pharmaceuticals

Novel Anti-proliferative Agents

Edited by
Valentina Onnis

mdpi.com/journal/pharmaceuticals

MDPI

Novel Anti-proliferative Agents

Novel Anti-proliferative Agents

Editor

Valentina Onnis

Editor
Valentina Onnis
University of Cagliari
Cagliari
Italy

This is a reprint of articles from the Special Issue published online in the open access journal *Pharmaceuticals* (ISSN 1424-8247) (available at: https://www.mdpi.com/journal/pharmaceuticals/special_issues/Antiproliferative_Agents).

For citation purposes, cite each article independently as indicated on the article page online and as indicated below:

Lastname, A.A.; Lastname, B.B. Article Title. *Journal Name* **Year**, *Volume Number*, Page Range.

Contents

Editorial

Special Issue "Novel Anti-Proliferative Agents"

Valentina Onnis

Department of Life and Environmental Sciences, University of Cagliari, 09042 Monserrato, CA, Italy; vonnis@unica.it

Cancer is a disease that can affect any organ and spread to other nearby or distant organs. Cancer is the second most frequent cause of morbidity and mortality in industrialized countries. The American Cancer Society estimates that 1,958,310 new cancer cases and 609,820 cancer deaths will occur in the United States in 2023 [1]. For the same year, 1,261,990 cancer deaths were predicted in EU-27 countries [2]. The availability of anticancer drugs based on the study of oncogenes and tumor suppressors which are involved in the emergence of human cancers has reduced the death rate and increased both the quality of life and life expectancy of tumor patients [3–6]. However, the failure of cancer therapies is still an urgent challenge due to reactions to existing treatments and multidrug chemoresistance [7–9].

In this Special Issue, different studies were reported relating to kinase inhibitors. Among antitumoral drugs, small molecule inhibitors of epidermal growth factor receptors (EGFR), including Erlotinib and its analogs [10], as well as monoclonal antibodies (e.g., cetuximab, necitumumab), are used in the therapy of non-small-cell lung cancer (NSCLC), breast, colon, pancreatic and thyroid cancer. Recently, studies have identified gene mutations targeting the kinase domain of the EGFR that are related to the response to inhibitors. Most EGFR mutations predict a higher benefit from treatment compared with wild-type receptors and are correlated with clinical features related to better outcomes; some EGFR mutations, however, confer drug resistance [11]. In this Special Issue, Youssif and co-workers described thiazole [12], purine/pteridine [13] and quinolone derivatives [14], dual EGFR/BRAFV600E inhibitors, as potential drugs in resistant NSCLC, in which BRAF mutation can cause resistance, even through EGFR stimulation. The same authors also described indole derivatives [15] as inducing apoptosis by EGFR and CDK2 dual inhibition. In NSCLC, both EGFR and its mutations, L858R/T790M, are overexpressed. New idantoine derivatives have been reported by Beshr and collaborators as potent inhibitors of these kinases [16].

In this Special Issue, two studies were dedicated to altering the tumor microenvironment [17,18] as a target for antiproliferative drugs. Death-associated protein kinase 1 (DAPK-1) is a positive mediator of gamma interferon-induced programmed cell death, and the loss- and gain-of-function of DAPK1 is associated with various cancer and neurodegenerative diseases, respectively [19]. Roh and collaborators reported on the anti-proliferative activity of aryl carboxamide derivatives acting as DAPK-1 inhibitors [20]. The c-Myc oncogene is a master regulator that has a very important role in regulating the transformed phenotype. The effects induced by c-Myc can occur either as a primary oncogene, which is activated by amplification or translocation, or as a downstream effect of other activated oncogenes. c-Myc is expressed in multiple types of cancer, comprising head and neck squamous cell carcinoma where it plays a fundamental role in tumor prognosis [21]. Diomede and collaborators underlined the functional relevance of c-Myc and HIF-Myc on oral squamous cell carcinoma (OSCC). In particular, their results indicated that c-Myc, c-Jun, Bcl-2, hypoxia inducible factor-1α (HIF-1α), vascular endothelial growth factor, matrix metalloproteinase-9, ERK 1/2 and pERK1/2 were overexpressed in OSCC [22]. In tumor cells, HIF-1α is activated by a deficient oxygen supply. HIF-1α activates the Carbonic Anhydrase (CA) IX and XII genes, leading to an improved resistance from tumoral cells to the

acidic extracellular environment [23]. Shchekotikhin and collaborators described indoline-5-sulfonamide derivatives as CAIX and CAXII inhibitors exhibiting hypoxic selectivity, suppressing the growth of MCF7 cells and causing partial inhibition of hypoxia-induced CA IX expression in A431 skin cancer cells [24].

Another approach to contrast tumoral cell proliferation is acting in the mitotic stage of the cell cycle with microtubule binding agents [25] and telomerase inhibitors [26]. In this Special Issue, Viola and collaborators described 2-anilino-triazolopyrimidines as tubuluin polymerization inhibitors [27], Pérez-Pérez and collaborators reported salicylamides as affecting tubulin polymerization and/or STAT3 phosphorylation [28], Shakeel and collaborators studied pyrazole hybrid chalcones that arrested the cell cycle, induced apoptosis in a dose-dependent manner and inhibited the polymerization of tubulin [29], and El-Hamamsy and collaborators reported on selective non-nucleoside potent telomerase inhibitor BIBR1532 derivatives that were demonstrated to inhibit telomerase inside living cancer cells [30].

The methyltransferase-like proteins 3 (METTL3) and 14 (METTL14) in cancers have been shown to be closely associated with the proliferation, apoptosis, metastasis and differentiation processes in the progression of various human cancers [31,32]. In this Special Issue, Kim and collaborators reported on Eltrombopag. This compound exhibited selective inhibitory activity in the most active catalytic form of the METTL3–14 complex, interacting at a putative allosteric binding site in METTL3 [33].

The Wnt/β-catenin pathway has been identified as one of the most important oncogenic signaling pathways related to immune evasion [34,35]. In this Special Issue, Kadletz-Wanke and collaborators reported that the inhibitor of the CBP/Beta-Catenin interaction ICG-001 produces cytotoxic and anti-migratory effects on human papillomavirus-positive head and neck squamous cell carcinoma [36].

In this Special Issue, the antiproliferative or cytotoxic activity of various small synthetic, natural-derived molecules and their hybrids was discussed. Kim and collaborators reported on phenylisoquinoline derivatives endowed with antiproliferative activity against MDA-MB-231, HeLa and HepG2 cancer cell lines [37]. Ammazzalorso and collaborators described the antiproliferative activity of benzothiazole derivatives on AsPC-1, Capan-2 and BxPC-3 pancreatic cancer cell lines [38]. Tuyun and collaborators reported that plastoquinone derivatives exerted notable cytotoxicity toward colon cancer HCT-116 and breast MCF-7 cells compared to cisplatin [39]. Abdala-Díaz and collaborators reported that ulvan polysaccharides obtained from *Ulva rigida* demonstrated antiproliferative activity on the HCT-116 tumor cell line [40]. Lokeshwar and collaborators demonstrated that the conjugation of the poor bioavailable antiproliferative compounds Curcumin and dichloroacetate by aminoacidic linkers improves bioavailability and reduced the growth of several breast cancer cell lines and tumor growth and metastasis on transgenic mouse breast cancer (BC) and metastatic BC tumor-bearing mice without showing signs of toxicity [41].

Curcumine and other naturally occurring agents have been proposed as cancer chemopreventive agents and were proposed for treating human malignancy [42,43]. Natural products have played an important role in chemotherapy and chemoprevention by providing antitumor drugs such as camptothecin, doxorubicin, paclitaxel, vinblastine and vincristine, as well as understanding the cellular and molecular mechanisms underlying antitumor activity. Natural products are a rich source of bioactive molecules endowed by a great variety of chemical scaffolds. Natural compounds are often used in traditional medicine and used to build semisynthetic molecules with improved biological properties [44–46]. In this context, Shuvalov and collaborators reviewed the information about plants and mushrooms, as well as their active compounds with antitumor properties. Plants and mushrooms were divided based on the regions where they are used in ethnomedicine to treat malignancies [47].

In conclusion, this Special Issue presented recent findings on antiproliferative compounds and highlighted possible routes to discover new drugs against cancer. I hope that this Special Issue can be of inspiration to readers working in cancer research and

stimulate the distinct fields involved in the continuous search for novel strategies for anticancer therapy. Finally, I would like to thank all of the authors and reviewers for their valuable contributions.

Conflicts of Interest: The author declares no conflict of interest.

References

1. Siegel, R.L.; Miller, K.D.; Wagle, N.S.; Jemal, A. Cancer statistics, 2023. *CA Cancer J Clin.* **2022**, *73*, 17–48. [CrossRef] [PubMed]
2. Malvezzi, M.; Santucci, C.; Boffetta, P.; Collatuzzo, G.; Levi, F.; La Vecchia, C.; Negri, E. European cancer mortality predictions for the year 2023 with focus on lung cancer. *Ann. Oncol.* **2023**, *34*, 410–419. [CrossRef] [PubMed]
3. Zhong, L.; Li, Y.; Xiong, L.; Wang, W.; Wu, M.; Yuan, T.; Yang, W.; Tian, C.; Miao, Z.; Wang, T.; et al. Small Molecules in Targeted Cancer Therapy: Advances, Challenges, and Future Perspectives. *Signal. Transduct. Target. Ther.* **2021**, *6*, 201. [CrossRef]
4. Botta, L.; Dal Maso, L.; Guzzinati, S.; Panato, C.; Gatta, G.; Trama, A.; Massimo Rugge, M.; Tagliabue, G.; Casella, C.; Caruso, B.; et al. Changes in life expectancy for cancer patients over time since diagnosis. *J. Adv. Res.* **2019**, *20*, 153–159. [CrossRef]
5. Capocaccia, R.; Gatta, G.; Dal Maso, L. Life expectancy of colon, breast, and testicular cancer patients: An analysis of US-SEER population-based data. *Ann. Oncol.* **2015**, *26*, 1263–1268. [CrossRef]
6. Yeh, J.M.; Ward, Z.J.; Chaudhry, A.; Liu, Q.; Yasui, Y.; Armstrong, G.T.; Gibson, T.M.; Howell, R.; Hudson, M.M.; Krull, K.R.; et al. Life Expectancy of Adult Survivors of Childhood Cancer Over 3 Decades. *JAMA Oncol.* **2020**, *6*, 350–357. [CrossRef] [PubMed]
7. Emran, T.B.; Shahriar, A.; Mahmud, A.R.; Rahman, T.; Abir, M.H.; Siddiquee, M.F.; Ahmed, H.; Rahman, N.; Nainu, F.; Wahyudin, E.; et al. Multidrug Resistance in Cancer: Understanding Molecular Mechanisms, Immunoprevention and Therapeutic Approaches. *Front. Oncol.* **2022**, *12*, 891652. [CrossRef]
8. Bukowski, K.; Kciuk, M.; Kontek, R. Mechanisms of Multidrug Resistance in Cancer Chemotherapy. *Int. J. Mol. Sci.* **2020**, *21*, 3233. [CrossRef]
9. Assaraf, Y.G.; Brozovic, A.; Gonçalves, A.C.; Jurkovicova, D.; Linē, A.; Machuqueiro, M.; Saponara, S.; Sarmento-Ribeiro, A.B.; Xavier, C.P.R.; Vasconcelos, M.H. The multi-factorial nature of clinical multidrug resistance in cancer. *Drug Resist. Updat.* **2019**, *46*, 100645. [CrossRef]
10. Abourehab, M.A.S.; Alqahtani, A.M.; Youssif, B.G.M.; Gouda, A.M. Globally Approved EGFR Inhibitors: Insights into Their Syntheses, Target Kinases, Biological Activities, Receptor Interactions, and Metabolism. *Molecules* **2021**, *26*, 6677. [CrossRef]
11. Shah, R.; Lester, J.F. Tyrosine Kinase Inhibitors for the Treatment of EGFR Mutation-Positive Non-Small-Cell Lung Cancer: A Clash of the Generations. *Clin. Lung Cancer* **2020**, *21*, e216–e228. [CrossRef] [PubMed]
12. Al-Wahaibi, L.H.; El-Sheref, E.M.; Hassan, A.A.; Bräse, S.; Nieger, M.; Youssif, B.G.M.; Ibrahim, M.A.A.; Tawfeek, H.N. Synthesis and Structure Determination of Substituted Thiazole Derivatives as EGFR/BRAFV600E Dual Inhibitors Endowed with Antiproliferative Activity. *Pharmaceuticals* **2023**, *16*, 1014. [CrossRef] [PubMed]
13. El-Kalyoubi, S.A.; Gomaa, H.A.M.; Abdelhafez, E.M.N.; Ramadan, M.; Agili, F.; Youssif, B.G.M. Design, Synthesis, and Anti-Proliferative Action of Purine/Pteridine-Based Derivatives as Dual Inhibitors of EGFR and BRAFV600E. *Pharmaceuticals* **2023**, *16*, 716. [CrossRef] [PubMed]
14. Al-Wahaibi, L.H.; El-Sheref, E.M.; Hammouda, M.M.; Youssif, B.G.M. One-Pot Synthesis of 1-Thia-4-azaspiro[4.4/5]alkan-3-ones via Schiff Base: Design, Synthesis, and Apoptotic Antiproliferative Properties of Dual EGFR/BRAFV600E Inhibitors. *Pharmaceuticals* **2023**, *16*, 467. [CrossRef]
15. Al-Wahaibi, L.H.; Mostafa, Y.A.; Abdelrahman, M.H.; El-Bahrawy, A.H.; Trembleau, L.; Youssif, B.G.M. Synthesis and Biological Evaluation of Indole-2-Carboxamides with Potent Apoptotic Antiproliferative Activity as EGFR/CDK2 Dual Inhibitors. *Pharmaceuticals* **2022**, *15*, 1006. [CrossRef]
16. Hassanin, M.A.; Mustafa, M.; Abourehab, M.A.S.; Hassan, H.A.; Aly, O.M.; Beshr, E.A.M. Design and Synthesis of New Hydantoin Acetanilide Derivatives as Anti-NSCLC Targeting EGFRL858R/T790M Mutations. *Pharmaceuticals* **2022**, *15*, 857. [CrossRef]
17. Hinshaw, D.C.; Shevde, L.A. The Tumor Microenvironment Innately Modulates Cancer Progression. *Cancer Res.* **2019**, *79*, 4557–4566. [CrossRef]
18. Wang, J.X.; Choi, S.Y.C.; Niu, X.; Kang, N.; Xue, H.; Killam, J.; Wang, Y. Lactic Acid and an Acidic Tumor Microenvironment suppress Anticancer Immunity. *Int. J. Mol. Sci.* **2020**, *21*, 8363. [CrossRef]
19. Singh, P.; Ravanan, P.; Talwar, P. Death Associated Protein Kinase 1 (DAPK1): A Regulator of Apoptosis and Autophagy. *Front. Mol. Neurosci.* **2016**, *9*, 46. [CrossRef]
20. Elkamhawy, A.; Paik, S.; Ali, E.M.H.; Hassan, A.H.E.; Kang, S.J.; Lee, K.; Roh, E.J. Identification of Novel Aryl Carboxamide Derivatives as Death-Associated Protein Kinase 1 (DAPK1) Inhibitors with Anti-Proliferative Activities: Design, Synthesis, In Vitro, and In Silico Biological Studies. *Pharmaceuticals* **2022**, *15*, 1050. [CrossRef]
21. Miller, D.M.; Thomas, S.D.; Islam, A.; Muench, D.; Sedoris, K. c-Myc and cancer metabolism. *Clin. Cancer Res.* **2012**, *18*, 5546–5553. [CrossRef] [PubMed]
22. Marconi, G.D.; Della Rocca, Y.; Fonticoli, L.; Melfi, F.; Rajan, T.S.; Carradori, S.; Pizzicannella, J.; Trubiani, O.; Diomede, F. C-Myc Expression in Oral Squamous Cell Carcinoma: Molecular Mechanisms in Cell Survival and Cancer Progression. *Pharmaceuticals* **2022**, *15*, 890. [CrossRef] [PubMed]

23. Angeli, A.; Carta, F.; Nocentini, A.; Winum, J.-Y.; Zalubovskis, R.; Akdemir, A.; Onnis, V.; Eldehna, W.M.; Capasso, C.; Simone, G.D.; et al. Carbonic Anhydrase Inhibitors Targeting Metabolism and Tumor Microenvironment. *Metabolites* **2020**, *10*, 412. [CrossRef] [PubMed]

24. Krymov, S.K.; Scherbakov, A.M.; Dezhenkova, L.G.; Salnikova, D.I.; Solov'eva, S.E.; Sorokin, D.V.; Vullo, D.; De Luca, V.; Capasso, C.; Supuran, C.T.; et al. Indoline-5-Sulfonamides: A Role of the Core in Inhibition of Cancer-Related Carbonic Anhydrases, Antiproliferative Activity and Circumventing of Multidrug Resistance. *Pharmaceuticals* **2022**, *15*, 1453. [CrossRef]

25. Dumontet, C.; Jordan, M.A. Microtubule-binding agents: A dynamic field of cancer therapeutics. *Nat. Rev. Drug Discov.* **2010**, *9*, 790–803. [CrossRef]

26. Andrews, L.G.; Tollefsbol, T.O. Methods of telomerase inhibition. *Methods Mol. Biol.* **2007**, *405*, 1–8. [CrossRef] [PubMed]

27. Romagnoli, R.; Oliva, P.; Prencipe, F.; Manfredini, S.; Budassi, F.; Brancale, A.; Ferla, S.; Hamel, E.; Corallo, D.; Aveic, S.; et al. Design, Synthesis and Biological Investigation of 2-Anilino Triazolopyrimidines as Tubulin Polymerization Inhibitors with Anticancer Activities. *Pharmaceuticals* **2022**, *15*, 1031. [CrossRef]

28. Gargantilla, M.; Persoons, L.; Kauerová, T.; del Río, N.; Daelemans, D.; Priego, E.-M.; Kollar, P.; Pérez-Pérez, M.-J. Hybridization Approach to Identify Salicylanilides as Inhibitors of Tubulin Polymerization and Signal Transducers and Activators of Transcription 3 (STAT3). *Pharmaceuticals* **2022**, *15*, 835. [CrossRef]

29. Alam, M.J.; Alam, O.; Perwez, A.; Rizvi, M.A.; Naim, M.J.; Naidu, V.G.M.; Imran, M.; Ghoneim, M.M.; Alshehri, S.; Shakeel, F. Design, Synthesis, Molecular Docking, and Biological Evaluation of Pyrazole Hybrid Chalcone Conjugates as Potential Anticancer Agents and Tubulin Polymerization Inhibitors. *Pharmaceuticals* **2022**, *15*, 280. [CrossRef]

30. Tawfik, H.O.; El-Hamaky, A.A.; El-Bastawissy, E.A.; Shcherbakov, K.A.; Veselovsky, A.V.; Gladilina, Y.A.; Zhdanov, D.D.; El-Hamamsy, M.H. New Genetic Bomb Trigger: Design, Synthesis, Molecular Dynamics Simulation, and Biological Evaluation of Novel BIBR1532-Related Analogs Targeting Telomerase against Non-Small Cell Lung Cancer. *Pharmaceuticals* **2022**, *15*, 481. [CrossRef]

31. Fiorentino, F.; Menna, M.; Rotili, D.; Valente, S.; Mai, A. METTL3 from Target Validation to the First Small-Molecule Inhibitors: A Medicinal Chemistry Journey. *J. Med. Chem.* **2023**, *66*, 1654–1677. [CrossRef] [PubMed]

32. Li, X.; Ma, S.; Deng, Y.; Yi, P.; Yu, J. Targeting the RNA m6A modification for cancer immunotherapy. *Mol. Cancer* **2022**, *21*, 76. [CrossRef] [PubMed]

33. Lee, J.-H.; Choi, N.; Kim, S.; Jin, M.S.; Shen, H.; Kim, Y.-C. Eltrombopag as an Allosteric Inhibitor of the METTL3-14 Complex Affecting the m6A Methylation of RNA in Acute Myeloid Leukemia Cells. *Pharmaceuticals* **2022**, *15*, 440. [CrossRef] [PubMed]

34. Fu, C.; Liang, X.; Cui, W.; Ober-Blobaum, J.L.; Vazzana, J.; Shrikant, P.A.; Lee, K.P.; Clausen, B.E.; Mellman, I.; Jiang, A. Beta-catenin in dendritic cells exerts opposite functions in cross-priming and maintenance of CD8+ T cells through regulation of IL-10. *Proc. Natl. Acad. Sci. USA* **2015**, *112*, 2823–2828. [CrossRef] [PubMed]

35. Spranger, S.; Gajewski, T.F. A new paradigm for tumor immune escape: Beta-catenin-driven immune exclusion. *J. Immunother. Cancer* **2015**, *3*, 43. [CrossRef] [PubMed]

36. Brkic, F.F.; Stoiber, S.; Maier, T.; Gurnhofer, E.; Kenner, L.; Heiduschka, G.; Kadletz-Wanke, L. Targeting Wnt/Beta-Catenin Signaling in HPV-Positive Head and Neck Squamous Cell Carcinoma. *Pharmaceuticals* **2022**, *15*, 378. [CrossRef]

37. Choi, O.K.; Sun, Y.H.; Lee, H.; Lee, J.K.; Lee, T.H.; Kim, H. Synthesis of Novel (S)-3-(1-Aminoethyl)-8-pyrimidinyl-2-phenylisoquinolin-1(2H)-ones by Suzuki–Miyaura Coupling and Their Cell Toxicity Activities. *Pharmaceuticals* **2022**, *15*, 64. [CrossRef]

38. Amoroso, R.; De Lellis, L.; Florio, R.; Moreno, N.; Agamennone, M.; De Filippis, B.; Giampietro, L.; Maccallini, C.; Fernández, I.; Recio, R.; et al. Benzothiazole Derivatives Endowed with Antiproliferative Activity in Paraganglioma and Pancreatic Cancer Cells: Structure–Activity Relationship Studies and Target Prediction Analysis. *Pharmaceuticals* **2022**, *15*, 937. [CrossRef]

39. Ciftci, H.; Sever, B.; Bayrak, N.; Yıldız, M.; Yıldırım, H.; Tateishi, H.; Otsuka, M.; Fujita, M.; Tuyun, A.F. In Vitro Cytotoxicity Evaluation of Plastoquinone Analogues against Colorectal and Breast Cancers along with In Silico Insights. *Pharmaceuticals* **2022**, *15*, 1266. [CrossRef]

40. García-Márquez, J.; Moreira, B.R.; Valverde-Guillén, P.; Latorre-Redoli, S.; Caneda-Santiago, C.T.; Acién, G.; Martínez-Manzanares, E.; Marí-Beffa, M.; Abdala-Díaz, R.T. In Vitro and In Vivo Effects of Ulvan Polysaccharides from Ulva rigida. *Pharmaceuticals* **2023**, *16*, 660. [CrossRef]

41. Panda, S.S.; Tran, Q.L.; Rajpurohit, P.; Pillai, G.G.; Thomas, S.J.; Bridges, A.E.; Capito, J.E.; Thangaraju, M.; Lokeshwar, B.L. Design, Synthesis, and Molecular Docking Studies of Curcumin Hybrid Conjugates as Potential Therapeutics for Breast Cancer. *Pharmaceuticals* **2022**, *15*, 451. [CrossRef] [PubMed]

42. Wang, J.; Jiang, Y.F. Natural compounds as anticancer agents: Experimental evidence. *World J. Exp. Med.* **2012**, *2*, 45–57. [CrossRef] [PubMed]

43. Subramaniam, S.; Selvaduray, K.R.; Radhakrishnan, A.K. Bioactive Compounds: Natural Defense Against Cancer? *Biomolecules* **2019**, *9*, 758. [CrossRef]

44. Muk-Lan Lee, M.M.-L.; Chan, B.D.; Wong, W.-Y.; Leung, T.-W.; Qu, Z.; Huang, J.; Zhu, L.; Lee, C.-S.; Chen, S.; Tai, W.C.-S. Synthesis and Evaluation of Novel Anticancer Compounds Derived from the Natural Product Brevilin A. *ACS Omega* **2020**, *5*, 14586–14596. [CrossRef] [PubMed]

45. Ahmed, I.A.; Hafiz, S.; van Ginkel, S.; Pondugula, S.R.; Abdelhaffez, A.S.; Sayyed, H.G.; Mansour, M.M. Augmentation of Docetaxel-Induced Cytotoxicity in Human PC-3 Androgen-Independent Prostate Cancer Cells by Combination With Four Natural Apoptosis-Inducing Anticancer Compounds. *Nat. Prod. Commun.* **2023**, *18*, 5. [CrossRef]
46. Patel, P.; Patel, V.; Modi, A.; Kumar, S.; Shukla, Y.M. Phytofactories of anti-cancer compounds: A tissue culture perspective. *Beni-Suef Univ. J. Basic Appl. Sci.* **2022**, *11*, 43. [CrossRef]
47. Kirdeeva, Y.; Fedorova, O.; Daks, A.; Barlev, N.; Shuvalov, O. How Should the Worldwide Knowledge of Traditional Cancer Healing Be Integrated with Herbs and Mushrooms into Modern Molecular Pharmacology? *Pharmaceuticals* **2022**, *15*, 868. [CrossRef]

Article

Synthesis and Structure Determination of Substituted Thiazole Derivatives as EGFR/BRAF^{V600E} Dual Inhibitors Endowed with Antiproliferative Activity

Lamya H. Al-Wahaibi [1,*], Essmat M. El-Sheref [2], Alaa A. Hassan [2], S. Bräse [3,*], M. Nieger [4], Bahaa G. M. Youssif [5,*], Mahmoud A. A. Ibrahim [2,6] and Hendawy N. Tawfeek [2,7]

1   Department of Chemistry, College of Sciences, Princess Nourah Bint Abdulrahman University, Riyadh 11564, Saudi Arabia
2   Chemistry Department, Faculty of Science, Minia University, El Minia 61519, Egypt; essmat_elsheref@mu.edu.eg (E.M.E.-S.); alaahassan2001@mu.edu.eg (A.A.H.); m.ibrahim@compchem.net (M.A.A.I.); hendawy1976@yahoo.com (H.N.T.)
3   Institute of Biological and Chemical Systems, IBCS-FMS, Karlsruhe Institute of Technology, 76131 Karlsruhe, Germany
4   Department of Chemistry, University of Helsinki, P.O. Box 55 (A. I. Virtasen aukio 1), 00014 Helsinki, Finland; martin.nieger@helsinki.fi
5   Pharmaceutical Organic Chemistry Department, Faculty of Pharmacy, Assiut University, Assiut 71526, Egypt
6   School of Health Sciences, University of KwaZulu-Natal, Westville Campus, Durban 4000, South Africa
7   Unit of Occupational of Safety and Health, Administration Office of Minia University, El-Minia 61519, Egypt
*   Correspondence: lhalwahaibi@pnu.edu.sa (L.H.A.-W.); stefan.braese@kit.edu (S.B.); bgyoussif2@gmail.com (B.G.M.Y.)

Abstract: 2,3,4-trisubstituted thiazoles **3a–i**, having a methyl group in position four, were synthesized by the reaction of 1,4-disubstituted thiosemicarbazides with chloroacetone in ethyl acetate/Et₃N at room temperature or in ethanol under reflux. The structures of new compounds were determined using NMR spectroscopy, mass spectrometry, and elemental analyses. Moreover, the structure of compound **3a** was unambiguously confirmed with X-ray analysis. The cell viability assay of **3a–i** at 50 μM was greater than 87%, and none of the tested substances were cytotoxic. Compounds **3a–i** demonstrated good antiproliferative activity, with GI₅₀ values ranging from 37 to 86 nM against the four tested human cancer cell lines, compared to the reference erlotinib, which had a GI₅₀ value of 33 nM. The most potent derivatives were found to be compounds **3a**, **3c**, **3d**, and **3f**, with GI₅₀ values ranging from 37 nM to 54 nM. The EGFR-TK and BRAF^{V600E} inhibitory assays' results matched the antiproliferative assay's results, with the most potent derivatives, as antiproliferative agents, also being the most potent EGFR and BRAF^{V600E} inhibitors. The docking computations were employed to investigate the docking modes and scores of compounds **3a**, **3c**, **3d**, and **3f** toward BRAF^{V600E} and EGFR. Docking computations demonstrated the good affinity of compound **3f** against BRAF^{V600E} and EGFR, with values of −8.7 and −8.5 kcal/mol, respectively.

Keywords: thiazole; thiosemicarbazide; X-ray; viability; antiproliferative; molecular modeling

1. Introduction

Kinases control many essential cancer processes, including tumor growth, metastasis, neovascularization, and treatment resistance. Hence, the development of kinase inhibitors has become a top priority, with several of them receiving FDA approval for a variety of cancer purposes [1–5].

One approach for simultaneously inhibiting two or more targets is combination chemotherapy. However, two or more drugs' pharmacokinetic profiles and metabolic stabilities frequently differ. Furthermore, drug–drug interactions may occur during combination chemotherapy [6–8]. An alternative method for addressing these issues is to

use a single drug to suppress two or more targets [9–12]. This approach may even make patients' treatment easier. The FDA has approved many dual-target or multi-target cancer treatments. Dasatinib is a multi-targeted kinase inhibitor that can potentially be a highly effective anticancer medication [13–17].

The acquired BRAF^{V600E} mutation was suggested as a resistance mechanism after therapy with an EGFR inhibitor [18,19]. The development of resistance in colorectal cancer was also linked to the feedback stimulation of EGFR signaling [20–22]. Additionally, BRAF inhibition can cause EGFR to become active, promoting tumor growth [23,24]. A BRAF/EGFR combination was used to adopt these issues. In a number of studies, the BRAF/EGFR combination was found to have a significant therapeutic effect in patients with metastatic colorectal cancer that had BRAF^{V600E} mutations [18,25,26]. As a result, sequentially inhibiting the two kinases may provide a solution to the EGFR activation problem.

Thiazole and its derivatives are also among the most active chemicals, ranking first in anticancer activity [27–29]. As well, thiazole-containing molecules were identified in a number of therapeutically available anticancer medicines (Figure 1), including tiazofurin (**I**) [30], dasatinib (**II**) [31,32], and dabrafenib (**III**) [33,34].
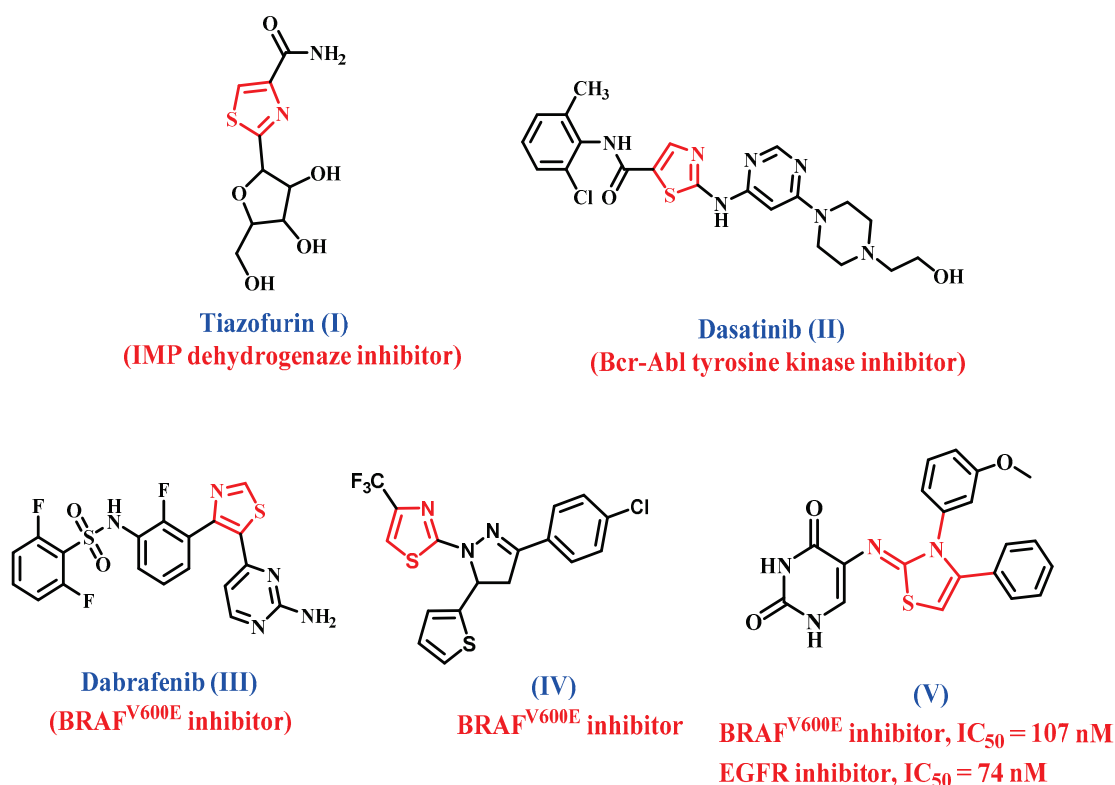
Figure 1. Structures of thiazole-based anticancer drugs **I**–**III** and compounds **IV** and **V**.

Abdel-Maksoud et al. [35] investigated several thiazole-based compounds as potential BRAF^{V600E} inhibitors. Compound **IV** (Figure 1) had the most potent antiproliferative activity, with a competitive BRAF^{V600E} inhibitory action (IC$_{50}$ = 0.05 μM). Furthermore, compound **IV** significantly affected dose-dependent apoptosis.

We recently reported on the design and synthesis of two series of thiazole-based compounds as potent antiproliferative agents targeting EGFR and BRAF^{V600E} [36]. Compound **V** (Figure 1) was shown to be the most potent derivative of all synthesized compounds, with a GI$_{50}$ value of 0.90 μM against the four evaluated cancer cell lines when compared to the reference doxorubicin (GI$_{50}$ = 1.10 μM). Compound **V** inhibited EGFR and BRAF^{V600E} with IC$_{50}$ values of 74 ± 7 and 107 ± 10 nM, respectively, and was more effective than erlotinib against EGFR (IC$_{50}$ = 80 nM).

Moreover, the sulfonamide moiety is commonly employed in medicinal chemistry as efficient bioisosteres of the carboxylic group [37,38]. The sulfonamide motif could build a network of hydrogen bonds similar to the carboxylic group. As the carboxylic group's bioisosteres, it could avoid some of the carboxylic group's limitations, such as metabolic instability, toxicity, and limited passive diffusion across biological membranes [37]. As a result, the sulfonamide moiety gained popularity in medicinal chemistry, and a wide range of sulfonamide derivatives with diverse biological properties, such as anticancer activity [39–41], were produced.

In light of the aforementioned information, and as part of our enduring effort to develop potent antiproliferative agents that are dual inhibitors of EGFR and BRAF^{V600E} [42–45], we describe the synthesis of a new set of thiazole-based compounds **3a–i** (Figure 2) in this article as antiproliferative agents that target EGFR and/or mutant BRAF. Scaffold A and B molecules had a methyl group in position 4, a hydrazo group in position 2, a physiologically active tosyl group for the scaffold B compounds, and a 2,4-dinitrophenyl group for the scaffold A compounds (Figure 2). The cell viability of the novel derivatives was tested against a normal human mammary gland epithelial (MCF-10A) cell line. The antiproliferative action of **3a–i** was tested on a panel of four human cancer cell lines. The ability to inhibit EGFR and mutant BRAF was further assessed for the most active antiproliferative derivatives. Finally, the most potent compounds' binding modes and docking scores toward BRAF^{V600E} and EGFR targets were investigated.

Scaffold A (3a-f)

3a, R = CH$_2$C$_6$H$_5$
3b, R = CH$_2$CH$_3$
3c, R = CH$_2$CH=CH$_2$
3d, R = C$_6$H$_{11}$
3e, R = C$_6$H$_5$
3f, R = 4-CH$_3$C$_6$H$_6$

Scaffold B (3g-i)

3g, R = C$_6$H$_5$
3h, R = CH$_2$CH=CH$_2$
3i, R = CH$_2$CH$_3$
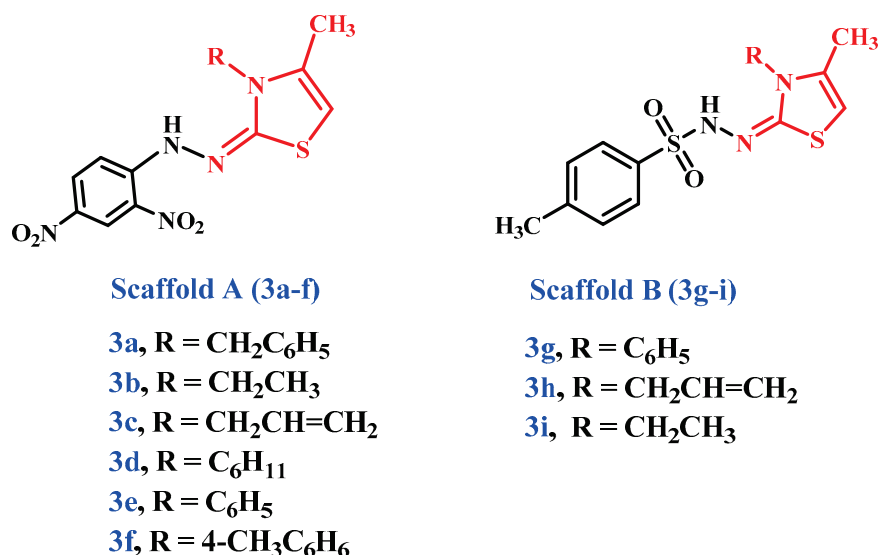
Figure 2. The new target compounds' **3a–i** structures.

2. Results and Discussion

2.1. Chemistry

This study aimed to develop new thiazole derivatives in a straightforward manner. Indeed, a novel series of *(Z)*-3-substituted-2-(2-substituted)-hydrazinylidene)-4-methyl-2,3-dihydrothiazoles **3a–i** were synthesized in an excellent yield of 78–99% via a mixture of substituted hydrazine-carbothioamides **1a–i** [46–49] and chloroacetone (**2**) in ethyl acetate as a solvent. Et$_3$N catalyzed the reaction by stirring overnight at room temperature or refluxing in ethanol for 6–10 hrs (Scheme 1). For example, compound **3a** was obtained in (AcOEt/Et$_3$N: 98%) and (EtOH: 85%) yield after recrystallization (Table 1). The structure assignment for all obtained products **3a–i** was confirmed by IR, NMR analysis (Supplementary File Figures S2–S32) of the expected chemical shifts, mass spectrometry, elemental analysis, and X-ray crystallography.

Scheme 1. Syntheses of substituted thiazoles **3a–i**.
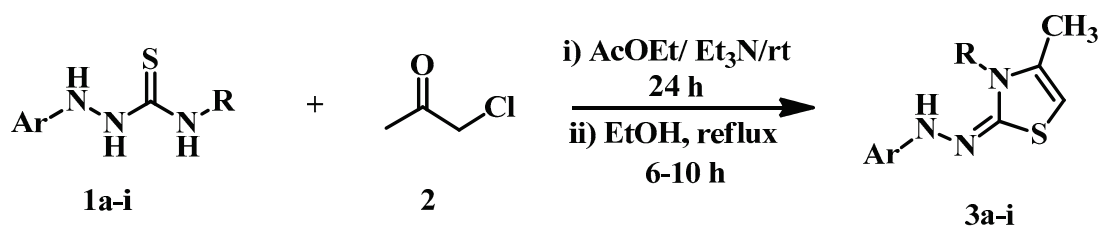
1,3: a, Ar = 2,4-di-NO_2-C_6H_3-, R = -$CH_2C_6H_5$ **g,** Ar = *p*-CH_3-$C_6H_4SO_2$-, R = -C_6H_5
b, Ar = 2,4-di-NO_2-C_6H_3-, R = -CH_2CH_3 **h,** Ar = *p*-CH_3-$C_6H_4SO_2$-, R = -$CH_2CH=CH_2$
c, Ar = 2,4-di-NO_2-C_6H_3-, R = -$CH_2CH=CH_2$ **i,** Ar = *p*-CH_3-$C_6H_4SO_2$-, R = -CH_2CH_3
d, Ar = 2,4-di-NO_2-C_6H_3-, R = -C_6H_{11}
e, Ar = 2,4-di-NO_2-C_6H_3-, R = -C_6H_5
f, Ar = 2,4-di-NO_2-C_6H_3-, R = 4-CH_3-C_6H_5-

Table 1. Yield percentage of **3a–i** via method **A** and method **B**.

Compound	3a	3b	3c	3d	3e	3f	3g	3h	3i
Method A	98	99	96	94	94	92	90	89	87
Method B	85	84	83	78	83	86	83	83	78

Compound **3a** was chosen as a representative example, which was assigned as (*Z*)-3-benzyl-2-(2-(2,4-dinitrophenyl)hydrazinylidene)-4-methyl-2,3-dihydrothiazole and exhibited a molecular formula $C_{17}H_{15}N_5O_4S$ with mass *m/z* (385). Elemental analysis and mass spectrometry confirmed that **3a** was formed by an interaction between one mole of *N*-benzyl-2-(2,4-dinitrophenyl)hydrazinecarbothioamide (**1a**) and one mole of chloroacetone (**2**), with the loss of a molecule of HCl and another molecule of H_2O. FTIR analysis of thiazole compound **3a** showed different peaks at 3286 cm^{-1} due to hydrazo-NH stretching, 3085 cm^{-1} for aromatic stretching-CH, and 2978 cm^{-1} for aliphatic-CH as well as two peaks at 1609 and 1548 cm^{-1} for C=N and C=C, respectively. IR showed a peak at 1399 and 1117 cm^{-1} for the NO_2 group. Further, in the ^{1}H NMR spectrum of **3a**, five singlet signals were distinguished at δ_H = 1.98, 5, 6.42, 8.68, and 10.38 ppm, which were assigned as CH_3, benzyl-CH_2, thiazole-H, 2,4-dinitrophenyl-H-3, and hydrazono-NH, respectively (Figure 3). The ^{13}C NMR spectrum for compound **3a** revealed signals at δ_C = 13.78, 47.16, and 94.49 ppm, which were assigned as CH_3, benzyl-CH_2, and thiazole-C5, respectively. Moreover, C4 and C2 gave signals at δ_C = 135.13 and 164.14 ppm, respectively.
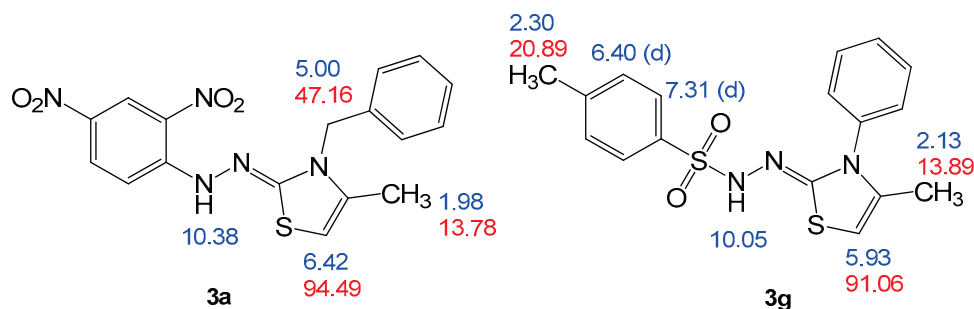
Figure 3. Structure elucidation of compounds **3a** and **3g**.

To make comparable results, we chose another compound, **3g**, which was assigned as (*Z*)-4-methyl-*N'*-(4-methyl-3-phenylthiazol-2(3*H*)-ylidene) benzenesulfonohydrazide, with a molecular formula $C_{17}H_{17}N_3O_2S_2$ (*m/z* = 359). Compound **3g** is analogous for

the above compound by replacing the benzyl group and 2,4-dinitrophenyl with phenyl and 4-methyl-benzensulfonoyl groups, respectively. The ^{1}H NMR for this compound is similar for compound **3a** unless the 1,4-disubstituted benzene gives characteristic signals as a doublet at δ_H = 6.40 (d, 2H) and 7.31 ppm (d, 2H), which were assigned as H-*m* and H-*o*, respectively. Moreover, by comparing the data for the two compounds, as shown in Figure 3, it is clear that the reaction behaves the same with the difference in the substitutes and that the difference is a slight difference in the chemical shift's results for the difference only in the nature of the substituted groups.

Another example is compound **3b,** which was assigned as (Z)-2-(2-(2,4-dinitrophenyl)-hydrazinylidene)-3-ethyl-4-methyl-2,3-dihydrothiazole and has the same spectral data as compound **3a** except that the benzyl group was replaced with ethyl, which gives two characteristic signals as triplet–quartet and appears in its ^{1}H NMR spectrum at δ_H = 1.28–1.38 (t, *J* = 3 Hz; 3H, ethyl-CH$_3$) and 3.88–3.98 ppm (q, *J* = 3 Hz; 2H, ethyl-CH$_3$) and was confirmed from its ^{13}C NMR spectrum, with two signals at δ_H = 12.98 (ethyl-CH$_3$) and 30.67 ppm (ethyl-CH$_2$).

Furthermore, the structures for the obtained products were confirmed via X-ray crystallography. Moreover, the X-ray measurements of compound **3b** showed that the molecule (except the C-atom of the ethyl substituent, C21) is virtual planar. The aromatic ring is coplanar with the thiazole ring, and the ethyl group has the hours conformation structure. The angle between the thiazole and the aromatic ring is 6.37(7)°, between the thiazole and the hydrazinylidene moiety is 2.98(14)°, and between the aromatic ring and the hydrazinylidene moiety is 6.56(9)° (angle between the L.S. planes of the moieties). In addition, the geometric structure around the exocyclic C=N has cissoid geometry concerning the thiazole *S*-atom and the hydrazo-group (Figure 4). The geometrical parameters (selected bond distance, bond angles, and dihedral angles; see Table 2) are in good correlation with the theoretical values.
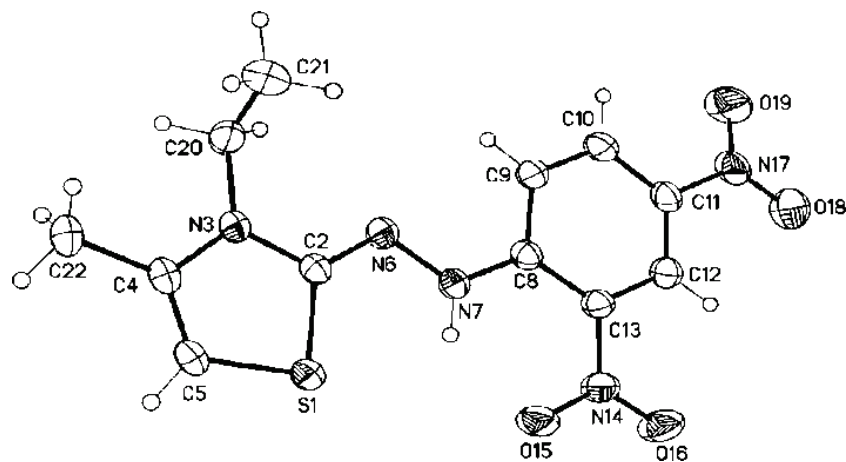
Figure 4. The crystal structure of *(Z)*-2-(2-(2,4-dinitrophenyl)hydrazinylidene)-3-ethyl-4-methyl-2,3-dihydrothiazole **3b**.

Table 2. Selected geometric parameters (Å, °) for **3b**.

S1—C5	1.742 (2)	N3—C4	1.394 (2)
S1—C2	1.7465 (19)	C4—C5	1.327 (3)
C2—N6	1.298 (2)	N6—N7	1.377 (2)
C2—N3	1.370 (2)	N7—C8	1.337 (2)
C5—S1—C2	90.45 (9)	N3—C4—C22	119.73 (19)
N6—C2—N3	121.44 (17)	C4—C5—S1	112.19 (14)

Table 2. *Cont.*

N6—C2—S1	128.53 (15)	C4—C5—H5	123.9
N3—C2—S1	110.03 (13)	S1—C5—H5	123.9
C2—N3—C4	113.80 (16)	C2—N6—N7	113.44 (16)
C2—N3—C20	120.49 (17)	C8—N7—N6	121.10 (17)
C4—N3—C20	125.43 (18)	C8—N7—H7	119.5
C5—C4—N3	113.50 (17)	N6—N7—H7	119.5
C5—C4—C22	126.76 (19)		
N3—C2—N6—N7	−179.55 (16)	N6—N7—C8—C9	1.6 (3)
S1—C2—N6—N7	0.1 (3)	N6—N7—C8—C13	−178.62 (16)
C2—N6—N7—C8	−174.03 (17)		

Based on the above results and the X-ray confirmation of our obtained products, the proposed mechanism is as follows. First, the nucleophilic attack of sulfur on the primary carbon atom results in the formation of the intermediate, **B** (S-alkylation), via the transition state, **A**. Another nucleophilic attack on the nitrogen atom on the carbonyl carbon gives the intermediate, **C**, followed by water molecule (dehydration) loss to give the target product. The reaction mechanism proceeds via the $S_N{}^2$ reaction type (Scheme 2).
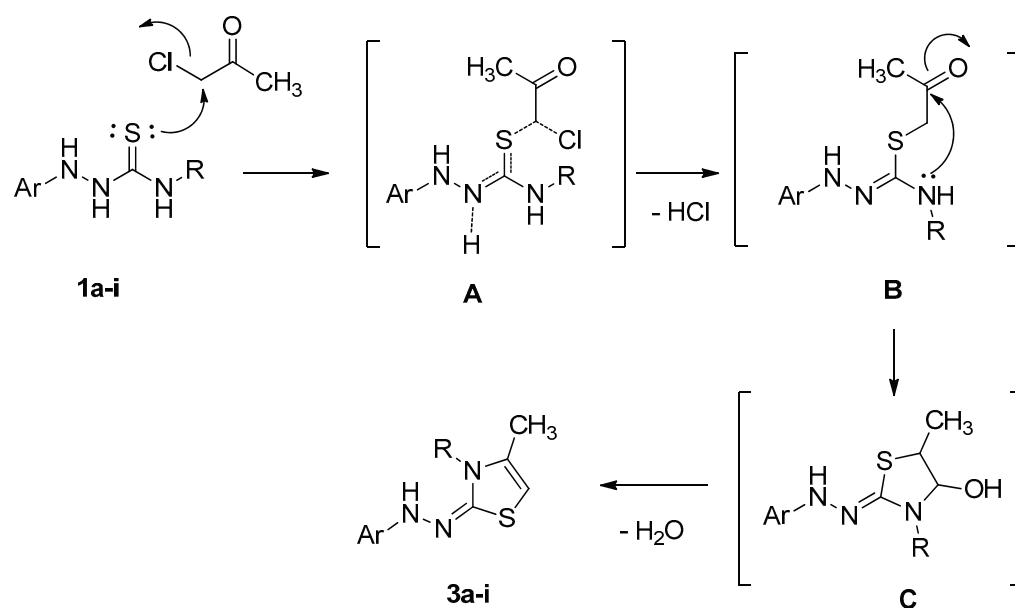
Scheme 2. The hypothesized mechanism for the synthesis of thiazole compounds **3a–i**.

2.2. Biology

2.2.1. Cell Viability Assay

The human mammary gland epithelial (MCF-10A) cell line was used to test the viability of the novel compounds [50,51]. After four days of incubation on MCF-10A cells, the vitality of compounds **3a–i** was determined using the MTT method. According to Table 3, the cell viability at 50 μM was greater than 87% for all tested agents, and none of the tested substances were cytotoxic.

Table 3. IC$_{50}$ values of compounds **3a–i** against four cancer cell lines.

Compound	Cell Viability %	Antiproliferative Activity IC$_{50}$ ± SEM (nM)				
		A-549	MCF-7	Panc-1	HT-29	Average
3a	89	45 ± 4	49 ± 4	48 ± 4	48 ± 4	48
3b	91	78 ± 7	82 ± 8	80 ± 8	80 ± 8	80
3c	90	50 ± 5	56 ± 5	54 ± 5	54 ± 5	54
3d	92	43 ± 4	47 ± 4	46 ± 4	46 ± 4	46
3e	87	71 ± 7	74 ± 7	72 ± 7	72 ± 7	72
3f	89	35 ± 3	40 ± 3	37 ± 3	37 ± 3	37
3g	90	58 ± 5	63 ± 6	60 ± 6	58 ± 5	60
3h	92	63 ± 6	68 ± 6	65 ± 6	65 ± 6	65
3i	95	84 ± 8	89 ± 8	86 ± 8	86 ± 8	86
Erlotinib	-	30 ± 3	40 ± 3	30 ± 3	30 ± 3	33

2.2.2. Antiproliferative Assay

The MTT assay was used to investigate the antiproliferative activity of **3a–i** against four human cancer cell lines: the colon cancer (HT-29) cell line, pancreatic cancer (Panc-1) cell line, lung cancer (A-549) cell line, and breast cancer (MCF-7) cell line, using erlotinib as the reference [52,53]. Table 3 shows the median inhibitory concentration (IC$_{50}$).

In general, the examined compounds **3a–i** displayed good antiproliferative activity, with average IC$_{50}$ (GI$_{50}$) values ranging from 37 to 86 nM against the four tested human cancer cell lines, compared to the reference erlotinib (GI$_{50}$ = 33 nM).

The most potent derivatives were compounds **3a**, **3c**, **3d**, and **3f**, with GI$_{50}$ values ranging from 37 nM to 54 nM. Compound **3f** (Ar = 2,4-di-NO$_2$-C$_6$H$_3$, R = 4-CH$_3$-C$_6$H$_5$) was the most potent derivative of all synthesized compounds, with a GI$_{50}$ value of 37 nM against the four tested human cancer cell lines, comparable to the reference erlotinib (GI$_{50}$ = 33 nM). By replacing the *p*-tolyl group in compound **3f** with a cyclohexyl moiety, compound **3d** (Ar = 2,4-di-NO$_2$-C$_6$H$_3$, R = C$_6$H$_{11}$) was found to be the second-most potent compound, with a GI$_{50}$ value of 46 nM, being 1.3-fold less potent than compound **3f**, demonstrating the importance of the *p*-tolyl moiety in antiproliferative activity.

The benzyl derivative, **3a** (Ar = 2,4-di-NO$_2$-C$_6$H$_3$, R = CH$_2$-C$_6$H$_5$), was less potent than **3f** and **3d**, with a GI$_{50}$ value of 48 nM against the tested four cancer cell lines, while the allyl derivatives, **3c** (Ar = 2,4-di-NO$_2$-C$_6$H$_3$, R = CH$_2$CH = CH$_2$), showed moderate antiproliferative activity, with a GI$_{50}$ value more than 50 nM. These findings show that allyl and benzyl groups are not preferred for the antiproliferative activity of scaffold A compounds **3a–f**.

The remaining scaffold A compounds, **3b** (Ar = 2,4-di-NO$_2$-C$_6$H$_3$, R = CH$_2$CH$_3$) and **3e** (Ar = 2,4-di-NO$_2$-C$_6$H$_3$, R = C$_6$H$_5$), had GI$_{50}$ values of 80 nM and 72 nM, respectively. Compounds **3b** and **3e** were 2.2- and 2-fold less potent than **3f**, respectively, indicating weak antiproliferative activity (Table 3).

With GI$_{50}$ values of 60 nM, 65 nM, and 86 nM, scaffold B compounds **3g**, **3h**, and **3i** demonstrated moderate-to-weak antiproliferative activity. Compound **3i** (Ar = *p*-CH$_3$-C$_6$H$_4$-SO$_2$, R = CH$_2$CH$_3$) was the least potent derivative of any of the synthesized compounds, with a GI$_{50}$ value of 86 nM, which is less potent than its congeners, **3b** (scaffold A), which has the same structure, but the aryl moiety was *p*-CH$_3$-C$_6$H$_4$-SO$_2$, while in **3b** it was 2,4-di-NO$_2$-C$_6$H$_3$. These findings demonstrated that 2,4-di-NO$_2$-C$_6$H$_3$ significantly affects the antiproliferative action of the newly synthesized compounds.

2.2.3. Assay for EGFR Inhibition

The most promising antiproliferative compounds, **3a**, **3c**, **3d**, and **3f**, were further evaluated for their suppressive impact on EGFR as a probable target for their mechanism of action [50,54,55]. Table 4 compares the IC_{50} values to erlotinib, which worked as a control.

Table 4. IC_{50} of compounds **3a**, **3c**, **3d**, and **3f** against EGFR and BRAF^{V600E}.

Compound	EGFR Inhibition $IC_{50} \pm SEM$ (nM)	BRAF^{V600E} Inhibition $IC_{50} \pm SEM$ (nM)
3a	93 ± 8	117 ± 10
3c	98 ± 9	126 ± 11
3d	91 ± 7	112 ± 10
3f	89 ± 7	93 ± 8
Erlotinib	80 ± 5	60 ± 5

The EGFR-TK inhibitory assay results matched the antiproliferative assay results, with the most potent derivatives, as antiproliferative agents, also being the most potent EGFR inhibitors. Compounds **3a**, **3c**, **3d**, and **3f** inhibited EGFR, with IC_{50} values ranging from 89 to 98 nM, but the tested compounds were less potent than erlotinib (IC_{50} = 80 nM). The most potent antiproliferative agent, compound **3f** (Ar = 2,4-di-NO_2-C_6H_3, R = 4-CH_3-C_6H_5), was also the most potent EGFR inhibitor, with an IC_{50} value of 89 ± 7, being 1.1-fold less potent than standard erlotinib.

Compounds **3a** (Ar = 2,4-di-NO_2-C_6H_3, R = CH_2-C_6H_5) and **3d** (Ar = 2,4-di-NO_2-C_6H_3, R = C_6H_{11}) ranked third and second in EGFR suppression, with IC_{50} values of 93 ± 8 and 91 ± 7 nM, respectively, being 1.15-fold less potent than erlotinib (IC_{50} = 80 ± 5 nM). These findings suggest that EGFR-TK could be a molecular target for the tested compound's antiproliferative action.

2.2.4. BRAF^{V600E} Inhibitory Assay

Derivatives **3a**, **3c**, **3d**, and **3f** were further investigated as possible BRAF^{V600E} inhibitors [56]. Table 4 displays the IC_{50} values compared to erlotinib, which was used as a control. According to Table 4, the evaluated derivatives had a promising BRAF^{V600E} suppressive action, with IC_{50} values ranging from 93 to 126 nM, making them approximately 1.5-fold less effective than erlotinib (IC_{50} = 60 nM). Compound **3f**, the most potent derivative in the antiproliferative and EGFR suppressive assays, was also the most effective derivative as anti-BRAF^{V600E} (IC_{50} = 93 ± 8 nM). These findings show that compound **3a** has potent antiproliferative activity as a dual EGFR/BRAF^{V600E} inhibitor, implying that further structural modifications may be required to obtain a more potent lead compound for future development.

2.3. In Silico Study

AutoDock4.2.6 software was used to investigate the binding scores and poses of compounds **3a**, **3c**, **3d**, and **3f** against BRAF^{V600E} and EGFR. The estimated docking features and scores are listed in Table 5. As tabulated in Table 5, all inspected compounds revealed good docking scores against BRAF^{V600E} and EGFR targets, ranging from −7.8 to −8.7 kcal/mol and from −7.9 to −8.5 kcal/mol, respectively. The good docking scores of the inspected compounds toward BRAF^{V600E} and EGFR may be imputed to their capability of forming H-bonds and vdW, pi-based, and hydrophobic interactions with the proximal residues within the active sites of the investigated targets (Table 5).

Table 5. Predicted binding features and docking scores for the top investigated compounds toward EGFR and BRAF[V600E].

Compound	EGFR		BRAF[V600E]	
	Docking Scores (kcal/mol)	Binding Features	Docking Scores (kcal/mol)	Binding Features [a]
3a	−8.0	CYS773 (2.21 Å)	−8.4	LYS483 (2.15 Å), THR529 (2.38 Å), ASP594 (2.12 Å)
3c	−7.9	CYS773 (2.15 Å)	−7.8	LYS483 (2.13 Å) ASP594 (1.93 Å)
3d	−8.1	CYS773 (2.17 Å)	−8.5	LYS483 (1.93 Å), GLY596 (2.32 Å), THR529 (2.66 Å), ASP594 (2.14 Å)
3f	−8.5	CYS773 (2.18 Å)	−8.7	LYS483 (2.15 Å), THR529 (2.38 Å), ASP594 (2.12 Å)
Erlotinib	−8.6	MET769 (1.62 Å), CYS773 (1.91 Å)	−8.4	THR529 (2.07), CYS532 (2.02)

[a] Only hydrogen bonds are presented in Å.

Compound **3f** demonstrated superior docking scores of −8.7 and −8.5 kcal/mol against BRAF[V600E] and EGFR, respectively. Inspecting the docking mode of compound **3f** with the EGFR active site unveiled that this compound formed one H-bond with CYS773 (2.18 Å). Moreover, compound **3f** exhibited two carbon–hydrogen bonds with LEU768 and pi–anion interaction with ASP831. On the other hand, compound **3f**, complexed with BRAF[V600E], demonstrated three H-bonds with LYS483 (2.15 Å), THR529 (2.38 Å), and ASP594 (2.12 Å). Additionally, compound **3f** established pi–cation interaction with LYS483 and pi–pi stacking interaction with PHE583 and TRP531 residues (Figure 5).

(a)

(b)
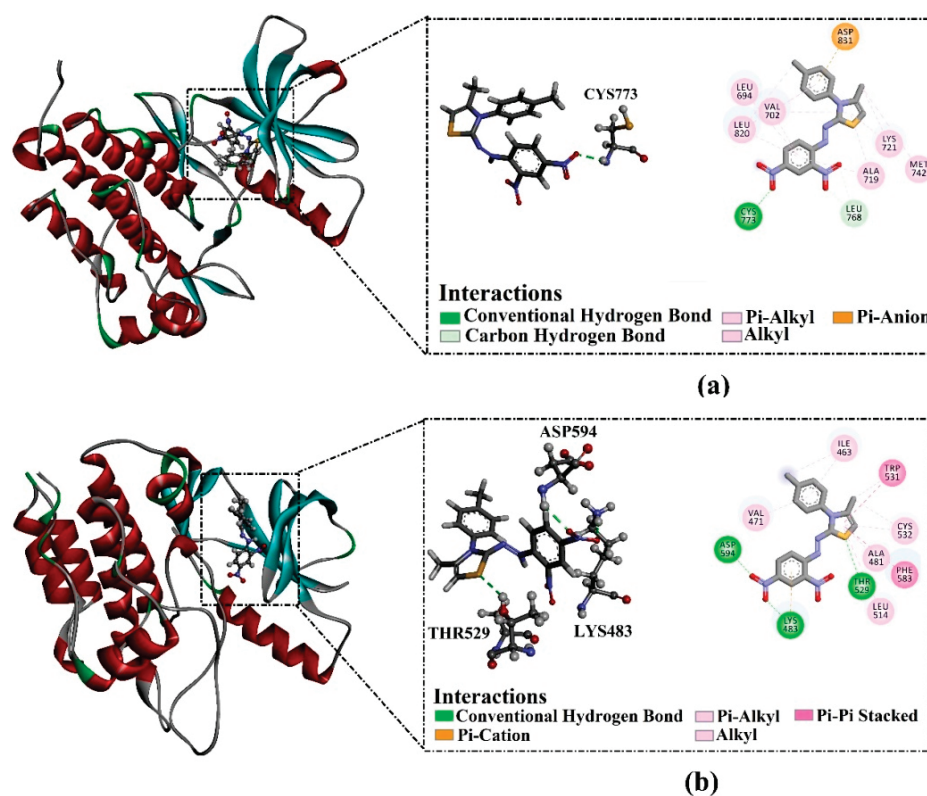
Figure 5. Molecular interactions of compound **3f** within (**a**) EGFR and (**b**) BRAF[V600E] active sites.

Compound **3d** showed the second-lowest docking score, with values of −8.5 and −8.1 kcal/mol against BRAF^{V600E} and EGFR, respectively. Compound **3d** displayed one hydrogen bond with the CYS773 (2.17 Å) within the active site of EGFR. However, compound **3d** demonstrated four H-bonds with the LYS483 (1.93Å), GLY596 (2.32 Å), THR529 (2.66 Å), and ASP594 (2.14 Å) of BRAF^{V600E}.

Compound **3a** exposed the third-lowest docking score, with values of −8.4 and −8.0 kcal/mol against BRAF^{V600E} and EGFR, respectively (Table 5). Compound **3a** made one H-bond with **the** CYS773 (2.21 Å) of EGFR, while compound **3a** exhibited three H-bonds with the LYS483 (2.15 Å), THR529 (2.38 Å), and ASP594 (2.12 Å) within the BRAF^{V600E} binding pocket.

Compound **3c** also unveiled good docking scores, with values of −7.8 and −7.9 kcal/mol against BRAF^{V600E} and EGFR, respectively (Table 5). Observably, compound **3c** established one H-bond with the CYS773 (2.15 Å) of EGFR and two H-bonds with the LYS483 (2.13 Å) and ASP593 (1.93 Å) of BRAF^{V600E}.

Erlotinib, a reference drug, showed docking scores of −8.4 and −8.6 kcal/mol toward BRAFV^{600E} and EGFR, respectively (Table 5). From Table 5, erlotinib demonstrated two H-bonds with the CYS773 (1.91 Å) and MET769 (1.62 Å) within the EGFR binding pocket. In addition, erlotinib also displayed two H-bonds with CYS532 (2.02 Å) and THR529 (2.07 Å).

3. Material and Methods

3.1. Chemistry

General information: refer to Supplementary Information.

The starting materials, **1a–i**, were synthesized in accordance with the documented methods [46–48]

3.1.1. General Procedure of Synthesis of Trisubstituted Thiazoles **3a–i**

Method A

In a conical flask containing 10 mL ethyl acetate and two drops of Et$_3$N as a catalyst, 0.092 gm of chloroacetone were dissolved (**2**). To this mixture, 1 mmol of thiosemicarbazides **1a–i** in 10 mL ethyl acetate was added drop by drop while stirring. After addition was complete, the reaction mixture was stirred for 24 h. The reaction mixture was monitored with TLC. After the reaction was completed, the formed precipitate was filtered off and recrystallized from ethanol to afford products **3a–i** as fine crystals.

Method B

In a 50 mL round-bottom flask containing 20 mL absolute ethanol, a molar ratio (1:1) mixture of chloroacetone and substituted thiosemicarbazides **1a–i** was added. The flask was fitted with a condenser and was refluxed for 6–10 h. The reaction was monitored with TLC to assure the reaction completion. Then, the reaction mixture was cooled to room temperature, and the formed precipitate was filtered off and recrystallized from ethanol to afford products **3a–i**.

(Z)-3-Benzyl-2-(2-(2,4-Dinitrophenyl)Hydrazineylidene)-4-Methyl-2,3-Dihydrothiazole (**3a**)

This compound was found as red crystals from methanol in (98% and 85%) yield, with m.p., 215–217 °C; ^{1}H NMR (DMSO-d_6): δ 1.98 (s, 3H, CH$_3$), 5.00 (s, 2H, benzyl-CH$_2$), 6.42 (s, 1H, H-5), 7.10–8.28 (m, 6H, Ar-H), 7.96–8.01 (d, 1H, Ar-H), 8.68 (s, 1H, Ar-H), 10.38 (s, 1H, NH) ppm; ^{13}C NMR (DMSO-d_6): δ 13.7 (CH$_3$), 47.1 (benzyl-CH$_2$), 94.5 (C5), 115.5, 123.4, 126.6, 127.4, 127.7, 128.7 (Ar-CH), 129.5, 136.7, 136.7, 144.3 (Ar-C), 135.1 (C4), 164.1 (C2) ppm; IR: ν = 3286 (NH),3085 (Ar-CH), 2978 (ali-CH), 1609 (C=N), 1548 (Ar-C=C), 1399, 1117 (NO$_2$) cm^{-1}; MS (70 eV): *m/z* (%) = 385 (M$^+$, 30). *Anal. Calcd. For* C$_{17}$H$_{15}$N$_5$O$_4$S (385.40): C, 52.98; H, 3.92; N, 18.17; S, 8.32. Found: C, 52.89; H, 3.81; N, 18.06; S, 8.23.

(Z)-2-(2-(2,4-Dinitrophenyl)Hydrazineylidene)-3-Ethyl-4-Methyl-2,3-Dihydrothiazole (3b)

This compound was found as red crystals from methanol in (99% and 84%) yield, with m.p., 176–177 °C; ^{1}H NMR (DMSO-d_6): δ 1.28–1.38 (t, 3H, $J = 3$, CH$_3$), 2.1 (s, 3H, CH$_3$), 3.88–3.98 (q, 2H, $J = 3$, CH$_2$), 6.14 (s, 1H, H-5), 7.48–7.54 (d, 1H, Ar-H), 8.22–8.28 (d, 1H, Ar-H), 8.82 (s, 1H, Ar-H), 10.46 (s, 1H, NH) ppm; ^{13}C NMR (DMSO-d_6): δ 12.9 (ethyl-CH$_3$), 13.4 (CH$_3$), 30.6 (ethyl-CH$_2$), 94.0 (C5), 115.5, 123.4, 127.6 (Ar-CH), 129.7, 136.8, 144.3 (Ar-C), 135.0 (C4), 163.6 (C2) ppm. IR: ν = 3115 (NH), 3078 (Ar-CH), 2988 (ali-CH), 1612 (C=N), 1557 (Ar-C=C), 1373, 1132 (NO$_2$). MS (70 eV): *m/z* (%) = 323 (M$^+$, 54). *Anal. Calcd. For* C$_{12}$H$_{13}$N$_5$O$_4$S (323.33): C, 44.58; H, 4.05; N, 21.66; S, 9.92. Found: C, 44.46; H, 3.98; N, 21.57; S, 9.87.

(Z)-3-Allyl-2-(2-(2,4-Dinitrophenyl)Hydrazineylidene)-4-Methyl-2,3-Dihydrothiazole (3c)

This compound was found as red crystals from methanol in (96% and 83%) yield, with m.p. 197–198 °C; ^{1}H NMR (DMSO-d_6): δ 2.16 (s, 3H, CH$_3$), 4.52–4.58 (m, 2H, allyl-CH$_2$), 5.10–5.28 (m, 2H, allyl-CH$_2$=), 5.96–6.06 (m, 1H, allyl-CH=), 6.16 (s, 1H, H-5), 7.46–7.52 (d, 1H, Ar-H), 8.22–8.28 (d, 1H, Ar-H), 8.85 (s, 1H, Ar-H), 10.48 (s, 1H, NH) ppm; ^{13}C NMR (DMSO-d_6): δ 13.4 (CH$_3$), 46.1 (allyl-CH$_2$), 94.17 (C5), 116.6 (allyl-CH$_2$=), 115.6, 123.4, 128.3 (Ar-CH), 129.7, 136.9, 144.3 (Ar-C), 135.2 (C4), 136.9 (allyl-CH=), 164.4 (C2) ppm. IR: ν = 3105 (NH), 3093 (Ar-CH), 2978 (ali-CH), 1606 (C=N), 1562 (Ar-C=C), 1374, 1206 (NO$_2$). MS (70 eV): *m/z* (%) = 335 (M$^+$, 93). *Anal. Calcd. For* C$_{13}$H$_{13}$N$_5$O$_4$S (335.34): C, 46.56; H, 3.91; N, 20.88; S, 9.56. Found: C, 46.48; H, 3.85; N, 20.79; S, 9.47.

(Z)-3-Cyclohexyl-2-(2-(2,4-Dinitrophenyl)Hydrazineylidene)-4-Methyl-2,3-Dihydrothi-Azole (3d)

This compound was found as red crystals from methanol in (94% and 78%) yield, with m.p., 204–206 °C; ^{1}H NMR (DMSO-d_6): δ 1.34–1.46 (m, 10H, cyclohexyl-CH$_2$), 1.69–184 (m, 1H, cyclohexyl-CH), 2.21 (s, 3H, CH$_3$), 6.10 (s, 1H, H-5), 7.36–7.39 (d, 1H, Ar-H), 8.29–8.32 (dd, 1H, Ar-H), 8.84–8.85 (d, 1H, Ar-H), 10.48 (s, 1H, NH) ppm. IR: ν = 3110 (NH), 3015 (Ar-CH), 2925 (ali-CH), 1608 (C=N), 1544 (Ar-C=C), 1323, 1034 (NO$_2$). MS (70 eV): *m/z* (%) = 377 (M$^+$, 80) *Anal. Calcd. For* C$_{16}$H$_{19}$N$_5$O$_4$S (377.42): C, 50.92; H, 5.07; N, 18.56; S, 8.49. Found: C, 50.82; H, 4.93; N, 18.48; S, 8.43.

(Z)-2-(2-(2,4-Dinitrophenyl)Hydrazineylidene)-4-Methyl-3-Phenyl-2,3-Dihydrothiazole (3e)

This compound was found as red crystals from methanol in (94% and 83%) yield, with m.p., 231–233 °C; ^{1}H NMR (DMSO-d_6): δ 1.80 (s, 3H, CH$_3$), 6.34 (s, 1H, H-5), 7.14–7.17 (d, 1H, Ar-H), 7.49–7.36 (m, 5H, Ar-H), 8.26–8.30 (dd, 1H, Ar-H), 8.85–8.86 (d, 1H, Ar-H), 10.47 (s, 1H, NH) ppm; ^{13}C NMR (DMSO-d_6): δ 14.5 (CH$_3$), 95.3 (C5), 115.5, 123.3, 127.8, 128.5, 128.9, 129.6 (Ar-CH), 129.7, 136.2, 136.5, 144.5 (Ar-C), 135.2 (C4), 165.5 (C2) ppm; IR: ν = 3226 (NH), 3118 (Ar-CH), 2975 (ali-CH), 1603 (C=N), 1555 (Ar-C=C), 1355, 1133 (NO$_2$) cm^{-1}; MS (70 eV): *m/z* (%) = 371 (M$^+$, 8). *Anal. Calcd. For* C$_{16}$H$_{13}$N$_5$O$_4$S (371.37): C, 51.75; H, 3.53; N, 18.86; S, 8.63. Found: C, 51.68; H, 3.49; N, 18.79; S, 8.52.

(Z)-2-(2-(2,4-Dinitrophenyl)Hydrazineylidene)-4-Methyl-3-(p-Tolyl)-2,3-Dihydrothi-Azole (3f)

This compound was found as red crystals from methanol in (92% and 86%) yield, with m.p., 198–199 °C; ^{1}H NMR (DMSO-d_6): δ 1.87 (s, 3H, CH$_3$), 2.40 (s, 3H, tolyl-CH$_3$), 6.32 (s, 1H, H-5), 7.14–7.17 (d, 1H, Ar-H), 7.35–7.39 (m, 4H, Ar-H), 8.19–8.24 (dd, 1H, Ar-H), 8.81–8.83 (d, 1H, Ar-H), 10.47 (s, 1H, NH) ppm; ^{13}C NMR (DMSO-d_6): δ 14.5 (CH$_3$), 20.7 (tolyl-CH$_3$), 95.1 (C5), 115.5, 123.6, 127.8, 128.2, 129.7 (Ar-CH), 130.1, 134.1, 137.5, 138.4, 144.4 (Ar-C), 136.1 (C4), 165.4 (C2) ppm. IR: ν = 3226 (NH), 3088 (Ar-CH), 2945 (ali-CH), 1607 (C=N), 1559 (Ar-C=C), 1383, 1172 (NO$_2$). MS (70 eV): *m/z* (%) = 385 (M$^+$, 13). *Anal. Calcd. For* C$_{17}$H$_{15}$N$_5$O$_4$S (385.40): C, 52.98; H, 3.92; N, 18.17; S, 8.32. Found: C, 52.89; H, 3.87; N, 18.11; S, 8.25.

(Z)-4-Methyl-N′-(4-Methyl-3-Phenylthiazol-2(3H)-Ylidene) Benzenesulfonohydrazide (**3g**)

This compound was found as pale-yellow crystals from methanol in (90% and 83%) yield, with m.p., 193–194 °C; ^{1}H NMR (DMSO-d_6): δ 2.13 (s, 3H, CH$_3$), 2.30 (s, 3H, tolyl-CH$_3$), 5.93 (s, 1H, H-5), 6.40 (d, 2H, tolyl-H-*m*), 6.93 (m, 1H, Ar-H), 7.19 (m, 2H, Ar-H), 7.31 (d, 2H, tolyl-H-*o*), 7.69 (m, 2H, Ar-H), 10.92 (s, 1H, NH) ppm; ^{13}C NMR (DMSO-d_6): δ 13.8 (CH$_3$), 20.9 (tolyl-CH$_3$), 91.0 (C5), 120.5, 122.9, 127.7, 128.9, 129.2 (Ar-CH), 137.6, 143.5, 148.5 (Ar-C), 136.0 (C4), 155.2 (C2) ppm. IR: ν = 3130 (NH),3062 (Ar-CH), 2920 (ali-CH), 1595 (C=N), 1561 (Ar-C=C). MS (70 eV): *m/z* (%) = 359 (M$^+$, 100). *Anal. Calcd. For* C$_{17}$H$_{17}$N$_3$O$_2$S$_2$ (359.46): C, 56.80; H, 4.77; N, 11.69; S, 17.84. Found: C, 56.73; H, 4.69; N, 11.63; S, 17.73.

(Z)-N′-(3-Allyl-4-Methylthiazol-2(3H)-Ylidene)-4-Methyl Benzenesulfonohydrazide (**3h**)

This compound was found as pale-yellow crystals from methanol in (89% and 83%) yield, with m.p., 236–238 °C. IR: ν = 3115 (NH),3078 (Ar-CH), 2988 (ali-CH), 1612 (C=N), 1557 (Ar-C=C), 1373, 1132 (NO$_2$) cm^{-1}. MS (70 eV): *m/z* (%) = 323 (M$^+$, 100). *Anal. Calcd. For* C$_{14}$H$_{17}$N$_3$O$_2$S$_2$ (323.43): C, 51.99; H, 5.30; N, 12.99; S, 19.83. Found: C, 51.91; H, 5.23; N, 12.92; S, 19.78.

(Z)-N′-(3-Ethyl-4-Methylthiazol-2(3H)-Ylidene)-4-Methyl Benzenesulfonohydrazide (**3i**)

This compound was found as pale-yellow crystals from methanol in (87% and 78%) yield, with m.p., 236–238 °C. ^{1}H NMR (DMSO-d_6): δ 1.26–1.39 (t, 3H, CH$_3$), 2.12 (s, 3H, CH$_3$), 3.80–3.96 (q, 2H, CH$_2$), 5.91 (s, 1H, H-5), 6.42 (d, 2H, Ar-H), 7.13 (d, 2H, Ar-H), 10.89 ppm (s, 1H, NH). IR: ν = 3112 (NH), 3044 (Ar-CH), 2946 (ali-CH), 1613 (C=N), 1545 (Ar-C=C), cm^{-1};. MS (70 eV): *m/z* (%) = 311 (M$^+$, 65). *Anal. Calcd. For* C$_{13}$H$_{17}$N$_3$O$_2$S$_2$ (311.42): C, 50.14; H, 5.50; N, 13.49; O, 10.27; S, 20.59. Found: C, 50.09; H, 5.41; N, 13.39; S, 20.53.

3.1.2. Crystal X-ray Structure Determination of **3b**

Compound **3b** was obtained as single crystals by recrystallization from methanol. Bruker D8 Venture diffractometer with Photon II detector at 298(2) K using Cu-Kα radiation ($λ$ = 1.54178 Å) was used to study the single-crystal X-ray diffraction. Moreover, we used dual space methods (SHELXT for **5a**) [57,58] for the structure solution, and refinement was carried out using SHELXL-2014 (full-matrix least-squares on F^2) [59]. Hydrogen atoms were localized by difference electron density determination and refined using a riding model. Semi-empirical absorption corrections and a general RIGU restraint were applied.

3b: red crystals, C$_{12}$H$_{13}$N$_5$O$_4$S, M_r = 323.33, crystal size 0.20 × 0.04 × 0.02 mm, triclinic, space group *P-1* (No. 2), a = 7.0981(2) Å, b = 8.2929(2) Å, c = 13.0081(4) Å, $α$ = 101.598(1)°, $β$ = 103.030(1)°, $γ$ = 92.366(1)°, V = 727.74(4) Å^3, Z = 2, $ρ$ = 1.476 Mg/m^{-3}, $μ$(Cu-K$_α$) = 2.24 mm^{-1}, $F(000)$ = 336, T = 298 K, $2θ_{max}$ = 144.4°, 13,774 reflections, of which 2874 were independent (R_{int} = 0.058), 200 parameters, 165 restraints (see cif-file for details), R_1 = 0.063 (for 2692 I > 2σ(I)), wR_2 = 0.170 (all data), S = 1.07, largest diff. peak/hole = 0.78/−0.40 e Å^{-3}.

CCDC 2265616 (**3b**) contains the supplementary crystallographic data for this paper. These data can be obtained free of charge from the Cambridge Crystallographic Data Centre via www.ccdc.cam.ac.uk/data_request/cif (accessed on 24 June 2023).

3.2. Biology

3.2.1. Cell Viability Assay

The human mammary gland epithelial (MCF-10A) cell line was used to test the viability of compounds **3a–i** [50,60]. See Supplementary Information.

3.2.2. Antiproliferative Assay

The MTT assay was used to investigate **3a–i**'s antiproliferative activity versus four human cancer cell lines: colon cancer (HT-29) cell line, pancreatic cancer (Panc-1) cell line, lung cancer (A-549) cell line, and breast cancer (MCF-7) cell line, using erlotinib as the reference [52,53]. See Supplementary Information.

3.2.3. EGFR Inhibitory Assay

Compounds **3a**, **3c**, **3d**, and **3f** were further evaluated for their suppressive effect versus EGFR as a probable molecular target for their mechanism of action [50,54]. See Supplementary Information.

3.2.4. BRAF^{V600E} Inhibitory Assay

Derivatives **3a**, **3c**, **3d**, and **3f** were further investigated as possible BRAF^{V600E} inhibitors [61]. See Supplementary Information.

3.3. In Silico Study

The crystal structures of BRAF^{V600E} and EGFR, with PDB codes 3OG7 [62] and 1M17 [63], respectively, were prepared for all docking computations. All heteroatoms, water molecules, ligands, and ions were removed to prepare the PDB files. Modeler software was applied to construct all missing amino acids [64,65]. The protonation state of titratable residues of the investigated targets was estimated using PropKa software at pH 7.0 [66]. The 3D structure of the investigated compounds was energetically minimized using the MMFF94S force field within SZYBKI software [67,68].

For docking computations, AutoDock4.2.6 software was utilized [69]. All docking parameters were set to default values, except *GA* run and energy evaluation, which were 250 and 25,000,000, respectively. The active site of the investigated targets was inspected by a grid box with a size of 50 Å × 50 Å × 50 Å. The grid maps were generated using the AutoGrid program with a spacing of 0.375 Å. Gasteiger–Marsili method was employed to assign the atomic charges of the chemical compounds [70]. Discovery Studio module of Biovia software 17.1.0.115 was utilized to visualize all drug–protein interactions [71].

4. Conclusions

Using simple interactions between thiosemicarbazides and chloroacetone, a novel set of heterocycles with thiazole rings was developed. All obtained derivatives were validated using various spectral data such as IR, NMR, mass spectrometry, elemental analysis, and X-ray crystallography. The newly synthesized compounds, **3a–i**, were evaluated against a panel of four human cancer cell lines, with compounds **3a**, **3c**, **3d**, and **3f** being the most potent variants. The in vitro assay results demonstrated that compound 3f possesses potent antiproliferative activity as a dual EGFR/BRAF^{V600E} inhibitor, signaling that further structural modifications may be needed to establish a more potent lead molecule for future development. Finally, the docking analysis results showed that all inspected compounds revealed good docking scores toward BRAF^{V600E} and EGFR.

References

1. Falzone, L.; Salomone, S.; Libra, M. Evolution of Cancer Pharmacological Treatments at the Turn of the Third Millennium. *Front. Pharmacol.* **2018**, *9*, 1300. [CrossRef] [PubMed]
2. Bin Emran, T.; Shahriar, A.; Mahmud, A.R.; Rahman, T.; Abir, M.H.; Siddiquee, M.F.-R.; Ahmed, H.; Rahman, N.; Nainu, F.; Wahyudin, E.; et al. Multidrug Resistance in Cancer: Understanding Molecular Mechanisms, Immunoprevention and Therapeutic Approaches. *Front. Oncol.* **2022**, *12*, 2581. [CrossRef] [PubMed]
3. Housman, G.; Byler, S.; Heerboth, S.; Lapinska, K.; Longacre, M.; Snyder, N.; Sarkar, S. Drug Resistance in Cancer: An Overview. *Cancers* **2014**, *6*, 1769–1792. [CrossRef] [PubMed]
4. Bhullar, K.S.; Lagarón, N.O.; McGowan, E.M.; Parmar, I.; Jha, A.; Hubbard, B.P.; Rupasinghe, H.P.V. Kinase-targeted cancer therapies: Progress, challenges and future directions. *Mol. Cancer* **2018**, *17*, 48. [CrossRef]
5. Nishal, S.; Jhawat, V.; Gupta, S.; Phaugat, P. Utilization of kinase inhibitors as novel therapeutic drug targets: A review. *Oncol. Res.* **2023**, *30*, 221–230. [CrossRef]
6. Al-Wahaibi, L.H.; Gouda, A.M.; Abou-Ghadir, O.F.; Salem, O.I.; Ali, A.T.; Farghaly, H.S.H.; Abdelrahman, M.H.; Trembleau, L.; Abdu-Allah, H.H.; Youssif, B.G. Design and synthesis of novel 2,3-dihydropyrazino[1,2-a]indole-1,4-dione derivatives as antiproliferative EGFR and BRAFV600E dual inhibitors. *Bioorg. Chem.* **2020**, *104*, 104260. [CrossRef]
7. Jarvinen, T.A.; Liu, E.T. Simultaneous amplification of HER-2 (ERBB2) and topoisomerase IIα (TOP2A) genes-molecular basis for combination chemotherapy in cancer. *Curr. Cancer Drug Targets* **2006**, *6*, 579–602. [CrossRef]
8. Gurunathan, S.; Kang, M.-H.; Qasim, M.; Kim, J.-H. Nanoparticle-Mediated Combination Therapy: Two-in-One Approach for Cancer. *Int. J. Mol. Sci.* **2018**, *19*, 3264. [CrossRef]
9. Lehár, J.; Krueger, A.S.; Avery, W.; Heilbut, A.M.; Johansen, L.M.; Price, E.R.; Rickles, R.J.; Iii, G.F.S.; Staunton, J.E.; Jin, X.; et al. Synergistic drug combinations tend to improve therapeutically relevant selectivity. *Nat. Biotechnol.* **2009**, *27*, 659–666. [CrossRef]
10. Kendall, J.M. Designing a research project: Randomised controlled trials and their principles. *Emerg. Med. J.* **2003**, *20*, 164–168. [CrossRef]
11. Lim, Z.-F.; Ma, P.C. Emerging insights of tumor heterogeneity and drug resistance mechanisms in lung cancer targeted therapy. *J. Hematol. Oncol.* **2019**, *12*, 134. [CrossRef]
12. Hoelder, S.; Clarke, P.A.; Workman, P. Discovery of small molecule cancer drugs: Successes, challenges and opportunities. *Mol. Oncol.* **2012**, *6*, 155–176. [CrossRef] [PubMed]
13. Shah, K.N.; Bhatt, R.; Rotow, J.; Rohrberg, J.; Olivas, V.; Wang, V.E.; Hemmati, G.; Martins, M.M.; Maynard, A.; Kuhn, J.; et al. Aurora kinase A drives the evolution of resistance to third-generation EGFR inhibitors in lung cancer. *Nat. Med.* **2019**, *25*, 111–118. [CrossRef] [PubMed]
14. Wu, C.-P.; Murakami, M.; Wu, Y.-S.; Lin, C.-L.; Li, Y.-Q.; Huang, Y.-H.; Hung, T.-H.; Ambudkar, S.V. The multitargeted tyrosine kinase inhibitor SKLB610 resensitizes ABCG2-overexpressing multidrug-resistant cancer cells to chemotherapeutic drugs. *Biomed. Pharmacother.* **2022**, *149*, 112922. [CrossRef]
15. Kanojia, D.; Garg, M.; Martinez, J.; MT, A.; Luty, S.B.; Doan, N.B.; Said, J.W.; Forscher, C.; Tyner, J.W.; Koeffler, H.P. Kinase profiling of liposarcomas using RNAi and drug screening assays identified druggable targets. *J. Hematol. Oncol.* **2017**, *10*, 173. [CrossRef]
16. Sun, D.; Zhao, Y.; Zhang, S.; Zhang, L.; Liu, B.; Ouyang, L. Dual-target kinase drug design: Current strategies and future directions in cancer therapy. *Eur. J. Med. Chem.* **2020**, *188*, 112025. [CrossRef]
17. Zou, X.; Tang, X.-Y.; Qu, Z.-Y.; Sun, Z.-W.; Ji, C.-F.; Li, Y.-J.; Guo, S.-D. Targeting the PDGF/PDGFR signaling pathway for cancer therapy: A review. *Int. J. Biol. Macromol.* **2022**, *202*, 539–557. [CrossRef]
18. Ho, C.-C.; Liao, W.-Y.; Lin, C.-A.; Shih, J.-Y.; Yu, C.-J.; Yang, J.C.-H. Acquired BRAF V600E Mutation as Resistant Mechanism after Treatment with Osimertinib. *J. Thorac. Oncol. Off. Publ. Int. Assoc. Study Lung Cancer* **2017**, *12*, 567–572. [CrossRef] [PubMed]
19. Nana, F.A.; Ocak, S. Targeting *BRAF* Activation as Acquired Resistance Mechanism to EGFR Tyrosine Kinase Inhibitors in *EGFR*-Mutant Non-Small-Cell Lung Cancer. *Pharmaceutics* **2021**, *13*, 1478. [CrossRef]
20. Hyman, D.M.; Puzanov, I.; Subbiah, V.; Faris, J.E.; Chau, I.; Blay, J.-Y.; Wolf, J.; Raje, N.S.; Diamond, E.L.; Hollebecque, A.; et al. Vemurafenib in Multiple Nonmelanoma Cancers with *BRAF* V600 Mutations. *N. Engl. J. Med.* **2015**, *373*, 726–736. [CrossRef]
21. Amodio, V.; Yaeger, R.; Arcella, P.; Cancelliere, C.; Lamba, S.; Lorenzato, A.; Arena, S.; Montone, M.; Mussolin, B.; Bian, Y.; et al. EGFR Blockade Reverts Resistance to KRASG12C Inhibition in Colorectal Cancer. *Cancer Discov.* **2020**, *10*, 1129–1139. [CrossRef] [PubMed]
22. Prahallad, A.; Sun, C.; Huang, S.; Di Nicolantonio, F.; Salazar, R.; Zecchin, D.; Beijersbergen, R.L.; Bardelli, A.; Bernards, R. Unresponsiveness of colon cancer to BRAF(V600E) inhibition through feedback activation of EGFR. *Nature* **2012**, *483*, 100–103. [CrossRef] [PubMed]

23. Desai, J.; Markman, B.; Ananda, S.; Tebbutt, N.C.; Michael, M.; Solomon, B.J.; McArthur, G.A.; Tie, J.; Gibbs, P.; Ritchie, D.; et al. A phase I/II trial of combined BRAF and EGFR inhibition in patients (pts) with BRAF V600E mutated (BRAFm) metastatic colorectal (mCRC): The EViCT (Erlotinib and Vemurafenib in Combination Trial) study. *J. Clin. Oncol.* **2017**, *35*, 3557. [CrossRef]

24. Liu, H.; Nazmun, N.; Hassan, S.; Liu, X.; Yang, J. BRAF mutation and its inhibitors in sarcoma treatment. *Cancer Med.* **2020**, *9*, 4881–4896. [CrossRef]

25. Corcoran, R.B.; André, T.; Atreya, C.E.; Schellens, J.H.; Yoshino, T.; Bendell, J.C.; Hollebecque, A.; McRee, A.J.; Siena, S.; Middleton, G. Combined BRAF, EGFR, and MEK Inhibition in Patients with BRAFV600E-Mutant Colorectal Can-cerBRAF/EGFR/MEK Inhibition in BRAFV600E Colorectal Cancer. *Cancer Discov.* **2018**, *8*, 428–443. [CrossRef]

26. Bahrami, A.; Hesari, A.; Khazaei, M.; Hassanian, S.M.; Ferns, G.A.; Avan, A. The therapeutic potential of targeting the BRAF mutation in patients with colorectal cancer. *J. Cell Physiol.* **2017**, *233*, 2162–2169. [CrossRef]

27. Lozynskyi, A.; Zimenkovsky, B.; Lesyk, R. Synthesis and anticancer activity of new thiopyrano [2, 3-d] thiazoles based on cinnamic acid amides. *Sci. Pharm.* **2014**, *82*, 723–734. [CrossRef] [PubMed]

28. Janowska, S.; Khylyuk, D.; Bielawska, A.; Szymanowska, A.; Gornowicz, A.; Bielawski, K.; Noworól, J.; Mandziuk, S.; Wujec, M. New 1,3,4-Thiadiazole Derivatives with Anticancer Activity. *Molecules* **2022**, *27*, 1814. [CrossRef]

29. Arshad, M.F.; Alam, A.; Alshammari, A.A.; Alhazza, M.B.; Alzimam, I.M.; Alam, A.; Mustafa, G.; Ansari, S.; Alotaibi, A.M.; Alotaibi, A.A.; et al. Thiazole: A Versatile Standalone Moiety Contributing to the Development of Various Drugs and Biologically Active Agents. *Molecules* **2022**, *27*, 3994. [CrossRef]

30. Franchetti, P.; Cappellacci, L.; Grifantini, M.; Barzi, A.; Nocentini, G.; Yang, H.; O'Connor, A.; Jayaram, H.N.; Carrell, C.; Goldstein, B.M. Furanfurin and Thiophenfurin: Two Novel Tiazofurin Analogs. Synthesis, Structure, Antitumor Activity, and Interactions with Inosine Monophosphate Dehydrogenase. *J. Med. Chem.* **1995**, *38*, 3829–3837. [CrossRef]

31. Li, X.; He, Y.; Ruiz, C.H.; Koenig, M.; Cameron, M.D. Characterization of Dasatinib and Its Structural Analogs as CYP3A4 Mechanism-Based Inactivators and the Proposed Bioactivation Pathways. *Drug Metab. Dispos.* **2009**, *37*, 1242–1250. [CrossRef] [PubMed]

32. Hughes, T.P.; Laneuville, P.; Rousselot, P.; Snyder, D.S.; Rea, D.; Shah, N.P.; Paar, D.; Abruzzese, E.; Hochhaus, A.; Lipton, J.H.; et al. Incidence, outcomes, and risk factors of pleural effusion in patients receiving dasatinib therapy for Philadelphia chromosome-positive leukemia. *Haematologica* **2018**, *104*, 93–101. [CrossRef] [PubMed]

33. Hu-Lieskovan, S.; Mok, S.; Moreno, B.H.; Tsoi, J.; Robert, L.; Goedert, L.; Pinheiro, E.M.; Koya, R.C.; Grae-ber, T.G.; Comin-Anduix, B. Improved antitumor activity of immunotherapy with BRAF and MEK inhibitors in BRAF V600E melanoma. *Sci. Transl. Med.* **2015**, *7*, 279ra41. [CrossRef]

34. Argenziano, G.; Banzi, C.; De Blasio, S.; Lallas, A.; Longo, C.; Moscarella, E.; Alfano, R. Dabrafenib: A new opportunity for the treatment of BRAF V600-positive melanoma. *OncoTargets Ther.* **2016**, *ume 9*, 2725–2733. [CrossRef]

35. Abdel-Maksoud, M.S.; Kim, M.-R.; El-Gamal, M.I.; El-Din, M.M.G.; Tae, J.; Choi, H.S.; Lee, K.-T.; Yoo, K.H.; Oh, C.-H. Design, synthesis, in vitro antiproliferative evaluation, and kinase inhibitory effects of a new series of imidazo [2, 1-b] thiazole derivatives. *Eur. J. Med. Chem.* **2015**, *95*, 453–463. [CrossRef] [PubMed]

36. Aly, A.A.; Alshammari, M.B.; Ahmad, A.; Gomaa, H.A.M.; Youssif, B.G.M.; Bräse, S.; Ibrahim, M.A.A.; Mohamed, A.H. Design, synthesis, docking and mechanistic studies of new thiazolyl/thiazolidinylpyrimidine-2,4-dione antiproliferative agents. *Arab. J. Chem.* **2023**, *16*, 104612. [CrossRef]

37. Ballatore, C.; Huryn, D.M.; Smith, A.B. Carboxylic Acid (Bio)Isosteres in Drug Design. *Chemmedchem* **2013**, *8*, 385–395. [CrossRef] [PubMed]

38. Ammazzalorso, A.; De Filippis, B.; Giampietro, L.; Amoroso, R. *N*-acylsulfonamides: Synthetic routes and biological potential in medicinal chemistry. *Chem. Biol. Drug Des.* **2017**, *90*, 1094–1105. [CrossRef]

39. Ghorab, M.M.; Alsaid, M.S.; El-Gaby, M.S.; Safwat, N.A.; Elaasser, M.M.; Soliman, A.M. Biological evaluation of some new N-(2,6-dimethoxypyrimidinyl) thioureido benzenesulfonamide derivatives as potential antimicrobial and anticancer agents. *Eur. J. Med. Chem.* **2016**, *124*, 299–310. [CrossRef]

40. Alaoui, S.; Dufies, M.; Driowya, M.; Demange, L.; Bougrin, K.; Robert, G.; Auberger, P.; Pagès, G.; Benhida, R. Synthesis and anti-cancer activities of new sulfonamides 4-substituted-triazolyl nucleosides. *Bioorg. Med. Chem. Lett.* **2017**, *27*, 1989–1992. [CrossRef]

41. Wan, Y.; Fang, G.; Chen, H.; Deng, X.; Tang, Z. Sulfonamide derivatives as potential anti-cancer agents and their SARs elucidation. *Eur. J. Med. Chem.* **2021**, *226*, 113837. [CrossRef]

42. Al-Wahaibi, L.H.; Mahmoud, M.A.; Mostafa, Y.A.; Raslan, A.E.; Youssif, B.G. Novel piperine-carboximidamide hybrids: Design, synthesis, and antiproliferative activity via a multi-targeted inhibitory pathway. *J. Enzym. Inhib. Med. Chem.* **2023**, *38*, 376–386. [CrossRef] [PubMed]

43. Gomaa, H.A.; Shaker, M.E.; Alzarea, S.I.; Hendawy, O.; Mohamed, F.A.; Gouda, A.M.; Ali, A.T.; Morcoss, M.M.; Abdelrahman, M.H.; Trembleau, L.; et al. Optimization and SAR investigation of novel 2,3-dihydropyrazino[1,2-a]indole-1,4-dione derivatives as EGFR and BRAFV600E dual inhibitors with potent antiproliferative and antioxidant activities. *Bioorg. Chem.* **2022**, *120*, 105616. [CrossRef]

44. Mohassab, A.M.; Hassan, H.A.; Abdelhamid, D.; Gouda, A.M.; Youssif, B.G.M.; Tateishi, H.; Fujita, M.; Otsuka, M.; Abdel-Aziz, M. Design and synthesis of novel quinoline/chalcone/1,2,4-triazole hybrids as potent antiproliferative agent targeting EGFR and BRAFV600E kinases. *Bioorg. Chem.* **2020**, *106*, 104510. [CrossRef] [PubMed]

45. Youssif, B.G.; Abdelrahman, M.H.; Abdelazeem, A.H.; Ibrahim, H.M.; Salem, O.I.; Mohamed, M.F.; Treambleau, L.; Bukhari, S.N.A. Design, synthesis, mechanistic and histopathological studies of small-molecules of novel in-dole-2-carboxamides and pyrazino [1, 2-a] indol-1 (2H)-ones as potential anticancer agents effecting the reactive oxygen species production. *Eur. J. Med. Chem.* **2018**, *146*, 260–273. [CrossRef]

46. Noto, R.; Meo, P.L.; Gruttadauria, M.; Werber, G. A quantitative study of substituent effects on oxidative cycliza-tion of some 2-aryl-substituted aldehyde thiosemicarbazones induced by ferric chloride and cupric perchlorate. *J. Heterocycl. Chem.* **1999**, *36*, 667–674. [CrossRef]

47. Krishna, P.M.; Reddy, N.G.; Harish, B.; Patil, Y.P.; Nethaji, M. Synthesis, structural studies, molecular docking and DNA binding studies of 4N-substituted hydrazinecarbothioamides. *J. Mol. Struct.* **2019**, *1175*, 97–104. [CrossRef]

48. Munir, R.; Zia-ur-Rehman, M.; Murtaza, S.; Zaib, S.; Javid, N.; Awan, S.J.; Iftikhar, K.; Athar, M.M.; Khan, I. Micro-wave-Assisted Synthesis of (Piperidin-1-yl) quinolin-3-yl) methylene) hydrazinecarbothioamides as Potent Inhibitors of Cholinesterases: A Biochemical and In silico Approach. *Molecules* **2021**, *26*, 656. [CrossRef]

49. Basri, R.; Ullah, S.; Halim, S.A.; Alharthy, R.D.; Rauf, U.; Khan, A.; Hussain, J.; Al-Ghafri, A.; Al-Harrasi, A.; Shafiq, Z. Synthesis, biological evaluation, and molecular docking study of chromen-linked hydrazine carbothioamides as potent α-glucosidase inhibitors. *Drug Dev. Res.* **2023**. [CrossRef]

50. Al-Wahaibi, L.H.; Mostafa, Y.A.; Abdelrahman, M.H.; El-Bahrawy, A.H.; Trembleau, L.; Youssif, B.G.M. Synthesis and Biolog-ical Evaluation of Indole-2-Carboxamides with Potent Apoptotic Antiproliferative Activity as EGFR/CDK2 Dual Inhibitors. *Pharmaceuticals* **2022**, *15*, 1006. [CrossRef]

51. Riss, T.L.; Moravec, R.A.; Niles, A.L.; Duellman, S.; Benink, H.A.; Worzella, T.J.; Minor, L. Cell Viability Assays, Assay Guidance Manual [Internet]. 2016. Available online: https://www.ncbi.nlm.nih.gov/books/NBK144065/ (accessed on 11 July 2023).

52. Mahmoud, M.A.; Mohammed, A.F.; Salem, O.I.; Gomaa, H.A.; Youssif, B.G. New 1, 3, 4-oxadiazoles linked with the 1, 2, 3-triazole moiety as antiproliferative agents targeting the EGFR tyrosine kinase. *Arch. Pharm.* **2022**, *355*, 2200009. [CrossRef] [PubMed]

53. Mahmoud, M.A.; Mohammed, A.F.; Salem, O.I.; Rabea, S.M.; Youssif, B.G. Design, synthesis, and antiproliferative properties of new 1,2,3-triazole-carboximidamide derivatives as dual EGFR/VEGFR-2 inhibitors. *J. Mol. Struct.* **2023**, *1282*, 135165. [CrossRef]

54. Mohamed, F.A.; Gomaa, H.A.; Hendawy, O.; Ali, A.T.; Farghaly, H.S.; Gouda, A.M.; Abdelazeem, A.H.; Ab-delrahman, M.H.; Trembleau, L.; Youssif, B.G. Design, synthesis, and biological evaluation of novel EGFR inhibitors con-taining 5-chloro-3-hydroxymethyl-indole-2-carboxamide scaffold with apoptotic antiproliferative activity. *Bioorg. Chem.* **2021**, *112*, 104960. [CrossRef] [PubMed]

55. Abbas, S.Y.; Al-Harbi, R.A.; El-Sharief, M.A.S. Synthesis and anticancer activity of thiourea derivatives bearing a benzodioxole moiety with EGFR inhibitory activity, apoptosis assay and molecular docking study. *Eur. J. Med. Chem.* **2020**, *198*, 112363. [CrossRef] [PubMed]

56. Zhang, J.; Yao, T.-W.; Hashizume, R.; Hariono, S.; Barkovich, K.J.; Fan, Q.-W.; Prados, M.; James, C.D.; Weiss, W.A.; Nicolaides, T. Combined BRAF V600E and MEK blockade for BRAF V600E-mutant gliomas. *J. Neurooncol.* **2017**, *131*, 495–505. [CrossRef] [PubMed]

57. Sheldrick, G.M. SHELXT–Integrated space-group and crystal-structure determination. *Acta Crystallogr. Sect. A Found. Adv.* **2015**, *71*, 3–8. [CrossRef]

58. Zhou, G.; Yang, T.; Huang, Z. Structure determination of a low-crystallinity covalent organic framework by three-dimensional electron diffraction. *Commun. Chem.* **2023**, *6*, 116. [CrossRef]

59. Sheldrick, G.M. Crystal structure refinement with SHELXL. *Acta Crystallogr. Sect. C Struct. Chem.* **2015**, *71*, 3–8. [CrossRef]

60. Abou-Zied, H.A.; Youssif, B.G.; Mohamed, M.F.; Hayallah, A.M.; Abdel-Aziz, M. EGFR inhibitors and apoptotic inducers: Design, synthesis, anticancer activity and docking studies of novel xanthine derivatives carrying chalcone moiety as hybrid molecules. *Bioorg. Chem.* **2019**, *89*, 102997. [CrossRef]

61. Youssif, B.G.; Gouda, A.M.; Moustafa, A.H.; Abdelhamid, A.A.; Gomaa, H.A.; Kamal, I.; Marzouk, A.A. Design and synthesis of new triarylimidazole derivatives as dual inhibitors of BRAFV600E/p38α with potential antiproliferative activity. *J. Mol. Struct.* **2021**, *1253*, 132218. [CrossRef]

62. Bollag, G.; Hirth, P.; Tsai, J.; Zhang, J.; Ibrahim, P.N.; Cho, H.; Spevak, W.; Zhang, C.; Zhang, Y.; Habets, G.; et al. Clinical efficacy of a RAF inhibitor needs broad target blockade in BRAF-mutant melanoma. *Nature* **2010**, *467*, 596–599. [CrossRef] [PubMed]

63. Stamos, J.; Sliwkowski, M.X.; Eigenbrot, C. Structure of the Epidermal Growth Factor Receptor Kinase Domain Alone and in Complex with a 4-Anilinoquinazoline Inhibitor. *J. Biol. Chem.* **2002**, *277*, 46265–46272. [CrossRef] [PubMed]

64. Martí-Renom, M.A.; Stuart, A.C.; Fiser, A.; Sánchez, R.; Melo, F.; Šali, A. Comparative Protein Structure Modeling of Genes and Genomes. *Annu. Rev. Biophys. Biomol. Struct.* **2000**, *29*, 291–325. [CrossRef]

65. Muthumanickam, S.; Boomi, P.; Subashkumar, R.; Palanisamy, S.; Sudha, A.; Anand, K.; Balakumar, C.; Saravanan, M.; Poorani, G.; Wang, Y. An Insight of Protein Structure Predictions Using Homology Modeling. In *Computation in Bioinformatics: Multidisciplinary Applications*; John Wiley & Sons, Inc.: Hoboken, NJ, USA; Scrivener Publishing LLC: Beverly, MA, USA, 2021; pp. 265–277.

66. Olsson, M.H.M.; Søndergaard, C.R.; Rostkowski, M.; Jensen, J.H. PROPKA3: Consistent Treatment of Internal and Surface Residues in Empirical pKa Predictions. *J. Chem. Theory Comput.* **2011**, *7*, 525–537. [CrossRef] [PubMed]

67. Halgren, T.A. MMFF VI. MMFF94s option for energy minimization studies. *J. Comput. Chem.* **1999**, *20*, 720–729. [CrossRef]

68. OpenEye Scientific. *SZYBKI 1.9.0.3. 1.9.0.3*; OpenEye Scientific Software: Santa Fe, NM, USA, 2016.

69. Morris, G.M.; Huey, R.; Lindstrom, W.; Sanner, M.F.; Belew, R.K.; Goodsell, D.S.; Olson, A.J. AutoDock4 and Auto-DockTools4: Automated docking with selective receptor flexibility. *J. Comput. Chem.* **2009**, *30*, 2785–2791. [CrossRef]
70. Gasteiger, J.; Marsili, M. Iterative partial equalization of orbital electronegativity—A rapid access to atomic charges. *Tetrahedron* **1980**, *36*, 3219–3228. [CrossRef]
71. Discovery Studio Visualizer (D.S.V.). *Dassault Systèmes BIOVIA. Version 2019*; Dassault Systèmes: San Diego, CA, USA, 2019.

Article

Design, Synthesis, and Anti-Proliferative Action of Purine/Pteridine-Based Derivatives as Dual Inhibitors of EGFR and BRAF^{V600E}

Samar A. El-Kalyoubi [1,*], Hesham A. M. Gomaa [2], Elshimaa M. N. Abdelhafez [3], Mohamed Ramadan [4], Fatimah Agili [5] and Bahaa G. M. Youssif [6,*]

1   Department of Pharmaceutical Organic Chemistry, Faculty of Pharmacy, Port Said University, Port Said 42511, Egypt
2   Department of Pharmacology, College of Pharmacy, Jouf University, Sakaka 72341, Aljouf, Saudi Arabia
3   Medicinal Chemistry Department, Faculty of Pharmacy, Minia University, Minia 61519, Egypt
4   Pharmaceutical Organic Chemistry Department, Faculty of Pharmacy, Al-Azhar University, Assiut Branch, Assiut 11651, Egypt
5   Chemistry Department, Faculty of Science (Female Section), Jazan University, Jazan 82621, Jazan, Saudi Arabia
6   Pharmaceutical Organic Chemistry Department, Faculty of Pharmacy, Assiut University, Assiut 71526, Egypt
*   Correspondence: s.elkalyoubi@hotmail.com (S.A.E.-K.); bahaa.youssif@pharm.aun.edu.eg or bgyoussif2@gmail.com (B.G.M.Y.); Tel.: +02-01098294419 (B.G.M.Y.)

Abstract: The investigation of novel EGFR and BRAF^{V600E} dual inhibitors is intended to serve as targeted cancer treatment. Two sets of purine/pteridine-based derivatives were designed and synthesized as EGFR/BRAF^{V600E} dual inhibitors. The majority of the compounds exhibited promising antiproliferative activity on the cancer cell lines tested. Compounds **5a**, **5e**, and **7e** of purine-based and pteridine-based scaffolds were identified as the most potent hits in anti-proliferative screening, with GI$_{50}$ values of 38 nM, 46 nM, and 44 nM, respectively. Compounds **5a**, **5e**, and **7e** demonstrated promising EGFR inhibitory activity, with IC$_{50}$ values of 87 nM, 98 nM, and 92 nM, respectively, when compared to erlotinib's IC$_{50}$ value of 80 nM. According to the results of the BRAF^{V600E} inhibitory assay, BRAF^{V600E} may not be a viable target for this class of organic compounds. Finally, molecular docking studies were carried out at the EGFR and BRAF^{V600E} active sites to suggest possible binding modes.

Keywords: cancer; EGFR; BRAF; anti-proliferative; purine; pteridine; docking

1. Introduction

Enhanced understanding of therapeutic targets plays a significant role in the advancement of new drugs in cancer research. This approach is based on the assumption that altering a particular cancer biomarker will lead to a positive treatment result [1]. The selectivity of anti-cancer drugs can significantly enhance their effectiveness in damaging cancer cells while minimizing adverse reactions on healthy cells [2]. However, due to drug resistance, suppressing just one target often has only a temporary impact. To obtain optimal outcomes, it is essential to target multiple targets simultaneously due to the diversity in cancers [3,4].

One strategy for simultaneously blocking two or more targets is combined chemotherapy. Yet there are frequently discrepancies between the pharmacokinetic properties and metabolic stabilities of two or more medications. Moreover, the use of multiple medications at the same time may result in hazardous medication interactions [5]. These issues might be addressed by combining two drugs within a single molecule that affects multiple targets [6]. Multi-target medications, commonly referred to as "hybrid" molecules, were shaped by fusing two or more distinct pharmacophore moieties into a single molecule. These drugs have attracted a lot of attention lately [7].

It has been demonstrated that kinases control a wide range of essential tumour behaviours, including tumour development, metastasis, neovascularization, and chemotherapeutic resistance. As a consequence, the FDA has recently validated many kinase blockers for use in a wide variety of cancers, making them a key focus of therapeutic development [8].

The established BRAF^{V600E} mutation was expected to be a resistance mechanism after EGFR blocker therapy [9]. The feedback activation of EGFR signalling has also been connected to the resistance that develops in colorectal cancer [10]. Furthermore, EGFR may be activated by BRAF suppression, leading to continuing tumour development [11]. To address these problems, a BRAF/EGFR combination was utilized. Much research in cases of metastatic colorectal cancer with BRAF^{V600E} mutations discovered that the BRAF–EGFR combination might lead to critical therapeutic action [9]. Hence, sequential suppression of the two kinases may provide a solution for the EGFR activation issue.

Several studies have been conducted to investigate the potential activity of 1,3-dimethyl-1*H*-purine-2,6(3*H*,7*H*)-dione derivatives (methylxanthines) on tumour cell molecular aspects and growth [12–14]. Theophylline and caffeine, two well-known methylxanthine derivatives, have the ability to suppress cell proliferation in addition to the metastatic behaviour of melanoma cancer cells [15]. Substitution at N-7 and/or C-8 of the xanthine ring subsequently drew the attention of many researchers seeking novel anti-tumour agents [16–19].

Earlier, we mentioned the synthesis of a series of purine-2,6-dione derivatives with possible anti-proliferative properties, with compound **I** (Figure 1) being the most effective derivative against the investigated cell lines. Compound **I** demonstrated promising EGFR suppressive effect, with an IC$_{50}$ of 0.32 µM [16]. In another series [20], Compound **II** (Figure 1) demonstrated promising anti-proliferative activity with a GI$_{50}$ value of 1.60 µM against four cancer cell lines tested. Compound **II** was tested for EGFR inhibitory activity. The study findings revealed that **II** had an IC$_{50}$ against the target enzyme of 0.30 µM, that is more potent than the reference staurosporine (IC$_{50}$ = 0.4 µM). In contrast to the reference drug methotrexate, compound **III** (Figure 1) demonstrated good anti-proliferative action versus the lung carcinoma cell line (A549), with an IC$_{50}$ value of 12.2 µM [21].

Compound I
EGFR inhibitor, IC$_{50}$ = 0.32 µM

Compound II
EGFR inhibitor, IC$_{50}$ = 0.30 µM

Compound III
Anticancer (A549, IC$_{50}$ = 12.2 µM)
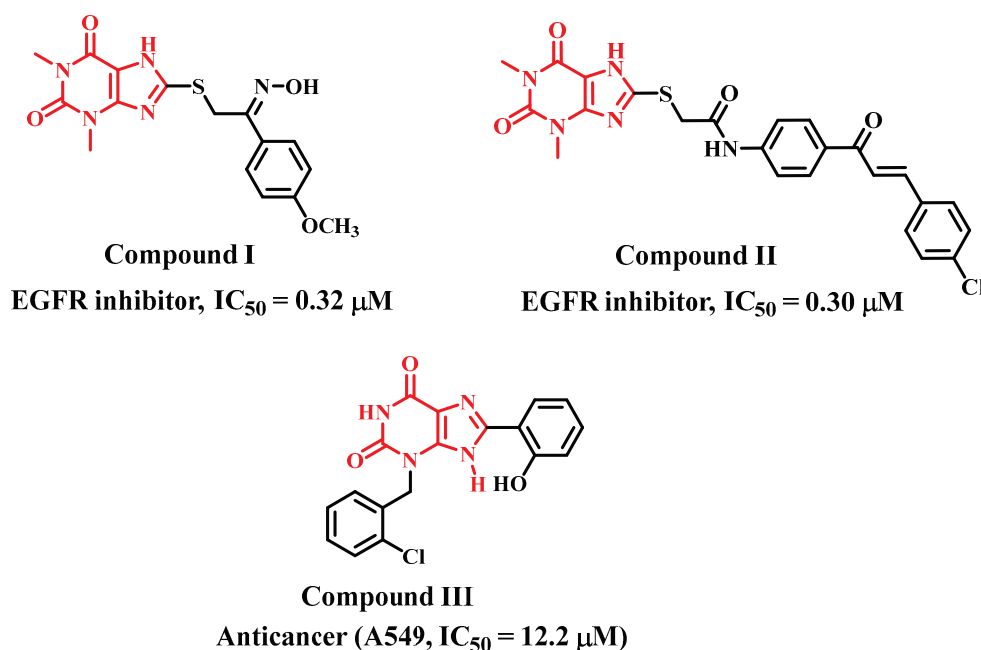
Figure 1. Purine-based derivatives **I**, **II**, and **III** with anti-proliferative activity.

Spiro scaffolds, on the other hand, are an additional class of building block with potential medicinal chemistry features.

During the process of developing a new drug, chemists include a rigid ring to significantly minimize the entropic cost upon binding to the target protein. A spiro ring fusion is another appealing method for achieving conformational restriction.

Their inherent three-dimensional and atypical structural properties make them particularly useful in the exploration and design of novel drugs. Inhibitors of protein–protein interactions (e.g., p53–MDM2 interaction) and enzyme inhibitors (aspartyl proteases, kinases, renin, and BACE1) have effectively included spiro ring structures in recent years [22].

Pteridines are compounds with pyrimido[4,5-*b*]pyrazine rings **IV** (Figure 2). Many living organisms produce these bicyclic compounds, which serve many biological functions. The majority of naturally occurring pteridines are known as pterins **V** (Figure 2) because they have a carbonyl and an amino group at ring positions 4 and 2, respectively (Figure 2) [23].
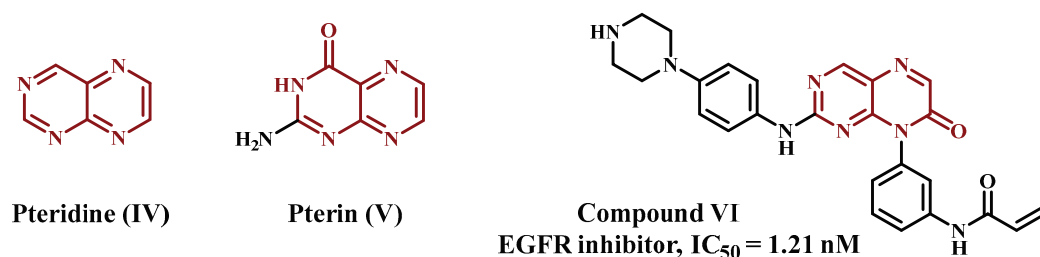
Figure 2. Pteridine-based derivatives with anti-proliferative activity.

Due to their significance in both health and sickness, pteridines have long been the subject of medicinal and biomedical chemistry research. In order to target a broad range of human pathologies, such as neoplasms, microbial infections, chronic inflammatory disorders, and others, many pteridine derivatives have been synthesised and evaluated for biological actions. It has shown that these compounds have a high potential for drug development [24]. Zhou et al., prepared and optimised a series of pteridine-7(8*H*)-dione derivatives and assessed their suppressor potential against wild-type epidermal growth factor receptor (EGFR^{WT}) and the mutant-type (EGFR$^{L858R/T790M}$). Compound **VI** (Figure 2) was the most effective in the series, suppressing both mutant enzyme EGFR$^{L858R/T790M}$ (IC$_{50}$ = 0.68 nM) and wild EGFR^{WT} (IC$_{50}$ = 1.21 nM) [25].

In the context of cancer, molecular docking can be used to identify potential drugs that could target specific proteins involved in cancer cell growth and survival, such as oncogenes or proteins involved in angiogenesis. By identifying molecules that bind to these targets with high affinity, researchers can develop drugs that specifically target cancer cells, while minimizing side effects. However, it is important to note that molecular docking is only a computational prediction and must be validated experimentally. It is also limited by the accuracy of the protein structure and the quality of the small molecule library used for screening. Therefore, molecular docking should be considered a complementary tool in drug discovery rather than a replacement for experimental methods.

In keeping with our previous investigations on the anti-proliferative aspects of purine-based derivatives [16,20,21], and inspired by the promising anti-proliferative and EGFR inhibitory activities of pteridine derivatives [25], we present the synthesis and design of two series of new compounds, **5a**–**e** and **7a**–**f** (Figure 3). The newly synthesized elements are from two different scaffolds. Scaffold A elements **5a**–**e** were purine-based derivatives with a spiro moiety in their backbone structure. The second series consists of pteridine-based derivatives **7a**–**f**. Four distinct cancer cell lines were used to assess the newly created chemicals' anti-proliferative ability. Furthermore, the most potent elements from the two series were studied further for their suppressive impact on BRAF^{V600E} and EGFR. Molecular docking analysis was utilised to evaluate how these molecules attach to the active sites of BRAF^{V600E} and EGFR.

5a-e (Scaffold A)   **7a-f (Scaffold B)**
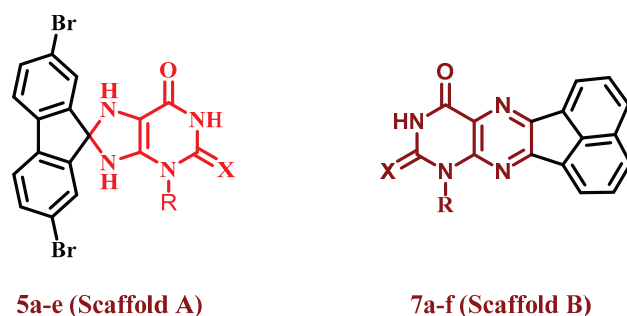
Figure 3. Structures of target compounds **5a–e** and **7a–f**.

2. Results and Discussion

2.1. Chemistry

Scheme 1 depicts the synthetic route used to synthesize purine-based derivatives **5a–e**. In situ, nitrosation of 6-amino-1-alkyluracils **1a–f** [21,26,27] with HNO_2 afforded compounds **2a–f** in high yields, which were then reduced with ammonium sulphide to produce 5,6-diaminouracils **3a–f**. The nucleophilic attack of the amino group of diaminouracils **3a–e** on the carbonyl group of 2,7-dibromo-9*H*-fluoren-9-one (**4**) takes place to form intermediate **VII** followed by the elimination of a water molecule to form intermediate **VIII** (Scheme 2), which underwent intramolecular aza-Michael addition that resulted in the formation of compounds **5a–e** in reasonable yields (59–68%). The structures of compounds **5a–e** were completely consistent with their ^{1}H NMR, ^{13}C NMR, mass spectra, and elemental analyses, with compound **5a** used as an example to discuss structure confirmation. The ^{1}H NMR spectrum of **5a** revealed the disappearance of the signals of the 5,6-diamino-groups at δ_H 6.0–7.5 ppm and the appearance of characteristic protons of the two NH of the dihydropurine ring at δ_H 7.50 and 7.19 ppm. In addition to the appearance of a spiro carbon characteristic signal in the ^{13}C NMR spectrum at δ 102.1 ppm. Compound **5a** has a molecular weight of 476 based on elemental analysis. The molecular ion peak in the mass spectrum of **5a** corresponds to the molecular weight of $m/z = 476$, with the appearance of M$^+$ + 2 at $m/z = 478$ and M$^+$ + 4 at $m/z = 480$.

1a–e   **2a–e**   **3a–e**

3a–e   **4**   **5a–e**

1,2,3,5 a   X=O, R= Me
b   X=O, R= Et
c   X=S, R= Me
d   X=O, R= Bn
e   X=O, R= 2-Cl.Bn
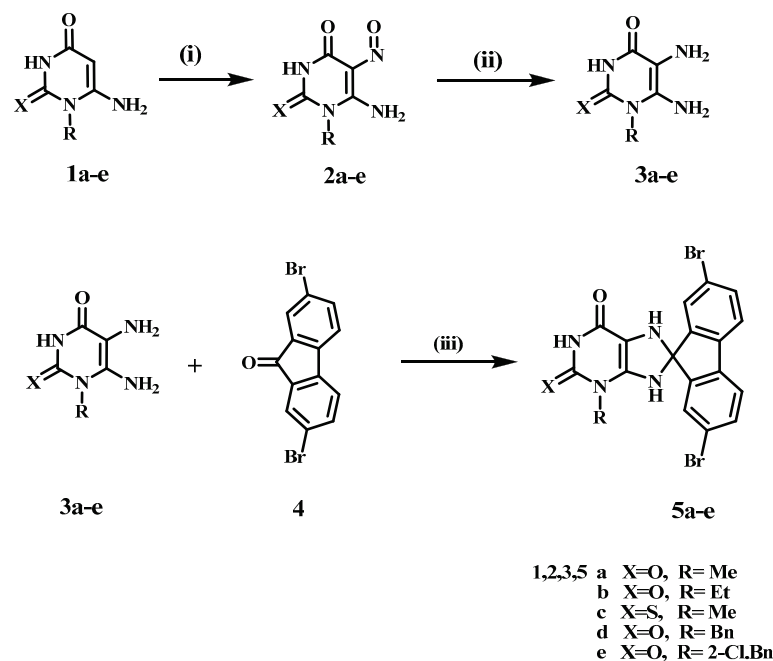
Scheme 1. Synthesis of compounds **5a–e**. Reagents and conditions: (i) HNO_2, r.t., 30 min; (ii) $(NH_4)_2S$, 75 °C, 15 min, (iii) DMF, heat under fusion for 20 min, 59–68%.
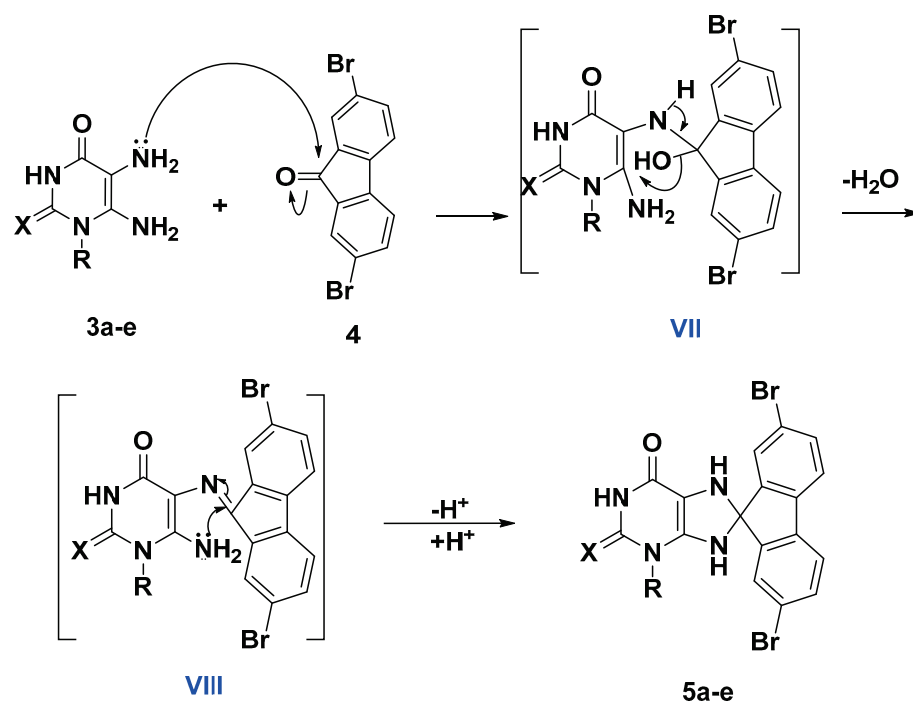
Scheme 2. Proposed mechanism for the formation of compounds **5a–e**.

Scheme 3 describes the synthesis of acenaphtho [1,2-*g*] pteridines **7a–f**. Ram and Pandy previously prepared compounds **7a** and **7d** by dissolving diaminouracil hydrochloride salts in water and then refluxing with acenaphthoquinone **6** in acetic acid for 6 h [28]. In the current study, we prepared compounds **7a–f** by condensation of 5,6-diaminouracils **3a–f** with acenaphthoquinone (**6**) under reflux conditions for 4 h in the presence of catalytic amounts of acetic acid (yields 60–71%). Another method for preparing compounds **7a–f** was to heat under fusion 5,6-diaminouracils **3a–f** with acenaphthoquinone (**6**) for 15 min in presence of drops of DMF, which resulted in slightly higher yields (69–79%). Compounds **7a–f** elemental analyses, NMR, and mass spectra all agreed with the assigned product structures. The disappearance of the two NH$_2$ group signals of uracils and the appearance of the deshielded aromatic protons was revealed by ^{1}H NMR. Furthermore, the characteristic signal of uracil NH was found at δ 11.63–12.16 ppm, as well as thiouracil NH at δ 13.09 ppm.

3a-f + **6** → **7a-f**

method A; 60-71% yield
method B; 69-79% yield
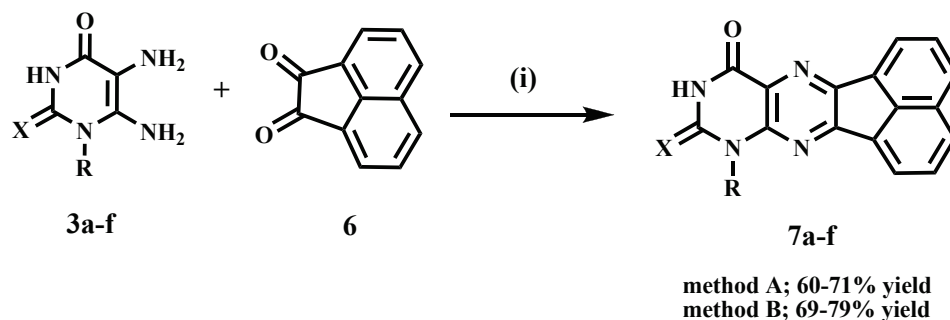
3, 7	a	X=O,	R= Me
	b	X=O,	R= Et
	c	X=S,	R= Me
	d	X=O,	R= Bn
	e	X=O,	R= 2-Cl.Bn
	f	X=O,	R= H

Scheme 3. Synthesis of compounds **7a–f**. Reagents and conditions: (i) Method (A) AcOH, reflux, 4 h. Method (B) heating under fusion for 15 min.

2.2. Biology

2.2.1. Cell Viability Assay

To evaluate the survivability of novel substances, the human mammary gland epithelial (MCF-10A) cell line was utilized [29,30]. The vitality of compounds **5a–e** and **7a–f** was assessed using the MTT method after incubation on MCF-10A cells for four days. Cell viability at 50 μM was more than 88% for all of the agents evaluated, according to Table 1, and none of the substances evaluated had any harmful impacts.

Table 1. IC_{50} of compounds **5a–e** and **7a–f**.
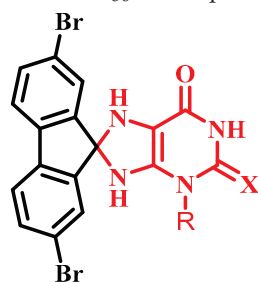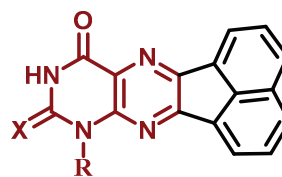
5a-e (Scaffold A)   **7a-f (Scaffold B)**

Comp.	R	X	Cell Viability %	Anti-Proliferative Activity $IC_{50} \pm$ SEM (nM)				
				A-549	MCF-7	Panc-1	HT-29	Average (GI_{50})
5a	Me	O	89	36 ± 3	40 ± 3	38 ± 3	38 ± 3	38
5b	Et	O	91	85 ± 8	88 ± 8	86 ± 8	86 ± 8	86
5c	Me	S	90	98 ± 9	103 ± 10	100 ± 9	102 ± 10	101
5d	Bn	O	91	52 ± 5	55 ± 5	54 ± 5	52 ± 5	53
5e	2-Cl-Bn	O	89	44 ± 4	48 ± 4	46 ± 4	46 ± 4	46
7a	Me	O	92	56 ± 5	60 ± 6	58 ± 5	58 ± 5	58
7b	Et	O	90	64 ± 6	69 ± 6	66 ± 6	68 ± 6	67
7c	Me	S	89	80 ± 8	83 ± 8	80 ± 8	80 ± 8	81
7d	Bn	O	91	90 ± 9	96 ± 9	90 ± 9	92 ± 9	92
7e	2-Cl-Bn	O	88	41 ± 4	46 ± 4	44 ± 4	44 ± 4	44
7f	H	O	90	76 ± 7	79 ± 7	75 ± 7	75 ± 7	76
Erlotinib	-	-	ND	30 ± 3	40 ± 3	30 ± 3	30 ± 3	33

2.2.2. Anti-Proliferative Assay

With erlotinib serving as the reference medication, the MTT assessment was utilized to evaluate the anti-proliferative effect of **5a–e** and **7a–f** against four human cancer cell lines: HT-29 (colon cancer cell line), Panc-1 (pancreatic cancer cell line), A-549 (lung cancer cell line), and MCF-7 (breast cancer cell line) [31–33]. Table 1 reveals the median inhibitory concentration (IC_{50}).

Compounds **5a–e** "Scaffold A" and **7a–f** "Scaffold B" demonstrated promising antiproliferative effect, with GI_{50} ranging from 38 nM to 101 nM for **5a–e** and 44 nM to 92 nM for **7a–f**. All were less effective than the reference erlotinib (GI_{50} = 33 nM). With a GI_{50} value of 38 nM against the four cancer cell lines evaluated, molecule **5a** (R = Me, X = O, Scaffold A) was the most effective of all synthesized derivatives and was equivalent to the reference drug erlotinib.

Substitution of the oxygen atom at position 2 of compound **5a** with a sulphur atom results in compound **5c** (R = Me, X = S, Scaffold A), which has significantly reduced antiproliferative activity, with a GI_{50} value of 101 nM, being 2.7 times less effective than **5a**,

suggesting the significance of the oxygen atom at position 2 of "Scaffold A" compounds for anti-proliferative action. The same pattern holds true when the methyl group at position 3 of compound **5a** is replaced with an ethyl group as in molecule **5b** (R = Et, X = O, Scaffold A), resulting in a marked reduction in anti-proliferative action with a GI_{50} of 86 nM, making **5b** 2.3-fold less effective than **5a**. These results revealed the significance of both the oxygen atom in the second position and the methyl group in the third position of Scaffold A compounds for antiproliferative activity.

Surprisingly, compounds **5d** (R = Bn, X = O, Scaffold A) and **5e** (R = 2-Cl-Bn, X = O, Scaffold A) where the methyl group in compound **5a** has been replaced by benzyl and 2-chlorobenzyl moieties, respectively, revealed encouraging anti-proliferative action, with GI_{50} values of 50 nM and 46 nM, respectively, being 1.4-fold and 1.2-fold less effective than **5a**, but much stronger than the ethyl derivative, **5b** (GI_{50} = 86 nM). These findings suggest that the nature of the third-position substitution in Scaffold A compounds plays a significant role in anti-proliferative activity, with activity increasing in the order: methyl > 2-chlorobenzyl > benzyl > ethyl.

As previously stated, "Scaffold B" compounds **7a–f** demonstrated moderate antiproliferative effect, with GI_{50} values ranging from 44 nM to 92 nM. Compound **7e** (R = 2-chlorobenzyl, X = O, Scaffold B) was the most significant derivative in this series, with a GI_{50} value of 44 nM versus the four cancer cell lines evaluated, but it was 1.3-fold less effective than the reference erlotinib. Molecule **7e** was similar to its congener **5e**, which has the same substitution pattern but with Scaffold A" in its backbone structure.

Compound **7a** (R = Me, X = O, Scaffold B) demonstrated moderate anti-proliferative action with a GI_{50} value of 58 nM, being 1.5-fold less potent than its congener **5a** (R = Me, X = O, Scaffold A). Once again, the replacement of the methyl group in **7a** with the ethyl group in **7b** (R = Et, X = O, Scaffold B) led to a reduction in anti-proliferative effect, with a GI_{50} value of 67 nM for **7b**. Furthermore, replacing the oxygen atom with a sulphur atom, as in compound **7c** (R = Me, X = S, Scaffold B), reduces activity, with **7c**; GI_{50} equal to 81 nM.

Compounds **7d** (R = benzyl, X = O, Scaffold B) and **7e** (R = 2-chlorobenzyl, X = O, Scaffold B), in which the methyl group in **7a** was replaced by benzyl and *o*-chlorobenzyl moiety, respectively, demonstrated a significant difference in anti-proliferative activity. Compound **7d** demonstrated a marked decrease in anti-proliferative action with a GI_{50} value of 92 nM, being 1.5-fold less effective than **7a**, whereas **7e** outperformed **7a** in activity with a GI_{50} value of 44 nM.

Finally, the unsubstituted derivative, **7f** (R = H, X = O, Scaffold B), showed weak anti-proliferative action with a GI_{50} value of 76 nM, being 1.3-fold less effective than the methyl derivative, **7a** (R = Me, X = O, Scaffold A), indicating that the free NH group in the third position is not favoured for activity. Unfortunately, due to a lack of a sufficient number of compounds, such a rule cannot be generalized, necessitating further research on this topic in the future.

2.2.3. EGFR Inhibitory Assay

The most potential anti-proliferative derivatives, **5a**, **5d**, **5e**, **7a**, and **7e**, were further assessed for their suppressive effect against EGFR, as a possible molecular target for their mechanism of action [34,35]. Table 2 lists the IC_{50} values against erlotinib, which was utilized as a reference.

The compounds assessed revealed promising EGFR inhibitory action, with IC_{50} values ranging from 87 nM to 112 nM, in contrast to erlotinib that has an IC_{50} value of 80 nM. The results of this assay are the same as the results of the anti-proliferative assay, where compound **5a** (R = Me, X = O, Scaffold A), the most potent anti-proliferative agent, was determined to be the most effective EGFR suppressor, with an IC_{50} value of 87 ± 07 nM, equal to erlotinib (IC_{50} = 80 nM).

Table 2. IC$_{50}$ of compounds **5a**, **5d**, **5e**, **7a**, and **7e** against EGFR and BRAF^{V600E}.

Compd.	EGFR Inhibition IC$_{50}$ ± SEM (nM)	BRAF^{V600E} Inhibition IC$_{50}$ ± SEM (nM)
5a	87 ± 07	92 ± 07
5d	105 ± 09	164 ± 15
5e	98 ± 08	137 ± 12
7a	112 ± 10	183 ± 17
7e	92 ± 07	109 ± 09
Erlotinib	80 ± 05	60 ± 05

Molecules **7e** (R = 2-chlorobenzyl, X = O, Scaffold B) and **5e** (R = 2-chlorobenzyl, X = O, Scaffold A) ranked second and third in terms of action with comparable IC$_{50}$ values of 92 ± 07 and 98 ± 08, respectively. Finally, compounds **5d** (R = benzyl, X = O, Scaffold A) and **7a** (R = Me, X = O, Scaffold B) showed weak EGFR suppressive action with IC$_{50}$ values greater than 100 nM. These findings imply that EGFR can be a potential target for compounds **5a**, **5e**, and **7e**, which required more in-depth structural investigation to obtain a lead compound for future development.

2.2.4. BRAF^{V600E} Inhibitory Assay

Molecules **5a**, **5d**, **5e**, **7a**, and **7e** were further explored as potential BRAF^{V600E} inhibitors [36]. Table 2 shows the IC$_{50}$ values in comparison to erlotinib that was utilized as a control. Findings from Table 2 revealed that the assessed molecules had weak BRAF^{V600E} suppressive action, with IC$_{50}$ values ranging from 92 nM to 183 nM, being at least 1.5-fold less effective than erlotinib (IC$_{50}$ = 60 nM). Once again, compound **5a**, the most potent derivative in both the anti-proliferative assay and EGFR suppressive assay, was the most effective derivative against BRAF^{V600E} (IC$_{50}$ = 92 ± 07 nM). These results suggest that BRAF may not be a viable target for this group of organic molecules.

2.3. Docking Study

The most effective molecules **5a**, **5d**, **5e**, **7a**, and **7e** were selected for further study of their probability of interaction modes through active sites of EGFR and BRAF using erlotinib as a reference compound. Molecular docking simulations inside the EGFR active site were used to evaluate the "Scaffold A" group's potency as EGFR inhibitors, as shown in Table 3. Compound **5a** revealed the greatest docking scores −7.05 and −6.69 (S; kcal/mol) within the five test compounds compared to the reference compound (erlotinib) at −7.06 and −8.02, respectively.

Table 3. Binding Interactions of **5a**, **5d**, **5e**, **7a**, **7e** and erlotinib within the EGFR (PDB ID: 1M17) active sites.

	5a	5c	5d	5e	7a	7c	7e	Erlotinib
				EGFR (PDB ID): 1M17				
S (kcal/mol)	−7.05	−5.53	−6.34	−4.75	−6.28	−4.9	−6.70	−7.06
RMSD (Å)	1.44	1.53	1.39	1.9	1.43	2.	1.84	0.75
Amino acids residues binding interactions and their bond length (Å)	2Met 742 (3.61) [c] Asp 831 (3.0) [a]	Asp 776 (3.53) [c] Gly 695 (3.37) [a]	Asp 776 (3.57) [c] Gly 695 (3.41) [b]	Leu 694 (4.13) [b]	Glu 738 (3.43) [c] Met 742 (4.11) [c]	Lys 721 (2.97) [a], 2 Val 702 (4.26) [b]	Lys 721 (2.80) [a] Val 702 (3.98) [b]	Met 769 (2.70) [a] H$_2$O 10 (2.78) [a] Lys 721 (4.62) [b]

[a] H-acceptor; [b] pi-H; [c] H-donor.

The five test compounds' best docking positions with the co-crystallized ligand (erlotinib) revealed stability of the compounds within the cavity of the active sites with a number of H-bonds and pi-H hydrophobic interactions with several residues of amino acids around the active site, as illustrated in Figure 4 (See also Supplementary File, Figure S12) Compound **5a** within the active sites of EGFR has three hydrogen bonds with Met

742 and Asp 831 whereas erlotinib forms two hydrogen bonds with Met 769 and a water molecule and a pi-H hydrophobic interaction with Lys 721.
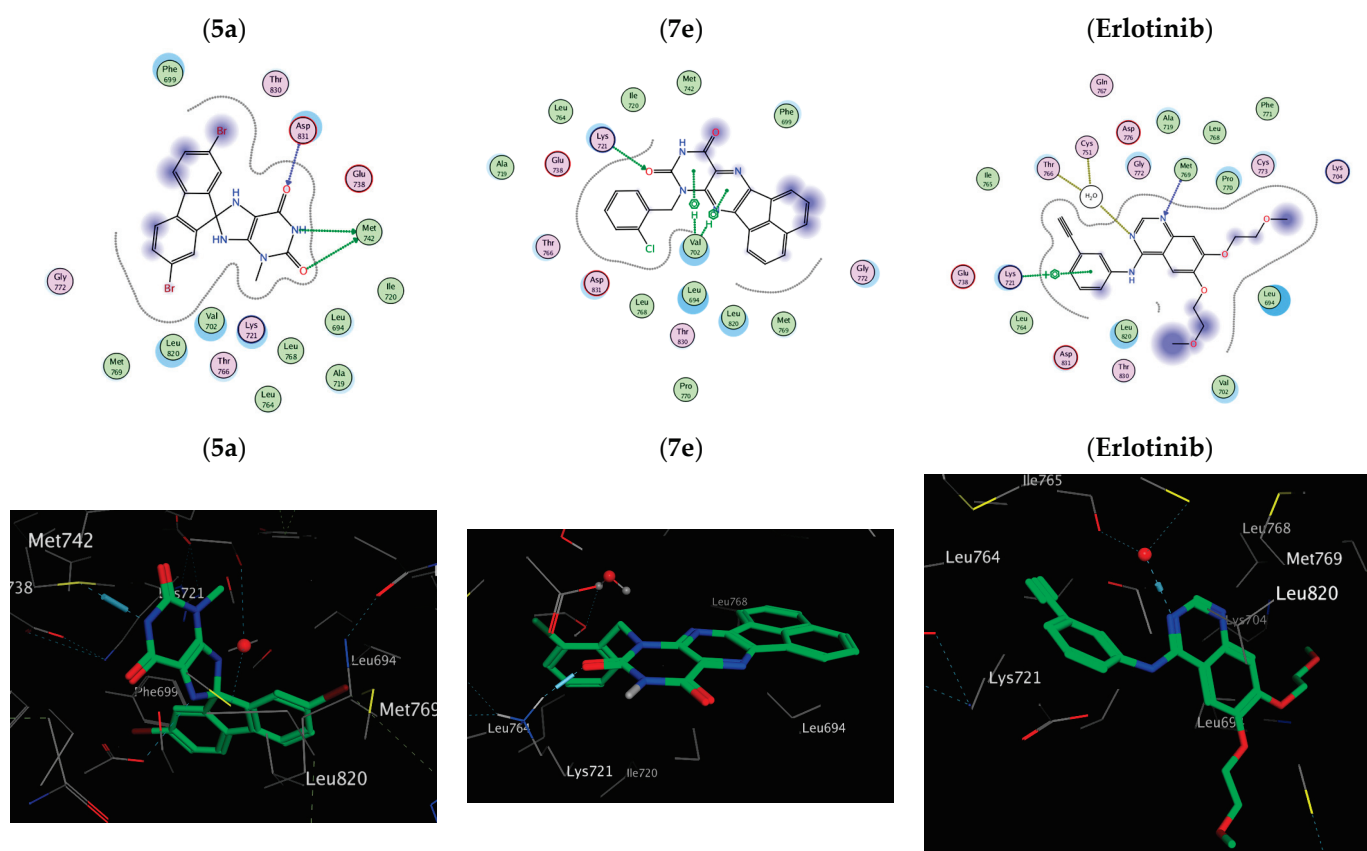
Figure 4. Two-dimensional and three-dimensional interaction diagram of **5a, 7e** and erlotinib within EGFR (PDB ID: 1M17).

On the other hand, compound **5a** within the active sites of BRAF has two hydrogen bonds with Ser 536 and Gly 466 and a pi-H hydrophobic interaction Phe 583. The order of the docking scores fitted with the results of the biochemical tests. Additionally, Substitution of the oxygen atom at position 2 of compounds **5a** and **7a** with a sulphur atom results in compound **5c** and **7c**, respectively where (R = Me, X = S), which showed a reduction in the docking scores (S) in both EGFR active sites (−4.75, −4.95) and BRAF active sites (3.88, 4.92) due to an absence/decrease in hydrogen bonds, Table 4, Figure 5 (See also Supplementary File, Figure S13). Therefore, it is obvious that the stated docking results are in agreement with the biological findings.

Table 4. Binding Interactions of **5a, 5d, 5e, 7a, 7e** and erlotinib within BRAF[V600E] (PDB ID: 5JRQ) active sites.

	5a	5c	5d	5e	7a	7c	7e	Erlotinib
				BRAF[V600E] (PDB ID: 5JRQ)				
S (kcal/mol)	−6.69	−3.88	−5.03	−5.34	−5.82	−4.92	−6.30	−8.02
RMSD (Å)	0.89	1.95	2.02	1.87	1.26	1.79	1.55	1.27
Amino acid residues' binding interactions and their bond length (Å)	Asn 580 (2.94) [c] Lys 578 (3.36) [a]	Ile463 (4.52) [b] Gln 461 (4.38) [b]	Ser 536 (2.74) [a] Phe 583 (3.72) [b]	Ile 463 (3.36) [c]	Thr 529 (3.31) [c] Cys 532 (2.80) [a] Val 471 (4.62) [b]	Ser 535 (4.62) [b] Phe 583 (3.88) [b]	Asp 594 (3.1) [a] Phe 583 (3.85) [b]	Cys 532 (2.95) [a]

[a] H-acceptor; [b] pi-H; [c] H-donor.

(5a)   **(7e)**   **(Erlotinib)**
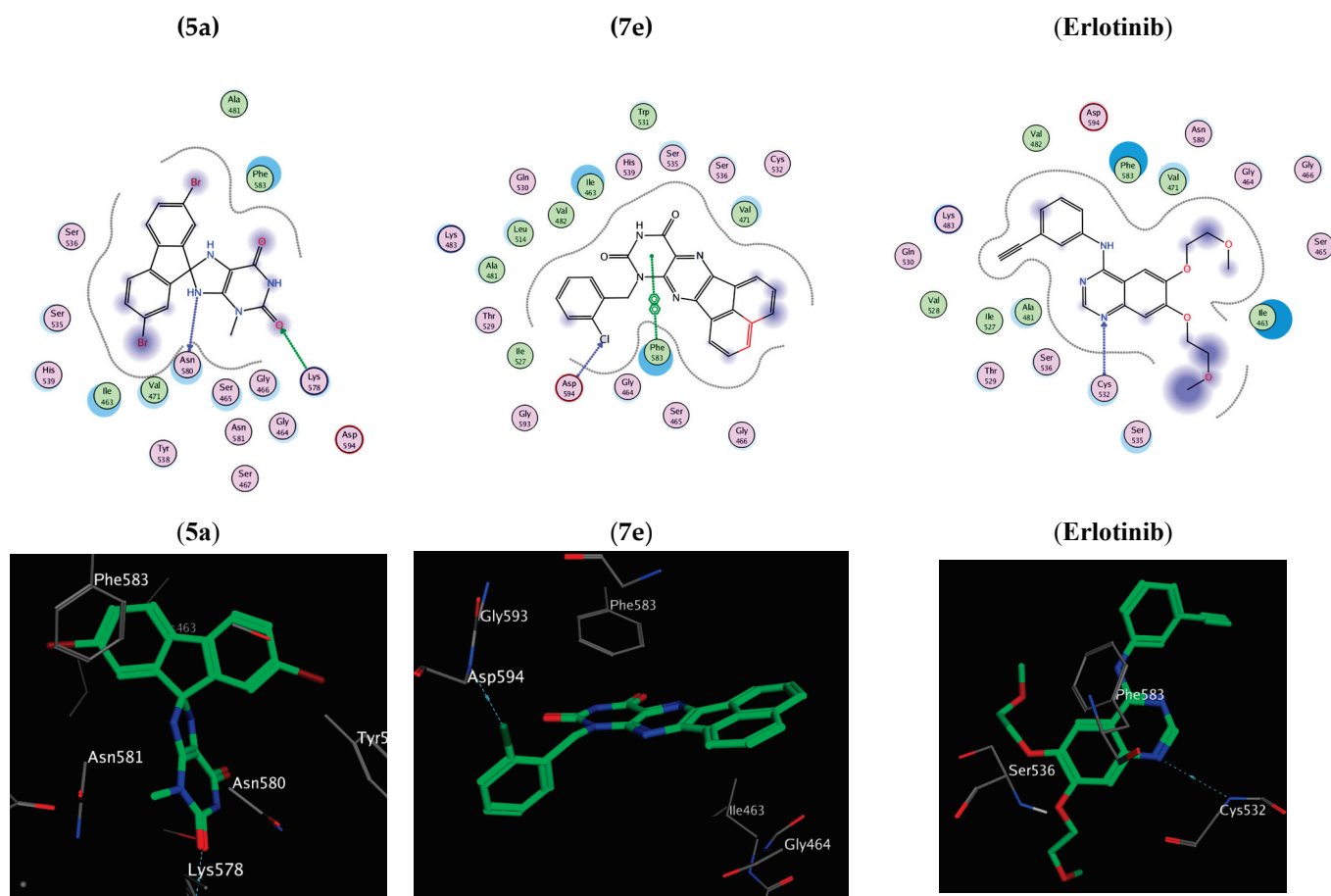
(5a)   **(7e)**   **(Erlotinib)**

Figure 5. Two-dimensional and three-dimensional interaction diagram of **5a, 7e** and **erlotinib** within BRAF[V600E] (PDB ID: 5JRQ).

3. Experimental

3.1. Chemistry

General details: Refer to Supplementary File S1

Compounds 5,6-diaminouracils **3a–f** were prepared according to the reported method [21,26,27].

3.1.1. General Procedures for the Synthesis of 2,7-Dibromo-3′-ethyl-7′,9′-dihydrospiro-[fluorene-9,8′-purines] **5a–e**

A mixture of 5,6-diaminouracils (**3a–e**) (0.9 mmol) and 2,7-Dibromo-9-fluorenone (**4**) (0.9 mmol) and drops of DMF were heated in fusion for 20 min. The residue was treated with an appropriate amount of ethanol. The precipitate was washed with methanol, filtered, and crystallized from DMF.

2,7-Dibromo-3′-methyl-7′,9′-dihydrospiro[fluorene-9,8′-purine]-2′,6′(1′*H*,3′*H*)-dione (**5a**)

Deep orange solid, Yield: 64%; mp > 300 °C; IR (KBr) ν_{max} (cm^{-1}): 3162, 3120 (NH), 3049 (CH Ar), 2839 (CH aliph), 1695 (C=O), 1489 (C=C), 735, 729 (monosubstituted phenyl); ^{1}H NMR (400 MHz, DMSO-d_6) δ_H 11.00 (s, 1H, NH), 8.02 (s, 1H, Ar), 7.74 (d, *J* = 7.8 Hz, 2H, Ar), 7.70–7.62 (m, 1H, Ar), 7.57–7.56 (m, 2H, Ar), 7.50 (s, 1H, NH), 7.19 (s, 1H, NH), 3.38 (s, 3H, CH$_3$) ppm. ^{13}C NMR (DMSO-d_6, 100 MHz) δ_C: 153.7, 153.4, 151.6, 149.3, 140.9, 138.9, 137.7, 134.2, 132.2, 132.0, 130.6, 125.3, 121.8, 121.5, 121.1, 120.7, 102.1, 29.6 ppm. MS: *m/z* (rel. int.) = 480 (M$^+$ + 4, 22), 478 (M$^+$ + 2, 11), 476 (M$^+$, 21), 438 (100), 302 (91), 129 (47). Anal. Calcd for C$_{18}$H$_{12}$Br$_2$N$_4$O$_2$ (476.12): C, 45.41; H, 2.54; N, 11.77; Found: C, 45.59; H, 2.70; N, 11.98%.

2,7-Dibromo-3′-ethyl-7′,9′-dihydrospiro[fluorene-9,8′-purine]-2′,6′(1′*H*,3′*H*)-dione (5b)

Red solid, Yield: 68%; mp > 300 °C; IR (KBr) ν_{max} (cm^{-1}): 3196, 3167 (NH), 3075 (CH Ar), 2977 (CH aliph), 1707, 1622 (C=O), 1516 (C=C), 759, 733 (monosubstituted phenyl); ^{1}H NMR (400 MHz, DMSO-d_6) δ_H 11.01 (s, 1H, NH), 8.04 (s, 1H, Ar), 7.79 (d, *J* = 7.9, 2H, Ar), 7.60 (d, *J* = 7.9 Hz, 2H, Ar), 7.54 (s, 2H, Ar, NH), 7.18 (s, 1H, NH), 3.99 (q, *J* = 6.9 Hz, 2H, CH$_2$), 1.21 (t, *J* = 6.9 Hz, 3H, CH$_3$) ppm. ^{13}C NMR (DMSO-d_6, 100 MHz) δ_C 153.9, 153.2, 152.1, 149.5, 141.3, 139.4, 138.2, 134.7, 132.6, 132.5, 131.1, 125.8, 122.3, 122.0, 121.6, 121.2, 102.4, 37.8, 13.5 ppm. MS: *m/z* (rel. int.) = 494 (M$^+$ + 4, 44), 492 (M$^+$ + 2, 63), 490 (M$^+$, 35), 430 (52), 428 (87), 345 (35), 343 (31), 341 (26), 309 (100), 294 (69), 174 (83). Anal. Calcd for C$_{19}$H$_{14}$Br$_2$N$_4$O$_2$ (490.16): C, 46.56; H, 2.88; N, 11.43; Found: C, 46.82; H, 3.07; N, 11.65%.

2,7-Dibromo-3′-methyl-2′-thioxo-2′,3′,7′,9′-tetrahydrospiro[fluorene-9,8′-purin]-6′(1′*H*)-one (5c)

Brown solid, Yield: 60%; mp: 298–300 °C; IR (KBr) ν_{max} (cm^{-1}): 3184, 3141 (NH), 3050 (CH Ar), 2980, 2837 (CH aliph), 1650 (C=O), 1498 (C=C), 761, 725 (monosubstituted phenyl); ^{1}H NMR (400 MHz, DMSO-d_6) δ_H 12.42 (s, 1H, NH), 8.04 (s, 1H, Ar), 7.79 (d, *J* = 7.9 Hz, 2H, Ar), 7.67–7.59 (m, 2H, Ar), 7.57 (s, 2H, Ar, NH), 7.22 (s, 1H, NH), 3.86 (s, 3H, CH$_3$) ppm. ^{13}C NMR (DMSO-d_6, 100 MHz) δ_C 173.7, 154.1, 152.4, 150.9, 140.5, 139.3, 138.1, 134.2, 132.9, 132.8, 130.7, 125.8, 122.1, 121.8, 121.3, 120.9, 105.7, 36.5 ppm. MS: *m/z* (rel. int.) = 496 (M$^+$ + 4, 18), 492 (M$^+$, 36), 470 (16), 468 (40), 466 (33), 464 (30), 308 (72), 387 (70), 281 (100), 160 (58). Anal. Calcd for C$_{18}$H$_{12}$Br$_2$N$_4$OS (492.19): C, 43.93; H, 2.46; N, 11.38; Found: C, 44.17; H, 2.62; N, 11.60%.

3′-Benzyl-2,7-dibromo-7′,9′-dihydrospiro[fluorene-9,8′-purine]-2′,6′(1′*H*,3′*H*)-dione (5d)

Yellow solid, Yield: 61%; mp >300 °C; IR (KBr) ν_{max} (cm^{-1}): 3154 (NH), 3049, 3030 (CH Ar), 2833 (CH aliph), 1682 (C=O), 1486 (C=C), 756, 735 (monosubstituted phenyl); ^{1}H NMR (400 MHz, DMSO-d_6) δ_H 11.69 (s, 1H, NH), 8.06–8.03 (m, 1H, Ar), 7.90–7.81 (m, 2H, Ar), 7.63–7.58 (m, 2H, Ar), 7.50–7.46 (m, 3H, Ar, NH), 7.40–7.27 (m, 5H, Ar, NH), 5.36–5.19 (dd, 2H, CH$_2$) ppm. ^{13}C NMR (DMSO-d_6, 100 MHz) δ_C 154.9, 154.0, 151.9, 151.0, 148.1, 145.6, 139.6, 138.4, 137.6, 135.3, 129.1 (2), 129.0 (2), 128.9, 128.2, 127.4, 126.8, 124.0, 123.5, 122.1 (2), 100.0, 46.4 ppm. MS: *m/z* (rel. int.) = 556 (M$^+$ + 4, 16), 554 (M$^+$ + 2, 25), 552 (M$^+$, 10), 323 (28), 321 (48), 319 (37), 317 (29), 270 (94), 223 (100), 162 (42). Anal. Calcd for C$_{24}$H$_{16}$Br$_2$N$_4$O$_2$ (552.23): C, 52.22; H, 2.92; N, 10.15; Found: C, 52.46; H, 3.17; N, 10.32%.

2,7-Dibromo-3′-(2-chlorobenzyl)-7′,9′-dihydrospiro[fluorene-9,8′-purine]-2′,6′(1′*H*,3′*H*)-dione (5e)

Bright orange solid, Yield: 59%; mp > 300 °C; IR (KBr) ν_{max} (cm^{-1}): 3183, 3156 (NH), 3056, 3033 (CH Ar), 2837 (CH aliph), 1683 (C=O), 1484 (C=C), 756, 730 (monosubstituted phenyl); ^{1}H NMR (400 MHz, DMSO-d_6) δ_H 11.21 (s, 1H, NH), 8.06 (s, 1H, Ar), 7.84–7.81 (m, 2H, Ar), 7.63 (d, *J* = 6.9 Hz, 2H, Ar), 7.58 (s, 2H, Ar, NH), 7.55–7.53 (m, 1H, Ar), 7.37–7.35 (m, 2H, Ar), 7.31 (s, 1H, NH), 7.10–7.08 (m, 1H, Ar), 5.20 (s, 2H, CH$_2$) ppm. ^{13}C NMR (DMSO-d_6, 100 MHz) δ_C: 153.6, 153.3, 151.6, 148.5, 148.1, 144.1, 143.9, 142.6, 142.4, 138.4, 138.0, 134.0, 127.8, 127.7, 124.1, 123.2, 100.0, 46.5 ppm. MS: *m/z* (rel. int.) = 590 (M$^+$ + 4, 19), 588 (M$^+$ + 2, 17), 586 (M$^+$, 74). Anal. Calcd for C$_{24}$H$_{15}$Br$_2$ClN$_4$O$_2$ (586.67): C, 49.14; H, 2.58; N, 9.55; Found: C, 49.08; H, 2.69; N, 9.73%.

3.1.2. General Procedures for the Synthesis of Acenaphtho[1,2-*g*]pteridines (7a–f)

Method A: A mixture of 5,6-diaminouracils **3a–f** (1.2 mmol) and acenaphthoquinone (**6**) (1.2 mmol) in acetic acid (3 mL) was heated under reflux for 4 h. The formed precipitate was filtered, washed with ethanol and recrystallized from acetic acid.

Method B: A mixture of 5,6-diaminouracils **3a–f** (1.2 mmol) and acenaphthoquinone (**6**) (1.2 mmol) was heated under fusion with drops of DMF for 15 min. An adequate amount of ethanol was added to the residue, the precipitate was filtered and washed with methanol.

8-Methylacenaphtho[1,2-*g*]pteridine-9,11(8*H*,10*H*)-dione (7a)

Canary yellow solid, Yield: method A: 65%, method B: 73%; mp > 300 °C [28]; IR (KBr) ν_{max} (cm^{-1}): 3170 (NH), 3057 (CH Ar), 2961(CH aliph), 1707, 1674 (C=O), 1449 (C=C); ^{1}H NMR (400 MHz, DMSO-d_6) δ_H 11.97 (s, 1H, NH), 8.45 (d, *J* = 7.0 Hz, 1H, Ar), 8.38 (d, *J* = 8.2 Hz, 1H, Ar), 8.35 (d, *J* = 7.0 Hz, 1H, Ar), 8.27 (d, *J* = 8.2 Hz, 1H, Ar), 7.94 (m, 2H, Ar), 3.64 (s, 3H, CH$_3$) ppm. ^{13}C NMR (DMSO-d_6, 100 MHz) δ_C 160.8, 150.6, 149.2, 148.0, 133.8, 132.2, 130.8, 130.3, 130.1, 129.8, 129.7, 129.6, 127.6, 125.9, 124.8, 123.1, 29.0 ppm. MS: *m/z* (rel. int.) = 302 (M$^+$, 11), 270 (64), 212 (45), 162 (100), 65 (67). Anal. Calcd for C$_{17}$H$_{10}$N$_4$O$_2$ (302.29): C, 67.55; H, 3.33; N, 18.53; Found: C, 67.68; H, 3.49; N, 18.80%.

8-Ethylacenaphtho[1,2-*g*]pteridine-9,11(8*H*,10*H*)-dione (7b)

Canary yellow solid, Yield: method A: 64%, method B: 71%; mp > 300 °C; IR (KBr) ν_{max} (cm^{-1}): 3174 (NH), 3080 (CH Ar), 2934 (CH aliph), 1689 (C=O), 1499 (C=C); ^{1}H NMR (400 MHz, DMSO-d_6) δ_H 11.95 (s, 1H, NH), 8.48 (d, *J* = 6.9 Hz, 1H, Ar), 8.39 (d, *J* = 8.2 Hz, 1H, Ar), 8.36 (d, *J* = 6.9 Hz, 1H, Ar), 8.29 (d, *J* = 8.2 Hz, 1H, Ar), 7.99–7.92 (m, 2H, Ar), 4.37 (q, *J* = 7.0 Hz, 2H, CH$_2$), 1.33 (t, *J* = 7.0 Hz, 3H, CH$_3$) ppm. ^{13}C NMR (100 MHz, DMSO) δ_C 160.7, 158.0, 155.7, 150.1, 132.2, 130.8, 130.4, 130.0, 129.9, 129.8, 129.7, 129.5, 124.7, 123.0, 25.1, 13.9 ppm. MS: *m/z* (rel. int.) = 316 (M+, 21), 308 (49), 299 (73), 252(100), 251 (82), 57 (72), 56 (76). Anal. Calcd for C$_{18}$H$_{12}$N$_4$O$_2$ (316.32): C, 68.35; H, 3.82; N, 17.71; Found: C, 68.17; H, 3.98; N, 17.98%.

8-Methyl-9-thioxo-9,10-dihydroacenaphtho[1,2-*g*]pteridin-11(8*H*)-one (7c)

Yellow solid, Yield: method A: 71%, method B: 79%; mp > 300 °C; IR (KBr) ν_{max} (cm^{-1}): 3210 (NH), 3044 (CH Ar), 2935 (CH aliph), 1712 (C=O), 1488 (C=C); ^{1}H NMR (400 MHz, DMSO-d_6) δ_H 13.09 (s, 1H, NH), 8.46–8.25 (m, 4H, Ar), 7.98–7.92 (m, 2H, Ar), 4.08 (s, 3H, CH$_3$) ppm. MS: *m/z* (rel. int.) = 318 (M$^+$, 49), 315 (46), 295 (100), 277 (95), 133 (99), 83 (67). Anal. Calcd for C$_{17}$H$_{10}$N$_4$OS (318.35): C, 64.14; H, 3.17; N, 17.60; Found: C, 64.31; H, 3.40; N, 17.86%.

8-Benzylacenaphtho[1,2-*g*]pteridine-9,11(8*H*,10*H*)-dione (7d)

Deep orange solid, Yield: method A: 70%, method B: 78%; mp > 300 °C [28]; IR (KBr) ν_{max} (cm^{-1}): 3168 (NH), 3044 (CH Ar), 2918 (CH aliph), 1696, 1673 (C=O), 1499 (C=C); ^{1}H NMR (400 MHz, DMSO-d_6) δ_H 12.08 (s, 1H, NH), 8.35 (d, *J* = 7.2 Hz, 2H, Ar), 8.32–8.28 (m, 1H, Ar), 8.23 (d, *J* = 8.6 Hz, 1H, Ar), 7.92–7.89 (m, 2H, Ar), 7.53 (d, *J* = 8.6 Hz, 2H, Ar), 7.33 (t, *J* = 7.8 Hz, 2H, Ar), 7.25 (t, *J* = 7.8 Hz, 1H, Ar), 5.48 (s, 2H, CH$_2$) ppm. ^{13}C NMR (DMSO-d_6, 100 MHz) δ_C 160.7, 155.5, 150.6, 148.4, 137.7, 133.8, 132.3, 130.7, 130.2, 130.1, 129.8, 129.7, 129.5, 128.9, 128.4, 127.7, 125.9, 124.8, 123.1, 44.8 ppm. MS: *m/z* (rel. int.) = 378 (M$^+$, 35), 313 (68), 210 (53), 205 (97), 193 (100), 115 (60). Anal. Calcd for C$_{23}$H$_{14}$N$_4$O$_2$ (378.39): C, 73.01; H, 3.73; N, 14.81; Found: C, 72.93; H, 3.94; N, 14.98%.

8-(2-Chlorobenzyl)acenaphtho[1,2-*g*]pteridine-9,11(8*H*,10*H*)-dione (7e)

Light yellow solid, Yield: method A: 60%, method B: 69%; mp > 300 °C; IR (KBr) ν_{max} (cm^{-1}): 3168 (NH), 3045 (CH Ar), 2845 (CH aliph), 1714, 1679 (C=O), 1497 (C=C); ^{1}H NMR (400 MHz, DMSO-d_6) δ_H 12.16 (s, 1H), 8.39 (d, *J* = 7.6 Hz, 1H, Ar), 8.36 (d, *J* = 8.8 Hz, 1H, Ar), 8.31 (d, *J* = 7.6 Hz, 1H, Ar), 8.29 (d, *J* = 8.8 Hz, 1H, Ar), 7.96–7.90 (m, 2H, Ar), 7.55 (d, *J* = 7.4 Hz, 1H, Ar), 7.35–7.28 (m, 2H, Ar), 7.22 (t, *J* = 7.4 Hz, 1H, Ar), 5.57 (s, 2H, CH$_2$) ppm. ^{13}C NMR (DMSO-d_6, 100 MHz) δ_C 158.3, 151.3, 148.6, 146.2, 141.9, 134.7, 132.2, 130.7, 130.3, 130.2, 130.1, 129.7, 129.6, 129.2, 128.7, 128.6, 128.2, 127.9, 127.8, 126.3, 46.5 ppm. MS: *m/z* (rel. int.) = 414 (M + 2, 12), 412 (M+, 49), 334 (16), 332 (73), 185 (77), 84 (38), 82 (100). Anal. Calcd for C$_{23}$H$_{13}$ClN$_4$O$_2$ (412.83): C, 66.92; H, 3.17; N, 13.57; Found: C, 66.80; H, 3.41; N, 13.79%.

Acenaphtho [1,2-*g*]pteridine-9,11(8*H*,10*H*)-dione (7f)

Yellow solid, Yield: method A: 69%, method B: 77%; mp > 300 °C; IR (KBr) ν_{max} (cm^{-1}): 3208 (NH), 3036 (CH Ar), 2819 (CH aliph), 1688, 1643 (C=O), 1486 (C=C); ^{1}H NMR (400 MHz, DMSO-d_6) δ_H 11.63 (s, 1H, NH), 11.29 (s, 1H, NH), 8.34–8.28 (m, 1H, Ar), 8.17 (m, 1H, Ar), 8.09 (m, 2H, Ar), 7.93–7.76 (m, 2H, Ar) ppm. ^{13}C NMR (DMSO-d_6, 100 MHz)

δ 161.8, 156.4, 150.3, 149.1, 133.8, 132.8, 132.1, 131.0, 130.3, 129.8, 129.7, 129.5, 129.0, 124.5, 122.7, 121.7 ppm. MS: m/z (rel. int.) = 288 (M$^+$, 17), 264 (53), 186 (50), 107 (62), 63 (100). Anal. Calcd for $C_{16}H_8N_4O_2$ (288.27): C, 66.67; H, 2.80; N, 19.44; Found: C, 66.73; H, 2.91; N, 11.65%.

3.2. Biology

3.2.1. Cell Viability Assay

The normal human mammary gland epithelial (MCF-10A) cell line was used to test the viability of new compounds [29,30]. See Supplementary File S1.

3.2.2. Anti-Proliferative Assay

The antiproliferative activity of compounds **5a–e** and **7a–f** was tested against the four human cancer cell lines Panc-1 (pancreatic cancer cell line), MCF-7 (breast cancer cell line), HT-29 (colon cancer cell line), and A-549 (lung cancer cell line) using the MTT assay and erlotinib as the reference drug [11–31]. See Supplementary File S1.

3.2.3. EGFR Inhibitory Assay

Compounds **5a, 5d, 5e 7a**, and **7e** were tested for EGFR inhibitory activity as a potential target for their antiproliferative activity [34,35]. See Supplementary File S1.

3.2.4. BRAF^{V600E} Inhibitory Assay

Compounds **5a**, **5d**, **5e 7a**, and **7e** were further tested for BRAF^{V600E} inhibitory activity as a potential target for their antiproliferative activity [36]. See Supplementary File S1.

3.3. Protocol of Docking Studies

The automated docking simulation study was performed using Molecular Operating Environment (MOE®) version 2014.09. The X-ray crystallographic structure of the target EGFR and BRAF was obtained from the protein data bank (PDB: 1M17, 5JRQ), respectively. The target compounds were constructed in a three-dimensional model using the builder interface of the MOE® program. After checking their structures and the formal charges on atoms by two-dimensional depiction, the following steps were carried out: The target compounds were subjected to a conformational search. All conformers were subjected to energy minimization; all the minimizations were performed with MOE until a RMSD gradient of 0.01 Kcal/mole and RMS distance of 0.1 Å with MMFF94X force-field and the partial charges were automatically calculated. The protein was prepared for docking studies by adding hydrogen atoms to the system with their standard geometry. The atoms connection and type were checked for any errors with automatic correction. Selection of the receptor and its atoms potential were fixed. MOE Alpha Site Finder was used for the active site search in the enzyme structure using all default items. Dummy atoms were created from the obtained alpha spheres [37,38].

4. Conclusions

In summary, two sets of purine/pteridine-based analogues **5a–e** and **7a–f** were designed and synthesised. The newly synthesised compounds were tested for anti-proliferative activity, and compounds **5a**, **5e**, and **7e** were found to be the most effective. SAR analysis revealed that replacing the oxygen atom in position 2 of compounds **5a** or **7a** with a sulphur atom resulted in compounds **5c** and **7c**, which had significantly lower anti-proliferative activity. When compared to erlotinib's IC$_{50}$ value of 80 nM, compounds **5a**, **5e**, and **7e** demonstrated promising EGFR inhibitory activity, with IC$_{50}$ values of 87 nM, 98 nM, and 92 nM, respectively. These findings suggest that EGFR could be a potential target for compounds **5a**, **5e**, and **7e**, which would necessitate more in-depth structural investigation to identify a lead compound for future development. Furthermore, the molecular docking study was performed on the EGFR and BRAF^{V600E} active sites revealing good interactions with the enzymes.

References

1. Stanković, T.; Dinić, J.; Podolski-Renić, A.; Musso, L.; Burić, S.S.; Dallavalle, S.; Pešić, M. Dual Inhibitors as a New Challenge for Cancer Multidrug Resistance Treatment. *Curr. Med. Chem.* **2019**, *26*, 6074–6106. [CrossRef] [PubMed]

2. Raghavendra, N.M.; Pingili, D.; Kadasi, S.; Mettu, A.; Prasad, S.V.U.M. Dual or multi-targeting inhibitors: The next generation anticancer agents. *Eur. J. Med. Chem.* **2018**, *143*, 1277–1300. [CrossRef] [PubMed]

3. Fu, R.-G.; Sun, Y.; Sheng, W.-B.; Liao, D.-F. Designing multi-targeted agents: An emerging anticancer drug discovery paradigm. *Eur. J. Med. Chem.* **2017**, *136*, 195–211. [CrossRef] [PubMed]

4. Zha, G.-F.; Qin, H.-L.; Youssif, B.G.; Amjad, M.W.; Raja, M.A.G.; Abdelazeem, A.H.; Bukhari, S.N.A. Discovery of potential anticancer multi-targeted ligustrazine based cyclohexanone and oxime analogs overcoming the cancer multidrug resistance. *Eur. J. Med. Chem.* **2017**, *135*, 34–48. [CrossRef] [PubMed]

5. Palmeira, A.; Sousa, E.; Vasconcelos, M.H.; Pinto, M.M. Three Decades of P-gp Inhibitors: Skimming Through Several Generations and Scaffolds. *Curr. Med. Chem.* **2012**, *19*, 1946–2025. [CrossRef] [PubMed]

6. Zheng, W.; Zhao, Y.; Luo, Q.; Zhang, Y.; Wu, K.; Wang, F. Multi-targeted anticancer agents. *Curr. Top. Med. Chem.* **2017**, *17*, 3084–3098. [CrossRef] [PubMed]

7. Mahboobi, S.; Sellmer, A.; Winkler, M.; Eichhorn, E.; Pongratz, H.; Ciossek, T.; Baer, T.; Maier, T.; Beckers, T. Novel Chimeric Histone Deacetylase Inhibitors: A Series of Lapatinib Hybrides as Potent Inhibitors of Epidermal Growth Factor Receptor (EGFR), Human Epidermal Growth Factor Receptor 2 (HER2), and Histone Deacetylase Activity. *J. Med. Chem.* **2010**, *53*, 8546–8555. [CrossRef]

8. Bhullar, K.S.; Lagarón, N.O.; McGowan, E.M.; Parmar, I.; Jha, A.; Hubbard, B.P.; Rupasinghe, H.P.V. Kinase-targeted cancer therapies: Progress, challenges and future directions. *Mol. Cancer* **2018**, *17*, 48. [CrossRef]

9. Ho, C.-C.; Liao, W.-Y.; Lin, C.-A.; Shih, J.-Y.; Yu, C.-J.; Yang, J.C.-H. Acquired BRAF V600E Mutation as Resistant Mechanism after Treatment with Osimertinib. *J. Thorac. Oncol.* **2017**, *12*, 567–572. [CrossRef]

10. Hyman, D.M.; Puzanov, I.; Subbiah, V.; Faris, J.E.; Chau, I.; Blay, J.-Y.; Wolf, J.; Raje, N.S.; Diamond, E.L.; Hollebecque, A.; et al. Vemurafenib in Multiple Nonmelanoma Cancers with *BRAF* V600 Mutations. *N. Engl. J. Med.* **2015**, *373*, 726–736. [CrossRef]

11. Desai, J.; Markman, B.; Ananda, S.; Tebbutt, N.C.; Michael, M.; Solomon, B.J.; McArthur, G.A.; Tie, J.; Gibbs, P.; Ritchie, D.; et al. A phase I/II trial of combined BRAF and EGFR inhibition in patients (pts) with BRAF V600E mutated (BRAFm) metastatic colorectal (mCRC): The EViCT (Erlotinib and Vemurafenib in Combination Trial) study. *J. Clin. Oncol.* **2017**, *35*, 3557. [CrossRef]

12. Makower, D.; Malik, U.; Novik, Y.; Wiernik, P.H. Therapeutic efficacy of theophylline in chronic lymphocytic leukemia. *Med. Oncol.* **1999**, *16*, 69–71. [CrossRef]

13. Sabisz, M.; Skladanowski, A. Modulation of cellular response to anticancer treatment by caffeine: Inhibition of cell cycle checkpoints, DNA repair and more. *Curr. Pharm. Biotechnol.* **2008**, *9*, 325–336. [CrossRef] [PubMed]

14. Tenzer, A.; Pruschy, M. Potentiation of DNA-damage-induced cytotoxicity by G2checkpoint abrogators. *Curr. Med. Chem. Anti-Cancer Agents* **2003**, *3*, 35–46. [CrossRef]

15. Lentini, A.; Kleinman, H.K.; Mattioli, P.; Autuori-Pezzoli, V.; Nicoli, L.; Pietrini, A.; Abbruzzese, A.; Cardinali, M.; Beninati, S. Inhibition of melanoma pulmonary metastasis by methylxanthines due to decreased invasion and proliferation. *Melanoma Res.* **1998**, *8*, 131–138. [CrossRef] [PubMed]

16. Hisham, M.; Youssif, B.G.; Osman, E.E.A.; Hayallah, A.M.; Abdel-Aziz, M. Synthesis and biological evaluation of novel xanthine derivatives as potential apoptotic antitumor agents. *Eur. J. Med. Chem.* **2019**, *176*, 117–128. [CrossRef] [PubMed]

17. Kim, D.; Lee, H.; Jun, H.; Hong, S.-S.; Hong, S. Fluorescent phosphoinositide 3-kinase inhibitors suitable for monitoring of intracellular distribution. *Bioorg. Med. Chem.* **2011**, *19*, 2508–2516. [CrossRef]

18. Lee, K.; Jeong, K.-W.; Lee, Y.; Song, J.Y.; Kim, M.S.; Lee, G.S.; Kim, Y. Pharmacophore modeling and virtual screening studies for new VEGFR-2 kinase inhibitors. *Eur. J. Med. Chem.* **2010**, *45*, 5420–5427. [CrossRef]

19. Ruddarraju, R.R.; Murugulla, A.C.; Kotla, R.; Tirumalasetty, M.C.B.; Wudayagiri, R.; Donthabakthuni, S.; Maroju, R.; Baburao, K.; Parasa, L.S. Design, synthesis, anticancer, antimicrobial activities and molecular docking studies of theophylline containing acetylenes and theophylline containing 1,2,3-triazoles with variant nucleoside derivatives. *Eur. J. Med. Chem.* **2016**, *123*, 379–396. [CrossRef]

20. Abou-Zied, H.A.; Youssif, B.G.; Mohamed, M.F.; Hayallah, A.M.; Abdel-Aziz, M. EGFR inhibitors and apoptotic inducers: Design, synthesis, anticancer activity and docking studies of novel xanthine derivatives carrying chalcone moiety as hybrid molecules. *Bioorg. Chem.* **2019**, *89*, 102997. [CrossRef]

21. El-Kalyoubi, S.; Agili, F. Synthesis, In Silico Prediction and In Vitro Evaluation of Antitumor Activities of Novel Pyrido [2,3-*d*] pyrimidine, Xanthine and Lumazine Derivatives. *Molecules* **2020**, *25*, 5205. [CrossRef] [PubMed]

22. Zheng, Y.; Tice, C.M.; Singh, S.B. The use of spirocyclic scaffolds in drug discovery. *Bioorg. Med. Chem. Lett.* **2014**, *24*, 3673–3682. [CrossRef] [PubMed]

23. Carmona-Martínez, V.; Ruiz-Alcaraz, A.J.; Vera, M.; Guirado, A.; Martínez-Esparza, M.; García-Peñarrubia, P. Therapeutic potential of pteridine derivatives: A comprehensive review. *Med. Res. Rev.* **2018**, *39*, 461–516. [CrossRef] [PubMed]

24. Kompis, I.M.; Islam, K.; Then, R.L. DNA and RNA Synthesis: Antifolates. *Chem. Rev.* **2005**, *105*, 593–620. [CrossRef] [PubMed]

25. Zhou, W.; Liu, X.; Tu, Z.; Zhang, L.; Ku, X.; Bai, F.; Zhao, Z.; Xu, Y.; Ding, K.; Li, H. Discovery of Pteridin-7(8*H*)-one-Based Irreversible Inhibitors Targeting the Epidermal Growth Factor Receptor (EGFR) Kinase T790M/L858R Mutant. *J. Med. Chem.* **2013**, *56*, 7821–7837. [CrossRef]

26. El-Kalyoubi, S.; Agili, F.; Zordok, W.A.; El-Sayed, A.S.A. Synthesis, In Silico Prediction and In Vitro Evaluation of Antimicrobial Activity, DFT Calculation and Theoretical Investigation of Novel Xanthines and Uracil Containing Imidazolone Derivatives. *Int. J. Mol. Sci.* **2021**, *22*, 10979. [CrossRef]

27. El-Kalyoubi, S.; Agili, F.; Adel, I.; Tantawy, M.A. Novel uracil derivatives depicted potential anticancer agents: In Vitro, molecular docking, and ADME study. *Arab. J. Chem.* **2022**, *15*, 103669. [CrossRef]

28. Ram, V.J.; Pandey, H.K.; Vlietinck, A.J. Synthesis of 2,4-substituted 6,7-phenanthreno-and 6,7-acenaphthenopteridines. *J. Heterocycl. Chem.* **1981**, *18*, 55–57. [CrossRef]

29. Gomaa, H.A.; Shaker, M.E.; Alzarea, S.I.; Hendawy, O.; Mohamed, F.A.; Gouda, A.M.; Ali, A.T.; Morcoss, M.M.; Abdelrahman, M.H.; Trembleau, L.; et al. Optimization and SAR investigation of novel 2,3-dihydropyrazino[1,2-a]indole-1,4-dione derivatives as EGFR and BRAFV600E dual inhibitors with potent antiproliferative and antioxidant activities. *Bioorg. Chem.* **2022**, *120*, 105616. [CrossRef]

30. Youssif, B.G.; Gouda, A.M.; Moustafa, A.H.; Abdelhamid, A.A.; Gomaa, H.A.; Kamal, I.; Marzouk, A.A. Design and synthesis of new triarylimidazole derivatives as dual inhibitors of BRAFV600E/p38α with potential antiproliferative activity. *J. Mol. Struct.* **2021**, *1253*, 132218. [CrossRef]

31. Mahmoud, M.A.; Mohammed, A.F.; Salem, O.I.; Gomaa, H.A.; Youssif, B.G. New 1,3,4-oxadiazoles linked with the 1,2,3-triazole moiety as antiproliferative agents targeting the EGFR tyrosine kinase. *Arch. Pharm.* **2022**, *355*, 2200009. [CrossRef] [PubMed]

32. Mahmoud, M.A.; Mohammed, A.F.; Salem, O.I.; Rabea, S.M.; Youssif, B.G. Design, synthesis, and antiproliferative properties of new 1,2,3-triazole-carboximidamide derivatives as dual EGFR/VEGFR-2 inhibitors. *J. Mol. Struct.* **2023**, *1282*, 135165. [CrossRef]

33. Mekheimer, R.A.; Allam, S.M.; Al-Sheikh, M.A.; Moustafa, M.S.; Al-Mousawi, S.M.; Mostafa, Y.A.; Youssif, B.G.; Gomaa, H.A.; Hayallah, A.M.; Abdelaziz, M.; et al. Discovery of new pyrimido [5,4-c] quinolines as potential antiproliferative agents with multitarget actions: Rapid synthesis, docking, and ADME studies. *Bioorg. Chem.* **2022**, *121*, 105693. [CrossRef]

34. Abdel-Aziz, S.A.; Taher, E.S.; Lan, P.; Asaad, G.F.; Gomaa, H.A.; El-Koussi, N.A.; Youssif, B.G. Design, synthesis, and biological evaluation of new pyrimidine-5-carbonitrile derivatives bearing 1,3-thiazole moiety as novel anti-inflammatory EGFR inhibitors with cardiac safety profile. *Bioorg. Chem.* **2021**, *111*, 104890. [CrossRef] [PubMed]

35. Mohamed, F.A.; Gomaa, H.A.; Hendawy, O.; Ali, A.T.; Farghaly, H.S.; Gouda, A.M.; Abdelazeem, A.H.; Abdelrahman, M.H.; Trembleau, L.; Youssif, B.G. Design, synthesis, and biological evaluation of novel EGFR inhibitors containing 5-chloro-3-hydroxymethyl-indole-2-carboxamide scaffold with apoptotic antiproliferative activity. *Bioorg. Chem.* **2021**, *112*, 104960. [CrossRef] [PubMed]

36. El-Sherief, H.A.; Youssif, B.G.; Abdelazeem, A.H.; Abdel-Aziz, M.; Abdel-Rahman, H.M. Design, synthesis and antiproliferative evaluation of novel 1, 2, 4-triazole/schiff base hybrids with EGFR and B-RAF inhibitory activities. *Anti-Cancer Agents Med. Chem.* **2019**, *19*, 697–706. [CrossRef] [PubMed]

37. Ibrahim, T.S.; Bokhtia, R.; Al-Mahmoudy, A.M.; Taher, E.S.; AlAwadh, M.; Elagawany, M.; Abdel-Aal, E.H.; Panda, S.; Gouda, A.M.; Asfour, H.Z.; et al. Design, synthesis and biological evaluation of novel 5-((substituted quinolin-3-yl/1-naphthyl) methylene)-3-substituted imidazolidin-2,4-dione as HIV-1 fusion inhibitors. *Bioorg. Chem.* **2020**, *99*, 103782. [CrossRef]

38. Shaykoon, M.S.; Marzouk, A.A.; Soltan, O.M.; Wanas, A.S.; Radwan, M.M.; Gouda, A.M.; Youssif, B.G.; Abdel-Aziz, M. Design, synthesis and antitrypanosomal activity of heteroaryl-based 1,2,4-triazole and 1,3,4-oxadiazole derivatives. *Bioorg. Chem.* **2020**, *100*, 103933. [CrossRef]

Article

One-Pot Synthesis of 1-Thia-4-azaspiro[4.4/5]alkan-3-ones via Schiff Base: Design, Synthesis, and Apoptotic Antiproliferative Properties of Dual EGFR/BRAF^{V600E} Inhibitors

Lamya H. Al-Wahaibi [1], Essmat M. El-Sheref [2], Mohamed M. Hammouda [3,4] and Bahaa G. M. Youssif [5,*]

[1] Department of Chemistry, College of Sciences, Princess Nourah Bint Abdulrahman University, Riyadh 11564, Saudi Arabia
[2] Chemistry Department, Faculty of Science, Minia University, El Minia 61519, Egypt
[3] Department of Chemistry, College of Science and Humanities in Al-Kharj, Prince Sattam Bin Abdulaziz University, Al-Kharj 11942, Saudi Arabia
[4] Chemistry Department, Faculty of Science, Mansoura University, Mansoura 35516, Egypt
[5] Pharmaceutical Organic Chemistry Department, Faculty of Pharmacy, Assiut University, Assiut 71526, Egypt
[*] Correspondence: bahaa.youssif@pharm.aun.edu.eg or bgyoussif2@gmail.com; Tel.: +20-109-829-4419

Abstract: In this investigation, novel 4-((quinolin-4-yl)amino)-thia-azaspiro[4.4/5]alkan-3-ones were synthesized via interactions between 4-(2-cyclodenehydrazinyl)quinolin-2(1*H*)-one and thioglycolic acid catalyzed by thioglycolic acid. We prepared a new family of spiro-thiazolidinone derivatives in a one-step reaction with excellent yields (67–79%). The various NMR, mass spectra, and elemental analyses verified the structures of all the newly obtained compounds. The antiproliferative effects of **6a–e**, **7a**, and **7b** against four cancer cells were investigated. The most effective antiproliferative compounds were **6b**, **6e**, and **7b**. Compounds **6b** and **7b** inhibited EGFR with IC$_{50}$ values of 84 and 78 nM, respectively. Additionally, **6b** and **7b** were the most effective inhibitors of BRAF^{V600E} (IC$_{50}$ = 108 and 96 nM, respectively) and cancer cell proliferation (GI$_{50}$ = 35 and 32 nM against four cancer cell lines, respectively). Finally, the apoptosis assay results revealed that compounds **6b** and **7b** had dual EGFR/BRAF^{V600E} inhibitory properties and showed promising antiproliferative and apoptotic activity.

Keywords: thioglycolic acid; schiff base; spiro; apoptosis; antiproliferative; mechanism

1. Introduction

The development of new drugs in anti-cancer research depends on a better understanding of druggable targets. According to this strategy, changing particular cancer biomarkers will produce beneficial therapeutic effects [1]. Selective anti-cancer medications must be more effective at destroying tumors while having fewer side effects on normal cells [2]. Single-target therapy has been recognized as causing chemotherapeutic resistance [3]. Recently, combination therapy (drug cocktails combining two or more therapeutic agents with different modes of action and non-overlapping toxicities) was authorized as an alternative to single-target chemotherapy for cancer [4]. Despite the possibility of additive and synergistic effects, combination therapy frequently results in unexpected adverse effects, such as increased toxicity. Alternatives to combination therapy include drugs with two or more targets, a reduced risk of drug interactions, enhanced pharmacokinetics (PK), and improved safety profiles [5]. Additionally, a dual-target kinase may inhibit drug interactions, harmful off-target impacts, poor patient compliance, and elevated costs of production [5].

Combining tyrosine kinase (TK) and BRAF inhibitors has proven useful in preventing tumor growth and minimizes resistance in clinical trials. Combining vemurafenib and EGFR inhibitors in thyroid carcinoma may help overcome resistance to BRAF inhibitors [6]. This combination has also been effective in BRAF^{V600E} colorectal cancer [7]. Additionally, several in vitro substances have been developed, including EGFR/VEGFR-2 and

BRAF, which contain the essential pharmacophoric groups necessary to suppress tyrosine kinase [8,9]. In summary, dual/multi-targeted kinase inhibitors can be turned into effective anti-cancer medications [10].

In medicinal chemistry, nitrogen heterocycles are crucial structural components. The chemical and biological uses of quinoline, one of many heterocyclic compounds, have been studied by numerous research groups [11,12]. The FDA recently approved quinazoline derivatives, such as gefitinib and erlotinib (Figure 1), as EGFR inhibitors for treating non-small cell breast and lung cancers [13–15]. In addition, Thr766 in the EGFR pocket forms a water-mediated hydrogen bond with the nitrogen atom at position 3 of the quinazoline core [16,17]. New quinoline derivatives, such as pelitinib and neratinib, which are potent EGFR inhibitors, were developed through the bioisosteric replacement of the quinazoline core with a quinoline ring (Figure 1) [18–22]. The bioisosteric substitution did not require water molecules to facilitate the interaction with amino acid residue Thr766 [23].
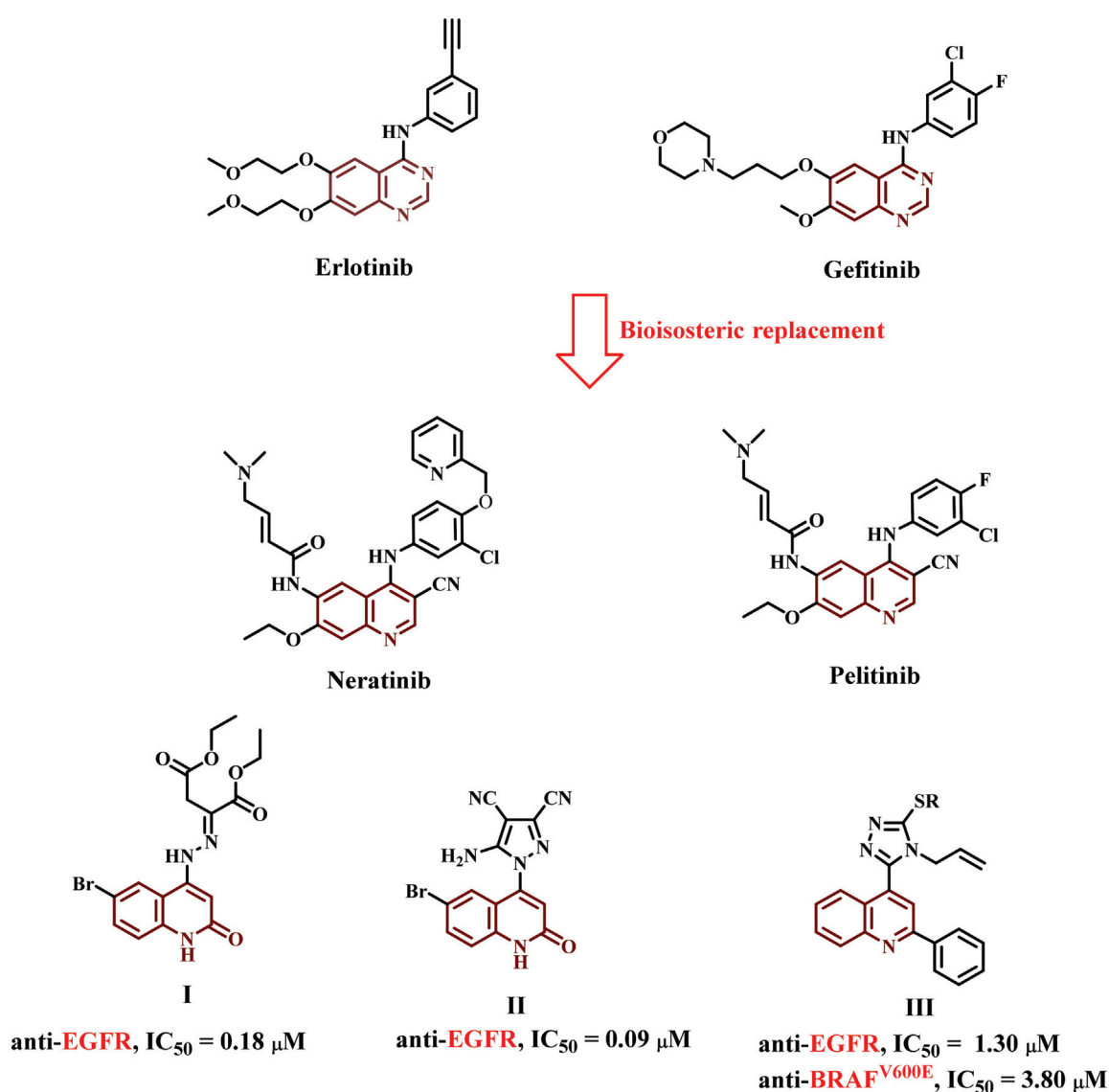
Figure 1. Structure of Erlotinib, Gefitinib, Neratinib, Pelitinib, and compounds **I**–**III**.

We previously reported synthesizing two novel series of quinoline-2-one-based derivatives as potential apoptotic antiproliferative agents targeting the EGFR inhibitory pathway [24]. Compounds **I** and **II** (Figure 1) inhibited EGFR effectively, with IC$_{50}$ values of 0.18 and 0.09 µM, respectively. Furthermore, the two compounds significantly increased the

apoptotic markers caspase-3, caspase-8, and the Bax levels while decreasing antiapoptotic Bcl2. In another study [25], compound **III**, a quinoline-based derivative, was developed as a dual EGFR and BRAF^{V600E} inhibitor with IC$_{50}$ values of 1.30 and 3.8 μM, respectively.

The Spiro scaffold is another building material with potential applications in medicinal chemistry. Chemists have introduced a ring for rigidity when designing new drugs to potentially reduce the entropic penalties upon binding to target proteins. Conformational restriction can also be achieved by spiro ring fusion. They are frequently used in the design and discovery of drugs due to their inherent three-dimensionality and novel structural characteristics. Previously, spiro ring systems were efficiently integrated into enzyme inhibitors, with kinases topping the list, as well as protein–protein interaction inhibitors [26–28].

On the other hand, the thiazole moiety has piqued researchers' interest due to its robust biological properties [29,30]. Regarding anti-cancer activity, thiazole and its derivatives rank among the most active compounds [31–36]. Furthermore, several clinically available anti-cancer drugs contain thiazole-containing compounds, such as dabrafenib (**IV**, Figure 2) (BRAF inhibitor) [37].

Dabrafenib (IV)
BRAF^{V600E} inhibitor

(V)
BRAF^{V600E} inhibitor
IC$_{50}$ = 0.05 μM

VI
BRAF^{V600E} inhibitor, IC$_{50}$ = 74 nM
EGFR inhibitor, IC$_{50}$ = 107 nM
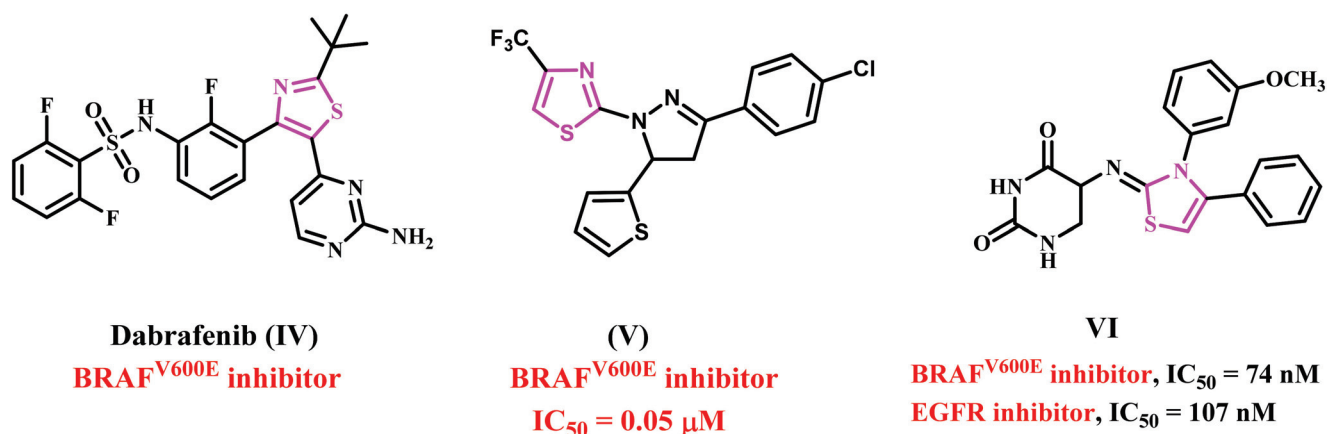
Figure 2. Structures of some thiazole-based anticancer agents **IV**–**VI**.

Abdel-Maksoud et al. also developed a novel series of thiazole-based derivatives for testing as BRAF^{V600E} inhibitors. Compound **V** (Figure 2) exhibited the most potent antiproliferative activity, with potent BRAF^{V600E} inhibitory activity and an IC$_{50}$ value of 0.05 μM [38]. We recently reported the synthesis of novel thiazole-based derivatives that act as dual EGFR and BRAF^{V600E} inhibitors [39]. Compound **VI** (Figure 2) demonstrated significant antiproliferative activity against EGFR and BRAF^{V600E}, with IC$_{50}$ values of 74 and 107 nM, respectively.

Following our previous study on dual targeting strategies and motivated by the findings above [40–42], we synthesized new spiro-compounds that combine quinolinone, thiazolidinone, and spiro-cyclic in a single molecule via the reaction of thioglycolic acid and 4-(2-cyclodenehydrazinyl)4uinoline-2(1*H*)-one. As a result, two new compounds, **6a**–**e** (Scaffold A) and **7a** and **7b** (Scaffold B), were developed to generate new potent antiproliferative agents targeting EGFR and/or BRAF^{V600E}, as shown in Figure 3.

The new compounds underwent a cell viability assay test to determine their influence on the vitality of normal cell lines. They were also tested against a panel of four cancer cell lines as antiproliferative agents. Furthermore, the most active compounds were tested for antiproliferative activity against EGFR and BRAF^{V600E}. Finally, we tested the most active compounds for apoptotic potential against caspase 3, caspase 8, Bax, and the antiapoptotic Bcl2.
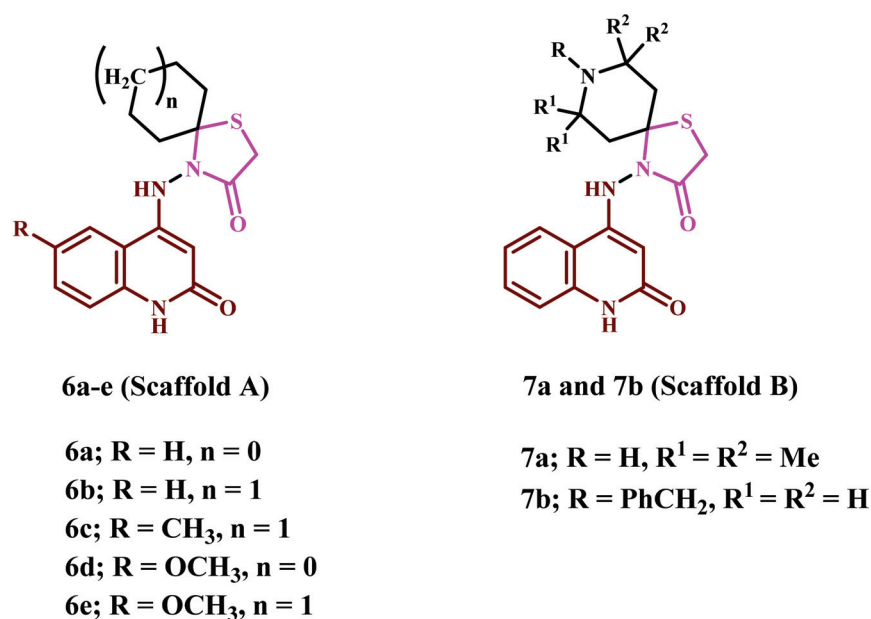
Figure 3. Structures of new compounds **6a–e**, **7a**, and **7b**.

2. Results and Discussion

2.1. Chemistry

We aimed to develop a novel series of spiro-compounds, namely **6a–e**, **7a** and **7b**. Scheme 1 depicts the steps taken to obtain our target 4-((6-substituted-2-oxo-1,2-dihydroquinolin-4-yl)amino)-1-thia-4-azaspiroalkan-3-ones (**6a–e**) in high yields via the interaction between 4-(2-cyclodenehydrazinyl)5uinoline-2(1*H*)-ones (**5a–e**) [43–45] and thioglycolic acid refluxed under dry benzene with a free catalyst at a molar ratio of 1:20 for 20 h.
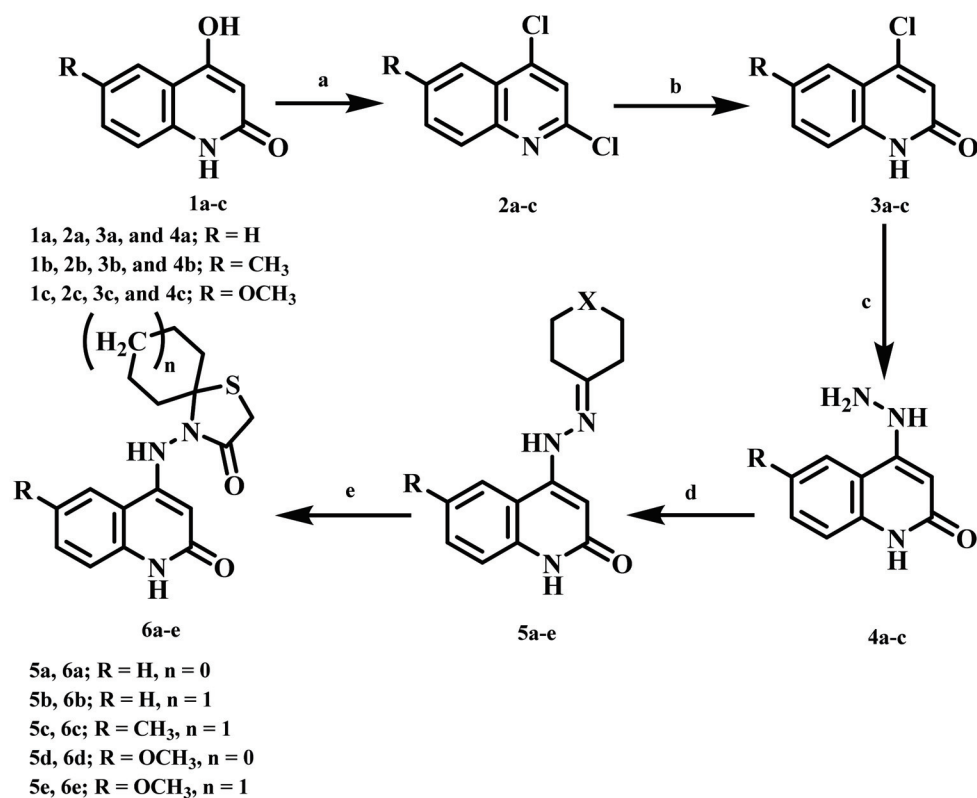
Scheme 1. Synthesis of azaspiroalkan-3-one **6a–e**.

Reagents and reaction conditions: (**a**) POCl$_3$/stirring for 1 h, 70 °C; (**b**) AcOH/H$_2$O/refluxing overnight; (**c**) Hydrazine/EtOH/refluxing for 3 h; (**d**) Cyclic ketone/EtOH/refluxing for 3 h; I Thioglycolic acid/Benzene/refluxing for 24 h.

The structures of our obtained products, **6a–e**, were confirmed using NMR, mass spectrometry, and elemental analysis. All of the spectral data show that the acquired molecular formula for **6a–e** comprises one molecule from compounds **5a–e** and one molecule of thioglycolic acid, with the elimination of the H$_2$O molecule. Compound **6b** [4-((2-oxo-1,2-dihydroquinolin-4-yl)amino)-1-thia-4-azaspiro-[4.5]decan-3-one], with the chemical formula C$_{17}$H$_{19}$N$_3$O$_2$S and a detectable molecular ion peak at *m/z* = 329, was used as a representative example. Moreover, the ^{1}H NMR spectra of compound **6b** revealed two broad singlet signals at δ_H = 11.01 and 10.07 ppm, respectively, indicative of NH-1 and exo-NH-4b. Two singlet signals at δ_H = 6.11 and 3.74 ppm were assigned as H-3 and H-2′, respectively, in addition to quinolinone-CH between 7.97 and 7.12 ppm (m, 4H). The ^{13}C NMR spectra for compound **6b** had four downfield-lying lines at δ_C = 167.56 (C-3′), 162.85 (C-2), 151.76 (C-4), and 139.06 (C-8a) ppm, respectively. C-5 resonated at δ_C = 61.27 ppm and was characteristic of a spiro-structure.

The possibility of an isomeric structure in compound **6b′** (Figure 4) was ruled out by ^{1}H NMR, which revealed an NH chemical shift at 10.07 ppm due to hydrogen bonding with the carbonyl group (C-3′). Furthermore, the ^{15}N NMR spectrum revealed a signal at δ_N = 131.7 ppm, which produced an HSQC correlation with the proton at δ_H = 10.07 ppm. An HMBC correlation with two protons at δ_H = 10.07 and 6.11 ppm, assigned as NH-4b and H-3, was also indicated (Figure 5). The latter applies to structure **6b** but not **6b′**. Furthermore, the two signals at δ_N = 142.1 ppm, designated as NH-1, show an HSQC correlation with the proton at H 6.11 ppm, designated as H-3. These correlations are not possible for structure **6b′**.
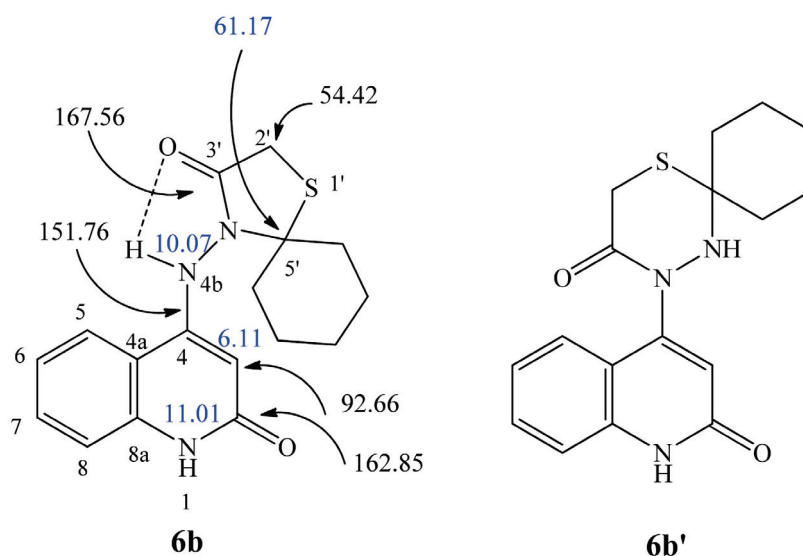
Figure 4. Structure of compound **6b** and its isomeric structure **6b′**.

We also investigated the reaction of thioglycolic acid with 4-(2-(2,2,6,6-tetramethylpiperidin-4-ylidene)hydrazinyl)quinolin-2(1*H*)-one (**5f**) and 4-(2-(1-benzylpiperidin-4-ylidene) hydrazinyl)quinolin-2(1*H*)-one (**5g**). The reaction followed the same pattern and produced similar products, **7a** and **7b**, in high yields (Scheme 2).
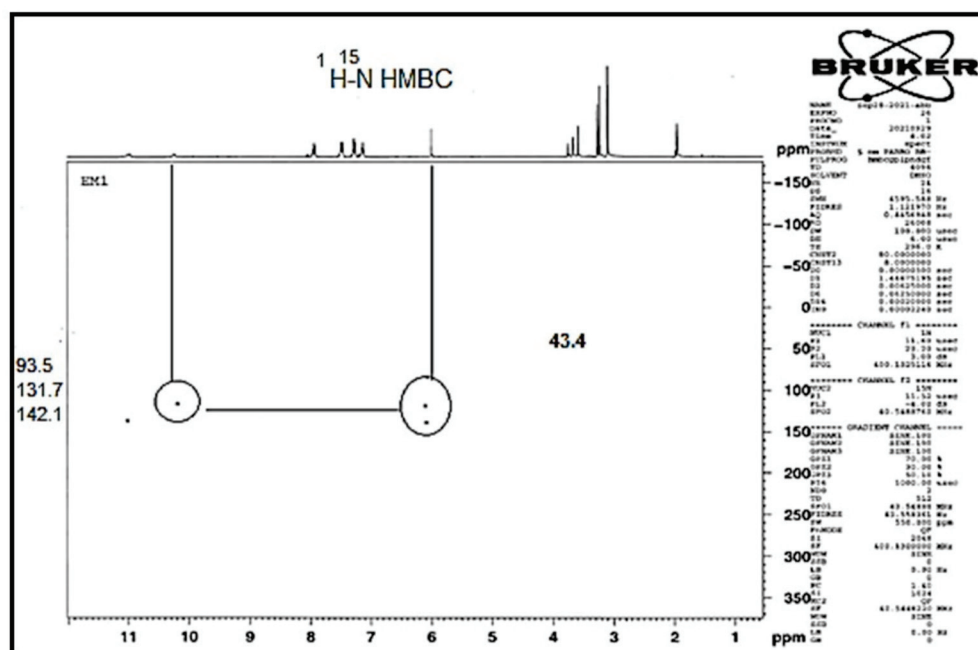
Figure 5. ^{1}H -^{15}N HMBC for compound **6b**.

5f and **7a**; R = H, R^1 = R^2 = Me

5g and **7b**; R = PhCH$_2$, R^1 = R^2 = H
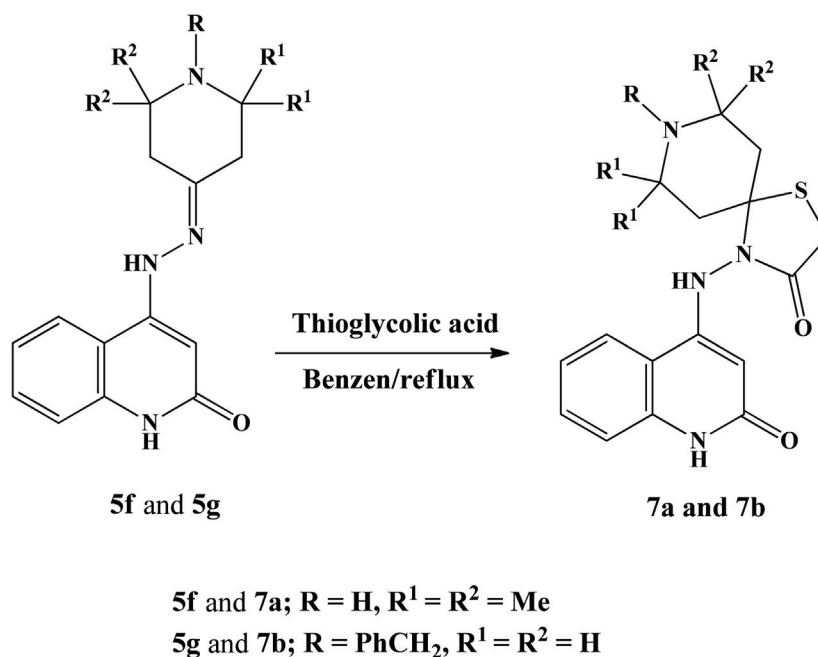
Scheme 2. Synthesis of azaspiroalkan-3-one **7a,b**.

For example, consider compound **7b**, which was designated as 8-benzyl-4-((2-oxo-1,2-dihydroquinolin-4-yl)amino)-1-thia-4,8-diazaspiro[4.5]decan-3-one with the molecular formula $C_{23}H_{24}N_4O_2S$ (Figure 6, Table 1). The ^{1}H NMR of compound **7b** revealed that H-3 was distinctive as the vinylic singlet at δ_H 6.08 ppm, with its attached carbon appearing at δ_C 92.33 ppm. Furthermore, H-3 exhibits an HMBC correlation with both protonated nitrogens at δ_N 141.9 and 132.0 ppm. The latter could be N-1 and N-4b, although it is unclear which was which. Furthermore, N-1 exhibits an HMBC correlation with the proton resonance at δ_H 7.28 ppm, implying that H-8 is present. Of the two carbons that exhibit an HSQC correlation with this proton, the one at δ_C 115.45 ppm exhibits an HMBC correlation with the protons in the quinoline ring, designated as C-8. The only visible 1H doublet in

the aromatic region appears at δ_H 7.98 ppm and is assigned to H-5, whose attached carbon appears at δ_C 122.44 ppm. H-5 establishes a COSY correlation with the dd at δ_H 7.12 ppm, designated as H-6. The attached carbon appears at δ_C 120.31 ppm in H-6, establishing a COSY correlation with the other dd, at δ_H 7.46, designated as H-7. Attached carbon appears at δ_C 130.13 ppm in H-7. In turn, H-7 establishes a COSY correlation with H-8. The carbon at δ_C 139.23 establishes an HMBC correlation with H-5 and H-7, designated as C-8a. The carbon at δ_C 112.26 establishes a strong HMBC correlation with H-3, NH-4b, H-6, and H-8, designated as C-4a. These six HMBC correlations are three-bond correlations. The carbon at δ_C 162.90 establishes an HMBC correlation with H-3 and (weakly) NH-4b, designated as C-2. The carbon at δ_C 149.51 establishes an HMBC correlation with H-3, NH-4b, H-5, and (weakly) H-8, designated as C-4. This arrangement constituted the quinolinone structure.
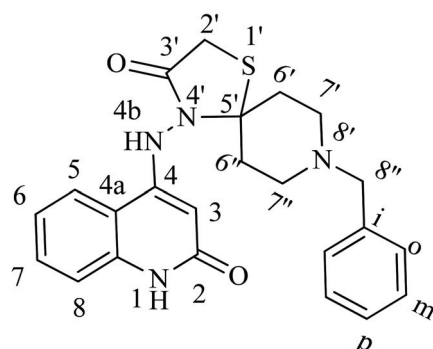
Figure 6. Structure of compound **7b**.

Furthermore, H-8″ is distinctive as the 2H singlet at δ_H 3.56, whose attached carbon appears at δ_C 61.36 ppm., and establishes an HMBC correlation with the signal at δ_C 128.73 ppm, designated as C-*o*. Both C-*o* and C-*m* establish HSQC correlations with the m-signal at δ_H 7.35 ppm. Furthermore, the carbon at δ_C 126.93 establishes a COSY correlation with both H-*o* and H-*m*, and HSQC correlations with the signal at 7.28 ppm. This carbon must be C-*p*, as shown in Table 1.

Compounds **6a–e** were synthesized by cyclizing the corresponding hydrazones **5a–e** with thioglycolic acid according to the suggested mechanism in Scheme 3. Compounds **5a–c** were catalyzed with thioglycolic acid to form tertiary carbocation 8 and a nucleophilic addition of HS-thioglycolic, followed by rearrangement with the loss of an H+-proton to produce the intermediate 9. Nucleophilic attacks from NH-2 to the carbonyl group eliminated an H_2O molecule, yielding the corresponding products 6a–e via intermediates 9 and 10. Compounds **7a** and **7b** were also formed via a similar mechanism.

Table 1. Spectral data for compound **7b**.

^{1}H NMR	^{1}H-^{1}H COSY	Assignment
11.01 (bs; 1H)	6.08	NH-1
10.09 (s; 1H)		NH-4b
7.98 (d, J = 8.1; 1H)	7.46, 7.12	H-5
7.46 (dd, J = 7.7, 7.5; 1H)	7.98, 7.28, 7.12	H-7
7.35 (m; 4H)	7.28	H-*o, m*
7.28 (m; 3H)	7.46, 7.35, 7.12	H-8, *p*
7.12 (dd, J = 7.7, 7.4; 1H)	7.98, 7.46, 7.28	H-6
6.08 (s; 1H)	11.01	H-3
3.71 (s; 2H)		H-2′
3.56 (s; 2H)		H-8″
2.67 (t, J = 5.6; 2H)	2.55, 2.44	H-6′/6″
2.55 (m; 4H)	2.67, 2.44	H-7′,7″
2.44 (t, J = 5.4; 2H)	2.67, 2.55	H-6″/6′

Table 1. *Cont.*

^{13}C NMR	HSQC	HMBC	Assignment
167.33		10.09, 3.71	C-3′
162.90		10.09, 6.08	C-2
149.51		10.09, 7.98, 7.28, 6.08	C-4
139.23		7.98, 7.46	C-8a
138.31		7.35, 7.28, 3.56	C-*i*
130.13	7.46	7.98, 7.46, 7.28	C-7
128.73	7.35	7.35, 7.35, 3.56	C-*o*
128.16	7.35	7.35, 7.35	C-*m*
126.93	7.28	7.28	C-*p*
122.44	7.98	7.98, 7.46, 6.08	C-5
120.31	7.12	7.28, 7.12	C-6
115.45	7.28	7.46, 7.12	C-8
112.26		10.09, 7.98, 7.28, 7.12, 6.08	C-4a
92.33	6.08	10.09, 6.08	C-3
61.36		3.56, 2.55	C-8″
54.11	3.71	2.67, 244	C-2′
53.23, 52.07	2.55	3.56, 2.67, 2.55, 2.55, 2.44	C-7′,7″
47.33	3.56	2.67, 2.44	C-5′
34.46	2.44	2.67, 2.55	C-6′/6″
27.26	2.67	2.67, 2.55, 2.55	C-6″/6′

^{15}N NMR:	HSQC	HMBC	Assignment
141.9	11.00	7.28, 6.08	N-1
132.0	10.09	10.09, 6.08	N-4b
49.7		2.67, 2.44	N-8′
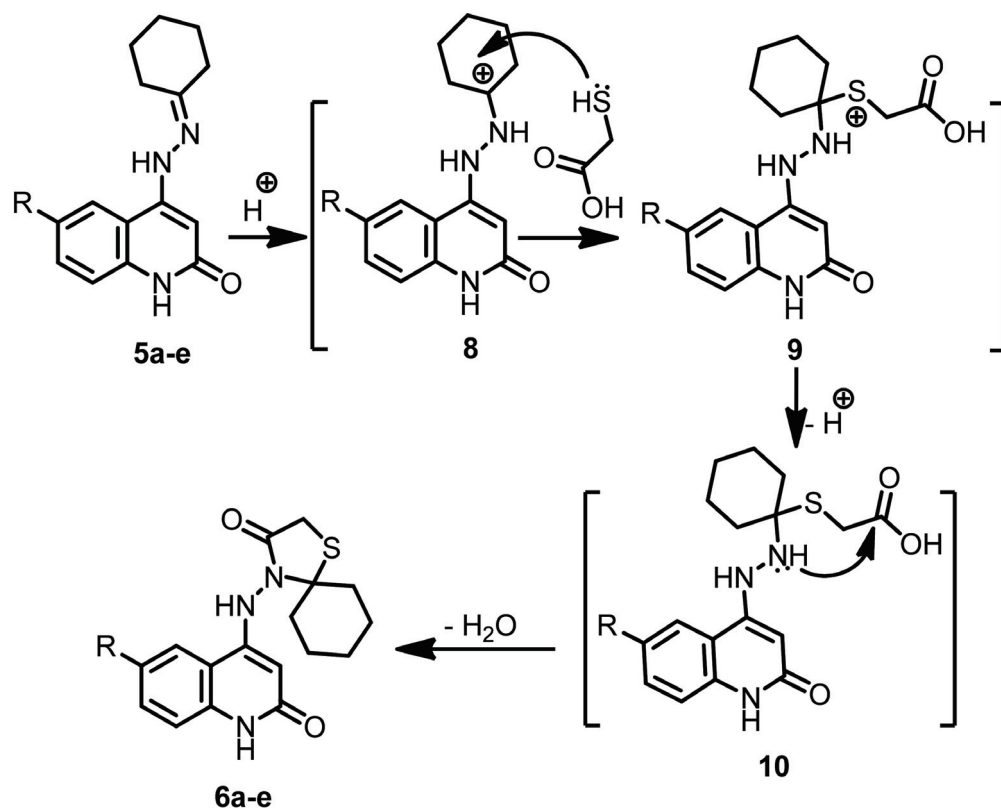
Scheme 3. Suggested mechanism which rationalizes compounds **6a–e**.

2.2. Biology

2.2.1. Cell Viability Assay

The epithelial (MCF-10A) cell line of a normal human mammary gland was used to test the viability of the new substances. Compounds **6a–e**, **7a**, and **7b** were incubated on MCF-10A cells for four days before being tested for viability using the MTT assay [46,47]. According to Table 2, none of the tested substances revealed cytotoxic impacts, and the cell viability for the compounds tested at 50 μM was >89%.

Table 2. IC_{50} of compounds **6a–e**, **7a**, **7b**, and Erlotinib against four cancer cell lines.

Compd.	Cell Viability %	Antiproliferative Activity $IC_{50} \pm$ SEM (μM)				
		A-549	MCF-7	Panc-1	HT-29	Average (GI_{50})
6a	90	40 ± 4	44 ± 4	46 ± 4	48 ± 4	45
6b	89	33 ± 3	35 ± 3	36 ± 3	36 ± 3	35
6c	91	72 ± 7	74 ± 7	73 ± 7	72 ± 7	73
6d	91	48 ± 4	52 ± 5	54 ± 5	54 ± 5	52
6e	92	36 ± 3	40 ± 3	42 ± 4	42 ± 4	40
7a	89	80 ± 8	82 ± 8	81 ± 8	81 ± 8	81
7b	91	30 ± 3	34 ± 3	32 ± 3	32 ± 3	32
Erlotinib	ND	30 ± 3	40 ± 3	30 ± 3	30 ± 3	33

ND: Not Determined.

2.2.2. Antiproliferative Assay

The antiproliferative role of **6a–e**, **7a**, and **7b** was tested against the four human cancer cell lines, namely MCF-7 (breast cancer cell line), Panc-1 (pancreatic cancer cell line), A-549 (lung cancer cell line), and HT-29 (colon cancer cell line), using the MTT assay and erlotinib as the reference drug [48,49]. Table 2 shows the median inhibitory concentration of each tested compound (IC_{50}).

Overall, the recently screened derivatives **6a–e**, **7a**, and **7b** showed encouraging antiproliferative action against the four cancer cell lines tested, with an average IC_{50} (GI_{50}) ranging between 32 and 81 nM compared to the reference erlotinib, which had a GI_{50} of 33 nM. Compounds **6b**, **6e**, and **7b** had the highest antiproliferative activity, with GI_{50} values of 35, 40, and 32 nM, respectively. Compound 7b (R = Ph-CH$_2$, R^1 = R^2 = H, Scaffold B) was the most effective derivative, with a GI_{50} value of 32 nM. It was comparable to, and even more effective than, erlotinib (GI_{50} = 33 nM) against the MCF-7 cell line, as shown in Table 3. The other Scaffold B compound 7a (R = H, R^1 = R^2 = CH$_3$) was the least effective derivative, with GI_{50} values of 81 nM. It was 2.5-fold less potent than **7b**, suggesting the significance of the N-benzyl piperidine moiety for antiproliferative activity.

Compounds **6b** (R = H, *n* = 1, Scaffold A) and 6e (R = OCH$_3$, *n* = 1, Scaffold A) were the second and third most active compounds, with GI_{50} values of 35 and 40 nM, respectively. They were 1.1- and 1.25-fold less potent than **7b**. Additionally, compound **6c** (R = CH$_3$, *n* = 1, Scaffold A) showed modest antiproliferative activity with a GI_{50} value of 73 nM against the four cancer cell lines tested. Compound 6c was 2.1- and 1.8-folds less potent than 6b and 6e, respectively.

Compound **6a** (R = H, *n* = 0, Scaffold A) was 1.3-fold less potent than compound **6b** (R = H, *n* = 1, Scaffold A) against the four cancer cell lines, with a GI50 value of 45 nM. The same pattern was observed when comparing compounds 6d (R = OCH3, *n* = 0, Scaffold A) and 6e (R = OCH3, *n* = 1, Scaffold A). Compound **6d** had a GI50 of 52 nM, whereas 6e had a GI50 of 40 nM. These results showed that the spiro moiety's ring size and the type of substitution at the quinoline moiety's 6-position significantly impacted the antiproliferative function. Regarding the ring size, the cyclohexyl ring moiety was more

tolerated for antiproliferative activity than the cyclopentyl ring moiety. Furthermore, the nature of substitution at the quinoline 6-position was associated with an increase in the antiproliferative activity, in the order H > OCH3 > CH3.

Table 3. IC$_{50}$ of compounds **6a–e**, **7a**, **7b**, and Erlotinib against EGFR and BRAF^{V600E}.

Compd.	EGFR Inhibition IC$_{50}$ $\pm$ SEM (nM)	BRAF^{V600E} Inhibition IC$_{50}$ $\pm$ SEM (nM)
6a	97 $\pm$ 07	137 $\pm$ 12
6b	84 $\pm$ 06	108 $\pm$ 09
6c	135 $\pm$ 11	164 $\pm$ 15
6d	104 $\pm$ 08	159 $\pm$ 14
6e	92 $\pm$ 07	129 $\pm$ 10
7a	149 $\pm$ 12	187 $\pm$ 16
7b	78 $\pm$ 05	96 $\pm$ 8
Erlotinib	80 $\pm$ 05	60 $\pm$ 05

2.2.3. EGFR Inhibitory Assay

As potential targets for their antiproliferative activity, compounds **6a–e**, **7a**, and **7b** were tested for EGFR inhibitory activity [50]. Table 3 displays these results as IC$_{50}$ values. The outcomes of this test align with the antiproliferative test, where the two most effective antiproliferative derivatives, compounds **7b** (R = Ph-CH$_2$, R^1 = R^2 = H, Scaffold B) and **6b** (R = H, *n* = 1, Scaffold A), were the most effective EGFR inhibitors, with IC values of 78 $\pm$ 05 and 84 $\pm$ 06 nM, respectively. They were also equipotent to the reference erlotinib (IC$_{50}$ = 80 $\pm$ 05).

Compounds **6a** (R = H, *n* = 0, Scaffold A), **6d** (R = OCH$_3$, *n* = 0, Scaffold A), and **6e** (R = OCH$_3$, *n* = 1, Scaffold A) displayed significant anti-EGFR activity with IC$_{50}$ values of 97 $\pm$ 07, 104 $\pm$ 08, and 92 $\pm$ 07 nM, respectively. They were 1.2- to 1.3-folds less potent than erlotinib.

Once again, compounds **6c** (R = CH$_3$, *n* = 1, Scaffold A) and **7a** (R = H, R^1 = R^2 = CH$_3$, Scaffold B) had the lowest activity as EGFR inhibitors, with IC$_{50}$ values of 135 $\pm$ 11 and 149 $\pm$ 12 nM, respectively. These findings demonstrated that compounds **6b** and **7b** are workable antiproliferative candidates with substantial EGFR inhibitory properties.

2.2.4. BRAF^{V600E} Inhibitory Assay

The anti-BRAF^{V600E} activity of compounds **6a–e**, **7a**, and **7b** was also investigated in vitro [51], using erlotinib as a reference compound; the results are displayed in Table 3. According to the enzyme testing results, the investigated compounds had moderate to good BRAF^{V600E} inhibitory activity, with IC$_{50}$ values between 96 and 187 nM. In every instance, the compounds were less effective than the standard drug erlotinib (IC$_{50}$ = 60 nM).

Table 3 shows that the most potent EGFR inhibitors, compounds **7b** (R = Ph-CH$_2$, R^1 = R^2 = H, Scaffold B) and **6b** (R = H, *n* = 1, Scaffold A), were also the most potent BRAF^{V600E} inhibitors, with IC values of 96 $\pm$ 8 and 108 $\pm$ 9 nM, respectively. Compounds **7b** and **6b** were roughly equivalent to erlotinib as antiproliferative agents; however, as BRAF^{V600E} inhibitors, they were 1.6- and 1.8-fold less potent. Compounds **6a**, **6c**, **6d**, **6e**, and **7a** showed weak to moderate anti-BRAF activity with IC$_{50}$ values ranging between 129 and 187 nM, as shown in Table 3. The in vitro assay findings revealed that compounds 6b and 7b are potent antiproliferative agents that can act as dual EGFR/BRAF^{V600E} inhibitors.

2.2.5. Apoptotic Markers Activation Assay

Numerous biochemical and morphological processes are involved in apoptosis, also called programmed cell death [52]. Antiapoptotic proteins such as Bcl-2 and Bc-W coexist

with proapoptotic proteins such as Bad and Bax [53]. Proapoptotic proteins stimulate the release of cytochrome-c, whereas antiapoptotic proteins control apoptosis by inhibiting the release of cytochrome-c. The outer mitochondrial membrane becomes permeable when the ratio of proapoptotic proteins exceeds that of antiapoptotic proteins, setting off a series of events. The release of cytochrome c triggers both caspase-3 and caspase-9. Then, caspase-3 induces apoptosis by attacking several of the vital proteins that the cell requires [53].

Caspase 3 Activation Assay

Compounds **6b** and **7b** were tested as caspase-3 activators against the human pancreatic (Panc-1) cancer cell line [54]; the findings are shown in Table 4. Our results showed that derivatives **6b** and **7b** had a significant overexpression of caspase-3 protein levels (487.50 ± 4 and 544.50 ± 5 pg/mL, respectively) compared to the reference staurosporine (503.00 ± 4 pg/mL). The highest active substance, **7b**, caused caspase-3 protein overexpression (544.50 ± 5 pg/mL) in the Panc-1 cancer cell line, which was 8.5-fold higher than the control with untreated cells, and even higher than staurosporine. Compound **6b** (487.50 ± 4 pg/mL) showed comparable caspase-3 activation to the reference staurosporine. The above findings suggest that apoptosis may have contributed to the antiproliferative action of the tested compounds and caspase-3 overexpression.

Table 4. Caspase-3 induction of compounds **6b** and **7b**.

Compound Number	Caspase-3	
	Conc (Pg/mL)	Fold Change
6b	487.50 ± 4	7.50
7b	544.50 ± 5	8.5
Staurosporine	503.00 ± 4	8.0
Control	65.50	1

Caspase-8, Bax and Bcl-2 Levels Assay

Compounds **6b** and **7b** were investigated for their impact on the Bacl-2, Bax, and caspase-8 levels against the Panc-1 cancer cell line, with staurosporine as a reference [55]. Our results are presented in Table 5.

Table 5. Caspase-8, Bax and Bcl-2 levels for compounds **6b**, **7b**, and Staurosporine.

Compound Number	Caspase-8		Bax		Bcl-2	
	Conc (ng/mL)	Fold Change	Conc (Pg/mL)	Fold Change	Conc (ng/mL)	Fold Reduction
6b	1.50	17	220	28	1.30	4
7b	1.90	21	295	37	1.00	5
Staurosporine	1.80	20	280	35	1.10	5
Control	0.09	1	8	1	5	1

Our findings demonstrated that the investigated substances significantly increased the Bax and caspase-8 levels compared to staurosporine. Compound **7b** had the highest level of caspase-8 overexpression (1.90 ng/mL), followed by compound **6b** (1.50 ng/mL) and the reference staurosporine (1.80 ng/mL). Additionally, **7b** showed a comparable induction of Bax (295 pg/mL) to staurosporine (280 pg/mL), which was 37-fold higher than the control with untreated Panc-1 cancer cells. Finally, compound 7b caused the equipotent downregulation of the Bcl-2 protein level (1.00 ng/mL), followed by compound 6b (1.30 ng/mL) in the Panc-1 cell line, and the reference staurosporine (1.10 ng/mL). The apoptosis assay

results revealed that compounds **6b** and **7b** possess dual EGFR/BRAF inhibitory properties and show promising antiproliferative and apoptotic activity.

3. Conclusions

We designed and synthesized a small set of novel compounds, 4-((quinolin-4-yl)amino) thia-azaspiro[4.4/5]alkan-3-ones **6a–e**, **7a**, and **7b**, in order to develop new dual-targeting antiproliferative agents. The MTT assay was used to investigate the antiproliferative effects of the new compounds against a panel of four cancer cell lines. Compounds **6b**, **6e**, and **7b** had higher antiproliferative activity, with GI_{50} values of 35, 40, and 32 nM, than erlotinib, which had a GI_{50} of 33 nM. The most potent compounds were then tested for EGFR and $BRAF^{V600E}$ inhibition. Our results showed that compounds **6b**, **6e**, and **7b** were the most potent EGFR inhibitors, with IC_{50} values of 84, 92, and 78 nM, respectively. Furthermore, **6b**, **6e**, and **7b** showed promising $BRAF^{V600E}$ inhibitory activity, with IC_{50} values of 108, 129, and 96 nM, respectively. Therefore, they can be considered effective antiproliferative agents that act as dual $EGFR/BRAF^{V600E}$ inhibitors. The most active derivative in Panc-1 cells, **7b**, induces apoptosis via caspase 3 overexpression and an increased ratio of *Bax/Bcl-2* genes compared to the control cells. In the future, more in vitro and in vivo studies, as well as chemical modifications, may be required to develop highly effective antiproliferative agents.

4. Experimental
4.1. Chemistry

General details: See Appendix SA (Supplementary File).

The 4-(2-substitutedhydrazinyl)-6-substituted-quinolin-2(1*H*)-one **5a–g** were prepared as reported [36–38], the thioglycolic acid (Aldrich) was used as received.

General procedure for preparation of compounds **6a–e** and **7a**,**b**

The **5a–g** (1 mmol) and thioglycolic acid (20 mmol) were refluxed in 20 mL dray benzene in a round-bottom flask for 20 h. The reaction mixture was allowed to cool, and a white precipitate formed. The precipitate was suction filtrated and washed four times with 25 mL of 3% Na_2CO_3 solution to remove unreacted thioglycolic acid before being thoroughly dried to yield the products **6a–e**, **7a**, and **7b**.

4.1.1. 4-((2-Oxo-1,2-dihydroquinolin-4-yl)amino)-1-thia-4-azaspiro[4.4]nonan-3-one (**6a**)

White ppt (69%), m.p 215–17 °C; ^{1}H NMR (DMSO-d_6): δ_H = 11.01 (bs, 1H; NH-1), 10.07 (bs, 1H; NH-4b), 7.97 (d, *J* = 8.1 Hz; 1H, H-5), 7.47 (dd, *J* = 8.1, 7.2 Hz; 1H, H-7), 7.28 (d, *J* = 7.8 Hz; 1H, H-8), 7.13 (t, *J* = 8, 7.2 Hz, H-6), 6.09 (s, 1H; H-3), 3.74 (s, 2H; H-2′), 1.1–1.95 ppm (m, 8H; cyclopentyl-CH_2), ^{13}C NMR (DMSO-d_6): δ_C = 167.54 (C-3′), 162.89 (C-2), 149.69 (C-4), 139.05 (C-8a), 130.64 (C-7), 122.09 (C-5), 120.93 (C-6), 115.54 (C-8), 111.98 (C-4a), 92.64 (C-3), 54.40 (C-2′), 47.12 (C-5′), 34.11, 26.11, 25.25 ppm (Cyclopentyl-CH_2), ^{15}N NMR (DMSO-d_6): δ_N = 142 (N-1), 128,6 (N-4b), 93.3 ppm (N-4′). *m/z*, Ms = 315 (M$^+$, 12). *Anl. Calcd.* For $C_{16}H_{17}N_3O_2S$: C, 60.93; H, 5.43; N, 13.32; S, 10.17. Found: C, 61.08; H, 5.33; N, 13.43; S, 10.29.

4.1.2. 4-((2-Oxo-1,2-dihydroquinolin-4-yl)amino)-1-thia-4-azaspiro[4.5]decan-3-one (**6b**)

White ppt (70%), m.p 194–96 °C; ^{1}H NMR (DMSO-d_6): δ_H = 11.05 (bs, 1H; NH-1), 10.09 (bs, 1H; NH-4b), 7.97 (m, 1H; H-5), 7.49 (m, 1H; H-6), 7.27 (m, 1H; H-7), 7.12 (m, 1H; H-8), 6.11 (s, 1H; H-3), 3.74 (s, 2H; H-2′), 1.11–1.92 ppm (m, 10H; cyclohexyl-CH_2), ^{13}C NMR (DMSO-d_6): δ_C = 167.56 (C-3′), 162.85 (C-2), 149.76 (C-4), 139.06 (C-8a), 130.34 (C-7), 122.09 (C-5), 120.69 (C-6), 115.53 (C-8), 111.99 (C-4a), 92.66 (C-3), 54.42 (C-2′), 47.17 (C-5′), 34.18, 26.17 ppm (Cyclohexyl-CH), ^{15}N NMR (DMSO-d_6): δ_N = 142.1 (N-1), 131,7 (N-4b), 93.5 ppm (N-4′). *m/z*, Ms = 329 (M$^+$, 10). *Anl. Calcd.* For $C_{17}H_{19}N_3O_2S$: C, 61.98; H, 5.81; N, 12.76; S, 9.73. Found: C, 62.11; H, 5.77; N, 12.83; S, 9.66.

4.1.3.
4-((6-Methyl-2-oxo-1,2-dihydroquinolin-4-yl)amino)-1-thia-4-azaspiro[4.5]decan-3-one (**6c**)

White ppt (75%), m.p 160–62 °C; ^{1}H NMR (DMSO-d$_6$): δ_H = 10.93 (bs, 1H; NH-1), 10.05 (bs, 1H; NH-4b), 7.78 (s, 1H, H-8), 7.33 (m, 1H; H-8), 7.17 (m, 1H; H-5), 6.07 (s, 1H; H-3), 3.24 (s, 2H; H-2′), 1.11–1.93 (m, 10H; Ali-CH), 2.11 ppm (s, 3H, CH$_3$), ^{13}C NMR (DMSO-d$_6$): δ_C = 167.49 (C-3′), 162.15 (C-2), 149.75 (C-4), 139.16 (C-8a), 131.48 (C-7), 129.60 (C-6), 121.77 (C-5), 115.45 (C-8), 111.84 (C-4a), 92.61 (C-3), 54.33 (C-2′), 46.98 (C-5′), 33.90, 25.98 (Cyclohexyl-CH), 20.58 ppm (CH$_3$). *m/z*, Ms = 343 (M$^+$, 10). *Anl. Calcd. For* C$_{18}$H$_{21}$N$_3$O$_2$S: C, 62.95; H, 6.16; N, 12.23; S, 9.34. Found: C, 63.10; H, 6.22; N, 12.43; S, 9.21.

4.1.4.
4-((6-Methoxy-2-oxo-1,2-dihydroquinolin-4-yl)amino)-1-thia-4-azaspiro[4.4]nonan-3-one (**6d**)

White ppt (67%), m.p 236–38 °C; ^{1}H NMR (DMSO-d$_6$): δ_H = 11.12 (bs, 1H; NH-1), 10.07 (bs, 1H; NH-4b), 7.99–7.11 (m, 3H; H-5,7,8), 6.06 (s, 1H; H-3), 3.70 (s, 3H; OMe), 3.35 (s, 2H; H-2′), 1.12–1.95 ppm (m, 8H; Cyclpentyl-CH$_2$), ^{13}C NMR (DMSO-d$_6$): δ_C = 167.52 (C-3′), 162.84 (C-2), 149.11 (C-4), 136.07 (C-8a), 133.40 (C-6), 128.28 (C-7), 119.52 (C-5), 115.52 (C-8), 111.98 (C-4a), 92.67 (C-3), 55.55 (C-2′), 54.94 (OMe), 47.44 (C-5′), 32.77, 25.90, 23.77 ppm (Cyclopentyl-CH). *Anl. Calcd. For* C$_{17}$H$_{19}$N$_3$O$_3$S: C, 59.11; H, 5.54; N, 12.17; S, 9.28. Found: C, 59.23; H, 5.44; N, 11.99; S, 9.18.

4.1.5.
4-((6-Methoxy-2-oxo-1,2-dihydroquinolin-4-yl)amino)-1-thia-4-azaspiro[4.5]decan-3-one (**6e**)

White ppt (79%), m.p 238–40 °C; ^{1}H NMR (DMSO-d$_6$): δ_H = 10.93 (bs, 1H; NH-1), 10.07 (bs, 1H; NH-4b), 7.50–7.34 (m, 1H; H-,8), 7.22–7.13 (m, 2H; H-5,7), 6.06 (s, 1H; H-3), 3.71 (s, 3H; OMe), 3.33 (s, 2H; H-2′), 1.14–1.92 ppm (m, 10H; Cyclohexyl-CH$_2$), ^{13}C NMR (DMSO-d$_6$): δ_C = 167.60 (C-3′), 162.49 (C-2), 149.49 (C-4), 136.90 (C-8a), 133.46 (C-6), 128.28 (C-7), 119.52 (C-5), 116.82 (C-8), 112.29 (C-4a), 92.99 (C-3), 55.62 (C-2′), 55.42 (OMe), 47.56 (C-5′), 33.0, 25.94, 23.91 ppm (Cyclohexyl-CH). *Anl. Calcd. For* C$_{18}$H$_{21}$N$_3$O$_3$S: C, 60.15; H, 5.89; N, 11.69; S, 8.92. Found: C, 60.25; H, 5.77; N, 11.80; S, 8.88.

4.1.6. 7,7,9,9-Tetramethyl-4-((2-oxo-1,2-dihydroquinolin-4-yl)amino)-1-thia-4,8-diazaspiro-[4.5]decan-3-one (**7a**)

White ppt (78%), m.p 165–67 °C; ^{1}H NMR (DMSO-d$_6$): δ_H = 11.07 (bs, 1H; NH-1), 10.26 (s, 1H; NH-4b), 7.78 (t, 1H; H-5), 7.65 (m,1H; H-7), 7.05 (m, 2H; NH, H-6), 6.05 (s, 1H; H-3), 3.51 (s, 2H; H-2′), 2.67 (s, 4; H-6′), 2.44 (s, 12H; 4CH$_3$), ^{13}C NMR (DMSO-d$_6$): δ_C = 167.57 (C-3′), 162.68 (C-2), 149.68 (C-4), 139.02 (C-8a), 130.35 (C-7), 122.14 (C-5), 120.72 (C-6), 115.54 (C-8), 111.99 (C-4a), 92.87 (C-3), 55.55 (C-2′), 47.11 (C-5′), 34.0 (C-6′), 26.33, 25.25 ppm (CH$_3$). *Anl. Calcd. For* C$_{20}$H$_{26}$N$_4$O$_2$S: C, 62.15; H, 6.78; N, 14.50; S, 8.30. Found: C, 62.29; H, 6.88; N, 14.38; S, 8.36.

4.1.7. 8-Benzyl-4-((2-oxo-1,2-dihydroquinolin-4-yl)amino)-1-thia-4,8-diazaspiro[4.5]decan-3-one (**7b**)

White ppt (71%), m.p 180–82 °C; ^{1}H NMR (DMSO-d$_6$): δ_H = 11.01 (bs; 1H, NH-1), 10.09 (s; 1H, NH-4b), 7.98 (d, *J* = 8.1 Hz; 1H, H-5), 7.46 (dd, *J* = 7.7, 7.5 Hz; 1H, H-7), 7.35 (m; 4H, H-*o*, *m*), 7.28 (m; 3H, H-8, *p*), 7.12 (dd, *J* = 7.7, 7.4 Hz; 1H, H-6), 6.08 (s; 1H, H-3), 3.71 (s; 2H, H-2′), 3.56 (s; 2H, H-8″), 2.67 (t, *J* = 5.6 Hz; 2H, H-6′/6″), 2.55 (m; 4H, H-7′/7″), 2.44 ppm (t, *J* =5.4 Hz; 2H, H-6″/6′), ^{13}C NMR (DMSO-d$_6$): δ_C = 167.33 (C-3′), 162.90 (C-2), 149.51 (C-4), 139.23 (C-8a), 138.31 (C-*i*), 130.13 (C-7), 128.73 (C-*o*), 128.16 (C-*m*), 126.93 (C-*p*), 122.44 (C-5), 120.31 (C-6), 115.45 (C-8), 112.26 (C-4a), 92.33 (C-3), 61.36 (C-8″), 54.11 (C-2′), 53.23, 52.07 (C-7′/7″), 47.33 (C-5′), 34.46 (C-6′/6″), 27.26 ppm (C-6″/6′). *Anl. Calcd. For* C$_{23}$H$_{24}$N$_4$O$_2$S: C, 65.69; H, 5.75; N, 13.32; S, 7.62. Found: C, 65.51; H, 5.89; N, 13.22; S, 7.55.

4.2. Biology

4.2.1. Cell Viability Assay

The normal human mammary gland epithelial (MCF-10A) cell line was used to test the viability of the new compounds [46,47]. See Appendix SA (Supplementary File).

4.2.2. Antiproliferative Assay

The antiproliferative activity of **6a–e**, **7a**, and **7b** was tested against the four human cancer cell lines, Panc-1 (pancreatic cancer cell line), MCF-7 (breast cancer cell line), HT-29 (colon cancer cell line), and A-549 (lung cancer cell line), using the MTT assay and Erlotinib as the reference drug [48,49]. See Appendix SA (Supplementary File).

4.2.3. EGFR Inhibitory Assay

Compounds **6a–e**, **7a**, and **7b** were tested for EGFR inhibitory activity as a potential target for their antiproliferative activity [50]. See Appendix SA (Supplementary File).

4.2.4. BRAF^{V600E} Inhibitory Assay

The anti-BRAF^{V600E} activity of compounds **6a–e**, **7a**, and **7b** was also investigated in vitro [51] using Erlotinib as a reference compound. See Appendix SA (Supplementary File).

4.2.5. Apoptotic Markers Assay

Caspase 3 Activation Assay

Compounds **6b** and **7b** were tested as caspase-3 activators against the human pancreatic (Panc-1) cancer cell line [52–54]. See Appendix SA (Supplementary File).

Caspase-8, Bax and Bcl-2 Levels Assay

Compounds **6b** and **7b** were further investigated for their impact on the caspase-8, Bax, and Bacl-2 levels against the Panc-1 cancer cell line and staurosporine as a reference [55]. See Appendix SA (Supplementary File).

References

1. Stanković, T.; Dinić, J.; Podolski-Renić, A.; Musso, L.; Burić, S.S.; Dallavalle, S.; Pešić, M. Dual Inhibitors as a New Challenge for Cancer Multidrug Resistance Treatment. *Curr. Med. Chem.* **2019**, *26*, 6074–6106. [CrossRef] [PubMed]
2. Raghavendra, N.M.; Pingili, D.; Kadasi, S.; Mettu, A.; Prasad, S.V.U.M. Dual or multi-targeting inhibitors: The next generation anti-cancer agents. *Eur. J. Med. Chem.* **2018**, *143*, 1277–1300. [CrossRef] [PubMed]
3. Hughes, D.; Andersson, D.I. Evolutionary consequences of drug resistance: Shared principles across diverse targets and organisms. *Nat. Rev. Genet.* **2015**, *16*, 459–471. [CrossRef] [PubMed]

4. Staunton, J.E.; Jin, X.; Lee, M.S.; Zimmermann, G.R.; Borisy, A.A. Synergistic drug combinations tend to improve therapeutically relevant selectivity. *Nat. Biotechnol.* **2009**, *27*, 659–666. [CrossRef]

5. Shah, K.N.; Bhatt, R.; Rotow, J.; Rohrberg, J.; Olivas, V.; Wang, V.E.; Hemmati, G.; Martins, M.M.; Maynard, A.; Kuhn, J.; et al. Aurora kinase A drives the evolution of resistance to third-generation EGFR inhibitors in lung cancer. *Nat. Med.* **2019**, *25*, 111–118. [CrossRef]

6. Notarangelo, T.; Sisinni, L.; Condelli, V.; Landriscina, M. Dual EGFR and BRAF blockade overcomes resistance to vemurafenib in BRAF mutated thyroid carcinoma cells. *Cancer Cell Int.* **2017**, *17*, 86–94. [CrossRef]

7. Mondaca, S.; Lacouture, M.; Hersch, J.; Yaeger, R. Balancing RAF, MEK, and EGFR inhibitor doses to achieve clinical responses and modulate toxicity in BRAF V600E colorectal cancer. *JCO Precis. Oncol.* **2018**, *10*, 1–5. [CrossRef]

8. Zhang, Q.; Diao, Y.; Wang, F.; Fu, Y.; Tang, F.; You, Q.; Zhou, H. Design and discovery of 4-anilinoquinazoline ureas as multikinase inhibitors targeting BRAF, VEGFR-2 and EGFR. *MedChemComm* **2013**, *4*, 979–986. [CrossRef]

9. Okaniwa, M.; Hirose, M.; Imada, T.; Ohashi, T.; Hayashi, Y.; Miyazaki, T.; Arita, T.; Yabuki, M.; Kakoi, K.; Kato, J.; et al. Design and synthesis of novel DFG-out RAF/vascular endothelial growth factor receptor 2 (VEGFR2) inhibitors. 1. Exploration of [5,6]-fused bicyclic scaffolds. *J. Med. Chem.* **2012**, *55*, 3452–3478. [CrossRef]

10. Roskoski, R., Jr. Properties of FDA-approved small molecule protein kinase inhibitors. *Pharmacol. Res.* **2019**, *144*, 19–50. [CrossRef]

11. Prajapati, S.M.; Patel, K.D.; Vekariya, R.H.; Panchal, S.N.; Patel, H.D. Recent advances in the synthesis of quinolines: A review. *RSC Adv.* **2014**, *4*, 24463–24476. [CrossRef]

12. Navneetha, O.; Deepthi, K.; Rao, A.M.; Jyostna, T.S. A review on chemotherapeutic activities of quinolone. *Int. J. Pharm. Chem. Biol. Sci.* **2017**, *7*, 364–372.

13. Barlési, F.; Tchouhadjian, C.; Doddoli, C.; Villani, P.; Greillier, L.; Kleisbauer, J.P.; Thomas, P.; Astoul, P. Gefitinib (ZD1839, Iressa®) in non-small-cell lung cancer: A review of clinical trials from a daily practice perspective. *Fund. Clin. Pharmacol.* **2005**, *19*, 385–393. [CrossRef]

14. Iyer, R.; Bharthuar, A. A review of erlotinib–an oral, selective epidermal growth factor receptor tyrosine kinase inhibitor. *Exp. Opin. Pharmacother.* **2010**, *11*, 311–320. [CrossRef]

15. Bao, B.; Mitrea, C.; Wijesinghe, P.; Marchetti, L.; Girsch, E.; Farr, R.L.; Boerner, J.L.; Mohammad, R.; Dyson, G.; Terlecky, S.R.; et al. Treating triple negative breast cancer cells with erlotinib plus a select antioxidant overcomes drug resistance by targeting cancer cell heterogeneity. *Sci. Rep.* **2017**, *7*, 44125. [CrossRef]

16. Stamos, J.; Sliwkowski, M.X.; Eigenbrot, C. Structure of the epidermal growth factor receptor kinase domain alone and in complex with a 4-anilinoquinazoline inhibitor. *J. Biol. Chem.* **2002**, *277*, 46265–46272. [CrossRef]

17. Wissner, A.; Berger, D.M.; Boschelli, D.H.; Floyd, M.B.; Greenberger, L.M.; Gruber, B.C.; Johnson, B.D.; Mamuya, N.; Nilakantan, R.; Reich, M.F.; et al. 4-Anilino-6,7-dialkoxyquinoline-3-carbonitrile inhibitors of epidermal growth factor receptor kinase and their bioisosteric relationship to the 4-anilino-6,7-dialkoxyquinazoline inhibitors. *J. Med. Chem.* **2000**, *43*, 3244–3256. [CrossRef]

18. Wissner, A.; Mansour, T.S. The development of HKI-272 and related compounds for the treatment of cancer. *Arch. Pharm.* **2008**, *341*, 465–477. [CrossRef]

19. Kiesel, B.F.; Parise, R.A.; Wong, A.; Keyvanjah, K.; Jacobs, S.; Beumer, J.H. LC–MS/MS assay for the quantitation of the tyrosine kinase inhibitor neratinib in human plasma. *J. Pharm. Biomed. Anal.* **2017**, *134*, 130–136. [CrossRef]

20. Pisaneschi, F.; Nguyen, Q.-D.; Shamsaei, E.; Glaser, M.; Robins, E.; Kaliszczak, M.; Smith, G.; Spivey, A.C.; Aboagye, E.O. Development of a new epidermal growth factor receptor positron emission tomography imaging agent based on the 3-cyanoquinoline core: Synthesis and biological evaluation. *Bioorg. Med. Chem.* **2010**, *18*, 6634–6645. [CrossRef]

21. Lü, S.; Zheng, W.; Ji, L.; Luo, Q.; Hao, X.; Li, X.; Wang, F. Synthesis, characterization, screening and docking analysis of 4-anilinoquinazoline derivatives as tyrosine kinase inhibitors. *Eur. J. Med. Chem.* **2013**, *61*, 84–94. [CrossRef]

22. Luethi, D.; Durmus, S.; Schinkel, A.H.; Schellens, J.H.M.; Beijnen, J.H.; Sparidans, R.W. Liquid chromatography–tandem mass spectrometry assay for the EGFR inhibitor pelitinib in plasma. *J. Chromatogr. B* **2013**, *934*, 22–25. [CrossRef] [PubMed]

23. Pawar, V.G.; Sos, M.L.; Rode, H.B.; Rabiller, M.; Heynck, S.; van Otterlo, W.A.L.; Thomas, R.K.; Rauh, D. Synthesis and biological evaluation of 4-anilinoquinolines as potent inhibitors of epidermal growth factor receptor. *J. Med. Chem.* **2010**, *53*, 2892–2901. [CrossRef] [PubMed]

24. Elbastawesy, M.A.I.; Aly, A.A.; Ramadan, M.; Elshaier, Y.A.M.M.; Youssif, B.G.M.; Brown, A.B.; Abuo-Rahma, G.E.A. Novel Pyrazoloquinolin-2-ones: Design, Synthesis, Docking Studies, and Biological Evaluation as Antiproliferative EGFR-TK Inhibitors. *Bioorg. Chem.* **2019**, *90*, 103045–103060. [CrossRef] [PubMed]

25. Mohassab, A.M.; Hassan, H.A.; Abdelhamid, D.; Gouda, A.M.; Youssif, B.G.M.; Tateishi, H.; Fujita, M.; Otsuka, M.; Abdel-Aziz, M. Design and Synthesis of Novel quinoline/chalcone/1,2,4-triazole hybrids as potent antiproliferative agent targeting EGFR and BRAF^{V600E} kinases. *Bioorg. Chem.* **2021**, *106*, 104510. [CrossRef]

26. Zheng, Y.; Tice, C.M.; Singh, S.B. The use of spirocyclic scaffolds in drug discovery. *Bioorg. Med. Chem. Lett.* **2014**, *24*, 3673–3682. [CrossRef]

27. Batista, V.F.; Pinto, D.C.G.A.; Silva, A.M.S. Recent *in vivo* advances of spirocyclic scaffolds for drug discovery. *Expert Opin. Drug Discov.* **2022**, *17*, 603–618. [CrossRef]

28. Hiesinger, K.; Dar'in, D.; Proschak, E.; Krasavin, M. Spirocyclic Scaffolds in Medicinal Chemistry. *J. Med. Chem.* **2021**, *64*, 150–183. [CrossRef]

29. Ayati, A.; Emami, S.; Asadipour, A.; Shafiee, A.; Foroumadi, A. Recent applications of 1,3-thiazole core structure in the identification of new lead compounds and drug discovery. *Eur. J. Med. Chem.* **2015**, *97*, 699–718. [CrossRef]

30. Sharma, P.C.; Jain, A.; Yar, M.S.; Pahwa, R.; Singh, J.; Chanalia, P. Novel fluoroquinolone derivatives bearing N-thiomide linkage with 6-substituted-2-aminobenzothiazoles: Synthesis and antibacterial evaluation. *Arab. J. Chem.* **2017**, *10*, S568–S575. [CrossRef]

31. Petrou, A.; Fesatidou, M.; Geronikaki, A. Thiazole Ring—A Biologically Active Scaffold. *Molecules* **2021**, *26*, 3166. [CrossRef]

32. Othman, I.M.M.; Alamshany, Z.M.; Tashkandi, N.Y.; Gad-Elkareem, M.A.M.; Abd El-Karim, S.S.; Nossier, E.S. Synthesis and biological evaluation of new derivatives of thieno-thiazole and dihydrothiazolo-thiazole scaffolds integrated with a pyrazoline nucleus as anticancer and multi-targeting kinase inhibitor. *RSC Adv.* **2022**, *12*, 561–577. [CrossRef]

33. Nafie, M.S.; Kishk, S.M.; Mahgoub, S.; Amer, A.M. Quinoline-based thiazolidinone derivatives as potent cytotoxic and apoptosis-inducing agents through EGFR inhibition. *Chem. Biol. Drug Des.* **2022**, *99*, 547–560. [CrossRef]

34. Xiong, L.; He, H.; Fan, M.; Hu, L.; Wang, F.; Song, X.; Shi, S.; Qi, B. Discovery of novel conjugates of quinoline and thiazolidinone urea as potential anti-colorectal cancer agent. *J. Enzym. Inhib. Med. Chem.* **2022**, *37*, 2334–2347. [CrossRef]

35. Yadav, J.; Chaudhary, R.P. A review on advances in synthetic methodology and biological profile of spirothiazolidin-4-ones. *J. Heterocycl. Chem.* **2022**, *59*, 1839–1878. [CrossRef]

36. Lozynskyi, A.; Zimenkovsky, B.; Lesyk, R. Synthesis and Anticancer Activity of New Thiopyrano[2,3-*d*]thiazoles Based on Cinnamic Acid Amides. *Sci. Pharm.* **2014**, *82*, 723–733. [CrossRef]

37. Hu-Lieskovan, S.; Mok, S.; Homet Moreno, B.; Tsoi, J.; Robert, L.; Goedert, L.; Pinheiro, E.; Koya, R.; Graeber, T.; Comin-Anduix, B.; et al. Improved antitumor activity of immunotherapy with BRAF and MEK inhibitors in BRAFV600E melanoma. *Sci. Transl. Med.* **2015**, *7*, 279ra41. [CrossRef]

38. Abdel-Maksoud, M.S.; Kim, M.-R.; El-Gamal, M.I.; Gamal El-Din, M.M.; Tae, J.; Choi, H.S.; Lee, K.-T.; Yoo, K.H.; Oh, C.-H. Design, synthesis, in vitro antiproliferative evaluation, and kinase inhibitory effects of a new series of imidazo[2,1-b]thiazole derivatives. *Eur. J. Med. Chem.* **2015**, *95*, 453–463. [CrossRef]

39. Aly, A.A.; Alshammari, M.B.; Ahmad, A.; Gomaa, H.A.M.; Youssif, B.G.M.; Bräse, S.; Ibrahim, M.A.A.; Mohamed, A.H. Design, synthesis, docking, and mechanistic studies of new thiazolyl/thiazolidinylpyrimidine-2,4-dione antiproliferative agents. *Arab. J. Chem.* **2023**, *16*, 104612. [CrossRef]

40. Al-Wahaibi, L.H.; Gouda, A.M.; Abou-Ghadir, O.F.; Salem, O.I.A.; Ali, A.T.; Farghaly, H.S.; Abdelrahman, M.H.; Trembleau, L.; Abdu-Allah, H.H.M.; Youssif, B.G.M. Design and synthesis of novel 2,3-dihydropyrazino[1,2-a]indole-1,4-dione derivatives as antiproliferative EGFR and BRAF^{V600E} dual inhibitors. *Bioorg. Chem.* **2020**, *104*, 104260. [CrossRef]

41. Gomaa, H.A.M.; Shaker, M.E.; Alzarea, S.I.; Hendawy, O.M.; Mohamed, F.A.M.; Gouda, A.M.; Ali, A.T.; Morcoss, M.M.; Abdelrahman, M.H.; Trembleau, L.; et al. Optimization and SAR investigation of novel 2,3-dihydropyrazino[1,2-a]indole-1,4-dione derivatives as EGFR and BRAF^{V600E} dual inhibitors with potent antiproliferative and antioxidant activities. *Bioorg. Chem.* **2022**, *120*, 105616. [CrossRef] [PubMed]

42. Alshammari, M.B.; Aly, A.A.; Youssif, B.G.M.; Bräse, S.; Ahmad, A.; Brown, A.B.; Ibrahim, M.A.A.; Mohamed, A.H. Design and synthesis of new thiazolidinone/uracil derivatives as antiproliferative agents targeting EGFR and/or BRAF^{V600E}. *Front. Chem.* **2022**, *10*, 1076383. [CrossRef] [PubMed]

43. Buckle, D.R.; Cantello, B.C.C.; Smith, H.; Spicer, B.A. 4-Hydroxy-3-nitro-2-quinolones and related compounds as inhibitors of allergic reactions. *J. Med. Chem.* **1975**, *18*, 726–732. [CrossRef] [PubMed]

44. Bhudevi, B.; Ramana, P.V.; Mudiraj, A.; Reddy, A.R. Synthesis of 4-hydroxy-3-formylideneamino-lH/methyl/phenylquinolin2-ones. *Indian J. Chem. B* **2009**, *48*, 255–260.

45. Yang, Z.; Sun, P. Compare of three ways of synthesis of simple Schiff bas. *Molbank* **2006**, *2006*, M514. [CrossRef]

46. Mahmoud, M.A.; Mohammed, A.F.; Salem, O.I.A.; Gomaa, H.A.M.; Youssif, B.G.M. New 1,3,4-oxadiazoles linked 1,2,3-triazole moiety as antiproliferative agents targeting EGFR-TK. *Arch. Der Pharm.* **2022**, *355*, e2200009. [CrossRef]

47. Ramadan, M.; Abd El-Aziz, M.; Elshaier, Y.A.M.M.; Youssif, B.G.M.; Brown, A.B.; Fathy, H.M.; Aly, A.A. Design and synthesis of new pyranoquinolinone heteroannulated to triazolopyrimidine of potential apoptotic antiproliferative activity. *Bioorg. Chem.* **2020**, *105*, 104392. [CrossRef]

48. Al-Sanea, M.M.; Gotina, L.; Mohamed, M.F.A.; Parambi, D.G.T.; Gomaa, H.A.M.; Mathew, B.; Youssif, B.G.M.; Alharbi, K.S.; Elsayed, Z.M.; Abdelgawad, M.A.; et al. Design, Synthesis and Biological Evaluation of New HDAC1 and HDAC2 Inhibitors Endowed with Ligustrazine as a Novel Cap Moiety. *Drug Des. Dev. Ther.* **2020**, *14*, 497–508. [CrossRef]

49. Hisham, M.; Hassan, H.A.; Gomaa, H.A.M.; Youssif, B.G.M.; Hayallah, A.M.; Abdel-Aziz, M. Structure-based design, synthesis and antiproliferative action of new quinazoline-4-one/chalcone hybrids as EGFR inhibitors. *J. Mol. Struct.* **2022**, *1254*, 132422. [CrossRef]

50. Mohamed, F.A.M.; Gomaa, H.A.M.; Hendawy, O.M.; Ali, A.T.; Farghaly, H.S.; Gouda, A.M.; Abdelazeem, A.H.; Abdelrahman, M.H.; Trembleau, L.; Youssif, B.G.M. Design, synthesis, and biological evaluation of novel EGFR inhibitors containing 5-chloro-3-hydroxymethyl-indole-2-carboxamide scaffold with apoptotic antiproliferative activity. *Bioorg. Chem.* **2021**, *112*, 104960. [CrossRef]

51. Abou-Zied, H.A.; Beshr, E.A.M.; Gomaa, H.A.M.; Mostafa, Y.A.; Youssif, B.G.M.; Hayallah, A.M.; Abdel-Aziz, M. Discovery of new cyanopyridine/chalcone hybrids as dual inhibitors of EGFR/BRAF^{V600E} with promising antiproliferative properties. *Arch. Der Pharm.* **2022**, *355*, e2200464. [CrossRef]

52. Hisham, M.; Youssif, B.G.M.; Osman, E.E.A.; Hayallah, A.M.; Abdel-Aziz, M. Synthesis and biological evaluation of novel xanthine derivatives as potential apoptotic antitumor agents. *Eur. J. Med. Chem.* **2019**, *176*, 117–128. [CrossRef] [PubMed]

53. Martin, S.J. Caspases: Executioners of apoptosis. *Pathobiol. Hum. Dis.* **2014**, *145*, 145–152.

54. Abdelbaset, M.S.; Abdel-Aziz, M.; Abuo-Rahma, G.E.A.; Abdelrahman, M.H.; Ramadan, M.; Youssif, B.G.M. Novel quinoline derivatives carrying nitrones/oximes nitric oxide donors: Design, synthesis, antiproliferative and caspase-3 activation activities. *Arch. Der Pharm.* **2018**, *352*, 1800270. [CrossRef] [PubMed]

55. Abou-Zied, H.A.; Youssif, B.G.M.; Mohamed, M.F.A.; Hayallah, A.M.; Abdel-Aziz, M. EGFR inhibitors and apoptotic inducers: Design, synthesis, anticancer activity and docking studies of novel xanthine derivatives carrying chalcone moiety as hybrid molecules. *Bioorg. Chem.* **2019**, *89*, 102997. [CrossRef]

Article

Indoline-5-Sulfonamides: A Role of the Core in Inhibition of Cancer-Related Carbonic Anhydrases, Antiproliferative Activity and Circumventing of Multidrug Resistance

Stepan K. Krymov [1], Alexander M. Scherbakov [2], Lyubov G. Dezhenkova [1], Diana I. Salnikova [2], Svetlana E. Solov'eva [1], Danila V. Sorokin [2], Daniela Vullo [3], Viviana De Luca [4], Clemente Capasso [4], Claudiu T. Supuran [3,*] and Andrey E. Shchekotikhin [1,*]

[1] Gause Institute of New Antibiotics, 11 B. Pirogovskaya Street, 119021 Moscow, Russia
[2] Department of Experimental Tumor Biology, Blokhin N.N. National Medical Research Center of Oncology, 115522 Moscow, Russia
[3] Department of NEUROFARBA, Section of Pharmaceutical and Nutraceutical Sciences, University of Florence, 50122 Florence, Italy
[4] Institute of Biosciences and Bioresources, CNR, Via Pietro Castellino 111, 80131 Napoli, Italy
[*] Correspondence: claudiu.supuran@unifi.it (C.T.S.); shchekotikhin@gause-inst.ru (A.E.S.)

Abstract: The overexpression and activity of carbonic anhydrase (CA, EC 4.2.1.1) isoforms CA IX and CA XII promote the accumulation of exceeding protons and acidosis in the extracellular tumor environment. Sulfonamides are effective inhibitors of most families of CAs. In this study, using scaffold-hopping, indoline-5-sulfonamide analogs **4a–u** of the CA IX-selective inhibitor **3** were designed and synthesized to evaluate their biological properties. 1-Acylated indoline-5-sulfonamides demonstrated inhibitory activity against tumor-associated CA IX and XII with K_I values up to 132.8 nM and 41.3 nM. Compound **4f**, as one of the most potent inhibitors of CA IX and XII, exhibits hypoxic selectivity, suppressing the growth of MCF7 cells at 12.9 μM, and causes partial inhibition of hypoxia-induced CA IX expression in A431 skin cancer cells. **4e** and **4f** reverse chemoresistance to doxorubicin of K562/4 with overexpression of P-gp.

Keywords: indoline-5-sulfonamide; carbonic anhydrase IX; antiproliferative activity; hypoxia; breast cancer; skin cancer; multidrug resistance; carbonic anhydrase XII; P-glycoprotein

1. Introduction

One of the factors of the reduced effectiveness of chemo- and radiotherapy is hypoxic regions of tumors [1–3]. The deficient oxygen supply leads to the activation of transcriptional factor HIF-1α in tumor cells. In its turn, HIF-1α conceives expression of many proteins that advantage the development of aggressive phenotype of cancer cells [4]. One of the features of hypoxic cancer cells is the acidic extracellular pH (pHe) [5]. Increased level of protons causes resistance to the widely applied chemotherapeutic agents, including doxorubicin (Dox) [6] and cisplatin [7]. Aside from resistance development, acidic pHe destructs extracellular matrix and declines cell adhesion resulting in invasion and metastasis of tumors [8,9].

The acidic extracellular tumor environment arises from the coordinated work of transmembrane carbonic anhydrase (CA) IX and CA XII with sodium-hydrogen exchanger-1 [10]. CA IX and CA XII genes have a hypoxia response element that indicates their activation under the control of HIF-1α [11]. CA IX and CA XII are among 13 zinc metalloproteins of the α-carbonic anhydrases family with enzymatic activity [12]. Both enzymes are anchored in the cell membrane with active sites located in the extracellular milieu [13]. Utilizing the Zn^{2+} ion and His residues, CA IX and CA XII catalyze the hydration of CO_2 to HCO_3^- and H^+ [14]. CA IX presence in normal tissue is limited to GI mucosa, whereas its expression

in tumor cells is widespread and found in highly aggressive types of cancer, including breast, lung, brain, colon, rectum and kidney tumors [12,15]. Numerous studies have shown that the expression of CA IX is the prediction of a poor outcome [16–19]. However, CA XII, along with expression in several types of tumors, was also found in breast and colon normal tissues [20,21] and can correlate with a positive [22] as well as a negative prognosis [23,24]. Despite such uncertainty, several studies demonstrated the significance of CA XII in cancer severity [25,26]. For example, CA XII expression was increased in chemoresistant cells and influenced P-glycoprotein (P-gp) activity [27]. The development of CA XII as a pharmacological target for cancer therapy has led to successful reports of selective CA XII inhibitors overcoming multidrug resistance (MDR) in vivo [28,29].

Coordinating with the Zn^{2+} ion, sulfonamides such as acetazolamide (**1**) and SLC-0111 (**2**) (Figure 1) are the most studied inhibitors of the CA enzyme family [30–38]. SLC-0111 is the selective CA IX inhibitor; it reduces acidic pH, leading to the tumor and metastasis regression in preclinical models [39–41]. Combinations of different chemotherapeutic agents with SLC-0111 demonstrate a high potential for CA IX inhibition to treat aggressive and resistant types of cancer [42–44]. For example, the combination of the SLC-0111 with gemcitabine increased survival and enhanced tumor cell death of highly hypoxic and resistant pancreatic ductal adenocarcinomas in vivo [45].
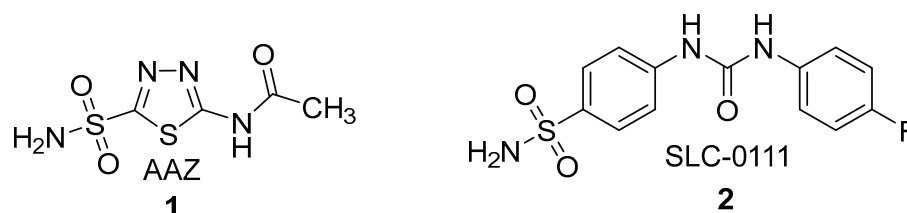
Figure 1. Chemical structures of clinically used diuretic AAZ (**1**) and CA IX inhibitor under clinical trial on diarylcarbamide scaffold (**2**).

Different groups have reported successful approaches to inhibit cancer-related CA IX and CA XII by indole-based sulfonamides [46–48]. Earlier, we studied 1-substituted isatin-5-sulfonamides as new CAs inhibitors, which suppressed the growth of tumor cells at low micromolar concentrations [49]. At this stage, we continue the work on modifying the structure of 5-indanesulfonamide derivative **3**, which selectively inhibits CA IX [50] and enhances the therapeutic effect of tumor irradiation in vivo [51]. However, 1-aminoindane-5-sulfonamide **3** has a limited antiproliferative effect on tumor cells [49], so the development of carbonic anhydrase inhibitors with improved anticancer potencies is a pivotal task. Scaffold hopping is an effective method to discover novel biologically active compounds by central core modification of the known lead compound [52–56]. Based on the selectivity of **3** toward CA IX and the known antiproliferative effect of indoline derivatives [57–59], we applied the scaffold hopping approach to replace 1-aminoindane to indoline core **4**, varying the structure of hydrophobic tail for the best binding to the targets (Figure 2).
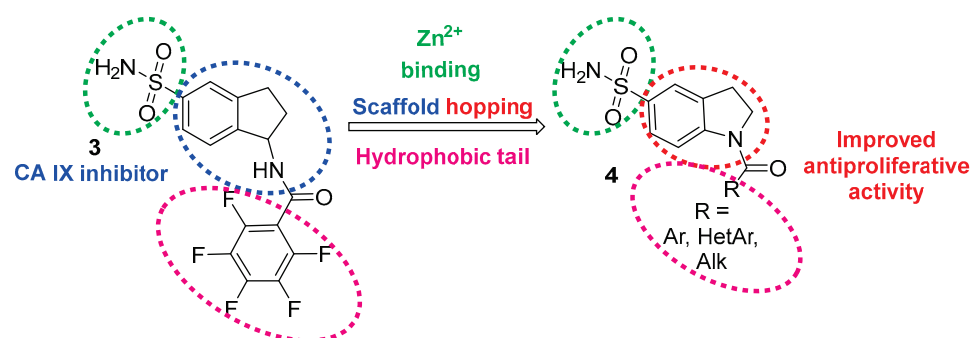
Figure 2. Scaffold hopping approach for the design of novel CA inhibitors based on indoline-5-sulfonamide core **4**.

To examine the results of the scaffold hopping for the discovery of new carbonic anhydrase inhibitors, we docked indane-5-sulfonamide **3** with indoline-5-sulfonamide analog **4** in the active site of CA IX (Figure 3). According to the modeling, **3** and perfluoro benzoyl derivative **4** demonstrate a similar orientation in the active site of CA IX. Both ligands interact with Zn^{2+} ions as sulfonamidate anions and form identical hydrogen bonds with Thr 199 and arene-H interactions with Leu 198 residues. The distinction of indoline ligand **4** from indane **3** lies in the orientation of the perfluorobenzoyl group that allows indoline inhibitor **4** to form novel interactions with the amino acid residue of CA IX. Thus, the additional hydrogen bond between the amides group of indoline ligand **4** and Gln 92 and the similar binding mode of central cores point to a promising potential of 1-acylindoline-5-sulfonamides **4** as new CA IX inhibitors.
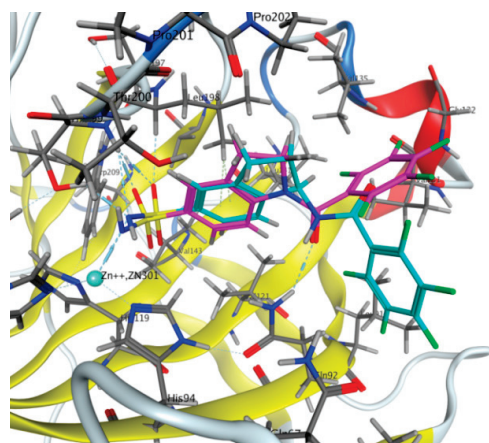
Figure 3. Modelling of aminoindanesulfoamide **3** (blue) and indoline analog **4e** (purple) in the active site of CA IX (PDB 5sz5).

2. Results

2.1. Chemistry

Indolines exhibit chemical properties close to N-substituted anilines. Developed methods of indole reduction and reverse dehydrogenation open the convenient synthetic way to 5-substituted indoles. In particular, Terent'ev and Preobrazhenskaya applied this method to obtain indole-5-sulfonamide [60]. Firstly, to carry out an electrophilic substitution, indoline (**5**) was protected with acetic anhydride in quantitative yield (Scheme 1). Next, 1-acetylindoline (**6**) was treated with chlorosulfuric acid, which led to 1-acetylindloine-5-sulfochloride (**7**) in a good yield (81%). The following interaction of sulfochloride **7** with ammonia in THF resulted in the formation of 1-acetylindoline-5-sulfonamide (**8**) with an 89% yield. In the next step, hydrolysis of indoline **8** by hydrochloric acid gave indoline-5-sulfonamide (**9**) with 81% yield.
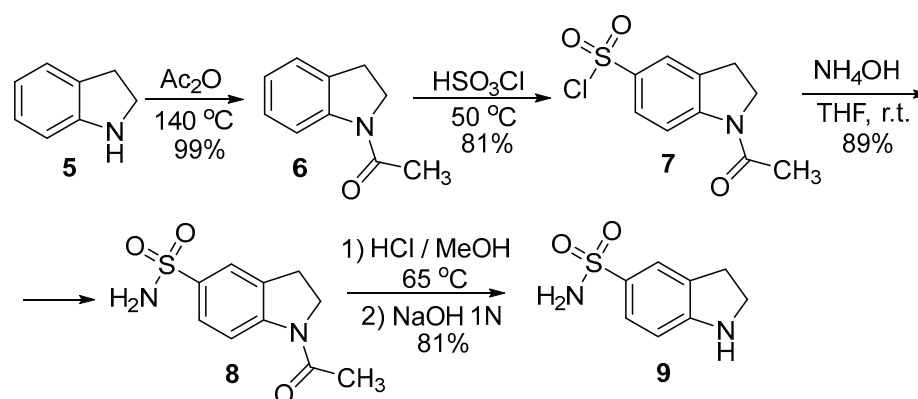
Scheme 1. The synthesis of indoline-5-sulfonamide **9**.

To synthesize a library of 1-acylindoline-5-sulfonamides **4**, indoline-5-sulfonamide **9** was acylated by a series of acyl chlorides in the presence of pyridine in CHCl$_3$ (Scheme 2). For the synthesis of isonicotinic derivative **4q**, the corresponding acid was activated by CDI and then treated with indoline-5-sulfonamide **9** in the presence of DMAP in THF. Applying these procedures, a library of 21 1-acylindoline-5-sulfonamides **4a–4u** was synthesized with 50–79% yields.
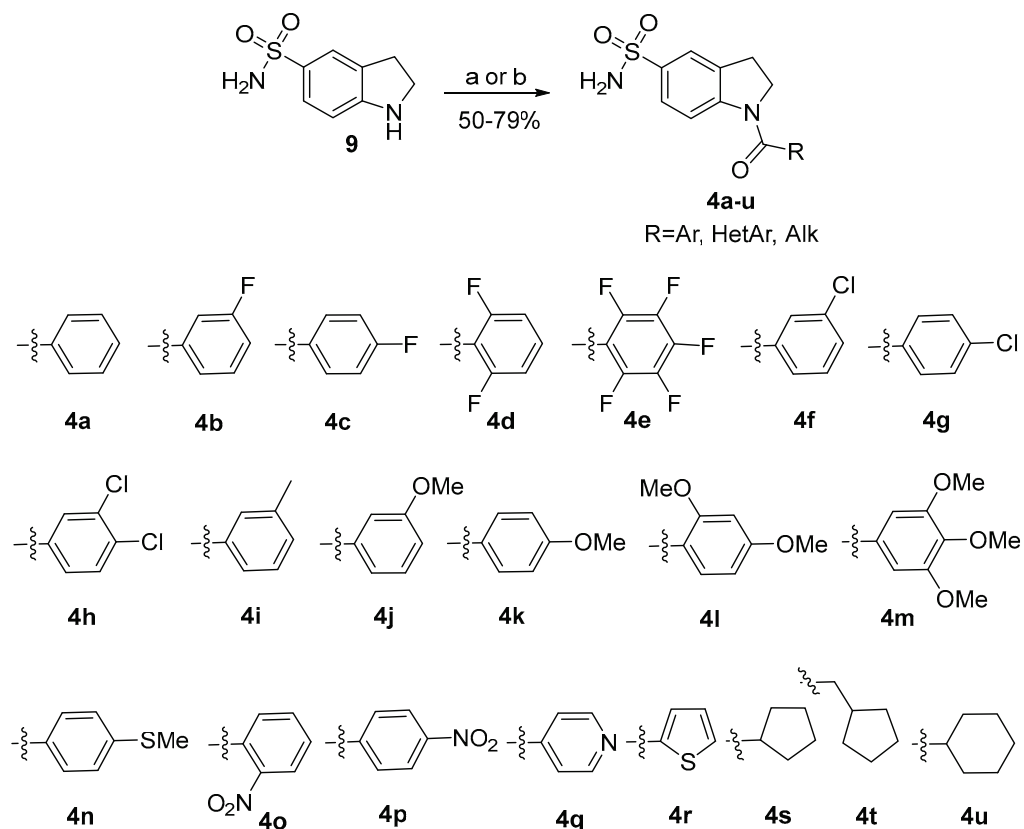
Scheme 2. The synthesis of 1-acylindoline-5-sulfonamides **4a–4u**. Reagents and conditions: (a) acyl chloride, Py, CHCl$_3$; r.t., (b) CDI, DMAP, THF, 40 °C.

To extend structure-activity relationships data, indoline-5-sulfonamide **9** was alkylated by benzyl bromide in MeCN in the presence of K$_2$CO$_3$ that yielded 1-benzyl-5-sulfonamide **10** (Scheme 3).
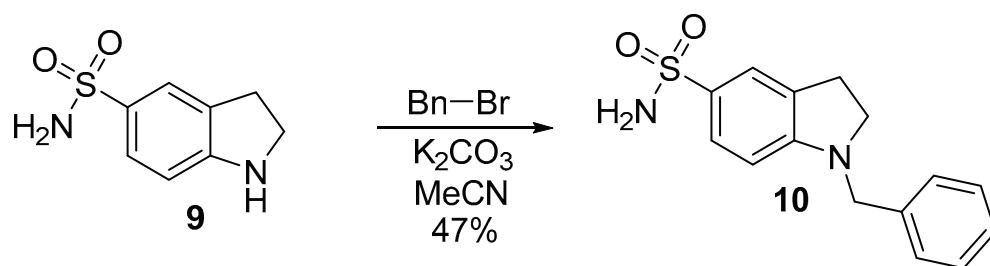
Scheme 3. The synthesis of 1-benzylindoline-5-sulfonamide **10**.

2.2. Carbonic Anhydrase Inhibition Assay

Synthesized indoline-5-sulfonamide derivatives **4a–4u**, **10** were evaluated against hCA I, hCA II, hCA IX and hCA XII by a stopped-flow technique (Table 1).

Table 1. Inhibition of hCAs I, II, IX and XII with indoline-5-sulfonamides **4a–4u**, **10** and AAZ and **3** as standards.

Cmp	K_I (nM) *			
	hCA I	hCA II	hCA IX	hCA XII
4a	79.0	5.4	>10^4	258.5
4b	65.9	5.6	>10^4	>10^4
4c	88.3	9.5	2246.9	>10^4
4d	268.1	9.1	1330.2	41.3
4e	52.2	3.4	1297.5	126.7
4f	303.9	31.3	141.2	111.7
4g	242.1	66.2	>10^4	57.0
4h	350.1	54.0	>10^4	56.0
4i	220.1	36.1	>10^4	93.9
4j	67.7	9.2	>10^4	110.0
4k	77.7	9.3	173.0	>10^4
4l	71.5	4.0	203.2	112.5
4m	49.0	3.0	>10^4	103.0
4n	71.4	9.3	1990.1	91.0
4o	83.4	4.5	>10^4	119.6
4p	60.5	42.2	2109.4	198.1
4q	64.0	12.5	2394.3	>10^4
4r	42.2	5.0	176.7	147.3
4s	60.9	7.1	132.8	88.1
4t	51.6	3.5	176.8	>10^4
4u	67.0	1.8	222.6	>10^4
10	41.0	3.0	>10^4	>10^4
AAZ	250	12.1	25.7	5.7
3 **	770	490	3.5	N.T.

* Mean from three different assays, by a stopped-flow technique (errors were in the range of $\pm$ 5–10% of the reported values); ** K_I data for compound **3** taken from previous research [50]; N.T.—not tested.

CA I and CA II are cytosolic proteins, that are widely expressed in erythrocytes, the eye, the GI tract, osteoclasts, and kidney cells [61]. CA II inhibitors are used in the clinical setting as diuretics and for glaucoma-related intraocular hypertension [62]. At the same time, CA I and CA II are considered the main off-target isoforms for the development of cancer-related CA IX and CA XII inhibitors [63].

The majority of indoline-5-sulfonamides **4a–4u**, **10** inhibits CA I at concentrations less than 100 nM. Structure-activity relationship points out that derivatives of benzoic acids with chlorine atoms **4f**, **g**, **h** demonstrate lower affinity toward this off-target isoform. At the same time, replacement of the phenyl **4a** by pyridine **4q**, thiophene **4r** or cycloalkanes **4s**, **t**, **u** does not affect K_I notably.

Indolines **4a–u** inhibit CA II at much lower concentrations despite its structural similarity to indane derivative **3**. However, a group of indoline-5-sulfonamides **4f–4i**, **4p** has somewhat higher K_I at 31–66 nM. Interestingly, previously studied 6-chloro-5-sulfamylindolines as potential furosemide analogs did not show notable diuretic activity in vivo [64].

3-Chlorophenyl **4f**, thiophene **4r** and cyclopentyl **4s**, **t** derivatives are the most potent derivatives inhibiting CA IX around 100 nM. These compounds outperform a group of the least active derivatives by more than 100 times, which indicates the high importance of the structure of the lipophilic fragment for CA IX inhibition. Additionally, a comparison of indane **3** with indoline analog **4e** reveals that 1-aminoindane scaffold appears as a preferred scaffold toward CA IX isoform. Thereby, the affinity of 1-acylindoline-5-sulfonamides **4a–u** for CA IX mainly depends on the structure of acyl moiety and is notably enhanced by 3-chlorophenyl and five-membered rings of aromatic and saturated nature.

1-Acylated indoline-5-sulfonamides **4d**, **g**, **h** are potent inhibitors of CA XII. Notably, for indoline-5-sulfonamides, the introduction of acyl group (**4a**), compared to less polar alkyl fragment (**10**), leads to a clear gain of activity against CA XII. The majority of 1-

acylated indoline-5-sulfonamides inhibit CA XII around 100 nM. Additionally, 4-chloro **4g** and 3,4-dichloro derivatives **4h** demonstrate selectivity over CA I and CA IX isoforms and have similar K_I with CA II. Based on the CA inhibition profile, 3-chlorobenzoyl derivative **4f**, as one of the most potent compounds toward CA IX and CA XII, was selected as the lead compound for further investigation.

2.3. Docking Studies

To investigate the difference of K_I against CA IX in 1-acylindoline-5-sulfonamides, we docked compound **4f** (Figure 4) in the active site of CA IX and compared it to a model of **4e**. As in the case with perfluoro derivative **4e**, **4f** displays coordination with Zn^{2+} ion as a sulfonamidate anion. Additionally, both ligands are acceptors of hydrogen bonds of Thr 199 residue. The differences between **4e** and **4f** occurred in interactions of indoline and acyl fragments. In particular, ligand **4f**, compared with **4e**, lacks arene-H interaction with Leu 198 but interacts with Gln 67 instead of Gln 92. Almost 10-fold higher activity of **4f** in vitro may be explained by the strength of interactions and physicochemical properties of compounds.
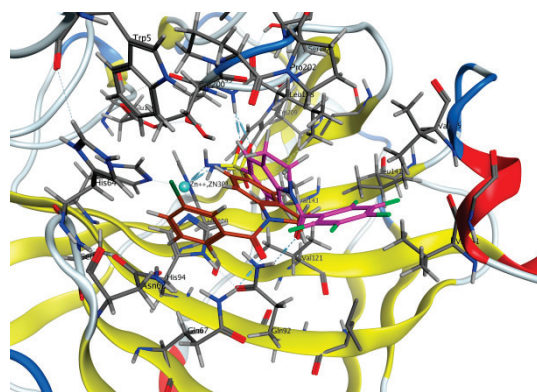
Figure 4. Docking of 3-chlorobenzoyl derivative **4f** (brown) and **4e** (purple) in the active site of CA IX (PDB 5sz5).

2.4. Antiproliferative Activity of Indoline-5-sulfonamides

A series of synthesized indoline-5-sulfonamides was tested on the MCF7 cancer cell line under normoxia and hypoxia using the MTT test. According to the results presented in Table 2, indoline-5-sulfonamides demonstrate a moderate antiproliferative effect. In general, indoline-5-sulfonamides do not lose their activity under hypoxia, which is the common reason for resistance to current antitumor agents. Comparing MTT results of **3** and indoline analog **4e**, we observed a clear gain of antiproliferative activity for the indoline derivative against the MCF7 line in normoxia and hypoxia. Again, indoline-5-sulfonamide **4f** as the most potent compound against MCF7 cells under hypoxia conditions (IC_{50} = 12.9 μM) demonstrates two-fold higher activity compared to normoxia conditions.

To evaluate the influence of CA inhibition on the antiproliferative activity, we selected five compounds **4b**, **f**, **m**, **n** and **10** with different inhibition profiles against CA IX for in-depth testing on cancer cells with increased CA IX expression. The database www. proteinatlas.org (accessed on 13 October 2022) contains data on gene expression in various cell lines. According to the data obtained from this database, A431 cells express CA IX at a very high level, which distinguishes them from human cell lines belonging to other tissues [https://www.proteinatlas.org/ENSG00000107159-CA9/cell+line (accessed on 13 October 2022)]. A431 cells are skin cancer cells, and their growth has already been intensely analyzed in hypoxia [65–67]. Hypoxia significantly alters the activity of signaling pathways in these cells; some of the revealed changes may be related to the induced activity of CAs. Moreover, Ren and colleagues described that hypoxia modulates cellular pathways in A431 cells, which are associated with radioresistance and enhanced migration [65]. Given the observations described above, we were expecting to reveal the high antiproliferative

activity of the selected compounds against skin cancer cells. Surprisingly, the activity turned out to be at a moderate level. The cell growth curves are shown in Figure 5A–E. As can be seen in normoxia, the compounds inhibit cell growth by no more than 20%. Compounds **4b** and **4m** were the least active in normoxia; this finding may be associated with their low activity against CA IX (Table 1). In hypoxia, the activity of tested compounds was increased, but the 50% inhibition of growth was never achieved.

Table 2. Antiproliferative activity of indoline-5-sulfonamides **4a**–**4u**, **10** (the MTT assay after 72 h exposure; IC$_{50}$, µM).

Compound	IC$_{50}$ [a] against MCF7 Cells, µM	
	Normoxia	**Hypoxia**
4a	>50	36.9 ± 3.5
4b	>50	>50
4c	40.6 ± 3.8	32.7 ± 2.8
4d	>50	35.9 ± 3.4
4e	29.9 ± 2.7	20.2 ± 2.0
4f	24.5 ± 1.9	12.9 ± 1.2
4g	36.5 ± 3.3	24.2 ± 2.1
4h	35.2 ± 3.5	48.7 ± 4.5
4i	>50	43.6 ± 4.0
4j	46.2 ± 3.6	>50
4k	>50	>50
4l	37.0 ± 3.0	>50
4m	29.6 ± 2.2	36.7 ± 3.2
4n	18.4 ± 1.6	>50
4o	43.7 ± 3.7	39.5 ± 3.4
4p	48.8 ± 4.4	39.9 ± 3.5
4q	>50	>50
4r	47.7 ± 3.8	39.1 ± 3.9
4s	>50	>50
4t	38.0 ± 3.5	36.0 ± 3.3
4u	37.1 ± 3.5	39.2 ± 3.4
10	23.6 ± 2.0	34.8 ± 3.2
3	>50	>50

[a] IC$_{50}$ values represent an average of at least three independent experiments.
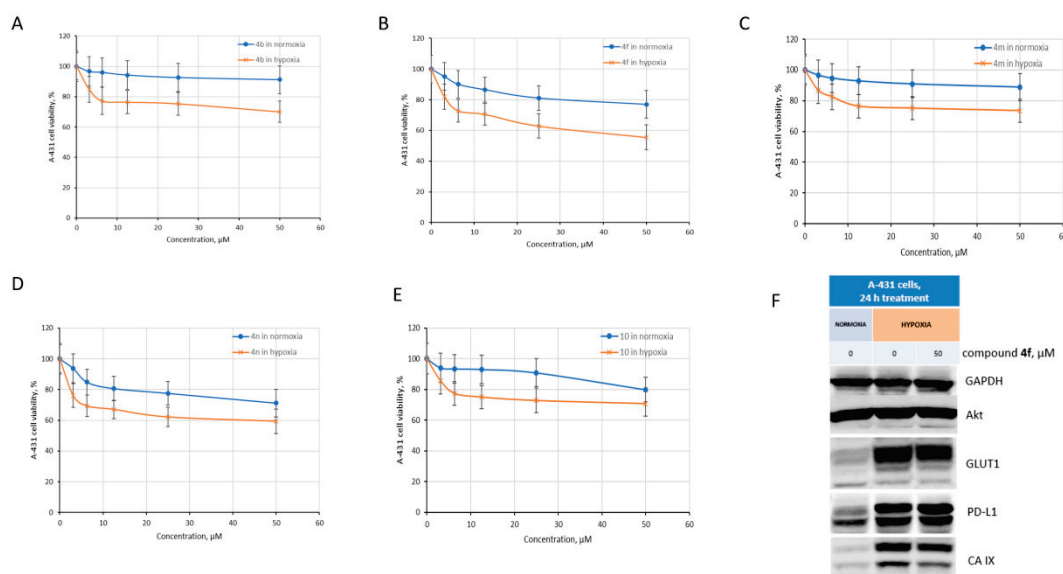
Figure 5. The activity of compounds **4b**, **f**, **m**, **n** and **10** against A431 skin cancer cells in normoxia and hypoxia. (**A**–**E**) antiproliferative evaluation; (**F**) immunoblotting with antibodies against Akt, GLUT1, PD-L1, CA IX; GAPDH antibodies were used as loading controls.

Compound **4f** was the most active under hypoxic conditions, inhibiting the growth of A431 cells by 44%. We wondered whether compound **4f** affected CA IX expression or whether its activity was limited to inhibiting the enzyme activity reported above (Table 1). To induce CA IX expression, cells were placed in hypoxia for 24 h, and then protein expression was analyzed by immunoblotting. Because the data on the expression of hypoxia-related proteins in the literature are highly inconsistent, we introduced additional controls. Antibodies to hypoxia-regulated and "non-hypoxic" proteins were used [68,69]. The expression of kinase Akt, which is not regulated directly by hypoxia/HIF-1α, was not altered under hypoxia conditions (Figure 5F). On the contrary, the expression of proteins (CA IX, PD-L1, GLUT1) associated with hypoxia pathways was significantly increased. Thus, these data again support a high expression of CA IX in A431 cells. In A431 cells treated with compound **4f**, a moderate decrease in CA IX expression was observed, whereas the expression of hypoxia-regulated proteins PD-L1 and GLUT1 did not change. Thus, lead compound **4f** not only blocks the enzyme activity of CA IX, but also causes partial inhibition of hypoxia-induced CA IX expression in skin cancer cells.

Next, we examined the activity of the whole series of indoline-5-sulfonamides against leukemia cell line K562. Surprisingly, among all tested compounds, only perfluoro derivative **4e** demonstrated significant activity and inhibited the growth of the cells at 10 μM. Other indoline derivatives showed low activity against K562 cells at 50 μM or the highest concentrations.

Earlier, Kopecka and colleagues have shown that CA XII can interact with P-gp and influence its activity [27]. Subsequently, silencing or inhibition of CA XII by chemical agents may restore the sensitivity to Dox of resistant K562 and other tumor cells [70,71]. Given the potent inhibition of **4f** against CA XII and the activity of **4e** against K562, we examined their ability to reverse the chemoresistance of K562/4 with P-gp to Dox. MTT-test results summarized in Figure 6 show that **4e** and **4f** have low cytotoxic activity against MDR subline K562/4 as monoagents. However, treatment of K562/4 cells with combinations of Dox with **4e** and **4f** led to the decline of viable K562/4 cells. Specifically, the combination of Dox with perfluoro derivative **4e** demonstrated a clear dose-dependent antiproliferative effect against K562/4 cells.
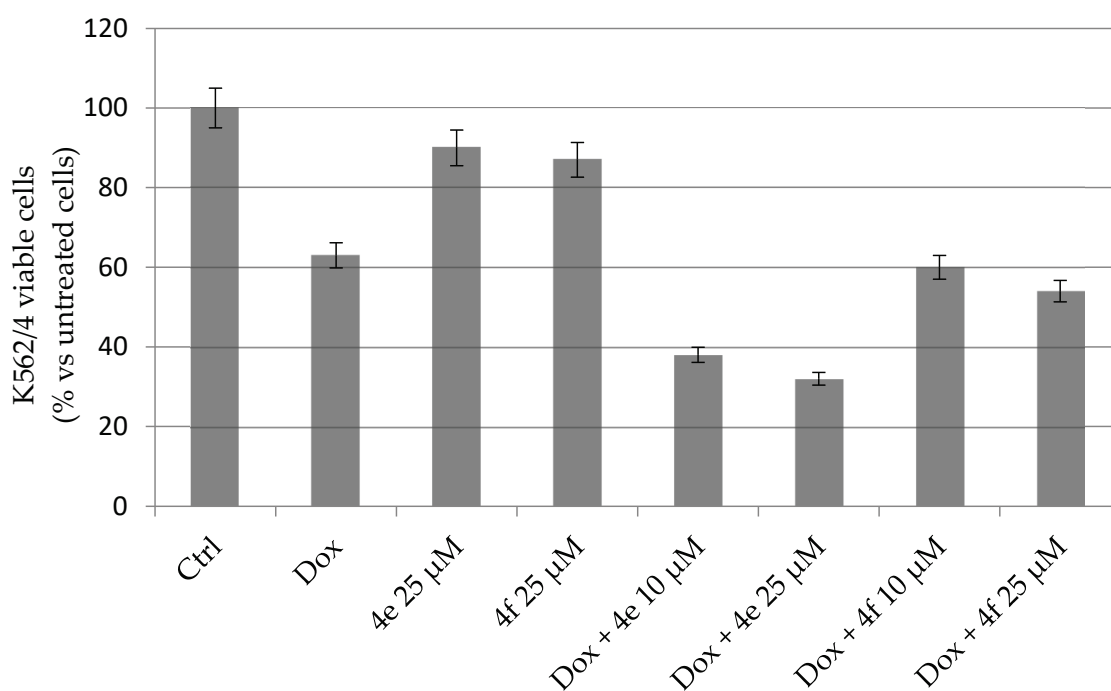
Figure 6. Susceptibility of resistant K562/4 line to combinations of Dox (25 μM) with indoline-5-sulfonamides **4e** and **4f**. Data are presented as means $\pm$ SD (*n* = 3).

3. Discussion

Scaffold hopping makes it possible to reveal previously unknown data on the structure-activity relationships. It is especially important for the search for selective inhibitors of enzymes with off-target isoforms. In addition to a Zn^{2+} binding sulfonamide group, inhibitors of tumor-associated CA IX require a lipophilic fragment responsible for interaction with the hydrophobic side of the enzyme. Thus, in the structure of the CA IX-selective sulfonamide **3**, we replaced the 1-aminoindane with an indoline fragment and varied the hydrophobic tail to create new inhibitors of CA IX. As a result, we have obtained a broad series of 1-substituted indoline-5-sulfonamides exhibiting a broad spectrum of K_I against four CA isoforms. In general, replacement of 1-aminoindane scaffold with indoline led to a significant increase of activity against cytosolic CA I and CA II isoforms. Simultaneously, inhibition of CA IX and CA XII by 1-acylindoline-5-sulfonamides **4a–4u** can vary in the range of two orders. Among indoline-5-sulfonamides with a high affinity toward cancer-related isoforms, indoline **4f** demonstrated a decreased activity toward cytosolic CA I and CA II.

The antiproliferative activity of the indoline-5-sulfonamides **4a–4u** series indicated the good activity of potent CA IX and CA XII inhibitor **4f**, which exhibits hypoxic selectivity and inhibits the growth of MCF7 cells at 12.9 μM. At the same time, indoline analog **4e** outperforms indane analog **3** against the MCF7 line. MTT-test of chosen indoline-5-sulfonamides did not reveal a high antiproliferative activity against A431 cells with a high expression of CA IX. However, immunoblotting has shown that the lead **4f** not only inhibits CA IX, but also suppresses CA IX expression under hypoxic conditions in A431 skin cancer cells.

The good inhibitory activity of some indoline-5-sulfonamides against CA XII, a new target for overcoming MDR, made it compelling to study **4e** and **4f** ability to overcome the resistance of K562/4 cells with the expression of P-gp. Combinations of compounds **4e** and **4f** with Dox pointed to their ability to increase the suppression of resistant cells K562/4.

Overall, 1-acylated indoline-5-sulfonamides represent a new scaffold of nanomolar inhibitors and suppressors of tumor-associated CA IX and CA XII that points out their potential as adjuvant and MDR-overcoming agents (Supplementary Materials).

4. Materials and Methods

4.1. Synthesis

4.1.1. Instruments and General Information

NMR spectra were recorded on a Varian VXR-400 instrument operated at 400 MHz (^{1}H NMR) and 100 MHz (^{13}C NMR). Chemical shifts were measured in DMSO-d6, using tetramethylsilane as an internal standard. Analytical TLC was performed on Silica Gel F254 plates (Merck), column chromatography with a SilicaGel Merck 60. Melting points were determined using a Buchi SMP-20 apparatus and were uncorrected. High-resolution mass spectra were recorded with electron spray ionization on a Bruker Daltonics microOTOF-QII instrument. HPLC was performed using a Shimadzu Class-VP V6.12SP1 system. IR spectra were recorded on a Nicolet iS10 Fourier transform IR spectrometer (Nicolet iS10 FT-IR, Madison, WI). All solvents, chemicals and reagents were obtained commercially and used without purification. The purity of final compounds **4a–4u**, **10** was ≥95% as determined by HPLC analysis.

Indoline-5-sulfonamide **9** was synthesized from indoline **5** according to a previously reported procedure [72].

4.1.2. 1-Acetylindoline (**6**)

To a stirring acetic anhydride (15 mL, 0.16 mol) was added indoline (**5**, 4 g, 0.034 mol). The reaction mixture was refluxed for 10 min, cooled to room temperature and poured onto ice. The pinkish precipitate was filtered and washed with water to obtain 5.39 g (99%) of *N*-acetylindoline, m.p. = 102–104 °C (102–104 °C lit.).

4.1.3. 1-Acetyl-5-(chlorosulfonyl)indoline (7)

To a stirring chlorosulfonic acid (15 mL, 0.225 mol) cooled in an ice bath was added *N*-acetylindoline (**6**, 5.4 g, 0.034 mol) portionwise at 0–5 °C. The resulting mixture was heated to 50 °C for 2 h. Upon completion, the reaction mixture was cooled and poured onto ice, and the precipitate was filtered and washed with cold water twice to obtain 7.0 g (81%) of 5-(chlorosulfonyl)-*N*-acetylindoline as a white solid, m.p. = 167–169 °C (167–169 °C lit.).

4.1.4. 1-Acetylindoline-5-sulfonamide (8)

To a solution of 5-(chlorosulfonyl)-*N*-acetylindoline (**7**, 7.0 g, 0.027 mol) in THF (40 mL) was added NH_4OH (10 mL, 0.098 mol, 18% solution) at room temperature. The reaction mixture was stirred for 1 h and then concentrated in vacuo. The residue was diluted with water and adjusted to a pH of 7–8 with 1 N aq. HCl solution to give 5.8 g (89%) of *N*-acetylindoline-5-sulfonamide as a white solid, m.p. = 223–225 °C (223–224 °C lit.).

4.1.5. Indoline-5-sulfonamide (9)

To a suspension of *N*-acetylindoline-5-sulfonamide (**8**, 5.8 g, 0.024 mol) in MeOH (30 mL) was added concentrated HCl (10 mL, 0.1 mol). The mixture was refluxed for 2 h, cooled, and the solvent was removed in vacuo. The product was dissolved in water (40 mL), and the solution was adjusted to a pH of 7–8 with 1N aq. NaOH solution. The brown precipitate was filtered and purified by flash chromatography to obtain 3.9 g (81%) of pure indoline-5-sulfonamide. ^{1}H NMR (400 MHz, DMSO-d_6): δ 7.39 (s, 1H, Ar), 7.35 (dd, J^1 = 8.3, J^2 = 1.6 Hz, 1H, Ar), 6.88 (s, 2H, NH_2), 6.46 (d, J = 8.3 Hz, 1H, Ar), 6.19 (d, 1H, Ar), 3.49 (t, J = 8.4 Hz, 2H, CH_2), 2.94 (t, J = 8.4 Hz, 2H, CH_2). ^{13}C NMR (100 MHz, DMSO-d_6): δ 155.9, 131.6, 129.2, 126.8, 122.5, 106.5, 46.9, 28.8.

4.1.6. 1-Benzoylindoline-5-sulfonamide (4a)

To a solution of indoline-5-sulfonamide (**9**, 80 mg, 0.4 mmol) and pyridine (66 µL, 0.8 mmol) in $CHCl_3$ (3 mL) was added 56 µL (0.48 mmol) of benzoyl chloride in $CHCl_3$ (2 mL) at 0–5 °C. The resulting mixture was stirred at room temperature for 2 h, and the solvent was removed in vacuo. The residue was diluted with water (7 mL) and adjusted to a pH of 4–5 with 1 N aq. HCl solution and filtrated. The crude product was crystallized from MeOH to get 96 mg (79%) of pure 1-benzoylindoline-5-sulfonamide **4a**. A white powder, mp > 250 °C. HPLC (LW = 300 nm, gradient B 30/70/30% (35 min)) t_R = 11.7 min, purity 99%. ^{1}H NMR (400 MHz, DMSO-d_6): δ 7.96 (br s, 1H, Ar), 7.69 (s, 1H, Ar), 7.64 (d, J = 6.4 Hz, 1H, Ar), 7.59 (d, J = 7.2 Hz, 2H, Ar), 7.54–7.45 (m, 3H, Ar), 7.27 (s, 2H, NH_2), 4.04 (t, J = 8.2 Hz, 2H, CH_2), 3.12 (t, J = 8.2 Hz, 2H, CH_2). ^{13}C NMR (100 MHz, DMSO-d_6): δ 169.1, 145.9, 139.6, 136.9, 134.2, 130.9, 129.0 (2C), 127.4 (2C), 125.7, 123.0, 116.3, 51.3, 27.9. HRMS (ESI) (*m/z*) [M+H]$^+$: calculated for $C_{15}H_{15}N_2O_3S$ 303.0798, found 303.0811.

4.1.7. 1-(3-Fluorobenzoyl)indoline-5-sulfonamide (4b)

This compound was prepared from **9** and 3-fluorobenzoyl chloride as described for **4a**. A white powder, yield 67%, mp > 250 °C. HPLC (LW = 300 nm, gradient B 30/70/30% (35 min)) t_R = 13.7 min, purity 99%. ^{1}H NMR (400 MHz, DMSO-d_6): δ 8.07 (br s, 1H, Ar), 7.69 (s, 1H, Ar), 7.65 (d, J = 7.3 Hz, 1H, Ar), 7.59–7.51 (m, 1H, Ar), 7.51–7.42 (m, 2H, Ar), 7.45 (m, 1H, Ar), 7.26 (s, 2H, NH_2), 4.05 (t, J = 8.2 Hz, 2H, CH_2), 3.14 (t, J = 8.2 Hz, 2H, CH_2). ^{13}C NMR (100 MHz, DMSO-d_6): δ 167.5, 162.2 (d, J = 245.4 Hz, C-F), 145.6, 139.8, 139.1 (d, J = 6.9 Hz, C-F), 134.2, 131.3 (d, J = 7.7 Hz), 125.8, 123.6, 123.0, 117.7 (d, J = 20.7 Hz), 116.4, 114.5 (d, J = 22.2 Hz), 51.2, 27.9. HRMS (ESI) (*m/z*) [M+H]$^+$: calculated for $C_{15}H_{14}FN_2O_3S$ 321.0704, found 321.0679.

4.1.8. 1-(4-Fluorobenzoyl)indoline-5-sulfonamide (4c)

This compound was prepared from **9** and 4-fluorobenzoyl chloride as described for **4a**. A white powder, yield 73%, mp > 250 °C. HPLC (LW = 300 nm, gradient B 30/70/30% (35 min)) t_R = 13.2 min, purity 100%. ^{1}H NMR (400 MHz, DMSO-d_6): δ 7.90 (br s, 1H,

Ar), 7.74–7.61 (m, 4H, Ar), 7.32 (m, 2H, Ar), 7.27 (s, 2H, NH$_2$), 4.06 (t, J = 8.2 Hz, 2H, CH$_2$), 3.13 (t, J = 8.2 Hz, 2H, CH$_2$). ^{13}C NMR (100 MHz, DMSO-d_6): δ 168.1, 163.5 (d, J = 247.7 Hz, C-F), 145.8, 139.6, 134.2, 133.4, 130.3 (d, J = 8.4 Hz, 2C), 125.7, 123.0, 116.4, 116.0 (d, J = 21.5 Hz, 2C), 51.3, 27.9. HRMS (ESI) (m/z) [M+H]$^+$: calculated for C$_{15}$H$_{14}$FN$_2$O$_3$S 321.0704, found 321.0721.

4.1.9. 1-(2,6-Difluorobenzoyl)indoline-5-sulfonamide (4d)

This compound was prepared from **9** and 2,6-difluorobenzoyl chloride as described for **4a**. A white powder, yield 72%, mp = 244–246 °C. HPLC (LW = 300 nm, gradient B 30/70/30% (35 min)) t$_R$ = 13.5 min, purity 98%. ^{1}H NMR (400 MHz, DMSO-d_6): δ 8.24 (d, J = 8.6 Hz, 1H, Ar), 7.79–7.70 (m, 2H, Ar), 7.62 (m, 1H, Ar), 7.32 (s, 2H, NH$_2$), 7.31–7.22 (m, 2H, Ar), 3.93 (t, J = 8.6 Hz, 2H, CH$_2$), 3.21 (t, J = 8.6 Hz, 2H, CH$_2$). ^{13}C NMR (100 MHz, DMSO-d_6): δ 159.6, 158.4 (d, J = 248.4 Hz, C-F), 158.3 (d, J = 248.4 Hz, C-F), 144.6, 140.7, 134.3, 133.2 (t, J = 9.2 Hz), 126.1, 123.2, 116.3, 114.6 (t, J = 23.0 Hz), 112.9 (d, J = 23.0 Hz, 2C), 49.5, 27.5. HRMS (ESI) (m/z) [M+H]$^+$: calculated for C$_{15}$H$_{13}$F$_2$N$_2$O$_3$S 339.0609, found 339.0609.

4.1.10. 1-(Perfluorobenzoyl)indoline-5-sulfonamide (4e)

This compound was prepared from **9** and perfluorobenzoyl chloride as described for **4a**. A white powder, yield 72%, mp = 187–189 °C. HPLC (LW = 300 nm, gradient B 30/70/30% (35 min)) t$_R$ = 20.9 min, purity 99%. ^{1}H NMR (400 MHz, DMSO-d_6): δ 8.19 (d, J = 8.6 Hz, 1H, Ar), 7.77–7.70 (m, 2H, Ar), 7.35 (s, 2H, NH$_2$), 4.05 (t, J = 8.2 Hz, 2H, CH$_2$), 3.13 (t, J = 8.2 Hz, 2H, CH$_2$). ^{13}C NMR (100 MHz, DMSO-d_6): δ 156.3, 144.2, 141.6 (m, C-F, 2C), 141.2, 139.1 (m, C-F, 2C), 134.7, 126.1, 125.2, 123.3, 116.5, 111.6 (m, C-F), 49.6, 27.5. HRMS (ESI) (m/z) [M+H]$^+$: calculated for C$_{15}$H$_{10}$F$_5$N$_2$O$_3$S 393.0327, found 393.0332. IR ν max, (film) cm^{-1} 3373 m, 3283 m, 1654 s, 1597 m, 1552 w, 1529 m, 1486 s, 1434 m, 1419 w, 1394 s, 1342 s, 1321 w, 1303 w, 1283 w, 1252 w, 1225 w, 1183 m, 1149 m, 1137 w, 1107 m, 1070 s, 988 s, 936 m, 916 m, 891 w, 832 s, 813 w, 785 m, 702 m, 677 m.

4.1.11. 1-(3-Chlorobenzoyl)indoline-5-sulfonamide (4f)

This compound was prepared from **9** and 3-chlorobenzoyl chloride as described for **4a**. A white powder, yield 75%, mp > 250 °C. HPLC (LW = 300 nm, gradient B 30/70/30% (35 min)) t$_R$ = 17.0 min, purity 99%. ^{1}H NMR (400 MHz, DMSO-d_6): δ 8.25–7.90 (br s, 1H, Ar), 7.72–7.62 (m, 3H, Ar), 7.62–7.48 (m, 3H, Ar), 7.26 (s, 2H, NH$_2$), 4.04 (t, J = 8.2 Hz, 2H, CH$_2$), 3.13 (t, J = 8.2 Hz, 2H, CH$_2$). ^{13}C NMR (100 MHz, DMSO-d_6): δ 167.4, 145.6, 139.8, 138.9, 134.2, 133.7, 131.0, 130.7, 127.3, 126.1, 125.8, 123.0, 116.4, 51.2, 27.9. HRMS (ESI) (m/z) [M+H]$^+$: calculated for C$_{15}$H$_{14}$ClN$_2$O$_3$S 337.0408, found 337.0386. IR ν max, (film) cm^{-1} 3336 s, 3189 m, 3079 w, 1644 s, 1592 m, 1566 w, 1539 m, 1482 s, 1433 s, 1394 s, 1333 s, 1315 s, 1257 m, 1194 s, 1169 m, 1152 s, 1111 w, 1079 s, 999 w, 912 s, 892 s, 869 s, 835 s, 802 s, 772 w, 741 w, 714 m, 683 w.

4.1.12. 1-(4-Chlorobenzoyl)indoline-5-sulfonamide (4g)

This compound was prepared from **9** and 4-chlorobenzoyl chloride as described for **4a**. A white powder, yield 74%, mp > 250 °C. HPLC (LW = 300 nm, gradient B 30/70/30% (35 min)) t$_R$ = 17.1 min, purity 99%. ^{1}H NMR (400 MHz, DMSO-d_6): δ 8.15–7.90 (br s, 1H, Ar), 7.69 (s, 1H, Ar), 7.68–7.61 (m, 3H, Ar), 7.56 (d, J = 8.2 Hz, 2H, Ar), 7.26 (s, 2H, NH$_2$), 4.05 (t, J = 8.2 Hz, 2H, CH$_2$), 3.13 (t, J = 8.2 Hz, 2H, CH$_2$). ^{13}C NMR (100 MHz, DMSO-d_6): δ 168.0, 145.7, 139.7, 135.7 135.6, 134.2, 129.5 (2C), 129.1 (2C), 125.8, 123.0, 116.4, 51.2, 27.9. HRMS (ESI) (m/z) [M+H]$^+$: calculated for C$_{15}$H$_{14}$ClN$_2$O$_3$S 337.0408, found 337.0409.

4.1.13. 1-(3,4-Dichlorobenzoyl)indoline-5-sulfonamide (4h)

This compound was prepared from **9** and 3,4-dichlorobenzoyl chloride as described for **4a**. A white powder, yield 73%, mp > 250 °C. HPLC (LW = 300 nm, gradient B 30/70/30% (35 min)) t$_R$ = 21.5 min, purity 97%. ^{1}H NMR (400 MHz, DMSO-d_6): δ 8.35–8.02 (br s, 1H, Ar), 7.90 (d, J = 1.4 Hz, 1H, Ar), 7.76 (d, J = 8.6 Hz, 1H, Ar), 7.69 (s, 1H, Ar), 7.68–7.63(m,

1H, Ar), 7.60 (dd, *J* = 8.6 Hz, *J* = 1.4 Hz, 1H, Ar),7.26 (s, 2H, NH$_2$), 4.05 (t, *J* = 8.2 Hz, 2H, CH$_2$), 3.13 (t, *J* = 8.2 Hz, 2H, CH$_2$). ^{13}C NMR (100 MHz, DMSO-*d$_6$*): δ 166.5, 145.5, 139.9, 137.3, 134.2, 133.6, 131.9, 131.4, 129.6, 127.8, 125.8, 123.0, 116.5, 51.2, 27.9. HRMS (ESI) (*m/z*) [M+H]$^+$: calculated for C$_{15}$H$_{13}$Cl$_2$N$_2$O$_3$S 371.0018, found 371.0005.

4.1.14. 1-(3-Methylbenzoyl)indoline-5-sulfonamide (4i)

This compound was prepared from **9** and 3-methylbenzoyl chloride as described for **4a**. A white powder, yield 69%, mp = 247–249 °C. HPLC (LW = 300 nm, gradient B 30/70/30% (35 min)) t$_R$ = 15.3 min, purity 99%. ^{1}H NMR (400 MHz, DMSO-*d$_6$*): δ 8.05–7.83 (br s, 1H, Ar), 7.68 (s, 1H, Ar), 7.63 (d, *J* = 6.6 Hz, 1H, Ar), 7.43–7.30 (m, 4H, Ar), 7.24 (s, 2H, NH$_2$), 4.04 (t, *J* = 8.6 Hz, 2H, CH$_2$), 3.12 (t, *J* = 8.6 Hz, 2H, CH$_2$). ^{13}C NMR (100 MHz, DMSO-*d$_6$*): δ 169.2, 145.9, 139.5, 138.4, 136.9, 134.1, 131.5, 128.9, 127.8, 125.7, 124.4, 123.0, 116.2, 51.2, 27.9, 21.4. HRMS (ESI) (*m/z*) [M+H]$^+$: calculated for C$_{16}$H$_{17}$N$_2$O$_3$S 317.0954, found 317.0981.

4.1.15. 1-(3-Methoxybenzoyl)indoline-5-sulfonamide (4j)

This compound was prepared from **9** and 3-methoxybenzoyl chloride as described for **4a**. A white powder, yield 62%, mp = 225–227 °C. HPLC (LW = 300 nm, gradient B 30/70/30% (35 min)) t$_R$ = 13.1 min, purity 99%. ^{1}H NMR (400 MHz, DMSO-*d$_6$*): δ 7.97 (br s, 1H, Ar), 7.68 (s, 1H, Ar), 7.63 (d, *J* = 6.9 Hz, 1H, Ar), 7.40 (t, *J* = 7.8 Hz 1H, Ar), 7.25 (s, 2H, NH$_2$), 7.16–7.11 (m, 2H, Ar), 7.08 (dd, *J* = 7.8, *J* = 2.4 Hz, 1H, Ar), 4.04 (t, *J* = 8.2 Hz, 2H, CH$_2$), 3.78 (s, 3H, OMe), 3.12 (t, *J* = 8.2 Hz, 2H, CH$_2$). ^{13}C NMR (100 MHz, DMSO-*d$_6$*): δ 168.7, 159.6, 145.8, 139.6, 138.3, 134.2, 130.3, 125.7, 123.0, 119.4, 116.5, 116.3, 112.7, 55.8, 51.2, 27.9. HRMS (ESI) (*m/z*) [M+H]$^+$: calculated for C$_{16}$H$_{17}$N$_2$O$_4$S 333.0904, found 333.0907.

4.1.16. 1-(4-Methoxybenzoyl)indoline-5-sulfonamide (4k)

This compound was prepared from **9** and 4-methoxybenzoyl chloride as described for **4a**. A white powder, yield 64%, mp = 240–242 °C. HPLC (LW = 300 nm, gradient B 30/70/30% (35 min)) t$_R$ = 12.2 min, purity 99%. ^{1}H NMR (400 MHz, DMSO-*d$_6$*): δ 7.82–7.73 (br s, 1H, Ar), 7.68 (s, 1H, Ar), 7.65–7.56 (m, 3H, Ar), 7.24 (s, 2H, NH$_2$), 7.02 (d, *J* = 8.2 Hz, 2H, Ar), 4.10 (t, *J* = 8.2 Hz, 2H, CH$_2$), 3.81 (s, 3H, OMe), 3.12 (t, *J* = 8.2 Hz, 2H, CH$_2$). ^{13}C NMR (100 MHz, DMSO-*d$_6$*): δ 168.8, 161.4, 146.2, 139.3, 134.0, 129.8 (2C), 128.8, 125.7, 122.9, 116.3, 114.2 (2C), 55.8, 51.5, 28.0. HRMS (ESI) (*m/z*) [M+H]$^+$: calculated for C$_{16}$H$_{17}$N$_2$O$_4$S 333.0904, found 333.0882.

4.1.17. 1-(2,4-Dimethoxybenzoyl)indoline-5-sulfonamide (4l)

This compound was prepared from **9** and 2,4-dimethoxybenzoyl chloride as described for **4a**. A white powder, yield 64%, mp = 249–251 °C. HPLC (LW = 300 nm, gradient B 30/70/30% (35 min)) t$_R$ = 12.9 min, purity 97%. ^{1}H NMR (400 MHz, DMSO-*d$_6$*): δ 8.18 (br s, 1H, Ar), 7.66 (s, 2H, Ar), 7.24 (br s, 3H, NH$_2$, Ar), 6.66 (s, 1H, Ar), 6.61 (d, *J* = 7.8 Hz, 1H, Ar), 3.81 (s, 8H, CH$_2$, 2OMe) 3.11 (t, *J* = 8.2 Hz, 2H, CH$_2$). ^{13}C NMR (100 MHz, DMSO-*d$_6$*): δ 167.7, 162.2, 156.9, 145.7, 139.4, 134.0, 129.3, 125.9, 123.0, 119.5, 116.0, 106.0, 99.1, 56.2, 55.9, 49.5, 27.5. HRMS (ESI) (*m/z*) [M+H]$^+$: calculated for C$_{17}$H$_{19}$N$_2$O$_5$S 363.1009, found 363.0993.

4.1.18. 1-(3,4,5-Trimethoxybenzoyl)indoline-5-sulfonamide (4m)

This compound was prepared from **9** and 3,4,5-trimethoxybenzoyl chloride as described for **4a**. A white powder, yield 58%, mp = 248–250 °C. HPLC (LW = 300 nm, gradient B 30/70/30% (35 min)) t$_R$ = 10.9 min, purity 99%. ^{1}H NMR (400 MHz, DMSO-*d$_6$*): δ 7.85 (br s, 1H, Ar), 7.68 (s, 1H, Ar), 7.64 (d, *J* = 8.3 Hz, 1H, Ar), 7.24 (s, 2H, NH$_2$), 6.90 (s, 2H, Ar), 4.10 (t, *J* = 8.2 Hz, 2H, CH$_2$), 3.79 (s, 6H, 2OMe), 3.71 (s, 3H, OMe), 3.13 (t, *J* = 8.2 Hz, 2H, CH$_2$). ^{13}C NMR (100 MHz, DMSO-*d$_6$*): δ 168.7, 153.3 (2C), 145.9, 139.5 (2C), 134.1, 132.2, 125.7, 122.9, 116.3, 105.1 (2C), 60.6, 56.6 (2C), 51.3, 27.8. HRMS (ESI) (*m/z*) [M+H]$^+$: calculated for C$_{18}$H$_{21}$N$_2$O$_6$S 393.1115, found 333.1106. IR *ν* max, (film) cm^{-1} 3336 s, 3189 m, 3079 w,

1644 s, 1592 m, 1566 w, 1539 w, 1482 s, 1433 m, 1394 s, 1333 s, 1315 s, 1257 m, 1194 s, 1169 m, 1152 s, 1111 w, 1079 s, 999 w, 912 s, 892 s, 869 s, 835 s, 802 s, 772 w, 741 w, 714 m, 683 w.

4.1.19. 1-(4-(Methylthio)benzoyl)indoline-5-sulfonamide (**4n**)

This compound was prepared from **9** and 4-(methylthio)benzoyl chloride as described for **4a**. A white powder, yield 63%, mp = 245–247 °C. HPLC (LW = 300 nm, gradient B 30/70/30% (35 min)) t_R = 16.4 min, purity 99%. ^{1}H NMR (400 MHz, DMSO-d_6): δ 7.98–7.76 (br s, 1H, Ar), 7.68 (s, 1H, Ar), 7.63 (d, J = 7.8 Hz, 1H, Ar), 7.55 (d, J = 8.2 Hz, 2H, Ar), 7.33 (d, J = 8.2 Hz, 2H, Ar), 7.26 (s, 2H, NH$_2$), 4.08 (t, J = 8.6 Hz, 2H, CH$_2$), 3.13 (t, J = 8.6 Hz, 2H, CH$_2$). ^{13}C NMR (100 MHz, DMSO-d_6): δ 168.6, 146.0, 142.3, 139.5, 134.1, 132.7, 128.3 (2C), 125.7, 125.5 (2C), 123.0, 116.3, 51.4, 28.0, 14.6. HRMS (ESI) (m/z) [M+H]$^+$: calculated for C$_{16}$H$_{17}$N$_2$O$_3$S$_2$ 349.0675, found 349.0642.

4.1.20. 1-(2-Nitrobenzoyl)indoline-5-sulfonamide (**4o**)

This compound was prepared from **9** and 2-nitrobenzoyl chloride as described for **4a**. A white powder, yield 66%, mp = 238–240 °C. HPLC (LW = 300 nm, gradient B 30/70/30% (35 min)) t_R = 11.7 min, purity 100%. ^{1}H NMR (400 MHz, DMSO-d_6): δ 8.27 (d, J = 8.2 Hz, 1H, Ar), 8.20 (d, J = 8.2 Hz, 1H, Ar), 7.30 (s, 2H, NH$_2$), 3.83 (t, J = 8.2 Hz, 2H, CH$_2$), 3.17 (t, J = 8.2 Hz, 2H, CH$_2$). ^{13}C NMR (100 MHz, DMSO-d_6): δ 165.6, 145.3, 144.9, 140.1, 135.9, 133.9, 132.7, 131.4, 128.6, 126.1, 125.3, 123.1, 116.1, 50.2, 27.7. HRMS (ESI) (m/z) [M+H]$^+$: calculated for C$_{15}$H$_{14}$N$_3$O$_5$S 348.0649, found 348.0612.

4.1.21. 1-(4-Nitrobenzoyl)indoline-5-sulfonamide (**4p**)

This compound was prepared from **9** and 4-nitrobenzoyl chloride as described for **4a**. A white powder, yield 64%, mp = 247–249 °C. HPLC (LW = 300 nm, gradient B 30/70/30% (35 min)) t_R = 14.2 min, purity 97%. ^{1}H NMR (400 MHz, DMSO-d_6): δ 8.33 (d, J = 8.2 Hz, 2H, Ar), 8.19 (br s, 1H, Ar), 7.88 (d, J = 8.2 Hz, 2H, Ar), 7.71 (s, 2H, Ar), 7.30 (s, 2H, NH$_2$), 4.02 (t, J = 8.2 Hz, 2H, CH$_2$), 3.15 (t, J = 8.2 Hz, 2H, CH$_2$). ^{13}C NMR (100 MHz, DMSO-d_6): δ 167.2, 148.7, 145.4, 142.8, 140.1, 134.3, 128.9 (2C), 125.8, 124.3 (2C), 123.0, 116.7, 51.1, 28.0. HRMS (ESI) (m/z) [M+H]$^+$: calculated for C$_{15}$H$_{14}$N$_3$O$_5$S 348.0649, found 348.0654. IR ν max, (film) cm^{-1} 3352 m, 3258 s, 1650 s, 1593 m, 1512 s, 1476 s, 1431 m, 1392 s, 1335 s, 1313 m, 1290 w, 1254 m, 1192 m, 1146 s, 1108 m, 1079 s, 1016 m, 921 w, 907 m, 885 w, 861 s, 831 s, 737 w, 722 w, 702 s.

4.1.22. 1-Isonicotinoylindoline-5-sulfonamide (**4q**)

To a solution of isonicotinic acid (90 mg, 0.73 mmol) in THF (5 mL) was added CDI (119 mg, 0.73 mmol). After 30 min until the end of the release of bubbles, a solution of indoline-5-sulfonamide (**9**, 110 mg, 0.6 mmol) in THF (5 mL) was added dropwise. The resulting mixture was heated to 40 °C for 2 h, cooled, and the solvent was removed in vacuo. The residue was diluted with water (7 mL) and filtrated. The crude product was crystallized from EtOH to get 84 mg (50%) of pure 1-isonicotinoylindoline-5-sulfonamide. A white powder, mp > 250 °C. HPLC (LW = 300 nm, gradient B 30/70/30% (35 min)) t_R = 8.8 min, purity 96%. ^{1}H NMR (400 MHz, DMSO-d_6): δ 8.73 (d, J = 5.7 Hz, 2H, Ar), 8.25–8.11 (br s, 1H, Ar), 7.70 (s, 1H, Ar), 7.59 (d, J = 5.7 Hz, 2H, Ar), 7.27 (s, 2H, NH$_2$), 4.01 (t, J = 8.2 Hz, 2H, CH$_2$), 3.15 (t, J = 8.2 Hz, 2H, CH$_2$). ^{13}C NMR (100 MHz, DMSO-d_6): δ 166.9, 150.7 (2C), 145.4, 144.1, 140.1, 134.2, 125.9, 123.0, 121.5 (2C), 116.6, 51.0, 28.0. HRMS (ESI) (m/z) [M+H]$^+$: calculated for C$_{14}$H$_{14}$N$_3$O$_3$S 304.0750, found 304.0752. IR ν max, (film) cm^{-1} 3350 w, 3180 w, 3072 w, 1638 s, 1591 m, 1545 m, 1484 s, 1440 m, 1400 s, 1332 m, 1308 s, 1255 w, 1224 w, 1197 w, 1144 s,1110 w, 1086 m, 1073 m, 992 w, 938 m, 898 w, 882 w, 832 s, 757 m, 729 w.

4.1.23. 1-(Thiophene-2-carbonyl)indoline-5-sulfonamide (**4r**)

This compound was prepared from **9** and thiophene-2-carbonyl chloride as described for **4a**. A white powder, yield 62%, mp > 250 °C. HPLC (LW = 300 nm, gradient B 30/70/30%

(35 min)) t_R = 11.0 min, purity 99%. ^{1}H NMR (400 MHz, DMSO-d_6): δ 8.11 (d, *J* = 8.2 Hz, 1H, Ar), 7.90 (d, *J* = 4.7 Hz, 1H, Ar), 7.79 (d, *J* = 3.9 Hz, 1H, Ar), 7.70 (s, 1H, Ar), 7.67 (d, *J* = 8.2 Hz, 1H, Ar) 7.27 (s, 2H, NH$_2$), 7.21 (t, *J* = 3.9 Hz, *J* = 4.7 Hz, 1H, Ar), 4.47 (t, *J* = 8.2 Hz, 2H, CH$_2$), 3.25 (t, *J* = 8.2 Hz, 2H, CH$_2$). ^{13}C NMR (100 MHz, DMSO-d_6): δ 161.6, 146.3, 139.7, 139.4, 133.8, 132.4, 131.2, 128.5, 125.8, 122.9, 116.9, 51.1, 28.3. HRMS (ESI) (*m/z*) [M+H]$^+$: calculated for C$_{13}$H$_{13}$N$_2$O$_3$S$_2$ 309.0362, found 309.0372.

4.1.24. 1-(Cyclopentanecarbonyl)indoline-5-sulfonamide (**4s**)

This compound was prepared from **9** and cyclopentanecarbonyl chloride as described for **4a**. A white powder, yield 58%, mp = 233–235 °C. HPLC (LW = 300 nm, gradient B 30/70/30% (35 min)) t_R = 14.2 min, purity 99%. ^{1}H NMR (400 MHz, DMSO-d_6): δ 8.15 (d, *J* = 7.8 Hz, 1H, Ar), 7.64–7.57 (m, 2H, Ar), 7.19 (s, 2H, NH$_2$), 4.20 (t, *J* = 8.6 Hz, 2H, CH$_2$), 3.18 (t, *J* = 8.6 Hz, 2H, CH$_2$), 3.07–2.96 (m, 1H, CH), 1.93–1.82 (m, 2H, CH$_2$), 1.78–1.69 (m, 2H, CH$_2$), 1.68–1.60 (m, 2H, CH$_2$), 1.59–1.50 (m, 2H, CH$_2$). ^{13}C NMR (100 MHz, DMSO-d_6): δ 175.3, 146.4, 138.8, 133.3, 125.9, 122.7, 115.8, 48.5, 43.7, 29.9(2C), 27.6, 26.2 (2C). HRMS (ESI) (*m/z*) [M+H]$^+$: calculated for C$_{14}$H$_{19}$N$_2$O$_3$S 295.1111, found 295.1133.

4.1.25. 1-(2-Cyclopentylacetyl)indoline-5-sulfonamide (**4t**)

This compound was prepared from **9** and 2-cyclopentylacetyl chloride as described for **4a**. A white powder, yield 60%, mp = 184–186 °C. HPLC (LW = 300 nm, gradient B 30/70/30% (35 min)) t_R = 18.5 min, purity 100%. ^{1}H NMR (400 MHz, DMSO-d_6): δ 8.14 (d, *J* = 8.2 Hz, 1H, Ar), 7.63–7.58 (m, 2H, Ar), 7.19 (s, 2H, NH$_2$), 4.13 (t, *J* = 8.6 Hz, 2H, CH$_2$), 3.16 (t, *J* = 8.6 Hz, 2H, CH$_2$), 2.30–2.18 (m, 1H, CH), 1.86–1.74 (m, 2H, CH$_2$), 1.65–1.53 (m, 2H, CH$_2$), 1.52–1.43 (m, 2H, CH$_2$). ^{13}C NMR (100 MHz, DMSO-d_6): δ 171.9, 146.2, 138.7, 133.1, 125.9, 122.8, 115.5, 48.4, 41.6, 35.7, 32.6 (2C), 27.5, 25.0 (2C). HRMS (ESI) (*m/z*) [M+H]$^+$: calculated for C$_{15}$H$_{21}$N$_2$O$_3$S 309.1267, found 309.1263.

4.1.26. 1-(Cyclohexanecarbonyl)indoline-5-sulfonamide (**4u**)

This compound was prepared from **9** and cyclohexanecarbonyl chloride as described for **4a**. A white powder, yield 61%, mp > 250 °C. HPLC (LW = 300 nm, gradient B 30/70/30% (35 min)) t_R = 17.3 min, purity 100%. ^{1}H NMR (400 MHz, DMSO-d_6): δ 8.15 (d, *J* = 7.6 Hz, 1H, Ar), 7.62 (s, 1H, Ar), 7.60 (d, *J* = 7.6 Hz, 1H, Ar), 7.19 (s, 2H, NH$_2$), 4.21 (t, *J* = 8.2 Hz, 2H, CH$_2$), 3.17 (t, *J* = 8.2 Hz, 2H, CH$_2$), 2.61–2.50 (m, 1H, CH), 1.77 (m, 4H, 2CH$_2$), 1.65 (d, *J* = 11.9 Hz, 1H, CH$_2$), 1.45–1.24 (m, 4H, 2CH$_2$), 1.23–1.13 (m, 1H, CH$_2$). ^{13}C NMR (100 MHz, DMSO-d_6): δ 175.1, 146.3, 138.9, 133.3, 125.8, 122.7, 115.9, 48.4, 43.1, 29.1(2C), 27.6, 25.9, 25.5 (2C). HRMS (ESI) (*m/z*) [M+H]$^+$: calculated for C$_{15}$H$_{21}$N$_2$O$_3$S 309.1267, found 309.1223.

4.1.27. 1-Benzylindoline-5-sulfonamide (**10**)

To a suspension of 100 mg (0.5 mmol) of indoline-5-sulfonamide **9** in MeCN (5 mL) was added 209 mg (1.5 mmol) of K$_2$CO$_3$ and 72 μL (0.6 mmol) of benzyl bromide at room temperature. After completion of the reaction monitored by TLC, the mixture was diluted with water (20 mL), adjusted to pH 7–8 with 1N HCl and extracted with EtOAc twice. The combined organic phases were dried over anhydrous Na$_2$SO$_4$, filtered, and concentrated in vacuum. The residue was purified by flash column chromatography (EtOAc/Hexane 1:2) to afford 70 mg of 1-benzylindoline-5-sulfonamide **10**. A white powder, yield 47%, mp = 144–146 °C. HPLC (LW = 300 nm, gradient B 30/70/30% (35 min)) t_R = 20.6 min, purity 99%. ^{1}H NMR (400 MHz, DMSO-d_6): δ 7.45 (dd, *J* = 8.2, *J* = 1.5 Hz, 1H, Ar), 8.19 (d, *J* = 1.5 Hz, 1H, Ar), 7.36–7.23 (m, 5H, Ar), 6.95 (s, 2H, NH$_2$), 6.60 (d, *J* = 8.2, 1H, Ar), 4.38 (s, 2H, CH$_2$), 3.42 (t, *J* = 8.6 Hz, 2H, CH$_2$), 2.96 (t, *J* = 8.6 Hz, 2H, CH$_2$). ^{13}C NMR (100 MHz, DMSO-d_6): δ 154.9, 137.9, 131.9, 130.1, 129.0 (2C), 128.2 (2C), 127.6, 126.9, 122.5, 105.1, 52.5, 51.2, 27.9. HRMS (ESI) (*m/z*) [M+H]$^+$: calculated for C$_{15}$H$_{17}$N$_2$O$_2$S 289.1005, found 289.0982.

4.2. CA Inhibitory Assay

The CO_2 hydration activity of the four hCA isoforms was monitored using an Applied Photophysics stopped-flow instrument [73]. Phenol red (at a concentration of 0.2 mM) was used as an indicator, working at the absorbance maximum of 557 nm, with 10 mM HEPES (pH 7.4) as a buffer, and 20 mM $NaClO_4$ (for maintaining constant the ionic strength), following the initial rates of the CA-catalyzed CO_2 hydration reaction for a period of 10–100 s. To determine the kinetic parameters by Lineweaver-Burk plots and the inhibition constants, a concentration of CO_2 between 1.7 to 17 mM was used. At least six measurements of the original 5–10% reaction were used to assess the initial velocity for each inhibitor. The uncatalyzed rates were determined and detracted from the total observed rates. Stock inhibitor solutions (10–100 mM) were prepared in distilled-deionized water, and dilutions up to 0.1 nM were done with the buffer test. Inhibitor and enzyme solutions were preincubated together for 15 min at room temperature prior to assay in order to allow for the formation of the E-I complex or for the eventual active site-mediated hydrolysis of the inhibitor. The inhibition constants were obtained by non-linear least-squares methods using PRISM 6 and the Cheng-Prusoff equation, as reported earlier [74–76], and represent the mean from at least three different determinations. All enzymes were recombinant proteins obtained in-house, and their concentration in the assay system was 4.5–12 nM.

4.3. Molecular Modelling Studies

Molecular modelling was performed using Molecular Operating Environment (MOE) version 2014.09; Chemical Computing Group Inc., 1010 Sherbrooke St. West, Suite #910, Montreal, QC, Canada, H3A 2R7, 2014. CA IX structure was read from a PDB file 5sz5. Structural issues were automatically corrected using the Structure Preparation application. The hydrogen bond network and charges were optimized. Tethered energy minimization was performed using an AMBER10:EHT force field. The binding pocket of the receptor was specified by proximity to the cocrystallized ligand atoms. Chosen compounds were prepared using the wash command, and then partial charges were calculated. Ligand's energy minimization was done using an MMFF94x force field. Deprotonation of strong acids and protonation of strong bases were checked in the wash panel. Docking placement was done using the triangle matcher algorithm with the 'rotate bonds' option. The 1st scoring function was London dG, and the 2nd scoring function was GBVI/WSA dG. MOE-Dock performed 30 independent docking runs. Docked complexes were ranked based on the docking scores (S). Finally, predicted complexes were analyzed for molecular interactions using the MOE window.

4.4. Cells and Antiproliferative Evaluation

The MCF7 human breast, A431 human skin cancer cells and K562 (ATCC CCL-243) chronic myelogenous leukemia cells were obtained from the ATCC collection. The MDR subline K562/4 [77] (kind gift of Dr. Alexander Shtil, Blokhin N.N. National Medical Research Center of Oncology) was obtained by stepwise selection of K562 cells for survival under continuous exposure to Dox. This subline expresses the MDR1 gene and functional P-gp and is characterized by a high resistance index for Dox [78]. The MCF7 and A431 cells were cultured in standard 4.5 g/L glucose DMEM medium (Gibco) supplemented with 10% FCS (HyClone), 2 mM L-glutamine, 50 U/mL penicillin, 50 μg/mL streptomycin (PanEco), 100 μg/mL sodium pyruvate (Santa Cruz) at 37 °C, 5% CO_2 and 80–85% humidity in Nu-Aire incubator. Suspension myelogenous leukemia cells (K562, K562/4) were propagated in RPMI-1640 (PanEco) with 5% FCS (HyClone), 2 mM L-glutamine, 100 U/mL penicillin, and 100 μg/mL streptomycin at 37 °C, 5% CO_2, and 80–85% humidity in Binder incubator. Cells in the logarithmic phase of growth were used in the experiments. The growth inhibitory activity of compounds was assessed by the MTT test based on the metabolism of the MTT reagent (3-[4,5-dimethylthiazol-2-yl]-2,5-diphenyltetrazolium bromide) (Applichem) in living cells, with modifications as described previously in [49]. Compounds at different concentrations in 100 μL of the appropriate medium were added, and the cells were grown

for 72 h. The hypoxia (1% O_2) conditions were simulated in Binder multigas incubator, as described in [49]. After incubation with compounds, the medium was removed, the MTT reagent that was dissolved in the medium was added to the final concentration of 0.2 mg/mL to each well, and the incubation was performed for 2 h. Then the cell supernatants were removed, and purple formazan crystals were dissolved in 100% DMSO (350 μL per well). Culture plates were gently shaken, and the absorbance was measured at 571 nm with a reference wavelength of 630 nm on a MultiScan reader (ThermoFisher, Waltham, MA, USA). The viability of the cells was expressed as a percentage of the control. Dose-response curves were analyzed by regression analysis using sigmoid curves (Log(concentration) vs. normalized absorbance).

4.5. Statistical Analysis

All results were reported as means ± SD. One-way analysis of variance was used for the analysis of data. Differences were defined as significant at $p < 0.05$. GraphPad Prism7 (GraphPad Software, San Diego, CA, USA) was used for the determination of the half-maximal inhibitory concentration (IC_{50}) values.

4.6. Immunoblotting

A431 cells were seeded on 100 mm dishes (Corning, Corning, NY, USA), and after 24 h growth, the compound **4f** was added to a fresh medium. To prepare cell extracts, A431 cells were twice washed in phosphate buffer and incubated for 10 min on ice in the modified lysis buffer containing 50 mM Tris-HCl, pH 7.5, 0.5% Igepal CA-630, 150 mM NaCl, 1 mM EDTA, 1 mM DTT, 1 mM PMSF, 0.1 mM sodium orthovanadate and aprotinin, leupeptin and pepstatin (1 μg/mL each) as described earlier in the work [79]. The protein content was determined by the Bradford method.

A431 cell lysates were separated in 10% SDS-PAGE under reducing conditions, transferred to a nitrocellulose membrane (GE HealthCare, Chicago, IL, USA), and processed according to a standard protocol. Akt, GLUT1, PD-L1, and CA IX antibodies were obtained from Cell Signaling Technology (Danvers, MA, USA); the antibodies against GAPDH (Cell Signaling Technology) were added to standardize loading. Goat anti-rabbit IgGs (Jackson ImmunoResearch, West Grove, PA, USA) conjugated to horseradish peroxidase were used as secondary antibodies. Signals were detected using the ECL reagent as described in Mruk and Cheng's protocol [80] and an ImageQuant LAS4000 system (GE HealthCare).

Author Contributions: Conceptualization and methodology, A.E.S. and C.T.S.; investigation, S.K.K., L.G.D., D.I.S., S.E.S., D.V.S., D.V. and V.D.L.; data curation S.K.K. and A.M.S., writing—original draft preparation, S.K.K.; writing—review and editing A.M.S.; supervision, A.E.S., A.M.S., C.C. and C.T.S. All authors have read and agreed to the published version of the manuscript.

Institutional Review Board Statement: Not applicable.

Informed Consent Statement: Not applicable.

Data Availability Statement: Data is contained within the article.

Conflicts of Interest: The authors declare no conflict of interest.

References

1. Liang, Y.; Zheng, T.; Song, R.; Wang, J.; Yin, D.; Wang, L.; Liu, H.; Tian, L.; Fang, X.; Meng, X.; et al. Hypoxia-mediated sorafenib resistance can be overcome by EF24 through Von Hippel-Lindau tumor suppressor-dependent HIF-1α inhibition in hepatocellular carcinoma. *Hepatology* **2013**, *57*, 1847–1857. [CrossRef]

2. Xu, K.; Zhan, Y.; Yuan, Z.; Qiu, Y.; Wang, H.; Fan, G.; Wang, J.; Li, W.; Cao, Y.; Shen, X.; et al. Hypoxia Induces Drug Resistance in Colorectal Cancer through the HIF-1α/miR-338-5p/IL-6 Feedback Loop. *Mol. Ther.* **2019**, *27*, 1810–1824. [CrossRef] [PubMed]

3. Morotti, M.; Bridges, E.; Valli, A.; Choudhry, H.; Sheldon, H.; Wigfield, S.; Gray, N.; Zois, C.E.; Grimm, F.; Jones, D.; et al. Hypoxia-induced switch in SNAT2/SLC38A2 regulation generates endocrine resistance in breast cancer. *Proc. Natl. Acad. Sci. USA* **2019**, *116*, 12452–12461. [CrossRef] [PubMed]

4. Jing, X.; Yang, F.; Shao, C.; Wei, K.; Xie, M.; Shen, H.; Shu, Y. Role of hypoxia in cancer therapy by regulating the tumor microenvironment. *Mol. Cancer* **2019**, *18*, 157. [CrossRef] [PubMed]

5. Švastová, E.; Hulíková, A.; Rafajová, M.; Zaťovičová, M.; Gibadulinová, A.; Casini, A.; Cecchi, A.; Scozzafava, A.; Supuran, C.T.; Pastorek, J.; et al. Hypoxia activates the capacity of tumor-associated carbonic anhydrase IX to acidify extracellular pH. *FEBS Lett.* **2004**, *577*, 439–445. [CrossRef]

6. Mellor, H.R.; Callaghan, R. Accumulation and distribution of doxorubicin in tumour spheroids: The influence of acidity and expression of P-glycoprotein. *Cancer Chemother. Pharmacol.* **2011**, *68*, 1179–1190. [CrossRef]

7. Federici, C.; Petrucci, F.; Caimi, S.; Cesolini, A.; Logozzi, M.; Borghi, M.; D'Ilio, S.; Lugini, L.; Violante, N.; Azzarito, T.; et al. Exosome release and low pH belong to a framework of resistance of human melanoma cells to cisplatin. *PLoS ONE* **2014**, *9*, e88193. [CrossRef]

8. Chiche, J.; Ilc, K.; Laferrière, J.; Trottier, E.; Dayan, F.; Mazure, N.M.; Brahimi-Horn, M.C.; Pouysségur, J. Hypoxia-Inducible Carbonic Anhydrase IX and XII Promote Tumor Cell Growth by Counteracting Acidosis through the Regulation of the Intracellular pH. *Cancer Res.* **2008**, *69*, 358–368. [CrossRef]

9. Estrella, V.; Chen, T.; Lloyd, M.; Wojtkowiak, J.; Cornnell, H.H.; Ibrahim-Hashim, A.; Bailey, K.; Balagurunathan, Y.; Rothberg, J.M.; Sloane, B.F.; et al. Acidity Generated by the Tumor Microenvironment Drives Local Invasion. *Cancer Res.* **2013**, *73*, 1524–1535. [CrossRef]

10. Becker, H.M. Carbonic anhydrase IX and acid transport in cancer. *Br. J. Cancer* **2020**, *122*, 157–167. [CrossRef] [PubMed]

11. Wykoff, C.C.; Beasley, N.J.; Watson, P.; Turner, K.J.; Pastorek, J.; Sibtain, A.; Wilson, G.; Turley, H.; Talks, K.L.; Maxwell, P.; et al. Hypoxia-inducible expression of tumor-associated carbonic anhydrases. *Cancer Res.* **2000**, *60*, 7075–7083. [PubMed]

12. Pastorekova, S.; Gillies, R.J. The role of carbonic anhydrase IX in cancer development: Links to hypoxia, acidosis, and beyond. *Cancer Metastasis Rev.* **2019**, *38*, 65–77. [CrossRef] [PubMed]

13. Pastoreková, S.; Pastorek, J. Cancer-related carbonic anhydrase isozymes and their inhibition. In *Carbonic Anhydrase*; CRC Press: Boca Raton, FL, USA, 2004.

14. Angeli, A.; Carta, F.; Nocentini, A.; Winum, J.-Y.; Zalubovskis, R.; Akdemir, A.; Onnis, V.; Eldehna, W.; Capasso, C.; Simone, G.; et al. Carbonic Anhydrase Inhibitors Targeting Metabolism and Tumor Microenvironment. *Metabolites* **2020**, *10*, 412. [CrossRef] [PubMed]

15. Ivanov, S.; Liao, S.-Y.; Ivanova, A.; Danilkovitch-Miagkova, A.; Tarasova, N.; Weirich, G.; Merrill, M.J.; Proescholdt, M.A.; Oldfield, E.H.; Lee, J.; et al. Expression of Hypoxia-Inducible Cell-Surface Transmembrane Carbonic Anhydrases in Human Cancer. *Am. J. Pathol.* **2001**, *158*, 905–919. [CrossRef]

16. Nordfors, K.; Haapasalo, J.; Korja, M.; Niemelä, A.; Laine, J.; Parkkila, A.-K.; Pastorekova, S.; Pastorek, J.; Waheed, A.; Sly, W.S.; et al. The tumour-associated carbonic anhydrases CA II, CA IX and CA XII in a group of medulloblastomas and supratentorial primitive neuroectodermal tumours: An association of CA IX with poor prognosis. *BMC Cancer* **2010**, *10*, 148. [CrossRef]

17. Trastour, C.; Benizri, E.; Ettore, F.; Ramaioli, A.; Chamorey, E.; Pouysségur, J.; Berra, E. HIF-1α and CA IX staining in invasive breast carcinomas: Prognosis and treatment outcome. *Int. J. Cancer* **2007**, *120*, 1451–1458. [CrossRef]

18. Driessen, A.; Landuyt, W.; Pastorekova, S.; Moons, J.; Goethals, L.; Haustermans, K.; Nafteux, P.; Penninckx, F.; Geboes, K.; Lerut, T.; et al. Expression of Carbonic Anhydrase IX (CA IX), a Hypoxia-Related Protein, Rather Than Vascular-Endothelial Growth Factor (VEGF), a Pro-Angiogenic Factor, Correlates with an Extremely Poor Prognosis in Esophageal and Gastric Adenocarcinomas. *Ann. Surg.* **2006**, *243*, 334–340. [CrossRef]

19. Loncaster, J.A.; Harris, A.L.; Davidson, S.E.; Logue, J.P.; Hunter, R.D.; Wycoff, C.C.; Pastorek, J.; Ratcliffe, P.J.; Stratford, I.J.; West, C.M. Carbonic anhydrase (CA IX) expression, a potential new intrinsic marker of hypoxia: Correlations with tumor oxygen measurements and prognosis in locally advanced carcinoma of the cervix. *Cancer Res.* **2001**, *61*, 333–340.

20. Wykoff, C.C.; Beasley, N.; Watson, P.H.; Campo, L.; Chia, S.K.; English, R.; Pastorek, J.; Sly, W.S.; Ratcliffe, P.; Harris, A.L. Expression of the Hypoxia-Inducible and Tumor-Associated Carbonic Anhydrases in Ductal Carcinoma in Situ of the Breast. *Am. J. Pathol.* **2001**, *158*, 1011–1019. [CrossRef]

21. Kivelä, A.; Parkkila, S.; Saarnio, J.; Karttunen, T.J.; Kivelä, J.; Parkkila, A.-K.; Waheed, A.; Sly, W.S.; Grubb, J.H.; Shah, G.; et al. Expression of a Novel Transmembrane Carbonic Anhydrase Isozyme XII in Normal Human Gut and Colorectal Tumors. *Am. J. Pathol.* **2000**, *156*, 577–584. [CrossRef]

22. Watson, P.H.; Chia, S.K.; Wykoff, C.C.; Han, C.; Leek, R.D.; Sly, W.S.; Gatter, K.C.; Ratcliffe, P.; Harris, A.L. Carbonic anhydrase XII is a marker of good prognosis in invasive breast carcinoma. *Br. J. Cancer* **2003**, *88*, 1065–1070. [CrossRef] [PubMed]

23. Ochi, F.; Shiozaki, A.; Ichikawa, D.; Fujiwara, H.; Nakashima, S.; Takemoto, K.; Kosuga, T.; Konishi, H.; Komatsu, S.; Okamoto, K.; et al. Carbonic Anhydrase XII as an Independent Prognostic Factor in Advanced Esophageal Squamous Cell Carcinoma. *J. Cancer* **2015**, *6*, 922. [CrossRef] [PubMed]

24. Chien, M.-H.; Ying, T.-H.; Hsieh, Y.-H.; Lin, C.-H.; Shih, C.-H.; Wei, L.-H.; Yang, S.-F. Tumor-associated carbonic anhydrase XII is linked to the growth of primary oral squamous cell carcinoma and its poor prognosis. *Oral Oncol.* **2012**, *48*, 417–423. [CrossRef]

25. Guerrini, G.; Criscuoli, M.; Filippi, I.; Naldini, A.; Carraro, F. Inhibition of smoothened in breast cancer cells reduces CAXII expression and cell migration. *J. Cell. Physiol.* **2018**, *233*, 9799–9811. [CrossRef] [PubMed]

26. Hsieh, M.-J.; Chen, K.-S.; Chiou, H.-L.; Hsieh, Y.-S. Carbonic anhydrase XII promotes invasion and migration ability of MDA-MB-231 breast cancer cells through the p38 MAPK signaling pathway. *Eur. J. Cell Biol.* **2010**, *89*, 598–606. [CrossRef]

27. Kopecka, J.; Campia, I.; Jacobs, A.; Frei, A.P.; Ghigo, D.; Wollscheid, B.; Riganti, C. Carbonic anhydrase XII is a new therapeutic target to overcome chemoresistance in cancer cells. *Oncotarget* **2015**, *6*, 6776–6793. [CrossRef]

28. Salaroglio, I.C.; Mujumdar, P.; Annovazzi, L.; Kopecka, J.; Mellai, M.; Schiffer, D.; Poulsen, S.-A.; Riganti, C. Carbonic Anhydrase XII Inhibitors Overcome P-Glycoprotein–Mediated Resistance to Temozolomide in Glioblastoma. *Mol. Cancer Ther.* **2018**, *17*, 2598–2609. [CrossRef]

29. Mujumdar, P.; Kopecka, J.; Bua, S.; Supuran, C.T.; Riganti, C.; Poulsen, S.-A. Carbonic Anhydrase XII Inhibitors Overcome Temozolomide Resistance in Glioblastoma. *J. Med. Chem.* **2019**, *62*, 4174–4192. [CrossRef]

30. Nocentini, A.; Angeli, A.; Carta, F.; Winum, J.-Y.; Zalubovskis, R.; Carradori, S.; Capasso, C.; Donald, W.A.; Supuran, C.T. Reconsidering anion inhibitors in the general context of drug design studies of modulators of activity of the classical enzyme carbonic anhydrase. *J. Enzym. Inhib. Med. Chem.* **2021**, *36*, 561–580. [CrossRef]

31. Berrino, E.; Michelet, B.; Martin-Mingot, A.; Carta, F.; Supuran, C.T.; Thibaudeau, S. Modulating the Efficacy of Carbonic Anhydrase Inhibitors through Fluorine Substitution. *Angew. Chem.* **2021**, *60*, 23068–23082. [CrossRef]

32. Supuran, C.T. Emerging role of carbonic anhydrase inhibitors. *Clin. Sci.* **2021**, *135*, 1233–1249. [CrossRef] [PubMed]

33. McDonald, P.C.; Chafe, S.C.; Supuran, C.T.; Dedhar, S. Cancer Therapeutic Targeting of Hypoxia Induced Carbonic Anhydrase IX: From Bench to Bedside. *Cancers* **2022**, *14*, 3297. [CrossRef] [PubMed]

34. Kumar, A.; Siwach, K.; Supuran, C.T.; Sharma, P.K. A decade of tail-approach based design of selective as well as potent tumor associated carbonic anhydrase inhibitors. *Bioorganic Chem.* **2022**, *126*, 105920. [CrossRef] [PubMed]

35. Tawfik, H.O.; Petreni, A.; Supuran, C.T.; El-Hamamsy, M.H. Discovery of new carbonic anhydrase IX inhibitors as anticancer agents by toning the hydrophobic and hydrophilic rims of the active site to encounter the dual-tail approach. *Eur. J. Med. Chem.* **2022**, *232*, 114190. [CrossRef] [PubMed]

36. Tawfik, H.O.; Belal, A.; Abourehab, M.A.S.; Angeli, A.; Bonardi, A.; Supuran, C.T.; El-Hamamsy, M.H. Dependence on linkers' flexibility designed for benzenesulfonamides targeting discovery of novel hCA IX inhibitors as potent anticancer agents. *J. Enzyme Inhib. Med. Chem.* **2022**, *37*, 2765–2785. [CrossRef]

37. Arrighi, G.; Puerta, A.; Petrini, A.; Hicke, F.J.; Nocentini, A.; Fernandes, M.X.; Padrón, J.M.; Supuran, C.T.; Fernández-Bolaños, J.G.; López, Ó. Squaramide-Tethered Sulfonamides and Coumarins: Synthesis, Inhibition of Tumor-Associated CAs IX and XII and Docking Simulations. *Int. J. Mol. Sci.* **2022**, *23*, 7685. [CrossRef]

38. Manzoor, S.; Angeli, A.; Zara, S.; Carradori, S.; Rahman, A.; Raza, K.; Supuran, C.T.; Hoda, N. Development of benzene and benzothiazole-sulfonamide analogues as selective inhibitors of the tumor-associated carbonic anhydrase IX. *Eur. J. Med. Chem.* **2022**, *243*, 114793. [CrossRef]

39. Lock, F.E.; McDonald, P.C.; Lou, Y.; Serrano, I.; Chafe, S.C.; Ostlund, C.; Aparicio, S.; Winum, J.-Y.; Supuran, C.T.; Dedhar, S. Targeting carbonic anhydrase IX depletes breast cancer stem cells within the hypoxic niche. *Oncogene* **2013**, *32*, 5210–5219. [CrossRef]

40. Pacchiano, F.; Carta, F.; McDonald, P.C.; Lou, Y.; Vullo, D.; Scozzafava, A.; Dedhar, S.; Supuran, C.T. Ureido-Substituted Benzenesulfonamides Potently Inhibit Carbonic Anhydrase IX and Show Antimetastatic Activity in a Model of Breast Cancer Metastasis. *J. Med. Chem.* **2011**, *54*, 1896–1902. [CrossRef]

41. Lou, Y.; McDonald, P.C.; Oloumi, A.; Chia, S.; Ostlund, C.; Ahmadi, A.; Kyle, A.; Keller, U.A.D.; Leung, S.; Huntsman, D.; et al. Targeting Tumor Hypoxia: Suppression of Breast Tumor Growth and Metastasis by Novel Carbonic Anhydrase IX Inhibitors. *Cancer Res* **2011**, *71*, 3364–3376. [CrossRef]

42. Kalinin, S.; Malkova, A.; Sharonova, T.; Sharoyko, V.; Bunev, A.; Supuran, C.T.; Krasavin, M. Carbonic Anhydrase IX Inhibitors as Candidates for Combination Therapy of Solid Tumors. *Int. J. Mol. Sci.* **2021**, *22*, 13405. [CrossRef]

43. Boyd, N.H.; Walker, K.; Fried, J.; Hackney, J.R.; McDonald, P.C.; Benavides, G.A.; Spina, R.; Audia, A.; Scott, S.E.; Libby, C.J.; et al. Addition of carbonic anhydrase 9 inhibitor SLC-0111 to temozolomide treatment delays glioblastoma growth in vivo. *JCI Insight* **2017**, *2*, e92928. [CrossRef] [PubMed]

44. Hedlund, E.-M.E.; McDonald, P.C.; Nemirovsky, O.; Awrey, S.; Jensen, L.D.; Dedhar, S. Harnessing Induced Essentiality: Targeting Carbonic Anhydrase IX and Angiogenesis Reduces Lung Metastasis of Triple Negative Breast Cancer Xenografts. *Cancers* **2019**, *11*, 1002. [CrossRef] [PubMed]

45. McDonald, P.C.; Chafe, S.C.; Brown, W.S.; Saberi, S.; Swayampakula, M.; Venkateswaran, G.; Nemirovsky, O.; Gillespie, J.A.; Karasinska, J.M.; Kalloger, S.E.; et al. Regulation of pH by Carbonic Anhydrase 9 Mediates Survival of Pancreatic Cancer Cells With Activated KRAS in Response to Hypoxia. *Gastroenterology* **2019**, *157*, 823–837. [CrossRef]

46. Güzel-Akdemir, Ö.; Demir-Yazıcı, K.; Vullo, D.; Supuran, C.T.; Akdemir, A. New Pyridinium Salt Derivatives of 2-(Hydrazinocarbonyl)-3-phenyl-1H-indole-5-sulfonamide as Selective Inhibitors of Tumour-Related Human Carbonic Anhydrase Isoforms IX and XII. *Anti-Cancer Agents Med. Chem.* **2022**, *22*, 2637–2646. [CrossRef] [PubMed]

47. Singh, P.; Goud, N.S.; Swain, B.; Sahoo, S.K.; Choli, A.; Angeli, A.; Kushwah, B.S.; Yaddanapudi, V.M.; Supuran, C.T.; Arifuddin, M. Synthesis of a new series of quinoline/pyridine indole-3-sulfonamide hybrids as selective carbonic anhydrase IX inhibitors. *Bioorganic Med. Chem. Lett.* **2022**, *70*, 128809. [CrossRef] [PubMed]

48. Kumar, S.; Rulhania, S.; Jaswal, S.; Monga, V. Recent advances in the medicinal chemistry of carbonic anhydrase inhibitors. *Eur. J. Med. Chem.* **2020**, *209*, 112923. [CrossRef] [PubMed]

49. Krymov, S.K.; Scherbakov, A.M.; Salnikova, D.I.; Sorokin, D.V.; Dezhenkova, L.G.; Ivanov, I.V.; Vullo, D.; De Luca, V.; Capasso, C.; Supuran, C.T.; et al. Synthesis, biological evaluation, and in silico studies of potential activators of apoptosis and carbonic anhydrase inhibitors on isatin-5-sulfonamide scaffold. *Eur. J. Med. Chem.* **2021**, *228*, 113997. [CrossRef]

50. Thiry, A.; Ledecq, M.; Cecchi, A.; Dogné, J.-M.; Wouters, J.; Supuran, C.T.; Masereel, B. Indanesulfonamides as Carbonic Anhydrase Inhibitors. Toward Structure-Based Design of Selective Inhibitors of the Tumor-Associated Isozyme CA IX. *J. Med. Chem.* **2006**, *49*, 2743–2749. [CrossRef]

51. Dubois, L.; Peeters, S.; Lieuwes, N.G.; Geusens, N.; Thiry, A.; Wigfield, S.; Carta, F.; Mcintyre, A.; Scozzafava, A.; Dogné, J.-M.; et al. Specific inhibition of carbonic anhydrase IX activity enhances the in vivo therapeutic effect of tumor irradiation. *Radiother. Oncol.* **2011**, *99*, 424–431. [CrossRef]

52. Langdon, S.R.; Ertl, P.; Brown, N. Bioisosteric Replacement and Scaffold Hopping in Lead Generation and Optimization. *Mol. Inform.* **2010**, *29*, 366–385. [CrossRef] [PubMed]

53. Hu, Y.; Stumpfe, D.; Bajorath, J. Recent Advances in Scaffold Hopping. *J. Med. Chem.* **2016**, *60*, 1238–1246. [CrossRef] [PubMed]

54. Böhm, H.-J.; Flohr, A.; Stahl, M. Scaffold hopping. *Drug Discov. Today: Technol.* **2004**, *1*, 217–224. [CrossRef] [PubMed]

55. Dick, A.; Cocklin, S. Bioisosteric Replacement as a Tool in Anti-HIV Drug Design. *Pharmaceuticals* **2020**, *13*, 36. [CrossRef]

56. Alhadrami, H.A.; Sayed, A.M.; Al-Khatabi, H.; Alhakamy, N.A.; Rateb, M.E. Scaffold Hopping of α-Rubromycin Enables Direct Access to FDA-Approved Cromoglicic Acid as a SARS-CoV-2 M^{Pro} Inhibitor. *Pharmaceuticals* **2021**, *14*, 541. [CrossRef]

57. Wang, S.-Y.; Liu, X.; Meng, L.-W.; Li, M.-M.; Li, Y.-R.; Yu, G.-X.; Song, J.; Zhang, H.-Y.; Chen, P.; Zhang, S.-Y.; et al. Discovery of indoline derivatives as anticancer agents via inhibition of tubulin polymerization. *Bioorganic Med. Chem. Lett.* **2021**, *43*, 128095. [CrossRef]

58. Thakur, A.; Singh, A.; Kaur, N.; Ojha, R.; Nepali, K. Steering the antitumor drug discovery campaign towards structurally diverse indolines. *Bioorganic Chem.* **2019**, *94*, 103436. [CrossRef]

59. Fu, D.-J.; Li, M.; Zhang, S.-Y.; Li, J.-F.; Sha, B.; Wang, L.; Zhang, Y.-B.; Chen, P.; Hu, T. Discovery of indoline derivatives that inhibit esophageal squamous cell carcinoma growth by Noxa mediated apoptosis. *Bioorganic Chem.* **2019**, *92*, 103190. [CrossRef]

60. Preobrazhenskaya, M.N. Synthesis of Substituted Indoles via Indolines. *Russ. Chem. Rev.* **1967**, *36*, 753–771. [CrossRef]

61. Supuran, C.T. Structure and function of carbonic anhydrases. *Biochem. J.* **2016**, *473*, 2023–2032. [CrossRef]

62. Mishra, C.B.; Tiwari, M.; Supuran, C.T. Progress in the development of human carbonic anhydrase inhibitors and their pharmacological applications: Where are we today? *Med. Res. Rev.* **2020**, *40*, 2485–2565. [CrossRef]

63. Supuran, C.T. Novel carbonic anhydrase inhibitors. *Future Med. Chem.* **2021**, *13*, 1935–1937. [CrossRef] [PubMed]

64. Glamkowski, E.J.; Reitano, P.A. Synthesis and evaluation for diuretic activity of 1-substituted 6-chloro-5-sulfamylindolines. *J. Med. Chem.* **1979**, *22*, 106–109. [CrossRef] [PubMed]

65. Ren, Y.; Hao, P.; Dutta, B.; Cheow, E.S.H.; Sim, K.H.; Gan, C.S.; Lim, S.K.; Sze, S.K. Hypoxia Modulates A431 Cellular Pathways Association to Tumor Radioresistance and Enhanced Migration Revealed by Comprehensive Proteomic and Functional Studies. *Mol. Cell. Proteom.* **2013**, *12*, 485–498. [CrossRef] [PubMed]

66. Ren, Y.; Hao, P.; Law, S.K.A.; Sze, S.K. Hypoxia-induced Changes to Integrin α 3 Glycosylation Facilitate Invasion in Epidermoid Carcinoma Cell Line A431. *Mol. Cell. Proteom.* **2014**, *13*, 3126–3137. [CrossRef]

67. Misra, A.; Pandey, C.; Sze, S.K.; Thanabalu, T. Hypoxia Activated EGFR Signaling Induces Epithelial to Mesenchymal Transition (EMT). *PLoS ONE* **2012**, *7*, e49766. [CrossRef]

68. Boström, P.; Thoms, J.; Sykes, J.; Ahmed, O.; Evans, A.; van Rhijn, B.G.; Mirtti, T.; Stakhovskyi, O.; Laato, M.; Margel, D.; et al. Hypoxia Marker GLUT-1 (Glucose Transporter 1) is an Independent Prognostic Factor for Survival in Bladder Cancer Patients Treated with Radical Cystectomy. *Bladder Cancer* **2016**, *2*, 101–109. [CrossRef]

69. Smith, V.; Mukherjee, D.; Lunj, S.; Choudhury, A.; Hoskin, P.; West, C.; Illidge, T. The effect of hypoxia on PD-L1 expression in bladder cancer. *BMC Cancer* **2021**, *21*, 1–11. [CrossRef] [PubMed]

70. Teodori, E.; Braconi, L.; Bua, S.; Lapucci, A.; Bartolucci, G.; Manetti, D.; Romanelli, M.N.; Dei, S.; Supuran, C.T.; Coronnello, M. Dual P-Glycoprotein and CA XII Inhibitors: A New Strategy to Reverse the P-gp Mediated Multidrug Resistance (MDR) in Cancer Cells. *Molecules* **2020**, *25*, 1748. [CrossRef]

71. Kopecka, J.; Rankin, G.M.; Salaroglio, I.C.; Poulsen, S.-A.; Riganti, C. P-glycoprotein-mediated chemoresistance is reversed by carbonic anhydrase XII inhibitors. *Oncotarget* **2016**, *7*, 85861–85875. [CrossRef]

72. Borror, A.L.; Chinoporos, E.; Filosa, M.P.; Herchen, S.R.; Petersen, C.P.; Stern, C.A.; Onan, K.D. Regioselectivity of electrophilic aromatic substitution: Syntheses of 6- and 7-sulfamoylindolines and -indoles. *J. Org. Chem.* **1988**, *53*, 2047–2052. [CrossRef]

73. Khalifah, R.G. The carbon dioxide hydration activity of carbonic anhydrase. I. Stop-flow kinetic studies on the native human isoenzymes B and C. *J. Biol. Chem.* **1971**, *246*, 2561–2573. [CrossRef] [PubMed]

74. Del Prete, S.; Vullo, D.; De Luca, V.; Carginale, V.; di Fonzo, P.; Osman, S.M.; AlOthman, Z.; Supuran, C.T.; Capasso, C. Anion inhibition profiles of the complete domain of the η-carbonic anhydrase from Plasmodium falciparum. *Bioorganic Med. Chem.* **2016**, *24*, 4410–4414. [CrossRef] [PubMed]

75. Del Prete, S.; Vullo, D.; De Luca, V.; Carginale, V.; di Fonzo, P.; Osman, S.M.; AlOthman, Z.; Supuran, C.T.; Capasso, C. Anion inhibition profiles of α-, β- and γ-carbonic anhydrases from the pathogenic bacterium Vibrio cholerae. *Bioorganic Med. Chem.* **2016**, *24*, 3413–3417. [CrossRef]

76. De Luca, V.; Vullo, D.; Del Prete, S.; Carginale, V.; Osman, S.M.; AlOthman, Z.; Supuran, C.T.; Capasso, C. Cloning, characterization and anion inhibition studies of a γ-carbonic anhydrase from the Antarctic bacterium Colwellia psychrerythraea. *Bioorganic Med. Chem.* **2016**, *24*, 835–840. [CrossRef]

77. Sagnou, M.; Novikov, F.N.; Ivanova, E.S.; Alexiou, P.; Stroylov, V.S.; Titov, I.Y.; Tatarskiy, V.V.; Vagida, M.S.; Pelecanou, M.; Shtil, A.A.; et al. Novel curcumin derivatives as P-glycoprotein inhibitors: Molecular modeling, synthesis and sensitization of multidrug resistant cells to doxorubicin. *Eur. J. Med. Chem.* **2020**, *198*, 112331. [CrossRef]

78. Shchekotikhin, A.E.; Dezhenkova, L.G.; Susova, O.Y.; Glazunova, V.A.; Luzikov, Y.N.; Sinkevich, Y.B.; Buyanov, V.N.; Shtil, A.A.; Preobrazhenskaya, M.N. Naphthoindole-based analogues of tryptophan and tryptamine: Synthesis and cytotoxic properties. *Bioorganic Med. Chem.* **2007**, *15*, 2651–2659. [CrossRef]

79. Scherbakov, A.M.; Lobanova, Y.S.; Shatskaya, V.A.; Onopchenko, O.V.; Gershtein, E.S.; Krasil'nikov, M.A. Activation of mitogenic pathways and sensitization to estrogen-induced apoptosis: Two independent characteristics of tamoxifen-resistant breast cancer cells? *Breast Cancer Res. Treat.* **2006**, *100*, 1–11. [CrossRef]

80. Mruk, D.D.; Cheng, C.Y. Enhanced chemiluminescence (ECL) for routine immunoblotting: An inexpensive alternative to commercially available kits. *Spermatogenesis* **2011**, *1*, 121–122. [CrossRef]

Article

Identification of Novel Aryl Carboxamide Derivatives as Death-Associated Protein Kinase 1 (DAPK1) Inhibitors with Anti-Proliferative Activities: Design, Synthesis, In Vitro, and In Silico Biological Studies

Ahmed Elkamhawy [1,2], Sora Paik [3], Eslam M. H. Ali [4,5], Ahmed H. E. Hassan [6], So Jin Kang [7], Kyeong Lee [1] and Eun Joo Roh [3,8,*]

[1] BK21 FOUR Team and Integrated Research Institute for Drug Development, College of Pharmacy, Dongguk University-Seoul, Goyang 10326, Korea
[2] Department of Pharmaceutical Organic Chemistry, Faculty of Pharmacy, Mansoura University, Mansoura 35516, Egypt
[3] Chemical and Biological Integrative Research Center, Korea Institute of Science and Technology (KIST), Seoul 02792, Korea
[4] Department of Medicinal Chemistry and Molecular Pharmacology, Purdue University, 575 West Stadium Avenue, West Lafayette, IN 47907, USA
[5] Pharmaceutical Chemistry Department, Faculty of Pharmacy, Modern University for Technology and Information (MTI), Cairo 12055, Egypt
[6] Department of Medicinal Chemistry, Faculty of Pharmacy, Mansoura University, Mansoura 35516, Egypt
[7] Department of Biotechnology, Graduate School Korea University, Seoul 02841, Korea
[8] Division of Bio-Medical Science & Technology, University of Science and Technology, Daejeon 34113, Korea
* Correspondence: r8636@kist.re.kr

Abstract: Death-associated protein kinase 1 (DAPK1) is a serine/threonine protein kinase involved in diverse fundamental cellular processes such as apoptosis and autophagy. DAPK1 isoform plays an essential role as a tumor suppressor and inhibitor of metastasis. Consequently, DAPK1 became a promising target protein for developing new anti-cancer agents. In this work, we present the rational design and complete synthetic routes of a novel series of eighteen aryl carboxamide derivatives as potential DAPK1 inhibitors. Using a custom panel of forty-five kinases, a single dose of 10 μM of the picolinamide derivative **4a** was able to selectively inhibit DAPK1 kinase by 44.19%. Further investigations revealed the isonicotinamide derivative **4q** as a promising DAPK1 inhibitory lead compound with an IC_{50} value of 1.09 μM. In an in vitro anticancer activity assay using a library of 60 cancer cell lines including blood, lung, colon, CNS, skin, ovary, renal, prostate, and breast cancers, four compounds (**4d**, **4e**, **4o**, and **4p**) demonstrated high anti-proliferative activity with mean % GI ~70%. Furthermore, the most potent DAPK1 inhibitor (**4q**) exhibited remarkable activity against leukemia (K-562) and breast cancer (MDA-MB-468) with % GI of 72% and 75%, respectively.

Keywords: death-associated protein kinase 1 (DAPK1); kinase inhibitors; DAPK1 inhibitors; anti-proliferative activity; aryl carboxamides

1. Introduction

Death-associated protein kinase 1 (DAPK1) (a Ca^{2+}/calmodulin dependent Ser/Thr kinase) is an essential mediator in cell death and autophagy related signals [1,2]. It consists of 1430 residues and is the largest member in the DAPK protein family, including a Ca^{2+}/CaM autoregulatory domain, a death domain, and a serine-rich C-terminal tail whose phosphorylation activity is known to be responsible for specific forms of apoptosis [3,4]. It coordinates cell-death signaling pathways in response to various stimuli such as death receptor activation, cytokines, matrix detachment, ceramide, ischemia, and glutamate toxicity [5]. As previously discussed in various studies, DAPK1 as a stress-responsive kinase is

a crucial component that transmits ER stress signals into two distinct directions, caspase activation (via regulating type I apoptotic caspase-dependent cell death) and autophagy (by controlling type II autophagic caspase-independent cell death) [5–13].

Among novel effective approaches to hinder apoptosis pathways, some fusion proteins have been reported [14]. However, a peptide-based strategy has certain potential scientific and technical cautions, such as lack of cell selectivity, instability, as well as uncertainty of the effective therapeutic concentration, which influences the peptide cargo in addition to suffering from rapid degradation after administration orally [15]. Hence, the rational drug design of small molecule inhibitors could be a unique way to overcome such drawbacks. Although DAPK1 has gained a lot of interest regarding the comprehension of its functions, only a small number of chemical scaffolds, comprehensively discussed in our recent review [4], have been found in the literature with DAPK1 inhibitory activity, i.e., aminopyridazine [16,17], imidazo [1,2-*b*]pyridazine [18], pyridin-3-ylmethylene-1,3-oxazol-5-one [19,20], pyrazolo [3,4-*d*]pyrimidinone [21,22], and 1*H*-pyrrolo [2,3-*b*]pyridine (7-azaindole) [23] (Figure 1). Inspired by the various unsolved issues of reported scaffolds, such as instability in biological systems, low potency, low selectivity profile, and/or insufficient toxicity studies, in addition to the absence of a current promising clinical candidate or an FDA-approved specific DAPK1 inhibitor, our institute has launched a project aimed at designing novel leads for DAPK1 activity modulation with potential anticancer activities.

I, IC_{50} = 13 μM
Aminopyridazine

II, IC_{50} = 0.247 μM
Imidazo[1,2-*b*]pyridazine

III, IC_{50} = 0.148 μM
Pyridin-3-ylmethylene-1,3-oxazol-5-one

IV, IC_{50} = 0.069 μM
Pyridin-3-ylmethylene-1,3-oxazol-5-one

V, IC_{50} = 0.2 μM
Pyrazolo[3,4-*d*]pyrimidine

VI, % inhibition at 0.2 μM = 87%
1*H*-pyrrolo[2,3-*b*]pyridine (7-azaindole)
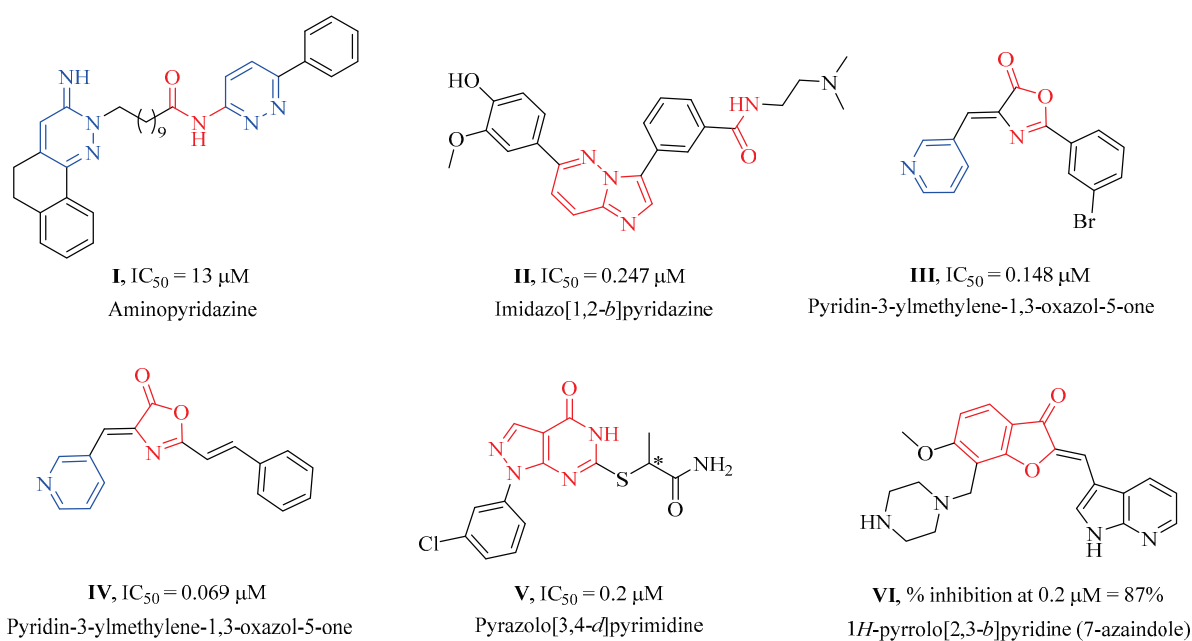
Figure 1. Reported synthetic small molecules bearing different chemical scaffolds and their IC_{50} values or % inhibition against DAPK1 kinase.

In previous studies, a structure-based virtual screening strategy was followed to develop an oxazol-5-one derivative **III** and its related analogues as DAPK inhibitors. Further in silico studies were conducted to define the structure–activity relationship (SAR) of the developed inhibitors [19,24]. The SAR studies stated that a nitrogen containing group, such as pyridinyl moiety, is essential for DAPK activity due to the role of the N-atom in H-bond formation with the backbone NH of Val96 in the hinge region at the ATP binding site. In addition, substitution on the terminal phenyl ring was found to improve potency against DAPK compared to the unsubstituted analogues, which might be explained by the increase in electron density of the phenyl ring which allows for ring contribution in hydrophobic interactions at the ATP binding site. Regarding phenyl ring substitution, the studies reported that meta-substitution seems to be more appropriate for binding at the ATP binding site than para-substitution because of electronic effects. Additionally, substitution with electron withdrawing groups at meta-positions is more effective for activity than

electron donating ones. It was also observed that the phenyl ring is located near Asp161 in a very tight area of the binding pocket, so bulky substitution would badly affect inhibitor affinity to the binding site and reduce their stability and activity, as well. Finally, docking of compound **III** in DAPK binding sites illustrated an observed vacancy around the phenyl group, which is considered a point of optimization for developing new DAPK inhibitors with extended substitution on the phenyl ring.

Relying on the aforementioned SAR studies, structural optimizations of the reported inhibitor **III** were conducted, while keeping the essential binding interactions, with the aim of producing a novel series of DAPK inhibitors (**4a–r**) (Figure 2). In the current work, the designed carboxamide derivatives (**4a–r**) were designed to retain the hinge binding interaction with the Val96 backbone by introducing different nitrogen containing groups (pyridine, pyridazine, and pyrazine). However, the principal modification was the ring opening of the central oxazole into carboxamide moiety, which has been reported in many DAPK inhibitors. The lateral phenyl group of the designed series was substituted by an electron withdrawing meta-chloro group that was reported for better hydrophobic interaction. The new designed compounds possessed a unique extension in the hydrophobic area via additional phenoxy substitutions on the terminal phenyl group in an attempt to boost molecular interaction with the enzyme pocket.
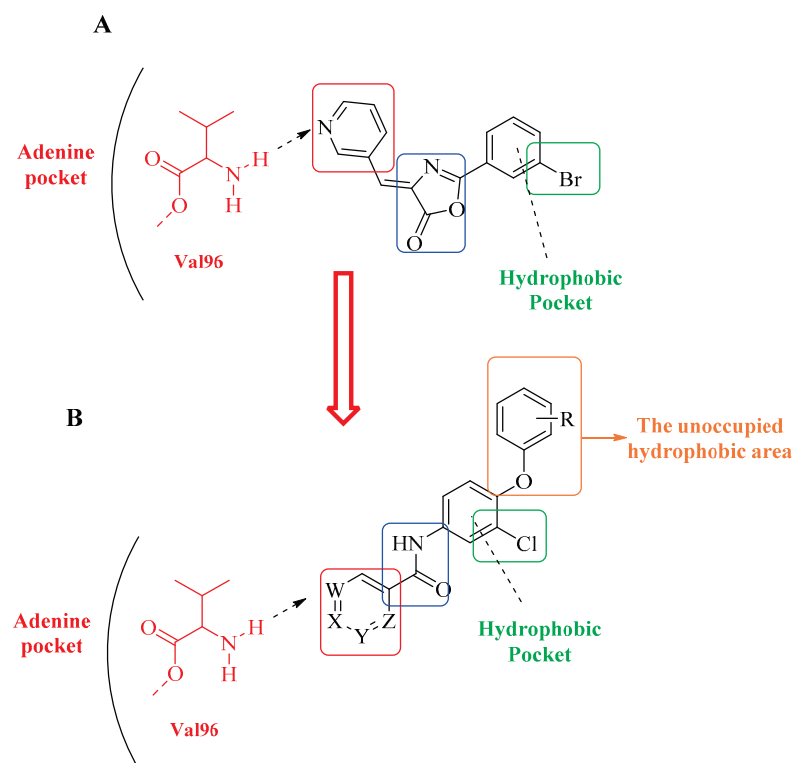
Figure 2. Diagrammatic representation of the structural modifications of compound **III** for developing new DAPK inhibitor candidates: (**A**) molecular interactions of compound **III** into the DAPK active site; (**B**) proposed binding interaction of the new synthesized derivatives **4a–r** into the DAPK kinase domain (W, X, Y, and Z could be C or N atoms).

2. Results and Discussion

2.1. Chemistry

The chemical synthesis of the target compounds **4a–r** was carried out as illustrated in Scheme 1. A nucleophilic aromatic substitution reaction of the commercially available starting material 2-chloro-1-fluoro-4-nitrobenzene (**1**) was performed via adding the appropriate phenolic derivative and a catalytic amount of potassium carbonate to generate 2-chloro-4-nitrophenoxybenzene derivatives (**2a–c**). Catalytic hydrogenation of compounds **2a–c**

was performed using Pt/C catalyst under hydrogen atmosphere to yield compounds **3a–c**. Introduction of amide functionality to intermediate **3a–c** was achieved by coupling with the appropriate benzoic acid derivative using HATU to afford the final target compounds **4a–r** (Table 1).
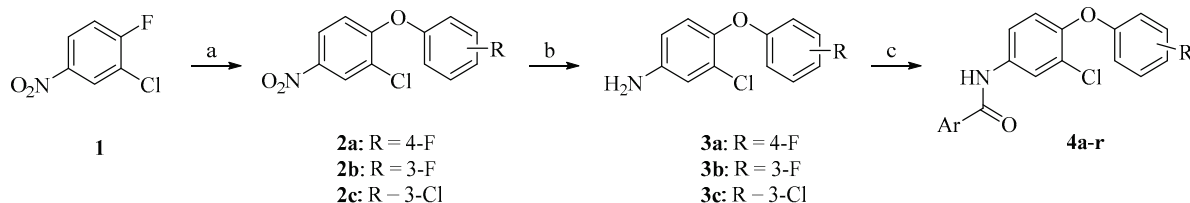
Scheme 1. Reagents and conditions: (**a**) appropriate phenol derivative, K_2CO_3, MeCN, 85 °C, 6 h; (**b**) H_2, Pt/C, MeOH, rt, 6 h; (**c**) appropriate benzoic acid derivative, DIPEA, HATU, THF, reflux, overnight.

Table 1. Key Structure of the final target compounds **4a–r**.

Cpd	R	Ar	Yield%	Cpd	R	Ar	Yield%
4a	4-F		73	**4j**	4-F		70
4b	3-F		50	**4k**	4-F		56
4c	3-F		63	**4l**	4-F		46
4d	3-F		59	**4m**	3-Cl		62
4e	3-F		23	**4n**	3-Cl		72
4f	3-F		29	**4o**	3-Cl		65
4g	3-F		62	**4p**	3-Cl		49
4h	4-F		82	**4q**	3-Cl		12
4i	4-F		86	**4r**	3-Cl		53

2.2. Biological Evaluation

2.2.1. Evaluation of Compound **4a** against a Panel of 45 Kinases

In an attempt to test our design hypothesis and discover if DAPK1 is the potential conceivable kinase target of the designed candidates, a kinase selectivity assay was carried out to the first synthesized derivative (**4a**) against a group of forty-five different kinases. Compound **4a** was evaluated at a single dose concentration of 10 μM and % inhibition was determined against each corresponding kinase (Table 2).

Table 2. % enzyme inhibition (relative to DMSO controls) of compound **4a** in a single-dose duplicate mode assay at a concentration of 10 μM against 45 kinases.

Kinase	DAPK1% Inhibition at 10 μM Dose [a]	Kinase	DAPK1% Inhibition at 10 μM Dose [a]
ABL1	12.29 ± 0.11	JAK1	8.11 ± 1.85
ACK1	0.53 ± 3.32	JNK1	−9.39 ± 0.22
AKT1	−6.56 ± 1.56	KDR/VEGFR2	−4.28 ± 0.11
AMPK(A1/B1/G1)	2.10 ± 2.96	LCK	−15.69 ± 0.45
Aurora A	−5.10 ± 0.78	LRRK2	23.80 ± 1.19
BRAF	−4.67 ± 0.03	MARK1	−3.12 ± 0.15
BRAF (V599E)	−9.72 ± 0.04	MEK1	−16.18 ± 0.42
BTK	1.97 ± 0.21	OSR1/OXSR1	−6.76 ± 1.93
CAMK1a	−49.53 ± 0.28	P38a/MAPK14	−22.83 ± 0.63
CDK1/cyclin A	−8.34 ± 0.93	PAK1	1.12 ± 2.73
CHK1	−7.21 ± 0.77	PDGFRa	19.18 ± 0.68
c-Kit	15.53 ± 3.14	RAF1	4.51 ± 1.32
CLK1	−0.14 ± 0.13	RET	−12.78 ± 0.99
c-MET	7.03 ± 0.34	ROCK1	−6.35 ± 1.35
c-Src	10.63 ± 1.61	ROCK2	2.96 ± 1.06
DAPK1	44.19 ± 1.95	ROS/ROS1	−7.04 ± 1.71
DDR1	5.76 ± 1.69	STK39/STLK3	−2.47 ± 1.50
ERBB2/HER2	−7.42 ± 1.74	SYK	−13.26 ± 0.10
FGFR1	−14.24 ± 0.24	TAK1	−4.08 ± 1.16
FLT3	0.13 ± 1.08	TIE2/TEK	−13.18 ± 2.15
FMS	3.36 ± 0.31	TLK1	−2.23 ± 3.33
IGF1R	−12.67 ± 0.72	TRKA	−8.71 ± 0.17
IKKb/IKBKB	−15.92 ± 0.74		

[a] Inhibition percentage values expressed as a mean of duplicate measurements ± S.E.M.

Interestingly, the preliminary data revealed a remarkable selectivity of compound **4a** towards DAPK1, with mean % inhibition of 44.19%. On the other hand, the results for the other 44 kinases showed no activity for most of the kinases and low activity (less than 25%) for a few of the tested kinases (Figure 3). An additional inspection of compound **4a** selectivity was carried out by evaluating its activity against other DAPK isoforms (DAPK2 and DAPK3). The obtained results showed no activity for compound **4a** with DAPK2 and DAPK3 isoforms (data not shown).

2.2.2. In Vitro DAPK1 Kinase Assay and Optimization towards Lead Development

Based on the previous panel of kinase data, a series of aryl carboxamide derivatives (**4b–r**) were synthesized and evaluated in vitro for their inhibitory activity against DAPK1 using the ELISA technique (enzyme-linked immune sorbent assay). The enzyme inhibition assay was conducted with a 10 μM dose of the tested compounds and the mean % inhibition was measured. As illustrated in Table 3, derivatives possessing the pyridinyl carboxamide moiety (**4c**, **4e**, **4f**, **4h**, **4j**, **4k**, **4m**, **4p**, and **4q**) exhibited the highest inhibitory activity (59–81%) in comparison to the pyridazine or pyrazine possessing derivatives (38–61%). In addition, the attachment point of these nitrogen heterocycles (pyridine, pyridazine, and pyrazine) with the amide group did not show a remarkable effect in terms of activity. In regard to the substitution on the terminal phenoxy moiety, the overall results showed that para-substitution with the fluoro group in compounds **4a** and **4h–l** has a better effect on activity than the meta-substituted derivatives **4b–g**, except for the pyridazine bearing derivatives **4a** and **4b**. Moreover, replacing the m-fluoro substitution with *m*-chloro in compounds **4m–r** showed a slight improvement in activity, except in compounds **4d** and **4o** where the chloro substitution dramatically reduced activity to 37.99%. Among the tested series, compounds **4h**, **4j**, **4k,** and **4q** revealed the highest activity of 81%, 79%, 80%, and 72%, respectively.
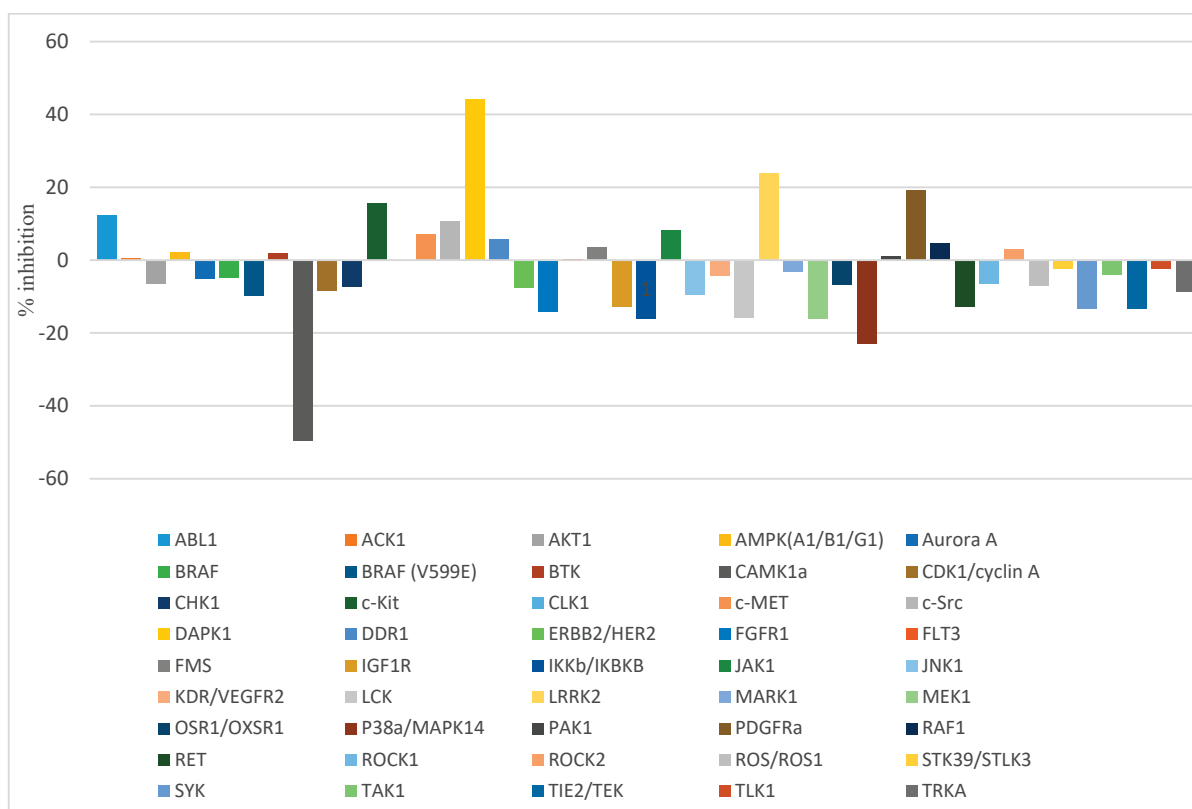
Figure 3. A schematic chart illustrating the enzyme inhibitory activity of compound **4a** (10 μM) against a panel of 45 oncogenic kinases.

Table 3. DAPK1 kinase % inhibition activity for the final target compounds **4a–r** at 10 μM.

Cpd	% Inhibition against DAPK1 [a]	Cpd	% Inhibition against DAPK1 [a]
4a	44.19	**4j**	79.06
4b	58.95	**4k**	80.61
4c	58.83	**4l**	61.83
4d	50.91	**4m**	61.73
4e	59.98	**4n**	61.54
4f	64.06	**4o**	37.99
4g	50.18	**4p**	61.48
4h	81.00	**4q**	72.10
4i	63.69	**4r**	59.98

[a] % enzyme inhibition (relative to DMSO controls) for all synthesized analogs in a single-dose duplicate mode assay at a concentration of 10 μM with DAPK1 kinase.

2.2.3. Dose-Dependent Assay of Compounds 4h, 4j, 4k, and 4q with DAPK1 Kinase

For more clarification of the structural activity relationship of the synthesized compounds, the most active derivatives (**4h**, **4j**, **4k** ,and **4q)** were subjected to a dose-dependent IC_{50} kinase assay. The selected candidates showed low micromolar IC_{50} values against DAPK1 kinase with a range of 1.09–7.26 μM. The data obtained in Table 4 revealed the impact of the attachment point of the pyridine moiety with the amide linker and, for the 4-F phenoxy derivatives, nicotinamide owing compound 4j exhibited the highest activity (IC_{50} = 1.7 μM). In contrast, substitution with picolinamide (**4h**) and isonicotinamide (**4k**) declined activity to 6.81 μM and 7.26 μM, respectively. Interestingly, the isonicotinamide derivative with the terminal *m*-chlorophenoxy moiety (**4q**) emerged to be the most potent inhibitor with an IC_{50} value of 1.09 μM. In order to determine its selectivity against DAPK1, compound **4q** was evaluated at a single dose concentration (10 μM) against the other two

isoforms (DAPK2/DAPK3). The two isoforms exhibited no inhibition at all by compound **4q** (data not shown), indicating the high potential of compound **4q** to be a promising selective DAPK1 inhibitory lead compound.

Table 4. IC_{50} values of compounds **4h**, **4j**, **4k**, and **4q** against DAPK1 kinase.

Cpd	DAPK1 [a], IC_{50} (µM)
4h	6.81
4j	1.70
4k	7.26
4q	1.09

[a] Mean values of duplicate mode 10-dose IC_{50} assays with DAPK1 kinase, with 3-fold serial dilution starting at 10 µM.

2.2.4. In Vitro Anticancer Assay

The anticancer effects of all newly synthesized compounds (**4a–r**) were assessed through determining their anti-proliferative activities against a panel of NCI-60 human cancer cell lines belonging to nine cancer types (leukemia, non-small cell lung cancer, colon cancer, CNS cancer, melanoma, ovarian cancer, renal cancer, prostate cancer, and breast cancer). All the subjected compounds were selected for one-dose 60 cell line assays. The tested compounds showed wide spectrum activity against the different human cancer cell lines with maximum mean inhibition of 71% (Figure 4). Among the tested compounds, only compounds **4d**, **4e**, **4o**, and **4p** displayed high anti-proliferative activities (67.02%, 67.87%, 70.83%, and 69.27%, respectively). The data obtained from NCI assays are analyzed in this section.
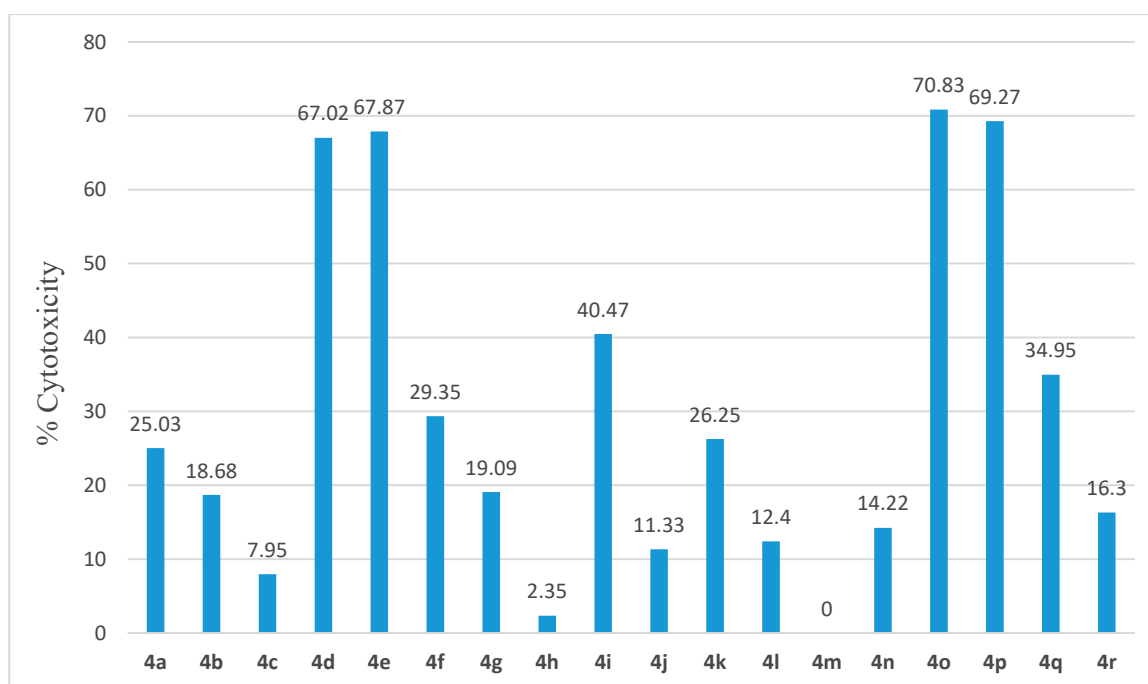
Figure 4. Mean % inhibition of NCI-60 cell lines after treatment with a single dose (10 µM) of compounds **4a–r**.

■ Anti-proliferative activity against leukemia:

The efficacy of the synthesized compounds against leukemia cell lines (CCRF-CEM, HL-60(TB), K-562, MOLT-4, RPMI-8226, and SR) is illustrated in Table 5. It was observed that leukemia cells (HL-60(TB) and K-562) are the most sensitive cell lines towards treatment with the tested compounds (Figure 5). The pyrazine carboxamide derivatives **4d** and **4o**,

with meta-(F or Cl) substitution on the terminal phenoxy group, totally inhibited the growth of the leukemia HL-60(TB) cell line with almost 100% inhibition and showed above 90% growth inhibition for leukemia K-562. Compounds **4e**, **4h**, and **4p** exhibited satisfactory inhibitory activity against both cell lines (78–83%), while most of the tested candidates showed moderate anti-proliferative activity against leukemia (30–60%).

Table 5. Anti-proliferative activities (% growth inhibition) of the target compounds **4a–r** against leukemia cell lines.

Cpd.	CCRF-CEM	HL-60(TB)	K-562	MOLT-4	RPMI-8226	SR
4a	24.87	43.74	44.47	40.16	37.38	2.35
4b	24.49	26.45	38.23	19.72	42.72	−6.10
4c	6.71	11.44	10.98	6.93	21.08	−4.05
4d	81.59	96.88	86.57	58.79	82.05	79.23
4e	76.04	87.94	83.79	59.83	84.21	76.25
4f	41.83	32.93	67.22	27.56	54.45	36.39
4g	40.77	30.04	44.68	24.07	55.39	8.58
4h	−5.45	−5.22	4.80	−24.34	−1.85	−26.54
4i	35.87	78.57	78.88	54.90	19.59	50.71
4j	−0.75	16.79	49.09	-5.20	12.69	24.85
4k	21.90	16.39	53.90	5.43	34.21	10.68
4l	21.39	15.06	19.57	12.50	33.55	−2.96
4m	−0.92	12.35	−7.67	−12.52	0.39	−26.02
4n	16.03	10.46	23.01	19.89	28.89	13.01
4o	83.35	98.50	86.78	73.85	81.94	73.68
4p	82.54	93.94	88.94	62.59	88.07	80.15
4q	43.23	40.60	71.93	32.16	59.20	18.60
4r	34.26	18.01	41.54	14.16	46.55	−11.83
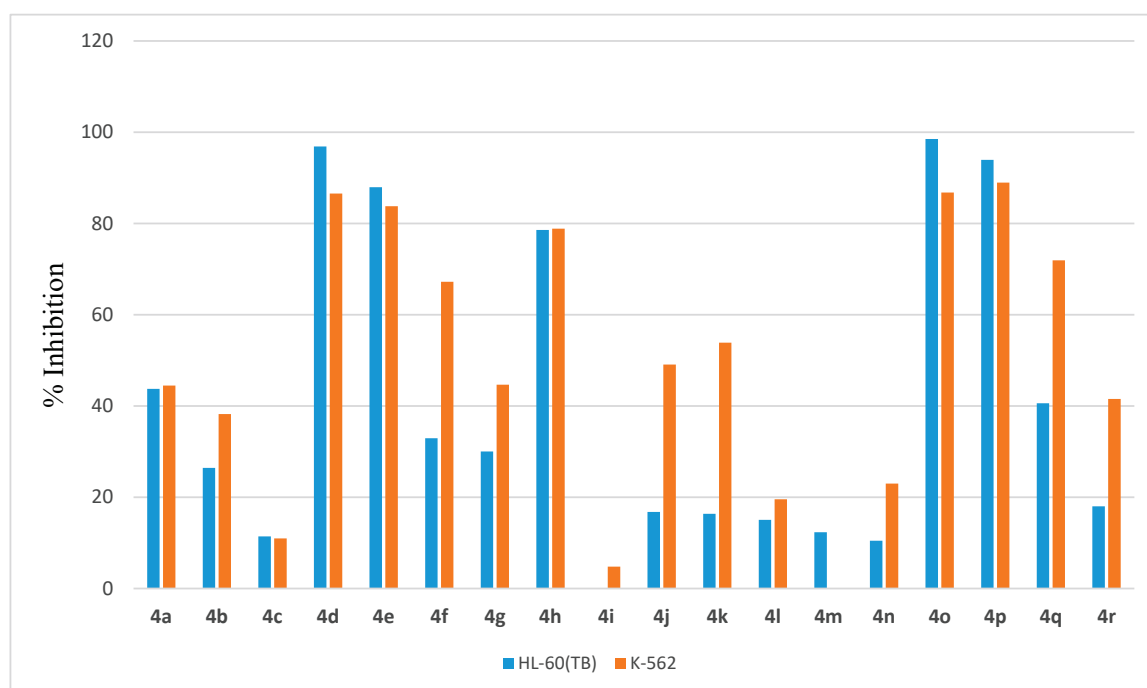
Figure 5. Mean % inhibition of the target compounds **4a–r** against leukemia cell lines (HL-60(TB) and K-562).

■ Anti-proliferative activity on non-small cell lung cancer:

The synthesized candidates were evaluated against a panel of nine NSCLCs (A549, EKVX, HOP62, HOP92, NCI-H226, NCI-H23, NCI-H322M, NCI-H460, and NCI-H522). The

results are represented in Table 6. Among the tested series, compounds **4d**, **4e**, **4o**, and **4p** were the most active anti-proliferative agents against the nine NSCLCs (% GI = 55–60%).

Table 6. Anti-proliferative activities (% growth inhibition) of the target compounds **4a–r** against non-small cell lung cancer cell lines.

Cpd	A549/ATCC	EKVX	HOP-62	HOP-92	NCI-H226	NCI-H23	NCI-H322M	NCI-H460	NCI-H522
4a	34.51	25.04	15.76	33.54	45.00	37.68	12.42	23.21	38.20
4b	32.62	25.29	0.90	17.89	30.57	23.57	6.18	3.78	27.10
4c	18.95	10.63	−7.22	15.05	1.09	6.75	2.94	0.03	17.87
4d	60.88	48.75	57.56	48.48	38.23	55.06	53.70	77.90	77.71
4e	64.48	50.41	65.97	36.59	43.08	55.14	49.18	75.35	63.79
4f	44.90	46.82	31.88	12.60	37.44	49.29	10.81	22.18	24.20
4g	36.08	35.47	10.18	NT	30.80	33.47	−0.14	11.06	22.76
4h	1.70	13.06	−8.34	7.68	5.54	14.36	1.66	0.15	20.06
4i	56.25	21.95	43.80	41.84	25.60	34.41	17.83	71.99	45.79
4j	14.04	18.08	−6.37	8.10	0.24	20.04	−0.70	3.01	27.70
4k	12.58	60.37	29.52	20.18	17.62	51.60	1.00	18.70	37.11
4l	24.02	19.22	1.57	16.91	26.86	25.71	7.09	5.29	20.81
4m	8.08	−0.64	−6.77	3.98	−8.86	−5.18	−5.68	−0.87	5.22
4n	24.70	12.67	−0.67	15.62	21.16	15.91	6.13	0.21	26.35
4o	76.05	46.82	59.01	37.99	35.91	53.91	52.07	84.28	87.52
4p	63.21	49.14	62.02	38.66	45.68	52.09	52.92	77.80	72.66
4q	50.61	47.56	33.07	13.96	42.84	55.74	19.25	28.11	35.65
4r	32.61	28.53	6.68	5.58	29.92	32.81	1.73	7.58	27.65

As depicted in Figure 6, NCI-H460 and NCI-H522 were the highest affected cell lines by the mentioned active compounds. NCI-H460 showed % GI of 77.9%, 75.34%, 84.28%, and 77.8%, while NCI- H522 growth was inhibited by 77.7%, 63.79%, 87.25%, and 72.65% upon treatment with 10 µM of **4d**, **4e**, **4o**, and **4p**, respectively. Compounds **4i** and **4q** elicited moderate activity with average inhibition of 40% and 36%, respectively. Meanwhile, the rest of the tested series did not exhibit significant activity towards NSCLCs (average % GI < 30%).
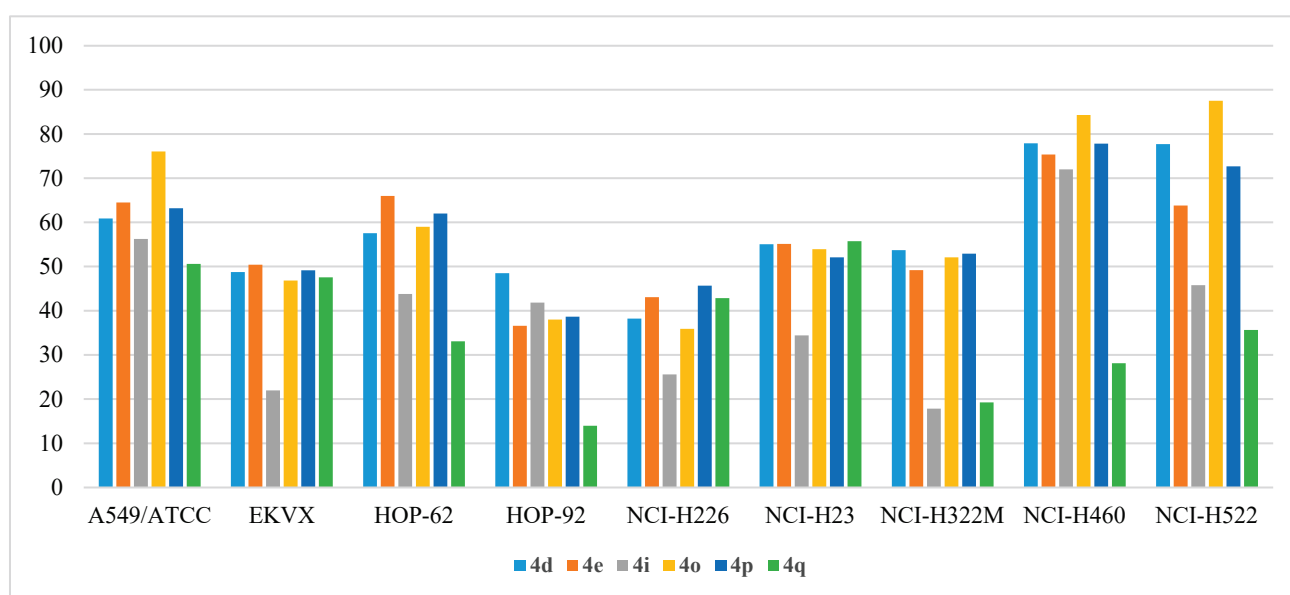
Figure 6. Anti-proliferative activities (% GI) of compounds **4d**, **4e**, **4i**, **4o**, **4p**, and **4q** against NSCLCs.

■ Anti-proliferative activity on colon cancers:

The target compounds were assayed against a panel of seven colon adenocarcinoma cell lines (COLO-205, HCC-2998, HCT-116, HCT-15, HT29, KM12, and SW-620) and the results are summarized in Table 7. The tested compounds revealed a wide range of inhibitory activity against the seven cell lines, with average % GI from 0% to 78%. The overall data indicated that compounds **4d**, **4e**, **4o**, and **4p** had the highest growth inhibitory activity and showed average % GI of 71.84%, 69.73%, 78.16%, and 71.11%, respectively (Figure 7). Compounds **4d** and **4e** significantly inhibited the growth of HOP92 adenocarcinoma with % GI of 90.87% and 87.13%, respectively. The two compounds also exhibited outstanding activity towards the COLO 205 cell line (% GI = 84.52% and 77.29%, respectively).

Table 7. Anti-proliferative activities (% growth inhibition) of the target compounds **4a–r** against colon adenocarcinoma cell lines.

Cpd	COLO 205	HCC-2998	HCT-116	HCT-15	HT29	KM12	SW-620
4a	−11.74	10.88	3.23	22.43	23.27	20.85	5.86
4b	−0.78	3.23	44.58	48.54	13.03	17.64	−3.69
4c	−10.09	7.89	14.49	24.71	15.35	4.65	−2.86
4d	84.52	43.81	67.97	68.78	90.87	69.66	77.31
4e	77.29	42.26	66.25	70.11	87.31	70.73	74.22
4f	9.29	−6.85	52.29	19.16	3.92	29.08	15.56
4g	1.75	−5.80	21.38	20.12	0.43	25.11	1.33
4h	−24.87	6.42	8.49	3.76	−3.35	1.13	5.68
4i	30.70	23.68	41.31	52.26	76.34	72.49	63.04
4j	−20.33	8.79	11.85	15.67	11.48	23.60	7.30
4k	4.83	27.39	56.60	13.33	1.72	22.04	14.96
4l	−2.63	3.36	6.44	9.12	12.54	10.52	−5.05
4m	−12.61	−17.45	−3.79	−0.91	−2.08	−1.10	−0.09
4n	−5.90	4.76	33.28	43.26	10.11	14.71	−4.84
4o	87.71	49.22	79.08	76.69	97.86	79.27	77.28
4p	84.61	42.04	70.09	63.16	91.43	71.89	74.59
4q	17.91	−0.82	55.73	24.37	15.41	32.88	23.45
4r	−1.57	−10.77	15.72	17.28	3.02	21.25	−0.48

Figure 7. Anti-proliferative activities (% GI) of compounds **4d**, **4e**, **4i**, **4o**, and **4p** against colon cancer cell lines.

Moreover, compounds **4o** and **4p** emerged to be the most potent inhibitors of HOP92 adenocarcinoma with % GI of 97.8% and 91.4%, respectively. Furthermore, the COLO 205 cell line was also inhibited by the two compounds with % GI of 87.71% and 84.61% for the two compounds. Compound **4i** moderately inhibited the growth of HCT-15, HT29,

KM12, and SW-620 and exhibited % GI of 52.26%, 76.34%, 72.49%, and 63.04%, respectively (Figure 7).

- Anti-proliferative activity on CNS cancers:

The anti-proliferative activities of the target derivatives were determined against six CNS cancer cell lines (SF-268, SF-295, SF-539, SNB-19, SNB-75, and U251) and the resulting % GIs were tabulated in Table 8. As illustrated, compounds **4d**, **4e**, **4o**, and **4p** kept their ranking among the tested derivatives as the most potent anti-proliferative agents. It was observed that SF-539 and SNB-75 were the most sensitive cell lines that showed growth inhibition around 100% upon treatment with 10 μM of compounds **4d**, **4o**, **4p**, **4e** (Figure 8). In addition, the mentioned derivatives broadly inhibited the growth of the remaining four cell lines (44.50–83.53%). Compound **4q** moderately inhibited the growth of SF-295 (67.42%), while there was no observable activity from the compound towards the other five cell lines.

Table 8. Anti-proliferative activities (% growth inhibition) of the target compounds **4a–r** against CNS cancer cell lines.

| Cpd	SF-268	SF-295	SF-539	SNB-19	SNB-75	U251
4a	19.64	26.63	14.50	33.85	12.24	37.09
4b	15.24	19.22	3.77	13.63	19.94	30.61
4c	3.67	6.83	−4.47	8.03	20.26	21.79
4d	44.50	63.96	103.46	59.62	99.15	74.34
4e	46.35	59.88	95.94	57.35	92.15	67.54
4f	15.83	59.58	17.49	32.89	10.07	27.52
4g	18.94	22.54	7.93	18.58	14.60	21.98
4h	−1.32	8.92	4.25	8.73	NT	12.52
4i	27.80	27.12	32.90	36.26	52.28	61.85
4j	5.00	14.00	5.58	6.79	NT	10.97
4k	16.97	58.92	18.58	26.78	NT	14.64
4l	18.14	14.27	4.69	11.91	28.81	15.77
4m	−1.72	5.99	−3.28	4.33	12.89	9.88
4n	16.12	17.78	4.69	10.47	22.28	23.31
4o	45.68	58.77	135.24	66.47	120.94	83.53
4p	46.58	58.61	108.37	58.71	123.19	76.10
4q	20.45	67.42	24.18	41.32	18.27	37.68
4r	17.40	27.73	4.39	18.63	12.21	19.46

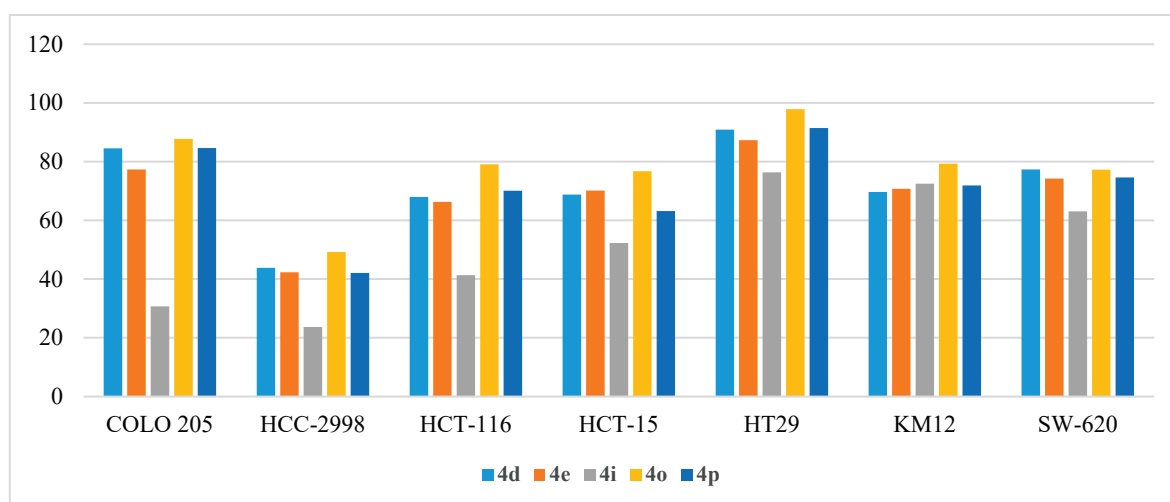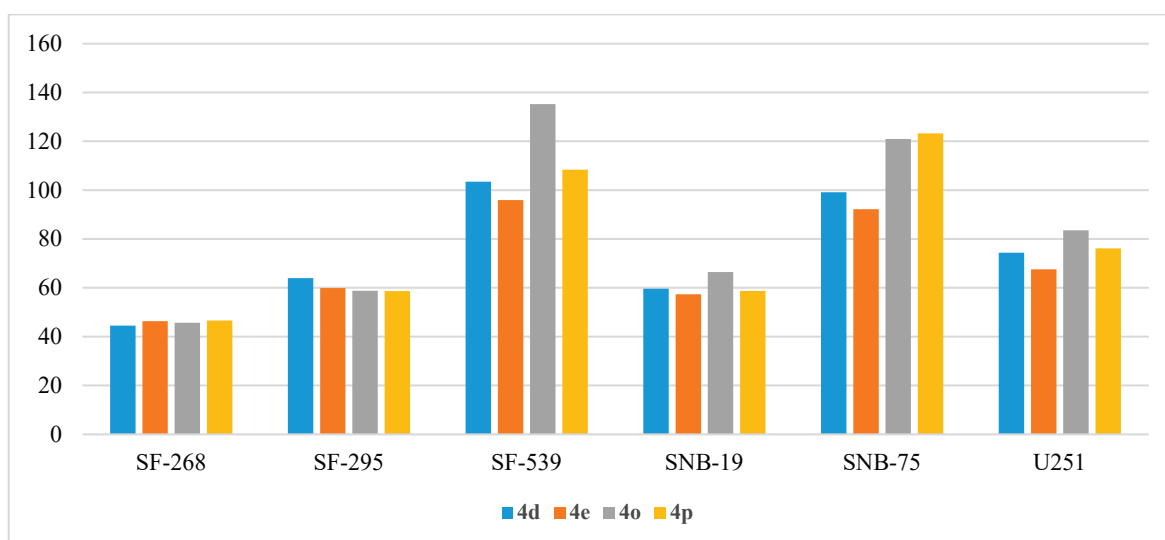**Figure 8.** Anti-proliferative activities (% GI) of compounds **4d**, **4e**, **4o**, and **4p** against CNS cancer cell lines.

■ Anti-proliferative activity on melanoma:

Melanoma anti-proliferative activity of the synthesized compounds was evaluated using a panel of nine melanoma cell lines (LOX IMVI, MALME-3M, M14, MDA-MB-435, SK-MEL-2, SK-MEL-28, SK-MEL-5, UACC-257, and UACC-62) with the % GI results illustrated in Table 9. The highest potency was observed on the MDA-MB-435 cell line which was strongly inhibited by compounds **4d**, **4e**, **4i**, **4o**, and **4p** (% GI = 121%, 98%, 102%, 139%, and 144%, respectively) (Figure 9). Compound **4e** exhibited high potency against the SK-MEL-5 cell line with % GI of 124%, while the same cell line was highly inhibited by **4d**, **4o**, **4p**, and **4q** (% GI of 90.39%, 74.19%, 85.47%, and 73.04%, respectively) and moderately inhibited by **4a**, **4f**, **4i**, and **4k** (% GI of 69.25%, 58.84%, 50.48%, and 67.41%, respectively). Moreover, compounds **4o** and **4p** showed moderate activity against the M14 cell line (80.21% and 78.15%, respectively) and UACC-62 cell line (71.64% and 62.37%, respectively).

Table 9. Anti-proliferative activities (% growth inhibition) of the target compounds **4a–r** against melanoma cell lines.

Cpd	LOX IMVI	MALME-3M	M14	MDA-MB-435	SK-MEL-2	SK-MEL-28	SK-MEL-5	UACC-257	UACC-62
4a	27.24	−4.65	−14.00	32.75	22.30	9.15	69.25	35.74	37.47
4b	25.22	7.97	7.10	19.00	8.32	1.43	32.67	7.10	31.60
4c	2.62	2.27	−1.30	8.65	5.50	−0.68	9.49	−9.00	16.27
4d	56.13	48.64	74.39	121.17	62.33	39.39	90.39	35.06	66.46
4e	47.19	52.84	84.06	98.36	63.46	45.96	123.95	43.92	68.80
4f	38.68	16.33	15.91	33.96	30.20	13.40	58.84	41.05	48.32
4g	18.38	−3.55	11.13	23.66	14.50	2.85	41.79	19.72	36.67
4h	3.90	−1.10	−5.94	5.26	−4.51	−14.37	2.21	−12.41	12.42
4i	48.55	29.89	7.62	102.80	46.40	23.13	50.48	20.25	49.67
4j	8.76	−2.94	2.72	58.51	8.69	−2.54	20.48	8.59	18.73
4k	29.89	8.49	6.80	28.75	40.51	1.54	67.41	23.72	40.20
4l	10.38	−2.67	5.36	10.47	2.21	−0.94	21.76	6.33	25.61
4m	-2.57	−9.79	−4.28	6.16	−7.38	0.87	−3.94	−4.90	6.68
4n	11.48	−3.78	7.23	22.44	−2.18	0.55	16.20	−3.76	25.33
4o	70.14	46.63	80.21	139.73	56.37	35.07	74.19	27.57	71.64
4p	48.29	49.87	78.15	144.28	55.91	36.16	85.47	35.81	62.37
4q	44.43	27.35	26.33	40.27	35.39	17.55	73.04	38.68	49.14
4r	14.41	2.90	15.11	21.71	14.60	5.10	29.20	16.23	33.19
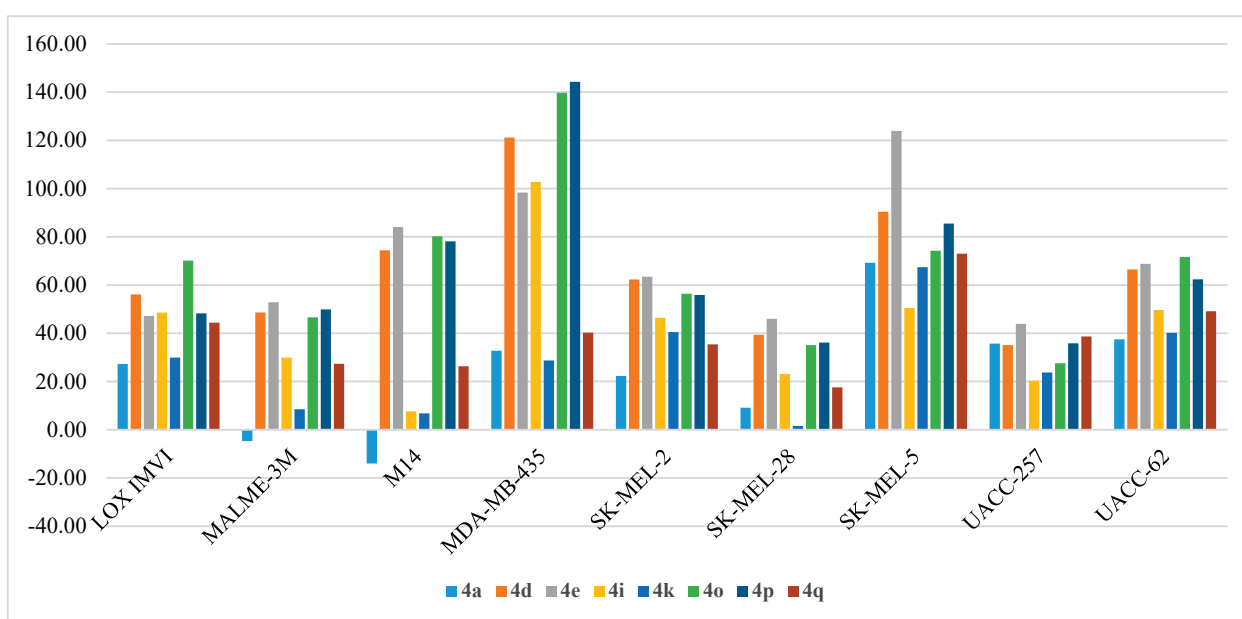
Figure 9. Anti-proliferative activities (% GI) of compounds **4a**, **4d**, **4e**, **4i**, **4k**, **4o**, **4p**, and **4q** against Melanoma cell lines.

■   Anti-proliferative activity on ovarian cancers:

The growth inhibition results of the tested compounds against a panel of six ovarian cancer cell lines are demonstrated in Table 10. Among the employed ovarian cell lines, OVCAR-3 emerged to be the most sensitive cell line, which was strongly inhibited by compounds **4d**, **4e**, **4o**, and **4p** with % GI of 117.85%, 93.03%, 107.23%, and 97.34%, respectively. The **4d**, **4e**, **4o**, and **4p** compounds also inhibited the growth of the NCI/ADR-RES cell line with % GI over 85%. OVCAR-3 and NCI/ADR-RES were moderately inhibited by compound **4i** (56.36% and 59.16%, respectively). In addition, moderate growth inhibition activity was detected against three cell lines: SK-OV-3 by compounds **4e** and **4p** (69.98% and 65.75%, respectively); OVCAR-8 by compounds **4d**, **4e**, **4o**, and **4p** (62.49%, 65.37%, 72.05%, and 67.92%, respectively); OVCAR-4 by compounds **4d**, **4e**, **4f**, **4o**, **4p,** and **4q** (55.46%, 53.83%, 54.30%, 61.05%, 52.16%, 56.18%, respectively); and IGROV1 by compounds **4d**, **4e**, **4o**, and **4p** (59.49%, 58.28%, 72.96%, 57.85%, respectively) (Figure 10).

Table 10. Anti-proliferative activities (% growth inhibition) of the target compounds **4a–r** against ovarian cancer cell lines.

| Cpd	IGROV1	OVCAR-3	OVCAR-4	OVCAR-5	OVCAR-8	NCI/ADR-RES	SK-OV-3
4a	2.39	26.40	NT	15.95	28.75	30.57	11.16
4b	7.95	21.21	38.86	3.48	6.93	7.85	−3.63
4c	5.29	5.30	21.99	2.65	−2.78	−3.02	−7.73
4d	59.49	117.85	55.46	43.39	62.49	90.94	14.03
4e	58.24	93.03	53.83	27.40	65.37	86.14	69.98
4f	10.32	24.90	54.30	−3.67	33.96	30.30	18.97
4g	−0.70	18.15	26.00	−8.04	11.94	8.76	−1.53
4h	1.79	−2.65	11.49	−5.31	−5.64	11.70	−14.73
4i	37.38	56.36	NT	18.94	28.56	59.16	−0.47
4j	4.59	14.21	14.85	0.07	1.40	14.87	−10.36
4k	7.73	31.85	22.92	7.00	27.11	36.38	19.08
4l	3.35	12.54	24.55	−2.71	9.85	7.17	3.83
4m	−4.42	−2.87	1.25	6.70	−3.01	−14.69	−3.50
4n	8.57	14.44	31.35	8.86	8.33	15.03	−2.30
4o	72.96	107.23	61.05	39.64	72.05	85.16	16.73
4p	57.85	97.34	52.16	28.80	67.92	88.11	65.75
4q	14.33	27.51	56.18	9.72	40.42	33.17	19.67
4r	7.86	14.64	31.04	−5.97	10.63	4.76	0.32
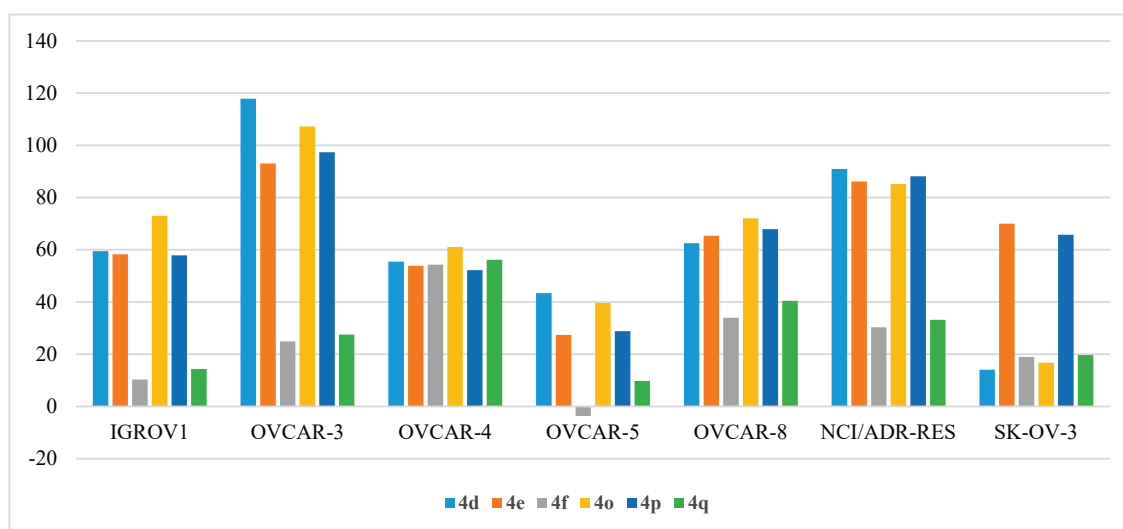
Figure 10. Anti-proliferative activities (% GI) of compounds **4d**, **4e**, **4f**, **4o**, **4p**, and **4q** against ovarian cancer cell lines.

■ Anti-proliferative activity on renal cancers:

The synthesized compounds **4a–r** exhibited a wide range of inhibitive activity towards a panel of eight renal cancer cell lines (786-0, A498, ACHN, CAKI-1, RXF 393, SN12C, TK-10, and UO-31), as shown in Table 11. The uppermost activity was observed against the growth of the RXF 393 cell line which was totally inhibited (% GI > 100%) by compounds **4o** and **4p** and greatly inhibited by compounds **4d** and **4e** (92.63% and 86.46%, respectively). Additionally, the A498 cell line showed inhibition of 100% by compound **4p** and 95.84% by compound **4e** (Figure 11). Modest activity was noticed against the 786-0 cell line by compounds **4d**, **4e**, **4o**, and **4p** (% GI of 53.47%, 59.13%, 55.36%, and 60.79%, respectively), the ACHN cell line by compounds **4d**, **4e**, **4o**, **4p**, and **4q** (% GI of 62.30%, 64.82%, 60.04%, 58.34%, and 52.45%, respectively), the CAKI-1 cell line by compounds **4d**, **4e**, **4o**, and **4p** (% GI of 74.84%, 67.45%, 78.37%, and 69.44%, respectively), the SN12C cell line by compounds **4d**, **4e**, **4o**, and **4p** (% GI of 54.42%, 63.63%, 55.60%, and 56.56%, respectively), and the UO-31 cell line by compounds **4d**, **4e**, **4o**, and **4p** (% GI of 56.60%, 60.28%, 62.66%, and 55.92%, respectively) (Figure 11).

Table 11. Anti-proliferative activities (% growth inhibition) of the target compounds **4a–r** against renal cancer cell lines.

Cpd	786-0	A498	ACHN	CAKI-1	RXF 393	SN12C	TK-10	UO-31
4a	−5.04	38.95	26.30	45.20	17.36	36.18	35.56	45.01
4b	23.45	21.77	14.60	24.59	20.89	15.74	25.76	33.84
4c	21.26	10.29	2.04	14.58	−4.88	7.62	22.97	17.68
4d	53.47	30.57	62.30	74.84	92.63	54.42	40.46	56.60
4e	59.13	95.84	64.82	67.45	86.46	63.63	40.07	60.28
4f	23.38	41.23	44.98	33.92	−6.80	18.18	22.50	31.83
4g	15.44	24.78	31.68	37.07	0.38	18.44	18.94	31.99
4h	5.85	22.23	−2.59	15.45	−0.44	−4.70	1.08	22.52
4i	18.95	32.33	5.89	50.35	27.74	30.22	14.22	34.97
4j	7.73	29.16	0.47	13.15	9.82	4.16	2.30	19.09
4k	16.26	56.91	25.12	30.56	8.16	16.37	15.85	28.68
4l	13.93	19.59	12.22	22.93	−11.93	14.96	18.03	40.38
4m	9.93	5.35	−1.09	7.21	−11.85	2.65	7.95	12.70
4n	22.57	12.65	2.11	19.24	9.70	16.79	24.95	35.06
4o	55.36	49.81	60.04	78.37	104.58	55.60	43.63	62.66
4p	60.79	103.10	58.34	69.44	100.14	56.56	40.23	55.92
4q	27.67	40.37	52.45	41.45	9.56	30.90	25.70	43.59
4r	14.13	27.83	26.38	33.64	−20.50	16.91	17.18	35.82
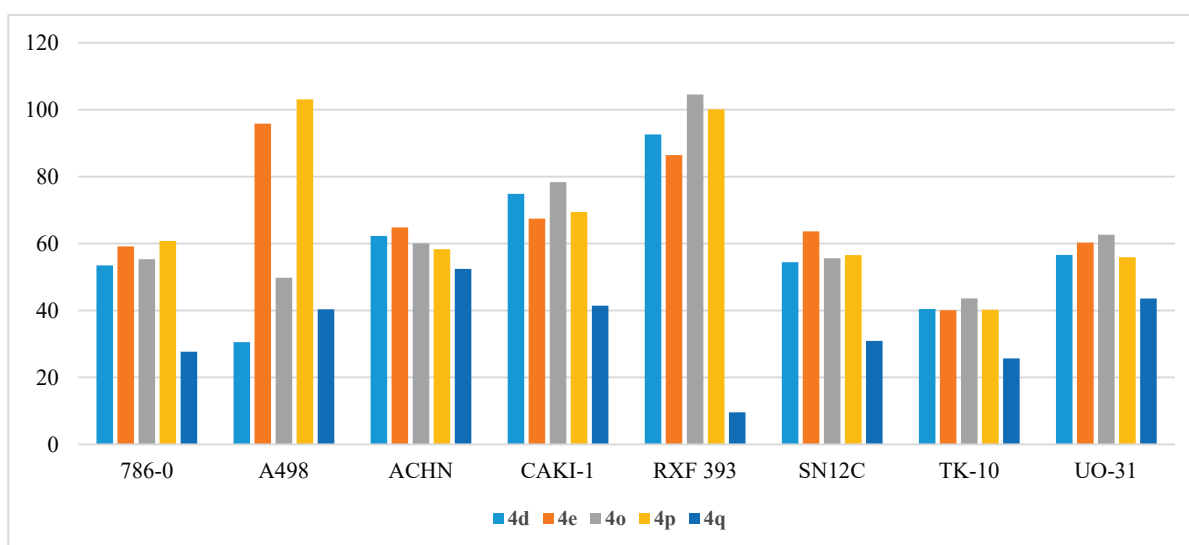
Figure 11. Anti-proliferative activities (% GI) of compounds **4d**, **4e**, **4o**, **4p**, and **4q** against renal cancer cell lines.

■ Anti-proliferative activity on prostate cancers:

Two prostate cancer cell lines (PC-3 and DU-145) were used for the anti-proliferative evaluation of the target compounds **4a–r** (Table 12). Among the tested series, only compounds **4d**, **4e**, **4o**, and **4p** exhibited satisfactory potency against the two cell lines. The four candidates inhibited the growth of the PC-3 cell line by % GI of 83.31%, 75.41%, 88.90%, and 85.15%, respectively. However, the DU-145 cell line was inhibited by % GI of 80.87%, 78.17%, 77.35%, and 83.88% by the four compounds, respectively (Figure 12).

Table 12. Anti-proliferative activities (% growth inhibition) of the target compounds **4a-r** against prostate cancer cell lines.

Cpd	PC-3	DU-145
4a	35.59	23.29
4b	47.62	17.49
4c	33.62	8.58
4d	83.31	80.87
4e	75.41	78.17
4f	20.74	9.42
4g	28.39	16.44
4h	2.71	3.23
4i	23.96	20.47
4j	9.30	12.96
4k	24.42	22.70
4l	13.07	5.67
4m	9.03	−3.53
4n	42.83	13.68
4o	88.90	77.35
4p	85.15	83.88
4q	25.02	22.55
4r	19.59	15.68
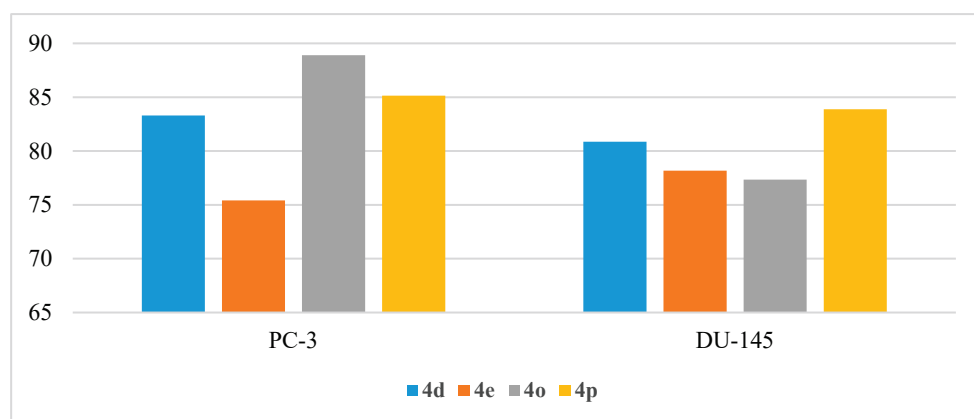
Figure 12. Anti-proliferative activities (% GI) of compounds **4d**, **4e**, **4o**, and **4p** against prostate cancer cell lines.

■ Anti-proliferative activity on breast cancers:

Finally, the target compounds were evaluated as anti-proliferative agents against six different breast cancer cell lines (MCF7, MDA-MB-231/ATCC, HS 578T, BT-549, T-47D, and MDA-MB-468) and the results were summarized. As shown in Table 13, the growth of the MDA-MB-468 cell line was completely inhibited (100–109%) by compounds **4d**, **4e**, **4o**, and **4p**, while its growth was moderately inhibited by compounds **4a**, **4f**, **4g**, **4i**, **4k**, **4q**, and **4r** (52–76%). The MCF7 cell line was less sensitive to the tested compounds and showed maximum growth inhibition of 82.54% and 80.44% with compounds **4d** and **4e**,

respectively. The HS 578T and T-47D cell lines were moderately inhibited by compounds **4a**, **4d**, **4e**, **4o**, and **4p** (% GI 59.27–81.27%). MDA-MB-231/ATCC and BT-549 were the most resistant cell lines to the tested compounds, except for compound **4o** that inhibited the growth of MDA-MB-231/ATCC by % GI of 68.29% (Figure 13).

Table 13. Anti-proliferative activities (% growth inhibition) of the target compounds **4a–r** against breast cancer cell lines.

| Cpd	MCF7	MDA-MB-231/ATCC	HS 578T	BT-549	T-47D	MDA-MB-468
4a	34.71	11.88	4.36	−3.11	62.39	60.73
4b	12.80	6.93	−4.53	15.34	42.13	41.58
4c	11.41	−0.05	1.61	7.71	23.18	14.77
4d	82.54	46.50	72.17	40.15	61.71	99.92
4e	80.44	39.78	68.75	51.44	66.51	109.22
4f	44.11	14.71	7.30	40.61	46.75	76.00
4g	18.46	1.84	8.39	8.12	39.23	55.16
4h	13.86	0.09	−0.49	2.31	27.84	20.32
4i	70.32	41.29	37.62	−0.40	57.08	68.17
4j	23.32	6.34	8.51	7.52	29.40	42.77
4k	39.38	19.70	6.71	36.00	56.60	78.17
4l	9.28	9.19	−7.24	5.75	30.08	36.63
4m	3.69	−2.42	3.47	1.02	−4.39	−2.35
4n	8.35	4.49	−6.22	1.47	27.64	36.69
4o	79.69	68.29	81.27	42.55	59.27	99.57
4p	78.44	41.02	68.95	46.72	64.41	109.21
4q	56.26	20.80	10.84	40.15	51.56	74.71
4r	14.03	5.90	2.82	1.87	38.96	52.01
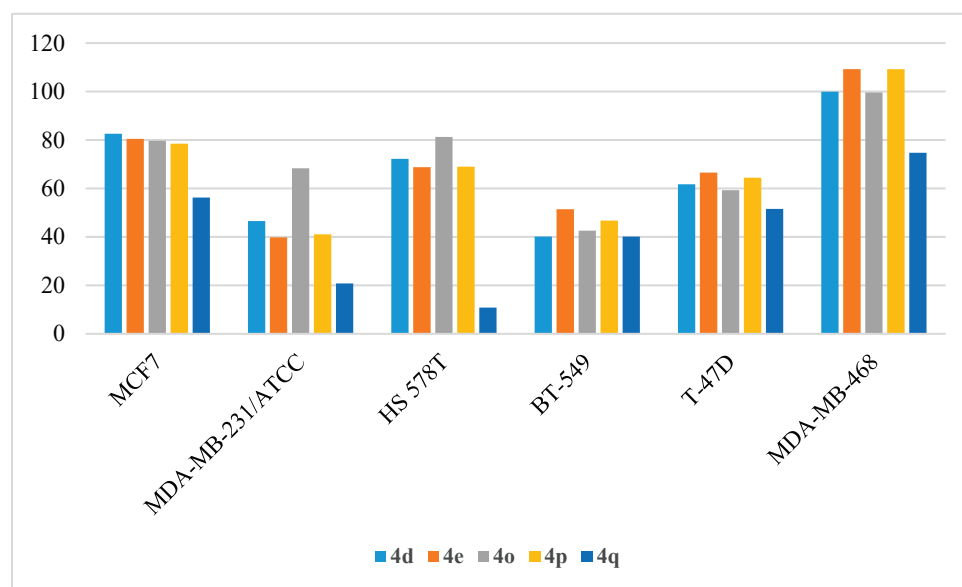
Figure 13. Anti-proliferative activities (% GI) of compounds **4d**, **4e**, **4o**, **4p**, and **4q** against breast cancer cell lines.

2.2.5. Docking Study

In an attempt to introduce a reasonable explanation for the observed DAPK1 kinase activity with respect to the inhibitors' binding affinity, the potent inhibitor **4j** was subjected to a molecular docking study as a representative example of the designed inhibitors. In this study, Molecular Operating Environment (MOE, 2014) software was used to operate the docking protocol. The X-ray crystallographic structures of DAPK1 in complex with Genistein (PDB ID: 5AUZ) were downloaded from the protein data bank (PDB). Validation

of the docking protocol was achieved by re-docking of the co-crystalized ligand, Genistein, in the binding site of DAPK1. The re-docked ligand retained the same binding manner in the DAPK1 active site (docking score= −6.1511 kcal/mol) with an RMSD value of 0.8894 Å. As illustrated in Figure 14A, the iso-flavone moiety of the native ligand, Genistein, is binding in the adenine pocket via H-bonding between the hydroxyl group and Glu100 residue while the pyran ring is additionally embedded in the pocket by AreneH interaction with Val27. Furthermore, the DAPK1 hydrophobic pocket is occupied by the lateral hydroxy phenyl moiety, which exhibits H-bonding between its para-hydroxyl group and the Glu94 residue. Accordingly, the target compounds should conserve the binding mode of the native ligand, which in turn would also be an indication of their binding affinity and enzymatic activity. In Figure 14B, docking of compound **4j** in the active site of DAPK1 (docking score= -5.5545 kcal/mol) illustrates that the NH of the amide linker is introduced to the adenine pocket and forms H-bonding with Glu100, while the phenoxy moiety is inserted deeply in the pocket via Arene-H interaction with Val27. On the other hand, the pyridine ring, which is substituted on the amide linker, exhibits additional H-bonding with Arg150.
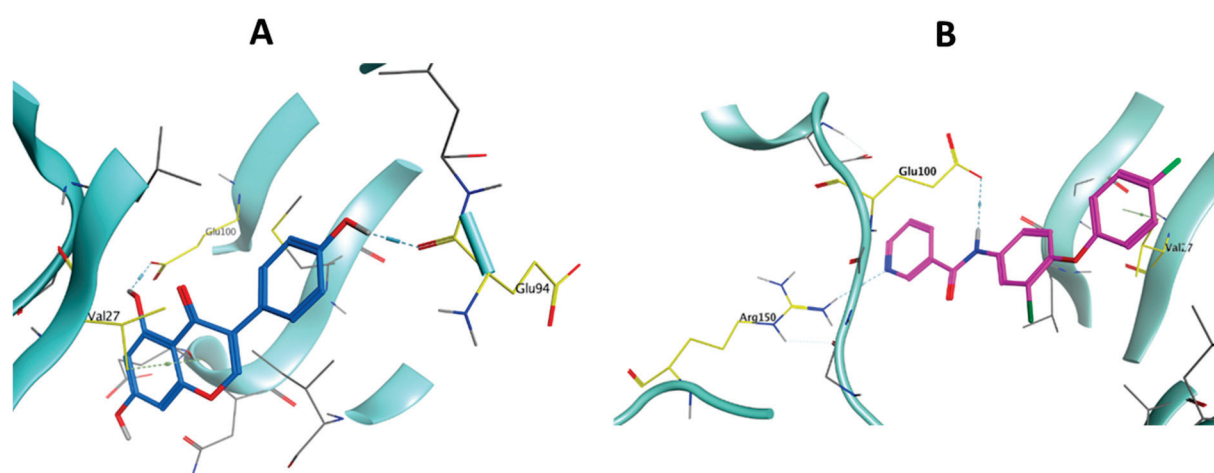
Figure 14. 3D representation of Genistein (**A**) and compound **4j** (**B**) molecular interactions in the DAPK1 kinase.

3. Materials and Methods

3.1. Chemistry

General: All reactions and manipulations were performed in a nitrogen atmosphere using standard Schlenk techniques. All reaction solvents and reagents were purchased from commercial suppliers and used without further purification. The NMR spectra were obtained with a Bruker Avance 400 (400 MHz ^{1}H and 100.6 MHz ^{13}C NMR). ^{1}H NMR spectra were referenced to tetramethylsilane (δ = 0.00 ppm) as an internal standard and were reported as follows: chemical shift, multiplicity (b = broad, s = singlet, d = doublet, t = triplet, dd = doublet of doublet, m = multiplet). Column chromatography was performed on Merck Silica Gel 60 (230–400 mesh) and eluting solvents for all of these chromatographic methods were noted as appropriated-mixed solvent with given volume-to-volume ratios. TLC was carried out using glass sheets pre-coated with silica gel 60 F_{254} purchased by Merk. For more details, see Supplementary Files.

3.1.1. General Procedure of 2-Chloro-4-nitrophenoxybenzene Derivatives (**2a–c**)

Potassium carbonate (1.25 mmol) and the appropriate phenol (1 mmol) were added to a solution of commercially available 2-chloro-1-fluoro-4-nitrobenzene (1 mmol) in MeCN (12 mL). The reaction mixture was heated at 85 °C for 6 h. The mixture was extracted with EtOAc and water. The organic layer was dried over Na_2SO_4 and concentrated under reduced pressure to give the target compound.

2-Chloro-1-(4-fluorophenoxy)-4-nitrobenzene (**2a**)

Yellowish white solid, yield: 77%, mp: 76.3−92.4 °C, ^{1}H NMR (400 MHz, CDCl$_3$) δ 6.76 (d, *J* = 8.9 Hz, 1H), 7.00−7.09 (m, 4H), 7.98 (d, *J* = 8.9 Hz, 1H), 8.31 (s, 1H) [25,26].

2-Chloro-1-(3-fluorophenoxy)-4-nitrobenzene (**2b**)

Yellow oil, yield: 96%, ^{1}H NMR (400 MHz, CDCl$_3$) δ 6.80−6.87 (m, 2H), 6.95−7.00 (m, 2H), 7.40 (dd, *J* = 8.2 Hz, 14.6 Hz, 1H), 8.10 (dd, *J* = 2.7 Hz, 9.0 Hz, 1H), 8.40 (d, *J* = 2.7 Hz, 1H). ^{13}C NMR (100.6 MHz, CDCl$_3$) δ 107.68 (J_{C-F} = 24.1 Hz), 112.49 (J_{C-F} = 21.1 Hz), 115.27 (J_{C-F} = 3.0 Hz), 117.91, 123.69, 125.39, 126.66, 131.27 (J_{C-F} = 9.1 Hz), 143.29, 115.83 (J_{C-F} = 10.1 Hz), 158.07, 163.58 (J_{C-F} = 248.5 Hz) [27].

2-Chloro-1-(3-chlorophenoxy)-4-nitrobenzene (**2c**)

Yellow solid, yield: 90%, mp: 92.4−93.1 °C, ^{1}H NMR (400 MHz, CDCl$_3$) δ 6.95−6.98 (m, 2H), 7.09 (s, 1H), 7.24 (d, *J* = 8.0 Hz, 1H), 7.37 (t, *J* = 8.1 Hz, 1H), 8.09 (dd, *J* = 2.0 Hz, 9.0 Hz, 1H), 8.38 (d, *J* = 2.0 Hz, 1H). ^{13}C NMR (100.6 MHz, CDCl$_3$) δ 117.84, 117.91, 120.22, 123.71, 125.36, 125.71, 126.67, 131.15, 135.73, 143.28, 155.41, 158.07 [28].

3.1.2. General Procedure of 3-Choro-4-phenoxyaniline Derivatives (**3a–c**)

Pt/C catalyst was added to a solution of the appropriate 2-chloro-4-nitrophenoxybenzene derivative (0.1 mmol) in MeOH (15 mL) under hydrogen atmosphere. The mixture was stirred at room temperature for 6 h. The reaction mixture was filtered with celite and washed with MeOH. The filtrate was evaporated in vacuo. The residue was purified by column chromatography to give the target compound.

3-Chloro-4-(4-fluorophenoxy) aniline (**3a**)

Brown oil, yield: 65%, ^{1}H NMR (400 MHz, DMSO-*d$_6$*) δ 5.34 (s, 2H), 6.55 (d, *J* = 8.8 Hz, 1H), 6.72 (s, 1H), 6.80–6.84 (m, 2H), 6.90 (d, *J* = 8.6 Hz, 1H), 7.13 (t, *J* = 8.2 Hz, 2H) [29].

3-Chloro-4-(3-fluorophenoxy) aniline (**3b**)

Yellow oil, yield: 78%, ^{1}H NMR (400 MHz, DMSO-*d$_6$*) δ 5.40 (s, 2H), 6.57 (d, *J* = 8.6 Hz, 1H), 6.63 (d, *J* = 8.4 Hz, 2H), 6.73 (s, 1H), 6.86 (t, *J* = 8.5 Hz, 1H), 6.96 (d, *J* = 8.8 Hz, 1H), 7.33 (t, *J* = 8.0 Hz, 1H) [27,30].

3-Chloro-4-(3-chlorophenoxy) aniline (**3c**)

Brown oil, yield: 60%, ^{1}H NMR (400 MHz, DMSO-*d$_6$*) δ 5.41 (s, 2H), 6.58 (dd, *J* = 2.6 Hz, 8.7 Hz, 1H), 6.73 (d, *J* = 2.6 Hz, 1H), 6.77–6.82 (m, 2H), 6.96 (d, *J* = 8.6 Hz, 2H), 7.09 (dd, *J* = 1.0 Hz, 8.0 Hz, 1H), 7.34 (t, *J* = 8.1 Hz, 1H) [28,30].

3.1.3. General Procedure of Target Compounds **4a–r**

The appropriate 3-chloro-4-phenoxyaniline derivative (0.1 mmol) was dissolved in THF (12 mL), followed by adding DIPEA (0.27 mmol), HATU (0.11 mmol), and the appropriate benzoic acid derivative (0.1 mmol). The reaction mixture was refluxed overnight. The mixture was extracted with EtOAc, water, and brine. The organic layer was dried over Na$_2$SO$_4$ and concentrated under reduced pressure. The residue was purified by column chromatography to give the target compound.

N-(3-chloro-4-(4-fluorophenoxy) phenyl) picolinamide (**4a**)

Brown solid, mp: 95.6–97.0 °C, ^{1}H NMR (400 MHz, CDCl$_3$) δ 6.91–6.95 (m, 2H), 7.01 (dd, *J* = 8.8 Hz, 17.2 Hz, 3H), 7.49–7.52 (m, 1H), 7.60 (dd, *J* = 2.4 Hz, 8.8 Hz, 1H), 7.92 (t, *J* = 7.6 Hz, 1H), 8.03 (d, *J* = 2.4 Hz, 1H), 8.29 (d, *J* = 7.8 Hz, 1H), 8.61 (d, *J* = 4.6 Hz, 1H), 10.04 (s, 1H). ^{13}C NMR (100.6 MHz, CDCl$_3$) δ 116.30 (J_{C-F} = 23.1 Hz), 118.91, 119.16 (J_{C-F} = 31.2 Hz), 121.03, 121.97, 122.48, 126.22, 126.72, 134.55, 137.82, 148.05, 148.89, 149.37, 153.14, 158.69 (J_{C-F} = 241.4 Hz), 162.02. HRMS (ESI) *m/z* calculated for C$_{17}$H$_{11}$ClFN$_3$NaO$_2$ [M+Na]$^+$: 366.0416, found: 366.0408.

N-(3-chloro-4-(4-fluorophenoxy) phenyl) pyridazine-3-carboxamide (**4b**)

White solid, mp: 134.1–134.9 °C, ¹H NMR (400 MHz, CDCl₃) δ 6.95–7.06 (m, 5H), 7.57 (d, *J* = 8.8 Hz, 1H), 7.77 (dd, *J* = 5.4 Hz, 7.9 Hz, 1H), 8.08 (s, 1H), 8.43 (d, *J* = 8.3 Hz, 1H), 9.36 (d, *J* = 4.4 Hz, 1H), 10.11 (s, 1H). ¹³C NMR (100.6 MHz, CDCl₃) δ 116.37 (J_{C-F} = 23.1 Hz), 119.15, 119.40 (J_{C-F} = 34.2 Hz), 120.86, 122.32, 125.90, 126.23, 128.09, 133.80, 149.54, 157.27, 152.92, 153.17, 158.80 (J_{C-F} = 241.4 Hz), 160.15. HRMS (ESI) *m/z* calculated for $C_{17}H_{11}ClFN_3NaO_2$ [M+Na]⁺: 366.0416, found: 366.0420.

N-(3-chloro-4-(4-fluorophenoxy) phenyl) pyrazine-2-carboxamide (**4c**)

White solid, mp: 155.5–156.0 °C, ¹H NMR (400 MHz, CDCl₃) δ 6.92–7.05 (m, 5H), 7.59 (dd, *J* = 2.4 Hz, 8.8 Hz, 1H), 7.99 (d, *J* = 2.4 Hz, 1H), 8.60 (s, 1H), 8.84 (d, *J* = 2.2 Hz, 1H), 9.51 (s, 1H), 9.67 (s, 1H). ¹³C NMR (100.6 MHz, CDCl₃) δ 116.35 (J_{C-F} = 23.1 Hz), 119.10, 119.33 (J_{C-F} = 27.2 Hz), 120.86, 122.18, 126.20, 133.85, 142.40, 143.98, 144.72, 147.81, 149.45, 152.92, 158.79 (J_{C-F} = 242.4 Hz), 160.67. HRMS (ESI) *m/z* calculated for $C_{18}H_{13}ClFN_2O_2$ [M+H]⁺: 343.0644, found: 343.0638.

N-(3-chloro-4-(4-fluorophenoxy) phenyl) nicotinamide (**4d**)

White solid, mp: 112.0–113.2 °C, ¹H NMR (400 MHz, CDCl₃) δ 6.89–6.93 (m, 3H), 7.02 (t, *J* = 9.1 Hz, 2H), 7.38–7.41 (m, 1H), 7.46 (dd, *J* = 2.5 Hz, 8.8 Hz, 1H), 7.83 (d, *J* = 2.4 Hz, 1H), 8.18 (dt, *J* = 1.8 Hz, 8.0 Hz, 1H), 8.71 (dd, *J* = 1.5 Hz, 4.8 Hz, 1H), 9.05 (s, 1H). ¹³C NMR (100.6 MHz, CDCl₃) δ 116.38 (J_{C-F} = 23.1 Hz), 118.85, 119.26 (J_{C-F} = 8.0 Hz), 120.49 (J_{C-F} = 12.1 Hz), 123.15, 123.81, 125.91, 130.43, 130.04, 135.57, 147.91, 149.70, 152.52, 152.77, 158.82 (J_{C-F} = 241.4 Hz), 164.20. HRMS (ESI) *m/z* calculated for $C_{17}H_{12}ClFN_3O_2$ [M+H]⁺: 344.0597, found: 343.0600.

N-(3-chloro-4-(4-fluorophenoxy) phenyl) isonicotinamide (**4e**)

White solid, mp: 57.0–58.5 °C, ¹H NMR (400 MHz, CDCl₃) δ 6.90–6.93 (m, 3H), 7.00–7.04 (m, 2H), 7.46 (dd, *J* = 2.5 Hz, 8.8 Hz, 1H), 7.68–7.70 (m, 2H), 7.83 (d, *J* = 2.5 Hz, 1H), 8.70–8.71 (m, 3H). ¹³C NMR (100.6 MHz, CDCl₃) δ 116.41 (J_{C-F} = 24.1 Hz), 118.82, 119.35 (J_{C-F} = 9.1 Hz), 120.43 (J_{C-F} = 10.1 Hz), 123.12, 125.91, 133.74, 141.74, 149.92, 150.58, 152.68, 158.87 (J_{C-F} = 241.4 Hz), 164.10. HRMS (ESI) *m/z* calculated for $C_{18}H_{13}ClFN_2O_2$ [M+H]⁺: 343.0644, found: 343.0640.

N-(3-chloro-4-(4-fluorophenoxy) phenyl) pyridazine-4-carboxamide (**4f**)

White solid, mp: 164.2–165.2 °C, ¹H NMR (400 MHz, DMSO-*d₆*) δ 7.02 (s, 2H), 7.16–7.23 (m, 3H), 7.69–7.79 (m, 1H), 8.11 (d, *J* = 6.1 Hz, 2H), 9.52 (d, *J* = 4.6 Hz, 1H), 9.65 (s, 1H), 10.89 (s, 1H). ¹³C NMR (100.6 MHz, DMSO-*d₆*) δ 117.07 (J_{C-F} = 23.1 Hz), 119.40 (J_{C-F} = 8.0 Hz), 121.19, 121.88, 122.61 (J_{C-F} = 11.1 Hz), 124.90, 125.01, 132.39, 135.97, 148.45, 149.34, 152.62, 153.35, 158.46 (J_{C-F} = 225.3 Hz), 162.98.

N-(3-chloro-4-(3-fluorophenoxy) phenyl) picolinamide (**4g**)

White solid, mp: 79.0–80.0 °C, ¹H NMR (400 MHz, CDCl₃) δ 6.65 (dt, *J* = 2.4 Hz, 10.2 Hz, 1H), 6.72 (dd, *J* = 2.2 Hz, 8.3 Hz, 1H), 6.75–6.80 (m, 1H), 7.09 (d, *J* = 8.8 Hz, 1H), 7.23–7.28 (m, 1H), 7.48–7.51 (m, 1H), 7.64 (dd, *J* = 2.6 Hz, 8.8 Hz, 1H), 7.92 (td, *J* = 1.7 Hz, 7.7 Hz, 1H), 8.05 (d, *J* = 2.6 Hz, 1H), 8.29 (d, *J* = 7.8 Hz, 1H), 8.61 (dt, *J* = 0.64 Hz, 4.12 Hz, 1H), 10.08 (s, 1H). ¹³C NMR (100.6 MHz, CDCl₃) δ 104.73 (J_{C-F} = 25.2 Hz), 109.76 (J_{C-F} = 21.1 Hz), 112.49 (J_{C-F} = 3.0 Hz), 119.36, 121.91, 122.44, 122.50, 126.77, 127.05, 130.53 (J_{C-F} = 10.1 Hz), 135.34, 137.82, 147.49, 148.07, 149.30, 158.83 (J_{C-F} = 10.1 Hz), 162.07, 163.55 (J_{C-F} = 246.5 Hz). HRMS (ESI) *m/z* calculated for $C_{17}H_{12}ClFN_3O_2$ [M+H]⁺: 344.0597, found: 344.0601.

N-(3-chloro-4-(3-fluorophenoxy) phenyl) pyridazine-3-carboxamide (**4h**)

White solid, mp: 130.3–131.2 °C, ¹H NMR (400 MHz, CDCl₃) δ 6.65–6.82 (m, 3H), 7.12 (d, *J* = 8.8 Hz, 1H), 7.27 (dd, *J* = 8.0 Hz, 15.0 Hz, 1H), 7.62 (dd, *J* = 1.8 Hz, 8.6 Hz, 1H), 7.75–7.79 (m, 1H), 8.10 (d, *J* = 1.8 Hz, 1H), 8.44 (d, *J* = 8.3 Hz, 1H), 9.37 (d, *J* = 4.3 Hz, 1H), 10.16 (s, 1H). ¹³C NMR (100.6 MHz, CDCl₃) δ 104.90 (J_{C-F} = 25.2 Hz), 109.93

(J_{C-F} = 21.1 Hz), 112.64 (J_{C-F} = 3.0 Hz), 119.62, 120.33, 121.61, 122.33 (J_{C-F} = 9.1 Hz), 125.91, 127.13, 128.09, 130.55 (J_{C-F} = 10.1 Hz), 134.60, 148.13, 152.22, 153.19, 160.19, 160.5 (J_{C-F} = 366.2 Hz).

N-(3-chloro-4-(3-fluorophenoxy) phenyl) pyrazine-2-carboxamide (**4i**)

White solid, mp: 156.6–157.2 °C, ^{1}H NMR (400 MHz, DMSO-d_6) δ 6.75 (d, *J* = 8.4 Hz, 1H), 6.83 (d, *J* = 10.3 Hz, 1H), 6.96 (t, *J* = 8.2 Hz, 1H), 7.30 (d, *J* = 8.9 Hz, 1H), 7.41 (dd, *J* = 8.2 Hz, 15.4 Hz, 1H), 7.95–7.97 (m, 1H), 8.28 (d, *J* = 2.0 Hz, 1H), 8.85 (s, 1H), 8.97 (d, *J* = 2.1 Hz, 1H), 9.33 (s, 1H), 11.05 (s, 1H). ^{13}C NMR (100.6 MHz, DMSO-d_6) δ 104.75 (J_{C-F} = 25.2 Hz), 110.26 (J_{C-F} = 21.1 Hz), 112.87, 120.26, 121.45, 122.87 (J_{C-F} = 31.2 Hz), 125.56, 131.81 (J_{C-F} = 10.1 Hz), 136.70, 143.74, 144.63, 145.21, 146.89, 148.37, 158.88 (J_{C-F} = 11.1 Hz), 162.45, 163.38 (J_{C-F} = 244.5 Hz). HRMS (ESI) *m/z* calculated for $C_{17}H_{11}ClFN_3NaO_2$ [M+Na]$^+$: 366.0416, found: 366.0415.

N-(3-chloro-4-(3-fluorophenoxy) phenyl) nicotinamide (**4j**)

White solid, mp: 117.3–118.2 °C, ^{1}H NMR (400 MHz, MeOD) δ 6.63 (dt, *J* = 2.3 Hz, 10.4 Hz, 1H), 6.69 (dd, *J* = 2.3 Hz, 8.4 Hz, 1H), 6.81 (td, *J* = 1.9 Hz, 8.4 Hz, 1H), 7.12 (d, *J* = 8.8 Hz, 1H), 7.27–7.32 (m, 1H), 7.55–7.59 (m, 1H), 7.65 (dd, *J* = 2.5 Hz, 8.8 Hz, 1H), 8.02 (d, *J* = 2.5 Hz, 1H), 8.34 (dt, *J* = 1.8 Hz, 8.1 Hz, 1H), 8.72 (dd, *J* = 1.5 Hz, 5.0 Hz, 1H), 9.09 (d, *J* = 1.5 Hz, 1H). HRMS (ESI) *m/z* calculated for $C_{18}H_{13}ClFN_2O_2$ [M+H]$^+$: 343.0644, found: 343.0648.

N-(3-chloro-4-(3-fluorophenoxy) phenyl) isonicotinamide (**4k**)

White solid, mp: 49.8–51.0 °C, ^{1}H NMR (400 MHz, CDCl$_3$) δ 6.63 (d, *J* = 10.1 Hz, 1H), 6.70 (d, *J* = 8.2 Hz, 1H), 6.75–6.81 (m, 1H), 7.04 (t, *J* = 8.7 Hz, 1H), 7.26 (dd, *J* = 8.2 Hz, 14.9 Hz, 1H), 7.52–7.62 (m, 1H), 7.70 (d, *J* = 4.8 Hz, 2H), 7.88 (d, *J* = 1.8 Hz, 1H), 8.71 (d, *J* = 5.0 Hz, 2H), 8.81 (s, 1H). ^{13}C NMR (100.6 MHz, CDCl$_3$) δ 104.95 (J_{C-F} = 24.1 Hz), 110.07 (J_{C-F} = 21.1 Hz), 112.73, 120.24 (J_{C-F} = 25.2 Hz), 121.11, 122.10, 122.49, 123.02, 126.88, 130.61 (J_{C-F} = 10.1 Hz), 134.71, 148.43, 150.57, 158.43 (J_{C-F} = 10.1 Hz), 163.21 (J_{C-F} = 187.1 Hz), 164.74. HRMS (ESI) *m/z* calculated for $C_{18}H_{13}ClFN_2O_2$ [M+H]$^+$: 343.0644, found: 343.0639.

N-(3-chloro-4-(3-fluorophenoxy) phenyl) pyridazine-4-carboxamide (**4l**)

Yellow solid, mp: 141.3–142.7 °C, ^{1}H NMR (400 MHz, CDCl$_3$) δ 6.64 (d, *J* = 10.1 Hz, 1H), 6.72 (d, *J* = 8.4 Hz, 1H), 6.80 (t, *J* = 8.1 Hz, 1H), 7.06 (d, *J* = 8.7 Hz, 1H), 7.27 (dd, *J* = 8.0 Hz, 15.0 Hz, 1H), 7.58–7.68 (m, 1H), 7.95–8.02 (m, 2H), 9.30 (d, *J* = 5.0 Hz, 1H), 9.59 (s, 1H), 9.82 (s, 1H). ^{13}C NMR (100.6 MHz, CDCl$_3$) δ 105.04 (J_{C-F} = 25.2 Hz), 110.15 (J_{C-F} = 21.1 Hz), 112.84 (J_{C-F} = 3.0 Hz), 120.07, 120.56, 122.05, 123.22, 125.23, 126.87, 130.63 (J_{C-F} = 10.1 Hz), 133.09, 134.57, 148.67, 151.96, 158.29, 162.13, 163.52 (J_{C-F} = 247.5 Hz). HRMS (ESI) *m/z* calculated for $C_{17}H_{12}ClFN_3O_2$ [M+H]$^+$: 344.0597, found: 344.0596.

N-(3-chloro-4-(3-chlorophenoxy) phenyl) picolinamide (**4m**)

Brown solid, mp: 92.7–93.5 °C, ^{1}H NMR (400 MHz, CDCl$_3$) δ 6.82 (dd, *J* = 1.9 Hz, 8.3 Hz, 1H), 6.92 (t, *J* = 2.1 Hz, 1H), 7.03–7.08 (m, 2H), 7.22 (t, *J* = 8.1 Hz, 1H), 7.47–7.50 (m, 1H), 7.63 (dd, *J* = 2.5 Hz, 8.8 Hz, 1H), 7.90 (td, *J* = 1.6 Hz, 7.7 Hz, 1H), 8.05 (d, *J* = 2.5 Hz, 1H), 8.28 (d, *J* = 7.8 Hz, 1H), 8.59 (d, *J* = 4.5 Hz, 1H), 10.07. ^{13}C NMR (100.6 MHz, CDCl$_3$) δ 115.18, 119.38, 121.91, 122.35, 122.47, 123.09, 126.76, 126.99, 130.52, 135.11, 135.35, 137.80, 147.43, 148.06, 149.27, 158.27, 162.06. HRMS (ESI) *m/z* calculated for $C_{18}H_{13}Cl_2N_2O_2$ [M+H]$^+$: 359.0349, found: 359.0346.

N-(3-chloro-4-(3-chlorophenoxy) phenyl) pyridazine-3-carboxamide (**4n**)

Light brown solid, mp: 138.0–139.6 °C, ^{1}H NMR (400 MHz, DMSO-d_6) δ 6.90 (dd, *J* = 1.9 Hz, 8.2 Hz, 1H), 7.01 (t, *J* = 2.0 Hz, 1H), 7.18 (d, *J* = 8.0 Hz, 1H), 7.31 (d, *J* = 8.9 Hz, 1H), 7.40 (t, *J* = 8.1 Hz, 1H), 7.99–8.02 (m, 2H), 8.32–8.36 (m, 2H), 9.50 (dd, *J* = 1.4 Hz, 4.9 Hz, 1H), 11.40 (s, 1H). ^{13}C NMR (100.6 MHz, DMSO-d_6) δ 115.63, 116.98, 121.63, 122.86, 123.12, 123.46, 125.59, 126.67, 129.19, 131.96, 134.50, 136.81, 146.78, 153.40, 154.13, 158.49, 162.23. HRMS (ESI) *m/z* calculated for $C_{17}H_{11}Cl_2N_3NaO_2$ [M+Na]$^+$: 382.0121, found: 382.0123.

N-(3-chloro-4-(3-chlorophenoxy) phenyl) pyrazine-2-carboxamide (**4o**)

Light brown solid, mp: 153.2–154.6 °C, ^{1}H NMR (400 MHz, DMSO-d_6) δ 6.90 (d, *J* = 8.0 Hz, 1H), 7.00 (s, 1H), 7.19 (d, *J* = 8.1 Hz, 1H), 7.30 (d, *J* = 8.8 Hz, 1H), 7.40 (t, *J* = 8.0 Hz, 1H), 7.96 (dd, *J* = 2.0 Hz, 8.8 Hz, 1H), 8.28 (d, *J* = 1.8 Hz, 1H), 8.84 (s, 1H), 8.96 (s, 1H), 9.32 (s, 1H), 11.05 (s, 1H). ^{13}C NMR (100.6 MHz, DMSO-d_6) δ 115.61, 116.98, 121.47, 122.72, 123.08, 123.45, 125.59, 131.94, 134.50, 136.76, 143.73, 144.63, 145.17, 146.75, 148.37, 158.47, 162.43. HRMS (ESI) *m/z* calculated for $C_{17}H_{12}Cl_2N_3O_2$ [M+H]$^+$: 360.0301, found: 360.0304.

N-(3-chloro-4-(3-chlorophenoxy) phenyl) nicotinamide (**4p**)

White solid, mp: 141.0–141.5 °C, ^{1}H NMR (400 MHz, DMSO-d_6) δ 6.89 (dd, *J* = 1.6 Hz, 8.4 Hz, 1H), 6.99 (s, 1H), 7.18 (d, *J* = 9.0 Hz, 1H), 7.30 (d, *J* = 8.8 Hz, 1H), 7.40 (t, *J* = 8.2 Hz, 1H), 7.58–7.61 (m, 1H), 7.77 (dd, *J* = 2.4 Hz, 8.9 Hz, 1H), 8.14 (d, *J* = 2.4 Hz, 1H), 8.30 (d, *J* = 8.1 Hz, 1H), 8.78–8.79 (m, 1H), 9.12 (d, *J* = 1.6 Hz, 1H), 10.66 (s, 1H). ^{13}C NMR (100.6 MHz, DMSO-d_6) δ 115.61, 116.93, 121.10, 122.34, 123.23, 123.45, 124.04, 125.65, 130.68, 131.96, 134.51, 135.97, 137.39, 146.53, 149.16, 152.83, 158.53, 164.73. HRMS (ESI) *m/z* calculated for $C_{18}H_{13}Cl_2N_2O_2$ [M+H]$^+$: 359.0349, found: 359.0351.

N-(3-chloro-4-(3-chlorophenoxy) phenyl) isonicotinamide (**4q**)

White solid, mp: 124.3–126.0 °C, ^{1}H NMR (400 MHz, DMSO-d_6) δ 6.91–7.00 (m, 2H), 7.19 (s, 1H), 7.28–7.40 (m, 2H), 7.78–7.88 (m, 3H), 8.15 (s, 1H), 8.82 (s, 2H), 10.72 (s, 1H).

N-(3-chloro-4-(3-chlorophenoxy) phenyl) pyridazine-4-carboxamide (**4r**)

Yellow solid, mp: 133.2–134.0 °C, ^{1}H NMR (400 MHz, DMSO-d_6) δ 6.91 (dd, *J* = 2.2 Hz, 8.3 Hz, 1H), 7.01 (s, 1H), 7.20 (d, *J* = 8.0 Hz, 1H), 7.32 (d, *J* = 8.8 Hz, 1H), 7.42 (t, *J* = 8.2 Hz, 1H), 7.76 (dd, *J* = 2.4 Hz, 8.9 Hz, 1H), 8.13 (d, *J* = 2.3 Hz, 2H), 9.53 (d, *J* = 5.2 Hz, 1H), 9.67 (s, 1H), 10.92 (s, 1H). ^{13}C NMR (100.6 MHz, DMSO-d_6) δ 115.74, 117.09, 121.22, 122.49, 123.18, 123.57, 125.01, 125.65, 131.97, 132.34, 134.53, 136.74, 147.03, 149.32, 152.62, 158.38, 163.04. HRMS (ESI) *m/z* calculated for $C_{17}H_{12}Cl_2N_3O_2$ [M+H]$^+$: 360.0301, found: 360.0304.

3.2. Biological Evaluation

3.2.1. In Vitro Kinase Screening

Kinase assays were performed at the Reaction Biology Corporation (Malvern, PA) using the "HotSpot" assay platform. All the target compounds were evaluated according to the Reaction Biology Corp implemented protocol as reported on their website (http://www.reactionbiology.com/ 25 January 2019).

3.2.2. NCI Cell Line Screening

The target compounds were evaluated for their anti-proliferative activity at the National Cancer Institute (NCI), Bethesda, Maryland, USA, applying the standard protocol of the NCI (http://www.dtp.nci.nih.gov/).

3.2.3. Docking Methodology

The X-ray crystal structures of DAPK1 kinase in complex with Genistein (PDB ID: 5AUZ) were downloaded from the protein data bank (www.rcsb.org) in PDB format. The 2D structure of compound **4j** was drawn using ChemDraw software. Molecular Operating Environment (MOE, 2014.0901) software was used for the molecular docking operation docking protocol. DAPK1 kinase was prepared for the molecular docking procedure by applying 3D protonation of both enzyme amino acids and the native ligand (Genistein). In addition, water from crystallization was removed from the kinase domain. The active site was isolated. The grid space was determined from the coordinates of the reference ligand (−22.780412, 2.367623, −10.682060) and expanded to cover all amino acid residues in the DAPK1 active site cavity (r = 8.383472). The docking protocol was validated by re-docking of Genistein with RMSD = 0.8894 Å and retained the same binding pose in the DAPK1 active site.

4. Conclusions

In the current study, a series of 3-chloro-4-(phenoxy)phenyl carboxamide derivatives featuring different substituents on the terminal phenoxy group, along with diverse nitrogen containing heterocycles on the carboxamide linker, has been designed and synthesized as DAPK1 inhibitors with potential anti-proliferative activity. A preliminary kinase inhibition evaluation was conducted on the first synthesized compound **4a** in an attempt to explore its DAPK1 activity and selectivity. Among the 45 panel kinases, compound **4a** exhibited higher activity and selectivity against DAPK1 kinase. Hence, DAPK1 inhibitory activity of the synthesized derivatives was detected; pyridinyl moiety owing derivatives **4h**, **4j**, **4f**, and **4q** displayed the highest activity and were subjected to 10-dose evaluation. The IC_{50} values of the mentioned compounds were determined and compound **4q** emerged to be the most potent DAPK1 inhibitor (IC_{50} =1.09 μM). Additionally, all the target compounds were evaluated for their cytotoxic activity against a panel of 60 NCI cancer cell lines at 10 μM concentration. Out of the tested series, compounds **4d**, **4e**, **4o**, and **4p** revealed the highest anti-proliferative activities against most of the employed cell lines (67.02%, 67.87%, 70.83%, and 69.27%. Moreover, two leukemia cell lines (HL-60(TB) and K-562) exhibited the highest sensitivity towards the tested candidates.

References

1. Deiss, L.P.; Feinstein, E.; Berissi, H.; Cohen, O.; Kimchi, A. Identification of a novel serine/threonine kinase and a novel 15-kD protein as potential mediators of the gamma interferon-induced cell death. *Genes Dev.* **1995**, *9*, 15–30. [CrossRef] [PubMed]
2. Bialik, S.; Kimchi, A. The death-associated protein kinases: Structure, function, and beyond. *Annu. Rev. Biochem.* **2006**, *75*, 189–210. [CrossRef] [PubMed]
3. Singh, P.; Ravanan, P.; Talwar, P. Death Associated Protein Kinase 1 (DAPK1): A Regulator of Apoptosis and Autophagy. *Front. Mol. Neurosci.* **2016**, *9*, 46. [CrossRef] [PubMed]
4. Farag Ahmed, K.; Roh Eun, J. Death-associated protein kinase (DAPK) family modulators: Current and future therapeutic outcomes. *Med. Res. Rev.* **2018**, *39*, 349–385. [CrossRef]
5. Pelled, D.; Raveh, T.; Riebeling, C.; Fridkin, M.; Berissi, H.; Futerman, A.H.; Kimch, A. Death-associated protein (DAP) kinase plays a central role in ceramide-induced apoptosis in cultured hippocampal neurons. *J. Biol. Chem.* **2002**, *277*, 1957–1961. [CrossRef]
6. Bialik, S.; Kimchi, A. DAP-kinase as a target for drug design in cancer and diseases associated with accelerated cell death. *Semin. Cancer Biol.* **2004**, *14*, 283–294. [CrossRef]
7. Hainsworth, A.H.; Allsopp, R.C.; Jim, A.; Potter, J.F.; Lowe, J.; Talbot, C.J.; Prettyman, R.J. Death-associated protein kinase (DAPK1) in cerebral cortex of late-onset Alzheimer's disease patients and aged controls. *Neuropathol. Appl. Neurobiol.* **2010**, *36*, 17–24. [CrossRef]

8. Gade, P.; Manjegowda, S.B.; Nallar, S.C.; Maachani, U.B.; Cross, A.S.; Kalvakolanu, D.V. Regulation of the Death-Associated Protein Kinase 1 Expression and Autophagy via ATF6 Requires Apoptosis Signal-Regulating Kinase 1. *Mol. Cell. Biol.* **2014**, *34*, 4033–4048. [CrossRef]

9. Gozuacik, D.; Bialik, S.; Raveh, T.; Mitou, G.; Shohat, G.; Sabanay, H.; Mizushima, N.; Yoshimori, T.; Kimchi, A. DAP-kinase is a mediator of endoplasmic reticulum stress-induced caspase activation and autophagic cell death. *Cell Death Differ.* **2008**, *15*, 1875–1886. [CrossRef]

10. Shohat, G.; Spivak-Kroizman, T.; Cohen, O.; Bialik, S.; Shani, G.; Berrisi, H.; Eisenstein, M.; Kimchi, A. The Pro-apoptotic Function of Death-associated Protein Kinase Is Controlled by a Unique Inhibitory Autophosphorylation-based Mechanism. *J. Biol. Chem.* **2001**, *276*, 47460–47467. [CrossRef]

11. Li, Y.; Grupe, A.; Rowland, C.; Nowotny, P.; Kauwe, J.S.K.; Smemo, S.; Hinrichs, A.; Tacey, K.; Toombs, T.A.; Kwok, S.; et al. DAPK1 variants are associated with Alzheimer's disease and allele-specific expression. *Hum. Mol. Genet.* **2006**, *15*, 2560–2568. [CrossRef] [PubMed]

12. Mor, I.; Carlessi, R.; Ast, T.; Feinstein, E.; Kimchi, A. Death-associated protein kinase increases glycolytic rate through binding and activation of pyruvate kinase. *Oncogene* **2011**, *31*, 683. [CrossRef]

13. Velentza, A.V.; Wainwright, M.S.; Zasadzki, M.; Mirzoev, S.; Schumacher, A.M.; Haiech, J.; Focia, P.J.; Egli, M.; Watterson, D.M. An aminopyridazine-based inhibitor of a pro-apoptotic protein kinase attenuates hypoxia-ischemia induced acute brain injury. *Bioorganic Med. Chem. Lett.* **2003**, *13*, 3465–3470. [CrossRef]

14. Herce, H.D.; Deng, W.; Helma, J.; Leonhardt, H.; Cardoso, M.C. Visualization and targeted disruption of protein interactions in living cells. *Nat. Commun.* **2013**, *4*, 2660. [CrossRef] [PubMed]

15. Wang, F.; Wang, Y.; Zhang, X.; Zhang, W.; Guo, S.; Jin, F. Recent progress of cell-penetrating peptides as new carriers for intracellular cargo delivery. *J. Control. Release* **2014**, *174*, 126–136. [CrossRef] [PubMed]

16. Watterson, D.M.; Velentza, A.V.; Zasadzki, M.; Craft, J.M.; Haiech, J.; van Eldik, L.J. Discovery of a new class of synthetic protein kinase inhibitors that suppress selective aspects of glial activation and protect against β-amyloid induced injury. *J. Mol. Neurosci.* **2003**, *20*, 411–423. [CrossRef]

17. Mirzoeva, S.; Sawkar, A.; Zasadzki, M.; Guo, L.; Velentza, A.V.; Dunlap, V.; Bourguignon, J.-J.; Ramstrom, H.; Haiech, J.; van Eldik, L.J.; et al. Discovery of a 3-Amino-6-phenyl-pyridazine Derivative as a New Synthetic Antineuroinflammatory Compound. *J. Med. Chem.* **2002**, *45*, 563–566. [CrossRef]

18. Wilbek, T.S.; Skovgaard, T.; Sorrell, F.J.; Knapp, S.; Berthelsen, J.; Strømgaard, K. Identification and characterization of a small-molecule inhibitor of death-associated protein kinase 1. *ChemBioChem* **2015**, *16*, 59–63. [CrossRef]

19. Okamoto, M.; Takayama, K.; Shimizu, T.; Ishida, K.; Takahashi, O.; Furuya, T. Identification of Death-Associated Protein Kinases Inhibitors Using Structure-Based Virtual Screening. *J. Med. Chem.* **2009**, *52*, 7323–7327. [CrossRef]

20. Al-Ghabkari, A.; Deng, J.-T.; McDonald, P.C.; Dedhar, S.; Alshehri, M.; Walsh, M.P.; MacDonald, J.A. A novel inhibitory effect of oxazol-5-one compounds on ROCKII signaling in human coronary artery vascular smooth muscle cells. *Sci. Rep.* **2016**, *6*, 32118. [CrossRef] [PubMed]

21. Carlson, D.A.; Franke, A.S.; Weitzel, D.H.; Speer, B.L.; Hughes, P.F.; Hagerty, L.; Fortner, C.N.; Veal, J.M.; Barta, T.E.; Zieba, B.J.; et al. Fluorescence Linked Enzyme Chemoproteomic Strategy for Discovery of a Potent and Selective DAPK1 and ZIPK Inhibitor. *ACS Chem. Biol.* **2013**, *8*, 2715–2723. [CrossRef] [PubMed]

22. MacDonald, J.A.; Sutherland, C.; Carlson, D.A.; Bhaidani, S.; Al-Ghabkari, A.; Swärd, K.; Haystead, T.A.J.; Walsh, M.P. A Small Molecule Pyrazolo[3,4-d]Pyrimidinone Inhibitor of Zipper-Interacting Protein Kinase Suppresses Calcium Sensitization of Vascular Smooth Muscle. *Mol. Pharmacol.* **2016**, *89*, 105–117. [CrossRef] [PubMed]

23. Irie, T.; Sawa, M. 7-Azaindole: A Versatile Scaffold for Developing Kinase Inhibitors. *Chem. Pharm. Bull.* **2018**, *66*, 29–36. [CrossRef]

24. Okamoto, M.; Takayama, K.; Shimizu, T.; Muroya, A.; Furuya, T. Structure–activity relationship of novel DAPK inhibitors identified by structure-based virtual screening. *Bioorganic Med. Chem.* **2010**, *18*, 2728–2734. [CrossRef]

25. Yang, Z.-X.; Chen, H.B.; Zou, Y.-Z.; Hou, Y.; Wang, T.-P.; Liang, Y. Synthesis of 7-chloro-4-hydroxy-6-(phenoxy)-3-quinolinecarboxylic acid ethyl ester derivatives and determination of their activity as coccidiostats. *Youji Huaxue* **2008**, *28*, 432–435.

26. Marafie, J.A.; Moseley, J.D. The application of stop-flow microwave technology to scaling-out SNAr reactions using a soluble organic base. *Org. Biomol. Chem.* **2010**, *8*, 2219–2227. [CrossRef]

27. Hennequin, L.F.A.; Chen, H.; Zou, Y.; Zhu, J.; Wang, Y. *Preparation of Quinazolines as Antitumor Agents*; AstraZeneca AB: Södertälje, Sweden; AstraZeneca UK Limited: Cambridge, UK, 2003; p. 218.

28. Bolea, C. *Preparation of Amido Derivatives and Their Use as Positive Allosteric Modulators of Metabotropic Glutamate Receptors*; Addex Pharma S.A.: Geneva, Switzerland, 2009; p. 68.

29. Yang, Z.; Chen, H.; Zou, Y.; Zhu, J.; Wang, Y. Method for Synthesizing 6-aryloxy-7-chloro-4-hydroxyl-3-quinolinecarboxylate. CN 200610022419, 11 July 2007.

30. Ishikawa, T.; Seto, M.; Banno, H.; Kawakita, Y.; Oorui, M.; Taniguchi, T.; Ohta, Y.; Tamura, T.; Nakayama, A.; Miki, H. Design and Synthesis of Novel Human Epidermal Growth Factor Receptor 2 (HER2)/Epidermal Growth Factor Receptor (EGFR) Dual Inhibitors Bearing a Pyrrolo [3,2-d] pyrimidine Scaffold. *J. Med. Chem.* **2011**, *54*, 8030–8050. [CrossRef] [PubMed]

Article

Synthesis and Biological Evaluation of Indole-2-Carboxamides with Potent Apoptotic Antiproliferative Activity as EGFR/CDK2 Dual Inhibitors

Lamya H. Al-Wahaibi [1], **Yaser A. Mostafa** [2], **Mostafa H. Abdelrahman** [3], **Ali H. El-Bahrawy** [4], **Laurent Trembleau** [5] **and Bahaa G. M. Youssif** [2,*]

[1] Department of Chemistry, College of Sciences, Princess Nourah bint Abdulrahman University, Riyadh 11671, Saudi Arabia
[2] Pharmaceutical Organic Chemistry Department, Faculty of Pharmacy, Assiut University, Assiut 71526, Egypt
[3] Department of Pharmaceutical Organic Chemistry, Faculty of Pharmacy, Al-Azhar University, Assiut 71524, Egypt
[4] Department of Pharmacology and Toxicology, Faculty of Pharmacy, Al-Azhar University, Assiut 71524, Egypt
[5] School of Natural and Computing Sciences, University of Aberdeen, Meston Building, Aberdeen AB24 3UE, UK
*   Correspondence: bgyoussif@ju.edu.sa; Tel.: +201098294419

Abstract: The apoptotic antiproliferative actions of our previously reported CB1 allosteric modulators 5-chlorobenzofuran-2-carboxamide derivatives **VIIa–j** prompted us to develop and synthesise a novel series of indole-2-carboxamide derivatives **5a–k**, **6a–c**, and **7**. Different spectroscopic methods of analysis were used to validate the novel compounds. Using the MTT assay method, the novel compounds were examined for antiproliferative activity against four distinct cancer cell lines. Compounds **5a–k**, **6a–c**, and **7** demonstrated greater antiproliferative activity against the breast cancer cell line (MCF-7) than other tested cancer cell lines, and **5a–k** (which contain the phenethyl moiety in their backbone structure) demonstrated greater potency than **6a–c** and **7**, indicating the importance of the phenethyl moiety for antiproliferative action. Compared to reference doxorubicin (GI$_{50}$ = 1.10 μM), compounds **5d**, **5e**, **5h**, **5i**, **5j**, and **5k** were the most effective of the synthesised derivatives, with GI$_{50}$ ranging from 0.95 μM to 1.50 μM. Compounds **5d**, **5e**, **5h**, **5i**, **5j**, and **5k** were tested for their inhibitory impact on EGFR and CDK2, and the results indicated that the compounds tested had strong antiproliferative activity and are effective at suppressing both CDK2 and EGFR. Moreover, the studied compounds induced apoptosis with high potency, as evidenced by their effects on apoptotic markers such as Caspases 3, 8, 9, Cytochrome C, Bax, Bcl2, and p53.

Keywords: indole; carboxamide; apoptosis; antiproliferative; multi-target

1. Introduction

In response to increased global morbidity and mortality rates from so-called incurable diseases, medication research and development has never been static but has grown increasingly dynamic. Traditionally, therapeutic drug discovery has relied on the design of highly selective chemical entities that target a single biological entity assumed to play a dominant role in a particular disease [1,2]. By means of this method, researchers hoped to eliminate any unwanted side effects and ensure that drug candidates had more drug-like properties. Highly selective or specific therapeutic medicines focused on single molecular targets, on the other hand, have shown to be ineffective, particularly in the treatment of complicated disorders. Drug resistance has been linked to the use of highly selective therapeutic agents.

However, due to the low efficacy of single target medications against multifactorial disorders whose aetiology is based on a collection of biochemical processes and many bioreceptors acting concurrently, drug design methodologies have to be reconsidered. Over the

last few years, medicinal chemistry has been exploring new tools and alternatives to attain more agility, security, and efficiency in the synthesis and prospection of drug candidates.

Because of the ineffectiveness of certain single-drug therapies, the hunt for improved clinical outcomes has prompted the introduction of polypharmacology as a novel therapeutical technique. Polypharmacology is the development or application of pharmacological drugs that operate on several molecular targets or metabolic pathways. This multi-target strategy can take several forms, such as drug associations, drug combinations, or a single agent with numerous ligands, all of which are aimed at multiple targets. HIV/AIDS treatment, cancer treatment, TB treatment, and hypertension medication are all examples of combination therapy [3–5]. However, the inefficiency of combination therapy, as well as the negative consequences of drug–drug interactions, different pharmacokinetics, toxicity, and costs, has fuelled the development of new drug discovery methodologies. This current technique promotes combining diverse structural components in a single scaffold to allow molecular recognition by more than one bioreceptor, operating in many targets associated with biochemical networks responsible for multifactorial disease pathophysiology [6–8].

A breakdown of balance between cell proliferation and apoptosis is a symptom that enhances the inability of damaged cells to be removed by apoptosis. Activating apoptotic pathways in tumour cells is a critical practise for cancer treatment [9]. Apoptosis is triggered by extracellular or intracellular cues, which initiate a signalling cascade with characteristics such as nuclear condensation and DNA fragmentation [10]. Furthermore, the deregulations responsible for cancer genesis and progression involve hundreds of genes or signalling cascades [11]

Caspase, a highly specialized family of cysteine proteases, is known to mediate an important stage of the apoptotic process [12]. Numerous in vitro and in vivo research demonstrated that aberrant caspase activation control is critical to avoiding cancer cell death [13]. Furthermore, other genes, including Bcl-2 and p53, are known to be involved in apoptotic pathways. Overexpression of anti-apoptotic Bcl-2 has been linked to a variety of cancers [14]. The suppression of caspase proteins is thought to be the mechanism by which Bcl-2 prevents apoptosis [15]. p53 has been discovered to be required for cellular senescence caused by mutations in genes involved in mitosis and chromosomal segregation [16]. To maintain genomic integrity, the p53 gene can activate cell cycle checkpoints, DNA repair, and apoptosis (Ahmad et al., 2012). Most malignancies are caused by p53 mutations or deletions [17].

Antiproliferative actions have been documented for cannabinoids such as THC (**I**) and the CB1 allosteric modulator CBD (**II**) [18–22], but no data for other CB1 allosteric modulators such as the 5-chloroindole-2-carboxamide derivatives **III** and **IV**, and their furan congeners **V** and **VI** have been reported (Figure 1). Recently, we reported on the antiproliferative action of 5-chlorobenzofuran-2-carboxamide CB1 allosteric modulators **V** and **VI** for the first time [23]. Based on this, we designed and synthesised a novel series of 5-chlorobenzofuran-2-carboxamide derivatives **VIIa–j** (Figure 1). The newly synthesized compounds were tested for their antiproliferative effects in A549 lung, MCF-7 breast, Panc-1 Pancreatic, and HT-29 colon cancer cell lines. **VIIa–j** compounds showed significant antiproliferative action, the most potent derivative of **VIIa–j** had a GI_{50} value of 1.35 μM against the four examined cell lines, being equipotent to the reference doxorubicin (mean GI_{50} = 1.13 μM) and even more potent than doxorubicin in MCF-7. The compounds examined had a strong apoptotic effect, with significant increases in caspase 3, 8, and 9, as well as Cytochrome C levels. Furthermore, compared to doxorubicin, the investigated compounds triggered a significant rise in Bax levels and a decrease in anti-apoptotic Bcl-2 protein levels in MCF-7 cells [23].
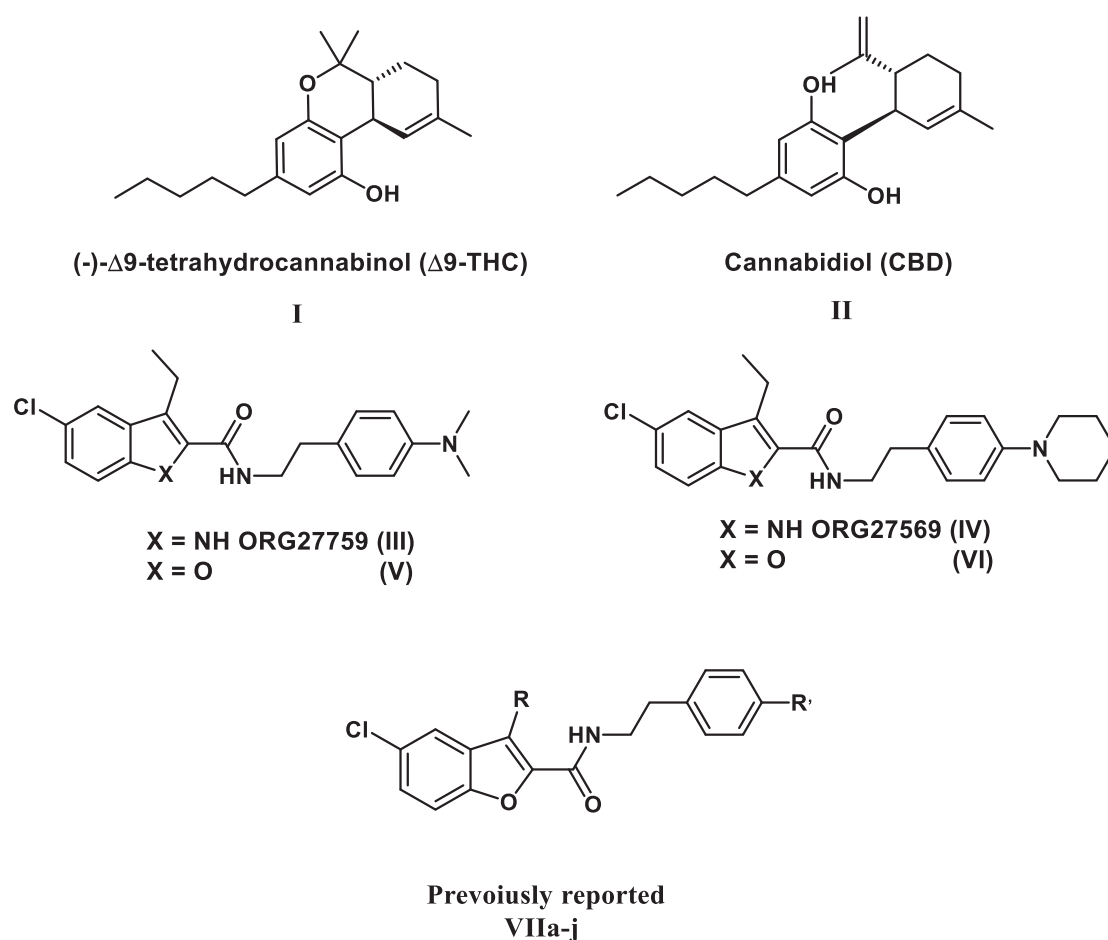
Figure 1. Structures of compounds **I–VI** and **VIIa–j**.

In the present work, the apoptotic antiproliferative actions of our previously reported 5-chlorobenzofuran-2-carboxamide derivatives **VIIa–j** (Figure 1) prompted us to develop and synthesise a novel series of indole-2-carboxamide derivatives **5a–k**, **6a–c**, and **7** (Figure 2). A small library of fifteen new compounds in which the methyl group was kept as a substituent at C3. To investigate the effect of substituent modification, the *para* positions of the phenethyl tails in the newly synthesised compounds were left unsubstituted or substituted with 4-dimethylamino, morpholin-4-yl, piperidin-1-yl, or 2-methylpyrrolidine-1-yl. To investigate the impact of the linker nature on anticancer activity, the phenethyl amino carbonyl moieties were modified to 4 phenylpiperazin-1-yl carbonyl as in compounds **6a–c** or benzyl carbonyl as in compound **7**. The position and number of halogen atoms on the indole moiety's phenyl ring were also investigated. The antiproliferative activity of compounds **5a–k**, **6a–c**, and **7** against a panel of cancer cell lines were investigated. The most active compounds were evaluated for mechanistic activity as multi-targeted kinase inhibitors such as EGFR and CDK2. Furthermore, the compounds were evaluated for apoptotic activity against caspases 3, 8, and 9, as well as Cytochrome C, Bax, Bcl2, and p53.
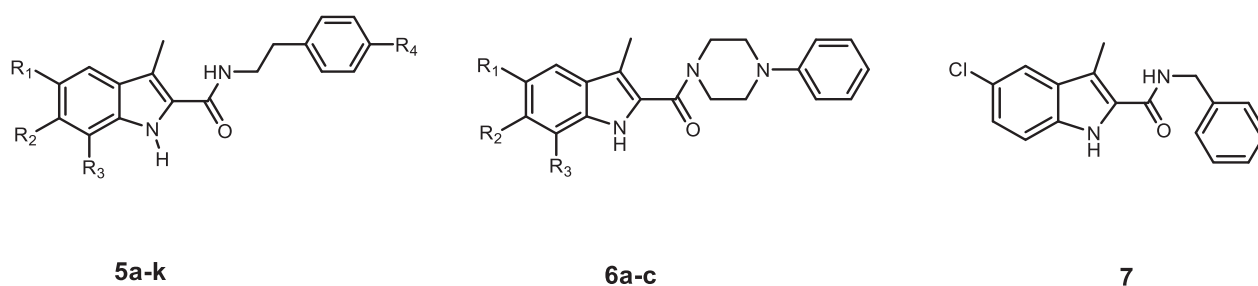
Figure 2. Structures of new compounds **5a–k**, **6a–c**, and **7**.

2. Results and Discussion

2.1. Chemistry

Scheme 1 depicts the synthesis of target compounds **5a–k**, **6a–c**, and **7**. Derivatives of phenyl hydrazine Hydrochloride **1a–d** under Fisher Indole cyclization were reacted with 2-oxopropanoic acid **2** in the presence of PTSA (*p*-toluenesulfonic acid) to provide 3-methylindole-2-carboxylates **3a–d** [24]. The carboxylic acids **4a–d** was obtained by alkaline hydrolysis of the esters **3a–d** [25]. The appropriate amines were coupled with carboxylic acids **4a–d** in the presence of DIPEA in DCM using BOP as a coupling reagent [23], yielding target carboxamides **5a–k**, **6a–c**, and **7**. ^{1}H NMR, ^{13}C NMR, and HRESI-MS were used to identify the newly synthesised derivatives. The ^{1}H NMR spectrum of **5d** revealed the appearance of three singlet signals: one at δ 11.34 ppm (1H) consistent with indole NH, one at δ 7.89 ppm (1H) relating to amidic NH, and one at δ 2.41 ppm (3H) corresponding to the methyl group. The spectrum also indicated the existence of signals corresponding to ethylene protons at δ 3.48 (q, *J* = 7.1 Hz, 2H, NHCH$_2$) and δ 2.77 (t, *J* = 7.4 Hz, 2H, NHCH$_2$), in addition to the morpholine group's distinctive signals at δ 3.70 (t, *J* = 4.8 Hz, 4H, morph-H) and δ 3.02 (t, *J* = 4.8 Hz, 4H, morph-H). HRESI-MS revealed a peak for [M + H]$^+$ at *m/z* 398.1629, which corresponds to the molecular formula $C_{22}H_{25}ClN_3O_2$.

2.2. Evaluation of Biological Activities

2.2.1. In Vitro Anticancer Activity
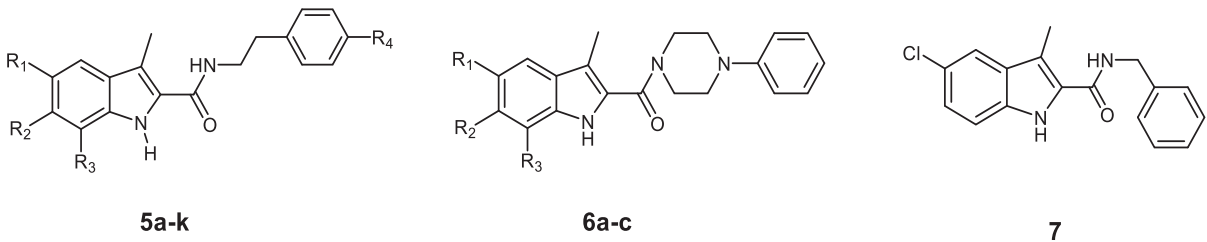
Cell Viability Assay

The MCF-10A (human mammary gland epithelial) cell line was used in the cell viability experiment. Compounds **5a–k**, **6a–c**, and **7** were incubated with MCF-10A cells for 4 days at 50 μM concentration, and the viability of cells was determined using the 3-(4,5-dimethylthiazol-2-yl)-2,5-diphenyltetrazolium bromide (MTT) test. [26]. All compounds had no cytotoxic effects, and the vitality of the cells was more than 83% for most of the compounds examined.

Antiproliferative Activity

Using the MTT assay with doxorubicin as the reference drug, the antiproliferative activities of **5a–k**, **6a–c**, and **7** against four human cancer cell lines, including pancreas cancer cell line (Panc-1), breast cancer cell line (MCF-7), colon cancer cell line (HT-29), and epithelial cancer cell line (A-549) were investigated [27]. Table 1 shows the results of calculating the median inhibitory concentration (IC$_{50}$) for all derivatives. Generally, compounds **5a–k**, **6a–c**, and **7** demonstrated greater antiproliferative activity against the breast cancer cell line (MCF-7) than other tested cancer cell lines, and **5a–k** (which contain the phenethyl moiety in their backbone structure) demonstrated greater potency than **6a–c** and **7**, indicating the importance of the phenethyl moiety for antiproliferative action.

1a, 3a, 4a; R$_1$ = Cl, R$_2$ = R$_3$ = H
1b, 3b, 4b; R$_2$ = Cl, R$_1$ = R$_3$ = H
1c, 3c, 4c; R$_1$ = R$_3$ = Cl, R$_2$ = H
1d, 3d, 4d; R$_1$ = R$_3$ = F, R$_2$ = H

5a; R$_1$ = Cl, R$_2$ = R$_3$ = R$_4$ = H
5b; R$_1$ = Cl, R$_2$ = R$_3$ = H; R$_4$ = N(CH$_3$)$_2$
5c; R$_1$ = Cl, R$_2$ = R$_3$ = H; R$_4$ = piperidin-1-yl
5d; R$_1$ = Cl, R$_2$ = R$_3$ = H; R$_4$ = morpholin-4-yl
5e; R$_1$ = Cl, R$_2$ = R$_3$ = H; R$_4$ = 2-methylpyrrolidin-1-yl
5f; R$_2$ = Cl, R$_1$ = R$_3$ = R$_4$ = H
5g; R$_2$ = Cl, R$_1$ = R$_3$ = H; R$_4$ = piperidin-1-yl
5h; R$_1$ = R$_3$ = Cl, R$_2$ = H; R$_4$ = piperidin-1-yl
5i; R$_1$ = R$_3$ = Cl, R$_2$ = H; R$_4$ = morpholin-4-yl
5j; R$_1$ = R$_3$ = F, R$_2$ = R$_4$ = H
5k; R$_1$ = R$_3$ = F, R$_2$ = H; R$_4$ = piperidin-1-yl

6a; R$_1$ = Cl, R$_2$ = R$_3$ = H
6b; R$_2$ = Cl, R$_1$ = R$_3$ = H
6c; R$_1$ = R$_3$ = F, R$_2$ = H
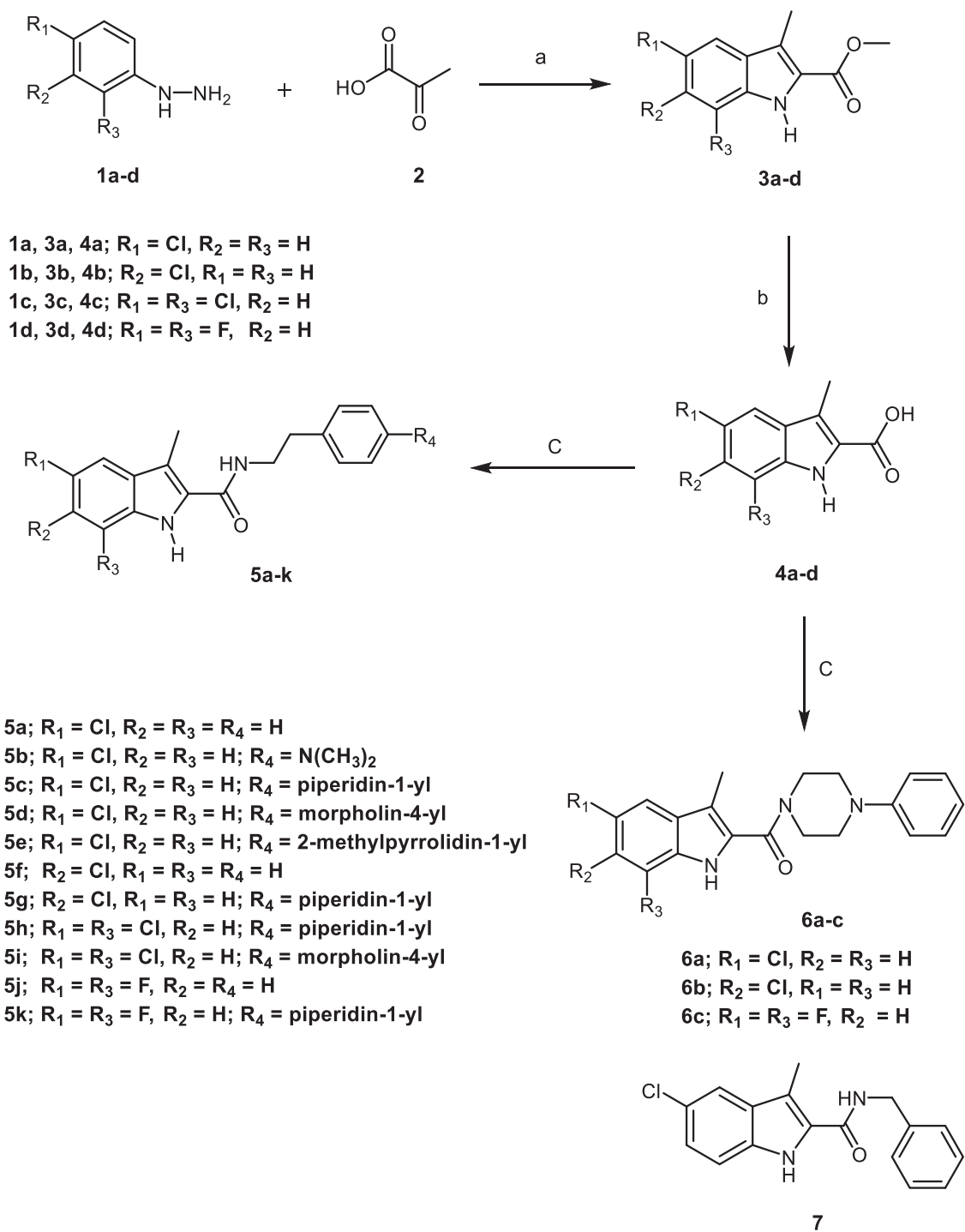
Scheme 1. Synthesis of the target compounds **5a–k**, **6a–c**, and **7**. Reagents and conditions: (a) PTSA, EtOH, reflux, 20 h, 82%; (b) 5% NaOH, EtOH, 40 °C, overnight, 95%; (c) BOP, DIPEA, DCM, rt, overnight, 75–94%.

Table 1. Antiproliferative activity of compounds **5a–k**, **6a–c**, **7**, and **Doxorubicin**.

Compd.	Cell Viability %	Antiproliferative Activity IC$_{50}$ $\pm$ SEM (μM)				
		A-549	**MCF-7**	**Panc-1**	**HT-29**	**Average**
5a	89	3.70 ± 0.30	3.20 ± 0.30	3.90 ± 0.30	3.90 ± 0.30	3.70
5b	87	3.20 ± 0.30	2.90 ± 0.30	3.50 ± 0.30	3.60 ± 0.30	3.30
5c	87	1.70 ± 0.20	1.40 ± 0.20	1.80 ± 0.20	1.80 ± 0.20	1.70
5d	89	1.05 ± 0.10	0.90 ± 0.10	1.10 ± 0.10	1.10 ± 0.10	1.05
5e	93	0.95 ± 0.05	0.80 ± 0.05	1.00 ± 0.20	1.10 ± 0.10	0.95
5f	90	1.90 ± 0.20	1.70 ± 0.20	2.10 ± 0.20	2.10 ± 0.20	1.95
5g	89	4.90 ± 0.50	4.80 ± 0.50	5.20 ± 0.50	5.10 ± 0.50	5.00
5h	87	1.00 ± 0.10	0.90 ± 0.10	1.20 ± 0.10	1.20 ± 0.10	1.10
5i	90	1.55 ± 0.20	1.30 ± 0.10	1.60 ± 0.20	1.65 ± 0.20	1.50
5j	83	1.20 ± 0.10	1.00 ± 0.10	1.30 ± 0.10	1.30 ± 0.10	1.20
5k	87	1.40 ± 0.20	1.20 ± 0.10	1.50 ± 0.20	1.50 ± 0.20	1.40
6a	90	2.90 ± 0.30	2.60 ± 0.20	2.80 ± 0.20	2.90 ± 0.20	2.80
6b	91	2.50 ± 0.20	2.30 ± 0.20	2.65 ± 0.20	2.80 ± 0.20	2.60
6c	89	2.20 ± 0.20	2.10 ± 0.20	2.40 ± 0.20	2.50 ± 0.20	2.30
7	91	4.10 ± 0.40	4.00 ± 0.40	4.40 ± 0.40	4.60 ± 0.40	4.30
Doxorubicin	-	1.20 ± 0.20	0.90 ± 0.10	1.40 ± 0.20	1.00 ± 0.10	1.10

The 2-methylpyrrolidin-4-yl phenethyl derivative **5e** (R_1 = Cl, R_2 = R_3 = H, R_4 = 2-methylpyrrolidin-1-yl) was the most potent derivative, with a GI$_{50}$ value of 0.95 μM against the four cell lines, being more potent than the reference doxorubicin (GI$_{50}$ = 1.10 μM) and also it was more potent than doxorubicin in A-549, MCF-7, and Panc-1 cell lines (IC$_{50}$ = 0.95, 0.80, and 1.00 μM, respectively, while for doxorubicin IC$_{50}$ = 1.20, 0.90, and 1.40 μM, respectively). The unsubstituted derivative **5a** (R_1 = Cl, R_2 = R_3 = R_4 = H) was roughly four-fold less effective than **5e**, with a GI$_{50}$ = 3.70 μM, whereas the 4-dimethylamino derivative **5b** (R_1 = Cl, R_2 = R_3 = H, R_4 = dimethylamino) had a GI$_{50}$ = 3.30 μM.

Compound **5d** (R_1 = Cl, R_2 = R_3 = H, R_4 = morpholin-4-yl) rated second in activity with a GI$_{50}$ of 1.05 μM against the four cancer cell lines, being somewhat less potent (1.1-fold) than **5e** but equipotent to doxorubicin and even more potent than doxorubicin against A-549 and Panc-1 cell lines.

Replacement of the 2-methylpyrrolidin-4-yl moiety in compound **5e** or the morpholin-4-yl in **5d** by 4-piperidin-1-yl in compound **5c** resulted in at least 1.8- and 1.6-fold reduction of the mean GI$_{50}$ values, respectively, signifying the importance of the 2-methylpyrrolidin-4-yl and 4-morpholinophenethyl moieties for the antiproliferative activity.

The 5-substitution impact was also investigated. As indicated in Table 1, compound **5g** (R_2 = Cl, R_1 = R_3 = H, R_4 = 4-piperidin-1-yl) had much lower antiproliferative efficacy (3 times) than compound **5c** (R_1 = Cl, R_2 = R_3 = H, R_4 = 4-piperidin-1-yl). Compound **5f** (R_2 = Cl, R_1 = R_3 = H = R_4 = H) was, on the other hand, more potent (1.9 times) than compound **5a** (R_1 = Cl, R_2 = R_3 = R_4 = H).

Furthermore, we attempt to explore the effect of increasing the number of halogen atoms on antiproliferative activity. For instance, the dihalo derivatives **5h** (R_1 = R_3 = Cl, R_2 = H, R_4 = 4-piperidin-1-yl) and **5k** (R_1 = R_3 = F, R_2 = H, R_4 = 4-piperidin-1-yl) had higher antiproliferative activity than the monohalo derivative **5c** (R_1 = Cl, R_2 = R_3 = H, R_4 = 4-piperidin-1-yl) with GI$_{50}$ values of 1.10 μM and 1.40 μM, respectively, compared to **5c** (GI$_{50}$ = 1.70 μM), indicating the relevance of dihalo atoms for antiproliferative activity and

that the chlorine atom is better tolerated than the fluorine one. The same is true for **5j** ($R_1 = R_3 = F$, $R_2 = R_4 = H$), which has higher potency ($GI_{50} = 1.20$ μM) than **5a** ($R_1 = Cl$, $R_2 = R_3 = R_4 = H$, $GI_{50} = 3.7$ μM) and **5f** ($R_2 = Cl$, $R_1 = R_3 = H = R_4 = H$, $GI_{50} = 1.95$ μM). The situation is somewhat different in the case of 5,7-dichloro derivative **5i** ($R_1 = R_3 = Cl$, $R_2 = H$, $R_4 =$ morpholin-4-yl), which demonstrated lower potency ($GI_{50} = 1.50$ μM) than the 5-chloro derivative **5d** ($R_1 = Cl$, $R_2 = R_3 = R_4 =$ morpholin-4-yl) with a GI_{50} value of 1.05 μM.

Furthermore, among the tested compounds, the 4-benzyl carbonyl derivative **7** and the 4-phenylpiperazin-1-yl carbonyl derivatives **6a–c** had the lowest mean GI_{50} values, implying that the *N*-phenethyl carboxamide architecture is important for antiproliferative action and correlating with previous SAR studies [23].

2.2.2. EGFR Inhibitory Activity

The inhibitory efficacy of **5d**, **5e**, and **5h–k** against EGFR was evaluated using the EGFR-TK assay [28], and the findings are presented in Table 2. The results of this test supplement the findings of the cancer-cell-based investigation. All the tested derivatives (**5d**, **5e**, and **5h–k**) inhibited EGFR significantly, with IC_{50} values ranging from 89 to 137 nM. Based on the findings given, three derivatives **5d**, **5e**, and **5j** were found to be the most potent, with EGFR inhibitory effects ($IC_{50} = 89 \pm 6$ nM and 93 ± 8 nM, and 98 ± 8 nM, respectively) comparable to the positive erlotinib ($IC_{50} = 80 \pm 5$ nM). Again, the 2-methylpyrrolidin-1-yl phenethyl derivative **5e** ($R_1 = Cl$, $R_2 = R_3 = H$, $R_4 =$ 2-methylpyrrolidin-1-yl) and the 4-morpholin-4-yl phenethyl 5d ($R_1 = Cl$, $R_2 = R_3 = H$, $R_4 =$ morpholin-4-yl) were the most potent of all synthesized derivatives, with IC_{50} value of 93 nM and 89 nM being equipotent to the reference erlotinib.

2.2.3. CDK2 Inhibitory Assay

Compounds **5d**, **5e**, and **5h–k** were further examines for their ability to inhibit the CDK2 enzyme [29]. The IC_{50} values are shown in Table 2. In comparison to the reference dinaciclib ($IC_{50} = 20$ nM), all investigated derivatives inhibited CDK2 effectively, with IC_{50} values ranging from 11 nM to 34 nM. Three derivatives, **5e**, **5h**, and **5k**, were shown to be superior to the standard dinaciclib as CDK2 inhibitors, with IC_{50} values of 13, 11, and 19 nM, respectively. Compound **5e**, the most potent antiproliferative derivative, displayed significant anti-CDK2 activity with an IC_{50} value of 13 nM, which is 1.5-fold more active than the reference dinaciclib. On the other hand, compounds **5d**, **5i**, **5j**, and **5k** exhibited significant activity against CDK2 ($IC_{50} = 23$, 27, 34, and 19 μM) comparable to dinaciclib. The findings of the EGFR and CDK2 tests revealed that the examined compounds exhibit significant antiproliferative activity and are efficient at suppressing both CDK2 and EGFR.

2.2.4. Apoptosis Assay

A previous report has shown that **CBD** (**2**), a CB1 allosteric modulator, can trigger apoptosis [30]. Therefore, to assess the proapoptotic potential of our target compounds, we evaluated the most active compounds **5d**, **5e**, and **5h** for their capacity to initiate the apoptosis cascade in the breast cancer (MCF-7) cell line.

Activation of Proteolytic Caspases Cascade

Caspases play a crucial role in the initiation and completion of the apoptotic process [31]. Caspase-3 is a crucial caspase that cleaves a variety of proteins in cells, causing apoptosis [32]. The effects of compounds **5d**, **5e**, and **5h** on caspase 3 were assessed and compared to doxorubicin, which was used as a control [33]. The results showed that when compared to control cells, the tested compounds increased the level of active caspase 3 by 8–10 folds and that **5d**, **5e**, and **5h** induce outstanding overexpression of caspase-3 protein level (570.00 ± 5.00, 635.50 ± 5.50 and 537.50 ± 5.00 pg/mL, respectively) compared to doxorubicin (503.50 ± 4.50 pg/mL). In comparison to the control untreated cells, the most active antiproliferative derivative **5e** increases caspase 3 levels by 9.70 times.

Table 2. Effects of compounds **5d**, **5e**, **5h–k**, and **Erlotinib** on EGFR and Dinaciclib.
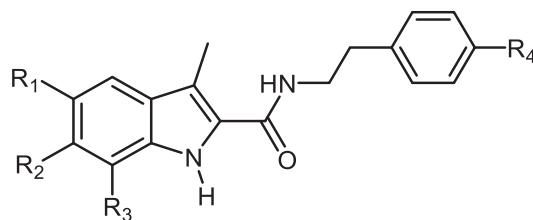
5d, 5e, and **5h-k**

Compd.	R_1	R_2	R_3	R_4	EGFR Inhibition $IC_{50} \pm SEM$ (nM)	CDK2 Inhibition $IC_{50} \pm SEM$ (nM)
5d	Cl	H	H	N-morpholine	89 ± 6	23 ± 2
5e	Cl	H	H	2-methylpyrrolidine	93 ± 8	13 ± 1
5h	Cl	H	Cl	N-piperidine	118 ± 10	11 ± 1
5i	Cl	H	Cl	N-morpholine	137 ± 12	27 ± 3
5j	F	H	F	H	98 ± 8	34 ± 3
5k	F	H	F	N-piperidine	129 ± 11	19 ± 2
Erlotinib	–	–	–	–	80 ± 5	ND
Dinaciclib	–	–	–	–	ND	20 ± 2

The impact of compounds **5d**, **5e**, and **5h** on caspases 8 and 9 was also investigated to highlight the involvement of the intrinsic and extrinsic apoptotic pathways in the antiproliferative actions of these compounds, Table 3. When compared to control cells, compound **5e** increased caspase 8 and 9 levels by 10.90 and 18.15 folds, respectively, while compound **5d** increased caspase 8 and 9 levels by 9.70 and 17.80 folds, respectively, indicating activation of both intrinsic and extrinsic pathways with a stronger effect on the intrinsic pathway because caspase 9 levels were higher [34].

Table 3. Effects of compounds **5d**, **5e**, **5h** and doxorubicin on active Caspases 3, 8, 9 and Cytochrome C in MCF-7 breast cancer cell line.

Compound Number	Caspase-3 Conc (pg/mL)	Caspase-3 Fold Change	Caspase-8 Conc (ng/mL)	Caspase-8 Fold Change	Caspase-9 Conc (ng/mL)	Caspase-9 Fold Change	Cytochrome C Conc (ng/mL)	Cytochrome C Fold Change
5d	570.00 ± 5.00	8.70	1.94	9.70	16.90	17.80	0.70	14
5e	635.50 ± 5.50	9.70	2.17	10.90	17.25	18.15	0.80	16
5h	537.50 ± 5.00	8.20	1.88	9.50	16.65	17.50	0.65	13
Doxorubicin	503.50 ± 4.50	7.70	1.80	9.00	16.25	17.00	0.60	12
Control	65.50	1	0.20	1	0.95	1	0.05	1

Cytochrome C Assay

The quantity of cytochrome C within the cell is important for activating caspases and commencing the intrinsic apoptosis process [35]. Table 3 shows the findings of testing indole-2-carboxamide derivatives **5d**, **5e**, and **5h** as Cytochrome C activators in the MCF-7 human breast cancer cell line. Compounds **5d**, **5e**, and **5h** increased Cytochrome C levels in the MCF-7 human breast cancer cell line by 14, 16, and 13 times, respectively, compared to untreated control cells. The findings add to the evidence that apoptosis can be attributed to Cytochrome C overexpression and activation of the intrinsic apoptotic pathway triggered by the investigated compounds.

Bax and Bcl-2 Levels Assay

The most potent caspase activators, **5d** and **5e**, were investigated further for their influence on Bax and Bacl-2 levels in a breast cancer cell line (MCF-7) using doxorubicin as a control [36]. Table 4 shows that **5d** and **5e** caused a significant increase in Bax levels when compared to doxorubicin. Compound **5e** demonstrated a comparable induction of Bax (296.50 pg/mL) compared to doxorubicin (276 pg/mL) with a 36-fold increase over control untreated breast cancer cells, followed by compound 5d (290 pg/mL and 35-fold rise). Finally, compound **5e** reduced the anti-apoptotic Bcl-2 protein levels to 0.87 ng/mL in MCF-7 cells, followed by compound **5d** (0.89 ng/mL) in comparison to doxorubicin (0.98 ng/mL).

Table 4. Effects of compounds **5d**, **5e**, and doxorubicin on Bax and Bcl-2.

Compd. No.	Bax		Bcl-2	
	Conc (pg/mL)	Fold Change	Conc (ng/mL)	Fold Change
5d	289.70 ± 2.50	35	0.89	5.70
5e	296.50 ± 2.50	36	0.87	5.90
Doxorubicin	275.80 ± 2.50	33	0.98	5.20
Cont.	8.25	1	5.10	1.00

Effect of Compounds **5d** and **5e** on p53 Transcription in MCF-7

p53 is a unique protein that participates in several physiological processes such as cell metabolism [37], stem cell maintenance [38], and cell adhesion [39]. Because p53 is frequently inactivated in cancer cells, the cells are unable to undergo apoptosis [40,41]. Similarly, activating, or stabilizing p53 aids cancer cells in normalizing p53-controlled physiological processes and increasing apoptotic activity [42]. The effects of **5d** and **5e** on p53 transcription were evaluated and compared to doxorubicin as a control [43], Table 5. The results revealed an increase of at least 27-folds in p53 level compared to the test cells and that the p53 protein level of **5d** and **5e** was significantly inductive (1375 and 1435 pg/mL, respectively) in relation to doxorubicin (1265 pg/mL).

Table 5. Effects of compounds **5d**, **5e**, and doxorubicin on p53.

Compd. No.	p53	
	Conc (pg/mL)	Fold Change
5d	1375 ± 15	27
5e	1435 ± 15	28
Doxorubicin	1265 ± 10	25
Cont.	51.50	1

2.3. Docking Study

Interestingly, running docking simulations of compounds **5d** and **5e** within EGFR active site revealed docking scores (S; −6.90 and −6.79 kcal/mol; respectively), so much close to that of co-crystallized ligand, erlotinib (−7.30 kcal/mol), which co-insides with

what obtained in-vitro against EGFR enzyme (as shown in Table 2). Moreover, visual inspection of the best docking poses of compounds **5d** and **5e** showed their close distance to key amino acids lining EGFR active site. Additionally, compounds **5d** and **5e** showed a number of H-bonding and pi–H interactions with LEU 694 and THR 766 amino acid residues (as listed in Table 6 and shown in Figure 3).

Table 6. MD of compounds **5d** and **5e** within EGFR and CDK2 active sites.

Compd.	EFGR (PDB ID: 1M17)					CDK2 (PDB ID: 1PYE)				
			Binding Interactions					Binding Interactions		
	S [a]	RMSD (Å)	a.a. Residue	Type	Distance (Å)	S	RMSD (Å)	a.a. Residue	Type	Distance (Å)
5d	−6.90	1.49	THR 766	H-acceptor	2.91	−6.03	1.77	GLN 131	H-donor	3.60
			LEU 694	pi-H	3.99					
5e	−6.79	1.51	LEU 694	pi-H	3.70	−6.99	1.68	LYS 33	pi-cation	4.65
Ref	−7.3 [b]	1.28	GLN 767	H-donor	3.15	−5.89 [c]	1.84	GLU 81	H-donor	3.05
			MET 769	H-acceptor	2.70			LEU 83	H-acceptor	3.07

[a] S: docking score (kcal/mol); [b] Ref: co-crystallized ligand (Erlotinib); [c] Ref: co-crystallized ligand (Dinaciclib).

Figure 3. Schematic 2D representation of best docking poses of **5d** (**left**) and **5e** (**right**) within EGFR (PDB ID: 1M17) active site showing pi-H (green-dotted line) and H-acceptor interactions (green arrow).

Both compounds **5d** and **5e** showed a common settling profile within EGFR active represented by U-shaped bending of the whole molecule, so its indole ring interacts with LEU 694 (as shown in Figure 3). On the other hand, compound **5d** showed additional H-acceptor bonding with THR 766 that resulted in its better docking score over its congener, compound **5e**.

Additionally, and as shown in Table 6, MDs of compound **5e** within the CDK2 active site revealed its better docking score (S = −6.99 kcal/mol) over its congener **5d** (S = −6.03 kcal/mol), although its inability to have strong H-bonding with amino acid residues lining active site, its close proximity to key amino acid residues (revealed by its proximity contour as shown in Figure 4) could explain its better scoring over **5d**.
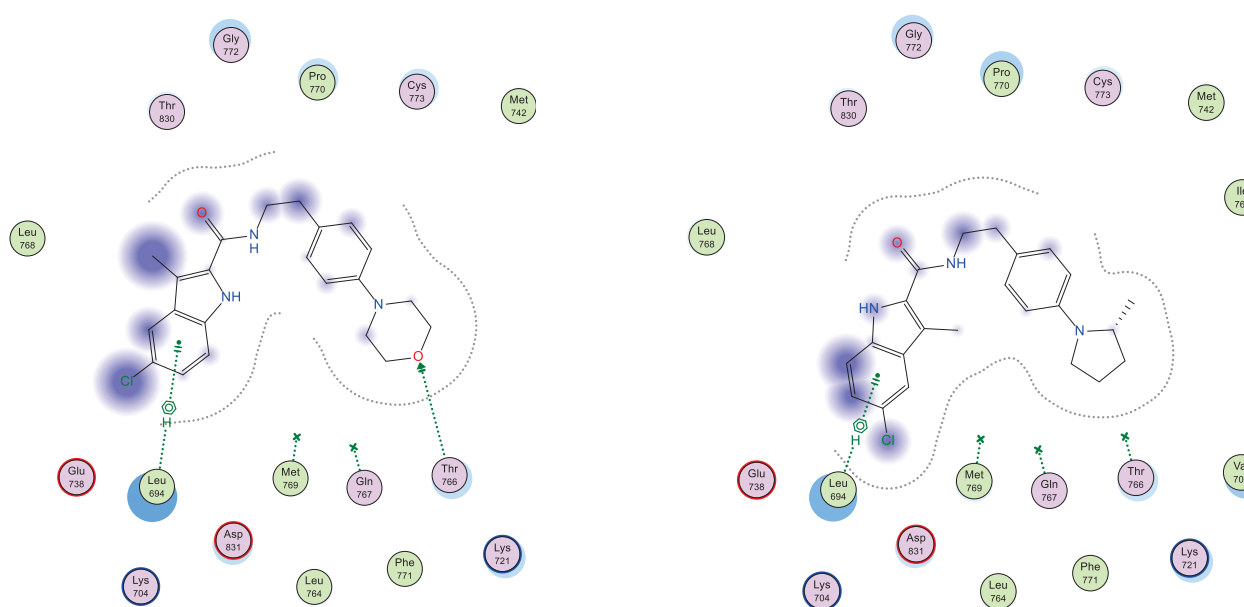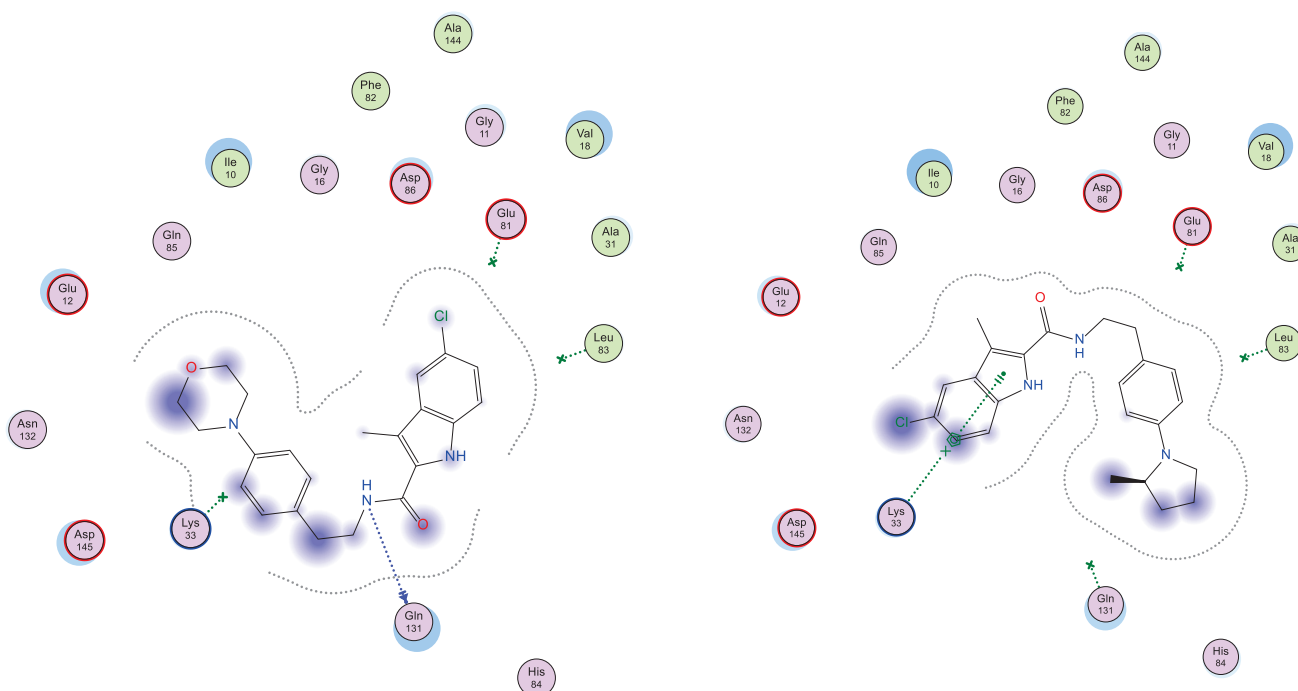
Figure 4. Schematic 2D representation of best docking poses of **5d** (**left**) and **5e** (**right**) within CDK2 (PDB ID: 1PYE) active site showing pi-cation (green-dotted line) and H-donor interactions (blue arrow).

3. Materials and Methods

3.1. Chemistry

3-Methylindole-2-carboxylates **3a–d** [24], carboxylic acids **4a–d** [25], and carboxamides **5a–k**, **6a–c**, and **7** [23] were synthesized according to previously reported procedures.

3.1.1. 5-Chloro-3-methyl-N-phenethyl-1H-indole-2-carboxamide (**5a**)

Yield % 91, m.p 182–184 °C, ^{1}H NMR (400 MHz, CDCl$_3$) δ 9.21 (s, 1H, indole NH), 7.53 (d, *J* = 2.2 Hz, 1H, Ar-H), 7.39–7.17 (m, 7H, Ar-H), 5.97 (s, 1H, amide NH), 3.81 (q, *J* = 6.4 Hz, 2H, NHCH$_2$), 2.97 (t, *J* = 6.8 Hz, 2H, NHCH$_2$CH$_2$), 2.26 (s, 3H, CH$_3$). ^{13}C NMR (101 MHz, CDCl$_3$) δ 162.10 (C=O), 138.50, 133.32, 128.85, 128.81, 128.53, 126.84, 125.53, 125.00, 119.38, 112.79, 110.80, 40.83, 35.51, 9.88. HRESI-MS *m/z* calcd for [M + H]$^+$ C$_{18}$H$_{18}$ClN$_2$O: 313.1102, found: 313.1104.

3.1.2. 5-Chloro-N-(4-(dimethylamino)phenethyl)-3-methyl-1H-indole-2-carboxamide (**5b**)

Yield % 89, m.p 202–204 °C. ^{1}H NMR (400 MHz, DMSO-d_6) δ 11.34 (s, 1H, indole NH), 7.87 (t, *J* = 5.6 Hz, 1H, amide NH), 7.62 (d, *J* = 2.0 Hz, 1H, Ar-H), 7.37 (d, *J* = 8.6 Hz, 1H, Ar-H), 7.16 (dd, *J* = 8.7, 2.1 Hz, 1H, Ar-H), 7.06 (d, *J* = 8.6 Hz, 2H, Ar-H), 6.66 (d, *J* = 8.7 Hz, 2H, Ar-H), 3.46 (q, *J* = 6.7 Hz, 2H, NHCH$_2$), 2.82 (s, 6H, N(CH$_3$)$_2$), 2.74 (t, *J* = 6.6 Hz, 2H, NHCH$_2$CH$_2$), 2.41 (s, 3H, CH$_3$). ^{13}C NMR (101 MHz, DMSO-d_6) δ 162.01 (C=O), 149.54, 134.07, 129.94, 129.59, 129.55, 127.31, 124.06, 123.97, 119.35, 113.92, 113.13, 112.93, 41.47, 40.79, 34.69, 9.98. HRESI-MS *m/z* calcd for [M + H]$^+$ C$_{20}$H$_{23}$ClN$_3$O: 356.1524, found: 356.1522.

3.1.3. 5-Chloro-3-methyl-N-(4-(piperidin-1-yl)phenethyl)-1H-indole-2-carboxamide (**5c**)

Yield % 92, m.p 216–218 °C, ^{1}H NMR (400 MHz, CDCl$_3$) δ 9.17 (s, 1H, indole NH), 7.53 (s, 1H, Ar-H), 7.29 (d, *J* = 8.6 Hz, 1H, Ar-H), 7.20 (dd, *J* = 8.6, 0.7 Hz, 1H, Ar-H), 7.13 (d, *J* = 8.6 Hz, 2H, Ar-H), 6.92 (d, *J* = 8.6 Hz, 2H, Ar-H), 5.97 (s, 1H, amide NH), 3.76 (q, *J* = 6.6 Hz, 2H, NHCH$_2$), 3.17–3.09 (m, 4H, piperidin-H), 2.87 (t, *J* = 6.7 Hz, 2H, NHCH$_2$CH$_2$), 2.27 (s, 3H, CH$_3$), 1.74–168 (m, 4H, piperidin-H), 1.63–1.53 (m, 2H, piperidin-H). ^{13}C NMR (101

MHz, CDCl$_3$) δ 162.03 (C=O), 151.21, 133.26, 129.74, 129.37, 128.77, 128.68, 125.48, 124.90, 119.37, 116.95, 112.75, 110.71, 50.82, 40.92, 34.48, 25.79, 24.25, 9.94. HRESI-MS *m/z* calcd for [M + H]$^+$ C$_{23}$H$_{27}$ClN$_3$O: 396.1837, found: 396.1837.

3.1.4. 5-Chloro-3-methyl-N-(4-morpholinophenethyl)-1H-indole-2-carboxamide (**5d**)

Yield % 91, m.p 210–212 °C. ^{1}H NMR (400 MHz, DMSO-*d*$_6$) δ 11.34 (s, 1H, indole NH), 7.89 (t, *J* = 5.6 Hz, 1H, amide NH), 7.62 (s, 1H, Ar-H), 7.38 (d, *J* = 8.6 Hz, 1H, Ar-H), 7.21–7.08 (m, 3H, Ar-H), 6.85 (d, *J* = 8.3 Hz, 2H, Ar-H), 3.70 (t, *J* = 4.8 Hz, 4H, morph-H), 3.48 (q, *J* = 7.1 Hz, 2H, NHCH$_2$), 3.02 (t, *J* = 4.8 Hz, 4H, morph-H), 2.77 (t, *J* = 7.4 Hz, 2H, NHCH$_2$), 2.41 (s, 3H, CH$_3$). ^{13}C NMR (101 MHz, DMSO-*d*$_6$) δ 162.05 (C=O), 149.99, 134.08, 130.44, 129.91, 129.62, 129.59, 124.08, 124.00, 119.36, 115.72, 113.94, 112.98, 66.57, 49.17, 41.29, 34.71, 9.98. HRESI-MS *m/z* calcd for [M + H]$^+$ C$_{22}$H$_{25}$ClN$_3$O$_2$: 398.1630, found: 398.1629.

3.1.5. 5-Chloro-3-methyl-N-(4-(2-methylpyrrolidin-1-yl)phenethyl)-1H-indole-2 -carboxamide (**5e**)

Yield % 85, m.p 186–188 °C. ^{1}H NMR (400 MHz, CDCl$_3$) δ 9.67 (s, 1H, indole NH), 7.53 (d, *J* = 2.0 Hz, 1H, Ar-H), 7.32 (d, *J* = 8.6 Hz, 1H, Ar-H), 7.20 (dd, *J* = 8.7, 2.0 Hz, 1H, Ar-H), 7.10 (d, *J* = 8.5 Hz, 2H, Ar-H), 6.57 (d, *J* = 8.5 Hz, 2H, Ar-H), 6.07 (t, *J* = 5.5 Hz, 1H, amide NH), 3.91–3.71 (m, 3H, pyrrolidin-H, NHCH$_2$), 3.47–3.37 (m, 1H, pyrrolidin-H), 3.18–3.12 (m, 1H, pyrrolidin-H), 2.87 (t, *J* = 6.7 Hz, 2H, NHCH$_2$CH$_2$), 2.31 (s, 3H, CH$_3$), 2.15–1.94 (m, 3H, pyrrolidin-H), 1.73–1.70 (m, 1H, pyrrolidin-H), 1.17 (d, *J* = 6.2 Hz, 3H, CHCH$_3$). ^{13}C NMR (101 MHz, CDCl$_3$) δ 162.23 (C=O), 146.18, 133.48, 129.68, 129.54, 128.78, 125.34, 124.78, 124.45, 119.29, 112.92, 112.16, 110.77, 53.67, 48.26, 41.25, 34.42, 33.09, 23.28, 19.29, 10.01. HRESI-MS *m/z* calcd for [M + H]$^+$ C$_{23}$H$_{27}$ClN$_3$O: 396.1837, found: 396.1832.

3.1.6. 6-Chloro-3-methyl-N-phenethyl-1H-indole-2-carboxamide (**5f**)

Yield % 80, m.p 170–172 °C, ^{1}H NMR (400 MHz, CDCl$_3$) δ 9.67 (s, 1H, indole NH), 7.46 (d, *J* = 8.6 Hz, 1H, Ar-H), 7.42–7.22 (m, 6H, Ar-H), 7.07 (dd, *J* = 8.6, 1.9 Hz, 1H, Ar-H), 6.00 (s, 1H, amide NH), 3.82 (q, *J* = 6.4 Hz, 2H, NHCH$_2$), 2.98 (t, *J* = 6.7 Hz, 2H, NHCH$_2$CH$_2$), 2.28 (s, 3H, CH$_3$). ^{13}C NMR (101 MHz, CDCl$_3$) δ 162.39 (C=O), 138.53, 135.49, 130.42, 128.84, 128.83, 127.88, 127.20, 126.81, 120.92, 120.67, 111.61, 40.89, 35.53, 9.94. HRESI-MS *m/z* calcd for [M + H]$^+$ C$_{18}$H$_{18}$ClN$_2$O: 313.1102, found: 313.1101.

3.1.7. 6-Chloro-3-methyl-N-(4-(piperidin-1-yl)phenethyl)-1H-indole-2-carboxamide (**5g**)

Yield % 75, m.p 218–220 °C, ^{1}H NMR (400 MHz, CDCl$_3$) δ 9.19 (s, 1H, indole NH), 7.47 (d, *J* = 8.6 Hz, 1H, Ar-H), 7.37 (d, *J* = 1.8 Hz, 1H, Ar-H), 7.13 (d, *J* = 8.6 Hz, 2H, Ar-H), 7.08 (dd, *J* = 8.6, 1.8 Hz, 1H, Ar-H), 6.92 (d, *J* = 8.6 Hz, 2H, Ar-H), 5.97 (s, 1H, amide NH), 3.76 (q, *J* = 6.6 Hz, 2H, NHCH$_2$), 3.17–3.09 (m, 4H, piperidin-H), 2.88 (t, *J* = 6.6 Hz, 2H, NHCH$_2$CH$_2$), 2.29 (s, 3H, CH$_3$), 1.76–1.66 (m, 4H, piperidin-H), 1.64–1.54 (m, 2H, piperidin-H). ^{13}C NMR (101 MHz, CDCl$_3$) δ 162.12 (C=O), 151.17, 135.22, 130.41, 129.39, 128.87, 128.04, 127.32, 120.95, 120.70, 116.97, 111.44, 111.39, 50.86, 40.93, 34.51, 25.79, 24.24, 9.97. HRESI-MS *m/z* calcd for [M + H]$^+$ C$_{23}$H$_{27}$ClN$_3$O: 396.1837, found: 396.1837.

3.1.8. 5,7-Dichloro-3-methyl-N-(4-(piperidin-1-yl)phenethyl)-1H-indole-2 -carboxamide (**5h**)

Yield % 85, m.p 178–180 °C, ^{1}H NMR (400 MHz, DMSO-*d*$_6$) δ 11.43 (s, 1H, indole NH), 8.36 (t, *J* = 5.6 Hz, 1H, amide NH), 7.66 (d, *J* = 1.8 Hz, 1H, Ar-H), 7.36 (d, *J* = 1.9 Hz, 1H, Ar-H), 7.07 (d, *J* = 8.0 Hz, 2H, Ar-H), 6.83 (d, *J* = 8.3 Hz, 2H, Ar-H), 3.45 (q, *J* = 7.3 Hz, 2H, NHCH$_2$), 3.03 (t, *J* = 5.4 Hz, 4H, piperidin-H), 2.75 (t, *J* = 7.5 Hz, 2H, NHCH$_2$CH$_2$), 2.46 (s, 3H, CH$_3$), 1.63–1.43 (m, 6H, piperidin-H). ^{13}C NMR (101 MHz, DMSO-*d*$_6$) δ 161.24 (C=O), 150.70, 131.41, 130.65, 130.24, 129.68, 129.53, 124.16, 123.24, 118.73, 117.38, 116.60, 116.52, 50.33, 41.27, 34.69, 25.76, 24.34, 10.19. HRESI-MS *m/z* calcd for [M + H]$^+$ C$_{23}$H$_{26}$Cl$_2$N$_3$O: 430.1447, found: 430.1448.

3.1.9. 5,7-Dichloro-3-methyl-N-(4-morpholinophenethyl)-1H-indole-2-carboxamide (**5i**)

Yield % 84, m. p 185–187 °C. ^{1}H NMR (400 MHz, CDCl$_3$) δ 9.25 (s, 1H, indole NH), 7.43 (d, *J* = 1.7 Hz, 1H, Ar-H), 7.25 (d, *J* = 1.8 Hz, 1H, Ar-H), 7.15 (d, *J* = 8.5 Hz, 2H, Ar-H), 6.88 (d, *J* = 8.7 Hz, 2H, Ar-H), 6.02 (s, 1H, amide NH), 3.90–3.83 (m, 4H, morph-H), 3.77 (q, *J* = 6.6 Hz, 2H, NHCH$_2$), 3.17–3.09 (m, 4H, morph-H), 2.89 (t, *J* = 6.7 Hz, 2H, NHCH$_2$CH$_2$), 2.28 (s, 3H, CH$_3$). ^{13}C NMR (101 MHz, CDCl$_3$) δ 161.59 (C=O), 150.23, 130.98, 130.33, 129.69, 129.53, 129.33, 125.41, 123.94, 118.19, 117.65, 116.11, 111.86, 66.86, 49.47, 41.01, 34.48, 10.12. HRESI-MS *m/z* calcd for [M + H]$^+$ C$_{22}$H$_{24}$Cl$_2$N$_3$O$_2$: 432.1240, found: 432.1240.

3.1.10. 5,7-Difluoro-3-methyl-N-phenethyl-1H-indole-2-carboxamide (**5j**)

Yield % 82, m.p 198–200 °C, ^{1}H NMR (400 MHz, DMSO-*d$_6$*) δ 11.95 (s, 1H, indole NH), 8.45 (t, *J* = 5.6 Hz, 1H, amide NH), 7.69–7.50 (m, 6H, Ar-H), 7.42 (t, *J* = 11.6 Hz, 1H, Ar-H), 3.86 (q, *J* = 7.8 Hz, 2H, NHCH$_2$), 3.20 (t, *J* = 7.4 Hz, 2H, NHCH$_2$CH$_2$), 2.75 (s, 3H, CH$_3$). ^{13}C NMR (101 MHz, DMSO-*d$_6$*) δ 161.91 (C=O), 140.15, 130.98, 129.46, 129.17, 126.95, 120.88, 116.06, 101.43, 101.15, 99.81, 99.61, 99.50, 41.29, 35.83, 10.49. HRESI-MS *m/z* calcd for [M + H]$^+$ C$_{18}$H$_{17}$F$_2$N$_2$O: 315.1303, found: 315.1305.

3.1.11. 5,7-Difluoro-3-methyl-N-(4-(piperidin-1-yl)phenethyl)-1H-indole-2 -carboxamide (**5k**)

Yield % 88, m.p 192–194 °C, ^{1}H NMR (400 MHz, DMSO-*d$_6$*) δ 11.61 (s, 1H, indole NH), 8.07 (s, 1H, amide NH), 7.25 (dd, *J* = 9.3, 2.2 Hz, 1H, Ar-H), 7.13–7.04 (m, 3H, Ar-H), 6.84 (d, *J* = 8.6 Hz, 2H, Ar-H), 3.46 (q, *J* = 7.2 Hz, 2H, NHCH$_2$), 3.05 (t, *J* = 5.4 Hz, 4H, piperidin-H), 2.74 (t, *J* = 7.4 Hz, 2H, NHCH$_2$CH$_2$), 2.42 (s, 3H, CH$_3$), 1.64–1.55 (m, 4H, piperidin-H), 1.51–1.48 (m, 2H, piperidin-H). ^{13}C NMR (101 MHz, DMSO-*d$_6$*) δ 161.50 (C=O), 157.34, 155.00, 150.69, 147.63, 131.03, 129.65, 120.65, 116.52, 115.77, 101.08, 99.44, 99.24, 50.33, 41.24, 34.64, 25.76, 24.35, 10.17. HRESI-MS *m/z* calcd for [M + H]$^+$ C$_{23}$H$_{26}$F$_2$N$_3$O: 398.2038, found: 398.2038.

3.1.12. (5-Chloro-3-methyl-1H-indol-2-yl)(4-phenylpiperazin-1-yl)methanone (**6a**)

Yield % 85, m.p 165–167 °C, ^{1}H NMR (400 MHz, CDCl$_3$) δ 9.0 (s, 1H, indole NH), 8.25 (d, *J* = 8.8 Hz, 1H, Ar-H), 7.56 (d, *J* = 2.0 Hz, 1H, Ar-H), 7.40 (dd, *J* = 8.7, 2.0 Hz, 1H, Ar-H), 7.35–7.21 (m, 5H, Ar-H), 3.76 (t, *J* = 7.6 Hz, 4H, piperazin-H), 3.00 (t, *J* = 8.0 Hz, 4H, piperazin-H), 2.65 (s, 3H, CH$_3$). ^{13}C NMR (101 MHz, CDCl$_3$) δ 164.41 (C=O), 150.78, 134.46, 129.28, 128.23, 127.44, 125.47, 124.14, 120.80, 119.61, 118.01, 116.80, 112.67, 49.87, 18.26, 14.76. HRESI-MS *m/z* calcd for [M + H]$^+$ C$_{20}$H$_{21}$ClN$_3$O: 354.1368, found: 354.1367.

3.1.13. (6-Chloro-3-methyl-1H-indol-2-yl)(4-phenylpiperazin-1-yl)methanone (**6b**)

Yield % 80, m.p 180–182 °C, ^{1}H NMR (400 MHz, CDCl$_3$) δ 9.68 (s, 1H, indole NH), 7.47 (d, *J* = 8.5 Hz, 1H, Ar-H), 7.37–7.25 (m, 2H, Ar-H), 7.08 (d, *J* = 8.0 Hz, 1H, Ar-H), 6.95–6.92 (m, 3H, Ar-H), 3.88 (t, *J* = 5.1 Hz, 4H, piperazin-H), 3.22 (t, *J* = 5.3 Hz, 4H, piperazin-H), 2.38 (s, 3H, CH$_3$). ^{13}C NMR (101 MHz, CDCl$_3$) δ 164.69 (C=O), 150.82, 136.51, 129.76, 129.29, 127.52, 126.64, 120.73, 120.67, 120.56, 116.78, 112.10, 111.53, 49.88, 10.18. HRESI-MS *m/z* calcd for [M + H]$^+$ C$_{20}$H$_{21}$ClN$_3$O: 354.1368, found: 354.1368.

3.1.14. (5,7-Difluoro-3-methyl-1H-indol-2-yl)(4-phenylpiperazin-1-yl)methanone (**6c**)

Yield % 82, m.p 171–173 °C, ^{1}H NMR (400 MHz, CDCl$_3$) δ 9.61 (s, 1H, indole NH), 7.29 (t, *J* = 7.9 Hz, 2H, Ar-H), 7.13–6.66 (m, 5H, Ar-H), 3.89 (t, *J* = 5.8 Hz, 4H, piperazin-H), 3.23 (t, *J* = 5.7 Hz, 4H, piperazin-H), 2.34 (s, 3H, CH$_3$). ^{13}C NMR (101 MHz, CDCl$_3$) δ 163.99 (C=O), 150.78, 129.34, 129.28, 120.79, 116.82, 100.35, 100.31, 100.12, 100.08, 99.28, 99.08, 98.78, 49.94, 10.12. HRESI-MS *m/z* calcd for [M + H]$^+$ C$_{20}$H$_{20}$F$_2$N$_3$O: 356.1569, found: 356.1568.

3.1.15. N-Benzyl-5-chloro-3-methyl-1H-indole-2-carboxamide (**7**)

Yield % 84, m.p 203–205 °C, ^{1}H NMR (400 MHz, DMSO-*d$_6$*) δ 11.38 (s, 1H, indole NH), 8.43 (t, *J* = 5.9 Hz, 1H, amide NH), 7.64 (d, *J* = 2.1 Hz, 1H, Ar-H), 7.41–7.20 (m, 6H,

Ar-H), 7.17 (dd, *J* = 8.7, 2.1 Hz, 1H, Ar-H), 4.50 (d, *J* = 5.9 Hz, 2H, NHCH$_2$), 2.48 (s, 3H, CH$_3$). ^{13}C NMR (101 MHz, DMSO-d_6) δ 162.16 (C=O), 139.83, 134.16, 129.66, 129.56, 128.76, 127.82, 127.28, 124.10, 119.41, 113.96, 113.46, 42.92, 10.07. HRESI-MS *m/z* calcd for [M + H]$^+$ C$_{17}$H$_{16}$ClN$_2$O: 299.0946, found: 299.0946.

3.2. Biology

3.2.1. In Vitro Anticancer Activity

Cell Viability Assay

The MCF-10A (human mammary gland epithelial) cell line was used in the cell viability experiment. Compounds **5a–k**, **6a–c**, and **7** were incubated with MCF-10A cells for 4 days at 50 μM concentration, and the viability of cells was determined using the 3-(4,5-dimethylthiazol-2-yl)-2,5-diphenyltetrazolium bromide (MTT) test [26].

Antiproliferative Activity

Using the MTT assay with doxorubicin as the reference drug, the antiproliferative activities of **5a–k**, **6a–c**, and **7** against four human cancer cell lines, including pancreas cancer cell line (Panc-1), breast cancer cell line (MCF-7), colon cancer cell line (HT-29), and epithelial cancer cell line (A-549) were investigated [27].

3.2.2. EGFR Inhibitory Activity

The inhibitory efficacy of **5d**, **5e**, and **5h–k** against EGFR was evaluated using the EGFR-TK assay [28].

3.2.3. CDK2 Inhibitory Assay

Compounds **5d**, **5e**, and **5h–k** were further examined for their ability to inhibit the CDK2 enzyme [29].

3.2.4. Apoptosis Assay

Activation of Proteolytic Caspases Cascade

The effects of compounds **5d**, **5e**, and **5h** on caspases 3, 8, and 9 were assessed and compared to doxorubicin, which was used as a control [33].

Cytochrome C Assay

Indole-2-carboxamide derivatives **5d**, **5e**, and **5h** were evaluated as Cytochrome C activators in the MCF-7 human breast cancer cell line [35].

Bax and Bcl-2 Levels Assay

The most potent caspase activators, **5d** and **5e**, were investigated for their influence on Bax and Bacl-2 levels in a breast cancer cell line (MCF-7) using doxorubicin as a control [36].

Effect of Compounds **5d** and **5e** on p53 Transcription in MCF-7

The effects of **5d** and **5e** on p53 transcription were evaluated and compared to doxorubicin as a control [43].

4. Conclusions

A new series of EGFR/CDK2 dual inhibitors containing indole-2-carboxamides has been reported. A total of fifteen target compounds were synthesized and evaluated in vitro against four cancer cell lines as well as these two kinases. The majority of the compounds examined had promising antiproliferative activity. The most effective of these compounds were **5d**, **5e**, **5h**, **5i**, **5j**, and **5k**. The novel compounds induced apoptosis and increased Caspase 3, 8, 9, and Cytochrome C levels. Furthermore, the investigated compounds increased Bax and p53 levels while decreasing anti-apoptotic Bcl2 protein levels. Following optimization, these compounds form a novel class of compounds capable of acting as potent apoptotic anticancer agents for both EGFR and CDK2.

References

1. Medina-Franco, J.L.; Giulianotti, M.A.; Welmaker, G.S.; Houghten, R.A. Shifting from the single to the multitarget paradigm in drug discovery. *Drug Discov. Today* **2013**, *18*, 495–501. [CrossRef] [PubMed]
2. Ramsay, R.R.; Popovic-Nikolic, M.R.; Nikolic, K.; Uliassi, E.; Bolognesi, M.L. A perspective on multi-target drug discovery and design for complex diseases. *Clin. Transl. Med.* **2018**, *7*, 3–17. [CrossRef] [PubMed]
3. Msomi, N.Z.; Shode, F.O.; Pooe, O.J.; Mazibuko-Mbeje, S.; Simelane, M.B.C. Iso-Mukaadial Acetate from Warburgia salutaris Enhances Glucose Uptake in the L6 Rat Myoblast Cell Line. *Biomolecules* **2019**, *9*, 520. [CrossRef] [PubMed]
4. Liu, C.; Zhang, M.; Hu, M.; Guo, H.-F.; Li, J.; Yu, Y.-L.; Jin, S.; Wang, X.-T.; Liu, L.; Liu, X.-D. Increased glucagon-like peptide-1 secretion may be involved in antidiabetic effects of ginsenosides. *J. Endocrinol.* **2013**, *217*, 185–196. [CrossRef]
5. Zhou, P.; Xie, W.; He, S.; Sun, Y.; Meng, X.; Sun, G.; Sun, X. Ginsenoside Rb1 as an anti-diabetic agent and its underlying mechanism analysis. *Cells* **2019**, *8*, 204. [CrossRef]
6. Qaseem, A.; Barry, M.J.; Humphrey, M.J.; Forciea, M.A.; Fitterman, N.; Horwitch, C.; Kansagara, D.; McLean, R.M.; Wilt, T.J. Oral pharmacologic treatment of type 2 diabetes mellitus: A clinical practice guideline update from the American college of physicians. *Ann. Intern. Med.* **2017**, *166*, 279–290. [CrossRef] [PubMed]
7. Garber, A.J.; Abrahamson, M.J.; Barzilay, J.I.; Blonde, L.; Bloomgarden, Z.T.; Bush, M.A.; Dagogo-Jack, S.; Davidson, M.B.; Einhorn, D.; Garvey, W.T.; et al. American Association of Clinical Endocrinologists' comprehensive diabetes management algorithm 2013 consensus statement—Executive summary. *Endocr. Pract.* **2013**, *19*, 536–557. [CrossRef]
8. Hussein, Z.; Wentworth, J.M.; Nankervis, A.J.; Proietto, J.; Colman, P.G. Effectiveness, and side effects of thiazolidinediones for type 2 diabetes: Real-life experience from a tertiary hospital. *Med. J. Aust.* **2004**, *181*, 536–539. [CrossRef]
9. Elkady, A.I.; Abuzinadah, O.A.; Baeshen, N.A.; Rahmy, T.R. Differential control of growth, apoptotic activity, and gene expression in human breast cancer cells by extracts derived from medicinal herbs *Zingiber officinale*. *J. Biomed. Biotechnol.* **2012**, *2012*, 614356. [CrossRef]
10. Ahmad, J.; Ahamed, M.; Akhtar, M.J.; Alrokayan, S.A.; Siddiqui, M.A.; Musarrat, J.; Al-Khedhairy, A.A. Apoptosis induction by silica nanoparticles mediated through reactive oxygen species in human liver cell in eHepG2. *Toxicol. Appl. Pharmacol.* **2012**, *259*, 160–168. [CrossRef]
11. Teiten, M.H.; Eifes, S.; Dicato, M.; Diederich, M. Curcumin–the paradigm of a multi-target natural compound with applications in cancer prevention and treatment. *Toxins* **2010**, *2*, 128–162. [CrossRef] [PubMed]
12. Pourhassanali, N.; Roshan-Milani, S.; Kheradmand, F.; Motazakker, M.; Bagheri, M.; Saboory, E. Zinc attenuates ethanol-induced Sertoli cell toxicity and apoptosis through caspase-3 mediated pathways. *Reprod. Toxicol.* **2016**, *61*, 97–103. [CrossRef] [PubMed]
13. Olsson, M.; Zhivotovsky, B. Caspases and cancer. *Cell Death Differ.* **2011**, *8*, 1441–1449. [CrossRef] [PubMed]
14. Guo, R.; Overman, M.; Chatterjee, D.; Rashid, A.; Shroff, S.; Wang, H.; Katz, M.H.; Fleming, J.B.; Varadhachary, G.R.; Abbruzzese, J.L.; et al. Aberrant expression of p53, p21, cyclinD1, and BCL2 and their clinicopathological correlation in ampullary adenocarcinoma. *Hum. Pathol.* **2014**, *45*, 1015–1023. [CrossRef]
15. Shi, L.; Teng, H.; Zhu, M.; Li, C.; Huang, K.; Chen, B.; Dai, Y.; Wang, J. Paeoniflorin inhibits nucleus pulposus cell apoptosis by regulating the expression of BCL2 family proteins and caspase-9 in a rabbit model of intervertebral disc degeneration. *Exp. Ther. Med.* **2015**, *10*, 257–262. [CrossRef] [PubMed]
16. Fan, Y.; Lu, H.; An, L.; Wang, C.; Zhou, Z.; Feng, F.; Ma, H.; Xu, Y.; Zhao, Q. Effect of active fraction of *Eriocaulon* sieboldianum on human leukemia K562 cells via proliferation inhibition, cell cycle arrest and apoptosis induction. *Environ. Toxicol. Pharmacol.* **2016**, *43*, 13–20. [CrossRef]
17. Lohrum, M.A.E.; Vousden, K.H. Regulation and function of the p53-related proteins: Same family, different rules (Electronic version). *Trends Cell Biol.* **2000**, *10*, 197–202. [CrossRef]
18. Shrivastava, A.; Kuzontkoski, P.M.; Groopman, J.E.; Prasad, A. Cannabidiol induces programmed cell death in breast cancer cells by coordinating the crosstalk between apoptosis and autophagy. *Mol. Cancer Ther.* **2011**, *10*, 1161–1172. [CrossRef]

19. McAllister, S.D.; Murase, R.; Christian, R.T.; Lau, D.; Zielinski, A.J.; Allison, J.; Almanza, C.; Pakdel, A.; Lee, J.; Limbad, C.; et al. Pathways mediating the effects of cannabidiol on the reduction of breast cancer cell proliferation, invasion, and metastasis. *Breast Cancer Res. Treat.* **2011**, *129*, 37–47. [CrossRef] [PubMed]

20. Blazquez, C.; Casanova, M.L.; Planas, A.; Gomez Del Pulgar, T.; Villanueva, C.; Fernandez-Acenero, M.J.; Aragones, J.; Huffman, J.W.; Jorcano, J.L.; Guzman, M. Inhibition of tumor angiogenesis by cannabinoids. *FASEB J.* **2003**, *17*, 529–531. [CrossRef]

21. Vaccani, A.; Massi, P.; Colombo, A.; Rubino, T.; Parolaro, D. Cannabidiol inhibits human glioma cell migration through a cannabinoid receptor-independent mechanism. *Br. J. Pharmacol.* **2005**, *144*, 1032–1036. [CrossRef] [PubMed]

22. Ramer, R.; Bublitz, K.; Freimuth, N.; Merkord, J.; Rohde, H.; Haustein, M.; Borchert, P.; Schmuhl, E.; Linnebacher, M.; Hinz, B. Cannabidiol inhibits lung cancer cell invasion and metastasis via intercellular adhesion molecule 1. *FASEB J.* **2012**, *26*, 1535–1548. [CrossRef] [PubMed]

23. Youssif, B.G.M.; Mohamed, A.M.; Osman, E.E.A.; Abou-Ghadir, O.F.; Elnaggar, D.H.; Abdelrahman, M.H.; Treamblu, L.; Gomaa, H.A. 5-Chlorobenzofuran-2-carboxamides: From allosteric CB1 modulators to potential apoptotic antitumor agents. *Eur. J. Med. Chem.* **2019**, *177*, 1–11. [CrossRef]

24. Abdelrahman, M.H.; Aboraia, A.S.; Youssif, B.G.M.; Elsadek, B.E.M. Design, synthesis and pharmacophoric model building of new 3-alkoxymethyl/3-phenyl indole-2-carboxamides with potential antiproliferative activity. *Chem. Biol. Drug Des.* **2017**, *90*, 64–82. [CrossRef] [PubMed]

25. Gomaa, H.A.M.; Shaker, M.E.; Alzarea, S.I.; Hendawy, O.M.; Mohamed, F.A.M.; Gouda, A.M.; Ali, A.T.; Morcoss, M.M.; Abdelrahman, M.H.; Tremblau, L.; et al. Optimization and SAR investigation of novel 2,3-dihydropyrazino[1,2-a]indole-1,4-dione derivatives as EGFR and BRAF^V600E dual inhibitors with potent antiproliferative and antioxidant activities. *Bioorg. Chem.* **2022**, *120*, 105616. [CrossRef]

26. Al-Wahaibi, L.H.; Gouda, A.M.; Abou-Ghadir, O.F.; Salem, O.I.A.; Ali, A.T.; Farghaly, H.S.; Abdelrahman, M.H.; Trembleau, L.; Abdu-Allah, H.H.M.; Youssif, B.G.M. Design, and synthesis of novel 2,3-dihydropyrazino[1,2-a]indole-1,4-dione derivatives as antiproliferative EGFR and BRAF^V600E dual inhibitors. *Bioorg. Chem.* **2020**, *104*, 104260. [CrossRef]

27. El-Sheref, E.M.; Elbastawesy, M.A.I.; Brown, A.B.; Shawky, A.M.; Gomaa, H.A.M.; Bräse, S.; Youssif, B.G.M. Design and Synthesis of (2-oxo-1, 2-Dihydroquinolin-4-yl)-1,2,3-triazole derivatives via Click Reaction: Potential Apoptotic Antiproliferative Agents. *Molecules* **2021**, *26*, 6798. [CrossRef] [PubMed]

28. Abdel-Aziz, S.A.; Taher, E.S.; Lan, P.; Asaad, G.F.; Gomaa, H.A.M.; El-Koussi, N.A.; Youssif, B.G.M. Design, synthesis, and biological evaluation of new pyrimidine-5-carbonitrile derivatives bearing 1, 3-thiazole moiety as novel anti-inflammatory EGFR inhibitors with cardiac safety profile. *Bioorg. Chem.* **2021**, *111*, 104890. [CrossRef]

29. Mekheimer, R.A.; Allam, S.M.R.; Al-Sheikh, M.A.; Moustafa, M.S.; Al-Mousawi, S.M.; Mostafa, Y.A.; Youssif, B.G.M.; Gomaa, H.A.M.; Hayallah, A.M.; Abdel Aziz, M.; et al. Discovery of new pyrimido [5,4-c] quinolines as potential antiproliferative agents with multitarget actions: Rapid synthesis, docking, and ADME studies. *Bioorg. Chem.* **2022**, *121*, 105693. [CrossRef]

30. Khurana, L.; Mackie, K.; Piomelli, D.; Kendall, D.A. Modulation of CB1 cannabinoid receptor by allosteric ligands: Pharmacology and therapeutic opportunities. *Neuropharmacology* **2017**, *124*, 3–12. [CrossRef]

31. Nguyen, T.; Li, J.X.; Thomas, B.F.; Wiley, J.L.; Kenakin, T.P.; Zhang, Y. Allosteric Modulation: An Alternate Approach Targeting the Cannabinoid CB1 Receptor. *Med. Res. Rev.* **2017**, *37*, 441–474. [CrossRef] [PubMed]

32. Cohen, G.M. Caspases: The executioners of apoptosis. *Biochem. J.* **1997**, *236*, 1–16. [CrossRef] [PubMed]

33. Abou-Zied, H.A.; Youssif, B.G.M.; Mohamed, M.F.A.; Hayallah, A.M.; Abdel-Aziz, M. EGFR inhibitors and apoptotic inducers: Design, synthesis, anticancer activity, and docking studies of novel xanthine derivatives carrying chalcone moiety as hybrid molecules. *Bioorg. Chem.* **2019**, *89*, 102997. [CrossRef] [PubMed]

34. Slee, E.A.; Adrain, C.; Martin, S.J. Executioner caspase-3, -6, and -7 perform distinct, non-redundant roles during the demolition phase of apoptosis. *J. Biol. Chem.* **2001**, *276*, 7320–7326. [CrossRef]

35. Hisham, M.; Youssif, B.G.M.; Osman, E.E.A.; Hayallah, A.M.; Abdel-Aziz, M. Synthesis and biological evaluation of novel xanthine derivatives as potential apoptotic antitumor agents. *Eur. J. Med. Chem.* **2019**, *176*, 117–128. [CrossRef]

36. Mitupatum, T.; Aree, K.; Kittisenachai, S.; Roytrakul, S.; Puthong, S.; Kangsadalampai, S.; Rojpibulstit, P. mRNA Expression of Bax, Bcl-2, p53, Cathepsin B, Caspase-3 and Caspase-9 in the HepG2 Cell Line Following Induction by a Novel Monoclonal Ab Hep88 mAb: Cross-Talk for Paraptosis and Apoptosis. *Asian Pac. J. Cancer Prev.* **2016**, *17*, 703–712. [CrossRef]

37. Gatza, C.; Moore, L.; Dumble, M.; Donehower, L.A. Tumor suppressor dosage regulates stem cell dynamics during aging. *Cell Cycle* **2007**, *6*, 52–55. [CrossRef]

38. Godar, S.; Ince, T.A.; Bell, G.W.; Feldser, D.; Donaher, J.L.; Bergh, J.; Liu, A.; Miu, K.; Watnick, R.S.; Reinhardt, F.; et al. Growth-inhibitory and tumor-suppressive functions of p53 depend on its repression of CD44 expression. *Cell* **2008**, *134*, 62–73. [CrossRef]

39. Finlay, C.A.; Hinds, P.W.; Levine, A.J. The p53 proto-oncogene can act as a suppressor of transformation. *Cell* **1989**, *57*, 1083–1093. [CrossRef]

40. Levine, A.J.; Hu, W.; Feng, Z. The p53 pathway: What questions remain to be explored? *Cell Death Differ.* **2006**, *13*, 1027–1036. [CrossRef]

41. Kim, N.H.; Kim, H.S.; Kim, N.-G.; Lee, I.; Choi, H.-S.; Li, X.-Y.; Kang, S.E.; Cha, S.Y.; Ryu, J.K.; Na, J.M.; et al. p53 and MicroRNA-34 are suppressors of canonical Wnt signaling. *Sci. Signal.* **2011**, *4*, 197. [CrossRef] [PubMed]

42. Junttila, M.R.; Evan, G.I. p53 a Jack of all trades but master of none. *Nat. Rev. Cancer* **2009**, *9*, 821–829. [CrossRef]
43. Gomaa, H.A.M.; El-Sherief, H.A.M.; Hussein, S.; Gouda, A.M.; Salem, O.I.A.; Alharbi, K.S.; Hayallah, A.M.; Youssif, B.G.M. Novel 1, 2,4-triazole derivatives as apoptotic inducers targeting p53: Synthesis and antiproliferative activity. *Bioorg. Chem.* **2020**, *105*, 104369. [CrossRef] [PubMed]

Article

Design and Synthesis of New Hydantoin Acetanilide Derivatives as Anti-NSCLC Targeting EGFR$^{L858R/T790M}$ Mutations

Moamen A. Hassanin [1], Muhamad Mustafa [2,*], Mohammed A. S. Abourehab [3], Heba A. Hassan [1], Omar M. Aly [4,*] and Eman A. M. Beshr [1]

[1] Department of Medicinal Chemistry, Faculty of Pharmacy, Minia University, Minia 61519, Egypt; moamenawad15@gmail.com (M.A.H.); hebahassan2009@live.com (H.A.H.); emanbeshr@yahoo.com (E.A.M.B.)

[2] Department of Medicinal Chemistry, Faculty of Pharmacy, Deraya University, Minia 61111, Egypt

[3] Department of Pharmaceutics, Faculty of Pharmacy, Umm Al-Qura University, Makkah 21955, Saudi Arabia; maabourehab@uqu.edu.sa

[4] Department of Medicinal Chemistry, Faculty of Pharmacy, Port Said University, Port Said 42511, Egypt

* Correspondence: muhamad_mustafa99@yahoo.com or muhamad.mustafa@deraya.edu.eg (M.M.); omarsokkar@yahoo.com or omarsokkar@mu.edu.eg (O.M.A.); Tel.: +20-1007620894 (M.M.); +20-1065607771 (O.M.A.)

Abstract: Epidermal Growth Factor Receptor (EGFR), its wild type and mutations L858R/T790M, is overexpressed in non-small cell lung cancer (NSCLC) patients and is considered an inevitable oncology target. However, while the potential EGFR inhibitors have been represented in the literature, their cellular activity failed to establish broad potency against EGFR and its mutations. This study identifies a new series of EGFR$^{L858R/T790M}$ inhibitors bearing hydantoin acetanilides. Most compounds revealed strong antiproliferative activity in a range of NSCL cancer models (A549, H1975, and PC9), in which **5a** and **5f** were the most potent. Compounds **5a** and **5f** possessed potent anticancer activity on H1975 cells with IC$_{50}$ values of 1.94 and 1.38 μM, respectively, compared to 9.70 μM for erlotinib. Favorably, **5a** and **5f** showed low activity on WI-38 normal cells. Western blotting and an EGFR kinase assay test proved the significant EGFR inhibitory activity of **5a**. Besides, active hydantoin derivative **5a** strongly arrested the cell cycle at the sub G1 and S phases and triggered apoptosis in A549 cells. These results imply that **5a** could be considered a promising lead compound for additional development as a potential active agent for anticancer therapy.

Keywords: EGFR; mutation; hydantoin; anticancer; molecular docking

1. Introduction

The Epidermal Growth Factor family (EGFR) is a transmembrane protein that plays a critical role in cell proliferation, survival, migration, adhesion, and differentiation [1]. Unfortunately, overexpression of the EGFR gene initiates diverse downstream signaling pathways, resulting in cancer aggressiveness and invasiveness [2]. Non-small cell lung cancer (NSCLC) is one of the major causes of cancer-related mortality and morbidity globally, accounting for about 80–90% of all lung malignancies [2–5]. EGFR overexpression and mutation (L858R and T790M) is highly prevalent in NSCLC [6,7]. Approximately 10–50% of NSCLC patients harbor EGFR containing the activating mutations [8]. Therefore, EGFR is a valuable clinically proven therapeutic target for anticancer therapy, particularly in the treatment of NSCLC.

The approved first-generation EGFR tyrosine kinase inhibitors, such as gefitinib and erlotinib (Figure 1), provided significant clinical benefits in patients with activating mutations, resulting in marked tumor shrinkage [9–11]. However, acquired drug resistance

usually develops after approximately a year of gefitinib or erlotinib treatment [4]. According to reports, around 60% of EGFR-mutant NSCLC patients have the EGFR[T790M] mutation, which renders first-generation EGFR inhibitors less effective in these patients [1]. Drastically, the T790M mutation boosts the affinity of the EGFR receptor for ATP, leading to a lowering of the ability of EGFR inhibitors to compete with ATP effectively [12]. In the T790M mutation, a secondary Thr790 to Met790 mutation occurs in the gatekeeper site of the EGFR catalytic domain, whereas the L858R mutation is a single-nucleotide substitution that replaces leucine with arginine at position 858 [3,4]. In the case of the latter mutation, the EGFR receptor shows a 50-fold of raised catalytic activity, symbolizing a vital hub for cancer cells in rising cell growth, downstream signaling, and metastasis [13]. As a result, the binding of these inhibitors is sterically blocked by the bulky methionine moiety, which disrupts water-mediated hydrogen bond formation between the inhibitors and the T790M of EGFR [4,12]. In this respect, second-generation inhibitors (afatinib and dacomitinib) have been developed to overcome the resistance associated with the T790M mutation (Figure 1) [14,15]. However, they have poor kinase selectivity between EGFR[T790M] mutants and the wild type (WT) EGFR. In addition, these inhibitors are associated with dose-limiting toxicities [2,16]. Seminal work was conducted to discover the third-generation EGFR inhibitors, rociletinib and Osimertinib, that block both activating mutations and the T790M drug resistance mutation of EGFR (Figure 1) [17–20]. As a result, they have the benefits of a better selectivity profile, an increased time to resistance, and better toxicity profiles. Among these third-generation inhibitors, osimertinib was identified as a breakthrough drug for treating mutant NSCLC and was authorized by the FDA in 2015 to treat NSCLC patients with the T790M EGFR mutation. Subsequently, it is still important to discover more compounds that could target EGFR and its mutations. Moreover, hydantoin moiety is emerging as a cornerstone scaffold in potential anticancer agents, particularly EGFR inhibitors (Figure 2) [21–23].

Gefitinib, I

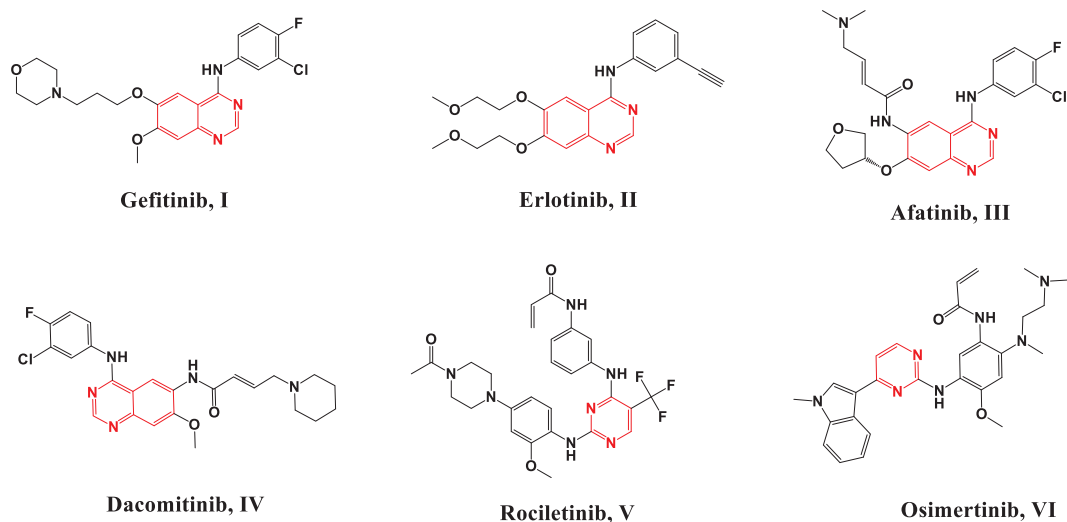**Erlotinib, II**

Afatinib, III

Dacomitinib, IV

Rociletinib, V

Osimertinib, VI

Figure 1. Chemical structures of the FDA-approved EGFR inhibitors.
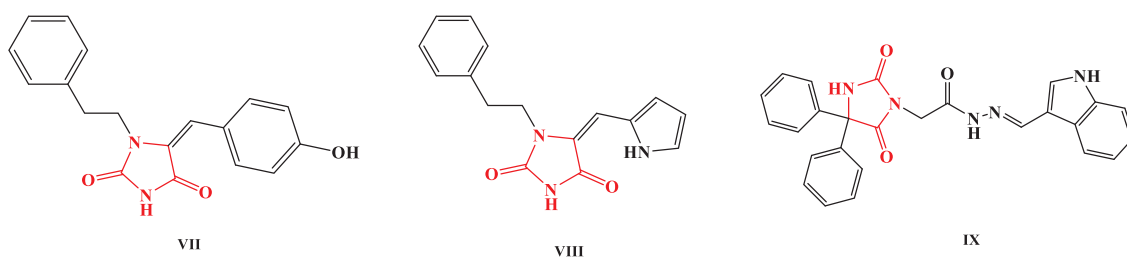

VII

VIII

IX

Figure 2. Hydantoin-based EGFR inhibitors.

As part of our ongoing efforts to discover new probes in our armamentarium for treating cancer, a new series of hydantoin acetanilide derivatives were designed and synthesized to conquer NSCLC through inhibiting EGFR[WT] and its mutations EGFR[L858R/T790M]. The prepared derivatives **5a–5n** were evaluated for their anti-NSCLC activity in A549, H1975, and PC9 cell lines. The most potent members **5a** and **5f** were tested for their safety on the normal fibroblast WI-38 cells, and their EGFR[WT/L858R/T790M] inhibitory activity. The effect of **5a** on the EGFR downstream signaling transduction pathways Akt and ERK was investigated. Molecular docking was performed within the EGFR[T790M] binding site to gain further insights into possible modes of action.

Rational Design of EGFR Inhibitors

Designing an inhibitor with a higher affinity to Met790 in NSCLC is our aim to overcome the resistance associated with the T790M mutation in which Met790 replaces Thr790 (Figure 3). The hydantoin group was designed to interact with Met790 in a manner similar to ribose of the agonist ATP, whereas the phenyl ring needs to interact with Leu777 and Asp855 similar to the adenine group of the ATP. The carbonyl group of the hydantoin group interacts with Thr854 similar to that of gefitinib. The carbonyl of the acetamide group binds with Lys745 by hydrogen bonding similar to ATP but ATP interacts with Lys745 by an ionic bond. The acetamide N-substituted phenyl group showed hydrophobic bonding with Cys797 of the kinase hinge area. The design of the target compounds shows the advantage of combining the binding properties of both ATP and gefitinib.
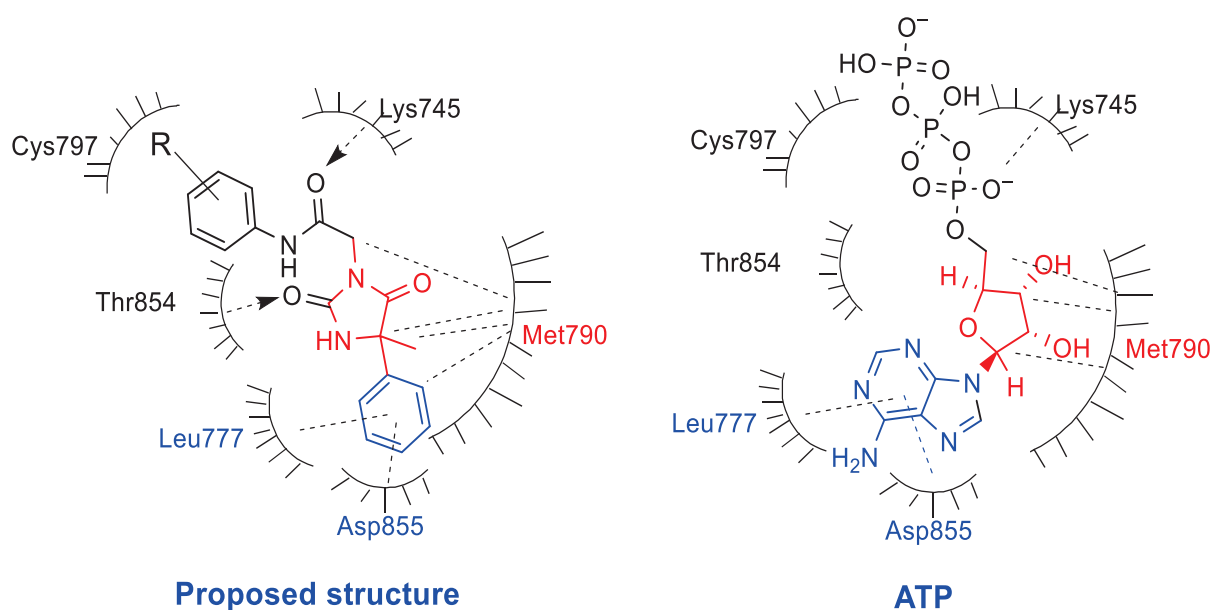
Figure 3. Design of 4-phenyl hydantoin acetanilide derivatives as EGFR inhibitors.

2. Results and Discussion

2.1. Chemistry

The synthesis of the alkylated hydantoin derivatives **5a–5n** (Table 1) is outlined in Scheme 1. The anilines **1a–1n** were treated with chloroacetyl chloride in the presence of triethylamine (TEA) to afford the corresponding acetylated anilines **2a–2n**. The parent hydantoin (5-methyl-5-phenylimidazolidine-2,4-dione) **4** was prepared in a good yield, via the non-stereospecific Bucherer–Bergs reaction, by refluxing acetophenone **3** with potassium cyanide and anhydrous ammonium carbonate [24]. In the presence of potassium carbonate and potassium iodide, hydantoin **4** was alkylated with the appropriate acylated aniline **2a–2n** to afford the targeted alkylated hydantoin derivatives **5a–5n**. The synthesized compounds were identified by ^{1}HNMR, ^{13}CNMR, and mass spectroscopy, and further confirmed by elemental analyses. The purity of compound **5a** was checked by HPLC

analysis using a gradient elution of methanol: water mixture at a rate of 1.0 mL/min leading to elution of **5a** as a single peak after 19.94 min at λmax of 254 nm (supp info). ^{1}H NMR spectra of compounds **5a**–**5n** showed the hydantoin methyl protons as a singlet integrated for three protons at approximately δ 1.69–1.74 ppm. The hydantoin amidic NH proton appeared as a singlet at δ 9.03–8.92 ppm, whereas the other amide proton appeared more downfield shifted as a singlet at 10.71–9.48 ppm due to the anisotropic effect of the benzene ring.

Table 1. Variable attachment points and substituents of the prepared compounds.

Cpd	R_1	R_2	R_3	R_4	Cpd	R_1	R_2	R_3	R_4
5a	H	OCH_3	OCH_3	H	**5h**	H	F	F	H
5b	H	SO_2NH_2	H	H	**5i**	F	F	F	H
5c	H	Cl	OCH_3	H	**5j**	CH_3	H	OCH_3	H
5d	OCH_3	H	H	CH_3	**5k**	H	Cl	F	H
5e	H	H	F	H	**5l**	H	H	OC_2H_5	H
5f	F	H	H	H	**5m**	OCH_3	H	H	H
5g	H	F	H	H	**5n**	H	OCH_3	H	H
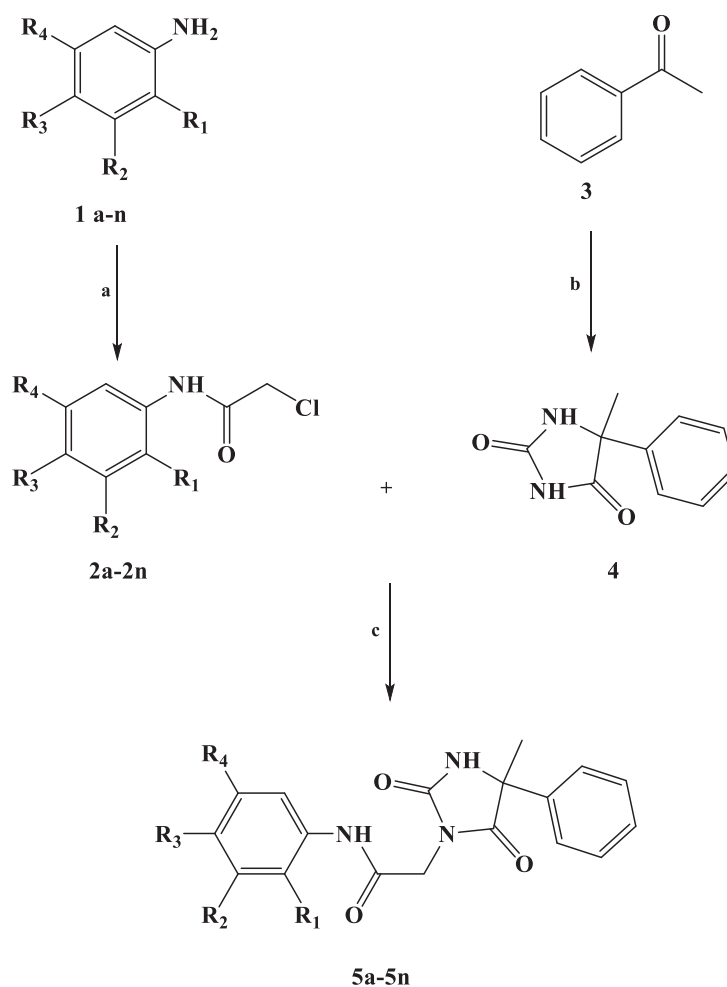
Scheme 1. Synthetic approach of compounds **5a**–**5n**. (a) $ClCH_2COCl$, TEA, CH_2Cl_2; (b) KCN, $(NH_4)_2CO_3$, 60% ETOH, 58–61 °C, 48 h; (c) (i) K_2CO_3, acetonitrile, 25 °C, 30 min, (ii) KI, an appropriate acylated aniline (**2a**–**2n**), Reflux, 3–6 h.

2.2. In Vitro Antiproliferative Activity

The synthesized hydantoin acetanilide derivatives **5a**–**5n** were evaluated for their anticancer activity in three various cells derived from NSCLC tumor subpanels, including A549 (harbor EGFR^{WT}), H1975 (harbor EGFR$^{L858R/T790M}$), and PC9 (harbor EGFR^{L858R}) cells, using the MTT assay (Table 2). Erlotinib was used as a positive control. Interestingly, six hydantoin derivatives exhibited promising activity. Among them, **5a**, **5b**, **5e**, **5f**, **5i**, and **5n** were the most potent against the three evaluated cell lines (average IC$_{50}$ = 2.57–9.29 μM). The synthesized compounds' half-maximal inhibitory concentration (IC$_{50}$) revealed a substantial ability of **5a**, **5e**, **5f**, **5i**, **5j**, **5l**, and **5n** to inhibit A549 lung cancer growth; their IC$_{50}$ values were superior to erlotinib. On the other hand, compounds **5b**, **5h**, and **5m** possessed moderate potency (IC$_{50}$ = 7.19–14.54 μM), whereas compounds **5c**, **5d**, **5g**, and **5k** showed a low potency (IC$_{50}$ = 35.82–91.39 μM). Regarding H1975 cells, compounds **5a**, **5b**, **5e**, **5f**, **5g**, **5k**, and **5m** showed better activity than the reference erlotinib, in which **5a** and **5f** showed their activity in low micromolar concentrations. Interestingly, all the prepared compounds showed better anticancer activity in the PC9 cell line than the reference erlotinib, except **5c** and **5m**. These results revealed that the synthesized hydantoin acetanilide derivatives possessed promising anticancer potency, and among them **5a** and **5f** were the most potent.

Table 2. IC$_{50}$ (μM) values for the target hydantoin acetanilide against A549, H1975, and PC9 cell lines compared to erlotinib.

Cpd	IC$_{50}$ (μM)				Cpd	IC$_{50}$ (μM)			
	A549	H1975	PC9	Average		A549	H1975	PC9	Average
5a	2.26 ± 0.12	1.94 ± 0.25	10.19 ± 0.53	4.79	**5i**	0.73 ± 0.05	14.00 ± 0.76	6.06 ± 0.35	6.93
5b	14.54 ± 0.92	8.20 ± 0.45	5.12 ± 0.56	9.29	**5j**	4.11 ± 0.26	30.90 ± 1.68	9.97 ± 1.08	14.99
5c	91.39 ± 5.75	55.30 ± 3.01	21.34 ± 2.31	56.01	**5k**	68.57 ± 4.32	5.84 ± 0.32	3.25 ± 0.35	25.89
5d	35.82 ± 2.26	11.90 ± 0.65	7.50 ± 0.81	18.41	**5l**	2.37 ± 0.15	43.80 ± 2.39	6.69 ± 0.73	17.62
5e	7.19 ± 0.45	9.34 ± 0.51	2.52 ± 0.27	6.35	**5m**	12.33 ± 0.78	2.27 ± 0.12	28.34 ± 3.08	14.31
5f	1.94 ± 0.12	1.38 ± 0.07	4.40 ± 0.48	2.57	**5n**	0.42 ± 0.03	18.80 ± 1.02	6.87 ± 0.75	8.70
5g	37.65 ± 2.37	6.84 ± 0.37	11.50 ± 1.25	18.66	Erloinib	7.81 ± 0.43	9.70 ± 0.53	16.26 ± 0.84	11.26
5h	11.94 ± 0.75	21.30 ± 1.16	15.41 ± 1.67	16.22					

2.3. In Vitro EGFR Inhibition Assay

As our rationale was to target EGFR and its mutations, activities of the most potent derivatives **5a** and **5f** were evaluated against EGFR^{WT}, EGFR^{L858R}, and EGFR^{T790M} using EGFR kinase assay tests. Erlotinib was used as a positive control. The results in Table 3 showed that **5a** and **5f** have potent EGFR^{WT} inhibitory activity, however, they were approximately three and seven-folds lower than the reference erlotinib, respectively. On the other hand, **5a** showed approximately the same EGFR^{L858R} and EGFR^{T790M} inhibitory activities (IC$_{50}$ = 0.05 and 0.09 μM, respectively) compared to erlotinib (IC$_{50}$ = 0.03 and 0.07 μM, respectively), whereas **5f** showed a five and four-fold decrease in EGFR^{L858R} and EGFR^{T790M} inhibitory activities compared to erlotinib, respectively. These results revealed that **5a** was potent against the mutations of EGFR.

Table 3. EGFR tyrosine kinase (wild type and mutations) inhibitory activities of the hydantoin acetanilide derivatives **5a**–**5n**.

Cpd	EGFR Enzymatic Inhibition, IC$_{50}$, (μM)		
	WT	L858R	T790M
5a	0.03 ± 0.005	0.05 ± 0.001	0.09 ± 0.002
5f	0.06 ± 0.011	0.17 ± 0.003	0.26 ± 0.005
Erlotinib	0.09 ± 0.002	0.03 ± 0.001	0.07 ± 0.002

2.4. In Vitro Inhibition of the EGFR Downstream Pathway

The ability of **5a** to inhibit Akt and ERK, the downstream signaling transduction of EGFR, was investigated using Akt and ERK enzyme assays. Treating A549 cells with the IC_{50} value of **5a** resulted in a substantial inhibition of Akt and ERK (IC_{50} = 33.75 and 25.76 nM, respectively) (Table 4). Besides, **5a** revealed a comparable Akt and ERK inhibition compared to the reference erlotinib (IC_{50} = 25.41 and 17.46 nM, respectively). Interestingly, these findings indicated that the hydantoin derivative 5a targeted EGFR and inhibited its related downstream proteins ERK and Akt.

Table 4. Effect of **5a** on the downstream signaling transduction Akt and ERK in A549 cells.

Cpd	Enzymatic Inhibition, IC_{50}, (nM)	
	Akt	**ERK**
5a	33.75 ± 0.55	25.76 ± 41
Erlotinib	22.97 ± 0.20	17.46 ± 0.18

2.5. Inhibition of EGFR Phosphorylation Expression Using Western Blot Analysis

To further investigate the biochemical effects of the most active compound **5a** on EGFR, Western blot analysis was conducted on A549 cell lines. In addition, the obtained data were attuned to β-actin expression to exclude the deviations further. The hydantoin derivative **5a** maintained a strong EGFR inhibitory activity; treating A549 cells with 0.03 μM of **5a** significantly lessened the expression level of EGFR phosphorylation and showed a 2.5-fold decrease in the expression compared to the control A549 cells (Figure 4).
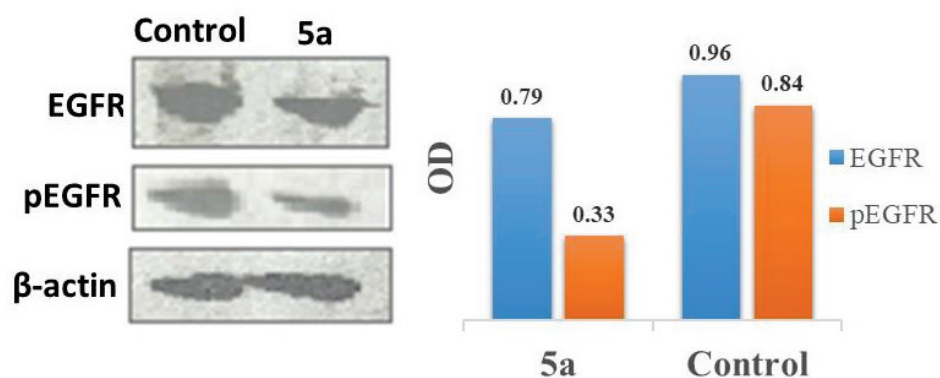
Figure 4. Western blot and statistical analysis of the expression level of EGFR and pEGFR in A549 cells treated by **5a**.

2.6. In Vitro Cytotoxic Activity towards Normal Fibroblast (WI-38) Cells

An MTT in vitro cytotoxic assay was conducted on the normal fibroblast WI-38 cells to examine the safety of **5a** and **5f**. Erlotinib was used as a positive control (Table 5). The obtained IC_{50} values revealed that both hydantoin derivatives possessed low cytotoxicity on the normal fetal lung WI-38 cells, in which **5a** and **5f** were 2.6 and 2.3-folds superior to the reference erlotinib, respectively. These results implied that **5a** and **5f** were barely cytotoxic on the normal WI-38 cell line.

Table 5. The concentration of 50% growth inhibition (IC_{50}, μM $\pm$ SEM) of compounds **5a** and **5f** on WI-38 normal cells.

Compound	WI-38, IC50 (μM)
5a	49.30 ± 2.75
5f	42.45 ± 2.32
Erlotinib	18.62 ± 1.24

2.7. Cell Cycle Analysis and Detection of Apoptosis

The active hydantoin derivative **5a** was further investigated for its effect on cell cycle progression and the induction of apoptosis in A549 cells. Exposure of A549 cells to **5a** at its IC_{50} value led to an interference with the normal cell cycle distribution of the cell (Figure 5). We observed that compound **5a** arrested the cell cycle at sub G1 and S phases (35.25% and 40.40%, respectively). Interestingly, **5a** caused a substantial boost of cells at pre-G1 by 22-folds compared to the control. Meanwhile, **5a** was evaluated for its ability to induce apoptosis in A549 cells by staining with propidium iodide and Annexin V-FITC. After treatment with its IC_{50} concentration, the acquired data showed a significant ability of **5a** to induce apoptosis and increase the early and late apoptotic cells by 3.77% and 19.89%, respectively (Figure 6). Interestingly, **5a** elevated the early and late apoptotic cells 77 and 9-folds compared to the negative control, respectively. These results implied that the hydantoin acetanilide derivatives arrested cells at the sub G1 and S phases and exhibited most of their antiproliferative activity by inducing cellular apoptosis and dissipating cellular integrity.

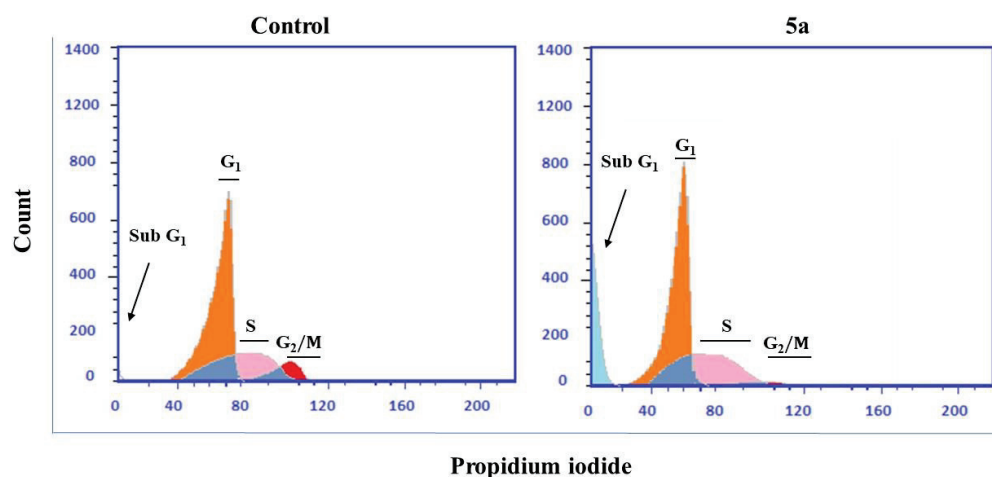**Figure 5.** Compound **5a** arrested the cell cycle at the sub G1 and S phases in A549 cells. Representative cell cycle distribution data are shown by flow cytometric analysis upon incubation with **5a** or DMSO as a negative control for 24 h.
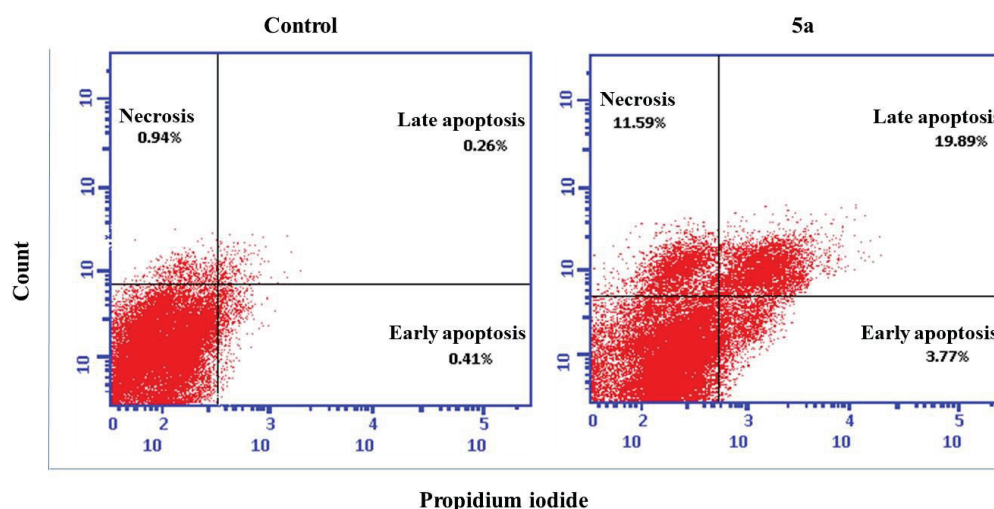

Figure 6. Apoptotic effect of compound **5a** on A549 cells. Representative cytograms of apoptotic A549 cells stimulated with **5a** or DMSO as a negative control for 24 h.

2.8. Wound Healing Assay Tau Aggregation Inhibition in a Cell Model of Tauopathy and Western Blot Analysis

Various articles have highlighted the role of EGFR in the migration of tumor cells [25]. Accordingly, the migratory effects of **5a** in A549 cells were assessed using a wound healing assay. Compound **5a** reduced the wound closure and the migration of A549 cells substantially in a dose-dependent manner (Figure 7).
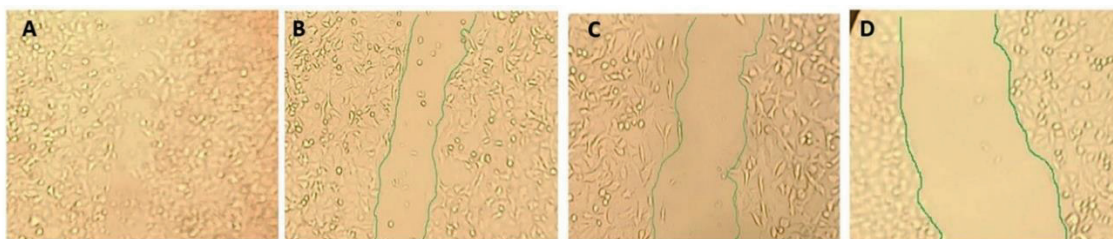
Figure 7. Wound closure and cell migration in A549 cells. (**A**) control cells; (**B**) cells treated with 0.5 μM of **5a**; (**C**) cells treated with 1 μM of **5a**; (**D**) cells treated with 2 μM of **5a**.

2.9. Molecular Docking Study

The docking study on the EGFR (PDB: 5GTY) showed that all the target compounds **5a–5n** could interact with the active sites of the co-crystallized ligand binding sites with Met790 by hydrogen bonds [24]. Moreover, all compounds showed a hydrogen bonding interaction with Thr854 while the formed pi-H interaction with Leu777 in addition to hydrogen bonding with Lys745. The most potent derivative **5a** formed two hydrogen bonds with the gatekeeper mutant Met790, whereas the p-methoxy group was in a higher proximity to Cys797 of the kinase hinge (Figure 8). Conversely, erlotinib showed no binding interaction with Met790 which may explain the superiority of the target compound in the in vitro inhibition of the mutated EGFR growth (Figure S1). The target compounds showed docking scores (kcal/mole) ranging from −7.9294 to −9.2064 while gefitinib (Figure S2), erlotinib, and ATP showed −9.5254, −9.5245, and −9.54906, respectively. Interestingly, **5a** approximately occupied the EGFR pocket the same as the native ligand, and ATP (Figure 9).
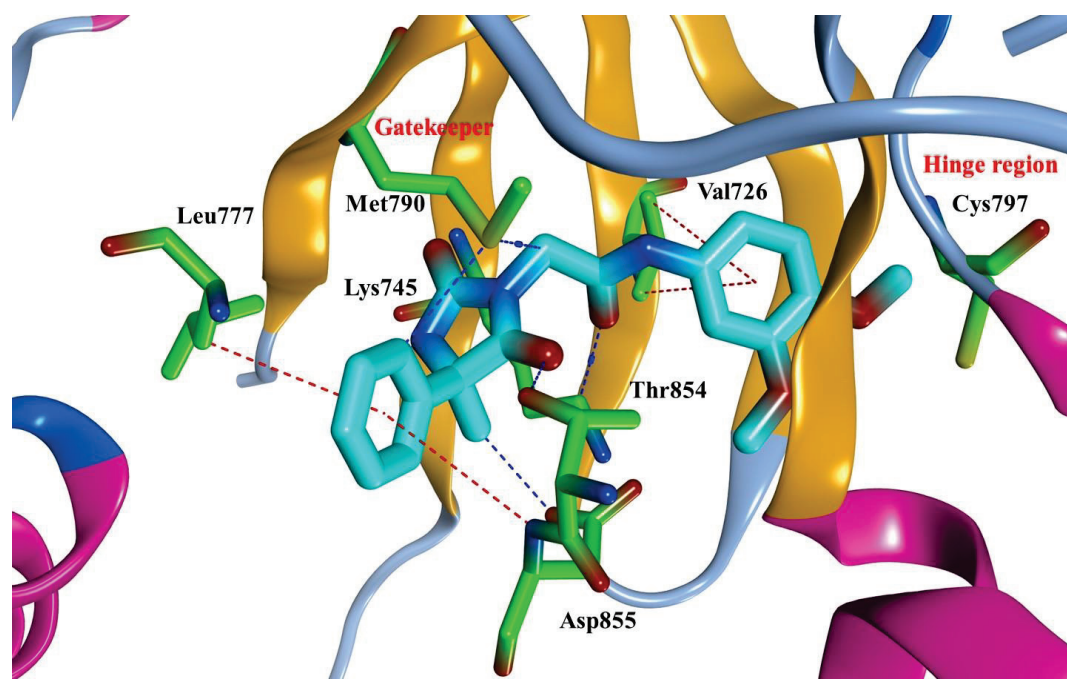
Figure 8. Three-dimensional representation of compound **5a** (cyan) within the EGFR active site.
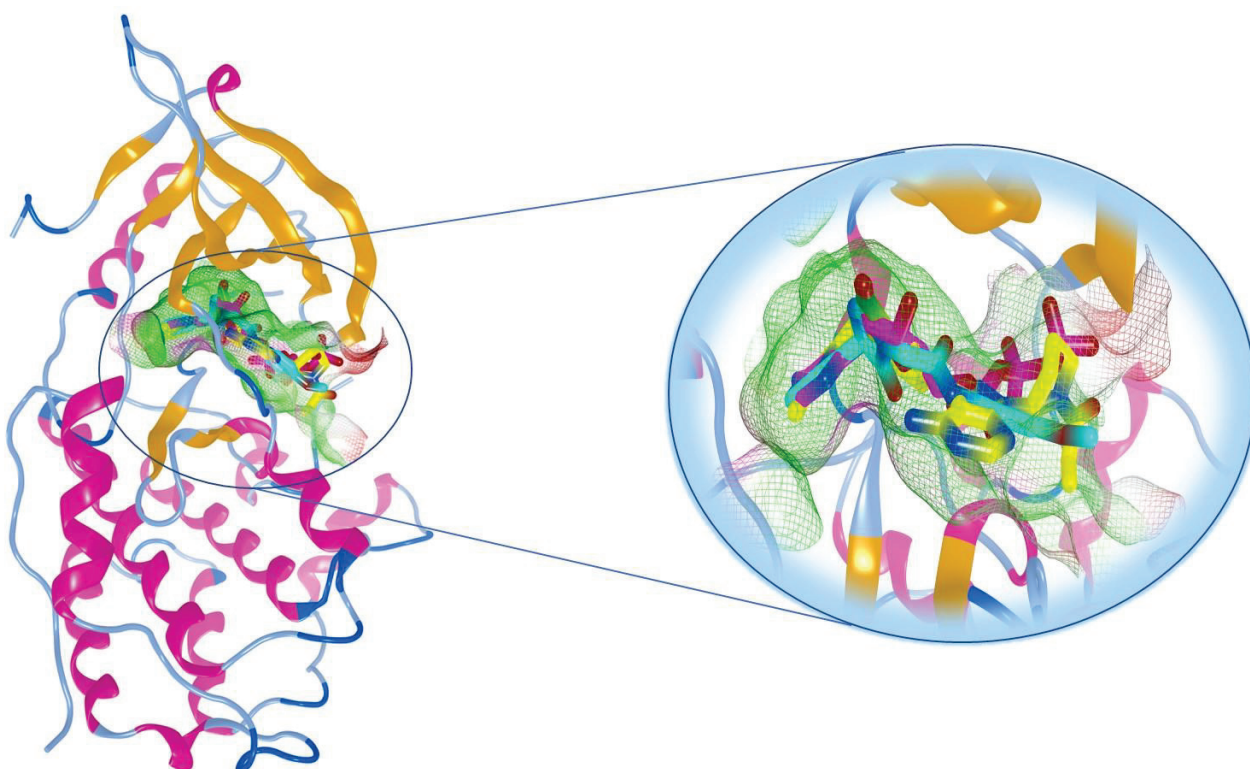
Figure 9. Superimposition of compound **5a** (cyan), co-crystallized ligand (yellow), and ATP (magenta) within the EGFR active site.

3. Materials and Methods

3.1. Chemistry

Chemicals were purchased from Aldrich (Burlington, MA, USA), Merck (Darmstadt, Germany), and El-Nasr pharmaceutical chemicals companies (Qalyubia, Egypt), and used without further purification. Reactions were monitored by thin layer chromatography (TLC), using Merck9385 pre-coated aluminum plate silica gel (Kieselgel 60) 5 × 20 cm plates with a layer thickness of 0.2 mm. The spots were detected by exposure to a UV lamp at 254 nm. Melting points were determined on Stuart electro thermal melting point apparatus and were uncorrected. NMR spectra were carried out using a Bruker Avance 400 MHz ^{1}HNMR spectrometer and 100 MHz ^{13}CNMR spectrometer (Beni Sweif, Egypt), using TMS as internal reference. Chemical shifts (δ values are given in parts per million (ppm) relative to TMS DMSO-d_6 (2.5 and 3.5 ppm for ^{1}HNMR and 76.9 ppm for ^{13}CNMR) and coupling constants (J) were measured in Hertz. Splitting patterns were designated as follows: s, singlet; d, doublet; t, triplet; q, quartet; m, multiplet. Elemental analyses were recorded on Shimadzu GC/MS-QP5050A, Regional center for Mycology and Biotechnology, Al-Azhar University, Cairo, Egypt. Mass spectra were recorded on an Advion compact mass spectrometer (CMS) and reported as mass/charge (*m/z*), Nawah scientific center for research, Almokattam, Cairo, Egypt. HPLC analysis of compound **5a** was performed on a Waters 2690 Alliance HPLC system equipped with a Waters 996 photodiode array detector, and UV detection at λ_{max} 254 nm, and HPLC run data were processed at Nawah Scientific, Egypt.

3.2. General Procedure for the Synthesis of Compounds **2a–2n**

The appropriate aniline **1a–1n** (1 mmol) was dissolved in DCM, TEA (2 mmol) was added, and the reaction mixture was stirred in an ice bath. Chloroacetyl chloride (2 mmol) was added dropwise to the reaction mixture. The progress of the reaction was monitored by TLC. After the reaction was completed, the organic solvent evaporated, and the product was washed with distilled water.

123

3.3. General Procedure for the Synthesis of Compound **4**

In a stoppered flask, acetophenone (1 mmol) was dissolved in a mixture of ethanol and distilled water (1:1). Potassium cyanide (3 mmol) and anhydrous ammonium carbonate (7 mmol) were carefully added. The mixture was heated in an oil bath at 58–61 °C for 48 h. After the reaction was completed, the mixture was concentrated under a vacuum to the third of its initial volume and diluted with water and acidified with diluted hydrochloric acid. The precipitate formed was filtered off, washed with water, and recrystallized from water ethanol mixture.

General procedure for the synthesis of compounds **5a–5n** was as follows.

The hydantoin 4 (190, 1 mmol) was stirred with K_2CO_3 (10 mmol) in CH_3CN for 30 min. The appropriate acylated aniline derivative **2a–2n** (1 mmol) was then added portion wise then KI (10 mmol) was added. The mixture was heated at reflux for 3–6 h. The reaction progress was monitored by TLC, then concentrated under reduced pressure. The residue was triturated with ethyl acetate (3 × 30 mL) and the combined organic phase was washed with water (3 × 30 mL), dried over anhydrous sodium sulphate, and evaporated to dryness. The obtained product was recrystallized from a mixture of ethyl acetate and petroleum ether.

***N*-(3,4-dimethoxyphenyl)-2-(4-methyl-2,5-dioxo-4-phenylimidazolidin-1-yl)acetamide (5a).**

Pale pink powder (165 mg, 43% yield); mp 145–148 °C; ^{1}HNMR (400 MHz, DMSO-d_6) δ (ppm): 10.11 (s, 1H, CO-NH-Ar), 8.96 (s, 1H, CO-NH), 7.5–7.49 (m, 2H, Ar-H), 7.40 (t, *J* = 7.5 Hz, 2H, Ar-H), 7.33 (t, *J* = 7.2 Hz, 1H, Ar-H), 7.21 (d, *J* = 2.3 Hz, 1H, Ar-H), 7.02 (dd, *J* = 8.7, 2.3 Hz, 1H, Ar-H), 6.86 (d, *J* = 8.7 Hz, 1H, Ar-H), 4.15 (s, 2H, CO-CH$_2$-N), 3.69 (s, 3H, O-CH$_3$), 3.69 (s, 3H, O-CH$_3$), 1.71 (s, 3H, CH$_3$); ^{13}CNMR (100 MHz, DMSO-d_6) δ (ppm): 175.36 (C=O), 164.17 (C=O), 155.36 (C=O), 148.60 (C quaternary), 144.99 (C quaternary), 139.51 (C quaternary), 132.18 (C quaternary), 128.52 (CH), 128.01 (CH), 125.68 (CH), 112.10 (CH), 110.98 (CH), 104.18 (CH), 63.12 (C quaternary), 55.71 (O-CH$_3$), 55.39 (O-CH$_3$), 40.67 (CH$_2$), 24.96 (CH$_3$); ESI/MS: *m/z* Calcd. for [M + Na]$^+$: 406.1, Found: 405.8; Anal. Calcd for $C_{20}H_{21}N_3O_5$ (383.1): C, 62.65; H, 5.52; N, 10.96. Found: C, 62.93; H, 5.80; N, 11.23; HPLC-analysis: gradient elution H_2O-MeOH (90:10) for 20 min, followed by with H_2O-MeOH (20:80) for 5 min, and finally with a further isocratic elution with H_2O-MeOH (90:10) for 5 min at a flow rate 1 ml/min, Rt = 19.947 min.

***N*-(4-aminosulphonylphenyl)-2-(4-methyl-2,5-dioxo-4-phenylimidazolidin-1-yl)acetamide (5b).**

Pale yellow powder (137 mg, 35% yield); mp 122–125 °C; ^{1}HNMR (400 MHz, DMSO-d_6) δ (ppm):10.60 (s, 1H, CO-NH-Ar), 9.01 (s, 1H, CO-NH), 7.57–7.47 (m, 4H, Ar-H), 7.45–7.31 (m, 5H, Ar-H), 4.24 (s, 2H, CO-CH$_2$-N), 2.87 (s, 1H, SO$_2$NH), 2.72 (s, 1H, SO$_2$NH), 1.73 (s, 3H, CH$_3$); ^{13}CNMR (100 MHz, DMSO-d_6) δ (ppm): 175.32 (C=O), 165.13 (C=O), 155.27 (C=O), 144.74 (C quaternary), 139.44 (C quaternary), 138.88 (C quaternary), 129.61 (CH), 128.53 (CH), 128.02 (CH), 125.66 (CH), 121.92 (CH), 120.61 (CH), 116.08 (CH), 63.16 (C quaternary), 40.79 (CH$_2$), 24.87 (CH$_3$); ESI/MS: *m/z* Calcd. for [M + Na]$^+$: 425.1, Found: 424.8; Anal. Calcd for $C_{18}H_{18}N_4O_5S$ (402.1): C, 53.72; H, 4.51; N, 13.92; S, 7.97. Found: C, 53.94; H, 4.59; N, 13.75; S, 8.04.

***N*-(3-chloro-4-methoxyphenyl)-2-(4-methyl-2,5-dioxo-4-phenylimidazolidin-1-yl)acetamide (5c).**

Pale black powder (192 mg, 50% yield); mp 163–166 °C; ^{1}HNMR (400 MHz, DMSO-d_6) δ (ppm):10.29 (s, 1H, CO-NH-Ar), 8.98 (s, 1H, CO-NH), 7.71 (d, *J* = 2.5 *Hz*, 1H, Ar-H), 7.55–7.49 (m, 2H, Ar-H), 7.44–7.30 (m, 4H, Ar-H), 7.09 (d, J = 9.0 *Hz*, 1H, Ar-H), 4.18 (s, 2H, CO-CH$_2$-N), 3.80 (s, 3H, O-CH$_3$), 1.72 (s, 3H, CH$_3$); ^{13}CNMR (100 MHz, DMSO-d_6) δ (ppm): 175.33 (C=O), 164.54 (C=O), 155.31 (C=O), 150.64 (C quaternary), 139.46 (C quaternary), 132.23 (C quaternary), 128.52 (C quaternary), 128.00 (CH), 125.67 (CH), 125.32 (CH), 120.66 (CH), 118.91 (CH), 113.02 (CH), 63.13 (C quaternary), 56.16 (O-CH$_3$), 40.66 (CH$_2$), 24.84 (CH$_3$); ESI/MS: *m/z* Calcd. for [M + Na]$^+$: 410.1, Found: 410.0; Anal. Calcd for $C_{19}H_{18}ClN_3O_4$ (387.1): C, 58.84; H, 4.68; N, 10.84. Found: C, 58.95; H, 4.80; N, 11.02.

***N*-(2-methoxy-5-methylphenyl)-2-(4-methyl-2,5-dioxo-4-phenylimidazolidin-1-yl)acetamide (5d).**

Pale yellow powder (203 mg, 55% yield); mp 170–173 °C; ^{1}HNMR (400 MHz, DMSO-d_6) δ (ppm): 9.48 (s, 1H, CO-NH-Ar), 8.97 (s, 1H, CO-NH), 7.75 (s, 1H, Ar-H), 7.55–7.50 (m, 2H, Ar-H), 7.41 (t, *J* = 7.4 Hz, 2H, Ar-H), 7.36–7.31 (m, 1H, Ar-H), 6.93–6.85 (m, 2H, Ar-H), 4.27 (s, 2H, CO-CH$_2$-N), 3.80 (s, 3H, O-CH$_3$), 2.20 (s, 3H, Ar-CH$_3$), 1.72 (s, 3H, CH$_3$); ^{13}CNMR (100 MHz, DMSO-d_6) δ (ppm): 175.37 (C=O), 164.79 (C=O), 155.36 (C=O), 147.24 (C quaternary), 139.50 (C quaternary), 129.02 (C quaternary), 128.51 (C quaternary), 127.97 (CH), 126.50 (CH), 125.65 (CH), 124.65 (CH), 122.12 (CH), 111.06 (CH), 63.08 (C quaternary), 55.75 (O-CH$_3$), 40.81 (CH$_2$), 24.90 (CH$_3$), 20.42 (CH$_3$); ESI/MS: *m/z* Calcd. for [M + Na]$^+$: 390.2, Found: 390.0; Anal. Calcd for C$_{20}$H$_{21}$N$_3$O$_4$ (367.2): C, 65.38; H, 5.76; N, 11.44. Found: C, 65.46; H, 5.94; N, 11.65.

***N*-(4-fluorophenyl)-2-(4-methyl-2,5-dioxo-4-phenylimidazolidin-1-yl)acetamide (5e).**

Pale gray powder (120 mg, 35% yield); mp 226–228 °C; ^{1}HNMR (400 MHz, DMSO-d_6) δ (ppm): 10.33 (s, 1H, CO-NH-Ar), 8.97 (s, 1H, CO-NH), 7.58–7.49 (m, 4H, Ar-H), 7.40 (t, *J* = 7.5 Hz, 2H, Ar-H), 7.35–7.30 (m, 1H, Ar-H), 7.13 (t, *J* = 8.9 Hz, 2H, Ar-H), 4.19 (s, 2H, CO-CH$_2$-N), 1.71 (s, 3H, CH$_3$); ^{13}CNMR (100 MHz, DMSO-d_6) δ (ppm): 175.37 (C=O), 164.62 (C=O), 159.30 (C=O), 155.33 (C quaternary), 139.47 (C quaternary), 134.95 (C quaternary), 128.51 (CH), 128.01 (CH), 125.69 (CH), 120.81 (CH), 115.32 (CH), 63.13 (C quaternary), 40.69 (CH$_2$), 24.79 (CH$_3$); ESI/MS: *m/z* Calcd. for [M + Na]$^+$: 364.1, Found: 364.0; Anal. Calcd for C$_{18}$H$_{16}$FN$_3$O$_3$ (341.1): C, 63.34; H, 4.72; N, 12.31. Found: C, 63.57; H, 4.79; N, 12.39.

***N*-(2-fluorophenyl)-2-(4-methyl-2,5-dioxo-4-phenylimidazolidin-1-yl)acetamide (5f).**

Pale yellow powder (100 mg, 30% yield); mp 153–155 °C; ^{1}HNMR (400 MHz, DMSO-d_6) δ (ppm): 10.14 (s, 1H, CO-NH-Ar), 8.99 (s, 1H, CO-NH), 7.94–7.84 (m, 1H, Ar-H), 7.55–7.52 (m, 2H, Ar-H), 7.41 (t, *J* = 7.5 Hz, 2H, Ar-H), 7.38–7.31 (m, 1H, Ar-H), 7.30–7.23 (m, 1H, Ar-H), 7.21–7.11 (m, 2H, Ar-H), 4.30 (s, 2H, CO-CH$_2$-N), 1.73 (s, 3H, CH$_3$); ^{13}CNMR (100 MHz, DMSO-d_6) δ (ppm): 175.36 (C=O), 165.28 (C=O), 155.30 (C=O), 154.49 (C quaternary), 152.06 (C quaternary), 139.46 (C quaternary), 128.51 (CH), 128.00 (CH), 125.68 (CH), 124.47 (CH), 123.64 (CH), 115.63 (CH), 115.44 (CH), 63.12 (C quaternary), 40.62 (CH$_2$), 24.76 (CH$_3$); ESI/MS: *m/z* Calcd. for [M + Na]$^+$: 364.1, Found: 363.9; Anal. Calcd for C$_{18}$H$_{16}$FN$_3$O$_3$ (341.1): C, 63.34; H, 4.72; N, 12.31. Found: C, 63.50; H, 4.88; N, 12.42.

***N*-(3-fluorophenyl)-2-(4-methyl-2,5-dioxo-4-phenylimidazolidin-1-yl)acetamide (5g).**

Pale yellow powder (240 mg, 70% yield); mp 182–185 °C; ^{1}HNMR (400 MHz, DMSO-d_6) δ (ppm): 10.52 (s, 1H, CO-NH-Ar), 8.99 (s, 1H, CO-NH), 7.55–7.47 (m, 3H, Ar-H), 7.40 (t, *J* = 7.5 Hz, 2H, Ar-H), 7.35–7.30 (m, 2H, Ar-H), 7.25 (d, *J* = 8.2 Hz, 1H, Ar-H), 6.91–6.84 (m, 1H, Ar-H), 4.21 (s, 2H, CO-CH$_2$-N), 1.71 (s, 3H, CH$_3$); ^{13}CNMR (100 MHz, DMSO-d_6) δ (ppm): 175.33 (C=O), 165.11 (C=O), 163.34 (C=O), 160.94 (C quaternary), 155.28 (C quaternary), 139.43 (C quaternary), 130.50 (CH), 128.52 (CH), 128.02 (CH), 125.67 (CH), 114.84 (CH), 110.12 (CH), 106.03 (CH), 63.15 (C quaternary), 40.81 (CH$_2$), 24.83 (CH$_3$); ESI/MS: *m/z* Calcd. for [M + Na]$^+$: 364.1, Found: 363.9; Anal. Calcd for C$_{18}$H$_{16}$FN$_3$O$_3$ (341.1): C, 63.34; H, 4.72; N, 12.31. Found: C, 63.49; H, 4.86; N, 12.34.

***N*-(3,4-difluorophenyl)-2-(4-methyl-2,5-dioxo-4-phenylimidazolidin-1-yl)acetamide (5h).**

Pale yellow powder (110 mg, 31% yield); mp 195–198 °C; ^{1}HNMR (400 MHz, DMSO-d_6) δ (ppm): 10.71 (s, 1H, CO-NH-Ar), 9.03 (s, 1H, CO-NH), 7.57–7.51 (m, 2H, Ar-H), 7.42 (t, *J* = 7.5 Hz, 2H, Ar-H), 7.38–7.32 (m, 1H, Ar-H), 7.29–7.22 (m, 2H, Ar-H), 6.98–6.88 (m, 1H, Ar-H), 4.24 (s, 2H, CO-CH$_2$-N), 1.74 (s, 3H, CH$_3$); ^{13}CNMR (100 MHz, DMSO-d_6) δ (ppm): 175.27 (C=O), 165.49 (C=O), 163.61 (C=O), 161.35 (C quaternary), 155.20 (C quaternary), 140.95 (C quaternary), 139.40 (C quaternary), 128.53 (CH), 128.03 (CH), 125.65 (CH), 102.15 (CH), 101.86 (CH), 98.75 (CH), 63.17 (C quaternary), 40.86 (CH$_2$), 24.85 (CH$_3$); ESI/MS: *m/z* Calcd. for [M + Na]$^+$: 382.1, Found: 381.8; Anal. Calcd for C$_{18}$H$_{15}$F$_2$N$_3$O$_3$ (359.1): C, 60.17; H, 4.21; N, 11.69. Found: C, 60.41; H, 4.37; N, 11.88.

***N*-(2,3,4-trifluorophenyl)-2-(4-methyl-2,5-dioxo-4-phenylimidazolidin-1-yl)acetamide (5i).**

Yellow powder (110 mg, 30% yield); mp 205–210 °C; ^{1}HNMR (400 MHz, DMSO-d_6) δ (ppm): 10.36 (s, 1H, CO-NH-Ar), 9.00 (s, 1H, CO-NH), 7.69–7.59 (m, 1H, Ar-H), 7.56–7.49 (m, 2H, Ar-H), 7.41 (t, *J* = 7.4 Hz, 2H, Ar-H), 7.34 (t, *J* = 7.3 Hz, 1H, Ar-H), 7.31–7.24 (m, 1H, Ar-H), 4.29 (s, 2H, CO-CH$_2$-N), 1.72 (s, 3H, CH$_3$); ^{13}CNMR (100 MHz, DMSO-d_6) δ (ppm): 175.30 (C=O), 165.55 (C=O), 155.21 (C=O), 139.41 (C quaternary), 128.51 (C quaternary), 128.01 (C quaternary), 127.81 (C quaternary), 125.66 (C quaternary), 125.32 (CH), 123.55 (CH), 118.42 (CH), 111.96 (CH), 111.78 (CH), 63.13 (C quaternary), 40.52 (CH$_2$), 24.73 (CH$_3$); ESI/MS: *m/z* Calcd. for [M + Na]$^+$: 400.1, Found: 399.9; Anal. Calcd for C$_{18}$H$_{14}$F$_3$N$_3$O$_3$ (377.1): C, 57.30; H, 3.74; N, 11.14. Found: C, 57.46; H, 3.90; N, 11.30.

N-(4-methoxy-2-methylphenyl)-2-(4-methyl-2,5-dioxo-4-phenylimidazolidin-1-yl)acetamide (5j).

Pale yellow powder (112 mg, 30% yield); mp 143-146 °C; ^{1}HNMR (400 MHz, DMSO-d_6) δ (ppm): 9.48 (s, 1H, CO-NH-Ar), 8.92 (s, 1H, CO-NH), 7.50 (d, *J* = 7.4 Hz, 2H, Ar-H), 7.38 (t, *J* = 7.4 Hz, 2H, Ar-H), 7.31 (t, *J* = 7.2 *Hz*, 1H, Ar-H), 7.17 (d, *J* = 8.7 *Hz*, 1H, Ar-H), 6.77 (d, *J* = 2.7 Hz, 1H, Ar-H), 6.70 (dd, *J* = 8.7, 2.7 Hz, 1H, Ar-H), 4.19 (s, 2H, CO-CH$_2$-N), 3.69 (s, 3H, O-CH$_3$), 2.13 (s, 3H, Ar-CH$_3$), 1.69 (s, 3H, CH$_3$); ^{13}CNMR (100 MHz, DMSO-d_6) δ (ppm): 175.44 (C=O), 164.93 (C=O), 156.90 (C=O), 155.42 (C quaternary), 139.55 (C quaternary), 133.83 (C quaternary), 128.63 (C quaternary), 128.49 (CH), 127.99 (CH), 126.52 (CH), 125.73 (CH), 115.42 (CH), 111.24 (CH), 63.08 (C quaternary), 55.16 (O-CH$_3$), 40.42 (CH$_2$), 24.72 (CH$_3$), 17.97 (CH$_3$); ESI/MS: *m/z* Calcd. for [M + Na]$^+$: 390.2, Found: 390.1; Anal. Calcd for C$_{20}$H$_{21}$N$_3$O$_4$ (367.2): C, 65.38; H, 5.76; N, 11.44. Found: C, 65.49; H, 5.84; N, 11.57.

N-(3-chloro-4-fluorophenyl)-2-(4-methyl-2,5-dioxo-4-phenylimidazolidin-1-yl)acetamide (5k).

Pale yellow powder (195 mg, 55% yield); mp 170–173 °C; ^{1}HNMR (400 MHz, DMSO-d_6) δ (ppm): 10.53 (s, 1H, CO-NH-Ar), 9.01 (s, 1H, CO-NH), 7.86 (dd, *J* = 6.8, 2.3 Hz, 1H, Ar-H), 7.56–7.51 (m, 2H, Ar-H), 7.46–7.39 (m, 3H, Ar-H), 7.38–7.32 (m, 2H, Ar-H), 4.22 (s, 2H, CO-CH$_2$-N), 1.73 (s, 3H, CH$_3$); ^{13}CNMR (100 MHz, DMSO-d_6) δ (ppm): 175.30 (C=O), 165.05 (C=O), 155.24 (C=O), 154.43 (C quaternary), 152.01 (C quaternary), 139.42 (C quaternary), 135.74 (C quaternary), 128.52 (CH), 128.01 (CH), 125.65 (CH), 120.48 (CH), 119.36 (CH), 116.99 (CH), 63.15 (C quaternary), 40.72 (CH$_2$), 24.83 (CH$_3$); ESI/MS: *m/z* Calcd. For [M + Na]$^+$: 398.1, Found: 397.9; Anal. Calcd for C$_{18}$H$_{15}$ClFN$_3$O$_3$ (375.1): C, 57.53; H, 4.02; N, 11.18. Found: C, 57.75; H, 4.21; N, 11.40.

N-(4-ethoxyphenyl)-2-(4-methyl-2,5-dioxo-4-phenylimidazolidin-1-yl)acetamide (5l).

Pale brown powder (225 mg, 62% yield); mp 153–155 °C; ^{1}HNMR (400 MHz, DMSO-d_6) δ (ppm): 10.12 (s, 1H, CO-NH-Ar), 8.97 (s, 1H, CO-NH), 7.56–7.51 (m, 2H, Ar-H), 7.47–7.39 (m, 4H, Ar-H), 7.35 (t, *J* = 7.3 Hz, 1H, Ar-H), 6.87 (d, *J* = 9.0 Hz, 2H, Ar-H), 4.18 (s, 2H, CO-CH$_2$-N), 3.97 (q, J = 7.0 Hz, 2H, O-CH$_2$CH$_3$), 1.73 (s, 3H, -CH$_3$), 1.30 (t, *J* = 7.0 Hz, 3H, -CH$_3$CH$_2$); ^{13}CNMR (100 MHz, DMSO-d_6) δ (ppm): 175.39 (C=O), 164.10 (C=O), 155.38 (C=O), 154.61 (C quaternary), 139.50 (C quaternary), 131.63 (C quaternary), 128.50 (CH), 127.98 (CH), 125.70 (CH), 120.56 (CH), 114.47 (CH), 63.09 (C quaternary), 63.09 (O-CH$_2$), 40.63 (CH$_2$), 24.80 (CH$_3$), 14.68 (CH$_3$); ESI/MS: *m/z* Calcd. for [M + Na]$^+$: 390.2, Found: 389.9; Anal. Calcd for C$_{20}$H$_{21}$N$_3$O$_4$ (367.2): C, 65.38; H, 5.76; N, 11.44. Found: C, 65.46; H, 5.89; N, 11.56.

N-(2-methoxyphenyl)-2-(4-methyl-2,5-dioxo-4-phenylimidazolidin-1-yl)acetamide (5m).

Yellow powder (160 mg, 45% yield); mp 85–90 °C; ^{1}HNMR (400 MHz, DMSO-d_6) δ (ppm): 9.56 (s, 1H, CO-NH-Ar), 8.98 (s, 1H, CO-NH), 7.93 (d, *J* = 7.8 Hz, 1H, Ar-H), 7.57–7.50 (m, 2H, Ar-H), 7.42 (t, *J* = 7.4 Hz, 2H, Ar-H), 7.34 (t, *J* = 7.3 Hz, 1H, Ar-H), 7.11–7.02 (m, 2H, Ar-H), 6.92–6.87 (m, 1H, Ar-H), 4.30 (s, 2H, CO-CH$_2$-N), 3.85 (s, 3H, O-CH$_3$), 1.73 (s, 3H, -CH$_3$); ^{13}CNMR (100 MHz, DMSO-d_6) δ (ppm): 175.42 (C=O), 164.89 (C=O), 155.38 (C=O), 149.31 (C quaternary), 139.49 (C quaternary), 128.50 (C quaternary), 127.99 (CH), 126.79 (CH), 125.68 (CH), 124.53 (CH), 121.53 (CH), 120.27 (CH), 111.21 (CH), 63.10 (C quaternary), 55.69 (O-CH$_3$), 40.85 (CH$_2$), 24.79 (CH$_3$); ESI/MS: *m/z* Calcd. for [M + Na]$^+$: 376.1, Found: 375.9; Anal. Calcd for C$_{19}$H$_{19}$N$_3$O$_4$ (353.1): C, 64.58; H, 5.42; N, 11.89. Found: C, 64.31; H, 5.31; N, 11.70.

N-(3-methoxyphenyl)-2-(4-methyl-2,5-dioxo-4-phenylimidazolidin-1-yl)acetamide (5n).
Pale yellow powder (230 mg, 65% yield); mp 148–151 °C; ^{1}HNMR (400 MHz, DMSO-d_6)
δ (ppm): 10.25 (s, 1H, CO-NH-Ar), 8.98 (s, 1H, CO-NH), 7.55–7.49 (m, 2H, Ar-H), 7.40 (t,
J =7.5 Hz, 2H, Ar-H), 7.33 (t, J = 7.2 Hz, 1H, Ar-H), 7.22–7.20 (m, 1H, Ar-H), 7.20–7.17 (m,
1H, Ar-H), 7.06 (d, J = 8.0 Hz, 1H, Ar-H), 6.63 (dd, J = 8.1, 2.2 Hz, 1H, Ar-H), 4.18 (s, 2H,
CO-CH$_2$-N), 3.70 (s, 3H, O-CH$_3$), 1.71 (s, 3H, -CH$_3$); ^{13}CNMR (100 MHz, DMSO-d_6) δ (ppm):
175.36 (C=O), 164.71 (C=O), 159.58 (C=O), 155.34 (C quaternary), 139.73 (C quaternary),
139.48 (C quaternary), 129.69 (CH), 128.52 (CH), 128.01 (CH), 125.68 (CH), 111.33 (CH),
109.01 (CH), 104.82 (CH), 63.14 (C quaternary), 55.01 (O-CH$_3$), 40.80 (CH$_2$), 24.88 (CH$_3$);
ESI/MS: m/z Calcd. for [M + Na]$^+$: 376.1, Found: 375.9; Anal. Calcd for C$_{19}$H$_{19}$N$_3$O$_4$
(353.1): C, 64.58; H, 5.42; N, 11.89. Found: C, 64.79; H, 5.56; N, 11.96.

3.4. Anti-Proliferative Activities against A549, H1975, PC9, WI-38 Cell Lines

The new prepared candidates **5a–5n** were evaluated for their antitumor activities
against four selected cell lines, the adenocarcinomic human alveolar basal epithelial
cells NCI-A549, NCI-H1975, human pulmonary adenocarcinoma PC9, and the caucasian
fibroblast-like fetal lung cells WI-38 (purchased from American Type Culture Collection
(ATCC), United States of America), using an MTT assay [26], as described earlier [27].

3.5. EGFR Inhibition Assay

The EGFR inhibitory assay was performed using EGFR (wild, L858R, or T790M) Kinase
Assay Kits (Cat. # 40321, 40324, or 40323, respectively, BPS Bioscience, San Diego, CA, USA)
as described earlier [28,29].

3.6. In Vitro Inhibition of EGFR Downstream Pathway

3.6.1. Akt Enzyme Assay

Akt expression level was assayed using the Phospho Sandwich Akt (Phospho-Ser473)
ELISA Kit (Cat. # MBS9511022, MyBioSource, San Diego, CA, USA) containing the com-
ponents necessary for the semi-quantitative determination of Akt concentrations within
experimental cell lysate samples. The assay was performed according to company proto-
cols: the lysates were diluted with assay diluent and 100 µL/well was dispensed, wrapped
with parafilm, and incubated for 2 h. They were shaken with RT or overnight at 4 °C. The
plate was washed 3 times with 1× Wash Buffer 300 µL/well with a vacuum-based plate
washer. Then, the plate was stricken on absorbent paper to remove as much residual liquid
as possible. The Detection Antibody was diluted to 1× and 100 µL/well was dispensed,
wrapped with parafilm, and incubated on a shaker for 2 hrs at RT, and the washing step was
repeated. Streptavidin-HRP was diluted to 1× and 100 µL/well was dispensed, wrapped
with parafilm, and incubated on a shaker for 30 min at RT. Ready-to-use substrate was
brought to RT and 100 µL/well was dispensed and the reaction was allowed to incubate on
an orbital shaker for 20–30 min. The reaction was stopped with stop solution 100 µL/well.
The wells turned from blue to yellow and were read at 450 nm.

3.6.2. ERK Enzyme Assay

ERK ELISA Kit (Cat. # E4317-100, BioVision, Inc., Waltham, MA, USA) was used
for the in vitro quantitative determination of Human ERK. Firstly, the plate was washed
2 times with Wash Solution before the standard, sample, and control wells were added.
A total of 100 µL of each standard or sample was added into appropriate wells. It was
covered well and incubated for 1.5 h at 37 °C. The cover was removed and the plate content
was discarded without washing or letting the wells completely dry. A total of 0.1 mL of
Biotin-detection antibody work solution was added into the above wells. The plate was
sealed and incubated at 37 °C for 60 min. The solution was discarded and washed 3 times
with Wash Solution. It was washed by filling each well with Wash Buffer (350 µL) using
a multi-channel pipette or auto-washer. It was soaked for 1–2 min, and then all residual
wash-liquid was removed from the wells by aspiration. After the last wash, any remaining

wash buffer was removed by aspirating or decanting. The plate was clapped on absorbent filter papers or other absorbent materials. A total of 0.1 mL of SABC working solution was added into each well, and the plate was covered and incubated at 37 °C for 30 min. The solution was discarded and washed 5 times with wash solution as mentioned before. A total of 90 μL of TMB substrate was added into each well, the plate was covered and incubated at 37 °C in the dark within 15–30 min. The shades of blue were seen in the first 3–4 wells by the end of the incubation. A total of 50 μL of Stop Solution was added to each well. The result was read at 450 nm within 20 min.

3.7. Inhibition of EGFR Phosphorylation Expression Using Western Blot Analysis

The western blot experiment was performed according to the same procedure described earlier [30].

3.8. Cell Cycle Analysis and Detection of Apoptosis

Cell cycle analysis and Annexin V-FITC apoptosis assay were performed as described earlier [26].

3.9. Wound Healing Assay

Wound healing assay of **5a** was performed using CytoSelect™ 24-well Wound Healing Assay kit (Cat. # CBA-120, Cell Biolabs Inc., Cambridge, UK) per manufacturer's instructions. In brief, the 24-well plate wound healing inserts were allowed to warm up at room temperature for 10 min., then to each well, 500 μL of A549 cells suspension (1.0×106) in media containing 10% fetal bovine serum (FBS) was added. Cells were kept in a cell culture incubator until a monolayer formed. Carefully, the insert was removed from the well. The media were slowly aspirated and discarded from the wells. The wells were washed with media to remove dead cells and debris. Finally, the media were added to wells to keep cells hydrated, then wells were visualized under a light microscope. Media containing the indicated concentrations of compound **5a** (0.5, 1, or 2 μM) were then added into the wells for 72 h. the wound closure was monitored with a light microscope. The percent closure of the cells into the wound field was measured.

3.10. Molecular Docking to EGFR Active Site

All processes of docking algorithms and visualization were performed within the EGFR active site, using Molecular Operating Environment (MOE) 2019.01 (Chemical Computing Group, Montreal, QC, Canada) software (PDB: 5GTY) [31], downloaded from the Protein Data Bank [32]. The protein structure (PDB: 5GTY) was prepared through the Quick-Prep suite executed in MOE. Then, all the structures of the docked hydantoin acetanilides were built, and their energies were minimized using the default force field, AMBER10. The native ligand was re-docked into EGFR active site to validate the docking study at the binding site using the default parameters. The top ranked re-docked pose had energy score of −10.82 kcal/mol and an RMSD value of 1.3070 Å. The acetanilides were docked in the EGFR active site using rigid receptor docking protocol, where ligand placement was performed with Triangle Matcher method using AMBER10 as a default force field and eventually ranking the docking poses by the London dG scoring function. The generated poses of the best binding affinities were considered.

4. Conclusions

A series of hydantoin acetanilide derivatives **5a–5n** were designed and synthesized as potent inhibitors of EGFR[L858R/T790M]. The synthesized derivatives exhibited potent activity on NSCLC tumor subpanels A549, H1975, and PC9 cells. Interestingly, compounds **5a** and **5f** showed a strong ability to EGFR with better affinity to the mutations L858R/T790M than the wild type and were safer than the reference erlotinib on the normal cells WI-38. Western blotting revealed a significant decrease in the expression of EGFR in A549 cells upon the treatment of **5a** at its IC$_{50}$ value. Besides, **5a** inhibited EGFR related downstream

proteins (ERK and Akt), induced cellular apoptosis, and arrested sub G1 and S phases of the cell cycle. The wound healing assay revealed the substantial ability of **5a** to decrease A549 cells' migration in a dose-dependent manner. Eventually, it is conceivable that further in vivo investigation will be of significant interest to afford promising recipes to overcome the obstacle of EGFR resistance.

Supplementary Materials: The following supporting information can be downloaded at: https://www.mdpi.com/article/10.3390/ph15070857/s1, Figure S1: 3D representation of erlotinib within EGFR active site; Figure S2: 3D representation of gefitinib within EGFR active site; Figure S3: ^{1}H-NMR spectrum of compound **5a** in DMSO-d_6 at 400 MHz; Figure S4: ^{13}C-NMR spectrum of compound **5a** in DMSO-d_6 at 100 MHz; Figure S5: ESI mass spectrum of compound **5a**; Figure S6: HPLC analysis for compound **5a**, retention time (19.947 min); Figure S7: ^{1}H-NMR spectrum of compound **5b** in DMSO-d_6 at 400 MHz; Figure S8: ^{13}C-NMR spectrum of compound **5b** in DMSO-d_6 at 100 MHz; Figure S9: ESI mass spectrum of compound **5b**; Figure S10: ^{1}H-NMR spectrum of compound **5c** in DMSO-d_6 at 400 MHz; Figure S11: ^{13}C-NMR spectrum of compound **5c** in DMSO-d_6 at 100 MHz; Figure S12: ESI mass spectrum of compound **5c**; Figure S13: ^{1}H-NMR spectrum of compound **5d** in DMSO-d_6 at 400 MHz; Figure S14: ^{13}C-NMR spectrum of compound **5d** in DMSO-d_6 at 100 MHz; Figure S15: ESI mass spectrum of compound **5d**; Figure S16: ^{1}H-NMR spectrum of compound **5e** in DMSO-d_6 at 400 MHz; Figure S17: ^{13}C-NMR spectrum of compound **5e** in DMSO-d_6 at 100 MHz; Figure S18: ESI mass spectrum of compound **5e**;Figure S19: ESI mass spectrum of compound **5e**; Figure S20: ^{13}C-NMR spectrum of compound **5f** in DMSO-d_6 at 100 MHz; Figure S21: ESI mass spectrum of compound **5f**; Figure S22: ^{1}H-NMR spectrum of compound **5g** in DMSO-d_6 at 400 MHz; Figure S23: ^{13}C-NMR spectrum of compound **5g** in DMSO-d_6 at 100 MHz; Figure S24: ESI mass spectrum of compound **5g**; Figure S25: ^{1}H-NMR spectrum of compound **5h** in DMSO-d_6 at 400 MHz; Figure S26: ^{13}C-NMR spectrum of compound **5h** in DMSO-d_6 at 100 MHz; Figure S27: ESI mass spectrum of compound **5h**; Figure S28: ^{1}H-NMR spectrum of compound **5i** in DMSO-d_6 at 400 MHz; Figure S29: ^{13}C-NMR spectrum of compound **5i** in DMSO-d_6 at 100 MHz; Figure S30: ESI mass spectrum of compound **5i;** Figure S31: ^{1}H-NMR spectrum of compound **5j** in DMSO-d_6 at 400 MHz; Figure S32: ^{13}C-NMR spectrum of compound **5j** in DMSO-d_6 at 100 MHz; Figure S33: ESI mass spectrum of compound **5j**; Figure S34: ^{1}H-NMR spectrum of compound **5k** in DMSO-d_6 at 400 MHz; Figure S35: ^{13}C-NMR spectrum of compound **5k** in DMSO-d_6 at 100 MHz; Figure S36: ESI mass spectrum of compound **5k**; Figure S37: ^{1}H-NMR spectrum of compound **5l** in DMSO-d_6 at 400 MHz; Figure S38: ^{13}C-NMR spectrum of compound **5l** in DMSO-d_6 at 100 MHz; Figure S39: ESI mass spectrum of compound **5l**; Figure S40: ^{1}H-NMR spectrum of compound **5m** in DMSO-d_6 at 400 MHz; Figure S41: ^{13}C-NMR spectrum of compound **5m** in DMSO-d_6 at 100 MHz; Figure S42: ESI mass spectrum of compound **5m**; Figure S43: ^{1}H-NMR spectrum of compound **5n** in DMSO-d_6 at 400 MHz; Figure S44: ^{13}C-NMR spectrum of compound **5n** in DMSO-d_6 at 100 MHz; Figure S45: ESI mass spectrum of compound **5n**; Figure S46: Western blotting analysis measuring the expression of **5a** on EGFR.

Author Contributions: Conceptualization, O.M.A. and M.M.; methodology, M.A.H., O.M.A. and M.M.; software, O.M.A. and M.M.; validation, O.M.A., M.M., E.A.M.B. and H.A.H.; formal analysis and investigation, M.A.H. and E.A.M.B.; resources, O.M.A., M.M., E.A.M.B. and H.A.H.; data curation, M.A.H. writing—original draft preparation, O.M.A., M.M., E.A.M.B., H.A.H. and M.A.H.; writing—review and editing, O.M.A., M.M., E.A.M.B., H.A.H. and M.A.H.; visualization, O.M.A. and M.M.; supervision, O.M.A., E.A.M.B. and H.A.H.; project administration, O.M.A.; funding acquisition, M.A.S.A., O.M.A. and M.A.H. All authors have read and agreed to the published version of the manuscript.

Institutional Review Board Statement: Not applicable.

Informed Consent Statement: Not applicable.

Data Availability Statement: The data presented in this study are available in article and Supplementary Material.

Conflicts of Interest: The authors declare no conflict of interest.

References

1. Meng, Y.; Yu, B.; Huang, H.; Peng, Y.; Li, E.; Yao, Y.; Song, C.; Yu, W.; Zhu, K.; Wang, K.; et al. Discovery of dosimertinib, a highly potent, selective, and orally efficacious deuterated EGFR targeting clinical candidate for the treatment of non-small-cell lung cancer. *J. Med. Chem.* **2021**, *64*, 925–937. [CrossRef]

2. An, B.; Pan, T.; Hu, J.; Pang, Y.; Huang, L.; Chan, A.S.; Li, X.; Yan, J. The discovery of a potent and selective third-generation EGFR kinase inhibitor as a therapy for EGFR L858R/T790M double mutant non-small cell lung cancer. *Eur. J. Med. Chem.* **2019**, *183*, 111709. [CrossRef] [PubMed]

3. Li, W.-Q.; Cui, J.-W. Non-small cell lung cancer patients with ex19del or exon 21 L858R mutation: Distinct mechanisms, different efficacies to treatments. *J. Cancer Res. Clin. Oncol.* **2020**, *146*, 2329–2338. [CrossRef] [PubMed]

4. Pawara, R.; Ahmad, I.; Nayak, D.; Wagh, S.; Wadkar, A.; Ansari, A.; Belamkar, S.; Surana, S.; Kundu, C.N.; Patil, C.; et al. Novel, selective acrylamide linked quinazolines for the treatment of double mutant EGFR-L858R/T790M Non-Small-Cell lung cancer (NSCLC). *Bioorg. Chem.* **2021**, *115*, 105234. [CrossRef] [PubMed]

5. Zhang, Y.; Lv, H.; Luo, L.; Xu, Y.; Pan, Y.; Wang, Y.; Lin, H.; Xiong, J.; Guo, P.; Zhang, J.; et al. Design, synthesis and pharmacological evaluation of N4,N6-disubstituted pyrimidine-4,6-diamine derivatives as potent EGFR inhibitors in non-small cell lung cancer. *Eur. J. Med. Chem.* **2018**, *157*, 1300–1325. [CrossRef] [PubMed]

6. Patel, H.M.; Pawara, R.; Ansari, A.; Noolvi, M.; Surana, S. Design and synthesis of quinazolinones as EGFR inhibitors to overcome EGFR resistance obstacle. *Bioorg. Med. Chem.* **2017**, *25*, 2713–2723. [CrossRef]

7. Lee, J.Y.; Yang, H.; Kim, D.; Kyaw, K.Z.; Hu, R.; Fan, Y.; Lee, S.K. Antiproliferative Activity of a New Quinazolin-4(3*H*)-One Derivative via Targeting Aurora Kinase A in Non-Small Cell Lung Cancer. *Pharmaceuticals* **2022**, *15*, 698. [CrossRef] [PubMed]

8. Ding, S.; Dong, X.; Gao, Z.; Zheng, X.; Ji, J.; Zhang, M.; Liu, F.; Wu, S.; Li, M.; Song, W.; et al. Design, synthesis and biological evaluation of novel N-(3-amino-4-methoxyphenyl)acrylamide derivatives as selective EGFRL858R/T790M kinase inhibitors. *Bioorg. Chem.* **2021**, *118*, 105471. [CrossRef]

9. Cohen, M.H.; Williams, G.A.; Sridhara, R.; Chen, G.; Pazdur, R. FDA Drug Approval Summary: Gefitinib (ZD1839) (Iressa®) Tablets. *Oncologist* **2003**, *8*, 303–306. [CrossRef]

10. Sordella, R.; Bell, D.W.; Haber, D.A.; Settleman, J. Gefitinib-Sensitizing *EGFR* Mutations in Lung Cancer Activate Anti-Apoptotic Pathways. *Science* **2004**, *305*, 1163–1167. [CrossRef]

11. Miyamoto, S.; Azuma, K.; Ishii, H.; Bessho, A.; Hosokawa, S.; Fukamatsu, N.; Kunitoh, H.; Ishii, M.; Tanaka, H.; Aono, H.; et al. Low-dose erlotinib treatment in elderly or frail patients with EGFR mutation–positive non–small cell lung cancer: A multicenter phase 2 trial. *JAMA Oncol.* **2020**, *6*, e201250. [CrossRef] [PubMed]

12. Yun, C.-H.; Mengwasser, K.E.; Toms, A.V.; Woo, M.S.; Greulich, H.; Wong, K.K.; Meyerson, M.; Eck, M.J. The T790M mutation in EGFR kinase causes drug resistance by increasing the affinity for ATP. *Proc. Natl. Acad. Sci. USA* **2008**, *105*, 2070–2075. [CrossRef] [PubMed]

13. Juchum, M.; Günther, M.; Döring, E.; Sievers-Engler, A.; Lämmerhofer, M.; Laufer, S. Trisubstituted imidazoles with a rigidized hinge binding motif act as single digit nM inhibitors of clinically relevant EGFR L858R/T790M and L858R/T790M/C797S mutants: An example of target hopping. *J. Med. Chem.* **2017**, *60*, 4636–4656. [CrossRef]

14. Marquez-Medina, D.; Popat, S. Afatinib: A second-generation EGF receptor and ErbB tyrosine kinase inhibitor for the treatment of advanced non-small-cell lung cancer. *Futur. Oncol.* **2015**, *11*, 2525–2540. [CrossRef] [PubMed]

15. Mitsudomi, T. Dacomitinib: Another option for EGFR-mutant lung cancer? *Lancet Oncol.* **2014**, *15*, 1408–1409. [CrossRef]

16. Sequist, L.V.; Besse, B.; Lynch, T.J.; Miller, V.A.; Wong, K.K.; Gitlitz, B.; Eaton, K.; Zacharchuk, C.; Freyman, A.; Powell, C.; et al. Neratinib, an irreversible pan-ErbB receptor tyrosine kinase inhibitor: Results of a phase II trial in patients with advanced non–small-cell lung cancer. *J. Clin. Oncol.* **2010**, *28*, 3076–3083. [CrossRef] [PubMed]

17. Wu, Y.L.; John, T.; Grohe, C.; Majem, M.; Goldman, J.W.; Kim, S.W.; Kato, T.; Laktionov, K.; Vu, H.V.; Wang, Z.; et al. Postoperative Chemotherapy Use and Outcomes From ADAURA: Osimertinib as Adjuvant Therapy for Resected EGFR-Mutated NSCLC. *J. Thorac. Oncol.* **2021**, *17*, 423–433. [CrossRef]

18. Yan, X.E.; Ayaz, P.; Zhu, S.J.; Zhao, P.; Liang, L.; Zhang, C.H.; Wu, Y.C.; Li, J.L.; Choi, H.G.; Huang, X.; et al. Structural basis of AZD9291 selectivity for EGFR T790M. *J. Med. Chem.* **2020**, *63*, 8502–8511. [CrossRef]

19. Shen, J.; Zhang, T.; Zhu, S.J.; Sun, M.; Tong, L.; Lai, M.; Zhang, R.; Xu, W.; Wu, R.; Ding, J.; et al. Structure-based design of 5-methylpyrimidopyridone derivatives as new wild-type sparing inhibitors of the epidermal growth factor receptor triple mutant (EGFRL858R/T790M/C797S). *J. Med. Chem.* **2019**, *62*, 7302–7308. [CrossRef]

20. Cheng, H.; Nair, S.K.; Murray, B.W.; Almaden, C.; Bailey, S.; Baxi, S.; Behenna, D.; Cho-Schultz, S.; Dalvie, D.; Dinh, D.M.; et al. Discovery of 1-{(3 R, 4 R)-3-[({5-Chloro-2-[(1-methyl-1 H-pyrazol-4-yl) amino]-7 H-pyrrolo [2, 3-d] pyrimidin-4-yl} oxy) methyl]-4-methoxypyrrolidin-1-yl} prop-2-en-1-one (PF-06459988), a Potent, WT Sparing, Irreversible Inhibitor of T790M-Containing EGFR Mutants. *J. Med. Chem.* **2016**, *59*, 2005–2024.

21. Azizmohammadi, M.; Khoobi, M.; Ramazani, A.; Emami, S.; Zarrin, A.; Firuzi, O.; Miri, R.; Shafiee, A. 2H-chromene derivatives bearing thiazolidine-2,4-dione, rhodanine or hydantoin moieties as potential anticancer agents. *Eur. J. Med. Chem.* **2013**, *59*, 15–22. [CrossRef] [PubMed]

22. Alkahtani, H.M.; Alanazi, M.M.; Aleanizy, F.S.; Alqahtani, F.Y.; Alhoshani, A.; Alanazi, F.E.; Almehizia, A.A.; Abdalla, A.N.; Alanazi, M.G.; El-Azab, A.S.; et al. Synthesis, anticancer, apoptosis-inducing activities and EGFR and VEGFR2 assay mechanistic studies of 5,5-diphenylimidazolidine-2,4-dione derivatives: Molecular docking studies. *Saudi Pharm. J.* **2019**, *27*, 682–693. [CrossRef] [PubMed]

23. Mourad, A.A.; Farouk, N.; El-Sayed, E.-S.H.; Mahdy, A.R. EGFR/VEGFR-2 dual inhibitor and apoptotic inducer: Design, synthesis, anticancer activity and docking study of new 2-thioxoimidazolidin-4one derivatives. *Life Sci.* **2021**, *277*, 119531. [CrossRef]

24. Kucwaj-Brysz, K.; Kurczab, R.; Jastrzębska-Więsek, M.; Żesławska, E.; Satała, G.; Nitek, W.; Partyka, A.; Siwek, A.; Jankowska, A.; Wesołowska, A.; et al. Computer-aided insights into receptor-ligand interaction for novel 5-arylhydantoin derivatives as serotonin 5-HT 7 receptor agents with antidepressant activity. *Eur. J. Med. Chem.* **2018**, *147*, 102–114. [CrossRef] [PubMed]

25. Li, Y.; Chang, Y.; Fu, J.; Ding, R.; Zhang, L.; Liang, T.; Liu, Y.; Liu, Y.; Hu, J. Design, synthesis and biological evaluation of aminopyrimidine derivatives bearing a 4,5,6,7-tetrahydrothieno [3,2-c]pyridine as potent EGFR inhibitors. *Eur. J. Med. Chem.* **2021**, *226*, 113845. [CrossRef]

26. Mosmann, T. Rapid colorimetric assay for cellular growth and survival: Application to proliferation and cytotoxicity assays. *J. Immunol. Methods* **1983**, *65*, 55–63. [CrossRef]

27. Mustafa, M.; Anwar, S.; Elgamal, F.; Ahmed, E.R.; Aly, O.M. Potent combretastatin A-4 analogs containing 1,2,4-triazole: Synthesis, antiproliferative, anti-tubulin activity, and docking study. *Eur. J. Med. Chem.* **2019**, *183*, 111697. [CrossRef]

28. Mghwary, A.E.-S.; Gedawy, E.M.; Kamal, A.M.; Abuel-Maaty, S.M. Novel thienopyrimidine derivatives as dual EGFR and VEGFR-2 inhibitors: Design, synthesis, anticancer activity and effect on cell cycle profile. *J. Enzym. Inhib. Med. Chem.* **2019**, *34*, 838–852. [CrossRef]

29. El-Deen, E.M.M.; Anwar, M.M.; El-Gwaad, A.A.A.; Karam, E.A.; El-Ashrey, M.K.; Kassab, R.R. Design and synthesis of some novel pyridothienopyrimidine derivatives and their biological evaluation as antimicrobial and anticancer agents targeting EGFR enzyme. *Arab. J. Chem.* **2022**, *15*, 103751. [CrossRef]

30. Mustafa, M.; Abuo-Rahma, G.E.; Abd El-Hafeez, A.A.; Ahmed, E.R.; Abdelhamid, D.; Ghosh, P.; Hayallah, A.M. Discovery of antiproliferative and anti-FAK inhibitory activity of 1, 2, 4-triazole derivatives containing acetamido carboxylic acid skeleton. *Bioorg. Med. Chem. Lett.* **2021**, *40*, 127965. [CrossRef]

31. Hu, C.; Wang, A.; Wu, H.; Qi, Z.; Li, X.; Yan, X.-E.; Chen, C.; Yu, K.; Zou, F.; Wang, W.; et al. Discovery and characterization of a novel irreversible EGFR mutants selective and potent kinase inhibitor CHMFL-EGFR-26 with a distinct binding mode. *Oncotarget* **2017**, *8*, 18359–18372. [CrossRef] [PubMed]

32. Mustafa, M.; Abd El-Hafeez, A.A.; Abdelhamid, D.; Katkar, G.D.; Mostafa, Y.A.; Ghosh, P.; Hayallah, A.M.; Abuo-Rahma, G.E. A first-in-class anticancer dual HDAC2/FAK inhibitors bearing hydroxamates/benzamides capped by pyridinyl-1,2,4-triazoles. *Eur. J. Med. Chem.* **2021**, *222*, 113569. [CrossRef] [PubMed]

Article

Hybridization Approach to Identify Salicylanilides as Inhibitors of Tubulin Polymerization and Signal Transducers and Activators of Transcription 3 (STAT3)

Marta Gargantilla [1], Leentje Persoons [2], Tereza Kauerová [3], Natalia del Río [1], Dirk Daelemans [2], Eva-María Priego [1], Peter Kollar [3],* and María-Jesús Pérez-Pérez [1],*

1   Instituto de Quimica Medica (IQM, CSIC) c/Juan de la Cierva 3, 28006 Madrid, Spain; mgargantilla@iqm.csic.es (M.G.); natalia.delrio@iqm.csic.es (N.d.R.); empriego@iqm.csic.es (E.-M.P.)
2   KU Leuven Department of Microbiology, Immunology and Transplantation, Laboratory of Virology and Chemotherapy, Rega Institute for Medical Research, KU Leuven, Herestraat 49, 3000 Leuven, Belgium; leentje.persoons@kuleuven.be (L.P.); dirk.daelemans@kuleuven.be (D.D.)
3   Department of Pharmacology and Toxicology, Faculty of Pharmacy, Masaryk University, Palackeho tr. 1946/1, 612 42 Brno, Czech Republic; kauerovat@pharm.muni.cz
*   Correspondence: kollarp@pharm.muni.cz (P.K.); mjperez@iqm.csic.es (M.-J.P.-P.); Tel.: +420-541-562-892 (P.K.); +34-91-2587516 (M.-J.P.P.)

Abstract: The superimposition of the X-ray complexes of cyclohexanediones (i.e., TUB015), described by our research group, and nocodazole, within the colchicine binding site of tubulin provided an almost perfect overlap of both ligands. This structural information led us to propose hybrids of TUB015 and nocodazole using a salicylanilide core structure. Interestingly, salicylanilides, such as niclosamide, are well-established signal transducers and activators of transcription (STAT3) inhibitors with anticancer properties. Thus, different compounds with this new scaffold have been synthesized with the aim to identify compounds inhibiting tubulin polymerization and/or STAT3 signaling. As a result, we have identified new salicylanilides (**6** and **16**) that showed significant antiproliferative activity against a panel of cancer cells. Both compounds were able to reduce the levels of p-STAT3^{Tyr705} without affecting the total expression of STAT3. While compound **6** inhibited tubulin polymerization and arrested the cell cycle of DU145 cells at G2/M, similar to TUB015, compound **16** showed a more potent effect on inhibiting STAT3 phosphorylation and arrested the cell cycle at G1/G0, similar to niclosamide. In both cases, no toxicity towards PBMC cells was detected. Thus, the salicylanilides described here represent a new class of antiproliferative agents affecting tubulin polymerization and/or STAT3 phosphorylation.

Keywords: tubulin polymerization inhibitors; colchicine site; salicylanilides; niclosamide; signal transducer and activator of transcription (STAT3) inhibitors

1. Introduction

Compounds binding in the colchicine site at the αβ-tubulin interface have been extensively studied as antimitotic agents, although their therapeutic applications could be much wider than their effect on mitosis [1]. Colchicine (**1**, Figure 1) is used for the treatment of gout and familial Mediterranean fever [2]. Its anti-inflammatory properties have led to its inclusion as a therapeutic agent for COVID-19 [3], although its use outside clinical trials has been discouraged [4]. The natural stilbene combretastatin A-4 (CA-4, **2**), which also binds to tubulin at the colchicine site, has been shown to have vascular disrupting activity in the tumor microenvironment and its phosphate prodrug fosbretabulin has progressed to phase III clinical trials [5]. The therapeutic interest related to compounds binding at the colchicine site in tubulin has made these compounds an extremely active area of research, and different chemical classes have been described [6–8].
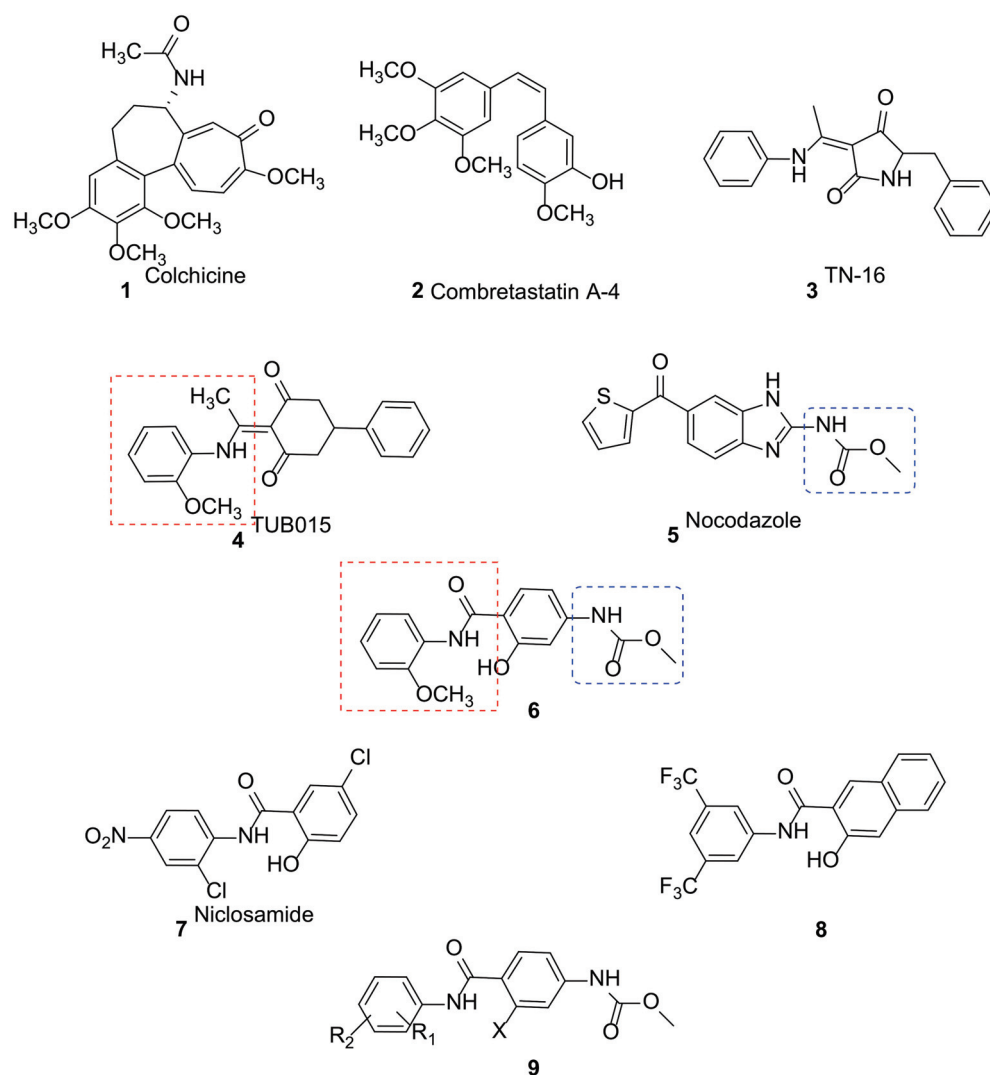
Figure 1. Chemical structures of colchicine-site binders in tubulin (**1**–**5**) and different salicylanilides (**6**–**9**) including niclosamide (**7**) and the here addressed compounds (**6**,**9**).

Our group has been involved in the identification and optimization of new scaffolds that are able to bind at the colchicine site in tubulin. Performing a ligand-based virtual screening approach, using TN-16 (**3**) as the model compound, we identified a series of cyclohexanediones that are potent colchicine-site binders [9]. Recently, the binding mode of these cyclohexanediones [i.e., TUB015 (**4**), Figure 1] into the colchicine site in tubulin has been determined by X-ray diffraction [10]. As expected, the compound binds in a similar way to TN-16 into the deeper part of the β-subunit (Figure 2A). The 5-phenyl ring of the cyclohexanedione is lodged into a cavity lined by residues βIle4, βTyr52, βGln136, βPhe169, βTyr202, βThr239, βLeu242, and βLeu252, among others, while there is a polar interaction between one of the carbonyls of the cyclohexanedione and the side chain of βGlu200. On the other hand, the 2-methoxyaniline of TUB015 is stabilized by hydrophobic interactions. Among the published structures of colchicine ligands with tubulin, nocodazole (**5**, Figure 1) occupies the same deep pocket as TUB015, and, interestingly, it also interacts with βGlu200 (Figure 2B) [11]. Indeed, when the binding modes of TUB015 and nocodazole are superimposed, there is almost a perfect fit, as shown in Figure 2C.

Figure 2. (**A**) X-ray complex structure of TUB015 (**4**, magenta sticks) in tubulin (α-tubulin shown in blue marine and β-tubulin in cyan). (**B**) X-ray complex structure of nocodazole (**5**, violet sticks) in tubulin (α-tubulin is shown in orange and β-tubulin in light orange). (**C**) Superimposition of X-ray structures of TUB015 (**4**) and nocodazole (**5**). Selected residues of the binding pocket are shown in sticks and labeled. Dashed lines represent hydrogen bonds.

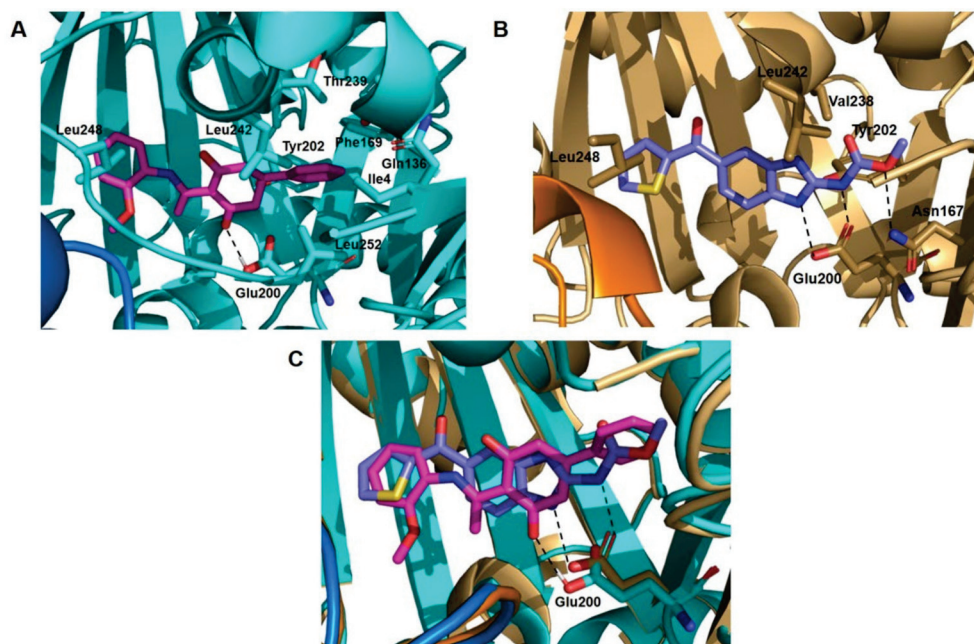In our aim to identify new scaffolds able to bind at the colchicine binding site of tubulin, we designed the hybrid molecule **6** (Figure 1), carrying a methyl carbamate as in nocodazole, an OH able to interact with βGlu200, and a 2-methoxyaniline as in TUB015. The resulting molecule **6** is a salicylanilide that can be structurally considered as a niclosamide analog. Niclosamide (**7**) is extensively studied for anticancer purposes affecting different pathways [12,13]. Among the described activities, niclosamide has been reported to inhibit the cytoplasmic signal transducer and activator of transcription-3 (STAT3) signaling [14,15], a pathway regulating important processes for tumorigenesis such as cell proliferation, cell cycle progression, or apoptosis. While in normal cells the levels of STAT3 remain transient, in a high number of solid tumors and hematological cancers, STAT3 is constitutively active [16]. Cytoplasmic STAT3 is activated through the phosphorylation at residue Tyr705 by Janus associated kinase (JAK) or other kinases, leading to its dimerization and translocation into the nucleus where STAT3 activates the transcription of a wide variety of genes related to cell proliferation and differentiation, immune response, or apoptosis among others [17]. Very recently, niclosamide has been shown to increase the efficacy of PD-1/PD-L1 immune checkpoint by the blockage of phosphorylated STAT3 to the promoter of PD-1 [18], opening new possibilities for cancer immunotherapy through targeting STAT3 [19].

Other salicylanilides based on hydroxynaphthalene carboxamides have also been recently described as STAT3 inhibitors [20]. Interestingly, in this naphthalene series, the best results were obtained with compound **8** (Figure 1), carrying a 3,5-diCF$_3$ aniline. Thus, we hypothesized that compounds with the general structure **9**, with one or two substituents (R$_1$ and R$_2$) at the aniline moiety, including a 3,5-diCF$_3$ substitution, may constitute a new class of antiproliferative agents by combining tubulin-binding at the colchicine site (similar to TUB015) and STAT3 inhibition based on the reported activities for niclosamide and hydroxynaphthalene derivatives exemplified by compound **8**. Additionally, the importance of the phenolic OH in this series has been studied by its replacement with F (**9**, X = F). Besides the synthesis of this new family of salicylanilides, their antiproliferative activity against a panel of cancer cell lines is reported here. Moreover, additional assays have been

performed to propose tubulin and STAT3 signaling as relevant targets that account for the antiproliferative effects.

2. Results and Discussion

2.1. Synthesis

The synthesis of the hybrid molecule **6** was addressed by reaction of 4-amino-2-hydroxybenzoic acid (**10**) with methyl chloroformate in ethyl acetate as reported in other hydroxyanilines [21] to provide a 95% yield of carbamate **11** (Scheme 1). Further reaction of **11** with o-anisidine was performed by heating in toluene to 150 °C under MW irradiation in the presence of PCl_3 [22] to yield the target compound **6**. Similarly, acid **11** reacted with m- or p-anisidine (PCl_3, toluene, 150 °C, MW) to afford the salicylanilides **12** and **13** in 43 and 35% yields, respectively, where the methoxy group is located at positions 3 or 4 in the aniline moiety. In the cyclohexanedione series exemplified by TUB015, the 2-OMe could be replaced by a 2-Cl without a significant loss in antiproliferative activity [9]. Thus, a chlorine substituent was also introduced at positions 2 or 3 of the aniline in the salicylanilide series (compounds **14** and **15**). Compound **14** was obtained by reaction of **11** with 2-chloroaniline in the presence of N,N′-dicyclohexylcarbodiimide in DMF [23] after 20 min of irradiation in the MW at 100 °C, while compound **15** was obtained by the standard procedure with PCl_3.
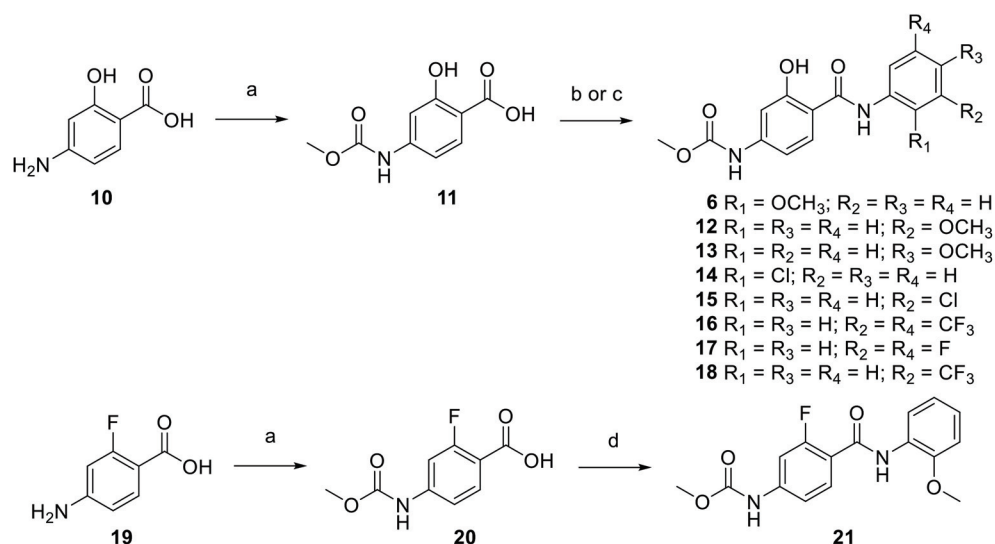
Scheme 1. Reagents and conditions: (a) Methyl chloroformate, ethyl acetate, 80 °C, 1.5–3 h, (**11**, 95% yield; **20**, 62% yield); (b) for **6, 12, 13, 15–17** appropriate aniline, PCl_3, anhydrous toluene, MW: 150 °C, 10 min, (**6**, 27% yield; **12**, 43% yield; **13**, 35% yield; **15**, 34% yield; **16**, 29% yield; **17**, 35% yield); (c) for **14, 18**: appropriate aniline, N,N′-dicyclohexylcarbodiimide, DMF, MW, 100 °C, 20 min (**14**, 35% yield; **18**, 31% yield); (d) o-anisidine, PCl_3, anhydrous toluene, 110 °C, 3 h, 66% yield.

Based on the antiproliferative activity and mechanism of action described for compound **8** [20], the synthesis of **16** was addressed by reaction of **11** with the 3,5-bis-(trifluoromethyl)aniline using PCl_3. Furthermore, the 3,5-bis-fluoro derivative **17** was synthesized following the same approach. As will be later discussed, compound **16** afforded potent antiproliferative activity; thus, the monosubstituted compound with a CF_3 at position 3 (compound **18**) was also synthesized. In all cases (**6, 12–18**), the ^{1}H NMR spectra registered in DMSO-d_6 showed the presence of a broad singlet at 11.66–12.31 ppm corresponding to the phenol, as described for other salicylanilides. [24] Finally, in order to study the influence of the hydroxyl substituent of **6**, the synthesis of the corresponding fluorinated derivative was accomplished. The reaction between 2-fluoro-4-aminobenzoic acid (**19**) and methyl chloroformate provided the acid **20,** which further reacted with o-anisidine to give the benzamide **21** in 66% yield. It should be mentioned that the ^{1}H NMR

spectrum of compound **21** showed the signal corresponding to the NH of the amide as a doublet, with a coupling constant of 11 Hz. By recording a fluorine-decoupled ^{1}H NMR spectrum, this signal was observed as a broad singlet, indicating that the splitting is due to a long-range coupling with the fluorine (see Supplementary Materials). This splitting has been reported in similar compounds [25,26].

2.2. Biological Evaluation

2.2.1. Antiproliferative Activity

The synthesized compounds were evaluated against a panel of cancer cell lines, as shown in Table 1. Compounds TUB015, niclosamide, and nocodazole were included as reference compounds.

Table 1. Antiproliferative activity of the synthesized compounds against different tumor cell lines.

	IC_{50} (μM) [a]						
Comp	**Capan-1** [b]	**HCT-116** [b]	**NCI-H460** [b]	**DND-41** [b]	**HL-60** [b]	**K-562** [b]	**Z-138** [b]
6	1.3 ± 0.1	1.4 ± 3.5	2.8 ± 1.6	1.3 ± 0.5	1.5 ± 0.1	1.3 ± 0.1	1.3 ± 0.7
12	>100	>100	>100	>100	>100	≥84.5	>100
13	35.3 ± 20.1	39.8 ± 25.0	33.3 ± 0.2	≥39.4	37.3 ± 20.4	≥67.8	>100
14	2.5 ± 0.6	10.4 ± 1.6	15.2 ± 6.3	3.8 ± 0.2	9.1 ± 1.9	2.9 ± 1.1	13.5 ± 3.3
15	>100	>100	>100	≥74.1	≥89.6	≥75.8	≥88.4
16	6.9 ± 1.6	4.6 ± 0.07	9.2 ± 3.9	8.7 ± 1.2	4.8 ± 4.5	6.7 ± 2.4	12.2 ± 4.0
17	49.9 ± 28.5	≥47.1	>100	>100	3.3 ± 1.1	35.7 ± 21.0	>100
18	28.0 ± 0.7	71.4 ± 40.4	62.3 ± 12.0	29.9 ± 3.0	68.0 ± 1.4	26.3 ± 13.3	60.2 ± 35.9
21	>100	>100	>100	>100	>100	>100	>100
TUB015	0.06 ± 0.003	1.1 ± 0.3	0.30 ± 0.01	0.40 ± 0.007	0.6 ± 0.1	0.5 ± 0.1	0.1 ± 0.06
Nic [b]	1.35 ± 0.6	0.4 ± 0.3	0.9 ± 0.3	0.45 ± 0.4	2.1 ± 0.6	0.7 ± 0.7	0.3 ± 0.4
Noc [b]	0.018 ± 0.01	0.070 ± 0.04	0.20 ± 0.10	0.21 ± 0.16	0.13 ± 0.09	0.095 ± 0.04	0.088 ± 0.04

[a] IC_{50}: Concentration of compound at which 50% of cell proliferation is inhibited. Mean value of two independent experiments ±SEM. [b] Capan-1: pancreatic adenocarcinoma; HCT-116: colorectal carcinoma; NCI-H460: lung carcinoma; DND-41: acute lymphoblastic leukemia; HL-60: acute myeloid leukemia; K-562: chronic myeloid leukemia; Z-138: non-Hodgkin lymphoma. [b] Nic stands for niclosamide; Noc stands for nocodazole.

Compound **6** showed marked antiproliferative activity against the different cancer cell lines tested, either carcinoma or leukemia cells, with IC_{50} values in the low μM range. Moving the methoxy substituent to position three of the aniline (**12**) resulted in an inactive compound, while the incorporation of the same substituent at position four (**13**) led to moderate antiproliferative activity. A similar trend was observed with the chloro substitution in the aniline, with the 2-Cl derivative (**14**) showing antiproliferative activity in the low μM range while the 3-Cl derivative (**15**) was inactive. Interestingly, the salicylanilide bis-substituted with a trifluoromethyl group at positions 3 and 5 (**16**) also showed clear antiproliferative activity against all the cell lines tested with IC_{50} values in the low μM range, while the 3,5-diF compound (**17**) was barely active against most cell lines tested, except for the HL-60 cell line. The monosubstitution with a CF_3 at position 3 (**18**) led to a significantly less active compound than the 3,5-disubstituted analog **16**. Finally, the replacement of the phenolic OH in compound **6** by an F atom (**21**) resulted in the annulation of the antiproliferative activity.

Thus, compounds **6** and **16** were selected for additional assays in order to gain insights into their mechanism of action as antiproliferative agents.

2.2.2. Inhibition of Tubulin Polymerization

In order to determine whether the observed antiproliferative activity was due to interaction with tubulin, compounds **6** and **16**, as well as controls TUB015, niclosamide, and nocodazole were tested in a cell-free tubulin polymerization assay, as shown in Figure 3A. Polymerization of tubulin is followed by fluorescence enhancement caused by the incorporation of a fluorescent reporter into the microtubules as polymerization occurs. Without

treatment (DMSO control, dashed line), tubulin subunits assemble to form microtubules in a time-dependent manner. Microtubule-destabilizing agents TUB015 and nocodazole prevent tubulin polymerization in a clear dose-dependent manner, with the highest concentration tested (10 μM) completely blocking polymerization (Figure 3A). Compound **6** exhibited a similar dose-dependent effect on tubulin polymerization confirming that compound **6** directly inhibited tubulin polymerization. The highest dose tested (100 μM) fully suppressed polymerization, and 30 and 10 μM also inhibited the polymerization almost completely. At 3 μM, compound **6** slowed down the rate of the polymerization but could not completely suppress it. The IC_{50} value of the effect of compound **6** in tubulin polymerization (3.9 μM) was comparable to those obtained for the positive control compounds TUB015 and nocodazole (Figure 3B). Compound **16** did not show a significant effect on tubulin polymerization, providing curves similar to the DMSO control or the negative control drug niclosamide.
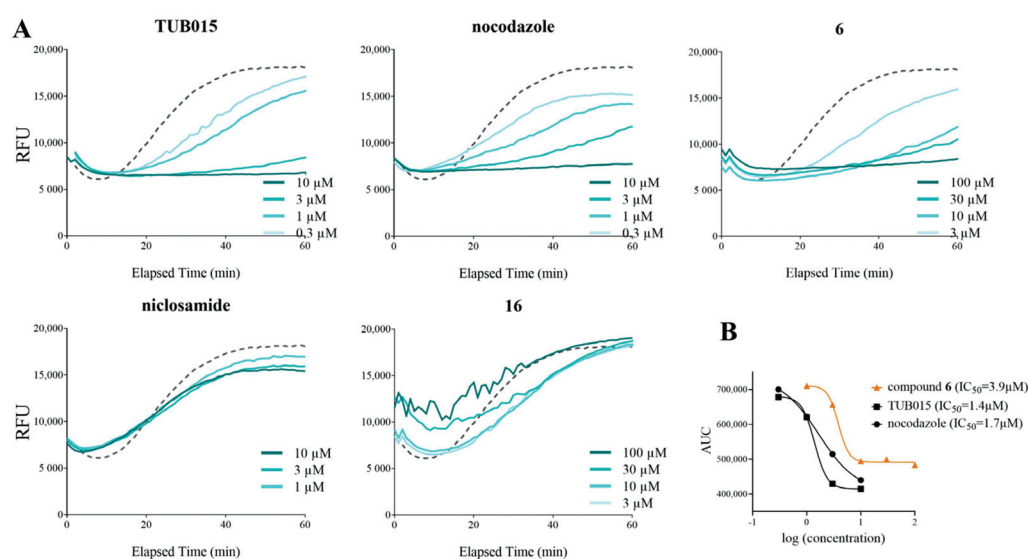

Figure 3. Compound **6** inhibits the rate and extent of tubulin polymerization in vitro. (**A**) Dose dependent effect on in vitro tubulin polymerization in the presence of vehicle (DMSO, dashed line) or a range of concentrations of TUB015 (**4**), nocodazole (**5**), compound **6**, (upper panel), or niclosamide (**7**) and compound **16** (lower panel). All conditions were tested in duplicate, and graphs represent average values of two (*n* = 2) independent experiments. (**B**) The measured IC_{50} values for tubulin polymerization inhibition induced by compound **6**, TUB015 (**4**), and nocodazole (**5**).

Moreover, immunofluorescence staining of α-tubulin in HEp-2 cells illustrated that salicylanilide **6** disrupts tubulin polymerization in a dose-dependent manner, similarly to TUB015 or nocodazole (see Supplementary Figure S1), further supporting that compound **6** promotes tubulin disassembly. Docking studies performed with compound **6** using the coordinates of the TUB015-tubulin complex indicated that the compound fits in this binding site (see Supplementary Figure S2).

2.2.3. Antiproliferative Activity in Human Prostate Cancer Cells DU145

As mentioned in the introduction, niclosamide and other recently reported salicylanilides (exemplified by compound **8**) have been shown to inhibit STAT3 signaling. In order to determine if our salicylanilides **6** and **16** were also interfering with this signaling pathway, proliferation assays were performed in human DU145 prostate cancer cells where STAT3 is constitutively activated [27]. As shown in Table 2, both compounds were able to considerably inhibit DU145 proliferation as determined by WST-1 analysis; this effect was most pronounced after 48 to 72 h. Compound **16** was significantly more active than compound **6** in this cell line, although both compounds showed IC_{50} values higher than those of the reference drug niclosamide.

Table 2. Cell proliferation analysis in DU145 cells. Cell proliferation was determined using WST-1 assay after 24, 48, and 72 h incubation with serial dilutions of tested compounds **6**, **16,** and niclosamide.

Compound	Incubation Time (h)	IC$_{50}$ (µM) [a]
6	24	>30
	48	11.87 ± 0.69
	72	10.81 ± 1.83
16	24	13.67 ± 1.82
	48	1.95 ± 0.63
	72	1.83 ± 0.49
Niclosamide	24	0.94 ± 0.13
	48	0.36 ± 0.12
	72	0.25 ± 0.04

[a] Values shown are the mean ± SD from three independent experiments, each performed in triplicate.

2.2.4. Effects of Compounds **6** and **16** in Regulating STAT3 Signaling Pathway In Vitro

To investigate the effect of compounds **6** and **16** on the regulation of STAT3 signaling, the phosphorylation of STAT3 at Tyr705 was measured in DU145 cells using niclosamide as a positive control. The levels of STAT3 and p-STAT3^{Tyr705} were examined by immunoblot after 24 h or 48 h of treatment to better describe the kinetics of phosphorylation changes induced by the compounds under study. Both compounds were tested at concentrations ranging from 1 to 20 µM for a 24 h incubation period and from 0.5 to 10 µM for a 48 h incubation period, while niclosamide was used at a fixed concentration of 5 µM. Compounds **6** and **16** markedly reduced phosphorylation of STAT3 at Tyr705 in a concentration-dependent manner both after 24 h (Figure 4A) or after 48 h (Figure 4B), while the total expression of STAT3 was not affected.

Figure 4. Compounds **6** and **16** reduced phosphorylation of STAT3 in human prostate cancer cells. DU145 cells were treated with both compounds at indicated concentrations for (**A**) 24 h and (**B**) 48 h. The levels of STAT3 and its phosphorylated form (p-STAT3^{Tyr705}) were detected by immunoblot analysis using appropriate antibodies. Samples treated with 5 µM of niclosamide (Nic) for 24 h and 48 h were used as positive controls. Representative immunoblots of one out of three experiments are shown. CTRL, drug-free control.

The levels of p-STAT3^{Tyr705} were quantified and represented as fold-change relative to control in Figure 5. After treatment with either compound **6** or **16**, p-STAT3^{Tyr705} phosphorylation decreased with time of exposure and concentration of the tested compounds. At both time points (24 h, Figure 5A or 48 h, Figure 5B), the effect on STAT3 phosphorylation was more significant for compound **16** than for **6**. Indeed, the reduction of the levels of p-STAT3^{Tyr705} after 48 h of treatment with compound **16** at 10 µM was very relevant, being quite comparable to the effect observed with niclosamide at 5 µM. Thus, we may conclude

that both compounds are able to reduce STAT3 phosphorylation, and in this way, they might affect STAT3 signaling.
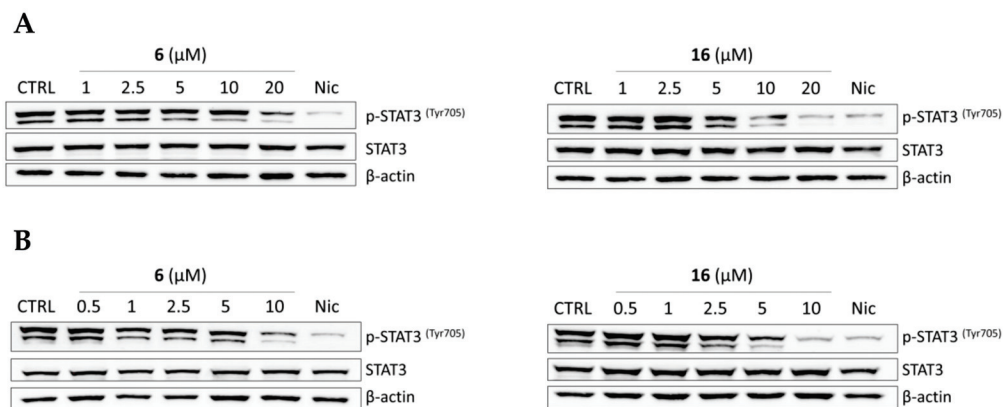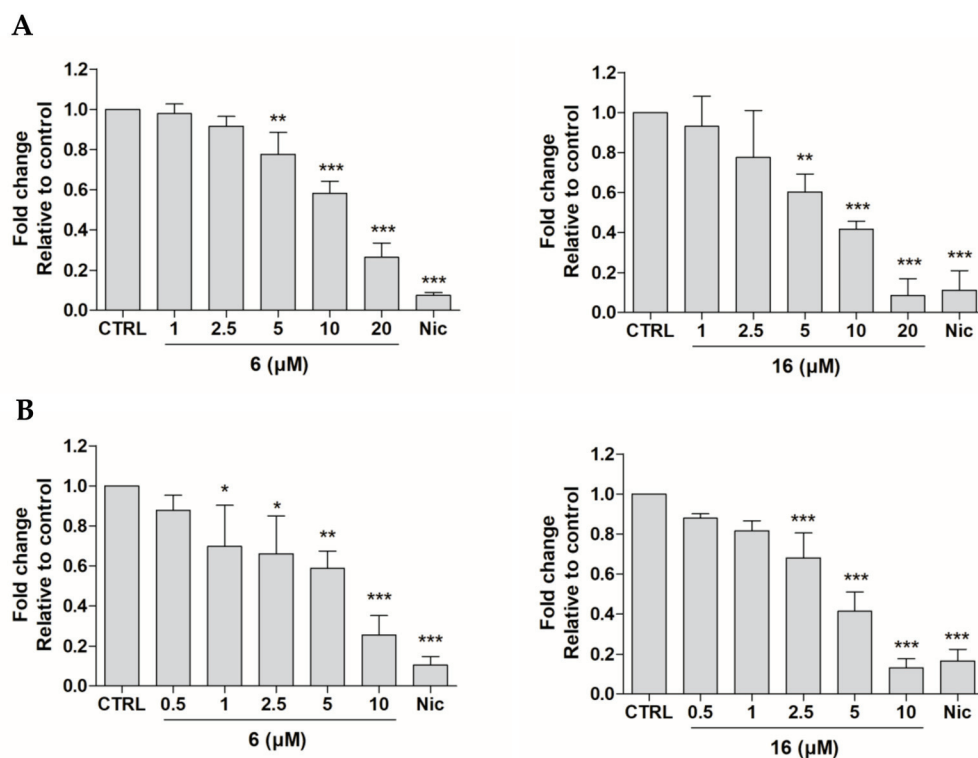

Figure 5. Compounds **6** and **16** reduced phosphorylation of STAT3 in human prostate cancer cells. DU145 cells were treated with both compounds at indicated concentrations for (**A**) 24 h and (**B**) 48 h. The levels of the phosphorylated form (p-STAT3^{Tyr705}) were detected by immunoblot analysis using an appropriate antibody. Samples treated with 5 µM of niclosamide (Nic) for 24 h and 48 h were used as positive controls. Summary data of p-STAT3^{Tyr705} levels, where the values shown are means $\pm$ SD of three independent experiments. The levels of p-STAT3^{Tyr705} protein are expressed in relative units following normalization for the intensity of the corresponding β-actin bands. * $p < 0.05$, ** $p < 0.01$, *** $p < 0.001$, significantly different from drug-free control.

2.2.5. STAT3 Translocation Experiments

Once phosphorylated, STAT3 forms dimers that are translocated to the cell nucleus, where it binds to specific DNA sequences and induces transcription of the target genes [28]. It has been described that niclosamide inhibits the step of phosphorylation of STAT3 and reduces STAT3 nuclear translocation [14]. Our results showed that compound **16,** similarly to niclosamide, suppressed the EGF-induced nuclear translocation of STAT3 in DU145 cells (Figure 6), while the total amount of cellular STAT3 was not affected by any of the tested compounds. Interestingly, only slight suppression of STAT3 nuclear translocation was observed upon treatment by 20 µM of compound **6**. Thus, we can assume that salicylanilide **16**, similar to niclosamide, might interfere with STAT3 signaling by suppressing its translocation into the cell nucleus.
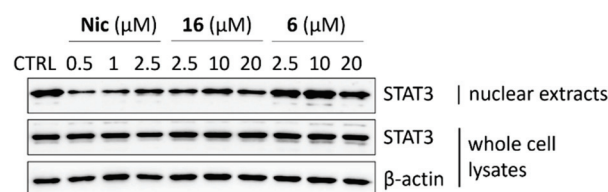
Figure 6. Compound **16** suppresses the EGF-induced nuclear translocation of STAT3 in human prostate cancer cells. Serum-starved DU145 cells were treated with compounds **6** and **16** at indicated concentrations for 2 h. Then the cells were stimulated with EGF (100 ng/mL) for 15 min, and the levels of STAT3 were detected by immunoblot analysis in nuclear extracts and whole cell lysates using an appropriate antibody. Samples treated by indicated concentrations of niclosamide (Nic) for 2 h were used as positive controls. Representative immunoblots of one out of at least three experiments are shown. CTRL, drug-free control.

2.2.6. Effects of Compounds **6** and **16** in Cell Cycle Progression

Since the tested compounds showed an antiproliferative effect in DU145 cells, we further investigated how they affected progression through cell cycle phases. As seen in Figure 7A, compound **6** at 2.5 µM induced accumulation of cells in the G2/M phase as described for TUB015 and similarly to other colchicine site binders [9]. However, compound **16** increased the proportion of cells in G1/G0 phases together with a decrease in the percentage of cells in the S phase (Figure 7B). Similarly, exposure of cells to niclosamide also led to cell accumulation in the G1/G0 phase of the cell cycle (Figure 7C).

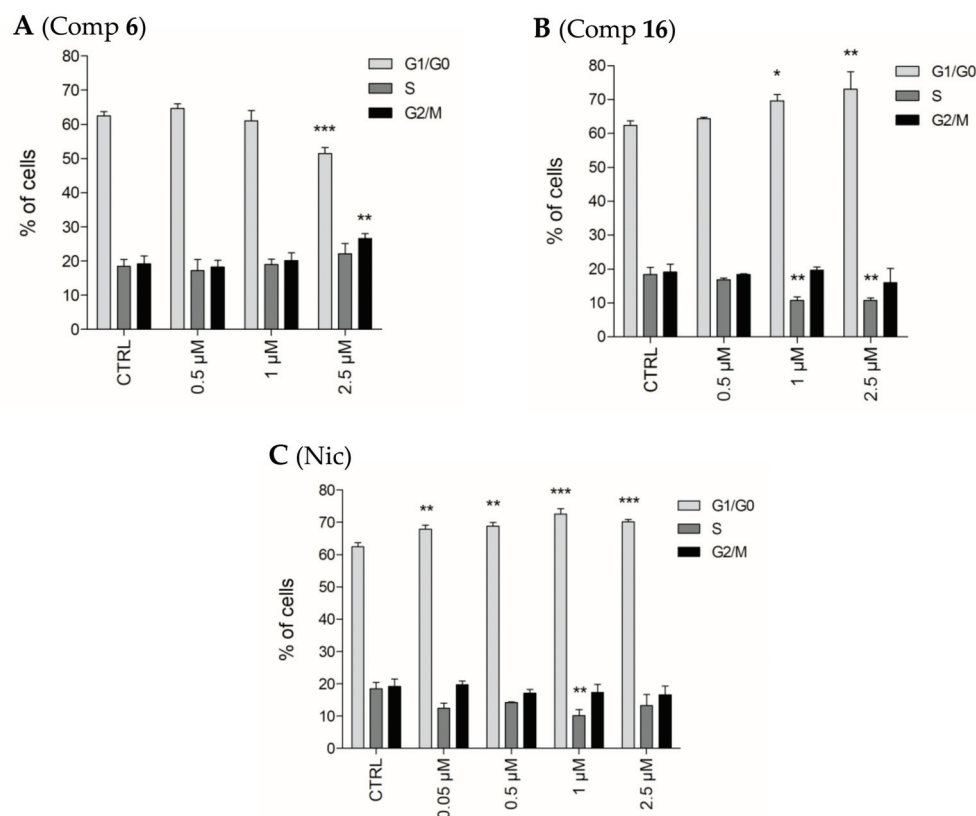**Figure 7.** Distribution of DU145 cells in cell cycle phases after 48 h treatment with each compound. Results are expressed as the mean $\pm$ SD from three independent experiments. * $p < 0.05$, ** $p < 0.01$, *** $p < 0.001$, significantly different from drug-free control (CTRL). (**A**) shows the results obtained with **6**; (**B**), results obtained with **16,** and (**C**) results obtained with niclosamide.

2.2.7. Analysis of Apoptosis Induction in PBMC

Compounds **6**, **16**, TUB015, nocodazole, and niclosamide were tested in peripheral blood mononuclear cells (PBMC) in order to evaluate their selectivity toward non-cancerous cells. Compounds **6** and **16** were tested at five different concentrations ranging up to 100 µM, while for the rest of the compounds, the highest concentration tested was 10 µM. As shown in Figure 8 compound **6** did not affect the viability of normal cells, in line with the profile seen for the other microtubule targeting agents TUB015 and nocodazole. For compound **16,** an increase in the number of dead PBMCs is detected only at the highest concentration tested (100 µM). Still, this slightly toxic effect is lower than that observed with niclosamide at 10 or even 3 µM. These results indicate that compounds that mainly target microtubules showed almost no impact on the percentages of live cells even at high concentrations, while those acting as STAT3 inhibitors showed a higher proportion of dead and apoptotic cells.
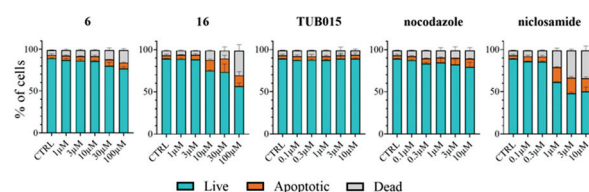

Figure 8. Percentages of live (cyan), apoptotic (orange), and dead (light grey) peripheral blood mononuclear cells (PBMC) after treatment for 72 h with compounds as **6**, **16**, TUB015, nocodazole, and niclosamide at the indicated concentration points. Results are reported as mean ± SD of two (*n* = 2) experiments.

3. Materials and Methods

3.1. Chemistry Procedures

Melting points were measured on an M170 apparatus (Mettler Toledo, Columbus, OH, USA) and are uncorrected. The elemental analysis was performed with a CHN-O-RAPID instrument (Heraus, Hanau, Germany). The elemental compositions of the compounds agreed within ±0.4% of the calculated values.

^{1}H and ^{13}C NMR spectra were recorded on a Varian INNOVA-300 (now Agilent, Santa Clara, CA, USA) operating at 299 MHz (^{1}H) and 75 MHz (^{13}C), respectively, and a Varian INNOVA-400 operating at 399 MHZ (^{1}H) and 99 MHz (^{13}C), respectively, and a VARIAN SYSTEM-500 operating at 499 MHz (^{1}H) and 125 MHz (^{13}C), respectively. Monodimensional ^{1}H and ^{13}C spectra were obtained using standard conditions.

Compounds were also analyzed by HPLC/MS with an e2695 LC (Waters, Milford, MA, USA), coupled to a Waters 2996 photodiode array detector and a Waters Micromass ZQ. The column used is a Waters SunFire C18 2.1 mm × 50 mm, 3.5 µm, and the mobile phases were A: acetonitrile and B: H_2O, together with a constant 5% of C (H_2O with 2% formic acid) to assure 0.1% of formic acid along the run.

Analytical TLC was performed on silica gel 60 F_{254} (Merck, Dramstand, Germany)-precoated plates (0.2 mm). Spots were detected under UV light (254 nm) and/or charring with ninhydrin or phosphomolybdic acid.

Separations on silica gel were performed by preparative centrifugal circular thin-layer chromatography (CCTLC) on a Chromatotron^{R} (Kiesegel 60 PF_{254} gipshaltig Merck), with a layer thickness of 1 and 2 mm and a flow rate of 4 or 8 mL/min, respectively.

The following is the general procedure for the reaction of 2-hydroxybenzoic acids with anilines (General procedure A): the appropriate aniline (1.0–2.0 mmol) in toluene (5–10 mL), PCl_3 (0.5–1.0 mmol) was added to a microwaveable vial containing the corresponding 2-hydroxybenzoic acid (1.0 mmol). The reaction vessel was sealed and heated in a microwave reactor at 150 °C for 10 min. The reaction mixture was diluted with DCM (20 mL) and washed with a saturated solution of NH_4Cl (10 mL). The organic layer was dried over Na_2SO_4, filtered, and evaporated to dryness. The residue was purified by CCTLC in the Chromatotron as specified.

2-Hydroxy-4-((methoxycarbonyl)amino)benzoic acid (**11**)

4-Aminosalicylic acid (**10**) (1 g, 6.53 mmol) was dissolved in ethyl acetate (45 mL). After heating to reflux for 15 min, methyl chloroformate (253 μL, 3.26 mmol) was slowly added. The final mixture was heated to reflux for 1.5 h and cooled. The mixture was filtered, and the filtrate was concentrated to yield 654 mg (95%) of compound **11** as an amorphous white solid. MS (ES, positive mode): m/z 212 (M + H)$^+$. ^{1}H NMR (400 MHz, DMSO-d$_6$) δ: 3.69 (s, 3H, OCH$_3$), 6.97 (dd, J = 8.7, 2.2 Hz, 1H, Ar), 7.15 (d, J = 2.1 Hz, 1H, Ar), 7.68 (d, J = 8.7 Hz, 1H, Ar), 10.00 (br s, 1H, NH), 11.34 (br s, 1H, OH), 13.61 (br s, 1H, COOH).

Methyl (3-hydroxy-4-((2-methoxyphenyl)carbamoyl)phenyl)carbamate (**6**)

Following the general procedure A, the acid **11** (100 mg, 0.47 mmol) and o-anisidine (64 μL, 0.57 mmol) reacted in the presence of PCl$_3$ (41 μL, 0.47 mmol) in anhydrous toluene (4.7 mL). After workup, the residue was purified by CCTLC in the Chromatotron (hexane/ethyl acetate/ammonia solution 30%, 2:1:0.03) to yield 41 mg (27%) of compound **6** as a white solid. Mp 199–201 °C. MS (ES, positive mode): m/z 317 (M + H)$^+$. ^{1}H NMR (400 MHz, DMSO-d$_6$) δ: 3.69 (s, 3H, OCH$_3$), 3.87 (s, 3H, OCH$_3$), 6.95 (m, 1H, Ar), 6.99 (dd, J = 8.7, 2.0 Hz, 1H, Ar), 7.06–7.08 (m, 2H, Ar), 7.34 (d, J = 2.0 Hz, 1H, Ar), 7.91 (d, J = 8.7 Hz, 1H, Ar), 8.35 (d, J = 7.7 Hz, 1H, Ar), 9.92 (br s, 1H, NH), 10.64 (br s, 1H, NH), 11.71 (br s, 1H, OH). ^{13}C NMR (101 MHz, DMSO-d$_6$) δ: 52.3, 56.5 (OCH$_3$), 105.6, 110.1, 111.4, 113.4, 120.8, 121.0, 124.1, 128.5, 131.8, 144.1, 149.1 (Ar), 154.2 (CO), 157.6 (Ar), 163.8 (CO). Analysis calculation for (C$_{16}$H$_{16}$N$_2$O$_5$): C, 60.76; H, 5.10; N, 8.86. Found: C, 60.60; H, 5.01; N, 8.72.

Methyl (3-hydroxy-4-((3-methoxyphenyl)carbamoyl)phenyl)carbamate (**12**)

Following the general procedure A, the acid **11** (200 mg, 0.95 mmol) and m-anisidine (220 μL, 1.89 mmol) reacted in the presence of PCl$_3$ (41 μL, 0.47 mmol) in anhydrous toluene (4.5 mL). After workup, the residue was purified by CCTLC in the Chromatotron (hexane/ethyl acetate/ammonia solution 30%, 1:2:0.03) to yield 132 mg (43%) of compound **12** as a white solid. Mp 196–198 °C. MS (ES, positive mode): m/z 317 (M + H)$^+$. ^{1}H NMR (400 MHz, DMSO-d$_6$) δ: 3.69 (s, 3H, OCH$_3$), 3.76 (s, 3H, OCH$_3$), 6.71 (dt, J = 7.6, 2.2 Hz, 1H, Ar), 7.01 (dd, J = 8.9, 2.1 Hz, 1H, Ar), 7.19–7.29 (m, 3H, Ar), 7.37 (br s, 1H, Ar), 7.91 (d, J = 8.8 Hz, 1H, Ar), 9.94 (br s, 1H, NH), 10.20 (br s, 1H, NH), 12.08 (br s, 1H, OH). ^{13}C NMR (101 MHz, DMSO-d$_6$) δ: 52.3, 55.5 (OCH$_3$), 105.8, 107.1, 109.4, 110.0, 111.4, 113.6, 129.9, 130.2, 139.8, 144.7 (Ar), 154.2 (CO), 159.9, 160.3 (Ar), 167.0 (CO). Analysis calculation for (C$_{16}$H$_{16}$N$_2$O$_5$·0.5H$_2$O): C, 59.07; H, 5.27; N, 8.61. Found: C, 59.20; H, 5.57; N, 8.40.

Methyl (3-hydroxy-4-((4-methoxyphenyl)carbamoyl)phenyl)carbamate (**13**)

Following the general procedure A, the acid **11** (100 mg, 0.47 mmol) and p-anisidine (116 mg, 0.95 mmol) reacted in the presence of PCl$_3$ (41 μL, 0.47 mmol) in anhydrous toluene (4 mL). After workup, the residue was purified by CCTLC in the Chromatotron (hexane/ethyl acetate/ammonia solution 30%, 1:1:0.02) to yield 52 mg (35%) of compound **13** as a pale yellow solid. Mp 203–205 °C. MS (ES, positive mode): m/z 317 (M + H)$^+$. ^{1}H NMR (400 MHz, DMSO-d$_6$) δ: 3.69 (s, 3H, OCH$_3$), 3.75 (s, 3H, OCH$_3$), 6.94 (d, J = 9.0 Hz, 2H, Ar), 7.00 (dd, J = 8.8, 2.1 Hz, 1H, Ar), 7.18 (d, J = 2.1 Hz, 1H, Ar), 7.56 (d, J = 9.0 Hz, 2H, Ar), 7.92 (d, J = 8.8 Hz, 1H, Ar), 9.92 (br s, 1H, NH), 10.12 (br s, 1H, NH), 12.31 (br s, 1H, OH). ^{13}C NMR (101 MHz, DMSO-d$_6$) δ: 52.3, 55.7 (OCH$_3$), 105.8, 109.3, 110.8, 114.3 123.4, 129.7, 131.4, 144.6 (Ar), 154.2 (CO), 156.4, 160.9 (Ar), 167.2 (CO). Analysis calculation for (C$_{16}$H$_{16}$N$_2$O$_5$): C, 60.76; H, 5.10; N, 8.86. Found: C, 60.69; H, 5.02; N, 8.77.

Methyl (4-((2-chlorophenyl)carbamoyl)-3-hydroxyphenyl)carbamate (**14**)

To a mixture of compound **11** (80 mg, 0.38 mmol), 2-chloroaniline hydrochloride (124 mg, 0.76 mmol) and triethylamine (106 μL, 0.76 mmol) in anhydrous DMF (1.5 mL) in a microwaveable vial, DCC (156 mg, 0.76 mmol) was added. The reaction vessel was sealed and heated in a microwave reactor at 100 °C for 20 min. The solvent was removed, and the residue was dissolved in ethyl acetate (20 mL) and washed with a saturated solution of NH$_4$Cl (10 mL). The organic layer was dried over Na$_2$SO$_4$, filtered, and evaporated to dryness. The residue was purified by CCTLC in the Chromatotron (hexane/ethyl acetate, 3:1) to yield 42 mg (35%) of compound **14** as a white solid. Mp 197–199 °C. MS (ES, positive mode): m/z 321 (M + H)$^+$. ^{1}H NMR (400 MHz, DMSO-d$_6$) δ: 3.69 (s, 3H, OCH$_3$), 7.01 (dd,

J = 8.7, 2.1 Hz, 1H, Ar), 7.15 (td, J = 7.7, 1.6 Hz, 1H, Ar), 7.34–7.40 (m, 2H, Ar), 7.54 (dd, J = 8.0, 1.5 Hz, 1H, Ar), 7.93 (d, J = 8.7 Hz, 1H, Ar), 8.38 (dd, J = 8.3, 1.6 Hz, 1H, Ar), 9.97 (br s, 1H, NH), 10.76 (br s, 1H, NH), 11.97 (br s, 1H, OH). ^{13}C NMR (101 MHz, DMSO-d$_6$) δ: 52.3 (OCH$_3$), 105.6, 110.2, 112.6, 123.3, 123.9, 125.4, 128.3, 129.8, 131.8, 135.9, 144.6 (Ar), 154.2 (CO), 158.0 (Ar), 164.4 (CO). Analysis calculation for (C$_{15}$H$_{13}$ClN$_2$O$_4$·H$_2$O): C, 53.19; H, 4.46; N, 8.27. Found: C, 53.23; H, 4.37; N, 8.24.

Methyl (4-((3-chlorophenyl)carbamoyl)-3-hydroxyphenyl)carbamate (**15**)

Following the general procedure A, the acid **11** (70 mg, 0.33 mmol) and 3-chloroaniline (70 μL, 0.66 mmol) reacted in the presence of PCl$_3$ (14 μL, 0.17 mmol) in anhydrous toluene (1.7 mL). After workup, the residue was purified by CCTLC in the Chromatotron (DCM/ethyl acetate, 20:1) to yield 36 mg (34%) of **15** as a white solid. Mp 213–215 °C. MS (ES, positive mode): m/z 321 (M + H)$^+$ with a Cl isotopic pattern. ^{1}H NMR (400 MHz, DMSO-d$_6$) δ: 3.69 (s, 3H, OCH$_3$), 7.01 (dd, J = 8.8, 2.1 Hz, 1H, Ar), 7.18 (dd, J = 8.0, 2.1 Hz, 1H, Ar), 7.24 (d, J = 2.1 Hz, 1H, Ar), 7.38 (t, J = 8.1 Hz, 1H, Ar), 7.59 (dd, J = 8.1, 2.0 Hz, 1H, Ar), 7.86–7.93 (m, 2H, Ar), 9.97 (br s, 1H, NH), 10.34 (br s, 1H, NH), 11.91 (br s, 1H, OH). ^{13}C NMR (101 MHz, DMSO-d$_6$) δ: 52.4 (OCH$_3$), 105.7, 109.5, 111.4, 119.6, 120.7, 124.1, 130.3, 130.8, 133.5, 140.2, 144.8 (Ar), 154.2 (CO), 160.1 (Ar), 167.0 (CO). Analysis calculation for (C$_{15}$H$_{13}$ClN$_2$O$_4$): C, 56.17; H, 4.09; N, 8.73. Found: C, 56.05; H, 3.95; N, 8.67.

Methyl (4-((3,5-bis(trifluoromethyl)phenyl)carbamoyl)-3-hydroxyphenyl) carbamate (**16**)

Following the general procedure A, **11** (80 mg, 0.38 mmol) and 3,5-bis (trifluoromethyl) aniline (61 μL, 0.38 mmol) reacted in the presence of PCl$_3$ (31 μL, 0.38 mmol) in anhydrous toluene (3.8 mL). After workup, the residue was purified by CCTLC in the Chromatotron (hexane/ethyl acetate/ammonia solution 30%, 2:1:0.02) to yield 47 mg (29%) of compound **16** as a white solid. Mp 228–230 °C. MS (ES, positive mode): m/z 423 (M + H)$^+$. ^{1}H NMR (400 MHz, DMSO-d$_6$) δ: 3.70 (s, 3H, OCH$_3$), 7.03 (dd, J = 8.7, 2.1 Hz, 1H, Ar), 7.28 (d, J = 2.2 Hz, 1H, Ar), 7.81 (s, 1H, Ar), 7.87 (d, J = 8.7 Hz, 1H, Ar), 8.44 (s, 2H, Ar), 9.99 (br s, 1H, NH), 10.70 (br s, 1H, NH), 11.66 (br s, 1H, OH). ^{13}C NMR (101 MHz, DMSO-d$_6$) δ: 52.4 (OCH$_3$), 105.7, 109.6, 111.5 (Ar), 117.0 (m, C4'), 187.4 (q, CF$_3$), 120.9 (d, J = 4.6 Hz, C2'/C6'), 130.5 (Ar), 131.3 (q, J = 33.1 Hz, C3'/C5'), 140.9, 145.1 (Ar), 154.2 (CO), 160.0 (Ar), 167.3 (CO). Analysis calculation for (C$_{17}$H$_{12}$F$_6$N$_2$O$_4$): C, 48.35; H, 2.86; N, 6.63. Found: C, 47.98; H, 3.14; N, 6.47.

Methyl (4-((3,5-difluorophenyl)carbamoyl)-3-hydroxyphenyl)carbamate (**17**)

Following the described procedure A, **11** (80 mg, 0.38 mmol) and 3,5-difluoroaniline (50 mg, 0.38 mmol) reacted in the presence of PCl$_3$ (31 μL, 0.38 mmol) in anhydrous toluene (3.8 mL). After workup, the residue was purified by CCTLC in the Chromatotron (hexane/ethyl acetate/ammonia solution 30%, 2:1:0.02) to yield 42 mg (35%) of compound **17** as a white solid. Mp 231–233 °C. MS (ES, positive mode): m/z 323 (M + H)$^+$. ^{1}H NMR (400 MHz, DMSO-d$_6$) δ: 3.69 (s, 3H, OCH$_3$), 6.96 (tt, 6.96 (tt, J$_{H,F}$ = 9.3 Hz, J$_{H,H}$ = 2.5 Hz, 1H1H, Ar), 7.01 (dd, J = 8.7, 2.1 Hz, 1H, Ar), 7.26 (d, J = 2.1 Hz, 1H, Ar), 7.49 (dd, J$_{H,F}$ = 9.3 Hz, J$_{H,H}$ = 2.4 Hz 2H, Ar), 7.84 (d, J = 8.7 Hz, 1H, Ar), 9.96 (br s, 1H, NH), 10.45 (br s, 1H, NH), 11.73 (br s, 1H, OH). ^{13}C NMR (101 MHz, DMSO-d$_6$) δ: 52.3 (OCH$_3$), 99.3 (t, J = 26.2 Hz, C4'), 103.8 (m, C2'/C6'), 105.7, 109.6, 111.8, 130.6 (Ar), 141.4 (t, J = 13.8 Hz, C1'), 144.9 (Ar), 154.2 (CO), 159.7 (Ar), 162.8 (dd, J = 242.8, 15.2 Hz, C3'/C-5'), 166.8 (CO). Analysis calculation for (C$_{15}$H$_{12}$N$_2$O$_4$): C, 55.91; H, 3.75; N, 8.69. Found: C, 55.79; H, 3.60; N, 8.58.

Methyl (3-hydroxy-4-((3-(trifluoromethyl)phenyl)carbamoyl)phenyl)carbamate (**18**)

Following a synthetic procedure similar to the one described for **14**, the acid **11** (60 mg, 0.28 mmol) and 3-(trifluoromethyl)aniline (71 μL, 0.57 mmol) reacted in the presence of DCC (117 mg, 0.57 mmol) in anhydrous DMF (1.1 mL). After workup, the residue was purified by CCTLC in the Chromatotron (DCM/ethyl acetate, 20:1). The fractions containing the compound were evaporated and the residue obtained was purified by CCTLC in the Chromatotron (hexane/ethyl acetate 1:1) to yield 31 mg (31%) of compound **18** as a white solid. Mp (decomp at 212 °C). MS (ES, positive mode): m/z 355 (M + H)$^+$. ^{1}H NMR (400 MHz, DMSO-d$_6$) δ: 3.69 (s, 3H, OCH$_3$), 7.02 (dd, J = 8.8, 2.1 Hz, 1H, Ar), 7.25 (d,

J = 2.1 Hz, 1H, Ar), 7.47 (d, J = 7.8 Hz, 1H, Ar), 7.60 (t, J = 8.0 Hz, 1H, Ar), 7.87–7.96 (m, 2H, Ar), 8.19 (t, J = 2.0 Hz, 1H, Ar), 9.99 (br s, 1H, NH), 10.47 (br s, 1H, NH), 11.89 (br s, 1H, OH). ^{13}C NMR (101 MHz, DMSO-d$_6$) δ: 52.4 (OCH$_3$), 105.8, 109.6, 111.5, 117.4 (q, J = 4.1 Hz, Ar), 120.8 (d, J = 4.0 Hz, Ar), 124.7 (q, J = 272.4 Hz, CF$_3$), 124.9 (Ar), 129.8 (q, J = 31.8 Hz, Ar), 130.5, 139.7, 145.0 (Ar), 154.3 (CO), 160.3 (Ar), 167.3 (CO). Analysis calculation for (C$_{16}$H$_{13}$F$_3$N$_2$O$_4$): C, 54.24; H, 3.70; N, 7.91. Found: C, 54.23; H, 3.62; N, 7.99.

2-Fluoro-4-((methoxycarbonyl)amino)benzoic acid (**20**)

As described for the synthesis of compound **11**, a mixture of 4-amino-2-fluorobenzoic acid (**19**) (500 mg, 3.2 mmol) and methyl chloroformate (126 μL, 1.6 mmol) in ethyl acetate (23 mL) was refluxed for 3 h. The reaction was filtered, and the filtrate was concentrated to yield 422 mg (62%) of compound **20** as an amorphous white solid. MS (ES, negative mode): m/z 212 (M−H)$^-$. ^{1}H NMR (400 MHz, DMSO-d$_6$) δ: 3.71 (s, 3H, OCH$_3$), 7.29 (dd, J = 8.7, 2.1 Hz, 1H, Ar), 7.45 (dd, J = 13.7, 2.1 Hz, 1H, Ar), 7.82 (t, J = 8.6 Hz, 1H, Ar), 10.23 (br s, 1H, NH), 12.90 (br s, 1H, OH).

Methyl (3-fluoro-4-((2-methoxyphenyl)carbamoyl)phenyl)carbamate (**21**)

Adapting the general procedure A, to a mixture of compound **20** (100 mg, 0.47 mmol) and o-anisidine (66 μL, 0.56 mmol) in anhydrous toluene (2.5 mL) in a pressure flask, PCl$_3$ was added (83 μL, 0.94 mmol). The reaction was stirred and heated to 110 °C for 3 h. The reaction mixture was dissolved in DCM (20 mL) and washed with HCl 1M (10 mL) and NaCl (10 mL). The organic layer was dried over Na$_2$SO$_4$, filtered and evaporated to dryness. The residue was purified by column chromatography on silica gel (DCM/MeOH, 20:1) to yield 99 mg (66% yield) of compound **21** as a white solid. Mp 216–218 °C. MS (ES, positive mode): m/z 319 (M + H)$^+$. ^{1}H NMR (400 MHz, DMSO-d$_6$) δ: 3.71 (s, 3H, OCH$_3$), 3.87 (s, 3H, OCH$_3$), 6.96 (ddd, J = 7.9, 6.6, 2.2 Hz, 1H, Ar), 7.06–7.16 (m, 2H, Ar), 7.34 (dd, J = 8.7, 2.1 Hz, 1H, Ar), 7.53 (dd, J = 14.7, 2.0 Hz, 1H, Ar), 7.86 (t, J = 8.8 Hz, 1H, Ar), 8.20 (d, J = 8.0 Hz, 1H, Ar), 9.24 (d, J = 11.3 Hz, NH), 10.23 (br s, 1H, NH). ^{13}C NMR (101 MHz, DMSO-d$_6$) δ: 52.6, 56.5 (OCH$_3$), 105.2 (d, J = 29.9 Hz), 111.6, 114.5 (d, J = 2.5 Hz), 115.8 (d, J = 12.5 Hz), 121.0, 121.2, 125.0, 127.7, 132.3 (d, J = 3.7 Hz), 144.6 (d, J = 12.3 Hz), 149.4 (Ar), 154.2 (CO), 160.6 (d, J = 244.8 Hz, Ar), 161.5 (CO). Analysis calculation for (C$_{16}$H$_{15}$FN$_2$O$_4$): C, 60.37; H, 4.75; N, 8.80. Found: C, 60.21; H, 4.82; N, 8.64.

3.2. Biological Assays

3.2.1. Cell Culture and Reference Compounds

Cancer cell lines Capan-1, HCT-116, NCI-H460, HL-60, K-562, and Z-138 were acquired from the American Type Culture Collection (ATCC, Manassas, VA, USA). The DND-41 cell line was purchased from the Deutsche Sammlung von Mikroorganismen und Zellkulturen (DSMZ Leibniz-Institut, Brunswick, Germany). All cell lines were cultured as recommended by the suppliers. Culture media were purchased from Gibco Life Technologies and supplemented with 10% fetal bovine serum (HyClone, GE Healthcare Life Sciences, Chicago, IL, USA).

A human prostate cancer cell line DU145 was obtained from ATCC and cultivated in RPMI 1640 supplemented with the antibiotic solution (100 U/mL of penicillin, 100 μg/mL of streptomycin (HyClone, GE Healthcare Life Sciences, Chicago, IL, USA), and 10% fetal bovine serum. Cells were maintained in a humidified incubator with 5% CO$_2$ at 37 °C and were regularly tested for the presence of mycoplasma contamination.

TUB015 was obtained as previously described [9]. Niclosamide was purchased from Acros (Acros Organics, Geel, Belgium) and Abcam (Cambridge, UK), and nocodazole from TCI (TCI Chemicals, Zwijndrecht, Belgium).

Tested compounds were dissolved in dimethyl sulfoxide (DMSO) from Sigma Aldrich (St. Louis, MO, USA). The final concentration of DMSO in the assays never exceeded 0.1% (*v/v*).

3.2.2. Cell Proliferation Assays

Adherent cell lines HCT-116, NCI-H460, and Capan-1 cells were seeded at a density between 500 and 1500 cells per well in 384-well tissue culture plates (Greiner). After overnight incubation, cells were treated with different concentrations of the test compounds. Suspension cell lines HL-60, K-562, Z-138, and DND-41 were seeded at densities ranging from 2500 to 5500 cells per well in 384-well culture plates containing the test compounds at the same concentration points. The plates were incubated and monitored at 37 °C for 72 h in an IncuCyte (Essen BioScience Inc., Sartorius; Göttingen, Germany for real-time imaging of cell proliferation. Brightfield images were taken every 3 h, with one field imaged per well under 10× magnification. Cell growth was then quantified based on the percent cellular confluence, as analyzed by the IncuCyte image analysis software and used to calculate IC_{50} values. Compounds were tested in at least two independent experiments and represented as mean ± SEM.

3.2.3. WST-1 Analysis of Cell Proliferation

DU145 cells were seeded at 7×10^3 cells/100 µL per well in 96-well plates and allowed to attach to the wells for 24 h. Cells were then treated with various concentrations of compound **6** or **16** to reach the final concentration range of 0.1–30 µM, and with various concentrations of niclosamide to reach the final concentration range of 0.01–10 µM. Cells were then incubated for 24 h, 48 h, or 72 h. Cell proliferation of DU145 cells was determined using Cell Proliferation Reagent WST-1 (2-(4-iodophenyl)-3-(4-nitrophenyl)-5-(2,4-disulfophenyl)-2H-tetrazolium) (Roche Diagnostics, Mannheim, Germany), as it was previously described [29,30]. WST-1 analysis was performed in three independent experiments, with each condition tested in triplicate. The IC_{50} values were determined using the nonlinear regression four-parameter logistic model using GraphPad Prism 5.03 software (GraphPad Software, San Diego, CA, USA).

3.2.4. In Vitro Tubulin Polymerization Assay

In vitro tubulin polymerization was carried out using the fluorescence-based tubulin polymerization assay (BK011P, Cytoskeleton, Denver, CO, USA) as described by the manufacturer. Briefly, half area 96-well plates were warmed to 37 °C 10 min prior to assay start. Test compounds and reference drugs were prepared at 10× stock solutions and added in 5 µL in duplicate wells. Ice-cold tubulin polymerization buffer (2 mg mL^{-1} tubulin in 80 nM Pipes, 2 mM MgCl$_2$, 0.5 mM EGTA, pH 6.9, and 10 µM fluorescent reporter + 15% glycerol + 1 mM GTP) was added into each well, followed by reading with a Tecan Spark fluorimeter in kinetic mode, 61 cycles of 1 reading per minute at 37 °C, 4 reads per well (Ex. 350 nm and Em. 435 nm).

3.2.5. Tubulin Immunofluorescence Staining

HEp-2 cells (human cervix carcinoma) were seeded at 15,000 c/well in 8-well chamber slides (Ibidi). After overnight incubation, cells were treated with test compounds or reference drugs for 3 h and then fixed with 4% PFA, washed, and permeabilized. Standard immunofluorescence procedures were performed using primary mouse anti-alpha tubulin antibody (sc-5286, Santa Cruz Biotechnology) and secondary goat anti-mouse IgG conjugated to Alexa Fluor® 488 (A11001, Invitrogen). Nuclei were counterstained with DAPI. Images were taken with a Leica TCS SP5 confocal microscope using an HCX PL APO 63x (NA 1.2)/water immersion objective.

3.2.6. Western Blotting

Cell lysates were prepared using radioimmunoprecipitation assay (RIPA) buffer supplemented with phenylmethanesulfonylfluoride (PMSF, 1 mM), both from Cell Signaling Technology (Danvers, MA, USA) and protease and phosphatase inhibitor cocktails (Roche Diagnostics, Mannheim, Germany). SDS-PAGE and western blotting were performed according to the previously described protocols [20]. Membranes were stained with

anti-β-actin antibody (Santa Cruz Biotechnology, Santa Cruz, CA, USA) to assess equal sample loading. Antibodies against STAT3 (79D7, 4904) and p-STAT3 [Tyr 705] (D3A7, 9145) were purchased from Cell Signaling Technology. The intensity of bands was semi-quantitatively analyzed using the ImageJ software (National Institute of Mental Health, Bethesda, MD, USA).

3.2.7. Analysis of STAT3 Nuclear Translocation

DU145 cells were serum-starved overnight and treated with the indicated concentrations of compounds **6**, **16,** and niclosamide for 2 h. After that, the cells were stimulated with 100 ng/mL EGF (Abcam, Cambridge, UK) for 15 min. Nuclear extracts were prepared using Nuclear Extraction Kit (Abcam, Cambridge, UK) according to the manufacturer's instructions. Whole cell lysates were prepared by use of RIPA buffer supplemented with PMSF (1 mM) and protease and phosphatase inhibitor cocktails. DU145 cells were detached with trypsin/EDTA and counted with a hemocytometer. For nuclear extract preparation, cells were centrifuged for 5 min at 1000 rpm, and the supernatant was discarded. The cell pellet was resuspended in 100 µL of 1X Pre-Extraction Buffer per 10^6 cells and incubated on ice for 10 min. Then, samples were centrifuged for 1 min at 12,000 rpm, and the cytoplasmic extract was removed from the nuclear pellet. Extraction Buffer containing DTT and PIC was added to the nuclear pellet (10 µL per 10^6 cells). After 15 min of incubation on ice, samples were centrifuged for 10 min at 14,000 rpm at 4 °C. Then, supernatants were collected, and the protein concentration of the nuclear extracts was measured using Roti®-Quant universal (Carl Roth, Karlsruhe, Germany) according to the manufacturer's instructions. Western blotting was performed according to the previously described protocol [20].

3.2.8. Cell Cycle Analysis

Sub-confluent DU145 cells were treated and subsequently incubated with indicated concentrations of compounds **6**, **16,** and niclosamide for 48 h. Cell cycle analysis was performed as it was previously described [29]. The cell cycle distribution was analyzed using a flow cytometer BriCyte-E6 (Mindray, Shenzhen, China). The quantification of cell cycle distribution was carried out using the software ModFit LT™ (Verity Software House, Topsham, ME, USA). A total number of 2×10^4 cells were analyzed per sample.

3.2.9. Statistical Analysis

Experimental data are expressed as the mean ± standard deviation (SD). Statistical significance between values was evaluated by one-way analysis of variance (ANOVA) paired with Dunnett's post hoc test using GraphPad Prism 5.00 software (GraphPad Software, San Diego, CA, USA) at levels of * $p < 0.05$, ** $p < 0.01$ and *** $p < 0.001$.

3.2.10. Apoptosis Induction Assay

Buffy coat preparations from healthy donors were obtained from the Blood Transfusion Center in Leuven, Belgium. Peripheral blood mononuclear cells (PBMC) were isolated by density gradient centrifugation over Lymphoprep (d = 1.077 g/mL) (Nycomed, Oslo, Norway) and cultured in cell culture medium (DMEM/F12, Gibco Life Technologies, Europe, Merelbeke, Belgium) containing 8% FBS. PBMC were seeded at 28,000 cells per well in 384-well, black-walled, clear-bottomed tissue culture plates containing the test and reference compounds at five different concentrations. Propidium iodide was added at a final concentration of 1 µg/mL, and IncuCyte® Annexin V Green Reagent was added as recommended by the supplier. The plates were incubated and monitored at 37 °C for 72 h in the IncuCyte®. Images were taken every 3 h in the brightfield and the green and red fluorescence channels, with one field imaged per well under 10× magnification. Quantification of the fluorescent signal after 72 h in both channels using the IncuCyte® image analysis software allowed for the calculation of the percentage of live, dead, and apoptotic cells. All compounds were tested in two independent experiments, implying PBMC originated from two different donors.

4. Conclusions

Molecular hybridization is considered an interesting approach in drug design to identify new compounds that may present dual modes of action while reducing non-desired side effects. Here we have undertaken a double strategy based on the binding mode of our cyclohexanediones, exemplified by TUB015, at the colchicine site in tubulin and its almost perfect overlap with the binding mode of nocodazole, in the search for novel chemical series that inhibit tubulin polymerization and affect STAT3 signaling. First, we have identified a central core of salicylanilide that could replace the cyclohexanedione of TUB015, employing a scaffold hopping strategy, while the functionalization of both ends of this scaffold has been performed following a hybridization approach incorporating a methoxycarbonylamino, present in nocodazole and a 2-methoxyphenylamino, similar to TUB015, resulting in compound **6**. Since salicylanilides, including niclosamide, have been reported to inhibit STAT3, different anilines were also assayed to replace the 2-methoxyaniline, being particularly relevant for compound **16,** functionalized with a 3,5-diCF$_3$-anilide. Compounds **6** and **16**, which showed antiproliferative activity against a panel of cancer cell lines with IC$_{50}$ values in the low μM range, were tested as tubulin polymerization inhibitors (similarly to TUB015) and as STAT3 inhibitors, using niclosamide as a reference compound. Interestingly, compound **6**, with a 2-methoxyaniline as the amidine, inhibited tubulin polymerization with IC$_{50}$ values close to those of nocodazole or TUB015 and arrested the cell cycle of DU145 cells at G2/M but also showed a moderate effect on inhibiting STAT3 phosphorylation. On the other hand, compound **16**, with a 3,5-diCF$_3$-anilide, significantly affected STAT3 phosphorylation, inhibited STAT3 nuclear translocation, and arrested the cell cycle at G0/G1 phases, similar to niclosamide, while no effect on tubulin polymerization was observed. Thus, the substitution pattern on the aniline on the same scaffold determines the mechanism of action underlying the antiproliferative activity of this new family of salicylanilides. Interestingly, both compounds did not show significant toxicity to PBMC cells up to 100 μM, while for niclosamide there are dead and apoptotic cells already at concentrations of 1 to 3 μM. The lack of toxicity in PBMC and the involvement of two different and complementary targets in their antiproliferative activity makes these salicylanilides a promising family of anticancer compounds that will be further explored. Moreover, our results also support the general strategy that molecular hybridization may lead to new molecules being able to achieve high efficacy through a multi-target mechanism of action whilst also reducing toxicity.

References

1. Bates, D.; Eastman, A. Microtubule Destabilising Agents: Far More than Just Antimitotic Anticancer Drugs. *Br. J. Clin. Pharmacol.* **2017**, *83*, 255–268. [CrossRef]
2. Leung, Y.Y.; Yao Hui, L.L.; Kraus, V.B. Colchicine—Update on Mechanisms of Action and Therapeutic Uses. *Semin. Arthritis Rheum.* **2015**, *45*, 341–350. [CrossRef] [PubMed]
3. Reyes, A.Z.; Hu, K.A.; Teperman, J.; Wampler Muskardin, T.L.; Tardif, J.-C.; Shah, B.; Pillinger, M.H. Anti-Inflammatory Therapy for COVID-19 Infection: The Case for Colchicine. *Ann. Rheum. Dis.* **2021**, *80*, 550–557. [CrossRef] [PubMed]
4. Colchicine. COVID-19 Treatment Guidelines. Available online: https://www.covid19treatmentguidelines.nih.gov/therapies/immunomodulators/colchicine/ (accessed on 22 February 2022).
5. Greene, L.M.; Meegan, M.J.; Zisterer, D.M. Combretastatins: More than Just Vascular Targeting Agents? *J. Pharmacol. Exp. Ther.* **2015**, *355*, 212–227. [CrossRef] [PubMed]
6. Pérez-Pérez, M.-J.; Priego, E.-M.; Bueno, O.; Martins, M.S.; Canela, M.-D.; Liekens, S. Blocking Blood Flow to Solid Tumors by Destabilizing Tubulin: An Approach to Targeting Tumor Growth. *J. Med. Chem.* **2016**, *59*, 8685–8711. [CrossRef]
7. McLoughlin, E.C.; O'Boyle, N.M. Colchicine-Binding Site Inhibitors from Chemistry to Clinic: A Review. *Pharmaceuticals* **2020**, *13*, 8. [CrossRef]
8. Lu, Y.; Chen, J.; Xiao, M.; Li, W.; Miller, D.D. An Overview of Tubulin Inhibitors That Interact with the Colchicine Binding Site. *Pharm. Res.* **2012**, *29*, 2943–2971. [CrossRef]
9. Canela, M.-D.; Pérez-Pérez, M.-J.; Noppen, S.; Sáez-Calvo, G.; Díaz, J.F.F.; Camarasa, M.-J.; Liekens, S.; Priego, E.-M. Novel Colchicine-Site Binders with a Cyclohexanedione Scaffold Identified through a Ligand-Based Virtual Screening Approach. *J. Med. Chem.* **2014**, *57*, 3924–3938. [CrossRef]
10. Bueno, O.; Estévez Gallego, J.; Martins, S.; Prota, A.E.; Gago, F.; Gómez-Sanjuan, A.; Camarasa, M.J.; Barasoain, I.; Steinmetz, M.O.; Díaz, J.F.; et al. High-Affinity Ligands of the Colchicine Domain in Tubulin Based on a Structure-Guided Design. *Sci. Rep.* **2018**, *8*, 4242. [CrossRef]
11. Wang, Y.; Zhang, H.; Gigant, B.; Yu, Y.; Wu, Y.; Chen, X.; Lai, Q.; Yang, Z.; Chen, Q.; Yang, J. Structures of a Diverse Set of Colchicine Binding Site Inhibitors in Complex with Tubulin Provide a Rationale for Drug Discovery. *FEBS J.* **2016**, *283*, 102–111. [CrossRef]
12. Satoh, K.; Zhang, L.; Zhang, Y.; Chelluri, R.; Boufraqech, M.; Nilubol, N.; Patel, D.; Shen, M.; Kebebew, E. Identification of Niclosamide as a Novel Anticancer Agent for Adrenocortical Carcinoma. *Clin. Cancer Res.* **2016**, *22*, 3458–3466. [CrossRef]
13. Chen, W.; Mook, R.A., Jr.; Premont, R.T.; Wang, J. Niclosamide: Beyond an Antihelminthic Drug. *Cell Signal* **2018**, *41*, 89–96. [CrossRef]
14. Ren, X.; Duan, L.; He, Q.; Zhang, Z.; Zhou, Y.; Wu, D.; Pan, J.; Pei, D.; Ding, K. Identification of Niclosamide as a New Small-Molecule Inhibitor of the STAT3 Signaling Pathway. *ACS Med. Chem. Lett.* **2010**, *1*, 454–459. [CrossRef]
15. Li, R.; You, S.; Hu, Z.; Chen, Z.G.; Sica, G.L.; Khuri, F.R.; Curran, W.J.; Shin, D.M.; Deng, X. Inhibition of STAT3 by Niclosamide Synergizes with Erlotinib against Head and Neck Cancer. *PLoS ONE* **2013**, *8*, e74670. [CrossRef]
16. Kusaba, T.; Nakayama, T.; Yamazumi, K.; Yakata, Y.; Yoshizaki, A.; Inoue, K.; Nagayasu, T.; Sekine, I. Activation of STAT3 Is a Marker of Poor Prognosis in Human Colorectal Cancer. *Oncol. Rep.* **2006**, *15*, 1445–1451. [CrossRef]
17. Huang, Q.; Zhong, Y.; Dong, H.; Zheng, Q.; Shi, S.; Zhu, K.; Qu, X.; Hu, W.; Zhang, X.; Wang, Y. Revisiting Signal Transducer and Activator of Transcription 3 (STAT3) as an Anticancer Target and Its Inhibitor Discovery: Where Are We and Where Should We Go? *Eur. J. Med. Chem.* **2020**, *187*, 111922. [CrossRef]
18. Luo, F.; Luo, M.; Rong, Q.-X.; Zhang, H.; Chen, Z.; Wang, F.; Zhao, H.-Y.; Fu, L.-W. Niclosamide, an Antihelmintic Drug, Enhances Efficacy of PD-1/PD-L1 Immune Checkpoint Blockade in Non-Small Cell Lung Cancer. *J. Immunother. Cancer* **2019**, *7*, 245. [CrossRef]
19. Zou, S.; Tong, Q.; Liu, B.; Huang, W.; Tian, Y.; Fu, X. Targeting STAT3 in Cancer Immunotherapy. *Mol. Cancer* **2020**, *19*, 145. [CrossRef]
20. Kauerová, T.; Goněc, T.; Jampílek, J.; Hafner, S.; Gaiser, A.-K.; Syrovets, T.; Fedr, R.; Souček, K.; Kollar, P. Ring-Substituted 1-Hydroxynaphthalene-2-Carboxanilides Inhibit Proliferation and Trigger Mitochondria-Mediated Apoptosis. *Int. J. Mol. Sci.* **2020**, *21*, 3416. [CrossRef]
21. Maly, D.J.; Leonetti, F.; Backes, B.J.; Dauber, D.S.; Harris, J.L.; Craik, C.S.; Ellman, J.A. Expedient Solid-Phase Synthesis of Fluorogenic Protease Substrates Using the 7-Amino-4-Carbamoylmethylcoumarin (ACC) Fluorophore. *J. Org. Chem.* **2002**, *67*, 910–915. [CrossRef]
22. Dahlgren, M.K.; Kauppi, A.M.; Olsson, I.-M.; Linusson, A.; Elofsson, M. Design, Synthesis, and Multivariate Quantitative Structure−Activity Relationship of Salicylanilides Potent Inhibitors of Type III Secretion in Yersinia. *J. Med. Chem.* **2007**, *50*, 6177–6188. [CrossRef]

23. Singh, M.; Singh, S.K.; Gangwar, M.; Nath, G.; Singh, S.K. Design, Synthesis and Mode of Action of Some Benzothiazole Derivatives Bearing an Amide Moiety as Antibacterial Agents. *RSC Adv.* **2014**, *4*, 19013–19023. [CrossRef]

24. Kang, S.; Min, H.-J.; Kang, M.-S.; Jung, M.-G.; Kim, S. Discovery of Novel 2-Hydroxydiarylamide Derivatives as TMPRSS4 Inhibitors. *Bioorg. Med. Chem. Lett.* **2013**, *23*, 1748–1751. [CrossRef]

25. Li, C.; Ren, S.-F.; Hou, J.-L.; Yi, H.-P.; Zhu, S.-Z.; Jiang, X.-K.; Li, Z.-T. F···H–N Hydrogen Bonding Driven Foldamers: Efficient Receptors for Dialkylammonium Ions. *Angew. Chem. Int. Ed.* **2005**, *44*, 5725–5729. [CrossRef]

26. Racine, E.; Monnier, F.; Vors, J.-P.; Taillefer, M. A Simple Copper-Catalyzed Synthesis of Tertiary Acyclic Amides. *Org. Lett.* **2011**, *13*, 2818–2821. [CrossRef]

27. Shin, D.-S.; Kim, H.-N.; Shin, K.D.; Yoon, Y.J.; Kim, S.-J.; Han, D.C.; Kwon, B.-M. Cryptotanshinone Inhibits Constitutive Signal Transducer and Activator of Transcription 3 Function through Blocking the Dimerization in DU145 Prostate Cancer Cells. *Cancer Res.* **2009**, *69*, 193–202. [CrossRef]

28. Furtek, S.L.; Backos, D.S.; Matheson, C.J.; Reigan, P. Strategies and Approaches of Targeting STAT3 for Cancer Treatment. *ACS Chem. Biol.* **2016**, *11*, 308–318. [CrossRef]

29. Kauerova, T.; Kos, J.; Gonec, T.; Jampilek, J.; Kollar, P. Antiproliferative and Pro-Apoptotic Effect of Novel Nitro-Substituted Hydroxynaphthanilides on Human Cancer Cell Lines. *Int. J. Mol. Sci.* **2016**, *17*, 1219. [CrossRef]

30. Kollár, P.; Bárta, T.; Závalová, V.; Smejkal, K.; Hampl, A. Geranylated Flavanone Tomentodiplacone B Inhibits Proliferation of Human Monocytic Leukaemia (THP-1) Cells. *Br. J. Pharmacol.* **2011**, *162*, 1534–1541. [CrossRef]

Article

New Genetic Bomb Trigger: Design, Synthesis, Molecular Dynamics Simulation, and Biological Evaluation of Novel BIBR1532-Related Analogs Targeting Telomerase against Non-Small Cell Lung Cancer

Haytham O. Tawfik [1,*], Anwar A. El-Hamaky [1], Eman A. El-Bastawissy [1], Kirill A. Shcherbakov [2], Alexander V. Veselovsky [2], Yulia A. Gladilina [2], Dmitry D. Zhdanov [2,3,*] and Mervat H. El-Hamamsy [1]

[1] Department of Pharmaceutical Chemistry, Faculty of Pharmacy, Tanta University, Tanta 31527, Egypt; anwaramin@pharm.tanta.edu.eg (A.A.E.-H.); emanesmat@pharm.tanta.edu.eg (E.A.E.-B.); mhamamsy@pharm.tanta.edu.eg (M.H.E.-H.)

[2] Laboratory of Medical Biotechnology, Institute of Biomedical Chemistry, Pogodinskaya St. 10/8, 119121 Moscow, Russia; kirill.soff@gmail.com (K.A.S.); veselov@ibmh.msk.su (A.V.V.); leonova_y@mail.ru (Y.A.G.)

[3] Department of Biochemistry, Peoples' Friendship University of Russia (RUDN University), Miklukho-Maklaya St. 6, 117198 Moscow, Russia

[*] Correspondence: haytham.omar.mahmoud@pharm.tanta.edu.eg (H.O.T.); zhdanovdd@gmail.com (D.D.Z.)

Abstract: Telomeres serve a critical function in cell replication and proliferation at every stage of the cell cycle. Telomerase is a ribonucleoprotein, responsible for maintaining the telomere length and chromosomal integrity of frequently dividing cells. Although it is silenced in most human somatic cells, telomere restoration occurs in cancer cells because of telomerase activation or alternative telomere lengthening. The telomerase enzyme is a universal anticancer target that is expressed in 85–95% of cancers. **BIBR1532** is a selective non-nucleoside potent telomerase inhibitor that acts by direct noncompetitive inhibition. Relying on its structural features, three different series were designed, and 30 novel compounds were synthesized and biologically evaluated as telomerase inhibitors using a telomeric repeat amplification protocol (TRAP) assay. Target compounds **29a**, **36b**, and **39b** reported the greatest inhibitory effect on telomerase enzyme with IC_{50} values of 1.7, 0.3, and 2.0 μM, respectively, while **BIBR1532** displayed $IC_{50} = 0.2$ μM. Compounds **29a**, **36b**, and **39b** were subsequently tested using a living-cell TRAP assay and were able to penetrate the cell membrane and inhibit telomerase inside living cancer cells. Compound **36b** was tested for cytotoxicity against 60 cancer cell lines using the NCI (USA) procedure, and the % growth was minimally impacted, indicating telomerase enzyme selectivity. To investigate the interaction of compound **36b** with the telomerase allosteric binding site, molecular docking and molecular dynamics simulations were used.

Keywords: 2-Amino-3-cyanothiophene; **BIBR1532**; telomerase enzyme; TRAP assay; molecular dynamics simulation; inhibitors; lung cancer

1. Introduction

Telomeres are unique structures composed of noncoding hexanucleotide tandem repeats $5'$-(TTAGGG)$_n$-$3'$ with 4–12 kb as a double-strand, followed by 50–400 nucleotides as a single strand overhang located at the ends of eukaryotic chromosomes [1–3]. Telomeres play a crucial role in the replication and proliferation of most somatic cells, as in each cell division, the telomere length gradually shortens [4]. After reaching approximately 50 cycles of cell division (Hayflick limit) [4,5], the telomere becomes too short for adopting the T-loop configuration, eliciting the DNA damage signaling pathway [1,4,6,7]. In case the linear telomere has sufficient length (7–4 kb) for binding with shelterin proteins, it will be protected from fusions by activation of p53. p53 activation resulting in cell cycle arrest at

the G1 phase is known as replicative senescence or mortality stage 1 (M1). Some cells can escape from senescence by p53 suppression, resulting in further replication producing a shorter telomere. A too-short linear telomere with a critical length (2–3 kb) cannot bind with shelterin proteins, resulting in replicative crisis or mortality stage 2 (M2) [1]. By these mechanisms, telomeres function as a mitotic clock granting the cells a finite capacity for replication, and as a genetic time bomb limiting tumor growth [8–11].

Telomerase is a ribonucleoprotein complex composed of two essential components: the catalytic core subunit *hTERT* (human telomerase reverse transcriptase) and the template RNA *hTERC* (human telomerase RNA component) [12]. Telomerase is responsible for maintaining telomere length and chromosomal integrity of the frequently dividing cells [13]. Despite being silent in most human somatic cells, cancer cells undergo telomere restoration via telomerase activation or alternative telomere lengthening (ALT) [4,14,15]. Interestingly, 85–90% of human cancers are concomitant with the reactivation of the telomerase enzyme to maintain the chromosomal ends during cellular proliferation, resulting in unlimited proliferation and immortalization of tumor cells [13,16].

Telomerase activity has been identified in various types of human cancers such as breast, kidney, colon, cervix, lung, liver, pancreas, thyroid, prostate, and urinary bladder cancers [4].

Most of the chemotherapeutic drugs used are not selective to cancer cells, consequently affecting normal and healthy cells [4]. Telomerase has emerged as a potent and selective molecular target for cancer treatment that is only activated in cancerous cells [4]. Unlike growth factor receptors, the gene nonredundancy of telomerase makes tumors less likely to develop resistance to telomerase-based therapies [9,17]. A potential drawback is the delay needed for telomere consumption [18]. Therefore, telomerase inhibitors cannot be used as the first line of cancer treatment [19]. Instead, they can prevent the reactivation of cancer cells that have survived after standard treatment [19].

Lung cancer is the world's second most common cancer and the leading cause of cancer mortality [20–22]. NSCLC (non-small cell lung cancer) accounts for about 84% of lung cancer cases, with telomerase activity seen in 80% [21,23]. The telomerase enzyme has been reactivated in NSCLC due to *hTERT* promoter (*hTERTp*) mutations, *hTERTp* methylation, or *hTERT* gene amplification [24,25]. Chemotherapies for advanced NSCLC are usually associated with tumor recurrences requiring additional treatments in the second- and third-line settings [26]. This recurrence is due to cancer heterogeneity and acquired resistance [24,27]. Therefore, there is an outstanding need to develop novel approaches that work across resistant types to provide patients with enduring remission [19]. Accordingly, telomerase inhibitors can be used as adjuvant therapy to block the regrowth of residual cancer cells [19].

The development or synthesis of compounds that may effectively interfere with numerous essential factors in carcinogenesis is one of the potential approaches to overcome the above mentioned disadvantages, and a number of dual-hybrid carbonic anhydrase-hTERT inhibitors have been discovered [28,29].

Telomerase targeting strategies range from immunotherapies such as the *hTERT* vaccine (GV1001) in phase III clinical trials to direct and indirect telomerase inhibitors [30]. Indirect telomerase inhibitors can be classified as G-quadruplex stabilizers and telomere-disrupting nucleoside analogs [30]. G-quadruplex stabilizers are small molecules that can stabilize telomeric G-quadruplex structures and make them unavailable for the action of telomerase, but toxicity is expected by binding to nontelomeric G-quadruplexes [30,31]. 6-Thio-dG (6-thio-2′-deoxyguanosine) is an example of a telomere-disrupting nucleoside analog that is in phase II of clinical trials (Figure 1) [30,32]. It acts as an uncapping agent by its incorporation into the telomere, impeding shelterin complex binding and resulting in the activation of the DNA damage response (DDR) [30]. Direct telomerase inhibitors can either act on *hTERC* as oligonucleotide inhibitors or on *hTERT* as small molecule inhibitors [30]. Imetelstat (GRN163L) is a lipid-conjugated thiophosphoramidate oligonucleotide that is complementary to the *hTERC* template region (Figure 1) [30]. However, in phase II clin-

ical trials, no improvement in overall survival was evident in patients with advanced non-small cell lung cancer [30,33]. **BIBR1532** is a selective non-nucleoside potent telomerase inhibitor that acts by direct noncompetitive inhibition of the *hTERT* allosteric site (Figure 1) [34]. It decreases telomere length, obstructs cell proliferation, and cell senescence in a dose-dependent manner in vitro [35].

6-Thio-dG   Imetelstat (GRN163L)   BIBR1532
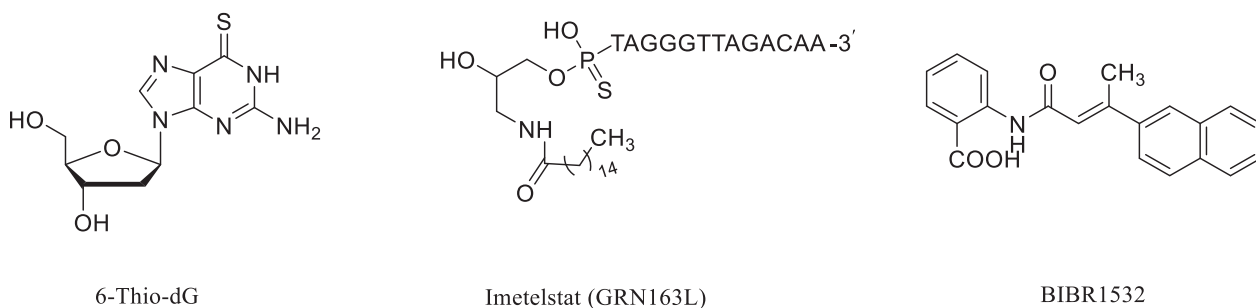
Figure 1. Chemical structures of 6-Thio-dG, Imetelstat, and **BIBR1532** as inhibitors of telomerase enzyme.

Unfortunately, **BIBR1532** suffers from poor pharmacokinetics and low cellular uptake, which limits its progress from preclinical to clinical trials [9,30,36]. Moreover, optimization of **BIBR1532** by the synthesis of various derivatives was not satisfactory [37]. The aim of the research project is to design and synthesize novel **BIBR1532** related analogous as inhibitors of telomerase enzyme, considering the **BIBR1532** pharmacophoric features.

2. Results and Discussion

2.1. Rational Design

The design of our target compounds was based on the pharmacophoric features deduced from the crystal complex of *Tribolium castaneum TERT* (*tcTERT*) with **BIBR1532** (PDB ID: 5CQG), in addition to valuable structure activity relationship studies (SARs) [37–39]. **BIBR1532** lays in a shallow, solvent-accessible, hydrophobic FVYL pocket that is conserved between *tcTERT* and *hTERT* [38]. **BIBR1532** displayed a dog bone shaped structure with two lipophilic heads separated by a four-atom linker made of an α,β-unsaturated secondary amide (Figure 2), which was essential for activity [39]. The introduction of the nitrile group is an important lead optimization approach that could enhance the ligand–receptor interaction [39]. Accordingly, 2-amino-3-cyanothiophene analogs were constructed as an advantageous lipophilic scaffold offering the amine part for our model. To enhance the lipophilicity of the amines, analog 2-amino-3-cyanocyclopenta[b]thiophene **2a** and 2-amino-3-cyano-tetrahydrobenzothiophene **2b** were prepared. Each amine was then connected to an amide linker to form an acetamide core as 2-Cyano-N-(3-cyano-4,5,6,7-tetrahydro-1-benzothiophen-2-yl)acetamide (**9b**) which has an anticancer activity [40–42].The second lipophilic head was designed to enclose three different series of aromatic compounds comprising monocyclic, bicyclic, and fused-ring structures (Figure 3), pointing to improved biological activity. Finally, the two lipophilic heads were connected with the essential four-atom of the α,β-unsaturated amide linker with the same geometry that mimics **BIBR1532**. Three different series were designed, and thirty novel compounds were synthesized as demonstrated in Figure 3.
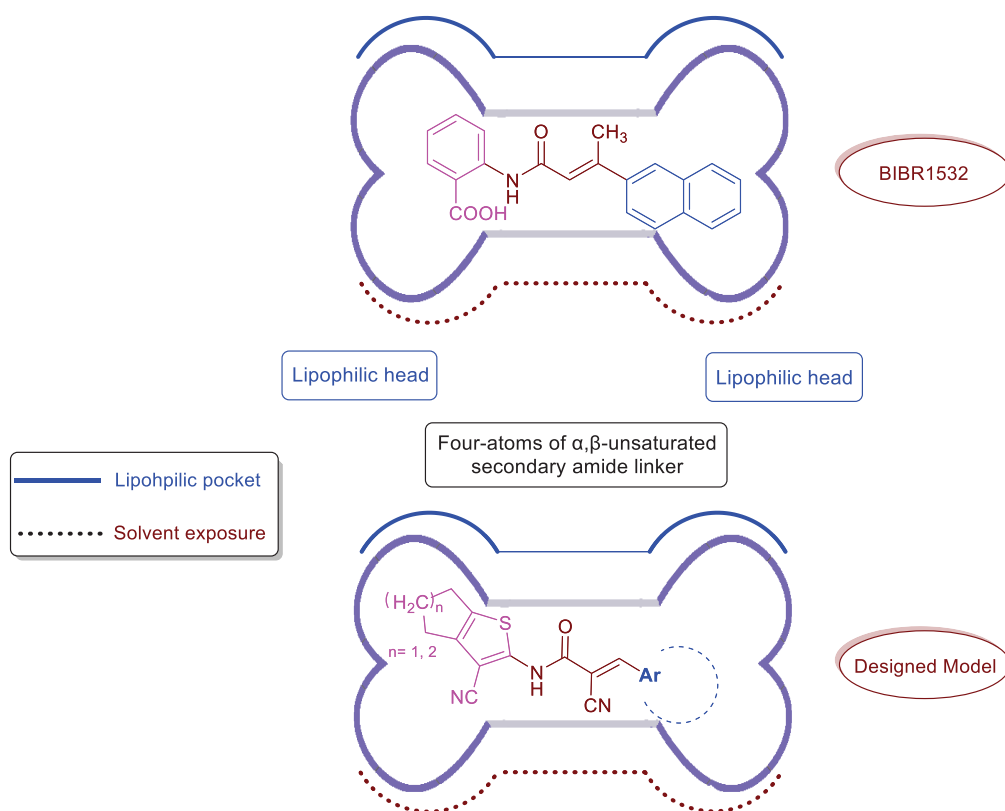
Figure 2. Rational design of our target compounds relying on the dog-bone-shaped structure of **BIBR1532**.
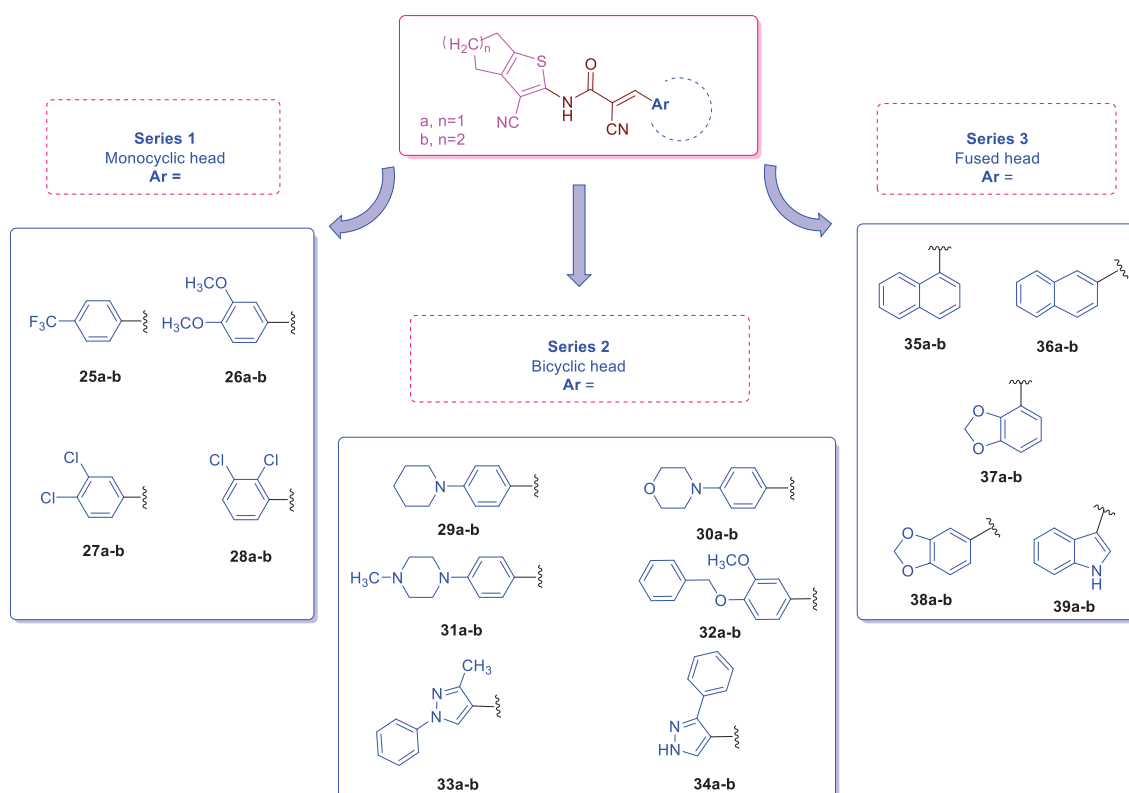
Figure 3. The workflow of three different series showing the chemical structures of 30 novel compounds designed as telomerase inhibitors.

2.2. Chemistry

A total of 30 compounds were designed and synthesized. Preparation of the anticipated amines, 2-amino-3-cyanothiophene derivatives **3a** and **3b**, was accomplished by the one-pot Gewald reaction of three components: cyclic ketone (cyclopentanone **1a** or cyclohexanone **1b**), malononitrile **2**, and elemental sulfur, using morpholine as a basic catalyst [43–45]. For linker construction, two subsequent reactions were employed, starting with the reaction between hydrazine hydrate (99%) **4** and ethyl cyanoacetate **5** in ethanol at 5 °C to give cyanoacetic acid hydrazide **6** [46,47], which was then reacted with acetyl acetone **7** in acidified distilled water (aq. HCl: 32%) at room temperature to yield 1-cyanoacetyl-3,5-dimethylpyrazole **8** (Scheme 1) [48,49].

For effective N-cyanoacetylation of 2-amino-3-cyanothiophene derivatives **3a** and **3b**, cyanoacetic acid hydrazide **6** was converted to 1-cyanoacetyl-3,5-dimethylpyrazole **8** [48,49]. 1-Cyanoacetyl-3,5-dimethylpyrazole **8** consumed less time and produced a higher yield of products than **9a** and **9b** compared to the direct use of ethyl cyanoacetate **5** [50]. Finally, amine derivatives **3a** and **3b** were heated under reflux with 1-cyanoacetyl-3,5-dimethylpyrazole **8** in toluene to form N-cynoacetylated compounds **9a** and **9b**, while 3,5-dimethylpyrazole evolved as a highly soluble leaving group (Scheme 1) [50,51].
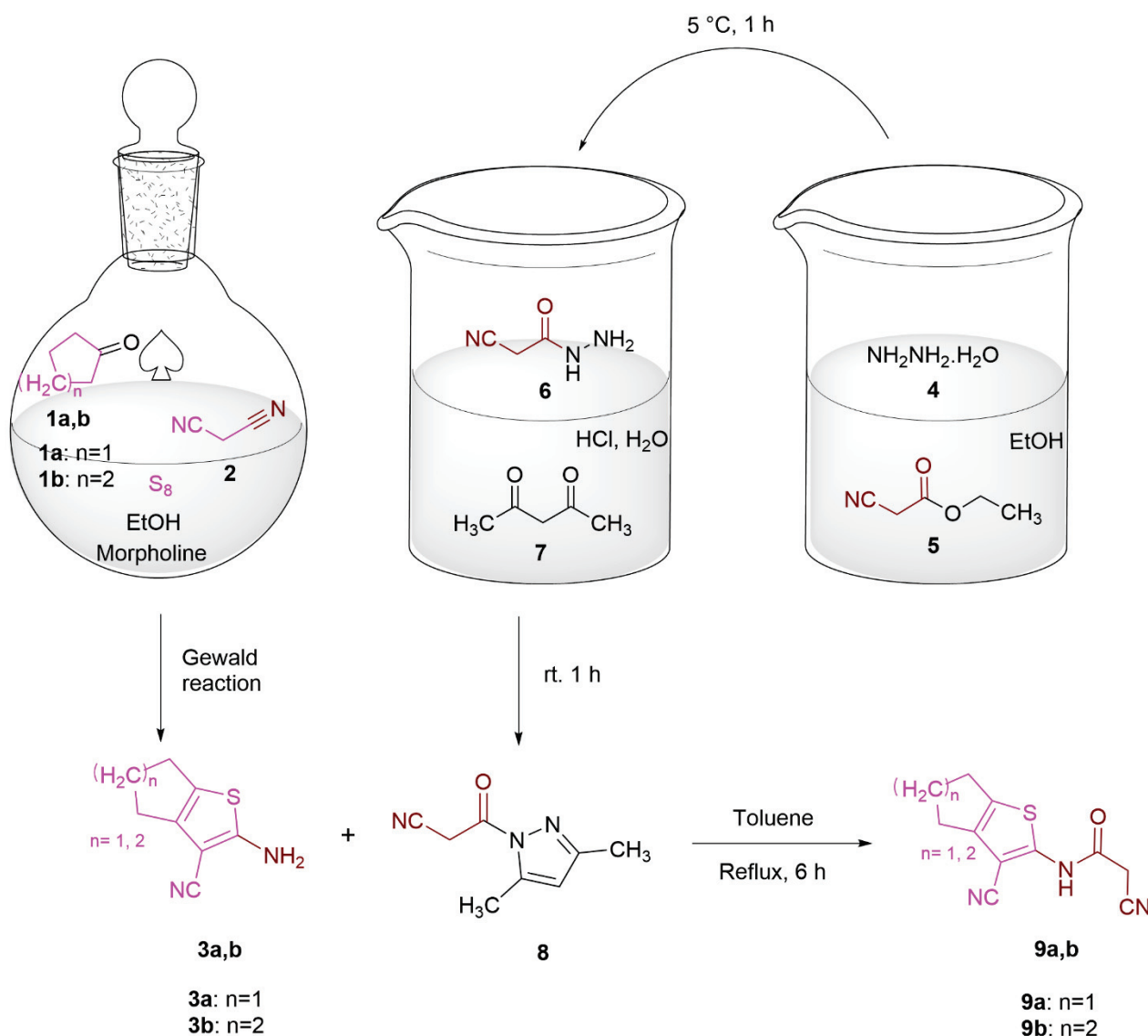
Scheme 1. Chemical synthesis of compounds **9a** and **9b**.

The target compounds **25a–39b** were synthesized via a Knoevenagel condensation reaction to construct the α,β-unsaturated amide linker between the two lipophilic heads for series 1, 2, and 3 (Scheme 2). Thereby, the aldehydes **10–24** were heated under the reflux for 6 h with the active methylene group containing compounds **9a–9b** using piperidine as a catalyst (Scheme 2) [52]. To confirm whether the designed compounds were in *E* or *Z* configuration, compound **38b** was subjected to 2D NOESY NMR. If compound **38b** was in *Z* configuration, we would notice that the vinyl and nitrogen protons were close in space, unlike the *E* configuration, in which the vinyl and nitrogen protons were not close in space (Figure S92 in Supplementary File). In case of *Z* configuration, we would expect a cross peak because of coupling between nitrogen and vinyl protons by drawing a line from both 8.30 ppm (vinyl H) and 8.96 ppm (NH) signals. In our case, the absence of this cross peak at (8.30, 8.96 ppm) refers to the fact that our compound is in *E* configuration (Figure S93 in Supplementary File). Another evidence is calculation of the potential energy. The potential energy of compound **38b** was calculated by MOE 2020.9010 software and was 77.50 and 79.95 for both *E* and *Z* configurations, respectively [53]. Therefore, compound **38b** is in *E* configuration, which is more stable, and the geometry of 24 synthesized analogs is in the stable *E*-isomer form. However, compounds **25a**, **26a**, **26b**, **27a**, **27b**, and **28a** were obtained as mixtures of *E* and *Z* isomers. It was reported that telomerase inhibition is not affected by geometrical isomerism [37,39]. Resolution of geometrical isomers for compounds **26a** and **26b** was accomplished by fractional crystallization [54].
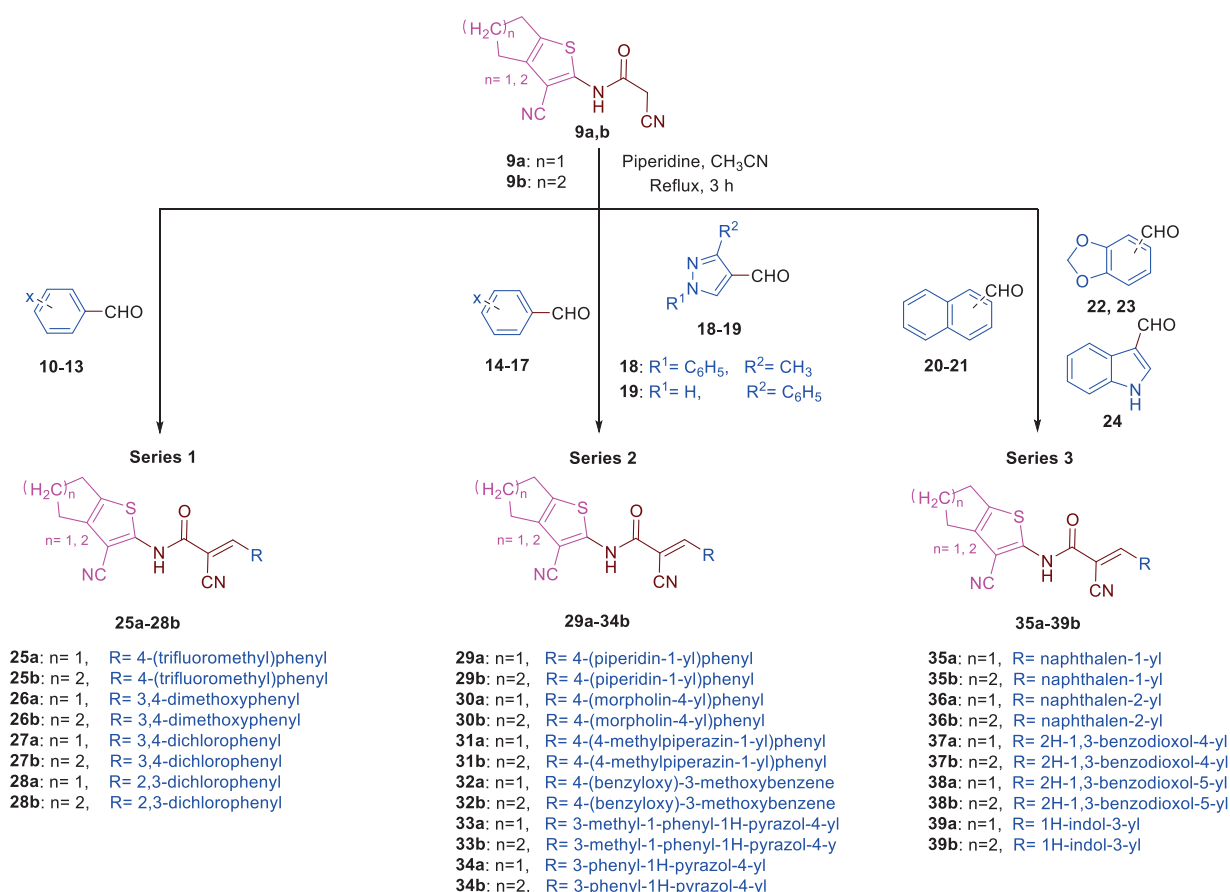
Scheme 2. Synthesis of target compounds **25a–39b**.

Aldehydes **14–16** were synthesized via an aromatic nucleophilic substitution reaction of *p*-fluorobenzaldehyde with different amines, such as piperidine, morpholine, and N-methylpiperazine (Scheme 3) [55,56].
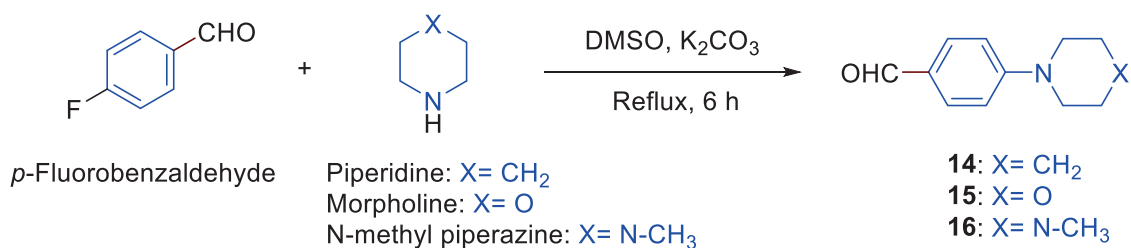
Scheme 3. Synthesis of aldehydes **14–16**.

The chemical structures of the target compounds in series 1, 2, and 3 were confirmed by elemental analysis and spectroscopic data (^{1}H, ^{13}C NMR, and mass spectrometry) as reported in the experimental section. The ^{1}H NMR spectra for compounds **9a** and **9b** were characterized by singlet signals at δ = 4.12 and 3.72 ppm, representing the two protons of the active methylene group, respectively. The disappearance of this signal in the ^{1}H NMR spectra of compounds **25a–39b** is an indication of the completion of the Knoevenagel reaction, in addition to the appearance of the characteristic singlet signal of the alkenyl proton in the range of δ from 7.98 to 9.06 ppm. Another evidence of the completion of the Knoevenagel reaction is the 2D NOESY NMR. For compound **38b**, the vinyl proton at 8.30 ppm is coupled to both C^6-*H* of benzodioxole ring at 7.47 ppm and C^4-*H* of benzodioxole at 7.71 ppm (Figure 4).

Figure 4. 2D NOESY NMR for compound **38b** showing dipolar interactions at (8.30, 7.47 ppm) and (8.30, 7.71 ppm).

The IR spectrum of compound **38b** showed the characteristic peaks at 1279.83 cm^{-1} (C-O of benzodioxole ring), 1648.26 cm^{-1} (C=O of amide), 1673.84 cm^{-1} (C=C), 2223.38 cm^{-1} (CN), 2931.53 cm^{-1} (aliphatic protons), 3002.25 cm^{-1} (aromatic protons), and 3433.83 cm^{-1} (NH of amide).
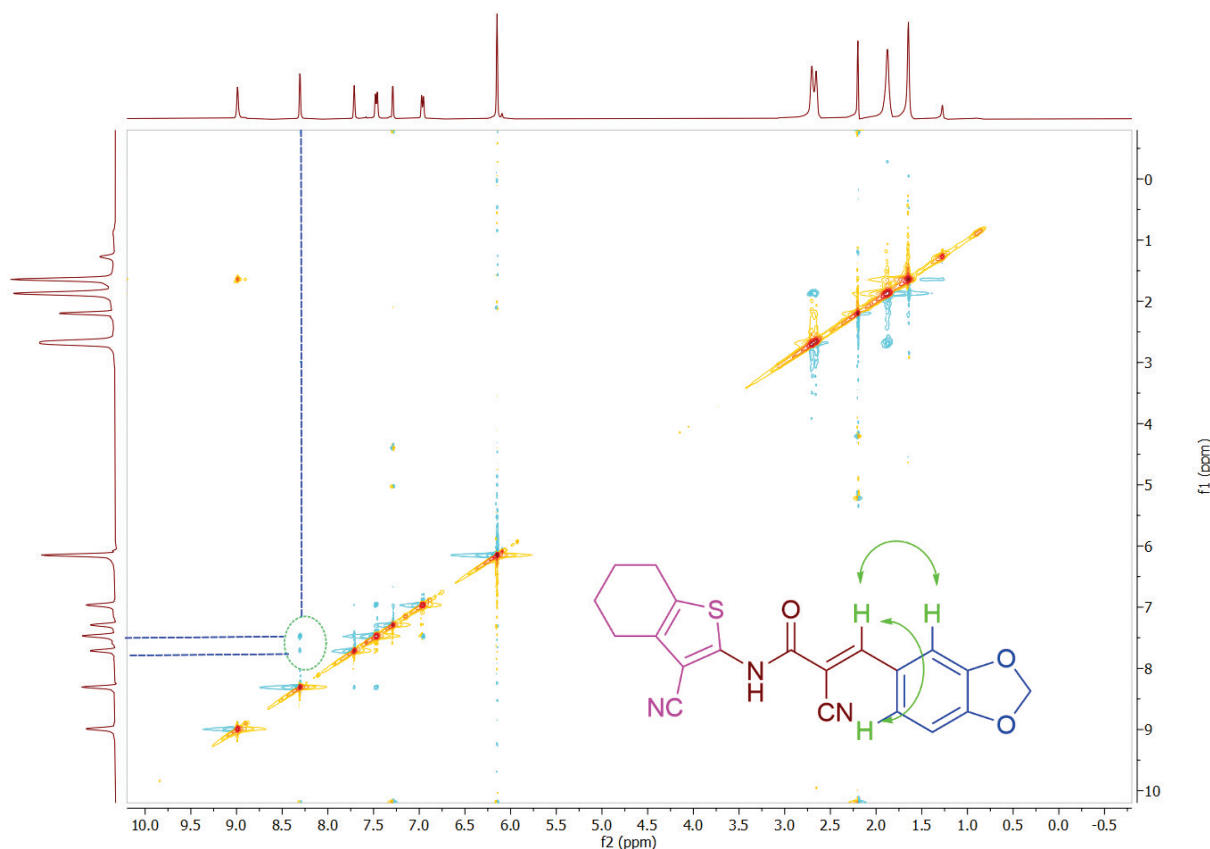
2.3. Biological Studies

2.3.1. In Vitro Inhibition of Telomerase Enzyme

A TRAP-based assay was used to assess telomerase inhibitory activity of target compounds **25a**–**39b**. In cell-free investigations, human A549 (epithelial cell lung carcinoma) lysates were utilized to evaluate telomerase with various inhibitor concentrations. We used a highly selective telomerase and reverse transcriptase inhibitor, **BIBR1532**, as a positive control [37]. All tested compounds demonstrated dose-dependent telomerase inhibition within the range of $0.1-100$ µM (Figure 5). Compounds **29a**, **36b**, and **39b** exhibited the best inhibition profile compared to the control.
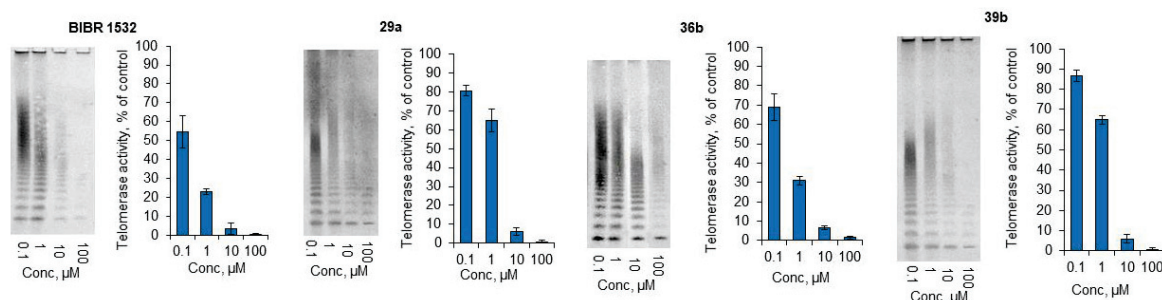
Figure 5. Suppression of telomerase activity in A549 cell-free lysates treated with several concentrations of inhibitors **29a**, **36b**, and **39b**. Representative telomeric repeat amplification protocol (TRAP) gel electrophoresis for treated lysates and quantification of TRAP. For each of the experiments, one representative TRAP gel out of a total of four is presented. The mean $\pm$ SEM is used to present the results.

The IC_{50} and IC_{90} values for **25a**–**39b** are presented in Table 1. Compounds **29a**, **36b**, and **39b** exhibited the best IC_{50} values. The most active compound, **36b**, exhibited $IC_{50} = 0.3$ µM. Compound **36b** revealed the strongest potency compared to **BIBR1532**, $IC_{50} = 0.2$ µM (Table 1).

Table 1. The IC_{50} and IC_{90} values were determined for all tested target compounds as telomerase inhibitors, using **BIBR1532** as a positive control.

Compound	IC_{50} (µM)	IC_{90} (µM)	Compound	IC_{50} (µM)	IC_{90} (µM)
25a	20.9 ± 0.7	108.7 ± 3.2	**33a**	205.3 ± 4.0	643.0
25b	25.8 ± 1.0	140.2 ± 4.7	**33b**	177.5 ± 3.3	573.8
26a	13.5 ± 0.6	153.5	**34a**	188.8 ± 6.4	1078.1
26b	53.6 ± 1.8	750.8	**34b**	38.8 ± 1.0	284.2 ± 6.6
27a	6.5 ± 0.3	163.6	**35a**	5.1 ± 0.2	31.1 ± 1.1
27b	12.5 ± 0.6	138.0	**35b**	5.3 ± 0.2	18.6 ± 0.9
28a	6.7 ± 0.1	67.8	**36a**	5.2 ± 0.2	34.9 ± 1.6
28b	8.3 ± 0.3	57.4	**36b**	0.3 ± 0.01	6.2 ± 0.3
29a	1.7 ± 0.04	6.3 ± 0.3	**37a**	23.5 ± 0.9	136.6 ± 2.6
29b	4.8 ± 0.2	32.8 ± 1.5	**37b**	97.8 ± 2.6	173.9
30a	5.2 ± 0.2	112.5 ± 3.6	**38a**	25.4 ± 1.0	282.4
30b	5.9 ± 0.2	119.4 ± 4.6	**38b**	40.3 ± 1.7	339.4
31a	98.5 ± 3.8	200.5	**39a**	2.5 ± 0.1	9.5 ± 0.3
31b	89.9 ± 3.6	165.2	**39b**	2.0 ± 0.03	7.1 ± 0.3
32a	6.4 ± 0.2	177.4	**BIBR1532**	0.2 ± 0.01	5.6 ± 0.02
32b	109.7 ± 3.7	180.8			

2.3.2. Living-Cell TRAP Assay

To determine whether the target compounds can affect telomerase inside living cancer cells, we incubated cancer cells A549, HCC-44, or NCI-H23 with the most potent inhibitors, **29a**, **36b**, and **39b**, and then measured telomerase activity using the TRAP assay protocol (Table 2).

Table 2. Telomerase activity in cancer cells as a percent of control cells with target compounds **29a**, **36b**, and **39b**.

Compound	% Telomerase Activity in Cancer Cells		
	A549	HCC44	NCI-H23
29a	$22.1 \pm 4.8\%$	$66.1 \pm 2.4\%$	$28.2 \pm 3.9\%$
36b	$18.1 \pm 5.4\%$	$54.4 \pm 4.4\%$	$25.1 \pm 3.2\%$
39b	$41.5 \pm 6.9\%$	$75.6 \pm 7.9\%$	$50.3 \pm 5.1\%$

Fortunately, the results indicated that all the assessed compounds suppressed telomerase in all investigated cell lines (Figure 6a,b). The most potent inhibitor was compound **36b**, which induced the most significant decrease in telomerase activity in all tested cancer cell lines. Compound **39b** demonstrated the lowest ability to inhibit telomerase up to $75.6 \pm 7.9\%$ in HCC-44 cells, while compound **29a** established moderate activity. The highest telomerase inhibition activity was observed in A549 cells. Moreover, A549 cancer cells were the most sensitive to all three tested compounds. The most active compound, **36b**, reduced telomerase activity up to $18.1 \pm 5.4\%$. HCC-44 initially demonstrated low telomerase activity and was more resistant to inhibition (up to $54.4 \pm 4.4\%$ for **36b**). NCI-H23 demonstrated reasonable sensitivity for the tested inhibitors, and **36b** reduced telomerase up to $25.1 \pm 3.2\%$. The results of this experiment revealed that target compounds that demonstrated significant antitelomerase activity in cell-free lysates effectively penetrated the cell membrane and inhibited telomerase inside living cancer cells.
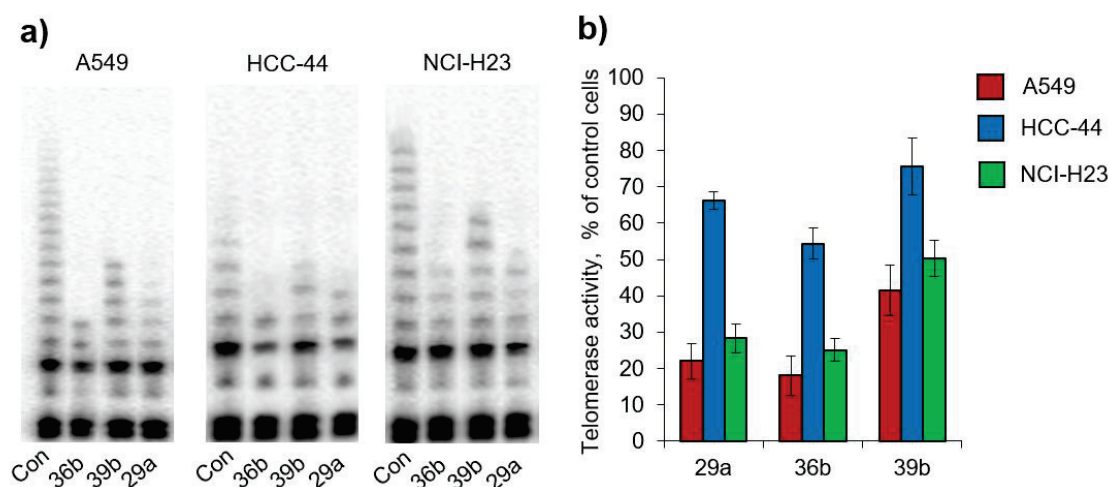
Figure 6. Compounds **29a**, **36b**, and **39b** suppress the activity of telomerase. (**a**) Electrophoresis of A549, HCC-44, or NCI-H23 cells treated for 48 h with 10 µM compounds **29a**, **36b**, and **39b** on a TRAP gel. (**b**) For live cells, TRAP quantification. The mean $\pm$ SEM is used to display the results. Con, control intact cells.

2.3.3. Telomerase Selectivity and Safety

Telomerase inhibitors exhibit a delayed onset for their cytotoxic effect to be recognized and, consequently, can be used to solve the problem of cancer relapse. The selectivity and lack of off-target effects toward other enzymes are important requirements for novel telomerase inhibitors to avoid side effects. Compound **36b** was submitted for in vitro anticancer screening to the National Cancer Institute in Bethesda, Maryland, USA [57]. NCI-60 cell line anticancer screening was implemented to ensure that compound **36b** was free from any cellular targets other than telomerase, where the incubation with cells was performed for 48 h. From the results in Table 3, we can observe that the growth percentage is barely affected by compound **36b**, suggesting the selectivity to telomerase enzyme and safety of compound **36b**.

Table 3. The percentage growth of compound **36b** in vitro anticancer screening against NCI-subpanel 60 tumor cell lines at a dose of 10 μM.

Cell Line	Growth Percent	Cell Line	Growth Percent	Cell Line	Growth Percent
Leukemia		KM12	101.43	OVCAR-5	104.98
CCRF-CEM	104.69	SW-620	103.69	OVCAR-8	102.91
HL-60(TB)	99.47	CNS cancer		NCI/ADR-RES	99.44
K-562	99.98	SF-268	104.45	SK-OV-3	89.18
MOLT-4	100.37	SF-295	95.53	Renal cancer	
RPMI-8226	99.85	SF-539	98.71	786-0	101.2
SR	95.72	SNB-19	100.30	A498	99.38
Lung cancer (NSCLC)		SNB-75	101.09	ACHN	103.29
A549/ATCC	100.18	U251	98.73	CAKI-1	94.28
EKVX	92.47	Melanoma		RXF 393	111.16
HOP-62	98.36	LOX IMVI	102.88	SN12C	100.72
HOP-92	90.75	MALME-3M	109.97	TK-10	113.35
NCI-H226	89.78	M14	94.57	UO-31	81.95
NCI-H23	94.56	MDA-MB-435	101.92	Prostate cancer	
NCI-H322M	98.58	SK-MEL-2	100.31	PC-3	104.77
NCI-H460	102.88	SK-MEL-28	102.31	DU-145	99.89
NCI-H522	94.31	SK-MEL-5	97.65	Breast cancer	
Colon cancer		UACC-257	102.32	MCF7	92.41
COLO 205	103.10	UACC-62	91.73	MDA-MB-231/ATCC	92.15
HCC-2998	114.98	Ovarian cancer		HS 578T	103.54
HCT-116	100.18	IGROV1	103.06	BT-549	107.71
HCT-15	99.95	OVCAR-3	98.78	T-47D	97.26
HT29	112.60	OVCAR-4	100.16	MDA-MB-468	90.36

2.4. In Silico Study

2.4.1. Molecular Docking

A molecular docking was performed on the allosteric binding site, since our compounds have some similarity to allosteric inhibitor **BIBR1532**. The docking results showed that all compounds interact in similar poses, and the values of the scoring functions varied from −7.6 kcal/mol to −10.0 kcal/mol. Slight correlation of scoring function to the experimental inhibitory values was observed. The compounds interact with allosteric site by hydrophobic forces, hydrogen bonds, and π-cation interactions (Figure 7).
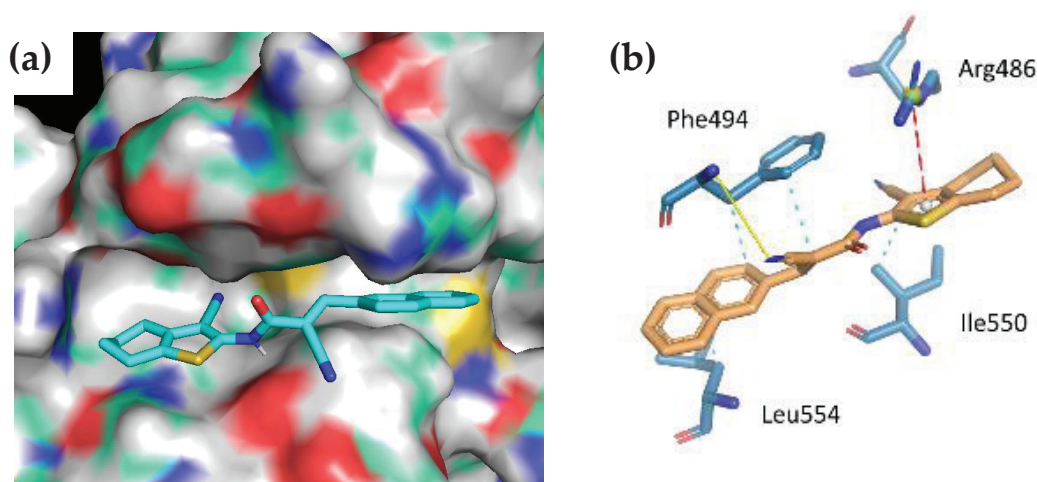
Figure 7. Position of compound **36b** in the allosteric site of telomerase as predicted by molecular docking. (**a**) Structure of telomerase presented as molecular surface. (**b**) The main interaction of compound **36b** with allosteric site. The H-bond is represented by the yellow line, π-cation interaction by the red dashed line, and hydrophobic interaction by the cyan dashed lines.

2.4.2. Molecular Dynamics Simulation

To evaluate the stability of the obtained docking pose, the simulation of molecular dynamics with the most potent inhibitor **36b** was performed. The root-mean-square deviation (RMSD) values for the heavy atoms of telomerase in the complex with compound **36b** are displayed (Figure 8). The amino acid residues deviated rapidly from the initial protein structure, stabilized between 3 and 5 Å, and were still stable over the time scale of the simulation. The RMSD value for compound **36b** in the complex was also stable.
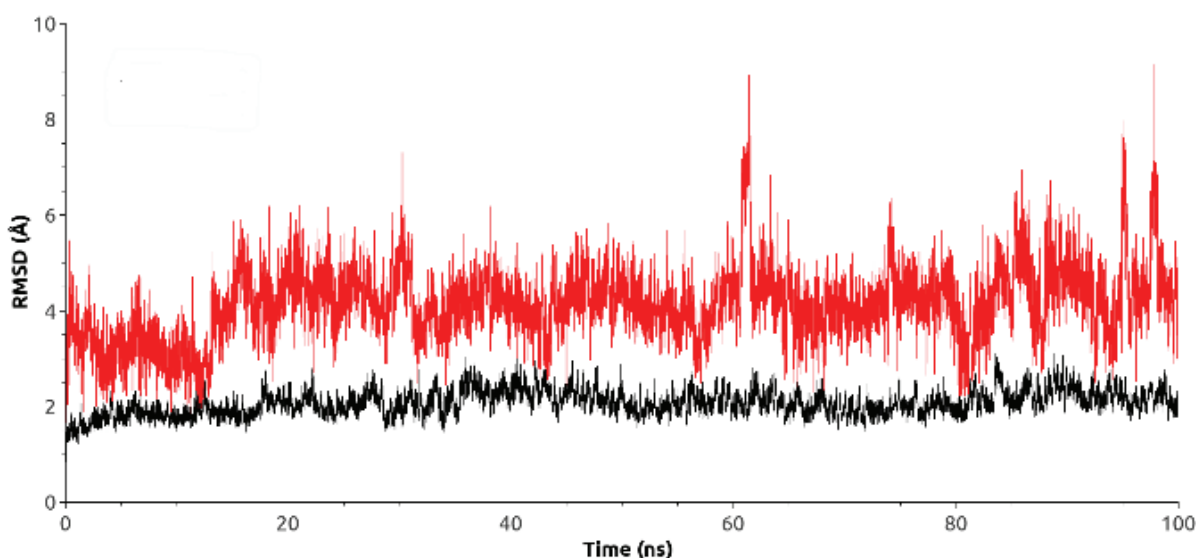
Figure 8. Root-mean-square deviation (RMSD) during molecular dynamics simulation of telomerase (red) in complex with compound **36b** (black).

2.4.3. In Silico Pharmacokinetic, Physicochemical Prediction, and PAINS Filters

SwissADME is a free web tool developed by the Swiss Institute of Bioinformatics (SIB) (http://www.swissadme.ch/, accessed on 20 December 2021) [58]. We applied SwissADME tools to predict the pharmacokinetic and physicochemical properties of the most potent inhibitor, **36b**. Compound **36b** exhibited a predicted $\log P_{o/w} = 3.04$, high GIT absorption with no blood–brain barrier (BBB) permeability. Accordingly, compound **36b** has a good CNS safety profile.

The brain or intestinal estimated permeation (BOILED-Egg) model was developed by calculating both lipophilicity using the Wildman $\log P$ method (WLOGP) and polarity expressed in topological polar surface area (tPSA), followed by plotting the relationship between them in a BOILED-Egg diagram, as illustrated in Figure 9 [59]. Therefore, we can predict both gastrointestinal absorption and BBB permeability for the tested compound. BOILED-Egg was assembled for compounds **36b** and **BIBR1532** (Figure 9). With no BBB permeability, compound **36b** appeared in the zone of human intestinal absorption (HIA). However, **BIBR1532** exists in the BBB zone, giving a privilege to compound **36b** by avoiding CNS side effects. Moreover, both inhibitors are not P-glycoprotein substrates (negative Pgp); thus, they are not susceptible to the efflux mechanism by the Pgp transporter, which is a mechanism that emerged by some tumor cells as a drug resistance strategy (Figure 9) [60].
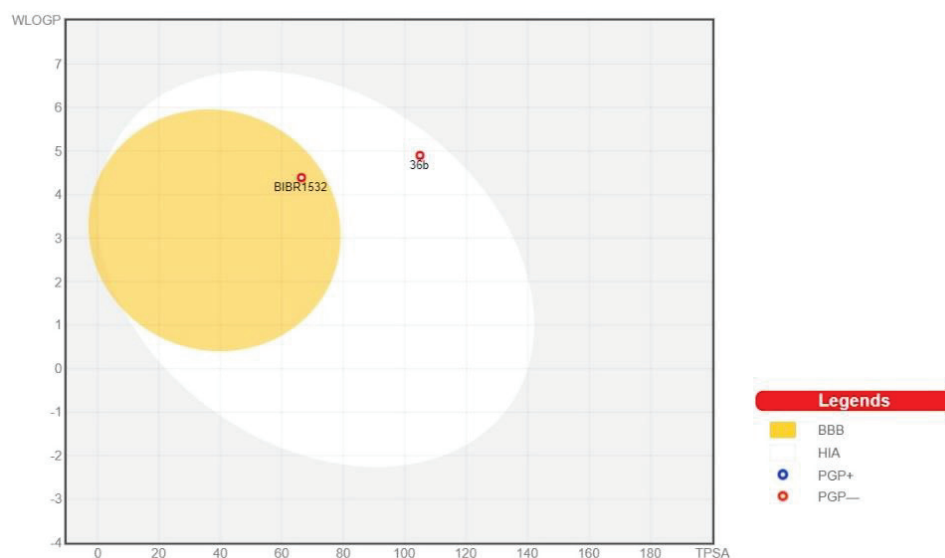
Figure 9. Predicted BOILED-Egg for both compound **36b** and **BIBR1532**. BBB (blood–brain barrier), HIA (human intestinal absorption), PGP+ (P-glycoprotein substrate), PGP− (not P-glycoprotein substrate).

In addition, the bioavailability radar was constructed for inhibitors **36b** and **BIBR1532**. It is composed of six axes bearing six physicochemical properties, which are size (SIZE), lipophilicity (LIPO), solubility (INSOLU), polarity (POLAR), saturation (INSATU), and flexibility (FLEX) (Figure 10) [58]. Compound **36b** showed an improvement in fraction Csp3 (as illustrated by the INSATU property in the bioavailability radar) compared to **BIBR1532**, explaining the importance of the aliphatic portion attached to the thiophene ring. Both compounds **36b** and **BIBR1532** pass the Lipinski (Pfizer), Ghose (Amgen), Veber (GSK), and Egan (Pharmacia) filters, which are used by some pharmaceutical companies to define drug-like qualities.
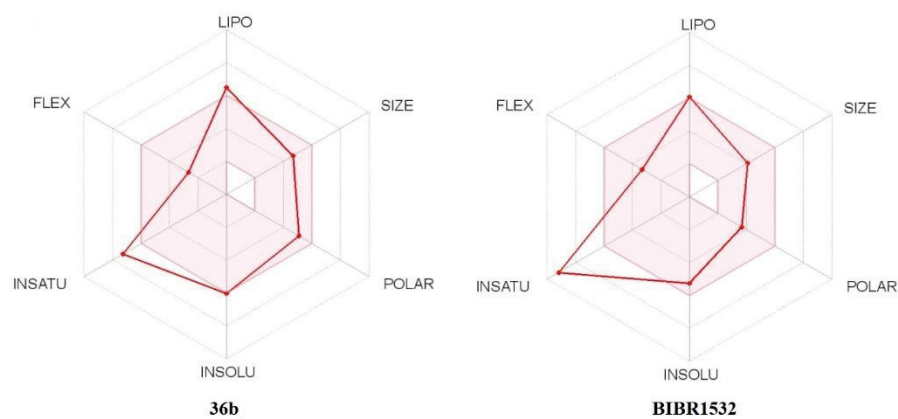
Figure 10. Bioavailability radar for compounds **36b** and **BIBR1532**. The red line represents each structure, and the range of optimal property values for oral bioavailability is shown in pink.

SwissADME-achieved data classified compound **36b** as non-PAINS (pan-assay interference compounds), signifying the high selectivity of our target compound **36b**. It did not display a potent response in assays other than its target which is consistent with the NCI-60 cell line panel assay.

2.5. Structure-Activity Relationship (SAR)

Telomerase inhibitory activities for target compounds were accomplished by a modified TRAP assay [61–63], since **BIBR1532** served as a positive control. Thirty novel inhibitors, **25a–39b**, disclosed IC$_{50}$ values ranging from 0.3 μM to 205.3 μM compared to

BIBR1532, IC_{50} = 0.2 µM. The TRAP assay results (IC_{50} and IC_{90}), recorded in Table 1, specified that we designed and synthesized three series of novel telomerase inhibitors. Sixteen compounds showed the strongest inhibitory effect, with IC_{50} values ranging between 0.3 and 13.5 µM. Seven compounds revealed a moderate inhibitory effect, with IC_{50} values ranging between 20.9 and 53.6 µM, while seven compounds displayed the weakest activity, with IC_{50} values ranging between 89.9 and 205.3 µM. Regarding the ring size of the amine part, where (n = 1 or 2), it was observed that target compounds having cyclopenta[b]thiophen amine, (n = 1), were stronger telomerase inhibitors than tetrahydrobenzothiophene (n = 2), analogs except for compounds **31**, **33**, **34**, **36**, and **39**. Meanwhile, the aldehyde part revealed that in series 3, inhibitors with lipophilic fused aromatic analogs, such as naphthalene in **35a**–**b** and **36a**–**b** and indole in **39a**–**b**, exhibited the best activity, with IC_{50} values ranging between 0.3 and 5.3 µM. The presence of the less lipophilic benzodioxole ring in compounds **37a**–**b** and **38a**–**b** reduced the activity, and the reported IC_{50} values ranging from 23.5 to 97.8 µM. In series 1, the presence of electron withdrawing groups, such as chloride and trifluoromethyl groups, enhanced the potency. Compounds **27a**–**b** and **28a**–**b** disclosed a dichlorobenzyl group bearing two chloride atoms either in the *ortho*, *meta*, or *meta*-*para* positions, and exhibited IC_{50} values ranging from 6.5 to 12.5 µM. Meanwhile, inhibitors **25a**–**b** with the *p*-trifluorometheylbenzyl group revealed IC_{50} values of 20.9 and 25.8 µM, respectively. In contrast, the presence of electron-donating groups reduced the potency, as revealed in compounds **26a**–**b** with *m,p*-dimethoxybenzyl group, which reported IC_{50} values of 13.5 and 53.6 µM, respectively. In series 2, having inhibitors with substituted benzaldehyde revealed that the presence of piperidine and morpholine rings in the *para* position enhanced the activity and displayed strong telomerase inhibition (**29a**–**b** and **30a**–**b**) with IC_{50} values ranging between 1.7 and 5.9 µM. The presence of the N-methylpiperazinyl group in the *para* position of the benzene ring in compounds **31a**–**b** showed a significant decrease in activity, as their polarity is not consistent with the lipophilic portion of the active site. Compounds **31a**–**b** displayed IC_{50} values of 98.5 and 89.9 µM, respectively. Moreover, compound **32b** with *m*-methoxy-*p*-benzyloxybenzyl group and n = 2 showed IC_{50} = 109.7 µM. Compound **32a** was an exception in the *m*-methoxy-*p*-benzyloxybenzyl group, and n = 1 showed IC_{50} = 6.4 µM. The presence of the polar pyrazole ring in compounds, **33a**–**b** and **34a**–**b** significantly decreased their activity (Figure 11).
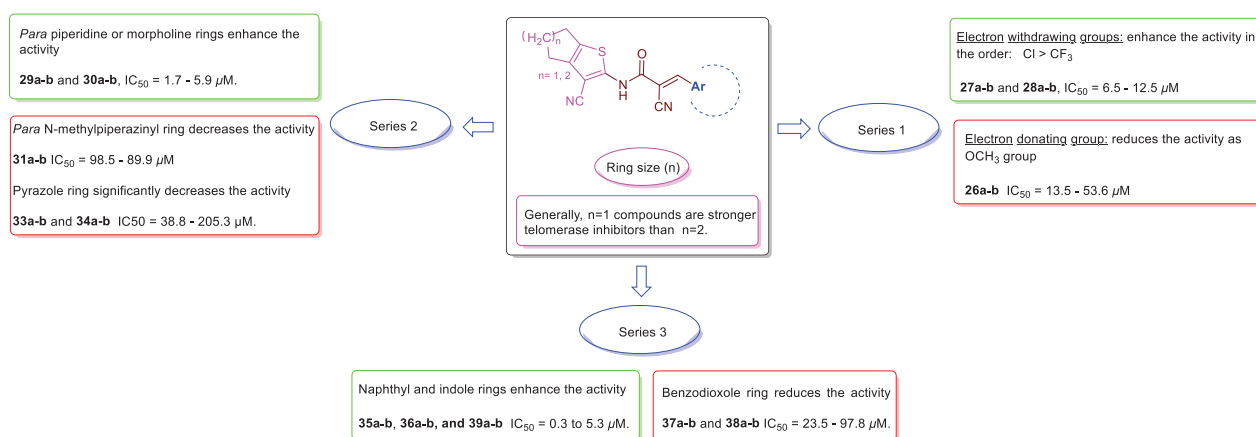
Figure 11. Structure–activity relationship summary for compounds **25a**–**39b** as telomerase inhibitors.

3. Materials and Methods

3.1. Chemistry

Sigma-Aldrich, Alfa Aesar, and Merck provided all of the organic reagents used in this research. The open capillary method was used to determine melting points on the electrothermal melting point apparatus (Stuart SMP10), and the results were reported uncorrected. TLC was used to monitor reactions on a precoated sheet (Fastman Kodak,

Silica 60 F$_{254}$) with the following developing system: *n*-hexane:ethyl acetate (66.7:33.3) and UV light at 254 nm. The elemental analysis was conducted using a PerkinElmer 2400 CHNS analyzer (% C, H, N, and S). It was measured at Nasr City, Cairo, Egypt, at Al-Azhar University's Regional Center for Mycology and Biotechnology. ^{1}H, ^{13}C NMR, and 2D NOESY spectra were recorded using CDCl$_3$, DMSO-*d$_6$*, or CF$_3$COOD as a solvent and tetramethylsilane (TMS) as an internal reference on a Bruker FT-NMR spectrometer at 400 MHz and 100 MHz, respectively, and a JEOL ECA-500 II FT-NMR spectrometer at 500 MHz and 125 MHz. All values of chemical shift, coupling constants, *J*, and splitting [singlet (s), doublet (d), triplet (t), quintet (quint), multiplet (m), broad(br)] are expressed in ppm and Hz. The Faculty of Pharmacy at Mansoura University in Egypt and the Faculty of Science at Mansoura University in Egypt both provided ^{1}H and ^{13}C NMR spectra. Except for compounds **25a**, **26a**, **26b**, **27a**, **27b**, and **28a**, which had the *E-Z* mixture, all remaining compounds were obtained in the *E* configuration. Absence of some signals in compounds **25a**, **26b**, **30b**, **31b**, **32a**, **32b**, and **38a** was due to very low solubility. At Tanta University's Central Laboratory, infrared (IR) spectroscopy measurements were performed at using a Bruker to record infrared spectra in the range 4000–500 cm^{-1}. Thermo-Scientific ISQ Single Quadruple MS was used to record electron ionization mass spectra (EI-MS) using a 70-eV ionization energy and helium gas (carrier gas) at a constant flow rate of 1 mL/min. The mass spectrometry was performed in Nasr City, Cairo, Egypt, at Al-Azhar University's Regional Center for Mycology and Biotechnology.

3.1.1. General Procedure for the Preparation of **3a,b**

At room temperature, a stirred solution of suitable ketone **1a,b** (10 mmol) and malononitrile **2** (10 mmol) in ethanol (20 mL) was added with sulfur (10 mmol). After heating the reaction mixture to 60 °C, morpholine (12 mmol) was added dropwise and stirred for 30 min. The reaction mixture was permitted to cool and stirred for 5 h at rt. The formed precipitates **3a,b** were filtered and rinsed with cold MeOH and then recrystallized from EtOH [43–45].

2-Amino-4H,5H,6H-cyclopenta[b]thiophene-3-carbonitrile (**3a**). Compound **3a** was synthesized according to typical procedure using cyclopentanone **1a**. The yield was (1.31 g, 79.94%) as brown powder with m.p. 159–161 °C [43–45].

2-Amino-4,5,6,7-tetrahydro-1-benzothiophene-3-carbonitrile (**3b**). Compound **3b** was synthesized according to typical procedure using cyclohexanone **1b**. The yield was (1.49 g, 84.09%) as off-white powder with m.p. 149–151 °C [43–45].

3.1.2. Cyanoacetic Acid Hydrazide (**6**)

Hydrazine hydrate (99%) **4** (10 mmol) was added to a solution of ethyl cyanoacetate **5** (10 mmol) in ethanol (20 mL) and stirred for 1 h at 0 °C. The formed crystals were then filtered and rinsed with cold MeOH and recrystallized from EtOH. The yield was (0.89 g, 89.91%) as colorless crystals with m.p. 114–116 °C [46,47].

3.1.3. 1-Cyanoacetyl-3,5-dimethylpyrazole (**8**)

Acetyl acetone **7** (10 mmol) was added to a solution of cyanoacetic acid hydrazide **6** (10 mmol) in distilled water (20 mL) containing a catalytic amount of HCl (32%) and stirred for 1 h at rt. The formed precipitate was filtered and washed with water. The yield was (1.38 g, 84.99%) as white powder with m.p. 124–126 °C [48,49].

3.1.4. General Procedure for the Preparation of **9a,b**

1-Cyanoacetyl-3,5-dimethylpyrazole **8** (1.2 mmol), and either **3a** or **3b** (1 mmol) in dry toluene (20 mL) were heated under reflux for 6 h [50,51]. Filtered precipitates **9a,b** were washed in diethyl ether before being recrystallized from EtOH.

2-Cyano-N-{3-cyano-4H,5H,6H-cyclopenta[b]thiophen-2-yl}acetamide (**9a**). Compound **9a** was synthesized according to typical procedure using **3a** as a starting material. The yield was (0.15 g, 64.85%) as brown powder with m.p. 239–241 °C. ^{1}H NMR (400 MHz, DMSO-*d$_6$*)

δ (ppm): 2.37 (2H, quint., *J* = 8.0 Hz, CH$_2$ of C^5-*H*s of cyclopenta[b]thiophen ring), 2.74 (2H, t, *J* = 8.0 Hz, CH$_2$ of C^4-*H*s of cyclopenta[b]thiophen ring), 2.85 (2H, t, *J* = 8.0 Hz, CH$_2$ of C^6-*H*s of cyclopenta[b]thiophen ring), 4.12 (2H, s, CH$_2$), 11.96 (1H, s, NH).

2-Cyano-N-(3-cyano-4,5,6,7-tetrahydro-1-benzothiophen-2-yl)acetamide (**9b**). Compound **9b** was synthesized according to typical procedure using **3b** as a starting material. The yield was (0.17 g, 69.71%) as grayish-white precipitate with m.p. 244–246 °C [50,51]. ^{1}H NMR (400 MHz, CDCl$_3$) δ (ppm): 1.80–2.10 (4H, m, 2 CH$_2$ of C^{5,6}-*H*s of tetrahydrobenzothiophene ring), 2.60–2.75 (4H, m, 2 CH$_2$ of C^{4,7}-*H*s of tetrahydrobenzothiophene ring), 3.72 (2H, s, CH$_2$), 9.85 (1H, s, NH).

3.1.5. General Procedure for the Preparation of **14–16**

Suitable aliphatic cyclic amines piperidine, morpholine, or N-methyl piperazine (15 mmol), and *p*-fluorobenzaldehyde (15 mmol) in DMSO (30 mL) were heated under reflux in the presence of potassium carbonate anhydrous (16 mmol) as a base for 6 h [55,56]. After pouring the reaction mixture into distilled water (30 mL), ethyl acetate was used to extract it (3 × 30 mL). The extracts were collected, brine-washed, dried over anhydrous MgSO4, and then evaporated in vacuo.

4-(Piperidin-1-yl)benzaldehyde (**14**). Compound **14** was synthesized according to typical procedure using piperidine as a starting material. The yield was (1.99 g, 69.99%) as a pink powder with m.p. 63–65 °C [55].

4-(Morpholin-4-yl)benzaldehyde (**15**). Compound **15** was synthesized according to typical procedure using morpholine as a starting material. The yield was (2.09 g, 72.96%) as a yellow powder with m.p. 65–67 °C [55].

4-(4-Methylpiperazin-1-yl)benzaldehyde (**16**). Compound **16** was synthesized according to typical procedure using N-methyl piperazine as a starting material. The yield was (2.05 g, 66.96%) as a yellow powder with m.p. 56–58 °C [55].

3.1.6. General Procedure for the Preparation of **25a–39b**

In CH$_3$CN (10 mL), a suitable aldehyde **10–24** (1 mmol), and either **9a** or **9b** (1 mmol) were heated under reflux with piperidine (three drops) as a catalyst [53]. The **25a–39b** precipitate was filtered and washed in acetone before being recrystallized from EtOH.

(2E/2Z)-2-Cyano-N-{3-cyano-4H,5H,6H-cyclopenta[b]thiophen-2-yl}-3-[4-(trifluoromethyl) phenyl]prop-2-enamide (**25a**). Compound **25a** was synthesized according to the typical procedure using **9a** and 4-(trifluoromethyl)benzaldehyde **10** as starting materials. The yield was (0.25 g, 64.53%) as off-white powder with m.p. 354–356 °C. ^{1}H NMR (500 MHz, CF$_3$COOD) δ (ppm): 2.65–2.75 (2H, m, CH$_2$ of C^5-*H*s of cyclopenta[b]thiophen ring), 3.08–3.14 (2H, t, *J* = 7.0 Hz, CH$_2$ of C^4-*H*s of cyclopenta[b]thiophen ring), 3.14–3.23 (2H, t, *J* = 7.0 Hz, CH$_2$ of C^6-*H*s of cyclopenta[b]thiophen ring), 7.65 (2H, d, *J* = 8.0 Hz, 2 CH of C^{2,6}-*H*s of phenyl ring), 7.85 (2H, d, *J* = 8.0 Hz, 2 CH of C^{3,5}-*H*s of phenyl ring), 8.30 (1H, s, vinyl-*H*), 8.53 (1H, s, NH). ^{13}C NMR (125 MHz, CF$_3$COOD) δ (ppm): 29.76, 30.59, 30.90, 103.02, 115.41, 128.73 (2C), 131.53 (2C), 140.22, 149.91, 153.08, 159.37 (2C), 171.17, 184.12. EI-MS: *m/z*: 387.39 [M$^+$]. Anal. Calcd. for C$_{19}$H$_{12}$F$_3$N$_3$OS: C, 58.91; H, 3.12; N, 10.85; S, 8.28. Found: C, 59.17; H, 3.29; N, 11.08; S, 8.37.

(2E)-2-Cyano-N-(3-cyano-4,5,6,7-tetrahydro-1-benzothiophen-2-yl)-3-[4-(trifluoromethyl) phenyl]prop-2-enamide (**25b**). Compound **25b** was synthesized according to the typical procedure using **9b** and 4-(trifluoromethyl)benzaldehyde **10** as starting materials. The yield was (0.22 g, 54.56%) as a yellow powder with m.p. 225–227 °C. ^{1}H NMR (500 MHz, DMSO-*d*$_6$) δ (ppm): 1.70–1.85 (4H, m, 2 CH$_2$ of C^{5,6}-*H*s of tetrahydrobenzothiophene ring), 2.50–2.55 (2H, m, CH$_2$ of C^7-*H*s of tetrahydrobenzothiophene ring), 2.60–2.65 (2H, m, CH$_2$ of C^4-*H*s of tetrahydrobenzothiophene ring), 7.97 (2H, d, *J* = 8.5 Hz, CH of C^{2,6}-*H*s of phenyl ring), 8.15 (2H, d, *J* = 8.5 Hz, CH of C^{3,5}-*H*s of phenyl ring), 8.45 (1H, s, vinyl-*H*), 12.03 (1H, s, NH). ^{13}C NMR (125 MHz, DMSO-*d*$_6$) δ (ppm): 21.43, 22.33, 23.85, 24.56, 94.41, 104.80, 114.98, 117.42, 125.42, 126.21 (2C), 127.47 (2C), 133.37, 134.05, 136.50, 145.08, 148.00, 157.40,

157.91. EI-MS: *m/z*: 401.08 [M$^+$]. Anal. Calcd. for C$_{20}$H$_{14}$F$_3$N$_3$OS: C, 59.84; H, 3.52; N, 10.47; S, 7.99. Found: C, 59.70; H, 3.72; N, 10.68; S, 8.15.

(2E)-2-Cyano-N-{3-cyano-4H,5H,6H-cyclopenta[b]thiophen-2-yl}-3-(3,4-dimethoxyphenyl) prop-2-enamide (**26a**). Compound **26a** was synthesized according to typical procedure using **9a** and 3,4-dimethoxybenzaldehyde **11** as starting materials. In fractional crystallization, compound **26a** was subjected to hot dioxane, where the *E* isomer was dissolved, leaving the *Z* isomer insoluble. The hot dioxane was filtered to remove the insoluble *Z* isomer and then allowed to cool to give the *E* isomer. The yield was (0.26 g, 68.52%) as a yellow powder with m.p. 249–251 °C. ^{1}H NMR (500 MHz, DMSO-d_6) δ (ppm): 2.30–2.45 (2H, m, CH$_2$ of C^5-*H*s of cyclopenta[b]thiophen ring), 2.60–2.95 (4H, m, 2 CH$_2$ of C^{4,6}-*H*s of cyclopenta[b]thiophen ring), 3.81 (3H, s, CH$_3$ of OCH$_3$ at C^3 of phenyl ring), 3.87 (3H, s, CH$_3$ of OCH$_3$ at C^4 of phenyl ring), 7.19 (1H, d, *J* = 7.5 Hz, CH of C^5-*H* of phenyl ring), 7.68 (1H, d, *J* = 7.5 Hz, CH of C^6-*H* of phenyl ring) 7.73 (1H, s, CH of C^2-*H* of phenyl ring), 8.26 (1H, s, vinyl-*H*), 11.72 (1H, s, NH). ^{13}C NMR (125 MHz, CF$_3$COOD) δ (ppm): 29.24, 29.32, 30.77. 57.12 (2C), 96.92, 109.67, 113.22, 113.93, 117.25, 126.63, 132.36, 140.10, 150.50, 152.88, 154.28, 155.00, 156.87, 157.08, 171.60. EI-MS: *m/z*: 379.2 [M$^+$]. Anal. Calcd. for C$_{20}$H$_{17}$N$_3$O$_3$S: C, 63.31; H, 4.52; N, 11.07; S, 8.45. Found: C, 63.49; H, 4.68; N, 11.29; S, 8.52.

(2E)-2-Cyano-N-(3-cyano-4,5,6,7-tetrahydro-1-benzothiophen-2-yl)-3-(3,4-dimethoxyphenyl) prop-2-enamide (**26b**). Compound **26b** was synthesized according to typical procedure using **9b** and 3,4-dimethoxybenzaldehyde **11** as starting materials. In fractional crystallization, compound **26b** was subjected to hot dioxane, where the *E* isomer was dissolved, leaving the *Z* isomer insoluble. The hot dioxane was filtered to remove the insoluble *Z* isomer and then allowed to cool to give the *E* isomer. The yield was (0.25 g, 62.78%) as a yellow powder with m.p. 264–266 °C. ^{1}H NMR (500 MHz, DMSO-d_6) δ (ppm): 1.70–1.80 (4H, m, 2 CH$_2$ of C^{5,6}-*H*s of tetrahydrobenzothiophene ring), 2.50–2.55 (2H, m, CH$_2$ of C^7-*H*s of tetrahydrobenzothiophene ring), 2.60–2.65 (2H, m, CH$_2$ of C^4-*H*s of tetrahydrobenzothiophene ring), 3.81 (3H, s, CH$_3$ of OCH$_3$ at C^3 of phenyl ring), 3.87 (3H, s, CH$_3$ of OCH$_3$ at C^4 of phenyl ring), 7.19 (1H, d, *J* = 9.0 Hz, CH of C^5-*H* of phenyl ring), 7.68 (1H, d, *J* = 9.0 Hz, CH of C^6-*H* of phenyl ring) 7.73 (1H, s, CH of C^2-*H* of phenyl ring), 8.26 (1H, s, vinyl-*H*), 11.74 (1H, s, NH). ^{13}C NMR (125 MHz, DMSO-d_6) δ (ppm): 21.67, 22.56, 23.48, 23.60, 55.53, 55.91, 111.98, 112.59 (2C), 124.24, 126.27, 148.73 (2C), 153.19 (2C), 160.67. EI-MS: *m/z*: 393.64 [M$^+$]. Anal. Calcd. for C$_{21}$H$_{19}$N$_3$O$_3$S: C, 64.11; H, 4.87; N, 10.68; S, 8.15. Found: C, 64.38; H, 4.92; N, 10.85; S, 8.34.

(2E/2Z)-2-Cyano-N-{3-cyano-4H,5H,6H-cyclopenta[b]thiophen-2-yl}-3-(3,4-dichlorophenyl) prop-2-enamide (**27a**). Compound **27a** was synthesized according to the typical procedure using **9a** and 3,4-dichlorobenzaldehyde **12** as starting materials. The yield was (0.21 g, 54.09%) as a gray powder with m.p. 329–331 °C. ^{1}H NMR (500 MHz, CF$_3$COOD) δ (ppm): 2.70–2.80 (2H, m, CH$_2$ of C^5-*H*s of cyclopenta[b]thiophen ring), 3.10–3.25 (4H, m, 2 CH$_2$ of C^{4,6}-*H*s of cyclopenta[b]thiophen ring), 7.38 (1H, s, CH of C^5-*H* of phenyl ring), 7.60–7.85 (2H, m, 2 CH of C^{2,6}-*H* of phenyl ring), 8.32 (1H, s, vinyl-*H*), 8.65 (1H, s, NH). ^{13}C NMR (125 MHz, CF$_3$COOD) δ (ppm): 29.65, 30.49, 30.81, 103.10, 112.48, 112.71, 115.33, 129.62, 132.58, 133.66, 136.67, 139.37, 140.09, 144.09, 149.80, 152.58, 158.01, 158.94. EI-MS: *m/z*: 388.5 [M$^+$]. Anal. Calcd. for C$_{18}$H$_{11}$Cl$_2$N$_3$OS: C, 55.68; H, 2.86; N, 10.82; S, 8.26. Found: C, 55.87; H, 3.15; N, 11.04; S, 8.42.

(2E/2Z)-2-Cyano-N-(3-cyano-4,5,6,7-tetrahydro-1-benzothiophen-2-yl)-3-(3,4-dichlorophenyl) prop-2-enamide (**27b**). Compound **27b** was synthesized according to typical procedure using **9b** and 3,4-dichlorobenzaldehyde **12** as starting materials. The yield was (0.23 g, 57.42%) as a gray powder with m.p. 376–378 °C. ^{1}H NMR (500 MHz, CF$_3$COOD) δ (ppm): 1.85–1.95 (4H, m, 2 CH$_2$ of C^{5,6}-*H*s of tetrahydrobenzothiophene ring), 2.55–2.65 (2H, m, CH$_2$ of C^7-*H*s of tetrahydrobenzothiophene ring), 2.70–2.80 (2H, m, CH$_2$ of C^4-*H*s of tetrahydrobenzothiophene ring), 7.39 (1H, d, *J* = 7.0 Hz, CH of C^5-*H* of phenyl ring), 7.67 (2H, m, 2 CH of C^{2,6}-*H* of phenyl ring), 8.56 (1H, s, vinyl-*H*), 8.88 (1H, s, NH). ^{13}C NMR (125 MHz, CF$_3$COOD) δ (ppm): 22.89, 25.71, 26.19, 27.39, 114.72, 115.50, 116.97, 117.80, 129.53, 130.16, 132.00, 132.47, 133.57, 134.77, 136.56, 145.67, 146.33, 158.30, 158.90. EI-MS: *m/z*: 402.98 [M$^+$].

Anal. Calcd. for $C_{19}H_{13}Cl_2N_3OS$: C, 56.73; H, 3.26; N, 10.45; S, 7.97. Found: C, 56.81; H, 3.42; N, 10.69; S, 7.92.

(2E/2Z)-2-Cyano-N-{3-cyano-4H,5H,6H-cyclopenta[b]thiophen-2-yl}-3-(2,3-dichlorophenyl) prop-2-enamide (**28a**). Compound **28a** was synthesized according to typical procedure using **9a** and 2,3-dichlorobenzaldehyde **13** as starting materials. The yield was (0.27 g, 70.57%) as a gray powder with m.p. 302–304 °C. ^{1}H NMR (500 MHz, DMSO-d_6) δ (ppm): 2.37 (2H, quint, J = 7.0 Hz, CH_2 of C^5-*H*s of cyclopenta[b]thiophen ring), 2.76 (2H, t, J = 7.0 Hz, CH_2 of C^4-*H*s of cyclopenta[b]thiophen ring), 2.87 (2H, t, J = 7.0 Hz, CH_2 of C^6-*H*s of cyclopenta[b]thiophen ring), 7.61 (1H, t, J = 8.0 Hz, CH of C^5-*H* of phenyl ring), 7.80 (1H, d, J = 8.0 Hz, CH of C^6-*H* of phenyl ring), 7.94 (1H, d, J = 8.0 Hz, CH of C^4-*H* of phenyl ring), 8.48 (1H, s, vinyl-*H*), 11.99 (1H, s, NH). ^{13}C NMR (125 MHz, DMSO-d_6) δ (ppm): 27.48, 27.67, 29.27, 93.08, 110.58, 114.31, 114.68, 128.69, 128.97, 131.85, 132.81, 133.55, 136.11, 141.98, 149.26 (2C), 159.11 (2C). EI-MS: *m/z*: 388.33 [M$^+$]. Anal. Calcd. for $C_{18}H_{11}Cl_2N_3OS$: C, 55.68; H, 2.86; N, 10.82; S, 8.26. Found: C, 55.79; H, 3.04; N, 11.03; S, 8.44.

(2E)-2-Cyano-N-(3-cyano-4,5,6,7-tetrahydro-1-benzothiophen-2-yl)-3-(2,3-dichlorophenyl) prop-2-enamide (**28b**). Compound **28b** was synthesized according to typical procedure using **9b** and 2,3-dichlorobenzaldehyde **13** as starting materials. The yield was (0.31 g, 77.06%) as a dark yellow powder with m.p. 232–234 °C. ^{1}H NMR (500 MHz, DMSO-d_6) δ (ppm): 1.70–1.80 (4H, m, 2 CH_2 of $C^{5,6}$-*H*s of tetrahydrobenzothiophene ring), 2.50–2.55 (2H, m, CH_2 of C^7-*H*s of tetrahydrobenzothiophene ring), 2.60–2.65 (2H, m, CH_2 of C^4-*H*s of tetrahydrobenzothiophene ring), 7.61 (1H, t, J = 8.0 Hz, CH of C^5-*H* of phenyl ring), 7.87 (1H, d, J = 8.0 Hz, CH of C^6-*H* of phenyl ring), 7.94 (1H, d, J = 8.0 Hz, CH of C^4-*H* of phenyl ring), 8.48 (1H, s, vinyl-*H*), 12.02 (1H, s, NH). ^{13}C NMR (125 MHz, DMSO-d_6) δ (ppm): 21.62, 22.53, 23.50, 23.59, 96.90, 110.64, 114.00, 114.70, 128.65, 128.94, 130.00, 131.83 (2C), 132.79, 133.00, 149.18 (2C), 159.10 (2C). EI-MS: *m/z*: 402.54 [M$^+$]. Anal. Calcd. for $C_{19}H_{13}Cl_2N_3OS$: C, 56.73; H, 3.26; N, 10.45; S, 7.97. Found: C, 56.85; H, 3.44; N, 10.78; S, 7.89.

(2E)-2-Cyano-N-{3-cyano-4H,5H,6H-cyclopenta[b]thiophen-2-yl}-3-[4-(piperidin-1-yl)phenyl] prop-2-enamide (**29a**). Compound **29a** was synthesized according to typical procedure using **9a** and 4-(piperidin-1-yl)benzaldehyde **14** as starting materials. The yield was (0.28 g, 70.55%) as a dark red powder with m.p. 262–264 °C. ^{1}H NMR (500 MHz, DMSO-d_6) δ (ppm): 1.50–1.65 (6H, m, 3 CH_2 of $C^{3,4,5}$-*H*s of piperdine ring), 2.30–2.40 (2H, quint, J = 6.5 Hz, CH_2 of C^5-*H*s of cyclopenta[b]thiophen ring), 2.70–2.80 (2H, t, J = 6.5 Hz, CH_2 of C^4-*H*s of cyclopenta[b]thiophen ring), 2.80–2.90 (2H, t, J = 6.5 Hz, CH_2 of C^6-*H*s of cyclopenta[b]thiophen ring), 3.45–3.55 (4H, m, 2 CH_2 of $C^{2,6}$-*H*s of the piperdine ring), 7.04 (2H, d, J = 8.0 Hz, 2 CH of $C^{3,5}$-*H*s of phenyl ring), 7.91 (2H, d, J = 8.0 Hz, 2 CH of $C^{2,6}$-*H*s of phenyl ring), 8.10 (1H, s, vinyl-*H*), 11.45 (1H, s, NH). ^{13}C NMR (125 MHz, DMSO-d_6) δ (ppm): 23.96, 25.00 (2C), 27.45, 27.64, 29.17, 47.40 (2C), 94.93, 113.21 (2C), 117.67, 119.18, 133.65 (2C), 141.55, 152.52, 153.57, 161.32. EI-MS: *m/z*: 402.67 [M$^+$]. Anal. Calcd. for $C_{23}H_{22}N_4OS$: C, 68.63; H, 5.51; N, 13.92; S, 7.96. Found: C, 68.80; H, 5.62; N, 14.20; S, 8.05.

(2E)-2-Cyano-N-(3-cyano-4,5,6,7-tetrahydro-1-benzothiophen-2-yl)-3-[4-(piperidin-1-yl)phenyl] prop-2-enamide (**29b**). Compound **29b** was synthesized according to typical procedure using **9b** and 4-(piperidin-1-yl)benzaldehyde **14** as starting materials. The yield was (0.28 g, 66.26%) as an orange powder with m.p. 262–264 °C. ^{1}H NMR (500 MHz, DMSO-d_6) δ (ppm): 1.55–1.65 (6H, m, 3 CH_2 of $C^{3,4,5}$-*H*s of piperdine ring), 1.70–1.80 (4H, m, 2 CH_2 of $C^{5,6}$-*H*s of tetrahydrobenzothiophene ring), 2.45–2.55 (2H, m, CH_2 of C^7-*H*s of tetrahydrobenzothiophene ring), 2.60–2.65 (2H, m, CH_2 of C^4-*H*s of tetrahydrobenzothiophene ring), 3.49 (4H, t, J = 5.0 Hz, 2 CH_2 of $C^{2,6}$-*H*s of piperdine ring), 7.06 (2H, d, J = 8.5 Hz, 2 CH of $C^{3,5}$-*H*s of phenyl ring), 7.91 (2H, d, J = 8.5 Hz, 2 CH of $C^{2,6}$-*H*s of phenyl ring), 8.10 (1H, s, vinyl-*H*), 11.43 (1H, s, NH). ^{13}C NMR (125 MHz, DMSO-d_6) δ (ppm): 21.68, 22.57, 23.45, 23.59, 23.99 (2C), 25.02 (2C), 47.40, 94.98, 95.80, 113.22 (2C), 114.20, 117.72, 119.18, 128.80, 131.39, 133.67 (2C), 146.24, 152.56, 153.58, 161.29. EI-MS: *m/z*: 416.22 [M$^+$]. Anal. Calcd. for $C_{24}H_{24}N_4OS$: C, 69.20; H, 5.81; N, 13.45; S, 7.70. Found: C, 69.43; H, 5.96; N, 13.72; S, 7.81.

(2E)-2-Cyano-N-{3-cyano-4H,5H,6H-cyclopenta[b]thiophen-2-yl}-3-[4-(morpholin-4-yl)phenyl] prop-2-enamide (**30a**). Compound **30a** was synthesized according to the typical procedure using **9a** and 4-(morpholin-4-yl)benzaldehyde **15** as starting materials. The yield was (0.28 g, 69.96%) as an orange powder with m.p. 296–298 °C. ^{1}H NMR (500 MHz, DMSO-d_6) δ (ppm): 2.35 (2H, quint, *J* = 6.5 Hz, CH$_2$ of C^5-*H*s of cyclopenta[b]thiophen ring), 2.74 (2H, t, *J* = 6.5 Hz, CH$_2$ of C^4-*H*s of cyclopenta[b]thiophen ring), 2.85 (2H, t, *J* = 6.5 Hz, CH$_2$ of C^6-*H*s of cyclopenta[b]thiophen ring), 3.35–3.45 (4H, m, 2 CH$_2$ of C^{3,5}-*H*s of morpholine ring), 3.65–3.75 (4H, m, 2 CH$_2$ of C^{2,6}-*H*s of morpholine ring), 7.09 (2H, d, *J* = 9.0 Hz, 2 CH of C^{3,5}-*H*s of phenyl ring), 7.95 (2H, d, *J* = 9.0 Hz, 2 CH of C^{2,6}-*H*s of phenyl ring), 8.15 (1H, s, vinyl-*H*), 11.54 (1H, s, NH). ^{13}C NMR (125 MHz, DMSO-d_6) δ (ppm): 27.45, 27.64, 29.18, 46.30 (2C), 65.74 (2C), 92.11, 96.65, 113.42 (2C), 114.47, 117.36, 120.56, 133.22 (2C), 135.25, 141.60, 152.65, 153.90 (2C), 161.13. EI-MS: *m/z*: 404.62 [M$^+$]. Anal. Calcd. for C$_{22}$H$_{20}$N$_4$O$_2$S: C, 65.33; H, 4.98; N, 13.85; S, 7.93. Found: C, 65.47; H, 5.12; N, 14.09; S, 7.81.

(2E)-2-Cyano-N-(3-cyano-4,5,6,7-tetrahydro-1-benzothiophen-2-yl)-3-[4-(morpholin-4-yl) phenyl]prop-2-enamide (**30b**). Compound **30b** was synthesized according to typical procedure using **9b** and 4-(morpholin-4-yl)benzaldehyde **15** as starting materials. The yield was (0.29 g, 69.05%) as an orange powder with m.p. 246–248 °C. ^{1}H NMR (500 MHz, DMSO-d_6) δ (ppm): 1.70–1.82 (4H, m, 2 CH$_2$ of C^{5,6}-*H*s of tetrahydrobenzothiophene ring), 2.49–2.54 (2H, m, CH$_2$ of C^7-*H*s of tetrahydrobenzothiophene ring), 2.59–2.64 (2H, m, CH$_2$ of C^4-*H*s of tetrahydrobenzothiophene ring), 3.40 (4H, t, *J* = 5.0 Hz, 2 CH$_2$ of C^{3,5}-*H*s of morpholine ring), 3.72 (4H, t, *J* = 5.0 Hz, 2 CH$_2$ of C^{2,6}-*H*s of morpholine ring), 7.10 (2H, d, *J* = 9.0 Hz, 2 CH of C^{3,5}-*H*s of phenyl ring), 7.95 (2H, d, *J* = 9.0 Hz, 2 CH of C^{2,6}-*H*s of phenyl ring), 8.14 (1H, s, vinyl-*H*), 11.52 (1H, s, NH). ^{13}C NMR (125 MHz, DMSO-d_6) δ (ppm): 21.71, 22.60, 23.48, 23.60, 46.31 (2C), 65.77 (2C), 113.44 (2C), 114.30, 117.48, 120.64, 126.82, 130.60, 131.37, 133.20 (2C), 146.70, 153.88, 161.19. EI-MS: *m/z*: 418.81 [M$^+$]. Anal. Calcd. for C$_{23}$H$_{22}$N$_4$O$_2$S: C, 66.01; H, 5.30; N, 13.39; S, 7.66. Found: C, 66.28; H, 5.47; N, 13.58; S, 7.85.

(2E)-2-Cyano-N-{3-cyano-4H,5H,6H-cyclopenta[b]thiophen-2-yl}-3-[4-(4-methylpiperazin-1-yl)phenyl]prop-2-enamide (**31**). Compound **31a** was synthesized according to typical procedure using **9a** and 4-(4-methylpiperazin-1-yl)benzaldehyde **16** as starting materials. The yield was (0.29 g, 69.45%) as a red powder with m.p. 254–256 °C. ^{1}H NMR (500 MHz, MHz, DMSO-d_6) δ (ppm): 2.25–2.35 (2H, m, CH$_2$ of C^5-*H*s of cyclopenta[b]thiophen ring), 2.44 (3H, s, CH$_3$ of N-methyl of piperazine ring), 2.60–2.85 (8H, m, 2 CH$_2$ of C^{4,6}-*H*s of cyclopenta[b]thiophen ring and 2 CH$_2$ of C^{3,5}-*H*s of piperazine ring), 3.40–3.55 (4H, m, 2 CH$_2$ of C^{2,6}-*H*s of piperazine ring), 7.06 (2H, d, *J* = 7.5 Hz, 2 CH of C^{3,5}-*H*s of phenyl ring), 7.87 (2H, d, *J* = 7.5 Hz, 2 CH of C^{2,6}-*H*s of phenyl ring), 7.98 (1H, s, vinyl-*H*), 10.39 (1H, br s, NH). ^{13}C NMR (125 MHz, CF$_3$COOD) δ (ppm): 29.20, 29.31, 30.76, 45.25, 50.40 (2C), 54.37 (2C), 100.28, 109.91, 117.14, 120.24, 130.83, 135.88 (2C), 140.28 (2C), 149.49, 150.87, 151.99, 154.82, 163.01, 164.10. EI-MS: *m/z*: 417.73 [M$^+$]. Anal. Calcd. for C$_{23}$H$_{23}$N$_5$OS: C, 66.16; H, 5.55; N, 16.77; S, 7.68. Found: C, 66.34; H, 5.67; N, 16.89; S, 7.76.

(2E)-2-Cyano-N-(3-cyano-4,5,6,7-tetrahydro-1-benzothiophen-2-yl)-3-[4-(4-methylpiperazin-1-yl)phenyl]prop-2-enamide (**31b**). Compound **31b** was synthesized according to typical procedure using **9b** and 4-(4-methylpiperazin-1-yl)benzaldehyde **16** as starting materials. The yield was (0.32 g, 74.14%) as a golden powder with m.p. 257–259 °C. ^{1}H NMR (500 MHz, CF$_3$COOD) δ (ppm): 2.00–2.10 (4H, m, 2 CH$_2$ of C^{3,5}-*H*s of piperazine ring), 2.95–3.15 (4H, m, 2 CH$_2$ of C^{5,6}-*H*s of tetrahydrobenzothiophene ring), 3.21 (3H, s, CH$_3$ of N-methyl of piperazine ring), 3.70–3.80 (2H, m, CH$_2$ of C^7-*H*s of tetrahydrobenzothiophene ring), 4.05–4.15 (4H, m, 2 CH$_2$ of C^{2,6}-*H*s of piperazine ring), 4.30–4.35 (2H, m, CH$_2$ of C^4-*H*s of tetrahydrobenzothiophene ring), 7.68 (2H, d, *J* = 9.5 Hz, 2 CH of C^{3,5}-*H*s of phenyl ring), 8.29 (2H, d, *J* = 9.5 Hz, 2 CH of C^{2,6}-*H*s of phenyl ring), 8.71 (1H, s, vinyl-*H*), 9.39 (1H, s, NH), 8.91 (1H, s, NH$_4$$^+$ of piperazine ring as a result of ionization). ^{13}C NMR (125 MHz, CF$_3$COOD) δ (ppm): 20.72, 22.64, 23.11, 26.58, 45.41, 49.44 (2C), 54.84 (2C), 98.84, 115.15, 117.50, 121.69, 131.41, 135.38, 136.29 (2C), 145.36 (2C), 151.06, 152.93, 155.62, 167.26. EI-MS:

m/z: 431.25 [M$^+$]. Anal. Calcd. for C$_{24}$H$_{25}$N$_5$OS: C, 66.80; H, 5.84; N, 16.23; S, 7.43. Found: C, 67.04; H, 5.98; N, 16.48; S, 7.60.

(2E)-3-[4-(Benzyloxy)-3-methoxyphenyl]-2-cyano-N-{3-cyano-4H,5H,6H-cyclopenta[b]thiophen-2-yl}prop-2-enamide (**32a**). Compound **32a** was synsized according to typical procedure using **9a** and 4-(benzyloxy)-3-methoxybenzaldehyde **17** as starting materials. The yield was (0.22 g, 48.30%) as a yellow powder with m.p. 233–235 °C. ^{1}H NMR (500 MHz, pyridine-d_5) δ (ppm): 2.05–2.15 (2H, m, CH$_2$ of C^5-*H*s of cyclopenta[b]thiophen ring), 2.55–2.75 (4H, m, 2 CH$_2$ of C^{4,6}-*H*s of cyclopenta[b]thiophen ring), 3.78 (3H, s, CH$_3$ of OCH$_3$ at C^3 of phenyl ring), 5.21 (2H, s, benzylic CH$_2$), 7.08 (1H, d, *J* = 9.0 Hz, C^5-*H* of phenyl ring), 7.22 (1H, hindered by solvent peak, C^4-*H* of benzyl group), 7.32 (2H, d, *J* = 6.5 Hz, C^{2,6}-*H*s of benzyl group), 7.38 (2H, t, *J* = 6.5 Hz, C^{3,5}-*H*s of benzyl group), 7.58 (1H, hindered by solvent peak, C^6-*H* of phenyl ring), 7.80 (1H, s, C^2-*H* of phenyl ring), 8.53 (1H, s, vinyl-*H*). ^{13}C NMR (125 MHz, pyridine-d_5) δ (ppm): 27.93, 28.05, 29.49, 55.68, 70.79, 93.85, 101.89, 112.84, 113.30, 127.02, 128.10 (2C), 128.46, 128.90 (2C), 153.49, 161.37. EI-MS: *m/z*: 455.3 [M$^+$]. Anal. Calcd. for C$_{26}$H$_{21}$N$_3$O$_3$S: C, 68.55; H, 4.65; N, 9.22; S, 7.04. Found: C, 68.74; H, 4.82; N, 9.43; S, 7.18.

(2E)-3-[4-(Benzyloxy)-3-methoxyphenyl]-2-cyano-N-(3-cyano-4,5,6,7-tetrahydro-1-benzothiophen-2-yl)prop-2-enamide (**32b**). Compound **32b** was synsized according to typical procedure using **9b** and 4-(benzyloxy)-3-methoxybenzaldehyde **17** as starting materials. The yield was (0.20 g, 42.38%) as yellow powder with m.p. 220–222 °C. ^{1}H NMR (500 MHz, DMSO-d_6) δ (ppm): 1.70–1.85 (4H, m, 2 CH$_2$ of C^{5,6}-*H*s of tetrahydrobenzothiophene ring), 2.45–2.55 (2H, m, CH$_2$ of C^7-*H*s of tetrahydrobenzothiophene ring), 2.55–2.65 (2H, m, CH$_2$ of C^4-*H*s of tetrahydrobenzothiophene ring), 3.82 (3H, s, CH$_3$ of OCH$_3$ at C^3 of phenyl ring), 5.22 (2H, s, benzylic CH$_2$), 7.28 (1H, d, *J* = 8.5 Hz, C^5-*H* of phenyl ring), 7.35 (1H, d, *J* = 6.5 Hz, C^4-*H* of benzyl group), 7.40 (2H, t, *J* = 6.5 Hz, C^{3,5}-*H*s of benzyl group), 7.45 (2H, d, *J* = 6.5 Hz, C^{2,6}-*H*s of benzyl group), 7.65 (1H, d, *J* = 8.5 Hz, C^6-*H* of phenyl ring), 7.74 (1H, s, C^2-*H* of phenyl ring), 8.25 (1H, s, vinyl-*H*), 11.72 (1H, s, NH). ^{13}C NMR (125 MHz, DMSO-d_6) δ (ppm): 21.74, 22.64, 23.57, 23.67, 55.65, 70.10, 112.96, 113.30, 116.82, 116.86, 124.58, 126.00, 128.14 (2C), 128.26, 128.62 (2C), 131.62, 136.31, 149.00, 152.17, 160.78. EI-MS: *m/z*: 469.13 [M$^+$]. Anal. Calcd. for C$_{27}$H$_{23}$N$_3$O$_3$S: C, 69.06; H, 4.94; N, 8.95; S, 6.83. Found: C, 69.34; H, 4.81; N, 9.17; S, 7.01.

(2E)-2-Cyano-N-{3-cyano-4H,5H,6H-cyclopenta[b]thiophen-2-yl}-3-(3-methyl-1-phenyl-1H-pyrazol-4-yl)prop-2-enamide (**33a**). Compound **33a** was synsized according to typical procedure using **9a** and 3-methyl-1-phenyl-1*H*-pyrazole-4-carbaldehyde **18** as starting materials. The yield was (0.32 g, 78.8%) as a yellow powder with m.p. 267–269 °C. ^{1}H NMR (500 MHz, CDCl$_3$) δ (ppm): 1.58 (3H, s, CH$_3$ at C^4 of pyrazole ring), 2.46 (2H, quint, *J* = 7.0 Hz, CH$_2$ of C^5-*H*s of cyclopenta[b]thiophen ring), 2.84 (2H, t, *J* = 7.0 Hz, CH$_2$ of C^4-*H*s of cyclopenta[b]thiophen ring), 2.92 (2H, t, *J* = 7.0 Hz, CH$_2$ of C^6-*H*s of cyclopenta[b]thiophen ring), 7.39 (1H, t, *J* = 8.0 Hz, C^4-*H* of phenyl ring), 7.51 (2H, t, *J* = 8.0 Hz, 2 CH of C^{3,5}-*H* of phenyl ring), 7.72 (2H, d, *J* = 8.0 Hz, 2 CH of C^{2,6}-*H* of phenyl ring), 8.34 (1H, s, C5-H of pyrazole ring), 8.80 (1H, s, vinyl-*H*), 8.93 (1H, s, NH). ^{13}C NMR (125 MHz, CDCl$_3$) δ (ppm): 11.74, 28.06, 28.13, 29.44, 91.28, 97.32, 113.86, 116.11, 116.75, 119.83 (2C), 128.13, 128.76, 129.70 (2C), 136.20, 138.69, 141.58, 145.45, 149.73, 154.23, 157.67. EI-MS: *m/z*: 399.8 [M$^+$]. Anal. Calcd. for C$_{22}$H$_{17}$N$_5$OS: C, 66.15; H, 4.29; N, 17.53; S, 8.03. Found: C, 66.42; H, 4.36; N, 17.79; S, 8.21.

(2E)-2-Cyano-N-(3-cyano-4,5,6,7-tetrahydro-1-benzothiophen-2-yl)-3-(3-methyl-1-phenyl-1H-pyrazol-4-yl)prop-2-enamide (**33b**). Compound **33b** was synsized according to typical procedure using **9b** and 3-methyl-1-phenyl-1*H*-pyrazole-4-carbaldehyde **18** as starting materials. The yield was (0.33 g, 78.59%) as a yellow powder with m.p. 256–258 °C. ^{1}H NMR (500 MHz, CDCl$_3$) δ (ppm): 1.80–1.90 (4H, m, 2 CH$_2$ of C^{5,6}-*H*s of tetrahydrobenzothiophene ring), 2.50 (3H, s, CH$_3$ at C^4 of pyrazole ring), 2.62 (2H, t, *J* = 6.0 Hz, CH$_2$ of C^7-*H*s of tetrahydrobenzothiophene ring), 2.67 (2H, t, *J* = 5.5 Hz, CH$_2$ of C^4-*H*s of tetrahydrobenzothiophene ring), 7.39 (1H, t, *J* = 7.5 Hz, C^4-*H* of phenyl ring), 7.50 (2H, t, *J* = 7.5 Hz, 2 CH of C^{3,5}-*H* of phenyl ring), 7.72 (2H, d, *J* = 7.5 Hz, 2 CH of C^{2,6}-*H* of phenyl ring), 8.34 (1H, s, C^5-*H* of pyrazole ring), 8.81 (1H, s, vinyl-*H*), 8.92 (1H, s, NH). ^{13}C NMR (125 MHz,

CDCl$_3$) δ (ppm): 11.73, 21.99, 22.99, 23.97, 24.01, 95.54, 97.38, 113.60, 116.09, 116.73, 119.79 (2C), 128.10, 128.73, 129.69 (2C), 129.86, 131.65, 138.67, 144.98, 145.45, 154.21, 157.66. EI-MS: *m/z*: 413.27 [M$^+$]. Anal. Calcd. for C$_{23}$H$_{19}$N$_5$OS: C, 66.81; H, 4.63; N, 16.94; S, 7.75. Found: C, 67.09; H, 4.81; N, 17.15; S, 7.94.

(2E)-2-Cyano-N-{3-cyano-4H,5H,6H-cyclopenta[b]thiophen-2-yl}-3-(3-phenyl-1H-pyrazol-4-yl)prop-2-enamide (**34a**). Compound **34a** was synthesized according to typical procedure using **9a** and 3-phenyl-1*H*-pyrazole-4-carbaldehyde **19** as starting materials. The yield was (0.24 g, 60.96%) as golden powder with m.p. 226–228 °C. ^{1}H NMR (400 MHz, DMSO-*d$_6$*) δ (ppm): 2.30–2.50 (2H, m, CH$_2$ of C^5-*H*s of cyclopenta[b]thiophen ring), 2.70–2.95 (4H, m, 2 CH$_2$ of C^{4,6}-*H*s of cyclopenta[b]thiophen ring), 7.65 (5H, m, 5 CH of C^{2,3,4,5,6}-*H*s of phenyl ring), 8.14 (1H, s, vinyl-*H*), 8.56 (1H, br s, NH), 11.71 (1H, s, C^5-*H* of pyrazole ring), 14.16 (1H, br s, NH of pyrazole ring). ^{13}C NMR (100 MHz, DMSO-*d$_6$*) δ (ppm): 27.94, 28.10, 29.66, 92.88, 100.33, 112.64, 113.33, 114.86, 117.35, 129.49 (4C), 129.68, 136.00, 142.10 (3C), 151.02, 160.92 (2C). EI-MS: *m/z*: 385.48 [M$^+$]. Anal. Calcd. for C$_{21}$H$_{15}$N$_5$OS: C, 65.44; H, 3.92; N, 18.17; S, 8.32. Found: C, 65.67; H, 4.09; N, 18.30; S, 8.58.

(2E)-2-Cyano-N-(3-cyano-4,5,6,7-tetrahydro-1-benzothiophen-2-yl)-3-(3-phenyl-1H-pyrazol-4-yl)prop-2-enamide (**34b**). Compound **34b** was synthesized according to typical procedure using **9b** and 3-phenyl-1*H*-pyrazole-4-carbaldehyde **19** as starting materials. The yield was (0.24 g, 60.07%) as a yellow powder with m.p. 263–265 °C. ^{1}H NMR (400 MHz, DMSO-*d$_6$*) δ (ppm): 1.70–1.85 (4H, m, 2 CH$_2$ of C^{5,6}-*H*s of tetrahydrobenzothiophene ring), 2.55–2.65 (4 H, m, 2 CH$_2$ of C^{4,7}-*H*s of tetrahydrobenzothiophene ring), 7.65 (5H, m, 5 CH of C^{2,3,4,5,6}-*H*s of phenyl ring), 8.13 (1H, s, vinyl-*H*), 8.54 (1H, br s, NH), 11.70 (1H, s, C^5-*H* of pyrazole ring), 14.14 (1H, br s, NH of pyrazole ring). ^{13}C NMR (125 MHz, DMSO-*d$_6$*) δ (ppm): 21.65, 22.56, 23.47, 23.58, 96.36, 99.89, 112.14, 114.06, 116.86, 129.02 (4C), 129.21, 129.35 (2C), 131.50 (2C), 145.69 (2C), 160.46 (2C). EI-MS: *m/z*: 399.22 [M$^+$]. Anal. Calcd. for C$_{22}$H$_{17}$N$_5$OS: C, 66.15; H, 4.29; N, 17.53; S, 8.03. Found: C, 65.97; H, 4.38; N, 17.71; S, 8.14.

(2E)-2-Cyano-N-{3-cyano-4H,5H,6H-cyclopenta[b]thiophen-2-yl}-3-(naphthalen-1-yl)prop-2-enamide (**35a**). Compound **35a** was synthesized according to typical procedure using **9a** and 1-naphthaldehyde **20** as starting materials. The yield was (0.24 g, 64.69%) as a dark orange powder with m.p. 238–240 °C. ^{1}H NMR (500 MHz, DMSO-*d$_6$*) δ (ppm): 2.38 (2H, quint, *J* = 7.0 Hz, CH$_2$ of C^5-*H*s of cyclopenta[b]thiophen ring), 2.77 (2H, t, *J* = 7.0 Hz, CH$_2$ of C^4-*H*s of cyclopenta[b]thiophen ring), 2.89 (2H, t, *J* = 7.0 Hz, CH$_2$ of C^6-*H*s of cyclopenta[b]thiophen ring), 7.67 (1H, t, *J* = 7.0 Hz, C^6-*H* of naphthalene ring), 7.70 (2H, t, *J* = 8.0 Hz, 2 CH of C^{3,7}-*H*s of naphthalene ring), 8.07 (1H, d, *J* = 8.0 Hz, C^4-*H* of naphthalene ring), 8.12 (1H, d, *J* = 7.0 Hz, C^5-*H* of naphthalene ring), 8.18 (1H, d, *J* = 8.0 Hz, C^2-*H* of naphthalene ring), 8.26 (1H, d, *J* = 8.0 Hz, C^8-*H* of naphthalene ring), 9.06 (1H, s, vinyl-*H*), 12.06 (1H, s, NH). ^{13}C NMR (125 MHz, DMSO-*d$_6$*) δ (ppm): 27.50, 27.71, 29.28, 92.48, 108.92, 114.48, 115.73, 124.02, 125.56 (2C), 127.06, 127.72 (2C), 128.90, 129.19, 130.85, 132.59, 133.09, 135.65, 141.91, 151.43, 160.14. EI-MS: *m/z*: 369.21 [M$^+$]. Anal. Calcd. for C$_{22}$H$_{15}$N$_3$OS: C, 71.52; H, 4.09; N, 11.37; S, 8.68. Found: C, 71.38; H, 4.23; N, 11.58; S, 8.90.

(2E)-2-Cyano-N-(3-cyano-4,5,6,7-tetrahydro-1-benzothiophen-2-yl)-3-(naphthalen-1-yl)prop-2-enamide (**35b**). Compound **35b** was synthesized according to typical procedure using **9b** and 1-naphthaldehyde **20** as starting materials. The yield was (0.24 g, 63.1%) as a yellow powder with m.p. 265–267 °C. ^{1}H NMR (500 MHz, DMSO-*d$_6$*) δ (ppm): 1.73–1.83 (4H, m, 2 CH$_2$ of C^{5,6}-*H*s of tetrahydrobenzothiophene ring), 2.52–2.58 (2H, m, CH$_2$ of C^7-*H*s of tetrahydrobenzothiophene ring), 2.63–2.69 (2H, m, CH$_2$ of C^4-*H*s of tetrahydrobenzothiophene ring), 7.66 (1H, t, *J* = 7.0 Hz, C^6-*H* of naphthalene ring), 7.70 (2H, t, *J* = 8.0 Hz, 2 CH of C^{3,7}-*H*s of naphthalene ring), 8.07 (1H, d, *J* = 8.0 Hz, C^4-*H* of naphthalene ring), 8.11 (1H, d, *J* = 7.0 Hz, C^5-*H* of naphthalene ring), 8.18 (1H, d, *J* = 8.0 Hz, C^2-*H* of naphthalene ring), 8.26 (1H, d, *J* = 8.0 Hz, C^8-*H* of naphthalene ring), 9.06 (1H, s, vinyl-*H*), 12.06 (1H, s, NH). ^{13}C NMR (125 MHz, DMSO-*d$_6$*) δ (ppm): 21.67, 22.56, 23.50, 23.63, 96.33, 114.64, 116.25, 124.03, 125.55, 127.05, 127.71, 127.75, 128.89, 129.20, 129.30, 130.83, 132.57, 133.08, 133.17, 133.58, 133.65, 151.51, 160.12. EI-MS: *m/z*: 383.23 [M$^+$]. Anal. Calcd. for C$_{23}$H$_{17}$N$_3$OS: C, 72.04; H, 4.47; N, 10.96; S, 8.36. Found: C, 71.88; H, 4.69; N, 11.23; S, 8.49.

(2E)-2-Cyano-N-{3-cyano-4H,5H,6H-cyclopenta[b]thiophen-2-yl}-3-(naphthalen-2-yl)prop-2-enamide (**36a**). Compound **36a** was synthesized according to typical procedure using **9a** and 2-naphthaldehyde **21** as starting materials. The yield was (0.19 g, 51.42%) as a dark orange powder with m.p. 228–230 °C. ^{1}H NMR (500 MHz, DMSO-d_6) δ (ppm): 2.25–2.35 (2H, m, CH$_2$ of C^5-Hs of cyclopenta[b]thiophen ring), 2.65–2.80 (4H, m, 2 CH$_2$ of C^{4,6}-Hs of cyclopenta[b]thiophen ring), 7.54–7.66 (2H, m, C^{6,7}-Hs of naphthalene ring), 7.92–8.02 (3H, m, C^{3,5,8}-Hs of naphthalene ring), 8.15 (1H, d, J = 8.0 Hz, C^4-H of naphthalene ring), 8.38 (1H, s, C^1-H of naphthalene ring), 8.38 (1H, s, vinyl-H). ^{13}C NMR (125 MHz, DMSO-d_6) δ (ppm): 27.06, 27.95, 29.63, 87.54, 113.98, 118.68 (2C), 125.09, 126.97, 127.72, 127.83, 128.55, 128.76, 130.00 (2C), 131.03, 131.09, 132.75, 134.00, 139.05, 146.09, 162.53. EI-MS: m/z: 369.53 [M$^+$]. Anal. Calcd. for C$_{22}$H$_{15}$N$_3$OS: C, 71.52; H, 4.09; N, 11.37; S, 8.68. Found: C, 71.69; H, 4.21; N, 11.62; S, 8.79.

(2E)-2-Cyano-N-(3-cyano-4,5,6,7-tetrahydro-1-benzothiophen-2-yl)-3-(naphthalen-2-yl)prop-2-enamide (**36b**). Compound **36b** was synthesized according to typical procedure using **9b** and 2-naphthaldehyde **21** as starting materials. The yield was (0.19 g, 49.5%) as a dark yellow powder with m.p. 252–254 °C. ^{1}H NMR (500 MHz, DMSO-d_6) δ (ppm): 1.73–1.81 (4H, m, 2 CH$_2$ of C^{5,6}-Hs of tetrahydrobenzothiophene ring), 2.50–2.55 (2H, m, CH$_2$ of C^7-Hs of tetrahydrobenzothiophene ring), 2.59–2.65 (2H, m, CH$_2$ of C^4-Hs of tetrahydrobenzothiophene ring), 7.63 (1H, t, J = 7.5 Hz, C^6-H of naphthalene ring), 7.68 (1H, t, J = 7.5 Hz, C^7-H of naphthalene ring), 8.01 (1H, d, J = 8.0 Hz, C^5-H of naphthalene ring), 8.06 (1H, d, J = 8.0 Hz, C^8-H of naphthalene ring), 8.10 (1H, d, J = 9.0 Hz, C^3-H of naphthalene ring), 8.19 (1H, d, J = 9.0 Hz, C^4-H of naphthalene ring), 8.44 (1H, s, C^1-H of naphthalene ring), 8.51 (1H, s, vinyl-H), 11.94 (1H, s, NH). ^{13}C NMR (125 MHz, CF$_3$COOD) δ (ppm): 23.03, 25.17, 25.73, 26.23, 114.74, 115.16, 124.92, 125.31, 129.68, 129.80, 130.02, 130.16, 130.90, 131.55, 131.88, 134.64, 135.02, 135.96, 136.88, 146.66, 151.79, 158.56, 162.32. EI-MS: m/z: 383.26 [M$^+$]. Anal. Calcd. for C$_{23}$H$_{17}$N$_3$OS: C, 72.04; H, 4.47; N, 10.96; S, 8.36. Found: C, 71.92; H, 4.65; N, 11.18; S, 8.47.

(2E)-3-(2H-1,3-Benzodioxol-4-yl)-2-cyano-N-{3-cyano-4H,5H,6H-cyclopenta[b]thiophen-2-yl}prop-2-enamide (**37a**). Compound **37a** was synthesized according to typical procedure using **9a** and 2,3-methylenedioxybenzaldehyde **22** as starting materials. The yield was (0.30 g, 82.55%) as a yellow powder with m.p. 286–288 °C. ^{1}H NMR (500 MHz, DMSO-d_6) δ (ppm): 2.36 (2H, quint, J = 7.0 Hz, CH$_2$ of C^5-Hs of cyclopenta[b]thiophen ring), 2.75 (2H, t, J = 7.0 Hz, CH$_2$ of C^4-Hs of cyclopenta[b]thiophen ring), 2.86 (2H, t, J = 7.0 Hz, CH$_2$ of C^6-Hs of cyclopenta[b]thiophen ring), 6.21 (2H, s, CH$_2$ of C^2-Hs of benzodioxole ring), 7.04 (1H, t, J = 7.75 Hz, C^6-H of benzodioxole ring), 7.16 (1H, d, J = 7.75 Hz, C^5-H of benzodioxole), 7.63 (1H, d, J = 7.75 Hz, C^7-H of benzodioxole ring), 8.23 (1H, s, vinyl-H), 11.91 (1H, s, NH). ^{13}C NMR (125 MHz, CF$_3$COOD) δ (ppm): 29.46, 29.59, 30.98, 100.17, 104.41, 110.21, 115.87, 116.37, 117.46, 121.20, 124.79, 140.53, 149.70, 150.43, 151.23, 152.48, 152.65, 163.39, 171.42. EI-MS: m/z: 363.33 [M$^+$]. Anal. Calcd. for C$_{19}$H$_{13}$N$_3$O$_3$S: C, 62.80; H, 3.61; N, 11.56; S, 8.82. Found: C, 63.04; H, 3.78; N, 11.82; S, 8.98.

(2E)-3-(2H-1,3-Benzodioxol-4-yl)-2-cyano-N-(3-cyano-4,5,6,7-tetrahydro-1-benzothiophen-2-yl)prop-2-enamide (**37b**). Compound **37b** was synthesized according to typical procedure using **9b** and 2,3-methylenedioxybenzaldehyde **22** as starting materials. The yield was (0.20 g, 52.99%) as a yellow powder with m.p. 226–228 °C. ^{1}H NMR (500 MHz, CDCl$_3$) δ (ppm): 1.80–1.90 (4H, m, 2 CH$_2$ of C^{5,6}-Hs of tetrahydrobenzothiophene ring), 2.60–2.70 (4H, m, 2 CH$_2$ of C^{4,7}-Hs of tetrahydrobenzothiophene ring), 6.10 (2H, s, CH$_2$ of C^2-Hs of benzodioxole ring), 6.93–6.99 (2H, m, C^{5,6}-Hs of benzodioxole ring), 6.75 (1H, d, J = 7.5 Hz, C^7-H of benzodioxole ring), 8.55 (1H, s, vinyl-H), 8.93 (1H, br s, NH). ^{13}C NMR (100 MHz, CDCl$_3$) δ (ppm): 22.03, 23.03, 24.02, 24.08, 95.97, 102.00, 102.16, 113.02, 113.54, 114.24, 115.98, 119.78, 122.52, 130.17, 131.81, 144.78, 147.02, 148.21, 149.58, 157.11. EI-MS: m/z: 377.13 [M$^+$]. Anal. Calcd. for C$_{20}$H$_{15}$N$_3$O$_3$S: C, 63.65; H, 4.01; N, 11.13; S, 8.49. Found: C, 63.89; H, 4.23; N, 11.41; S, 8.60.

(2E)-3-(2H-1,3-Benzodioxol-5-yl)-2-cyano-N-{3-cyano-4H,5H,6H-cyclopenta[b]thiophen-2-yl}prop-2-enamide (**38a**). Compound **38a** was synthesized according to typical procedure

using **9a** and 3,4-methylenedioxybenzaldehyde **23** as starting materials. The yield was (0.22 g, 60.54%) as a golden powder with m.p. 219–221 °C. ^{1}H NMR (500 MHz, DMSO-d_6) δ (ppm): 2.25–2.35 (2H, m, CH$_2$ of C^5-*H*s of cyclopenta[b]thiophen ring), 2.60–2.80 (4H, m, 2 CH$_2$ of C^{4,6}-*H*s of cyclopenta[b]thiophen ring), 6.19 (2H, s, CH$_2$ of C^2-*H*s of benzodioxole ring), 7.15 (1H, d, *J* = 10.0 Hz, C^7-*H* of benzodioxole ring), 7.58 (1H, d, *J* = 10.0 Hz, C^6-*H* of benzodioxole ring), 7.65 (1H, s, C^4-*H* of benzodioxole), 8.24 (1H, s, vinyl-*H*), 11.73 (1H, s, NH). ^{13}C NMR (125 MHz, DMSO-d_6) δ (ppm): 27.53, 27.73, 29.28, 92.59, 101.39, 102.64, 108.19, 109.26, 114.45, 116.49, 129.09, 135.71, 141.87, 148.27, 150.47, 151.83, 152.86, 160.55. EI-MS: *m/z*: 363.13 [M$^+$]. Anal. Calcd. for C$_{19}$H$_{13}$N$_3$O$_3$S: C, 62.80; H, 3.61; N, 11.56; S, 8.82. Found: C, 63.07; H, 3.49; N, 11.80; S, 8.65.

(2E)-3-(2H-1,3-Benzodioxol-5-yl)-2-cyano-N-(3-cyano-4,5,6,7-tetrahydro-1-benzothiophen-2-yl)prop-2-enamide (**38b**). Compound **38b** was synthesized according to typical procedure using **9b** and 3,4-methylenedioxybenzaldehyde **23** as starting materials. The yield was (0.20 g, 52.99%) as a yellow powder with m.p. 204–206 °C. FT-IR (KBr) ν$_{max}$ (cm^{-1}): 1279.83 (C-O of benzodioxole ring), 1648.26 (C=O of amide), 1673.84 (C=C), 2223.38 (CN), 2931.53 (aliphatic protons), 3002.25 (aromatic protons), 3433.83 (NH of amide). ^{1}H NMR (400 MHz, CDCl$_3$) δ (ppm): 1.80–1.90 (4H, m, 2 CH$_2$ of C^{5,6}-*H*s of tetrahydrobenzothiophene ring), 2.60–2.75 (4H, m, 2 CH$_2$ of C^{4,7}-*H*s of tetrahydrobenzothiophene ring), 6.14 (2H, s, CH$_2$ of C^2-*H*s of benzodioxole ring), 6.96 (1H, d, *J* = 8.0 Hz, C^7-*H* of benzodioxole ring), 7.47 (1H, d, *J* = 8.0 Hz, C^6-*H* of benzodioxole ring), 7.71 (1H, s, C^4-*H* of benzodioxole ring), 8.30 (1H, s, vinyl-*H*), 8.96 (1H, s, NH). NOESY: dipolar interaction detected between C^6-*H* of benzodioxole ring (7.47, d) and vinyl-*H* (8.30, s) and between C^4-*H* of benzodioxole ring (7.71, s) and vinyl-*H* (8.30, s). ^{13}C NMR (100 MHz, CDCl$_3$) δ (ppm): 17.30, 18.30, 19.28, 19.33, 91.04, 93.89, 97.76, 104.07, 104.39, 108.82, 111.69, 121.20, 125.24, 125.60, 127.01, 140.22, 144.12, 148.12, 149.74, 152.96. EI-MS: *m/z*: 377.53 [M$^+$]. Anal. Calcd. for C$_{20}$H$_{15}$N$_3$O$_3$S: C, 63.65; H, 4.01; N, 11.13; S, 8.49. Found: C, 63.81; H, 4.23; N, 11.40; S, 8.65.

(2E)-2-Cyano-N-{3-cyano-4H,5H,6H-cyclopenta[b]thiophen-2-yl}-3-(1H-indol-3-yl)prop-2-enamide (**39a**). Compound **39a** was synthesized according to typical procedure using **9a** and indole-3-carboxaldehyde **24** as starting materials. The yield was (0.23 g, 65.28%) as a golden powder with m.p. 284–286 °C. ^{1}H NMR (500 MHz, DMSO-d_6) δ (ppm): 2.30–2.40 (2H, m, CH$_2$ of C^5-*H*s of cyclopenta[b]thiophen ring), 2.70–2.95 (4H, m, 2 CH$_2$ of C^{4,6}-*H*s of cyclopenta[b]thiophen ring), 7.25–7.35 (2H, m, 2 CH of C^{5,6}-*H*s of indole ring), 7.57 (1H, d, *J* = 6.5 Hz, C^7-*H* of indole ring), 7.99 (1H, d, *J* = 5.5 Hz, C^4-*H* of indole ring), 8.57 (1H, s, C^4-*H* of indole ring), 8.64 (1H, s, vinyl-*H*), 11.52 (1H, s, NH), 12.54 (1H, s, NH of indole ring). ^{13}C NMR (100 MHz, DMSO-d_6) δ (ppm): 27.92, 28.13, 29.66, 92.49, 95.20, 110.47, 113.44, 115.06, 118.74, 119.10, 122.51, 124.11, 127.62, 132.39, 135.61, 136.65, 142.03, 145.62, 151.53, 161.66. EI-MS: *m/z*: 358.42 [M$^+$]. Anal. Calcd. for C$_{20}$H$_{14}$N$_4$OS: C, 67.02; H, 3.94; N, 15.63; S, 8.94. Found: C, 66.85; H, 4.12; N, 15.79; S, 9.08.

(2E)-2-Cyano-N-(3-cyano-4,5,6,7-tetrahydro-1-benzothiophen-2-yl)-3-(1H-indol-3-yl)prop-2-enamide (**39b**). Compound **39b** was synthesized according to typical procedure using **9b** and indole-3-carboxaldehyde **24** as starting materials. The yield was (0.20 g, 53.69%) as dark yellow powder with m.p. 284–286 °C. ^{1}H NMR (400 MHz, DMSO-d_6) δ (ppm): 1.60–1.90 (4H, m, 2 CH$_2$ of C^{5,6}-*H*s of tetrahydrobenzothiophene ring), 2.60–2.70 (4 H, m, 2 CH$_2$ of C^{4,7}-*H*s of tetrahydrobenzothiophene ring), 7.20–7.40 (2H, m, 2 CH of C^{5,6}-*H*s of indole ring), 7.61 (1H, s, C^7-*H* of indole ring), 8.02 (1H, s, C^4-*H* of indole ring), 8.61 (1H, s, C^2-*H* of indole ring), 8.67 (1H, s, vinyl-*H*), 11.57 (1H, s, NH), 12.58 (1H, s, NH of indole ring). ^{13}C NMR (100 MHz, CDCl$_3$) δ (ppm): 22.17, 23.07, 23.95, 24.09, 31.19, 95.28, 110.46, 113.46, 114.74, 118.76, 119.15, 122.51, 124.11, 127.61, 129.33, 131.91, 132.43, 136.67, 145.70, 146.61, 161.69. EI-MS: *m/z*: 372.18 [M$^+$]. Anal. Calcd. for C$_{21}$H$_{16}$N$_4$OS: C, 67.72; H, 4.33; N, 15.04; S, 8.61. Found: C, 67.51; H, 4.60; N, 15.28; S, 8.73.

3.2. In Vitro Telomerase Activity Assay

The tested compound and **BIBR1532** (R&D Systems, Minneapolis, MN, USA) were dissolved in an appropriate solvent (according to recommendations from TSCA certification)

at stock concentrations of 10 mM, and further diluted to appropriate concentrations in assay buffer. The Telomeric Repeat Amplification Protocol (TRAP) [61] was used to evaluate the activity of telomerase, with some changes that we have previously described [62,63]. A549 cells (human epithelial cell lung carcinoma, ATCC, Manassas, VA) were lysed in (10 mM) Tris-HCl, pH 7.5, (1 mM) EGTA, (1 mM) $MgCl_2$, (5 mM) 2-mercaptoethanol, (0.1 mM) PMSF, (0.5%) CHAPS, and (10%) glycerol (Sigma-Aldrich, St. Louis, MO, USA) and centrifugation. The supernatants were kept at -80 °C. The BCA-1 Protein Assay Kit was used to assess the protein concentration in cell extracts (Sigma-Aldrich, St. Louis, MO, USA). An amount of 5 µg total protein and appropriate amounts of AZT and **BIBR1532** were added to a reaction mixture of (67 mM) Tris-HCl, pH 8.8, (1.5 mM) $MgCl_2$, (0.01%) Tween-20, (16.6 mM) $(NH_4)_2SO_4$, and (1 mM) EGTA (Sigma-Aldrich, St. Louis, MO, USA), (0.25 mM) each dNTP (Evrogen, Moscow) (TS-primer) (5′-AATCCGTCGAGCAGAGTT-3′). To inactivate telomerase, the cells were elongated for 30 min at 37 °C and 10 min at 96 °C. Copy CX-primer was added to the elongation mixture along with 0.1 µL (5′-CCCTTACCCTTACCCTTACCCTAA-3′) and 2.5 units Taq-polymerase, followed by the following PCR: 94 °C for 5 min; 30 cycles of 94 °C for 30 s, 50 °C for 30 s, and 72 °C for 40 s, and 72 °C for 5 min. TBE buffer and (12%) nondenaturing PAAG electrophoresis were used to visualize the PCR product. 10 µL of each sample was placed in each well of gel comb. The gels were stained with the SYBR Green I (Invitrogen, Grand Island, NY, USA), then photographed under the UV light in ChemiDocTM XRS imaging system and analyzed with GelAnalyzer 2010.

3.3. Cell Lines and Incubation with the Compounds

The human A549 (epithelial cell lung carcinoma, ATCC, Manassas, VA, USA), HCC44 (non-small cell lung adenocarcinoma, Leibniz Institute DSMZ-German Collection of the Microorganisms and the Cell Cultures, Braunschweig, Germany), and NCI-H23 (non-small cell lung adenocarcinoma, ATCC, Manassas, VA, USA) cell lines (compounds **29a**, **36b**, and **39b**) were diluted to 10 µM and incubated for 48 h before being tested using the TRAP method.

3.4. In Vitro Anticancer Screening

The cancer screening panel's human tumor 60 cell lines were cultured in the RPMI 1640 medium with (5%) fetal bovine serum and (2 mM) L-glutamine. For a screening experiment, cells were injected onto 96-well microtiter plates (100 µL), with plating densities varying from 5 to 40×10^3 cells per well, depending on different cell lines' doubling times. Before introducing experimental drugs, the microtiter plates were incubated overnight at 37 °C, 95% air, 5% CO_2, and 100% relative humidity after cell injection. TCA was employed to keep each cell line in place overnight, resembling a computation of the cell population for every cell line at the time of the addition of the drug. The experimental drugs were chilled after solubilization in DMSO at 400 times the final maximum test concentration. At the moment of the addition of the drug, the aliquot of the frozen concentrate was thawed and diluted to twice the required final maximum concentration with the complete medium containing (50 µg/mL) gentamicin. The required final concentration of the drug (10 µM) was reached by adding 100 µL aliquots of these definite dilutions of the drug to suitable microtiter wells previously holding a medium of 100 µL. The same technique was utilized for controls containing only DMSO and phosphate-buffered saline at identical dilutions. Following drug addition, the plates were incubated for a further two days at 37 °C, 95% air, 5% CO_2, and 100% relative humidity. The experiment was finished with addition of cold TCA. The cells were fixed in situ by adding (50 µL) cold 50% (*w/v*) TCA (final concentration: 10% TCA) and incubating for 1 hr at 4 °C. The plates were rinsed numerous times with distilled water and dried after the supernatant was removed. Sulforhodamine B (SRB) solution (100 µL) containing 0.4% (*w/v*) sulforhodamine in 1% acetic acid was added and plates were incubated at rt for 10 min. The unbound dye was washed away numerous times with (1%) acetic acid after the staining, and plates were dried. The bound

dye was then solubilized with a (10 mM) trizma base, and absorbance was calculated at 515 nm on an automatic reader. The process was typical for suspension cells, except that the experiment was finished by gradually adding (50 µL) of 80% TCA to fix settling cells at the bottoms of the wells (final conccentration:, 16% TCA). The % growth of treated cells was established using seven absorbance measurements and compared to untreated control cells [57].

3.5. Statistical Analysis

Analysis was carried out using SPSS 25 software, a 2-way ANOVA, and a student's *t*-test (IBM SPSS Statistics, Armonk, NY, USA). The mean ± SEM is used to express the findings. The significance level was set at $p \leq 0.05$. An amount of 1 µL was submitted to the Real-Time Quantitative Telomeric Repeat Amplification Protocol Assay (RTQ-TRAP) as reported by Hou M., et al. to obtain the IC_{50} and IC_{90} values (inhibitor concentrations where the response is decreased by 50% and 90%, respectively) [64]. According to Sebaugh J.L., et al.'s guidelines, the values were assessed using the Prism 6 software (GraphPad, San Diego, CA, USA) [65].

3.6. Molecular Docking

The RSCB Protein Data Bank was employed to get the structure of telomerase from *Tribolium castaneum* (PDB ID: 5CQG) for complex modelling [66]. The SYBYL 8.1 suite was used to design the structures of compound **36b**. The structure was optimized in a vacuum using a Tripos force field and energy minimization. The Gasteiger–Huckel method was used to compute the partial atomic charges. The AutoDock Vina package was used to perform the docking [67]. The docking parameters were established using the AutoDock Tools package. Based on the values of their scoring functions and poses in the binding site, the ligand poses acquired via docking were graded and chosen. Ligand positions from crystal structures were used as a reference template to assess the accuracy of the docked molecules' poses. The PLIP server and the PyMol package were used to study intermolecular interactions between proteins and docked molecules [68].

3.7. Molecular Dynamics Simulation

The Gromacs-2020 software package was used to simulate molecular dynamics, with the explicit solvent (TIP3P) and Na+ ions used to neutralize the system. For atomic parametrization of protein molecules, the AMBER99SB-ILDN forcefield was employed, while for ligand molecules, the GAFF forcefield was used. Steepest descent minimization with a solvent was performed for 50,000 steps. The minimization was followed by a 5 ns NVT equilibration, which was followed by a 5 ns NPT equilibration. During both phases of equilibration, movements of protein- and ligand-heavy atoms were restricted. The equilibrated structure was used as a starting point for MD. MD calculations were performed during 100 ns trajectories. An integrator step was set to 2 fs. The values of the temperature and the pressure were set to 300 K and 1 atm, respectively. The Berendsen thermostat was used for temperature coupling, and the Parrinelo–Ranman barostat was used for pressure coupling. Hydrogen atoms were restricted with the LINCS algorithm. The particle mesh Ewald (PME) was utilized to treat long-range electrostatic interactions. The cutoff distance for nonbonded interactions was set to 12 Å. Data frames were saved every 10 ps. To avoid nonequilibrium effects, the last 50 ns were used for analysis. For simulations, the docked pose of compound **36b** was employed as a starting point. The Gromacs-2020 built-in tools and VMD-1.9.1 software were used to perform trajectory analysis. The conformational changes in the interaction were identified using RMSD of protein structures and RMSF of residues.

3.8. In Silico Pharmacokinetic; Physicochemical Prediction and PAINS Filters

The Swiss Institute of Bioinformatics (SIB) provided the free SwissADME web tool for calculating physicochemical parameters, pharmacokinetic properties, drug-like nature, and

medicinal chemistry friendliness [58,59,69]. The structures of **BIBR1532** and compound **36b** were translated to the SMILES data and then uploaded to the online server for evaluation.

4. Conclusions

Our goal was to design a new, simply synthesized, and highly derivable chemical scaffold as a telomerase inhibitor. Therefore, 30 novel compounds were designed and simply synthesized using readily available and inexpensive starting materials. The activity of telomerase of all synthesized compounds was assessed through TRAP assay. Compounds **29a**, **36b**, and **39b** showed the greatest inhibitory effect on the telomerase enzyme. The most active compound was **36b**, with IC_{50} values of 0.3 μM. The IC_{50} of compounds **29a** and **39b** were 1.7 and 2 μM, respectively. To test whether these compounds (**29a**, **36b**, and **39b**) can penetrate the cells, a living-cell TRAP assay was performed using three NSCLC cell lines: A549, HCC44, and NCI-H23. All three compounds were successfully capable of penetrating the cell membrane. Compound **36b** was selected to investigate whether it can bind to another target using the NCI-60 cell line panel assay as a screening test. Surprisingly, the growth percentage of the 60 cell lines was barely affected, confirming the selectivity of compound **36b** along with the PAINS filter. According to SwissADME prediction, compound **36b** has a good CNS safety profile and enhanced bioavailability in comparison with **BIBR1532**. The simple synthesis, easily modifiable structure, and cellular penetration capability offer our new scaffold as a valuable new genetic bomb trigger.

References

1. Nassour, J.; Schmidt, T.T.; Karlseder, J. Telomeres and Cancer: Resolving the Paradox. *Annu. Rev. Cancer Biol.* **2021**, *5*, 59–77. [CrossRef] [PubMed]
2. Seimiya, H.; Nagasawa, K.; Shin-Ya, K. Chemical targeting of G-quadruplexes in telomeres and beyond for molecular cancer therapeutics. *J. Antibiot.* **2021**, *74*, 617–628. [CrossRef] [PubMed]
3. Shi, H.; Gao, T.; Shi, L.; Chen, T.; Xiang, Y.; Li, Y.; Li, G. Molecular imaging of telomerase and the enzyme activity-triggered drug release by using a conformation-switchable nanoprobe in cancerous cells. *Sci. Rep.* **2018**, *8*, 16341. [CrossRef] [PubMed]
4. Bajaj, S.; Kumar, M.S.; Peters, G.J.; Mayur, Y.C. Targeting telomerase for its advent in cancer therapeutics. *Med. Res. Rev.* **2020**, *40*, 1871–1919. [CrossRef]
5. Wu, L.; Fidan, K.; Um, J.Y.; Ahn, K.S. Telomerase: Key regulator of inflammation and cancer. *Pharmacol. Res.* **2020**, *155*, 1–12. [CrossRef]
6. Di Micco, R.; Krizhanovsky, V.; Baker, D.; d'Adda di Fagagna, F. Cellular senescence in ageing: From mechanisms to therapeutic opportunities. *Nat. Rev. Mol. Cell Biol.* **2021**, *22*, 75–95. [CrossRef]
7. Nassrally, M.S.; Lau, A.; Wise, K.; John, N.; Kotecha, S.; Lee, K.L.; Brooks, R.F. Cell cycle arrest in replicative senescence is not an immediate consequence of telomere dysfunction. *Mech. Ageing Dev.* **2019**, *179*, 11–22. [CrossRef]
8. Harley, C.B. Telomere loss: Mitotic clock or genetic time bomb? *Mutat. Res./DNAging* **1991**, *256*, 271–282. [CrossRef]

9. Harley, C.B. Telomerase and cancer therapeutics. *Nat. Rev. Cancer* **2008**, *8*, 167–179. [CrossRef]

10. Azarm, K.; Bhardwaj, A.; Kim, E.; Smith, S. Persistent telomere cohesion protects aged cells from premature senescence. *Nat. Commun.* **2020**, *11*, 3321. [CrossRef]

11. Graham, M.K.; Meeker, A. Telomeres and telomerase in prostate cancer development and therapy. *Nat. Rev. Urol.* **2017**, *14*, 607–619. [CrossRef] [PubMed]

12. Kaul, Z.; Cheung, C.T.Y.; Bhargava, P.; Sari, A.N.; Yu, Y.; Huifu, H.; Bid, H.; Henson, J.D.; Groden, J.; Reddel, R.R.; et al. Functional characterization of miR-708 microRNA in telomerase positive and negative human cancer cells. *Sci. Rep.* **2021**, *11*, 17052. [CrossRef] [PubMed]

13. Han, X.; Yu, Y.L.; Ma, D.; Zhang, Z.Y.; Liu, X.H. Synthesis, telomerase inhibitory and anticancer activity of new 2-phenyl-4H-chromone derivatives containing 1,3,4-oxadiazole moiety. *J. Enzym. Inhib. Med. Chem.* **2021**, *36*, 344–360. [CrossRef] [PubMed]

14. Asamitsu, S.; Shioda, N.; Sugiyama, H. Switching Off Cancer-Causing Telomerase Using Small Molecules. *Cell Chem. Biol.* **2019**, *26*, 1045–1047. [CrossRef]

15. Maciejowski, J.; de Lange, T. Telomeres in cancer: Tumour suppression and genome instability. *Nat. Rev. Mol. Cell Biol.* **2017**, *18*, 175–186. [CrossRef]

16. Vasina, D.A.; Zhdanov, D.D.; Orlova, E.V.; Orlova, V.S.; Pokrovskaya, M.V.; Aleksandrova, S.S.; Sokolov, N.N. Apoptotic endonuclease EndoG inhibits telomerase activity and induces malignant transformation of human CD4+ T cells. *Biochemistry* **2017**, *82*, 24–37. [CrossRef]

17. Camp, E.R.; Summy, J.; Bauer, T.W.; Liu, W.; Gallick, G.E.; Ellis, L.M. Molecular Mechanisms of Resistance to Therapies Targeting the Epidermal Growth Factor Receptor. *Clin. Cancer Res.* **2005**, *11*, 397–405. [CrossRef]

18. Damm, K.; Hemmann, U.; Garin-Chesa, P.; Hauel, N.; Kauffmann, I.; Priepke, H.; Niestroj, C.; Daiber, C.; Enenkel, B.; Guilliard, B.; et al. A highly selective telomerase inhibitor limiting human cancer cell proliferation. *EMBO J.* **2001**, *20*, 6958–6968. [CrossRef]

19. Burchett, K.M.; Etekpo, A.; Batra, S.K.; Yan, Y.; Ouellette, M.M. Inhibitors of telomerase and poly(ADP-ribose) polymerases synergize to limit the lifespan of pancreatic cancer cells. *Oncotarget* **2017**, *8*, 83754–83767. [CrossRef]

20. Ma, F.; Wang, T.T.; Jiang, L.; Zhang, C.Y. Ultrasensitive detection of telomerase activity in lung cancer cells with quencher-free molecular beacon-assisted quadratic signal amplification. *Anal. Chim. Acta* **2019**, *1053*, 122–130. [CrossRef]

21. American Cancer Society. What Is Lung Cancer? 1 October 2019. Available online: https://www.cancer.org/cancer/lung-cancer/about/what-is.html (accessed on 17 March 2022).

22. World Health Organization. Cancer. 3 February 2022. Available online: https://www.who.int/news-room/fact-sheets/detail/cancer (accessed on 17 March 2022).

23. Chen, K.Y.; Lee, L.N.; Yu, C.J.; Lee, Y.C.; Kuo, S.H.; Yang, P.C. Elevation of telomerase activity positively correlates to poor prognosis of patients with non-small cell lung cancer. *Cancer Lett.* **2006**, *240*, 148–156. [CrossRef] [PubMed]

24. Yang, L.; Li, N.; Wang, M.; Zhang, Y.H.; Yan, L.D.; Zhou, W.; Yu, Z.Q.; Peng, X.C.; Cai, J. Tumorigenic effect of TERT and its potential therapeutic target in NSCLC (Review). *Oncol. Rep.* **2021**, *46*, 1–12. [CrossRef] [PubMed]

25. Zhu, C.Q.; Cutz, J.C.; Liu, N.; Lau, D.; Shepherd, F.A.; Squire, J.A.; Tsao, M.S. Amplification of telomerase (hTERT) gene is a poor prognostic marker in non-small-cell lung cancer. *Br. J. Cancer* **2006**, *94*, 1452–1459. [CrossRef]

26. Mender, I.; LaRanger, R.; Luitel, K.; Peyton, M.; Girard, L.; Lai, T.P.; Batten, K.; Cornelius, C.; Dalvi, M.P.; Ramirez, M.; et al. Telomerase-Mediated Strategy for Overcoming Non-Small Cell Lung Cancer Targeted Therapy and Chemotherapy Resistance. *Neoplasia* **2018**, *20*, 826–837. [CrossRef] [PubMed]

27. Ding, X.; Cheng, J.; Pang, Q.; Wei, X.; Zhang, X.; Wang, P.; Yuan, Z.; Qian, D. BIBR1532, a Selective Telomerase Inhibitor, Enhances Radiosensitivity of Non-Small Cell Lung Cancer Through Increasing Telomere Dysfunction and ATM/CHK1 Inhibition. *Int. J. Radiat. Oncol. Biol. Phys.* **2019**, *105*, 861–874. [CrossRef]

28. Plyasova, A.A.; Berrino, E.; Khan, I.I.; Veselovsky, A.V.; Pokrovsky, V.S.; Angeli, A.; Ferraroni, M.; Supuran, C.T.; Pokrovskaya, M.V.; Alexandrova, S.S.; et al. Mechanisms of the Antiproliferative and Antitumor Activity of Novel Telomerase–Carbonic Anhydrase Dual-Hybrid Inhibitors. *J. Med. Chem.* **2021**, *64*, 11432–11444. [CrossRef]

29. Berrino, E.; Angeli, A.; Zhdanov, D.D.; Kiryukhina, A.P.; Milaneschi, A.; De Luca, A.; Bozdag, M.; Carradori, S.; Selleri, S.; Bartolucci, G.; et al. Azidothymidine "Clicked" into 1,2,3-Triazoles: First Report on Carbonic Anhydrase-Telomerase Dual-Hybrid Inhibitors. *J. Med. Chem.* **2020**, *63*, 7392–7409. [CrossRef]

30. Guterres, A.N.; Villanueva, J. Targeting telomerase for cancer therapy. *Oncogene* **2020**, *39*, 5811–5824. [CrossRef]

31. Huppert, J.L.; Balasubramanian, S. Prevalence of quadruplexes in the human genome. *Nucleic Acids Res.* **2005**, *33*, 2908–2916. [CrossRef]

32. Sanford, S.L.; Welfer, G.A.; Freudenthal, B.D.; Opresko, P.L. Mechanisms of telomerase inhibition by oxidized and therapeutic dNTPs. *Nat. Commun.* **2020**, *11*, 5288. [CrossRef]

33. Chiappori, A.A.; Kolevska, T.; Spigel, D.R.; Hager, S.; Rarick, M.; Gadgeel, S.; Blais, N.; Von Pawel, J.; Hart, L.; Reck, M.; et al. A randomized phase II study of the telomerase inhibitor imetelstat as maintenance therapy for advanced non-small-cell lung cancer. *Ann. Oncol.* **2015**, *26*, 354–362. [CrossRef] [PubMed]

34. Pascolo, E.; Wenz, C.; Lingner, J.; Hauel, N.; Priepke, H.; Kauffmann, I.; Garin-Chesa, P.; Rettig, W.J.; Damm, K.; Schnapp, A. Mechanism of human telomerase inhibition by BIBR1532, a synthetic, non-nucleosidic drug candidate. *J. Biol. Chem.* **2002**, *277*, 15566–15572. [CrossRef]

35. Parsch, D.; Brassat, U.; Brümmendorf, T.H.; Fellenberg, J. Consequences of Telomerase Inhibition by BIBR1532 on Proliferation and Chemosensitivity of Chondrosarcoma Cell Lines. *Cancer Investig.* **2008**, *26*, 590–596. [CrossRef] [PubMed]

36. Wu, Y.; Zhong, D.; Li, Y.; Wu, H.; Xu, X.; Yang, J.; Gu, Z. Tumor-Oriented Telomerase-Terminated Nanoplatform as Versatile Strategy for Multidrug Resistance Reversal in Cancer Treatment. *Adv. Healthc. Mater.* **2020**, *9*, 1–12. [CrossRef] [PubMed]

37. Barma, D.K.; Elayadi, A.; Falck, J.R.; Corey, D.R. Inhibition of telomerase by BIBR 1532 and related analogues. *Bioorg. Med. Chem. Lett.* **2003**, *13*, 1333–1336. [CrossRef]

38. Bryan, C.; Rice, C.; Hoffman, H.; Harkisheimer, M.; Sweeney, M.; Skordalakes, E. Structural Basis of Telomerase Inhibition by the Highly Specific BIBR1532. *Structure* **2015**, *23*, 1934–1942. [CrossRef]

39. Liu, C.; Zhou, H.; Sheng, X.B.; Liu, X.H.; Chen, F.H. Design, synthesis and SARs of novel telomerase inhibitors based on BIBR1532. *Bioorg. Chem.* **2020**, *102*, 1–16. [CrossRef]

40. Mohamed, M.; Attia, Y.; Shouman, S.; Abdelhamid, I. Anticancer Activities of New N-hetaryl-2-cyanoacetamide Derivatives Incorporating 4,5,6,7-Tetrahydrobenzo[b]thiophene Moiety. *Anticancer Agents Med. Chem.* **2017**, *17*, 1084–1092. [CrossRef]

41. Shams, H.Z.; Mohareb, R.M.; Helal, M.H.; Mahmoud, A.E. Novel Synthesis and Antitumor Evaluation of Polyfunctionally Substituted Heterocyclic Compounds Derived from 2-Cyano-N-(3-cyano-4,5,6,7-tetrahydrobenzo[b]thiophen-2-yl)-acetamide. *Molecules* **2011**, *16*, 52. [CrossRef]

42. Mohareb, R.; Ibrahim, R.; Wardakhan, W. Synthesis of pyridine, pyran and thiazole containing thiophene derivatives and their anti-tumor evaluations. *Med. Chem. Res.* **2016**, *25*, 2187–2204. [CrossRef]

43. Punetha, A.; Ngo, H.X.; Holbrook, S.Y.L.; Green, K.D.; Willby, M.J.; Bonnett, S.A.; Krieger, K.; Dennis, E.K.; Posey, J.E.; Parish, T.; et al. Structure-Guided Optimization of Inhibitors of Acetyltransferase Eis from Mycobacterium tuberculosis. *ACS Chem. Biol.* **2020**, *15*, 1581–1594. [CrossRef]

44. Rodrigues, K.A.; Dias, C.N.; Neris, P.L.; Rocha Jda, C.; Scotti, M.T.; Scotti, L.; Mascarenhas, S.R.; Veras, R.C.; de Medeiros, I.A.; Keesen Tde, S.; et al. 2-Amino-thiophene derivatives present antileishmanial activity mediated by apoptosis and immunomodulation in vitro. *Eur. J. Med. Chem.* **2015**, *106*, 1–14. [CrossRef] [PubMed]

45. Elrayess, R.; Abdel Aziz, Y.M.; Elgawish, M.S.; Elewa, M.; Elshihawy, H.A.; Said, M.M. Pharmacophore modeling, 3D-QSAR, synthesis, and anti-lung cancer evaluation of novel thieno[2,3-d][1,2,3]triazines targeting EGFR. *Arch. Pharm.* **2020**, *353*, 1–15. [CrossRef]

46. Assiri, M.A.; Al-Sehemi, A.G.; Pannipara, M. AIE based "on-off" fluorescence probe for the detection of Cu^{2+} ions in aqueous media. *Inorg. Chem. Commun.* **2019**, *99*, 11–15. [CrossRef]

47. Hosseini, H.; Bayat, M. Cyanoacetohydrazides in Synthesis of Heterocyclic Compounds. *Top. Curr. Chem.* **2018**, *376*, 1–67. [CrossRef] [PubMed]

48. Iraji, A.; Firuzi, O.; Khoshneviszadeh, M.; Tavakkoli, M.; Mahdavi, M.; Nadri, H.; Edraki, N.; Miri, R. Multifunctional iminochromene-2H-carboxamide derivatives containing different aminomethylene triazole with BACE1 inhibitory, neuroprotective and metal chelating properties targeting Alzheimer's disease. *Eur. J. Med. Chem.* **2017**, *141*, 690–702. [CrossRef] [PubMed]

49. Mohammed, E.Z.; Mahmoud, W.R.; George, R.F.; Hassan, G.S.; Omar, F.A.; Georgey, H.H. Synthesis, in vitro anticancer activity and in silico studies of certain pyrazole-based derivatives as potential inhibitors of cyclin dependent kinases (CDKs). *Bioorg. Chem.* **2021**, *116*, 105347. [CrossRef]

50. Almarhoon, Z.; Al Rasheed, H.H.; El-Faham, A. Ultrasonically Assisted N-Cyanoacylation and Synthesis of Alkyl(4-(3-cyano-4,6-dimethyl-2-oxopyridin-1(2H)-yl)benzoyl)amino Acid Ester Derivatives. *ACS Omega* **2020**, *5*, 30671–30678. [CrossRef]

51. Gewald, K.; Schäfer, H.; Sattler, K. Synthesen von 4-Amino-thieno[2,3—b]pyridinen. *Monatsh. Chem.* **1979**, *110*, 1189–1196. [CrossRef]

52. *Molecular Operating Environment (MOE)*; 2020.09; Chemical Computing Group ULC: Montreal, QC, Canada, 2022.

53. El Bialy, S.A.A.; Gouda, M.A. Cyanoacetamide in heterocyclic chemistry: Synthesis, antitumor and antioxidant activities of some new benzothiophenes. *J. Heterocycl. Chem.* **2011**, *48*, 1280–1286. [CrossRef]

54. Schoen, B.W.; Lira, C.T.; Lee, A. Separation and Solubility of Cis and Trans Isomers in Nanostructured Double-Decker Silsequioxanes. *J. Chem. Eng. Data* **2014**, *59*, 1483–1493. [CrossRef]

55. Hassan, A.S.; Askar, A.A.; Naglah, A.M.; Almehizia, A.A.; Ragab, A. Discovery of New Schiff Bases Tethered Pyrazole Moiety: Design, Synthesis, Biological Evaluation, and Molecular Docking Study as Dual Targeting DHFR/DNA Gyrase Inhibitors with Immunomodulatory Activity. *Molecules* **2020**, *25*, 2593. [CrossRef] [PubMed]

56. Allam, H.A.; Fahim, S.H.; Abo-Ashour, M.F.; Nocentini, A.; Elbakry, M.E.; Abdelrahman, M.A.; Eldehna, W.M.; Ibrahim, H.S.; Supuran, C.T. Application of hydrazino and hydrazido linkers to connect benzenesulfonamides with hydrophilic/phobic tails for targeting the middle region of human carbonic anhydrases active site: Selective inhibitors of hCA IX. *Eur. J. Med. Chem.* **2019**, *179*, 547–556. [CrossRef] [PubMed]

57. Skehan, P.; Storeng, R.; Scudiero, D.; Monks, A.; McMahon, J.; Vistica, D.; Warren, J.T.; Bokesch, H.; Kenney, S.; Boyd, M.R. New Colorimetric Cytotoxicity Assay for Anticancer-Drug Screening. *J. Natl. Cancer Inst.* **1990**, *82*, 1107–1112. [CrossRef]

58. Daina, A.; Michielin, O.; Zoete, V. SwissADME: A free web tool to evaluate pharmacokinetics, drug-likeness and medicinal chemistry friendliness of small molecules. *Sci. Rep.* **2017**, *7*, 42717. [CrossRef]

59. Daina, A.; Zoete, V. A BOILED-Egg To Predict Gastrointestinal Absorption and Brain Penetration of Small Molecules. *ChemMed-Chem* **2016**, *11*, 1117–1121. [CrossRef]

60. Robey, R.W.; Pluchino, K.M.; Hall, M.D.; Fojo, A.T.; Bates, S.E.; Gottesman, M.M. Revisiting the role of ABC transporters in multidrug-resistant cancer. *Nat. Rev. Cancer* **2018**, *18*, 452–464. [CrossRef]

61. Kim, N.W.; Piatyszek, M.A.; Prowse, K.R.; Harley, C.B.; West, M.D.; Peter, L.C.H.; Coviello, G.M.; Wright, W.E.; Weinrich, S.L.; Shay, J.W. Specific Association of Human Telomerase Activity with Immortal Cells and Cancer. *Science* **1994**, *266*, 2011–2015. [CrossRef]

62. Kovalenko, N.A.; Zhdanov, D.D.; Bibikova, M.V.; Gotovtseva, V.Y. The influence of compound aITEL1296 on telomerase activity and growth of cancer cells. *Biochem. Suppl. B. Biomed. Chem.* **2012**, *6*, 48–54. [CrossRef]

63. Zhdanov, D.D.; Vasina, D.A.; Grachev, V.A.; Orlova, E.V.; Orlova, V.S.; Pokrovskaya, M.V.; Alexandrova, S.S.; Sokolov, N.N. Alternative splicing of telomerase catalytic subunit hTERT generated by apoptotic endonuclease EndoG induces human CD4+ T cell death. *Eur. J. Cell Biol.* **2017**, *96*, 653–664. [CrossRef]

64. Hou, M.; Dw, X.; Björkholm, M.; Gruber, A. Real-Time Quantitative Telomeric Repeat Amplification Protocol Assay for the Detection of Telomerase Activity. *Clin. Chem.* **2001**, *47*, 519–524. [CrossRef]

65. Sebaugh, J.L. Guidelines for accurate EC50/IC50 estimation. *Pharm. Stat.* **2011**, *10*, 128–134. [CrossRef] [PubMed]

66. Berman, H.M.; Westbrook, J.; Feng, Z.; Gilliland, G.; Bhat, T.N.; Weissig, H.; Shindyalov, I.N.; Bourne, P.E. The Protein Data Bank. *Nucleic Acids Res.* **2000**, *28*, 235–242. [CrossRef]

67. Trott, O.; Olson, A.J. AutoDock Vina: Improving the speed and accuracy of docking with a new scoring function, efficient optimization, and multithreading. *J. Comput. Chem.* **2010**, *31*, 455–461. [CrossRef] [PubMed]

68. Salentin, S.; Schreiber, S.; Haupt, V.J.; Adasme, M.F.; Schroeder, M. PLIP: Fully automated protein–ligand interaction profiler. *Nucleic Acids Res.* **2015**, *43*, 443–447. [CrossRef]

69. Daina, A.; Michielin, O.; Zoete, V. iLOGP: A Simple, Robust, and Efficient Description of n-Octanol/Water Partition Coefficient for Drug Design Using the GB/SA Approach. *J. Chem. Inf. Model.* **2014**, *54*, 3284–3301. [CrossRef] [PubMed]

Article

Targeting Wnt/Beta-Catenin Signaling in HPV-Positive Head and Neck Squamous Cell Carcinoma

Faris F. Brkic [1,†], **Stefan Stoiber** [2,3,†], **Tobias Maier** [1], **Elisabeth Gurnhofer** [2], **Lukas Kenner** [2,3,4,5,*,‡], **Gregor Heiduschka** [1,‡] and **Lorenz Kadletz-Wanke** [1,‡]

[1] Department of Otorhinolaryngology and Head and Neck Surgery, Medical University of Vienna, 1090 Vienna, Austria; faris.brkic@meduniwien.ac.at (F.F.B.); tobias.maier@meduniwien.ac.at (T.M.); gregor.heiduschka@meduniwien.ac.at (G.H.); lorenz.kadletz-wanke@meduniwien.ac.at (L.K.-W.)

[2] Department of Pathology, Medical University of Vienna, 1090 Vienna, Austria; stefan.stoiber@meduniwien.ac.at (S.S.); elisabeth.gurnhofer@meduniwien.ac.at (E.G.)

[3] Christian Doppler Laboratory for Applied Metabolomics, 1090 Vienna, Austria

[4] Unit of Laboratory Animal Pathology, University of Veterinary Medicine, 1210 Vienna, Austria

[5] CBmed GmbH—Center for Biomarker Research in Medicine, 8010 Graz, Austria

[*] Correspondence: lukas.kenner@meduniwien.ac.at; Tel.: +43-140-400-51720

[†] These authors contributed equally to this work.

[‡] These authors contributed equally to this work.

Abstract: Wnt/Beta-Catenin signaling is involved in the carcinogenesis of different solid malignant tumors. The interaction of Creb-binding protein (CBP) with Beta-Catenin is a pivotal component of the Wnt/Beta-Catenin signaling pathway. The first aim of this study was to evaluate the association of CBP expression with survival in patients with human papillomavirus (HPV)-positive head and neck squamous cell carcinoma (HNSCC). Second, the in vitro effects of the inhibition of CBP/Beta-Catenin interaction were analyzed. In particular, the effects of ICG-001, an inhibitor of CBP/Beta-Catenin interaction, on proliferation, cell death, modulation of Wnt/Beta-Catenin target expression, and cell migration were examined in vitro. High CBP expression is significantly associated with better survival on mRNA and protein levels. Furthermore, we observed cytotoxic as well as anti-migratory effects of ICG-001. These effects were particularly more potent in the HPV-positive than in the -negative cell line. Mechanistically, ICG-001 treatment induced apoptosis and led to a downregulation of CBP, c-MYC, and Cyclin D1 in HPV-positive cells, indicating inhibition of Wnt/Beta-Catenin signaling. In conclusion, high CBP expression is observed in HPV-positive HNSCC patients with a good prognosis, and ICG-001 showed a promising antineoplastic potential, particularly in HPV-positive HNSCC cells. Therefore, ICG-001 may potentially become an essential component of treatment de-escalation regimens for HPV-positive HNSCC. Further studies are warranted for additional assessment of the mechanistic background of our in vitro findings.

Keywords: Wnt; Beta-Catenin; HPV; head and neck cancer; cell culture; immunohistochemistry

1. Introduction

Head and neck squamous cell carcinoma (HNSCC) derives from the mucosa of the larynx, oropharynx, hypopharynx, nasal cavity, and paranasal sinuses and nasopharynx. They account for almost half a million new cases annually and represent the sixth most common malignancy worldwide [1]. HNSCC is most commonly induced by carcinogens to which the mucosa of the upper aerodigestive tract is constantly exposed. Usually, exposure is a result of alcohol consumption and tobacco smoking. However, the numbers of users for these lifestyle habits are stable or slowly declining from a worldwide perspective [1,2]. In contrast, a rise in the incidence of oropharyngeal squamous cell carcinoma (OPSCC) has been observed, and the most probable underlying cause is the human papillomavirus (HPV) [2].

The role of double-stranded HPV in HNSCC, and OPSCC in particular, has been well known for the last two decades [3]. HPV is able to infect squamous cells of the upper aerodigestive tract. In particular, the oropharynx is most commonly affected. The crypts, which are widely spread in the epithelium of the tongue base and tonsils, facilitate the replication of HPV [4]. This potentially explains why HPV is found about five to ten times more often in malignancies of the oropharynx than in other head and neck areas [5].

In general, HPV-positive OPSCC is linked to excellent survival outcomes. Nevertheless, therapy for HPV-positive OPSCC is still very intense. To date, cisplatin is the most extensively used systemic agent in first-line therapeutic approaches for this type of cancer. Although cisplatin is very effective as systemic therapy, it is associated with multiple severe side effects which include, among others, acute kidney failure, hearing loss, and neuropathy [6].

In HPV-positive OPSCC, treatment de-escalation options are currently heavily discussed [7]. However, little focus lies on the identification of new tools to predict prognosis in those patients and new substances that show fewer side effects than cisplatin with similar survival outcomes. Interestingly, classical risk-factors and clinical outcome prognosticators in non-HPV HNSCC do not necessarily have the same prognostic value in HPV-positive malignancies [8]. Furthermore, a specific patient subset has a bad prognosis and/or develops distant metastases [2,9]. Finding markers that help to identify high-risk patients early might contribute to better patient care. Moreover, particularly those patients might benefit from new therapeutic targets in order to improve survival and quality of life. Currently, there are no available systemic treatment alternatives to cisplatin. For example, trials focusing on the usage of cetuximab as de-escalation treatment were inferior regarding the outcome in comparison to cisplatin [6]. Therefore, identification of novel substances that may reduce side effects while enhancing radiotherapy efficacy is warranted.

The Wnt/Beta-Catenin (WBC) pathway is an important, well-conserved signaling pathway in cancer. It is responsible for different processes during embryonic development, such as proliferation, migration, and differentiation [10]. Furthermore, it is already established that deregulation/activation of the WBC pathway can contribute to the carcinogenesis of different frequently diagnosed solid tumors, such as colorectal and ovarian cancer [11]. Recent studies indicated that activation of the canonical WBC pathway might contribute to disease progression in HNSCC [12]. However, the effects of deregulated WBC signaling in HPV-positive head and neck tumors are still unknown.

Bello et al. [13] hypothesized and reviewed the interaction between HPV infection and dysregulation of the WBC pathway. E6 and E7, two oncogenic HPV-associated proteins, significantly contribute to the malignant transformation of squamous epithelial cells. They inhibit apoptosis and induce suprabasal cell proliferation, but in addition, they may even play an important role in the deregulation of important core cancer pathways, such as the WBC pathway [14].

The small molecule inhibitor "ICG-001" blocks the interaction between Beta-Catenin and the Creb-binding protein (CBP), therefore inhibiting the WBC pathway [15]. Chemically, ICG-001 is a nitrogen-heterocyclic derivative of decahydronaphthalene with a molecular weight of 548.6 g/mol and has the molecular formula $C_{33}H_{32}N_4O_4$ [16]. Specifically, ICG-001 interacts with CBP and therefore competes with Beta-Catenin for CBP. Consequently, this leads to the inhibition of Beta-Catenin/CBP interaction and blocks the activation of the WBC signaling pathway, ultimately leading to a reduction of WBC-induced tumor-initiation and -proliferation [17]. Several studies have already assessed the anti-neoplastic effects and potential therapeutic value of ICG-001 for different malignant tumors, including oral [15], nasopharyngeal [18], gastric [19] and, pancreatic cancer [20].

However, to the best of our knowledge, no studies have analyzed its effects in HPV-positive malignancies yet. Therefore, our study aimed to assess the association of WBC signaling with survival in HPV-positive HNSCC. In particular, we aimed to assess the prognostic potential of CBP expression in silico. Furthermore, using in vitro experiments, we sought to analyze the antineoplastic effects of CBP/Beta-Catenin inhibition using a

small molecule inhibitor ICG-001 in an HPV-positive cell line as well as HPV-negative cell line serving as a control.

2. Results

2.1. High Expression of Crebbp at mRNA Level Associates with Better Survival

The data for a total of 41 patients with HPV-positive HNSCC were retrieved from "The Cancer Genome Atlas" (TCGA). Table 1 shows the patient characteristics for the whole cohort and stratified according to the *Crebbp* mRNA expression.

Table 1. TCGA cohort patient characteristics and distribution into the two groups post-stratification based on *Crebbp* expression. *Crebbp*; Creb-binding protein, T; T-stage, N; N-stage, M; M-stage, Tx/Nx/Mx; unknown stage.

	Crebbp **Low**	*Crebbp* **High**	**Total**
Number of patients	17	24	41
Age, median (years)	59.5	53.5	57.0
Range (years)	41.1–68.3	40.6–71.5	40.6–71.5
T4, n	4	4	8
T3, n	3	2	5
T2, n	7	14	21
T1, n	3	3	6
Tx, n	0	1	1
N3, n	0	1	1
N2, n	13	13	26
N1, n	1	4	5
N0, n	2	6	8
Nx, n	1	0	1
M0, n	15	23	38
Mx, n	2	1	3

The median overall survival (OS) for the whole cohort was 1.70 years (range 0.36–4.75 years). In order to test if *Crebbp* mRNA expression is associated with OS, the log-rank test was performed and showed significantly longer OS in the high expression group (median OS for both groups not reached due to a small number of events, $p = 0.016$). Figure 1 shows the Kaplan–Meier survival curve for the TCGA cohort stratified according to the optimized threshold value (OTV) of the *Crebbp* mRNA expression.

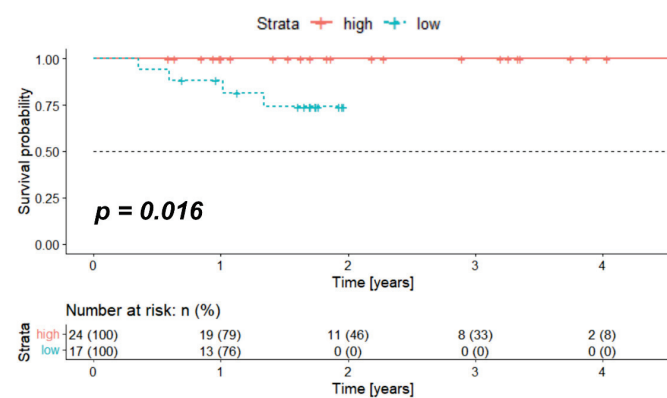**Figure 1.** High *Crebbp* mRNA expression is associated with better survival in HPV-positive OPSCC patients. Kaplan–Meier survival curve for patients with HPV-positive OPSCC extracted from the TCGA database and stratified according to the OTV of *Crebbp*. HPV; human papillomavirus, OPSCC; oropharyngeal squamous cell carcinoma, TCGA; The Cancer Genome Atlas, *Crebbp*; CREB-binding protein, OTV; optimized threshold value.

2.2. Association of CBP Protein Expression with Survival in the In-House Cohort

A total of 29 patients fulfilled the inclusion criteria and had available follow-up data. The detailed patient and tumor characteristics are presented in Table 2. Thirteen patients were female (44.8%). The median age of the whole cohort was 63.7 years (range 37.0–80.5 years). A smaller number of patients were presented with advanced local disease. Indeed, only five patients (17.2%) had a T3 or T4 tumor. Furthermore, the majority of patients had a regional cancer spread (N > 0 in 24 patients, 82.8%), and no distant metastases were observed during the initial work-up. All patients underwent a primary surgical resection, and 21 patients (72.4%) received postoperative radiotherapy.

Table 2. Patient and tumor characteristics of the in-house cohort. PORT; post-operative radiotherapy. y; years, T; T-stage, N; N-stage, M; M-stage.

Patients	**29**	
Age, median (y)	63.7	
Range (y)	37.0–80.5	
	n	*%*
Female	13	44.8
Male	16	55.2
T4	4	13.8
T3	1	3.4
T2	15	51.7
T1	9	31.0
N3	1	3.4
N2	13	44.8
N1	10	34.5
N0	5	17.2
M0	29	100.0
PORT		
Yes	21	72.4
No	8	27.6

The median OS and disease-free survival (DFS) for the whole cohort were 1.8 years (range 0.3–12.3 years) and 1.5 years (range 0.0–9.8 years), respectively. Analog to the TCGA analysis, significantly longer survival times were observed in the group with high CBP expression as calculated by the OTV and a minimum patient distribution of 20% per group (median OS and DFS for both groups not reached due to a small number of events, $p = 0.016$ and $p = 0.039$, respectively). Figure 2A,B present the Kaplan–Meier survival curves for OS and DFS, respectively. The number of patients in each group is noted in the respective figure. In addition, Figure 2C illustrates the measured CBP expression for every patient in the two groups (low CBP expression vs. high CBP expression) based on the stratification by the OTV for OS (left) and DFS (right). Figure 2D shows images from the immunohistochemistry (IHC) staining of three independent patients for each of the two groups (low CBP expression vs. high CBP expression) with low magnification (5× magnification, total view of the tissue microarray (TMA) core) and high magnification (20× magnfication, zoomed in to the center of the core).
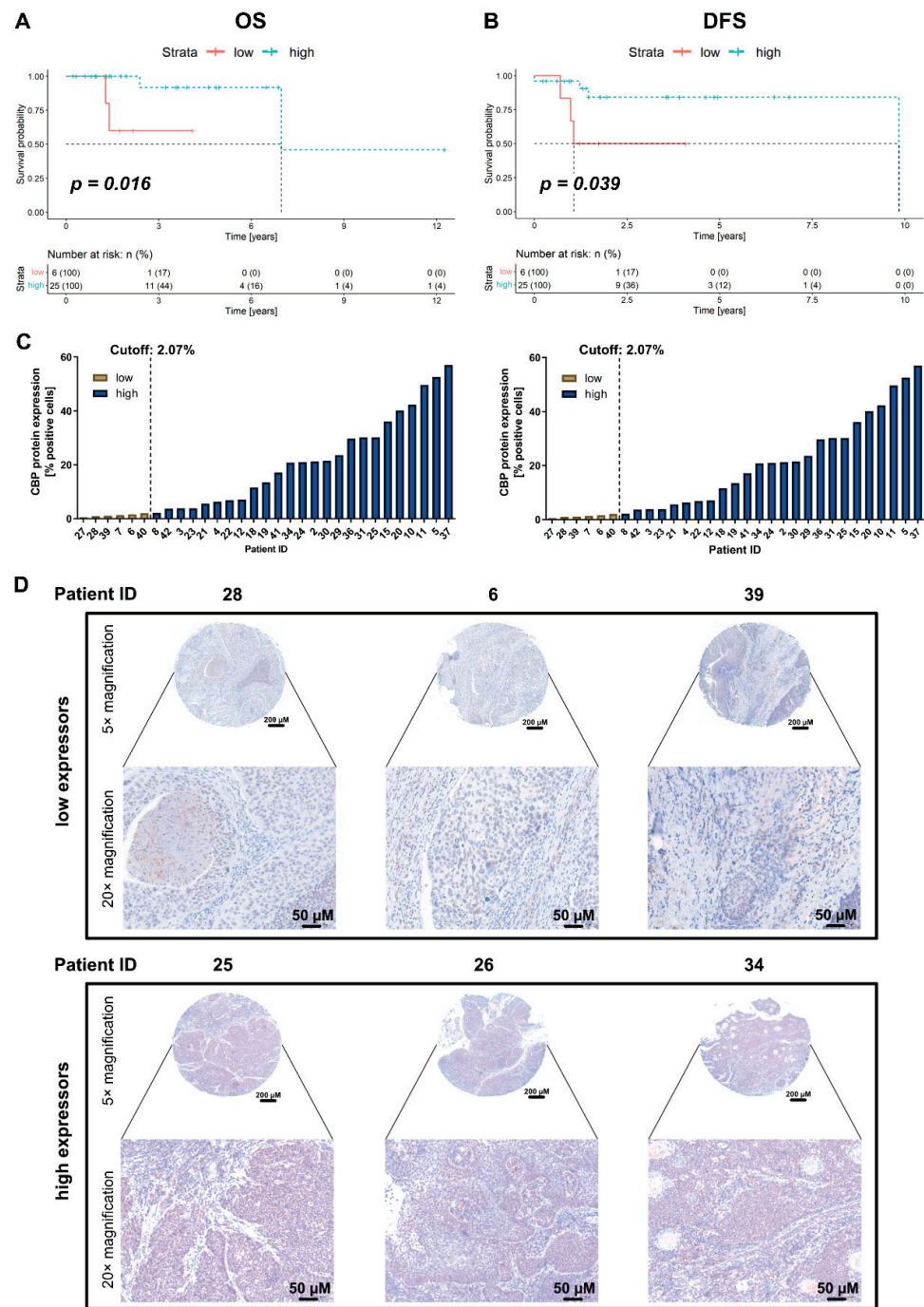
Figure 2. (**A**) Kaplan–Meier survival curve for OS stratified into a high and low group according to the OTV of the CBP expression. Significantly longer overall survival was observed in the group with high CBP protein expression (*p* = 0.016). (**B**) Kaplan–Meier survival curve for DFS stratified into high and low group according to the OTV of the CBP expression. Significantly longer disease-free survival was observed in the group with high CBP protein expression (*p* = 0.039). (**C**) Respective CPB expression values per patient stratified into the two groups ("low" [brown] and "high" [blue]) according to the OTV for OS (**left**) and DFS (**right**). (**D**) Representative images from the IHC staining for CBP, stratified into "low expressors" (**top**) and "high expressors" (**bottom**) according to the OTV. OS; overall survival, DFS; disease-free survival, CBP; Creb-binding protein, OTV; optimized threshold value, IHC; immunohistochemistry staining, μm; micrometer, low; the group with low CBP expression according to the OTV, high; the group with high CBP expression according to the OTV.

2.3. Combining ICG-001 with Irradiation Leads to a Decreased Cell Viability in a Dose-Dependent Manner in SCC154 and Cal27

Both cell lines were treated with a dilution series of ICG-001 (from 0–10 μM) in combination with irradiation (from 0–8 Grey (Gy)) in order to assess the cytotoxicity and a potential synergistic effect in combination treatment. The cell viability was measured 72 h post-treatment using a resazurin assay. A dose-dependent proliferation inhibition could be observed in both cell lines, and the IC_{50} was notably lower in the HPV-positive HNSCC cell line SCC154 than in HPV-HNSCC cell line Cal27 (0.88 μM and 4.65 μM, respectively; Figure 3A,B). The combinatorial effects of ICG-001 and irradiation are graphically illustrated in Figure 3C,D (Cal27 and SCC154, respectively). Relative mean Zip-synergy scores of 0.714 and 5.206 were calculated for SCC154 and Cal27, respectively. Overall, mostly additive effects were observed for both cell lines, and the strongest (synergistic) effects were calculated at a combination of 2 Gy irradiation and 2.5 μM of ICG-001 for Cal27 and 0.625 μM of ICG-001 for SCC154. According to calculated IC_{50} values for the two cell lines, different ICG-001 concentrations were used in subsequent experiments. In particular, SCC154 was treated with lower inhibitor concentrations than Cal27.
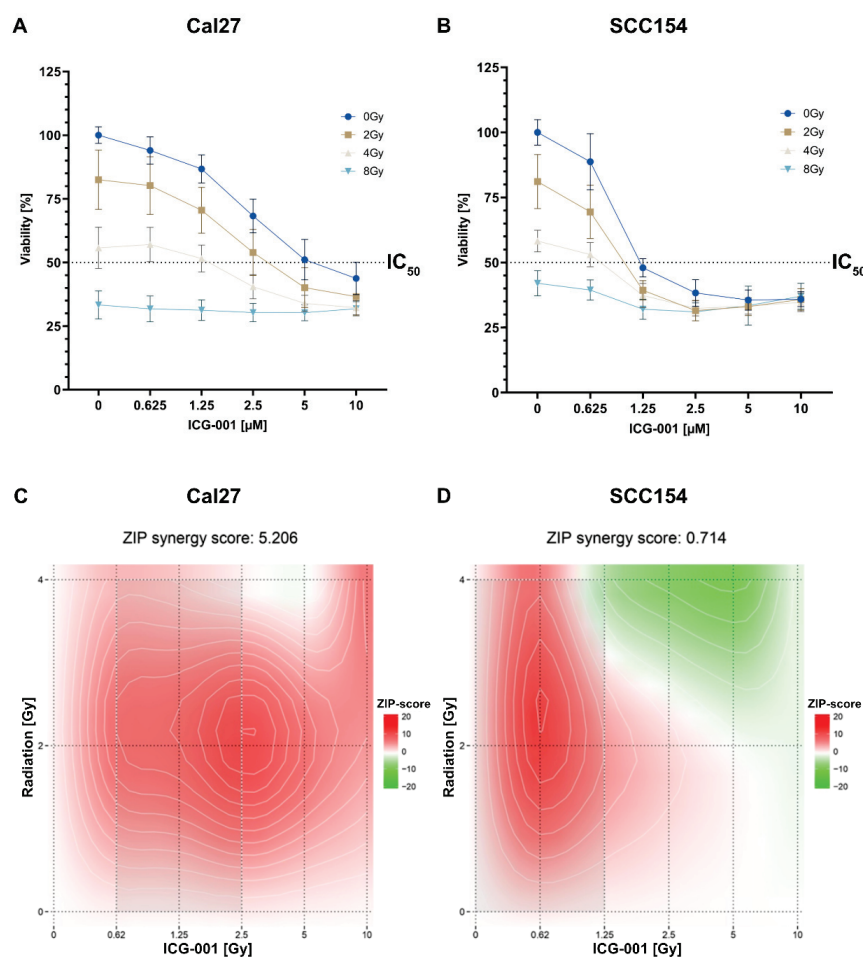

Figure 3. ICG-001 treatment specifically reduces cell proliferation in HPV-positive HNSCC cells in a dose-dependent manner, and its effect can be augmented by concomitant irradiation of the cells. Changes in cell viability in SCC154 (**A**) and Cal27 (**B**) cell lines following treatment with ICG-001 and irradiation. (**C,D**) Graphical illustration of the combinatorial analysis of ICG-001 inhibition and irradiation in regard to cell viability of Cal27 (**C**) and SCC154 (**D**) cell line. The Synergyfinder was used, and the Zip score reference model was applied. A score above 10 is regarded as synergistic interaction, between −10 and 10 as additive and less than −10 is regarded as antagonistic interaction. HPV; human papillomavirus, Gy; Gray, IC_{50}; half-maximal inhibitory concentration.

2.4. Treatment with ICG-001 Downregulates CBP and Shows Different Down-Stream Modulation of Cell-Cycle Control between HPV-Negative and HPV-Positive HNSCC Cells

We could generate evidence that ICG-001 treatment leads to a downregulation of CBP (Figure 4A,B). In addition, screening for two bona fide transcriptional targets of the WBC pathway revealed that ICG-001 treatment leads to a strong repression of Cyclin D1 and c-MYC (two strong drivers of cell survival and proliferation and WBC pathway target genes [10–12]) in the HPV-positive cell line SCC154, whereas in the HPV-negative cell line Cal27, an upregulation thereof was observed (Figure 4A,B). The increased levels of Cyclin D1 and c-MYC in the HPV-negative cell line (Cal27) post-ICG-001 treatment potentially compensate partially for the anti-neoplastic-effects of ICG-001 treatment—hence limiting the overall efficacy of ICG-001 in the HPV-negative Cal27 cell line.
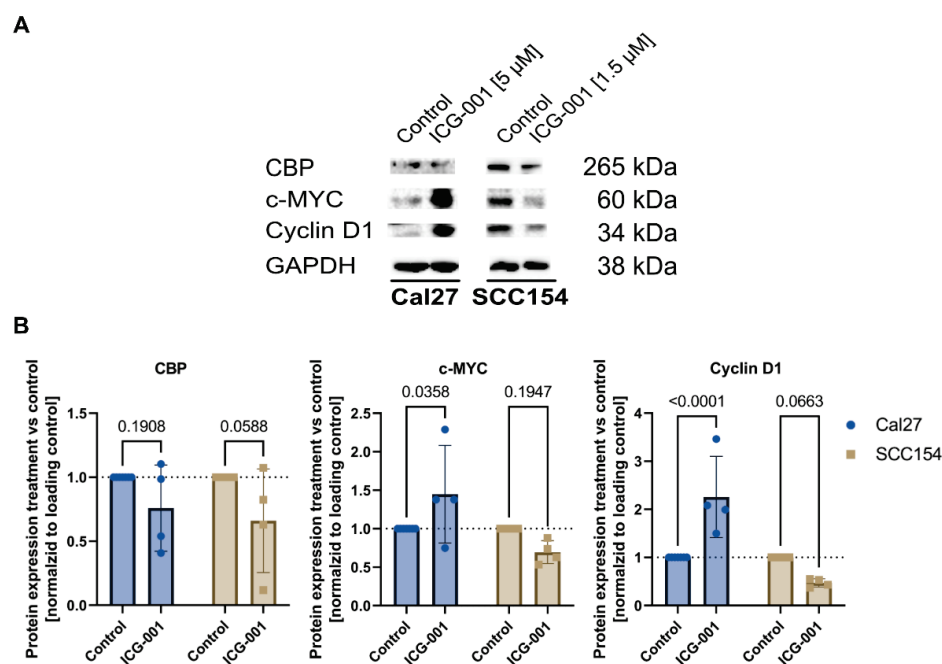

Figure 4. ICG-001 treatment leads to a downregulation of CBP and shows differential effects on WBC target genes in HPV-negative and HPV-positive HNSCC cells. (**A**,**B**) Representative immunoblotting results and quantification for CBP, c-MYC, and Cyclin D1 expression in control and ICG-001-treated cells. Cells were treated with ICG-001 for 72 h. Bar plots represent mean ± SD. Statistical differences between control and ICG-001-treated cells were assessed using the one-way ANOVA test. HPV; human papillomavirus, CBP; Creb-binding protein, WBC; Wnt/Beta-Catenin, SD; standard deviation.

2.5. Treatment with ICG-001 Induces Apoptosis in SCC154 and Cal27 Cells

A significant change in the amount of early apoptotic, late apoptotic, and dead cells could be observed in one or both tested cell lines post 72 h treatment with ICG-001 at 1.5 µM and 5 µM, respectively. In particular, the early apoptotic cell percentage increased significantly in Cal27 cells upon treatment (10.5 ± 1.8% vs. 17.5 ± 3.7%, Figure 5A,C). Moreover, a significant increase in dead cells could be detected in ICG-001-treated Cal27 cells (2.2 ± 0.8% vs. 5.9 ± 3.5%, Figure 5A,C). Interestingly, for the HPV-positive cell line (SCC154), the amount of late apoptotic cells significantly differed between control and ICG-001-treated cells (7.6 ± 3.0% vs. 18.9 ± 4.6%, Figure 5B,C)—potentially indicating that these cells already entered apoptosis earlier than the Cal27 cells. Furthermore, in both cell lines, the fraction of viable cells was significantly different between the control and treated sample (Cal27: 81.3 ± 2.7% vs. 70.4 ± 3.3%, SCC154: 78.3 ± 4.1% vs. 60.6 ± 4.2%, Figure 5A–C). Combined with the increase of cleaved PARP (c-PARP) in ICG-001-treated samples (Figure 5D), this strongly indicates that WBC pathway blockade via ICG-001 induces apoptosis in the tested cell lines, especially in the HPV-positive cell line SCC154.
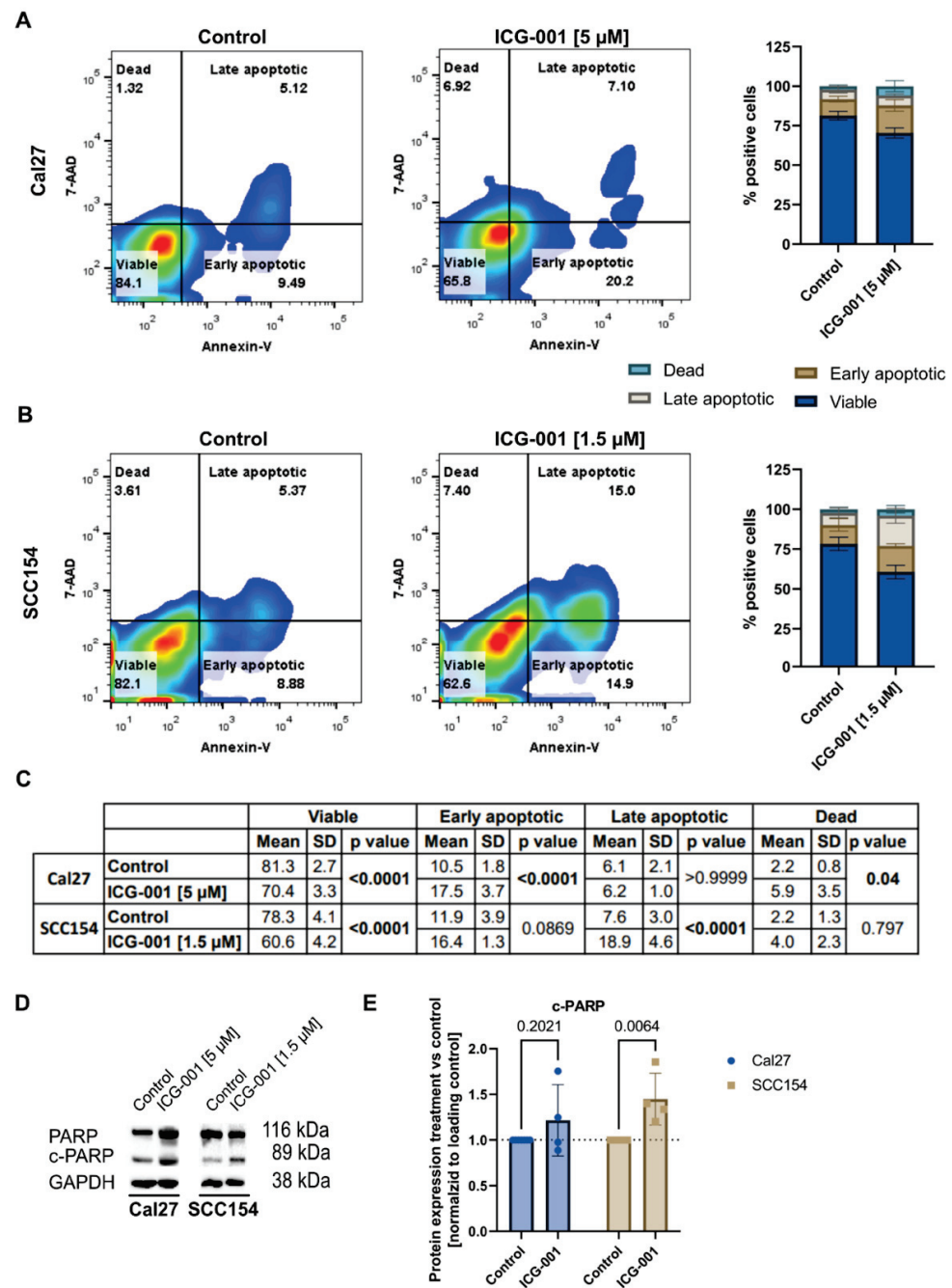
Figure 5. ICG-001 treatment induces apoptosis in HPV-negative and HPV-positive HNSCC cells. (**A**) Representative dot plots of Annexin V/7-AAD assay performed after 72 h of treatment with ICG-001. One plot each is shown for control (untreated) and ICG-001-treated cells for Cal27 and SCC154, respectively (**A**,**B**). Proportion of "viable", "early apoptotic", "late apoptotic", and "dead" cells in control and in treated cells was quantified and is shown in the staggered bar plots as mean ± SD (**A**,**B**). Numeric representation of the quantification of the Annexin V / 7-AAD assay (**C**). Immunoblotting results and quantification for PARP and c-PARP expression in control as well as in ICG-001-treated cells after 72 h of treatment. Bar plots represent mean ± SD (**D**,**E**). Statistical differences between control and ICG-001-treated cells were assessed using the one-way ANOVA test (Immunoblotting results) and the two-way ANOVA test (Annexin V/7-AAD results). HPV; human papillomavirus, PARP; Poly(ADP-ribose)-Polymerase, SD; standard deviation.

2.6. Treatment with ICG-001 Shows Antimigratory Effects In Vitro

Cal27 and SCC154 were treated with 1.5 and 6 µM, and 0.5 and 1 µM of ICG-001, respectively. The anti-migratory effects were assessed by the wound healing tool in ImageJ after 18 h in Cal27 and after 48 h in SCC154 (Figure 6A,B). Cal27 cells treated with ICG-001 showed a gap closure of 72.6% (1.5 µM, Figure 6A,C) and 36.81% (6 µM, Figure 6A,C), whereas DMSO-treated Cal27 cells showed a gap closure of 85.73% (Figure 6A,C. In SCC154 cells treated with ICG-001, the calculated gap closure measured 71.44% (0.5 µM, Figure 6B,D) and 33.76% (1 µM, Figure 6B,D) in contrast to 88.43% in the DMSO-treated control group (Figure 6B,D). Overall, ICG-001 treatment showed a significant reduction of cell migration for both cell lines; indeed, for SCC154 cells, lower concentrations were needed to obtain a similar inhibitory effect.
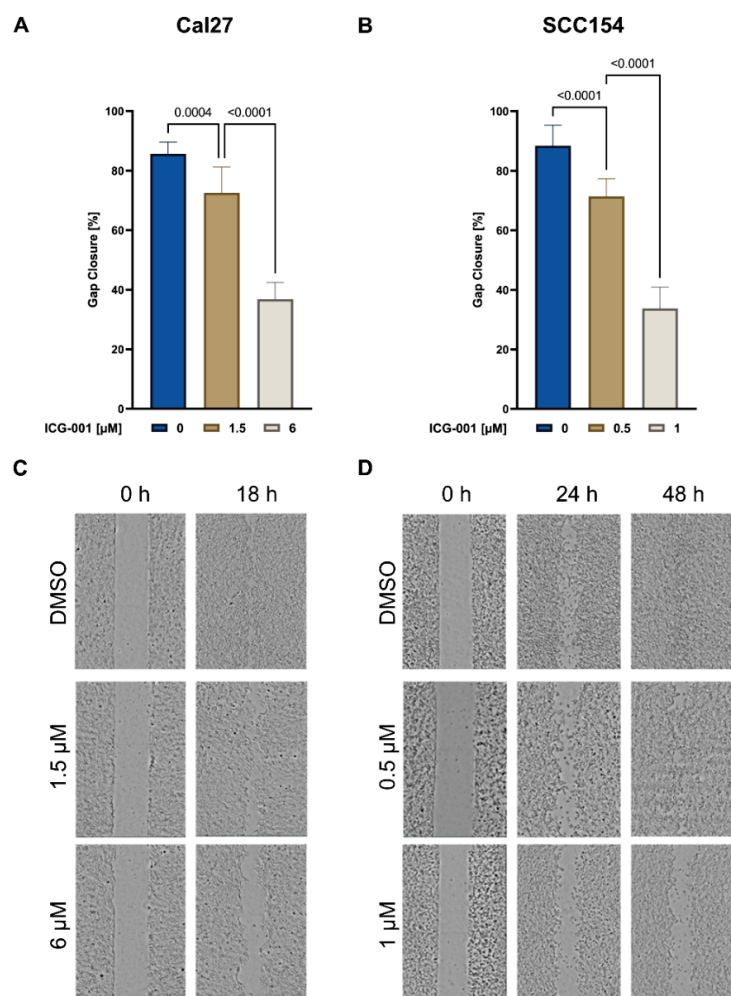
Figure 6. ICG-001 treatment reduces the migratory potential of HPV-negative and HPV-positive HNSCC cells. (**A,B**) Graphical illustration of the analyzed migration assay of Cal27 (0 and 18 h, (**A**) and SCC154 (0 and 48 h, (**B**)) cells treated with ICG-001 or vehicle control (DMSO). With lower inhibitor concentrations, a similar anti-migratory effect was observed in the SCC154. (**C,D**) Visualization performed with the TECAN reader for Cal27 (**C**) and for SCC154 (**D**) at the indicated time points. The free area was measured immediately after the gap generation, as well as after 24 h and 48 h in SCC154. Due to faster cell migration and gap closure, the second measurement was performed after 18 h in Cal27. Statistical differences between control and ICG-001-treated cells were assessed using the one-way ANOVA test. HPV; human papillomavirus, DMSO; dimethyl sulfoxide, SD; standard deviation.

2.7. Proposed Mechanism of ICG-001 in the Tested HNSCC Cell Lines

Our in vitro findings on the mechanism of action of ICG-001 in HPV-negative Cal27 and HPV-positive SCC154 cells are graphically summarized in Figure 7.
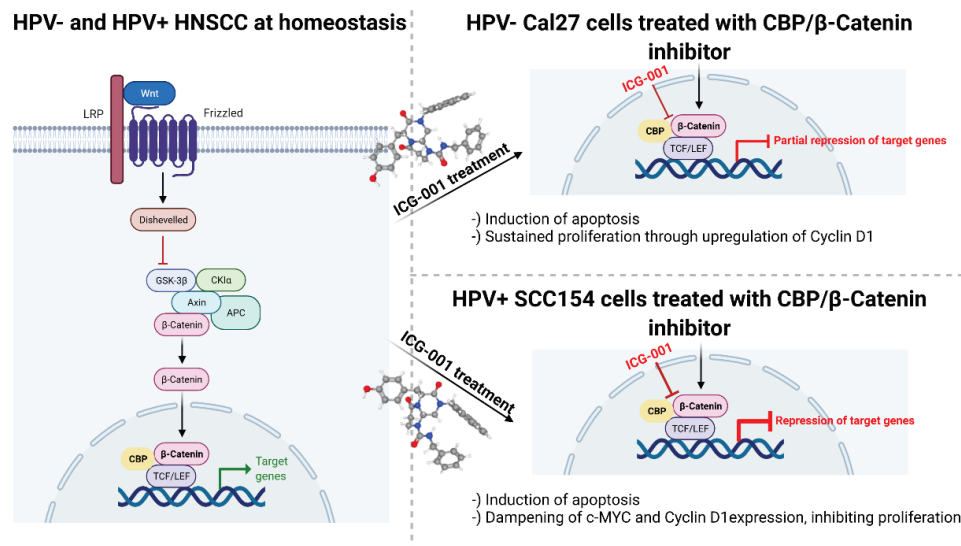

Figure 7. The mechanism of action of ICG-001 in HPV-negative and HPV-positive HNSCC cells. Schematic representation of WBC signaling at baseline (homeostasis) and the effects of CBP inhibition via ICG-001 (the molecular structure was retrieved from the publicly available and free reproducible source [16]) in HPV-negative and HPV-positive HNSCC tumor cells. The scheme was created with BioRender.com (accessed on 30 December 2021).

3. Discussion

The current study revolved around the role of the WBC pathway in HPV-positive HNSCC in terms of its prognostic relevance and therapeutic potential of its inhibition. First, we provided evidence that high *Crebbp* mRNA expression is associated with better survival in patients with HPV-associated HNSCC. These results could be validated in an independent, in-house cohort on protein level. Therefore, CBP expression can facilitate the identification of patients with a potentially better prognosis. Furthermore, in our in vitro experiments, we presented anti-migratory, proapoptotic, cytotoxic, as well as synergistic effects with radiotherapy of CBP/Beta-Catenin inhibition via ICG-001 in both cell lines, SCC154 and Cal27. Effects were indeed more potent in the HPV-positive cell line (SCC154). Moreover, downregulation of WBC transcriptional targets was observed in ICG-001-treated SCC154 cells, further supporting the hypothesis of HPV-induced deregulation of the WBC pathway.

The interaction between CBP and Beta-Catenin is an important component of the WBC pathway [21]. Therefore, we first evaluated the association of *Crebbp* mRNA and protein expression with survival in HPV-positive HNSCC in silico. High CBP expression was linked to better survival times. Similar results on protein level were shown by Rühlmann et al. [22] for patients with locally advanced rectal cancer. The mechanistic background behind the association of high CBP expression with better survival in HPV-positive HNSCC patients certainly warrants further elucidation. One possible explanation is the proposed association of higher HPV viral load with better survival in patients with an HPV-associated malignancy [23]. Higher viral load is supposed to induce a higher expression of HPV oncogenes E6 and E7. Rampias et al. [24] were able to observe an E6 and E7-mediated upregulation of Wnt/Beta-Catenin signaling. Thus, overexpression of Wnt-associated genes (including *Crebbp*) could be the result of a higher viral load and have a similar positive prognostic effect, such as the high viral load, in those tumors. Indeed, further studies are needed in order to decipher the exact mechanistic background behind this observation.

The above-noted interaction of the HPV with the WBC pathway via the HPV-associated oncoproteins E6 and E7 was further elucidated in a recent study by Muñoz-Bello et al. [25]. They were able to show that E6 with its spliced isoform upregulates the WBC signaling cascade through the transcription factor TCF-4. In particular, WBC target gene overexpression is achieved by upregulation of TCF-4 via E6 and its spliced isoform. We investigated the therapeutic potential of WBC inhibition by ICG-001 in HNSCC cell lines with a specific focus on the HPV-positive HNSCC cell line SCC154. We show here for the first time a downregulation of WBC signaling induced by CBP/Beta-Catenin inhibition via ICG-001. The treatment with ICG-001 resulted in pronounced early apoptotic and late apoptotic cell death, which was also observed in Cal27, albeit to a lesser extent than in SCC154. Treatment with ICG-001 specifically decreases cell proliferation in the HPV-positive HNSCC cell line in a dose-dependent manner, and its effect can be enhanced by simultaneous irradiation in both tested cell lines. Furthermore, our data support the observation that HPV-positive HNSCC shows a better response to radiotherapy [26] than HPV-negative tumors. Similarly, ICG-001 increased radiosensitivity in a hepatocellular carcinoma cell line [27] and reversed radiotherapy resistance in a non-small cell lung cancer cell line [28]. In addition, we show high anti-migratory effects of ICG-001 treatment on the HPV-positive cell line. Up to now, this was the first study analyzing the anti-migratory effects of ICG-001 for an HPV-positive HNSCC cell line (SCC154). Interestingly, lower inhibitor concentrations were needed to achieve a reduction of cellular migration in SCC154 compared to Cal27. Similarly, antiproliferative and proapoptotic effects were stronger in SCC154 than in Cal27. This further supports the hypothesis that HPV may interfere with the activation of the WBC pathway, and hence, stronger antineoplastic effects of CBP inhibition are observed in HPV-positive cancer cells. Hypothetically, HPV infection might lead to an overexpression of CBP by activating WBC pathway transcription via E6-regulated TCF-4. Moreover, the interaction between E6 and E7 HPV oncoproteins and the nuclear accumulation of active Beta-Catenin in HPV-positive oropharyngeal cell line was shown by Rampias et al. [24] They even proposed Beta-Catenin as a biomarker for developing an HPV-induced carcinoma.

In the study by Schultz et al. [29], the expression of the Beta-Catenin as well as of the c-kit was assessed in p16-positive, and HPV-negative HNSCC treated with imatinib. However, this study lacks in vitro analyses of the therapeutic potential of the Wnt/Beta-Catenin signaling blockade. On the other hand, we show here for the first-time mechanistic evidence that the antineoplastic effects induced by ICG-001 are specific for an HPV-positive HNSCC cell line (SCC154). ICG-001 strongly downregulated the transcriptional targets c-MYC and Cyclin D1 in the HPV-positive cell line SCC154, which was in contrast to the HPV negative cell line Cal27, where we observed an upregulation of both proteins. In our opinion, this different modulation may explain the dissimilar sensitivity of the two cell lines to ICG-001 in our experiments.

The various side-effects of cisplatin, including acute kidney failure or hearing loss [6], are well-known and impose an important limitation. Therefore, other chemotherapy options or add-on therapies for patients with HPV-positive OPSCC are certainly needed. On the other hand, small molecule inhibitors that are currently in clinical use or studies were associated with low side-effect-rates [30,31]. Furthermore, the safety of PRI-724, a small-molecule inhibitor of CBP/Beta-Catenin interaction and an analog of ICG-001, was demonstrated in phase 1 clinical trial of Kimura et al. [32]. Moreover, Lenz et al. [33] summarized preclinical and clinical studies regarding PRI-724 safety. The perhaps most interesting trial comprised 18 patients continuously receiving rising doses from 40 to 1280 mg/m^2/day for 1 week. Indeed, the cytotoxicity rate was acceptable, with only one patient developing hyperbilirubinemia [34]. Ko et al. [35] conducted a phase Ib study on PRI-724 with gemcitabine as a second-line treatment for advanced pancreatic adenocarcinoma. Similarly, a low side-effect profile, as well as the satisfactory clinical activity of PRI-724, were recorded. Although still not elucidated, it can be hypothesized that the clinical toxicity of ICG-001 should be comparable to PRI-724. Interestingly, CBP/Beta-Catenin inhibitors are not necessarily potential treatment agents only for tumors with

overexpressed canonical Wnt pathways. Indeed, Deng et al. [36] reported on the therapeutic effects of ICG-001 in *neurofibromin 2* gene mutated meningioma, using in vitro and in vivo xenograft models.

As noted, the majority of patients with HPV-positive OPSCC associate with good outcomes. Therefore, efforts are made to investigate possible treatment de-escalation regimens [7,37]. These should contribute to a reduction of treatment morbidity while maintaining comparable efficiency. As CBP was highly expressed in patients with good survival rates, the CBP/Beta-Catenin targeted chemotherapy agents, which are associated with low cytotoxicity, may potentially have future clinical utilization as a part of de-escalation regiments in HPV-positive OPSCC.

Limitations of the current study include that the size of the TCGA cohort is relatively small. Nevertheless, a significant association between high *Crebbp* expression and better survival outcome was observed in silico and validated on protein level in an independent cohort. For future validation studies of our in vitro data, additional HPV-negative and HPV-positive cell lines should be included. In addition, the current study did not provide information on the exact mechanistic effects of ICG-001 treatment in vitro, particularly for HPV-negative cells. Despite the above-mentioned shortcomings of the study, CBP expression may become a valuable survival biomarker for HPV-positive HNSCC. Moreover, the ICG-001 may become a candidate for targeted therapy in HPV-associated HNSCC. Taken together, we showed that CBP expression might be a valuable prognostic marker and the specific blockade of its interaction with Beta-Catenin a potential therapy option for low-risk patients with HPV-positive HNSCC.

4. Materials and Methods

4.1. The Cancer Genome Atlas (TCGA)—TCGA Cohort

First, the association of CBP expression on mRNA level (gene name of CBP: *Crebbp*) with OS in HPV-positive HNSCC was analyzed. The data were retrieved using the TCGA database (https://portal.gdc.cancer.gov/projects/TCGA-HNSC. accessed on 1 March 2021) [38]. All patients with a primary treated and HPV-positive HNSCC were included in the analysis. Besides all available clinical and follow-up data, gene expression results from Illumina HiSeq RNA sequencing (RNA-seq) were downloaded from the GDC Legacy Archive (https://portal.gdc.cancer.gov/legacy-archive/search/f. accessed on 30 December 2021) and normalized utilizing the R package "TCGA biolinks" (version 2.19.0) and processed in R (version 4.0.3, R Foundation for Statistical Computing, Vienna, Austria). Survival analysis was performed with packages "survival" and "survminer" (versions 3.2.13 and 0.4.9, respectively) in R. Kaplan–Meier curves were plotted with "ggplot" (version 3.3.3). The OTV of *Crebbp* expression in regard to OS was calculated (>OTV was considered as high expression) with a patient distribution of at least 20% per group. The whole cohort was stratified according to the OTV into high and low and a Kaplan–Meier survival curve for OS was calculated and plotted.

4.2. Immunohistochemistry—The MUV Cohort

All patients with a histologically verified HPV-positive HNSCC, primarily surgically treated in our institution from 1 January 2012 to 31 December 2019, were included in this study. Patients with recurrent disease or a second malignancy were excluded from the analysis. Furthermore, data on age, sex, tumor staging, and other clinically relevant data were retrieved. The association of CBP expression on protein level with OS and DFS was analyzed.

For this analysis, a TMA of formalin-fixed paraffin-embedded tumor samples of all included patients was constructed. This was performed with the computer-assisted tissue microarray platform (TMA Grand Master, 3D Histech, Budapest, Hungary). The subsequent staining was performed on 4 µm slices.

The immunohistochemical staining was performed with the Lab Vision UltraVision Kit (Thermo Scientific, Waltham, MA, USA, TL-060-HL), with colon tissue serving as a positive

control. For the staining, the TMA was first dewaxed and dehydrated. Then, antigen retrieval was performed using ethylenediaminetetraacetic acid in a microwave (10 min (min) at 600 Watt). Next, 3% H_2O_2 and Ultra V Block were used in order to block the endogenous peroxidase activity. Then, the samples were incubated for 1 h (h) with the primary antibody against CBP 1:100 (Santa Cruz, sc-7300) at room temperature. Subsequently, the primary antibody enhancer and horseradish peroxidase enhancer were applied for 10 and 15 min, respectively. In order to visualize the staining, the UltraVision Plus Detection System DAB Plus Substrate System (Thermo Scientific, Waltham, MA, USA, TL-060-HL) was utilized. The counterstaining of the tissues was performed with hematoxylin Gill II (Merck, Darmstadt, Germany, 105175). The tissues were scanned using the Panoramic Flash 250 II. The expression of the CBP was analyzed. We performed the quantification of the staining using QuPath (Version 0.2.3). Tissue was analyzed for the percentage (0–100%) of stained cells. The survival analysis was conducted with the R packages "survival" and "survminer" (R: A language and environment for statistical computing. R Foundation for Statistical Computing, Vienna, Austria. URL https://www.R-project.org/, accessed on 23 October 2020). The optimized threshold values in regards to overall and DFS were calculated, serving as a cutoff for the patient stratification into high and low CBP groups (>optimized threshold was considered as high). The calculation of the optimized threshold was performed with a patient distribution of at least 20% per group. Kaplan Meier curves were plotted with "ggplot".

4.3. Cell Culture

Next, we evaluated the effect of WBC pathway inhibition in vitro. For these experiments, we used the HPV-positive HNSCC cell line SCC154. The Cal27, an HPV-negative HNSCC, cell line served as a control. They were both acquired from the American Type Culture Collection (ATCC, Manassas, VA, USA) and were regularly tested for mycoplasma contamination. Dulbecco's modified eagle's medium (DMEM), Penicillin/Streptomycin (P/S) and fetal calf serum (FBS) were obtained from Gibco (Gibco, Thermo Fisher Scientific, Waltham, MA, USA). Cells were kept in a humidified environment at 37 °C and 5% CO_2 (Hera Cell 240, Heraeus Holding GmbH, Hanau, Germany) and cultivated in DMEM supplemented with 10% FBS and 1% P/S. Cells were split once per week by trypsinization. The inhibitor ICG-001 was acquired from Selleckchem (Selleckchem S2662, Houston, TX, USA). All in vitro experiments were performed at least three times. Mean values ± standard deviations (SD) were calculated and used for further analysis and graphical representation. Displayed graphical presentation show representative images.

4.4. Cytotoxicity Assay

In order to analyze cell proliferation, cells were seeded in 96-well plates (Sarstedt, Nürnbrecht, Germany) in the following fashion: SCC154 20,000 cells/100 μL/well; Cal27 5000 cells/100 μL/well. A set of five replicates for each dose was used. One day after seeding, cells were treated with 100 μL of inhibitor diluted in DMEM. Ascending inhibitor concentrations were used and ranged between 0.625 and 10 μM. Dimethyl sulfoxide (DMSO) (Sigma-Aldrich, D8418, St. Louis, MO, USA) treated cells served as control. Furthermore, cells were irradiated at 2, 4, and 8 Gy (YXLON International GmbH, Hamburg, Germany). The Synergyfinder tool (https://synergyfinder.org, accessed on 31 January 2021) was used for calculating synergistic/additive effects of irradiation and ICG-001 treatment.

After 72 h of treatment, the medium was removed, 100 μL of 56 μM Resazurin (Sigma-Aldrich, St. Louis, MO, USA), diluted in DMEM, was added to each well, and the cells were incubated. The measurements were performed with a TECAN Spark reader (Tecan Group, Männedorf, Switzerland); for Cal27 after 90 min of incubation and for SCC154 after 150 min.

Based on IC_{50} inhibitor values calculated in the cytotoxicity assay, corresponding inhibitor concentration ranges of ICG-001 were used in subsequent experiments for two cell lines.

4.5. Migration Assay

In order to assess the anti-migratory effects of WBC inhibition in a dose-dependent manner, the cells were seeded in 24-well plates (Greiner Bio-One, Frickenhausen, Germany) with 150,000 Cal27 cells/well and 700,000 SCC154 cells/well. The medium was prepared with DMEM containing 1% P/S and 1% FBS (in order to starve the cells, thereby limiting their proliferation). Cells were seeded at 100% confluency, and simultaneously, a migration gap was created by a culture insert (Ibidi, Gräfelfing, Germany) which was removed 24 h after seeding. Then, the cells were washed with 1x DPBS (Gibco, Thermo Fischer Scientific, Waltham, MA, USA) once followed by treatment with ICG-001. Concentrations of 1.5 and 6 µM in Cal27 and 0.5 and 1 µM in SCC154 of ICG-001 were used.

The initial visualization was performed immediately after treatment with a TECAN Spark reader. The same was performed after 24 and 48 h in SCC154 and after 18 h in Cal27 (as the gap was already closed after this time). Before visualization, cells were washed with 1x DPBS, and fresh DMEM was added (in order to remove dead and floating cells). The analysis and calculation of the gap closure percentage were performed with ImageJ 1.53e [39].

4.6. Cell Apoptosis: Fluorescence-Activated Cell Sorting (FACS)—Annexin V Assay

In order to assess cell apoptosis after treatment with ICG-001, a FACS Annexin V assay was performed. Firstly, 80,000 Cal27 and 150,000 SCC154 cells were seeded into each well on a 12-well plate. On the next day, the cells were either treated with DMSO (vehicle control) or the approximate IC_{50} concentrations of ICG-001 (5 µM for Cal27 and 1.5 µM for SCC154). After 72 h of treatment, the cells were trypsinized, washed, and pelleted, and the apoptotic cell death was determined by Annexin V (Invitrogen, Thermo Fisher Scientific, R37174, Waltham, MA, USA)/7-AAD (Abcam, ab228563, Cambridge, UK) co-staining, following the instructions from the manufacturer. Data from stained cells were acquired with a BD FACSCanto II (Becton Dickinson, Franklin Lakes, NJ, USA). Analysis of results was performed with the FACSDiva software 8.0.1 (Becton Dickinson, Franklin Lakes, NJ, USA).

4.7. Immunoblotting

After trypsinization, washing, and pelleting of the cells, the cell pellet was lysed in RIPA buffer (Sigma-Aldrich, D8418, St. Louis, MO, USA) supplemented with phosphatase (PhosSTOP™, Roche, Basel, Switzerland) and protease inhibitors (complete protease inhibitors, Roche, Basel, Switzerland). For all samples, equivalent amounts of protein were diluted in RIPA buffer and separated by a 10% SDS-PAGE. Next, proteins were transferred to a nitrocellulose membrane (Millipore, Burlington, MA, USA) with a Trans-Blot Turbo Transfer System (Bio-Rad, Hercules, CA, USA). In the following step, membranes were blocked with 5% BSA in 1 × TBS/0.1% Tween-20 for 1 h and incubated overnight at 4 °C on a roller shaker with the following primary antibody: β-TUBULIN (1:1000, Cell Signaling Technology, #86298, Danvers, MA, USA), PARP (1:1000, Cell Signaling Technology, #9542, Danvers, MA, USA), CBP (1:500, Santa Cruz, sc-7300, Santa Cruz Biotechnology, Dallas, TX, USA), c-MYC (1:500, Cell Signaling Technology, #18583, Danvers, MA, USA) and Cyclin D1 (1:1000, Cell Signaling Technology, #55506, Danvers, MA, USA). On the following day, membranes were incubated with the second antibody (specific for the host species of the primary antibody) at a dilution of 1:5000 (in 1× TBS / 0.1% Tween-20) for 1 h at room temperature. The target protein expression was visualized using the ECL™ Prime Western Blot System from Cytiva (Merck, Darmstadt, Germany) and the ChemiDoc XRS+ (Bio-Rad, Hercules, CA, USA). Quantification of results from immunoblotting was conducted using ImageJ 1.53e [39].

4.8. Statistics

The statistical analysis of the patient cohort data was performed with the R software. The level of statistical significance was set at 0.05, two-tailed. Survival analysis was

performed using R, as described above, and the log-rank test was used to assess if the two groups have a statistically significant difference in survival times.

In order to assess the differences in gap closure between different inhibitor concentrations in the migration assay and to analyze results from the Annexin V/7-AAD assay, the two-way ANOVA test was used. Differences in protein expression between treated and untreated cells were assessed using the one-way ANOVA test. Graphical presentation of cell culture results, as well as the one-way/two-way ANOVA analyses, were performed with GraphPad Prism (GraphPad Prism version 8.4.2 for Windows, GraphPad Software, www.graphpad.com. accessed on 5 December 2020).

5. Conclusions

In the current study, we provided novel insights into the potential therapeutic value of WBC inhibition in HNSCC, particularly in the HPV-positive cell line SCC154. ICG-001 treatment not only led to a decrease in cancer cell proliferation via apoptosis induction but also had synergistic effects with irradiation and showed anti-migratory potential in both tested cell lines (Cal27 and SCC154). The antineoplastic potential seems to be higher in SCC154, supporting the hypothesis of HPV-induced WBC pathway deregulation. Indeed, a strong downregulation of WBC transcriptional targets was observed in the HPV-positive cell line SCC154 treated with ICG-001. Furthermore, high CBP expression could possibly facilitate the identification of low-risk patients with HPV-positive HNSCC. Finally, ICG-001 may become a viable therapy option for these low-risk patients, particularly as a component of proposed treatment de-escalation regimens for this patient group. Indeed, further research is warranted in order to decipher the exact molecular effects of ICG-001, as well as to assess further in vitro and in vivo antineoplastic effects of ICG-001, particularly for HPV-positive HNSCC.

Author Contributions: Conceptualization, F.F.B., S.S. and L.K.-W.; methodology, F.F.B., S.S., T.M. and E.G.; software, F.F.B., S.S. and T.M.; validation, L.K., G.H. and L.K.-W.; formal analysis, F.F.B., S.S. and T.M.; investigation, F.F.B.; resources, F.F.B.; data curation, F.F.B.; writing—original draft preparation, F.F.B.; writing—review and editing, F.F.B., S.S., T.M., E.G., L.K., G.H. and L.K.-W.; visualization, F.F.B., S.S. and L.K.-W.; supervision, L.K., G.H. and L.K.-W.; project administration, F.F.B.; funding acquisition, F.F.B. All authors have read and agreed to the published version of the manuscript.

Institutional Review Board Statement: The study approval for the immunohistochemistry analysis and retrospective data sampling of patients treated in our center was obtained from the ethics committee of the Medical University of Vienna (approval number EK1262/2019, obtained on 15 May 2019 and subsequent annual extensions). For cell culture experiments, as well as analysis of the publicly available TCGA data, no ethics approval was needed according to the guidelines of our institution.

Informed Consent Statement: Not applicable.

Data Availability Statement: The data that support the findings of this study are available on request from the corresponding author.

Conflicts of Interest: The authors declare no conflict of interest.

References

1. Mirza, A.H.; Thomas, G.; Ottensmeier, C.H.; King, E.V. Importance of the immune system in head and neck cancer. *Head Neck* **2019**, *41*, 2789–2800. [CrossRef] [PubMed]
2. Brkic, F.F.; Kadletz-Wanke, L.; Kenner, L.; Füreder, T.; Jank, B.; Brunner, M.; Heiduschka, G. An analysis of distant metastasis cases from HPV-associated oropharyngeal squamous cell carcinoma. *J. Craniomaxillofac. Surg.* **2021**, *49*, 312–316. [CrossRef] [PubMed]
3. Ward, M.J.; Thirdborough, S.M.; Mellows, T.; Riley, C.; Harris, S.; Suchak, K.; Webb, A.; Hampton, C.; Patel, N.N.; Randall, C.J.; et al. Tumour-infiltrating lymphocytes predict for outcome in HPV-positive oropharyngeal cancer. *Br. J. Cancer* **2014**, *21*, 489–500. [CrossRef] [PubMed]

4. Timbang, M.R.; Sim, M.W.; Bewley, A.F.; Farwell, D.G.; Mantravadi, A.; Moore, M.G. HPV-related oropharyngeal cancer: A review on burden of the disease and opportunities for prevention and early detection. *Hum. Vaccin. Immunother.* **2019**, *15*, 1920–1928. [CrossRef] [PubMed]

5. Combes, J.D.; Franceschi, S. Role of human papillomavirus in non-oropharyngeal head and neck cancers. *Oral Oncol.* **2014**, *50*, 370–379. [CrossRef]

6. Mehanna, H.; Robinson, M.; Hartley, A.; Kong, A.; Foran, B.; Fulton-Lieuw, T.; Dalby, M.; Mistry, P.; Sen, M.; O'Toole, L.; et al. Radiotherapy plus cisplatin or cetuximab in low-risk human papillomavirus-positive oropharyngeal cancer (De-ESCALaTE HPV): An open-label randomised controlled phase 3 trial. *Lancet* **2019**, *393*, 51–60. [CrossRef]

7. Mirghani, H.; Blanchard, P. Treatment de-escalation for HPV-driven oropharyngeal cancer: Where do we stand? *Clin. Transl. Radiat. Oncol.* **2017**, *8*, 4–11. [CrossRef] [PubMed]

8. Iyer, N.G.; Dogan, S.; Palmer, F.; Rahmati, R.; Nixon, I.J.; Lee, N.; Patel, S.G.; Shah, J.P.; Ganly, I. Detailed Analysis of Clinicopathologic Factors Demonstrate Distinct Difference in Outcome and Prognostic Factors Between Surgically Treated HPV-Positive and Negative Oropharyngeal Cancer. *Ann. Surg. Oncol.* **2015**, *22*, 4411–4421. [CrossRef]

9. Brkic, F.F.; Mayer, C.; Besser, G.; Altorjai, G.; Herrmann, H.; Heiduschka, G.; Haymerle, G.; Kadletz-Wanke, L. Potential association of the prognostic index and survival in patients with p16-positive oropharyngeal squamous cell carcinoma. *Wien. Klin. Wochenschr.* **2021**, *133*, 1117–1121. [CrossRef] [PubMed]

10. Lee, S.H.; Koo, B.S.; Kim, J.M.; Huang, S.; Rho, Y.S.; Bae, W.J.; Kang, H.J.; Kim, Y.S.; Moon, J.H.; Lim, Y.C. Wnt/β-catenin signalling maintains self-renewal and tumourigenicity of head and neck squamous cell carcinoma stem-like cells by activating Oct4. *J. Pathol.* **2014**, *234*, 99–107. [CrossRef]

11. Zhan, T.; Rindtorff, N.; Boutros, M. Wnt signaling in cancer. *Oncogene* **2017**, *36*, 1461–1473. [CrossRef] [PubMed]

12. Moon, J.H.; Lee, S.H.; Lim, Y.C. Wnt/β-catenin/Slug pathway contributes to tumor invasion and lymph node metastasis in head and neck squamous cell carcinoma. *Clin. Exp. Metastasis* **2021**, *38*, 163–174. [CrossRef]

13. Bello, J.O.; Nieva, L.O.; Paredes, A.C.; Gonzalez, A.M.; Zavaleta, L.R.; Lizano, M. Regulation of the Wnt/β-Catenin Signaling Pathway by Human Papillomavirus E6 and E7 Oncoproteins. *Viruses* **2015**, *7*, 4734–4755. [CrossRef] [PubMed]

14. Manzo-Merino, J.; Contreras-Paredes, A.; Vázquez-Ulloa, E.; Rocha-Zavaleta, L.; Fuentes-Gonzalez, A.M.; Lizano, M. The role of signaling pathways in cervical cancer and molecular therapeutic targets. *Arch. Med. Res.* **2014**, *45*, 525–539. [CrossRef] [PubMed]

15. Kartha, V.K.; Alamoud, K.A.; Sadykov, K.; Nguyen, B.C.; Laroche, F.; Feng, H.; Lee, J.; Pai, S.I.; Varelas, X.; Egloff, A.M.; et al. Functional and genomic analyses reveal therapeutic potential of targeting β-catenin/CBP activity in head and neck cancer. *Genome Med.* **2018**, *10*, 54. [CrossRef] [PubMed]

16. National Center for Biotechnology Information. PubChem Compound Summary for CID 11238147. Available online: https://pubchem.ncbi.nlm.nih.gov/compound/icg-001 (accessed on 17 March 2022).

17. Lin, Z.; Li, Q.; Zhao, Y.; Lin, Z.; Cheng, N.; Zhang, D.; Liu, G.; Lin, J.; Zhang, H.; Lin, D. Combination of Auranofin and ICG-001 Suppress the Proliferation and Metastasis of Colon Cancer. *Front. Oncol.* **2021**, *11*, 738085. [CrossRef] [PubMed]

18. Chan, L.S.; Man, O.Y.; Kwok, H.H.; Chen, L.; Chan, K.C.; Lung, H.L.; Ngan, R.K.; Wong, R.N.; Lo, K.W.; Lee, A.W.; et al. The Wnt modulator ICG 001 mediates the inhibition of nasopharyngeal carcinoma cell migration in vitro via the miR 150/CD44 axis. *Int. J. Oncol.* **2019**, *54*, 1010–1020. [CrossRef]

19. Liu, Y.; Chen, H.; Zheng, P.; Zheng, Y.; Luo, Q.; Xie, G.; Ma, Y.; Shen, L. ICG-001 suppresses growth of gastric cancer cells and reduces chemoresistance of cancer stem cell-like population. *J. Exp. Clin. Cancer Res.* **2017**, *36*, 125. [CrossRef] [PubMed]

20. Arensman, M.D.; Telesca, D.; Lay, A.R.; Kershaw, K.M.; Wu, N.; Donahue, T.R.; Dawson, D.W. The CREB-binding protein inhibitor ICG-001 suppresses pancreatic cancer growth. *Mol. Cancer Ther.* **2014**, *13*, 2303–2314. [CrossRef]

21. Evangelisti, C.; Chiarini, F.; Cappellini, A.; Paganelli, F.; Fini, M.; Santi, S.; Martelli, A.M.; Neri, L.M.; Evangelisti, C. Targeting Wnt/β-catenin and PI3K/Akt/mTOR pathways in T-cell acute lymphoblastic leukemia. *J. Cell Physiol.* **2020**, *235*, 5413–5428. [CrossRef]

22. Rühlmann, F.; Windhof-Jaidhauser, I.M.; Menze, C.; Beißbarth, T.; Bohnenberger, H.; Ghadimi, M.; Dango, S. The prognostic capacities of CBP and p300 in locally advanced rectal cancer. *World J. Surg. Oncol.* **2019**, *17*, 224. [CrossRef] [PubMed]

23. Hashida, Y.; Higuchi, T.; Matsumoto, S.; Iguchi, M.; Murakami, I.; Hyodo, M.; Daibata, M. Prognostic significance of human papillomavirus 16 viral load level in patients with oropharyngeal cancer. *Cancer Sci.* **2021**, *112*, 4404–4417. [CrossRef] [PubMed]

24. Rampias, T.; Boutati, E.; Pectasides, E.; Sasaki, C.; Kountourakis, P.; Weinberger, P.; Psyrri, A. Activation of Wnt signaling pathway by human papillomavirus E6 and E7 oncogenes in HPV16-positive oropharyngeal squamous carcinoma cells. *Mol. Cancer Res.* **2010**, *8*, 433–443. [CrossRef] [PubMed]

25. Muñoz-Bello, J.O.; Olmedo-Nieva, L.; Castro-Muñoz, L.J.; Manzo-Merino, J.; Contreras-Paredes, A.; González-Espinosa, C.; López-Saavedra, A.; Lizano, M. HPV-18 E6 Oncoprotein and Its Spliced Isoform E6*I Regulate the Wnt/β-Catenin Cell Signaling Pathway through the TCF-4 Transcriptional Factor. *Int. J. Mol. Sci.* **2018**, *19*, 3153. [CrossRef] [PubMed]

26. Lacau St Guily, J.; Rousseau, A.; Baujat, B.; Périé, S.; Schultz, P.; Barry, B.; Dufour, X.; Malard, O.; Pretet, J.L.; Clavel, C.; et al. Oropharyngeal cancer prognosis by tumour HPV status in France: The multicentric Papillophar study. *Oral Oncol.* **2017**, *67*, 29–36. [CrossRef] [PubMed]

27. Huang, Y.; Sheng, H.; Xiao, Y.; Hu, W.; Zhang, Z.; Chen, Y.; Zhu, Z.; Wu, D.; Cao, C.; Sun, J. Wnt/β-catenin inhibitor ICG-001 enhances the antitumor efficacy of radiotherapy by increasing radiation-induced DNA damage and improving tumor immune microenvironment in hepatocellular carcinoma. *Radiother. Oncol.* **2021**, *162*, 34–44. [CrossRef] [PubMed]

28. Gökyildirim, M.Y.; Grandel, U.; Hattar, K.; Dahlem, G.; Schuetz, E.; Leinberger, F.H.; Eberle, F.; Sibelius, U.; Grimminger, F.; Seeger, W.; et al. Targeting CREB-binding protein overrides LPS induced radioresistance in non-small cell lung cancer cell lines. *Oncotarget* **2018**, *9*, 28976–28988. [CrossRef]

29. Schultz, J.D.; Sommer, J.U.; Hoedt, S.; Erben, P.; Hofheinz, R.D.; Faber, A.; Thorn, C.; Hörmann, K.; Sauter, A. Chemotherapeutic alteration of β-catenin and c-kit expression by imatinib in p16-positive squamous cell carcinoma compared to HPV-negative HNSCC cells in vitro. *Oncol. Rep.* **2012**, *27*, 270–280. [CrossRef]

30. Lorusso, P.M. Inhibition of the PI3K/AKT/mTOR Pathway in Solid Tumors. *J. Clin. Oncol.* **2016**, *34*, 3803–3815. [CrossRef] [PubMed]

31. Wang, L.; Wang, W. Safety and efficacy of anaplastic lymphoma kinase tyrosine kinase inhibitors in non-small cell lung cancer (Review). *Oncol. Rep.* **2021**, *45*, 13–28. [CrossRef]

32. Kimura, K.; Ikoma, A.; Shibakawa, M.; Shimoda, S.; Harada, K.; Saio, M.; Imamura, J.; Osawa, Y.; Kimura, M.; Nishikawa, K.; et al. Safety, Tolerability, and Preliminary Efficacy of the Anti-Fibrotic Small Molecule PRI-724, a CBP/β-Catenin Inhibitor, in Patients with Hepatitis C Virus-related Cirrhosis: A Single-Center, Open-Label, Dose Escalation Phase 1 Trial. *EBioMedicine* **2017**, *23*, 79–87. [CrossRef] [PubMed]

33. Lenz, H.J.; Kahn, M. Safely targeting cancer stem cells via selective catenin coactivator antagonism. *Cancer Sci.* **2014**, *105*, 1087–1092. [CrossRef] [PubMed]

34. El-Khoueiry, A.B.; Ning, Y.; Yang, D.; Cole, S.; Kahn, M.; Zoghbi, M.; Berg, J.; Fujimori, M.; Inada, T.; Kouji, H.; et al. A phase I first-in-human study of PRI-724 in patients (pts) with advanced solid tumors. *J. Clin. Oncol.* **2013**, *31*, 2501. [CrossRef]

35. Ko, A.H.; Chiorean, E.G.; Kwak, E.L.; Lenz, H.J.; Nadler, P.I.; Wood, D.L.; Fujimori, M.; Inada, T.; Kouji, H.; McWilliams, R.R. Final results of a phase Ib dose-escalation study of PRI-724, a CBP/beta-catenin modulator, plus gemcitabine (GEM) in patients with advanced pancreatic adenocarcinoma (APC) as second-line therapy after FOLFIRINOX or FOLFOX. *J. Clin. Oncol.* **2016**, *34*, e15721. [CrossRef]

36. Deng, J.; Hua, L.; Han, T.; Tian, M.; Wang, D.; Tang, H.; Sun, S.; Chen, H.; Cheng, H.; Zhang, T.; et al. The CREB-binding protein inhibitor ICG-001: A promising therapeutic strategy in sporadic meningioma with NF2 mutations. *Neurooncol. Adv.* **2020**, *2*, vdz055. [CrossRef] [PubMed]

37. Mirghani, H.; Amen, F.; Blanchard, P.; Moreau, F.; Guigay, J.; Hartl, D.M.; Lacau St Guily, J. Treatment de-escalation in HPV-positive oropharyngeal carcinoma: Ongoing trials, critical issues and perspectives. *Int. J. Cancer* **2015**, *136*, 1494–1503. [CrossRef] [PubMed]

38. The Cancer Genome Atlas Program. Available online: https://www.cancer.gov/tcga (accessed on 1 March 2021).

39. Schneider, C.A.; Rasband, W.S.; Eliceiri, K.W. NIH Image to ImageJ: 25 years of image analysis. *Nat. Methods* **2012**, *9*, 671–675. [CrossRef]

Article

Eltrombopag as an Allosteric Inhibitor of the METTL3-14 Complex Affecting the m^{6}A Methylation of RNA in Acute Myeloid Leukemia Cells

Je-Heon Lee [†], Namjeong Choi [†], Subin Kim, Mi Sun Jin *, Haihong Shen * and Yong-Chul Kim *

School of Life Sciences, Gwangju Institute of Science and Technology (GIST), Gwangju 61005, Korea;
jhl@gm.gist.ac.kr (J.-H.L.); njchoi@gist.ac.kr (N.C.); ksb1201@gm.gist.ac.kr (S.K.)
* Correspondence: misunjin@gist.ac.kr (M.S.J.); haihongshen@gist.ac.kr (H.S.); yongchul@gist.ac.kr (Y.-C.K.)
† These authors contributed equally to this work.

Abstract: N^{6}A-methyladenosine (m^{6}A) post-transcriptional modification, the most abundant internal RNA modification, is catalyzed by the METTL3-14 methyltransferase complex. Recently, attention has been drawn to the METTL3-14 complex regarding its significant roles in the pathogenesis of acute myeloid leukemia (AML), attracting the potential of novel therapeutic targets for the disease. Herein, we report the identification and characterization of eltrombopag as a selective allosteric inhibitor of the METTL3-14 complex. Eltrombopag exhibited selective inhibitory activity in the most active catalytic form of the METTL3-14 complex by direct binding, and the mechanism of inhibition was confirmed as a noncompetitive inhibition by interacting at a putative allosteric binding site in METTL3, which was predicted by cavity search and molecular docking studies. At a cellular level, eltrombopag displayed anti-proliferative effects in the relevant AML cell line, MOLM-13, in correlation with a reduction in m^{6}A levels. Molecular mechanism studies of eltrombopag using m^{6}A-seq analysis provided further evidence of its cellular function by determining the hypomethylation of leukemogenic genes in eltrombopag-treated MOLM-13 cells and the overlapping of the pattern with those of METTL3-knockdown MOLM-13 cells. In conclusion, eltrombopag was first disclosed as a functional METTL3-14 allosteric inhibitor in AML cells, which could be utilized for the further development of novel anti-AML therapy.

Keywords: eltrombopag; METTL3-14; allosteric inhibitor; acute myeloid leukemia

1. Introduction

Of the over 170 RNA modifications occurring in diverse cell systems, N^6-methyladenosine (m^{6}A) is the most prevalent and abundant internal modification of particular mRNAs in the long exon and 3′ untranslated region (3′ UTR) near the stop codon of mRNA with the consensus sequence RRACH (R = A or G, H = A, C or U) [1–4]. The mechanisms and functions of this modification have been recently explored, revealing regulatory functions in the fate of mRNA by affecting its nuclear export, splicing, stability, and translation efficiency [5–7]. Consequently, the m^{6}A modification turned out to be closely involved in multiple biological processes, including self-renewal, development, metabolism, homeostasis, and immunity [8–13]. As the components play various roles in m^{6}A modification, the N^6-methyltransferase complex (writers) and demethylases (erasers) catalyze the reversible regulatory functions by methylation and demethylation, respectively, and the resulting products are recognized by m^{6}A binding protein (readers) to further forward biological processes [14–16].

Among them, the N^6-methyltransferase complex consists of catalytic components, methyltransferase-like protein 3 (METTL3) and 14 (METTL14), and other regulatory m^{6}A-associated complexes, such as Wilms tumor 1-associated protein (WTAP), Vir-like m6A methyltransferase associated (VIRMA), Cbl protooncogene like 1 (CBLL1), RNA-binding

motif 15 (RBM15), and zinc finger CCCH-type containing 13 (ZC3H13) [17–20]. The individual METTL3 and METTL14 exhibit relatively weak catalytic activity in vitro, but their heterodimeric complex has a much higher activity, which is the physiologically relevant form in the nucleus [17,21]. The crystal structure of the heterodimeric complex of METTL3-14 demonstrated that METTL3 is mainly responsible for catalytic function, transferring a methyl group from S-(5′-adenosyl)-$_L$-methionine (SAM) to the N^6-amine of adenine, while METTL14 promotes METTL3 catalytic activity by providing an RNA-binding surface composed of positively charged residues [22–24].

Recent studies of METTL3 and METTL14 in cancers have shown that they are closely associated with the processes involved in the proliferation, apoptosis, metastasis, and differentiation in the progression of various human cancers [25–27]. In particular, acute myeloid leukemia (AML), one of the most common types of leukemia with diverse genetic and molecular abnormalities in adults, expresses higher levels of METTL3 and METTL14 compared with other cancer types in the analysis of The Cancer Genome Atlas (TCGA) dataset [28–31]. The significance of METTL3 and METTL14 in AML progression was further investigated by knockdown experiments of the AML cell line, which resulted in the induction of apoptosis and cell differentiation [30,32,33]. The role of METTL3 in tumorigenesis has been reported to promote the translation of c-MYC, BCL2, and PTEN in MOLM-13, a human AML cell line [32]. Another report showed that METTL3 is recruited at the transcription initiation site (TSS) by the CAATT enhancer binding protein zeta (CEBPZ), which resulted in the enhanced translation of oncogenes SP1 and SP2 to maintain the leukemic state [33]. In addition, METTL14 has been reported to play a critical oncogenic role by increasing the mRNA stability and translational efficiency of MYB and MYC through the m^{6}A modification in the NB4 human AML cell line [30]. Therefore, METTL3 and METTL14 have drawn increased attention as attractive new therapeutic targets for the treatment of AML.

As such, chemical inhibitors of METTL3-14 have been developed for the discovery of novel mechanism-based anti-AML therapies. At first, the enzyme reaction product S-(5′-adenosyl)-L-homocysteine (SAH) and non-selective nucleoside analog sinefungin (**1**) were reported as the inhibitors of METTL3-14 [34,35]. Until recently, only a few SAM competitive inhibitors of METTL3 have been developed, including adenine derivatives (**2**) [36], UZH1a (**3**) [37], UZH2 (**4**) [38], and STM2457 (**5**) [39] (Figure 1). Although some SAM competitive inhibitors have shown selective inhibition profiles in the methyltransferase panel screening, allosteric inhibitors are preferred to avoid possible nonselective inhibitions, since the SAM binding region was conserved in most of the methyltransferase enzyme family [40–42]. In that sense, our group recently reported 4-[2-[5-chloro-1-(diphenylmethyl)-2-methyl-1H-indol-3-yl]-ethoxy]benzoic acid (CDIBA) derivatives (**6**) as the first allosteric inhibitor of METTL3-14 [43].

In this article, we report the discovery of eltrombopag as another allosteric inhibitor of METTL3-14 identified by screening the drug library from the Korea Chemical Bank. Eltrombopag was first reported as a thrombopoietin receptor (TPO-R) agonist for the treatment of immune thrombocytopenia (ITP), and approved by the U.S. Food and Drug Administration for the treatment of chronic ITP and aplastic anemia in 2008 and 2014, respectively [44–46]. Herein, we present the identification and characterization of eltrombopag as a METTL3-14 allosteric inhibitor, including the prediction of a putative binding site, anti-proliferative effects on AML cell lines, and an analysis of the influences on the m^{6}A abundance on a cellular level. Furthermore, the molecular mechanism of eltrombopag was confirmed using m^{6}A-seq analysis.
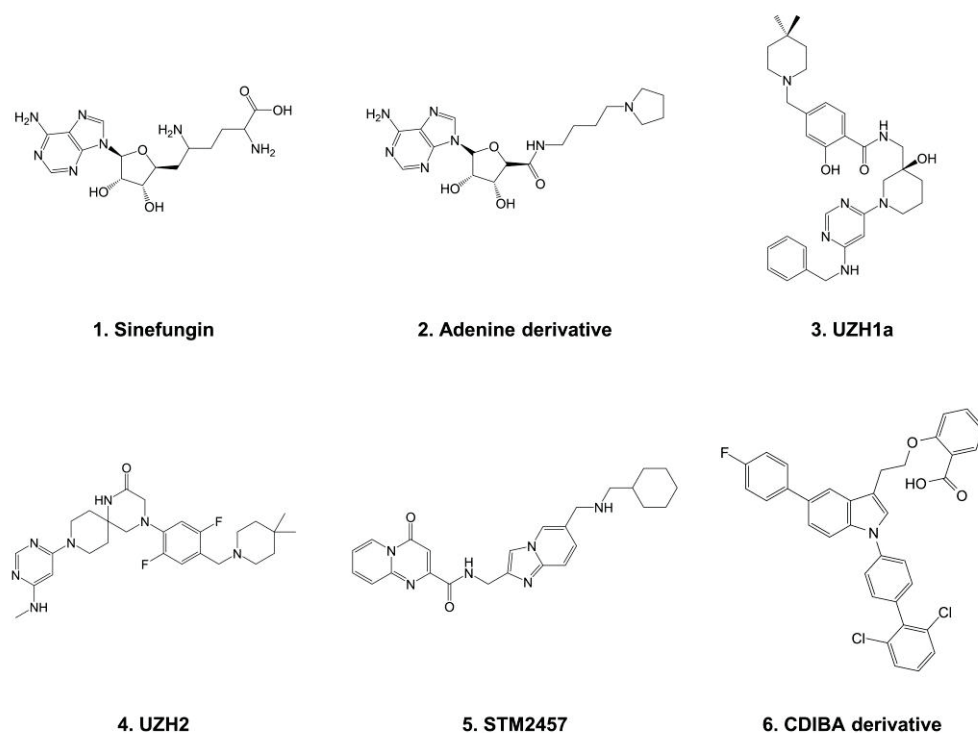
Figure 1. Chemical structures of current METTL3-14 inhibitors.

2. Results and Discussion

2.1. Enzyme Assay and Hit Identification of Eltrombopag as a METTL3-14 Inhibitor

To aid in the discovery of METTL3-14 inhibitors, we developed an enzyme-based bioluminescence assay protocol measuring the METTL3-14 enzymatic reaction product, SAH, by converting it to adenosine triphosphate (ATP), which could be quantitatively detected by the luminescence-mediated luciferase enzymatic activity. Then, the Michaelis–Menten of the kinetic parameters of METTL3-14 with SAM and RNA substrates were determined as the Km values with 98.6 nM and 70.5 nM for SAM and RNA, respectively (Figure S1), which are similar to those of the previously reported METTL3-14 assay systems [34,35].

Using the verified assay system, the drug compound library (2300 compounds) from the Korea Chemical Bank was initially screened at 25 μM, identifying 20 hit compounds with more than 70% inhibition (Figure 2A). After the exclusion of 9 false-positive compounds, which inhibit the coupled enzyme reaction processes converting SAH to ATP (Figure S2A), and further dose-response titration experiments of the true positive 11 compounds, eltrombopag (**7**) was discovered as the most potent final hit compound with an IC_{50} value of 3.65 μM (Figure 2B,C)—which was previously reported as a thrombopoietin receptor agonist [44]. The similar inhibitory potency (IC_{50} = 4.55 μM) of eltrombopag at METTL3-14 was additionally confirmed in a counter assay system using mass spectrometric analysis that measured the m^6A level of the single strand RNA substrate (Figure 2D). Moreover, the METTL3-14 inhibitory activity of eltrombopag was further clarified in the centrifugation experiment, which could exclude the possible false-positive inhibition induced by colloidal aggregation (Figure S2B).

To determine whether eltrombopag directly binds to the METTL3-14 complex, the dissociation constant between eltrombopag and the METTL3-14 complex was measured using surface plasmon resonance (Figure 3). As a result, the binding of eltrombopag was observed in a concentration dependent manner with 13.2 μM of the calculated K_D value, as shown in Figure 3, demonstrating that the inhibition of eltrombopag on the METTL3-14 enzyme activity could occur by direct binding. To explore the selectivity profile of eltrombopag for METTL3-14, seven other methyltransferase family enzymes were investigated, resulting in a relatively low inhibitory activity of 10 μM eltrombopag on the

SAM-dependent methyltransferases listed in Table 1. Taken together, our data suggest that eltrombopag has selective inhibitory activity at the METTL3-14 complex by direct binding to the enzyme protein.
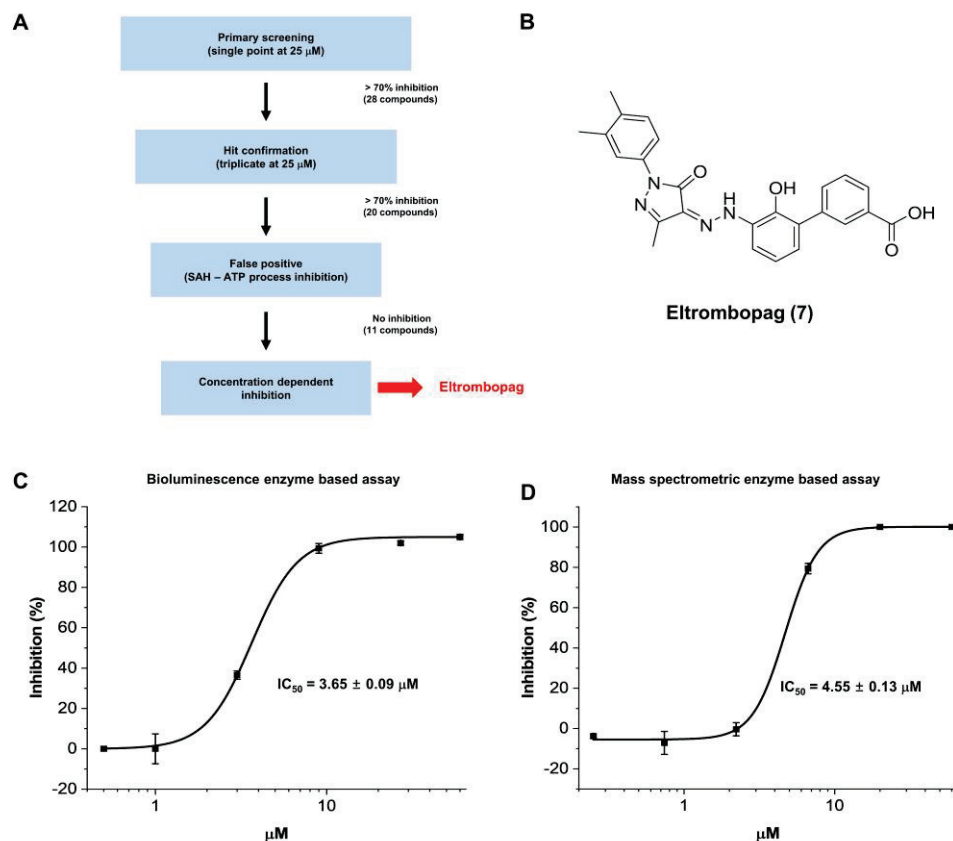

Figure 2. Identification of Eltrombopag as a novel inhibitor of the METTL3-14 complex through library screening. (**A**) Eltrombopag was discovered as a METTL3-14 inhibitor through the described procedure for screening of drug compound library. (**B**) Chemical structure of eltrombopag. (**C**) Concentration-dependent enzymatic inhibitory activity of eltrombopag on METTL3-14 was confirmed in a bioluminescence enzyme-based assay system with an IC_{50} value of 3.65 μM. (**D**) Enzymatic inhibitory activity of eltrombopag on METTL3-14 was confirmed in the mass spectrometric enzyme based assay system with an IC_{50} value of 4.55 μM.

Table 1. Methyltransferase selectivity profile of eltrombopag at 10 μM.

Methyltransferase	Remaining Activity (%) [1]	Control IC_{50} (μM) [2]	Control Compound
DOT1L	90.0 ± 2.8	0.217	Chaetocin
G9a	99.0 ± 3.3	0.762	SAH
MLL4 complex	70.9 ± 2.4	5.09	SAH
PRDM9	130 ± 4	4.16	SAH
PRMT1	96.1 ± 3.9	0.637	SAH
SETD2	97.3 ± 4.1	10.8	SAH
SMYD3	98.7 ± 5.7	35.3	SAH

[1] The remaining activity is the percentage of enzymatic activity in the presence of 10 μM eltrombopag to the buffer containing DMSO. [2] IC_{50} (50% inhibitory concentrations of activity) values were obtained based on the concentration−response curves.
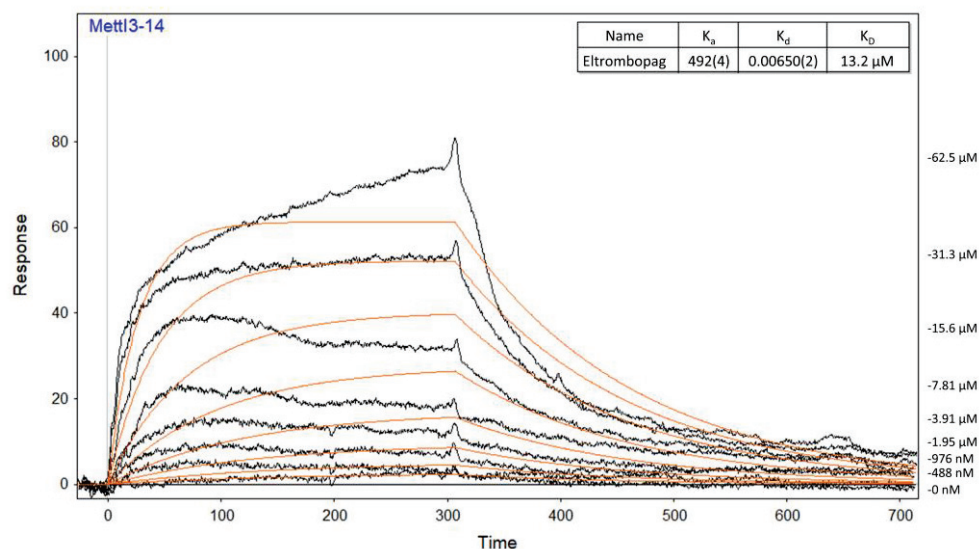
Figure 3. The Binding affinity of eltrombopag was evaluated by measuring the equilibrium dissociation constant (K_D value) to the METTL3-14 complex as 13.2 μM in surface plasmon resonance assay.

2.2. Mode of Enzyme Inhibition and Predicted Binding Mode of Eltrombopag in METTL3-14

To understand the mechanism of action of eltrombopag in the METTL3-14 complex, the tendency of its inhibitory activity was determined from a variation of IC_{50} values of eltrombopag depending on the different substrate concentrations. As shown in Figure 4, the IC_{50} values of eltrombopag were not affected even when the concentrations of the SAM and RNA substrates varied from 50 to 1600 nM and from 25 to 800 nM, respectively. These results suggest that eltrombopag acts as a noncompetitive inhibitor, possibly by binding to the allosteric site of METTL3-14 rather than to the catalytic active sites of the SAM or RNA substrate binding pockets. Although allosteric modulators generally show lower binding affinity than orthosteric ligands, they could have other advantages, such as potentially higher selectivity and fewer side effects than orthosteric ligands [47]. Therefore, further optimization studies of eltrombopag, to improve the binding affinity and inhibitory activities based on its binding mode in METTL3-14, could achieve distinguished novel inhibitors with higher selectivity than other SAM competitive inhibitors.
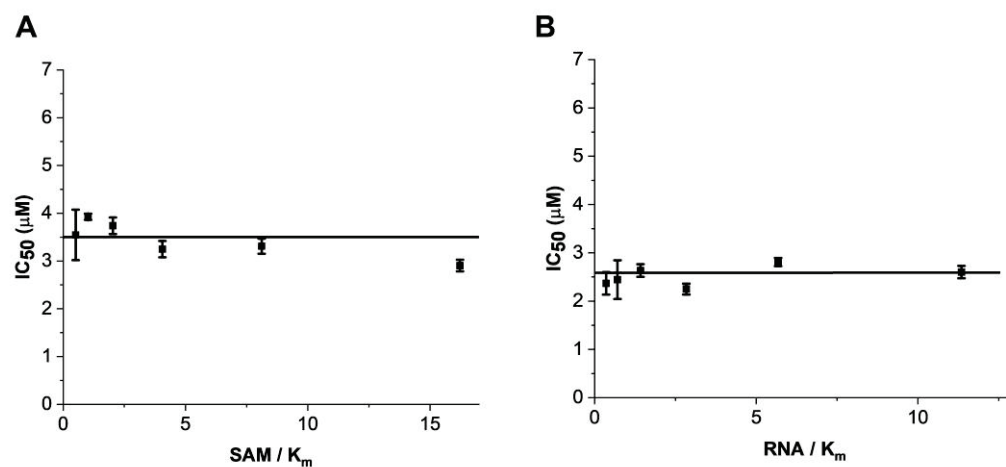
Figure 4. Studies on the mechanism of action showed that eltrombopag inhibited the METTL3-14 complex in a noncompetitive manner. (**A**) IC_{50} values of eltrombopag at increasing concentrations of SAM ranging from 50 to 1600 nM at fixed concentrations of RNA substrate (2 μM). (**B**) IC_{50} values of eltrombopag at increasing concentrations of RNA substrate ranging from 25 to 800 nM at fixed concentrations of SAM substrate (3 μM).

Next, in order to predict the allosteric binding site in which eltrombopag might interact and bind, its inhibitory activities were evaluated first at various enzyme forms of METTL3-14, such as each single form of METTL3 and METTL14 and the truncated form of METTL3-14 with only the methyltransferase domain (Figure 5A). As a result, eltrombopag maintained its inhibitory activity with an IC_{50} value of 7.04 μM in the single subunit enzyme form of METTL3, whereas a dramatically reduced partial inhibition was observed in the single subunit enzyme form of METTL14 with 59.3% at 36 μM. The profile of inhibitory activities suggests that the main interacting enzyme form of eltrombopag might be the METTL3 subunit rather than the METTL14 subunit. In the case of the truncated form of the METTL3-14 complex, of which the crystal structure was reported, eltrombopag maintained its full inhibitory activities with a 3.5-fold decreased IC_{50} value of 12.0 μM (Figure 5A). Therefore, it could be predicted that some part of the binding regions for eltrombopag might exist in the truncated form of the METTL3 monomer.
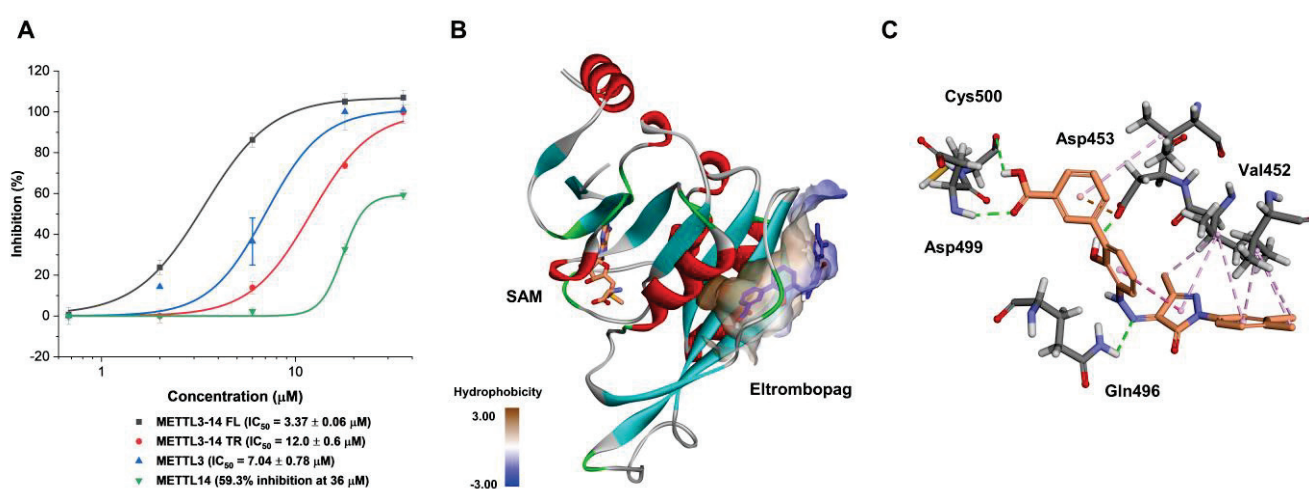

Figure 5. Predicted binding mode of eltrombopag with the METTL3 crystal structure. (**A**) Inhibitory activities of eltrombopag in various METTL3-14 enzyme forms (METTL3-14 FL: full length of METTL3-14, METTL3-14 TR: truncated form of METTL3-14 consisting of a methyltransferase domain). (**B**) Hydrophobicity surface view at the predicted allosteric binding pocket with the docked eltrombopag into METTL3 crystal structure (PDB: 5IL1 A chain). (**C**) Docking pose of eltrombopag with METTL3 (the green dashed lines represent hydrogen bond).

Consequently, potential allosteric binding pockets were investigated in the METTL3 crystal structure (PDB: 5IL1 A chain) through computational cavity searching algorithms using Allosite [48] and Discovery Studio software (version 3.5). As a result, a new allosteric binding pocket—distinct from the SAM binding site—was simultaneously predicted by both of the independent programs (Figure 5B). Then, a molecular docking experiment was performed on eltrombopag at the predicted allosteric binding pocket using the CDOCKER protocol of the Discovery Studio software. As illustrated in Figure 5B,C, eltrombopag was successfully docked to the predicted binding pocket, displaying several interactions with amino acids in the region. The putative binding modes include the hydrogen bonding interactions between the backbone amide group of Asp499 and Cys500 residues, the carboxylate group of Asp453, and the carboxamide group of Gln 496 with the carboxylic acid, the phenolic alcohol, and the hydrazine of eltrombopag, respectively. Additionally, some van der Waals interactions with aromatic groups of eltrombopag were predicted with several hydrophobic amino acids, including Val452, Val485, and Val487. It might be speculated that the putative binding could be further tightened by more interactions with the missing domains from the full-length METTL3-14 complex, such as the zinc finger domain.

The attempt of the X-ray analysis to verify the predicted binding site of eltrombopag at METTL3 was unfortunately not feasible since it was hard to generate a crystal of eltrom-

bopag with METTL3 due to the low water solubility of eltrombopag [49]. Therefore, the interactions of eltrombopag in the predicted binding site of METTL3-14 were indirectly investigated by evaluating the inhibitory activities of its derivatives, thereby disrupting the hydrogen bonding donors of eltrombopag, such as carboxylic acid or the phenol groups, which might be responsible moieties for the key interactions in docking results. Thus, compounds **14a** (removal of carboxylic acid), **14b** (carboxylate methyl ester), and **14d** (removal of phenol group) were synthesized as Scheme S1 in the Supplementary Materials and evaluated for their enzyme inhibitory activities.

As a result, compounds **14a**,**b** exhibited a significant loss of METTL3-14 inhibitory activities with only 23.3 and 23.7% inhibitions even at 60 μM, respectively, indicating that the acidic proton of the carboxylic acid moiety of eltrombopag is essential for maintaining the inhibitory activity (Figure 6). In addition, the importance of phenolic alcohol in maintaining the inhibitory activity of eltrombopag was also confirmed and observed in the 4-fold decreased inhibitory activity of compound **14d** with an IC_{50} value of 15.3 μM. Collectively, these results, consistent with the reduced docking scores in the molecular docking experiments, indirectly support the predicted binding mode of eltrombopag in a complex with METTL3.
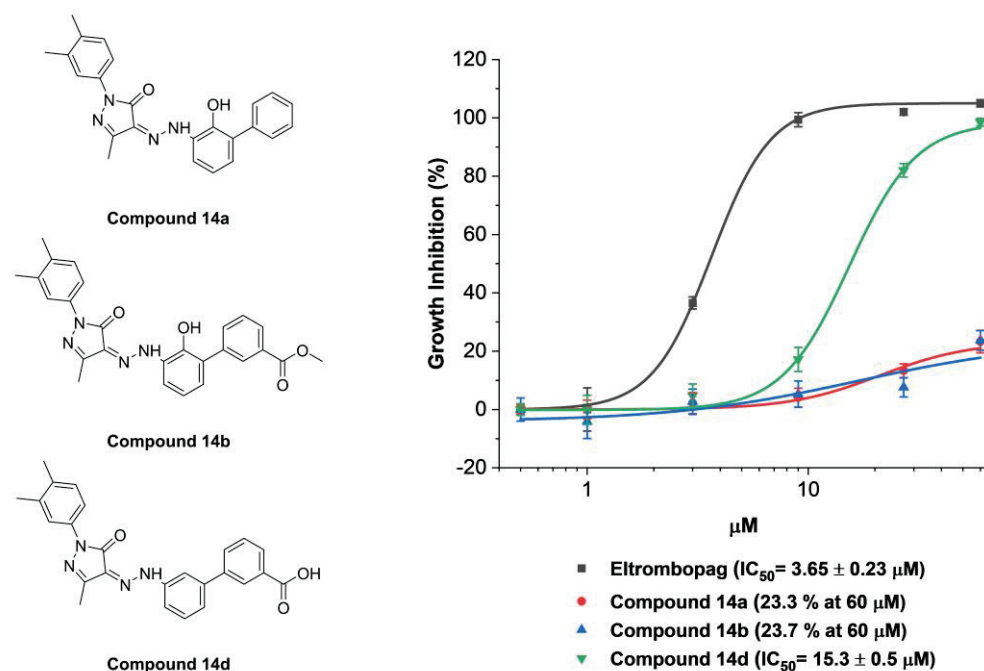
Figure 6. METTL3-14 enzymatic inhibitory activities of compounds **14a**, **14b**, and **14d** with structural modifications to disrupt the predicted hydrogen bonding interactions between METTL3-14 and eltrombopag.

2.3. Cellular Activity Evaluation of Eltrombopag on Acute Myeloid Leukemia Cell Lines

Based on the close relationship of METTL3-14 for the proliferation of AML, the cellular level of anti-leukemic potential associated with the inhibition of METTL3-14 was investigated by the anti-proliferative activity of eltrombopag in MOLM-13 as an AML cell line closely related with METTL3 for its growth [32,33]. As shown in Figure 7A, eltrombopag exhibited the growth inhibition of the MOLM-13 cell line with a GI_{50} value of 8.28 μM. In addition, dose-dependent inhibition of m^6A levels on poly-A^+-enriched mRNA was also confirmed in the MOLM-13 cell line after 24 h eltrombopag treatment (Figure 7B), indicating that eltrombopag exhibited anti-leukemic effects on the MOLM-13 cell line by a correlated reduction of the m^6A levels through the inhibition of METTL3-14. The maximum m^6A inhibition by eltrombopag in MOLM-13 cells was shown to be 50% at 40 μM, which was similar to those of the shMETTL3 treated case (Figure S4) and the previously reported

data (60–70%) with UZH1a [37]. Moreover, eltrombopag also showed the antiproliferative effects against other AML cell lines, including MOLM-14, HL60, MV4-11, and THP-1, with a range of GI_{50} values from 10~22 μM (Figure 7C).
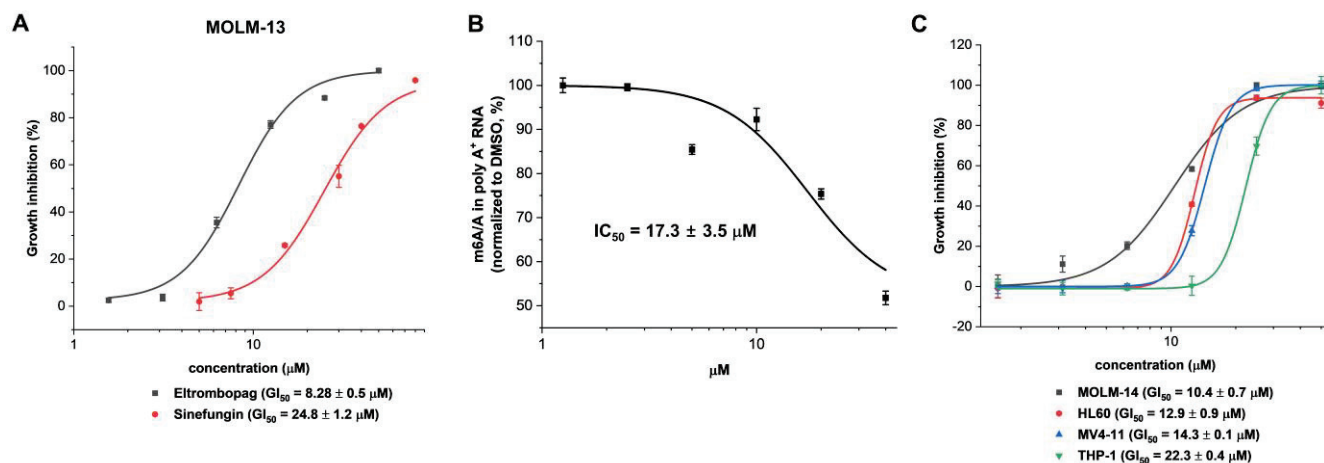

Figure 7. Anti-proliferative activity and cellular activity of eltrombopag on AML cell lines. (**A**) Anti-proliferative activity of eltrombopag against the MOLM-13 cell line. A global methyltransferase inhibitor, Sinefungin (**1**), was evaluated as a positive control in MOLM-13 cell line with a GI_{50} value of 24.8 μM. (Gilteritinib, an FLT3 targeted anti-AML drug, showed a GI_{50} value of 16.6 nM in Figure S3). (**B**) Dose-response curve of m^6A/A reduction on poly-A^+-enriched mRNA after 24 h of MOLM-13 treatment with eltrombopag. (**C**) Anti-proliferative activities of eltrombopag against AML cell lines including MOLM-14, HL60, MV4-11, and THP-1 cell lines.

The Steidl group has previously reported that eltrombopag displayed anti-proliferative activity, inducing the differentiation of human acute myeloid cells, which have an independent biological activity at the original target, TPO-R, without presenting a clear mechanism of eltrombopag for anti-leukemic effects [50]. In the present study, we have demonstrated that the mechanism of action of eltrombopag for its anti-leukemic effects would be direct inhibition of METTL3-14 and a consequent decrease of the m^6A levels of mRNA. In addition, the in–vivo anti-leukemic effect of eltrombopag, through prolonging the survival of a mouse model transplanted with an AML cell line, has been reported in the abovementioned paper [50]. Therefore, eltrombopag might be a starting point for the development of a novel mechanism-based drug candidate for the treatment of acute myeloid leukemia through a further optimization study of the chemical structure of eltrombopag based on its binding mode in METTL3-14.

To investigate the applicability of eltrombopag for combination therapy with current AML drugs, we evaluated the antiproliferative activity of combination treatments of eltrombopag and current AML drugs, including venetoclax, cytarabine, gilteritinib, and sorafenib, against MOLM-13. The synergy scores for each combination were calculated using the Highest Single Agent (HSA) model in the Synergyfinder software [51]. As a result, a clear synergistic inhibitory effect of the venetoclax/eltrombopag combination was determined with an average HSA synergy score of 11.68 and a peak value of 26.37 (Figure 8A,B). In addition, this synergistic effect of the venetoclax/eltrombopag combination was further confirmed from the analysis with the Zero Interaction Potency (ZIP), Loewe additivity model, and Bliss independence models in the Synergyfinder software [51]. In the case of the cytarabine/eltrombopag combination, a relatively weak synergistic effect was observed with an average HSA synergy score of 6.86 (Figure 8C,D), which was consistent with the previously reported result that eltrombopag enhanced the anticancer effect of cytarabine [52]. However, the treatments with the combination of eltrombopag with gilteritinib or sorafenib didn't display a significant synergistic effect (Figure S5). Collectively, the results indicated

that eltrombopag could have a potential for use in combination with current AML drugs, including venetoclax and cytarabine, for the treatment of AML.
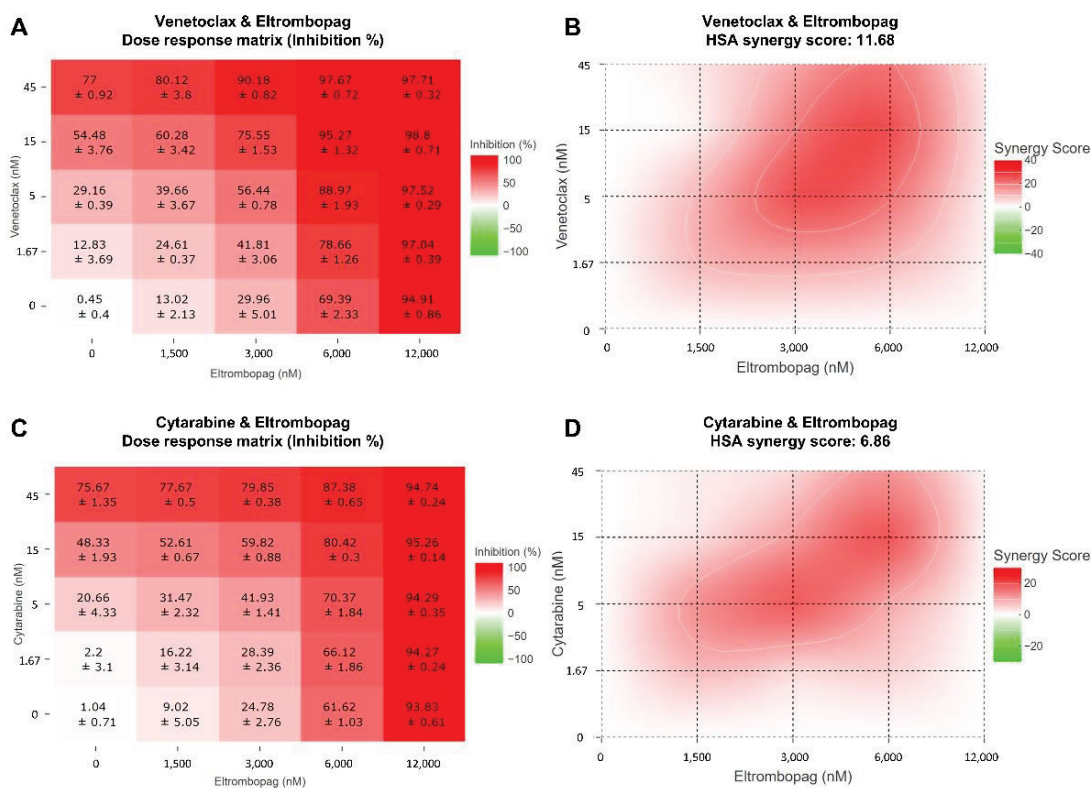

Figure 8. Synergistic effect of the combination treatment of eltrombopag and current AML drugs, venetoclax and cytarabine, on MOLM-13. (**A**) Dose-response matrix for the venetoclax/eltrombopag combination in MOLM-13 cell line. (**B**) 2D synergy maps and calculated HSA synergy scores for the venetoclax/eltrombopag combinations using Synergyfinder software. (**C**) Dose-response matrix for the cytarabine/eltrombopag combination in MOLM-13 cell line. (**D**) 2D synergy maps and calculated HSA synergy scores for the cytarabine/eltrombopag combinations using Synergyfinder software. Red and green areas represent synergy and antagonism, respectively. All experiments were repeated at least three times.

In clinical studies of eltrombopag, although monotherapy treatment didn't show any safety concerns, increased progression to acute myeloid leukemia was observed in the combination treatment with azacitidine compared with the treatment of azacitidine alone [53,54]. Therefore, attention to various safety concerns should be drawn when attempting a combination therapy of drugs with eltrombopag.

2.4. Identification of Anti-Leukemia Potential of Eltrombopag at Molecular Level

To determine whether eltrombopag has anti-leukemia potential on a molecular level, we performed N^6-methyladenosine-sequencing (m6A-seq) using the eltrombopag-treated MOLM-13 cell line and analyzed the differential m6A methylation sites in the transcriptome. As shown in Figure 9A and Table S1, we identified 10,723 differential m6A methylation sites, and 71% of them were hypomethylated, similarly to the previously reported METTL3 inhibitor STM2457 treatment [39]. Additionally, we found that about 30% of hypermethylation was also detected when treated with eltrombopag or STM2457. To find out whether this hypermethylation is specifically caused by chemical METTL3 inhibitors, we obtained m6A individual-nucleotide-resolution cross-linking and immunoprecipitation (miCLIP) sequencing results for the METTL3-deficient MOLM-13 cell line from the Gene Expression Omnibus (GEO) database [32] and re-analyzed the differential m6A methylation

sites. As a result, hypomethylation was predominant in the METTL3 knockdown cells, but hypermethylation was also observed (Figure S6, Table S2). Our observations regarding hypermethylation upon METTL3 inhibition suggest that it might be considered in the development of anti-AML therapies.

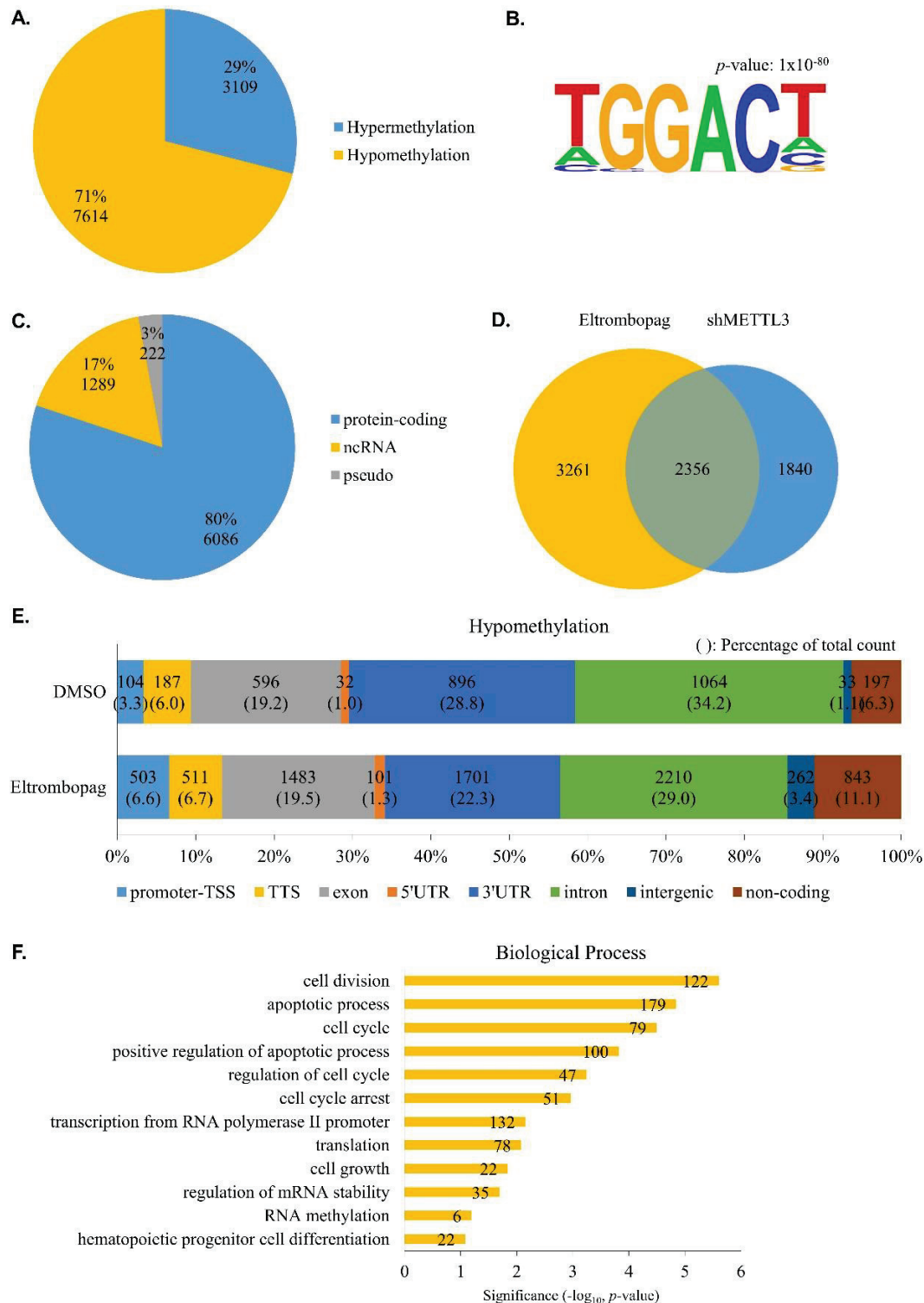**Figure 9.** Eltrombopag reduces m^6A levels in AML cells. (**A**) Distribution of significantly differentiated m6A methylated peaks detected in MOLM-13 cell line with 25 µM of eltrombopag. If diff.log2.fc is larger than 0 it is indicated as hypermethylation (blue), and if smaller than 0 it is indicated as hypomethylation (yellow). (**B**) Top consensus motif in eltrombopag-treated differentiated m^6A methylated

peaks with HOMER. GGAC, a subset of the m^6A common motif, was detected. (**C**) Distribution of hypomethylated gene identity. Protein-coding, non-coding RNA (ncRNA), and pseudogenes (pseudo) are shown in blue, yellow, and gray, respectively. (**D**) Common and unique hypomethylated peaks in eltrombopag-treated or shMETTL3-treated MOLM-13 cell lines. A proportional Venn diagram was drawn with VennDiagram. (**E**) Peak annotation of DMSO or eltrombopag-treated hypomethylation with HOMER. TSS, transcription start site (from −1 kb to +100 bp); TTS, transcription termination site (from −100 bp to +1 kb); UTR, untranslated region. (**F**) Gene ontology enrichment analysis of eltrombopag-treated hypomethylation genes. The number of genes associated with the GO term is shown at the end of the bar.

M^6A RNA methylation tends to occur in the RRACH consensus motif [2,4]. To investigate the specificity of eltrombopag-regulated m^6A methylation, we analyzed motifs in differentially methylated peaks. Figure 9B shows that GGAC, a subset of the m^6A common motif, is highly enriched in its differential methylation sites. Since eltrombopag acts as a METTL3 inhibitor, we focused on the hypomethylation genes in subsequent analyses. We further analyzed the types of hypomethylated genes, and, as a result, most of them were protein-coding (~80%), noncoding-RNA (ncRNA), and pseudogenes accounting for 17% and 3%, respectively (Figure 9C).

Next, we compared hypomethylated genes in eltrombopag-treated or METTL3 knockdown cells. As shown in Figure 9D, a significant number of them overlapped, suggesting that eltrombopag leads to gene hypomethylation through the METTL3 inhibitory effect. In addition to the overlapping regions, there were eltrombopag-specific hypomethylated genes, which may be due to eltrombopag not targeting METTL3 alone but inhibiting the roles of other components of the METTL3-14 complex. To further examine the m^6A peak distribution affected by eltrombopag, we performed a peak annotation analysis. As a result, hypomethylation in the 3′UTR and intron, in which the m^6A peak is widely distributed, was significantly decreased during eltrombopag treatment, whereas it was increased in the promoter-TSS and non-coding region (Figure 9E, Table S1).

Finally, we applied gene ontology enrichment analysis to an in-depth study of the biological process of differentially eltrombopag-treated hypomethylated genes. As shown in Figure 9F, hypomethylated genes were highly enriched in apoptotic processes, cell cycle and growth, and hematopoietic progenitor cell differentiation events, suggesting that eltrombopag might be involved in the physiological processes of AML cells. A recent study has shown that the N^6-methyltransferase complex, including METTL3-14, is recruited near the promoter and promotes RNA polymerase II pausing, leading to gene regulation [55]. The eltrombopag-treated m^6A peak distribution at the promoter-TSS and transcription-related events shown in the GO analysis suggest that eltrombopag may affect gene expression through the regulation of m^6A RNA methylation around promoter-TSS (Figure 9E, Table S3). Taken together, eltrombopag reduced m^6A levels in the MOLM-13 transcriptome, indicating the anti-leukemia potential of eltrombopag on a molecular level.

3. Materials and Methods

3.1. General Methods for Chemistry

All reagents and solvents were obtained from commercial sources and used without further purification. Eltrombopag (**1**) was purchased from Axonmedchem (SB 497115) (Groningen, The Netherlands). The ^{1}H and ^{13}C Nuclear magnetic resonance (NMR) spectra were recorded with a JEOL JNM-ECX 400p spectrometer at 400 MHz and 101 MHz, respectively. All spectra were taken using CDCl$_3$ and dimethyl sulfoxide (DMSO)-d$_6$. Mass spectroscopy was performed on a BEH C18 column (1.7 µM, 2.1 mm × 50 mm; Waters) and maintained at 40 °C during separation under isocratic conditions (mobile phase A: mobile phase B = 20:80) by using a Waters ACQUITY ultraperformance liquid chromatograph coupled to a triple quadrupole mass spectrometer (Micromass Quattro Micro, Waters, Milford, MA, USA). The mobile phase was as follows: A, water (LC-MS grade) with 0.1% formic acid

(*v/v*); and B, CH3CN (LC-MS grade) with 0.1% formic acid (*v/v*); flow rate, 0.2 mL/min. Synthetic procedures and characterization data for all the synthesized compounds are provided in the Supplementary Materials.

3.2. Cloning, Expression and Purification of METTL3 and METTL14

For recombinant protein production, genes encoding the full-length and MTase domain of human METTL3 (residues 369 to 580) or METTL14 (residues 106 to 396) were cloned between the XbaI and NotI sites in the pVL1393 baculovirus transfer vector (BD Biosciences, NJ, USA) with a thrombin-cleavable decahistidine ($10\times$ His) tag at the C-terminus and N-terminus. The plasmids were transfected into Spodoptera frugiperda (Sf9) cells using BestBac 2.0 linearized baculovirus DNA (Expression Systems, Davis, CA, USA) and Cellfectin II transfection reagent (Gibco, Waltham, MA, USA). The METTL3-METTL14 complex was obtained by co-infection of Trichoplusia ni (Hi5) cells with two recombinant baculoviruses. The transgenic cells were cultured for 72 h at 28 °C and harvested by centrifugation at $14,000\times$ *g* for 10 min at 4 °C.

The purification of the human METTL3 and METTL14 complex was performed with slight modifications [22]. Briefly, cells were re-suspended and broken using a sonicator (6 cycles of 10 s on/10 s off, 40% amplitude, Branson, CT, USA) in a lysis buffer containing 20 mM Tris-HCl pH 8.0, 200 mM NaCl, 10 μg/mL DNase I and 0.1 mM phenylmethylsulfonyl fluoride (PMSF). Cell debris was removed by ultracentrifugation at $240,000\times$ *g* for 1 h at 4 °C, and the supernatant was loaded onto Ni-NTA affinity resin (Goldbio, MO, USA). The resin was washed with 20 column volumes of lysis buffer containing 50 mM imidazole. The protein was eluted with a 100-, 300-, and 500-mM imidazole gradient. After cleavage by thrombin to remove the histidine tag, the protein was further purified by Hi-Trap Q (GE Healthcare, Chicago, IL, USA) anion exchange chromatography and Superdex 200 Increase (GE Healthcare) gel filtration chromatography in a buffer containing 25 mM Tris-HCl pH 8.0, 150 mM NaCl, and 3 mM DL-Dithiothreitol (DTT, Goldbio). Fractions containing the complex protein were pooled and concentrated to an amount of 1 mg/mL for functional assays. All purification steps were performed on ice or at 4 °C.

3.3. METTL3-14 Enzyme-Based Bioluminescence Assay (Screening Assay)

An enzymatic bioluminescence assay was established to identify the METTL3-14 inhibitor through screening. During the screening, all enzymatic reactions were performed in 96-well plates using a reaction buffer (20 mM Tris pH 7.5, 1 mM DTT, 0.01% Triton X-100, and 40 U of RNaseOUT (Invitrogen, Waltham, MA, USA) with a final reaction volume of 20 μL. In total, a final concentration of 30nM of METTL3-14 was incubated with 300 nM final concentration of SAM, 300 nM final concentration of RNA substrates (5'-ACGAGUCCUGGACUGAAACGGACUUGU-3'), and serially diluted compounds at 23 °C for 1 h. Furthermore, 5 μL of 5% trifluoroacetic acid was added to each well to stop the enzymatic reaction. After a 10-min incubation period, the reaction product, SAH, was converted to ATP as a substrate of luciferase using the MTase-Glo™ Methyltransferase Assay kit (Promega, Madison, WI, USA). METTL3-14 activity was assessed by measuring the luminescence using a Victor multilabel reader (PerkinElmer, Waltham, MA, USA). The IC_{50} values were calculated by a nonlinear regression analysis using OriginPro 9.1 software (OriginLab).

To confirm the mechanism of action of eltrombopag in the METTL3-14 complex, 30 nM METTL3-14 and serially diluted eltrombopag were reacted with various concentrations of SAM or RNA substrate and saturating concentrations of the other substrate (3 μM SAM or 2 μM RNA substrate) for 20 min. To evaluate the inhibitory activity in a single form of METTL3 and METTL14, 1 μM of METTL3 and 300 nM of METTL14 were incubated with 1 μM of SAM, 500 nM of RNA substrates, and serially diluted eltrombopag for 5 h. To measure the inhibitory activity in the truncated form of the METTL3-14 complex, 1 μM of the truncated METTL3-14 complex was reacted with 1 μM of SAM, 500 nM of RNA substrates, and serially diluted eltrombopag for 5 h.

3.4. METTL3-14 Enzyme-Based Bioluminescence Assay (False Positive Response Experiment)

To determine whether hit compounds are false positives that inhibit the coupled enzyme reaction processes converting SAH to ATP, 30 nM of METTL3-14, 300 nM of SAM, and 300 nM of RNA substrates were incubated at 23 °C for 1 h without a hit compound. After incubation, 5 µL of 5% trifluoroacetic acid was added to each well to stop the enzymatic reaction. Then, the hit compound was added to the reaction mixture at a concentration of 25 µM before the product SAH was converted to ATP. Finally, the reaction product, SAH, was converted to ATP as a substrate of luciferase using the MTase-GloTM Methyltransferase Assay kit (Promega). METTL3-14 activity was assessed by measuring the luminescence using a Victor multilabel reader (PerkinElmer). If it shows the inhibitory activity in a false positive response experiment, this hit compound is a false positive affecting the coupled enzyme system.

To investigate whether the hit compound was a false positive, thereby causing colloidal aggregation, a hit compound diluted in enzyme assay buffer was centrifuged at $15,000 \times g$ for 10 min at 4 °C. After centrifugation, the supernatant was used for the METTL3-14 enzyme-based bioluminescence assay as described above. According to this method, if it is not possible to identify the inhibitory activity in a false positive centrifugation test, the hit compound is a false positive that will lead to colloidal aggregation.

3.5. Mass Spectrometry Based METTL3-14 Enzyme Based Assay

The 30 nM of METTL3-14 was incubated with 300 nM of SAM, 300 nM of RNA substrates, and serially diluted compounds at 23 °C for 1 h as described above. The enzymatic reaction was stopped by heating at 80 °C for 10 min and centrifuged at $15,000 \times g$ for 10 min. Then, the reacted RNA in the supernatant was digested to nucleosides by using 2 units of nuclease P1 (NEB, Ipswich, MA, USA) and dephosphorylated by using 1 unit of alkaline phosphatase (NEB) at 37 °C for 2 h.

The produced nucleosides were detected by reversed-phase high-performance liquid chromatography on an ACQUITY BEH C18 column (1.7 µM, 2.1 mm × 50 mm; Waters) coupled with mass spectrometry detection using an EVOQ Elite ER LC-TQ (Bruker, Billerica, MA, USA). The adenosine and m^{6}A were quantified using an MRM transition as follows: m/z = 267.9 -> 136.1 and m/z = 282.1 -> 150.1, respectively. (Retention time 5 min). The m^{6}A/A nucleoside ratio of the eltrombopag-treated sample was normalized to the corresponding value of the DMSO treated negative control. The IC_{50} values were calculated by a nonlinear regression analysis using OriginPro 9.1 software (OriginLab).

3.6. Surface Plasmon Resonance

The interaction between eltrombopag and the METTL3-14 complex was explored using a Reichert SR7000DC instrument optical biosensor (Reichert Technologies, Depew, NY, USA) equipped with a carboxymethyl dextran sensor chip (part no. 13206066, Reichert Technologies). To activate the sensor chip, free carboxyl groups on the surface were modified by injecting a mixture of 0.1 M of 1-ethyl-3-(3-dimethylaminopropyl) carbodiimide hydrochloride and 0.05 M of N-hydroxysuccinimide at a flow rate of 10 µL/min to generate a reactive succinimide ester surface. Then, the METTL3-14 complex (9.5 µg/mL; prepared in 10 mM sodium acetate buffer, pH 4.5) was coupled to the sensor via free amine coupling to the immobilized succinimide and followed by the quenching of the remaining activated succinimide ester with 1 M of ethanolamine, pH 8.5. The eltrombopag was diluted in PBS that was supplemented with 0.005% Tween, thereby maintaining a final 5% DMSO concentration. The binding experiments were performed using a flow rate of 30 µL/min with an association time of 5 min and a dissociation time of 7 min. The regeneration of the surfaces was performed, when necessary, by 10 mM of NaOH. The Langmuir model of the Scrubber2 software was used to determine the equilibrium dissociation constant and kinetic dissociation and association constants.

3.7. Selectivity Profiling

The selectivity profile of eltrombopag was investigated by testing the level of inhibition in a methyltransferase panel. The inhibition of 7 RNA methyltransferase was tested at Reaction Biology (Malvern, PA, USA) using a gold standard radioisotope-based MT assay (MT HotSpot^{TM}) with 10 μM of eltrombopag in duplicate. SAH and chaetocin were used as positive controls in the methyltransferase panel screening.

3.8. Allosteric Binding Pocket Prediction and Molecular Docking

The potential allosteric binding pocket in METTL3 was independently predicted based on the METTL3 crystal structure (PDB ID: 5IL1 A chain) obtained from the Protein Data Bank via the "From Receptor Cavities" protocol in the Discovery Studio 3.5 software and Allosite 2.0 [48], which detects allosteric sites based on a structure-based machine learning method. After prediction, the protein preparation process was carried out using the "Prepare Protein" wizard included in Discovery Studio and a radius of 15 Å around the predicted allosteric binding pocket was set as a binding site. For the molecular docking, ligands applied with a CHARMM force field were docked into the above-predicted allosteric binding pocket in METTL3 using the CDOCKER protocol in Discovery Studio.

3.9. Cell Culture and shMETTL3 Knockdown

The MOLM-13, MOLM-14, and MV4-11 cell lines were supplied by the Leibniz Institute DSMZ-German Collection of Microorganisms and Cell Cultures GmbH (DSMZ) (Braunschweig, Germany). The HL60 and THP-1 cell lines were supplied by the Korea Cell Line Bank (KCLB) (Seoul, Korea). The MOLM-13, MOLM-14, HL60, MV4-11, and THP-1 cells were cultured in RPMI 1640 medium (HyClone, Logan, UT, USA) with 10% fetal bovine serum (Gibco) and 1% penicillin/streptomycin in 5% CO_2 at 37 °C in a humidified incubator. METTL3 shRNA was produced by transfection of shRNA plasmid DNA (Open Biosystems), psPAX2 (packaging plasmid), and pMD2.G (envelope plasmid) with polyethyleneimine (PEI) reagent into HEK293T cells. After 24 h, the media were freshly replaced, and 48 h after transfection the supernatant was passed through a 0.45 μm filter to obtain a viral supernatant. The viral supernatant was transfected into MOLM-13 cells using a polybrene reagent.

3.10. Anti-Proliferative Assay Protocol

The MOLM-13, MOLM-14, HL60, MV4-11, and THP-1 cells were seeded in white 96-well clear bottomed plates with 100 μL of medium (5000 cells/well). The plated cells were treated with serially diluted compounds and incubated for 72 h at 37 °C. After incubation, 10 μL of EZ-cytox kit reagent from the EZ-cytox cell viability assay kit (DaeiLab, Seoul, Korea) was added to each well and then incubated for 3 h at 37 °C. The absorbance of metabolically active cells was measured at a wavelength of 450 nm using a Victor multilabel reader (PerkinElmer). The GI_{50} values were calculated by nonlinear regression analysis using OriginPro 9.1 software (OriginLab).

3.11. Combinatorial Analysis of AML Drugs with Eltrombopag

The MOLM-13 cells were seeded in white 96-well clear bottomed plates with 50 μL of medium (5000 cells/well). The plated cells were treated with serially diluted eltrombopag and current AML drugs, including venetoclax, cytarabine, gilteritinib, and sorafenib, to a final volume of 100 μL and incubated for 72 h at 37 °C. After incubation, 10 μL of EZ-cytox kit reagent from the EZ-cytox cell viability assay kit (DaeiLab) was added to each well and then incubated for 3 h at 37 °C. The absorbance of metabolically active cells was measured at a wavelength of 450 nm using a Victor multilabel reader (PerkinElmer). The synergy scores of each combination were quantified by the HAS model, ZIP model, Loewe additivity model, and Bliss independence models using Synergyfinder software [51]. Positive or negative synergy scores obtained through these models represent synergy and antagonism, respectively.

3.12. Quantitative Analysis of m⁶A Level by Mass Spectrometry

The MOLM-13 cells were seeded in 10 cm^2 dishes at a density of 1.5×10^6 cells/mL with 10 mL of complete medium. After 24 h, the plated cells were treated with the vehicle (DMSO) or serial dilutions of eltrombopag and incubated for 24 h. Following incubation in the cell culture incubator, total RNA was extracted using TRIsure^{TM} (Bioline, Brisbane, Australia) according to the manufacturer's instructions. Then, poly-A$^+$-enriched mRNA was purified from the extracted total RNA using the Magnosphere^{TM} ultrapure mRNA purification kit (Takara, Shiga, Japan). One microgram of mRNA was digested to the nucleosides using 2 units of nuclease P1 (NEB) and dephosphorylated using 1 unit of alkaline phosphatase (NEB) at 37 °C for 2 h.

The produced nucleosides were detected by reversed-phase high-performance liquid chromatography on an ACQUITY BEH C18 column (1.7 μm, 2.1 mm × 50 mm; Waters) coupled with mass spectrometry detection using an EVOQ Elite ER LC-TQ (Bruker). The adenosine and m⁶A were quantified using MRM transition as follows: $m/z = 267.9 \rightarrow 136.1$ and $m/z = 282.1 \rightarrow 150.1$, respectively. (Retention time 5 min). The m⁶A/A nucleoside ratio of the eltrombopag-treated sample was normalized to the corresponding value of the DMSO treated negative control. The inhibition curves were plotted using OriginPro 9.1 software (OriginLab) and fitted using nonlinear regression analysis.

3.13. N⁶-Methyladenosine-Sequencing (m⁶A-seq) and Sequencing Data Analysis

mRNA was purified using a GenElute™ mRNA Miniprep Kit (SIGMA, MRN10-1KT, St. Louis, MO, USA) according to the manufacturer's protocol. Briefly, the total RNA was mixed with 2× Binding Solution and oligo(dT) beads, vortexed, and left for 10 min at room temperature. The beads:mRNA complex was passed through a GenElute spin filter/collection tube and washed twice with Wash Solution. The mRNA was eluted in an Elution Solution incubated at 70 °C.

m⁶A-seq was performed using the EpiMark® N⁶-Methyladenosine Enrichment Kit (NEB, E1610S). Briefly, 25 μL of Dynabeads™ Protein G (Invitrogen, 10004D) and 1 μL of N⁶-Methyladenosine Antibody were incubated in a 4 °C rotator for 2 h. The purified mRNA was fragmented at 95 °C for 10 min in a fragmentation buffer (100 mM Tris (pH 8.0), 8 mM MgCl$_2$) with spike-in control RNA (m⁶A and unmodified, 0.1 fmol of each RNA). The fragmented RNA was concentrated with RNA Clean & Concentrator™-5 (ZYMO RESEARCH, R1014, Irvine, CA, USA) and then 5% was saved as the input. The remaining 95% of the fragmented RNA was added to the beads/antibody complex. RNA was eluted in Buffer RLT (QIAGEN, 79216, Hilden, Germany), followed by ethanol precipitation and was used for sequencing library construction. All sequencing experiments were performed in triplicate via Novaseq. Adapter trimming and QC were performed using Trim Galore. Reads were mapped to hg38 by HISAT2 [56], and exomePeak [57] and HOMER [58] were used to analyze the differential methylation peaks, motifs, and gene annotations.

4. Conclusions

In this study, we reported on the use of eltrombopag as a METTL3-14 allosteric inhibitor that was identified through the screening of a drug library from the Korea Chemical Bank, and its mechanism of action was determined by various biochemical analyses. Eltrombopag exhibited selective inhibitory activity against the METTL3-14 complex with an IC$_{50}$ value of 3.65 μM, and its direct binding to the enzyme complex was confirmed by the analysis in surface plasmon resonance experiments. In addition, exploring the mode of enzyme inhibitory mechanisms revealed that eltrombopag acts as a noncompetitive inhibitor interacting at a putative allosteric binding site predicted by molecular docking studies and the main enzyme of its interaction was experimentally determined as the METTL3 subunit rather than the METTL14 subunit. On a cellular level, eltrombopag showed anti-leukemic activity in the relevant AML cell line, MOLM-13, in correlation with the reduction of m⁶A levels. Molecular mechanism studies of eltrombopag using m⁶A-seq analysis provided further evidence of its cellular function by determining the hypomethylation of leukemogenic

genes in eltrombopag-treated MOLM-13 cells and the overlapping of the pattern with those of the METTL3-knockdown MOLM-13 cells. Taken together, in this study, eltrombopag was identified as a METTL3-14 allosteric inhibitor with anti-leukemic activity against AML, which could provide a potential opportunity for the development of new drug candidates for AML via further optimization of the structure of eltrombopag at the binding site.

Supplementary Materials: The following supporting information can be downloaded at: https://www.mdpi.com/article/10.3390/ph15040440/s1, Scheme S1: Reagents and conditions: (a) Sodium acetate, AcOH, reflux, 24 h; (b) R^1-PhB(OH)$_2$, Pd(PPh$_3$)$_4$, K$_2$CO$_3$, THF/water/EtOH, 60 °C, 18 h; (c) Pd/c, THF/MeOH, rt, 3 h; (d) NaNO$_2$, NaHCO$_3$, MeOH, rt, 3 h; (e) KOH, MeOH, water, 60 °C, 18 h; Figure S1: Kinetic parameter determination of the METTL3-14 complex by using screening assay system, Figure S2: Confirmation of false-positive potential, Figure S3: The anti-proliferative activity of gilteritinib as positive control was confirmed a GI$_{50}$ value of 16.6 nM in MOLM-13. Figure S4: m^{6}A levels on poly-A+-enriched mRNA after 24 h of eltrombopag treatment (40 μM) or 4 days after post-transduction of siRNA in MOLM-13, Figure S5: Analysis of combination treatment of AML drugs, gilteritinib and sorafenib, with eltrombopag in MOLM-13, Figure S6: Distribution of significantly differential m^{6}A methylated peaks detected in shMETTL3-treated Molm-13 cells, Figure S7: NMR spectrum of compound **14a**, Figure S8: NMR spectrum of compound **14b**, Figure S9: NMR spectrum of compound **14d**, Table S1: Differential m^{6}A methylation sites and peak annotation in Eltrombopag-treated Molm-13 cells, Table S2: Differential m^{6}A methylation sites in shMETTL3-treated Molm-13 cells, Table S3: GO enrichment analysis of differentially m^{6}A methylated genes.

Author Contributions: Conceptualization, J.-H.L. and Y.-C.K.; methodology, J.-H.L., N.C. and S.K.; validation, J.-H.L., N.C. and S.K.; formal analysis, J.-H.L., N.C. and S.K.; investigation, J.-H.L., N.C. and S.K.; resources, M.S.J., H.S. and Y.-C.K.; writing—original draft preparation, J.-H.L., N.C. and S.K.; writing—review and editing, M.S.J., H.S. and Y.-C.K.; funding acquisition, Y.-C.K. All authors have read and agreed to the published version of the manuscript.

Institutional Review Board Statement: Not applicable.

Informed Consent Statement: Not applicable.

Data Availability Statement: Publicly available datasets were analyzed in this study. The m^{6}A-seq and RNA-seq data created in this study are openly available in the NCBI Sequence Read Archive at BioProject accession number PRJNA807459.

Conflicts of Interest: The authors declare no conflict of interest.

References

1. Desrosiers, R.C.; Friderici, K.H.; Rottman, F.M. Characterization of Novikoff Hepatoma MRNA Methylation and Heterogeneity in the Methylated 5′ Terminus. *Biochemistry* **1975**, *14*, 4367–4374. [CrossRef] [PubMed]
2. Dominissini, D.; Moshitch-Moshkovitz, S.; Schwartz, S.; Salmon-Divon, M.; Ungar, L.; Osenberg, S.; Cesarkas, K.; Jacob-Hirsch, J.; Amariglio, N.; Kupiec, M.; et al. Topology of the Human and Mouse M6A RNA Methylomes Revealed by M6A-Seq. *Nature* **2012**, *485*, 201–206. [CrossRef] [PubMed]
3. Harper, J.E.; Miceli, S.M.; Roberts, R.J.; Manley, J.L. Sequence Specificity of the Human MRNA N6-Adenosine Methylase in Vitro. *Nucleic Acids Res.* **1990**, *18*, 5735–5741. [CrossRef] [PubMed]
4. Meyer, K.D.; Saletore, Y.; Zumbo, P.; Elemento, O.; Mason, C.E.; Jaffrey, S.R. Comprehensive Analysis of MRNA Methylation Reveals Enrichment in 3′ UTRs and near Stop Codons. *Cell* **2012**, *149*, 1635–1646. [CrossRef]
5. Fustin, J.-M.; Doi, M.; Yamaguchi, Y.; Hida, H.; Nishimura, S.; Yoshida, M.; Isagawa, T.; Morioka, M.S.; Kakeya, H.; Manabe, I.; et al. RNA-Methylation-Dependent RNA Processing Controls the Speed of the Circadian Clock. *Cell* **2013**, *155*, 793–806. [CrossRef]
6. Zhao, X.; Yang, Y.; Sun, B.-F.; Shi, Y.; Yang, X.; Xiao, W.; Hao, Y.-J.; Ping, X.-L.; Chen, Y.-S.; Wang, W.-J.; et al. FTO-Dependent Demethylation of N6-Methyladenosine Regulates MRNA Splicing and Is Required for Adipogenesis. *Cell Res.* **2014**, *24*, 1403–1419. [CrossRef]

7. Zhao, B.S.; Roundtree, I.A.; He, C. Post-Transcriptional Gene Regulation by MRNA Modifications. *Nat. Rev. Mol. Cell Biol.* **2017**, *18*, 31–42. [CrossRef]

8. Wang, Y.; Li, Y.; Yue, M.; Wang, J.; Kumar, S.; Wechsler-Reya, R.J.; Zhang, Z.; Ogawa, Y.; Kellis, M.; Duester, G.; et al. N6-Methyladenosine RNA Modification Regulates Embryonic Neural Stem Cell Self-Renewal through Histone Modifications. *Nat. Neurosci.* **2018**, *21*, 195–206. [CrossRef]

9. Sui, X.; Hu, Y.; Ren, C.; Cao, Q.; Zhou, S.; Cao, Y.; Li, M.; Shu, W.; Huo, R. METTL3-Mediated m^{6}A Is Required for Murine Oocyte Maturation and Maternal-to-Zygotic Transition. *Cell Cycle* **2020**, *19*, 391–404. [CrossRef]

10. Wu, J.; Frazier, K.; Zhang, J.; Gan, Z.; Wang, T.; Zhong, X. Emerging Role of m^{6}A RNA Methylation in Nutritional Physiology and Metabolism. *Obes. Rev.* **2020**, *21*, e12942. [CrossRef]

11. Dorn, L.E.; Lasman, L.; Chen, J.; Xu, X.; Hund, T.J.; Medvedovic, M.; Hanna, J.H.; van Berlo, J.H.; Accornero, F. The N^6-Methyladenosine MRNA Methylase METTL3 Controls Cardiac Homeostasis and Hypertrophy. *Circulation* **2019**, *139*, 533–545. [CrossRef] [PubMed]

12. Winkler, R.; Gillis, E.; Lasman, L.; Safra, M.; Geula, S.; Soyris, C.; Nachshon, A.; Tai-Schmiedel, J.; Friedman, N.; Le-Trilling, V.T.K.; et al. M6A Modification Controls the Innate Immune Response to Infection by Targeting Type I Interferons. *Nat. Immunol.* **2019**, *20*, 173–182. [CrossRef] [PubMed]

13. Gu, J.; Zhan, Y.; Zhuo, L.; Zhang, Q.; Li, G.; Li, Q.; Qi, S.; Zhu, J.; Lv, Q.; Shen, Y.; et al. Biological Functions of M6A Methyltransferases. *Cell Biosci.* **2021**, *11*, 15. [CrossRef] [PubMed]

14. Roignant, J.-Y.; Soller, M. M 6 A in MRNA: An Ancient Mechanism for Fine-Tuning Gene Expression. *Trends Genet.* **2017**, *33*, 380–390. [CrossRef] [PubMed]

15. Yang, Y.; Hsu, P.J.; Chen, Y.-S.; Yang, Y.-G. Dynamic Transcriptomic M6A Decoration: Writers, Erasers, Readers and Functions in RNA Metabolism. *Cell Res.* **2018**, *28*, 616–624. [CrossRef] [PubMed]

16. Bi, Z.; Liu, Y.; Zhao, Y.; Yao, Y.; Wu, R.; Liu, Q.; Wang, Y.; Wang, X. A Dynamic Reversible RNA N^6-methyladenosine Modification: Current Status and Perspectives. *J. Cell Physiol.* **2019**, *234*, 7948–7956. [CrossRef] [PubMed]

17. Liu, J.; Yue, Y.; Han, D.; Wang, X.; Fu, Y.; Zhang, L.; Jia, G.; Yu, M.; Lu, Z.; Deng, X.; et al. A METTL3–METTL14 Complex Mediates Mammalian Nuclear RNA N6-Adenosine Methylation. *Nat. Chem. Biol.* **2014**, *10*, 93–95. [CrossRef]

18. Ping, X.-L.; Sun, B.-F.; Wang, L.; Xiao, W.; Yang, X.; Wang, W.-J.; Adhikari, S.; Shi, Y.; Lv, Y.; Chen, Y.-S.; et al. Mammalian WTAP Is a Regulatory Subunit of the RNA N6-Methyladenosine Methyltransferase. *Cell Res.* **2014**, *24*, 177–189. [CrossRef]

19. Schwartz, S.; Mumbach, M.R.; Jovanovic, M.; Wang, T.; Maciag, K.; Bushkin, G.G.; Mertins, P.; Ter-Ovanesyan, D.; Habib, N.; Cacchiarelli, D.; et al. Perturbation of M6A Writers Reveals Two Distinct Classes of MRNA Methylation at Internal and 5′ Sites. *Cell Rep.* **2014**, *8*, 284–296. [CrossRef]

20. Wen, J.; Lv, R.; Ma, H.; Shen, H.; He, C.; Wang, J.; Jiao, F.; Liu, H.; Yang, P.; Tan, L.; et al. Zc3h13 Regulates Nuclear RNA M6A Methylation and Mouse Embryonic Stem Cell Self-Renewal. *Mol. Cell* **2018**, *69*, 1028–1038.e6. [CrossRef]

21. Wang, Y.; Li, Y.; Toth, J.I.; Petroski, M.D.; Zhang, Z.; Zhao, J.C. N6-Methyladenosine Modification Destabilizes Developmental Regulators in Embryonic Stem Cells. *Nat. Cell Biol.* **2014**, *16*, 191–198. [CrossRef] [PubMed]

22. Wang, X.; Feng, J.; Xue, Y.; Guan, Z.; Zhang, D.; Liu, Z.; Gong, Z.; Wang, Q.; Huang, J.; Tang, C.; et al. Structural Basis of N6-Adenosine Methylation by the METTL3–METTL14 Complex. *Nature* **2016**, *534*, 575–578. [CrossRef] [PubMed]

23. Wang, P.; Doxtader, K.A.; Nam, Y. Structural Basis for Cooperative Function of Mettl3 and Mettl14 Methyltransferases. *Mol. Cell* **2016**, *63*, 306–317. [CrossRef] [PubMed]

24. Śledź, P.; Jinek, M. Structural Insights into the Molecular Mechanism of the M^{6}A Writer Complex. *eLife* **2016**, *5*, e18434. [CrossRef]

25. Chen, X.-Y.; Zhang, J.; Zhu, J.-S. The Role of M^{6}A RNA Methylation in Human Cancer. *Mol. Cancer* **2019**, *18*, 103. [CrossRef]

26. Lan, Q.; Liu, P.Y.; Haase, J.; Bell, J.L.; Hüttelmaier, S.; Liu, T. The Critical Role of RNA M^{6}A Methylation in Cancer. *Cancer Res.* **2019**, *79*, 1285–1292. [CrossRef]

27. Zeng, C.; Huang, W.; Li, Y.; Weng, H. Roles of METTL3 in Cancer: Mechanisms and Therapeutic Targeting. *J. Hematol. Oncol.* **2020**, *13*, 117. [CrossRef]

28. De Kouchkovsky, I.; Abdul-Hay, M. Acute Myeloid Leukemia: A Comprehensive Review and 2016 Update. *Blood Cancer J.* **2016**, *6*, e441. [CrossRef]

29. Kwok, C.-T.; Marshall, A.D.; Rasko, J.E.J.; Wong, J.J.L. Genetic Alterations of M6A Regulators Predict Poorer Survival in Acute Myeloid Leukemia. *J. Hematol. Oncol.* **2017**, *10*, 39. [CrossRef]

30. Weng, H.; Huang, H.; Wu, H.; Qin, X.; Zhao, B.S.; Dong, L.; Shi, H.; Skibbe, J.; Shen, C.; Hu, C.; et al. METTL14 Inhibits Hematopoietic Stem/Progenitor Differentiation and Promotes Leukemogenesis via MRNA M6A Modification. *Cell Stem. Cell* **2018**, *22*, 191–205.e9. [CrossRef]

31. Siegel, R.L.; Miller, K.D.; Fuchs, H.E.; Jemal, A. Cancer Statistics, 2021. *CA A Cancer J. Clin.* **2021**, *71*, 7–33. [CrossRef] [PubMed]

32. Vu, L.P.; Pickering, B.F.; Cheng, Y.; Zaccara, S.; Nguyen, D.; Minuesa, G.; Chou, T.; Chow, A.; Saletore, Y.; MacKay, M.; et al. The N6-Methyladenosine (M^{6}A)-Forming Enzyme METTL3 Controls Myeloid Differentiation of Normal Hematopoietic and Leukemia Cells. *Nat. Med.* **2017**, *23*, 1369–1376. [CrossRef] [PubMed]

33. Barbieri, I.; Tzelepis, K.; Pandolfini, L.; Shi, J.; Millán-Zambrano, G.; Robson, S.C.; Aspris, D.; Migliori, V.; Bannister, A.J.; Han, N.; et al. Promoter-Bound METTL3 Maintains Myeloid Leukaemia by M6A-Dependent Translation Control. *Nature* **2017**, *552*, 126–131. [CrossRef] [PubMed]

34. Li, F.; Kennedy, S.; Hajian, T.; Gibson, E.; Seitova, A.; Xu, C.; Arrowsmith, C.H.; Vedadi, M. A Radioactivity-Based Assay for Screening Human M^{6}A-RNA Methyltransferase, METTL3-METTL14 Complex, and Demethylase ALKBH5. *J. Biomol. Screen* **2016**, *21*, 290–297. [CrossRef] [PubMed]

35. Buker, S.M.; Gurard-Levin, Z.A.; Wheeler, B.D.; Scholle, M.D.; Case, A.W.; Hirsch, J.L.; Ribich, S.; Copeland, R.A.; Boriack-Sjodin, P.A. A Mass Spectrometric Assay of METTL3/METTL14 Methyltransferase Activity. *SLAS Discov. Adv. Sci. Drug Discov.* **2020**, *25*, 361–371. [CrossRef] [PubMed]

36. Bedi, R.K.; Huang, D.; Eberle, S.A.; Wiedmer, L.; Śledź, P.; Caflisch, A. Small-Molecule Inhibitors of METTL3, the Major Human Epitranscriptomic Writer. *ChemMedChem* **2020**, *15*, 744–748. [CrossRef]

37. Moroz-Omori, E.V.; Huang, D.; Bedi, R.K.; Cheriyamkunnel, S.J.; Elena, B.; Aymeric, D.; Rzeczkowski, M.D.; Lars, W.; Paweł, Ś.; Amedeo, C. METTL3 Inhibitors for Epitranscriptomic Modulation of Cellular Processes. *ChemMedchem* **2020**, *16*, 3035–3043. [CrossRef]

38. Dolbois, A.; Bedi, R.K.; Bochenkova, E.; Müller, A.; Moroz-Omori, E.V.; Huang, D.; Caflisch, A. 1,4,9-Triazaspiro[5.5]Undecan-2-One Derivatives as Potent and Selective METTL3 Inhibitors. *J. Med. Chem.* **2021**, *64*, 12738–12760. [CrossRef]

39. Yankova, E.; Blackaby, W.; Albertella, M.; Rak, J.; De Braekeleer, E.; Tsagkogeorga, G.; Pilka, E.S.; Aspris, D.; Leggate, D.; Hendrick, A.G.; et al. Small Molecule Inhibition of METTL3 as a Strategy against Myeloid Leukaemia. *Nature* **2021**, *593*, 597–601. [CrossRef]

40. Ianniello, Z.; Paiardini, A.; Fatica, A. N6-Methyladenosine (M^{6}A): A Promising New Molecular Target in Acute Myeloid Leukemia. *Front. Oncol.* **2019**, *9*, 251. [CrossRef]

41. Malone, T.; Blumenthal, R.M.; Cheng, X. Structure-Guided Analysis Reveals Nine Sequence Motifs Conserved among DNA Amino-Methyl-Transferases, and Suggests a Catalytic Mechanism for These Enzymes. *J. Mol. Biol.* **1995**, *253*, 618–632. [CrossRef] [PubMed]

42. Sun, Q.; Huang, M.; Wei, Y. Diversity of the Reaction Mechanisms of SAM-Dependent Enzymes. *Acta Pharm. Sin. B* **2021**, *11*, 632–650. [CrossRef] [PubMed]

43. Lee, J.; Kim, S.; Jin, M.S.; Kim, Y. Discovery of Substituted Indole Derivatives as Allosteric Inhibitors of m^{6}A-RNA Methyltransferase, METTL3-14 Complex. *Drug Dev. Res.* **2022**. *online ahead of print*. [CrossRef] [PubMed]

44. Erickson-Miller, C.L.; DeLorme, E.; Tian, S.-S.; Hopson, C.B.; Stark, K.; Giampa, L.; Valoret, E.I.; Duffy, K.J.; Luengo, J.L.; Rosen, J.; et al. Discovery and Characterization of a Selective, Nonpeptidyl Thrombopoietin Receptor Agonist. *Exp. Hematol.* **2005**, *33*, 85–93. [CrossRef]

45. Townsley, D.M.; Scheinberg, P.; Winkler, T.; Desmond, R.; Dumitriu, B.; Rios, O.; Weinstein, B.; Valdez, J.; Lotter, J.; Feng, X.; et al. Eltrombopag Added to Standard Immunosuppression for Aplastic Anemia. *N. Engl. J. Med.* **2017**, *376*, 1540–1550. [CrossRef]

46. Wang, J.; Dai, M.; Fu, Q.; Chen, S. Eltrombopag for the Treatment of Refractory Thrombocytopenia Associated with Connective Tissue Disease. *Sci. Rep.* **2021**, *11*, 5459. [CrossRef]

47. Lu, S.; He, X.; Ni, D.; Zhang, J. Allosteric Modulator Discovery: From Serendipity to Structure-Based Design. *J. Med. Chem.* **2019**, *62*, 6405–6421. [CrossRef]

48. Huang, W.; Lu, S.; Huang, Z.; Liu, X.; Mou, L.; Luo, Y.; Zhao, Y.; Liu, Y.; Chen, Z.; Hou, T.; et al. Allosite: A Method for Predicting Allosteric Sites. *Bioinformatics* **2013**, *29*, 2357–2359. [CrossRef]

49. Jayagopal, B.; Murugesh, S. QBD-Driven HPLC Method of Eltrombopag Olamine: Degradation Pathway Proposal, Structure Elucidation, and in Silico Toxicity Prediction. *J. Pharm. Biomed. Anal.* **2021**, *203*, 114231. [CrossRef]

50. Roth, M.; Will, B.; Simkin, G.; Narayanagari, S.; Barreyro, L.; Bartholdy, B.; Tamari, R.; Mitsiades, C.S.; Verma, A.; Steidl, U. Eltrombopag Inhibits the Proliferation of Leukemia Cells via Reduction of Intracellular Iron and Induction of Differentiation. *Blood* **2012**, *120*, 386–394. [CrossRef]

51. Zheng, S.; Wang, W.; Aldahdooh, J.; Malyutina, A.; Shadbahr, T.; Tanoli, Z.; Pessia, A.; Tang, J. SynergyFinder Plus: Toward Better Interpretation and Annotation of Drug Combination Screening Datasets. *Genom. Proteom. Bioinform.* **2022**. *online ahead of print*. [CrossRef] [PubMed]

52. Argenziano, M.; Tortora, C.; Paola, A.D.; Pota, E.; Martino, M.D.; Pinto, D.D.; Leva, C.D.; Rossi, F. Eltrombopag and Its Iron Chelating Properties in Pediatric Acute Myeloid Leukemia. *Oncotarget* **2021**, *12*, 1377–1387. [CrossRef] [PubMed]

53. Dickinson, M.; Cherif, H.; Fenaux, P.; Mittelman, M.; Verma, A.; Portella, M.S.O.; Burgess, P.; Ramos, P.M.; Choi, J.; Platzbecker, U. Azacitidine with or without Eltrombopag for First-Line Treatment of Intermediate- or High-Risk MDS with Thrombocytopenia. *Blood* **2018**, *132*, 2629–2638. [CrossRef] [PubMed]

54. Basood, M.; Oster, H.S.; Mittelman, M. Thrombocytopenia in patients with myelodysplastic syndromes—Still an unsolved problem. *Mediterr. J. Hematol. Infect. Dis.* **2018**, *10*, e2018046. [CrossRef] [PubMed]

55. Akhtar, J.; Renaud, Y.; Albrecht, S.; Ghavi-Helm, Y.; Roignant, J.-Y.; Silies, M.; Junion, G. M6A RNA Methylation Regulates Promoter- Proximal Pausing of RNA Polymerase II. *Mol. Cell* **2021**, *81*, 3356–3367.e6. [CrossRef] [PubMed]

56. Kim, D.; Paggi, J.M.; Park, C.; Bennett, C.; Salzberg, S.L. Graph-Based Genome Alignment and Genotyping with HISAT2 and HISAT-Genotype. *Nat. Biotechnol.* **2019**, *37*, 907–915. [CrossRef]

57. Meng, J.; Cui, X.; Rao, M.K.; Chen, Y.; Huang, Y. Exome-Based Analysis for RNA Epigenome Sequencing Data. *Bioinformatics* **2013**, *29*, 1565–1567. [CrossRef]

58. Heinz, S.; Benner, C.; Spann, N.; Bertolino, E.; Lin, Y.C.; Laslo, P.; Cheng, J.X.; Murre, C.; Singh, H.; Glass, C.K. Simple Combinations of Lineage-Determining Transcription Factors Prime Cis-Regulatory Elements Required for Macrophage and B Cell Identities. *Mol. Cell* **2010**, *38*, 576–589. [CrossRef]

Article

Design, Synthesis, Molecular Docking, and Biological Evaluation of Pyrazole Hybrid Chalcone Conjugates as Potential Anticancer Agents and Tubulin Polymerization Inhibitors

Md. Jahangir Alam [1], Ozair Alam [1,*], Ahmad Perwez [2], Moshahid Alam Rizvi [2], Mohd Javed Naim [1], Vegi G. M. Naidu [3], Mohd Imran [4], Mohammed M. Ghoneim [5], Sultan Alshehri [6] and Faiyaz Shakeel [6]

[1] Medicinal Chemistry and Molecular Modeling Lab, Department of Pharmaceutical Chemistry, School of Pharmaceutical Education and Research, Jamia Hamdard, New Delhi 110062, India; zahangir.jh@gmail.com (M.J.A.); javednaim88@rediffmail.com (M.J.N.)
[2] Genome Biology Lab, Department of Biosciences, Jamia Millia Islamia, New Delhi 110020, India; ahmad86.delhi@gmail.com (A.P.); rizvi_ma@yahoo.com (M.A.R.)
[3] National Institute of Pharmaceutical Education and Research, Guwahati 781101, India; vgmnaidu@gmail.com
[4] Department of Pharmaceutical Chemistry, Faculty of Pharmacy, Northern Border University, Rafha 91911, Saudi Arabia; imran.pchem@gmail.com
[5] Department of Pharmacy Practice, College of Pharmacy, Al-Maarefa University, Ad Diriyah 13713, Saudi Arabia; mghoneim@mcst.edu.sa
[6] Department of Pharmaceutics, College of Pharmacy, King Saud University, Riyadh 11451, Saudi Arabia; salshehri1@ksu.edu.sa (S.A.); fsahmad@ksu.esu.sa (F.S.)
* Correspondence: oalam@jamiahamdard.ac.in

Abstract: Some (*E*)-3-(3-(4-(benzyloxy)phenyl)-1-phenyl-1*H*-pyrazol-4-yl)-1-phenylprop-2-en-1-one conjugates **5a–r** were designed; synthesized; characterized by ^{1}H, ^{13}C NMR, and ESI-MS; and evaluated for tubulin polymerization inhibitory activity and in vitro cytotoxicity against breast (MCF-7), cervical (SiHa), and prostate (PC-3) cancer cell lines, as well as a normal cell line (HEK-293T). The compounds were also tested to determine their binding modes at the colchicine-binding site of tubulin protein (PDB ID-3E22), for in silico ADME prediction, for bioactivity study, and for PASS prediction studies. Among all the synthesized conjugates, compound **5o** exhibited excellent cytotoxicity with an IC$_{50}$ value of 2.13 ± 0.80 μM (MCF-7), 4.34 ± 0.98 μM (SiHa), and 4.46 ± 0.53 μM (PC-3) against cancer cell lines. The compound did not exhibit significant toxicity to the HEK cells. Results of the in silico prediction revealed that the majority of the conjugates possessed drug-like properties.

Keywords: pyrazole conjugate; anticancer; MTT assay; molecular docking; cytotoxicity; tubulin polymerization inhibitors

1. Introduction

Cancer is significantly the most common health issue worldwide. It is considered the second most recurrent death-causing factor after cardiovascular disorders [1,2]. It accounts for nearly 10 million deaths in 2020, with most deaths due to lung cancer, followed by colon, liver, stomach, and breast cancer [3]. The World Health Organization (WHO) has projected that by 2030, more than 13 million annual deaths are expected to occur from cancer globally [4]. Currently available chemotherapeutic agents that target cell division and angiogenesis, or induce cancer cell death through different signaling pathways comprise the major treatment options for cancer. While these therapies are effective in treating early-stage cancers, the efficacy against advanced cancers, especially multidrug-resistant cancers, is limited. Furthermore, these classes of drug molecules face numerous restrictions such as greater systemic toxicity and complex synthesis [5].

The microtubules are a dynamic polymeric network of two closely related 55 kDa proteins in cells known as α and β-tubulin dimers [6]. It is responsible for the formation of the mitotic spindle during cell division and the severance of duplicated chromosomes. It also plays a crucial role as an important target for cancer therapy because of its essential role in cell proliferation and angiogenesis [7]. Since rapidly dividing cancer cells are highly dependent on tubulin polymerization/depolymerization, interfering with tubulin dynamics has become an important approach for the development of mitotic inhibitors [8,9]. The tubulin inhibitors have been classified based on their binding domains to tubulin *viz*. microtubule destabilizers (e.g., Combretastatin A-4) [10], colchicine site-binding agents (e.g., colchicine and podophyllotoxin) [11,12], and the vinca site-binding agent (e.g., vinblastine and vincristine) [13]. The microtubule disrupters inhibit tubulin polymerization and consequently interfere with the formation of the necessary mitotic assembly required for cell division. On the other hand, microtubule stabilizers, such as taxanes [14], paclitaxel, docetaxel, and laulimalide, prevent the depolymerization of microtubules [15]. Both agents, which can disrupt as well as stabilize microtubules, have found clinical success as anticancer agents, therefore the compounds that can affect tubulin or microtubule stability may show potential against various cancers. That is why, nowadays, scientists draw attention to the drug discovery of microtubule-targeting agents/inhibitors for anticancer therapy. The trimethoxy/dimethoxy phenyl rings of reported ligands are well-defined pharmacophores that bind to the interface of the α-tubulin and β-tubulin of the colchicine-binding site, which destabilizes the microtubules [16–19]. In the past few years, several chalcone derivatives were found as the most effective tubulin polymerization inhibitors as well as safer anticancer molecules [20]. The three binding sites are present in tubulin as the colchicine-binding site, vinca-binding site, and taxane-binding site. The tubulin polymerization inhibitors are docked into the colchicine-binding site of the tubulin protein. The colchicines always interact and bind with the α-tubulin and β-tubulin interface, which was also established by molecular docking [21] (Figure 1). The colchicine forms hydrogen, bonding with the Cys-241 of the β subunit of tubulin.
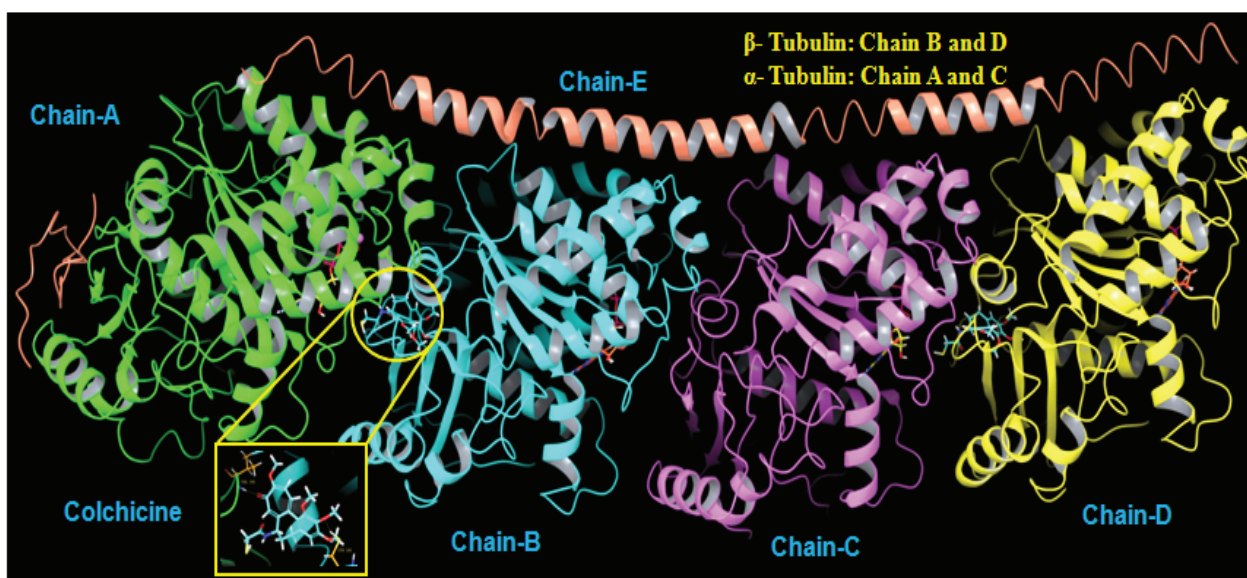
Figure 1. Colchicine-binding site (PDB: 1SA0).

Pyrazole is a significant class of heterocyclic compounds in pharmaceutical chemistry. Many pyrazole-based lead compounds have been evaluated for their biological effects, including anti-inflammatory, antimicrobial, antioxidant, anti-depressant, and anti-influenza activities [22,23]. Several recent reports suggested that pyrazole derivatives have shown promising anticancer activity, indicating their use in the development of new anticancer agents [24]. Among the anticancer pyrazole moieties, 1,3-diphenyl pyra-

zole derivatives have been shown as potent and effective cytotoxic agents [25]. Chalcone conjugates have shown wide pharmacological efficacy as well as synthetic applications in pharmaceutical chemistry [26,27]. Presently, colchicine (A), combretastatin A-4 (B) analogs, pyrazole linker chalcone congeners, and the marketed drug nocodazole (C) are the most important tubulin-binding agents that inhibit tubulin depolymerization [28]. In the recently reported literature, Peyrot et al. synthesized (*E*)-3-(4-(dimethylamino)phenyl)-1-(2,5-dimethoxyphenyl)-2-methylprop-2-en-1-one (D, MDL-27048) [29] as anti-mitotic agents with rapid and reversible binding to the colchicine-binding site for inhibiting its assembly to microtubules. Kamal et al. [30] designed and synthesized a novel scaffold (*Z*)-3-((3-phenyl-1*H*-pyrazol-5-yl)methylene)indolin-2-one (E), which has significant polymerization inhibitory activity. Moreover, various 1,3,4 thiadiazole ring-based cinnamide derivatives' tubulin (F) [31] also exhibited significant growth inhibition effects against MCF-7 and A549 cell lines apart from effectively inhibiting tubulin polymerization. Srinivasa and co-workers synthesized a new class of (*Z*)-1-(1,3-diphenyl-1*H*-pyrazol-4-yl)-3-(phenylamino)prop-2-en-1-one derivatives (G) as an effective anticancer agent with IC$_{50}$ values ranging from 1.25 to 3.98 μM [32]. In addition, Kamal and co-workers synthesized a series of pyrazole-linked arylcinnamides (H) as potential antiproliferative agents with significant tubulin polymerization inhibitory action (Figure 2) [33].
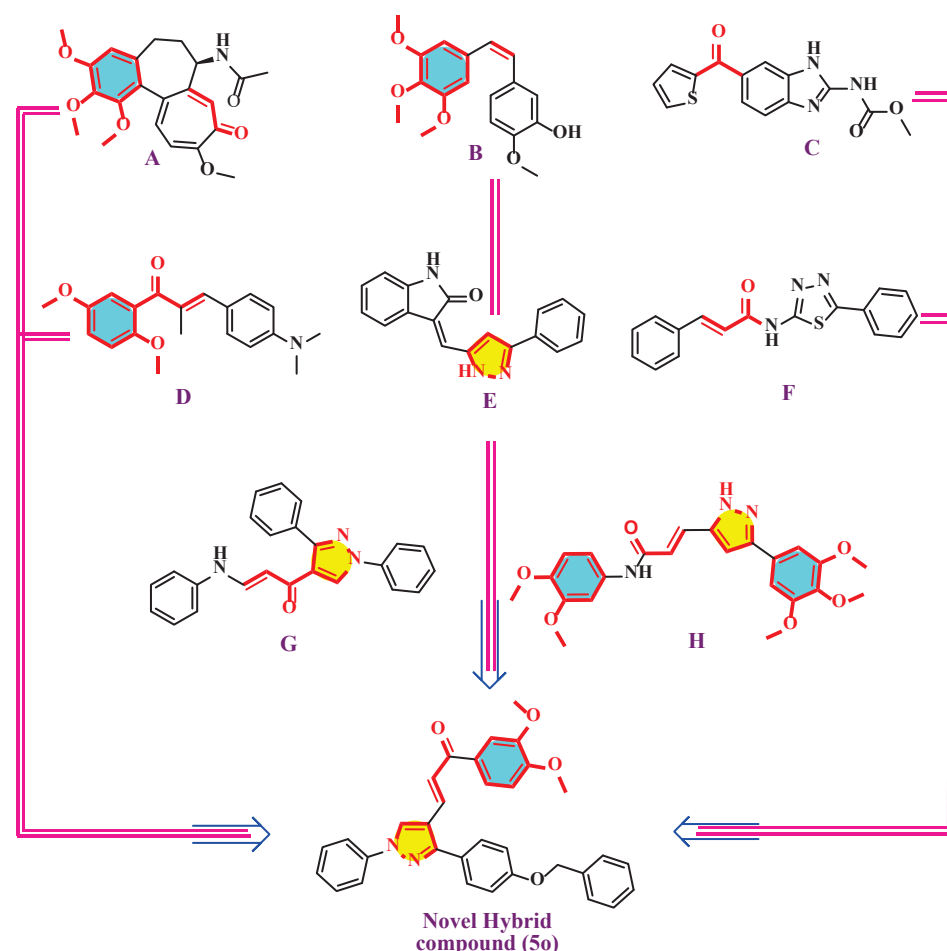
Figure 2. Structures of some potential cytotoxic agents and tubulin polymerization inhibitors: colchicine (**A**), combretastatin-A4 (**B**), nocodazole (**C**), MDL-27048 (**D**), reported pyrazole-linked conjugates (**E**), reported chalcone-linked conjugates (**F**), reported pyrazole-linked chalcone conjugates (**G,H**), and novel hybrid compound (**5o**).

Hybrid chalcone derivatives possess structural similarities to occurring moieties, such as Combretastatin A-4, obtained from the bark of *Combretum caffrum* [34]. It has

exhibited cytotoxicity against a broad range of human cancer cell lines by binding at the colchicine-binding site on β tubulin with a percentage of inhibition in the range of 28.42–66.40%. Furthermore, hybrid chalcones linked to other heterocyclic moieties have resulted in enhanced anticancer activity [35]. With this background, the present work was carried out to design and synthesize novel pyrazole-linked hybrid chalcone conjugates, and to evaluate their ability to inhibit tubulin polymerization and consequently prevent cancer growth.

2. Results and Discussion

2.1. Chemistry

The protocol for the synthesis of analog (**5a–r**) is described in Scheme 1. Compound **1** was prepared by reacting 4-hydroxyacetophenone and benzyl chloride. It was then reacted with phenylhydrazine (**2**) to give compound **3**, which was further cyclized in the presence of $POCl_3$ and DMF (Vilsmeier Haack reaction) to give 3-(4-(Benzyloxy) phenyl)-1-phenyl-1*H*-pyrazole-4-carbaldehyde (**4**). Equimolar quantities of compound **4** and various substituted acetophenones underwent Claisen–Schmidt condensation to yield the final pyrazole–chalcone conjugates. All compounds were characterized by FT-IR, ^{1}H NMR, ^{13}C NMR, and mass spectral data. The ^{1}H NMR, ^{13}C NMR, and mass spectra of lead compounds are presented in Figures S1–S14. The ^{1}H NMR spectra of the aldehydic proton in compound **4** appeared as a singlet at δ 9.82 ppm. The H-6 and H-7 of compound **5a** appeared as a doublet at δ 7.95 and δ 8.01 ppm, respectively, with the coupling constant (*J* = 15.6–15.7 Hz), which agrees with the trans-configuration of α,β-unsaturated ketone and the disappearance of the signal corresponding to the C-H of aldehyde. Moreover, in the ^{13}C NMR spectrum, the signal for C-1 was in the range of δ 127.8–139.6 ppm and the signal for C-7 appeared at δ 113.1–127.7 ppm, while the C=O carbon atom appeared at δ 186.3–196.1 ppm. The IR spectra showed absorption bands at 1755–1675, 1653–1590, and 1590–1512 cm^{-1}, corresponding to the C=O, C=N, and C=C functionalities, respectively. Mass spectra showed a molecular ion peak, i.e., (*m/z*) [M$^+$] with a characteristic fragmentation pattern involving the loss of the phenyl group in all cases.
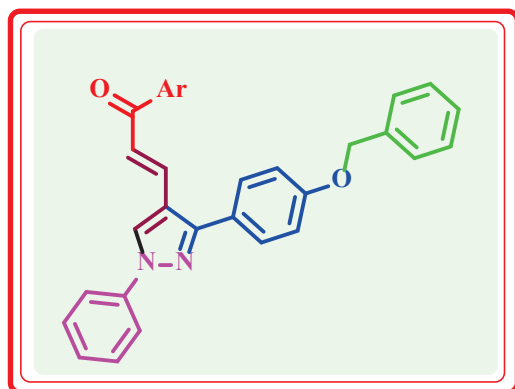
2.2. Molecular Docking Study

Molecular docking was performed to establish the binding ability of the newer synthesized compounds to the colchicine-binding site of tubulin (PDB code: 3E22). The docking scores of the compounds (**5a–r**) and co-crystal ligand colchicine are given in Table 1. The protein backbone of tubulin is depicted in purple and yellow colors for α and β chains, respectively. The favorable hydrogen bonding interactions are shown with yellow dashed lines and the amino acid residues that interact with the compounds are represented as purple and yellow tubes. The standard compounds were docked as co-crystal ligands at the colchicine-binding site of tubulin. Docking studies revealed that eighteen newer compounds (5a–r) exhibited a higher docking score than that of the co-crystal ligand, suggesting that the synthesized molecules have better interaction and better accommodation within the binding site. The different binding sites of tubulin protein complexes with **5o** viz. GTP, Mg^{+2}, and GDP are shown in Figure 3. The 3D docked images of compound **5o** and **5p** complexes with tubulin are represented in Figure 4. The most promising compound **5o** could fit well into the colchicine-binding site of the tubulin, making five hydrogen bond interactions with the most important active site residues ASN 249 (O....H$_2$N, 3.53 Å, β-), ALA 250 (O....H$_2$N, 3.70 Å) and LYS 254 (O....H$_3$N$^+$, 3.30 Å), SER 178 (O....HN, 3.65 Å), and TYR 224 (O....HO, 3.23 Å) pi-cation LYS 352 (pyrazole....H$_3$N$^+$, 6.17 Å, and phenyl....H$_3$N$^+$, 6.26 Å), as depicted in Figure 5a. The methoxy group of the 3,4-dimethoxy aryl moiety exhibited interaction with the side chain of SER 178 (O....H$_2$N, 1.93 Å) and TYR 224 (O....H$_2$N, 1.93 Å) in a similar manner as the co-crystal ligand colchicine. Introduction of a methoxy group at positions two and four of the aromatic ring of compounds leads to a slight decrease in the inhibitory activity primarily due to the changing of the orientation of the 2,4-dimethoxy group in the binding site, as observed for compound **5p**. The carbonyl group of **5p** also

showed hydrogen bond interaction with the side chain of ASN 249 (O....H$_2$N, 2.87 Å), ALA 250 (O....H$_2$N, 2.91 Å), and LYS 254 (O....H$_3$N$^+$, 3.10 Å).
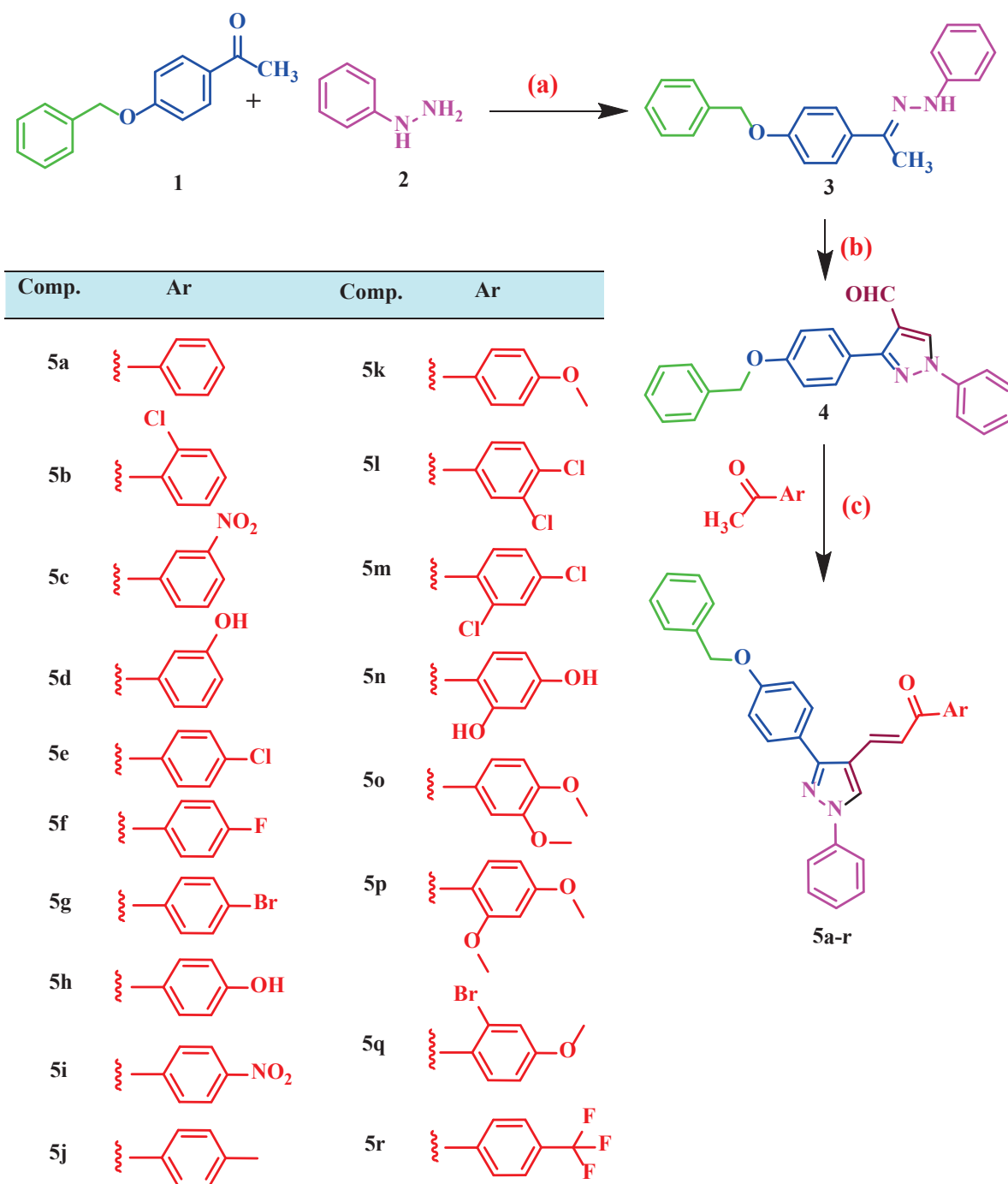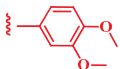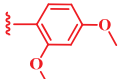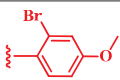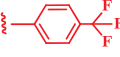
Scheme 1. General synthesis of (*E*)-3-(3-(4-(benzyloxy)phenyl)-1-phenyl-1*H*-pyrazol-4-yl)-1-phenylprop-2-en-1-one derivatives (**5a–r**). Reagents and conditions: (**a**) absolute ethanol and glacial acetic acid, 50–60 °C, refluxed for 6–8 h; (**b**) DMF and POCl$_3$, heated for 2 h on steam bath; and (**c**) absolute ethanol, 40% NaOH, reflux.

Table 1. Docking score and anti-tubulin activity of *E*-3-(3-(4-(benzyloxy) phenyl)-1-phenyl-1*H*-pyrazol-4-yl)-1-phenylprop-2-en-1-one analogs (**5a–r**).

Comp.	Ar	Docking Score	% Inhibition of Tubulin Polymerization at 10 μM [b]	Inhibition of Tubulin Polymerization IC$_{50}$ (μM) [a]
5a	phenyl	−5.994	Nd	Nd
5b	2-Cl-phenyl	−5.934	Nd	Nd
5c	3-NO$_2$-phenyl	−5.873	Nd	Nd
5d	3-OH-phenyl	−6.967	49.78	1.65 ± 0.06
5e	4-Cl-phenyl	−6.937	48.44	1.58 ± 0.04
5f	4-F-phenyl	−6.241	Nd	Nd
5g	4-Br-phenyl	−5.531	Nd	Nd
5h	4-OH-phenyl	−5.752	Nd	Nd
5i	4-NO$_2$-phenyl	−6.249	28.42	3.58 ± 0.83
5j	4-methyl-phenyl	−5.952	Nd	Nd
5k	4-methoxy-phenyl	−6.432	32.79	3.03 ± 0.44
5l	3,4-diCl-phenyl	−7.072	55.17	1.73 ± 0.04
5m	2,4-diCl-phenyl	−6.664	33.76	2.97 ± 0.03
5n	2,4-diOH-phenyl	−6.751	47.56	2.73 ± 0.07

Table 1. *Cont*.

Comp.	Ar	Docking Score	% Inhibition of Tubulin Polymerization at 10 μM [b]	Inhibition of Tubulin Polymerization IC$_{50}$ (μM) [a]
5o		−7.002	66.40	1.15 ± 0.06
5p		−7.277	51.11	1.93 ± 0.03
5q		−6.111	Nd	Nd
5r		−6.367	31.50	2.34 ± 0.63
Co-crystal–colchicine	—	−7.059	—	—
Control	—	—	0.0	0.0
Paclitaxel (3 μM)	—	—	−25.73	0.53 ± 0.12
Combretastatin A-4 (6 μM)	—	—	72.30	1.46 ± 0.05
Vincristine (3 μM)	—	—	75.45	1.54 ± 0.54

[a] Half-maximal inhibitory concentration: compound concentration required to inhibit tubulin polymerization by 50%; data are the mean ± SD of *n* = 3 independent experiments performed in triplicates. [b] Inhibition of tubulin polymerization at 10 μM (final volume = 10 mL); compounds were pre-incubated with tubulin at a final concentration of 10 μM.
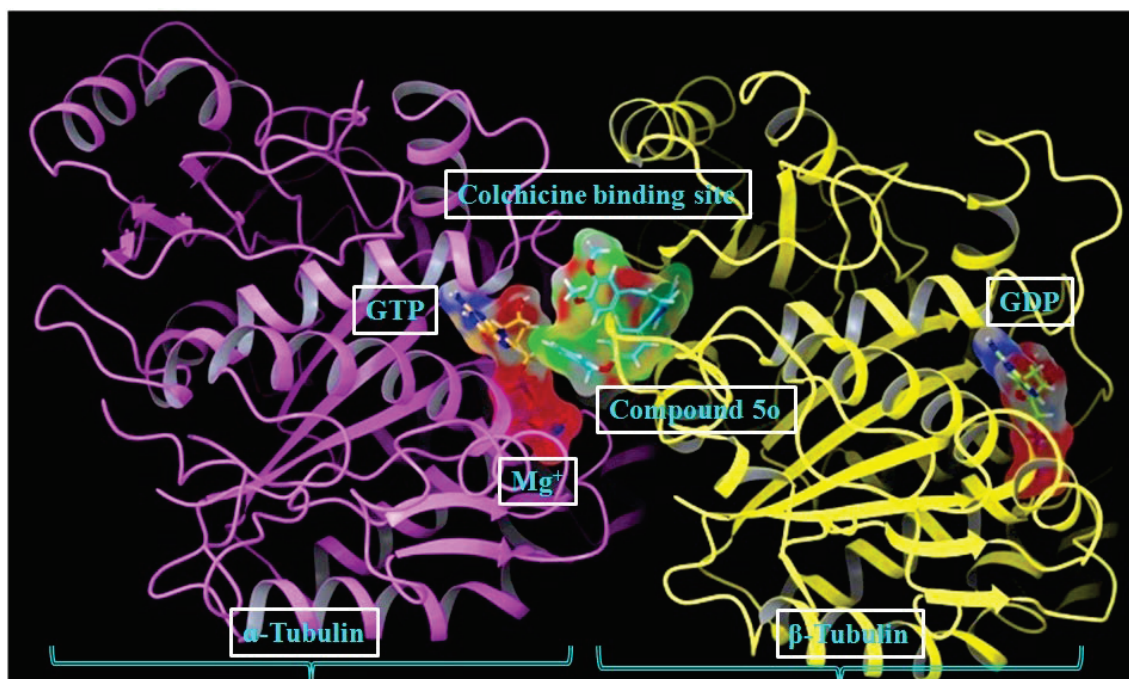
Figure 3. Different binding sites of tubulin protein complexes with **5o** (turquoise-color stick model), GTP, Mg^{+2}, and GDP. The α-chain is represented in purple color and the β-chain is represented in yellow color.
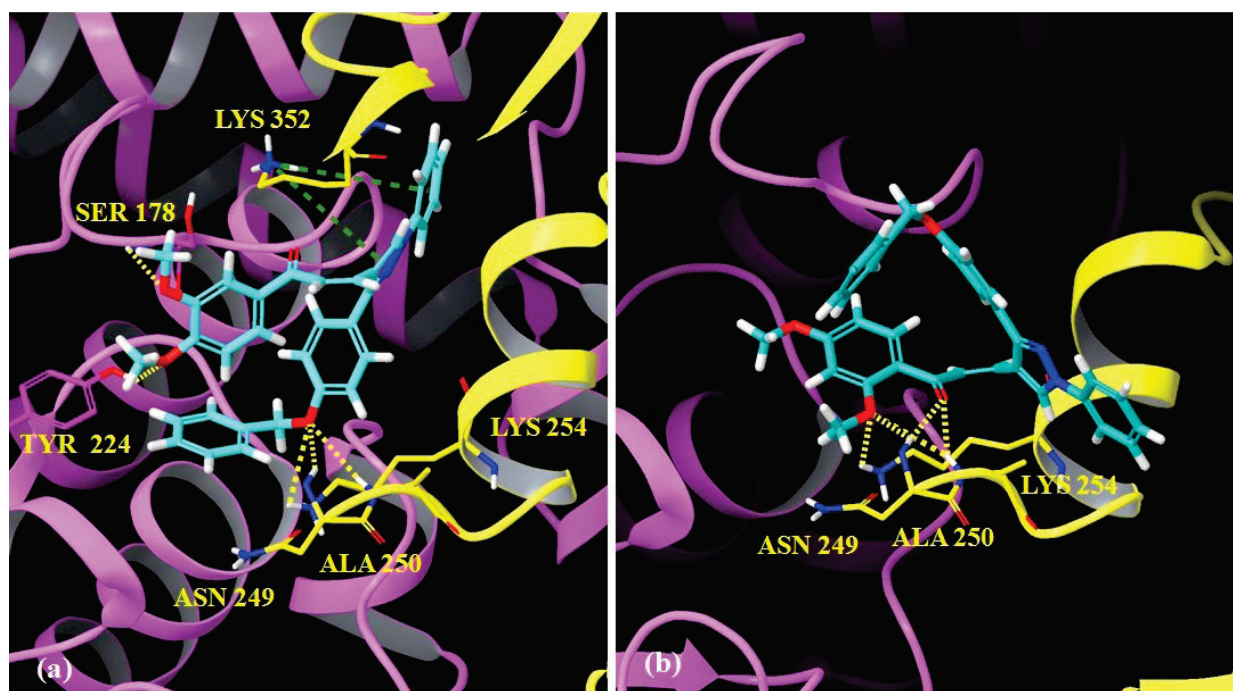
Figure 4. (**a**) Docked pose of compound **5o** (turquoise color) showing hydrogen bond interaction (yellow dashed lines) with ASN 249, ALA 250, LYS 254, SER 178, and TYR 224; pi-cation interaction with LYS 352 in the colchicine-binding site of tubulin. (**b**) Docked pose of compound **5p** (turquoise color) showing hydrogen bond interaction (yellow dashed lines) with ASN 249, ALA 250, and LYS 254 in the colchicine-binding site of tubulin. The α-chain is represented in a purple color cartoon and the β-chain is represented in a yellow color cartoon model.
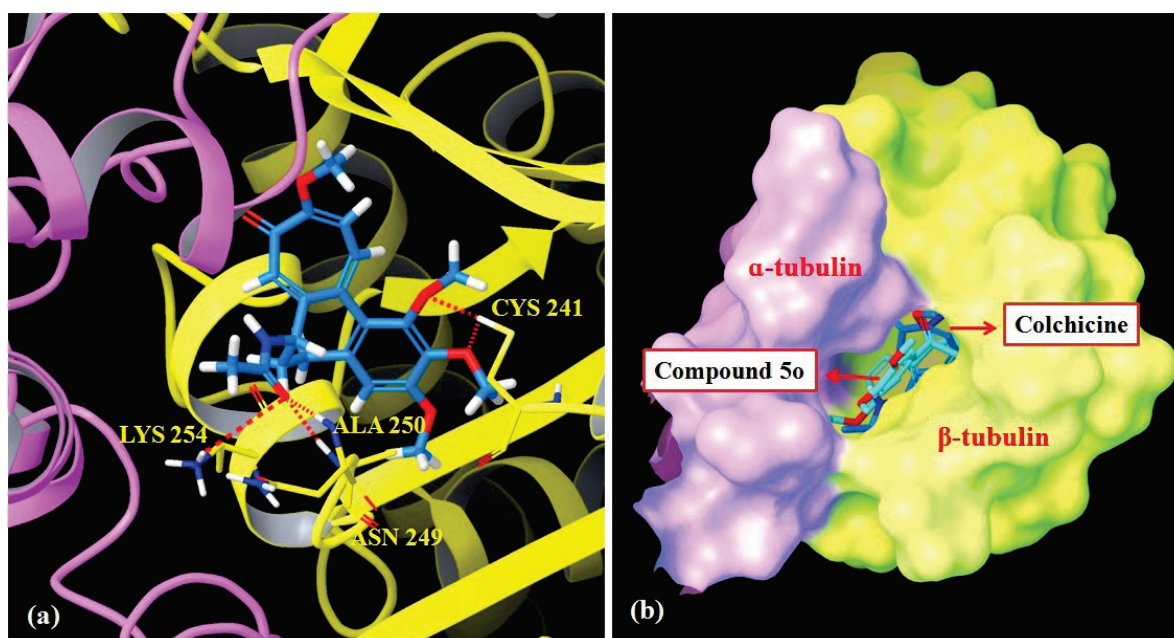
Figure 5. (**a**) Docked pose of colchicine (blue color) showing hydrogen bond interaction (red dashed lines) with ASN 249, ALA 250, LYS 254, and CYS 241 in the colchicine-binding site of tubulin. The α-chain is represented in a purple color cartoon and the β-chain is represented in a yellow color cartoon model. (**b**) Receptor surface of superimposing docked pose of compound **5o** (turquoise-color stick model) with colchicine (blue-color stick model) at colchicine-binding site of tubulin. The α-chain is represented in the purple color surface and the β-chain is represented in the yellow color surface.

The present study showed that the presence of methoxy groups at positions three and four of the aromatic ring of the ligand has a significant inhibitory effect on the tubulin polymerization at positions two and four. The positions of the methoxy (OCH_3) groups in these two (**5o** and **5p**) compounds showed slight differences in the in silico as well as in vitro studies. This could be due to the difference in the position of the substituents present in the aryl rings. These observations also provide a possible explanation as to why the 3,4-dimethoxy derivative **5o** is the only compound from the series which shows high affinity as well as a high docking score. The docked compound **5o** was superimposed with co-crystal ligand colchicine and its binding pattern was then compared (Figure 5a). The co-crystal ligand colchicine formed four hydrogen bond interactions with the most important active site residues ASN 249 (O....H_2N, 1.76 Å), ALA 250 (O....H_2N, 1.95 Å), LYS 254 (O....H_3N^+, 3.61 Å), and CYS 241 (O....HS, 2.40 Å and 2.61 Å). The receptor surface of the docked conformer **5o** complex with tubulin is presented in Figure 5b. The dG binding energy of the compounds was found in the range of −48.34 to −91.43 Kcal/mol for the receptor sites (Table 1). All compounds displayed a higher binding free energy (dG bond) for tubulin, which indicates that the compounds may have higher affinity and stability for the tubulin protein. To validate the molecular docking results, the synthesized compounds with higher dock scores were screened by the in vitro tubulin inhibitory assay. The outcome of molecular docking studies, along with the biological activity, revealed that compound **5o** was the most potent inhibitor.

2.3. Pharmacological Activities

2.3.1. In Vitro Cytotoxicity Activity

The resultant compounds were tested for their in vitro cytotoxic activity by MTT assay against breast (MCF-7), cervical (SiHa), and prostate (PC-3) cancer cell lines, and the human embryonic kidney cell line (HEK) [36]. The relative absorbance of the treated versus control (untreated) cells was used in determining the percentage viability and the IC_{50} value of Combretastatin A4 (CA4), which was used as the standard. IC_{50} values of various compounds in the MTT assay are presented in Table 2. Almost all synthesized conjugates were selectively cytotoxic against breast MCF-7 cancerous cells. Moreover, compounds **5d**, **5o**, and **5p** displayed pronounced growth inhibition on MCF-7 cells with IC_{50} values in the range of 2.13–4.10 μM, which were equivalent or better than the standard CA-4 (4.12–5.23 μM). The effective growth inhibitory activity was exhibited by compound **5o** (IC_{50} −2.13 ± 0.80 μM), followed by the compounds **5p** (IC_{50} 3.45 ± 1.28 μM) and **5d** (IC_{50} 4.10 ± 1.12 μM) against MCF-7 cancer cells. The other two cancer cell lines, SiHa and PC-3, also showed maximum sensitivity towards these two compounds with IC_{50} values of less than 6.52 μM. Moreover, compound **5n** showed higher potency against SiHa cells with an IC_{50} value of 3.60 ± 0.45 μM, while compound **5d** revealed selective potency against PC-3 cells with an IC_{50} value of 2.97 ± 0.88 μM. All compounds were further tested on non-cancerous HEK cells, where most compounds did not show any significant cytotoxicity (IC_{50} > 50 μM). The compounds **5r** and **5i** displayed moderate growth inhibition on HEK cells with IC_{50} values of 38.30 and 45.23 μM, respectively. These results expressed the selectivity of 1,3-diphenyl-1*H* pyrazole hybrids towards cancer cells compared to normal HEK cells. Therefore, the high cytotoxicity of the synthesized anticancer agents and their selectivity towards cancer cells were found to be characteristic factors. Subsequently, SAR studies were done by investigating the effect of substituents on cytotoxic activity. It has been shown that compounds with strong electron-donating groups on the aromatic ring (OH > OCH_3) exhibited potent cytotoxic activity. Furthermore, the compounds with electron-donating groups such as 3,4-dimethoxy substitution and 2,4-dimethoxy (**5o** and **5p**) exhibited higher potency than *para*-Methoxy substitutions (**5k**). Furthermore, compounds with electron-withdrawing groups such as para-chloro, para-nitro, 3,4-dichloro, and trifluoromethyl substitutions (**5e**, **5i**, **5l**, and **5r**) on the phenyl rings displayed good cytotoxic strength (Cl > NO_2 > CF_3) on cancerous cells (Figure 6). The majority of the compounds in this scheme exhibited moderate selectivity index values.

Moreover, the pharmacological efficacy of the synthesized entities **5d**, **5n**, **5o**, and **5p** has created a scope to explore their profound efficacy at the cellular level and particularly using the mechanism proposed for cytotoxic effects.

Table 2. In vitro cytotoxic effect (IC$_{50}$, μM) of the *E*-3-(3-(4-(benzyloxy) phenyl)-1-phenyl-1*H*-pyrazol-4-yl)-1-phenylprop-2-en-1-one against a panel of human cancer and normal cell lines.

Comp.	Cell Line (IC$_{50}$) [a]			
	MCF-7 [b]	SiHa [c]	PC3 [d]	HEK-293 [e]
5d	4.10 ± 1.12	4.85 ± 0.89	2.97 ± 0.88	>50
5e	11.50 ± 1.62	12.3 ± 1.32	9.68 ± 1.42	>50
5i	42.70 ± 0.34	34.53 ± 0.90	13.14 ± 1.6	45.23 ± 2.60
5k	7.23 ± 0.74	5.65 ± 0.71	5.45 ± 0.94	>50
5l	8.23 ± 1.45	11.70 ± 2.83	5.84 ± 1.65	>50
5m	17.14 ± 2.25	6.46 ± 1.52	11.22 ± 1.44	>50
5n	6.98 ± 1.12	3.60 ± 0.45	3.56 ± 0.63	>50
5o	2.13 ± 0.80	4.34 ± 0.98	4.46 ± 0.53	>50
5p	3.45 ± 1.28	4.98 ± 0.54	6.52 ± 1.23	>50
5r	14.82 ± 2.76	>50	>50	38.3 ± 1.72
CA-4	4.12 ± 0.38	5.23 ± 0.85	3.86 ± 0.39	19.25 ± 1.65

Cell lines were treated with different concentrations of compounds for 48 h as described under experimental protocol. Cell viability was measured by employing MTT assay. [a] IC$_{50}$ values are the concentrations causing 50% inhibition of cancer cell growth (μM). Data represent the mean values ± standard deviation of three independent experiments performed in triplicates. [b] Breast cancer, [c] cervical cancer, [d] prostate cancer cell line, and [e] human normal cell line CA-4: Combretastatin A-4.
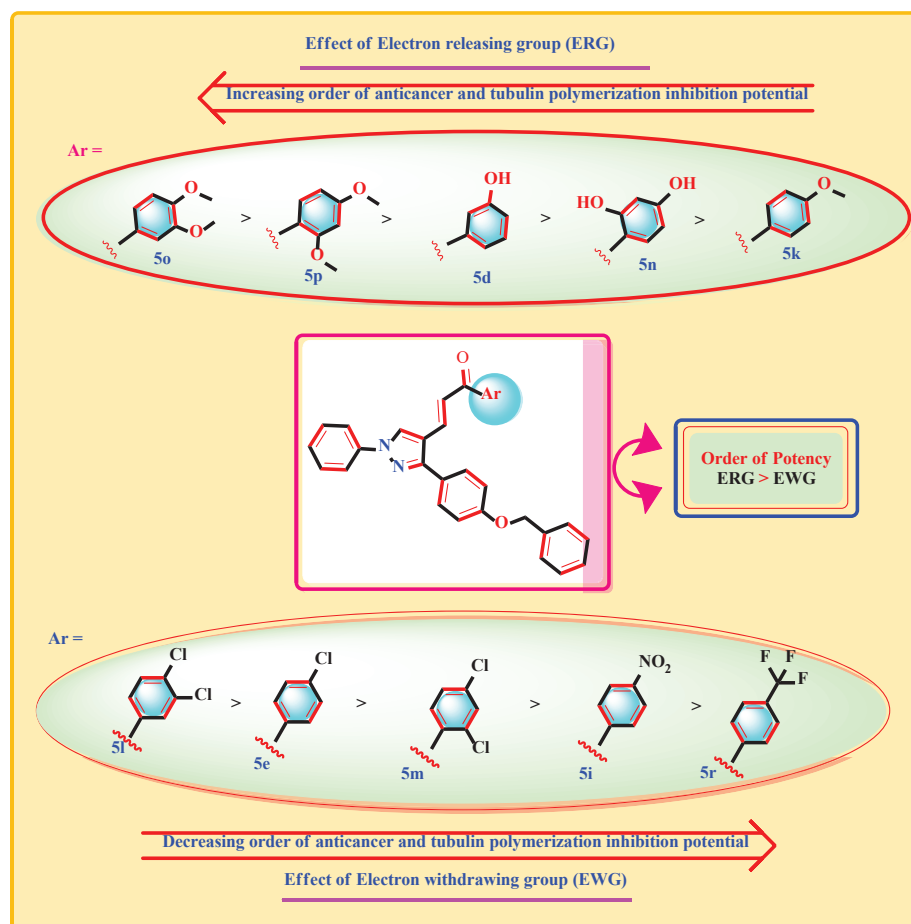

Figure 6. SAR of titled compounds.

2.3.2. Tubulin Polymerization Assay

The α and β tubulin subunits are recognized by heterodimers and self-assemble into a stable microtubule in a time-dependent manner. Assessment of the inhibitory effect of new pyrazolic chalcone conjugates on tubulin polymerization was also carried out. The progression of tubulin polymerization was thus examined by monitoring the increase in the fluorescence intensity at 450 nm (excitation wavelength of 360 nm) in a 384-plate for 1 h at 37 °C with and without the conjugate at 10 μM concentration. CA-4 (6 μM) and Vincristine (3 μM) were used as the positive control, whereas paclitaxel (3 μM) was used as the negative control. The effect of lead conjugates on tubulin polymerization is presented in Figure 5. The compounds **5d**, **5e**, **5i**, **5k**, **5l**, **5m**, **5n**, **5o**, **5p**, and **5r** exhibited 28.42–66.40% inhibition on tubulin polymerization (Figure 7). Among these compounds, **5o**, **5l**, and **5p** showed significant inhibition of tubulin polymerization with IC_{50} values of 1.15, 1.65, and 1.95 μM, respectively, as compared with 1.46 μM for Combretastatin A-4, as shown in Table 1. In general, these outcomes imply that the lead molecules **5o**, **5l**, and **5p** possess a potent inhibitory effect on microtubule assembly in vitro.
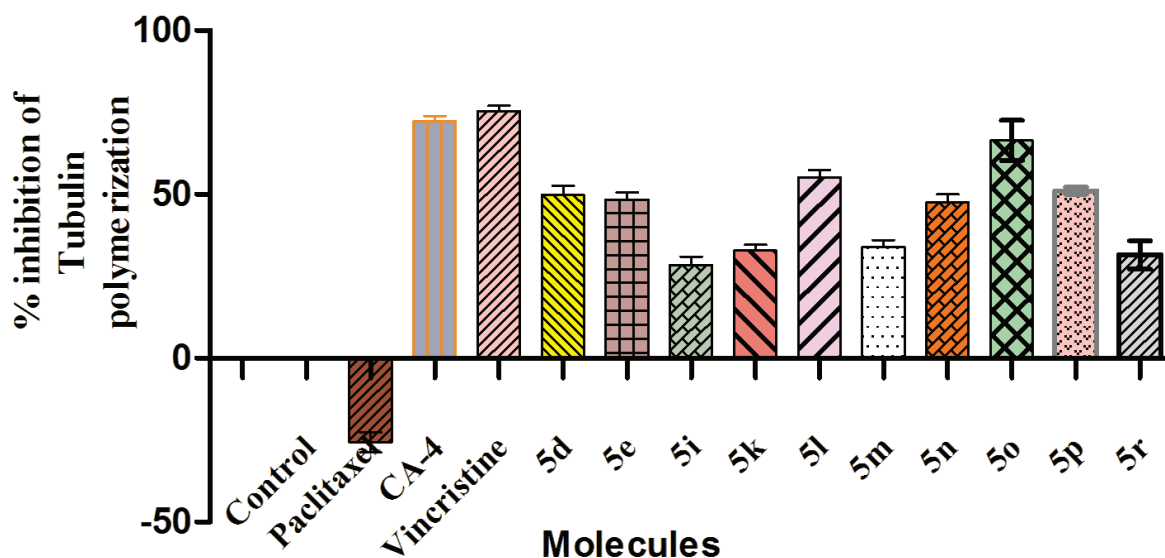

Figure 7. Effect of conjugates on in vitro tubulin polymerization. Values indicated are the mean ± SD of two different experiments performed in triplicates.

2.4. In Silico Computational Studies

Physicochemical properties of lead compounds are important for their development as anticancer agents with an inhibitory effect on tubulin polymerization agents. Improved lipophilicity with reduced water solubility is an essential factor. Different online software are available for the computation of these factors, such as the Molinspiration property calculation toolkit, Osiris Property explorer, PASS prediction, etc. The drug-like characters, such as water solubility (clogS), the number of rotatable bonds (NROTB), hydrophobicity (clogP), molecular weight (MW), and the drug-like score of Lipinski's rule of five [37–39], calculated for the lead compounds (**5a–r**) are represented in Table 3. Most of the synthesized compounds showed an acceptable range of solubility (clogS), which is less than (−4.6). The synthesized lead with a clogP-value < 5 is regarded as the compound with a better drug-likeness profile [40,41]. Most of the compounds were found to have a clogP-value of <5, which indicated their potential for oral administration. Parameters such as the TPSA (topological polar surface area) of new pyrazole derivatives (**5a–r**) were found to be within the acceptable range of 39.08–108.08 A°. The Molinspiration property calculation toolkit used for calculating the drug-likeness properties recommends that derivatives with negative or zero values should not be regarded as a drug-like candidates. However, all synthesized compounds, except **5c** and **5i**, were found to have scores > 0, as shown in

Table 3. The predicted toxicity risks of all the synthesized derivatives were envisaged by Osiris Property Explorer and are given in Table 3. The compounds, except for **5c**, **5i**, and **5j**, were found to be non-mutagenic and non-carcinogenic. PASS prediction was performed for the synthesized compounds to omit the compounds with a probability of activity (Pa) < 0.400 [42,43]. The remaining compounds were selected for evaluation based on the net probability of activity over inactivity (Pa-Pi), being more than 0.400 (Table 3).

Table 3. In silico physicochemical properties for oral bioavailability and bioactivity of the test compounds using computational predictive software.

Comp.	Cancer Treatment		cLogP	cLogS	*n* OHNH	*n* ON	MW	Rotatable Bonds	Drug Likeness	Drug Score	TPSA	Toxicity
	Pa	Pa-Pi										
5a	0.65	0.64	4.59	−4.60	0	4	456.18	8	0.97	0.34	61.80	NM, NC
5b	0.40	0.30	3.20	−2.23	1	4	491.88	8	1.23	0.24	63.08	NM. NC
5c	0.25	0.08	4.20	−3.42	1	4	501.17	8	−2.34	0.26	39.08	SR
5d	0.43	0.34	4.34	−3.36	0	4	472.18	8	3.45	0.35	65.08	NM, NC
5e	0.40	0.29	4.80	−2.07	1	4	491.88	8	4.62	0.05	68.08	NM, NC
5f	0.37	0.25	3.40	−4.34	0	4	477.70	8	2.82	0.36	63.60	NM, NC
5g	0.47	0.46	3.60	−3.45	0	4	535.09	8	1.24	0.32	70.08	NM, NC
5h	0.43	0.42	4.56	−2.67	1	4	472.18	8	2.87	0.23	62.07	NM, NC
5i	0.35	0.23	4.90	−3.60	1	4	501.17	8	−2.24	0.25	80.08	SM
5j	0.49	0.493	4.90	−3.78	1	4	471.20	8	1.37	0.11	102.30	SM
5k	0.44	0.36	2.34	−3.56	0	10	487.19	10	−1.92	0.34	87.00	NM, NC
5l	0.43	0.42	2.23	−4.02	1	7	524.11	9	3.45	0.25	62.90	NM, NC
5m	0.23	0.22	4.25	−3.35	2	5	524.11	8	2.64	0.15	59.31	NM, NC
5n	0.49	0.41	3.60	−2.54	1	5	488.17	9	−1.56	0.56	63.31	NM, NC
5o	0.47	0.40	3.45	−2.63	1	6	516.20	10	1.67	0.34	63.56	NM, NC
5p	0.48	0.41	2.50	−2.67	1	4	516.20	8	2.12	0.27	63.34	NM, NC
5q	0.29	0.13	5.20	−3.24	3	7	525.17	9	3.44	0.48	80.20	NM, NC
5r	0.31	0.16	4.50	−3.48	3	7	554.17	9	2.65	0.65	75.23	NM, NC

Pa: probability of being active; Pi: the probability of being inactive; cLogP: lipophilicity; cLogS: water solubility; *n* OHNH: number of hydrogen bond donors; *n* ON: number of hydrogen bond acceptors; MW: molecular weight; TPSA; topological polar surface area; NM: non-mutagenic; NC: non-carcinogenic; SM: slightly mutagenic; and SR: slightly reproducible.

3. Materials and Methods

3.1. General Chemistry

The chemicals and reagents employed were of LR grade and procured from Sigma Aldrich (Mumbai, India), E. Merck (Mumbai, India), S.D. Fine Chemicals Ltd. (Mumbai, India), and Qualigens (New Delhi, India). Thin-layer chromatography (TLC) was carried out to observe the advancement of the reactions using benzene and acetone (80:20, *v/v*), as well as toluene/ethyl acetate/formic acid (50:40:10, *v/v/v*) as a solvent system, and spots were traced using iodine vapor or UV-light (254 nm). Melting points of the synthesized molecules were calculated using an electrical melting point apparatus (open capillary method) and are uncorrected. The infrared spectra were noted in the region from the 4000 to 400 cm^{-1} range on the Shimadzu FT-IR spectrometer, while ^{1}H and ^{13}C-NMR spectra were recorded on the Bruker Advance-500 MHz and 125 MHz spectrometer using DMSO-d_6 or CDCl$_3$ as an NMR solvent. Synapt-mass spectrometric detection was performed on UPLC-MS (Q-TOF-ESI; Waters Corp., Milford, MA, USA) using the ESI technique. Elemental analysis was executed on the CHNOS-Elemental analyzer (Vario EL III) and found to be ±0.4%, i.e., within the theoretical values.

3.1.1. Synthesis of Substituted (*E*)-1-(1-(4-(Benzyloxy)phenyl)ethylidene)-2-phenylhydrazine (**3**)

A solution of **1** (10 mmol) and **2** (15 mmol) in absolute ethanol (30 mL) was refluxed for 6–8 h in the presence of glacial acetic acid (0.3 mL). The reaction advancement was determined by the TLC method using a mixture of ethyl acetate: hexane (8:2). The product obtained was then washed, dried in shade, and recrystallized from ethanol [44]; white solid, yield: 78%; m.p.: 123–125 °C.

3.1.2. Synthesis of Substituted (*E*)-3-(4-(Benzyloxy)phenyl)-1-phenyl-1*H*-pyrazole-4-carbaldehyde (**4**)

Compound **3** in dry dimethylformamide at a temperature of 0–5 °C in a 100 mL RBF was reacted with POCl$_3$ (drop-wise addition) for a time interval of 15–20 min and then heated in a steam bath for a period of 2 h; allowed to cool down to room temperature; poured in crushed ice; and then basified with a saturated solution of NaHCO$_3$. The product obtained was then filtered, washed 2–3 times with water, dried, and recrystallized from ethanol to get yellow crystals (needle-like) [45].

White solid, yield: 72%; m.p.: 127–129 °C, IR (KBr, cm^{-1}): 3093 (CH aromatic), 1710 (C=O), 1633 (C=N), and 1626 (C=C), 1255 (C-O). ^{1}H NMR (CDCl$_3$, 500 MHz) δ (ppm): 5.13 (s, 2H,-CH$_2$-benzyloxy), 6.57 (d, 2H, Ar-H, *J* = 8.0 Hz), 7.05 (d, 2H, Ar-H, *J* = 8.4 Hz), 7.21 (d, 1H, Ar-H, *J* = 8.2 Hz), 7.30–7.59 (m, 4H, Ar-H), 7.67 (d, 2H, Ar-H, *J* = 8.8 Hz), 7.75–7.99 (m, 3H, Ar-H), 8.45 (s, 1H, pyrazole-CH), and 9.82 (s, 1H, CHO). Analysis calculated for C$_{23}$H$_{18}$N$_2$O$_2$: C, 77.93; H, 5.11; and N, 7.90. Found: C, 77.81; H, 5.16; and N, 7.81.

3.1.3. Synthesis of (*E*)-3-(3-(4-(Benzyloxy)phenyl)-1-phenyl-1*H*-pyrazol-4-yl)-1-phenylprop-2-en-1-one derivatives (**5a–r**)

A mixture of 3-(4-(benzyloxy)phenyl)-1-phenyl-1*H*-pyrazole-4-carbaldehyde (**4**; 10 mmol) and different substituted acetophenones (10 mmol) were dissolved in 20 mL ethanol. To this mixture, sodium hydroxide (40%, 2 mL) was added at 0–5 °C and then stirred at room temperature for 24 h. Then, this reaction mixture was poured over crushed ice and acidified with dilute HCl (10%) until pH = 5. The light-yellow solid thus obtained was filtered, washed with water, dried, and recrystallized from ethanol to obtain the final product, i.e., (*E*)-3-(3-(4-(benzyloxy)phenyl)-1-phenyl-1*H*-pyrazol-4-yl)-1-phenylprop-2-en-1-one (**5a–r**) [46].

(*E*)-3-(3-(4-(benzyloxy)phenyl)-1-phenyl-1*H*-pyrazol-4-yl)-1-phenylprop-2-en-1-one (**5a**):

White solid, yield: 74%; m.p.: 190–194 °C; IR (KBr, cm^{-1}): 3045 (CH aromatic), 2930 (CH aliphatic), 1710 (C=O), 1643 (C=C), 1627 (C=N), and 1245 (C-O); ^{1}H NMR (CDCl$_3$, 500 MHz); δ (ppm): 5.15 (s, 2H, CH$_2$-benzyloxy), 7.12 (d, 2H, Ar-H, *J* = 8.4 Hz), 7.05 (d, 2H Ar-H, *J* = 8.4 Hz), 7.36 (t, 1H, Ar-H, *J* = 7.5 Hz), 7.54–7.62 (m, 5H, Ar-H), 7.64 (d, 2H, Ar-H, *J* = 8.8 Hz), 7.67 (d, 2H, Ar-H, *J* = 8.8 Hz), 7.74–7.85 (m, 3H, Ar-H), 7.89 (d, 2H, *J* = 7.7 Hz), 7.95 (d, 1H, chalcone H-7, *J* = 15.6 Hz), 8.01 (d, 1H, chalcone-H-6, *J* = 15.7 Hz), and 8.42 (s, 1H, pyrazole-H); ^{13}C NMR (CDCl$_3$, 125 MHz): δ (ppm) 71.1 (benzyloxy CH$_2$), 113.1, 114.8, 119.4, 125.2, 126.7, 127.1, 127.7 (chalcone-C-7), 127.8, 128.4, 128.6, 129.1, 129.8, 130.2 (pyrazole-C-5), 134.5, 136.8, 137.9, 139.6 (pyrazole phenyl-C-1), 145.1 (chalcone-C-6), 150.7 (pyrazole-C-3), 159.1, and 189.8 (C=O); ESI-MS (*m/z*): 456.18 (M$^+$). Analysis calculated for C$_{31}$H$_{24}$N$_2$O$_2$: C, 81.54; H, 5.29; N, 6.13; and O, 7.01. Found: C, 81.61; H, 5.22; and N, 6.17.

(*E*)-3-(3-(4-(benzyloxy)phenyl)-1-phenyl-1*H*-pyrazol-4-yl)-1-(2-chlorophenyl)prop-2-en-1-one (**5b**):

Off white solid, yield: 70%; m.p.: 182–184 °C; IR (KBr, cm^{-1}): 3050 (CH aromatic), 2935 (CH aliphatic), 1715 (C=O), 1640 (C=N), 1597 (C=C), and 1255 (C-O), 745 (C-Cl); ^{1}H NMR (CDCl$_3$, 500 MHz); δ (ppm): 5.19 (s, 2H, CH$_2$-benzyloxy), 6.97 (t, 2H, Ar-H, *J* = 8.7 Hz), 7.08 (d, 2H, Ar-H, *J* = 8.2 Hz), 7.31 (d, 2H, Ar-H, *J* = 9.6 Hz), 7.35 (t, 1H, Ar-H, *J* = 8.2 Hz), 7.57 (d, 2H, Ar-H, *J* = 8.3 Hz), 7.50–7.68 (m, 3H, Ar-H), 7.74 (d, 2H, Ar-H, *J* = 8.4 Hz), 7.96 (d, 2H, Ar-H, *J* = 7.6 Hz), 7.98 (d, 2H, Ar-H, *J* = 8.7 Hz), 7.93 (d, 1H, chalcone-H-7, *J* = 15.6 Hz), 8.06 (d, 1H, chalcone-H-6, *J* = 15.7 Hz), and 8.52 (s, 1H, pyrazole-H); and ^{13}C NMR (CDCl$_3$, 125 MHz): δ (ppm): 71.4 (benzyloxy-CH$_2$), 113.8, 114.7, 119.5, 125.6, 126.4, 127.2, 127.8 (chalcone-C-7), 127.9, 128.4, 128.8, 129.5, 130.4 (pyrazole-C-5), 130.6, 131.8 (C-Cl), 136.2, 137.9, 139.4 (pyrazole-phenyl-C-1), 144.7 (Chalcone-C-6), 150.5 (pyrazole-C-3), 159.4, and 189.4 (C=O). ESI-MS (*m/z*): 491.88 (M$^+$+1) and 492.75 (M$^+$+2). Analysis calculated for C$_{31}$H$_{23}$ClN$_2$O$_2$: C, 75.82; H, 4.71; and N, 5.70. Found: C, 75.91; H, 4.62; and N, 5.75.

(*E*)-3-(3-(4-(benzyloxy)phenyl)-1-phenyl-1*H*-pyrazol-4-yl)-1-(3-nitrophenyl)prop-2-en-1-one (**5c**):

Orange red solid, yield: 78%; m.p.: 203–205 °C; IR (KBr, cm^{-1}): 3046 (CH aromatic), 2940 (CH aliphatic), 1690 (C=O), 1625 (C=N), 1612 (C=C), 1510 and 1350 (NO$_2$), and 1245

(C-O); ^{1}H NMR (CDCl$_3$, 500 MHz); δ (ppm): 5.11 (s, 2H, CH$_2$-benzyloxy), 7.35 (d, 2H, Ar-H, *J* = 7.8 Hz), 7.44 (d, 2H, Ar-H, *J* = 7.8 Hz), 7.58 (t, 1H, Ar-H, *J* = 8.0 Hz), 7.63 (d, 2H, Ar-H, *J* = 8.8 Hz), 7.66–7.78 (m, 5H, Ar-H), 7.80 (d, 1H, chalcone-H-7, *J* = 15.5 Hz), 7.88 (d, 2H, Ar-H, *J* = 7.6 Hz), 8.00 (d, 1H, chalcone-H-6, *J* = 15.7 Hz), 8.02 (t, 1H, Ar-H, *J* = 8.8 Hz), 8.42 (s, 1H, Ar-H), 8.56 (d, 2H, Ar-H, *J* = 9.4 Hz), and 8.48 (s, 1H, pyrazole-H); ^{13}C NMR (CDCl$_3$, 125 MHz): δ (ppm) 71.2 (benzyloxy-CH$_2$), 113.3, 114.5, 119.2, 123.7, 125.6, 126.6, 127.1, 127.6 (chalcone-C-7), 128.3, 128.8, 129.2, 129.4, 130.2 (pyrazole-C-5), 130.6, 134.9, 136.8, 138.5, 139.6 (pyrazole-phenyl-C-1), 143.3 (chalcone-C-6), 148.6 (Ar-C-NO$_2$), 150.6 (pyrazole-C-3), 159.1, and 189.9 (C=O); ESI-MS (*m/z*): 501.17 (M$^+$). Analysis calculated for C$_{31}$H$_{23}$N$_3$O$_4$: C, 74.21; H, 4.61; and N, 8.31. Found: C, 74.26; H, 4.55; and N, 8.42.

(*E*)-3-(3-(4-(benzyloxy)phenyl)-1-phenyl-1*H*-pyrazol-4-yl)-1-(3-hydroxyphenyl)prop-2-en-1-one (**5d**):

White buff solid, yield: 64%; m.p.: 184–186 °C; IR (KBr, cm^{-1}): 3445 (OH), 3055 (CH aromatic), 2958 (CH aliphatic), 1705 (C=O), 1620 (C=N), 1597 (C=C), and 1245 (C-O); ^{1}H NMR (CDCl$_3$, 500 MHz); δ (ppm): 5.22 (s, 2H, CH$_2$-benzyloxy), 5.42 (s, 1H, OH), 6.72 (d, 2H, Ar-H, *J* = 7.6 Hz), 6.94 (d, 2H, Ar-H, *J* = 7.8 Hz), 7.14 (s, 1H, Ar-H), 7.24 (t, 2H, Ar-H, *J* = 6.8 Hz), 7.31 (d, 2H, Ar-H, *J* = 6.4 Hz), 7.42–7.53 (m, 3H, Ar-H), 7.74 (d, 1H, chalcone-H-7, *J* = 15.8 Hz), 7.58–7.76 (m, 4H, Ar-pyrazole), 7.94 (d, 1H, chalcone-H-6, *J* = 16.0 Hz), 7.98 (d, 2H, Ar-H, *J* = 7.8 Hz), and 8.03 (s, 1H. pyrazole-H); ^{13}C NMR (CDCl$_3$, 125 MHz): δ (ppm) 70.8 (benzyloxy-CH$_2$), 113.6, 114.7, 117.3, 119.4, 121.6, 123.2, 125.3, 126.3, 127.1, 127.4 (chalcone-C-7), 127.9, 128.3, 129.4, 130.5 (pyrazole-C-5), 131.4, 136.9, 137.3, 139.3 (pyrazole-phenyl-C-1), 146.4 (chalcone-C-6), 150.2 (pyrazole-C-3), 159.1, 164.8 (C-OH), and 196.1 (C=O); ESI-MS (*m/z*): 472.18 (M$^+$). Analysis calculated for C$_{31}$H$_{24}$N$_2$O$_3$: C, 78.80; H, 5.13; and N, 5.94. Found: C, 78.85; H, 5.17; and N, 5.89

(*E*)-3-(3-(4-(benzyloxy)phenyl)-1-phenyl-1*H*-pyrazol-4-yl)-1-(4-chlorophenyl)prop-2-en-1-one (**5e**):

White buff solid, yield: 76%; m.p.: 212–214 °C; IR (KBr, cm^{-1}): 3080 (CH aromatic), 2960 (CH aliphatic), 1720 (C=O), 1657 (C=C), 1610 (C=N), 1235 (C-O), and 790 (C-Cl); ^{1}H NMR (CDCl$_3$, 500 MHz); δ (ppm): 5.17 (s, 2H, CH$_2$-benzyloxy), 7.15 (d, 2H, Ar-H, *J* = 8.7 Hz), 7.28 (d, 2H, Ar-H, *J* = 7.8 Hz), 7.31–7.43 (m, 3H, Ar-H), 7.46–7.55 (m, 4H, Ar-H), 7.59 (d, 2H, Ar-H, *J* = 8.4 Hz), 7.64 (d, 2H, Ar-H, *J* = 8.4 Hz), 7.83 (t, 3H, Ar-H, *J* = 7.8 Hz), 7.95 (d, 1H, chalcone-H-7, *J* = 15.6 Hz), 8.05 (d, 1H, chalcone-H-6), and 8.38 (s, 1H, pyrazole-H); ^{13}C NMR (CDCl$_3$, 125 MHz): δ (ppm) 69.7 (benzyloxy-CH$_2$), 112.8, 115.9, 118.9, 119.2, 124.7, 126.1, 126.5, 128.5, 128.8 (chalcone-C-7), 128.9, 129.2, 129.9, 130.3 (pyrazole-C-5), 137.4, 139.9 (pyrazole-phenyl-C-1), 146.8 (chalcone-C-6), 150.7 (pyrazole-C-3), 158.6, and 189.7 (C=O); ESI-MS (*m/z*): 491.88 (M$^+$+1) and 492.75 (M$^+$+2). Analysis calculated for C$_{31}$H$_{23}$ ClN$_2$O$_2$: C, 75.82; H, 4.73, and N, 5.70. Found: C, 75.88; H, 4.69; and N, 5.75.

(*E*)-3-(3-(4-(benzyloxy)phenyl)-1-phenyl-1*H*-pyrazol-4-yl)-1-(4-fluorophenyl)prop-2-en-1-one (**5f**):

Off white solid, yield: 66%; m.p.: 168–170 °C; IR (KBr, cm^{-1}): 3105 (CH aromatic), 2950 (CH aliphatic), 1708 (C=O), 1605 (C=N), 1593 (C=C), 1210 (C-O), and 755 (C-F); ^{1}H NMR (CDCl$_3$, 500 MHz); δ (ppm): 5.18 (s, 2H, CH$_2$-benzyloxy), 7.16 (d, 2H, Ar-H, *J* = 8.7 Hz), 7.33 (t, 1H, Ar-H, *J* = 8.2 Hz), 7.43 (d, 2H Ar-H, *J* = 8.8 Hz), 7.54 (d, 2H, Ar-H, *J* = 8.2 Hz), 7.52–7.72 (m, 5H, Ar-H), 7.74 (d, 2H, Ar-H, *J* = 8.4 Hz), 7.76 (d, 1H, chalcone-H-7, *J* = 15.3 Hz), 7.96 (d, 2H, Ar-H, *J* = 7.6 Hz), 7.98 (d, 2H, Ar-H, *J* = 8.7 Hz), 8.06 (d, 1H, chalcone-H-6, *J* = 15.7 Hz), and 8.54 (s, 1H, pyrazole-H); ^{13}C NMR (CDCl$_3$, 125 MHz): δ (ppm) 70.7 (benzyloxy-CH$_2$), 113.2, 114.5, 116.0, 119.6, 125.3, 126.4, 127.2, 127.4 (chalcone-C-7), 127.8, 128.6, 129.4, 130.4 (pyrazole-C-5), 131.8, 133.6, 136.1, 136.6, 139.7 (pyrazole-phenyl-C-1), 145.3 (chalcone-C-6), 150.8 (C-3-pyrazole), 159.6, 164.8 (C-F), and 189.5 (C=O); ESI-MS (*m/z*): 477.70 (M$^+$+1). Analysis calculated for C$_{31}$H$_{23}$ FN$_2$O$_2$: C, 78.48; H, 4.90; and N, 5.92. Found: C, 78.55; H, 4.95; and N, 5.86.

(*E*)-3-(3-(4-(benzyloxy)phenyl)-1-phenyl-1*H*-pyrazol-4-yl)-1-(4-bromophenyl)prop-2-en-1-one (**5g**):

Off white solid, yield: 62%; m.p.: 178–180 °C; IR (KBr, cm^{-1}): 3095 (CH aromatic), 2965 (CH aliphatic), 1708 (C=O), 1610 (C=N), 1585 (C=C), 1210 (C-O), and 665 (C-Br); ^{1}H NMR (CDCl$_3$, 500 MHz); δ (ppm): 5.14 (s, 2H, CH$_2$-benzyloxy), 7.10–7.97 (m, 20H, aromatic H), 7.90 (d, 1H, CH=CH, Cis, *J* = 15.5 Hz), 7.83 (d, 1H, CH=CH, *J* = 9 Hz), and 8.33 (s, 1H, CH of pyrazole); ^{13}C NMR (CDCl$_3$, 125 MHz): δ (ppm) 70.1 (benzyloxy-CH$_2$), 115.24, 118.01, 119.36, 120.56, 124.96, 125.86, 127.28, 127.52, 127.76, 128.10, 128.68 (chalcone-C-7), 129.61 (pyrazole-C-5), 129.92, 130.10 (pyrazole-phenyl-C-1), 131.90, 136.19 (chalcone-C-6), 136.79 (pyrazole-C-3), 139.40, 153.78 (C-Br), 159.36, and 188.92 (C=O); ESI-MS (*m/z*): 537.09 (M$^+$+1). Analysis calculated for C$_{31}$H$_{23}$BrN$_2$O$_2$: C, 69.55; H, 4.31; and N, 5.24. Found: C, 69.62; H, 4.36; and N, 5.20.

(*E*)-3-(3-(4-(benzyloxy)phenyl)-1-phenyl-1*H*-pyrazol-4-yl)-1-(4-hydroxyphenyl)prop-2-en-1-one (**5h**):

White buff solid, yield: 65%; m.p.: 167–169 °C; IR (KBr, cm^{-1}): 3415 (OH), 3065 (CH aromatic), 2934 (CH aliphatic), 1695 (C=O), 1618 (C=N), 1605 (C=C), and 1248 (C-O); ^{1}H NMR (CDCl$_3$, 500 MHz); δ (ppm): 5.20 (s, 2H, CH$_2$-benzyloxy), 5.68 (s, 1H, OH), 6.56 (d, 2H, Ar-H, *J* = 7.2 Hz), 6.80 (d, 2H, Ar-H, *J* = 7.6 Hz), 7.27 (t, 2H, Ar-H, *J* = 7.3 Hz), 7.31 (d, 2H, Ar-H, *J* = 6.4 Hz), 7.38–7.48 (m, 3H, Ar-H), 7.66 (d, 1H, chalcone-H-7, *J* = 15.5 Hz), 7.69–780 (m, 4H, Ar-pyrazole), 7.82 (d, 1H, chalcone-H-6, *J* = 15.5 Hz), 7.92 (d, 2H, Ar-H, *J* = 7.4 Hz), and 8.01 (s, 1H. pyrzole-H); ^{13}C NMR (CDCl$_3$, 125 MHz): δ (ppm) 71.8 (benzyloxy-CH$_2$), 113.2, 114.5, 119.8, 125.8, 126.4, 127.2, 127.5 (chalcone-C-7), 127.9, 128.4, 128.8, 129.7, 130.5 (pyrazole-C-5), 130.8, 131.5, 136.8, 139.9 (pyrazole-phenyl-C-1), 146.4 (chalcone-C-6), 150.7 (pyrazole-C-3), 159.6, 164.5 (C-OH), and 189.8 (C=O); ESI-MS (*m/z*): 472.18 (M$^+$). Analysis calculated for C$_{31}$H$_{24}$N$_2$O$_3$: C, 78.79; H, 5.12; and N, 5.93. Found: C, 78.84; H, 5.16; and N, 5.88.

(*E*)-3-(3-(4-(benzyloxy)phenyl)-1-phenyl-1*H*-pyrazol-4-yl)-1-(4-nitrophenyl)prop-2-en-1-one (**5i**):

Orange red solid, yield: 82%; m.p.: 223–225 °C IR (KBr, cm^{-1}): 3035 (CH aromatic), 2956 (CH aliphatic), 1675 (C=O), 1630 (C=N), 1576 (C=C), 1505 and 1363 (NO$_2$), and 1238 (C-O); ^{1}H NMR (CDCl$_3$, 500 MHz); δ (ppm): 5.12 (s, 2H, CH$_2$-benzyloxy), 7.13 (d, 2H, Ar-H, *J* = 7.8 Hz), 7.42 (d, 2H, Ar-H, *J* = 8.6 Hz), 7.54 (t, 1H, Ar-H, *J* = 7.4 Hz), 7.62 (d, 2H, Ar-H, *J* = 8.8 Hz), 7.66–7.76 (m, 5H, Ar-H), 7.82 (d, 1H, chalcone-H-7, *J* = 15.6 Hz), 7.86 (d, 2H, Ar-H, *J* = 7.6 Hz), 8.08 (d, 1H, chalcone-H-6, *J* = 15.8 Hz), 8.16 (d, 2H, Ar-H, *J* = 8.6 Hz), 8.30 (d, 2H, Ar-H, *J* = 8.8 Hz), and 8.38 (s, 1H, pyrazole-H); ^{13}C NMR (CDCl$_3$, 125 MHz): δ (ppm) 69.5 (benzyloxy-CH$_2$), 113.3 (pyrazole-C-4), 115.2, 119.6, 122.4, 125.6, 126.6, 127.5, 127.4 (chalcone-C-7), 127.8, 128.1, 128.6, 129.2, 130.8 (pyrazole-C-5), 130.6, 136.5, 139.6 (pyrazole-phenyl-C-1), 142.5 (chalcone-C-6), 150.5 (pyrazole-C-3), 153.6 (C-NO$_2$), and 159.2, 189.3 (C=O); ESI-MS (*m/z*): 501.17 (M$^+$). Analysis calculated for C$_{31}$H$_{23}$N$_3$O$_4$: C, 74.27; H, 4.64; and N, 8.41. Found: C, 74.32; H, 4.58; and N, 8.46.

(*E*)-3-(3-(4-(benzyloxy)phenyl)-1-phenyl-1*H*-pyrazol-4-yl)-1-(p-tolyl)prop-2-en-1-one (**5j**):

Off white solid, yield: 78%; m.p.: 205–207 °C; IR (KBr cm^{-1}): 3028 (CH aromatic), 2960 (C-H str in CH$_3$), 2968 (CH aliphatic), 1724 (C=O), 1645 (C=N), 1618 (C=C), and 1205 (C-O); ^{1}H NMR (CDCl$_3$, 500 MHz); δ (ppm): 3.75 (s, 3H, CH$_3$), 5.16 (s, 2H, CH$_2$-benzyloxy), 7.14 (d, 2H, Ar-H, *J* = 7.1 Hz), 7.29 (d, 2H, Ar-H, *J* = 5.1 Hz), 7.54 (t, 3H, Ar-H, *J* = 8.1 Hz), 7.62 (d, 2H, Ar-H, *J* = 8.4 Hz), 7.64–7.72 (m, 3H, Ar-H), 7.74 (d, 1H, chalcone-H-7, *J* = 15.4 Hz), 7.76–7.81 (m, 4H, Ar-H), 7.86 (d, 1H, chalcone-H-6, *J* = 15.1 Hz), 7.95 (d, 2H, Ar-H, *J* = 7.5 Hz), and 8.52 (s, 1H. pyrazole-H); ^{13}C NMR (CDCl$_3$, 125 MHz): δ (ppm) 20.5 (Ar-CH$_3$), 70.8 (benzyloxy-CH$_2$), 11.9 (pyrazole-C-4), 115.3, 118.3, 119.2, 124.9, 126.1, 126.4, 128.2 (chalcone-C-7), 128.3, 128.9, 129.1, 129.7, 130.0 (pyrazole-C-5), 139.4 (pyrazol-phenyl-C-1), 146.8 (chalcone-C-6), 150.7 (pyrazole-C-3), 158.6, and 189.7 (C=O); ESI-MS (*m/z*): 471.20 (M$^+$+1). Analysis calculated for C$_{32}$H$_{26}$N$_2$O$_2$: C, 81.67; H, 5.59; and N, 5.96. Found: C, 81.73; H, 5.53; and N, 6.02.

(*E*)-3-(3-(4-(benzyloxy)phenyl)-1-phenyl-1*H*-pyrazol-4-yl)-1-(4-methoxyphenyl)prop-2-en-1-one (**5k**):

Greenish solid, yield: 68%; m.p.: 187–189 °C; IR (KBr, cm^{-1}): 3090 (CH aromatic), 2970 (CH aliphatic), 1745 (C=O), 1655 (C=N), 1633 (C=C), and 1267 (OCH$_3$), 1220 (C-O); ^{1}H NMR (CDCl$_3$, 500 MHz); δ (ppm): 3.86 (s, 3H, OCH$_3$), 5.14 (s, 2H, CH$_2$-benzyloxy), 7.10–7.97 (m, 20H, aromatic H), 7.90 (d, 1H, CH=CH Cis, *J* = 8.5 Hz), 7.83 (d, 1H, CH=CH, *J* = 8 Hz), and 8.53 (s, 1H, CH of pyrazole); ^{13}C NMR (CDCl$_3$, 125 MHz): δ (ppm) 70.1 (Ar-OCH$_3$), 70.5 (benzyloxy-CH$_2$), 115.15 (pyrazole-C-4), 119.34, 119.74, 122.36 (chalcone-C-7), 124.10, 127.53, 127.93, 128.13, 128.68 (pyrazole-C-5), 129.70, 130.70, 131.20 (phenyl-pyrazole-C-1), 136.70 (chalcone-C-6), 139.06 (pyrazole-C-3), 154.51, 159.75, and 185.24 (C=O); ESI-MS (*m/z*): 487.22 (M$^+$+1). Analysis calculated for C$_{32}$H$_{26}$N$_2$O$_3$: C, 78.97; H, 5.40; and N, 5.78. Found: C, 78.94; H, 5.34; and N, 5.84.

(*E*)-3-(3-(4-(benzyloxy)phenyl)-1-phenyl-1*H*-pyrazol-4-yl)-1-(3,4-dichlorophenyl)prop-2-en-1-one (**5l**):

Off white solid, yield: 76%; m.p.: 243–245 °C; IR (KBr, cm^{-1}): 3030 (CH aromatic), 2980 (CH aliphatic), 1745 (C=O), 1653 (C=N), 1637 (C=C), 1225 (C-O), and 785 (C-Cl); ^{1}H NMR (CDCl$_3$, 500 MHz); δ (ppm): 5.17 (s, 2H, CH$_2$-benzyloxy), 7.16 (d, 2H, Ar-H, *J* = 8.4 Hz), 7.25 (s, 1H Ar-H), 7.36 (d, 2H, Ar-H, *J* = 7.6 Hz), 7.48–7.51 (d, 2x 2H, Ar-H, *J* = 8.4 Hz), 7.55 (s, 1H, Ar-H), 7.56 (s, 1H, Ar-H), 7.58 (s, 1H, Ar-H), 7.67 (d, 2H, Ar-H, *J* = 8.4 Hz), 7.79–7.83 (m, 3H, Ar-H), 7.95 (d, 1H, chalcone-H, *J* = 15.6 Hz), 8.05 (d, 1H, chalcone-H, *J* = 16.2 Hz), and 8.37 (s, 1H, pyrazole-H); ^{13}C NMR (CDCl$_3$, 125 MHz): δ (ppm) 70.2 (benzyloxy-CH$_2$), 113.4, 114.4, 119.6, 125.5, 126.2, 127.2, 127.4 (chalcone-C-7), 127.7, 128.3, 128.6, 128.8, 129.5, 130.2 (pyrazole-C-5), 130.6, 131.4, 133.6, 136.6, 137.3, 139.3 (C-Cl), 139.8 (phenyl-C-1), 145.2 (chalcone-C-6), 150.3 (pyrazole-C-3), 159.1, and 189.5 (C=O); ESI-MS (*m/z*): 524.11 (M$^+$+1), 525.08 (M$^+$+2), and 526.06 (M$^+$+4). Analysis calculated for C$_{31}$H$_{22}$ Cl$_2$N$_2$O$_2$: C, 70.85; H, 4.23; and N, 5.31. Found: C, 70.92; H, 4.18; and N, 5.41.

(*E*)-3-(3-(4-(benzyloxy)phenyl)-1-phenyl-1*H*-pyrazol-4-yl)-1-(2,4dichlorophenyl)prop-2-en-1-one (**5m**):

Off white solid, yield: 67%; m.p.: 192–194 °C; IR (KBr, cm^{-1}): 3065 (CH aromatic), 2985 (CH aliphatic), 1753 (C=O), 1620 (C=N), 1598 (C=C), 1275 (C-O), and 785 (C-Cl); ^{1}H NMR (CDCl$_3$, 500 MHz); δ (ppm): 5.12 (s, 2H, CH$_2$-benzyloxy), 7.14 (d, 2H, Ar-H, *J* = 8.4 Hz), 7.53 (d, 2H, Ar-H, *J* = 8.4 Hz), 7.46–7.52 (d, 2x 2H, Ar-H, *J* = 8.4 Hz), 7.57 (s, 1H, Ar-H), 7.55 (s, 1H, Ar-H), 7.59 (d, 2H, Ar-H, *J* = 7.8 Hz), 7.72 (d, 2H, Ar-H, *J* = 8.4 Hz), 7.75–7.80 (m, 3H, Ar-H), 7.62 (d, 1H, chalcone-H, *J* = 15.5 Hz), 7.69 (d, 1H, chalcone-H, 15.3 Hz), and 8.47 (s, 1H, pyrazole-H); ^{13}C NMR (CDCl$_3$, 125 MHz): δ (ppm) 70.6 (benzyloxy-CH$_2$), 113.3, 114.6, 119.7, 125.4, 126.5, 127.2, 127.3 (chalcone-C-7), 127.6, 128.7, 129.2, 129.3, 129.7, 130.3 (pyrazole-C-5), 131.7 (C-Cl), 133.3, 135.4, 136.9, 139.7 (phenyl-C-1), 145.3 (chalcone-C-6), 146.3, 150.2 (pyrazole-C-7), 159.2, and 189.1 (C=O); ESI-MS (*m/z*): 524.11 (M$^+$+1), 525.08 (M$^+$+2), and 526.06 (M$^+$+4). Analysis calculated for C$_{31}$H$_{22}$ Cl$_2$N$_2$O$_2$: C, 70.85; H, 4.21; and N, 5.32. Found: C, 70.92; H, 4.18; and N, 5.41.

(*E*)-3-(3-(4-(benzyloxy)phenyl)-1-phenyl-1*H*-pyrazol-4-yl)-1-(2,4-dihydroxyphenyl)prop-2-en-1-one (**5n**):

White buff solid, yield: 72%; m.p.: 176–178 °C; IR (KBr, cm^{-1}): 3435 (OH), 3086 (CH aromatic), 2950 (CH aliphatic), 1782 (C=O), 1620 (C=N), 1603 (C=C), and 1250 (C-O); ^{1}H NMR (CDCl$_3$, 500 MHz); δ (ppm): 5.18 (s, 2H, CH$_2$-benzyloxy), 5.60 (s, 2H, 2x OH), 6.42 (s, 1H, Ar-H), 7.10 (t, 3H, Ar-H, *J* = 6.8 Hz), 7.38 (d, 2H, Ar-H, *J* = 6.4 Hz), 7.46–7.64 (m, 3H, Ar-H), 7.72 (d, 1H, chalcone-H-7, *J* = 15.2 Hz), 7.62–7.76 (m, 4H, Ar-pyrazole), 7.80 (d, 1H, chalcone-H-6, *J* = 15.8 Hz), 7.86 (d, 2H, Ar-H, *J* = 8.8 Hz), 7.90 (d, 2H, Ar-H, *J* = 7.6 Hz), and 8.05 (s, 1H. pyrazole-H); ^{13}C NMR (CDCl$_3$, 125 MHz): δ (ppm) 71.2 (benzyloxy-CH$_2$), 104.6, 113.2, 113.5, 114.3, 114.7, 119.6, 125.4, 126.4, 127.8, 127.4 (chalcone-C-7), 127.5, 128.5, 128.6, 129.4, 130.4 (pyrazole-C-5), 133.5, 136.4, 139.8 (pyrazole-phenyl-C-1), 145.2 (chalcone-C-6), 150.6 (pyrazole-C-3), 159.2, 165.4 (C'-4-OH), 166.8 (C'-2-OH), and 192.2 (C=O); ESI-MS (*m/z*): 488.17 (M$^+$). Analysis calculated for C$_{31}$H$_{24}$N$_2$O$_4$: C, 76.21; H, 4.95; and N, 5.73. Found: C, 76.28; H, 4.88; and N, 5.76.

(*E*)-3-(3-(4-(benzyloxy)phenyl)-1-phenyl-1*H*-pyrazol-4-yl)-1-(3,4-dimethoxyphenyl)prop-2-en-1-one (**5o**):

Green solid, yield: 79%; m.p.: 206–208 °C; IR (KBr, cm^{-1}): 3085 (CH aromatic), 2955 (CH aliphatic), 1730 (C=O), 1610 (C=N), 1596 (C=C), 1225 (OCH$_3$), and 1265 (C-O); ^{1}H NMR (CDCl$_3$, 500 MHz); δ (ppm): 3.96 (s, 6H, OCH$_3$), 5.12 (s, 2H, CH$_2$-benzyloxy), 6.91–7.97 (m, 19H, aromatic H), 7.90 (d, 1H, CH=CH, Cis, *J* = 13 Hz), 7.7 (d, 1H, CH=CH, *J* = 9 Hz), and 8.32 (s, 1H, CH of pyrazole); ^{13}C NMR (CDCl$_3$, 125 MHz): δ (ppm) 56.1 (C'-4-OCH$_3$), 70.1 (benzyloxy-CH$_2$), 109.9 (Pyrazole-C-4), 110.7, 115.2, 118.27, 119.33, 120.93, 122.79, 125.21, 126.83, 127.15, 127.52, 128.09, 128.68, 129.59 (Chalcone-C-7), 130.13, 131.36, 134.75 (pyrazole-C-5), 136.80, 139.50 (pyrazole-phenyl-C-1), 149.18 (chalcone-C-6), 151.15 (pyrazole-C-3), 153.51, 159.28 (C-4'-OCH$_3$), and 188.25 (C=O); ESI-MS (*m/z*): 517.19 (M$^+$). Analysis calculated for C$_{33}$H$_{28}$N$_2$O$_4$: C, 76.73; H, 5.46; and N, 5.42. Found: C, 76.78; H, 5.40; and N, 5.48.

(*E*)-3-(3-(4-(benzyloxy)phenyl)-1-phenyl-1*H*-pyrazol-4-yl)-1-(2,4-dimethoxyphenyl)prop-2-en-1-one (**5p**):

Green solid, yield: 76%; m.p.: 226–228 °C; IR (KBr, cm-1): 3096 (CH aromatic), 2967 (CH aliphatic), 1738 (C=O), 1625 (C=N), 1563 (C=C), 1245 (OCH$_3$), and 1272 (C-O); ^{1}H NMR (CDCl$_3$, 500 MHz); δ (ppm): 3.73–3.75 (s, 6H, 2xOCH$_3$), 5.17 (s, 2H, CH$_2$-benzyloxy), 7.14 (d, 2H, Ar-H, *J* = 8.6 Hz), 7.35 (d, 2H, Ar-H, *J* = 8.1 Hz), 7.38 (s, 1H, Ar-H), 7.39–7.60 (m, 10H, Ar-H), 7.67 (d, 2H, Ar-H, *J* = 8.7 Hz), 7.99 (d, 1H, chalcone-H-7, *J* = 15.3 Hz), 8.36 (s, 1H, chalcone-H-6), and 8.54 (s, 1H. pyrazole-H); ^{13}C NMR (CDCl$_3$, 125 MHz): δ (ppm) 56.3 (C'-4-OCH$_3$), 69.5 (benzyloxy-CH$_2$), 113.4 (pyrazole-C-4), 113.7, 114.2, 119.6, 119.1, 125.6, 126.3, 127.3, 127.65 (chalcone-C-7), 127.2, 128.3, 128.5, 129.4, 130.4 (pyrazole-C-5), 130.8, 133.7, 136.4, 139.3 (pyrazole-phenyl-C-1), 145.5 (chalcone-C-6), 150.7 (pyrazole-C-3), 151.2 (C-3'-OCH$_3$), 156.2 (C-4'-OCH$_3$), 159.5, and 189.5 (C=O); ESI-MS (*m/z*): 516.20 (M$^+$). Analysis calculated for C$_{33}$H$_{28}$N$_2$O$_4$: C, 76.73; H, 5.46; and N, 5.42. Found: C, 76.75; H, 5.38; and N, 5.45.

(*E*)-3-(3-(4-(benzyloxy)phenyl)-1-phenyl-1*H*-pyrazol-4-yl)-1-(2-bromo-4-methoxyphenyl)prop-2-en-1-one (**5q**):

Off white solid, yield: 56%; m.p.: 174–176 °C; IR (KBr, cm^{-1}): 3070 (CH aromatic), 2938 (CH aliphatic), 1765 (C=O), 1647 (C=N), 1588 (C=C), 1229 (C-OCH$_3$), 1260 (C-O), and 630 (C-Br); ^{1}H NMR (CDCl$_3$, 500 MHz); δ (ppm): 3.82 (s, 3H, OCH$_3$), 5.13 (s, 2H, CH$_2$-benzyloxy), 7.14 (d, 2H, Ar-H, *J* = 7.1 Hz), 7.21 (s, 1H, Ar-H), 7.38 (d, 2H, Ar-H, *J* = 6.4 Hz), 7.32–7.44 (m, 5H, Ar-H), 7.48 (s, 1H, Ar-H), 7.62 (d, 2H, Ar-pyrazole, *J* = 7.6 Hz), 7.64 (d, 2H, Ar-H, *J* = 7.6 Hz), 7.86 (d, 1H, chalcone-H-7, *J* = 15.5 Hz), 7.90 (d, 2H, Ar-H, *J* = 7.6 Hz), 8.32 (d, 1H, chalcone-H-6, *J* = 16.4 Hz), and 8.43 (s, 1H. pyrazole-H); ^{13}C NMR (CDCl$_3$, 125 MHz): δ (ppm) 56.3 (C'-4-OCH$_3$), 69.5 (benzyloxy-CH$_2$), 113.4 (pyrazole-C-4), 113.7, 114.2, 119.6, 119.1, 125.6, 126.3, 127.3, 127.65 (chalcone-C-7), 127.2, 128.3, 128.5, 129.4, 130.4 (pyrazole-C-5), 130.8, 133.7, 136.4, 139.3 (pyrazole-phenyl-C-1), 145.5 (chalcone-C-6), 150.7 (pyrazole-C-3), 151.2 (C-3'-OCH$_3$), 156.2 (C-4'-OCH$_3$), 159.5, and 189.5 (C=O); ESI-MS (*m/z*): 525.17 (M$^+$). Analysis calculated for C$_{32}$H$_{25}$BrN$_2$O$_3$: C, 67.97; H, 4.46; amd N, 4.95. Found: C, 68.02; H, 4.42; and N, 4.98.

(*E*)-3-(3-(4-(benzyloxy)phenyl)-1-phenyl-1*H*-pyrazol-4-yl)-1-(4-(trifluoromethyl)Phenyl)prop-2-en-1-one (**5r**):

White buff solid, yield: 68%; m.p.: 186–188 °C; IR (KBr, cm^{-1}): 3075 (CH aromatic), 2985 (CH aliphatic), 1760 (C=O), 1650 (C=N), 1520 (C=C), and 1265 (C-O), 780 (C-F); ^{1}H NMR (CDCl$_3$, 500 MHz); δ (ppm): 5.14 (s, 2H, CH$_2$-benzyloxy), 7.17 (d, 2H, Ar-H, *J* = 7.2 Hz), 7.36 (t, 1H, Ar-H, *J* = 7.3 Hz), 7.44–7.52 (m, 5H, Ar-H), 7.58 (d, 2H, Ar-H, *J* = 7.5 Hz), 7.69 (d, 2H Ar-H, *J* = 8.4 Hz), 7.74 (d, 2H, Ar-H, *J* = 8.4 Hz), 7.80 (d, 2H, Ar-H, *J* = 8.7 Hz), 7.88 (d, 1H, chalcone-H-7, *J* = 15.6 Hz), 7.92 (d, 2H, Ar-H, *J* = 8.6 Hz), 8.06 (d, 1H, chalcone-H-6, *J* = 15.76 Hz), and 8.34 (s, 1H, pyrazole-H); ^{13}C NMR (CDCl$_3$, 125 MHz): δ (ppm) 70.6 (benzyloxy-CH$_2$), 113.1, 114.9, 119.8, 124.5 (C-F$_3$), 125.4, 125.7, 126.2, 127.1, 127.4 (chalcone-C-7), 127.9, 128.5, 128.8, 129.4, 130.2 (C-2'), 130.3 (pyrazole-C-5), 136.4, 136.93 (C-4'), 139.8 (pyrazole-phenyl-C-1), 141.4, 145.7 (chalcone-C-6), 150.6 (pyrazole-C-3), 159.1, and 189.6 (C=O); ESI-MS (*m/z*): 554.17 (M$^+$+1). Analysis calculated for C$_{32}$H$_{23}$F$_3$N$_2$O$_2$: C, 73.27; H, 4.42; and N, 5.34. Found: C, 73.36; H, 4.36; and N, 5.42.

3.2. Molecular Docking Simulation

The molecular docking study of the designed molecules was carried out to assess their interaction and binding modes with the target receptors using Glide Extra precision (XP) Maestro 10.1 Schrodinger running on the Linux 64 operating system [47]. The 2D structure of the synthesized compounds was generated and then converted to their respective 3D structures using Ligprep. The PDB file of the X-ray crystal structure of the tubulin domain bound to colchicine (PDB ID:3E22) was downloaded from the RCSB Protein Data Bank. The protein preparation wizard was used to prepare the protein and the grid was generated for the co-crystal ligand using receptor grid generation. The water residues beyond 5 Å were eliminated. The protein was optimized by assigning H-bonds and the minimization of the OPLS 2005 force field. The docked pose of ligands and their interactions were analyzed after the end of the molecular docking.

3.3. Biological Activity

3.3.1. In Vitro Anticancer Activity by MTT Assay

Materials and Methods

(3-(4,5-Dimethyl-2-yl)-2,5-diphenyl tetrazolium bromide (MTT), Dulbecco's modified Eagle's medium (DMEM), 0.25% trypsin, and 0.02% EDTA mixture were purchased from HiMedia (Mumbai, India), and fetal bovine serum (FBS) was obtained from Gibco (Grand Island, NY, USA).

Cell Line and Culture Conditions

Human cervical cancer cell line SiHa, human breast cancer cell line MCF-7, human prostate cancer cell line PC-3, and human embryonic kidney HEK-293 cells were procured from the National Centre for Cell Sciences (NCCS) Pune, India. In this experiment, antibiotics (100 units/mL penicillin and 100 mg L^{-1} streptomycin were grown as a monolayer culture in Dulbecco's modified Eagle's medium containing 10% fetal bovine serum) were cultured in a humidified atmosphere of 5% CO_2 at 37 °C in T-75 flasks and subcultured twice a week.

In Vitro Cytotoxicity

The cytotoxic effects of the selected compounds were evaluated by MTT assay [48] on the above-mentioned cell lines. Initially, 2×10^4 cells/well were seeded into 96-well plates (150 μL/well) in triplicates and allowed to grow. The cells were incubated for 24 h and subsequently treated with varying concentrations of the compounds. After 48 h, the cells were incubated with 20 μL of MTT (5 mg/mL in PBS) in a fresh medium for 4 h at 37 °C. MTT is a metabolic substrate that is reduced to give formazan crystals, which were solubilized in DMSO (150 μL/well) and analyzed by reading the absorbance at 540 nm after 15 min of the incubation period on the iMark Microplate Reader (Bio-Rad). Percentage viability and IC_{50} values were used to determine the relative absorbance of treated versus control (untreated) cells.

3.3.2. In Vitro Tubulin Polymerization Assay

Tubulin polymerization is a dynamic process by enhancement of fluorescence intensity due to the combination of a fluorescent reporter into the microtubules as polymerization occurs [49]. Tubulin polymerization was performed by using a purified brain tubulin polymerization kit purchased from Cytoskeleton (BK110P, Denver, CO, USA). The tubulin polymerization assay was monitored by the increase in fluorescence over a 60 min period at 37 °C, with excitation at 360 nm and emission at 450 nm. The final buffer concentration for tubulin polymerization contained 80 mM PIPES, pH 6.9; 2 mM $MgCl_2$; 0.5 mM EGTA; 1μM GTP; and 15% glycerol. Firstly, 5 μL of the test compounds (final concentration of 10 μM) was added and then warmed to 37 °C for 1 min. The reaction was initiated by adding 50 μL of the tubulin reaction mix as specified for 6 min.

3.3.3. In Silico Bioactivity Study

All newly synthesized derivatives were screened for their physicochemical properties, oral bioavailability, toxicity, and online biological activity by using online software such as Molinspiration, Osiris Property Explorer, and the PASS prediction study. Hydrophobicity (c-log P), molecular weight (MW), number of rotatable bonds (NROTB) of Lipinski's rule of five [33], water solubility (c-log S), toxicity [35], and drug-likeness [34] were calculated using the online Molinspiration property calculation toolkit and online OSIRIS Property explorer. With the help of Osiris Property Explorer software, the toxicities of the synthesized derivatives were predicted, which showed that the newly synthesized compounds would be free of carcinogenicity, mutagenicity, reproductive adverse effects, and irritation. All these derivatives were also projected for their pharmacological activity by using the online PASS computer program (prediction of activity spectra for substances).

3.4. Statistical Analysis

Statistical analyses were performed using Graph Pad Prism 5 software. All data were analyzed by ANOVA, followed by Dunnett's multiple comparison test for $n = 6$; (a) $p < 0.05$ and (b) $p < 0.001$. Relative to normal and data were analyzed by paired Student's *t*-test for $n = 6$; (c) $p < 0.0001$ and (d) $p < 0.005$.

4. Conclusions

A series of *E*-3-(3-(4-(benzyloxy)phenyl)-1-phenyl-1*H*-pyrazol-4-yl)-1-phenylprop-2-en-1-one conjugates were synthesized, characterized, and evaluated for anticancer potential and tubulin polymerization inhibition. The conjugates **5d**, **5k**, **5n**, **5o**, and **5p** revealed potent cytotoxic activities against MCF-7 (human breast), SiHa (human cervical), PC-3 (human prostate), and non-cancerous cell lines using combretastatin A4 as the standard. Compound **5o** displayed the most potent cytotoxic activity with the IC$_{50}$ value of 2.13 ± 0.80 μM for the MCF-7 cancer cell line. Furthermore, compound **5o** considerably arrested the cell cycle, induced apoptosis in a dose-dependent manner, and inhibited polymerization of tubulin by 66.40%. Molecular docking studies of compound **5o** (highest docking score of −7.22) showed that the colchicine-binding site of tubulin established promising interactions with ASN 249, ALA 250, LYS 254, SER 178, and TYR 224, and pi-cation interaction with LYS 352 in the active site of tubulin. The in silico bioactivity study and PASS prediction studies exposed that most of the synthesized compounds displayed excellent physicochemical properties within the ideal range. These results established that compound 5o is a newer tubulin polymerization inhibitor and is commendable of advanced investigation in the future, directing to the progress of newer potential anticancer agents. Therefore, these conjugates can further be structurally modified to promote a new potential target for the optimization and development of anticancer agents.

Supplementary Materials: The following are available online at https://www.mdpi.com/article/10.3390/ph15030280/s1, Figure S1: ^{1}H NMR of (*E*)-3-(3-(4-(benzyloxy)phenyl)-1-phenyl-1*H*-pyrazol-4-yl)-1-(3,4-dimethoxyphenyl)prop-2-en-1-one; Figure S2: ^{13}C NMR of (*E*)-3-(3-(4-(benzyloxy)phenyl)-1-phenyl-1*H*-pyrazol-4-yl)-1-(3,4-dimethoxyphenyl)prop-2-en-1-one; Figure S3: ^{1}H NMR of (*E*)-3-(3-(4-(benzyloxy)phenyl)-1-phenyl-1*H*-pyrazol-4-yl)-1-(3,4-dimethoxyphenyl)prop-2-en-1-one; Figure S4: ^{13}C NMR of (*E*)-3-(3-(4-(benzyloxy)phenyl)-1-phenyl-1*H*-pyrazol-4-yl)-1-(3,4-dimethoxyphenyl)prop-2-en-1-one; Figure S5: Mass spectra of (*E*)-3-(3-(4-(benzyloxy)phenyl)-1-phenyl-1*H*-pyrazol-4-yl)-1-(3,4-dimethoxyphenyl)prop-2-en-1-one; Figure S6: ^{1}H NMR of (*E*)-3-(3-(4-(benzyloxy)phenyl)-1-phenyl-1*H*-pyrazol-4-yl)-1-(4-bromophenyl)prop-2-en-1-one; Figure S7: ^{1}H NMR of (*E*)-3-(3-(4-(benzyloxy)phenyl)-1-phenyl-1*H*-pyrazol-4-yl)-1-(4-bromophenyl)prop-2-en-1-one; Figure S8: ^{13}C NMR of (*E*)-3-(3-(4-(benzyloxy)phenyl)-1-phenyl-1*H*-pyrazol-4-yl)-1-(4-bromophenyl)prop-2-en-1-one; Figure S9: Mass spectra of (*E*)-3-(3-(4-(benzyloxy)phenyl)-1-phenyl-1*H*-pyrazol-4-yl)-1-(4-bromophenyl)prop-2-en-1-one; Figure S10: ^{1}H NMR of (*E*)-3-(3-(4-(benzyloxy)phenyl)-1-phenyl-1*H*-pyrazol-4-yl)-1-(4-methoxyphenyl)prop-2-en-1-one; Figure S11: ^{13}C NMR of (*E*)-3-(3-(4-(benzyloxy)phenyl)-1-phenyl-1*H*-pyrazol-4-yl)-1-(4-methoxyphenyl)prop-2-en-1-one; Figure S12: ^{1}H NMR of (*E*)-3-(4-(benzyloxy)phenyl)-1-phenyl-1*H*-pyrazol-4-yl)-1-(4-methoxyphenyl)prop-2-en-1-one; Figure S13:

[^13]C NMR of (*E*)-3-(3-(4-(benzyloxy)phenyl)-1-phenyl-1*H*-pyrazol-4-yl)-1-(4-methoxyphenyl)prop-2-en-1-one; Figure S14: Mass spectra of (*E*)-3-(3-(4-(benzyloxy)phenyl)-1-phenyl-1*H*-pyrazol-4-yl)-1-(4-methoxyphenyl)prop-2-en-1-one; and Figure S15: Effect of lead conjugates **5d**, **5e**, **5i**, **5k**, **5l**, **5m**, **5n**, **5o**, **5p**, and **5r** on tubulin polymerization. Tubulin polymerization was monitored by the increase in fluorescence at 360 nm (excitation) and 420 nm (emission) for 1 h at 37 °C. Combretastatin A-4 was used as the reference standard in this study.

Author Contributions: Conceptualization, O.A. and M.J.A.; methodology, M.J.A., A.P., M.A.R., M.J.N. and V.G.M.N.; software, M.I.; validation, S.A., M.M.G. and F.S.; formal analysis, M.I.; investigation, M.I., S.A. and F.S.; resources, O.A.; data curation, M.J.A.; writing—original draft preparation, O.A. and M.J.A.; writing—review and editing, S.A., F.S. and M.I.; visualization, O.A.; supervision, O.A.; project administration, O.A.; funding acquisition, S.A. and M.M.G. All authors have read and agreed to the published version of the manuscript.

References

1. Frankish, H. 15 million new cancer cases per year by 2020, says WHO. *Lancet* **2003**, *361*, 1278. [CrossRef]
2. American Cancer Society. *American Cancer Society: Cancer Facts and Figures 2016*; American Cancer Society: Atlanta, GA, USA, 2016.
3. Available online: https://www.who.int/news-room/fact-sheets/detail/cancer (accessed on 15 September 2021).
4. Belpomme, D.; Irigaray, P.; Sasco, A.J.; Newby, J.A.; Howard, V.; Clapp, R.; Hardell, L. The growing incidence of cancer: Role of lifestyle and screening detection (review). *Int. J. Oncol.* **2007**, *30*, 1037–1049. [CrossRef]
5. Kibria, G.; Hatakeyama, H.; Harashima, H. Cancer multidrug resistance: Mechanisms involved and strategies for circumvention using a drug delivery system. *Arch. Pharm. Res.* **2014**, *37*, 4–15. [CrossRef]
6. Negi, A.S.; Gautam, Y.; Alam, S.; Chanda, D.; Luqman, S.; Sarkar, J.; Khan, F.; Konwar, R. Natural anti-tubulin agents: Importance of 3,4,5-trimethoxyphenyl fragment. *Bioorg. Med. Chem.* **2015**, *23*, 373–389. [CrossRef]
7. Vindya, N.G.; Sharma, N.; Yadav, M.; Ethiraj, K.R. Tubulins—The target for anticancer therapy. *Curr. Top. Med. Chem.* **2015**, *15*, 73–82. [CrossRef]
8. Barbier, P.; Tsvetkov, P.O.; Breuzard, G.; Devred, F. Deciphering the molecular mechanisms of anti-tubulin plant-derived drugs. *Phytochem. Rev.* **2014**, *13*, 157–169. [CrossRef]
9. Field, J.J.; Kanakkanthara, A.; Miller, J.H. Microtubule-targeting agents are clinically successful due to both mitotic and interphase impairment of microtubule function. *Bioorg. Med. Chem.* **2014**, *22*, 5050–5059. [CrossRef]
10. Pettit, G.R.; Cragg, G.M.; Herald, D.L.; Schmidt, J.M.; Lohavanijaya, P. Isolation, and structure of combretastatin. *Can. J. Chem.* **1982**, *60*, 1374–1376. [CrossRef]
11. Ravelli, R.B.; Gigant, B.; Curmi, P.A.; Jourdain, I.; Lachkar, S.; Sobel, A.; Knossow, M. Insight into tubulin regulation from a complex with colchicine and a stathmin-like domain. *Nature* **2004**, *428*, 198–202. [CrossRef]
12. Bohlin, L.; Rosen, B. Podophyllotoxin derivatives: Drug discovery and development. *Drug Discov. Today* **1996**, *1*, 343–351. [CrossRef]
13. Kuehne, M.E.; Marko, I.; Brossi, A. (Eds.) *The Alkaloids*; Academic Press: San Diego, CA, USA, 1990; Volume 37, pp. 77–132.
14. Jimenez, C.; Ellahioui, Y.; Alvarez, R.; Aramburu, L.; Riesco, A.; Gonzalez, M.; Vicente, A.; Dandouh, A.; Ibn Mansour, A.; Jimenez, C.; et al. Exploring the size adaptability of the B ring binding zone of the colchicine site of the tubulin with para-nitrogen substituted isocombretastatins. *Eur. J. Med. Chem.* **2015**, *100*, 210–222. [CrossRef]
15. Nickel, H.C.; Schmidt, P.; Bohm, K.J.; Baasner, S.; Muller, K.; Gerlach, M.; Unger, E.; Gunthe, E.G.; Prinz, H. Synthesis, antiproliferative activity and inhibition of tubulin polymerization by 1,5- and 1,8-disubstituted 10H-anthracen-9-ones bearing a 10-benzylidene or 10-(2-oxo-2-phenylethylidene) moiety. *Eur. J. Med. Chem.* **2010**, *45*, 3420–3438. [CrossRef]

16. Pellegrini, F.; Budman, D.R. Review: Tubulin function, action of anti-tubulin drugs, and new drug development. *Cancer Investig.* **2005**, *23*, 264–273. [CrossRef]

17. Tron, G.C.; Pagliai, F.; Del Grosso, E.; Genazzani, A.A.; Sorba, G. Synthesis and cytotoxic evaluation of combretafurazans. *J. Med. Chem.* **2005**, *48*, 3260–3268. [CrossRef]

18. Doi, S.; Fujioka, N.; Ohtsuka, S.; Kondo, R.; Yamamoto, M.; Denda, M.; Magari, M.; Kanayama, N.; Hatano, N.; Morishita, R.; et al. Regulation of the tubulin polymerization-promoting protein by Ca2+/S100 proteins. *Cell Calcium.* **2021**, *96*, 102404. [CrossRef]

19. Liu, W.; Wang, G.; Peng, Z.; Li, Y. Design, synthesis and biological evaluation of novel 4-(4-methoxynaphthalen-1-yl)-5-arylpyrimidin-2-amines as tubulin polymerization inhibitors. *Chem. Pharm. Bull.* **2020**, *68*, 1184–1192. [CrossRef]

20. Kamal, A.; Kumar, G.B.; Vishnuvardhan, M.V.P.S.; Shaik, A.B.; Reddy, V.S.; Mahesh, R.; Sayeeda, I.B.; Kapure, J.S. Synthesis of phenstatin/isocombretastatin–chalcone conjugates as potent tubulin polymerization inhibitors and mitochondrial apoptotic inducers. *Org. Biomol. Chem.* **2015**, *13*, 3963–3981. [CrossRef]

21. Nakagawa-Goto, K.; Oda, A.; Hamel, E.; Ohkoshi, E.; Lee, K.-H.; Goto, M. Development of a novel class of tubulin inhibitor from desmosdumotin B with a hydroxylated bicyclic B-ring. *J. Med. Chem.* **2015**, *58*, 2378–2389. [CrossRef]

22. Kumar, V.; Kaur, K.; Gupta, G.K.; Sharma, A.K. Pyrazole containing natural products: Synthetic preview and biological significance. *Eur. J. Med. Chem.* **2013**, *69*, 735–753. [CrossRef]

23. Harras, M.F.; Sabour, R. Design, synthesis and biological evaluation of novel 1, 3, 4-trisubstituted pyrazole derivatives as potential chemotherapeutic agents for hepatocellular carcinoma. *Bioorg. Chem.* **2018**, *78*, 149–157. [CrossRef]

24. Kumar, H.; Saini, D.; Jain, S.; Jain, N. Pyrazole scaffold: A remarkable tool in the development of anticancer agents. *Eur. J. Med. Chem.* **2013**, *70*, 248–258. [CrossRef] [PubMed]

25. Liu, Y.R.; Luo, J.Z.; Duan, P.P.; Shao, J.; Zhao, B.X.; Miao, J.Y. Synthesis of pyrazole peptidomimetics and their inhibition against A549 lung cancer cells. *Bioorg. Med. Chem. Lett.* **2012**, *22*, 6882–6887. [CrossRef] [PubMed]

26. Shah, K.; Chhabra, S.; Shrivastava, S.K.; Mishra, P. Benzimidazole: A promising pharmacophore. *Med. Chem. Res.* **2013**, *22*, 5077–5104. [CrossRef]

27. Narasimhan, B.; Sharma, D.; Kumar, P. Benzimidazole: A medicinally important heterocyclic moiety. *Med. Chem. Res.* **2012**, *21*, 269–283. [CrossRef]

28. Sharp, S.Y.; Boxall, K.; Rowlands, M.; Prodromou, C.; Roe, S.M.; Maloney, A.; Powers, M.; Clarke, P.A.; Box, G.; Sanderson, S.; et al. In vitro biological characterization of a novel, synthetic diaryl pyrazole resorcinol class of heat shock protein 90 inhibitors. *Cancer Res.* **2007**, *67*, 2206–2216. [CrossRef] [PubMed]

29. Peyrot, V.; Leynadier, D.; Sarrazin, M.; Briand, C.; Menendez, M.; Laynez, J.; Andreu, J.M. Mechanism of binding of the new antimitotic drug MDL 27048 to the colchicine site of tubulin: Equilibrium studies. *Biochemistry* **1992**, *31*, 11125–11132. [CrossRef] [PubMed]

30. Kamal, A.; Shaik, A.B.; Jain, N.; Kishor, C.; Nagabhushana, A.; Supriya, B.; Kumar, G.B.; Chourasiya, S.S.; Suresh, Y.; Mishra, R.K. Design and synthesis of pyrazole-oxindole conjugates targeting tubulin polymerization as new anticancer agents. *Eur. J. Med. Chem.* **2013**, *92*, 501–513. [CrossRef]

31. Yang, X.H.; Wen, Q.; Zhao, T.T.; Sun, J.; Li, X.; Xing, M.; Lu, X.; Zhu, H.L. Synthesis, biological evaluation, and molecular docking studies of acyl 1,3,4-thiadiazole amide derivatives as novel anti-tubulin agents. *Bioorg. Med. Chem.* **2012**, *20*, 1181–1187. [CrossRef]

32. Srinivasa, R.T.; Ganga, R.V.; Kulhari, H.; Shukla, R.; Kamal, A.; Bansal, V. Synthesis of Z-1-(1,3-diphenyl-1H-pyrazol—4-yl)-3-(phenylamino)prop-2-en-one derivatives as potential anticancer and apoptosis inducing agents. *Eur. J. Med. Chem.* **2016**, *117*, 157–166. [CrossRef]

33. Kamal, A.; Shaik, A.B.; Bhaskara, R.B.; Khan, I.; Kumara, G.B.; Jainc, N. Design and synthesis of pyrazole/isoxazole linked arylcinnamides as tubulin polymerization inhibitors and potential antiproliferative agents. *Org. Biomol. Chem.* **2015**, *40*, 10162–10178. [CrossRef]

34. Nam, N.H. Combretastatin A-4 analogues as antimitotic antitumor agents. *Curr. Med. Chem.* **2003**, *10*, 1697–1722. [CrossRef] [PubMed]

35. Paul, K.; Bindal, S.; Luxami, V. Synthesis of new conjugated coumarin-benzimidazole hybrids and their anticancer activity. *Bioorg. Med. Chem.* **2013**, *15*, 3667–3672. [CrossRef] [PubMed]

36. Lagunin, A.; Stepanchikova, A.; Filimonov, D.; Poroikov, V. PASS: Prediction of activity spectra for biologically active substances. *Bioinformatics* **2000**, *16*, 747–748. [CrossRef] [PubMed]

37. PASS Software Free Molecular Property Calculation Services. Available online: http://www.pharmaexpert.ru/passonline/predict.php (accessed on 15 February 2019).

38. Mosmann, T.J. Rapid colorimetric assay for cellular growth and survival: Application to proliferation and cytotoxicity assays. *Immunol. Methods* **1983**, *65*, 55–63. [CrossRef]

39. Kaushik, D.; Khan, S.A.; Chawla, G.; Kumar, S. N′-[(5-chloro-3-methyl-1-phenyl-1H-pyrazol-4-yl)methylene] 2/4-substituted hydrazides: Synthesis and anticonvulsant activity. *Eur. J. Med. Chem.* **2010**, *45*, 3943–3949. [CrossRef] [PubMed]

40. Ragab, F.A.; Abdel Gawad, N.M.; Georgey, H.H.; Said, M.F. Synthesis of novel 1,3,4-trisubstituted pyrazoles as anti-inflammatory and analgesic agents. *Eur. J. Med. Chem.* **2013**, *63*, 645–654. [CrossRef]

41. Mehdi, S.J.; Ahmad, A.; Irshad, M.; Manzoor, N.; Rizvi, M.M.A. Cytotoxic effect of carvacrol on human cervical cancer cells. *Biol. Med.* **2011**, *2*, 307–312.

42. Kamal, A.; Srinivasa, R.T.; Vardhan, V.; Kumar, V.; Nimbarte, D.; Subba, A.V.R.; Srinivasulu, V.; Shankaraiah, N. Synthesis of 2-aryl-1,2,4-oxadiazolo-benzimidazoles: Tubulin polymerization inhibitors and apoptosis inducing agents. *Bioorg. Med. Chem.* **2015**, *23*, 4608–4623. [CrossRef]

43. LLC. *Schrodinger, Maestro, Version 10.1*; LLC: New York, NY, USA, 2018.

44. Huang, X.F.; Lu, X.; Zhang, Y.; Song, G.Q.; He, Q.L.; Li, Q.S.; Yang, X.H.; Wei, Y.; Zhu, H.L. Synthesis, biological evaluation, and docking studies of N-((1,3-diphenyl-1H-pyrazol-4yl)methyl)aniline derivatives as novel anticancer agents. *Bioorg. Med. Chem.* **2012**, *20*, 4895–4900. [CrossRef]

45. Hou, T.; Wang, J.; Zhang, W.; Xu, X.J. ADME evaluation in drug discovery. 6. Can oral bioavailability in humans be effectively predicted by simple molecular property-based rules? *Chem. Inf. Model.* **2007**, *47*, 460–463. [CrossRef]

46. Molinspiration Software or Free Molecular Property Calculation Services (2 Screens). Available online: www.molinspiration.com/cgi-bin/properties (accessed on 15 February 2021).

47. Sander, T. Osiris Property, Explore. 2001. Available online: http://www.organic-chemistry.org/prog/peo/ (accessed on 15 February 2018).

48. Meanwell, N.A. Improving drug candidates by design: A focus on physicochemical properties as a means of improving compound disposition and safety. *Chem. Res. Toxicol.* **2011**, *24*, 1420–1456. [CrossRef] [PubMed]

49. Hopkins, A.L.; Keserü, G.M.; Leeson, P.D.; Rees, D.C.; Reynolds, C.H. The role of ligand efficiency metrics in drug discovery. *Nat. Rev. Drug Discov.* **2014**, *13*, 105–121. [CrossRef] [PubMed]

Communication

Synthesis of Novel (*S*)-3-(1-Aminoethyl)-8-pyrimidinyl-2-phenylisoquinolin-1(2*H*)-ones by Suzuki–Miyaura Coupling and Their Cell Toxicity Activities

Ok Kyoung Choi [1,2], Yong Ho Sun [2], Hyemi Lee [2], Joon Kwang Lee [2], Tae Hoon Lee [1,*] and Hakwon Kim [1,*]

[1] Department of Applied Chemistry and Global Center for Pharmaceutical Ingredient Materials, Kyung Hee University, Yongin 17410, Korea; andante99@boryung.co.kr
[2] Process Research, Boryung R&D Institute, Ansan 15425, Korea; sunyh@boryung.co.kr (Y.H.S.); hmlee0325@samjinpharm.co.kr (H.L.); jklee@boryung.co.kr (J.K.L.)
* Correspondence: thlee@khu.ac.kr (T.H.L.); hwkim@khu.ac.kr (H.K.); Tel.: +82-31-201-5173 (T.H.L.); +82-31-201-2459 (H.K.)

Abstract: A series of (*S*)-3-(1-aminoethyl)-8-pyrimidinyl-2-phenylisoquinoline-1(2*H*)-ones **3a–3k** was synthesized in 40–98% yield through Suzuki–Miyaura coupling using $Pd(PPh_3)_2Cl_2$, Sphos, and K_2CO_3 in THF/H_2O mixed solvent. All newly synthesized compounds were evaluated for cell viability (IC_{50}) against MDA-MB-231, HeLa, and HepG2 cells. The antitumor activities of **3a–3k** were improved when various pyrimidine motifs were introduced at position C-8 of the isoquinolinone ring.

Keywords: (S)-3-(1-aminoethyl)-8-pyrimidinyl-2-phenylisoquinoline-1(2H)-one; Suzuki–Miyaura coupling; antitumor; cytotoxicity

Publisher's Note: MDPI stays neutral with regard to jurisdictional claims in published maps and institutional affiliations.

1. Introduction

Isoquinolin-1(2*H*)-one derivatives are heterocyclic compounds exhibiting various bioactivities [1]. For example, the isoquinolin-1(2*H*)-one structure is known as an important pharmacophore of an effective 5-HT3 antagonist [2] and an inhibitor for the production of tumor necrosis factor α (TNF-α) [3]. In particular, 2-phenylisoquinolin-1(2*H*)-one has been reported as the main structure of several anticancer drugs that have been recently developed [4–7]. Duvelisib, which is used for the treatment of chronic lymphocytic leukemia (CLL) and somatic cell lymphoma (SLL), contains 2-phenylisoquinolin-1(2*H*)-one as a basic structure [6]. BR1018018, which has recently been developed as a PI3K selective inhibitor by Boryung Pharmaceutical (Korea), also has a 2-phenylisoquinoline-1(2*H*)-one moiety (Figure 1) [7].
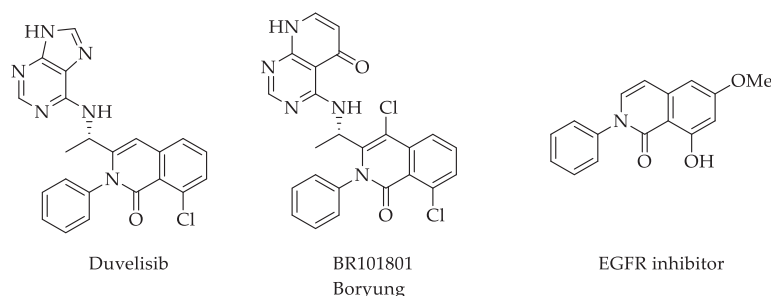

Figure 1. Examples of anti-cancer drugs containing the 2-phenylisoqunolin-1(2*H*)-one.

On the other hand, 2-substituted pyrimidines consist of the basic structure of several drugs with various pharmacological activities. Recently, 2-substituted pyrimidines in RhoJ (Rho-related GTP-binding protein) inhibitor [8], CDK (Cyclin-dependent kinase)

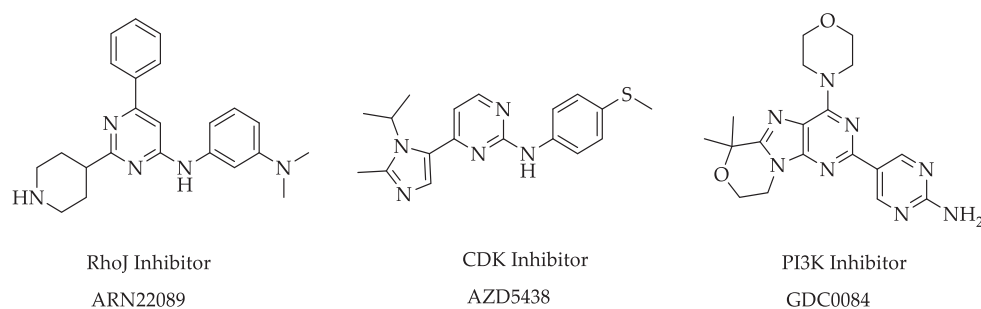inhibitor [9], and PI3K (phosphoinositide 3-kinase) inhibitor [10] are important basic structures (Figure 2).

Figure 2. Candidates for anticancer drugs with pyrimidine cores.

Based on these previous reports, we have become interested in whether 8-pyrimidinyl-2-phenylisoquinolin-1(2*H*)-one derivatives synthesized by the combination of 2-phenylisoquinolin-1(2*H*)-one and pyrimidine can be used as a new pharmacophore. Therefore, we investigated the synthesis of new (*S*)-3-(1-aminoethyl)-8-pyrimidinyl-2-phenylisoquinolin-1(2*H*)-one derivatives (**3**) by the Suzuki–Miyaura coupling (SMC) of (*S*)-3-(1-aminoethyl)-8-chloro-2-phenylisoquinolin-1(2*H*)-one (**1**) with various pyrimidinyl boronic acids **2** (Scheme 1). SMC is well known as the most common method for forming new carbon–carbon bonds in organic synthesis chemistry [11–13]. Well-known highly efficient SMC reactions, such as those using microwave chemistry, can be simply performed in a laboratory to produce a small amount of product by the column chromatography separation method [14]. However, there is a need to develop a mild, general, and practical SMC reaction capable of the bulk synthesis required in drug discovery research. Herein, we report an effective and mild synthesis method for (*S*)-3-(1-aminoethyl)-8-pyrimidinyl-2-phenylisoquinolin-1(2*H*)-one derivatives (**3**) and their anticancer activities.
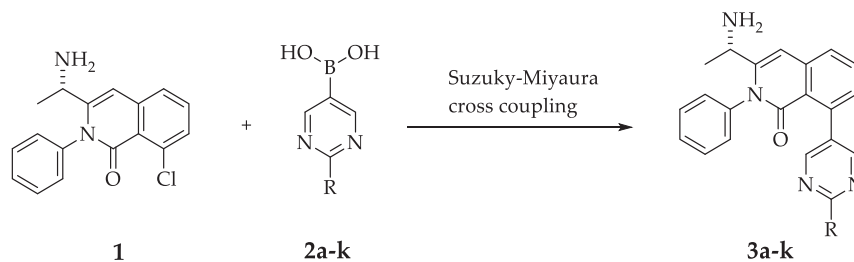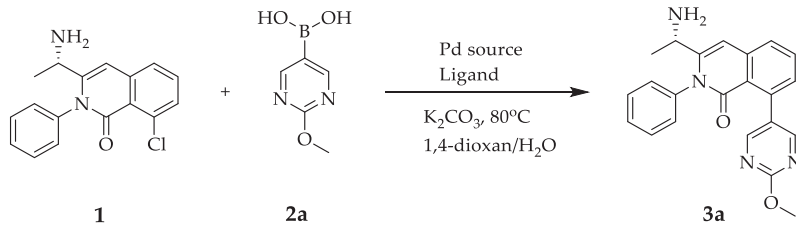

Scheme 1. Synthesis of novel pyrimidinyl-2-phenylisoquinolin-1(2*H*)-ones **3** using SMC.

2. Results and Discussion

2.1. Synthesis of Compounds

First, we compared the SMC reaction efficiencies of (*S*)-3-(1-aminoethyl)-8-chloro-2-phenylisoquinolin-1(2*H*)-one (**1**) prepared in a known method [15] with (2-methoxypyrimidin-5-yl)boronic acid (**2a**) on various Pd catalysts in dioxane/H_2O for 12 h at 80 °C with reference to a previously reported mixed solvent system [16,17]. To screen Pd catalysts in SMC reactions, the synthesis efficiencies of **3a** for various Pd catalyst systems were compared under the above reaction conditions, including 5 mol% of Pd complex and 10 mol% of ligand (Table 1, Entries 1–5). When $Pd(PPh_3)_2Cl_2$ and PPh_3 (Entry 5) were used, **3a** was obtained in a low yield of 39%. Lower yields were also observed when using other common catalysts, such as $Pd(PPh_3)_4$, $Pd(OAc)_2/PPh_3$, or $PdCl_2/PPh_3$.

Table 1. Screening of catalysts on the Suzuki–Miyaura cross-coupling of **1** with **2a** *.

Entry	Catalyst (Mol%)	Ligand (Mol%)	3a(%) [b]	1(%) [b]
1	Pd(PPh$_3$)$_4$ (5)	-	18.5	74.5
2	Pd(PPh$_3$)Cl$_2$ (5)	-	28.7	63.5
3	Pd(OAc)$_2$ (5)	PPh$_3$ (10)	19.4	73.3
4	PdCl$_2$ (5)	PPh$_3$ (10)	21.4	72.4
5	Pd(PPh$_3$)$_2$Cl$_2$ (5)	PPh$_3$ (10)	39.2	53.5
6	Pd(PPh$_3$)$_2$Cl$_2$ (2.5)	PPh$_3$ (5)	28.2	64.5
7	Pd(PPh$_3$)$_2$Cl$_2$ (2.5)	P(O-tol)$_3$ (5)	31.2	62.9
8	Pd(PPh$_3$)$_2$Cl$_2$ (2.5)	P(Cy)$_3$ (5)	66.2	27.4
9	Pd(PPh$_3$)$_2$Cl$_2$ (2.5)	Dppf (5)	35.6	58.4
10	Pd(PPh$_3$)$_2$Cl$_2$ (2.5)	Aphos (5)	76.9	17.8
11	Pd(PPh$_3$)$_2$Cl$_2$ (2.5)	Xantphos (5)	65.6	29.2
12	Pd(PPh$_3$)$_2$Cl$_2$ (2.5)	Xphos (5)	86.3	9.0
13	Pd(PPh$_3$)$_2$Cl$_2$ (2.5)	Sphos (5)	96.5 [a]	0
14	Pd(PPh$_3$)$_2$Cl$_2$ (2.5)	Ruphos (5)	96.4 [a]	0
15	Pd(PPh$_3$)$_2$Cl$_2$ (2.5)	Davephos (5)	96.1 [a]	0

* Reaction conditions: 1 (1.67 mmol), 2a (2.0 mmol), K$_2$CO$_3$ (5 mmol), 1,4-dioxane (5 mL), H$_2$O (5 mL), 12 h.
[a] Reaction time 2 h. [b] The yields were determined by HPLC (area%). HPLC system using an Kromasil 100-5 C18 column (4.6 mm × 250 mm, 5 μM). The mobile phase consisted of two eluents: A: Ammonium Acetate Buffer Solution (Accurately weighed 1.54 g of ammonium acetate buffer solution is completely dissolved in 1 L of water and the pH level is adjusted to pH 4.5 with acetic acid) and eluant B: Acetonitrile: Methanol (80:20).
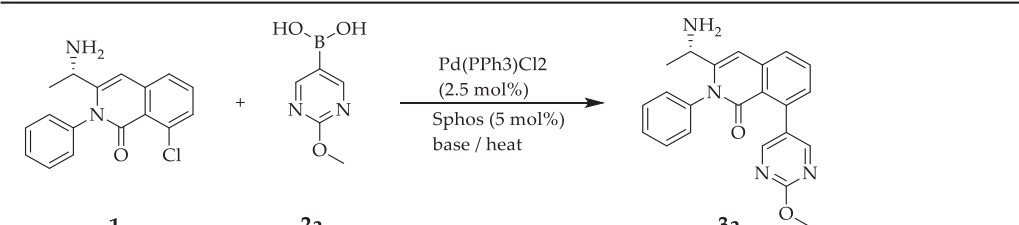
SMC reactions with Pd(PPh$_3$)$_2$Cl$_2$ (2.5 mol%), selected as a Pd catalyst, and various phosphine ligands (5 mol%) were studied under conditions in which the amount of catalyst used was reduced by half of that given above. First, the reaction efficiency was investigated by increasing the bulkiness of the ligand using mono-phosphine ligands (PPh$_3$ < P(O-tol)$_3$ < P(Cy)$_3$) (Entries 6–8) and di-phosphine ligands (dppf < Xantphos) (Entries 9,11). It was observed that mono-phosphine ligands or di-phosphine ligands [18] showed low reactivity (Entries 1–9,11). However, the yield increased in the electron-rich phosphine ligands, such as Aphos (Entry 10). Unlike the mono-aryl type Aphos, the yield as well as the reaction rate increased dramatically when using Buchwald ligands, such as Sphos, Ruphos, and Davephos, which are biaryl types (Entries 13–15). We attributed this to the structural characteristics of the electron-rich and bulky phosphine ligands substituted with cyclohexyl or biaryl groups. This is consistent with reports that electron-rich and bulky phosphine Buchwald ligands accelerate reductive elimination and oxidative addition in SMC reactions, resulting in increased reactivity [19–21].

Subsequently, base screening with various solvents was performed in SMC (Table 2).

The SMC reaction occurred in the highest yield in the THF/H$_2$O mixed solvent system. In addition, phase separation occurred in the THF/H$_2$O solvent system after the reaction was completed, but phase separation was not observed in the aqueous solution system mixed with other solvents. Therefore, in this solvent system, the separated organic layer was extracted with an acidic aqueous solution, neutralized, and then crystallized to easily obtain a high-purity product without a chromatographic separation, which is very advantageous for a large-scale synthesis process. To further develop this process, a design of experiments (DoE; using Design Expert 12) was performed and optimized. The optimal conditions established through the DoE were Pd(PPh$_3$)$_2$Cl$_2$ (0.5 mol%), Sphos (1.5 mol%), and K$_2$CO$_3$ (3.0 eq) in THF and H$_2$O mixed solvent. It was found that the amount of solvent

THF/H$_2$O used to facilitate phase separation between the organic layer and the aqueous layer after the reaction was more than 10 mL per gram of substrate **1**.

Table 2. Screening of base and solvent *.

Entry	Base	Solvent	T(°C)	3a(%) [c]	1(%) [c]
1	-	1,4-dioxane/H$_2$O [a]	80	0	96.0
2	K$_t$OBu	1,4-dioxane/H$_2$O [a]	80	31.4	0
3	Na$_2$CO$_3$	1,4-dioxane/H$_2$O [a]	80	96.0	0
4	KOH	1,4-dioxane/H$_2$O [a]	80	35.4	0
5	KOAc	1,4-dioxane/H$_2$O [a]	80	95.1	0.1
6	Cs$_2$CO$_3$	1,4-dioxane/H$_2$O [a]	80	96.9	0.1
7	K$_2$CO$_3$	1,4-dioxane/H$_2$O [a]	80	96.9	0
8	K$_2$CO$_3$	THF	64 [b]	25.1	70.3
9	K$_2$CO$_3$	1,4-dioxane	104 [b]	9.1	67.5
10	K$_2$CO$_3$	EtOH	80 [b]	87.4	0
11	K$_2$CO$_3$	H$_2$O	101 [b]	49.7	45.3
12	K$_2$CO$_3$	THF/H$_2$O [a]	65 [b]	99.0	0
13	K$_2$CO$_3$	EtOH/H$_2$O [a]	78 [b]	97.6	0
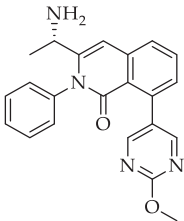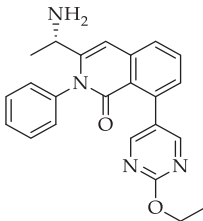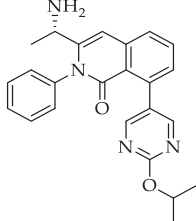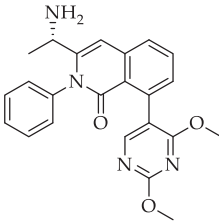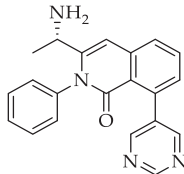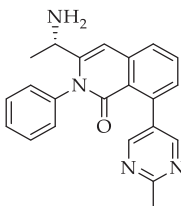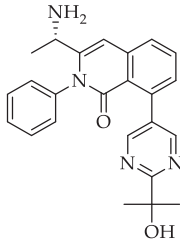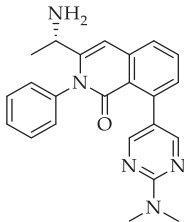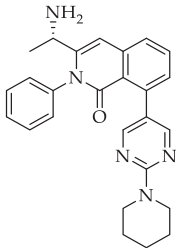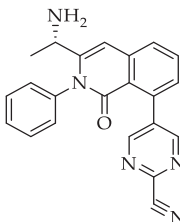
* Reaction condition: 1 (1.67 mmol), 2a (2.0 mmol), base (5 mmol), 12 h, solvent (10 mL). [a] Solvent (5 mL)/H$_2$O(5 mL). [b] Reflux. [c] The yields were determined by HPLC (area%).

Novel (*S*)-3-(1-aminoethyl)-8-pyrimidinyl-2-phenylisoquinolin-1(2*H*)-one derivatives (**3**) were synthesized by using SMC reactions under these optimized conditions (Table 3). The structure of **3a**–**3k** were confirmed by ^{1}H-NMR, ^{13}C-NMR spectrosco-py (Supplementary Materials Figures S1–S22). In the case of unstable boronic acid, pinacol boronate (in case of **3g** and **3k**) was used as a reactant. Electron-rich pyrimidinyl boronic acid substituted with methoxy, ethoxy, dimethylamino, and piperidinyl groups at the para position of the pyrimidine ring gave the product in good yield (**3a**, **3b**, **3i** and **3j**). In the case of other boronic acids with low reactivity, the reaction could be completed in good yield by increasing the amount of catalyst and ligand (**3c**, **3e**–**3g**). Boronic acids with steric hindrance, such as 2,4-dimethoxypyrimidinyl boronic acid, still showed low yield even when the amount of catalyst and ligand was increased (**3d**). In addition, electron-deficient boronic acid (e.g., 2-cyanopyrimidinyl boronic acid) showed the lowest reactivity (**3k**).

2.2. Anti-Cancer Activity

All newly synthesized compounds (**3a**–**3k**) were evaluated for cell viability (IC$_{50}$) against MDA-MB-231 (metallic breast cancer cells), HeLa (cervical epithelial carcinoma c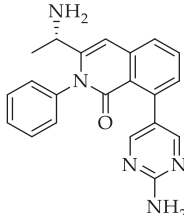ell), and HepG2 (hepatic carcinoma cell) to evaluate the effect of different pyrimidinyl groups on (*S*)-3-(1-aminoethyl)-8-chloro-2-phenylisoquinolin-1(2*H*)-one **1** (Table 4). The cell toxicity data of compounds **1**, **3a**–**3k** for MDA-MB 231, HeLa, HepG2 were de-scribed in Supplementary Materials Figures S23–S34.

Table 3. Various 8-pyrimidinyl-2-phenylisoquinolin-1(2*H*)-one derivatives **3** *.

3a 98% [a]	**3b** 97% [a]	**3c** 95% [b]	**3d** 45% [b]
3e 91% [b]	**3f** 95% [b]	**3g** 94% [c]	**3h** 61% [b]
3i 87% [a]	**3j** 92% [a]	**3k** 40% [d]	

* Reaction conditions: **1** (1.67 mmol), boronic acid or Pinacol boronate (2.0 mmol), Pd(PPh$_3$)$_2$Cl$_2$ (0.5~5 mol%), Sphos (1.5–15 mol%), K$_2$CO$_3$ (5.0 mmol), 12 hr, THF (5 mL)/H$_2$O (5 mL), Isolated yield. [a] boronic acid (2.0 mmol), Pd(PPh$_3$)$_2$Cl$_2$ (0.5 mol%), Sphos (1.5 mol%). [b] boronic acid (2.0 mmol), Pd(PPh$_3$)$_2$Cl$_2$ (5 mol%), Sphos (15 mol%) [c] Pinacol boronate (2.0 mmol), Pd(PPh$_3$)$_2$Cl$_2$ (1.0 mol%), Sphos (3 mol%). [d] Pinacol boronate (2.0 mmol), Pd(PPh$_3$)$_2$Cl$_2$ (5 mol%), Sphos (15 mol%).

Table 4. Selected IC$_{50}$ values of **3** against different cancer cell lines.

Entry	Compound	MDA-MB231 IC$_{50}$ (μM) [a]	HeLa IC$_{50}$ (μM) [a]	HepG2 IC$_{50}$ (μM) [a]
1	**1**	ND [b]	ND [b]	ND [b]
2	**3a**	ND [b]	5.07 ± 0.13	2.20 ± 0.26
3	**3b**	2.28 ± 0.10	1.55 ± 0.15	2.01 ± 0.05
4	**3c**	2.83 ± 0.10	1.86 ± 0.12	1.79 ± 0.13
5	**3d**	ND [b]	2.07 ± 0.46	4.85 ± 0.21
6	**3e**	ND [b]	2.12 ± 0.17	5.12 ± 0.23
7	**3f**	ND [b]	5.38 ± 0.22	5.22 ± 0.23
8	**3g**	5.25 ± 0.09	2.43 ± 0.25	5.27 ± 0.39
9	**3h**	2.72 ± 0.24	1.94 ± 0.11	2.93 ± 0.10
10	**3i**	2.29 ± 0.11	1.42 ± 0.19	3.08 ± 0.20
11	**3j**	1.62 ± 0.12	1.11 ± 0.70	3.87 ± 1.58
12	**3k**	1.18 ± 0.08	1.99 ± 0.28	1.57 ± 0.17

[a] MTT assay. [b] ND: Not determined. At the 10 μM, less than 50% cell death was observed. The viability test was performed in triplicate and repeated at least three times. The cell viability represents the mean ± SD from three independent experiments.

Compound **1** without a pyrimidine substituent showed less than 50% cell death in MDA-MB-231, HeLa, and HepG2 cells at a concentration of 10 μM, so its IC$_{50}$ value could not be determined. However, compound **3** substituted with various pyrimidines showed excellent cytotoxic activity in tumor cell lines. Since in MDA-MB-231 simple pyrimidinyl (**3e**), 4-methylpyrimidinyl (**3f**), 4-methoxypyrimidinyl (**3a**), or 2,4-dimethoxypyrimidinyl (**3d**) compounds had no cytotoxic activity, their IC$_{50}$ values could not be determined. On the other hand, 4-alkoxypyrimidinyl (**3b,3c**), 4-aminopyrimidinyl (**3h,3i**), 4-piperidinopyrimidinyl (**3j**), and 4-cyanopyrimidinyl (**3k**) compounds showed strong anticancer activity. In particular, the cytotoxic activity increased as the alkyl chain of the alkoxy substituent in the 4-alkoxypyrimidinyl compounds increased (**3a** < **3b,3c**). These results indicate that the cytotoxic activity of the novel synthetic 8-pyrimidinylisoquinolinones **3a–3k** on cancer cells was slightly different depending on the type of cell. Although cell viability assays, such as the MTT assay, alone cannot fully explain these results, overall cytotoxicity appears to be dependent on the polarity of the compound. In HeLa and HepG2 cells, all pyrimidine-substituted isoquinolinones **3a–3k** showed excellent cytotoxic activity. Although all compounds showed good cytotoxic activity, 4-alkoxypyrimidinyl (**3b**, **3c**), 4-aminopyrimidinyl (**3h**, **3i**), 4-piperidinopyrimidinyl (**3j**), and 4-cyanopyrimidinyl (**3k**) compounds showed higher activity than others. In particular, compound **3k**, which has an electron-withdrawing group (CN) in a pyrimidine ring, showed the lowest IC$_{50}$ value under this condition.

3. Materials and Methods

3.1. General

All commercially available materials from Sigma-Aldrich (Burlington, MA, USA), Daejung (Siheung, Korea), TCI (Tokyo, Japan), Chemieliva (Chongqing, China) and solvents were used without further purification. All small-scale screening reactions (≤10 mL of solvent) were performed in 50 mL round bottom flasks on a Radleys Carousel 6 Plus Reaction Station under an air atmosphere. HPLC was performed on a Hitachi LaChrom Elite HPLC system. ^{1}H NMR (400 MHz) and ^{13}C NMR (100 MHz) were measured on a Bruker Avance 400 spectrometer system. ^{1}H NMR spectra chemical shifts were expressed in parts per million (ppm) downfield from tetramethylsilane, and coupling constants were reported in Hertz (Hz). Splitting patterns are indicated as follows: s, singlet; d, doublet; t, triplet; and q, quartet; m, multiplet. ^{13}C NMR spectra were reported in ppm, referenced to deuterochloroform (77.16 ppm). Melting points were determined by DSC (Mettler Toledo). High resolution mass spectra (HRMS, JEOL MStation JMS-700) were obtained using an electron impact (EI) ionization technique (magnetic sector—electric sector double focusing mass analyzer) from the KBSI (Korea Basic Science Institute Daegu Center).

3.2. General Procedure for the Suzuki-Miyaura Coupling Reactions (**3a~3k**)

Suzuki–Miyaura coupling reactions (Table 3) were typically performed on a 1.67 mmol scale of the aryl halide **1**. A mixture of (*S*)-3-(1-aminoethyl)-8-chloro-2-phenylisoquinolin-1(2*H*)-one **1** (0.5 g, 1.67 mmol), 2-substituted pyrimidinyl boronic acid or 2-substituted pyrimidinyl pinacol boronate **2** (1.2 equiv, 2 mmol), K$_2$CO$_3$ (0.3 g, 2.17 mmol), Pd(PPh$_3$)$_2$Cl$_2$ (0.50–5 mol%), and Sphos (1.5–15 mol%) in mixed solvent (THF 5 mL, water 5 mL) was stirred at 65 °C in 50 mL round bottom flasks for 12 h. After the biphasic reaction solution was cooled to room temperature, the organic layer was separated. The organic layer was concentrated under vacuum and diluted with CH$_2$Cl$_2$ (20 mL) and 0.3 N HCl (20 mL). The aqueous layer was separated and washed with CH$_2$Cl$_2$ (20 mL). The aqueous layer was basified with aqueous NH$_4$OH (1 mL) and extracted two times with CH$_2$Cl$_2$ (2 × 20 mL). The organic phase was concentrated under vacuum. Further purification of product was isolated from a flash chromatography using silica gel (300–400 mesh) with CH$_2$Cl$_2$–methanol as an eluent.

3-[(1*S*)-1-aminoethyl]-8-(2-methoxypyrimidin-5-yl)-2-phenyl-isoquinolin-1-one (**3a**). White solid, [α]$_D^{20}$ −1.33 (c 0.01, CH$_3$CN), mp 210–214 °C. 610 mg, 98% yield. ^{1}H NMR (400 MHz, CDCl$_3$) δ 8.45 (s, 2H), 7.62–7.70 (m, 2H), 7.47–7.51 (m, 2H), 7.40–7.44 (m, 1H),

7.19–7.23 (m, 3H), 6.84 (s, 1H), 3.98 (s, 1H), 3.69 (q, J = 6.5 Hz, 1H), 1.53 (s, 2H), 1.28 (d, J = 6.5 Hz, 3H). ^{13}C NMR (100 MHz, CDCl$_3$) δ 164.3, 162.9, 157.9, 149.8, 139.0, 138.1, 137.2, 132.0, 130.5, 130.0, 129.8, 129.7, 129.2, 128.9, 128.7, 127.3, 122.1, 102.1, 54.8, 54.8, 46.9, 23.7 HRMS (EI$^+$): *m*/*z* [M + H] + calcd for C$_{22}$H$_{20}$N$_4$O$_2$ 372.1586, found 372.1584.

3-[(1*S*)-1-aminoethyl]-8-(2-ethoxypyrimidin-5-yl)-2-phenyl-isoquinolin-1-one (**3b**). White solid, $[\alpha]_D^{20}$ −3.51 (c 0.01, CH$_3$CN), mp 185–188 °C. 629 mg, 97% yield. ^{1}H NMR (400 MHz, CDCl$_3$) δ 8.44 (s, 2H), 7.60–7.69 (m, 2H), 7.47–7.51 (m, 2H), 7.40–7.44 (m, 1H), 7.19–7.23 (m, 3H), 6.83 (s, 1H), 4.39 (q, J = 7.1 Hz, 2H), 3.69 (q, J = 6.5 Hz, 1H), 1.41 (t, J = 7.1 Hz, 3H), 1.34 (s, 2H), 1.28 (d, J = 6.5 Hz, 3H). ^{13}C NMR (100 MHz, CDCl$_3$) δ 164.0, 162.9, 157.90, 149.8, 139.0, 138.1, 137.4, 132.0, 130.5, 129.8, 129.7, 129.3, 128.9, 128.7, 127.2, 122.1, 102.1, 63.3, 46.9, 23.7, 14.6 HRMS (EI$^+$): *m*/*z* [M + H] + calcd for C$_{23}$H$_{22}$N$_4$O$_2$ 386.1743, found 386.1743.

3-[(1*S*)-1-aminoethyl]-8-(2-isopropoxypyrimidin-5-yl)-2-phenyl-isoquinolin-1-one (**3c**). White solid, $[\alpha]_D^{20}$ −0.99 (c 0.01, CH$_3$CN), mp 142–148 °C. 638 mg, 95% yield. ^{1}H NMR (400 MHz, CDCl$_3$) δ 8.43 (s, 2H), 7.62–7.70 (m, 2H), 7.47–7.51 (m, 2H), 7.40–7.44 (m, 1H), 7.19–7.23 (m, 3H), 6.83 (s, 1H), 5.25(m, J = 6.2 Hz, 1H), 3.70 (q, J = 6.5 Hz, 1H), 1.52 (s, 2H), 1.37 (d, J = 6.2 Hz, 6H), 1.28 (d, J = 6.5 Hz, 3H). ^{13}C NMR (100 MHz, CDCl$_3$) δ 163.6, 163.0, 158.0, 149.7, 139.0, 138.2, 137.5, 132.0, 130.6, 129.9, 129.8, 129.6, 129.3, 128.9, 128.8, 127.2, 122.1, 102.1, 70.0, 46.9, 23.7, 22.1 HRMS (EI$^+$): *m*/*z* [M + H] + calcd for C$_{24}$H$_{24}$N$_4$O$_2$ 400.1899, found 400.1902.

3-[(1*S*)-1-aminoethyl]-8-(2,4-dimethoxypyrimidin-5-yl)-2-phenyl-isoquinolin-1-one (**3d**). White solid, $[\alpha]_D^{20}$ −1.82 (c 0.01, CH$_3$CN), 303 mg, 45% yield. ^{1}H NMR (400 MHz, CDCl$_3$) δ 8.04 (s, 1H), 7.65 (m, 1H), 7.58 (m, 1H), 7.43–7.50 (m, 3H), 7.19 (m, 3H), 6.79 (s, 0.5H), 6.75 (s, 0.5H), 3.95 (s, 3H), 3.87 (s, 0.5H), 3.85 (s, 0.5H), 3.67 (m, J = 6.3 Hz, 1H), 1.44 (s, 2H), 1.30 (d, J = 6.4 Hz, 1.5H), 1.26 (d, J = 6.4 Hz, 1.5H). ^{13}C NMR (100 MHz, CDCl$_3$) δ 168.6, 164.6, 162.8, 184.7, 154.6, 149.4, 149.3, 138.5, 138.4, 135.4, 132.1, 130.0, 130.0, 129.9, 129.8, 129.4, 129.2, 129.0, 128.9, 128.7, 127.0, 123.6, 123.5, 118.8, 102.0, 101.9, 54.7, 53.9, 47.0, 46.9, 23.8, 23.4 HRMS (EI$^+$): *m*/*z* [M + H] + calcd for C$_{23}$H$_{22}$N$_4$O$_3$ 402.1692, found 402.1689.

3-[(1*S*)-1-aminoethyl]-2-phenyl-8-pyrimidin-5-yl-isoquinolin-1-one (**3e**). White solid, $[\alpha]_D^{20}$ −2.24 (c 0.01, CH$_3$CN), mp 205–209 °C. 522 mg, 91% yield. ^{1}H NMR (400 MHz, CDCl3) δ 9.08 (s, 1H), 8.68 (s, 2H), 7.66–7.73 (m, 2H), 7.47–7.51 (m, 2H), 7.40–7.44 (m, 1H), 7.19–7.22 (m, 3H), 6.86 (s, 1H), 3.70 (q, J = 6.5 Hz, 1H), 2.12 (s, 2H), 1.28 (d, J = 6.5 Hz, 3H). ^{13}C NMR (100 MHz, CDCl$_3$) δ 162.8, 156.7, 155.6, 150.1, 139.0, 138.0, 137.0, 136.7, 132.0, 130.4, 129.9, 129.8, 129.2, 128.9, 128.7, 127.7, 122.1, 102.1, 46.9, 23.7 HRMS (EI$^+$): *m*/*z* [M + H] + calcd for C$_{21}$H$_{18}$N$_4$O 342.1481, found 342.1484.

3-[(1*S*)-1-aminoethyl]-8-(2-methylpyrimidin-5-yl)-2-phenyl-isoquinolin-1-one (**3f**). White solid, $[\alpha]_D^{20}$ −1.55 (c 0.01, CH$_3$CN), mp 221–237 °C. 567 mg, 95% yield. ^{1}H NMR (400 MHz, CDCl$_3$) δ 8.58 (s, 2H), 7.63–7.71 (m, 2H), 7.46–7.50 (m, 2H), 7.39–7.43 (m, 1H), 7.19–7.22 (m, 3H), 6.84 (s, 1H), 3.70 (q, J = 6.5 Hz, 1H), 2.71 (s, 3H), 1.50 (s, 2H), 1.28 (d, J = 6.5 Hz, 3H). ^{13}C NMR (100 MHz, CDCl$_3$) δ 165.7, 162.84, 155.6, 149.9, 139.0, 138.1, 137.3, 133.3, 13, 130.4, 129.8, 129.7, 129.2, 128.9, 128.7, 127.5, 122.1, 102.0, 46.9, 25.8, 23.7 HRMS (EI$^+$): *m*/*z* [M + H] + calcd for C$_{22}$H$_{20}$N$_4$O 356.1637, found 356.1639.

3-[(1*S*)-1-aminoethyl]-8-[2-(1-hydroxy-1-methyl-ethyl)pyrimidin-5-yl]-2-phenyl-isoquinolin-1-one (**3g**). White solid, $[\alpha]_D^{20}$ −2.44 (c 0.01, CH$_3$CN), mp 216–220 °C. 629 mg, 94% yield. ^{1}H NMR (400 MHz, CDCl$_3$) δ 8.68 (s, 2H), 7.68–7.75 (m, 2H), 7.50–7.52 (m, 2H), 7.44–7.47 (m, 1H), 7.21–7.24 (m, 3H), 6.88 (s, 1H), 3.71 (q, J = 6.5 Hz, 1H), 1.62 (s, 6H), 1.30 (d, J = 6.5 Hz, 3H). ^{13}C NMR (100 MHz, CDCl$_3$) δ 171.8, 162.9, 155.6, 150.1, 139.1, 138.1, 137.0, 134.1, 132.1, 130.8, 129.9, 129.2, 129.1, 128.7, 127.8, 122.1, 102.2, 73.1, 46.9, 30.0, 23.8 HRMS (EI$^+$): *m*/*z* [M + H] + calcd for C$_{24}$H$_{24}$N$_4$O$_2$ 400.1899, found 400.1898.

3-[(1*S*)-1-aminoethyl]-8-(2-aminopyrimidin-5-yl)-2-phenyl-isoquinolin-1-one (**3h**). White solid, $[\alpha]_D^{20}$ −1.83 (c 0.01, CH$_3$CN), mp 242–247 °C. 365 mg, 61% yield. 1H NMR (400 MHz, CDCl$_3$) δ 8.27 (s, 2H), 7.63–7.67 (m, 1H), 7.59–7.57 (m, 1H), 7.46–7.51 (m, 2H),7.40–7.43 (m, 1H), 7.19–7.23 (m, 3H), 6.80 (s, 1H), 5.11(s, 2H), 3.68 (q, J = 6.5 Hz, 1H), 1.47 (s, 2H), 1.27 (d, J = 6.5 Hz, 3H). ^{13}C NMR (100 MHz, CDCl$_3$) δ 163.0, 161.6, 157.2, 149.7, 139.0, 138.3, 138.2,

132.0, 130.4, 129.8, 129.7, 129.3, 128.8, 126.8, 126.6, 122.1, 102.1, 46.9, 23.7 HRMS (EI⁺): *m/z* [M + H] + calcd for $C_{21}H_{19}N_5O$ 357.1590, found 357.1593.

3-[(1*S*)-1-aminoethyl]-8-[2-(dimethylamino)pyrimidin-5-yl]-2-phenyl-isoquinolin-1-one (**3i**). White solid, $[\alpha]_D^{20}$ −7.03 (c 0.01, CH₃CN), mp 244–248 °C. 563 mg, 87% yield. ¹H NMR (400 MHz, CDCl₃) δ 8.30 (s, 2H), 7.62–7.66 (m, 1H), 7.54–7.56 (m, 1H), 7.45–7.49 (m, 2H), 7.38–7.42 (m, 1H), 7.19–7.22 (m, 3H), 6.78 (s, 1H), 3.68 (q, J = 6.5 Hz, 1H), 3.16 (s, 6H), 1.52 (s, 2H), 1.27 (d, J = 6.5 Hz, 3H). ¹³C NMR (100 MHz, CDCl₃) δ 163.0, 161.0, 156.7, 154.9, 149.4, 139.0, 138.9, 138.4, 132.0, 130.3, 129.7, 129.7, 129.4, 128.9, 128.7, 126.4, 123.6, 122.0, 102.0, 46.9, 37.3, 23.6 HRMS (EI⁺): *m/z* [M + H] + calcd for $C_{23}H_{23}N_5O$ 385.1903, found 385.1905.

3-[(1*S*)-1-aminoethyl]-2-phenyl-8-[2-(1-piperidyl)pyrimidin-5-yl]isoquinolin-1-one (**3j**). White solid, $[\alpha]_D^{20}$ −5.03 (c 0.01, CH₃CN), 655 mg, 92% yield. ¹H NMR (400 MHz, CDCl₃) δ 8.28 (s, 2H), 7.62–7.65 (m, 1H), 7.53–7.56 (m, 1H), 7.46–7.50 (m, 2H), 7.39–7.43 (m, 1H), 7.19–7.23 (m, 3H), 6.78 (s, 1H), 3.76 (t, J = 4.9 Hz, 4H), 3.69 (q, J = 6.5 Hz, 1H), 1.58-1.64 (m, 8H), 1.27 (d, J = 6.5 Hz, 3H). ¹³C NMR (100 MHz, CDCl₃) δ 163.0, 160.4, 156.8, 149.4, 139.0, 138.9, 138.4, 132.0, 130.0, 129.8, 129.7, 129.4, 128.9, 128.8, 126.4, 123.8, 122.0, 102.1, 46.9, 44.8, 25.9, 24.9, 23.6 HRMS (EI⁺): *m/z* [M + H] + calcd for $C_{26}H_{27}N_5O$ 425.2216, found 425.2212.

5-[3-[(1*S*)-1-aminoethyl]-1-oxo-2-phenyl-8-isoquinolyl]pyrimidine-2-carbonitrile (**3k**). White solid, $[\alpha]_D^{20}$ −3.54 (c 0.01, CH₃CN), 246 mg, 40% yield. ¹H NMR (400 MHz, CDCl₃) δ 8.74 (s, 2H), 7.74–7.75 (m, 2H), 7.42–7.52 (m, 3H), 7.20–7.21 (m, 3H), 6.91 (s, 1H), 3.71 (q, J = 6.3 Hz, 1H), 1.47 (s, 2H), 1.28 (d, J = 6.3 Hz, 3H). ¹³C NMR (100 MHz, CDCl₃) δ 162.8, 156.5, 150.5, 142.7, 139.2, 139.2, 137.7, 135.2, 132.2, 130.1, 130.0, 129.9, 129.2, 129.0, 128.7, 128.5, 121.8, 116.1, 102.3, 46.9, 24.9, 23.8 HRMS (EI⁺): *m/z* [M + H] + calcd for $C_{22}H_{17}N_5O$ 367.1433, found 367.1435.

3.3. Scale up Procedure for the Synthesis of 3-[(1S)-1-Aminoethyl]-8-(2-Methoxypyrimidin-5-yl)-2-Phenyl-Isoquinolin-1-one (*3a*)

In a 2 L three-neck round-bottom flask equipped with a condenser, a mechanical stirrer, and a thermometer maintained under air atmosphere was charged with (S)-3-(1-aminoethyl)-8-chloro-2-phenylisoquinolin-1(2H)-one **1** (100.0 g, 334.7 mmol), (2-methoxypyrimidin-5-yl)boronic acid **2a** (61.8 g, 401.6 mmol), Pd (PPh₃)₂Cl₂ (1.172 g, 0.5 mol%), Sphos (2.06 g, 1.5 mol%), K₂CO₃ (60.1 g, 435 mmol), THF (500 mL), and H₂O (500 mL). The reaction mixture was well-stirred (120 rpm) under reflux at 65 °C for 12 h. After the biphasic reaction solution was cooled to room temperature, the organic layer was separated. The organic layer was concentrated under vacuum and diluted with CH₂Cl₂ (1000 mL), H₂O (1000 mL), and conc. HCl (100 mL). The mixture was well-stirred (160 rpm) and left for 10 min. The aqueous layer was separated and washed with CH₂Cl₂ (500 mL). The aqueous layer was filtered and basified with NH₄OH (200 mL). The mixture was extracted two times with CH₂Cl₂ (2 × 1000 mL). The combined organic layer was concentrated in vacuo. The concentrated product was recrystallized with ethyl acetate (250 mL) and added n-heptane (500 mL). The mixture was stirred at room temperature for 1hr, and the solid was collected by filtration and dried to give **3a** (118.3 g, 94.9%) as a white solid.

3.4. Cell Culture and Viability Assay

Three types of human cancer cell lines, such as MDA-MB-231 (metallic breast cancer cells), HeLa (cervical epithelial carcinoma cell), and HepG2 (hepatic carcinoma cell), were cultured with Dulbecco's Modified Eagle Medium (DMEM, Welgene, Seoul, Korea) with 10% fetal bovine serum (FBS), 2 mM glutamine, and 100 units/mL antibiotics (Gibco BRL, Rockville, MD). The cells were incubated at 37 °C in a humidity atmosphere of 5% (*v/v*) air/CO₂. Cells for in vitro MTT assay were inoculated into 3 × 10⁵ cells/well in a 96-cell culture palate and were stored for 24 h in a 5% CO₂ incubator at 37 °C. Then, the cells were treated with indicated-differential concentrations of newly synthetic samples. After incubation for 24 h, 10 μL of the EZ cytox (DogenBio, Seoul, Korea) was added to each well, and the sample was further incubated for 30 min at 37 °C and 5% CO₂ according to the manufacturer's recommendation. The value of the cell viability was determined by

measuring the formazan production with a micro-plate UV-spectrophotometer (Thermo Fisher Scientific, Waltham, MA, USA) at an absorbance of 450 nm.

4. Conclusions

In this study, we developed an effective method of introducing various pyrimidine groups into (*S*)-3-(1-aminoethyl)-8-chloro-2-phenylisoquinolin-1(*2H*)-one (**1**) via SMC to provide new pyrimidine-substituted isoquinoline derivatives **3**. To evaluate the activity of the compounds **3**, their cell viability (IC$_{50}$) was measured in cancer cell lines of MDA-MB-231, HeLa, and HepG2. From the antitumor activity of compounds **3**, it was found that antitumor activity was increased when various pyrimidine rings were introduced instead of Cl at position 8 of the isoquinoline derivative **1**. This is further evidence that the pyrimidine functional group is a very good pharmacophore. In the future, we hope to identify more novel compounds with enhanced pharmacological activity using this synthetic method.

Supplementary Materials: The following are available online at https://www.mdpi.com/article/10.3390/ph15010064/s1. Analytical data for synthesized compounds. ^{1}H NMR, ^{13}C NMR for compounds **3a–3k**: Figure S1–S22; Cell toxicity data of compounds 1, **3a–3k** for MDA-MB 231, HeLa, HepG2: Figure S23–S34.

Author Contributions: Conceptualization, H.K. and T.H.L.; methodology, O.K.C. and Y.H.S.; software, O.K.C.; validation, J.K.L. and H.L.; bioassay analysis, T.H.L.; investigation, O.K.C.; data curation, O.K.C. and H.L.; writing—original draft preparation, O.K.C.; writing—review and editing, H.K. All authors have read and agreed to the published version of the manuscript.

Funding: This research was funded by the GRRC Program of Gyeonggi province (GRRC-KyungHee 2020(B04)), Korea.

Institutional Review Board Statement: Not applicable.

Informed Consent Statement: Not applicable.

Data Availability Statement: Data are contained within the article.

Conflicts of Interest: The authors declare no conflict of interest.

References

1. Glushkov, V.A.; Shklyaev, Y.V. Synthesis of 1(2H)-isoquinolones. *Chem. Heterocycl. Compd.* **2001**, *37*, 663. [CrossRef]
2. Matsui, T.; Sugiura, T.; Nakui, H.; Iguch, S.; Shigeoka, S.; Tukedu, H.; Odagaki, T.; Ushio, Y.; Ohmoto, K.; Iwamani, M.; et al. Novel 5-HT3A ntagonists. Isoquinolinones and 3-Aryl-2-pyridones. *J. Med. Chem.* **1992**, *35*, 3307. [CrossRef] [PubMed]
3. Chao, Q.; Deng, L.; Shih, H.; Leoni, L.M.; Genini, D.; Carson, D.A.; Cottam, H.B. Substituted Isoquinolines and Quinazolines as Potential Antiinflammatory Agents. Synthesis and Biologocal Evaluation of Inhibitors of Tumor Necrosis Factor α. *J. Med. Chem.* **1999**, *42*, 3860–3873. [CrossRef] [PubMed]
4. Evans, C.A.; Liu, T.; Lescarbeau, A.; Nair, S.J.; Grenier, L.; Pradeilles, J.A.; Glenadel, Q.; Tibbitts, T.; Rowley, A.M.; DiNitto, J.P.; et al. Discovery of a Selective Phosphoinositide-3-Kinase (PI3K)-γ Inhibitor (IPI-549) as an Immuno-Oncology Clinical Candidate. *ACS Med. Chem. Lett.* **2016**, *7*, 862–867. [CrossRef]
5. Kang, B.R.; Shan, A.L.; Li, Y.P.; Xu, J.; Lu, S.M.; Zhang, S.Q. Discovery of 2-aryl-8-hydroxy (or methoxy)-isoquinolin-1 (2H)-ones as Novel EGFR Inhibitor by Scaffold Hopping. *Bioorg. Med. Chem.* **2013**, *21*, 6956–6964. [CrossRef]
6. Rodrigues, D.A.; Sagrillo, F.S.; Fraga, C.A.M. Duvelisib: A 2018 Novel FDA-Approved Small Molecule Inhibiting Phosphoinositide 3-Kinases. *Pharmaceuticals* **2019**, *12*, 69. [CrossRef]
7. Son, M.K.; Jeon, B.; Wang, J.S.; Kim, B.K.; Lee, B.R.; Choi, Y.S.; Kim, N.H.; Myung, J.; Kim, D.H. BR101801: A first-in-class dual inhibitor of PI3Kδ and DNA-PK in non-Hodgkin's lymphoma. *Cancer Res.* **2018**, *78*, 871. [CrossRef]
8. Flesher, J.L.; Jahid, S.; Ortega, J.A.; Sala, G.L.; Brindani, N.; Arencibia, J.M.; Manigrasso, J.; Hachey, S.; Chen, C.; Hughes, C.; et al. Structure-based design of CDC42/RHOJ effector inhibitors for the treatment of cancer. *Cancer Res.* **2020**, *80*, 5324. [CrossRef]
9. Byth, K.F.; Thomas, A.; Hughes, G.; Forder, C.; McGregor, A.; Geh, C.; Oakes, S.; Green, C.; Walker, M.; Newcombe, N.; et al. AZD5438, a Potent Oral Inhibitor of Cyclin-Dependent Kinases 1, 2, And 9, Leads to Pharmacodynamic Changes and Potent Antitumor Effects in Human Tumor Xenografts. *Mol. Cancer Ther.* **2009**, *8*, 1856–1866. [CrossRef] [PubMed]
10. Heffron, T.P.; Ndubaku, C.O.; Salphati, L.; Alicke, B.; Cheong, J.; Drobnick, J.; Edgar, K.; Gould, S.E.; Lee, L.B.; Lesnick, J.D.; et al. Discovery of Clinical Development Candidate GDC-0084, a Brain Penetrant Inhibitor of PI3K and mTOR. *ACS Med. Chem. Lett.* **2016**, *7*, 351–356. [CrossRef]

11. Roy, D.; Uozumi, Y. Recent Advances in Palladium-Catalyzed Cross-Coupling Reactions at ppm to ppb Molar Catalyst Loadings. *Adv. Synth. Catal.* **2018**, *360*, 620. [CrossRef]

12. Littke, A.F.; Dai, C.; Fu, G.C. Versatile Catalysts for the Suzuki Cross-Coupling of Arylboronic Acids with Aryl and Vinyl Halides and Triflates under Mild Conditions. *J. Am. Chem. Soc.* **2000**, *122*, 4020–4028. [CrossRef]

13. Ashworth, I.W.; Campbell, A.D.; Cherryman, J.H.; Clark, J.; Crampton, A.; Eden-Rump, E.G.; Evans, M.; Jones, M.F.; McKeever-Abbas, S.; Meadows, R.E.; et al. Process development of a Suzuki reaction used in the manufacture of lanabecestat. *Org. Process Res. Dev.* **2018**, *22*, 1801–1808. [CrossRef]

14. Irfan, M.; Fuchs, M.; Glasnov, T.N.; Kappe, C.O. Microwave-Assisted Cross-Coupling and Hydrogenation Chemistry by Using Heterogeneous Transition-Metal Catalysts: An Evaluation of the Role of Selective Catalyst Heating. *Chem. Eur. J.* **2009**, *15*, 11608–11618. [CrossRef]

15. Lee, G.H.; Lim, H.J.; Cho, H.Y.; Park, W.K.; Kim, S.H.; Choi, J.H. Heteroaryl Derivative or Pharmaceutically Acceptable Salt Thereof, Preparation Method Therefor, and Pharmaceutical Composition for Preventing or Treating Diseases Associated with Pi3 Kinases, Containing Same as Active Ingredient. U.S. Patent WO2016204429, 22 December 2016.

16. Knapp, D.M.; Gillis, E.P.; Burke, M.D. A General Solution for Unstable Boronic Acids: Slow-Release Cross-Coupling from Air-Stable MIDA Boronates. *J. Am. Chem. Soc.* **2009**, *131*, 6961–6963. [CrossRef]

17. Bender, A.M.; Chopko, T.C.; Bridges, T.M.; Lindsley, C.W. Preparation of Unsymmetrical 1,2,4,5-Tetrazines via a Mild Suzuki Cross-Coupling Reaction. *Org. Lett.* **2017**, *19*, 5693–5696. [CrossRef]

18. Takahashi, R.; Kubota, K.; Ito, H. Air- and Moisture-Stable Xantphos-Ligated Palladium Dialkyl Complex as a Precatalyst for Cross-Coupling Reactions. *Chem. Commun.* **2020**, *56*, 407–410. [CrossRef]

19. Martin, R.; Buchwald, S.L. Palladium-Catalyzed Suzuki-Miyaura Cross-Coupling Reactions Employing Dialkylbiaryl Phosphine Ligands. *Acc. Chem. Res.* **2008**, *41*, 1461–1473. [CrossRef] [PubMed]

20. Wolfe, J.P.; Singer, R.A.; Yang, B.H.; Buchwald., S.L. Highly Active Palladium Catalysts for Suzuki Coupling Reactions. *J. Am. Chem. Soc.* **1999**, *121*, 9550–9561. [CrossRef]

21. Billingsley, K.; Buchwald, S.L. Highly Efficient Monophosphine-Based Catalyst for the Palladium-Catalyzed Suzuki-Miyaura Reaction of Heteroaryl Halides and Heteroaryl Boronic Acids and Esters. *J. Am. Chem. Soc.* **2007**, *129*, 3358–3366. [CrossRef] [PubMed]

Article

C-Myc Expression in Oral Squamous Cell Carcinoma: Molecular Mechanisms in Cell Survival and Cancer Progression

Guya Diletta Marconi [1], Ylenia Della Rocca [2], Luigia Fonticoli [2], Francesco Melfi [3], Thangavelu Soundara Rajan [4,5], Simone Carradori [3], Jacopo Pizzicannella [6,*], Oriana Trubiani [2,†] and Francesca Diomede [2,†]

[1] Department of Medical, Oral and Biotechnological Sciences, University "G. d'Annunzio" Chieti-Pescara, Via dei Vestini, 31, 66100 Chieti, Italy; guya.marconi@unich.it

[2] Department of Innovative Technologies in Medicine & Dentistry, University "G. d'Annunzio" Chieti-Pescara, Via dei Vestini, 31, 66100 Chieti, Italy; ylenia.dellarocca@unich.it (Y.D.R.); luigia.fonticoli@unich.it (L.F.); oriana.trubiani@unich.it (O.T.); francesca.diomede@unich.it (F.D.)

[3] Department of Pharmacy, University "G. d'Annunzio" Chieti-Pescara, Via dei Vestini 31, 66100 Chieti, Italy; francesco.melfi@unich.it (F.M.); simone.carradori@unich.it (S.C.)

[4] Department of Biotechnology, Karpagam Academy of Higher Education, Coimbatore 641021, India; drsoundararajan.t@kahedu.edu.in

[5] Karpagam Cancer Research Centre, Karpagam Academy of Higher Education, Coimbatore 641021, India

[6] Ss. Annunziata Hospital, ASL 02 Lanciano-Vasto-Chieti, 66100 Chieti, Italy

* Correspondence: jacopo.pizzicannella@unich.it

† These authors contributed equally to this work.

Abstract: Oral squamous cell carcinoma (OSCC) represents 90% of malignant epithelial cancer that occurs in the oral cavity. The c-Myc factor is expressed in multiple types of cancer, comprising head and neck squamous cell carcinoma (HNSCC), where it plays a fundamental role in tumor prognosis and in the self-renewal of tumor stem cells. However, the role of c-Myc in controlling OSCC cells is not well-known. The aim of the present study is the evaluation of the biological roles and regulatory mechanism of c-Myc in the pathogenesis of OSCC. Results indicated that c-Myc, c-Jun, Bcl-2, hypoxia inducible factor-1α (HIF-1α), vascular endothelial growth factor (VEGF), matrix metalloproteinase-9 (MMP-9), ERK 1/2 and pERK1/2 were overexpressed in a cellular model of squamous cell carcinoma, Cal-27. Doxorubicin (Doxo), a common chemotherapeutic agent, inhibited cell invasion, hypoxia, angiogenesis and inflammation in a cellular model of Cal-27 cells as indicated by downregulation of MMP-9, VEGF, ERK 1/2 and pERK 1/2 as well as promoted apoptosis as evidenced by the downregulation of Bcl-2 protein. This work aimed at underlying the functional relevance of c-Myc in OSCC and the HIF-Myc collaboration by integrating the knowledge on this molecular link in an OSCC tumor microenvironment. The results obtained showed for the first time the vital role of c-Myc in Cal-27 in cell survival/proliferation and tumor growth as well as the negative regulatory effect of Doxo against c-Myc signaling pathway.

Keywords: squamous cell carcinoma; doxorubicin; tumor microenvironment; c-Myc; Cal-27

1. Introduction

Head and neck squamous cell carcinomas (HNSCCs) have a great incidence worldwide, with a mortality rate of 40–50%. The tumors initiate in the epithelial cells of the mucosal layers in the oral cavity, oropharynx, larynx or hypopharynx [1] and they represent the most widespread malignancies that originate in the head and neck. Head and neck carcinoma is notably heterogeneous and is characterized by different etiologies and molecular alterations [2]. Different therapeutic approaches such as chemotherapy, radiotherapy and surgery are used to treat this complex malignancy. Due to the lack of efficient therapeutic approaches, the necessity to find a valuable target molecule against HNSCCs is strongly needed. c-Fos upregulation has been found in HNSCC cells and clinical data suggest that

c-Fos may be associated with lymph node metastasis in oral cancer [3,4]. c-Fos is a proto-oncogene that encodes for a nuclear DNA-binding protein, which then dimerizes with the c-Jun gene product and finally forms the transcription factor 1 activating protein (AP-1). Since the c-Fos protein is a member of the AP-1 family, it is mainly associated with signal transduction and cell differentiation/proliferation [5]. Furthermore, c-Fos is associated with lymphonoidal metastatic progression and poor differentiation, mainly in coexpression with c-Jun, especially the simultaneous co-expression of c-Jun/c-Fos/p53 in oral cell squamous carcinoma (OSCC) has been identified as a prognostic factor for survival [4]. c-Myc proto-oncogene is correlated with c-Fos and c-Jun in gene regulation for cell proliferation and this protein has many unusual features that are shared by some other oncogenes such as c-Fos. Myc, a multifunctional transcription factor, regulates many genes involved in multiple biological processes such as cell growth, proliferation and apoptosis. Moreover, it promotes invasion events by activating MEK–ERK pathways [6–8]. It is well-known that c-Myc is expressed in many different types of cancer, including HNSCCs, in which c-Myc overexpression is responsible for poor tumor prognosis as well as the self-renewal of tumor stem cells [9,10]. Based on the literature, oncogenic c-Myc has been shown to be necessary to maintain the constitutive level of hypoxia inducible factor-1α (HIF-1α) protein in multiple myeloma (MM) cells, and thus influences VEGF secretion and angiogenic activity [11]. The present work was aimed at studying the underlying functional relevance of c-Myc in OSCC and in the HIF-Myc collaboration in Cal-27 OSCC cell line by integrating the knowledge on the molecular links in OSCC tumor microenvironment. For this reason, the current study was based on the analysis of the molecular links of c-Myc/HIF-1α gene expression as well as on the expression of other markers such as c-Jun, ERK 1/2, pERK 1/2, VEGF, MMP-9, and Bcl-2, which are involved in Cal-27 survival/proliferation and tumor progression. Moreover, the biological effect of Doxorubicin (Doxo), a well-known chemotherapeutic agent, has been evaluated in the same pathways. Our work revealed the vital role of c-Myc/HIF-1α collaboration and the potential utilization of c-Myc as a potential target for OSCC clinical treatment.

2. Results

2.1. Effects of Doxo on Cal-27 Cell Viability

The effects of Doxo against the survival of Cal-27 cell line was studied by MTS assay. Initially, Doxo was tested at different concentrations ranging from 1 to 10 μM to evaluate the effect on cell viability, based on previous data obtained (data not shown). The cell-viability graph showed a cell-viability reduction in a dose-dependent manner. A total of 1 μM Doxo treatment on Cal-27 cell line showed a cell-viability percentage of 80% after 24 h, while 5 μM to 10 μM treatment exerted a cell-viability percentage of less than 50% (Figure 1A). Then, we extrapolated the IC$_{50}$ for Doxo using Graph Pad Prism result and obtained the value of 2.5 μM as the IC$_{50}$ value (Figure 1B). Hence, Doxo at 2.5 μM was used for further investigations. To evaluate the effects of Doxo at 2.5 μM, MTT assay was performed at 24, 48 and 72 h on Cal-27 cells. Cell viability was reduced at all considered endpoints, as reported in Figure 1C.
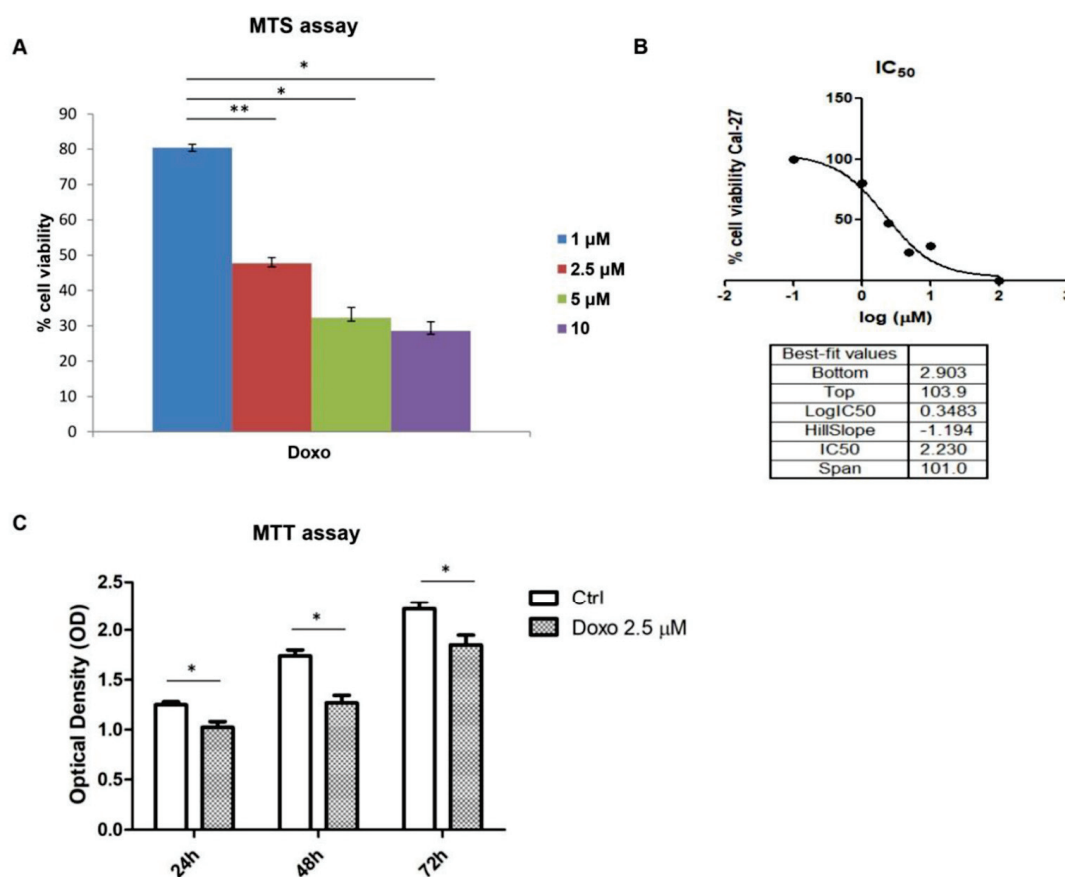
Figure 1. (**A**) Cell viability on Cal-27 cells treated with Doxo at 1, 2.5, 5 and 10 μM for 24 h. Cell viability was assessed using MTS assay and normalized to control cells treated with DMSO (0.2% as final concentration). ** $p < 0.01$; * $p < 0.05$. (**B**) the IC_{50} value graph for Doxo. (**C**) MTT assay reported the Doxo treatment on Cal-27 cells at 24, 48 and 72 h. * $p < 0.05$.

2.2. Expression Level of c-Myc, c-Jun, Bcl-2, HIF-1α, VEGF, MMP-9, ERK 1/2 and pERK 1/2 in Doxo-Treated Cells

Immunofluorescence results evidenced that c-Myc, c-Jun, Bcl-2, HIF-1α, VEGF, MMP-9, ERK 1/2 and pERK1/2 proteins were expressed significantly in Cal-27 untreated cells. On the contrary, Cal-27 cancer cells treated with 2.5 μM Doxo showed a marked reduction of these proteins compared to the untreated cells (Figures 2–5). These results were confirmed by Western blot analysis, in which the expression of c-Myc, c-Jun, Bcl-2, HIF-1α, VEGF, MMP-9, ERK 1/2 and pERK 1/2 were significantly reduced in Doxo-treated cells compared to the untreated cells (Figure 6). To evaluate the Doxo treatment on apoptosis-related markers, Western blotting analysis was performed on Cal-27 cells to evaluate the expression of caspase-3, caspase-9 and Bax. Caspase-3, caspase-9 and Bax showed a down-expression in Cal-27 Doxo-treated cells when compared to the CTRL group, as demonstrated by protein-specific bands (Figure 7A) and these results were confirmed by densitometric analyses (Figure 7B1–B3).
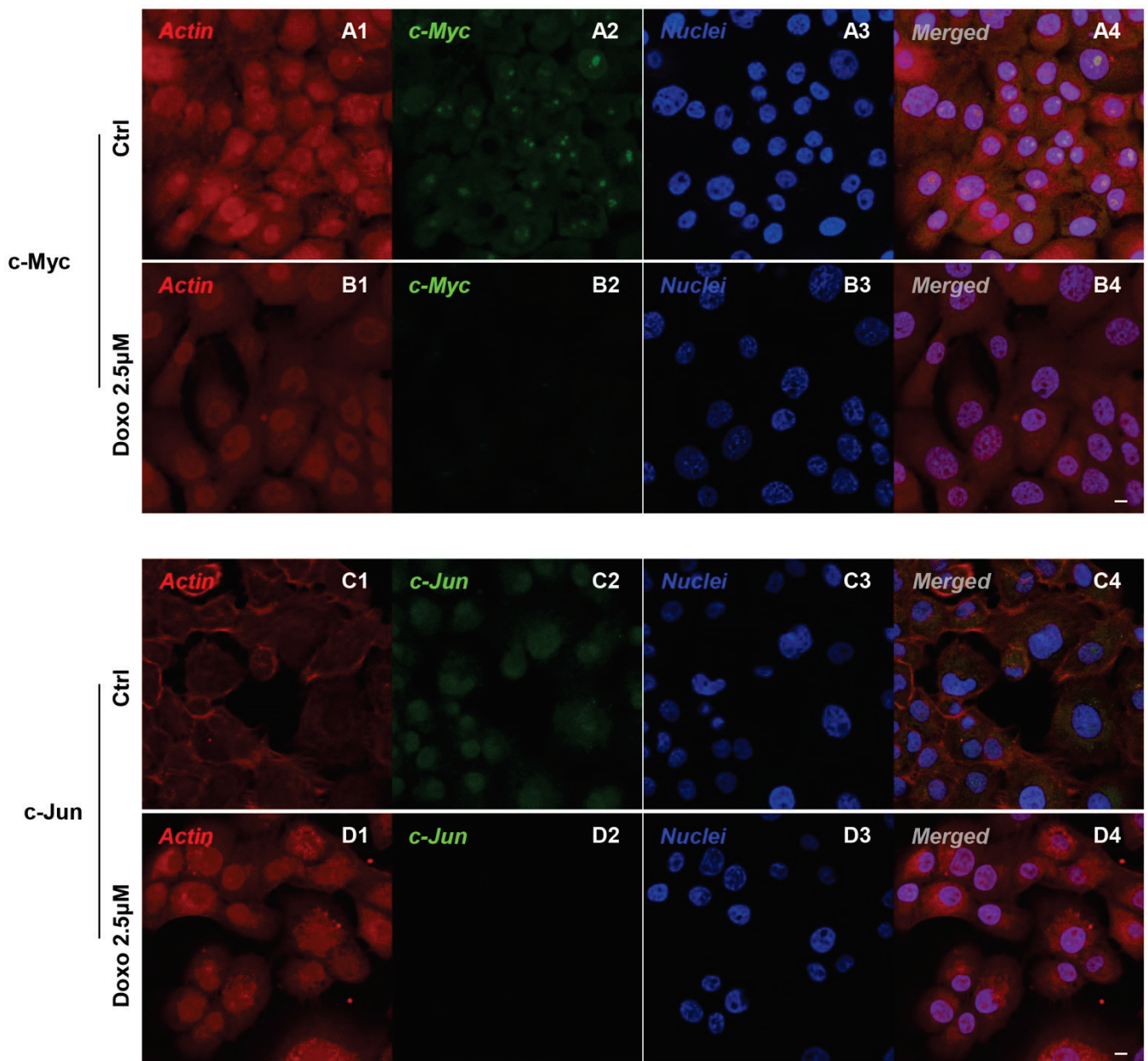
Figure 2. Confocal microscopic analysis on the expression of c-Myc and c-Jun in Cal-27 cell lines. Expression of c-Myc and c-Jun analyzed by confocal microscopy in untreated cells (CTRL) (**A1**–**A4**,**C1**–**C4**); expression of c-Myc and c-Jun expression in Cal-27 treated with Doxo 2.5 μM (**B1**–**B4**,**D1**–**D4**). Red fluorescence: cytoskeleton actin. Green fluorescence: c-Myc and c-Jun. Blue fluorescence: cell nuclei. Scale bar: 20 μm.
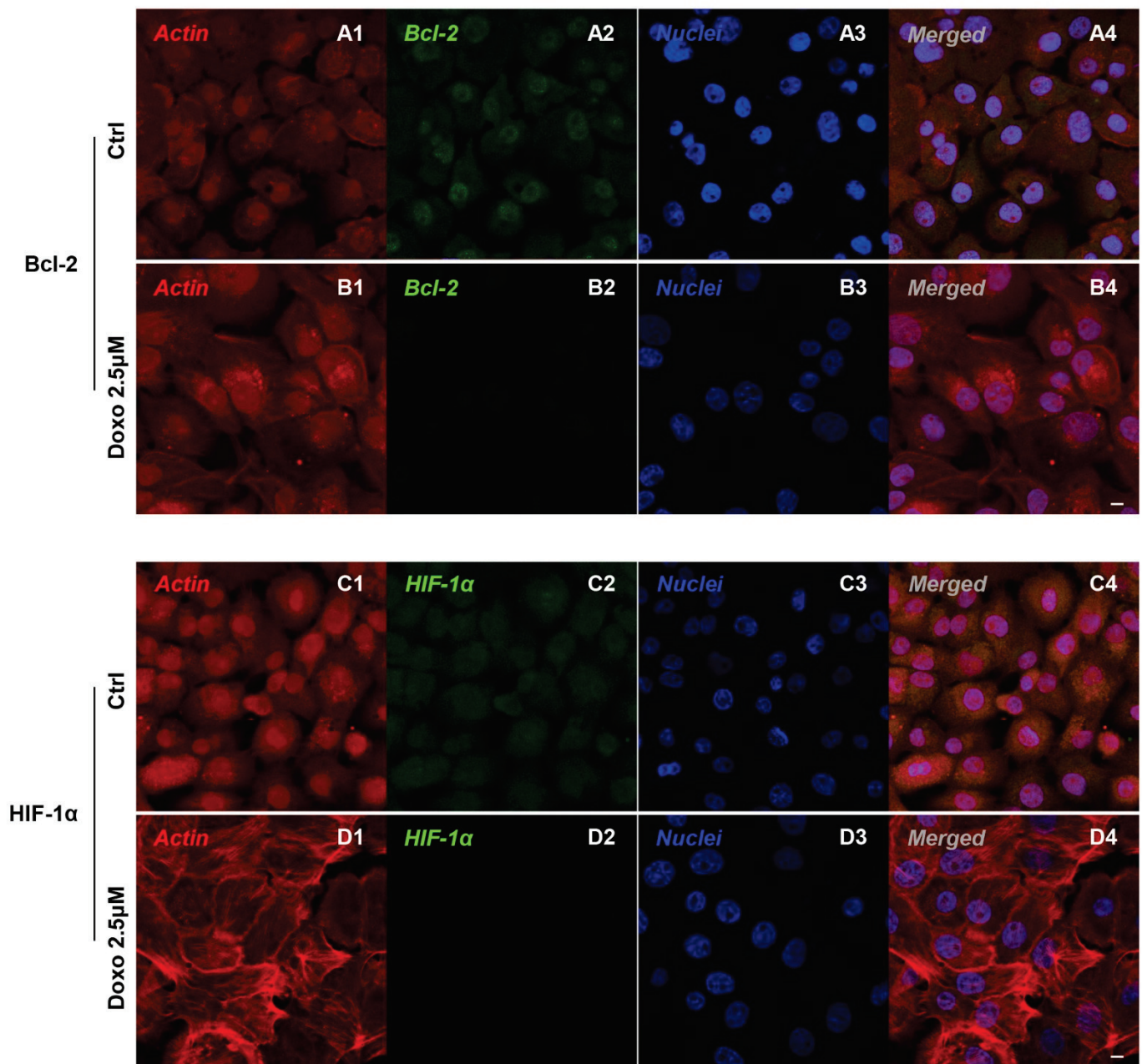
Figure 3. Confocal microscopic analysis on the expression of Bcl-2 and HIF-1α in Cal-27 cell lines. Expression of Bcl-2 and HIF-1α analyzed by confocal microscopy in untreated cells (CTRL) (**A1–A4**,**C1–C4**); expression of Bcl-2 and HIF-1α expression in Cal-27 treated with Doxo 2.5 µM (**B1–B4**,**D1–D4**). Red fluorescence: cytoskeleton actin. Green fluorescence: Bcl-2 and HIF-1α. Blue fluorescence: cell nuclei. Scale bar: 20 µm.
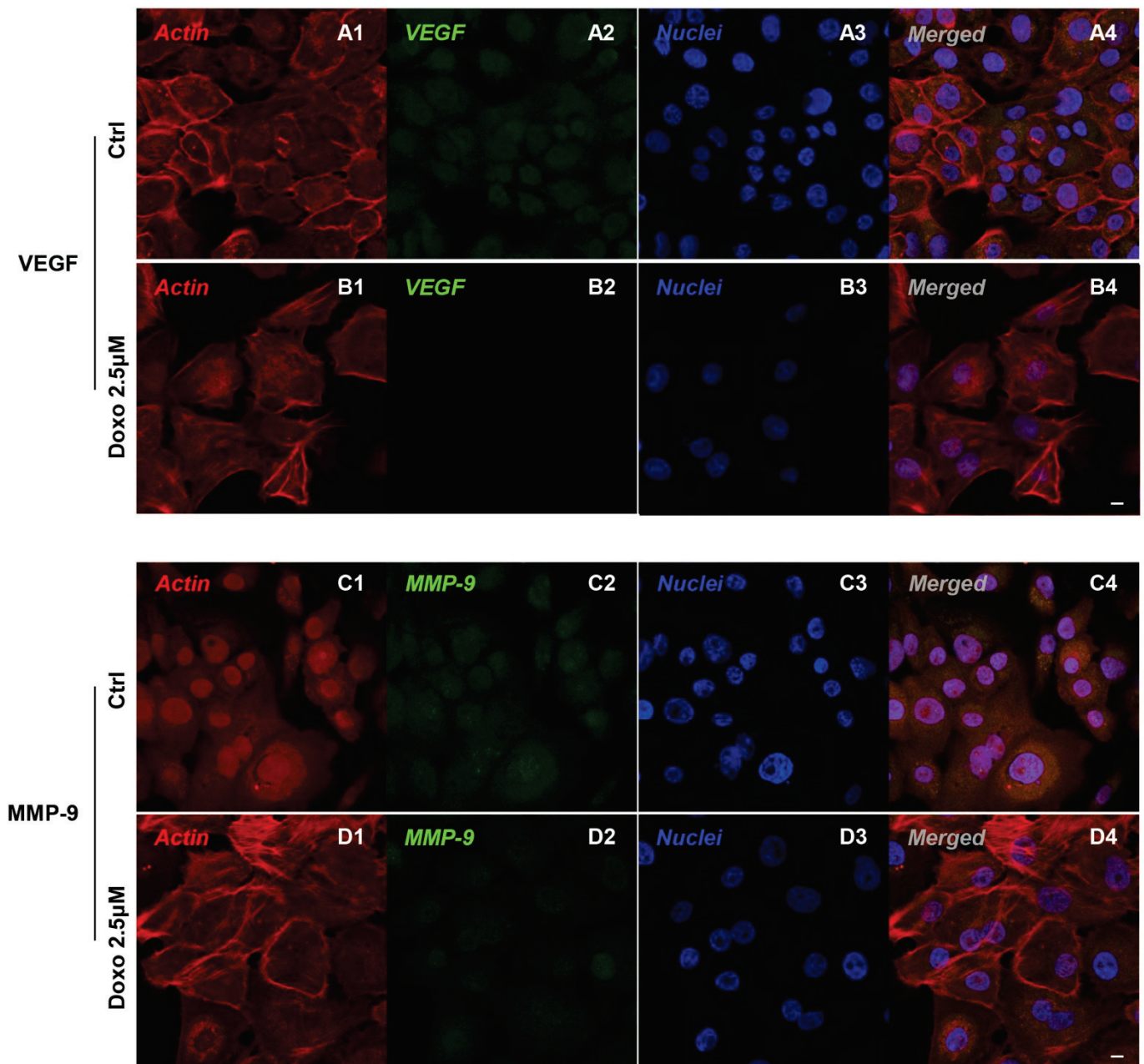
Figure 4. Confocal microscopic analysis on the expression of VEGF and MMP-9 in Cal-27 cell lines. Expression of VEGF and MMP-9 analyzed by confocal microscopy in untreated cells (CTRL) (**A1–A4**,**C1–C4**); expression of VEGF and MMP-9 analyzed by confocal microscopy in Cal-27 treated with Doxo 2.5 μM (**B1–B4**,**D1–D4**). Red fluorescence: cytoskeleton actin. Green fluorescence: VEGF, MMP-9, ERK 1/2 and pERK 1/2. Blue fluorescence: cell nuclei. Scale bar: 20 μm.
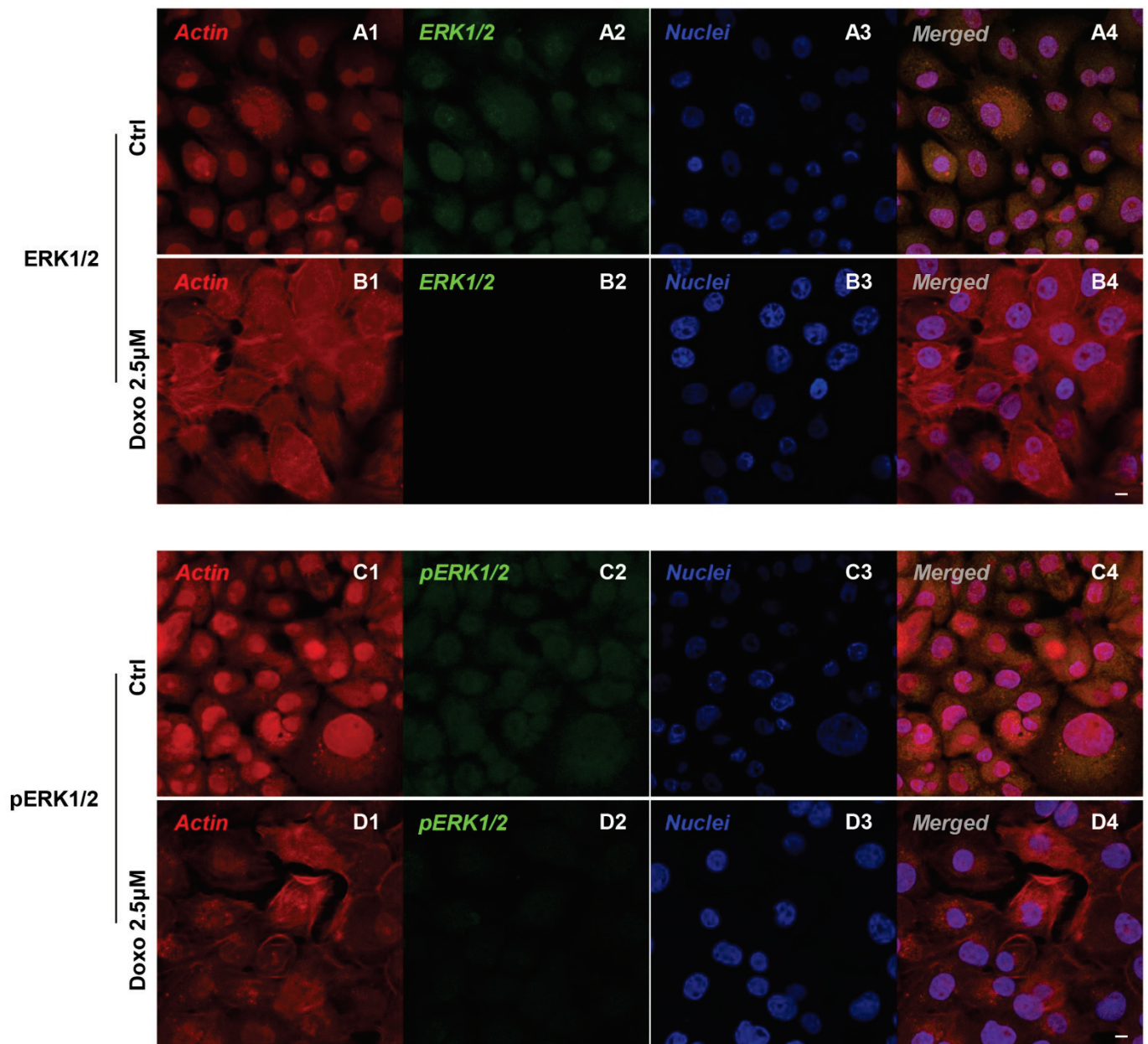
Figure 5. Confocal microscopic analysis on the expression of ERK 1/2 and pERK 1/2 in Cal-27cell lines. Expression of ERK 1/2 and pERK 1/2 analyzed by confocal microscopy in untreated cells (CTRL) (**A1–A4,C1–C4**); expression of ERK 1/2 and pERK 1/2 analyzed by confocal microscopy in Cal-27 treated with Doxo 2.5 μM (**B1–B4,D1–D4**). Red fluorescence: cytoskeleton actin. Green fluorescence: ERK 1/2 and pERK 1/2. Blue fluorescence: cell nuclei. Scale bar: 20 μm.
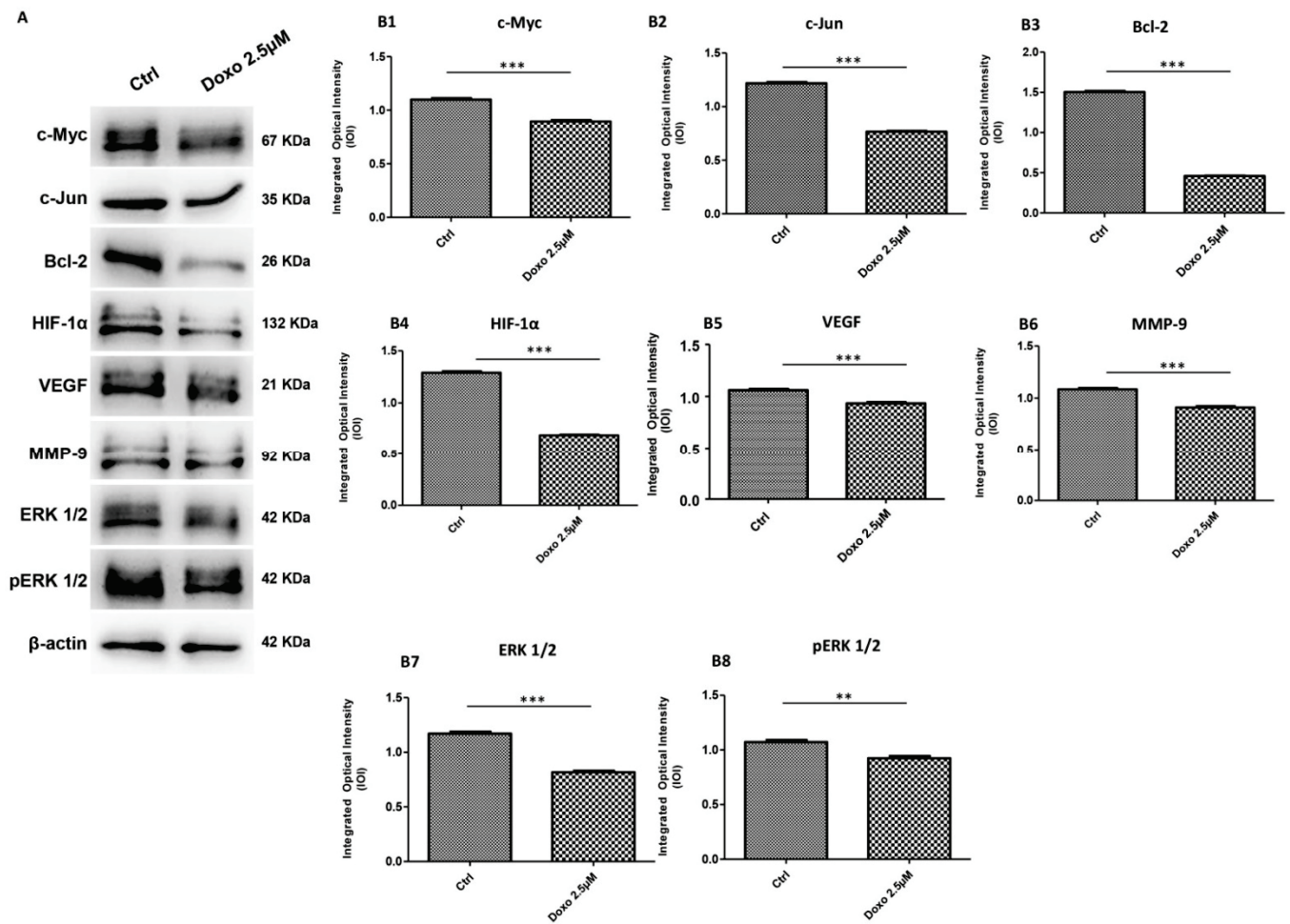
Figure 6. Western blotting analysis. (**A**) c-Myc, c-Jun, Bcl-2, HIF-1α, VEGF, MMP-9, ERK 1/2 and pERK1/2 proteins expression in Cal-27 cell line untreated and treated with 2.5 μM Doxo. Each membrane was probed with β-actin antibody to verify loading consistency. Western blot data shown are the representative data from three different experiments. (**B1–B8**) Histograms represent densitometric measurements of protein bands expressed as integrated optical intensity (IOI) mean of three separate experiments. The error bars show standard deviation (±SD). Densitometric values analyzed by *t*-test (unpaired *t*-test) return significant differences. *** $p < 0.001$, ** $p < 0.01$.
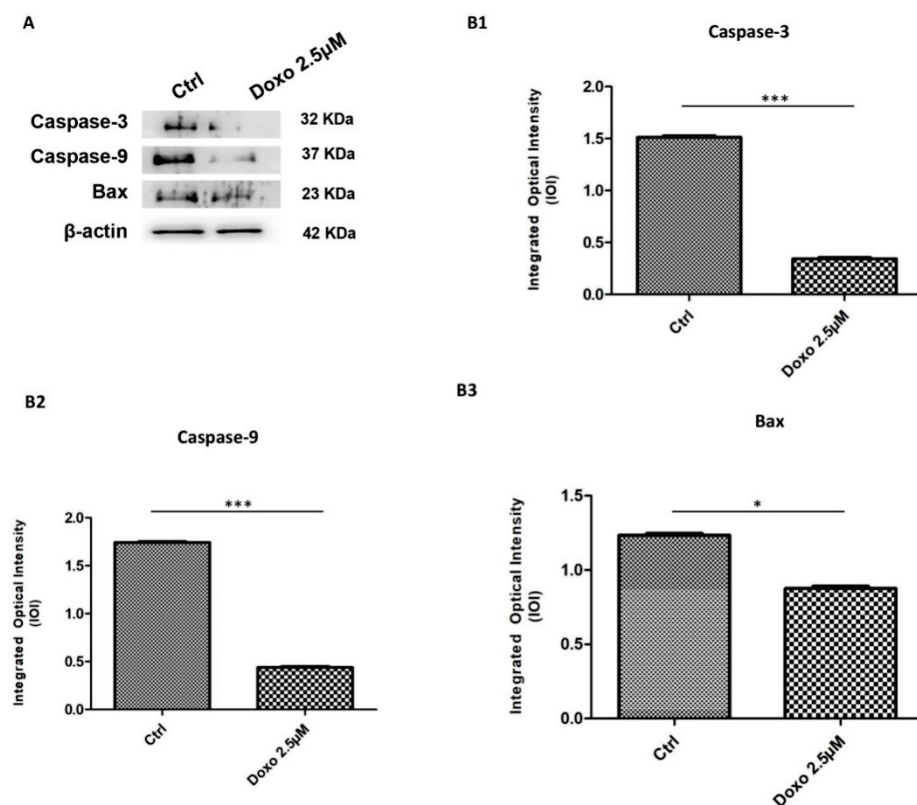
Figure 7. Western blotting analysis of apoptosis related markers. (**A**) Caspase-3, caspase-9 and Bax proteins expression in Cal-27 cell line untreated and treated with 2.5 μM Doxo. Each membrane was probed with β-actin antibody to verify loading consistency. Western blot data shown are the representative data from three different experiments. (**B1–B3**) Histograms represent densitometric measurements of proteins bands expressed as integrated optical intensity (IOI) mean of three separate experiments. The error bars show standard deviation (± SD). Densitometric values analyzed by *t*-test (unpaired *t*-test) return significant differences. *** $p < 0.001$, * $p < 0.05$.

3. Discussion

Tumor is a heterogeneous illness with complex molecular changes that consist of genetic and epigenetic alterations. OSCC is the eighth-most common oral malignancy, constituting 90% of all oral malignancies [12]. The main aspects of tumor biology are proliferation, apoptosis and differentiation.

Although Doxo is not considered the gold standard for chemotherapy in OSCC, some studies have been reported the use of Doxo for noninvasive diagnostic imaging and therapeutical application using multifunctional nanotechnology to increase the intracellular uptake [13,14]. In tumor advancement, proto-oncogenes such as c-Myc and Bcl-2 are considered as genes that regulate cellular proliferation and apoptosis [15].

C-MYC gene is involved in the initiation of cyclin-dependent kinases which promote transcription followed by cellular proliferation.

Chen et al. reported that the c-Myc inhibitor 10058-F4 could work synergistically with Doxo treatment to inhibit the proliferation of drug-resistant cells and promote their apoptosis in triple-negative breast cancer (TNBC) [16]. Doxo treatment is also related to the epithelial-to-mesenchymal transition (EMT) repression through targeting c-Myc in in vitro study in lung cancer [17]. EMT is a biological process through which epithelial cells are transformed into mesenchymal-phenotype and plays a pivotal role in regulating tumor pathogenesis [18].

Gonzalez-Gonzalez et al. reported the molecular mechanism that targets the EMT process in the HNSCC [19]. During EMT, the alteration of epithelium-specific adhesion proteins and the induction of mesenchymal proteins such as matrix metalloproteinases

(MMPs) was occurred. In tumor progression, the extracellular matrix (ECM) destruction and hypoxia are the main studied processes. In HNSCC MMP-9 plays an important role during tumor invasion [20], as well as the participation of ERK-1/2 and PI3K signaling pathways [21]. Several genes were reported in the promotion of carcinogenesis of HNSCC as c-Myc and cyclin D1 [22]. On the other hand, in OSCC, tumor progression and metastasis are also sustained by the presence of hypoxia-inducible factor (HIF) and related genes induced by hypoxia, such as VEGF, interleukin 1A (IL-1A), endothelin 1, platelet-derived growth factor B (PDGFB) and erythropoietin (EPO) [23].

BCL2 gene was first discovered in follicular B-cell lymphoma, which is connected to the immunoglobulin heavy-chain locus at the breakpoints of t(14;18) translocation. The effect of this translocation is the induction of Bcl-2 protein transcription. Bcl-2 protein preserves membrane integrity of mitochondria and was found to inhibit cell death [24]. *C-MYC* and *BCL2* oncogenes evidence parallel outcomes in cancer development. Previous studies documented the synergistic mechanism of Bcl-2 and c-Myc in the abrogation of apoptosis and facilitating abnormal proliferation of the cell. The role of these genes is still unspecified in the progression, aggressiveness and prognosis in OSCC. The role of *C-MYC* in regulating the proliferation of OSCC cells is not well-identified [25]. The antiapoptotic Bcl-2 protein is overexpressed in cancer cells, as demonstrated in the Intrahepatic cholangiocarcinoma (iCCA) model, in which the increase expression of BCL-2 and c-FLIP is associated with the reduction in apoptosis due to the lack of activation of the caspase cascade [26]. Our results showed an overexpression of Bcl-2, caspase-3, caspase-9 and Bax in untreated Cal-27 cells, while Doxo treatment showed a reduction in all considered proteins.

Emerging studies suggest that c-Myc and HIF also collaborate to induce cancer cell growth and progression [27]. C-Myc signaling plays a key part in controlling cancer-cell metabolism and vasculogenesis. The Myc oncoprotein is a master regulator of transcription that activates or represses gene expression to coordinate diverse cellular processes, including cellular differentiation, apoptosis and angiogenesis [28]. C-Myc and HIFs also cooperate to promote tumor angiogenesis and metastasis. Under hypoxic conditions, HIF-1α can stimulate the expression of various proangiogenic factors, including VEGF and matrix metalloproteinases (MMP-2 and MMP-9). Based on the literature, oncogenic c-Myc cooperates with HIF-1α to trigger VEGF production and release [29,30].

Our results showed the down-expression of c-Myc and HIF-1α after Doxo treatment in Cal-27 cells. It is also possible that the Myc-HIF link further interplays with other oncogenic pathways such as ERK/MAPK, Akt/mTOR and Notch signaling to alter cell metabolism, cell cycle, ribosome biogenesis and genomic stability in tumorigenesis.

High levels of c-Jun are found in multiple types of cancer [31], and c-Jun overexpression might lead to an overexpression of c-Myc, since in other types of tumors it has been shown that c-Jun controls the exposure of c-Myc binding directly to its promoter, and that induces an overexpression of c-Jun accelerating the c-Myc promoter activity [32]. Based on this knowledge, the c-Myc expression in a cellular model of squamous cell carcinoma, Cal-27, was investigated. The activity of the Raf/MEK/ERK signaling pathway plays an important role in the processes of proliferation, survival and metastasis in several types of cancers, in which ERK 1/2 are activated through phosphorylation by MAPK/ERK kinases, which are activated through phosphorylation by the upstream serine/threonine Raf protein kinases [33]. The KRAS mutant activates the Raf/MEK/ERK signaling pathway to upregulate c-Myc. In many types of cancer it has been shown that ERK is involved in the increase in c-Myc expression associated with development, growth and invasion [34]. Furthermore, the EGF receptor also activates the PI3K pathway, which is always correlated with c-Myc to stimulate the proliferation of tumor cells [35].

In the present study, we focused our attention on the biological roles and regulatory mechanism of c-Myc in OSCC. Obtained data showed that that c-Myc, c-Jun, Bcl-2, HIF-1α, VEGF, MMP-9, ERK 1/2 and pERK 1/2 were overexpressed in a cellular model of OSCC, Cal-27, as reported by confocal microscopy observations and protein-expression analysis.

All these proteins are associated with cell invasion, hypoxia, angiogenesis, migration and inflammation. On the other hand, Cal-27 cells treated with Doxo, at a concentration of 2.5 μM (IC$_{50}$ value obtained), showed a down-expression of the above-mentioned proteins.

The current study explores one of the molecular mechanisms targeting oral squamous cell carcinoma cells. Novel ideas are provided by an in-depth exploration of its signal pathways for treating OSCC from the molecular level. In conclusion, the functional relevance of c-Myc in OSCC and in the Myc-HIF collaboration by integrating the knowledge on this molecular link in the OSCC tumor microenvironment was investigated. The outcomes achieved showed for the first time the pivotal role of c-Myc in Cal-27 in cell survival/proliferation and cancer development as well as the inhibitory consequence of Doxo in downregulating the signaling pathways stimulated by c-Myc. These data suggest a possible route for the control of OSCC, even if further insights into the understanding of the Myc-HIF interplay are necessary for developing novel targeted therapeutics.

4. Materials and Methods

4.1. Reference Compound

Doxorubicin hydrochloride (98.0–102.0% purity as assessed by HPLC) was purchased from Sigma-Aldrich (Milan, Italy).

4.2. Cell-Culture Establishment

Cal-27 cells (ATCC, Manassas, Virginia, VA, USA) were maintained in Dulbecco's Modified Eagle's Medium (DMEM) supplemented with 10% fetal bovine serum (Euroclone, Milan, Italy). Cultures were incubated at 37 °C in a humidified atmosphere of 5% CO$_2$ in air and subcultured when they were 80% confluent.

4.3. Experimental Study Design

All experiments were performed in triplicate. The study was designed as follows:

(i)   Untreated Cal-27, used as negative control (CTRL);
(ii) Cal-27 treated with Doxo (2.5 μM) for 24 h.

4.4. Cell-Viability Assay

The Cal-27 cancer cells were seeded at the cell density of 15,000/well in a 96-well tissue culture plate. The cell viability was evaluated through the 3-(4,5-dimethylthiazol-2-yl)-5-(3-carboxymethoxyphenyl)-2-(4-sulfo-phenyl)-2*H*-tetrazolium (MTS) assay (CellTiter 96® Aqueous One Solution Cell Proliferation Assay, Promega, Madison, WI, USA). After 24 h of treatment with Doxo at 1, 2.5, 5 and 10μM concentration, 20 μL/well of MTS dye solution was added to culture medium, and cells were incubated for 3 h at 37 °C [36]. The amount of formazan product is directly proportional to the number of living cells in culture and it was detected by absorbance measurements at 490 nm wavelength utilizing the Synergy™ HT Multi-detection microplate reader (Biotech, Winooski, VT, USA). The MTS assay was executed in three independent experiments. To evaluate the Doxo effects at 2.5 μM concentration on Cal-27 cells3-(4,5-dimethyl-2-thiazolyl)-2,5-diphenyltetrazolium bromide (MTT) assay was used with a previously reported methodology [37].

4.5. Confocal Microscopy (CLSM)

The Cal-27 cells were seeded at 40,000/well on 8-well culture glass slides (Corning, Glendale, AZ, USA) treated with Doxo at 2.5 μM for 24 h. Then, the samples were fixed for 1 h with 4% paraformaldehyde in 0.1 M PBS (pH 7.4) (Lonza, Basel, Switzerland) at room temperature. After washing, cell samples were processed for the immunofluorescence staining as previously described [38]. Successively, the cells were permeabilized with 0.5% Triton X-100 in PBS (Lonza) for 10 min and blocked with 5% skimmed milk in PBS for 1 h. Then, the cells were incubated with the primary antibodies for 2 h at room temperature. The following primary antibodies were used in this experiment: anti-c-Myc (1:200) (sc-293072, Santa Cruz Biotechnology, Dallas, TX, USA), anti-c-Jun (1:200) (sc-8008,

Santa Cruz Biotechnology), anti-Bcl-2 (1:200) (sc-134306, Santa Cruz Biotechnology), anti-HIF-1α (1:200) (sc-53546, Santa Cruz Biotechnology), anti-VEGF (1:200) (sc-57496, Santa Cruz Biotechnology), anti-MMP-9 (1:200) (sc-21733, Santa Cruz Biotechnology), anti-ERK 1/2 (1:200) (sc 514302, Santa Cruz Biotechnology) and anti-pERK 1/2 (1:200) (sc-81492, Santa Cruz Biotechnology). Next, samples were incubated with Alexa Fluor 488 green fluorescent conjugated goat antirabbit secondary antibody (1:200) (A32731, Molecular Probes, Invitrogen, Eugene, OR, USA) or Alexa Fluor 488 green fluorescent conjugated goat antimouse secondary antibody (1: 200) (A32723, Invitrogen, Eugene, OR, USA) for 1 h at 37 °C. To stain the cytoskeleton actin, cells were treated with Alexa Fluor 568 phalloidin red conjugate (1:200) (A12380, Invitrogen, Eugene, OR, USA) for 1 h, and to stain the nuclei, cells were stained with TOPRO (1:200) (T3605, Invitrogen, Eugene, OR, USA) for 1 h. The Zeiss LSM800 confocal system (Carl Zeiss, Jena, Germany) was used to acquire microphotographs.

4.6. Western Blot

The cell lysates (50 μg) underwent electrophoresis and transferred to the polyvinylidenfluoride (PVDF) membrane. Successively, they were blocked in 5% of non-fat milk in PBS + 0.1% Tween-20. Then, the blotted membranes were incubated overnight at 4 °C with primary antibodies of anti-c-Myc (1:500) (sc-40, Santa Cruz Biotechnology, Dallas, TX, USA), anti-c-Jun (1:500) (397500, Life Technologies), anti-Bcl-2 (1:500) (sc-7382, Santa Cruz Biotechnology), anti-HIF-1α (1:500) (sc-53546, Santa Cruz Biotechnology), anti-VEGF (1:500) (sc-57496, Santa Cruz Biotechnology), anti-MMP-9 (1:500) (sc-21733, Santa Cruz Biotechnology), anti-ERK 1/2 (1:500) (sc-514302, Santa Cruz Biotechnology), anti-pERK1/2 (1:500) (sc-81492, Santa Cruz Biotechnology), anti-caspase-3 (1:500) (sc-56052, Santa Cruz Biotechnology), anti-caspase-9 (1:500) (sc-56076, Santa Cruz Biotechnology) and anti-Bax (1:500) (sc-493, Santa Cruz Biotechnology). β-actin was used as a loading control (1:750, Santa Cruz Biotechnology). After five washings in PBS containing 0.1% Tween-20, membranes were incubated for 1 h at room temperature with peroxidase-conjugated antimouse secondary antibody (A90-116P Goat antimouse; 1:5000 dilution in 2.5% milk made by 1X PBS and 0.1% Tween-20). Protein expression was visualized using the enhanced chemiluminescence detection method (ECL) (Amersham Pharmacia Biotech, Milan, Italy) with photo documenter Alliance 2.7 (Uvitec, Cambridge, UK). Signals were analyzed by ECL enhancing and evaluated through UVIband-1D gel analysis (Uvitec, Cambridge, UK). Data were normalized with densitometric values derived from β-actin, the loading control.

4.7. Statistical Analysis

Statistical significance was analyzed with GraphPad Prism 5 (GraphPad, San Diego, CA, USA) software using *t*-test. Values of $p < 0.05$ were considered statistically significant.

5. Conclusions

The present work reported the regulatory role of c-Myc in cell survival/proliferation and cancer progression in Cal-27 cells. Moreover, our results showed that Doxo treatment downregulated the activation of the c-Myc signaling pathway.

Author Contributions: Conceptualization, G.D.M., J.P. and F.D.; methodology, G.D.M., Y.D.R., L.F. and F.M.; formal analysis, G.D.M., J.P. and F.D.; investigation, G.D.M., Y.D.R., L.F., F.M. and S.C.; resources, G.D.M., J.P. and F.D.; data curation, G.D.M., Y.D.R., L.F., T.S.R., J.P., O.T. and F.D.; writing—original draft preparation, G.D.M., J.P. and F.D.; writing—review and editing, S.C. and T.S.R.; supervision, G.D.M., J.P., O.T. and F.D.; project administration, G.D.M., J.P. and F.D.; funding acquisition, G.D.M., J.P., O.T. and F.D. All authors have read and agreed to the published version of the manuscript.

Institutional Review Board Statement: Not applicable.

Informed Consent Statement: Not applicable.

Data Availability Statement: Data is contained within the article.

Conflicts of Interest: The authors declare no conflict of interest.

References

1. Verdonck-de Leeuw, I.M.; van Nieuwenhuizen, A.; Leemans, C.R. The value of quality-of-life questionnaires in head and neck cancer. *Curr. Opin. Otolaryngol. Head Neck Surg.* **2012**, *20*, 142–147. [CrossRef] [PubMed]
2. Johnson, D.E.; Burtness, B.; Leemans, C.R.; Lui, V.W.Y.; Bauman, J.E.; Grandis, J.R. Head and neck squamous cell carcinoma. *Nat. Rev. Dis. Primers* **2020**, *6*, 92. [CrossRef]
3. Muhammad, N.; Bhattacharya, S.; Steele, R.; Phillips, N.; Ray, R.B. Involvement of c-Fos in the Promotion of Cancer Stem-like Cell Properties in Head and Neck Squamous Cell Carcinoma. *Clin. Cancer Res.* **2017**, *23*, 3120–3128. [CrossRef] [PubMed]
4. Wang, S.; Xu, X.; Xu, F.; Meng, Y.; Sun, C.; Shi, L.; Zhao, E. Combined Expression of c-jun, c-fos, and p53 Improves Estimation of Prognosis in Oral Squamous Cell Carcinoma. *Cancer Investig.* **2016**, *34*, 393–400. [CrossRef] [PubMed]
5. Milde-Langosch, K. The Fos family of transcription factors and their role in tumourigenesis. *Eur. J. Cancer* **2005**, *41*, 2449–2461. [CrossRef]
6. Lin, S.H.; Wang, H.K.; Yeh, K.T.; Tai, H.C.; Wang, H.Y.; Huang, L.R.; Chiu, C.W.; Chung, C.M.; Velmurugan, B.K. c-MYC expression in T (III/IV) stage oral squamous cell carcinoma (OSCC) patients. *Cancer Manag. Res.* **2019**, *11*, 5163–5169. [CrossRef]
7. Cole, M.D. The myc oncogene: Its role in transformation and differentiation. *Annu. Rev. Genet.* **1986**, *20*, 361–384. [CrossRef]
8. Czarnecka, A.M.; Synoradzki, K.; Firlej, W.; Bartnik, E.; Sobczuk, P.; Fiedorowicz, M.; Grieb, P.; Rutkowski, P. Molecular Biology of Osteosarcoma. *Cancers* **2020**, *12*, 2130. [CrossRef]
9. Field, J.K.; Spandidos, D.A.; Stell, P.M.; Vaughan, E.D.; Evan, G.I.; Moore, J.P. Elevated expression of the c-myc oncoprotein correlates with poor prognosis in head and neck squamous cell carcinoma. *Oncogene* **1989**, *4*, 1463–1468.
10. Nakagawa, M.; Takizawa, N.; Narita, M.; Ichisaka, T.; Yamanaka, S. Promotion of direct reprogramming by transformation-deficient Myc. *Proc. Natl. Acad. Sci. USA* **2010**, *107*, 14152–14157. [CrossRef]
11. Podar, K.; Anderson, K.C. A therapeutic role for targeting c-Myc/Hif-1-dependent signaling pathways. *Cell Cycle* **2010**, *9*, 1722–1728. [CrossRef] [PubMed]
12. Pallavi, N.; Nalabolu, G.R.K.; Hiremath, S.K.S. Bcl-2 and c-Myc expression in oral dysplasia and oral squamous cell carcinoma: An immunohistochemical study to assess tumor progression. *J. Oral Maxillofac. Pathol. JOMFP* **2018**, *22*, 325–331. [CrossRef] [PubMed]
13. Gu, M.; Jiang, L.; Hao, L.; Lu, J.; Liu, Z.; Lei, Z.; Li, Y.; Hua, C.; Li, W.; Li, X. A novel theranostic nanoplatform for imaging-guided chemo-photothermal therapy in oral squamous cell carcinoma. *J. Mater. Chem. B* **2021**, *9*, 6006–6016. [CrossRef] [PubMed]
14. Li, R.; Wang, Y.; Du, J.; Wang, X.; Duan, A.; Gao, R.; Liu, J.; Li, B. Graphene oxide loaded with tumor-targeted peptide and anti-cancer drugs for cancer target therapy. *Sci. Rep.* **2021**, *11*, 1725. [CrossRef]
15. Garte, S.J. The c-myc oncogene in tumor progression. *Crit. Rev. Oncog.* **1993**, *4*, 435–449.
16. Chen, Y.; Feng, X.; Yuan, Y.; Jiang, J.; Zhang, P.; Zhang, B. Identification of a novel mechanism for reversal of doxorubicin-induced chemotherapy resistance by TXNIP in triple-negative breast cancer via promoting reactive oxygen-mediated DNA damage. *Cell Death Dis.* **2022**, *13*, 338. [CrossRef]
17. Tao, L.; Wang, S.-L.; Hao, J.-B.; Zhang, Y.; Hu, R.; Liu, X.-Q.; Cui, W.-J.; Zhou, L.-F. MiR-451a attenuates doxorubicin resistance in lung cancer via suppressing epithelialmesenchymal transition (EMT) through targeting c-Myc. *Biomed. Pharmacother.* **2020**, *125*, 109962. [CrossRef]
18. Zhu, Q.C.; Gao, R.Y.; Wu, W.; Qin, H.L. Epithelial-mesenchymal transition and its role in the pathogenesis of colorectal cancer. *Asian Pac. J. Cancer Prev. APJCP* **2013**, *14*, 2689–2698. [CrossRef]
19. Gonzalez-Gonzalez, R.; Ortiz-Sarabia, G.; Molina-Frechero, N.; Salas-Pacheco, J.M.; Salas-Pacheco, S.M.; Lavalle-Carrasco, J.; Lopez-Verdin, S.; Tremillo-Maldonado, O.; Bologna-Molina, R. Epithelial-Mesenchymal Transition Associated with Head and Neck Squamous Cell Carcinomas: A Review. *Cancers* **2021**, *13*, 3027. [CrossRef]
20. Libra, M.; Scalisi, A.; Vella, N.; Clementi, S.; Sorio, R.; Stivala, F.; Spandidos, D.A.; Mazzarino, C. Uterine cervical carcinoma: Role of matrix metalloproteinases (review). *Int. J. Oncol.* **2009**, *34*, 897–903. [CrossRef]
21. Zuo, J.H.; Zhu, W.; Li, M.Y.; Li, X.H.; Yi, H.; Zeng, G.Q.; Wan, X.X.; He, Q.Y.; Li, J.H.; Qu, J.Q.; et al. Activation of EGFR promotes squamous carcinoma SCC10A cell migration and invasion via inducing EMT-like phenotype change and MMP-9-mediated degradation of E-cadherin. *J. Cell. Biochem.* **2011**, *112*, 2508–2517. [CrossRef] [PubMed]
22. Tian, X.; Liu, Z.; Niu, B.; Zhang, J.; Tan, T.K.; Lee, S.R.; Zhao, Y.; Harris, D.C.; Zheng, G. E-cadherin/beta-catenin complex and the epithelial barrier. *J. Biomed. Biotechnol.* **2011**, *2011*, 567305. [CrossRef] [PubMed]
23. Joseph, J.P.; Harishankar, M.K.; Pillai, A.A.; Devi, A. Hypoxia induced EMT: A review on the mechanism of tumor progression and metastasis in OSCC. *Oral Oncol.* **2018**, *80*, 23–32. [CrossRef] [PubMed]
24. Tzifi, F.; Economopoulou, C.; Gourgiotis, D.; Ardavanis, A.; Papageorgiou, S.; Scorilas, A. The Role of BCL2 Family of Apoptosis Regulator Proteins in Acute and Chronic Leukemias. *Adv. Hematol.* **2012**, *2012*, 524308. [CrossRef]

25. Sabit, H.; Tombuloglu, H.; Cevik, E.; Abdel-Ghany, S.; El-Zawahri, E.; El-Sawy, A.; Isik, S.; Al-Suhaimi, E. Knockdown of c-MYC Controls the Proliferation of Oral Squamous Cell Carcinoma Cells in vitro via Dynamic Regulation of Key Apoptotic Marker Genes. *Int. J. Mol. Cell. Med.* **2021**, *10*, 45–55. [CrossRef]

26. Carnevale, G.; Carpino, G.; Cardinale, V.; Pisciotta, A.; Riccio, M.; Bertoni, L.; Gibellini, L.; De Biasi, S.; Nevi, L.; Costantini, D.; et al. Activation of Fas/FasL pathway and the role of c-FLIP in primary culture of human cholangiocarcinoma cells. *Sci. Rep.* **2017**, *7*, 14419. [CrossRef]

27. Li, Y.P.; Sun, X.X.; Qian, D.Z.; Dai, M.S. Molecular Crosstalk Between MYC and HIF in Cancer. *Front. Cell Dev. Biol.* **2020**, *8*, 590576. [CrossRef]

28. Masoud, G.N.; Li, W. HIF-1alpha pathway: Role, regulation and intervention for cancer therapy. *Acta Pharm. Sin. B* **2015**, *5*, 378–389. [CrossRef]

29. Hickey, M.M.; Simon, M.C. Regulation of angiogenesis by hypoxia and hypoxia-inducible factors. *Curr. Top. Dev. Biol.* **2006**, *76*, 217–257. [CrossRef]

30. Zimna, A.; Kurpisz, M. Hypoxia-Inducible Factor-1 in Physiological and Pathophysiological Angiogenesis: Applications and Therapies. *BioMed Res. Int.* **2015**, *2015*, 549412. [CrossRef]

31. Sioletic, S.; Czaplinski, J.; Hu, L.; Fletcher, J.A.; Fletcher, C.D.; Wagner, A.J.; Loda, M.; Demetri, G.D.; Sicinska, E.T.; Snyder, E.L. c-Jun promotes cell migration and drives expression of the motility factor ENPP2 in soft tissue sarcomas. *J. Pathol.* **2014**, *234*, 190–202. [CrossRef] [PubMed]

32. Shen, S.P.; Liang, J.; Liang, X.L.; Wang, G.Y.; Feng, B.; Guo, W.; Guo, Y.L.; Dong, Z.M. SNHG17, as an EMT-related lncRNA, promotes the expression of c-Myc by binding to c-Jun in esophageal squamous cell carcinoma. *Cancer Sci.* **2022**, *113*, 319–333. [CrossRef]

33. Cui, N.; Li, L.; Feng, Q.; Ma, H.M.; Lei, D.; Zheng, P.S. Hexokinase 2 Promotes Cell Growth and Tumor Formation Through the Raf/MEK/ERK Signaling Pathway in Cervical Cancer. *Front. Oncol.* **2020**, *10*, 581208. [CrossRef]

34. Ala, M. Target c-Myc to treat pancreatic cancer. *Cancer Biol. Ther.* **2022**, *23*, 34–50. [CrossRef] [PubMed]

35. Tanaka, T.; Kaida, T.; Yokoi, K.; Ishii, S.; Nishizawa, N.; Kawamata, H.; Katoh, H.; Sato, T.; Nakamura, T.; Watanabe, M.; et al. Critical relevance of genomic gains of PRL-3/EGFR/c-myc pathway genes in liver metastasis of colorectal cancer. *Oncol. Lett.* **2019**, *17*, 1257–1266. [CrossRef]

36. Marconi, G.D.; Della Rocca, Y.; Fonticoli, L.; Guarnieri, S.; Carradori, S.; Rajan, T.S.; Pizzicannella, J.; Diomede, F. The Beneficial Effect of Carvacrol in HL-1 Cardiomyocytes Treated with LPS-G: Anti-Inflammatory Pathway Investigations. *Antioxidants* **2022**, *11*, 386. [CrossRef] [PubMed]

37. Li, Y.; Qin, G.; Cheng, C.; Yuan, B.; Huang, D.; Cheng, S.; Cao, C.; Chen, G. Purification, characterization and anti-tumor activities of polysaccharides from Ecklonia kurome obtained by three different extraction methods. *Int. J. Biol. Macromol.* **2020**, *150*, 1000–1010. [CrossRef] [PubMed]

38. Marconi, G.D.; Fonticoli, L.; Guarnieri, S.; Cavalcanti, M.; Franchi, S.; Gatta, V.; Trubiani, O.; Pizzicannella, J.; Diomede, F. Ascorbic Acid: A New Player of Epigenetic Regulation in LPS-gingivalis Treated Human Periodontal Ligament Stem Cells. *Oxidative Med. Cell. Longev.* **2021**, *2021*, 6679708. [CrossRef]

Article

Benzothiazole Derivatives Endowed with Antiproliferative Activity in Paraganglioma and Pancreatic Cancer Cells: Structure–Activity Relationship Studies and Target Prediction Analysis

Rosa Amoroso [1,†], Laura De Lellis [1,2,†], Rosalba Florio [1], Nazaret Moreno [3], Mariangela Agamennone [1], Barbara De Filippis [1], Letizia Giampietro [1], Cristina Maccallini [1], Inmaculada Fernández [3], Rocío Recio [3], Alessandro Cama [1,2], Marialuigia Fantacuzzi [1,*] and Alessandra Ammazzalorso [1,*]

[1] Department of Pharmacy, "G. d'Annunzio" University of Chieti-Pescara, Via Dei Vestini 31, 66100 Chieti, Italy; rosa.amoroso@unich.it (R.A.); laura.delellis@unich.it (L.D.L.); rosalba.florio@unich.it (R.F.); mariangela.agamennone@unich.it (M.A.); barbara.defilippis@unich.it (B.D.F.); letizia.giampietro@unich.it (L.G.); cristina.maccallini@unich.it (C.M.); alessandro.cama@unich.it (A.C.)
[2] Center for Advanced Studies and Technology CAST, Via Luigi Polacchi 11, 66100 Chieti, Italy
[3] Departamento de Química Orgánica y Farmacéutica, Facultad de Farmacia, Universidad de Sevilla, C/Profesor García González, 2, 41012 Sevilla, Spain; nmoreno4@us.es (N.M.); inmaff@us.es (I.F.); rrecioj@us.es (R.R.)
*   Correspondence: marialuigia.fantacuzzi@unich.it (M.F.); alessandra.ammazzalorso@unich.it (A.A.)
†   These authors contributed equally to this work.

Abstract: The antiproliferative effects played by benzothiazoles in different cancers have aroused the interest for these molecules as promising antitumor agents. In this work, a library of phenylacetamide derivatives containing the benzothiazole nucleus was synthesized and compounds were tested for their antiproliferative activity in paraganglioma and pancreatic cancer cell lines. The novel synthesized compounds induced a marked viability reduction at low micromolar concentrations both in paraganglioma and pancreatic cancer cells. Derivative **4l** showed a greater antiproliferative effect and higher selectivity index against cancer cells, as compared to other compounds. Notably, combinations of derivative **4l** with gemcitabine at low concentrations induced enhanced and synergistic effects on pancreatic cancer cell viability, thus supporting the relevance of compound **4l** in the perspective of clinical translation. A target prediction analysis was also carried out on **4l** by using multiple computational tools, identifying cannabinoid receptors and sentrin-specific proteases as putative targets contributing to the observed antiproliferative activity.

Keywords: benzothiazole; antiproliferative; pancreatic cancer; paraganglioma; gemcitabine combination; target prediction

1. Introduction

Heterocycles represent precious scaffolds in natural and synthetic molecules, endowed with a great variety of biological activities. Benzothiazoles are members of the bicyclic heteroaromatic family, and they are widely used in medicinal chemistry as the scaffolds of several drugs, including antimicrobial, anti-inflammatory, anticonvulsant, neuroprotective and many others [1,2]. The easy functionalization of the aromatic ring of benzothiazole and the 2-amino or 2-mercapto substituents, which are frequently used as building blocks, makes them attractive and reactive components that are useful in organic and medicinal chemistry programs [3,4]. The development of benzothiazole-based drugs has led to a number of derivatives currently marketed to treat different pathologies, such as the neuroprotective agent riluzole, the diuretic ethoxzolamide, the antidiabetic zopolrestat, the immunosuppressant frentizole, or the diagnostic tool thioflavin T (Figure 1A).
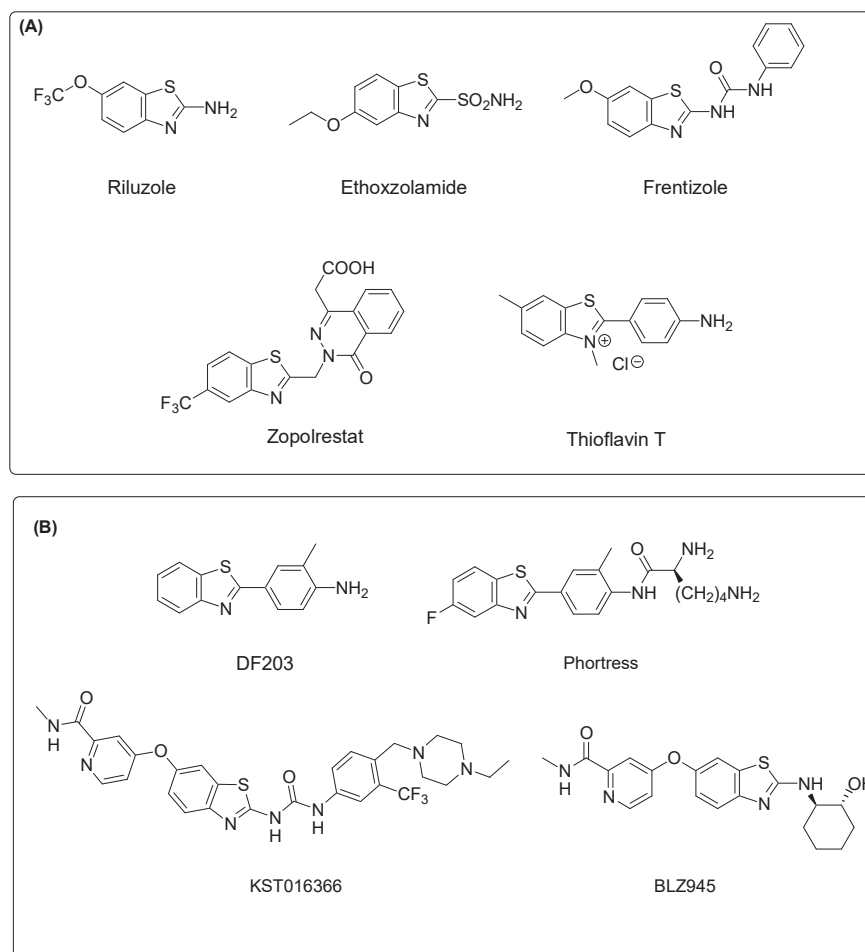
Figure 1. (**A**) Selected marketed drugs containing the benzothiazole nucleus; (**B**) Chemical structures of some benzothiazole derivatives endowed with strong antiproliferative effects in cancer cell models.

The potent antiproliferative effects exerted by benzothiazoles in different cancer models has elicited interest in these molecules as promising antitumor agents (Figure 1B) [5,6]. Considering that 2-phenylbenzothiazoles have been recognized as highly potent cytotoxic compounds, several derivatives were identified and tested in different cancer cell lines. In particular, the chemical manipulation of the lead compound DF203 [7], a 2-phenylbenzothiazole derivative, led to the development of the clinic candidate prodrug Phortress [8]. More recently, the derivative BLZ945, acting as a CSF-1R kinase inhibitor [9,10], has been identified, and it is currently under evaluation as single agent and in combination with spartalizumab for the treatment of advanced solid tumors in adults (ClinicalTrials.gov, NCT02829723) [11]. The 2-ureidobenzothiazole derivative KST016366 has been reported as a potent multikinase inhibitor, displaying a broad-spectrum antiproliferative activity against a wide panel of cancer cell lines [12].

In previous studies, our research group synthesized 2-mercaptobenzothiazole derivatives as Peroxisome Proliferator-Activated Receptor Alpha (PPARα) antagonists [13] (Figure 2). These compounds were able to antagonize PPARα at low micromolar concentrations, and displayed also interesting antiproliferative effects when tested in paraganglioma, glioblastoma, colorectal and pancreatic cancer cell models [14,15]. Interestingly, the benzothiazole derivative **2b** showed a marked cytotoxic effect, mainly in paraganglioma cells, with a dose-dependent inhibition profile and a potency comparable to that of the commercially available PPARα antagonist GW6471 [16,17]. However, it cannot be excluded that other mechanisms of action, or molecular targets, in addition to PPARα inhibition, may emerge for explaining the antiproliferative activity of this compound.
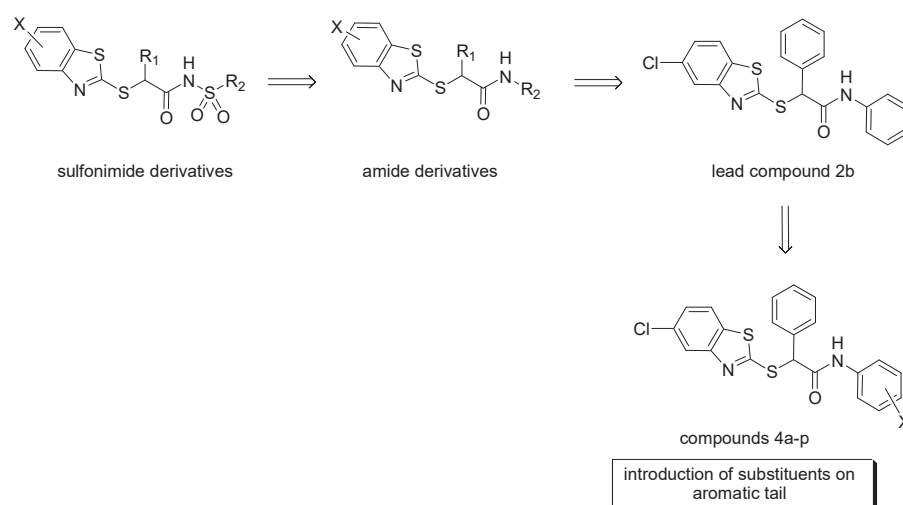
Figure 2. Cytotoxic 2-mercaptobenzothiazole derivatives containing sulfonimide or amide groups, and novel derivatives **4a**–**p** synthesized in this study.

To further explore the potential of this class of molecules as antiproliferative agents, we synthetized novel derivatives of the *lead compound* **2b** by keeping unaltered the benzothiazole scaffold and the amide functional group, and by introducing substituents on the distal aromatic ring. In particular, substituents with different electronic properties and steric hindrance were selected to obtain a series of *para*-substituted (**4a**–**f**), *meta*-substituted (**4g**–**l**) and disubstituted analogs that bear electron-withdrawing substituents (**4m**–**p**). These modifications were performed to test how this molecular portion could modulate the cytotoxic activity in different cancer cell lines.

In this regard, the synthesized compounds **4a**–**p** were tested for their antiproliferative activity in three distinct pancreatic cancer cell lines (AsPC-1, Capan-2, BxPC-3) and two paraganglioma cell lines (PTJ64i, PTJ86i) that have been established by Prof. Cama's research group at the University of Chieti [17]. Compounds of the series that consistently affected cell viability across the tested cancer cell lines more potently than the *lead compound* **2b** were further analyzed against normal HFF-1 fibroblast cells, to evaluate their toxicity. In the perspective of clinical translation, we also tested whether the most potent and less toxic derivatives could be usefully combined with already approved drugs by analyzing the effects of combined treatments on cancer and normal cell viability.

A target prediction study was also performed to shed light on the putative mechanisms of action contributing to the antiproliferative effects of novel compounds.

2. Results and Discussion

2.1. Chemistry

The synthesis of the planned compounds **4a**–**p** was carried out as depicted in Scheme 1. Briefly, the commercially available ethyl mandelate was treated with mesyl chloride and triethylamine in THF at 0 °C. The resulting mesylate **1** was reacted with 5-chloro-2-mercaptobenzothiazole and triethylamine in THF at 50 °C for 24 h; the ester **2** was hydrolyzed in a basic medium to afford acid **3**. The direct coupling of **3** with the proper amines HOBt, DCC, and *N*-methylmorpholine in DMF led to the amides **4a**–**p**. Crude products were purified by column chromatography or crystallization, obtaining desired amides in good purity and discrete yields.
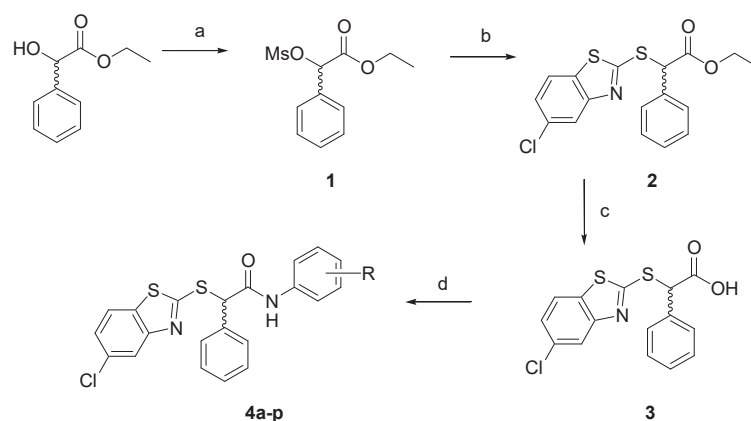
Scheme 1. Synthetic route to final compounds **4a**–**p**. Reagents and conditions: (a) mesyl chloride, TEA, THF, 0 °C-r.t.; (b) 5-chloro-2-mercaptobenzothiazole, TEA, THF, 0°-r.t.−50 °C; (c) NaOH 2N, THF, r.t.; (d) substituted aniline, DCC, HOBt, NMM, DMF, 0 °C-r.t.

Final compounds, including para-substituted **4a**–**f**, meta-substituted **4g**–**l** and a group of m–p disubstituted analogues **4m**–**p** bearing electron-withdrawing substituents, are reported in Table 1. For each compound, the method of purification, the yield, and the melting point are also specified.

Table 1. Final compounds **4a**–**p** synthesized in this study.

Cpd	R	Purification Conditions	Yield %	m.p.
4a	*p*-OCH$_3$	Silica gel, eluent chloroform	58	190 °C (dec)
4b	*p*-Cl	Silica gel, eluent chloroform	63	178–180 °C
4c	*p*-F	Silica gel, eluent dichloromethane	52	168–170 °C
4d	*p*-CF$_3$	Silica gel, eluent dichloromethane	47	183–185 °C
4e	*p*-NO$_2$	Silica gel, eluent dichloromethane	43	191–193 °C
4f	*p*-NHCOCH$_3$	Crystallization from ethyl acetate/methanol	59	243 °C (dec)
4g	*m*-OCH$_3$	Silica gel, eluent cyclohexane/ethyl acetate 7:1	44	160–162 °C
4h	*m*-Cl	Silica gel, eluent dichloromethane	76	175–177 °C
4i	*m*-F	Silica gel, eluent dichloromethane	51	151–153 °C
4j	*m*-CF$_3$	Silica gel, eluent cyclohexane/diethyl ether 4:1	45	155–157 °C
4k	*m*-NO$_2$	Silica gel, eluent dichloromethane	48	193–195 °C
4l	*m*-NHCOCH$_3$	Crystallization from chloroform	41	197–199 °C
4m	3,4-diCl	Silica gel, eluent dichloromethane	44	203–204 °C
4n	2-Br, 5-NO$_2$	Crystallization from cyclohexane/methanol	48	176–178 °C
4o	2-Br, 4-CF$_3$	Crystallization from petroleum ether/methanol	51	179–180 °C
4p	2-Br, 5-CF$_3$	Crystallization from petroleum ether	46	157–159 °C

2.2. Antiproliferative Activity

We analyzed by MTT assays the effects of synthesized compounds **4a**–**p** on the viability of three pancreatic cancer cell lines (AsPC-1, Capan-2, BxPC-3) and two paraganglioma cell models (PTJ64i, PTJ86i), based on relevant antiproliferative effects previously shown by the lead compound **2b** in the same cells [16].

Compounds **4a**–**p** were submitted to a preliminary MTT assay at a one-point screening concentration of 75 μM for 72 h, including **2b** as a reference compound (Figure 3). Overall, the majority of the tested compounds affected cancer cell viability, with a potency compara-

ble, or superior to, **2b** with the exception of **4g** (m-methoxy) and the 2-bromo-substituted derivatives **4n** (2-Br, 5-NO$_2$), **4o** (2-Br, 4-CF$_3$), and **4p** (2-Br, 5-CF$_3$). The presence of the electron-donating methoxy group decreased the activity of **2b**, in both the para and meta positions. Conversely, the introduction of electron-withdrawing substituents, such as halogens, nitro, trifluoromethyl and acetylamino groups, improved the antiproliferative activity of the lead compound **2b**, and this effect was observed for meta and para positions, including the m,p-dichloro derivative **4m**. This general trend was observed for **4a**–**p** in all the selected cancer cell lines. Starting from these data, we selected nine compounds displaying a greater antiproliferative activity than **2b** to perform concentration–response curves. Specifically, these compounds, namely **4d**, **4e**, **4f**, **4h**, **4i**, **4j**, **4k**, **4l**, and **4m**, were tested at concentrations of 3, 6, 12 and 24 μM for 72 h. In addition, the nine compounds, together with **2b**, were tested against human fibroblasts HFF-1, in order to evaluate their selectivity against tumor cells, as compared to normal cells. Effects on cancer or normal cell viability were extrapolated from concentration–response curves and are expressed as IC$_{50}$ values in Table 2.
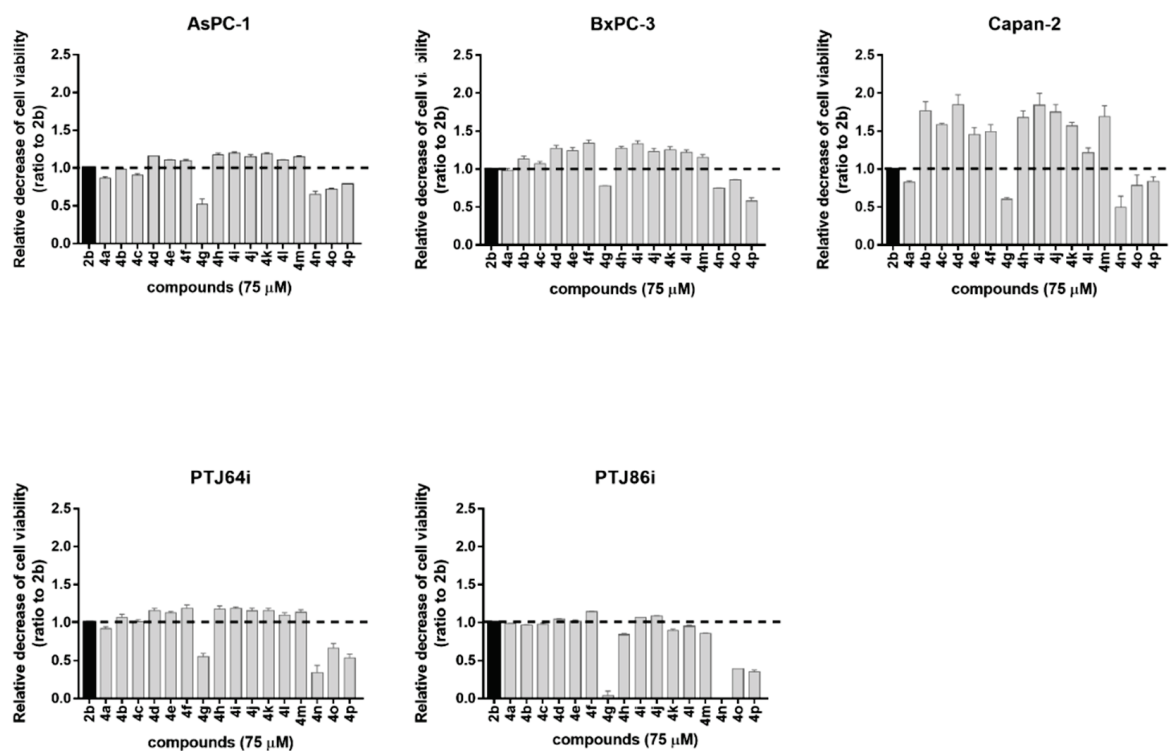
Figure 3. Screening of the effects of novel derivatives (**4a**–**p**) on the viability of pancreatic (AsPC-1, BxPC-3, and Capan-2) and paraganglioma (PTJ64i and PTJ86i) cancer cell lines. The *lead compound* **2b** was included as a reference and the histograms show the relative decrease of cancer cell viability observed after treatments, as compared to **2b**. Cell viability was assessed by an MTT assay using compounds at 75 μM for 72 h. Data shown are the means ± SD of duplicate experiments with quintuplicate determinations and are calculated as ratios relative to the reference compound **2b** (dashed line).

Notably, the compounds **4k** and **4l** displayed the greatest and most consistent selectivity index (SI) values across the tested cancer cell lines (Table 3 and Table S1), which supported their potential as effective and safe anticancer agents in pancreatic cancer and paraganglioma treatment.

Considering that gemcitabine is one of the first-line therapies in pancreatic cancer, to deepen the potential clinical relevance of compounds **4k** and **4l** we further analyzed the effects of the combinations between each of them and gemcitabine on pancreatic cancer cell line viability (Figure 4 and Figure S1, and Table 4).

Table 2. IC$_{50}$ values of **2b** and its nine most active derivatives on cancer and normal cell lines.

	IC$_{50}$ (µM)					
	Pancreatic Cancer			**Paraganglioma**		**Normal Cells**
	AsPC-1	**BxPC-3**	**Capan-2**	**PTJ64i**	**PTJ86i**	**HFF-1**
2b	12.44	14.99	19.65	8.49	16.70	21.37
4d	7.66	3.99	8.97	6.79	12.39	9.23
4e	12.77	10.69	14.11	9.81	18.87	16.69
4f	10.04	18.85	20.10	12.34	12.82	6.54
4h	12.16	11.99	17.67	7.27	16.58	11.55
4i	14.80	18.60	28.50	8.60	11.70	15.00
4j	9.53	13.96	24.18	11.20	17.46	18.10
4k	10.08	11.92	16.87	7.47	13.51	23.33
4l	14.78	13.67	33.76	10.13	19.88	67.07
4m	8.49	9.81	13.33	7.84	19.92	10.32

Note: IC$_{50}$ values for **2b** in paraganglioma cells were previously published [17].

Table 3. Selectivity index values for compounds **4k** and **4l**.

	Selectivity Index (SI) Values				
	Pancreatic Cancer			**Paraganglioma**	
	AsPC-1	**BxPC-3**	**Capan-2**	**PTJ64i**	**PTJ86i**
4k	2.31	1.96	1.38	3.12	1.73
4l	4.54	4.91	1.99	6.62	3.37
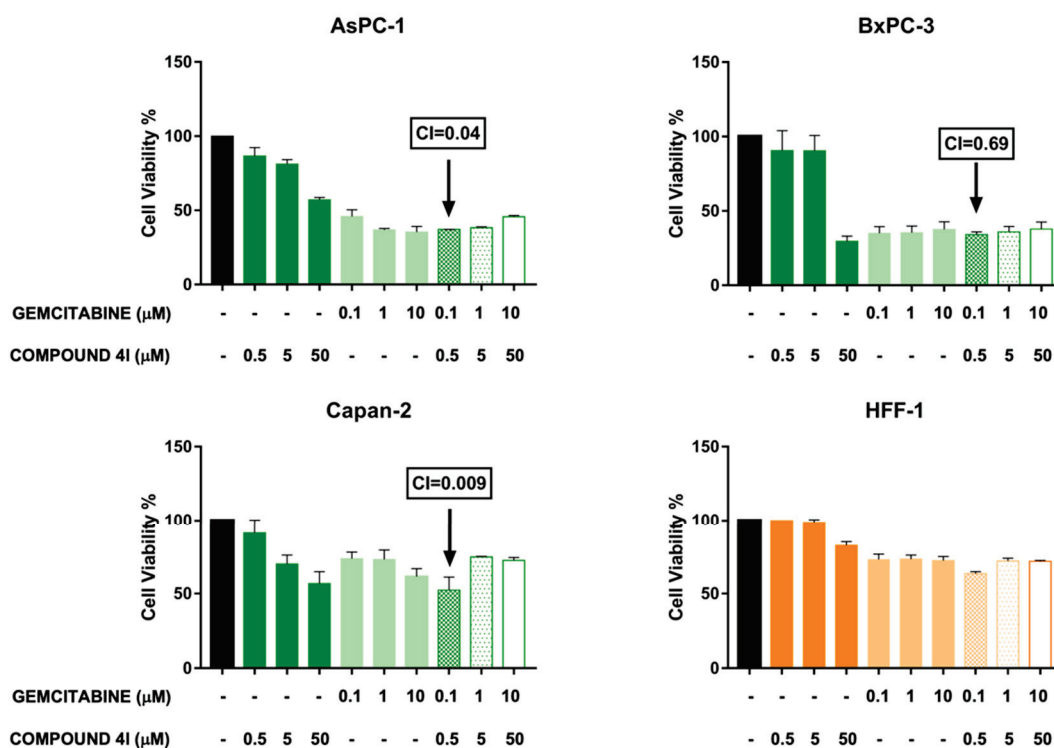
Figure 4. Effect of combined treatments with compound **4l** and gemcitabine on the viability of pancreatic cancer and normal fibroblast cells. Cell viability was assessed by MTT assays after a 72 h incubation of cells with **4l** and gemcitabine at the indicated concentrations, as single agents or in combination. Histograms represent the means ± SD of two independent experiments with quintuplicate determinations. Combination indexes (CIs) were calculated by CompuSyn software. Combinations assessed as synergistic by CIs < 1 are indicated.

Table 4. Percentage of cell viability inhibition after compound **4l** and gemcitabine treatments in PC and normal fibroblast cell lines.

	Inhibition Rate of Cell Viability, %			
	Pancreatic Cancer			Normal Cells
	AsPC-1	BxPC-3	Capan-2	HFF-1
4l–0.5 μM	13.40	6.00	9.34	0.00
4l–5 μM	18.87	9.54	30.25	1.00
4l–50 μM	42.97	70.50	43.30	17.69
GEM—0.1 μM	54.21	65.02	26.87	27.39
GEM—1 μM	63.25	64.65	27.22	25.43
GEM—10 μM	64.63	62.50	38.65	26.27
4l (0.5 μM) + GEM (0.1 μM)	62.85	65.98	47.66	36.69
4l (5 μM) + GEM (1 μM)	61.70	64.01	25.40	28.16
4l (50 μM) + GEM (10 μM)	54.27	64.09	27.79	25.19

Remarkably, the combination between the lowest concentrations of gemcitabine and **4l** (0.1 and 0.5 μM, respectively) decreased pancreatic cancer cell viability in a more marked and synergistic manner (CIs < 1) across the three pancreatic cancer cell lines, as compared to combinations with higher concentrations of the two agents (Figure 4 and Table 4). Notably, the combination with the lowest concentrations of the two compounds appeared safer in normal fibroblast HFF-1 cells, as compared with the pancreatic cancer cell lines (inhibition rate 37% in HFF-1, as compared with 63% in AsPC-1, 66% in BxPC-3 and 48% in Capan-2), supporting the relevance of compound **4l** in the perspective of clinical translation (Table 4).

2.3. Target Prediction Studies

In principle, there could be multiple putative molecular targets for explaining the cytotoxic activity of derivatives **4a**–**p**, and their identification may contribute to a more comprehensive understanding of their bioactivity. Since the high-throughput in vivo target profiling of compounds to identify a potential binding protein for a specific molecule could be expensive and time-consuming, an in silico target fishing study was applied to identify novel proteins possibly involved in the network of molecular events underlying the cytotoxic activity against the cancer cell lines. In silico target fishing (also known as target prediction or target identification) is emerging as an efficient alternative to predict the macromolecular target speedily [18]. A primary distinction divides these methods into ligand-based, i.e., comparing the characteristics (fingerprints) of the query molecule with those present in the databases, and structure-based, i.e., comparing the putative ligand with the features of the target protein's active site [19]. Various tools, freely accessible or not, have been designed to this aim.

In the present work, all query molecules were analyzed using different web-based tools including ligand-based methods such as SEA SEARCH, PLATO, PPB2, and SuperPred, and structure-based tools such as PharmMapper (Table 5). The resulting targets were filtered, selecting only those expressed in the human organism. Furthermore, as most tools retrieve many possible targets, only the highest-ranked (more reliable) were selected and analyzed. Results for the selected derivative **4l** are shown in Table 6, and the prediction results for other analogue compounds are very similar to those presented.

By analyzing the obtained results, to reduce the risk of false-positive prediction [30] we focused on the target protein classes more frequently retrieved by multiple tools, namely cannabinoid receptors (CBR1, CBR2, and G-protein coupled receptor 55—GPCR55—an orphan GPCR binding cannabinoid), which were predicted by four over six programs, as well as sentrin-specific proteases (SENP6, SENP7, SENP8), which were suggested by three over six programs (Table 6). To further assess the significance of our prediction, the potential role of these two targets in pancreatic cancer was explored by a literature research.

Table 5. Description, database, and target ranking criterion of the used web tools. The URL of each tool is indicated. All sites were accessed in 1 March 2022.

Web Tool	Description	Database	Target ranking	URL
SwissTargetPrediction [20]	A combination of 2D and 3D similarities with known ligands	ChEMBL23	Similarity threshold of compounds	http://www.swisstargetprediction.ch
PLATO [21–24]	Multifingerprint Similarity Predictive Approach	ChEMBL30	Similarity between query molecule and known target ligands using different fingerprints	http://plato.uniba.it/
SEA Search [25]	Similarity searching	ChEMBL27	E-value indicating the reliability of the prediction	https://sea.bkslab.org/
PPB2 [26]	Similarity searching combined with Machine Learning models	ChEMBL22	Score calculated by the applied model	http://ppb2.gdb.tools/
SuperPred [27]	Similarity searching by ECFP4 fingerprints	ChEMBL29	Similarity between query molecule and known target ligands	https://prediction.charite.de/subpages/target_prediction.php
ChemMapper [28]	Pharmacophore/shape superposition and statistical background distribution	database of 300M drug-like compounds (ChEMBL, BindingDB, DrugBank, KEGG, PDB)	Similarity between query molecule and known target ligands	http://www.lilab-ecust.cn\T1\guilsinglrightchemmapper
PharmMapper [29]	Reverse Pharmacophore screening	TargetBank DrugBank, BindingDB and PDTD.	Z-score based on fit score (match feature types and positions)	http://www.lilab-ecust.cn/pharmmapper/

Cannabinoid receptors belong to the Class A GPCR family and regulate several functions, such as neurotransmission, immune and inflammatory responses [31]. It is worth noting that the cannabinoid system is a well-known player in cancer biology [32]. The overexpression of both CB1 and CB2 receptors on pancreatic cancer cells, as compared to a very limited expression in healthy pancreatic cells, was revealed by a study in patients [33]. In addition, antagonists to these receptors seem to be extremely promising as antitumor agents, since they are selective in interacting with pancreatic tumor cells, as compared to healthy cells [34].

Sentrin-specific proteases, also known as SUMO-specific proteases, are cysteine proteases responsible for the DeSUMOylation of target proteins, an essential post-translational modification process [35]. To date, seven SENP isoforms have been identified, showing different localization and substrate preference [36]. Considering that SENPs regulate proteins involved in DNA repair, cell cycle, and neovascularization, the deregulation (overexpression or downregulation) of SENP activity results in cellular dysfunction associated with the development of different diseases, including prostate, thyroid, colon, lung, and pancreatic cancer [37]. For instance, the upregulation of SENP3 is a prognostic marker of pancreatic cancer according to the Cancer Genome Atlas (TCGA) [38]. For these reasons, in recent years SENP proteases have emerged as potential targets for cancer therapy [39]; the high sequence homology of members of human SENPs, along with the differences in substrate specificity and subcellular localization might be an interesting way to discover selective SENP inhibitors [40].

Table 6. Predicted targets for compound **4l**.

PLATO	SwissTargetPrediction	SEA	PPB2	SuperPRED	PharmMAPPER	ChemMapper
Peroxisome proliferator-activated receptor alpha	Dual specificity mitogen-activated protein kinase1	Potassium voltage-gated channel subfamily B member 2	Arachidonate 5-lipoxygenase	Glutaminase kidney isoform, mitochondrial	Cbp/p300-intE4:E27	Voltage-dependent T-type calcium channel subunit alpha-1H
Cathepsin K	ATP-binding cassette sub-family G member 2	Neuronal calcium sensor 1	Peroxisome proliferator-activated receptor alpha	Casein kinase II alpha/beta	Coagulation factor XIII A chain	G-protein coupled receptor 55
Cathepsin L	Voltage-gated potassium channel subunit Kv1.5	Ubiquitin carboxyl-terminal hydrolase BAP1	G-protein coupled receptor 55	Muscarinic acetylcholine receptor M3	Cold shock domain-containing protein E1	Cannabinoid receptor 2
Tyrosine-protein kinase LCK	Insulin receptor	Survival motor neuron protein	Cannabinoid CB1 receptor	ADAM10	Short-chain specific acyl-CoA dehydrogenase, mitochondrial	Cannabinoid receptor 1
C-C chemokine receptor type 3	Cannabinoid receptor 1	Potassium channel subfamily K member 9	Cannabinoid CB2 receptor	Aurora kinase B/Inner centromere protein	Homeobox protein Hox-B13	DNA dC->dU-editing enzyme APOBEC-3G
G-protein coupled receptor 55	ALK tyrosine kinase receptor	Cysteinyl leukotriene receptor 1	Vascular endothelial growth factor receptor 2	Caspase-8	Disheveled-associated activator of morphogenesis 1	Probable DNA dC->dU-editing enzyme APOBEC-3A
Carboxy-terminal domain RNA polymerase II polypeptide A small phosphatase 1	Receptor protein-tyrosine kinase erbB-4	Glutamate receptor ionotropic, kainate 1	Coagulation factor X	DNA topoisomerase I	Protection of telomeres protein 1	E3 ubiquitin-protein ligase Mdm2
11-beta-hydroxysteroid dehydrogenase 1	Peroxisome proliferator-activated receptor alpha	6-phosphofructo-2-kinase/fructose-2,6-bisphosphatase 4	Sentrin-specific protease 7	Galectin-3	Regulator of G-protein signaling 6	Eukaryotic translation initiation factor 4H
G-protein coupled receptor 35	MAP kinase p38 alpha	Sentrin-specific protease 8	Epidermal growth factor receptor erbB1	Indoleamine 2,3-dioxygenase	Heterogeneous nuclear ribonucleoprotein R	Polyadenylate-binding protein 1
Sentrin-specific protease 7	c-Jun *N*-terminal kinase 2	Sentrin-specific protease 7	Tyrosine-protein kinase SRC	Sphingosine kinase 1	Calpain-9	MCOLN3 protein
PI3-kinase p110-alpha subunit	Cyclin-dependent kinase 4	Probable G-protein coupled receptor 139	Beta-secretase 1	Adenosine A3 receptor	Glycogen phosphorylase, liver form	Estrogen receptor
Caspase-3	Serine/threonine-protein kinase AKT	Free fatty acid receptor 2	Adenosine A3 receptor	Integrin alpha-V/beta-3	Transcription initiation factor TFIID subunit 13	Putative hexokinase HKDC1
Cannabinoid CB2 receptor	Vascular endothelial growth factor receptor 2	Sentrin-specific protease 6	Dopamine D2 receptor	DNA (cytosine-5)-methyltransferase 1	Proto-oncogene tyrosine-protein kinase Fes/Fps	Hexokinase-1
C-C chemokine receptor type 1	Ribosomal protein S6 kinase alpha 3	Solute carrier family 22 member 6	Serine/threonine-protein kinase Aurora-A	Muscarinic acetylcholine receptor M5	Ig gamma-1 chain C region secreted form	Coagulation factor XII
Sentrin-specific protease 6	Phosphodiesterase 10A	Acyl-CoA (8–3)-desaturase	Vanilloid receptor	Protein-tyrosine phosphatase 2C	Cytochrome P450 2E1	Glyceraldehyde-3-phosphate dehydrogenase
Sentrin-specific protease 8	Pregnane X receptor	Trypsin-3	Induced myeloid leukemia cell differentiation protein Mcl-1	Muscarinic acetylcholine receptor M1	Threonine dehydratase biosynthetic	Induced myeloid leukemia cell differentiation protein Mcl-1
1-acylglycerol-3-phosphate O-acyltransferase beta	Cytochrome P450 19A1	10 kDa heat shock protein, mitochondrial	Adenosine A1 receptor	Glutathione S-transferase Pi	Heme oxygenase 1	Carboxy-terminal domain RNA polymerase II polypeptide A small phosphatase 1
	MAP kinase-activated protein kinase 2	60 kDa heat shock protein, mitochondrial	Serine/threonine-protein kinase Aurora-B	Histone deacetylase 4	Eukaryotic initiation factor 4A-I	Apoptotic protease-activating factor 1
	Carnitine O-palmitoyltransferase 1 liver isoform	Multidrug resistance-associated protein 4	Calcium sensing receptor	Neprilysin	72 kDa type IV collagenase	Tumor necrosis factor

2.4. Docking Studies

To further validate our predictions, docking calculations were carried out on two representative target proteins. Ligands were flexibly docked in the binding site of the Cannabinoid CB1 receptor (CBR1) using the crystallographic structure of CBR1 retrieved by the Protein Data Bank (PDB: 6KPG) [41].

Docked poses in the CBR1 binding site are pretty well conserved among studied compounds: Figure 5a reports the binding mode of compound **4l** highlighting the optimal fitting of the ligand in the CB1 binding pocket. The reported ligand establishes interactions with Phe108, Val110, Leu111, Asn112, Phe170, Phe174, His178, Phe189, Val196, Thr197, Ile267, Phe268, Leu359, Met363, Lys376, Phe379, Ala380, and Ser383 (Figure 5b). These contacts are common to the other ligands as demonstrated by the interaction diagram reported in the Supplementary Materials (Supplementary Figure S2).
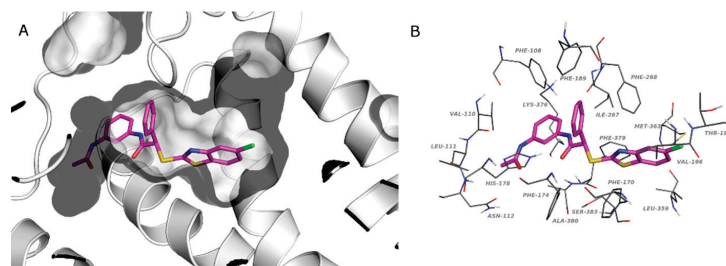

Figure 5. Predicted binding pose of **4l** in the catalytic site of CBR1 (PDB:6KPG). Panel (**A**) CBR1: gray cartoon, binding cavity: gray surface. Panel (**B**) Residues that interact with **4l**: gray lines. (**A**,**B**) Compound **4l,** magenta stick. (O, red; N, blue; S, yellow; Cl, green).

Since the crystallographic structure of SENP6 and SENP7 is not available, the chimeric form of SENP2 containing the SENP6 characteristic loop 1 (similar to SENP7) was used for the structure-based studies (PDB: 3ZO5) [42]. To explore the possible binding sites of the protein, the Sitemap tool was used. Among the identified sites, the one that was superimposable to the most studied SENPs was chosen for the grid generation. This binding site possesses a characteristic form that is able to host all studied compounds. The tridentate structure of the compounds fits well with the structure of the binding site. In Figure 6a, the binding mode of **4l** is shown by the surface representation of the protein, while in Figure 6b, the residues that make contacts with the ligand are reported. In detail, these residues are Leu401, Asn 423, Asn427, Val430, Lys434, Leu441, His442, Val443, Phe444, Ser445, Thr464, Val467, and Gln472. The interaction diagram of all compounds and residues is reported in Supplementary Figure S3.

Although the identified protein classes seem to be promising targets of our benzothiazole derivatives, further in vitro and in vivo studies will be necessary to validate our prediction.
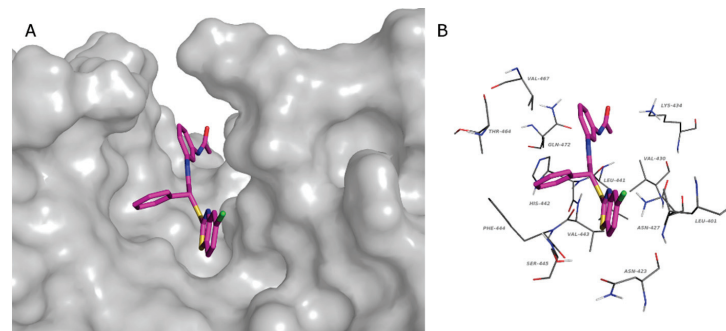

Figure 6. Predicted binding pose of **4l** in the catalytic site of the chimera SENP2-loop1 of SENP6 (PDB:3ZO5). (**A**) Chimera SENP2: gray surface. (**B**) Residues that interact with **4l**: gray lines. (**A**,**B**) Compound **4l,** magenta stick. (O, red; N, blue; S, yellow; Cl, green).

2.5. Physicochemical and Pharmacokinetic Properties Calculation

QikProp [43] calculations were carried out to predict the parameters affecting the drug-likeness and bioavailability of the studied benzothiazoles (Table 7). The calculated physicochemical and pharmacokinetic properties denote that the studied compounds have a drug-like profile, presenting at most one violation of the rule of five due to their lipophilicity (logPoct/water > 5). The predicted low solubility and possible HERG inhibition represent limiting aspects that need further optimization. On the other hand, our compounds present excellent oral absorption and remarkable cell permeability. Moreover, some of the analyzed compounds show good CNS activity and a promising brain/blood partition coefficient.

Table 7. Physicochemical and pharmacokinetic properties of the studied ligands.

ID	MW	accptHB	donorHB	QPlogPo/w	Rule OfFive	PSA	#Rotor	CIQP logS
2b	410.935	4	1	6.005	1	41.544	5	−7.236
4d	478.934	4	1	6.986	1	41.011	5	−8.646
4e	455.933	5	1	5.283	1	85.806	6	−7.758
4f	467.987	6.5	2	4.932	0	85.243	6	−7.325
4h	445.38	4	1	6.535	1	38.018	5	−7.949
4i	428.926	4	1	6.201	1	42.618	5	−7.608
4j	478.934	4	1	6.949	1	45.48	5	−8.646
4k	455.933	5	1	5.082	1	87.682	6	−7.758
4l	467.987	6.5	2	5.289	1	86.742	6	−7.325
4m	479.825	4	1	6.96	1	37.855	5	−8.665

ID	Percent Human Oral Absorption	QPPCaco	QPPMDCK	QPlogBB	QPlog HERG	QPlogKhsa	CNS	#metab
2b	100	4797.201	10,000	0.264	−7.033	0.884	1	4
4d	100	5598.932	10,000	0.616	−6.735	1.136	2	3
4e	95.015	629.287	1753.816	−0.773	−6.819	0.818	−1	4
4f	100	675.963	1383.764	−0.86	−7.087	0.69	−1	3
4h	100	5564.24	10,000	0.509	−7.021	0.991	2	4
4i	100	4890.181	10,000	0.387	−6.754	0.916	1	4
4j	100	3372.682	10,000	0.324	−7.26	1.185	1	5
4k	90.944	433.678	857.42	−1.064	−7.137	0.81	−2	5
4l	100	896.897	2297.395	−0.712	−7.352	0.763	−1	5
4m	100	5649.57	10,000	0.654	−6.934	1.096	2	3

QPlogPo/w: Predicted octanol/water partition coefficient (−2.0–6.5); RuleOfFive: Number of violations of Lipinski's rule of five; PSA: Van der Waals surface area of polar nitrogen and oxygen atoms and carbonyl carbon atoms (7–200); #rotor: Number of non-trivial (not CX3), non-hindered (not alkene, amide, small ring) rotatable bonds. (0–15); CIQPlogS: Conformation Independent predicted aqueous solubility, log S. S in mol dm^{-3} is the concentration of the solute in a saturated solution (−6.5–0.5); PercentHumanOralAbsorption: Predicted human oral absorption on a 0 to 100% scale; QPPCaco: Predicted apparent Caco-2 cell permeability in nm/sec. Caco-2 cells are a model for the gut–blood barrier (<25 poor, >500 great); QPPMDCK: Predicted apparent MDCK cell permeability in nm/sec. MDCK cells are considered to be a good mimic for the blood–brain barrier (<25 poor, >500 great); QPlogBB: Predicted brain/blood partition coefficient (−3.0–1.2); QPlogHERG: Predicted IC50 value for the blockage of HERG K+ channels (concern below −5); QPlogKhsa: Prediction of binding to human serum albumin (−1.5–1.5); CNS: Predicted central nervous system activity on a −2 (inactive) to +2 (active) scale; #metab: Number of likely metabolic reactions.

3. Materials and Methods

3.1. Chemistry

Melting points were determined with a Buchi Melting Point B-450 and were uncorrected. NMR spectra were recorded on a Varian Mercury 300 spectrometer with ^{1}H at 300.060 MHz and ^{13}C at 75.475 MHz. Proton chemical shifts were referenced to the TMS internal standard. Chemical shifts are reported in parts per million (ppm, δ units). Coupling constants are reported in units of Hertz (Hz). Splitting patterns are designed as s, singlet; d, doublet; t, triplet; q, quartet; dd, double doublet; m, multiplet; b, broad. Elemental analyses were carried out on a PerkinElmer 240B micro-analyzer, obtaining results within ± 0.4 % of the theoretical values. The purity of all compounds was over 98%. All commercial chemicals and solvents were reagent grade and were obtained from Merck; they were used without further purification, unless otherwise specified. Chemical reactions were monitored by thin layer chromatography on silica gel plates (60F-254, Sigma Aldrich, Italy) and the analysis of the plates was carried out using a UV lamp 254/365 nm. Flash chromatography was performed on silica gel 60 (Merck).

3.1.1. Synthesis of Ethyl 2-[(Methylsulfonyl)oxy]-2-phenylacetate 1

Triethylamine (834 μL, 6 mmol) was added to a solution of ethyl mandelate (162 mg, 1 mmol) in THF (8 mL) at 0 °C under stirring. Then methanesulfonyl chloride (232 μL, 3 mmol) was added dropwise, and the reaction was allowed to stir for two hours at room temperature. A saturated solution of ammonium chloride was added to the mixture, that was extracted with dichloromethane. Combined organic phases were washed with a saturated sodium chloride solution, dried on sodium sulfate, and the solvent was evaporated under reduced pressure. The crude material was purified by column chromatography on silica gel, with petroleum ether/ethyl acetate 8:2 as eluent. White solid, 93% yield, m.p. 60–61 °C; ^{1}H NMR (CDCl$_3$) δ 1.23 (t, 3H, *J* 7.2 Hz), 3.08 (s, 3H), 4.16–4.30 (m, 2H), 5.91 (s, 1H), 7.39–7.46 (m, 5H); ^{13}C NMR (CDCl$_3$) δ 13.9, 39.4, 62.3, 79.0, 127.7, 129.0, 129.9, 132.7, 167.7.

3.1.2. Synthesis of Ethyl 2-[(5-Chlorobenzo[*d*]thiazol-2-yl)thio]-2-phenylacetate 2

Triethylamine (278 μL, 2 mmol) was added to a solution of 5-cloro-2-mercaptobenzothiazole (202 mg, 1 mmol) in THF (10 mL) at 0 °C under stirring. After 30 min mesylate 1 (258 mg, 1 mmol) was added dropwise, and the temperature was allowed to reach room temperature. The mixture was then heated at 50 °C and stirred for 48 h. After the removal of THF, the resulting oil was dissolved in distilled water and extracted with dichloromethane. The organic phase was washed with a saturated solution of sodium chloride, dried on sodium sulfate, and evaporated under reduced pressure. The crude product was purified by column chromatography on silica gel, with petroleum ether/ethyl acetate 8:1 as eluent. Pale yellow solid, 87% yield; ^{1}H NMR (CDCl$_3$) δ 1.26 (t, 3H, *J* 6.9 Hz), 4.19 and 4.28 (dq, 2H, *J* 6.9 Hz), 5.76 (s, 1H), 7.25–7.38 (m, 5H), 7.52 (dd, 1H, *J* 8.4, 1.8 Hz), 7.64 (d, 1H, *J* 8.4 Hz), 7.83 (d, 1H, *J* 1.8 Hz); ^{13}C NMR (CDCl$_3$) δ 14.3, 54.8, 62.5, 121.7, 121.9, 125.0, 128.7, 129.1, 129.2, 132.3, 133.9, 153.9, 167.0, 169.6.

3.1.3. Synthesis of 2-[(5-Chlorobenzo[d]thiazol-2-yl)thio]-2-phenylacetic Acid 3

NaOH 2N (4 mL, 8 mmol) was added to ester 2 (363 mg, 1 mmol) in THF (5 mL) and the solution was stirred at room temperature overnight. THF was removed under reduced pressure, and the aqueous phase was acidified by HCl 2N, obtaining a precipitate that was collected by filtration under vacuum and recrystallized from cyclohexane. White crystals, 99% yield, m.p. 186–188 °C; ^{1}H NMR (CD$_3$OD) δ 5.79 (s, 1H), 7.31–7.41 (m, 5H), 7.54 (dd, 1H, *J* 8.4, 1.8 Hz), 7.81 (d, 1H, *J* 8.4 Hz), 7.84 (d, 1H, *J* 1.8 Hz); ^{13}C NMR (CD$_3$OD) δ 55.0, 120.9, 122.2, 124.8, 128.4, 128.7, 128.9, 132.2, 133.8, 135.0, 153.8, 167.9, 171.2.

3.1.4. General Procedure for the Synthesis of Amides **4a–p**

To a stirred solution of acid 3 (168 mg, 0.5 mmol) in DMF (5 mL) at 0 °C, *N,N'*-dicyclohexylcarbodiimide (DCC, 103 mg, 0.5 mmol) and hydroxybenzotriazole (HOBt, 77 mg, 0.5 mmol) were added. After 15 min, *N*-methylmorpholine (NMM, 55 μL, 0.5 mmol) and the selected amine (0.5 mmol) were added in sequence to the reaction mixture. The resulting solution was then stirred at room temperature for 24 h, concentrated and the residue was dissolved in dichloromethane, and washed with a saturated solution of sodium bicarbonate and brine. The combined organic layers were dried on sodium sulfate and concentrated under *vacuum* to provide the crude products, which were purified by column chromatography or crystallization.

2-[(5-Chlorobenzo[*d*]thiazol-2-yl)thio]-*N*-(4-methoxyphenyl)-2-phenylacetamide **4a**

Pale yellow solid (silica gel, chloroform), 58% yield; m.p. 190 °C (dec); ^{1}H NMR (CDCl$_3$) δ 3.76 (s, 3H), 5.81 (s, 1H), 6.82 (d, 2H, *J* 8.7 Hz), 7.30–7.42 (m, 6H), 7.54–7.57 (m, 2H), 7.67 (d, 1H, *J* 8.4 Hz), 7.91 (d, 1H, *J* 1.8 Hz), 9.01 (bs, 1H); ^{13}C NMR (CDCl$_3$) δ 55.0, 55.4, 114.1, 121.1, 121.4, 121.9, 125.3, 128.8, 128.9, 129.0, 130.8, 132.6, 133.5, 134.5, 152.9, 159.5, 166.4, 168.3. Calcd for C$_{22}$H$_{17}$ClN$_2$O$_2$S$_2$: C, 59.92; H, 3.89; N, 6.35. Found: C, 59.81; H, 3.90; N, 6.33.

2-[(5-Chlorobenzo[*d*]thiazol-2-yl)thio]-*N*-(4-chlorophenyl)-2-phenylacetamide **4b**

Pale yellow solid (silica gel, chloroform), 63% yield; m.p. 178–180 °C; ^{1}H NMR (CDCl$_3$) δ 5.83 (s, 1H), 7.26 (d, 1H, *J* 8.7 Hz), 7.34–7.56 (m, 9H), 7.70 (d, 1H, *J* 8.7 Hz), 7.95 (d, 1H, *J* 1.8 Hz), 9.39 (bs, 1H); ^{13}C NMR (CDCl$_3$) δ 54.8, 120.9, 121.0, 125.5, 128.8, 129.0, 129.1, 129.5, 132.7, 133.5, 134.1, 136.3, 152.8, 166.9, 168.5. Calcd for C$_{21}$H$_{14}$Cl$_2$N$_2$OS$_2$: C, 56.63; H, 3.17; N, 6.29. Found: C, 56.77; H, 3.18; N, 6.27.

2-[(5-Chlorobenzo[*d*]thiazol-2-yl)thio]-*N*-(4-fluorophenyl)-2-phenylacetamide **4c**

Pale yellow solid (silica gel, dichloromethane), 52% yield; m.p. 168–170 °C; ^{1}H NMR (CDCl$_3$) δ 5.77 (s, 1H), 6.98 (t, 2H, *J* 8.4 Hz), 7.32–7.55 (m, 8H), 7.67 (d, 1H, *J* 8.7 Hz), 7.91 (d, 1H, *J* 2.4 Hz), 9.23 (bs, 1H); ^{13}C NMR (CDCl$_3$) δ 54.8, 115.5, 115.8, 121.1, 121.3, 121.5, 122.0, 125.4, 128.8, 128.9, 129.0, 132.6, 133.7, 134.2, 153.1, 157.9, 161.4, 166.8. Calcd for C$_{21}$H$_{14}$ClFN$_2$OS$_2$: C, 58.80; H, 3.29; N, 6.53. Found: C, 58.69; H, 3.30; N, 6.54.

2-[(5-Chlorobenzo[*d*]thiazol-2-yl)thio]-2-phenyl-*N*-[4-(trifluoromethyl)phenyl] Acetamide **4d**

Pale yellow solid (silica gel, dichloromethane), 47% yield; m.p. 183–185 °C; ^{1}H NMR (CDCl$_3$) δ 5.79 (s, 1H), 7.34–7.41 (m, 4H), 7.51–7.56 (m, 4H), 7.64 (d, 2H, *J* 8.1 Hz), 7.70 (d, 1H, *J* 8.1 Hz), 7.93 (d, 1H, *J* 1.5 Hz), 9.71 (bs, 1H); ^{13}C NMR (CDCl$_3$) δ 54.6, 119.2, 121.0, 122.1, 125.6, 126.3 (q), 128.9, 129.0, 132.8, 133.5, 133.8, 140.8, 152.7, 167.3, 168.7. Calcd for C$_{22}$H$_{14}$ClF$_3$N$_2$OS$_2$: C, 55.17; H, 2.95; N, 5.85. Found: C, 55.22; H, 2.94; N, 5.84.

2-[(5-Chlorobenzo[*d*]thiazol-2-yl)thio]-*N*-(4-nitrophenyl)-2-phenylacetamide **4e**

Pale yellow solid (silica gel, dichloromethane), 43% yield, m.p. 191–193 °C; ^{1}H NMR (CDCl$_3$) δ 5.79 (s, 1H), 6.61 (d, 2H, *J* 9.3 Hz), 7.33–7.41 (m, 4H), 7.50–7.54 (m, 2H), 7.70 (d, 2H, *J* 8.7 Hz), 7.91 (d, 1H, *J* 1.8 Hz), 8.05 (d, 2H, *J* 9 Hz), 8.18 (d, 2H, *J* 9.3 Hz), 10.05 (bs, 1H); ^{13}C NMR (CDCl$_3$) δ 54.5, 113.3, 119.1, 120.9, 122.2, 125.1, 125.7, 126.3, 128.9, 129.1, 129.2, 133.0, 133.4, 143.6, 143.7, 152.5, 167.6, 168.9. Calcd for C$_{21}$H$_{14}$ClN$_3$O$_3$S$_2$: C, 55.32; H, 3.09; N, 9.22. Found: C, 55.57; H, 3.10; N, 9.24.

N-(4-Acetamidophenyl)-2-[(5-chlorobenzo[*d*]thiazol-2-yl)thio]-2-phenylacetamide **4f**

White cristals (from ethyl acetate/methanol), 59% yield; m.p. 243 °C (dec); ^{1}H NMR (DMSO-*d6*) δ 1.98 (s, 3H), 5.96 (s, 1H), 7.29–7.51 (m, 8H), 7.64–7.69 (m, 2H,), 7.86 (d, 1H, *J* 2.4 Hz), 8.03 (d, 1H, *J* 8.4 Hz), 9.89 (bs, 1H) 10.64 (bs, 1H); ^{13}C NMR (DMSO-*d6*) δ 24.3, 42.5, 110.0, 119.7, 120.2, 121.0, 123.9, 125.2, 128.7, 129.2, 131.7, 134.0, 135.9, 136.5,

153.7, 166.4, 167.0, 168.0, 168.4. Calcd for C$_{23}$H$_{18}$ClN$_3$O$_2$S$_2$: C, 59.03; H, 3.88; N, 8.98. Found: C, 59.08; H, 3.87; N, 8.96.

2-[(5-Chlorobenzo[*d*]thiazol-2-yl)thio]-*N*-(3-methoxyphenyl)-2-phenylacetamide **4g**

White solid (silica gel, cyclohexane/ethyl acetate 7:1), 44% yield; m.p. 160–162 °C; ^{1}H NMR (CDCl$_3$) δ 3.75 (s, 3H), 5.78 (s, 1H), 6.64 (dd, 1H, *J* 8.1, 2.4 Hz), 6.92 (d, 1H, *J* 8.1 Hz), 7.17 (t, 1H, *J* 8.1 Hz), 7.30–7.43 (m, 5H), 7.53 (dd, 2H, *J* 8.1, 2.4 Hz), 7.67 (d, 1H, *J* 8.1 Hz), 7.93 (d, 1H, *J* 1.8 Hz), 9.30 (bs, 1H); ^{13}C NMR (CDCl$_3$) δ 54.8, 55.2, 104.9, 110.8, 111.6, 121.1, 122.0, 125.3, 128.8, 128.9, 129.0, 129.7, 132.6, 133.6, 134.2, 139.0, 153.0, 160.1, 166.8, 168.4. Calcd for C$_{22}$H$_{17}$ClN$_2$O$_2$S$_2$: C, 59.92; H, 3.89; N, 6.35. Found: C, 59.80; H, 3.89; N, 6.37.

2-[(5-Chlorobenzo[*d*]thiazol-2-yl)thio]-*N*-(3-chlorophenyl)-2-phenylacetamide **4h**

White solid (silica gel, dichloromethane), 76% yield; m.p. 175–177 °C; ^{1}H NMR (CDCl$_3$) δ 5.77 (s, 1H), 7.08 (d, 1H, *J* 8.1 Hz), 7.20–7.41 (m, 6H), 7.52 (dd, 2H, *J* 8.1, 2.4 Hz), 7.69 (d, 1H, *J* 8.1 Hz), 7.72 (s, 1H), 7.93 (d, 1H, *J* 1.8 Hz), 9.42 (bs, 1H); ^{13}C NMR (CDCl$_3$) δ 54.7, 171.5, 119.8, 121.1, 122.0, 124.5, 125.5, 128.8, 129.0, 129.1, 130.0, 132.8, 133.5, 133.9, 134.7, 138.9, 152.8, 167.0. Calcd for C$_{21}$H$_{14}$Cl$_2$N$_2$OS$_2$: C, 56.63; H, 3.17; N, 6.29. Found: C, 56.67; H, 3.16; N, 6.27.

2-[(5-Chlorobenzo[*d*]thiazol-2-yl)thio]-*N*-(3-fluorophenyl)-2-phenylacetamide **4i**

White solid (silica gel, dichloromethane), 51% yield; m.p. 151–153 °C; ^{1}H NMR (CDCl$_3$) δ 5.77 (s, 1H), 6.79 (dt, 1H), 7.08–7.55 (m, 9H), 7.68 (d, 1H, *J* 8.1 Hz), 7.92 (d, 1H, *J* 2.4 Hz), 9.44 (bs, 1H); ^{13}C NMR (CDCl$_3$) δ 54.8, 107.1, 107.4, 111.1, 111.4, 114.8, 114.9, 121.1, 122.0, 125.4, 128.8, 128.9, 129.0, 130.0, 130.1, 132.7, 133.6, 134.1, 139.2, 152.9, 161.3, 164.5, 167.1. Calcd for C$_{21}$H$_{14}$ClFN$_2$OS$_2$: C, 58.80; H, 3.29; N, 6.53. Found: C, 58.63; H, 3.30; N, 6.55.

2-[(5-Chlorobenzo[*d*]thiazol-2-yl)thio]-2-phenyl-*N*-[3-(trifluoromethyl) phenyl]acetamide **4j**

White solid (silica gel, cyclohexane/diethyl ether 4:1), 45% yield; m.p. 155–157 °C; ^{1}H NMR (CDCl$_3$) δ 5.77 (s, 1H), 7.33–7.41 (m, 7H), 7.53 (d, 2H, *J* 6.3 Hz), 7.61 (d, 1H, *J* 8.1 Hz), 7.70 (d, 1H, *J* 8.7 Hz), 7.93 (s, 2H); ^{13}C NMR (CDCl$_3$) δ 54.6, 116.4 (q), 112.0, 121.0, 122.0, 122.4, 125.5, 128.8, 129.0, 129.5, 132.8, 133.6, 133.8, 138.3, 152.9, 167.2. Calcd for C$_{22}$H$_{14}$ClF$_3$N$_2$OS$_2$: C, 55.17; H, 2.95; N, 5.85. Found: C, 55.21; H, 2.96; N, 5.83.

2-[(5-Chlorobenzo[*d*]thiazol-2-yl)thio]-*N*-(3-nitrophenyl)-2-phenylacetamide **4k**

Pale yellow solid (silica gel, dichloromethane), 48% yield; m.p. 193–195 °C; ^{1}H NMR (CDCl$_3$) δ 5.77 (s, 1H), 7.34–7.54 (m, 7H), 7.70 (d, 1H, *J* 8.7 Hz), 7.83 (dd, 1H, *J* 8.1, 1.2 Hz), 7.92–7.95 (m, 2H), 8.47 (t, 1H, *J* 2.1 Hz), 9.88 (bs, 1H); ^{13}C NMR (CDCl$_3$) δ 54.6, 110.0, 114.5, 119.0, 121.0, 122.1, 125.1, 125.7, 128.8, 129.1, 129.8, 133.0, 133.6, 139.0, 148.5, 167.4. Calcd for C$_{21}$H$_{14}$ClN$_3$O$_3$S$_2$: C, 55.32; H, 3.09; N, 9.22. Found: C, 55.45; H, 3.08; N, 9.22.

N-(3-Acetamidophenyl)-2-[(5-chlorobenzo[*d*]thiazol-2-yl)thio]-2-phenylacetamide **4l**

White crystals (from chloroform), 41% yield; m.p. 197–199 °C; ^{1}H NMR (CDCl$_3$) δ 2.11 (s, 3H), 5.76 (s, 1H), 7.21 (d, 2H, *J* 5.4 Hz), 7.25–7.39 (m, 6H), 7.52 (dd, 2H, *J* 8.1, 2.4 Hz), 7.65 (d, 1H, *J* 8.7 Hz), 7.80 (s, 1H), 7.94 (d, 1H, *J* 1.8 Hz), 9.18 (bs, 1H); ^{13}C NMR (CDCl$_3$) δ 24.6, 55.2, 110.0, 110.9, 115.2, 115.7, 121.4, 121.9, 125.3, 128.8, 128.9, 129.0, 129.6, 132.6, 133.6, 134.2, 138.2, 138.5, 153.1, 166.9, 168.4. Calcd for C$_{23}$H$_{18}$ClN$_3$O$_2$S$_2$: C, 59.03; H, 3.88; N, 8.98. Found: C, 59.08; H, 3.89; N, 9.00.

2-[(5-Chlorobenzo[d]thiazol-2-yl)thio]-N-(3,4-dichlorophenyl)-2-phenyl Acetamide **4m**

White solid (silica gel, dichloromethane), 44% yield; m.p. 203–204 °C; ^{1}H NMR (DMSO-*d$_6$*) δ 5.96 (s, 1H), 7.33–7.47 (m, 5H), 7.54–7.64 (m, 3H), 7.85 (d, 1H, *J* 1.5 Hz), 7.94 (d, 1H, *J* 2.4 Hz), 8.03 (d, 1H, *J* 8.1 Hz), 11.03 (bs, 1H); ^{13}C NMR (DMSO-*d$_6$*) δ 56.2, 119.8, 120.9, 123.9, 125.1, 125.9, 128.7, 129.2, 129.4, 131.3, 131.6, 131.7, 134.0, 135.7, 138.9,

153.6, 167.3, 167.7. Calcd for $C_{21}H_{13}Cl_3N_2OS_2$: C, 52.57; H, 2.73; N, 5.84. Found: C, 52,44; H, 2.72; N, 5.85.

N-(2-Bromo-5-nitrophenyl)-2-[(5-chlorobenzo[*d*]thiazol-2-yl)thio]-2-phenyl Acetamide **4n**

White crystals (from cyclohexane/methanol), 48% yield; m.p. 176–178 °C; ^{1}H NMR (CDCl$_3$) δ 5.98 (s, 1H), 7.31–7.57 (m, 7H), 7.69 (d, 1H, *J* 8.7 Hz), 7.87–7.92 (m, 2H), 9.32 (d, 1H, *J* 3 Hz), 9.51 (bs, 1H); ^{13}C NMR (CDCl$_3$) δ 54.5, 116.7, 119.4, 121.5, 122.0, 125.4, 128.8, 129.2, 129.3, 129.6, 132.6, 133.5, 133.6, 135.5, 152.9, 167.7 Calcd for $C_{21}H_{13}BrClN_3O_3S_2$: C, 47.16; H, 2.45; N, 7.86. Found: C, 47.07; H, 2.46; N, 7.85.

N-[2-Bromo-4-(trifluoromethyl)phenyl]-2-[(5-chlorobenzo[*d*]thiazol-2-yl)thio]-2-phenylacetamide **4o**

White crystals (from petroleum ether/methanol), 51% yield; m.p. 179–180 °C; ^{1}H NMR (CDCl$_3$) δ 5.95 (s, 1H), 7.24–7.28 (m, 1H), 7.34–7.44 (m, 3H), 7.53–7.60 (m, 3H), 7.67 (d, 1H, *J* 8.7 Hz), 7.75 (s, 1H), 7.91 (d, 1H, *J* 1.8 Hz), 8.49 (d, 1H, *J* 8.7 Hz), 9.14 (bs, 1H); ^{13}C NMR (CDCl$_3$) δ 55.5, 113.3, 121.6, 121.7, 121.8, 125.3, 125.5, 125.6, 128.7, 129.2, 129.3, 129.4, 132.4, 133.6, 133.8, 153.2, 166.6, 167.3. Calcd for $C_{22}H_{13}BrClF_3N_2OS_2$: C, 47.37; H, 2.35; N, 5.02. Found: C, 47.39; H, 2.35; N, 5.01.

N-[2-Bromo-5-(trifluoromethyl)phenyl]-2-[(5-chlorobenzo[*d*]thiazol-2-yl)thio]-2-phenylacetamide **4p**

White crystals (from petroleum ether), 46% yield; m.p. 157–159 °C; ^{1}H NMR (CDCl$_3$) δ 5.96 (s, 1H), 7.20–7.32 (m, 2H), 7.39–7.44 (m, 3H), 7.56 (dd, 2H, *J* 7.5, 1.2 Hz), 7.61 (d, 1H, *J* 8.1 Hz), 7.67 (d, 1H, *J* 8.7 Hz), 7.92 (d, 1H, *J* 1.8 Hz), 8.67 (s, 1H), 9.16 (bs, 1H); ^{13}C NMR (CDCl$_3$) δ 55.2, 119.0, 121.7, 121.8, 121.9, 122.0, 125.2, 128.7, 129.2, 129.3, 132.4, 132.8, 133.9, 136.1, 153.2, 167.4. Calcd for $C_{22}H_{13}BrClF_3N_2OS_2$: C, 47.37; H, 2.35; N, 5.02. Found: C, 47.27; H, 2.35; N, 5.04.

3.2. Cell Lines, Treatments, and Cell Viability Assay

Pancreatic cancer (AsPC-1, BxPC-3, and Capan-2), paraganglioma (PTJ86i and PTJ64i) and normal fibroblast (HFF-1) cell lines were cultured as previously described [17]. All compounds were dissolved in DMSO (stock solutions) and then diluted in culture media to the final working concentrations. In this way, the solutions were completely clear and devoid of any undissolved material by microscopic inspection. The final concentration of DMSO in the experiments was at most 0.18% and showed no cell toxicity. The effects of compounds 4a-p and 2b on cancer cell viability were tested by an MTT assay (Sigma-Aldrich, St. Louis, MO, USA), as described by Florio et al. [17]. In the initial screening all compounds were tested at a one-point screening concentration of 75 μM for 72 h (five replica wells per each condition). Then, concentration–response curves were generated by incubating cancer or normal fibroblast cell lines for 72 h with compounds showing a greater antiproliferative activity than 2b, at concentrations ranging from 0 μ M to 24 μM (five replica wells per each condition). For combined treatments, the experimental design was made according to the Chou–Talalay method for drug combination studies, as previously described [44].

3.3. Calculation of Half Maximal Inhibitory Concentration (IC$_{50}$), Selectivity Index (SI), Combination Index (CI) Values and Statistical Analysis

IC$_{50}$ values were extrapolated from concentration–response curves and calculated using the CompuSyn software [45]. The interactions between compound 4l and gemcitabine were assessed by calculating the CI values using the CompuSyn software. Based on this analysis, a CI < 1 indicates synergism, a CI = 1 indicates additive effects and a CI > 1 indicates antagonism. SI values were calculated as previously described [46]. Comparisons of mean values were performed using an unpaired Student's *t*-test. For multiple compar-

isons, a one-way ANOVA followed by Dunnett's test were employed. A *p*-value < 0.05 was estimated as statistically significant.

3.4. In Silico Studies

The SMILE string of the selected compound was obtained from Marvin Sketch (ChemAxon). Swiss Target Prediction database (http://www.swisstargetprediction.ch/), PLATO (http://platomussel.uniba.it/), SEASearch (https://sea.bkslab.org/), PPB2 (http://ppb2.gdb.tools/), SuperPred (https://prediction.charite.de/subpages/target_prediction.php), ChemMapper (http://www.lilab-ecust.cn/chemmapper), and PharmMapper (http://www.lilab-ecust.cn/pharmmapper/) were used to predict potential targets. "Homo sapiens" as the organism and "cancer target" were chosen as an option when possible (SuperPred). In all other cases, the predicted targets were screened by UniProt database (http://www.uniprot.org/uniprot/) by entering the target protein names and selecting only those belonging the "Homo sapiens (Human)" organism and "cancer" as protein name or tissue. Finally, the targets that did not meet the setting parameters were removed. Since these programs use different methods to score the targets, only a max of 20 targets was taken into consideration. All used programs were accessed on 1 March 2022.

The structure-based analysis was carried out using the Schrödinger Life-Sciences Suite 2021–4 [43]. The 2D sketcher in Maestro was used to construct ligand structures that were submitted to LigPrep to obtain ligand 3D geometry, identify all potential tautomers, and protonation states at pH 7.0 ± 0.4. The resulting structures were minimized utilizing Macro-Model, the OPLS4 force field, and 5000 steps of the PRCG algorithm with a convergence criterion of 0.05 KJ/mol. Docking calculations were carried out on the 3D coordinates of CBR1 with PDB ID 6KPG and the chimeric form of SENP2 containing the SENP7 loop, PDB ID 3ZO5. Before docking calculations, protein structures were prepared using the Protein Preparation routine in Maestro [47] that fixes the protein structure and relaxes it through a constrained minimization. For the CBR1 the docking protocol was validated by reobtaining the X-ray geometry of the crystallographic ligand (RMSD 0.5135Å). To define the more proper binding site in SENP6, a SiteMap [48,49] calculation was carried out and the subsequent Glide Grid was generated on the predicted site. Glide [50,51] SP flexible docking calculations were carried out on both proteins

4. Conclusions

In conclusion, a library of phenylacetamide derivatives containing the benzothiazole nucleus was synthesized and tested for its antiproliferative activity in three pancreatic and two paraganglioma cancer cell lines. Most of the derivatives showed an improved antiproliferative activity, as compared to the *lead compound* 2b, allowing us to trace some preliminary structure–activity relationships. Considering both the antiproliferative activities and selectivity profiles, **4l** was further analyzed in combination with gemcitabine on the three pancreatic cancer cell lines. Notably, the combination of the two compounds when used at the lowest concentrations (0.1 μM gemcitabine and 0.5 μM **4l**, respectively) affected pancreatic cancer cell viability in a potent and synergistic manner. This synergistic effect supports the interest in this class of benzothiazoles in view of a possible translation into cancer treatment. A computational study was also conducted to predict the putative targets involved in the observed antiproliferative activity in pancreatic cancer cells: the different tools used to this aim identified the cannabinoid receptors and the sentrin-specific proteases as potential targets contributing to the bioactivity of this family of compounds. Docking studies on representative targets (CBR1 and SENP6) show that all compounds fit well in their binding site. Future in vitro and in vivo studies will be necessary to validate the predicted molecular targets of our compounds and gain novel insights into the under-explored potential of these molecules as antitumor agents in paraganglioma and pancreatic cancer treatment.

References

1. Sharma, P.C.; Sinhmar, A.; Sharma, A.; Rajak, H.; Pathak, D.P. Medicinal significance of benzothiazole scaffold: An insight view. *J. Enzyme Inhib. Med. Chem.* **2013**, *28*, 240–266. [CrossRef]

2. Weekes, A.A.; Westwell, A.D. 2-Arylbenzothiazole as a privileged scaffold in drug discovery. *Curr. Med. Chem.* **2009**, *16*, 2430–2440. [CrossRef]

3. Zhilitskaya, L.V.; Shainyan, B.A.; Yarosh, N.O. Modern approaches to the synthesis and transformations of practically valuable benzothiazole derivatives. *Molecules* **2021**, *26*, 2190. [CrossRef]

4. Keri, R.S.; Patil, M.R.; Patil, S.A.; Budagumpi, S. A comprehensive review in current developments of benzothiazole-based molecules in medicinal chemistry. *Eur. J. Med. Chem.* **2015**, *89*, 207–251. [CrossRef]

5. Irfan, A.; Batool, F.; Zahra Naqvi, S.A.; Islam, A.; Osman, S.M.; Nocentini, A.; Alissa, S.A.; Supuran, C.T. Benzothiazole derivatives as anticancer agents. *J. Enzyme Inhib. Med. Chem.* **2020**, *35*, 265–279. [CrossRef]

6. Ammazzalorso, A.; Carradori, S.; Amoroso, R.; Fernández, I.F. 2-substituted benzothiazoles as antiproliferative agents: Novel insights on structure-activity relationships. *Eur. J. Med. Chem.* **2020**, *207*, 112762. [CrossRef]

7. Bradshaw, T.D.; Stevens, M.F.; Westwell, A.D. The discovery of the potent and selective antitumour agent 2-(4-amino-3-methylphenyl)benzothiazole (DF 203) and related compounds. *Curr. Med. Chem.* **2001**, *8*, 203–210. [CrossRef]

8. Bradshaw, T.D.; Westwell, A.D. The development of the antitumour benzothiazole prodrug, Phortress, as a clinical candidate. *Curr. Med. Chem.* **2004**, *11*, 1009–1021. [CrossRef]

9. Strachan, D.C.; Ruffell, B.; Oei, Y.; Bissell, M.J.; Coussens, L.M.; Pryer, N.; Daniel, D. CSF1R inhibition delays cervical and mammary tumor growth in murine models by attenuating the turnover of tumor-associated macrophages and enhancing infiltration by CD8+ T cells. *Oncoimmunology* **2013**, *2*, e26968. [CrossRef]

10. Krauser, J.A.; Jin, Y.; Walles, M.; Pfaar, U.; Sutton, J.; Wiesmann, M.; Graf, D.; Pflimlin-Fritschy, V.; Wolf, T.; Camenisch, G.; et al. Phenotypic and metabolic investigation of a CSF-1R kinase receptor inhibitor (BLZ945) and its pharmacologically active metabolite. *Xenobiotica* **2015**, *45*, 107–123. [CrossRef]

11. Lin, C.-C.; Gil-Martin, M.; Bauer, T.M.; Naing, A.; Wan-Teck Lim, D.; Sarantopoulos, J.; Geva, R.; Ando, Y.; Fan, L.; Choudhury, S.; et al. Abstract nr CT171: Phase I study of BLZ945 alone and with spartalizumab (PDR001) in patients (pts) with advanced solid tumors [abstract]. *Cancer Res.* **2020**, *80* (Suppl. 16), CT171. [CrossRef]

12. El-Damasy, A.K.; Cho, N.C.; Nam, G.; Pae, A.N.; Keum, G. Discovery of a nanomolar multikinase inhibitor (KST016366): A new benzothiazole derivative with remarkable broad-spectrum antiproliferative activity. *ChemMedChem* **2016**, *11*, 1587–1595. [CrossRef]

13. Ammazzalorso, A.; D'Angelo, A.; Giancristofaro, A.; De Filippis, B.; Di Matteo, M.; Fantacuzzi, M.; Giampietro, L.; Linciano, P.; Maccallini, C.; Amoroso, R. Fibrate-derived *N*-(methylsulfonyl)amides with antagonistic properties on PPARα. *Eur. J. Med. Chem.* **2012**, *58*, 317–322. [CrossRef]

14. Ammazzalorso, A.; De Lellis, L.; Florio, R.; Bruno, I.; De Filippis, B.; Fantacuzzi, M.; Giampietro, L.; Maccallini, C.; Perconti, S.; Verginelli, F.; et al. Cytotoxic effect of a family of peroxisome proliferator-activated receptor antagonists in colorectal and pancreatic cancer cell lines. *Chem. Biol. Drug Des.* **2017**, *90*, 1029–1035. [CrossRef]

15. Benedetti, E.; d'Angelo, M.; Ammazzalorso, A.; Gravina, G.L.; Laezza, C.; Antonosante, A.; Panella, G.; Cinque, B.; Cristiano, L.; Dhez, A.C.; et al. PPARα antagonist AA452 triggers metabolic reprogramming and increases sensitivity to radiation therapy in human glioblastoma primary cells. *J. Cell Physiol.* **2017**, *232*, 1458–1466. [CrossRef] [PubMed]

16. Ammazzalorso, A.; De Lellis, L.; Florio, R.; Laghezza, A.; De Filippis, B.; Fantacuzzi, M.; Giampietro, L.; Maccallini, C.; Tortorella, P.; Veschi, S.; et al. Synthesis of novel benzothiazole amides: Evaluation of PPAR activity and anti-proliferative effects in paraganglioma, pancreatic and colorectal cancer cell lines. *Bioorg. Med. Chem. Lett.* **2019**, *29*, 2302–2306. [CrossRef]

17. Florio, R.; De Lellis, L.; di Giacomo, V.; Di Marcantonio, M.C.; Cristiano, L.; Basile, M.; Verginelli, F.; Verzilli, D.; Ammazzalorso, A.; Prasad, S.C.; et al. Effects of PPARα inhibition in head and neck paraganglioma cells. *PLoS ONE* **2017**, *12*, e0178995. [CrossRef]

18. Cereto-Massagué, A.; Ojeda, M.J.; Valls, C.; Mulero, M.; Pujadas, G.; Garcia-Vallve, S. Tools for in silico target fishing. *Methods* **2015**, *71*, 981–983. [CrossRef] [PubMed]

19. Sydow, D.; Burggraaff, L.; Szengel, A.; Van Vlijmen, H.W.T.; Ijzerman, A.P.; Van Westen, G.J.P.; Volkamer, A. Advances and challenges in computational target prediction. *J. Chem. Inf. Model.* **2019**, *59*, 1728–1742. [CrossRef]

20. Daina, A.; Michielin, O.; Zoete, V. Swiss Target Prediction: Updated data and new features for efficient prediction of protein targets of small molecules. *Nucleic Acids Res.* **2019**, *47*, W357–W364. [CrossRef] [PubMed]

21. Ciriaco, F.; Gambacorta, N.; Alberga, D.; Nicolotti, O. Quantitative polypharmacology profiling based on a multifingerprint similarity predictive approach. *J. Chem. Inf. Model.* **2021**, *61*, 4868–4876. [CrossRef]

22. Alberga, D.; Trisciuzzi, D.; Montaruli, M.; Leonetti, F.; Mangiatordi, G.F.; Nicolotti, O. A new approach for drug target and bioactivity prediction: The Multifingerprint Similarity Search Algorithm (MuSSeL). *J. Chem. Inf. Model.* **2019**, *59*, 586–596. [CrossRef] [PubMed]

23. Montaruli, M.; Alberga, D.; Ciriaco, F.; Trisciuzzi, D.; Tondo, A.R.; Mangiatordi, G.F.; Nicolotti, O. Accelerating drug discovery by early protein drug target prediction based on a multi-fingerprint similarity search. *Molecules* **2019**, *24*, 2233. [CrossRef]

24. Ciriaco, F.; Gambacorta, N.; Trisciuzzi, D.; Nicolotti, O. PLATO: A predictive drug discovery web platform for efficient target fishing and bioactivity profiling of small molecules. *Int. J. Mol. Sci.* **2022**, *23*, 5245. [CrossRef] [PubMed]

25. Keiser, M.J.; Roth, B.L.; Armbruster, B.N.; Ernsberger, P.; Irwin, J.J.; Shoichet, B.K. Relating protein pharmacology by ligand chemistry. *Nat. Biotechnol.* **2007**, *25*, 197–206. [CrossRef] [PubMed]

26. Awale, M.; Reymond, J.L. Polypharmacology browser PPB2: Target prediction combining nearest neighbors with machine learning. *J. Chem. Inf. Model.* **2019**, *59*, 10–17. [CrossRef] [PubMed]

27. Dunkel, M.; Günther, S.; Ahmed, J.; Wittig, B.; Preissner, R. SuperPred: Drug classification and target prediction. *Nucleic Acids Res.* **2008**, *36*, W55–W59. [CrossRef]

28. Gong, J.; Cai, C.; Liu, X.; Ku, X.; Jiang, H.; Gao, D.; Li, H. ChemMapper: A versatile web server for exploring pharmacology and chemical structure association based on molecular 3D similarity method. *Bioinformatics* **2013**, *29*, 1827–1829. [CrossRef]

29. Wang, X.; Shen, Y.; Wang, S.; Li, S.; Zhang, W.; Liu, X.; Lai, L.; Pei, J.; Li, H. PharmMapper 2017 update: A web server for potential drug target identification with a comprehensive target pharmacophore database. *Nucleic Acids Res.* **2017**, *45*, W356–W360. [CrossRef] [PubMed]

30. Wei, H.; Di Guan, Y.; Zhang, L.X.; Liu, S.; Lu, A.P.; Cheng, Y.; Cao, D.S. A combinatorial target screening strategy for deorphaning macromolecular targets of natural product. *Eur. J. Med. Chem.* **2020**, *204*, 112644. [CrossRef] [PubMed]

31. Mackie, K. Cannabinoid receptors: Where they are and what they do. *J. Neuroendocrinol.* **2008**, *20*, 10–14. [CrossRef] [PubMed]

32. Moreno, E.; Cavic, M.; Krivokuca, A.; Casadó, V.; Canela, E. The endocannabinoid system as a target in cancer diseases: Are we there yet? *Front. Pharmacol.* **2019**, *10*, 339. [CrossRef]

33. Michalski, C.W.; Oti, F.E.; Erkan, M.; Sauliunaite, D.; Bergmann, F.; Pacher, P.; Batkai, S.; Müller, M.W.; Giese, N.A.; Friess, H. Cannabinoids in pancreatic cancer: Correlation with survival and pain. *Int. J. Cancer* **2008**, *122*, 742–750. [CrossRef]

34. Garmpis, N.; Damaskos, C.; Dimitroulis, D.; Garmpi, A.; Diamantis, E.; Sarantis, P.; Georgakopoulou, V.E.; Patsouras, A.; Prevezanos, D.; Syllaios, A.; et al. Targeting the endocannabinoid system: From the need for new therapies to the development of a promising strategy. What about pancreatic cancer? *In Vivo* **2022**, *36*, 543–555. [CrossRef] [PubMed]

35. Celen, A.B.; Sahin, U. Sumoylation on its 25th anniversary: Mechanisms, pathology, and emerging concepts. *FEBS J.* **2020**, *287*, 3110–3140. [CrossRef]

36. Jia, Y.; Claessens, L.A.; Vertegaal, A.C.O.; Ovaa, H. Chemical tools and biochemical assays for SUMO specific proteases (SENPs). *ACS Chem. Biol.* **2019**, *14*, 2389–2395. [CrossRef]

37. Tokarz, P.; Woźniak, K. SENP proteases as potential targets for cancer therapy. *Cancers* **2021**, *13*, 2059. [CrossRef] [PubMed]

38. Available online: http://cancergenome.nih.gov/ (accessed on 1 March 2022).

39. Schneeweis, C.; Hassan, Z.; Schick, M.; Keller, U.; Schneider, G. The SUMO pathway in pancreatic cancer: Insights and inhibition. *Br. J. Cancer* **2021**, *124*, 531–538. [CrossRef] [PubMed]

40. Wang, Z.; Liu, Y.; Zhang, J.; Ullah, S.; Kang, N.; Zhao, Y.; Zhou, H. Benzothiophene-2-carboxamide derivatives as SENPs inhibitors with selectivity within SENPs family. *Eur. J. Med. Chem.* **2020**, *204*, 112553. [CrossRef]

41. Hua, T.; Li, X.; Wu, L.; Iliopoulos-Tsoutsouvas, C.; Wang, Y.; Wu, M.; Shen, L.; Brust, C.A.; Nikas, S.P.; Song, F.; et al. Activation and signaling mechanism revealed by cannabinoid receptor-Gi complex structures. *Cell* **2020**, *180*, 655–665. [CrossRef]

42. Alegre, K.O.; Reverter, D. Structural insights into the SENP6 Loop1 structure in complex with SUMO2. *Protein Sci.* **2014**, *23*, 433–441. [CrossRef]

43. *Schrödinger Release 2021-4: Maestro, Glide, Protein Preparation Wizard, Epik, SiteMap, QikProp, MacroModel*; Schrödinger, LLC.: New York, NY, USA, 2021.

44. Florio, R.; Veschi, S.; di Giacomo, V.; Pagotto, S.; Carradori, S.; Verginelli, F.; Cirilli, R.; Casulli, A.; Grassadonia, A.; Tinari, N.; et al. The benzimidazole-based anthelmintic parbendazole: A repurposed drug candidate that synergizes with gemcitabine in pancreatic cancer. *Cancers* **2019**, *11*, 2042. [CrossRef] [PubMed]

45. Chou, T.C. Drug combination studies and their synergy quantification using the Chou-Talalay method. *Cancer Res.* **2010**, *70*, 440–446. [CrossRef] [PubMed]

46. Ammazzalorso, A.; Bruno, I.; Florio, R.; De Lellis, L.; Laghezza, A.; Cerchia, C.; De Filippis, B.; Fantacuzzi, M.; Giampietro, L.; Maccallini, C.; et al. Sulfonimide and amide derivatives as novel PPARα antagonists: Synthesis, antiproliferative activity, and docking studies. *ACS Med. Chem. Lett.* **2020**, *11*, 624–632. [CrossRef] [PubMed]

47. Sastry, G.M.; Adzhigirey, M.; Day, T.; Annabhimoju, R.; Sherman, W. Protein and ligand preparation: Parameters, protocols, and influence on virtual screening enrichments. *J. Comput. Aid. Mol. Des.* **2013**, *27*, 221–234. [CrossRef]

48. Halgren, T.A. Identifying and characterizing binding sites and assessing druggability. *J. Chem. Inf. Model.* **2009**, *49*, 377–389. [CrossRef] [PubMed]

49. Halgren, T.A. New method for fast and accurate binding-site identification and analysis. *Chem. Biol. Drug Des.* **2007**, *69*, 146–148. [CrossRef]

50. Friesner, R.A.; Banks, J.L.; Murphy, R.B.; Halgren, T.A.; Klicic, J.J.; Mainz, D.T.; Repasky, M.P.; Knoll, E.H.; Shaw, D.E.; Shelley, M.; et al. Glide: A new approach for rapid, accurate docking and scoring. 1. Method and assessment of docking accuracy. *J. Med. Chem.* **2004**, *47*, 1739–1749. [CrossRef] [PubMed]

51. Halgren, T.A.; Murphy, R.B.; Friesner, R.A.; Beard, H.S.; Frye, L.L.; Pollard, W.T.; Banks, J.L. Glide: A new approach for rapid, accurate docking and scoring. 2. Enrichment factors in database screening. *J. Med. Chem.* **2004**, *47*, 1750–1759. [CrossRef]

Article

Design, Synthesis and Biological Investigation of 2-Anilino Triazolopyrimidines as Tubulin Polymerization Inhibitors with Anticancer Activities

Romeo Romagnoli [1,*], Paola Oliva [1], Filippo Prencipe [2], Stefano Manfredini [3], Federica Budassi [4], Andrea Brancale [5], Salvatore Ferla [6], Ernest Hamel [7], Diana Corallo [8], Sanja Aveic [8], Lorenzo Manfreda [9,10], Elena Mariotto [9,10], Roberta Bortolozzi [9,10] and Giampietro Viola [9,10,*]

1 Department of Chemical, Pharmaceutical and Agricultural Sciences, University of Ferrara, 44121 Ferrara, Italy
2 Department of Chemical and Pharmaceutical Sciences, University of Trieste, 34127 Trieste, Italy
3 Department of Life Sciences and Biotechnology, University of Ferrara, 44121 Ferrara, Italy
4 Medicinal Chemistry Department, Integrated Drug Discovery, Aptuit-An Evotec Company, 37135 Verona, Italy
5 School of Pharmacy and Pharmaceutical Sciences, Cardiff University, King Edward VII Avenue, Cardiff CF10 3NB, UK
6 Faculty of Medicine, Health and Life Science, Swansea University Medical School, Grove Building, Swansea University, Swansea SA2 8PP, UK
7 Molecular Pharmacology Branch, Developmental Therapeutics Program, Division of Cancer Treatment and Diagnosis, Frederick National Laboratory for Cancer Research, National Cancer Institute, National Institutes of Health, Frederick, MD 21702, USA
8 Laboratory of Target Discovery and Biology of Neuroblastoma, Istituto di Ricerca Pediatrica (IRP), Fondazione Città della Speranza, 35128 Padova, Italy
9 Department of Woman's and Child's Health, Hemato-Oncology Lab, University of Padova, 35131 Padova, Italy
10 Laboratory of Experimental Pharmacology, Istituto di Ricerca Pediatrica (IRP), Fondazione Città della Speranza, 35128 Padova, Italy
* Correspondence: rmr@unife.it (R.R.); giampietro.viola.1@unipd.it (G.V.)

Abstract: A further investigation aiming to generate new potential antitumor agents led us to synthesize a new series of twenty-two compounds characterized by the presence of the 7-(3′,4′,5′-trimethoxyphenyl)-[1,2,4]triazolo[1,5-*a*]pyrimidine pharmacophore modified at its 2-position. Among the synthesized compounds, three were significantly more active than the others. These bore the substituents *p*-toluidino (**3d**), *p*-ethylanilino (**3h**) and 3′,4′-dimethylanilino (**3f**), and these compounds had IC$_{50}$ values of 30–43, 160–240 and 67–160 nM, respectively, on HeLa, A549 and HT-29 cancer cells. The *p*-toluidino derivative **3d** was the most potent inhibitor of tubulin polymerization (IC$_{50}$: 0.45 μM) and strongly inhibited the binding of colchicine to tubulin (72% inhibition), with antiproliferative activity superior to CA-4 against A549 and HeLa cancer cell lines. In vitro investigation showed that compound **3d** was able to block treated cells in the G2/M phase of the cell cycle and to induce apoptosis following the intrinsic pathway, further confirmed by mitochondrial depolarization and caspase-9 activation. In vivo experiments conducted on the zebrafish model showed good activity of **3d** in reducing the mass of a HeLa cell xenograft. These effects occurred at nontoxic concentrations to the animal, indicating that **3d** merits further developmental studies.

Keywords: colchicine binding site; antitumor activity; [1,2,4]triazolo[1,5-*a*]pyrimidine; apoptosis; microtubule-targeting agents

1. Introduction

Eukaryotic cells possess a complex cytoskeletal system. One of its major components is the microtubule network, composed of polymeric protein structures formed by the assembly of αβ-tubulin heterodimers, which are in a dynamic equilibrium with the microtubules.

These are critical for several fundamental cellular functions, including cell division, where microtubules form the mitotic spindle required for proper chromosomal separation [1–4]. Since microtubules are critical in the proliferation of cancer cells, the design of new and improved molecules that exert their effects by interfering with microtubule dynamics continues to receive substantial attention [5–7].

Among the seven distinct classes of tubulin-binding agents that have been identified on the basis of their different mechanisms of action and binding sites on tubulin, only three groups of antimitotic agents are used clinically for cancer treatment [8,9]. First are the vinca alkaloids, typified by vinblastine, vincristine, vinorelbine and vinflunine, that destabilize microtubules by inhibiting polymerization of tubulin into microtubules [10–12]. Second is the halichondrin B analogue eribulin, which also inhibits tubulin polymerization. Third, are compounds that bind in the taxoid site and stabilize microtubules. This group includes paclitaxel, the structurally related compounds docetaxel and cabazitaxel and the epothilone analogue ixabepilone [13–15]. These drugs are in clinical use to treat both adult and pediatric cancers [16–19]. Taxoid site compounds, eribulin and vinca alkaloids all interact with β-tubulin, but at different binding sites [12,14]. Nevertheless, the clinical success of these three classes of compounds has stimulated intensive research aimed at discovering additional microtubule-targeting drugs with clinical potential [20–23].

The colchicine site agents that inhibit tubulin assembly belong to another important class of tubulin interactive compounds, due to the discovery of numerous natural products and synthetic compounds with wide structural heterogeneity that target this site [24–27]. The colchicine site is located on β-tubulin at its interface with α-tubulin and is distinct from the vinca and eribulin sites [25,26]. One of the most notable of these compounds, both for its potency and structural simplicity, is the naturally occurring polymethoxylated *cis*-stilbene derivative combretastatin A-4 (CA-4, **1a**, Figure 1) [28,29]. Moreover, several studies have documented that this compound also acts as a powerful vascular disrupting agent [30], particularly for the neovasculature of tumors. To improve its water solubility, the corresponding phosphate derivative of combretastatin A-4 (CA-4P, also known as fosbretabulin disodium, **1b**) was synthesized as a water-soluble pro-drug of CA-4 [31]. The European Medicines Agency (EMA) approved combretastatin CA-4P as an orphan drug for the treatment of anaplastic thyroid cancer and ovarian cancer, and CA-4P is in phase III clinical trials in combination with bevacizumab for recurrent ovarian cancer or with everolimus in neuroendocrine tumors [32,33].

While the vinca alkaloids and the taxoids have achieved notable success in the treatment of human cancers, no colchicine site inhibitor has yet been approved for cancer chemotherapy in human patients [34–36]. KXO1 (tirbanibulin or KX2–391), a dual Src and tubulin polymerization inhibitor acting at the colchicine site of β-tubulin [37], was approved by the FDA in December 2020 for the topical treatment of actinic or solar keratosis, the most common chronic and precancerous skin disease that occurs on skin damaged by long-term exposure to ultraviolet radiation [38].

Emerging multidrug resistance (MDR) due to the overexpression of membrane-bound drug efflux proteins, such as ATP binding cassette (ABC) transporters, along with aberrant expression of the βIII-tubulin isoform, has limited the use of taxoids and vinca alkaloids in clinical practice [39–42]. Resistance to different types of microtubule-targeting agents was recently suggested to be related to their binding sites and that βIII-tubulin-mediated drug resistance might be circumvented by colchicine site inhibitors [43–47]. These observations emphasize the need to discover novel scaffolds active at the colchicine site and amenable to rapid derivatization because such compounds could be readily prepared by rapid and concise synthetic procedures [48,49]. In addition, several colchicine site binders have been shown to be effective against p53-mutant cell lines and to circumvent P-glycoprotein-mediated multidrug resistance. This lack of susceptibility to MDR pumps further emphasizes the importance of novel inhibitors of tubulin assembly that have activity against drug-resistant tumors [50–52].
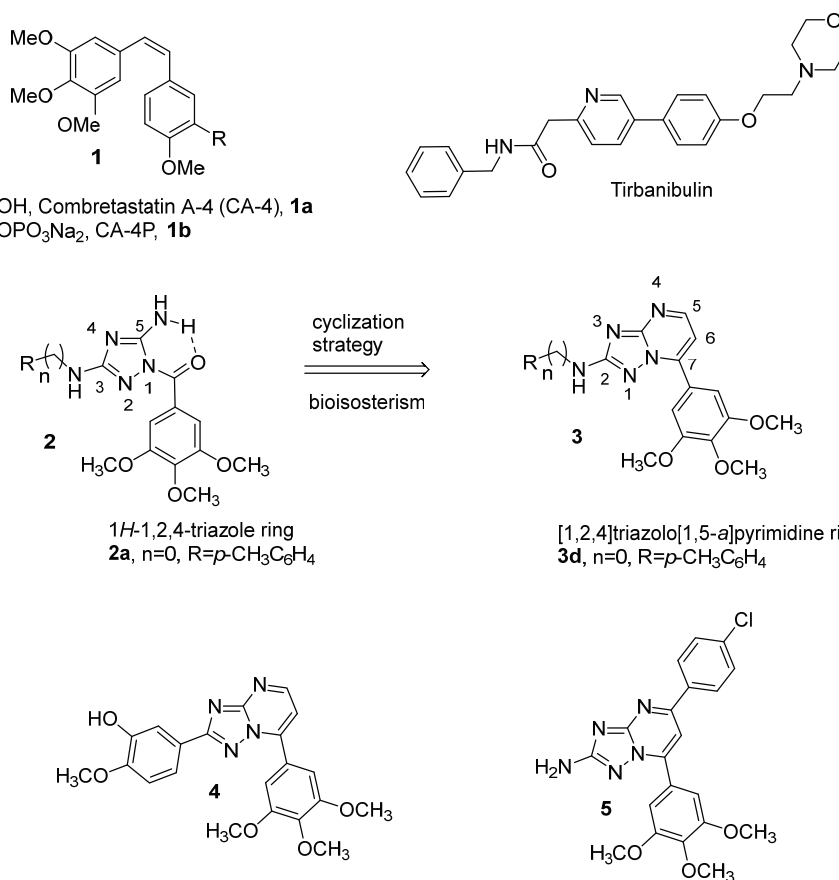
Figure 1. Structures of CA-4 (**1a**), CA-4P (**1b**), tirbanibulin, general structure (**2**) of 1-(3′,4′,5′-trimethoxybenzoyl)-5-amino-1,2,4-triazoles and [1,2,4]triazolo[1,5-*a*]pyrimidines reported in this manuscript (**3**) and reported in the literature (**4** and **5**).

In a previous article, we designed and synthesized a new class of antimitotic agents with general structure **2** based on the 3-arylamino-5-amino-1,2,4 triazole moiety [53]. The structure–activity relationship study was carried out on the phenyl ring of the anilino moiety present on the C-3 position of a triazole scaffold. Compound **2a**, with a para-methyl substitution on the phenyl ring, exhibited potent antiproliferative effects in the low nanomolar range on several cancer cell lines. This compound was almost twice as potent as CA-4 against inhibition of tubulin polymerization, displaying an IC_{50} value of 0.75 μM. The X-ray crystal structure of compound **2a** showed the formation of an intramolecular hydrogen bond between the carbonyl oxygen of the 3′,4′,5′-trimethoxybenzoyl function and the hydrogen of the amino moiety at the 1- and 5-position, respectively, of the 1,2,4-triazole ring. In the present study, a cyclization approach was adopted to form an additional six-membered fused pyrimidine ring that incorporated these elements, the carbonyl moiety and the amino group, to obtain the bicyclic [1,2,4]triazolo[1,5-*a*]pyrimidine framework **3**. This scaffold hopping approach strategy [54,55] also revealed a potential bioisosteric relationship between the 1-(3′,4′,5′-trimethoxybenzoyl)-5-amino-1,2,4-triazole structure and the 7-(3′,4′,5′-trimethoxyphenyl)[1,2,4]triazolo[1,5-*a*]pyrimidine system. In addition, several studies have shown that the carbonyl moiety is a metabolically labile site and that carbonyl reduction to a secondary alcohol is one of the major metabolic processes used by liver microsomes [56]. A promising approach to overcome this metabolic instability is by incorporating the carbonyl moiety into a five- or six-membered heterocyclic ring [57–60].

The [1,2,4]triazolo [1,5-*a*]pyrimidine scaffold incorporating the 1,2,4-triazole nucleus (Figure 1) was previously identified by us and others as a promising nucleus for the design of new microtubule-destabilizing agents [61–65]. Two different series of compounds that

retain the 3,4,5-trimethoxyphenyl ring at the 7-position of the triazolopyrimidine core variably functionalized at its 2-position were evaluated for their antitumor activity [62–64].

Yang et al. reported a novel series of 2,7-diaryl-[1,2,4]triazolo[1,5-*a*]pyrimidine derivatives substituted at the 2- and 7-positions as tubulin polymerization inhibitors [62,63]. By inversion of the C-2/C-7 substituents on the triazolopyrimidine ring, compound **4**, characterized by the presence of 4′-methoxy-3′-hydroxyphenyl and 3′,4′,5′-trimethoxyphenyl moieties at the 2- and 7-positions, respectively, of the triazolopyrimidine scaffold display potent and selective antiproliferative activity (IC$_{50}$: 60 nM) against HeLa cells [63]. The same compound showed reduced inhibitory activity against a panel of four cancer cell lines with IC$_{50}$ values of 3–18 μM. Mechanism studies indicate that **4** exerts antiproliferative effects by inhibition of tubulin assembly, with 3-fold greater potency than CA-4, and these data, together with data obtained with compound **5** recently identified by Mohamed et al. [64], confirm that the 3′,4′,5′-trimethoxyphenyl ring located at the 7-position of the triazolopyrimidine system contributes to maximal activity. This latter derivative, as an analogue of **4** where the aryl ring was moved from the 2- to the 5-position of the 7-(3′,4′,5′-trimethoxyphenyl) triazolopyrimidine scaffold and replaced by an amino group, exhibits significant antiproliferative activity (IC$_{50}$: 0.53 μM) against the HCT-116 cancer cell line, with four-fold less activity than CA-4 as a tubulin polymerization inhibitor (IC$_{50}$: 3.84 and 1.1 μM, respectively) [64].

Thus, once the 7-(3′,4′,5′-trimethoxyphenyl)-[1,2,4]triazolo[1,5-*a*]pyrimidine motif was identified as the minimum structural requirement for antimitotic activity, in the new class of designed **compounds 3a–v** reported in this article, modifications were focused on varying the substituent at the 2-position of the triazolopyrimidine ring to maximize activity against cancer cell lines (Figure 2). For the anilino derivative **3a**, we evaluated the replacement of phenyl with a bioisosteric pyrimidin-2-yl ring, to yield **3b**. For compounds **3c–o**, characterized by the presence of aromatic amines at the 2-position of the triazolopyrimidine scaffold, modifications were focused on varying the substituents on the phenyl ring of the anilino moiety, by introduction electron-withdrawing (F) or electron-releasing (alkyl or alkoxy) groups.

3a, n=0, R=C$_6$H$_5$
3b, n=0, R=3′-pyridinyl
3c, n=0, R=4′-F-C$_6$H$_4$
3d, n=0, R=4′-CH$_3$-C$_6$H$_4$
3e, n=0, R=3′-CH$_3$-C$_6$H$_4$
3f, n=0, R=3′,4′-(CH$_3$)$_2$-C$_6$H$_3$
3g, n=0, R=3′,5′-(CH$_3$)$_2$-C$_6$H$_3$
3h, n=0, R=4′-C$_2$H$_5$-C$_6$H$_4$
3i, n=0, R=4′-*n*-C$_3$H$_7$-C$_6$H$_4$
3j, n=0, R=4′-*i*-C$_3$H$_7$-C$_6$H$_4$
3k, n=0, R=4′-OCH$_3$-C$_6$H$_4$
3l, n=0, R=3′-OCH$_3$-C$_6$H$_4$
3m, n=0, R=4′-OC$_2$H$_5$-C$_6$H$_4$
3n, n=0, R=3′,4′-(OCH$_2$O)-C$_6$H$_3$
3o, n=0, R=3′,4′-(OCH$_2$CH$_2$O)-C$_6$H$_3$

3p, n=1, R=C$_6$H$_5$
3q, n=1, R=4′-Cl-C$_6$H$_4$
3r, n=1, R=4′-CH$_3$-C$_6$H$_4$
3s, n=1, R=4′-OCH$_3$-C$_6$H$_4$
3t, n=1, R=3′,4′-(OCH$_2$O)-C$_6$H$_3$
3u, n=2, R=C$_6$H$_5$
3v, n=3, R=C$_6$H$_5$

6a, n=1, R=4′-Cl-C$_6$H$_4$
6b, n=1, R=4′-CH$_3$-C$_6$H$_4$
6c, n=1, R=3′,4′-(OCH$_2$O)-C$_6$H$_3$
6d, n=3, R=C$_6$H$_5$

Figure 2. Chemical structures of newly synthesized compounds **3a–v** based on the 7-(3′,4′,5′-trimethoxyphenyl)[1,2,4]triazolo[1,5-*a*]pyrimidine scaffold and general molecular formula **6a–d** of triazolopyrimidines published by us (ref. [65]).

We also investigated a further structural modification by the synthesis of compounds **3p–v**, characterized by the presence of a methylene (-CH$_2$-), ethylene (-CH$_2$CH$_2$-) or propylene (-(CH$_2$)$_3$-) spacer between the nitrogen at the 2-position of the triazolopyrimidine

scaffold and the phenyl ring, to furnish compounds **3p–t**, **3u** and **3v**, respectively. By the preparation of this latter small series, we evaluated if an increased flexibility of the substituent at the 2-position of the triazolopyrimidine scaffold was correlated with further enhancement of antiproliferative activity. The design of the linker chain in derivatives **3p–t** was based on preserving 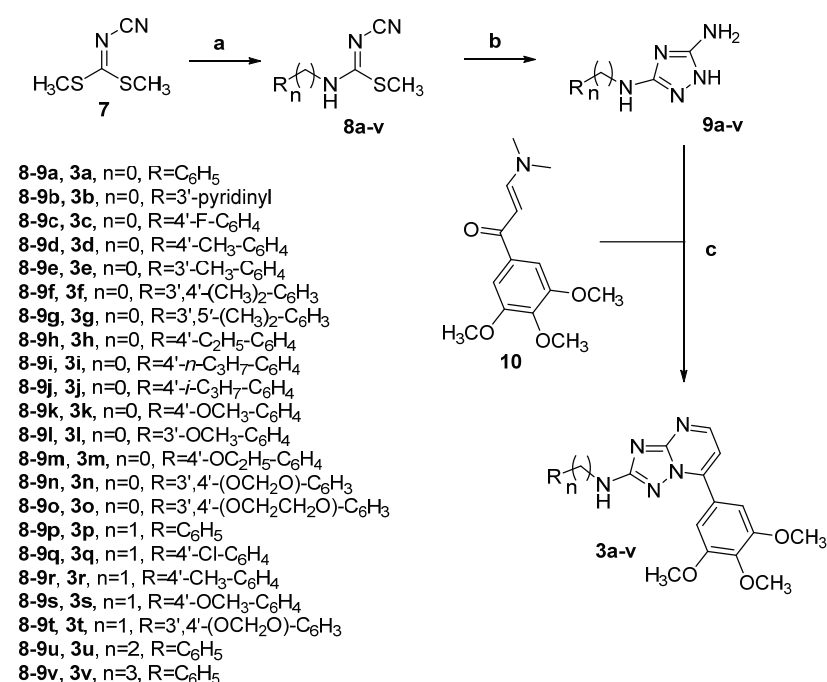flexibility similar to that of a series of compounds with general structure **6** previously published by us [65], characterized by a common 7-(3′,4′,5′-trimethoxyanilino)-[1,2,4]triazolo[1,5-*a*]pyrimidine scaffold and modified at its 2-position. Three benzylamino derivatives, **6a** (4′-Cl), **6b** (4′-Me) and **6c** (3′,4′-methylendioxy), along with the 3′-phenylpropylamino derivative **6d**, were the most active compounds identified in this series.

2. Results and Discussion

2.1. Chemistry

The 2-substituted-7-(3′,4′,5′-trimethoxyphenyl)[1,2,4]triazolo[1,5-*a*]pyrimidines **3a–v** were synthesized using a three-step synthetic procedure described in Scheme 1. The condensation of dimethyl cyanodithioimidocarbonate **7** with the appropriate amine (aniline or substituted aniline, benzylamine or substituted benzylamine, 2′-phenylethylamine or 3′-phenylpropylamine) resulted in the formation of imidates **8a–v**, which were cyclized into the corresponding 3-substituted 5-amino-1*H*-[1,2,4]-triazole derivatives **9a–v** in the presence of hydrazine hydrate in refluxing methanol.

8-9a, **3a**, n=0, R=C$_6$H$_5$
8-9b, **3b**, n=0, R=3′-pyridinyl
8-9c, **3c**, n=0, R=4′-F-C$_6$H$_4$
8-9d, **3d**, n=0, R=4′-CH$_3$-C$_6$H$_4$
8-9e, **3e**, n=0, R=3′-CH$_3$-C$_6$H$_4$
8-9f, **3f**, n=0, R=3′,4′-(CH$_3$)$_2$-C$_6$H$_3$
8-9g, **3g**, n=0, R=3′,5′-(CH$_3$)$_2$-C$_6$H$_3$
8-9h, **3h**, n=0, R=4′-C$_2$H$_5$-C$_6$H$_4$
8-9i, **3i**, n=0, R=4′-*n*-C$_3$H$_7$-C$_6$H$_4$
8-9j, **3j**, n=0, R=4′-*i*-C$_3$H$_7$-C$_6$H$_4$
8-9k, **3k**, n=0, R=4′-OCH$_3$-C$_6$H$_4$
8-9l, **3l**, n=0, R=3′-OCH$_3$-C$_6$H$_4$
8-9m, **3m**, n=0, R=4′-OC$_2$H$_5$-C$_6$H$_4$
8-9n, **3n**, n=0, R=3′,4′-(OCH$_2$O)-C$_6$H$_3$
8-9o, **3o**, n=0, R=3′,4′-(OCH$_2$CH$_2$O)-C$_6$H$_3$
8-9p, **3p**, n=1, R=C$_6$H$_5$
8-9q, **3q**, n=1, R=4′-Cl-C$_6$H$_4$
8-9r, **3r**, n=1, R=4′-CH$_3$-C$_6$H$_4$
8-9s, **3s**, n=1, R=4′-OCH$_3$-C$_6$H$_4$
8-9t, **3t**, n=1, R=3′,4′-(OCH$_2$O)-C$_6$H$_3$
8-9u, **3u**, n=2, R=C$_6$H$_5$
8-9v, **3v**, n=3, R=C$_6$H$_5$

Scheme 1. Reagents. **a**: Appropriate ArNH$_2$, *i*-PrOH, reflux, 18 h for the preparation of compounds **8a–o** or appropriate ArCH$_2$NH$_2$/C$_6$H$_5$(CH$_2$)$_2$NH$_2$/C$_6$H$_5$(CH$_2$)$_3$NH$_2$, *i*-PrOH, room temperature, 18 h for the synthesis of derivatives **8p–v**, 75–92%; **b**: NH$_2$NH$_2$.H$_2$O, MeOH, reflux, 18 h, 68–93%; **c**: AcOH, 80 °C, 2 h, 47–66%.
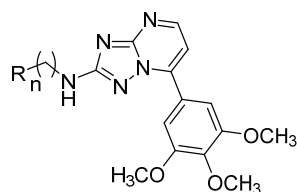
Finally, the cyclization reaction of compounds **9a–v** with enaminone **10** in glacial acetic acid at 80 °C for 2 h resulted in 2-substituted-7-(3′,4′,5′-trimethoxyphenyl)-[1,2,4]triazolo[1,5-*a*]pyrimidine derivatives **3a–v** in good yield. As reported in the literature, enaminone **10** was obtained by the condensation of 3′,4′,5′-trimethoxyacetophenone with dimethylformamide dimethyl acetal (DMF-DMA) as the solvent/reagent at 120 °C for 6 h [66]. The ^{1}H NMR and ^{13}C NMR spectra of derivatives **3a–v** are presented in the Supplementary Materials.

2.2. Biological Activity and Molecular Docking Studies

2.2.1. In Vitro Antiproliferative Activities

The series of 2-substituted 7-(3′,4′,5′-trimethoxyphenyl)[1,2,4]triazolo[1,5-*a*]pyrimidine derivatives **3a–v** was screened for antiproliferative activity against a panel of four different human cancer cell lines and compared with the reference compound CA-4 (**1a**) (Table 1). The cell lines used were a breast cancer cell (MDA-MB-231), a cervix carcinoma (HeLa), a non-small cell lung carcinoma (A549) and a colon adenocarcinoma (HT-29). CA-4 had single-digit nanomolar activity (IC$_{50}$: 4–5 nM) against MDA-MB-231 and HeLa cancer cell lines, while A549 and HT-29 cells were more resistant to CA-4, with IC$_{50}$ values of 180 and 3100 nM, respectively. Eight of twenty-two compounds were found to be more active than CA-4 against HT-29 cells, while only derivative **3d** was more potent (4-fold) than CA-4 against A549 cells. The compounds were generally less active against the MDA-MB-231 cells.

Table 1. In vitro cell growth inhibitory effects of compounds **3a–v** and CA-4 (**1a**).

Compound	R	n	IC$_{50}$ (μM) [a]			
			MDA-MB-231	**HeLa**	**A549**	**HT29**
3a	C$_6$H$_5$	0	2.27 ± 0.31	0.80 ± 0.09	1.56 ± 0.06	1.02 ± 0.67
3b	(pyridyl)	0	>10	>10	>10	3.42 ± 0.41
3c	4′-F-C$_6$H$_4$	0	>10	5.44 ± 1.05	>10	>10
3d	4′-CH$_3$-C$_6$H$_4$	0	0.43 ± 0.11	0.038 ± 0.009	0.043 ± 0.024	0.030 ± 0.003
3e	3′-CH$_3$-C$_6$H$_4$	0	>10	0.39 ± 0.02	1.87 ± 0.17	1.38 ± 0.09
3f	3′,4′-(CH$_3$)$_2$-C$_6$H$_3$	0	>10	0.067 ± 0.0023	0.16 ± 0.045	0.16 ± 0.041
3g	3′,5′-(CH$_3$)$_2$-C$_6$H$_3$	0	>10	>10	>10	>10
3h	4′-C$_2$H$_5$-C$_6$H$_4$	0	>10	0.24 ± 0.074	0.2 ± 0.044	0.16 ± 0.033
3i	4′-*n*-C$_3$H$_7$-C$_6$H$_4$	0	>10	>10	>10	>10
3j	4′-*i*-C$_3$H$_7$-C$_6$H$_4$	0	>10	4.7 ± 0.59	>10	>10
3k	4′-OCH$_3$-C$_6$H$_4$	0	5.2 ± 1.8	1.27 ± 0.08	5.32 ± 1.43	2.8 ± 0.20
3l	3′-OCH$_3$-C$_6$H$_4$	0	1.76 ± 0.9	0.44 ± 0.08	0.76 ± 0.18	0.76 ± 0.18
3m	4′-OC$_2$H$_5$-C$_6$H$_4$	0	>10	>10	>10	6.16 ± 0.97
3n	(benzodioxole)	0	6.1 ± 1.72	0.84 ± 0,19	1.44 ± 0.26	1.39 ± 0.06
3o	(benzodioxine)	0	>10	0.29 ± 0.031	2.42 ± 0.12	0.67 ± 0.12
3p	C$_6$H$_5$	1	9.3 ± 0.22	>10	>10	>10
3q	4′-Cl-C$_6$H$_4$	1	>10	>10	>10	>10
3r	4′-CH$_3$-C$_6$H$_4$	1	>10	>10	>10	>10
3s	4′-OCH$_3$-C$_6$H$_4$	1	>10	>10	>10	>10
3t	(benzodioxole)	1	>10	>10	>10	>10
3u	C$_6$H$_5$	2	8.7 ± 1.1	>10	>10	6.74 ± 0.50
3v	C$_6$H$_5$	3	>10	>10	>10	>10
CA-4 (**1a**)	-	-	0.005 ± 0.002	0.004 ± 0.001	0.18 ± 0.05	3.10 ± 0.03

[a] IC$_{50}$ = compound concentration required to inhibit tumor cell proliferation by 50% determined by a resazurin viability assay. Values are the mean ± SE from the dose–response curves of at least three independent experiments carried out in triplicate.

From a structure–activity point of view, the presence of a 3,4,5-trimethoxyphenyl ring at position 7 of the triazolopyrimidine scaffold combined with the *p*-toluidino moiety at position 2 were important structural features for this class of compounds. The *p*-toluidino

derivative **3d** was the most active compound of the series, showing similar activity toward the HeLa, A549 and HT29 cancer cell lines (IC$_{50}$: 38, 43 and 30 nM, respectively), with ten-fold reduced antiproliferative activity (IC$_{50}$: 0.43 μM) toward MDA-MB-231 cells. The activity of **3d** was 4- and 100-fold greater than that of the reference compound CA-4 against A549 and HT-29 cells, respectively, but was one and two orders of magnitude less potent than CA-4 against MDA-MB-231 and HeLa cells, respectively. Compound **3d** was 4–30-fold more potent as an antiproliferative agent than the corresponding 5-methyl-2-(*p*-toluidino)-7-(3′,4′,5′-trimethoxyanilino)-[1,2,4]triazolo[1,5-*a*]pyrimidine counterpart previously published by us (IC$_{50}$ 0.43–0.030 μM and 0.52–1.55 μM, respectively) [65].

While the aniline derivative **3a** showed antiproliferative activity ranging from 0.80 to 2.27 μM against the four cancer cell lines, increasing the length of the alkyl spacer between the phenyl ring and the nitrogen at the 2-position of the triazolopyrimidine scaffold from one (**3p**) to two (**3u**) to three (**3v**) methylene units caused a profound loss of activity compared with **3a**, with IC$_{50}$ values generally > 10 μM.

Replacement of the unsubstituted phenyl ring of compound **3a** with the bioisosteric pyridin-3-yl moiety (compound **3b**) also dramatically reduced antiproliferative activity against three of the four cancer cell lines (IC$_{50}$ > 10 μM), with a 3-fold reduction in potency against HT-29 cells (IC$_{50}$: 1.02 and 3.42 μM, respectively).

The substitution pattern on the phenyl ring of the arylamino moiety at the 2-position of the [1,2,4]triazolo[1,5-*a*]pyrimidine nucleus ring played an important role in antiproliferative activity. While the introduction of the electron-withdrawing fluorine atom at the para-position of the phenyl group, to furnish **3c**, was detrimental for activity relative to the unsubstituted phenyl derivative **3a**, the weak electron-releasing *p*-methyl group, to furnish compound **3d**, enhanced biological activity and resulted in the most active compound of the whole series.

The position of the methyl on the phenyl ring was critical for the antiproliferative activity of **3d**. Significant loss in activity (10–46-fold) occurred when the methyl group was moved from the para- to the meta-position, to obtain the isomeric derivative **3e**. The reduction in potency was most dramatic against MDA-MB-231 cells (IC$_{50}$ > 10 μM).

Relative to the activity of the *p*-toluidino derivative **3d**, the insertion of an additional methyl group at the meta-position of the *p*-tolyl moiety, to furnish the *m,p*-xylyl derivative **3f**, reduced antiproliferative activity 2–5-fold on three cancer cells, and the reduction in potency was most pronounced against MDA-MB-231 cells (IC$_{50}$ >10 μM), while the isomeric *m,m*′-xylyl analogue **3g** was completely inactive (IC$_{50}$ > 10 μM). Lengthening the alkyl chain from methyl (**3d**) to ethyl (**3h**) resulted in a 5–7-fold reduction in antiproliferative activity, most pronounced with the MDA-MB-231 cells (IC$_{50}$ > 10 μM).

The data showed that the homologation of the alkyl chain from ethyl to *n*-propyl or isopropyl (compounds **3i** and **3j**, respectively) at the para-position of the phenyl ring was not tolerated and provided a strong reduction in activity against all four cancer cell lines.

For the *p*-toluidine derivative **3d**, replacement of the methyl moiety by the stronger electron-releasing methoxy group, to furnish the *p*-anisidino analogue **3k**, was detrimental for antiproliferative activity, which was reduced 12–124-fold as compared to **3d**. In contrast to the two isomeric toluidine derivatives **3d** and **3e**, comparing the biological activities of the para- and meta-anisidino derivatives **3k** and **3l**, respectively, the highest antiproliferative activity was observed with the methoxy moiety at the meta-position of the phenyl ring. As observed for the *p*-toluidino derivative **3d**, with the *p*-anisidino **3k**, homologation of the alkyl chain from methoxy to ethoxy (compound **3m**) was detrimental for antiproliferative activity against all four cancer cell lines (IC$_{50}$ > 10 μM).

Replacement of the *p*-methoxy with a 3′,4′-methylendioxy moiety (compounds **3k** and **3n**, respectively) produced a 1.5- to 4-fold increase in antiproliferative activity against three of the four cancer cell lines, while **3k** and **3n** were equipotent against MDA-MB-231 cells. For derivative **3n**, the introduction of an additional methylene unit between the two oxygens, to yield the 3′,4′-ethylenedioxy homologue **3o**, had contrasting effects, producing

a reduction in potency against MDA-MB-231 and A549 cells, while **3o** was 2- and 3-fold more active than **3n** against HT-29 and HeLa cancer cells, respectively.

With the anilino derivatives **3a** (phenyl), **3d** (*p*-tolyl), **3k** (*p*-methoxyphenyl) and **3n** (3′,4′-methylendioxyphenyl), the corresponding benzylamino analogues **3p**, **3r**, **3s** and **3t**, respectively, showed a dramatic drop in potency (IC$_{50}$ > 10 μM).

In conclusion, SAR studies have underlined that the presence of small substituents such as methyl or ethyl at the para-position as well as two methyl groups at the meta- and para-positions (compounds **3d**, **3h** and **3f**, respectively) on the phenyl ring of the aniline moiety are critical for optimal antiproliferative activity. Electron-releasing substituents at the para-position of the phenyl ring showed antiproliferative activity in the order of Me > Et > OMe ≫ OEt = *n*-C$_3$H$_7$ = *i*-C$_3$H$_7$.

2.2.2. In Vitro Inhibition of Tubulin Polymerization and Colchicine Binding

To investigate whether the antiproliferative activities of tested compounds derived from an interaction with microtubules, the most active molecules **3d**, **3f**, **3h** and **3l** were selected to determine their inhibition of tubulin polymerization and for effects on the binding of [^{3}H]colchicine to tubulin (Table 2). For comparison, CA-4 was examined in contemporaneous experiments.

Table 2. Inhibition of tubulin polymerization and colchicine binding by compounds **3d**, **3f**, **3h**, **3l** and CA-4 (**1a**).

Compounds	Tubulin Assembly [a] IC$_{50}$ ± SD (μM)	Colchicine Binding [b] % Inhibition ± SD
3d	0.45 ± 0.1	72 ± 5
3f	0.80 ± 0.1	18 ± 5
3h	1.9 ± 0.2	21 ± 0.9
3l	2.2 ± 0.2	39 ± 5
CA-4 (**1a**)	0.75 ± 0.06	98 ± 2

[a] Inhibition of tubulin polymerization. Tubulin was at 10 μM. [b] Inhibition of [^{3}H]colchicine binding. Tubulin, [^{3}H]colchicine and tested compound were at 0.5, 5 and 5 μM concentrations, respectively.

In the assembly assay, compound **3d** was found to be the most active (IC$_{50}$: 0.45 μM), and it was almost twice as potent as CA-4 (IC$_{50}$: 0.75 μM), while **3f** was equipotent to CA-4. When comparing the inhibition of tubulin polymerization versus the growth inhibitory effect, we found that compound **3d,** although it was 2-fold more active than CA-4 as an inhibitor of tubulin assembly, was 10- and 100-fold less potent than CA-4 as an antiproliferative agent against HeLa and MDA-MB-231 cells, respectively. The reduced potency of **3d** on these two cancer cell lines can possibly be rationalized by any mechanism limiting the accessibility of this molecule to the cellular tubulin. Compounds **3h** and **3l** showed weak antitubulin polymerization activity (IC$_{50}$: 1.9 and 2.2 μM, respectively), which is consistent with their low antiproliferative activities.

In competition experiments, in reaction mixtures containing 0.5 μM tubulin and 5.0 μM [^{3}H]colchicine, compound **3d** strongly inhibited the binding of [^{3}H]colchicine to tubulin, with 72% inhibition occurring when **3d** and the radiolabeled drug were both at 5.0 μM in the reaction mixture. Compound **3d** was less potent than CA-4, which in these experiments inhibited colchicine binding by 98%, while **3f**, **3h** and **3l** inhibited colchicine binding by only 21, 18 and 39%, respectively.

In this small series of four compounds, the results obtained demonstrated that the antiproliferative activity was correlated with the inhibition of tubulin polymerization. Moreover, inhibition of tubulin assembly was correlated more closely with antiproliferative activity than with inhibition of [^{3}H]colchicine binding.

2.2.3. Molecular Modeling Studies

To rationalize the experimental data obtained for compounds **3d**, **3f**, **3h** and **3l**, a series of molecular docking simulations were performed.

The four derivatives occupy the tubulin colchicine site in a similar manner, mimicking the binding of the co-crystallized colchicine (Figure 3A–E), with the [1,2,4]triazolo[1,5-*a*]pyrimidine core lying on the central part of the binding site, the trimethoxyphenyl ring in position 7 placed in proximity of βCys241 and the differently substituted phenyl rings in position 2 sited at the interface between the two tubulin subunits, pointing toward a loop in the α-subunit (αSer178-αThr179).
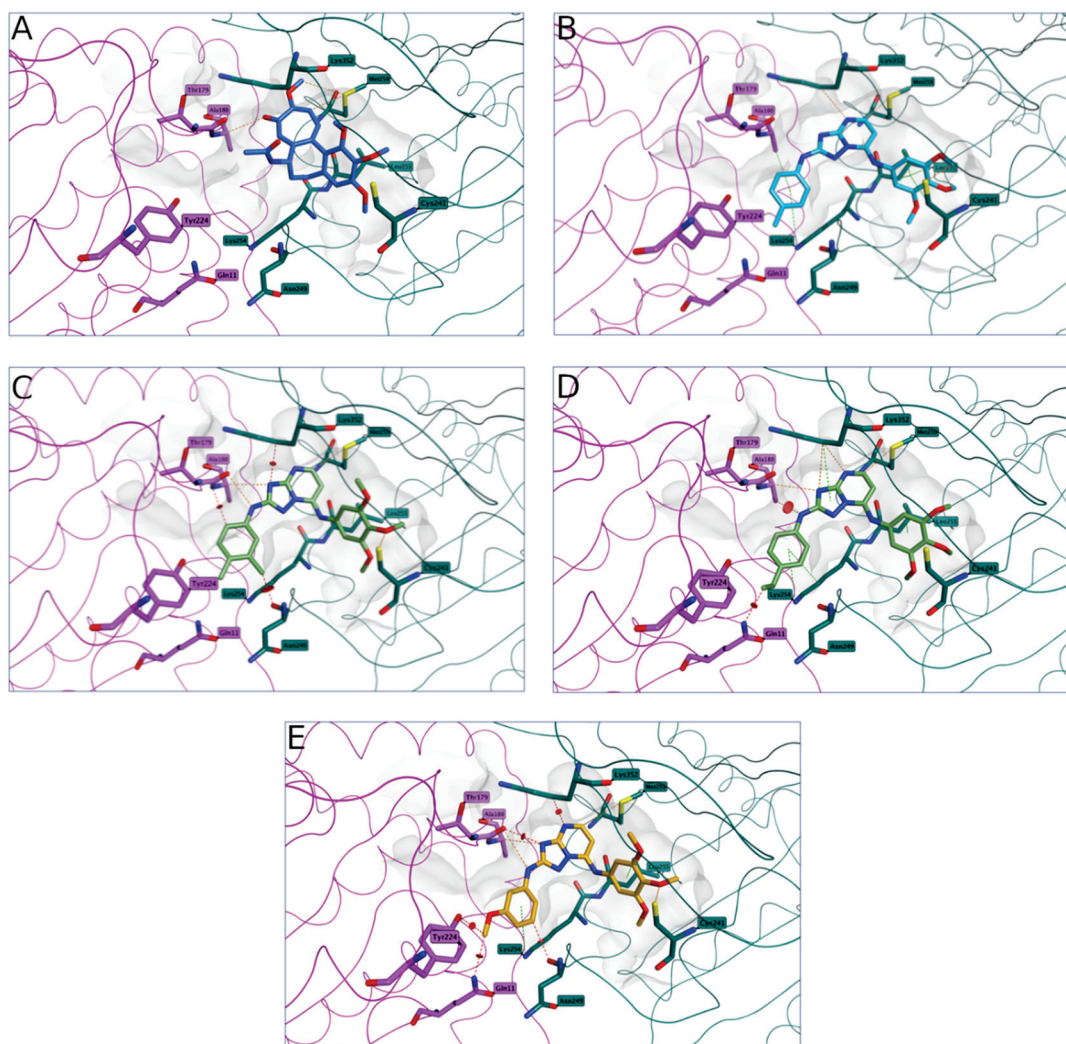

Figure 3. Colchicine binding conformation (**A**) and proposed binding for compounds **3d** (**B**), **3f** (**C**), **3h** (**D**) and **3l** (**E**) in the colchicine site. All the derivatives presented the trimethoxyphenyl ring in proximity to βCys241, while the substituted phenyl group at position 2 of the central core was sited at the interface between the two tubulin subunits, pointing toward a loop in the α-subunit (αSer178-αThr179). Compound **3d** presented two main interactions with βCys241, different anchoring contacts with the surrounding residues and no clashes with the tubulin structure. The rest of the compounds, even if conserving different interactions, including the important interaction with βCys241, presented different clashes with the surrounding residues, suggesting a non-optimal occupation of the colchicine site and indicating a reduced affinity for tubulin. The carbon atoms of the tubulin α unit residues are shown in lilac, while the carbon atoms of the β unit residues are represented in teal. Hydrogen bonds are shown as orange dashed lines, hydrophobic interactions as green dashed lines and distance clashes as red dashed lines.

According to this binding site occupation prediction, the four derivatives would bind in this area of tubulin in a similar manner. Analyzing in more detail the interactions and

any potential clash between the four molecules and the tubulin structure, some interesting observations were made.

The trimethoxyphenyl ring of **3d** presented two main interactions with βCys241 (Figure 3B), forming an important key contact point for inhibition of tubulin polymerization, and established different anchoring contacts with the surrounding residues (βLys254, βLeu255, βMet259, βLys352, αAla180), and these contacts further stabilized the compound–protein complex. Moreover, no clashes between the compound and the protein were present, indicating that **3d** had an optimal occupation of the colchicine site. This could then translate to **3d** being the best compound of the series in inhibiting tubulin polymerization and competing for the colchicine site.

Introduction of a second methyl group in the *m,p*-xylyl derivative **3f** did not seem to affect the interactions with the tubulin residues, including interaction with βCys241 (Figure 3C), but the additional methyl group at the meta-position did present a possible sterical clash with βAsn249, and this could affect the compound–protein complex, reducing its stability. Moreover, to accommodate the second methyl group, **3f** had a slightly different binding orientation as compared with compound **3d**, and this caused other possible steric clashes with the surrounding residues (βAsn249, βLys352, αAla180). The presence of these potential issues suggests that **3f** could not have an optimal occupation of the colchicine site, hence a reduced affinity towards tubulin, and therefore a detrimental effect in the inhibition of tubulin polymerization.

A similar effect was also observed for **3h** (*p*-ethyl, Figure 3D) and **3l** (*m*-methoxy, Figure 3E), where the longer ethyl chain in position 4′ and the presence of the methoxy groups in position 3′ for compounds **3h** and **3l**, respectively, caused some potential steric clashes with αGln11 and with αGln11/αTyr224, respectively. These negative structural features forced the compounds to adjust their binding, possibly reducing compound–protein complex stability. This could suggest a lower affinity for the binding site, negatively affecting the inhibition of tubulin polymerization.

2.2.4. Compound **3d** Induced G2/M Arrest of the Cell Cycle

With the aim of evaluating the effects of compound **3d** on the cell cycle, we analyzed HeLa cells after treatment for 24 h at 10, 25 or 50 nM. As shown in Figure 4A, compound **3d** caused a significant G2/M arrest in a concentration-dependent manner. The increase in G2/M cells was evident at 25 nM and accompanied by a concomitant reduction in both G1 and S phase cells.
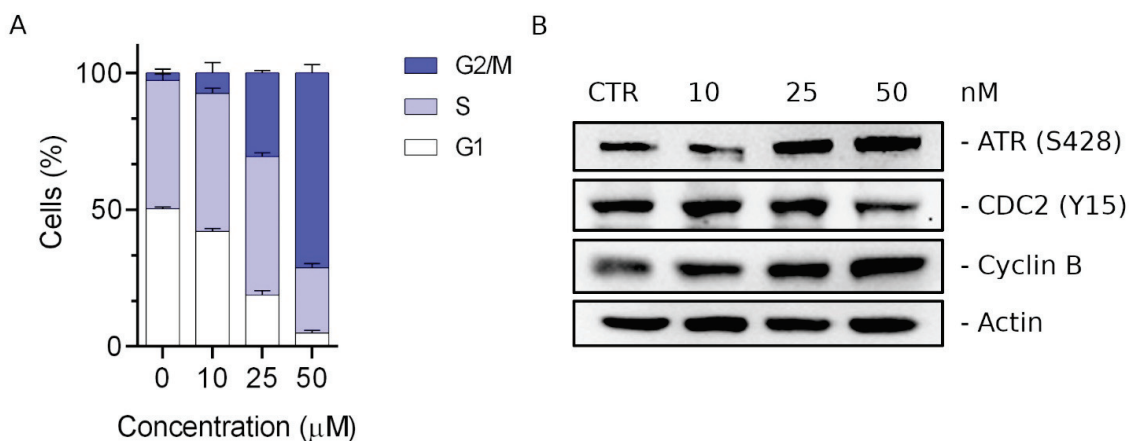

Figure 4. (Panel (**A**)) Quantitative analysis of cell cycle phase distribution in HeLa cells after a 24 h treatment with **3d**, at the concentrations of 10, 25 or 50 nM. Cells were stained with PI to analyze the DNA content by flow cytometry. Data are presented as means of three independent experiments ± SEM. (Panel (**B**)) Effects of compound **3d** on cell cycle regulatory proteins and DNA damage checkpoint proteins. HeLa cells were treated for 24 h with the indicated concentration of **3d**, and expression of ATR, cdc2 (Y15) and cyclin B was detected by Western blot analysis.

We then evaluated by Western blot analysis the effects of **3d** on the expression of several proteins regulating the mitotic checkpoint. When damage to the mitotic spindle occurs, the mitotic spindle assembly checkpoint is activated, causing an accumulation of cyclin B and the dephosphorylation of cdc2 [67,68]. We found (Figure 4B) that treatment with **3d** induced an increase in cyclin B expression and, at the same time, a significant reduction in cdc2 phosphorylation (Y15).

The prolonged arrest in metaphase induces the activation of a DNA damage signal cascade that involves primarily ATR kinase, which becomes phosphorylated at Ser428. As shown in Figure 4B, we found a considerable increase in ATR phosphorylation (Ser428) [69], suggesting that **3d** induced the activation of the DNA damage signaling response with consequent accumulation of cyclin B and a block of cells in the G2/M phase.

2.2.5. Compound **3d** Induced Apoptosis in HeLa Cells through Mitochondrial Depolarization

With the aim of evaluating the type of cell death induced by the treatment of compound **3d**, we treated HeLa cells with different concentrations of **3d**, and, after 24 or 48 h, we labeled the cells with both annexin-V conjugated with FITC and propidium iodide (PI). The cells were then subjected to flow cytometric analysis, and the results are shown in Figure 5. Compound **3d** induced, in a concentration- and time-dependent manner, apoptosis in the treated cells. The effect was evident at 25 nM and stronger still at 50 nM. With **3d** at 50 nM and at long incubation times, a fair percentage of cells (about 25%) became necrotic, being positive only for PI (A^-/PI^+).
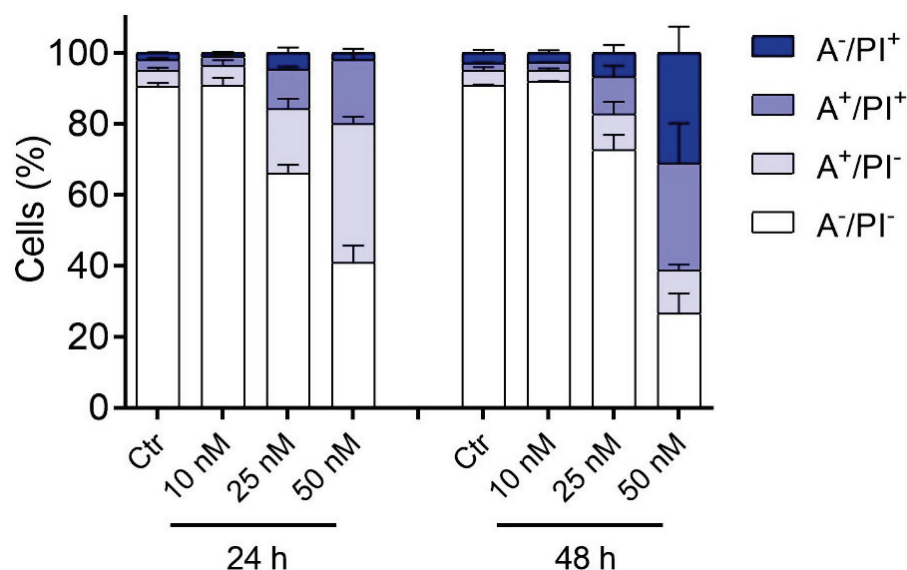

Figure 5. Apoptotic effects caused by **3d**. HeLa cells were treated with the indicated concentrations of **3d** for either 24 or 48 h and then were analyzed by flow cytometry after double staining with annexin-V-FITC and PI. A^-/PI^- Alive cells; A^+/PI^- Early apoptotic cells; A^+/PI^+ Late apoptotic cells; A^-/PI^+ Necrotic cells. In the histograms, data are represented as mean $\pm$ SEM of three independent experiments.

Since many drugs acting as inhibitors of tubulin polymerization induce apoptosis through mitochondrial depolarization [70–74], we wanted to investigate whether **3d**-induced apoptosis was accompanied by a reduction in mitochondrial potential. To do this, we treated the Hela cells with the compound, and after 24 or 48 h we labeled the cells with the fluorescent dye JC-1.

In physiological conditions, JC-1 aggregates and emits red fluorescence, while, in depolarization conditions, the dye disaggregates and forms monomers that emit green fluorescence. As can be seen from Figure 6, after a 24 h treatment, a significant increase in

the percentage of monomers was observed, and this percentage increased further at 48 h, in good agreement with the appearance of apoptotic cells described above.
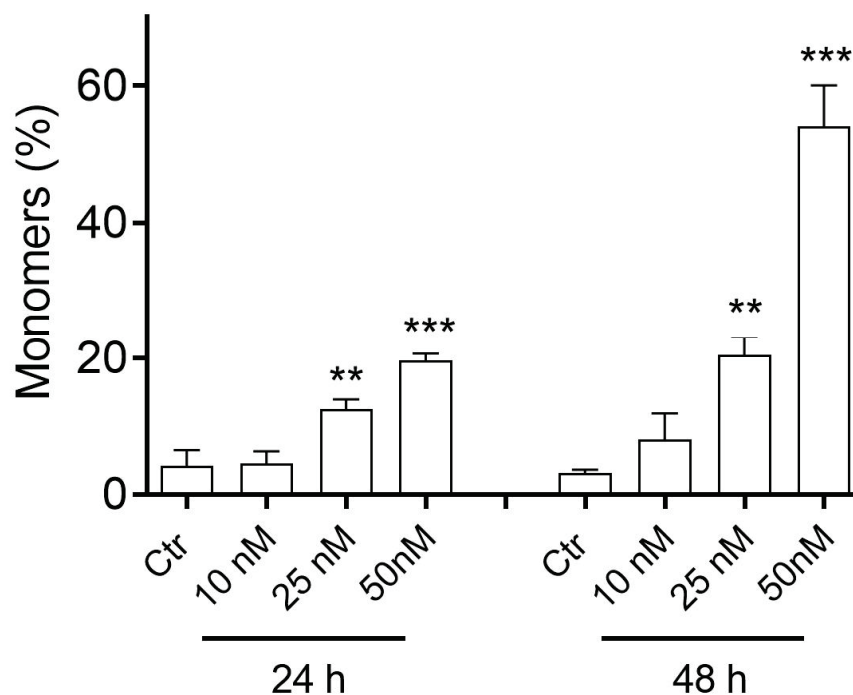

Figure 6. Assessment of mitochondrial depolarization after treatment with **3d**. HeLa cells were treated with the indicated concentrations of compound for 24 or 48 h. Data are represented as mean $\pm$ SEM of three independent experiments (** $p < 0.01$, *** $p < 0.001$).

2.2.6. Compound **3d** Induces Caspase-9 Activation and Causes a Decrease in the Expression of Bcl-2 Protein

To further study the **3d**-induced apoptosis process we evaluated the expression of caspase-9. As shown in Figure 7, we observed at both 25 and 50 nM **3d** the appearance of the cleaved fragment of caspase-9. In this context, many studies have demonstrated that activation of initiator pro-caspase-9 causes a decrease in Bcl-2 expression, thus indicating the occurrence of apoptosis [75].
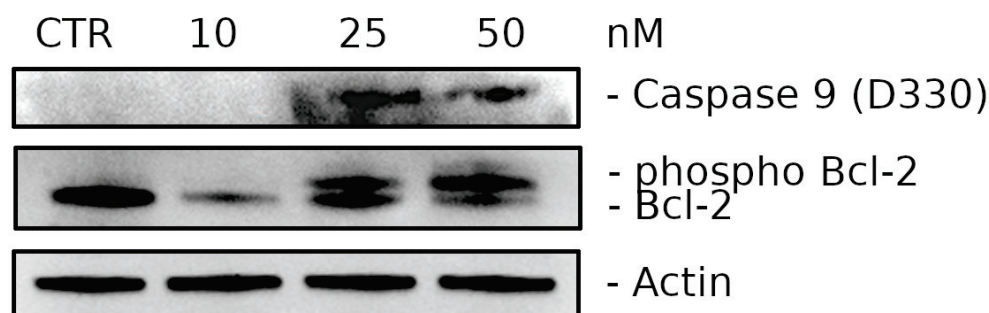

Figure 7. Western blot analysis of Caspase-9 (D330) (Cleaved form) and Bcl-2 levels. HeLa cells were treated for 24 h with **3d** at the indicated concentrations.

Western blot analysis showed that treatment with **3d** induced a reduction in Bcl-2 expression starting at 10 nM and, at higher concentrations, we also observed the appearance of the phosphorylated form of Bcl-2, a phenomenon frequently observed with antimitotic drugs and probably linked to mitotic death [76,77].

2.2.7. Effects of **3d** Treatments on Zebrafish Embryos

To evaluate the toxicity of **3d** in vivo, wild-type embryos were exposed to **3d** diluted in fish water to 30 and 300 nM. Three replicates were performed, and, for each one, 20 embryos were used per drug concentration (60 embryos in total). The embryos were exposed to chemicals from the shield stage (6 h post-fertilization (hpf)) to larval stage (72 hpf), and phenotypical observations were recorded every 24 h. As shown in Figure 8A, no morphological abnormalities or embryonic lethality were observed in embryos treated with the 30 nM dose. The compound at 300 nM generated a small yolk sac edema in the majority of 48 hpf embryos (red arrow), and the edema was completely re-absorbed within the next 24 h in all treated animals, suggesting that **3d** was well tolerated by the embryos.
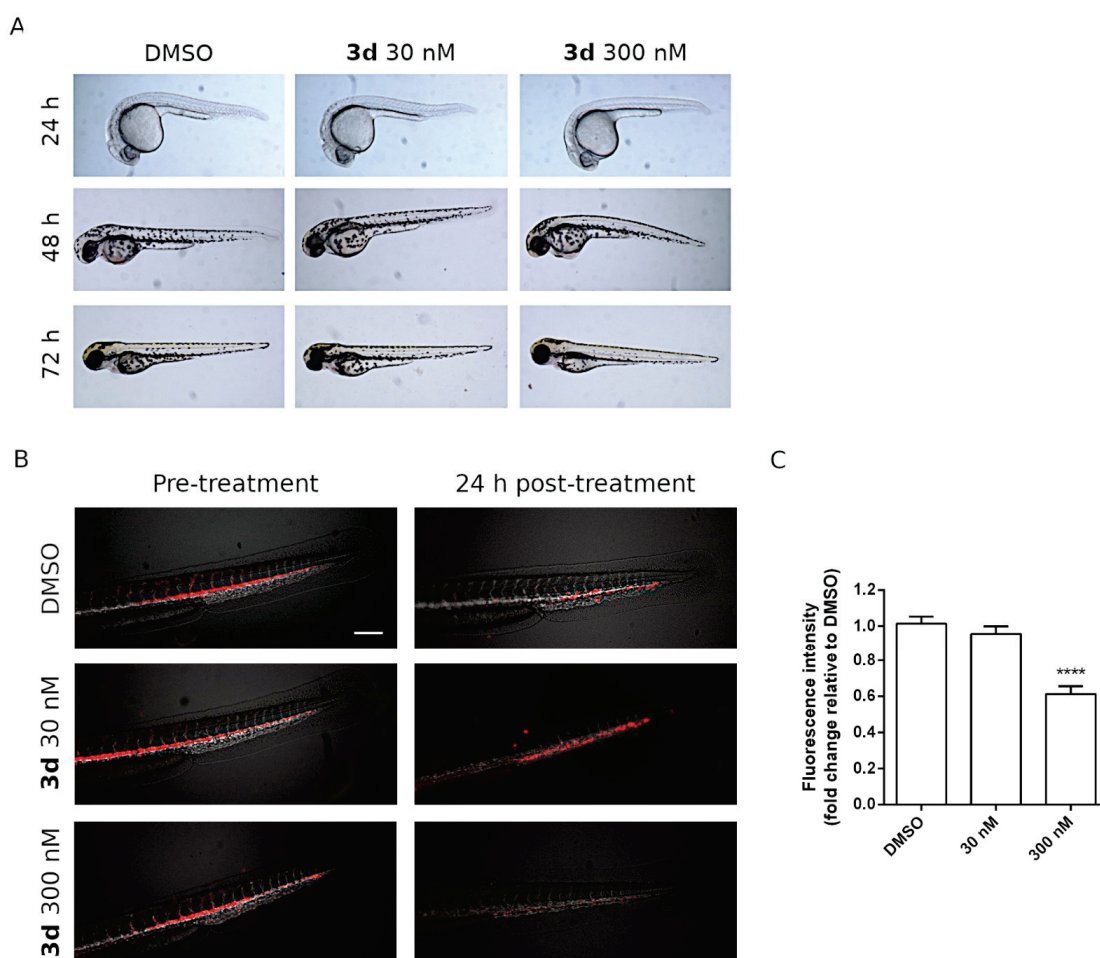

Figure 8. Effects of **3d** treatment on the zebrafish xenotransplantation model (**A**). Compound **3d** did not induce abnormal phenotypes or developmental anomalies in zebrafish embryos after 24, 48 and 72 h of incubation. DMSO-treated embryos were used as control. (**B**) Representative images of Tg(fli1:EGFP) zebrafish embryos (blood vessels shown in white) transplanted with DiI + HeLa cells (red). The embryos were treated with the indicated concentrations of **3d** for 24 h and then the fluorescence intensity was quantified as depicted in panel (**C**). Data are expressed as mean ± SD (**** $p < 0.001$). Scale bar, 200 μm. Effects of **3d** treatment on zebrafish embryos. No abnormal phenotypes or developmental defects were seen in comparison to DMSO-treated embryos (as a normal control) after 24, 48 and 72 h. (**B**) Effects of **3d** treatment on the zebrafish xenotransplantation model. Representative images of Tg(fli1:EGFP) zebrafish embryos (blood vessels shown in white) transplanted with DiI + HeLa cells (red). Embryos were treated for 24 h with DMSO (control group), 30 nM **3d** or 300 nM **3d**. (**C**) Histograms represent the fluorescence intensity of the tumor xenografts, indicating total HeLa cells present in each embryo after a 24 h treatment with **3d** at the indicated concentrations. Data are expressed as mean ± SD (**** $p < 0.001$). Scale bar, 200 μm.

2.2.8. In Vivo Antitumor Activity of Compound **3d** in a Zebrafish Xenograft Model

To evaluate the effects of **3d** on tumor maintenance and dissemination in vivo, we took advantage of a zebrafish xenograft model. About 200 DiI-labeled HeLa cells were injected within the duct of Cuvier of 48 hpf zebrafish embryos. After xenotransplantation, the animals were treated with **3d** at 30 or 300 nM and circulating tumor cells were visualized and quantified in real time through fluorescence microscopy.

Upon 24 h treatment, HeLa cells were engrafted into the trunk and tail regions of DMSO-treated zebrafish embryos (controls). Interestingly, **3d** significantly reduced the number of disseminated cancer cells (Figure 8B), in agreement with in vitro cytotoxic effects of this compound on HeLa cancer cells. Notably, as shown in Figure 8C, the fluorescence intensity decreased in a dose-dependent manner, reaching statistical significance at 300 nM, indicating the effectiveness of **3d** in eradicating DiI-positive tumor cells.

3. Materials and Methods

3.1. Chemistry

The ^{1}H and ^{13}C NMR spectra were recorded on a Varian 400 Mercury Plus spectrometer. Chemical shifts (δ) are given in ppm upfield, and the spectra were recorded in appropriate deuterated solvents, as indicated. Mass spectra were recorded by an ESI single quadrupole mass spectrometer (Waters ZQ 2000; Waters Instruments, UK), and the values are expressed as $[M+1]^+$. Melting points (mp) were determined on a Buchi-Tottoli apparatus and are uncorrected. All products reported showed ^{1}H and ^{13}C NMR spectra in agreement with the assigned structures. The purity of tested compounds was determined by combustion elemental analyses conducted by the Microanalytical Laboratory of the Chemistry Department of the University of Ferrara with a Yanagimoto MT-5 CHN recording elemental analyzer. All tested compounds yielded data consistent with a purity of at least 95% as compared with the theoretical values. Reaction courses and product mixtures were routinely monitored by TLC on silica gel (precoated F254 Merck plates), and compounds were visualized with aqueous $KMnO_4$. Flash chromatography was performed using 230–400 mesh silica gel and the indicated solvent system. Organic solutions were dried over anhydrous Na_2SO_4.

3.1.1. General Procedure A for the Synthesis of Compounds **8a–v**

To a solution of dimethyl cyanodithioimidocarbonate **7** (292 mg, 2 mmol) in isopropanol (10 mL) was added the appropriate amine (2 mmol, 1 equiv.), and the mixture was refluxed for 18 h for the synthesis of compounds **8a–o**, while the mixture was stirred at room temperature (18 h) for the preparation of compounds **8p–v**. After this time, the solvent was removed under reduced pressure, the resulting residue was washed with diethyl ether (10 mL) and filtered to furnish the final compound **8a–v** used for the next reaction without any purification. For the characterization of compounds **8a**, **8c–f**, **8h** and **8j–n** see reference [53]. The characterization of compounds **8p–v** was described previously [78].

(Z)-Methyl *N′*-Cyano-*N*-(pyridin-3-yl)carbamimidothioate (**8b**)

Following general procedure A, compound **8b** was obtained as a white solid, yield 89%, mp 188–190 °C; ^{1}H-NMR (DMSO-*d₆*) δ: 2.62 (s, 3H), 7.10 (d, J = 8.0 Hz, 1H), 7.26 (m, 1H), 7.69 (s, 1H), 8.62 (d, J = 8.0 Hz, 1H), 10.0 (s, 1H). MS (ESI): $[M+1]^+$ = 193.2.

(Z)-Methyl *N′*-Cyano-*N*-(3,5-dimethylphenyl)carbamimidothioate (**8g**)

Following general procedure A, compound **8g** was obtained as a white solid, yield 78%, mp 142–144 °C; ^{1}H-NMR (DMSO-*d₆*) δ: 2.22 (s, 6H), 2.44 (s, 3H), 6.36 (s, 1H), 7.10 (s, 2H), 10.0 (bs, 1H). MS (ESI): $[M+1]^+$ = 220.3.

(Z)-Methyl *N*-(4-n-Propylphenyl)-*N′*-cyanocarbamimidothioate (**8i**)

Following general procedure A, compound **8i** was obtained as a white solid, yield 84%, mp 154–156 °C; ^{1}H-NMR (DMSO-*d₆*) δ: 0.93 (t, J = 7.2 Hz, 3H), 1.60 (m, 2H), 2.53 (s,

3H), 2.62 (t, J = 7.2 Hz, 2H), 7.20 (d, J = 8.4 Hz, 2H), 7.24 (d, J = 8.4 Hz, 2H), 10.1 (bs, 1H). MS (ESI): [M+1]$^+$ = 234.3.

(Z)-Methyl *N'*-Cyano-*N*-(2,3-dihydrobenzo[b][1,4]dioxin-6-yl)carbamimidothioate (**8o**)

Following general procedure A, compound **8o** was obtained as a white solid, yield 92%, mp 202–204 °C; ^{1}H-NMR (DMSO-d_6) δ: 2.48 (s, 3H), 4.2 (s, 4H), 7.10 (d, J = 8.0 Hz, 1H), 6.84 (s, 2H), 6.94 (s, 1H), 10.0 (s, 1H). MS (ESI): [M+1]$^+$ = 250.2

3.1.2. General Procedure B for the Synthesis of Compounds **9a–v**

To a stirred suspension of compound **8a–v** (2 mmol) in methanol (10 mL) was added hydrazine monohydrate (0.2 mL, 4 mmol, 2 equiv.), and the mixture was heated under reflux for 18 h. After this time, the volatiles were removed, and the residue suspended with diethyl ether (10 mL) was sonicated for 10 min. The resultant solid was collected by filtration and then used for the next reaction without any purification. For the characterization of compounds **9a**, **9c–f**, **9h** and **9j–n** see reference [53].

N^3-(Pyridin-3-yl)-1*H*-1,2,4-triazole-3,5-diamine (**9b**)

Following general procedure B, compound **9b** was obtained as a grey solid. Yield 68%, mp 178–179 °C; ^{1}H-NMR (d_6-DMSO) δ: 5.76 (bs, 2H), 7.31 (dd, J = 7.7 and 4.8 Hz, 1H), 7.71 (dt, J = 7.8 and 1.8 Hz, 1H), 8.12–8.21 (m. 1H), 8.33 (s, 1H), 8.52 (d, J = 1.8 Hz. 1H), 11.0 (br. s., 1H). MS (ESI): [M+1]$^+$ = 177.2.

N^3-(3,5-Dimethylphenyl)-1*H*-1,2,4-triazole-3,5-diamine (**9g**)

Following general procedure B, compound **9g** was obtained as a white solid. Yield 88%, mp 188–190 °C; ^{1}H-NMR (d_6-DMSO) δ: 2.15 (s, 6H), 5.76 (bs, 2H), 6.34 (s, 1H), 7.09 (s, 2H), 8.40 (s, 1H), 11.0 (bs, 1H). MS (ESI): [M+1]$^+$ = 204.3.

N^3-(4-n-Propylphenyl)-1*H*-1,2,4-triazole-3,5-diamine (**9i**)

Following general procedure B, compound **9i** was obtained as a white solid. Yield 82%, mp 186–188 °C; ^{1}H-NMR (d_6-DMSO) δ: 0.88 (t, J = 7.0 Hz, 3H), 1.48 (m, 2H), 2.41 (t, J = 7.6 Hz, 2H), 5.80 (bs, 2H), 6.94 (d, J = 8.2 Hz, 2H), 7.36 (d, J = 8.2 Hz, 2H), 8.43 (bs, 1H), 11.1 (bs, 1H). MS (ESI): [M+1]$^+$ = 218.3.

N^3-(2,3-Dihydrobenzo[b][1,4]dioxin-6-yl)-1*H*-1,2,4-triazole-3,5-diamine (**9o**)

Following general procedure B, compound **9o** was obtained as a white solid. Yield 82%, mp 202–204 °C; ^{1}H-NMR (d_6-DMSO) δ: 4.10–4.16 (m, 4H), 5.73 (bs, 2H), 6.60 (d, J = 8.8 Hz, 1H), 6.82 (dd, J = 8.8 and 2.4 Hz, 1H), 7.15 (d, J = 2.4 Hz, 1H), 8.31 (s, 1H), 10.8 (bs, 1H). MS (ESI): [M+1]$^+$ = 234.2.

N^3-Benzyl-1*H*-1,2,4-triazole-3,5-diamine (**9p**)

Following general procedure B, compound **9p** was obtained as a white solid. Yield 75%, mp 203–205 °C; ^{1}H-NMR (d_6-DMSO) δ: 4.21 (d, J = 6.4 Hz, 2H), 5.32 (bs, 2H), 6.12 (t, J = 6.4 Hz, 1H), 7.18–7.20 (m, 1H), 7.27–7.30 (m, 4H), 10.6 (bs, 1H). MS (ESI): [M+1]$^+$ = 190.2.

N^3-(4-Chlorobenzyl)-1*H*-1,2,4-triazole-3,5-diamine (**9q**)

Following general procedure B, compound **9q** was obtained as a white solid. Yield 88%, mp 176–178 °C; ^{1}H-NMR (d_6-DMSO) δ: 4.20 (d, J = 6.4 Hz, 2H), 5.30 (bs, 2H), 5.86 (t, J = 6.4 Hz, 1H), 7.29-7.38 (m, 4H), 10.8 (bs, 1H). MS (ESI): [M+1]$^+$ = 224.7.

N^3-(4-Methylbenzyl)-1*H*-1,2,4-triazole-3,5-diamine (**9r**)

Following general procedure B, compound **9r** was obtained as a white solid. Yield 87%, mp 188–190 °C; ^{1}H-NMR (d_6-DMSO) δ: 2.25 (s, 3H), 4.14 (d, J = 6.2 Hz, 2H), 5.27 (bs,

2H), 5.85 (t, J = 6.2 Hz, 1H), 7.05 (d, J = 8.0 Hz, 2H), 7.16 (d, J = 8.0 Hz, 2H), 10.7 (bs, 1H). MS (ESI): [M+1]$^+$ = 203.9.

N^3-(4-Methoxybenzyl)-1*H*-1,2,4-triazole-3,5-diamine (9s)

Following general procedure B, compound **9s** was obtained as a white solid. Yield 88%, mp 198–200 °C; ^{1}H-NMR (d_6-DMSO) δ: 3.71 (s, 3H), 4.11 (d, J = 6.4 Hz, 2H), 5.28 (bs, 2H), 5.92 (t, J = 6.4 Hz, 1H), 6.82 (d, J = 8.6 Hz, 2H), 7.20 (d, J = 8.6 Hz, 2H), 10.8 (bs, 1H). MS (ESI): [M+1]$^+$ = 220.2.

N^3-(Benzo[d][1,3]dioxol-5-ylmethyl)-1*H*-1,2,4-triazole-3,5-diamine (9t)

Following general procedure B, compound **9t** was obtained as a white solid. Yield 93%, mp 204–206 °C; ^{1}H-NMR (d_6-DMSO) δ: 4.12 (d, J = 6.4 Hz, 2H), 4,24 (bs, 1H), 5.38 (bs, 2H), 5.97 (s, 2H), 6.74 (dd, J = 8.2 and 2.2 Hz, 1H), 6.80 (d, J = 8.2 Hz, 1H), 6.88 (d, J = 2.2 Hz, 1H), 10.8 (bs, 1H). MS (ESI): [M+1]$^+$ = 234.2.

N^3-(2-Phenylethyl)-1*H*-1,2,4-triazole-3,5-diamine (9u)

Following general procedure B, compound **9u** was obtained as a white solid. Yield 90%, mp 206–208 °C; ^{1}H-NMR (d_6-DMSO) δ: 2.82 (t, J = 7.2 Hz, 2H), 3.35–3.37 (m, 2H), 5.30 (bs, 2H), 6.22 (t, J = 6.4 Hz, 1H), 7.19–7.22 (m, 2H), 7.27–7.30 (m, 3H), 10.6 (bs, 1H). MS (ESI): [M+1]$^+$ = 204.2.

N^3-(3-Phenylpropyl)-1*H*-1,2,4-triazole-3,5-diamine (9v)

Following general procedure B, compound **9v** was obtained as a white solid. Yield 92%, mp 188–190 °C; ^{1}H-NMR (d_6-DMSO) δ: 1.74 (m, 2H), 2.55 (t, J = 7.2 Hz, 2H), 2.95–2.99 (m, 2H), 5.32 (bs, 2H), 6.14 (bs, 1H), 7.14–7.18 (m, 3H), 7.22–7.25 (m, 2H), 10.6 (bs, 1H). MS (ESI): [M+1]$^+$ = 218.3.

3.1.3. General Procedure C for the Synthesis of Compounds 3a–v

To a solution of (*E*)-3-(dimethylamino)-1-(3,4,5-trimethoxyphenyl)prop-2-en-1-one **10** (132 mg, 0.5 mmol) in glacial acetic acid (3 mL) was added the appropriate 3-substituted 5-amino-1,2,4-triazole **9a–v** (0.75 mmol, 1.5 equiv.), and the resulting mixtures were stirred for 2 h at 80 °C and then evaporated to dryness in vacuo. The residue was portioned between dichloromethane and a 2 M solution of Na_2CO_3 in water, the organic phase was separated, washed with brine, dried over sodium sulfate, filtered and concentrated. The crude residue was subjected to column chromatography on silica gel using a mixture of ethyl acetate–methanol as eluent or recrystallized from diethyl ether, yielding the appropriate 2-substituted-7-(3′,4′5′-trimethoxyphenyl)[1,2,4]triazolo[1,5-*a*]pyrimidines **3a–v**.

N-Phenyl-7-(3,4,5-trimethoxyphenyl)-[1,2,4]triazolo[1,5-*a*]pyrimidin-2-amine (3a)

Following general procedure C, the crude residue was purified by crystallization with diethyl ether to furnish **3a** as a yellow solid. Yield: 49%, mp 235–236 °C; ^{1}H-NMR (DMSO-d_6) δ: 3.79 (s, 3H), 3.91 (s, 6H), 6.94 (t, J = 8.4 Hz, 1H), 7.27 (t, J = 8.4 Hz, 2H), 7.52 (d, J = 4.8 Hz, 1H), 7.71 (s, 2H), 7.73 (t, J = 8.4 Hz, 2H), 8.66 (d, J = 4.8 Hz, 1H), 9.89 (s, 1H); ^{13}C-NMR (DMSO-d_6) δ: 56.60 (2C), 60.71, 107.70 (2C), 108.21, 117.39 (2C), 121.15, 125.36, 129.17 (2C), 140.69, 141.18, 145.52, 153.17 (2C), 153.36, 155.71, 163.57. MS (ESI): [M+1]$^+$ = 378.4. Anal. calcd for $C_{20}H_{19}N_5O_3$. C, 63.65; H, 5.07; N, 18.56; found: C, 63.48; H, 4.88; N, 18.34.

N-(Pyridin-3-yl)-7-(3,4,5-trimethoxyphenyl)-[1,2,4]triazolo[1,5-*a*]pyrimidin-2-amine (3b)

Following general procedure C, the crude residue was purified by crystallization with diethyl ether to furnish **3b** as a brown solid. Yield: 47%, mp 172–174 °C; ^{1}H-NMR (DMSO-d_6) δ: 3.79 (s, 3H), 3.81 (s, 6H), 7.31 (dd, J = 8.4 and 8.0 Hz, 1H), 7.55 (d, J = 4.8 Hz, 1H), 7.56 (s, 2H), 8.08–8.09 (m, 1H), 8.10–8.14 (m, 1H), 8.70 (d, J = 4.8 Hz, 1H), 8.97 (d, J = 2.8 Hz, 1H), 10.1 (s, 1H); ^{13}C-NMR (DMSO-d_6) δ: 56.62 (2C), 60.72, 107.69 (2C), 108.54, 123.78, 123.94, 125.27, 137.88, 139.51, 140.72, 142.18, 145.77, 153.19 (2C), 153.66, 155.75, 163.23. MS (ESI):

$[M+1]^+$ = 379.3. Anal. calcd for $C_{19}H_{18}N_6O_3$. C, 60.31; H, 4.79; N, 22.21; found: C, 60.12; H, 4.67; N, 22.03.

N-(4-Fluorophenyl)-7-(3,4,5-trimethoxyphenyl)-[1,2,4]triazolo[1,5-*a*]pyrimidin-2-amine (**3c**)

Following general procedure C, the crude residue was purified by crystallization with diethyl ether to furnish **3c** as a white solid. Yield: 58%, mp 234–235 °C; ^{1}H-NMR (DMSO-*d₆*) δ: 3.78 (s, 3H), 3.90 (s, 6H), 7.12 (t, J = 8.8 Hz, 2H), 7.50 (d, J = 4.8 Hz, 1H), 7.66 (s, 2H), 7.66–7.73 (m, 2H), 8.66 (d, J = 4.8 Hz, 1H), 9.91 (s, 1H); ^{13}C-NMR (DMSO-*d₆*) δ: 56.62 (2C), 60.71, 107.66 (2C), 108.30, 115.60 and 115.82 (J_{2CF} = 22.1 Hz, 2C), 118.75 and 118.82 (J_{3CF} = 6.9 Hz, 2C), 125.35, 137.67, 140.67, 145.57, 153.19 (2C), 153.36, 155.74, 155.95 and 158.31 (J_{1CF} = 236 Hz, 1C), 163.54. MS (ESI): $[M+1]^+$ = 396.2. Anal. calcd for $C_{20}H_{18}FN_5O_3$. C, 60.75; H, 4.59; N, 17.71; found: C, 60.56; H, 4.43; N, 17.48.

N-(p-Tolyl)-7-(3,4,5-trimethoxyphenyl)-[1,2,4]triazolo[1,5-*a*]pyrimidin-2-amine (**3d**)

Following general procedure C, the crude residue was crystallized with diethyl ether to furnish **3d** as a yellow solid. Yield: 58%, mp 208–209 °C; ^{1}H-NMR (DMSO-*d₆*) δ: 2.23 (s, 3H), 3.79 (s, 3H), 3.91 (s, 6H), 7.06 (d, J = 8.4 Hz, 2H), 7.50 (d, J = 4.8 Hz, 1H), 7.59 (d, J = 8.4 Hz, 2H), 7.68 (s, 2H), 8.64 (d, J = 4.8 Hz, 1H), 9.57 (s, 1H); ^{13}C-NMR (DMSO-*d₆*) δ: 20.77, 56.60 (2C), 60.71, 107.68 (2C), 108.09, 117.43 (2C), 125.39, 129.56 (2C), 129.90, 138.69, 140.66, 145.42, 153.16 (2C), 153.23, 155.74, 163.81. MS (ESI): $[M+1]^+$ = 392.4. Anal. calcd for $C_{21}H_{21}N_5O_3$. C, 64.44; H, 5.41; N, 17.89; found: C, 64.31; H, 5.18; N, 17.77.

N-(m-Tolyl)-7-(3,4,5-trimethoxyphenyl)-[1,2,4]triazolo[1,5-*a*]pyrimidin-2-amine (**3e**)

Following general procedure C, the crude residue was purified by crystallization with diethyl ether to furnish **3e** as a yellow solid. Yield: 62%, mp 229–230 °C; ^{1}H-NMR (DMSO-*d₆*) δ: 2.26 (s, 3H), 3.78 (s, 3H), 3.89 (s, 6H), 6.74 (d, J = 8.0 Hz, 1H), 7.14 (t, J = 8.0 Hz, 1H), 7.46 (d, J = 2.0 Hz, 1H), 7.48 (d, J = 4.8 Hz, 1H), 7.60 (d, J = 8.0 Hz, 1H), 7.65 (s, 2H), 8.66 (d, J = 4.8 Hz, 1H), 9.81 (s, 1H); ^{13}C-NMR (DMSO-*d₆*) δ: 21.79, 56.65 (2C), 60.71, 107.64 (2C), 108.22, 114.57, 117.97, 121.94, 125.44, 128.98, 138.32, 140.65, 141.14, 145.58, 153.17 (2C), 153.31, 155.67, 163.61. MS (ESI): $[M+1]^+$ = 392.6. Anal. calcd for $C_{21}H_{21}N_5O_3$. C, 64.44; H, 5.41; N, 17.89; found: C, 64.23; H, 5.31; N, 17.69.

N-(3,4-Dimethylphenyl)-7-(3,4,5-trimethoxyphenyl)-[1,2,4]triazolo[1,5-*a*]pyrimidin-2-amine (**3f**)

Following general procedure C, the crude residue was crystallized with diethyl ether to furnish **3f** as a yellow solid. Yield: 54%, mp 189–190 °C; ^{1}H-NMR (DMSO-*d₆*) δ: 2.14 (s, 3H), 2.16 (s, 3H), 3.78 (s, 3H), 3.89 (s, 6H), 7.02 (d, J = 8.4 Hz, 1H), 7.41 (d, J = 1.2 Hz, 1H), 7.47 (d, J = 4.8 Hz, 1H), 7.54 (dd, J = 8.4 and 1.2 Hz, 1H), 7.65 (s, 2H), 8.64 (d, J = 4.8 Hz, 1H), 9.68 (s, 1H); ^{13}C-NMR (DMSO-*d₆*) δ: 19.08, 20.24, 56.64 (2C), 60.70, 107.73 (2C), 108.08, 114.86, 118.81, 125.47, 128.72, 130.01, 138.74, 138.97, 140.62, 145.47, 153.17 (2C), 155.71, 158.64, 163.73. MS (ESI): $[M+1]^+$ = 406.4. Anal. calcd for $C_{22}H_{23}N_5O_3$. C, 65.17; H, 5.72; N, 17.27; found: C, 64.92; H, 5.53; N, 17.05.

N-(3,5-Dimethylphenyl)-7-(3,4,5-trimethoxyphenyl)-[1,2,4]triazolo[1,5-*a*]pyrimidin-2-amine (**3g**)

Following general procedure C, the crude residue was purified by flash chromatography, using ethyl acetate as eluent, to furnish **3g** as a yellow solid. Yield: 58%, mp 228–230 °C; ^{1}H-NMR (DMSO-*d₆*) δ: 2.21 (s, 6H), 3.77 (s, 3H), 3.87 (s, 6H), 6.55 (s, 1H), 7.32 (s, 2H), 7.44 (d, J = 4.8 Hz, 1H), 7.60 (s, 2H), 8.65 (d, J = 4.8 Hz, 1H), 9.72 (s, 1H); ^{13}C-NMR (DMSO-*d₆*) δ: 21.15 (2C), 56.13 (2C), 60.13, 107.22 (2C), 107.86, 114.64 (2C), 122.27, 124.98, 137.51 (2C), 140.01, 140.53, 145.10, 152.61 (2C), 152.71, 155.06, 163.07. MS (ESI): $[M+1]^+$ = 406.4. Anal. calcd for $C_{22}H_{23}N_5O_3$. C, 65.17; H, 5.72; N, 17.27; found: C, 64.97; H, 5.52; N, 17.11.

N-(4-Ethylphenin)-7-(3,4,5-trimethoxyphenyl)-[1,2,4]triazolo[1,5-*a*]pyrimidin-2-amine (**3h**)

Following general procedure C, the crude residue crystallized with diethyl ether furnished **3h** as a yellow solid. Yield: 63%, mp 199–200 °C; ^{1}H-NMR (DMSO-d_6) δ: 1.14 (t, J = 8.4 Hz, 3H), 2.52 (q, J = 8.4 Hz, 2H), 3.79 (s, 3H), 3.91 (s, 6H), 7.09 (d, J = 8.4 Hz, 2H), 7.50 (d, J = 4.8 Hz, 1H), 7.61 (d, J = 8.4 Hz, 2H), 7.69 (s, 2H), 8.64 (d, J = 4.8 Hz, 1H), 9.77 (s, 1H); ^{13}C-NMR (DMSO-d_6) δ: 16.34, 27.93, 56.59 (2C), 60.72, 107.68 (2C), 108.09, 117.56 (2C), 125.38, 128.16, 128.36 (2C), 136.52, 138.89, 140.66, 145.41, 153.16 (2C), 155.75, 163.71. MS (ESI): [M+1]$^+$ = 406.3. Anal. calcd for $C_{22}H_{23}N_5O_3$. C, 65.17; H, 5.72; N, 17.27; found: C, 64.91; H, 5.54; N, 17.12.

N-(4-Propylphenin)-7-(3,4,5-trimethoxyphenyl)-[1,2,4]triazolo[1,5-*a*]pyrimidin-2-amine (**3i**)

Following general procedure C, the crude residue crystallized with diethyl ether furnished **3i** as a yellow solid. Yield: 64%, mp 185–187 °C; ^{1}H-NMR (DMSO-d_6) δ: 0.86 (t, J = 7.2 Hz, 3H), 1.52–1.55 (m, 2H), 2.52 (q, J = 7.2 Hz, 2H), 3.78 (s, 3H), 3.91 (s, 6H), 7.07 (d, J = 8.4 Hz, 2H), 7.50 (d, J = 4.8 Hz, 1H), 7.60 (d, J = 8.4 Hz, 2H), 7.69 (s, 2H), 8.64 (d, J = 4.8 Hz, 1H), 9.77 (s, 1H); ^{13}C-NMR (DMSO-d_6) δ: 14.04, 24.75, 37.05, 56.59 (2C), 60.71, 107.68 (2C), 108.08, 117.50 (2C), 125.38, 128.95 (2C), 134.88, 138.90, 140.66, 145.40, 147.92, 153.16 (2C), 155.75, 163.71. MS (ESI): [M+1]$^+$ = 420.4. Anal. calcd for $C_{23}H_{25}N_5O_3$. C, 65.85; H, 6.01; N, 16.70; found: C, 65.69; H, 5.88; N, 16.52.

N-(4-Isopropylphenin)-7-(3,4,5-trimethoxyphenyl)-[1,2,4]triazolo[1,5-*a*]pyrimidin-2-amine (**3j**)

Following general procedure C, the crude residue crystallized with diethyl ether furnished **3j** as a yellow solid. Yield: 53%, mp 212–214 °C; ^{1}H-NMR (DMSO-d_6) δ: 1.12 (d, J = 6.8 Hz, 6H), 2.46–2.48 (m, 1H), 3.79 (s, 3H), 3.91 (s, 6H), 7.12 (d, J = 8.4 Hz, 2H), 7.50 (d, J = 4.8 Hz, 1H), 7.61 (d, J = 8.4 Hz, 2H), 7.69 (s, 2H), 8.64 (d, J = 4.8 Hz, 1H), 9.76 (s, 1H); ^{13}C-NMR (DMSO-d_6) δ: 24.52 (2C), 33.17, 56.59 (2C), 60.71, 107.69 (2C), 108.08, 115.95, 117.63 (2C), 125.38, 126.84 (2C), 138.95, 140.65, 141.25, 145.38, 153.16 (2C), 155.77, 163.73. MS (ESI): [M+1]$^+$ = 420.5. Anal. calcd for $C_{23}H_{25}N_5O_3$. C, 65.85; H, 6.01; N, 16.70; found: C, 65.70; H, 5.88; N, 16.51.

N-(4-Methoxyphenin)-7-(3,4,5-trimethoxyphenyl)-[1,2,4]triazolo[1,5-*a*]pyrimidin-2-amine (**3k**)

Following general procedure C, the crude residue was purified by crystallization with diethyl ether to furnish **3k** as a yellow solid. Yield: 62%, mp 213–215 °C; ^{1}H-NMR (DMSO-d_6) δ: 3.70 (s, 3H), 3.78 (s, 3H), 3.90 (s, 6H), 7.48 (d, J = 4.8 Hz, 1H), 6.85 (d, J = 8.8 Hz, 2H), 7.61 (d, J = 8.8 Hz, 2H), 7.68 (s, 2H), 8.62 (d, J = 4.8 Hz, 1H), 9.65 (s, 1H); ^{13}C-NMR (DMSO-d_6) δ: 55.69, 56.60 (2C), 60.71, 107.65 (2C), 107.98, 114.45 (2C), 118.90 (2C), 125.40, 134.54, 140.63, 145.30, 153.08, 153.16 (2C), 154.15, 155.82, 163.85. MS (ESI): [M+1]$^+$ = 408.4. Anal. calcd for $C_{21}H_{21}N_5O_4$. C, 61.91; H, 5.20; N, 17.19; found: C, 61.77; H, 5.02; N, 17.01.

N-(3-Methoxyphenin)-7-(3,4,5-trimethoxyphenyl)-[1,2,4]triazolo[1,5-*a*]pyrimidin-2-amine (**3l**)

Following general procedure C, the crude residue was purified by crystallization with diethyl ether to furnish **3l** as a yellow solid. Yield: 54%, mp 165–166 °C; ^{1}H-NMR (DMSO-d_6) δ: 3.70 (s, 3H), 3.78 (s, 3H), 3.90 (s, 6H), 6.54 (dd, J = 8.0 and 2.0 Hz, 1H), 7.19 (t, J = 8.4 Hz, 1H), 7.24 (dd, J = 8.0 and 2.0 Hz, 1H), 7.40 (d, J = 2.0 Hz, 1H), 7.49 (d, J = 4.8 Hz, 1H), 7.65 (s, 2H), 8.66 (d, J = 4.8 Hz, 1H), 9.88 (s, 1H); ^{13}C-NMR (DMSO-d_6) δ: 55.35, 56.59 (2C), 60.70, 103.88, 105.92, 107.69 (2C), 108.31, 110.17, 125.42, 129.92, 140.66, 142.29, 145.69, 153.19 (2C), 153.43, 155.61, 160.33, 163.48. MS (ESI): [M+1]$^+$ = 408.3. Anal. calcd for $C_{21}H_{21}N_5O_4$. C, 61.91; H, 5.20; N, 17.19; found: C, 61.72; H, 5.10; N, 17.02.

N-(4-Ethoxyphenin)-7-(3,4,5-trimethoxyphenyl)-[1,2,4]triazolo[1,5-*a*]pyrimidin-2-amine (**3m**)

Following general procedure C, the crude residue was purified by crystallization with diethyl ether to furnish **3m** as a yellow solid. Yield: 61%, mp 205–207 °C; ^{1}H-NMR (DMSO-d_6) δ: 1.28 (t, J = 6.8 Hz, 3H), 3.78 (s, 3H), 3.90 (s, 6H), 3.96 (q, J = 6.8 Hz, 2H), 6.83

(d, J = 9.2 Hz, 2H), 7.48 (d, J = 4.8 Hz, 1H), 7.60 (d, J = 8.8 Hz, 2H), 7.68 (s, 2H), 8.62 (d, J = 4.8 Hz, 1H), 9.65 (s, 1H); ^{13}C-NMR (DMSO-d_6) δ: 15.28, 56.59 (2C), 60.70, 63.60, 107.65 (2C), 107.97, 114.92, 115.03, 117.04, 118.88 (2C), 125.41, 134.45, 140.63, 145.29, 153.08, 153.16, 153.39, 155.82, 163.85. MS (ESI): [M+1]$^+$ = 422.4. Anal. calcd for $C_{22}H_{23}N_5O_4$. C, 62.70; H, 5.50; N, 16.62; found: C, 62.58; H, 5.38; N, 16.49.

N-(Benzo[d][1,3]dioxol-5-yl)-7-(3,4,5-trimethoxyphenyl)-[1,2,4]triazolo[1,5-*a*]pyrimidin-2-amine (**3n**)

Following general procedure C, the crude residue purified by crystallization with diethyl ether furnished **3n** as a white solid. Yield: 63%, mp 234–236 °C; ^{1}H-NMR (DMSO-d_6) δ: 3.78 (s, 3H), 3.90 (s, 6H), 5.95 (s, 2H), 6.82 (d, J = 8.4 Hz, 1H), 7.03 (dd, J = 8.4 and 2.0 Hz, 1H), 7.48-7.50 (m, 2H), 7.66 (s, 2H), 8.64 (d, J = 4.8 Hz, 1H), 9.76 (s, 1H); ^{13}C-NMR (DMSO-d_6) δ: 56.62 (2C), 60.70, 99.91, 101.24, 107.64 (2C), 108.11, 108.65, 109.97, 125.37, 135.89, 140.65, 141.62, 145.44, 147.78, 153.17 (2C), 153.27, 155.71, 163.64. MS (ESI): [M+1]$^+$ = 422.4. Anal. calcd for $C_{21}H_{19}N_5O_3$. C, 59.85; H, 4.54; N, 16.62; found: C, 59.72; H, 4.33; N, 16.48.

N-(2,3-Dihydrobenzo[b][1,4]dioxin-6-yl)-7-(3,4,5-trimethoxyphenyl)-[1,2,4]triazolo[1,5-*a*]pyrimidin-2-amine (**3o**)

Following general procedure C, the crude residue purified by crystallization with diethyl ether furnished **3o** as a white solid. Yield: 58%, mp 212–214 °C; ^{1}H-NMR (DMSO-d_6) δ: 3.78 (s, 3H), 3.91 (s, 6H), 4.16–4.22 (m, 4H), 6.74 (d, J = 8.4 Hz, 1H), 7.02 (dd, J = 8.4 and 2.4 Hz, 1H), 7.39 (d, J = 2.8 Hz, 1H), 7.48 (d, J = 4.8 Hz, 1H), 7.66 (s, 2H), 8.63 (d, J = 4.8 Hz, 1H), 9.67 (s, 1H); ^{13}C-NMR (DMSO-d_6) δ: 56.58 (2C), 60.69, 64.32, 64.74, 86.40, 106.42, 107.59 (2C), 108.06, 110.89, 117.31, 125.42, 135.04, 138.01, 140.62, 143.63, 145.44, 153.19 (2C), 155.71, 163.63. MS (ESI): [M+1]$^+$ = 436.4. Anal. calcd for $C_{22}H_{21}N_5O_5$. C, 60.68; H, 4.86; N, 16.08; found: C, 60.54; H, 4.72; N, 15.98.

N-Benzyl-7-(3,4,5-trimethoxyphenyl)-[1,2,4]triazolo[1,5-*a*]pyrimidin-2-amine (**3p**)

Following general procedure C, the crude residue was purified by flash chromatography, using ethyl acetate:methanol 9.5:0.5 as eluent, to furnish **3p** as a white solid. Yield: 58%, mp 144–146 °C; ^{1}H-NMR (DMSO-d_6) δ: 3.73 (s, 3H), 3.76 (s, 6H), 4.48 (d, J = 6.0 Hz, 2H), 7.22 (t, J = 8.4 Hz, 1H), 7.29 (t, J = 8.4 Hz, 2H), 7.34 (d, J = 8.4 Hz, 2H), 7.38 (d, J = 5.2 Hz, 1H), 7.59 (s, 2H), 7.61 (t, J = 6.4 Hz, 1H), 8.51 (d, J = 5.2 Hz, 1H); ^{13}C-NMR (DMSO-d_6) δ: 45.85, 56.49 (2C), 60.63, 107.38, 107.64 (2C), 125.45, 127.03, 127.29 (2C), 128.66 (2C), 140.44, 140.64, 144.61, 152.04, 153.02 (2C), 156.73, 167.43. MS (ESI): [M+1]$^+$ = 392.4. Anal. calcd for $C_{21}H_{21}N_5O_3$. C, 64.44; H, 5.41; N, 17.89; found: C, 64.24; H, 5.16; N, 17.67.

N-(4-Chlorobenzyl)-7-(3,4,5-trimethoxyphenyl)-[1,2,4]triazolo[1,5-*a*]pyrimidin-2-amine (**3q**)

Following general procedure C, the crude residue was purified by flash chromatography, using ethyl acetate:methanol 9:1 as eluent, to furnish compound **3q** as a yellow solid. Yield: 58%, mp 171–173 °C; ^{1}H-NMR (DMSO-d_6) δ: 3.76 (s, 6H), 3.81 (s, 3H), 4.47 (d, J = 6.4 Hz, 2H), 7.33–7.35 (m, 4H), 7.38 (d, J = 5.2 Hz, 1H), 7.57 (s, 2H), 7.68 (t, J = 6.4 Hz, 1H), 8.52 (d, J = 5.2 Hz, 1H); ^{13}C-NMR (DMSO-d_6) δ: 45.22, 56.48 (2C), 60.64, 107.48, 107.64 (2C), 125.42, 128.60 (2C), 129.14 (2C), 131.55, 139.73, 140,12, 144.70, 152.13 (2C), 153.03, 156.72, 167.30. MS (ESI): [M+1]$^+$ = 426.4. Anal. calcd for $C_{21}H_{20}ClN_5O_3$. C, 59.23; H, 4.73; N, 16.44; found: C, 59.11; H, 4.60; N, 16.33.

N-(4-Methylbenzyl)-7-(3,4,5-trimethoxyphenyl)-[1,2,4]triazolo[1,5-*a*]pyrimidin-2-amine (**3r**)

Following general procedure C, using ethyl acetate:methanol 9.5:0.5 as eluent, compound **3r** was obtained as a white solid. Yield: 61%, mp 156–158 °C; ^{1}H-NMR (DMSO-d_6) δ: 2.23 (s, 3H), 3.74 (s, 3H), 3.77 (s, 6H), 4.43 (d, J = 6.0 Hz, 2H), 7.07 (d, J = 8.0 Hz, 2H), 7.21 (d, J = 8.0 Hz, 2H), 7.38 (d, J = 4.8 Hz, 1H), 7.54 (t, J = 6.4 Hz, 1H), 7.59 (s, 2H), 8.51 (d, J = 4.8 Hz, 1H); ^{13}C-NMR (DMSO-d_6) δ: 20.61, 45.15, 56.02 (2C), 60.17, 106.88, 107.17 (2C), 125.00, 126.83 (2C), 128.72 (2C), 135.56, 137.09, 139.96, 144.11, 151.54, 152.57 (2C), 156.25,

166.95. MS (ESI): $[M+1]^+$ = 406.3. Anal. calcd for $C_{22}H_{23}N_5O_3$. C, 65.17; H, 5.72; N, 17.27; found: C, 65.03; H, 5.58; N, 17.18.

N-(4-Methoxybenzyl)-7-(3,4,5-trimethoxyphenyl)-[1,2,4]triazolo[1,5-*a*]pyrimidin-2-amine (**3s**)

Following general procedure C, the crude residue was purified by flash chromatography, using ethyl acetate:methanol 9.5:0.5 as eluent, to furnish **3s** as a white solid. Yield: 66%, mp 190–192 °C; ^{1}H-NMR (DMSO-d_6) δ: 3.69 (s, 3H), 3.74 (s, 3H), 3.79 (s, 6H), 4.40 (d, J = 6.4 Hz, 2H), 6.83 (d, J = 8.4 Hz, 2H), 7.26 (d, J = 8.4 Hz, 2H), 7.38 (d, J = 4.8 Hz, 1H), 7.53 (t, J = 6.4 Hz, 1H), 7.61 (s, 2H), 8.30 (d, J = 4.8 Hz, 1H); ^{13}C-NMR (DMSO-d_6) δ: 45.33, 55.46, 56.52 (2C), 60.64, 107.35, 107.67 (2C), 114.06 (2C), 125.48, 128.65 (2C), 132.53, 140.44, 144.57, 151.98, 153.03 (2C), 156.71, 158.56, 167.41. MS (ESI): $[M+1]^+$ = 422.4. Anal. calcd for $C_{22}H_{23}N_5O_4$. C, 62.70; H, 5.50; N, 16.62; found: C, 62.55; H, 5.36; N, 16.44.

N-(Benzo[d][1,3]dioxol-5-ylmethyl)-7-(3,4,5-trimethoxyphenyl)-[1,2,4]triazolo[1,5-*a*]pyrimidin-2-amine (**3t**)

Following general procedure C, the crude residue purified by flash chromatography, using ethyl acetate:methanol 9.5:0.5 as eluent, furnished **3t** as a white solid. Yield: 61%, mp 233–235 °C; ^{1}H-NMR (DMSO-d_6) δ: 3.74 (s, 3H), 3.79 (s, 6H), 4.38 (d, J = 6.0 Hz, 2H), 5.94 (s, 2H), 6.81 (s, 2H), 6.92 (s, 1H), 7.37 (d, J = 5.2 Hz, 1H), 7.57 (t, J = 8.4 Hz, 1H), 7.60 (s, 2H), 8.51 (d, J = 5.2 Hz, 1H); ^{13}C-NMR (DMSO-d_6) δ: 45.68, 56.51 (2C), 60.64, 101.19, 107.42, 107.65 (2C), 108.02, 108.41, 120.44, 125.49, 134.59, 140.45, 144.64, 146.37, 147.62, 152.03, 153.04 (2C), 156.70, 167.33. MS (ESI): $[M+1]^+$ = 436.4. Anal. calcd for $C_{22}H_{21}N_5O_5$. C, 60.68; H, 4.86; N, 16.08; found: C, 60.60; H, 4.77; N, 15.88.

N-Phenethyl-7-(3,4,5-trimethoxyphenyl)-[1,2,4]triazolo[1,5-*a*]pyrimidin-2-amine (**3u**)

Following general procedure C, the crude residue was purified by flash chromatography, using ethyl acetate:methanol 9.5:0.5 as eluent, to furnish **3u** as a white solid. Yield: 59%, mp 138–139 °C; ^{1}H-NMR (DMSO-d_6) δ: 2.44 (t, J = 7.6 Hz, 2H), 3.42-3.46 (m, 2H), 3.76 (s, 3H), 3.84 (s, 6H), 7.14 (t, J = 8.4 Hz, 1H), 7.23–7.27 (m, 5H), 7.38 (d, J = 4.8 Hz, 1H), 7.66 (s, 2H), 8.51 (d, J = 4.8 Hz, 1H); ^{13}C-NMR (DMSO-d_6) δ: 35.60, 44.23, 56.56 (2C), 60.66, 107.28, 107.73 (2C), 125.56, 126.48, 128.72 (2C), 129.07 (2C), 140.16, 144.61, 147.72, 151.96, 153.06 (2C), 156.83, 167.26. MS (ESI): $[M+1]^+$ = 406.3. Anal. calcd for $C_{22}H_{23}N_5O_3$. C, 65.17; H, 5.72; N, 17.27; found: C, 64.98; H, 5.59; N, 17.11.

N-(3-Phenylpropyl)-7-(3,4,5-trimethoxyphenyl)-[1,2,4]triazolo[1,5-*a*]pyrimidin-2-amine (**3v**)

Following general procedure C, the crude residue was purified by flash chromatography, using ethyl acetate:methanol 9:1 as eluent, to furnish **3v** as a light yellow solid. Yield: 58%, mp 98–100 °C; ^{1}H-NMR (DMSO-d_6) δ: 1.86–1.92 (m, 2H), 2.64 (t, J = 7.6 Hz, 2H), 3.25–3.30 (m, 2H), 3.75 (s, 3H), 3.83 (s, 6H), 7.09 (t, J = 8.4 Hz, 1H), 7.12–7.14 (m, 1H), 7.18-7.24 (m, 4H), 7.37 (d, J = 5.2 Hz, 1H), 7.64 (s, 2H), 8.50 (d, J = 5.2 Hz, 1H); ^{13}C-NMR (DMSO-d_6) δ: 31.27, 32.99, 42.12, 56.53 (2C), 60.64, 107.20, 107.65 (2C), 125.57, 126.15 (2C), 128.70 (2C), 128.74, 140.39, 142.22, 144.53, 151.89, 153.04 (2C), 156.69, 167.45. MS (ESI): $[M+1]^+$ = 419.9. Anal. calcd for $C_{23}H_{25}N_5O_3$. C, 65.85; H, 6.01; N, 16.70; found: C, 65.72; H, 5.89; N, 16.60.

3.2. Biological Assays and Computational Studies

3.2.1. Cell Cultures and Viability Assay

All the cell lines used in this paper were of human origin and purchased from the American Type Culture Collection (ATCC, Manassas, VA, USA). Colon adenocarcinoma (HT-29), non-small cell lung carcinoma (A549), cervix carcinoma (HeLa) and breast adenocarcinoma (MDA-MB-231) cells were grown in RPMI (HT29) or DMEM (A549, HeLa, MDA-MB-231) medium (Gibco, Milano, Italy). Both media were supplemented with 115 units/mL of penicillin G (Gibco, Milano, Italy), 115 μg/mL of streptomycin (Invitrogen, Milano, Italy) and 10% fetal bovine serum (Invitrogen, Milano, Italy). All cell lines were

grown at 37 °C in a humidified 5% CO_2 atmosphere. The cells were grown in 2 mL of complete medium.

Stock solutions were prepared for each compound by dissolving in DMSO at the final concentration of 10 mM.

The cells were seeded in 96-well plates at the appropriate density for each cell line. The respective cell line densities used for the antiproliferative assay were HeLa and HT29 5000 cells/well, A549 4000 cells/well and MDA-MB-231 7000 cells/well. The total volume of medium was 100 μL. After 24 h, the cells were treated by performing serial 5-fold dilutions of the tested compounds starting from a concentration of 10 μM. All experimental conditions were tested in triplicate for statistical analysis. After 72 h of incubation, 10 μL of 100 μg/mL resazurin solution was added to each well and the plate was re-incubated for 3–4 h. The fluorescence of the wells in each plate was monitored using a Spark 10M spectrophotometer (Tecan Group Ltd., Mannedorf, Switzerland) with a 535 nm excitation wavelength and a 600 nm emission wavelength.

The IC_{50} was defined as the compound concentration required to inhibit cell proliferation by 50%, in comparison with cells treated with the maximum amount of DMSO (0.25%), which was considered 100% viability.

3.2.2. Effects on Tubulin Polymerization and on Colchicine Binding to Tubulin

Bovine brain tubulin was purified as described previously [79]. To evaluate the effects of the compounds on tubulin assembly in vitro [80], varying concentrations were preincubated with 10 μM tubulin in 0.8 M monosodium glutamate (pH 6.6) at 30 °C and the reaction mixtures then cooled to 0 °C. After addition of GTP, the mixtures were transferred to 0 °C cuvettes in Beckman Coulter (Brea, CA, USA) DU-7400/DU-7500 recording spectrophotometers equipped with electronic temperature controllers and warmed to 30 °C, and the assembly of tubulin was observed turbidimetrically. The IC_{50} was defined as the compound concentration that inhibited the extent of assembly by 50% after a 20 min incubation. Inhibition of colchicine binding to tubulin was measured as described before [81], except that the reaction mixtures contained 0.5 μM tubulin and 5 μM each of [3H]colchicine and test compound. Only one DEAE-cellulose filter was used per sample, and filtration was by gravity.

Bovine brain tubulin (see ref. [79] for details of purification) was used to examine effects on tubulin polymerization [80] and colchicine binding [81]. Briefly, in the polymerization experiments, different compound concentrations were preincubated with 10 μM tubulin for 15 min at 30 °C and cooled on ice. After GTP was added to each reaction mixture, the samples were transferred to 0 °C cuvettes in recording spectrophotometers with electronic temperature controllers. The temperature was raised to 30 °C over about 30 s, and turbidity development was followed for 20 min at 350 nm. The IC50 was the compound concentration that inhibited net assembly by 50%. In the current studies, [3H]colchicine (from American Radiolabeled Corp., St. Louis, MO) binding was measured after 10 min at 37 °C. Reaction mixtures contained 0.5 μM tubulin and 5.0 μM each of the [3H]colchicine and the potential inhibitor, and a single DEAE-cellulose filter was used for each sample, with gravity filtration.

3.2.3. Molecular Modeling

All molecular docking studies were performed on a Viglen Genie Intel®CoreTM i7-3770 vPro CPU@ 3.40 GHz x 8 running Ubuntu 18.04. Molecular Operating Environment (MOE) 2022.02 [82] and Maestro (Schrödinger Release 2022-2) [83] were used as molecular modeling software. The tubulin structure was downloaded from the protein data bank, (http://www.rcsb.org/, accessed on 1 July 2022; PDB code 4O2B) and then the dimeric tubulin structure was prepared using the Schrödinger Protein Preparation Wizard by assigning bond orders, adding hydrogens and performing a restrained energy minimization of the added hydrogens using the OPLS_2005 force field. Compounds to be docked were built with MOE and then prepared using the Maestro LigPrep tool by energy minimizing

the structures (OPLS_2005 force filed), generating possible ionization states at pH 7 ± 2, tautomers and low-energy ring conformers. A 16 Å docking grid (inner-box 10 Å and outer-box 26 Å) was prepared using as centroid the co-crystallized colchicine. Glide SP precision was adopted for molecular docking studies, using the default parameters, and including 15 output poses per input ligand in the solution. The docking output database was saved as a mol2 file. The docking poses were visually inspected to evaluate their ability to bind in the colchicine binding site. Ligand–protein interactions and ligand–protein clashes were calculated using the MOE contacts tool.

3.2.4. Analysis of Cell Cycle by Flow Cytometry

For these experiments, HeLa cells were used, which were seeded in 6-well plates at a concentration of 5×10^5/well in a final volume of 2 mL culture medium. The cells were then treated with the test compounds for 24 h at the indicated concentrations. After this incubation period, the cells were detached with trypsin-EDTA and harvested by centrifugation. The pellet thus obtained was fixed in 70% ice-cold ethanol.

After this incubation period, the cells were detached with trypsin-EDTA and harvested by centrifugation. The pellet thus obtained was fixed in 70% ice-cold ethanol for at least 1 h. The cells thus fixed were treated with a 0.1% *v/v* solution of Triton_X-100 in phosphate buffered saline (PBS) containing RNAseA and propidium iodide (PI) at the final concentration of 0.02 mg/mL. The cells were incubated at room temperature for 30 min and then analyzed on a Cytomic FC500 flow cytometer (Beckman Coulter) in the FL3 channel. DNA histograms were analyzed using MultiCycle for Windows (Phoenix Flow Systems, San Diego, CA, USA).

3.2.5. Apoptosis Assay

The quantification of the apoptosis induced by the test compounds was carried out by flow cytometric analysis using the Annexin-V Fluos kit (Roche Diagnostics, Rotkreuz, Switzerland) following the manufacturer's instructions. The HeLa cells treated with the test compounds for different incubation times and at the indicated concentrations were then labeled with annexin V/FITC and PI and analyzed with Coulter Cytomics FC500 (Beckman Coulter) in the FL1 and FL3 channel, respectively.

3.2.6. Analysis of Mitochondrial Potential

The analysis of the mitochondrial potential was carried out by flow cytometric analysis. Briefly, the cells treated with the test compound were labeled with the JC-1 dye as previously described [53]. The labeled cells were analyzed using the Coulter Cytomics FC500 (Beckman Coulter) in the FL1 and FL2 channel, respectively.

3.2.7. Western Blot Analysis

Hela cells treated with the test compounds were harvested by centrifugation and then lysed with 0.1% (*v/v*) Triton X-100 containing RNase A at 0 °C. The protein content of the solutions was measured and analyzed as described previously [65]. The antibodies directed against cyclin B, cdc2 (Y15), ATR,Bcl-2, cleaved caspase-9 (D330) and actin were purchased from Cell Signaling. The membranes were visualized using ECL select (GE Healthcare, Uppsal, Sweden), and images were acquired using an Uvitec-Alliance imaging system.

3.2.8. In Vivo Experiments on Zebrafish Model
Husbandry and Maintenance

Zebrafish (*Danio rerio*) were obtained, staged and raised as described previously [65] and maintained according to the OPBA of the Istituto di Ricerca Pediatrica guidelines. All procedures were conducted following the recommendations and the guidelines of the Animal Use Ethics Committee concerning the protection of animals used for scientific purposes.

Drug Toxicity Assessment on Zebrafish Embryos

Wild-type AB zebrafish embryos were treated with chemicals from shield stage (6 hpf) to larval stage (72 hpf) in a 12-well plate, by adding 20 larvae/well for each experimental condition. The zebrafish embryos were treated with compound **3d** at the concentration of 30 nm and 300 nM. These concentrations were selected on the basis of the IC$_{50}$ found above in HeLa cells. The drugs were added directly to the fish water diluted directly from the stock solution in DMSO. Embryos treated with the highest dose of DMSO were used as negative controls and to confirm that this dose of vehicle does not cause any adverse effects towards zebrafish. Subsequently, the treated embryos were kept at a constant temperature (28.5 °C). Embryos are monitored daily through a stereo microscope (Nikon SMZ745T; Nikon, Japan) and the morphological changes as well as the number of dead embryos were evaluated and recorded.

Xenograft Model: Injection and Treatment

Prior to microinjections into Tg zebrafish embryos (fli1: EGFP) [84], HeLa tumor cells were labeled with the VybrantTM DiI dye (Invitrogen, ThermoFisher, Carlsbad, CA, USA). The fluorescent cells were loaded into borosilicate glass capillary needles (OD/ID: 1.00/0.75 mm, World Precision Instruments (WPI, Friedberg, Germany) and injected (200 cells), through a pneumatic picopump, into the Cuvier duct of 48 hpf embryos previously anesthetized with tricaine (0.02%, Sigma-Aldrich, Milan, Italy).

After injection, the xenograft-harboring larvae were incubated to recover at 34° C in fish water containing phenylthiourea (PTU) to inhibit the pigmentation process. After 2 h from the injection, the embryos were examined to ensure homogeneity of the xenografts. For drug treatments, only successfully injected xenograft larvae were selected, with approximately 200 HeLa fluorescent cells scattered around the caudal area.

The injected xenografts were exposed to the doses of **3d** used above with DMSO as control.

For cancer cell imaging and fluorescence quantification, anesthetized embryos were distributed to 96-well plates with one embryo/well. Initially (time 0 h, pre-treatment) and after one-day post-treatment, the tumors were photographed with a Zeiss AxioObserver microscope for live-cell imaging.

4. Conclusions

A series of twenty-two compounds, based on different amines at the 2-position of the 7-(3′,4′,5′-trimethoxyphenyl) [1,2,4]triazolo[1,5-*a*]pyrimidine pharmacophore, was synthesized by a facile and efficient three-step procedure. The modifications were focused at the 2-position of the triazolopyrimidine scaffold by using aromatic amines or arylalkyl amines such as benzylamines, 2-phenylethylamine and 3-phenylpropylamine, with the phenyl ring decorated with electron-releasing or electron-withdrawing groups.

Three of the synthesized aniline derivatives, **3d** (*p*-Me), **3f** (*m,p*-diMe) and **3h** (*p*-Et), had the best antiproliferative activities against the HeLa, A549 and HT-29 cell lines. Compounds **3d** and **3f** strongly inhibited tubulin assembly, with inhibitor potency superior to (**3d**) or comparable with (**3f**) that of CA-4. The *p*-toluidino derivative **3d** was the most potent inhibitor of tubulin polymerization and of colchicine binding (IC$_{50}$ = 0.45 μM for assembly, 72% inhibition of the binding of 5 μM colchicine, with tubulin and the inhibitor at 0.5 and 5 μM, respectively), and the antiproliferative activity of this molecule in terms of IC$_{50}$s ranged from 30 to 430 nM in the four tumor cell lines examined, superior to the IC$_{50}$ obtained with CA-4 against the A549 and HeLa lines.

In comparison with the 1-(3′,4′,5′-trimethoxybenzoyl)-5-amino-1,2,4-triazole **2a,** compound **3d** was almost 2-fold more potent as an inhibitor of tubulin assembly but about 1-2-fold less active as an antiproliferative agent against HeLa, HT-29 and A549 cells, suggesting that the previously published derivative **2a** may exert its potent antiproliferative effect by a mechanism other than inhibition of tubulin polymerization. Alternatively, the reduced potency of **3d** with respect to **2a** on the panel of cancer cell lines can possibly

be rationalized by a limited penetration into the cells or any other mechanism limiting the accessibility of this molecule to the cellular tubulin. As a result, the 7-(3′,4′,5′-trimethoxyphenyl)[1,2,4]triazolo[1,5-*a*]pyrimidine nucleus can be regarded as the same pharmacophore skeleton as the 1-(3′,4′,5′-trimethoxybenzoyl)-5-amino-1,2,4-triazole system.

In agreement with this consideration, we found, as expected, that **3d** in vitro led to cell cycle arrest in the G2/M phase. Immunoblot analysis also showed that treatment of HeLa cells induced the activation of ATR signaling, with the consequent increased expression of cyclin B and a reduction in cdc2 phosphorylation. Compound **3d** induced apoptosis associated with the loss of mitochondrial membrane potential. Moreover, we also demonstrated caspase-9 activation and phosphorylation of the anti-apoptotic Bcl-2 protein, two crucial events in the apoptotic cascade induced by antimitotic compounds.

In vivo experiments carried out in the zebrafish model showed that **3d** had significative anticancer activity because it reduced HeLa cell growth in xenografts implanted in zebrafish embryos and, more importantly, this effect occurred at concentrations that did not cause developmental toxicity.

References

1. Akhmanova, A.; Steinmetz, M.O. Control of microtubule organization and dynamics: Two ends in the limelight. *Nat. Rev. Mol. Cell. Biol.* **2015**, *16*, 711–726. [CrossRef] [PubMed]
2. Ludueña, R.F. A hypothesis on the origin and evolution of tubulin. In *International Review of Cell and Molecular Biology*; Jeon, K.W., Ed.; Academic Press: San Diego, CA, USA, 2013; pp. 41–185.
3. Knossow, M.; Campanacci, V.; Khodja, L.A.; Gigant, B. The mechanism of tubulin assembly into microtubules: Insights from structural studies. *iScience* **2020**, *23*, 101511. [CrossRef] [PubMed]
4. Mukhtar, E.; Adhami, V.M.; Mukhtar, H. Targeting microtubules by natural agents for cancer therapy. *Mol. Cancer Ther.* **2014**, *13*, 275–284. [CrossRef]
5. Karahalil, B.; Yardım-Akaydin, S.; Nacak Baytas, S. An overview of microtubule targeting agents for cancer therapy. *Arh. Hig. Rada Toksikol.* **2019**, *70*, 160–172. [CrossRef] [PubMed]
6. Čermák, V.; Dostál, V.; Jelínek, M.; Libusová, L.; Kovář, J.; Rösel, D.; Brábek, J. Microtubule-targeting agents and their impact on cancer treatment. *Eur. J. Cell Biol.* **2020**, *99*, 151075. [CrossRef]
7. Field, J.J.; Kanakkanthara, A.; Miller, J.H. Microtubule-targeting agents are clinically successful due to both mitotic and interphase impairment of microtubule function. *Bioorg. Med. Chem.* **2014**, *22*, 5050–5059. [CrossRef]

8. Cao, Y.N.; Zheng, L.L.; Wang, D.; Liang, X.X.; Gao, F.; Zhou, X.L. Recent advances in microtubule-stabilizing agents. *Eur. J. Med. Chem.* **2018**, *143*, 806–828. [CrossRef]

9. Seligmann, J.; Twelves, C. Tubulin: An example of targeted chemotherapy. *Future Med. Chem.* **2013**, *5*, 339–352. [CrossRef]

10. Gigant, B.; Wang, C.; Ravelli, R.B.G.; Roussi, F.; Steinmetz, M.O.; Curmi, P.A.; Sobel, A.; Knossow, M. Structural basis for the regulation of tubulin by vinblastine. *Nature* **2005**, *435*, 519–522. [CrossRef]

11. Ranaivoson, F.M.; Gigant, B.; Berritt, S.; Joullié, M.; Knossow, M. Structural plasticity of tubulin assembly probed by vinca-domain ligands. *Acta Crystallogr. Sect. D Biol. Crystallogr.* **2012**, *68*, 927–934. [CrossRef]

12. Coderch, C.; Morreale, A.; Gago, F. Tubulin-based structure-affinity relationships for antimitotic vinca alkaloids. *Anticancer Agents Med. Chem.* **2012**, *12*, 219–225. [CrossRef] [PubMed]

13. Parness, J.; Horwitz, S. Taxol binds to polymerized tubulin in vitro. *J. Cell Biol.* **1981**, *91*, 479–487. [CrossRef] [PubMed]

14. Prota, A.E.; Bargsten, K.; Zurwerra, D.; Field, J.J.; Diaz, J.F.; Altmann, K.H.; Steinmetz, M.O. Molecular mechanism of action of microtubule-stabilizing anticancer agents. *Science* **2013**, *339*, 587–590. [CrossRef] [PubMed]

15. Yang, C.H.; Horwitz, S.B. Taxol(®): The First Microtubule Stabilizing Agent. *Int. J. Mol. Sci.* **2017**, *18*, 1733. [CrossRef]

16. Katsetos, C.D.; Dráber, P. Tubulins as therapeutic targets in cancer: From bench to bedside. *Curr. Pharm. Des.* **2012**, *18*, 2778–2792. [CrossRef]

17. Steinmetz, M.O.; Prota, A.E. Microtubule-targeting agents: Strategies to hijack the cytoskeleton. *Trends Cell Biol.* **2018**, *28*, 776–792. [CrossRef]

18. Dumontet, C.; Jordan, M.A. Microtubule-binding agents: A dynamic field of cancer therapeutics. *Nat. Rev. Drug Discov.* **2010**, *9*, 790–803. [CrossRef]

19. Stanton, R.A.; Gernert, K.M.; Nettles, J.H.; Aneja, R. Drugs that target dynamic microtubules: A new molecular perspective. *Med. Res. Rev.* **2011**, *31*, 443–481. [CrossRef]

20. Arnst, K.E.; Banerjee, S.; Chen, H.; Deng, S.; Hwang, D.J.; Li, W.; Miller, D.D. Current advances of tubulin inhibitors as dual acting small molecules for cancer therapy. *Med. Res. Rev.* **2019**, *39*, 1398–1426. [CrossRef]

21. Florian, S.; Mitchison, T.J. Anti-microtubule drugs. *Methods Mol. Biol.* **2016**, *1413*, 403–421.

22. Vindya, N.G.; Sharma, N.; Yadav, M.; Ethiraj, K.R. Tubulins-the target for anticancer therapy. *Curr. Top. Med. Chem.* **2015**, *15*, 73–82. [CrossRef]

23. van Vuuren, R.J.; Visagie, M.H.; Theron, A.E.; Joubert, A.M. Antimitotic drugs in the treatment of cancer. *Cancer Chemother. Pharmacol.* **2015**, *76*, 1101–1112. [CrossRef] [PubMed]

24. Bukhari, S.N.A.; Kumar, G.B.; Revankar, H.M.; Qin, H.-L. Development of combretastatins as potent tubulin polymerization inhibitors. *Bioorg. Chem.* **2017**, *72*, 130–147. [CrossRef] [PubMed]

25. Li, W.; Sun, H.; Xu, S.; Zhu, Z.; Xu, J. Tubulin inhibitors targeting the colchicine binding site: A perspective of privileged structures. *Future Med. Chem.* **2017**, *9*, 1765–1794. [CrossRef] [PubMed]

26. Lu, Y.; Chen, J.J.; Xiao, M.; Li, W.; Miller, D.D. An overview of tubulin inhibitors that interact with the colchicine binding site. *Pharm. Res.* **2012**, *29*, 2943–2971. [CrossRef]

27. Kaur, R.; Kaur, G.; Gill, R.K.; Soni, R.; Bariwal, J. Recent developments in tubulin polymerization inhibitors: An overview. *Eur. J. Med. Chem.* **2014**, *87*, 89–124. [CrossRef]

28. Pettit, G.R.; Cragg, G.M.; Singh, S.B. Antineoplastic agents, 122. Constituents of Combretum caffrum. *J. Nat. Prod.* **1987**, *50*, 386–391. [CrossRef]

29. Lin, C.M.; Ho, H.H.; Pettit, G.R.; Hamel, E. Antimitotic natural products combretastatin A-4 and combretastatin A-2: Studies on the mechanism of their inhibition of the binding of colchicine to tubulin. *Biochemistry* **1989**, *28*, 6984–6991. [CrossRef]

30. Griggs, J.; Metcalfe, J.C.; Hesketh, R. Targeting tumour vasculature: The development of combretastatin A4. *Lancet Oncol.* **2001**, *2*, 82–87. [CrossRef]

31. Nagaiah, G.; Remick, S.C. Combretastatin A4 phosphate: A novel vascular disrupting agent. *Future Oncol.* **2010**, *6*, 1219–1228. [CrossRef]

32. Tewari, K.S.; Sill, M.W.; Coleman, R.L.; Aghajanian, C.; Mannel, R.; DiSilvestro, P.A.; Powell, M.; Randall, L.M.; Farley, J.; Rubin, S.C.; et al. Bevacizumab plus fosbretabulin in recurrent ovarian cancer: Overall survival and exploratory analyses of a randomized phase II NRG oncology/gynecologic oncology group study. *Gynecol. Oncol.* **2020**, *159*, 79–87. [CrossRef] [PubMed]

33. Chauhan, A.; Arnold, S.; Slone, S.A.; Flynn, H.; Weiss, H.; Anthony, L.B. A phase I/II study of fosbretabulin in combination with everolimus in neuroendocrine tumors that have progressed after at least one prior regimen for metastatic disease. *J. Clin. Oncol.* **2018**, *36*, TPS4148. [CrossRef]

34. Patil, P.O.; Patil, A.G.; Rane, R.A.; Patil, P.C.; Deshmukh, P.K.; Bari, S.B.; Patil, D.A.; Naphade, S.S. Recent advancement in discovery and development of natural product combretastatin-inspired anticancer agents. *Anticancer Agents Med. Chem.* **2015**, *15*, 955–969. [CrossRef] [PubMed]

35. Greene, L.M.; Meegan, M.J.; Zisterer, D.M. Combretastatins: More than just vascular targeting agents? *J. Pharmacol. Exp. Ther.* **2015**, *355*, 212–227. [CrossRef]

36. Mikstacka, R.; Stefański, T.; Różański, J. Tubulin-interactive stilbene derivatives as anticancer agents. *Cell Mol. Biol. Lett.* **2013**, *18*, 368–397. [CrossRef]

37. Niu, L.; Yang, J.; Yan, W.; Yu, Y.; Zheng, Y.; Ye, H.; Chen, X.Q.; Chen, L. Reversible binding of the anticancer drug KXO1(tirbanibulin) to the colchicine-binding site of tubulin explains KXO1's low clinical toxicity. *J. Biol. Chem.* **2019**, *294*, 18099–18108. [CrossRef]

38. Amirall. Almirall Announces FDA Approval of Klisyri®(Tirbanibulin), A New Innovative Topical Treatment for Actinic Keratosis. Available online: https://www.almirall.com/newsroom/news/almirall-announces-fda-approval-of-klisyri%C2%AE-tirbanibulin-a-new-innovative-topical-treatment-for-actinic-keratosis (accessed on 10 December 2020).

39. Mosca, L.; Ilari, A.; Fazi, F.; Assaraf, Y.G.; Colotti, G. Taxanes in cancer treatment: Activity, chemoresistance and its overcoming. *Drug Resist. Updates* **2021**, *54*, 100742. [CrossRef]

40. Martino, E.; Casamassima, G.; Castiglione, S.; Cellupica, E.; Pantalone, S.; Papagni, F.; Rui, M.; Siciliano, A.M.; Collina, S. Vinca alkaloids and analogues as anti-cancer agents: Looking back, peering ahead. *Bioorg. Med. Chem. Lett.* **2018**, *28*, 2816–2826. [CrossRef]

41. Kavallaris, M.; Tait, A.S.; Walsh, B.J.; He, L.F.; Horwitz, S.B.; Norris, M.D.; Haber, M. Multiple microtubule alterations are associated with Vinca alkaloid resistance in human leukemia cells. *Cancer Res.* **2001**, *61*, 5803–5809.

42. Verrills, N.M.; Kavallaris, M. Improving the targeting of tubulin-binding agents: Lessons from drug resistance studies. *Curr. Pharm. Des.* **2005**, *11*, 1719–1733. [CrossRef]

43. Fojo, A.T.; Menefee, M. Microtubule targeting agents: Basic mechanisms of multidrug resistance (MDR). *Semin. Oncol.* **2005**, *32*, S3–S8. [CrossRef] [PubMed]

44. Maloney, S.M.; Hoover, C.A.; Morejon-Lasso, L.V.; Prosperi, J.R. Mechanisms of taxane resistance. *Cancers* **2020**, *12*, 3323. [CrossRef] [PubMed]

45. Kavallaris, M. Microtubules and resistance to tubulin-binding agents. *Nat. Rev. Cancer* **2010**, *10*, 194–204. [CrossRef] [PubMed]

46. Stengel, C.; Newman, S.P.; Leese, M.P.; Potter, B.V.; Reed, M.J.; Purohit, A. Class III beta-tubulin expression and in vitro resistance to microtubule targeting agents. *Br. J. Cancer* **2010**, *102*, 316–324. [CrossRef]

47. Sève, P.; Dumontet, C. Is class III β-tubulin a predictive factor in patients receiving tubulin-binding agents? *Lancet Oncol.* **2008**, *9*, 168–175. [CrossRef]

48. Haider, K.; Rahaman, S.; Yar, M.S.; Kamal, A. Tubulin inhibitors as novel anticancer agents: An overview on patents (2013–2018). *Expert Opin. Ther. Pat.* **2019**, *29*, 623–641. [CrossRef]

49. Bates, D.; Eastman, A. Microtubule destabilising agents: Far more than just antimitotic anticancer drugs. *Br. J. Clin. Pharmacol.* **2017**, *83*, 255–268. [CrossRef]

50. McLoughlin, E.C.; O'Boyle, N.M. Colchicine-binding site inhibitors from chemistry to clinic: A review. *Pharmaceuticals* **2020**, *13*, 8. [CrossRef]

51. Wang, Z.; Chen, J.; Wang, J.; Ahn, S.; Li, C.M.; Lu, Y.; Loveless, V.S.; Dalton, J.T.; Miller, D.D.; Li, W. Novel tubulin polymerization inhibitors overcome multidrug resistance and reduce melanoma lung metastasis. *Pharm. Res.* **2012**, *29*, 3040–3052. [CrossRef]

52. Nainwal, L.M.; Alam, M.M.; Shaquiquzzaman, M.; Marella, A.; Kamal, A. Combretastatin-based compounds with therapeutic characteristics: A patent review. *Expert Opin. Ther. Pat.* **2019**, *29*, 703–731. [CrossRef]

53. Romagnoli, R.; Baraldi, P.G.; Kimatrai Salvador, M.; Prencipe, F.; Bertolasi, V.; Cancellieri, M.; Brancale, A.; Hamel, E.; Castagliuolo, I.; Consolaro, F.; et al. Synthesis, antimitotic and antivascular activity of 1-(3′,4′,5′-trimethoxybenzoyl)-3-arylamino-5-amino-1,2,4-triazoles. *J. Med. Chem.* **2014**, *57*, 6795–6808. [CrossRef] [PubMed]

54. Sun, H.; Tawa, G.; Wallqvist, A. Classification of scaffold-hopping approaches. *Drug Discov. Today* **2012**, *17*, 310–324. [CrossRef] [PubMed]

55. Lazzara, P.R.; Moore, T.W. Scaffold-hopping as a strategy to address metabolic liabilities of aromatic compounds. *RSC Med. Chem.* **2020**, *11*, 18–29. [CrossRef]

56. Li, C.M.; Lu, Y.; Narayanan, R.; Miller, D.D.; Dalton, J.T. Drug metabolism and pharmacokinetics of 4-substituted methoxybenzoyl-aryl-thiazoles. *Drug Metab. Dispos.* **2010**, *38*, 2032–2039. [CrossRef]

57. Lu, Y.; Chen, J.; Wang, J.; Li, C.M.; Ahn, S.; Barrett, C.M.; Dalton, J.T.; Li, W.; Miller, D.D. Design, synthesis, and biological evaluation of stable colchicine binding site tubulin inhibitors as potential anticancer agents. *J. Med. Chem.* **2014**, *57*, 7355–7366. [CrossRef]

58. Hwang, D.-J.; Wang, J.; Li, W.; Miller, D.D. Structural optimization of indole derivatives acting at colchicine binding site as potential anticancer agents. *ACS Med. Chem. Lett.* **2015**, *6*, 993–997. [CrossRef] [PubMed]

59. Ren, Y.; Wang, Y.; Li, G.; Zhang, Z.; Ma, L.; Cheng, B.; Chen, J. Discovery of novel benzimidazole and indazole analogues as tubulin polymerization inhibitors with potent anticancer activities. *J. Med. Chem.* **2021**, *64*, 4498–4515. [CrossRef]

60. Chen, H.; Deng, S.; Albadari, N.; Yun, M.-K.; Zhang, S.; Li, Y.; Ma, D.; Parke, D.N.; Yang, L.; Seagroves, T.N.; et al. Design, synthesis, and biological evaluation of stable colchicine-binding site tubulin inhibitors 6-aryl-2-benzoyl-pyridines as potential anticancer agents. *J. Med. Chem.* **2021**, *64*, 12049–12074. [CrossRef] [PubMed]

61. Zhang, N.; Ayral-Kaloustian, S.; Nguyen, T.; Afragola, J.; Hernandez, R.; Lucas, J.; Gibbons, J.; Beyer, C. Synthesis and SAR of [1,2,4]triazolo[1,5-*a*]pyrimidines, a class of anticancer agents with a unique mechanism of tubulin inhibition. *J. Med. Chem.* **2007**, *50*, 319–327. [CrossRef]

62. Yang, F.; Yu, L.Z.; Diao, P.C.; Jian, X.E.; Zhou, M.F.; Jiang, C.S.; You, W.W.; Ma, V.; Zhao, P.L. Novel[1,2,4]triazolo[1,5-*a*]pyrimidine derivatives as potent antitubulin agents: Design, multicomponent synthesis and antiproliferative activities. *Bioorg. Chem.* **2019**, *92*, 103260. [CrossRef]

63. Huo, X.-S.; Jian, X.-E.; Ou-Yang, J.; Chen, L.; Yang, F.; Lv, D.-X.; You, W.-W.; Rao, J.-J.; Zhao, P.-L. Discovery of highly potent tubulin polymerization inhibitors: Design, synthesis, and structure-activity relationships of novel 2,7-diaryl-[1,2,4]triazolo[1,5-*a*]pyrimidines. *Eur. J. Med. Chem.* **2021**, *220*, 113449. [CrossRef] [PubMed]

64. Mohamed, H.S.; Amin, N.H.; El-Saadi, M.T.; Abdel-Rahman, H.M. Design, synthesis, biological assessment, and in-silico studies of 1,2,4-triazolo[1,5-*a*]pyrimidine derivatives as tubulin polymerization inhibitors. *Bioorg. Chem.* **2022**, *121*, 105687. [CrossRef] [PubMed]

65. Oliva, P.; Romagnoli, R.; Cacciari, B.; Manfredini, S.; Padroni, C.; Brancale, A.; Ferla, S.; Hamel, E.; Corallo, D.; Aveic, S.; et al. Synthesis and biological evaluation of highly active 7-anilino triazolopyrimidines as potent antimicrotubule agents. *Pharmaceutics* **2022**, *14*, 1191. [CrossRef] [PubMed]

66. Kamal, A.; Dastagiri, D.; Ramaiah, M.J.; Reddy, J.S.; Bharathi, E.V.; Reddy, M.K.; Sagar, M.V.P.; Reddy, T.L.; Pushpavalli, S.N.C.V.L.; Pal-Bhadra, M. Synthesis and apoptosis inducing ability of new anilino substituted pyrimidine sulfonamides as potential anticancer agents. *Eur. J. Med. Chem.* **2011**, *46*, 5817–5824. [CrossRef] [PubMed]

67. Donzelli, M.; Draetta, G.F. Regulating mammalian checkpoints through cdc25 inactivation. *EMBO Rep.* **2003**, *4*, 671–677. [CrossRef]

68. Liu, K.; Zheng, M.; Lu, R.; Du, J.; Zhao, Q.; Li, Z.; Li, Y.; Zhang, S. The role of CDC25C in cell cycle regulation and clinical cancer therapy: A systematic review. *Cancer Cell Int.* **2020**, *20*, 213. [CrossRef]

69. Mollinedo, F.; Gajate, C. Microtubules, microtubule-interfering agents and apoptosis. *Apoptosis* **2003**, *8*, 413–450. [CrossRef]

70. Rovini, A.; Savry, A.; Braguer, D.; Carré, M. Microtubule-targeted agents: When mitochondria become essential to chemotherapy. *Biochim. Biophys. Acta-Bioenerg.* **2011**, *1807*, 679–688. [CrossRef]

71. Romagnoli, R.; Baraldi, P.G.; Lopez Cara, C.; Hamel, E.; Basso, G.; Bortolozzi, R.; Viola, G. Synthesis and biological evaluation of 2-(3′,4′,5′-trimethoxybenzoyl)-3-aryl/arylaminobenzo[*b*]thiophene derivatives as a novel class of antiproliferative agents. *Eur. J. Med. Chem.* **2010**, *45*, 5781–5791. [CrossRef]

72. Romagnoli, R.; Baraldi, P.G.; Kimatrai Salvador, M.; Preti, D.; Tabrizi, M.A.; Brancale, A.; Fu, X.-H.; Li, J.; Zhang, S.-Z.; Hamel, E.; et al. Discovery and optimization of a series of 2-aryl-4-amino-5-(3′,4′,5′-trimethoxybenzoyl)thiazoles as novel anticancer agents. *J. Med. Chem.* **2012**, *55*, 5433–5445. [CrossRef]

73. Romagnoli, R.; Baraldi, P.G.; Lopez-Cara, C.; Preti, D.; Aghazadeh Tabrizi, M.; Balzarini, J.; Bassetto, M.; Brancale, A.; Fu, X.-H.; Gao, Y.; et al. Concise synthesis and biological evaluation of 2-aroyl-5-amino benzo[*b*]thiophene derivatives as a novel class of potent antimitotic agents. *J. Med. Chem.* **2013**, *56*, 9296–9309. [CrossRef] [PubMed]

74. Romagnoli, R.; Baraldi, P.G.; Lopez-Cara, C.; Kimatrai Salvador, M.; Preti, D.; Aghazadeh Tabrizi, M.; Balzarini, J.; Nussbaumer, P.; Brancale, A.; Fu, X.-H.; et al. Design, synthesis and biological evaluation of 3,5-disubstituted 2-amino thiophene derivatives as a novel class of antitumor agents. *Bioorg. Med. Chem.* **2014**, *22*, 5097–5109. [CrossRef] [PubMed]

75. Singh, R.; Letai, A.; Sarosiek, K. Regulation of apoptosis in health and disease: The balancing act of BCL-2 family proteins. *Nat. Rev. Mol. Cell Biol.* **2019**, *20*, 175–193. [CrossRef] [PubMed]

76. Eichhorn, J.M.; Sakurikar, N.; Alford, S.E.; Chu, R.; Chambers, T.C. Critical role of anti-apoptotic Bcl-2 protein phosphorylation in mitotic death. *Cell Death Dis.* **2013**, *4*, e834. [CrossRef] [PubMed]

77. Whitaker, R.H.; Placzek, W.J. Regulating the BCL2 family to improve sensitivity to microtubule targeting agents. *Cells* **2019**, *8*, 346. [CrossRef] [PubMed]

78. Oliva, P.; Onnis, V.; Balboni, E.; Hamel, E.; Estévez-Sarmiento, F.; Quintana, J.; Estévez, F.; Brancale, A.; Ferla, S.; Manfredini, S.; et al. Synthesis and biological evaluation of 2-substituted benzyl/phenylethylamino-4-amino-5-aroyl thiazoles as apoptosis inducing anticancer agents. *Molecules* **2020**, *25*, 2177. [CrossRef]

79. Hamel, E.; Lin, C.M. Separation of active tubulin and microtubule-associated proteins by ultracentrifugation and isolation of a component causing the formation of microtubule bundles. *Biochemistry* **1984**, *23*, 4173–4184. [CrossRef]

80. Hamel, E. Evaluation of antimitotic agents by quantitative comparisons of their effects on the polymerization of purified tubulin. *Cell Biochem. Biophys.* **2003**, *38*, 1–21. [CrossRef]

81. Verdier-Pinard, P.; Lai, J.-Y.; Yoo, H.-D.; Yu, J.; Marquez, B.; Nagle, D.G.; Nambu, M.; White, J.D.; Falck, J.R.; Gerwick, W.H.; et al. Structure-activity analysis of the interaction of curacin A, the potent colchicine site antimitotic agent, with tubulin and effects of analogs on the growth of MCF-7 breast cancer cells. *Mol. Pharmacol.* **1998**, *53*, 62–67. [CrossRef]

82. Molecular Operating Environment (MOE), 2022.02. Chemical Computing Group ULC: Montreal, QC, Canada. Available online: http://www.chemcomp.com (accessed on 1 July 2022).

83. *Schrödinger Release 2022-2*; Maestro, Schrödinger, LLC: New York, NY, USA, 2022.

84. Lawson, N.D.; Weinstein, B.M. In vivo imaging of embryonic vascular development using transgenic zebrafish. *Dev. Biol.* **2002**, *248*, 307–318. [CrossRef]

Article

In Vitro Cytotoxicity Evaluation of Plastoquinone Analogues against Colorectal and Breast Cancers along with *In Silico* Insights

Halilibrahim Ciftci [1,2,3], Belgin Sever [2,4], Nilüfer Bayrak [5], Mahmut Yıldız [6], Hatice Yıldırım [7], Hiroshi Tateishi [2], Masami Otsuka [1,2], Mikako Fujita [2,*] and Amaç Fatih TuYuN [5,*]

[1] Department of Drug Discovery, Science Farm Ltd., Kumamoto 862-0976, Japan
[2] Medicinal and Biological Chemistry Science Farm Joint Research Laboratory, Faculty of Life Sciences, Kumamoto University, Kumamoto 862-0973, Japan
[3] Department of Molecular Biology and Genetics, Koc University, 34450 Istanbul, Turkey
[4] Department of Pharmaceutical Chemistry, Faculty of Pharmacy, Anadolu University, 26470 Eskisehir, Turkey
[5] Department of Chemistry, Faculty of Science, Istanbul University, Fatih, 34126 Istanbul, Turkey
[6] Chemistry Department, Gebze Technical University, Gebze, 41400 Kocaeli, Turkey
[7] Department of Chemistry, Faculty of Engineering, Istanbul University-Cerrahpasa, Avcılar, 34320 Istanbul, Turkey
*   Correspondence: mfujita@kumamoto-u.ac.jp (M.F.); aftuyun@istanbul.edu.tr (A.F.T.); Tel.: +81-96-371-4622 (M.F.); +90-212-4400000 (A.F.T.)

Abstract: Colorectal cancer (CRC) and breast cancer are leading causes of death globally, due to significant challenges in detection and management. The late-stage diagnosis and treatment failures require the discovery of potential anticancer agents to achieve a satisfactory therapeutic effect. We have previously reported a series of plastoquinone analogues to understand their cytotoxic profile. Among these derivatives, three of them (**AQ-11**, **AQ-12**, and **AQ-15**) were selected by the National Cancer Institute (NCI) to evaluate their *in vitro* antiproliferative activity against a panel of 60 human tumor cell lines. **AQ-12** exhibited significant antiproliferative activity against HCT-116 CRC and MCF-7 breast cancer cells at a single dose and further five doses. MTT assay was also performed for **AQ-12** at different concentrations against these two cells, implying that **AQ-12** exerted notable cytotoxicity toward HCT-116 (IC_{50} = 5.11 ± 2.14 μM) and MCF-7 (IC_{50} = 6.06 ± 3.09 μM) cells in comparison with cisplatin (IC_{50} = 23.68 ± 6.81 μM and 19.67 ± 5.94 μM, respectively). This compound also augmented apoptosis in HCT-116 (62.30%) and MCF-7 (64.60%) cells comparable to cisplatin (67.30% and 78.80%, respectively). Molecular docking studies showed that **AQ-12** bound to DNA, forming hydrogen bonding through the quinone scaffold. *In silico* pharmacokinetic determinants indicated that **AQ-12** demonstrated drug-likeness with a remarkable pharmacokinetic profile for future mechanistic anti-CRC and anti-breast cancer activity studies.

Keywords: colorectal cancer; breast cancer; plastoquinone; NCI-60; growth inhibition; cytotoxicity; apoptosis; DNA binding; pharmacokinetic determinants

1. Introduction

Colorectal cancer (CRC), the third most common cancer type and the fourth leading cause of cancer-related death, comprises nearly 10% of all annually diagnosed tumors across the world [1–4]. Male gender, old age, dietary habits, and environmental factors affect the pathogenesis of CRC as well as the genetic background [5]. In spite of advancements in CRC screening and treatment options such as surgery, radiotherapy, local ablative therapy, chemotherapy, targeted therapy, and immunotherapy, most of cases in particular diagnosed at an advanced stage with metastases, result in subsequent cancer-related deaths. The size, stage, and metastasis of tumor whether the therapy will be curative or palliative. Among CRC treatment options, chemotherapy incorporates single-agent therapy (primarily

fluoropyrimidine, oxaliplatin, irinotecan, and capecitabine) or combined regimens of these agents. Targeted therapy is another approach, which has been reported to extend survival of patients with CRC. However, the resistance and toxicity problems restrict the success of the therapy. Therefore, there is an urgency to find more effective and safer drugs [2,6].

The history of breast cancer was shown to be a risk factor for CRC in several studies, implying low or high relative risks. These risks were considered due to the common etiologic factors associated with the development of both cancers and administration of antihormone drugs in breast cancer treatment, which alter sex hormone levels and contribute to the development of CRC [7–11]. New efficacious therapeutic options have been also developed for the battle with breast cancer related to its clinical stage, histopathologic properties, and biomarker profiling. These options include traditional, personalized, neoadjuvant, and targeted therapies. The treatment still remains limited mainly in the breast cancer metastasis owing to heterogeneity of the disease, acquired and primary resistance, and toxicity problems during the treatment. New agents should be also developed to overcome or prevent these problems in breast cancer treatment [12–14].

Much effort to design and discover efficient and safe drug candidates led to identifying several hit compounds and analogues of natural products. *In silico* analyses were exploited to improve molecules with greater potential efficacy to cope with the adverse toxicological outcomes by emphasizing physicochemical parameters [15]. In addition, the study of the structure–activity relationship (SAR) has provided valuable information on the design of safe drug candidates with continuity about how structural changes can improve potency and bioavailability [16].

1,4-Quinones have been explored as attractive anticancer hit molecules to their multitargeted mode of actions [17–22]. In this field, a small library of amino-quinones based on bioactive natural products (fifty Plastoquinone (PQ) [23–25] and thirty-four LY83583 analogues [26,27]) that specifically target leukemia cancer cell lines, in the period 2017–2021, was generated for the purpose of discovering the SAR of various substituents in amino-quinones for their further mechanistic anticancer potential. Knowing that the PQ analogues are active toward some cancer cell lines, and considering our previous findings that demonstrated greater activity by the introduction of a chlorine atom in the quinone moiety, we also designed and evaluated the effect on inhibitory activity against some cancer cell lines caused by replacing the chlorine with a bromine atom in PQ analogues [28]. Regarding all PQ analogues, including halogenated (brominated and chlorinated) and non-halogenated analogues, a major breakthrough was the discovery of **AQ-11, AQ-12**, and **AQ-15** [25], as illustrated in Figure 1. These analogues showed consistent growth-inhibitory activities with low IC_{50} value against K562 human chronic myelogenous leukemia (CML) cell line and low toxicity toward human peripheral blood mononuclear cells (PBMCs) (healthy) (Table 1) [25].

Table 1. The cytotoxic effects of **AQ-11**, **AQ-12**, and **AQ-15** on K562 cells and PBMCs in comparison with imatinib [25].

Compound	Substitution Groups	Cell Type (IC_{50}, μM)		
	R	K562 [a]	PBMC [a]	SI [c]
AQ-11	H	0.75 ± 0.05	5.14 ± 1.76	6.85
AQ-12	*m*-CF$_3$	0.88 ± 0.06	3.00 ± 1.22	3.41
AQ-15	*p*-CH$_3$	0.76 ± 0.04	7.64 ± 1.58	10.05
	Imatinib [b]	5.58 ± 1.83	33.92 ± 4.19	6.08

[a] Cell lines include K562 leukemia cells and peripheral blood mononuclear cells (PBMC). [b] Used as a reference. [c] selectivity index (SI) = IC_{50} for PBMCs/IC_{50} for K562 cells.
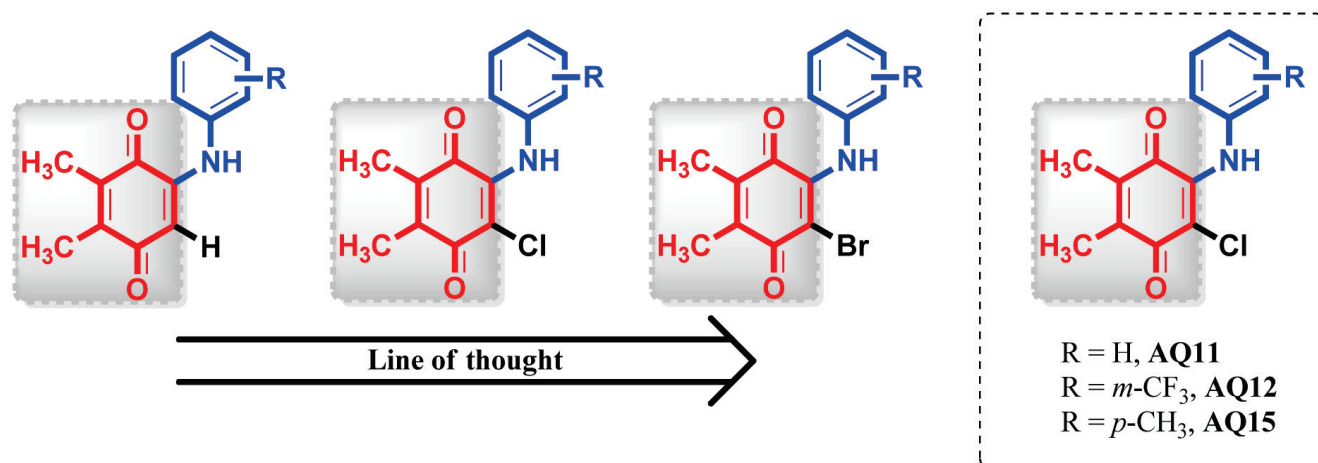
Figure 1. Line of thought. Structures of target molecules (**AQ-11**, **AQ-12**, and **AQ-15**).

Considering the encouraging results of the target PQ analogues, further studies were assessed aiming at the identification of new analogues for their antiproliferative activity against HCT-116 human CRC and MCF-7 human breast cancer cell lines. In addition, apoptosis-inducing activity in both cell lines, DNA binding characteristics, and a number of pharmacokinetic descriptors of the most effective anticancer analogue were examined.

2. Results

2.1. Anticancer Activity Assessment

2.1.1. *In Vitro* Screening of Tumor Cell Growth Inhibition at One Dose

Continuing our efforts on anticancer drug discovery, most effective PQ analogues from our previous study [25] were submitted to the National Cancer Institute (NCI) of Bethesda within the Developmental Therapeutics Program (DTP) for their *in vitro* anticancer activity with the protocol of the Drug Evaluation Branch, NCI. A single dose (10 μM) of all tested PQ analogues was used in the panel of 60 human cancer cell lines, including nine tumor subpanels, namely: leukemia, lung, CRC, central nervous system (CNS), melanoma, ovarian, renal, prostate, and breast cancer cell lines [29–31]. The *in vitro* growth inhibition and lethality were ascertained as percentages as follows: growth inhibition (G%) (values between 0 and 100) and lethality (values less than 0). Herein, three PQ analogues (**AQ-11**, NCI: D-827199/1; **AQ-12**, NCI: D-827200/1; and **AQ-15**, NCI: D-827201/1) were selected by the NCI for *in vitro* disease-oriented human-cell-screening panel assay.

The results of each tested PQ analogue were reported in terms of percent growth inhibition (GI% = 100 − G%) and lethality [32] (Table 2) and were also depicted as bars in the single-dose mean graphs (Supplementary Materials, Figures S1–S3). Overall, consistent with the previous data, PQ analogues showed the most notable anticancer activity against leukemia cancer cell lines. **AQ-11** and **AQ-15** were found ineffective against the other cancer cell lines except for significant anticancer effects of **AQ-11** on MDA-MB-231 breast cancer cell line with 84.65% inhibition percent. On the other hand, NCI-60 data suggested that **AQ-12** revealed prominent anticancer activity toward the subpanel cell line of CRC (HCT-116 cells, 66.14% inhibition; SW-620 cells, 82.93% inhibition) and breast cancer (MCF-7 cells, 64.64% inhibition; MDA-MB-231 cells, 81.04% inhibition). Additionally, this analogue also showed promising anticancer effects against NCI-H522 lung cancer cells.

Table 2. Anticancer activity results as per single-dose assay at 10 μM concentration as percent cell growth of **AQ-11, AQ-12**, and **AQ-15** after 48 h, based on Sulforhodamine B (SRB) assay at NCI.

Panel/Cancer Cell Line	Compound		
	AQ-11	**AQ-12**	**AQ-15**
	Growth Percentage of Cell Lines in NCI 60		
Leukemia			
CCRF-CEM	5.28	5.90	47.98
HL-60(TB)	45.64	38.46	73.23
K-562	15.93	3.78	54.03
MOLT-4	12.72	23.53	66.29
RPMI-8226	53.63	−3.12	87.67
SR	62.86	24.97	79.88
Non-Small Cell Lung Cancer			
A549/ATCC	99.81	96.78	101.90
EKVX	55.24	49.44	93.61
HOP-62	92.60	90.98	89.82
HOP-92	46.02	48.86	95.70
NCI-H226	96.94	90.87	101.59
NCI-H23	ND	ND	ND
NCI-H322M	99.29	100.88	104.93
NCI-H460	95.74	94.85	100.91
NCI-H522	83.46	17.73	93.90
CRC			
COLO 205	107.07	101.80	111.35
HCC-2998	ND	ND	ND
HCT-116	79.11	33.86	95.79
HCT-15	94.19	65.71	101.63
HT29	99.13	103.04	104.47
KM12	78.34	67.20	100.25
SW-620	96.49	17.07	102.49
CNS Cancer			
SF-268	95.39	94.34	95.65
SF-295	102.14	96.20	107.03
SF-539	95.42	93.40	97.15
SNB-19	88.79	92.41	96.00
SNB-75	65.44	66.47	65.44
U251	84.30	78.99	99.94
Melanoma			
LOX IMVI	ND	ND	ND
MALME-3M	107.98	94.35	102.03
M14	95.87	85.23	102.50
MDA-MB-435	102.30	98.46	107.59
SK-MEL-2	85.48	85.77	95.31
SK-MEL-28	106.11	98.26	104.07
SK-MEL-5	ND	ND	ND
UACC-257	90.27	78.53	106.17
UACC-62	90.28	80.22	96.80
Ovarian Cancer			
IGROV1	9.69	−7.20	80.83
OVCAR-3	101.79	70.40	105.64
OVCAR-4	−97.92	−80.41	99.38
OVCAR-5	103.60	100.01	100.88
OVCAR-8	94.89	87.14	104.55
NCI/ADR-RES	ND	ND	ND
SK-OV-3	ND	ND	ND
Renal Cancer			
786-0	99.18	101.74	104.29
A498	91.24	55.17	72.19
ACHN	100.46	−37.69	96.49
CAKI-1	96.08	92.74	91.53
RXF 393	96.80	97.82	108.41
SN12C	91.13	87.62	96.37
TK-10	128.28	183.73	142.33
UO-31	98.81	77.33	92.50
Prostate Cancer			
PC-3	73.87	64.35	86.95
DU-145	101.26	99.72	107.98
Breast Cancer			
MCF7	90.72	35.36	96.29
MDA-MB-231/ATCC	15.35	18.96	94.55
HS 578T	100.91	87.57	90.46
BT-549	113.97	120.60	119.94
T-47D	−38.88	−38.96	84.68
MDA-MB-468	−76.01	−65.55	52.82

2.1.2. *In Vitro* Full-Panel Five-Dose 60-Cell Lines Assay

From the single-dose assay data from the NCI screen, **AQ-12** was selected as a lead PQ analogue because of its pronounced anticancer selectivity compared with other PQ analogues. **AQ-12** exhibited the threshold inhibition criterion in the single-dose screening and was qualified for the evaluation in the full-panel five-dose *in vitro* anticancer screening at 10-fold dilutions in the range 0.01–100 μM. Three response parameters (50% cell growth inhibition (GI_{50}) (growth inhibitory activity), total cell growth inhibition (TGI) (cytostatic activity), and 50% cell death (LC_{50}) (cytotoxic activity)) [33] were used to establish biological potential of the tested **AQ-12**. The GI_{50} is an indicative concentration at 50% growth inhibitory activity, whereas TGI reflects total growth inhibition, and LC_{50} is an indicative concentration at which 50% of cancer cells are killed. In this assay, three parameters were calculated for each cell line from log concentration versus percent growth inhibition curves on nine panels of human cancer cell lines to generate dose response curves [31,34]. GI_{50} is the concentration of the test drug where $100 \times (T - T0)/(C - T0) = 50$. Herein, T explains the optical density of the test well after a 48 h period of treatment with the test drug; T0 explains the optical density at time zero; ultimately, C is the control (nondrug) optical density. The "50" is called the GI50PRCNT, a T/C-like parameter that can have values from +100 to −100. The TGI is the concentration of test drug where $100 \times (T - T0)/(C - T0) = 0$. LC_{50} is the concentration of the drug where $100 \times (T - T0)/T0 = -50$ [31].

The GI_{50}, TGI, and LC_{50} (in μM) values against subpanel cell lines are illustrated in Table 3, indicating that **AQ-12** displays high anticancer activity against all leukemia cell lines with GI_{50} values ranging from 1.32 to 2.59 μM. This compound also demonstrated superior cytotoxic activity against HL-60(TB) and RPMI-8226 cell lines with TGI values 6.54 and 7.32 μM, respectively. On the other hand, LC_{50} values were more than 100 μM against the entire panel of cancer cell lines. Moderate cytotoxicity was recorded against non-small cell lung cancer cells, except for EKVX cell line with a GI_{50} value of 1.49 μM, HOP-92 cell line with a GI_{50} value of 1.51 μM, and NCI-H522 cell line with a GI_{50} value of 2.24 μM. Moreover, good TGI values ranging from 3.04 to 32.20 μM were obtained against lung cancer cell lines. Additionally, **AQ-12** showed high activity with GI_{50} values ranging from 1.93 to 2.20 μM against some CRC cell lines (HCT-116 cells GI_{50} = 1.93 μM; HCT-15 cells GI_{50} = 2.20 μM; SW-620 cells GI_{50} = 2.09 μM). It also possessed notable TGI values against these three CRC cell lines in the range of 3.99–5.05 μM. Moderate cytotoxicity was recorded against CNS cancer with GI_{50} values ranging from 4.45 μM to 6.55 μM against most of the tested cancer cell lines. Moreover, important TGI values ranging from 13.60 to 28.60 μM were detected against CNS cell lines. **AQ-12** demonstrated pronounced cytotoxicity with GI_{50} values ranging from 3.36 to 9.96 μM, except for three cell lines (LOX IMVI, MALME-3M, and UACC-257 cells). Concerning the TGI values of **AQ-12**, the most prominent TGI value was observed with the LOX IMVI melanoma cell line (TGI = 3.32 μM). Furthermore, this analogue demonstrated notable anticancer activity against the entire panel of ovarian cancer cell lines with GI_{50} values ranging from 1.30 to 3.16 μM, as shown in (Table 3). Its TGI values ranged from 2.97 to 50.70 μM against all tested cancer cell lines. Finally, its LC_{50} values were found as 7.15, 5.58, and 8.61 μM against IGROV1, OVCAR-4, and OVCAR-5 cell lines; whereas, with regard to the lethality (LC_{50} values), **AQ-12** showed values exceeding 100 μM toward the other panel cancer cell lines. This analogue exhibited remarkable anticancer activity against the renal, prostate, and breast cancer cell lines with GI_{50} values ranging from 1.17 to 2.67 μM. Accepted pronounced TGI values were recorded against ACHN renal (TGI = 3.19 μM), RXF 393 renal (TGI = 2.85 μM), UO-31 renal (TGI = 4.18 μM), MCF-7 breast (TGI = 3.79 μM), MDA-MB-231 breast (TGI = 3.28 μM), T-47D breast (TGI = 3.60 μM), and MDA-MB-468 breast (TGI = 2.94 μM) cancer cell lines, together with PC-3 prostate (TGI = 12.80 μM) cancer cell line. All the five-dose response curves of **AQ-12** against the full panel of 60 human cancer cell lines are presented in Figure 2 and Table 3, which include nine tumor subpanels, namely: leukemia, melanoma, CRC, lung, CNS, ovarian, renal, prostate, and breast cancer cell lines.

Table 3. GI_{50}, TGI, and LC_{50} values (in μM) of anticancer activity data, as per five doses (0.01, 0.1, 1, 10, and 100 μM) of **AQ-12** after 48 h based on SRB assay at NCI.

| Panel/Cell Line	GI_{50}	TGI	LC_{50}
Leukemia			
CCRF-CEM	1.93	>100	>100
HL-60(TB)	2.34	6.54	>100
K-562	2.40	>100	>100
MOLT-4	2.22	>100	>100
RPMI-8226	1.32	7.32	>100
SR	2.59		>100
Non-Small Cell Lung Cancer			
A549/ATCC	13.30	>100	>100
EKVX	1.49	3.73	9.31
HOP-62	11.50	27.60	66.50
HOP-92	1.51	3.04	6.14
NCI-H226	10.80	34.90	>100
NCI-H23	6.87	24.00	65.40
NCI-H322M	22.70	>100	>100
NCI-H460	11.60	32.20	89.30
NCI-H522	2.24	5.66	>100
CRC			
COLO 205	13.00	29.30	66.00
HCC-2998	5.88	18.40	46.00
HCT-116	1.93	3.99	8.22
HCT-15	2.20	5.05	16.20
HT29	7.29	51.80	>100
KM12	3.58	25.70	>100
SW-620	2.09	4.73	>100
CNS Cancer			
SF-268	4.99	28.60	>100
SF-295	6.55	24.00	74.10
SF-539	2.40	6.61	24.80
SNB-19	5.83	23.40	77.40
SNB-75	1.16	13.60	91.00
U251	4.45	17.90	58.20
Melanoma			
LOX IMVI	1.69	3.32	6.51
MALME-3M	1.98	6.04	30.90
M14	9.96	32.70	>100
MDA-MB-435	5.98	19.50	49.20
SK-MEL-2	8.26	21.70	50.90
SK-MEL-28	3.36	10.80	36.00
SK-MEL-5	4.14	15.70	43.80
UACC-257	2.61	6.72	26.90
UACC-62	3.46	16.10	56.00
Ovarian Cancer			
IGROV1	1.42	3.19	7.15
OVCAR-3	2.31	5.58	>100
OVCAR-4	1.58	2.97	5.58
OVCAR-5	1.98	4.13	8.61
OVCAR-8	2.68	6.89	>100
NCI/ADR-RES	3.16	42.30	>100
SK-OV-3	1.30	50.70	>100
Renal Cancer			
786-0	10.60	24.30	55.70
A498	13.70	45.20	>100
ACHN	1.73	3.19	5.87
CAKI-1	1.94	9.11	32.40
RXF 393	1.49	2.85	5.44
SN12C	2.25	23.40	>100
TK-10	19.00	37.00	71.90
UO-31	1.46	4.18	14.20
Prostate Cancer			
PC-3	2.67	12.80	>100
DU-145	15.60	34.80	77.70
Breast Cancer			
MCF7	1.71	3.79	8.39
MDA-MB-231/ATCC	1.59	3.28	6.77
HS 578T	6.00	64.40	>100
BT-549	8.56	22.20	51.70
T-47D	1.17	3.60	>100
MDA-MB-468	1.24	2.94	7.00
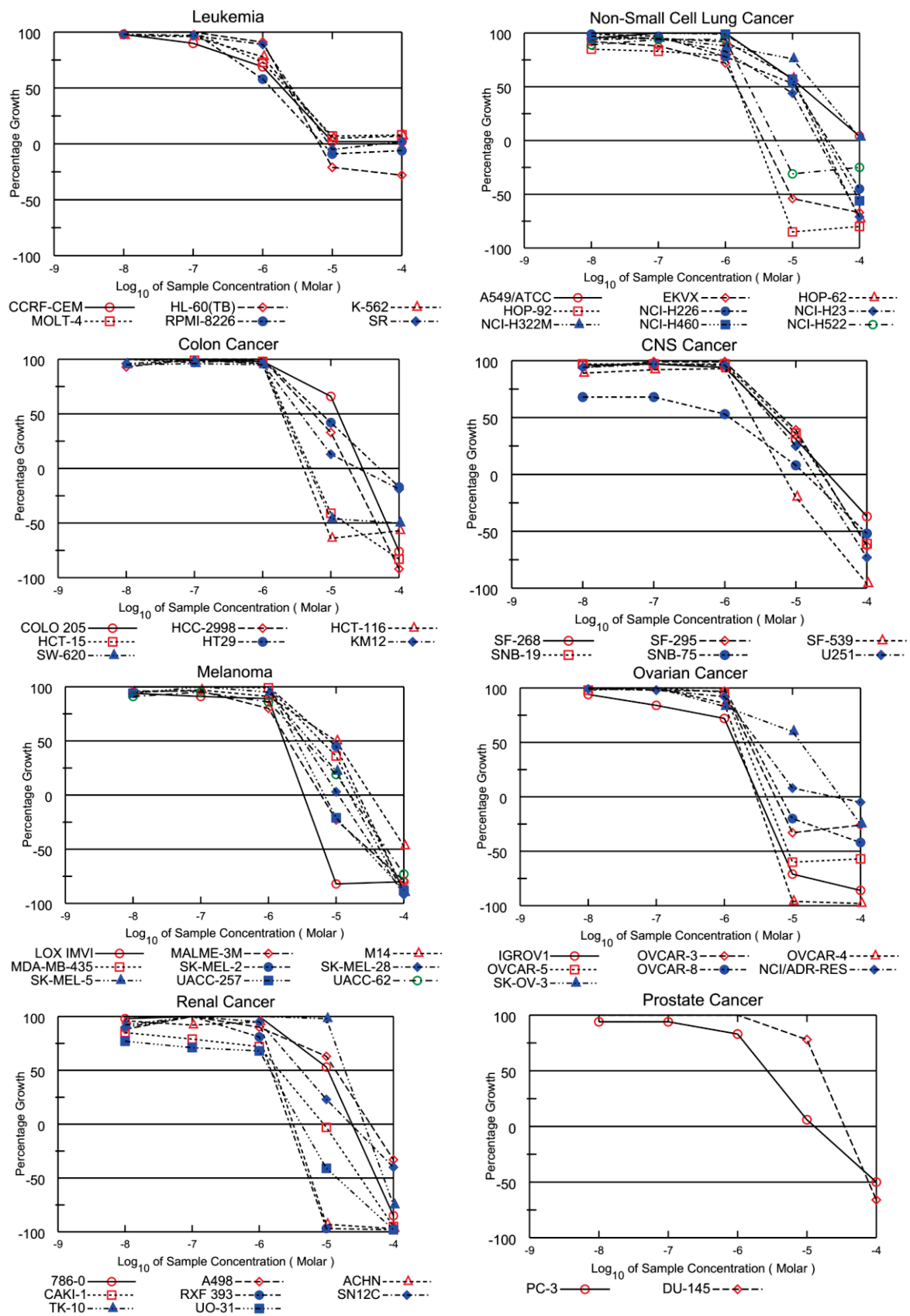
Figure 2. *Cont.*
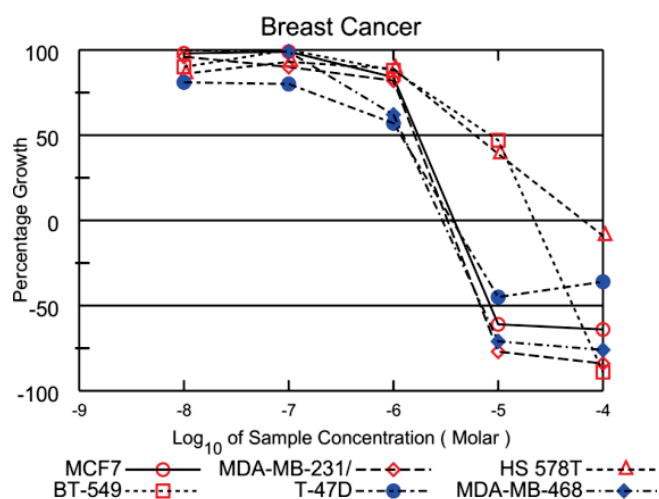
Figure 2. Graphical presentation of growth inhibition of the PQ analogue **AQ-12** at five dose concentrations (0.01, 0.1, 1, 10, and 100 μM) after 48 h based on SRB assay at NCI.

2.1.3. Cell Viability Assay on CRC and Breast Cancer Cells

AQ-12 was found to possess a superior sensitivity profile toward HCT-116 CRC and MCF-7 breast cancer cell lines with a higher growth inhibitory percent compared to **AQ-11** and **AQ-15**. **AQ-12** also displayed sensitivity toward MDA-MB-468 breast and NCI-H522 lung cancer cell lines. However, **AQ-11** also presented significant growth inhibitory effects on MDA-MB-468 breast cancer cells, restricting the selectivity of **AQ-12** against this cell line, and GI_{50}, TGI, and LC_{50} parameters were found very high against NCI-H522 lung cancer cells. Satisfactory results obtained from both single and five doses of NCI-60 screening toward HCT-116 CRC and MCF-7 breast cancer cells encouraged us to further investigate the anticancer effects of **AQ-12** against these two cell lines by MTT (3-(4,5-dimethyl-2-thiazolyl)-2,5-diphenyltetrazolium bromide) assay at five dose concentrations (1, 3, 10, 30, and 100 μM) in comparison with cisplatin, the reference agent.

Cisplatin, a metallic coordination compound leading to DNA damage and subsequently apoptosis induction in cancer cells, is one of the most important chemotherapeutic agents, which has been approved for the treatment of different fatal cancer types, including CRC and breast cancer [35–41].

Results indicated that **AQ-12** showed cytotoxic effects on HCT-116 and MCF-7 cells with IC_{50} values of 5.11 ± 2.14 μM and 6.06 ± 3.09 μM when compared with cisplatin (IC_{50} = 23.68 ± 6.81 μM for HCT-116 cells and 19.67 ± 5.94 μM for MCF-7 cells). The definite decline in percentage of viable cells was detected between 3 and 10 μM after **AQ-12** exposure while a similar decline was observed between 10 and 30 μM after cisplatin implementation (Figure 3, Table 4).

Table 4. The cytotoxic effects of **AQ-12** on MCF-7 and HCT-116 cells based on MTT assay at five dose concentrations (1, 3, 10, 30, and 100 μM).

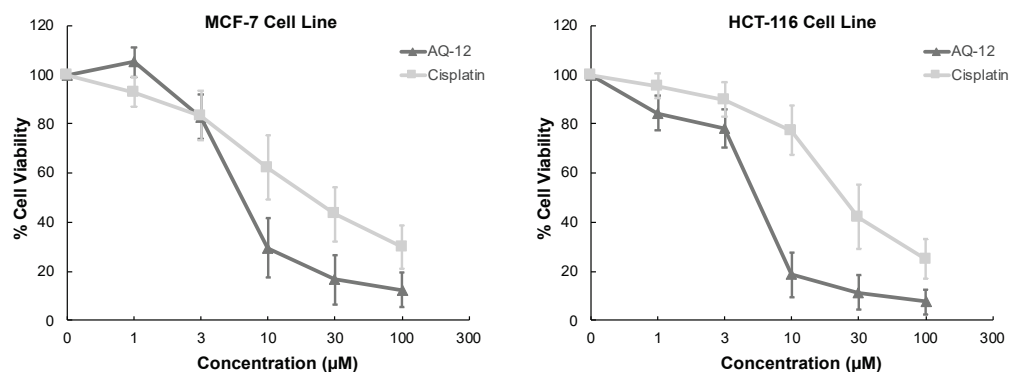| Compound	IC_{50} Value (μM)	
	MCF-7 Cells	**HCT-116 Cells**
AQ-12	6.06 ± 3.09	5.11 ± 2.14
Cisplatin	19.67 ± 5.94	23.68 ± 6.81

Figure 3. The cytotoxic effects of **AQ-12** and cisplatin at varying concentrations (1, 3, 10, 30, and 100 μM) on MCF-7 and HCT-116 cells based on MTT assay. All descriptive data are expressed as the mean ± standard deviation (SD). All experiments were repeated three times.

2.1.4. Cell Death Investigation

Based on significant anticancer activity results of **AQ-12** on HCT-116 and MCF-7 cells, we also further investigated potential effects of this compound on apoptosis in both cell lines using the annexin V/ethidium homodimer III staining procedure, which was observed by fluorescence microscopy, indicating apoptosis, necrosis or late apoptosis, and necrosis with green, yellow, and red staining, respectively (Figure 4A). **AQ-12** induced apoptotic behavior of HCT-116 cells (62.30%) in a similar manner with cisplatin (67.30%). This compound exhibited 21.30% late apoptotic/necrotic and 16.40% necrotic effects in HCT-116 cells compared to cisplatin (12.30% and 20.40%, respectively) (Figure 4B). The difference of apoptosis induction between **AQ-12** and cisplatin treatment in HCT-116 cells was found not significant, contrary to that of MCF-7 cells, which was found significant (Figure 4C). **AQ-12** enhanced apoptosis in MCF-7 cells significantly with 64.60% when compared with cisplatin (78.80%). **AQ-12**-treated MCF-7 cells underwent late apoptosis/necrosis and necrosis with 25.30% and 10.10%, respectively when compared with cisplatin (16.40% and 4.80%, respectively) (Figure 4B,C).
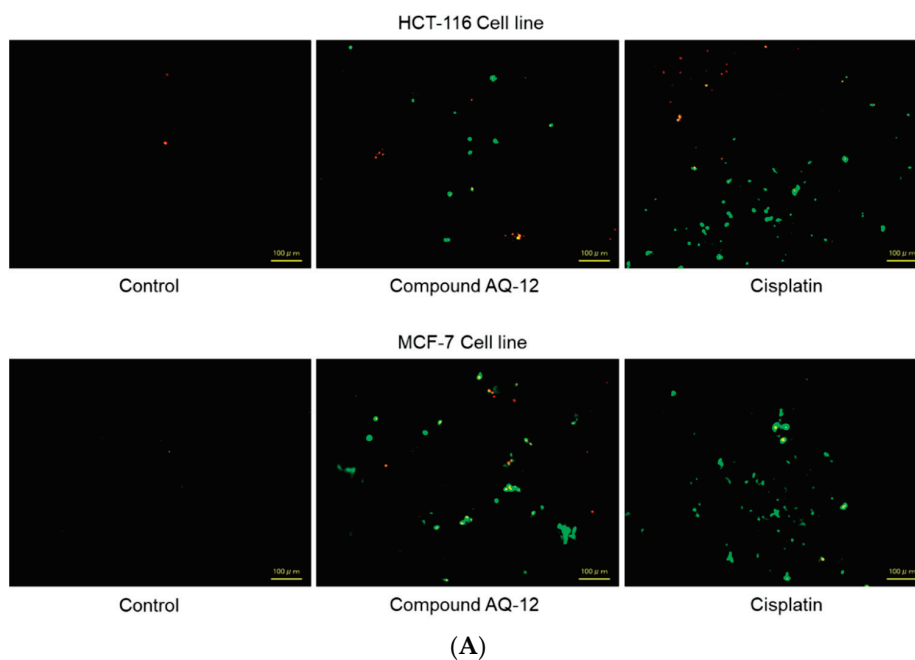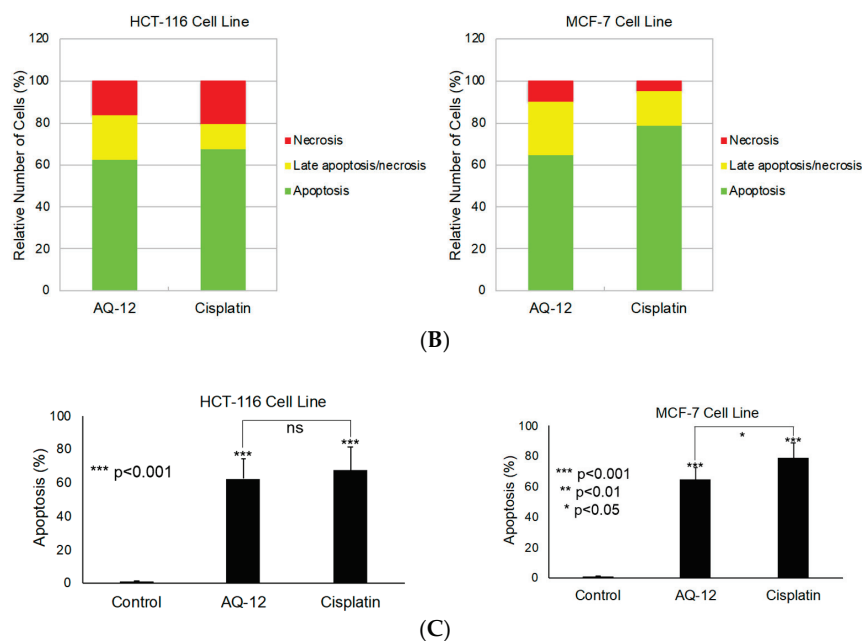

(A)

Figure 4. *Cont.*

Figure 4. (**A**) Alteration of HCT-116 and MCF-7 cells after treatment with IC_{50} concentration of the control (DMSO), **AQ-12,** and cisplatin (**B**) for 12 h. The percentage of apoptosis, late apoptosis/necrosis, and necrosis (green, yellow, and red, respectively) cells (**C**) was determined by analyzing 100 randomly selected stained cells in each experiment (ns: not statistically significant). Data from three independent experiments were expressed as means ± standard deviation and *p* values were determined using Student's test.

2.2. In Silico Studies

2.2.1. Molecular Docking

In our previous studies, we manifested that PQ analogues were able to bind DNA significantly [26,27,42]. In this study, the DNA binding effects of **AQ-11**, **AQ-12**, and **AQ-15** were also searched with molecular docking studies in the minor groove of the double helix of DNA (PDB ID: 2GWA) [43] via Maestro software [44]. Results corresponded to previous DNA cleavage outcomes, implying that **AQ-15** showed the most promising DNA binding potential through a key π-π interaction between DG-4 with its 4-methyl substituent. However, **AQ-11** and **AQ-12** displayed less binding capacity compared to **AQ-15,** forming hydrogen bonding with DT-5 and DG-4, respectively (Figure 5A,B). The docking scores were determined as −4.641 kcal/mol, −5.087 kcal/mol, and −5.097 kcal/mol for **AQ-11**, **AQ-12**, and **AQ-15,** indicating higher binding capacity of **AQ-15** compared to **AQ-11** and **AQ-12**.
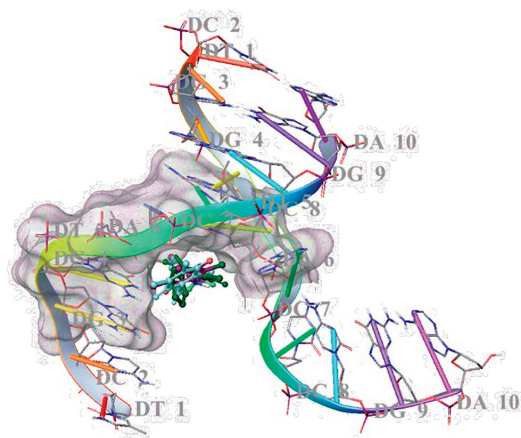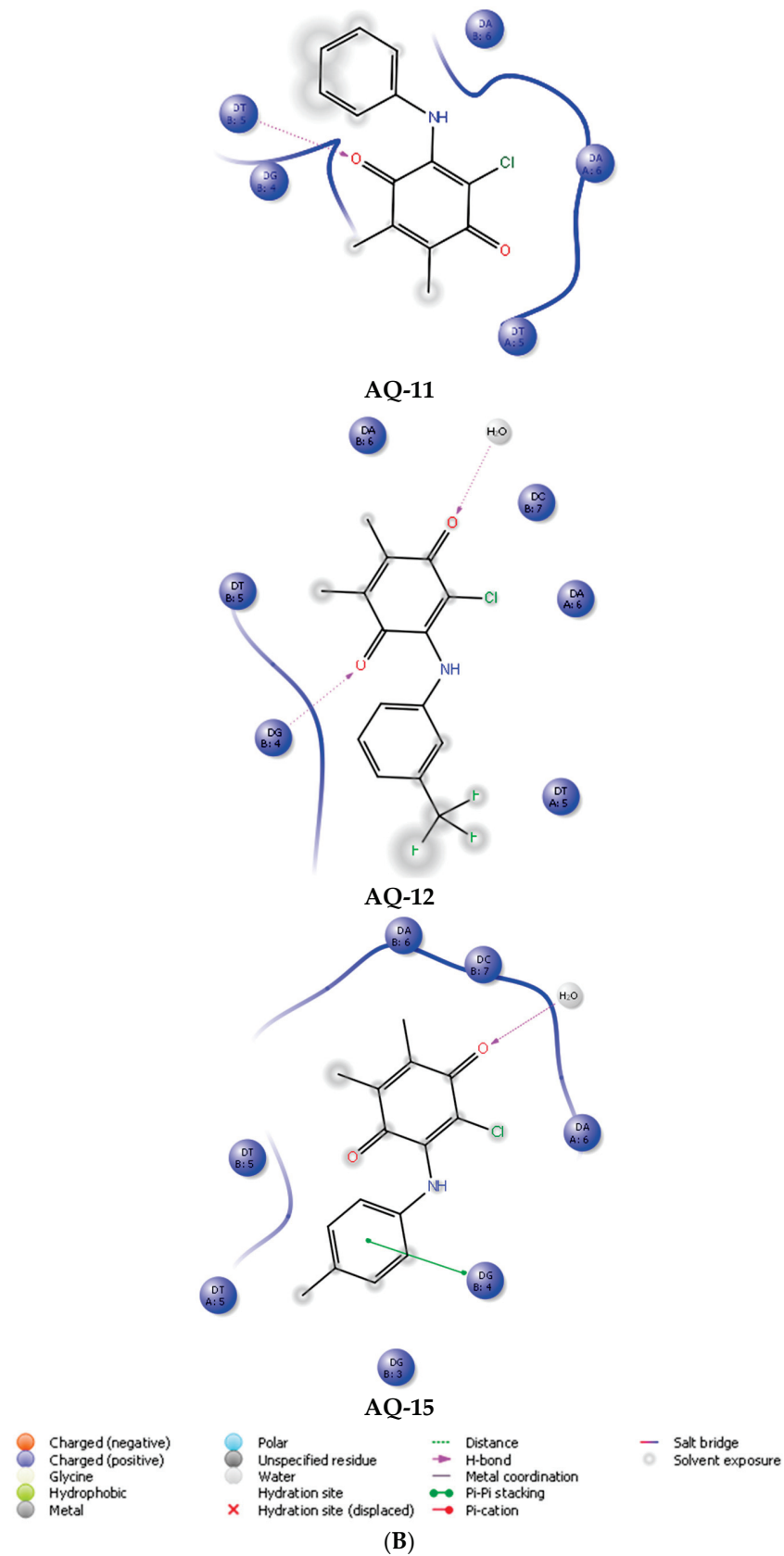

(**A**)

Figure 5. *Cont.*

Figure 5. Docking poses (**A**) and docking interactions (**B**) of **AQ-11**, **AQ-12**, and **AQ-15** in the minor groove of the DNA double helix (**AQ-11**, **AQ-12**, and **AQ-15** are shown in dark green, maroon, and turquoise, respectively) (PDB ID: 2GWA).

2.2.2. Estimation of Pharmacokinetic Parameters

AQ-12 was profiled *in silico* for various pharmacokinetic properties of interest such as octanol/water partition coefficient (QPlogPo/w), aqueous solubility (QPlogS), human serum albumin binding (QPlogKhsa), brain/blood partition coefficient (QPlogBB), and compliance to Lipinski's rule of five and Jorgensen's rule of three using the QikProp algorithm [45]. We also checked the *in silico* inhibitory potential of **AQ-12** on several cytochrome P450 (CYP) enzymes such as CYP1A2, CYP2C19, CYP2C9, CYP2D6, and CYP3A4, along with the evaluation of bioavailability and passive gastrointestinal absorption and brain penetration using the SwissADME web service [46,47].

AQ-12 represented a remarkable pharmacokinetic profile in which all the descriptors were found in appropriate ranges: QPlogPo/w, QPlogS, QPlogKhsa, and QPlogBB were computed with the values of 3.513, -5.035, 0.197, and 0.140, respectively, within the limits (-2 to 6.5, -6.5 to 0.5, -1.5 to 1.5, and -3 to 1.2, respectively). Additionally, **AQ-12** revealed robust human oral absorption (100%) and was found to possess of all the conditions of drug-likeness characters without any violation of Lipinski's rule of five and Jorgensen's rule of three.

The pink region of bioavailability radar (Figure 6) identifies the values of saturation (INSATU), size (SIZE), polarity (POLAR), solubility (INSOLU), lipophilicity (LIPO), and flexibility (FLEX) for oral bioavailability. **AQ-12** was found only beyond the saturation value for other values it was participating in, as shown in the pink area. **AQ-12** matched with CYP1A2, CYP2C19, CYP2C9, and CYP3A4 inhibition, apart from CYP2D6 inhibition, indicating that **AQ-12** could cause possible drug–drug or drug–food interactions. The boiled-egg model (Figure 7) explains whether a molecule has properties for the passive gastrointestinal absorption and blood–brain barrier (BBB) permeation. According to the results, **AQ-12** was predicted as brain-penetrant (in the yellow area) and not a substrate for P-glycoprotein (red dot), which decreased the possibility of its resistance by tumor cell lines through efflux [47–50].
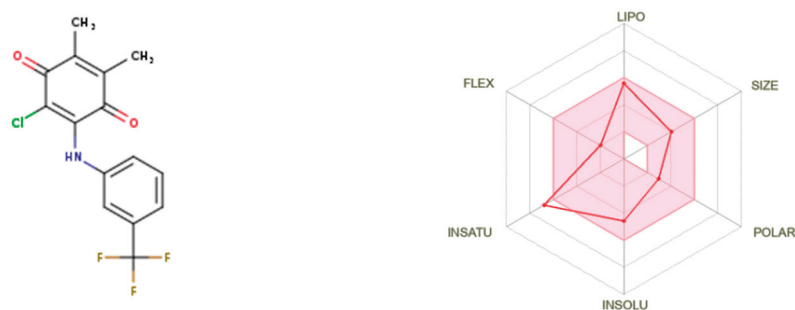

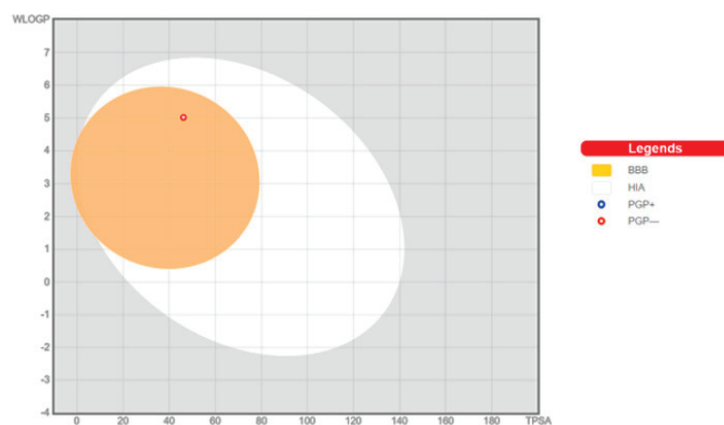**Figure 6.** Bioavailability radar for **AQ-12** from the SwissADME web tool.

Figure 7. Boiled-egg graph of **AQ-12** from the SwissADME web tool.

3. Discussion

Worldwide, CRC and breast cancer are prevalent and deadly cancers. The complete cure for both cancers is still far from success, albeit to increase overall survival rate obtained with new therapeutic options. Therefore, the discovery of new and better therapeutics is still needed [51,52]. In spite of numerous efforts in the search for more effective anticancer agents, quinone moiety still remains one of the most versatile members against cancer cell lines in drug discovery [53,54].

In our previous studies, we also reported the significant outcomes of quinone derivatives against CRC or breast cancer cell lines. We showed that compound **PQ11**, PQ analogue with *N*-phenylpiperazine (Figure 8), exhibited the most potent anticancer activity against MCF-7, MDA-MB-231, and UACC-2087 cell lines, with the IC_{50} values of 6.58, 16.66, and 38.52 μM [28]. In our recently published studies, we also confirmed anti-CRC and anti-breast cancer effects of PQ analogues. In the first study [42], the most significant cytotoxic effects were observed with **PQ2**, amino-1,4-benzoquinone (Figure 8), against HCT-116 CRC cells with an IC_{50} value of 4.97 ± 1.93 μM. In the latter one [55], compound **ClPQ1**, quinone-benzocaine hybrid molecule, (Figure 8) was found as the most effective anti-breast cancer agent against T47D and MCF-7 breast cancer cells, with IC_{50} values of 2.35 ± 0.30 and 6.53 ± 0.71 μM, respectively.

PQ11

MCF-7 cells (IC_{50}= 6.58 μM)
MDA-MB-231 cells (IC_{50}= 16.66 μM)
UACC-2087 cells (IC_{50}= 38.52 μM)

PQ2

HCT-116 cells (IC_{50}= 4.97±1.93 μM)
Apoptosis: 66%

ClPQ1

T47D cells (IC_{50}= 2.35 μM±0.30 μM)
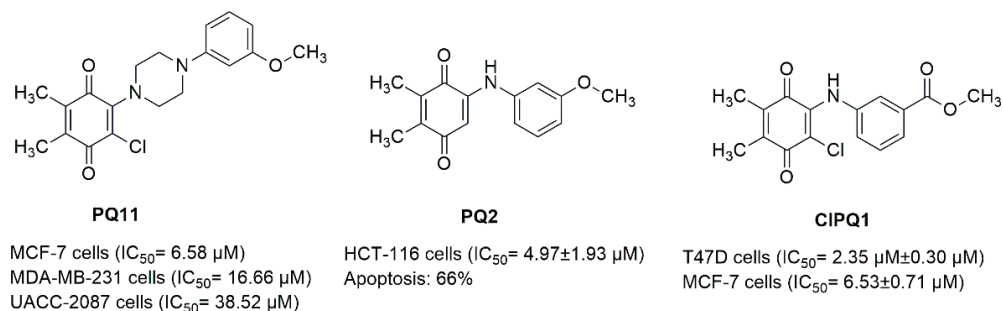MCF-7 cells (IC_{50}= 6.53±0.71 μM)

Figure 8. PQ analogues that were previously determined by our research group as potential anticancer agents against CRC and breast cancer.

In the current work, PQ analogues (**AQ-11**, **AQ-12**, and **AQ-15**) were selected by the NCI *in vitro* disease-oriented antitumor screening to be evaluated for their anticancer effects. Testing of the PQ analogues against the NCI-60 cell line panel revealed valuable information on their inhibitory activity across a broad variety of human cancer cell lines. In particular, **AQ-12** displayed potential growth inhibitory activity against HCT-116 and MCF-7 cell lines at a single dose and a super-sensitivity profile with low micromolar GI_{50}, TGI, and LC_{50} values against both cell lines at five doses. These findings indicated that meta trifluoromethyl substitution of **AQ-12** played an important role in its significant anti-CRC and anti-breast cancer activity when compared with the para methyl substitution of **AQ-15** and non-substitution of **AQ-11**. Moreover, **AQ-12** exerted similar cytotoxic effects against both cell lines in comparison with our aforementioned studies [28,42,55]. Current results once more confirmed that the presence of PQ moiety played an important role in anti-CRC and anti-breast cancer activity.

Genetically encoded programmed cell death (apoptosis) leads to elimination of cancer cells, and DNA degradation is one of the crucial indicators of apoptosis. Aberrant apoptotic activity can increase not only the pathogenesis of CRC and breast cancer, but also their resistance to current therapy options [56–59]. Regarding the anticancer efficacy of **AQ-12** in CRC and breast cancer cells, it was ascertained that **AQ-12** led to apoptosis in both cells with similar apoptotic pattern with **PQ2** (Figure 8) [42].

Molecular docking studies were carried out for **AQ-12** in order to discover its binding efficacy in the minor groove of the double helix of DNA (PDB ID: 2GWA). We previously showed that PQ analogues occupied this region with key interactions [26,27,42]. The 3,5-dimethyl phenyl [26] and benzodioxole [27] moieties were determined to be crucial in

binding with DNA, forming π-π stacking interactions with DA-17 and DG-16, and DA-5 and DG-4, respectively. In other our previous study [27], the methoxy substitution was also found to be important for high interaction between **PQ2** and DT-5 in the minor groove of DNA. In the current study, **AQ-12** was found less capable of binding DNA compared to **AQ-15**, albeit to hydrogen bonding with DG-4 through quinone moiety. The trifluoromethyl substitution of **AQ-12** played no significant role in binding with DNA. **AQ-15** bound to DG-4 through its *p*-methyl moiety, forming π-π stacking interactions. The docking score with the lowest energy (high negative scores) was found to pertain to **AQ-15,** followed by **AQ-12** and **AQ-11,** indicating their binding affinities. Compare to our previous studies, it can be concluded that CH_3 substitution ($-\sigma$ effect), OCH_3 substitution ($-\sigma$ effect), and ($-CH_2-O-CH_2-$) ($-\sigma$ effect) [26,27,42] were found to increase the binding capacity of the tested compounds, whereas CF_3 substitution ($+\sigma$ effect) was not detected to contribute to binding capacity of **AQ-12**. The higher docking score and the binding capacity of *p*-methyl-substituted **AQ-15** also complied with the previous data. This finding also suggested that the high apoptotic effect of **AQ-12** might be independent from DNA cleavage-associated cell death.

Absorption, distribution, metabolism, and excretion (ADME) parameters of a drug molecule have an enormous impact for successful drug discovery. Some of these essential parameters were predicted *in silico* for **AQ-12**. Lipophilicity is crucial for absorption, which is the process of movement of a drug into the systemic circulation crossing the lipid bilayers of cell membranes. On the other hand, optimum water solubility is also necessary since the active ingredient must be dissolved in aqueous compartments to some extent before drug absorption. The human serum albumin binding is directly associated with the volume of distribution and half-life of drugs. The transition of drugs from blood into brain is particularly important for brain metastases of other cancer types. According to the results of the QikProp module, **AQ-12** was endowed with drug-like properties. The outcomes of SwissADME web server signified that **AQ-12** was predicted not orally bioavailable. This was due to the out-of-limits for saturation, as shown in the bioavailability chart, in which a molecule must be entirely included in the pink area. **AQ-12** exerted inhibition against all tested CYP enzymes, except for CYP2D6, which had a higher risk for drug–drug interactions [60–63].

4. Materials and Methods

4.1. Chemistry

The synthesis and spectral analysis of **AQ-11**, **AQ-12**, and **AQ-15** were performed previously [25].

4.2. Anticancer Activity Studies

4.2.1. *In Vitro* Single-Dose Anticancer Screening by NCI

The PQ analogues were submitted to NCI, Bethesda, USA, and screened based on the procedures of NCI; all compounds were investigated for their cancer cell growth inhibitory activity at 10 μM concentration against a wide range of cancer cell lines stemming from leukemia, melanoma, CRC, non-small cell lung, CNS, ovarian, renal, prostate, and breast cancers. Tested compounds were added to the microtiter culture plates followed by incubation for 48 h at 37 °C. SRB was used for end point detection. The percent of growth of the treated cells was observed compared to the untreated control cells. Data from one-dose experiments corresponded to the percentage growth at 10 μM [29–31,34,64].

4.2.2. *In Vitro* Five-Dose Anticancer Screening by NCI

Initial DMSO stock solution was carried out for serial 5 × 10-fold dilution before incubation at each individual concentration. **AQ-12** was selected for a higher testing level by DTP-NCI to identify GI_{50}, TGI, and LC_{50} for each cell line after generating a dose response curve from 5 different concentrations (0.01, 0.1, 1, 10, and 100 μM). The definite protocol for the latter assay was explained in detail previously. The cells were assayed

by using the SRB method. The optical densities were measured by a plate reader and a microcomputer processed the optical densities into the special concentration parameters, as defined above [29,34,64,65].

4.2.3. Cell Culture, Drug Treatment, and MTT Assay

The HCT-116 cell line (provided by the RIKEN BRC through the National Bio-Resource Project of the MEXT/AMED, Japan (RCB2979)) and MCF-7 cell line (Precision Bioservices, Frederick, MD, USA) were incubated in Dulbecco's modified Eagle's medium (DMEM) (Wako Pure Chemical Industries, Osaka, Japan) and RPMI 1640 (Wako Pure Chemical Industries, Osaka, Japan), respectively. Ten percent fetal bovine serum (FBS) (Sigma Aldrich, St. Louis, MO, USA) and 89 µg/mL streptomycin (Meiji Seika Pharma, Tokyo, Japan) were added to total media (Wako Pure Chemical Industries) at 37 °C and 5% CO_2 atmosphere. HCT-116 and MCF-7 cells were cultured for 48 h in a 24-well plate (Iwaki brand Asahi Glass Co., Chiba, Japan) at 4×10^4 cells/mL concentration [42]. The stock solution of **AQ-12** and cisplatin in concentrations were prepared in DMSO (Wako Pure Chemical Industries, Osaka, Japan) (0.1 to 10 mM), and fresh culture medium was used for further dilution. The final DMSO concentration was set at 1% to prevent any effect of it on cell viability. MTT (Dojindo Molecular Technologies, Kumamoto, Japan) was used to examine the cytotoxic effects of **AQ-12** and cisplatin, as previously indicated [66]. HCT-116 and MCF-7 cells were treated with **AQ-12** and cisplatin at five dose concentrations (1, 3, 10, 30, and 100 µM) at 37 °C for 48 h, and then treated with MTT solution and incubated for 4 h. Eventually, 100 µL DMSO was added to each well following removal of supernatants. Infinite M1000 (Tecan, Mannedorf, Switzerland) was used for the analysis of the absorbance of the solution. All experiments were repeated three times, and IC_{50} values were calculated as the drug concentrations that diminished absorbance to 50% of control values.

4.2.4. Cell Death Analysis

The HCT-116 and MCF-7 cell lines were incubated with **AQ-12** and cisplatin at IC_{50} concentration for 12 h before the apoptotic/necrotic/detection kit (PromoKine, Heidelberg, Germany) was applied, with some alterations to the manufacturer's guidance [42]. HCT-116 and MCF-7 cells, treated with appropriate content including binding buffer and staining solution, were analyzed by an all-in-one fluorescence microscope, Biorevo Fluorescence BZ-9000 (Keyence, Osaka, Japan). Numbers of apoptotic, late apoptotic/necrotic, and necrotic cells were determined based on the staining with annexin V and ethidium homodimer III, as previously explained [66].

4.2.5. Statistical Analyses

All results were reported as means $\pm$ SD. One-way analysis of variance was used for the analysis of data. Differences were defined as significant at * $p < 0.05$, ** $p < 0.01$, and *** $p < 0.001$. GraphPad Prism7 (GraphPad Software, San Diego, CA, USA) was used for the determination of the IC_{50} values.

4.3. In Silico Studies
4.3.1. Molecular Docking

AQ-11, AQ-12, and **AQ-15** were prepared with energy minimization by applying the OPLS_2005 force field at physiological pH using the LigPrep module. The crystallographic structure of DNA was downloaded from the PDB server (PDB ID: 2GWA) [43,44] and prepared for the docking assessment by the PrepWizard module of Maestro. Then, the determined grid by Grid Generation was used for molecular docking with Glide/XP docking procedures [26,27,42].

4.3.2. ADME Prediction

The pharmacokinetic determinants of **AQ-12** were estimated by QikProp [45] and SwissADME web tool [46,47].

5. Conclusions

Our previous encouraging anticancer activity results obtained from PQ analogues guided us to analyze **AQ-11**, **AQ-12**, and **AQ-15** for further effects toward a wide spectrum of cancer cells by NCI-60 *in vitro* screening. **AQ-12** presented a promising growth inhibition in HCT-116 and MCF-7 cells at a single dose and submicromolar level anticancer activity at five doses. It was established that these two cell lines were found susceptible for further anticancer activity studies. The MTT assay outcomes also corresponded to notable anti-CRC and anti-breast cancer activity of **AQ-12** at different concentrations compared to cisplatin. This compound also enhanced apoptosis in both cell lines. Taken together, **AQ-12** could serve as a valuable lead molecule for CRC and breast cancer treatment with orally bioavailable favorable drug-like features.

References

1. Davies, R.J.; Miller, R.; Coleman, N. Colorectal cancer screening: Prospects for molecular stool analysis. *Nat. Rev. Cancer* **2005**, *5*, 199–209. [CrossRef] [PubMed]
2. Dekker, E.; Tanis, P.J.; Vleugels, J.L.A.; Kasi, P.M.; Wallace, M.B. Colorectal cancer. *Lancet* **2019**, *394*, 1467–1480. [CrossRef]
3. Dalal, N.; Jalandra, R.; Sharma, M.; Prakash, H.; Makharia, G.K.; Solanki, P.R.; Singh, R.; Kumar, A. Omics technologies for improved diagnosis and treatment of colorectal cancer: Technical advancement and major perspectives. *Biomed. Pharmacother.* **2020**, *131*, 110648. [CrossRef] [PubMed]
4. La Vecchia, S.; Sebastián, C. Metabolic pathways regulating colorectal cancer initiation and progression. *Semin. Cell Dev. Biol.* **2020**, *98*, 63–70. [CrossRef]
5. Jin, K.; Ren, C.; Liu, Y.; Lan, H.; Wang, Z. An update on colorectal cancer microenvironment, epigenetic and immunotherapy. *Int. Immunopharmacol.* **2020**, *89 (Pt A)*, 107041. [CrossRef]
6. Xie, Y.H.; Chen, Y.X.; Fang, J.Y. Comprehensive review of targeted therapy for colorectal cancer. *Signal Transduct. Target. Ther.* **2020**, *5*, 22. [CrossRef] [PubMed]
7. Howell, M.A. The association between colorectal cancer and breast cancer. *J. Chronic Dis.* **1976**, *29*, 243–261. [CrossRef]

8. Newschaffer, C.J.; Topham, A.; Herzberg, T.; Weiner, S.; Weinberg, D.S. Risk of colorectal cancer after breast cancer. *Lancet* **2001**, *357*, 837–840. [CrossRef]

9. Kmet, L.M.; Cook, L.S.; Weiss, N.S.; Schwartz, S.M.; White, E. Risk factors for colorectal cancer following breast cancer. *Breast Cancer Res. Treat.* **2003**, *79*, 143–147. [CrossRef] [PubMed]

10. Carney, P.A.; O'Malley, J.P.; Gough, A.; Buckley, D.I.; Wallace, J.; Fagnan, L.J.; Morris, C.; Mori, M.; Heintzman, J.D.; Lieberman, D. Association between documented family history of cancer and screening for breast and colorectal cancer. *Prev. Med.* **2013**, *57*, 679–684. [CrossRef] [PubMed]

11. Lu, Y.; Segelman, J.; Nordgren, A.; Lindström, L.; Frisell, J.; Martling, A. Increased risk of colorectal cancer in patients diagnosed with breast cancer in women. *Cancer Epidemiol.* **2016**, *41*, 57–62. [CrossRef] [PubMed]

12. Loibl, S.; Poortmans, P.; Morrow, M.; Denkert, C.; Curigliano, G. Breast cancer. *Lancet* **2021**, *397*, 1750–1769. [CrossRef]

13. Zubair, M.; Wang, S.; Ali, N. Advanced Approaches to Breast Cancer Classification and Diagnosis. *Front. Pharmacol.* **2021**, *11*, 632079. [CrossRef]

14. Lau, K.H.; Tan, A.M.; Shi, Y. New and Emerging Targeted Therapies for Advanced Breast Cancer. *Int. J. Mol. Sci.* **2022**, *23*, 2288. [CrossRef] [PubMed]

15. Meanwell, N.A. Improving drug candidates by design: A focus on physicochemical properties as a means of improving compound disposition and safety. *Chem. Res. Toxicol.* **2011**, *24*, 1420–1456. [CrossRef] [PubMed]

16. Guha, R. On exploring structure-activity relationships. *Methods Mol. Biol.* **2013**, *993*, 81–94. [PubMed]

17. Shrestha, J.P.; Subedi, Y.P.; Chen, L.H.; Chang, C.W.T. A mode of action study of cationic anthraquinone analogues: A new class of highly potent anticancer agents. *MedChemComm* **2015**, *6*, 2012–2022. [CrossRef]

18. Gholampour, M.; Seradj, H.; Pirhadi, S.; Khoshneviszadeh, M. Novel 2-amino-1,4-naphthoquinone hybrids: Design, synthesis, cytotoxicity evaluation and in silico studies. *Bioorg. Med. Chem.* **2020**, *28*, 115718. [CrossRef] [PubMed]

19. Kruschel, R.D.; Buzid, A.; Khandavilli, U.B.R.; Lawrence, S.E.; Glennon, J.D.; McCarthy, F.O. Isoquinolinequinone N-oxides as anticancer agents effective against drug resistant cell lines. *Org. Biomol. Chem.* **2020**, *18*, 557–568. [CrossRef]

20. Eyong, K.O.; Ketsemen, H.L.; Zhao, Z.; Du, L.Q.; Ingels, A.; Mathieu, V.; Kornienko, A.; Hull, K.G.; Folefoc, G.N.; Baskaran, S.; et al. Antiproliferative activity of naphthoquinones and indane carboxylic acids from lapachol against a panel of human cancer cell lines. *Med. Chem. Res.* **2020**, *29*, 1058–1066. [CrossRef]

21. Ravichandiran, P.; Subramaniyan, S.A.; Kim, S.Y.; Kim, J.S.; Park, B.H.; Shim, K.S.; Yoo, D.J. Synthesis and Anticancer Evaluation of 1,4-Naphthoquinone Derivatives Containing a Phenylaminosulfanyl Moiety. *ChemMedChem* **2019**, *14*, 532–544. [CrossRef] [PubMed]

22. Defant, A.; Mancini, I. Design, Synthesis and Cancer Cell Growth Inhibition Evaluation of New Aminoquinone Hybrid Molecules. *Molecules* **2019**, *24*, 2224. [CrossRef] [PubMed]

23. Bayrak, N.; Yıldırım, H.; Yıldız, M.; Radwan, M.O.; Otsuka, M.; Fujita, M.; Ciftci, H.I.; Tuyun, A.F. A novel series of chlorinated plastoquinone analogues: Design, synthesis, and evaluation of anticancer activity. *Chem. Biol. Drug Des.* **2020**, *95*, 343–354. [CrossRef] [PubMed]

24. Bayrak, N.; Yildirim, H.; Yildiz, M.; Radwan, M.O.; Otsuka, M.; Fujita, M.; Tuyun, A.F.; Ciftci, H.I. Design, synthesis, and biological activity of Plastoquinone analogues as a new class of anticancer agents. *Bioorg. Chem.* **2019**, *92*, 103255. [CrossRef] [PubMed]

25. Ciftci, H.I.; Bayrak, N.; Yildirim, H.; Yildiz, M.; Radwan, M.O.; Otsuka, M.; Fujita, M.; Tuyun, A.F. Discovery and structure-activity relationship of plastoquinone analogues as anticancer agents against chronic myelogenous leukemia cells. *Arch. Pharm.* **2019**, *352*, 1900170. [CrossRef] [PubMed]

26. Bayrak, N.; Ciftci, H.I.; Yildiz, M.; Yildirim, H.; Sever, B.; Tateishi, H.; Otsuka, M.; Fujita, M.; Tuyun, A.F. Structure based design, synthesis, and evaluation of anti-CML activity of the quinolinequinones as LY83583 analogues. *Chem. Biol. Interact.* **2021**, *345*, 109555. [CrossRef] [PubMed]

27. Ciftci, H.I.; Bayrak, N.; Yıldız, M.; Yıldırım, H.; Sever, B.; Tateishi, H.; Otsuka, M.; Fujita, M.; Tuyun, A.F. Design, synthesis and investigation of the mechanism of action underlying anti-leukemic effects of the quinolinequinones as LY83583 analogues. *Bioorg. Chem.* **2021**, *114*, 105160. [CrossRef] [PubMed]

28. Jannuzzi, A.T.; Yıldız, M.; Bayrak, N.; Yıldırım, H.; Shilkar, D.; Jayaprakash, V.; Tuyun, A.F. Anticancer agents based on Plastoquinone analogues with N-phenylpiperazine: Structure-activity relationship and mechanism of action in breast cancer cells. *Chem. Biol. Interact.* **2021**, *349*, 109673. [CrossRef] [PubMed]

29. DTP Developmental Therapeutics Program. Available online: https://dtp.cancer.gov/databases_tools/docs/compare/compare_methodology.htm#perform (accessed on 25 September 2022).

30. Kazakova, O.; Mioc, A.; Smirnova, I.; Baikova, I.; Voicu, A.; Vlaia, L.; Macașoi, I.; Mioc, M.; Drăghici, G.; Avram, Ş.; et al. Novel Synthesized *N*-Ethyl-Piperazinyl-Amides of C2-Substituted Oleanonic and Ursonic Acids Exhibit Cytotoxic Effects through Apoptotic Cell Death Regulation. *Int. J. Mol. Sci.* **2021**, *22*, 10967. [CrossRef] [PubMed]

31. Boyd, M.R.; Pauli, K.D. Some practical considerations and applications of the National-Cancer-Institute in vitro anticancer drug discovery screen. *Drug Dev. Res.* **1995**, *34*, 91–109. [CrossRef]

32. Cuartas, V.; Aragón-Muriel, A.; Liscano, Y.; Polo-Cerón, D.; Crespo-Ortiz, M.; Quiroga, J.; Abonia, R.; Insuasty, B. Anticancer activity of pyrimidodiazepines based on 2-chloro-4-anilinoquinazoline: Synthesis, DNA binding and molecular docking. *RSC Adv.* **2021**, *11*, 23310–23329. [CrossRef] [PubMed]

33. Rostom, S.A.; Shalaby, M.A.; El-Demellawy, M.A. Polysubstituted pyrazoles, part 5. Synthesis of new 1-(4-chlorophenyl)-4-hydroxy-1H-pyrazole-3-carboxylic acid hydrazide analogues and some derived ring systems. A novel class of potential antitumor and anti-HCV agents. *Eur. J. Med. Chem.* **2003**, *38*, 959–974. [CrossRef] [PubMed]

34. Monks, A.; Scudiero, D.; Skehan, P.; Shoemaker, R.; Paull, K.; Vistica, D.; Hose, C.; Langley, J.; Cronise, P.; Vaigrowlloff, A.; et al. Feasibility of a high-flux anticancer drug screen using a diverse panel of cultured human tumor cell lines. *J. Natl. Cancer Inst.* **1991**, *83*, 757–766. [CrossRef]

35. Sledge, G.W., Jr.; Loehrer, P.J., Sr.; Roth, B.J.; Einhorn, L.H. Cisplatin as first-line therapy for metastatic breast cancer. *J. Clin. Oncol.* **1988**, *6*, 1811–1814. [CrossRef] [PubMed]

36. Passalacqua, R.; Bisagni, G.; Cocconi, G.; Boni, C.; Di Blasio, B.; Ceci, G. Cisplatin and etoposide in advanced colorectal carcinoma. *Ann. Oncol.* **1991**, *2*, 687–688. [CrossRef]

37. Haller, D.G. Recent updates in the clinical use of platinum compounds for the treatment of gastrointestinal cancers. *Semin. Oncol.* **2004**, *31*, 10–16. [CrossRef]

38. Prabhakaran, P.; Hassiotou, F.; Blancafort, P.; Filgueira, L. Cisplatin induces differentiation of breast cancer cells. *Front. Oncol.* **2013**, *3*, 134. [CrossRef]

39. Shen, M.; Duan, W.M.; Wu, M.Y.; Wang, W.J.; Liu, L.; Xu, M.D.; Zhu, J.; Li, D.M.; Gui, Q.; Lian, L.; et al. Participation of autophagy in the cytotoxicity against breast cancer cells by cisplatin. *Oncol. Rep.* **2015**, *34*, 359–367. [CrossRef]

40. Wan, X.; Wang, C.; Huang, Z.; Zhou, D.; Xiang, S.; Qi, Q.; Chen, X.; Arbely, E.; Liu, C.Y.; Du, P.; et al. Cisplatin inhibits SIRT3-deacetylation MTHFD2 to disturb cellular redox balance in colorectal cancer cell. *Cell Death Dis.* **2020**, *11*, 649. [CrossRef]

41. Lynce, F.; Nunes, R. Role of Platinums in Triple-Negative Breast Cancer. *Curr. Oncol. Rep.* **2021**, *23*, 50. [CrossRef]

42. Ciftci, H.; Sever, B.; Ocak, F.; Bayrak, N.; Yıldız, M.; Yıldırım, H.; DeMirci, H.; Tateishi, H.; Otsuka, M.; Fujita, M.; et al. In Vitro and In Silico Study of Analogues of Plant Product Plastoquinone to Be Effective in Colorectal Cancer Treatment. *Molecules* **2022**, *27*, 693. [CrossRef] [PubMed]

43. Brogden, A.L.; Hopcroft, N.H.; Searcey, M.; Cardin, C.J. Ligand bridging of the DNA Holliday junction: Molecular recognition of a stacked-X four-way junction by a small molecule. *Angew. Chem. Int. Ed. Eng.* **2007**, *46*, 3850–3854. [CrossRef] [PubMed]

44. *Schrödinger Release 2016-2*; Schrödinger, LLC: New York, NY, USA, 2016.

45. *Schrödinger Release 2016-2: QikProp*; Schrödinger, LLC: New York, NY, USA, 2016.

46. SwissADME. Available online: http://www.swissadme.ch (accessed on 29 August 2022).

47. Daina, A.; Michielin, O.; Zoete, V. SwissADME: A free web tool to evaluate pharmacokinetics, drug-likeness and medicinal chemistry friendliness of small molecules. *Sci. Rep.* **2017**, *7*, 42717. [CrossRef]

48. Tukulula, M.; Little, S.; Gut, J.; Rosenthal, P.J.; Wan, B.; Franzblau, S.G.; Chibale, K. The design, synthesis, in silico ADME profiling, antiplasmodial and antimycobacterial evaluation of new arylamino quinoline derivatives. *Eur. J. Med. Chem.* **2012**, *57*, 259–267. [CrossRef]

49. Rasal, N.K.; Sonawane, R.B.; Jagtap, S.V. Potential 2,4-dimethyl-1H-pyrrole-3-carboxamide bearing benzimidazole template: Design, synthesis, in vitro anticancer and in silico ADME study. *Bioorg. Chem.* **2020**, *97*, 103660. [CrossRef] [PubMed]

50. Varano, F.; Catarzi, D.; Vigiani, E.; Vincenzi, F.; Pasquini, S.; Varani, K.; Colotta, V. Piperazine- and Piperidine-Containing Thiazolo[5,4-d]pyrimidine Derivatives as New Potent and Selective Adenosine A2A Receptor Inverse Agonists. *Pharmaceuticals* **2020**, *13*, 161. [CrossRef] [PubMed]

51. Waldner, M.J.; Neurath, M.F. The molecular therapy of colorectal cancer. *Mol. Aspects Med.* **2010**, *31*, 171–178. [CrossRef] [PubMed]

52. Howell, A.; Anderson, A.S.; Clarke, R.B.; Duffy, S.W.; Evans, D.G.; Garcia-Closas, M.; Gescher, A.J.; Key, T.J.; Saxton, J.M.; Harvie, M.N. Risk determination and prevention of breast cancer. *Breast Cancer Res.* **2014**, *16*, 446. [CrossRef]

53. Wellington, K.W. Understanding cancer and the anticancer activities of naphthoquinones—A review. *RSC Adv.* **2015**, *5*, 20309–20338. [CrossRef]

54. Tandon, V.K.; Kumar, S. Recent development on naphthoquinone derivatives and their therapeutic applications as anticancer agents. *Expert Opin. Ther. Pat.* **2013**, *23*, 1087–1108. [CrossRef]

55. Yilmaz Goler, A.M.; Jannuzzi, A.T.; Bayrak, N.; Yıldız, M.; Yıldırım, H.; Otsuka, M.; Fujita, M.; Radwan, M.O.; TuYuN, A.F. In Vitro and In Silico Study to Assess Toxic Mechanisms of Hybrid Molecules of Quinone-Benzocaine as Plastoquinone Analogues in Breast Cancer Cells. *ACS Omega* **2022**, *7*, 30250–30264. [CrossRef] [PubMed]

56. Davidson, N.E.; Hahm, H.A.; Armstrong, D.K. Apoptosis and Breast Cancer. In *Apoptosis and Cancer Chemotherapy. Cancer Drug Discovery and Development*; Hickman, J.A., Dive, C., Eds.; Humana Press: Totowa, NJ, USA, 1999; pp. 291–303.

57. Parton, M.; Dowsett, M.; Smith, I. Studies of apoptosis in breast cancer. *BMJ* **2001**, *322*, 1528–1532. [CrossRef] [PubMed]

58. Yang, S.Y.; Sales, K.M.; Fuller, B.; Seifalian, A.M.; Winslet, M.C. Apoptosis and colorectal cancer: Implications for therapy. *Trends Mol. Med.* **2009**, *15*, 225–233. [CrossRef] [PubMed]

59. Watson, A.J.M. Recent advances in basic science apoptosis and colorectal cancer. *Gut* **2004**, *53*, 1701–1709. [CrossRef] [PubMed]

60. Yamashita, F.; Hashida, M. In silico approaches for predicting ADME properties of drugs. *Drug Metab. Pharm.* **2004**, *19*, 327–338. [CrossRef] [PubMed]

61. Alqahtani, S. In silico ADME-Tox modeling: Progress and prospects. *Expert Opin. Drug Metab. Toxicol.* **2017**, *13*, 1147–1158. [CrossRef] [PubMed]

62. Honório, K.M.; Moda, T.L.; Andricopulo, A.D. Pharmacokinetic properties and in silico ADME modeling in drug discovery. *Med. Chem.* **2013**, *9*, 163–176. [CrossRef] [PubMed]

63. Durán-Iturbide, N.A.; Díaz-Eufracio, B.I.; Medina-Franco, J.L. In Silico ADME/Tox Profiling of Natural Products: A Focus on BIOFACQUIM. *ACS Omega* **2020**, *5*, 16076–16084. [CrossRef]

64. Grever, M.R.; Schepartz, S.A.; Chabner, B.A. The National-Cancer-Institute: Cancer drug discovery and development program. *Semin. Oncol.* **1992**, *19*, 622–638.

65. Skehan, P.; Storeng, R.; Scudiero, D.; Monks, A.; McMahon, J.; Vistica, D.; Warren, J.T.; Bokesch, H.; Kenney, S.; Boyd, M.R. New colorimetric cytotoxicity assay for anticancer-drug screening. *J. Natl. Cancer Inst.* **1990**, *82*, 1107–1112. [CrossRef]

66. Ciftci, H.I.; Can, M.; Ellakwa, D.E.; Suner, S.C.; Ibrahim, M.A.; Oral, A.; Sekeroglu, N.; Özalp, B.; Otsuka, M.; Fujita, M.; et al. Anticancer activity of Turkish marine extracts: A purple sponge extract induces apoptosis with multitarget kinase inhibition activity. *Investig. New Drugs* **2020**, *38*, 1326–1333. [CrossRef] [PubMed]

Review

How Should the Worldwide Knowledge of Traditional Cancer Healing Be Integrated with Herbs and Mushrooms into Modern Molecular Pharmacology?

Yulia Kirdeeva [1], Olga Fedorova [1], Alexandra Daks [1], Nikolai Barlev [1,2,*] and Oleg Shuvalov [1,2,*]

[1] Institute of Cytology, Russian Academy of Sciences, 194064 St. Petersburg, Russia;
    yulia.kirdeeva@yandex.ru (Y.K.); fedorovaolgand@gmail.com (O.F.); alexandra.daks@gmail.com (A.D.)

[2] Orekhovich Institute of Biomedical Chemistry, 119435 Moscow, Russia

*   Correspondence: barlev.nick@incras.ru (N.B.); oleg8988@mail.ru (O.S.); Tel.: +7-812-297-4519 (N.B. & O.S.)

Abstract: Traditional herbal medicine (THM) is a "core" from which modern medicine has evolved over time. Besides this, one third of people worldwide have no access to modern medicine and rely only on traditional medicine. To date, drugs of plant origin, or their derivates (paclitaxel, vinblastine, vincristine, vinorelbine, etoposide, camptothecin, topotecan, irinotecan, and omacetaxine), are very important in the therapy of malignancies and they are included in most chemotherapeutic regimes. To date, 391,000 plant and 14,000 mushroom species exist. Their medical and biochemical capabilities have not been studied in detail. In this review, we systematized the information about plants and mushrooms, as well as their active compounds with antitumor properties. Plants and mushrooms are divided based on the regions where they are used in ethnomedicine to treat malignancies. The majority of their active compounds with antineoplastic properties and mechanisms of action are described. Furthermore, on the basis of the available information, we divided them into two priority groups for research and for their potential of use in antitumor therapy. As there are many prerequisites and some examples how THM helps and strengthens modern medicine, finally, we discuss the positive points of THM and the management required to transform and integrate THM into the modern medicine practice.

Keywords: traditional medicine; ethnomedicine; medical plants and mushrooms; cancer; antineoplastic compounds; medical herbs; pharmacology; standardization; bioavailability; safety

1. Introduction

Cancer is the second greatest cause of mortality worldwide, accounting for nearly 10 million deaths in 2020 (World Health Organization, www.who.int/; accessed on 16 February 2022). Thus, this continuous challenge forces scientists to search for new antineoplastic drugs and approaches, and investigate their combinations, to better fight various types of malignancies.

Chemotherapy in combination with surgery is now the standard way to treat cancer. We analyzed the National Institutes of Health (NIH) list of cancer chemotherapeutic drugs (https://www.cancer.gov/about-cancer/treatment/drugs; accessed on 16 February 2022). Twenty-six of them (Table S1) are natural compounds derived from plants, actinomycetes, and marine organisms, or semi-synthetic derivates of these compounds. Despite the fact that this number does not look impressive, these compounds constitute the most frequently used drugs: doxorubicin, paclitaxel, docetaxel, etoposide, camptothecin, irino- and topotecan, vinblastine, vincristine, and vinorelbine. They are included in most chemotherapeutic regimes (Table S2) and have made a key impact on the chemotherapeutic cancer treatment. The chemical manipulation of these compounds continues to create new improved drugs.

However, our planet harbors a great biodiversity with about 391,000 plant species worldwide. These individual species produce tens of thousands of chemical compounds

with a wide range of biological activities. Undoubtedly, dozens of them possess antineoplastic activity and may become important anticancer therapeutics. This assumption is confirmed through the examples of the biological compounds already mentioned above, which have been successfully applied to cure various types of malignancies.

On the other hand, up to 2 billion people (approximately one third of the population) have no access to modern medicines. For instance, in high-income countries, where comprehensive medical services are generally accessible, more than 80% of children with cancer are cured, opposed to less than 30% in low- and middle-income countries [1]. Under these circumstances of economic disparity, people from poor countries have no other choice but to rely on traditional medicine, which represents empirically collected evidence over many hundreds of years. Firstly, traditional medicine relies on the application of plants which are reservoirs of thousands of biologically active compounds. Thus, different cultures have adapted to use certain plants in their region to treat a spectrum of illnesses, including malignancies.

The use of traditional medicine is beneficial not only due to a lack of access to modern medicine, but also through sociocultural factors. The best examples are India, China, and Japan.

The Ayurveda medical system, which has roots that are millennia old, is based on a holistic ("whole-body") healing system, which deals not only with the body but also with the mind and spirit [2,3]. A part of this system is associated with medical plants. Ayurvedic formulations are often complex and consist of several herbal-mineral ingredients, and are governed by well-described pharmacological principles of preparation, compatibility, and administration. With the support of the Government of India, a book in two parts—Ayurvedic Pharmacopoeia of India (API)—has been established. Part I (Volumes 1–6) of it contains information about natural substances (medical plants, minerals), whereas part II contains healing formulations which can be created from the constituents described in part I.

Ayurveda has been very popular in India for millennia and is of considerable interest all over the world. It applies dozens of plants with strong antineoplastic properties, which are now the focus of anticancer research [2,4].

Another example is traditional Chinese medicine (TCM). This is also a holistic body approach, which is aimed at restoring the body's balance and harmony between the natural opposing forces of "yin" and "yang", which can block the free circulation of internal "qi" energy and cause disease. Traditional Chinese medicine includes acupuncture, diet, herbal therapy, meditation, physical exercise, and massages. The material part of TCM has partially evolved into Chinese proprietary medicine (CPM). This takes the form of a finished product, such as a capsule, tablet, or injection, all featuring the effective ingredients for use are documented in TCM [5]. CPM is a modern from of TCM which, due to standardization, can be used in modern medicine [6]. China's government strongly supports this, exports CMP products to different countries for trials and therapy, and sets up research partnerships with the big international pharmaceutical companies [7,8].

Originally based on traditional Chinese medicine, Japan has created its own traditional medical system—Kampo—which has then evolved separately from TCM. Thus, Kampo is a uniquely Japanese form of medicine. It had been Japan's primary health care system for over 1500 years. Despite the government approval of the Medical Care Law in 1874, which called for the adoption of the German model of health care and legitimized only western medical licenses, Japanese physicians continued to use and develop Kampo. Thus, 148 Kampo formulation extracts, 241 crude drugs, and 5 crude drug preparations are reported to be officially approved by National Health Insurance system, as well as under the Good Manufacturing Practice (GMP) Law, which was established by the government in 1987 to ensure that all Kampo products are of uniformly high quality [9]. Kampo is mainly based on plant extracts and formulations and is prescribed in line with modern drugs to treat various diseases including cancer and takes part in various clinical evaluations [10–16].

All of these traditional medical systems use herbs to a large extent. Despite these three examples, various other regions have their own medical traditions where herbs play most important roles (the traditional medicine of Maya, New Guinea, Philippines, etc.), which are not discussed in this paper but have been described in detail in several reviews [17–19].

Many of the herbs and formulations empirically defined over the centuries have also proven to be effective in preclinical and clinical investigations. They affect tumor cells both directly and through the modulation of the immune system, as well as through interrupts with cellular signaling pathways, miRNAs, and metabolic pathways [20–22], etc. We discuss here the antineoplastic properties of folk medicine plants and mushrooms; the molecular mechanisms of their bioactive constituents; and the advantages and limitations of using plants, mushrooms, and their active compounds in parallel with modern antineoplastic drugs.

We collected information from the common databases (MEDLINE/PubMed, Google Scholar, Web of Science, Scopus, Elsevier, SpringerLink, Wiley Online Library), as well as from several books and dissertations, and open databases.

Below, we summarized the information about some plants and mushrooms which have been applied by ethnomedicine to cure malignancies on five continents for a long time. We considered their antineoplastic properties and will focus on the molecular mechanisms of their activity. Finally, based on the data collected, we suggest two priority groups from the selected plants, mushrooms, and their bioactive compounds, for research and potential use in antineoplastic therapy.

2. Cancer Features Affected by Natural Drugs

There are common features of malignant cells which are well established (Figure 1) [23]. It is clear that both the genetic background, and somatic factors including cell-to-cell interactions, immunity, humoral factors, microenvironmental conditions, metabolic alterations, and others, are orchestrated during neoplasia. As a result, the altered balance in the equilibrium between oncogenes and tumor suppressors favors malignization. This disbalance results in uncontrolled cell division, resistance to apoptosis, metabolic rewiring, altered interactions with the microenvironment, as well as the acquisition of the ability to migrate and invade neighboring tissues, induce angiogenesis, evade the immune system, and become resistant to therapeutics, etc.

The genetic background is associated with "switch-on" mutations in gene coding for important oncogenes and "switch-off" mutations in tumor suppressors. Many known "switch-on" mutations of oncogenes, which are frequently observed in different neoplasia, lead to the constant activation of signaling pathways, including phosphoinositide 3-kinase/AKT serine/threonine kinase 1 (PI3K/AKT), Kirsten rat sarcoma virus/mitogen-activated protein kinases (Ras/MAPKs), Wnt family member 1, and others, which in turn drive and maintain cancer development. On the other hand, "switch-off" mutations in tumor suppressors, such as p53 (tumor protein p53), retinoblastoma (Rb), phosphatase and tensin homolog (PTEN), von Hippel–Lindau (VHL) tumor suppressor, and CDK4 inhibitor P16-INK4 (p16INK4), turn off their functions and mitigate the ability to combat malignization [24]. This results in the abnormalities within signaling pathway networks.

Certainly, all of the signaling pathways in our cells are involved in neoplasia development including PI3K/AKT, the extracellular signal-regulated kinase/mitogen-activated protein kinase (ERK/MAPK), Wnt, the Janus kinase/signal transducer and activator of transcription (JAK/STAT), transforming growth factor beta 1 (TGF-β), Hippo (mammalian Ste20-like 1 and 2) kinase—yes-associated protein 1 and transcriptional coactivator with PDZ-binding motif (Hippo—YAP/TAZ), Notch, and others [25]. One of the key roles in malignant cells is occupied by the PI3K/AKT and ERK/MAPK signaling pathways. Different biological stimuli and other signaling pathways converge on them. Thus, various growth factors, such as the epidermal growth factor (EGF), the fibroblast growth factor (FGF), the insulin-like growth factor (IGF), and the vascular endothelial growth factor (VEGF), bind to and activate their tyrosine kinase receptors which induce the signal transduction following

the involvement of PI3K/AKT and ERK/MAPK signaling [26,27]. Thereby, the inhibition of these pathways is usually associated with the attenuation of tumor growth, migration, invasion, as well as the induction of apoptosis which makes them desirable drug targets.
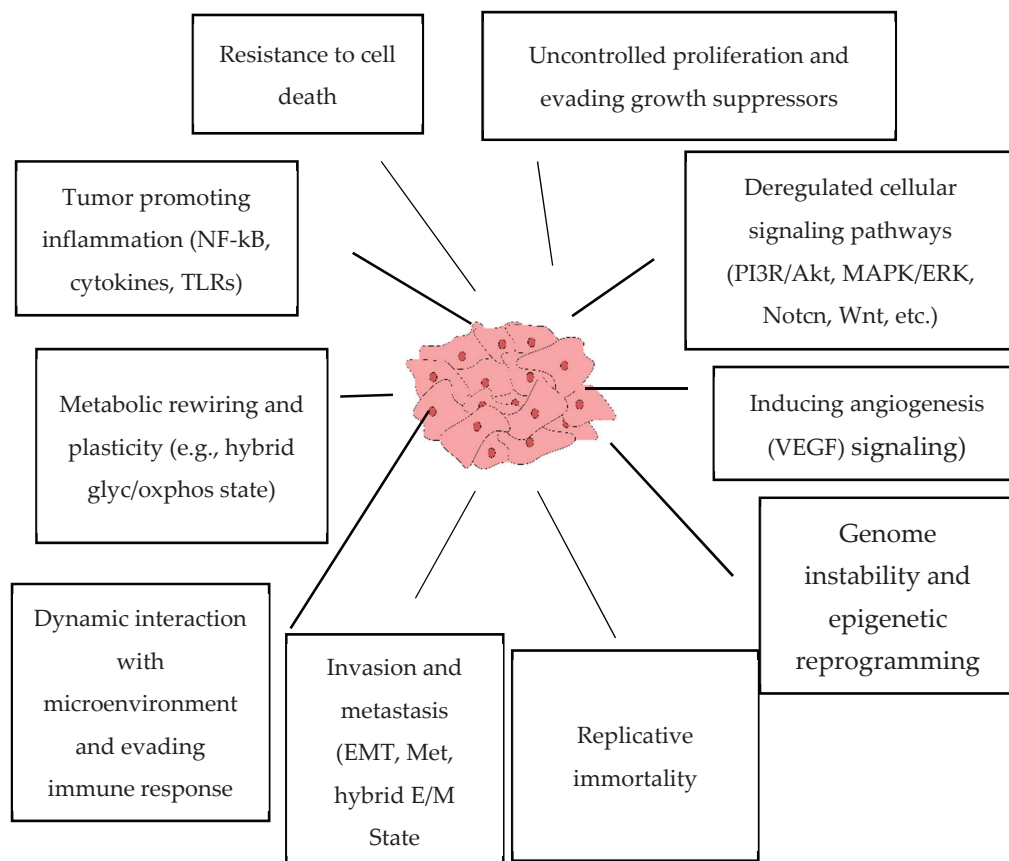

Figure 1. Main "hallmarks" of cancer.

AKT activates the master regulator of anabolism (mTOR) and deactivates AMP-activated protein kinase (AMPK) which is the inducer of autophagy. The inhibition of mTOR is one of the emerging successful strategies to kill malignant cells [28]. However, autophagy possesses a dual role in cancer. While it may contribute to cell death, it may also have cancer promoting properties including chemoresistance [29].

AMPK and mTOR are closely related to metabolic rewiring which is another "hallmark of cancer". This supplies cancer cells with the materials needed for growth and provides an adaptational plasticity to changing conditions [30–33]. As an antineoplastic strategy, the use of metabolic inhibitors first started in the 1950s [34]. Now, their use during successful cancer therapies is once again a hot topic for discussion. The metabolic inhibitors which have been used clinically are methotrexate and its analogs, as well as gemcitabine, 5-fluouracil, lonidamine, AZD3965, telaglenastat, and others [32]. Moreover, new drugs have been designed, and preclinical and clinical studies are underway.

The balance between the expression of oncogenes and tumor suppressors is also regulated by epigenetics [35,36]. DNA and histone methyl transferases, histone deacety-lases, and other chromatin-modifying participants are important targets for anti-cancer therapy [37–39].

As uncontrol growth and a resistance to programmed cell death are two major cancer cell features, the blocking of cell division and the induction of their death are the two key attributes of any chemotherapeutic methods. Several strategies can be implemented for this. The first relies on DNA-damaging agents, which stop the cell cycle and induce apoptosis (doxorubicin, cisplatin, etoposide, camptothecin, and others). Another way is

based on mitotic poisons disrupting microtubule dynamics (paclitaxel, vinblastine, and vincristine). One more is the application of targeted therapy—drugs which specifically inhibit important modulators of the cell cycle and apoptosis. Some examples of them are tyrosine kinase inhibitors (TKIs—gefitinib, lapatinib, and sunitinib [40]), inhibitors of cyclin-dependent kinase (CDK—palbociclib, ribociclib, and abemaciclib [41]), inhibitors of antiapoptotic proteins B-cell lymphoma 2 (Bcl-2), and myeloid leukemia cell differentiation protein (Mcl-1—venetoclax and navitoclax) [42].

Upon cancer, the main reason of death is metastasis which disrupts the functions of organs. The initiation of metastazing is associated with the epithelial–mesenchymal transition (EMT). Epithelial cancer cells which underwent EMT become able to invade surrounding tissues and blood and lymph vessels, disseminate across the body, extravasate into new related niches, and establish secondary tumors. To create new tumor heaths, cancer cells undergo the reverse to a EMT process—mesenchymal–epithelial transition (MET) [43]. Today, it is suggested that malignant cells dwell in hybrid E/M state which allows them to switch between EMT and MET if required [43,44]. The targeting invasive and migration properties of tumor cells is very important for all chemotherapeutic regimes.

Cancer stem cells (CSCs) are a small subpopulation of cells within malignancy groups with capabilities of self-renewal, differentiation, and tumorigenicity when transplanted into an animal host [45]. Generally, they are resistant to chemotherapeutics, possess tumor-initiating and metastasis-initiating capacities, and are responsible for tumor recurrence and development [46,47].

Immunity plays a critical role in the clearance from neoplasia. Various molecular mechanisms make the anticancer response of immune cells ineffective, e.g., macrophages, as well as B- and T- lymphocytes. Thus, stimulating the activity of immune system by various mechanisms represents a very promising approach [48,49].

In this review, we aimed to focus on those plants and mushrooms, whose biological activity in cancer treatment has been proven, and discuss the mechanisms of their action using the knowledge of modern molecular medicine.

3. Plants from Different Continents Used in Ethnomedicine for the Treatment of Malignancies

Ethnobotanical and ethnomedicine studies point to medical plants with certain properties. Below, we summarized data on plants with anti-neoplastic capabilities which are implicated to heal cancer by indigenous people from five continents.

3.1. Africa

Due to its weak economic development, Africa is a continent with an elevated level of poverty. For most people, modern methods of cancer treatment are not available, such as chemotherapy, irradiation, and surgical resection [50,51].

The most famous example of African plant with anticancer properties is Madagascar periwinkle plant, *Catharanthus roseus* G. Don (Syn. *Vinca roseus* Linn), which is a source of vincristine and vinblastine. These compounds are often used to treat different malignances worldwide.

Approximately 45,000 plant species grow in Africa [52] with the richest species diversity maximum in countries of West Sea coast from Gabon to Guinea, South African republic, and Western Africa (spanning Kenya, Tanzania, Uganda, Ethiopia, and South Sudan) [53].

According to a number of reviews, about a hundred of plants with anti-neoplastic properties are reported by ethnomedicine practitioners and are still used for a cancer treatment. However, for most of them, extremely limited information about their efficiency and selectivity in pre-clinical studies, active compounds, and molecular mechanisms of action is currently available.

Acacia nilotica (the *Fabacea* family, "*Egyptian mimosa*") which grows almost everywhere in Africa is widely used in traditional African medicine. It has been shown to possess

antispasmodic, anti-inflammatory, antithrombotic, antioxidant, antidiarrheal, antibacterial, antihypertensive, and anticancer properties [54].

The seeds of this plant are used by people to treat breast, colon, head, and neck tumors [55]. Several in vitro and in vivo studies have demonstrated anticancer properties of alcohol and methanol extracts derived from *A. nilotica*. This plant turned out to be toxic predominantly to a breast cancer model (MCF7) than for normal liver cells [56]. Other researches have shown anticancer activity of this plant against glioblastoma [57], colon cancer [58], and other types of malignant cell models [55].

In vivo study has shown the significantly decreased development of solid and ascitic tumors induced by Dalton's ascitic lymphoma in BALB/c mice [59], as well as *Helicobacter pylori*-induced colon tumors [60].

Foremost, the well-known chemicals quercetin, kaempferol, and ethyl-gallate are thought to be associated with antitumor and other activities of *A. nilotica* [54,61,62]. Pyrogallol was also shown to be the important anticancer chemical of *A. nilotica* which was able to strongly reduce colon tumors in mice models [58]. For all of these individual compounds, the significant anti-neoplastic properties have been demonstrated.

A detailed survey of *A. nilotica* traditional application, phytochemistry, and pharmacology is presented in review [54].

Guiera senegalensis is a small shrub (the *Combretaceae* family) which grows in the savannah region of West and Central Africa. It is widely used in African traditional medicine to treat different ailments including malignancies [55,63].

A number of phenolic compounds which may mediate antitumor effects of *G. senegalis* were identified: gisorhamnetin, eupatorin, alpinumisoflavone, procyanidin B3, syringin, gallic acid, galloylquinic acid derivatives, quercetin, rhamnetin, kamferol, myricetin, (−)-epicatechin, and alkaloid guieranone A, etc. [63,64].

Plant-derived aqueous and methanolic extracts were cytotoxic against breast cancer [64]. The alkaloid guieranone A isolated from *G. senegalensis* demonstrated cytotoxic activity rather similar to doxorubicin against a panel of malignant cell models but not to normal hepatocytes [65]. The authors have also demonstrated the significant inhibition of angiogenesis. The study of silver nanoparticles derived from the leaves extract of *G. senegalensis* has shown a significant antiproliferative effect on human prostate (PC3), breast (MCF7), and liver (HepG2) cell models [66].

Thus, despite the antineoplastic activity of this plant, there are still not many studies devoted to this subject. However, the composition of chemicals with anti-cancer properties makes this plant perspective for cancer research.

Combretum caffrum is the Eastern Cape South African bushwillow tree. The bark of this plant was shown to contain combretastatins—closely related stilbenes (combretastatins A), dihydrostilbenes (combretastatins B), phenanthrenes (combretastatins C), and macrocyclic lactones (combretastatins D).

Three common structural features of combtretastatins are: trimethoxy "A"-ring, a "B"-ring containing substituents o at C3' and C4', and (often) an ethene bridge between the two rings, which provides necessary structural rigidity and allows synthesis of different derivates [67].

The most promising and frequently tested compound in preclinical and clinical trials is water-soluble prodrug phospho-combretastatin A4 (CA-4P) which can be rapidly metabolized to combretastatin A4 (CA-4). This molecule exhibits anti-tumor properties by the attenuation of proliferation, and by targeting tumor vasculature paves [68]. It has a similar structure to colchicine, and binds tubulin at the same site. Moreover, CA-4 is effective against multidrug-resistant (MDR) cancer cells. A comprehensive overview of the structure, probable mechanisms of action, and potential applications is described in this review [68].

There are several detailed reviews systematizing the use of specific plants for the treatment of oncology in various regions of Africa: Western Africa [51,69], Central, Eastern, and North Africa [50], and South Africa [70–73].

There is no doubt that Africa, with its huge plant species diversity, is fraught with many currently unexplored plants and their biologically active compounds with strong antitumor properties. Some other African plants and their chemicals with anti-neoplastic activity are listed in Table 1.

Table 1. Some African plants and their compounds with anti-neoplastic activity.

Plant	Active Compounds	Effects	References
Aristolochia ringens	Triterpenes	Cytotoxic effects of root extract against several cancer cell lines, solid tumors, and leukemia models in vivo.	[74,75]
Beilschmiedia acuta	Flavonoids, saponins, alkaloids	Bark-derived extract inhibited proliferation and induced apoptosis in human leukemia CCRF-CEM cells, but was less toxic to human normal hepatocytes AML12 cells.	[76]
Dorstenia psilurus	Alkaloids, phenolic compounds, flavonoids	Cytotoxic and anti-proliferative effects in HeLa cancer cells; caspase 3/7 up-regulation and induction of apoptosis in HL-60 cells.	[77,78]
Echinops giganteus	Brominated oleanolide	Root extract inhibited proliferation and induced apoptosis in leukemia CCRF-CEM cells.	[79,80]
Imperata cylindrica	Saponins, flavonoids Antineoplastic activity: arundoin, daucosterol	Cytotoxicity against the panel of cancer cells. Root extracts induced apoptosis, increased caspase 3/7 activity, and significant down-regulated MMPs.	[77,81]
Piper capense	Alkaloids, polyphenols, saponins	Seeds extracts were cytotoxic for a number of cancer cell lines. Fruits extracts induced the shrinkage of tumor size in animal models by inhibiting the development of VM tubes and microvessel density.	[79,82]
Polyscia fulva	Anthocyanins, flavonoids, triterpenes, saponins	Roots extracted inhibited proliferation and induced apoptosis in leukemia CCRF-CEM cells via the enhanced production of ROS. It was significantly less toxic for human normal hepatocytes AML12 cells.	[76]

According to a review by Alves-Silva and colleagues [28], the frequency with which different parts of the plant are used for cancer treatment: seeds (27%), hole aerial parts of plants (23%), leaves (22%), followed by roots (8%), fruits (7%), flowers (4%), bulbs (2%), cortex (2%), stamen (2%), rhizome (1%), hole plant mass (1%), and rinds (1%). For sure, the long-standing ethnical knowledge about the use of specific parts of a particular plant may reflect the distribution and amount of biologically active compounds among the plant. As stated by the same authors, the preparation methods for consumption are as follows: decoction (30%), grind with honey (24%), infusion (20%), brut (6%), extraction (4%), powder (4%), oil (3%), pomade (2%), ingestion (2%), cataplasm (1%), chewing (1%), washing (1%), mouth washing (1%), and inhalation (1%). Diverse types of preparation can be associated with the specific assimilation of biologically active compounds required across the body for treatment certain types of malignancies.

3.2. South America

South America is the territory of growth for about 82,000 plant species [83] which is approximately 1.6 times more than in Africa. However, the degree of study of their biochemical diversity and antitumor properties is similar to Africa.

Tabebuia impetiginosa ("Lapacho", the *Bignoniaceae* family) is a tree with rosy or purple flowers widely distributed among South and Central America. This is a very important medical tree which is used to treat inflammatory diseases, bacterial and viral

infections, snake's venom, and cancer [84]. In Brazil, *T. impetiginosa* is the most used plant to cure neoplasia. The stem bark and/or inner bark of this tree is utilized. It contains iridoid, lignan, isocoumarin, phenylethanoid, and phenolic glycosides [85]. Naphthoquinones lapachol and β-lapachone are the most attractive compounds from a medical point of view.

The application of both *T. impetiginosa* extracts and lapachone exhibits strong antiproliferative and cytotoxic activities [86–89] for human breast, colon, and hepatic cancer cell models. Lapachone was sold in Brazil by the Pernambuco Pharmaceutical Laboratory (LAFEPE) and used to cure malignancies [90].

It was shown that lapachol is a pyruvate kinase M2 (PKM2) inhibitor [91], thus quenching glycolysis and anabolic capacities. PKM2 is an enzyme which branches glucose flux into biosynthetic pathways [92,93]. β-lapachone inhibited lung metastasis in colorectal cancer models [87]. It selectively killed NADPH quinone oxidoreductase 1 (NQO1)-overexpressing hepatoma cells which were accompanied by ROS induction and PARP1 hyperactivation, causing a decrease in NAD+ and ATP levels, as well as a dramatic increase in DNA double-strand break lesions [94]. NQO1 is a prognostic marker in HCC; it was increased 18-fold in HCC versus normal livers, and its high level predicts poor outcome [95,96].

Active studies of lapachones started in the 1960s when these compounds were isolated from *T. impetiginosa*, but then were terminated due to their side effects. However, further experiments have shown that β-lapachone, α-lapachone, and some of their synthetic analogs are safe and are promising antineoplastic compounds (for a comprehensive review, see [89,97]).

As an example, Rone and colleagues have created lapachone-containing ruthenium (II) complexes which enhanced lapachone toxicity to cancer cells relative to normal cells over 100-fold. The cytotoxic effects were mediated by Aurora-B down-regulation and G2/M-phase cell cycle arrest [98]. The other group [99] developed long-circulating lapachone nanoparticles which remarkably prolonged its half-life in the body and increased brain intake in order to affect glioma cells.

A number of patents cover promising synthetic derivates of lapachones. Further chemical modifications are required to improve their safety and bioavailability. Recently, positive results were obtained in phase I/Ib of a multi-center clinical trial (NCT02514031) of β-lapachone with gemcitabine/nab-paclitaxel in patients with advanced pancreatic cancer [100]. However, further insights into the molecular mechanisms of lapachone anticancer activity are required.

Besides lapachone, furanonaphthoquinones from *T. impetiginosa* possess anticancer capabilities. They were the key structures required to hamper signal transducer and activator of transcription 3 (STAT3) phosphorylation which inhibits the JAK/STAT pathway [101].

Taken together, these data demonstrate the potential of *T. impetiginosa* and lapachones in cancer healing.

Aloe vera* and *A. arborescence (the *Asphodelaceae* family) are stemless or very short-stemmed succulent plants of the genus Aloe. These species grow on several continents and are very frequently used to treat various diseases in Brazil including rheumatism, eczema, blood clots, diabetes, gastritis, inflammation, and malignancies.

A. vera and *A. arborescence* contain different biologically active secondary metabolites including anthraquinones, dihydroisocoumarins, naphthalenes, and polyketides [102]. Anthraquinones aloe-emodin, aloin A (barbaloin), and aloin B (isobarbaloin) are especially interesting for anticancer therapy. Extracts and individual compounds of Aloe induce cell cycle arrest [103,104] and apoptosis [105], exhibit antiangiogenic and antimetastatic properties [105,106], and decrease glucose flux and telomerase activity in a huge number of studies (including both solid and blood neoplasia) [107,108]. A comprehensive review of anticancer properties of *Aloe vera*, *A. arborescence*, and its active compounds is given in [108].

Aloe-emodin (Ae) exerts a plethora of important pharmacological properties including the anticancer ones (reviewed in [109]). The treatment of colorectal cancer cells with Ae induced ER stress and the activation of key components of the PERK pathway—glucose-

related protein 78 (GRP78) and transcriptional factor C/EBP homologous protein (CHOP) up-regulation, protein kinase R (PKR)-like ER kinase (p-PERK), and eukaryotic initiation factor-2α (p-eIF2α) [110]. In NSCLCs, this compound activated MAPK signaling and inhibited Akt/mTOR pathway which led to an increase in ROS and autophagy [111].

Wang's group have found that the AE compound is a competitive inhibitor of telomerase (hTERT) and a G-quadruplex structure stabilizer. In addition, Ae transcriptionally repressed tTERT via the up-regulation of E2F1 and the down-regulation of c-myc expressions [112]. G-quadruplexes are specific structures in DNA and RNA which are frequently observed in promotors of proliferation-related genes, chromosome ends, and telomeric regions, and are involved in transcription regulation. Due to the stability of G-quadruplexes and their presence within most human promoters of oncogenes, and at telomeres, G4 structures are promising targets and are currently being tested as a way to block the transcription of oncogenes and telomere elongation in cancer cells [113]. In line with this evidence, other groups have reported that Ae and Ae-8-glucoside are G4-binding ligands, especially for c-KIT and c-Myc oncogenes [114].

In melanoma cells, aloin down-regulates HMGB1 expression at the transcriptional level, preventing its translocation to the cytoplasm and interaction with TLR4, which indeed blocks HMGB1-mediated ERK activation [115]. In line with these data, in gastric cancer, the other group has shown an aloin-mediated inhibition of HMGB1 expression and release, as well as a HMGB1-induced activation of the Akt-mTOR-P70S6K and ERK-P90RSK-CREB signaling pathways [116].

Finally, aloin was shown to mitigate doxorubicin-induced cardiotoxicity by reducing proinflammatory cytokines—TNF-α, IL-1β, and IL-6 (Birari 2020) [117].

The polysaccharide acemannan exerts antitumor activity through the stimulation of the immune system and the production of antitumor cytokines, and has been approved by the U.S. Department of Agriculture (USDA) for treatment of fibrosarcoma in cats and dogs (Acemanna, CarraVet Acemannan immunostimulant) [108].

Although there have been numerous in vitro and in vivo studies, the antineoplastic potential of *Aloe* ssp. has not been fully studied. However, several clinical trials have been conducted. The combined adjuvant chemotherapy which includes Aloe arborescence, oxaliplatin, and 5-fluorouracil (5-FU), given to 240 patients with metastatic solid tumors, significantly improved tumor regressions and 3-year survival rates [118]. Two other trials have also indicated the potential of Aloe for anticancer therapy [119,120].

Despite the strong anticancer properties of Aloe, caution and further research is needed before its intake. Several studies have described the potential carcinogenic effects of Ae and aloin. Thus, Ae reportedly may have hepato- and nephrotoxicity [109] whereas aloin is able to induce the Wnt/β-catenin pathway [121].

Capsicum frutenese is a member of the *Solanaceae* family which is frequently used in South American ethnomedicine to treat cancer. Other pepper species, including *C. chinensies* (*Chili pepper*), are also used. The spicy taste of these plants is caused mainly by alkaloid capsaicin.

A huge number of studies have demonstrated the capsaicin-mediated anticancer effects [122,123]. In non-small cell lung cancer (NSCLC), capsaicin inhibits vascular endothelial growth factor (VEGF) expression and angiogenesis via the p53-HIF1-VEGF pathway [124]. It was also shown that capsaicin, in combination with sorafenib, inhibited epidermal growth factor receptor (EGFR) and PI3K/Akt/mTOR signaling [125]. This synergic effect attenuated the growth, migration, and invasion, and also induced apoptosis, in three hepatocellular carcinoma cell lines. In nasopharyngeal carcinoma, capsaicin extinguished the PI3K/Akt/mTOR pathway which induced autophagy and apoptosis [126].

It is interesting to note that Chang and colleagues [127] have shown that Ecto-NADPH oxidase disulfide thiol exchanger 2 (ENOX2) is a direct target of capsaicin. Authors have shown that capsaicin induces autophagy-related apoptosis in p53-mutant oral carcinoma cells, but only autophagy-dependent cytotoxicity (without apoptosis) in cells with wild-type p53.

However, several contrary results have also been reported, implicating capsaicin's pro-cancer properties [128]. For instance, high doses of capsaicin activated AMPK, and also induced autophagy, EMT, and chemoresistance [129]. These contradictions may depend on various factors including both the background of the cells and experimental conditions. While different studies report autophagy as a mechanism of capsaicin-mediated effects [129], the opposite results can also be linked to this fundamental process. It is already known that autophagy has a dual role in cancer, creating both pro-survival and antineoplastic effects [29]. Autophagy is typically associated with apoptosis. However, in other cases, it protects cancer cells from chemotherapy [130]. Arguably, the exact effects of capsaicin may depend on whether autophagy plays a pro- or anti-survival role in corresponding malignant cells.

Taken together, there is a possibility that capsaicin is a potential anticancer therapeutic; however, due to contradictory results, more detailed studies about its properties are required.

Some other South American plants and their compounds with anti-neoplastic activity are listed in Table 2.

Table 2. Some South American plants and their compounds with anti-neoplastic activity.

Plant	Active Compounds	Effects	References
Achyrocline satureioides	Achyrobichalcone, 3-*O*-methylquercetin, and other flavonoids	In vitro cytotoxicity and apoptosis in human breast cancer cells; inhibition of c-MYC and ERK/JNK in glioma cell lines.	[82,131]
Aloysia polystachya	Flavonoids	In vitro apoptosis in human colorectal cancer cells, and a decrease in the percentage of cancer stem cells (CSCs). In vivo inhibition of tumor growth in non-toxic doses.	[132]
Azorella glabra	Mulinic acid, azorellane terpenoids	G0/G1 cell cycle arrest and apoptosis in AML cell lines. A slight decrease in the survival of non-tumor cells	[133]
Ephedra chilensis	Terpens and fatty acids	IC50 of non-polar extracts for one breast cancer and three colon cell lines was at the level of doxorubicin; in vitro cytotoxicity for normal colon epithelium cells was less than doxorubicin.	[134]
Croton lechleri	Taspine	Leaf extracts exhibited cytotoxic antiproliferative effects on HeLa and SK23 cells in vitro, and antitumor effects in mice in vivo; moderate toxicity to mice.	[135,136]
Laetia corymbulosa	Corymbulosins B, C, D, E, F, G	Bark extract exhibited cytotoxicity to panel of cancer cells.	[137]
Lepidium meyenii	macamide and macaene fractions	Macadamine displayed anticancer activities against multiple cancer cell lines.	[138]
Leptocarpha rivularis	Leptocarpin	Cytotoxic effects against several cancer cell lines.	[139]
Passiflora alata	Flavonoids and saponins	In vitro cytotoxicity against the set of cancer cell lines, and in vivo antitumor activity against sarcoma S180-bearing mice with low general toxicity.	[140]
Thevetia peruviana	Thevetiaflavone, and individual cardiac glycosides	Fruit extract exhibited cytostatic and cytotoxic effects in cancer cell lines with moderate toxicity to non-tumor cells.	[141]

3.3. Asia

Asia occupies a vast territory with various climate zones which range from tropical to arctic. It is a habitat for 100,000 plant species, many of which have been medically used in ethnomedicine for centuries.

Cephalotaxus harringtonia (Japanese plum yew, the *Cephalotaxaceae* family) is an evergreen tree up which can grow up to 10 m tall and is native to Japan. Initially, the ethanolic extract from the seed of *Cephalotaxus harringtonia* showed antineoplastic activity against mouse leukemia L-1210 and P388 cells. Several alkaloids with potential antitumor activity were isolated from this extract and from other parts of the plant [142]. They are identified as cephalotaxin esters: harringtonine, isoharringtonine, homoharringtonine (HHT), and doxyharringtonine.

Clinical trials of HHT have been actively conducted in China and the USA in acute myeloid leukemia (AML) and chronic lymphocytic leukemia (CLL) [143]. The initial data obtained showed conflicting results; thus, interest among American scientists towards HHT has significantly weakened, unlike their Chinese colleagues.

Meanwhile, Chinese scientists continued clinical trials with varying regimes and HHT dosing. They carried out detailed studies and then successfully used HHT in a HAG combination scheme (homoharringtonine, cytarabine, and G-CSF) to treat hematological malignancies, including AML and myelodysplastic syndrome [144,145]. Thus, HHT became a part of the standard AML therapy in China [143]. In 2012, the Food and Drug Administration (FDA) approved omacetaxine—a semisynthetic purified HHT derivate for the treatment of patients with chronic myelogenous leukemia (CML) refractory or intolerance to two or more TKIs [146].

The mechanism of HHT and omacetaxine action is the inhibition of translation. These compounds compete with tRNA to bind the A-site cleft in the large ribosomal subunit which blocks elongation. Furthermore, another mechanism of HHT action in AML cells was discovered. It has been shown that HHT directly binds the NF-κB-repressing factor (NKRF) and arrests it in the cytoplasm, which in turn strengthens p65-NKRF interaction, thereby attenuating the transactivation activity of p65 on the MYC gene [147]. HHT was also shown to decrease p-JAK2, p-STAT5, and p-AKT, which suggests it may be a broad-spectrum PTK inhibitor [148]. Thus, multiple mechanisms of HHT activity may exist.

Oldenlandia diffusa (*Hedyotis diffusa*) or "Snake-Needle Grass" and *O. corymbose* are the annual plants widely distributed in China, Japan, and Korea. In China, this plant is actively used in traditional medicine. *Oldenlandia diffusa* has analgetic, antibacterial, anti-inflammatory, antitumor, cardiotonic, diuretic, and sedative effects on the body. Regarding cancer, it is well known in Chinese folk medicine, primarily for the treatment of liver, lung, and stomach malignancies [149].

O. diffusa has been extensively used as a part of adjuvant therapy for metastatic breast cancer and gastric cancer patients in traditional Chinese medicine (TCM) with proven efficacy [150,151]. Regarding breast cancer studies, extracts of *O. diffusa* possessed cytotoxicity towards highly invasive breast cancer cells, but not towards normal cells of different origins. It abrogates the expression of metalloproteinases (MMPs) and caveolin-1 [152]. The extract inhibited p-ERK, p-38, NF-κB, MMP-9, and Icam-1 [153], and may also inhibit AMPK [154].

Hedyotis diffusa contains various iridoids (asperuloside, geniposidic acid, diffusoside, and alpigenoside), triterpenes (arborinone, ursolic acid, and oleanolic acid), flavonoinds (quercetin, rutin, and kaempferol), athraquinones, phenolic acids (p-coumaric acid, caffeic acid, and caffeoyl-quinic acids), and a broad spectrum of volatile oils (reviewed in [155]). Such a diverse composition of compounds with antineoplastic properties may explain the use of *O. diffusa* by Chinese people as an anticancer substance for centuries.

Feng and colleagues have demonstrated that *Hedyotis diffusa* extract attenuated the phosphorylation of AKT, ERK1/2, JNK, p38, ribosomal protein S6 kinase beta-1 (p70S6K), STAT3, and the secretion of pro-inflammatory interleukins IL-1β, IL-6, and TNF-α. Additionally, at the time, it also induced anti-inflammatory IL-4 and IL-10 [156].

A number of studies have shown that oleanic and ursolic acids fractioned from this plant are very important compounds due to their antitumor properties. The ursolic-acid-mediated inhibition of the RAF/ERK, IKK/NF-κB [157], and STAT3 pathways [158] is reported. It has also been shown that ursolic acid suppressed proliferation and induced apoptosis in breast cancer cells, but not in non-malignant cells. Ursolic acid also repressed metastasis in both zebrafish and mouse models via the suppression of glycolysis through the activation of SP1/caveolin-1 signaling [159]. Another research group has demonstrated that ursolic acid inhibited energy metabolism. It inhibited Akt which was also associated with decreased HK2, PKM2, ATP, and lactate levels [160]. The derivate of ursolic acid mimics glucose, and competes with it for hexokinase 2 (HK2) binding [161].

Oleanolic acid (OA), which is another bioactive component of *Hedyotis diffusa*, similarly attenuates cancer development through several mechanisms [162]. In gastric cancer, OA was shown to down-regulate glucose uptake and aerobic glycolysis through the inhibition of YAP and HIF-1α [163], and through the induction of autophagic death by deactivating PI3K/AKT/mTOR and ERK/p38 MAPK [164,165].

OA was shown to activate ferroptosis in Hela cells by promoting the expression of ACSL4 [166] (Xiaofei, et al., 2021) in the purine salvage pathway. It suppressed the purine salvage pathway (PSP), thus interfering with nucleotide synthesis. OA induced the autophagy-dependent degradation of hypoxanthine–guanine phosphoribosyltransferase (HGPRT) and 5′-nucleotidase (5′-NT), i.e., two enzymes of PSP [167]. The other group was able to show that OA may suppress angiogenesis in colorectal cancer by blocking VEGFR2 signaling [168].

For medical purposes in China, *Hedytois diffusa* is often used in tandem with another plant—*Scutellaria barbata*. This pare is a "core" of Chinese herbal medicine (CHM) which is utilized to treat different types of tumors [151,169].

Scutellaria barbata (*SB*) is a perennial herb (the *Lamiaceae* family) living in southern central China. This medical plant is frequently used in TCM to cure malignancies, inflammation, infection, cirrhosis, etc. Among the chemical compounds identified, there are: flavonoids (scutellarein, scutellarin, carthamidin, isocarthamidin, wogonin, naringenin, apigenin, hispidulin, eriodictyol, and luteolin), diterpenoids (scutellones, scuterivulactones, barbatins, and scutebarbatines), and volatile oils (linalool, α-terpineol, thymol, and globulol) [155]. Flavonoids (scutellarein, scutellarin, and carthamidin) are thought to be the main compounds that are responsible for anticancer properties of SB.

BZL101 is an orally specified aqueous SB extract which has been extensively studied for the treatment of metastatic breast cancer. It provokes cell cycle arrest, apoptosis [170], inhibition of glycolysis, and OXPHOS [171].

Scutellarein inhibited the enhancer of zeste homolog 2 (EZH2), increased the expression of its target forkhead box protein O1 (FOXO1), and reduced tumor growth and metastasis [172]. Moreover, in HCC, scutellarein increased the level of PTEN—a negative regulator of Akt signaling pathway [173].

Another flavonoid compound—scutellarin—mitigates colitis-derived colorectal cancer by inhibiting the Wnt/β-catenin signaling pathway [174]. In gastric cancer cells, this compound up-regulates PTEN, which attenuates p-PI3K and EMT [167].

Extracts of this plant reduced p-STAT3, the expression of cyclin D1 and CDK4 [175], as well as the Wnt/β-catenin signaling pathway [176]. It may also attenuate the PI3K/AKT pathway, inhibit ABC transporters, and restore susceptibility to 5-FU [177].

Thus, the combination of *O. diffusa* and *S. barbata* extracts displays proven antineoplastic capacity and involves multiple mechanisms acting in a synergistic way. The study of a combination of extracts or individual compounds of these plants is a promising area of anticancer research.

The power of plants to fight cancer is exhaustively represented by traditional Chinese medicine (TCM) and Indian Ayurveda.

3.3.1. Traditional China Herbal Medicine

The herbal part of TCM relies on the application of a cocktail consisting of several herbs, used in the treatment of complex diseases such as cancer. It has at least 2000 years of history. According to Chen and colleagues, Chinese Pharmacopoeia (2015 edition) counted 25 formulations with antineoplastic properties [178].

Traditional personal medicine (TPM) is the improved and more standardized kind of TCM application. TPM includes herbal medicines in traditional Chinese medicine, modernized into a ready-to-use form (such as tablets, oral solutions, or dry suspensions), as opposed to herbs that require cooking (hot water extraction).

The benefit of TCM formulas in the therapy of various neoplasms is based on multiple components, which can target multiple signaling pathways, providing synergistic therapeutic effects. Plants described in the earlier section are often the components of various TCM formulations. The analysis of a number of TCM formulas uncovered the mechanisms of their antitumor activities and enumerates their bioactive anticancer compounds [178–181].

Wu and colleagues have analyzed the application of the top 15 TPMs and modern western drugs according to the frequency of their use in a particular type of malignancy and the cost per patient [5]. This statistical analysis has shown that TPMs are used with about the same frequency as western therapeutics, whereas the cost per patient was lower for TPMs. It is interesting to note that different TPMs can be applied to treat certain types of malignancy with varying frequencies. Moreover, TPMs are often applicated in combination with western medicines [5]. The most frequently used antineoplastic formulations are given in Table 3 with brief descriptions.

Table 3. Some frequently used traditional Chine's formulations for a cancer treatment.

Clinical Formulation	Composition	Type of Cancer	Effects	References
Aidi Injection	*Mylabris Phalerata, Astragalus Membranaceus, Panax Ginseng, Acanthopanax Senticosus*	Different solid tumors, gynecologic tumors	Suppression of proliferation, migration, invasion, angiogenesis, and metastasis. Decreased p-PI3K and Bcl-xL in liver cancer cells. Induction of apoptosis. *In Clinic*: improved overall survival, the quality of life, and the effectiveness of chemotherapy.	[182–184]
Fufangkushen Injection	*Sophora flavescens, Heterosmilacis Japonica*	Different solid tumors	Reduced proliferation, tumor growth, and TRPV1-ERK phosphorylation; decreased IFN-γ, IL-6, and KC levels in S-180 sarcoma. Induced apoptosis via up-regulation of caspase-3 and Fas in esophageal carcinoma. *In Clinic*: improved the quality of life and the effectiveness of chemotherapy.	[185,186]
Kanglaite injection	*Coix lacryma-jobi*	Non-small cell lung cancer, colorectal cancer, pancreatic cancer	In vitro suppressed cell growth and induced apoptosis via up-regulation of p53, Fas, and caspase-3. In vivo down-regulation of the PI3K/Akt/mTOR signaling pathway, and tumor growth suppression.	[187,188]
Kushen injection	*Sophorae Flavescentis, Radix, Smilacis Glabrae Rhixoma*	Different solid tumors	Immunomodulatory activity via regulation of macrophages and CD8+ T cells, TNFR1, NF-κB p65, and MAPK p38.	[189]

Table 3. *Cont.*

Clinical Formulation	Composition	Type of Cancer	Effects	References
Qing-Dai	*Baphicacanthus cusia, Polygonum tinctorium, Isatis indigotica*	Acute promyelocytic leukemia	Down-regulation of NF-κB, Iap1, Iap2, Bcl-2, BCL-xL, cyclin D1, and c-Myc; inhibition of angiogenesis by reducing JAK/STAT3, VEGFR2, ERK 1/2, Ang-1, PDGFB, and MMP2. Immunomodulatory activity through impact on CD4+ CD25+ Treg cells.	[190]
Tien-Hsien	*Cordyceps sinensis, Oldenlandia diffusa, Indigo Pulverata Levis, Polyporus umbellatus, Radix Astragali, Panax ginseng, Solanum nigrum, Pogostemon cablin, Atractylodis Macrocephalae Rhizoma, Trichosanthes Radix, Clematis Radix, Margarite, Ligustrum lucidum, Glycyrrhizae Radix*	Acute promyelocytic leukemia, breast cancer	Down-regulation of DNMT1, cyclin A, cyclin B1, p-AKT, Bcl-2, Akt/mTOR, Stat3, and ERK; induction of p21, p15, and apoptosis. Suppression of angiogenesis, metastasis, and tumor growth. Radiosensitization and immunomodulatory activity.	[191–193]
Zeng-Sheng-Ping	*Sophora tonkinensis, Polygonum bistorta, Prunella vulgaris, Sonchus brachyotus, Dictamnus dasycarpus, Dioscorea bulbifera*	Alimentary tract cancer; oral, lung, and bladder cancer	Inhibition of EGFR and Notch signaling. *In Clinic*: slowed down tumor growth and increased overall survival.	[194–196]

3.3.2. Ayurvedic Medicine

Ayurveda, translated from Sanskrit, meaning "life knowledge", is an ancient Indian traditional medical system which has been practiced for more than 5000 years and is still applied now by many cultural tribes in Indian sub-continent. Ayurvedic medicine is a unique holistic approach where herbal medicines, special diets, yoga, relaxation methods, and lifestyle management are key strategies for curing various chronic diseases such as diabetes, cancer, cardiovascular, neurological disorders, and many others.

As reported by Kuruppu and colleagues, between 70 and 80% of people in India, Nepal, and Shri Lanka practice this medical system [197]. Ayurveda attracts attention in other regions and countries, including the USA and Europe, as an alternative medical way for health recovery and maintenance [198,199].

About 1700 medical substances of herbal, animal, and mineral origin give birth to 40,000 different formulations for internal consumption and hundreds for external application (Sujatha, et al., 2021).

Ayurveda is supported by the government of India through the *Ayurvedic Pharmacopoeia of India* (API). This is a unique book divided in two parts. Part I (volumes 1–6) contains information about medical plants and their substances, whereas part II contains formulations from compounds described in part I. All in all, 450 medical herbs are listed in this book.

Bhandari and colleagues reported about 10 formulations which are readily available in the Indian market to cure neoplasia [200]. Thus, Ayurveda accounts a few dozen plants with anticancer properties [2,197,201]. Some of them have been also used in TCM and elsewhere, so they were described earlier. Several other very important anticancer ayurvedic plants are discussed below.

Withania somnifera (*WS*, "ashwagandha" or "winter cherry", the *Solanaceae* family) is an annual evergreen shrub which grows in India, the Middle East, and in some African regions. This is a very important Ayurvedic plant which is used as an energy balancer, and

to cure arthritis, anxiety, insomnia, bronchitis, male disfunctions, etc. Ashwagandha is also sold in western markets as a food supplement to increase energy and endurance [202].

The main biologically active chemical constituents of WS are alkaloids (isopelletier-ine, anaferine, cuseohygrine, anahygrine, etc.), steroidal lactones (withanolides and with-aferins), and saponins [203]. The extracts of Ashwagandha selectively killed cancer cells and inhibited xenograft's growth [204,205] through mitochondria-dependent apoptosis and G2/M cell cycle arrest. In other studies, extracts of *WS* suppressed the growth of malignant cell models and xenografts of breast, prostate, lung, gastrointestinal cancer, glioma, etc. This was associated with the down-regulation of p-AKT, VEGF, MMP-2, ERKp44/42 [206], cyclin D1, NF-kB, HSP-70, and NCAM, bcl-xl [207], as well as the reacti-vation of FOXO3a/Par4 [208]. The antineoplastic activity of WS is significantly associated with the presence of steroidal lactone whithaferin A.

A large number of studies have demonstrated the pleiotropic whithaferin-A-mediated down-regulation of cancer. This affects many characteristics of malignant cells (reviewed in [209,210]).

Withaferin A and withanone were able to attenuate EMT, driven by TNF-α and TGF-β in NSCLC cell lines H1299 and A549 [211]. Withaferin A inhibited glycolysis and complex III of the respiratory chain in breast cancer mouse models, indicating that it can interfere with metabolic rewiring in neoplasms [212]. A couple of studies reported that withaferin A can effectively target cancer stem cells (CSCs) [213,214].

Bearing in mind the safety and antitumor properties of *Withania somnifera* (Ashwa-gandha), its active constituent withaferin A should be studied in detail regarding therapeu-tical usage.

Curcuma longa ("Tumeric", the *Zingiberaceae* family) is a flowering plant, which is native to South Asia, India, and Indonesia. Its roots and rhizomes are widely used as a spice named "turmeric" which is a key ingredient in curry. This plant helps to reduce inflammation, hepatic and neurodegenerative disorders, metabolic syndrome, obesity, and other illnesses.

The major biologically active constituents of turmeric are diarylheptanoids, which occur in a mixture of dubbed curcuminoids (curcumin, desmethoxycurcumin, and bis-desmethoxycurcumin) that generally amount to approximately 1–6% of the plant by dry weight [215]. In addition, *C. longa* is another species of the Curcuma genus that contains a diverse composition of volatile (zingiberone, tumerone, and atlantone) compounds with a set of biological activities, including anticancer activity (reviewed in [216]).

However, the main pharmacological activity of *C. longa* is attributed to curcumin [217]. Curcumin acts through the modulation of multiple signaling pathways. It is known to inhibit the activity of transcriptional factors (STATs, Notch-1, NF-κB, PPAR-γ, WTG-1, and β-catechin), growth factors (FGF, VEGF, TGF-β1, TF, CTGF, and EGF), a number of receptors and kinases (EGFR, HER-2, CXCR4, MAPK, ERK1/2, RAK, PKA/B/C, Bcr-Abl, JNK, and IKK), and pro-survival proteins (Survivin, Mcl-1, Bcl-xL, cIAP-1, cIAP-2, and Bcl-2) [218,219].

Curcumin down-regulates cyclooxygenase (COX-2), EGFR, and ERK1/2 in lung and pancreatic cancer [220]. A number of literature sources report that curcumin activates autophagy in various malignancies, including melanoma, pancreatic [221] and gastric cancer [222], and glioma [223]. It may also target CSCs in esophageal carcinoma [224], hepa-tocellular carcinoma [225], and glioma [223]. Curcumin makes cancer cells more vulnerable to chemotherapeutic agents (doxorubicin, paclitaxel, 5-fluorouracil, and cisplatin) [226–229] and radiotherapy [230,231].

Zingiber officinale is a widely known plant because its whole rhizome—ginger—is widely used as a spice and in folk medicine. Its healing effects extend to diseases of the gastrointestinal tract, as well as the broncho pulmonary system.

Ginger is rich in phenolic compounds including gingerols (6-gingerol, 8-gingerol, and 10-gingerol), shogaols, paradols, quercetin, zingerone, gingerenone-A, and 6-dehydrogingerdione.

Moreover, ginger contains bioactive volatile oils. Its terpene compounds are zingiberene, β-bisabolene, α-curcumene, α-farnesene, and β-sesquiphellandrene [232,233].

There is a lot of evidence which shows the potential of ginger to prevent and suppress tumors, especially gastrointestinal cancer (GI). Ginger extracts and its individual constituents allow the multitargeted influence on cancer cells affecting Bcl2, p38/MAPK, EGFR, VEGF, AKT, ERK1/2, etc. [234].

In vivo studies have shown that ginger extract reduced NF-κB and TNF-α expression in rat livers with induced cancer [235]. Furthermore, 6-shogaol inhibits JAK2 and c-Src kinases [236], interleukin (IL)-6-induced STAT3, and TNF-α-induced NF-κB activation [237]. Zingerone and its derivates synergistically suppressed TGF-β-induced EMT and the invasion of hepatocellular carcinoma [238].

In addition, 6-shogaol reduced breast CSCs (CD44 + CD24−) and killed spheroids. This was associated with reduced Notch and its targets Hes1 and cyclin D1, and induced autophagy-based cell death [239].

In mice bearing Ehrlich carcinoma, the administration of doxorubicin in combination with ginger extract reduced the tumor volume and increased the survival rate by activating the AMPK pathway and reducing the cyclin D level [240]. In addition, both ginger extract and its isolated constituencies were shown to overcome methotrexate [241] and dodetaxel resistance [242] in AML and prostate cancer.

A more detailed description of ginger effects on the properties of various malignancies types is reviewed in [232,243,244].

Boswellia serrata and other *Boswellia* species are very important ayurveda plants which have been used for centuries to treat chronic ailments—arthritis, inflammatory bowel disease, diabetes, asthma, cancer, and others.

This plant is the source of "Frankincense", which is oleo gum resin extracted from the Boswellia species. Frankincense is a mixture of essential oils, polysaccharides, and resin acids. It contains a number of different types of boswellic acids (BAs) which are pentacyclic terpenoids. The main ones are: α- and β-BA, acetylated α- and β-BAs (ABA), 11-keto-β-BA (KBA), and 3-O-acetyl-11-keto-β-BA (AKBA) [245,246].

Essential oils are represented by α-thujene, α-terpineol, eudesmol, verbenene, thujone, pinocarveol, etc. [247,248]. Both BAs and volatile oils are responsible for Boswellia's antineoplastic properties [246].

A number of studies have shown the anticancer properties of frankincense [249]. A study on the cytotoxicity of oleo gum resin fractions revealed anticancer activity at the IC50 levels even lower than for doxorubicin and 5-fluouracil [250].

An in vivo study has demonstrated that frankincense suppressed melanoma in C57BL/6 mice with no detrimental effects on body weight; observable histopathologic differences in the brain, heart, liver, and kidney tissues; and hematological biochemical parameters [251]. The cytotoxicity was associated with a decreased Bcl2/BAX ratio.

A number of papers are devoted to the anticancer properties of BAs and their natural variants [246]. They down-regulate NF-kb and STAT3 [252,253], MAPK, AKT, ERK1/2, and other key signaling mediators.

As a possible mechanism of activity, Shen and colleagues [254] have shown that BAs may induce epigenetic alterations by modulating DNA methylation. The authors have shown that, in CRC cell lines, there was a modest increase in genome-wide DNA demethylation. This resulted in the re-expression of SAMD14 and co-suppressor genes SMPD3, as well as in the inhibition of DNMT activity. In line with this evidence, Mazzio and colleagues [255] have carried out transcriptomic profiling of TNBC MDA-MB-231 cells treated with *Boswellia serrata* or 3-O-acetyl-B-boswellic acid. They found that this treatment elicits the activation of several key components of the PERK pathway (unfolded protein response (UPR))—PERK, CHOP, GADD34, and ATF3), the induction of tumor suppressor genes and mTOR inhibitors (e.g., sestrin 2 (SESN2)), and Tribbles homolog 3 (TRIB3). On the contrary, this treatment inhibited the hyaluronan binding (CEMIP) of

oncogenes, transglutaminase 2 (TG2), and SRY box 9 (SOX9) which was associated with cell death induction.

Taken together, *Boswellia serrata* and BAs possess significant antineoplastic effects. BAs are considered to be excellent structures to develop lead compounds which may also be conjugated with other therapeutic drugs [256]. Numerous semisynthetic BAs have been developed with very good cytotoxicity [257].

The phase 1 clinical trial on Boswellia (which is the extract from frankincense) for breast cancer primary tumors (NCT03149081) is ongoing and intends to assess its influence on markers of proliferation, angiogenesis, and apoptosis.

Plants of the genus **Xanthium** (the *Asteraceae* family) are sources of bicyclic sesquiter-pene lactone xanthatin. Several species, including *Xanthium strumarium*, have been used as medical plants in Ayurveda, Chinese, and other traditional Asian medical systems.

In triple negative breast cancer MDA-MB-231 cells, xanthatin decreased the catalytic function of topoisomerase II, which led to GADD45γ up-regulation and arrested cells in the G2-M state [258]. Using the same breast cancer cell model and mouse xenografts, other authors have shown that xanthatin inhibits vascular endothelial growth factor receptor 2 (VEGFR2), reducing VEGF-stimulated angiogenesis, microvessel density, and tumor growth [259].

In A549 cells (NSCLCs), xanthatin disrupted NF-κB signaling and induced p53, which resulted in G2-M arrest and the activation of the intrinsic apoptotic pathway [260]. Xanthatin also suppressed NSCLC by diminishing STAT3 and GSK3β transcription factors [261,262].

Through its application to child retinoblastoma cell models and zebrafish xenografts, Yang and colleagues have shown that xanthatin targets polo-like kinase 1 (PLK1), mediating G2-M cell cycle arrest and apoptosis [263]. In colon cancer cells, xanthatin similarly stopped cells in G2-M. It elevated ROS, autophagy, and apoptotic response [264], while suppressing glycolysis and mTOR signaling [265].

Xanthatin induced the cell death of glioma cell lines and xenografts via the elevation of endoplasmic reticulum (ER) stress-related proteins, including glucose-regulated protein 78 C/EBP-homologous protein (CHOP) [266].

In this way, xanthatin is very interesting in terms of antitumor therapy.

In general, many Asian plants are known with neoplastic properties described in reviews [267–270]. In addition, other plants and their active substances with emerging antitumor activities have recently been identified [271,272], which indicates that there are many such plants that have not yet been discovered.

Other major medical plants traditionally used in ayurveda for cancer healing are described in the excellent review [2].

3.4. Europe

Hypericum perforatum (HP, St. John's wort, SJW, the *Hypericaceae* family) is a flowering plant native to Europe and Asia. It was also introduced to North and South America, South Africa, and Australia. HP is still used in folk medicine and now is commercially grown in different countries. It is effective in the treatment of anxiety and depression which is mediated by inhibiting the uptake of monoamine neurotransmitters (serotonin, dopamine, noradrenaline, GABA, and L-glutamate) [273]. *HP* is effective against inflammation and urinary cystitis.

The pharmacological properties of *Hypericum perforatum* are associated mainly with hyperforin (HPF) and hypericin, which usually present in a total hydro-alcoholic HP extract concentrations ranging between 1 and 5% and 0.1 and 0.3%, respectively [274]. Other *HP* constituents are hyperoside, rutin, quercetin, catechin polyphenols, acylphloroglucinols, and naphthodianthrones [275].

HP extracts and hyperforin decrease the inflammation by suppressing 5-lipoxygenase (5-LO), cytochrome c oxidase subunit I (COX-1) activity [276], and prostaglandin PGE2

production [277]. It also reduces ROS [278] and genotoxic stress [279]. These, and other, properties of *HP* protect from carcinogenesis [274].

In multiple studies, both *HP* extracts and hyperforin have demonstrated antineoplastic activity against different types of malignancies. They attenuated cell growth, angiogenesis, and metastases, while inducing apoptosis (reviewed in [274]). Hyperforin inhibited EGFR/ERK/NF-κB [280] and AKT [281] signaling pathways. It suppressed antiapoptotic proteins Bcl-2 and Mcl-1 [282]; reduced the production of angiogenic chemokines CXCL8 and CCL2 [283]; and decreased metalloproteasis MMP2, MMP9, elastase, and cathepsin, which are important for migration and invasiveness [284].

It is interesting to note that the mechanism of hyperforin's antineoplastic activity is thought to be associated with its protonophor properties. Due to a low ΔpH between intercellular space and cytosol in non-cancer cells, protonofor hyperforin does not significantly change their intracellular pH. At the same time, the ΔpH of cancer cells is much higher because of the acidic extracellular space and more basic cytoplasm. In this case, hyperforin induces the increased H+ influx which leads to cytosol acidification and interferes with biochemical processes in malignant cells [274,285].

The analysis of 87 HP samples which were collected from 14 countries concluded that there was limited chemical variability [286]. In view of HP's inclusion in European Pharmacopeia and standardization opportunities, it can be considered a potential antineoplastic substance.

Betula pubescens (*BP*, syn. *Betula alba*, the *Betulaceae* family), commonly known as white birch, is native and abundant throughout northern Europe and northern Asia. Its bark contains betulinic acid (BA)—a lupane-type pentacyclic triterpenoid saponin.

In tumor cells, BA activates the mitochondrial pathway of apoptosis. It permeabilized the outer mitochondrial membrane, and also induced cytochrome c release and caspase activation [287].

Several signaling pathways are shown to be affected by BA [288]. It dampens STAT3 and HIF-1α which reduce angiogenesis. BA augments the MAPK/p38 and JNK signaling pathways [289]. Guo and colleagues have shown that mTOR signaling was targeted by BA which initiated apoptosis [290]. In turn, another group has demonstrated that BA suppressed p-AKT and mTOR while inducing autophagy [291]. Apparently, this autophagic response can mitigate BA-induced mitochondria-dependent cell death [292].

In breast cancer cells, BA attenuated glycolysis and respiration [293]. It is important to note that BA attenuates the expression of multidrug resistance proteins P-gp, BCRP, and ABCB5, hence decreasing chemotherapeutic resistance mediated by mutant EGFR [294].

To improve the water solubility and antineoplastic activity of BA, different research groups are currently working on the synthesis of its soluble derivatives [295].

Glycyrrhiza glabra (*GG*, "Liquorice", the *Fabaceae* family) is an herbaceous perennial legume flowering plant native to Europe, Western and Central Asia, Siberia, and Northern Africa. This plant was used in folk medicine in ancient Egypt, Rome, Greece, and China, and has been included in Ayurveda.

GG has a rich biochemical composition as 400 compounds were isolated from this plant. The most important among them are triterpenoid glycyrrhizin; saponin glycyrrhizic acid; the flavonoids liquiritin and isoliquiritin; and the isoflavones glabridin and hispaglabridins A and B [296]. This set of chemicals mediate a huge number of beneficial pharmacological properties, including antitussive, expectorant, antimicrobial, anticoagulant, and memory-enhancing activity, as well as antioxidant, anti-inflammatory, antidiabetic, hepatoprotective, immunomodulator, and antineoplastic capabilities.

Regarding the antineoplastic properties of *GG*, isoliquiritigenin (2′,4′,4-trihydroxychalcone, ISL) is one of the most important compounds extracted from licorice roots. ISL displays a suite of antitumor properties [297]. In lung cancer cell models, ISL inhibited proliferation by interfering with AKT/mTOR [298] and FAK/Src signaling pathways [299]. Src family kinase (SFK) transmits signals from integrins, growth factors, and G protein-coupled receptors to AKT/mTOR, MAPK/ERK, and Hippo signaling pathways. Src/FAK mediates

modifications in the actin cytoskeleton and focal adhesion complexes, facilitating migration and invasion [300]. In renal carcinoma cells, ILS down-regulates Jak2/STAT3 and MDM2 ubiquitin ligase. MDM2 possesses oncogenic properties, i.e., the main negative regulator of the p53 tumor suppressor [301], as well as through various p53-independent ways [302,303]. ISL treatment of melanoma cells decreased miR-301b and recovered its target leucine-rich repeats and immunoglobulin-like domains 1 (LRIG1) which down-regulates tumor growth [304].

In silico docking experiments suggest that ISL can possibly directly target VEGF-2, both wild-type and double-mutant (L858R/T790M) EGFR, 78-kDa glucose-regulated protein (GRP78), sirtuin 1 (SIRT1), COX-2, and Ikkb [297].

Besides ILS, other compounds of GG (glycyrrhizin, glycyrrhizinic acid, etc.) possess antineoplastic activities (reviewed in [297]). This, together with the safety of GG, which is proven by centuries of use, makes this plant a very promising candidate for anticancer therapy studies.

Silybum marianum (***SM***, "milk thistle", the *Asteraceae* family) is a biennial herb, 30 to 200 cm tall with red-to-purple-colored flowers. Its native distribution area includes the Mediterranean Sea coast, the coast of southeast England, Iran, and Afghanistan. However, this plant was introduced to other continents and was cultivated due to its medical properties.

SM is important for medicine as a source of silymarine, which is the standardized extract from the thistle milk seeds, containing at least seven flavonolignans (silybin A, silybin B, isosilybin A, isosilybin B, silychristin, isosilychristin, and silydianin) and one flavonoid (taxifolin). Symilarin accounts for 65–80% of *SM* seeds. Its compounds provide the main SM pharmacological activity. The important pharmacological activity also has silybinin which is a semi-purified fraction of silymarin, consisting of a mixture of two diastereoisomers, silybin A and silybin B, in an approximate 1:1 ratio [305].

Silymarine possesses hepatoprotective (chronic hepatitis B and C, alcoholic hepatitis, fatty liver disease, and cirrhosis), antidiabetic, anti-ischemic, and skin-protective properties, as well as others [306]. In the oral cancer models, sylimarin induced the extrinsic apoptotic pathway, decreased tumor volumes, and prolonged mouse lifespan [307]. In human colorectal cancer cells, silymarin may down-regulate the Wnt signaling pathway through β-catenin proteasomal degradation and TCF4 transcriptional inhibition [308].

Silibinin also possesses anticancer activities: the inhibition of proliferation, migration, and metastasis; angiogenesis; and the induction of apoptosis due to the down-regulation of EGFR, Akt, MAPK, and Wnt signaling pathways [309,310]. Silibinin suppressed the growth of human gastric cancer cells by down-regulating MAPK signaling. In the TNBC cell line MDA-MB-231, this compound also reduced the TGF-β-mediated expression of fibronectin and metalloproteinases MMP2, MMP9, and metastasis in xenograft models [311]. In hepatocellular carcinoma models, the combination of silibinin with sorafenib was demonstrated to down-regulate Akt-STAT3 signaling, anti-apoptotic proteins (Bcl-2 and Mcl-1), and stemness-related proteins (homeobox transcription factor (NANOG)) and Krueppel-like factor 4 (Klf4) [312].

Several studies have demonstrated that silymarin is safe for humans and is tolerated even at a high dose of 700 mg three times a day for 24 weeks (reviewed in [313]). This obstacle, in light of its anti-neoplastic and hepatoprotective capabilities, as well as the presence of standardization, makes silymarin the excellent candidate for cancer treatment, especially for hepatocarcinoma.

Some other European plants and their compounds with anti-neoplastic activity are listed in Table 4.

Table 4. Some European plants and their compounds with anti-neoplastic activity.

Plant	Biologically Active Compounds	Effects	References
Allium sativum	Allicin, alliin, diallyl disulfide, diallyl trisulfide, Z-ajoene, S-allyl cysteine, S-propargyl-L-cysteine, S-allyl cysteine	Multiple anticancer effects and known molecular mechanisms of both crude extracts and individual compounds. Suppression of angiogenesis and migration in vivo.	[314]
Arctium lappa	Arctigenin, lappaol F, stigmasterol ß-sitosterol	Suppression of growth, invasion, and migration of cancer cell lines. Inhibition of hippo-signaling pathway. Reduction in tumor growth in vivo.	[315–317]
Centaurea solstitialis	Solstitialin A	Cytotoxic and cytostatic effects in a panel of cancer cell models	[276,318]
Ebenus boissieri		Antiproliferative and cytotoxic effects in human breast, cervical, and lung cancer cell lines. Induction of TNF-α expression.	[319–321]
Rosmarinus officinalis	Carnosol, carnosic acid, sageone, rosmarinic acid	Multiple antineoplastic effects in vitro and in vivo with known molecular mechanisms, including epigenetic regulation.	[322]
Menyanthes trifoliata	Betulinic acid, syringic acid, ellagic acid, rutin, chlorogenic acid	Cell cycle G2/M arrest and apoptosis in grade IV glioma. No toxicity to normal human astrocytes.	[323]
Vitis vinifera	Viniferin, resveratrol	Multiple anticancirogenic and antineoplastic effects with known molecular mechanisms.	[324,325]
Viscum album	Iscodor, helixor A, lectins (ML-I, ML-II, and ML-III), viscotoxins, polysaccharides, phenolic compounds	Cytostatic and cytotoxic effects in vitro and in vivo. Immunomodulatory activity and reduction in cancer-related fatigue in clinical studies. Helixor A and Iscador are used in Europe as adjuvants in cancer therapy.	[326,327]

3.5. North America

Panax quinquefolius (*PQ*, Panax americanus, the *Araliaceae* family) is a perennial herbaceous plant 30–100 cm high with a thick tuberous rhizome. It mainly grows in the USA, in the wooded areas of Maine and Missouri, and in Canada, in the provinces of Ontario, British Columbia, and Quebec. It is known that various Indian peoples took decoctions and infusions from the ginseng root to treat ulcers, asthma, and various inflammatory eye diseases, as well as to increase fertility levels. PA is a close relative of Panax ginseng which is the most widely used ginseng in China, Korea, and Japan. These plants have similar pharmacological properties.

According to the FDA, ginsengs are generally recognized as safe (GRAS) plants, and their inhibitory effects on malignant tumors have been widely accepted in the USA and Europe [328]. Ginseng is characterized by the presence of ginsenosides, which are ginsengs triterpenes saponins (Rx), considered to be the main bioactive compounds of ginseng. They are also metabolized by the gut microbiota to undergo sequential de-glycosylation and are finally converted to prosaposin or sapogenins within the human body. Based on the structure of aglicon, Rx may be divided into five types: panaxatriol saponin, protopanaxadiol, protopanaxatriol, oleanolic acid, and ocotillol types [329].

Various ginsenosides have demonstrated anticancer properties in vitro and in vivo following the inhibition of cell cycle, angiogenesis, and the induction of apoptosis in different types of malignancies [328,330].

Ginsenoside Rg3 reduced colon carcinoma in HCT116 cells, whereas its derivate 20(S)-protopanaxadiol effectively attenuated NF-κB, JNK, and MAPK/ERK signaling pathways [331]. Other ginsenosides, Rb3, R1, and Rc, bound Hsp90α, suppressing the activity

of SRC and PI3K kinases. This led to the inactivation of Akt and ERK pathways and lung cancer suppression [332]. In patient-derived xenograft mouse models and glioblastoma stem cell lines, ginsenosids Rg3 and Rh2 suppressed cell viability and the self-renewal capacity of GSCs via the inhibition of the Wnt/β-catenin signaling pathway [333]. In pancreatic cancer in vitro and in vivo models, Rg3 treatment reduced the levels of vasculogenic mimicry, matched with the decrease in VE-cadherin, EphA2, MMP-2, and MMP-9 mRNA [334].

The structure–activity relationships of ginsenosides and the molecular mechanisms of their actions are summarized in the following review [335]. According to literature data surveys, Rh1, Rh2, and Rg3 have strong anti-cancer activities. Because of a number of biologically active compounds identified, as well as FDA-reported safety concerns, Panax-standardized plant material and ginsenosides are promising candidates for anti-neoplastic adjuvant therapy.

Some other North American plants and their compounds with anti-neoplastic activity are listed in Table 5.

Table 5. Some others North American plants and their compounds with anti-neoplastic activity.

Plant	Biologically Active Compounds	Effects	References
Aristolochia foetida	β-sitosterol, stigmasterol, and other compounds	Apoptosis in MCF-7 cancer cells with less toxicity to non-tumor cells.	[336]
Asimina triloba	Acetogenins	Extracts from different parts of plant suppressed proliferation; induced apoptosis in AGS and HeLa cells; inhibited inflammatory makers NO, TNF-α, IL-6, and iNOS (inducible nitric oxide synthase).	[337]
Capraria biflora	Biflorin	Different anticancer effects in a number of tumor cell lines. Inhibition of c-MYC expression.	[338,339]
Echinacea purpurea	Echinacoside, alkylamides	Reduced proliferation, increased level of ROS, caspase 3 activity, and apoptosis in human lung cells. Inhibition of Wnt/β-catenin pathway. Immunomodulatory activity in vivo.	[340,341]
Sanguinaria canadensis	Sanguinarine, chelerythrine, berberine	Cytotoxic and antiproliferative effects in melanoma and child ALL cell lines. Induction of apoptosis by cIAP1, cIAP2, and XIAP suppression in pre-ALL cell lines. Sanguinarine and berberine binds G-quadruplex in oncogenes and telomeres.	[342–344]

3.6. Australia

Although Australia is a habitat for more than 21,000 plant species, there is extremely limited information about their medical use by indigenous peoples. There is especially little data on their anti-neoplastic properties. The well-known example is ***Eremophila galeata*** (*EG*, the *Scrophulariaceae* family), a flowering shrub which is endemic to Western Australia. This plant has a long history of use in medicine by indigenous peoples because of its valuable pharmacological properties [345].

Petersen and colleagues identified that the crude extract prepared from EG leaves significantly sensitized HT-29 cells to SN-38—a modern topoisomerase I inhibitor. One of its major compounds, the 5,3′,5′-trihydroxy-3,6,7,4′-tetramethoxyflavone, strongly suppressed the breast cancer resistance protein (BCRP/ABCG2) [346] which belongs to the family of ATP-binding cassette proteins. BCRP mediates multidrug resistance and promotes an efflux

of such potent drugs, such as methotrexate, irinotecan, topotecan, sorafenib, gefitinib, and doxorubicin, from cancer cells [347].

Some other medical Australian plants with anticancer properties are listed in Table 6. Thereby, Australian plants are extremely unstudied to date in terms of antitumor properties.

Table 6. Some other Australian plants and their compounds with anti-neoplastic activity.

Plant	Active Compounds	Effects	References
Terminalia ferdinandiana	Tannins, flavonoids: gallic acid, ellagic acid, lutein, hesperitin, kaempferol, luteolin, and quercetin	Antiproliferative and proapoptotic activity in cancer cell lines. No toxicity to human dermal fibroblasts and shrimp *Artemia franciscana* bioassay.	[348,349]
Tasmannia lanceolata	Phenolic acids: coumaric acid, chlorogenic acid. Flavonoids: quercetin, quercetin 3-rutinoside, and anthocyanin (cyanidin 3-rutinoside)	Cytotoxicity to different cancer cell models with non-significant effects on normal colon, stomach, and intestine cells.	[350]
Davidsonia pruriens	Anthocyanin compounds, flavanoids	Significant cytotoxicity to a panel of cancer cell models and low toxicity in the *Artemia nauplii* bioassay.	[351,352]
Elaeocarpus angustifolius	Not identified	Significant cytotoxicity to Hela and Caco-2 cell models and low toxicity in the *Artemia nauplii* bioassay.	[352]
Pittosporum angustifolium	Alcaloids, saponins	Antiproliferative effects of 7 saponins with IC50 values in a range of 1.74–34.1 μM for MCF7, HaCaT, LN18, and 5637 cancer cells.	[353]

4. Mushrooms

About 2.2–3.8 million fungi exist on our planet, including 14,000 mushroom species [354]. Interest in mushrooms as a medical supply is rooted in the mists of time and prevails to these days. Mushrooms are used in the traditional medicine of China, Ayurveda, East Asia, Europe, South America, etc. A number of mushroom species are implicated as food supplements to improve health in different regions, including the USA and Europe. Several big company sale food supplements contain, or are fully derived from, mushrooms. For instance, iHerb (USA, California, www.iherb.com; accessed on 30 March 2022), Fungi Perfecti (USA, Olympia, www.fungi.com; accessed on 30 March 2022), Ommushrooms (USA, Carlsbad, www.ommushrooms.com; accessed on 30 March 2022), Terezia (Czech Republic, Praha, https://www.terezia.eu/en/; accessed on 30 March 2022), Realmushrooms (Canada, Roberts Creek (BC), www.realmushrooms.com/; accessed on 30 March 2022), Time Health (UK, www.timehealth.co.uk; accessed on 30 March 2022), Zipvit (UK, Staffordshire, https://www.zipvit.co.uk/; accessed on 30 March 2022), Hangzhou Molai Biotech Co., Ltd. (China, Hangzhou, https://phytonutri.en.made-in-china.com; accessed on 30 March 2022), and Shaanxi Shineherb Biotech Co., Ltd. (China, Shaanxi, www.shineherb.en.made-in-china.com; accessed on 30 March 2022) are among them. The main mushrooms which are explored by humans as beneficial for health are reishi, cordyceps, turkey tail, maitake, lion's mane, chaga, and others.

Nowakowski and colleagues have summarized 92 mushroom species with antineoplastic activity, which could be effective against 38 various cancers [355]. Mushrooms display a great number of secondary metabolites with different biological activities [356–358]. In addition, these metabolites are different from secondary metabolites of plants. Regarding cancer healing, mushroom and fungi, in general, as well as their biochemical diversity, are almost fully unexplored to date.

Below, we give some examples of mushrooms that possess antitumor properties and have been used in traditional medicine.

Lentinula edodes is a mushroom that grows in East Asia. It is known as "Xianggu" in China and "Shiitake" in Japan. The mushroom has been used as food and in traditional Chinese medicine for at least 2000 years. It possesses analgesic, tonic, and antiparasitic activities [359].

Preclinical studies have identified that shiitake has immunostimulating, antibacterial, antiviral, hepatoprotective, antimutagenic, antihypercholemic, and anticancer properties due to the content of lentin, lignin, and erytadenine in the fruiting body [359].

Among others, shiitake chemical composition includes polysaccharides, polysaccharopeptides, lectinss, and lentinan, the last of which is especially focused on the medical attributes of this mushroom [355].

The polysaccharide lentinan (1,3 beta-D-glucan), when isolated from shiitake, has shown strong antitumor properties. There are studies demonstrating the existence of the direct cytotoxic effects of shiitake extracts on cancer cells in parallel with minimal impact on non-malignant cells. One group reports the direct apoptotic effects of shiitake mycelia extracts on human hepatocellular carcinoma cells with minimal toxicity to normal rat cells [360]. Other researchers have shown the direct cytotoxic effects of fruit bodies, but not mycelia extract, on MCF7 cells, with far less significant cytostatic effects on fibroblasts [361].

In several in vitro studies, the synergistic effects of lentinan with docetaxel, paclitaxel, and cisplatin on proliferation and apoptosis have been shown. Lentinan sensitized lung cancer cells to paclitaxel through ROS-TXNIP-NLRP3 inflammasome and ASK1/p38MAPK signaling pathways [362]. It also sensitized bladder cancer to gemcitabine [363] and gastric cancer cells to docetaxel and cisplatin [364]. Lentinan increased the sensitivity of HepG2 hepatoma cells and xenograft H22-bearing mice to oxaliplatin, which was associated with NF-kb, STAT3, and surviving suppression [365].

One more application may be doxorubicin-conjugated lentinan nanoparticles, which increased cytotoxicity for breast cancer while decreasing it for human normal cells [366].

The direct antitumor activity of water-extracted polysaccharide on cancer cells has also been demonstrated using athymic nude mice and human colon cancer cells [367]. In this model, lentinan-induced ROS mediated both TNF-α and mitochondria-dependent apoptosis.

Nevertheless, the main mechanism of the lentinan-mediated anticancer response is proposed to be associated with the stimulation of the immune system. Different mechanisms are suggested to be responsible for this. The modulation of the TLR4/dectin1-MAPK and Syk-PKC-NFκB signaling in immune cells is reported. In patients with digestive cancer, lentinan removed the dominant state of Th2 which restored Th1-Th2 lymphocyte (Tregs) balance [368–371]. Th1 cells possess antitumor activity and produce IFN-γ and IL-12, whereas Th2 is characterized by IL-4 and IL-10 production and may promote malignization [372,373].

In clinical concentrations, lentinan down-regulated PD-L1 which enhances the efficiency of adaptive immunity.

Lentinan decreased the granulocytes–lymphocytes (G/L) ratio in gastric cancer patients opposed to those who have only received chemotherapy, and prolonged their survival [374]. The G/L ratio (neutrophil–lymphocyte ratio) is suggested as a prognostic marker, and is associated with an increased tumor progression, invasion, and shortened survival in different types of malignancies including gastric cancer [375,376]. Solid tumors express granulocyte colony-stimulating factor (G-CSF) which induces the proliferation of leukocytes (neutrophils) and myeloid-derived suppressor cells (MDSCs). Both of them suppress the proliferation of lymphocytes and lymphocyte-activated tumor cells killing those which favor malignization [377]. Lentinan was shown to decrease the G-CSF serum level and inhibited MDSCs via a CARD9-NF-κB-Ido pathway which may be responsible for a decrease in the G/L ratio and partially responsible for anticancer properties [378,379].

Wang and colleagues reported that the addition of lentinan to the combination therapy of vinorelbine and cisplatin in a cohort of 73 patients with NSCLC resulted in an approxi-

mately two-fold increase in NKT-cells [379]. This was accompanied by the shift of Tregs status from Th2 to Th1, in accordance with the elevation of IFN-γ, TNF-α, and IL-12.

In China and Japan, lentinan was used as an adjuvant therapeutic drug. The meta-analysis of 650 gastric cancer patients has shown that lentinan significantly increased their survival and was mostly effective in patients with lymph node metastasis [380]. Lentinan also increased the lifespan of patients with hepatocellular carcinoma [381] and improved the quality of life of patients with unresectable pancreatic cancer [382].

Zhang and colleagues reported about 9500 cancer patients who were treated with lentinan for a period of 12 years [371]. A number of studies demonstrated that lentinan improved a patient's survival rate, seemingly irrespective of the tumor type [374,383].

Nevertheless, the mechanisms of this phenomenon are not fully understood today. In summary, shiitake and lentinan are valuable for cancer treatment, but further intensive studies of their antineoplastic mechanisms with possible side effects and limitations are required, as well as well-designed clinical trials.

Ganoderma lucidum (Gl) is a mushroom that grows on plum trees in many Asian countries. It is commonly known as "Reishi" in Japan and "Ling-zhi" in China. In traditional Chinese medicine, reishi has been called the "mushroom of immortality" or the "spirit plant" and has been actively used to prevent cardiovascular diseases; strengthen the immune system; and cure neurological afflictions, allergies, and liver disorders for many centuries [384]. Moreover, reishi is a part of adjuvant therapy of cancer and diabetes.

As in the case of shiitake, reishi suppresses tumor cells both directly and through fine-tuning of the immune system. Severe combined immunodeficient (SCID mice) cells, bearing human inflammatory breast cancer cells, when treated with *Gl* extract, significantly reduced tumor growth and weight, accompanied with the attenuation of Ki-67, vimentin, p-ERK1/2, Akt, and mTOR (as well as its targets p70S6K and eIF4G) [385]. The in vitro model has also proven the reishi-mediated suppression of protein synthesis and proliferation, whereas it was not toxic to non-tumor breast MCF10A cell lines [386]. The *Gl* extract was able to attenuate lamellipodia formation, thus inhibiting the motility of MDA-MB-231 breast cancer cell lines. This was associated with a reduction in Rac kinase activity, as well as p-FAK (Tyr925), Cdc42, and c-Myc expression [387].

Different compounds with medical properties have been identified in reishi extracts. Although the plethora of them may be responsible for antitumor activity, ganoderic acid (GA) and *Ganoderma lucidum polysaccharides* (*GLPs*) are proposed to be the most important of them [388]. The antineoplastic activity of reishi is manifested as both direct cytotoxicity to cancer cells or indirect cytotoxicity through the stimulation of the immune system [389].

GA is a natural triterpenoid whose molecular structure is similar to steroid hormones and has multiple isoforms [390]. It is proposed that GA targets several receptors (IGFR-1, VEGFR-1 and -2, and ER) [391] and is shown to inhibit the PI3K/Akt/mTOR pathway [392], induce DNA damage [393], down-regulate MMP-2 and -9 [394], and affect other oncogenic activities [388].

Ganoderma lucidum polysaccharides (*GLPs*) are considered to be the main antitumor compound of reishi [389,395]. *GLP* inhibited autophagic flux in colorectal and gastric cancer cells [396,397] and suppressed "aerobic glycolysis" (the Warburg effect) [398]. It down-regulated vimentin and EMT-associated TF Slug, and also inhibited the JAK/STAT5 pathway, motility, and the invasion of ovarian cancer cells [399]. Water-soluble glucose-enriched *Gl* polysaccharide attenuated the activation of EGFR and Akt, suppressed oral cancer cells, and sensibilized them to cisplatin, while protecting normal human oral epithelial cells from cisplatin-mediated cytotoxicity [400].

The major antitumor activity of GLP occurs through the modulation of the immune system [401]. GLP increased the proliferation and differentiation of B-lymphocytes, the activity of T-lymphocytes, and their IFN-γ production [402]. It increased several-fold the number of natural killer (NK) cells [403], and also increased the granulocyte–macrophage colony-stimulating factor (GM-CSF), the granulocyte colony-stimulating factor (G-CSF), and the macrophage colony-stimulating factor (M-CSF) [404].

Zhang and co-authors developed gold GLP composite nanoparticles which activated dendritic cells, promoted the proliferation of T killers and Tregs in splenocytes, elevated the percentage of CD4+/CD44+ memory T cells, and reduced tumor weight and metastasis in the 4T1 breast cancer mouse cell model [405].

GLP may be a promising prebiotic substance for the treatment of colorectal cancer. Using a mouse model of inflammatory colorectal cancer, Guo and colleagues reported that *GLP* treatment normalized dysbiosis; improved the gut barrier function; and suppressed IL-1β, iNOS, COX-2, and macrophage infiltration [406].

A randomized double-blind placebo-controlled study has shown beneficial effects for healthy volunteers upon *Gl* intake in terms of hepatoprotective and antioxidant activity [407]. An evaluation of 120 breast and lung cancer patients whose treatment was supplemented or not with *Gl* revealed the reverse correlation between *Gl* intake and immunosuppressive factors COX2 and TGF-β1 and positive correlation with anticancer IL-12 [408].

In conclusion, reishi is a safe non-toxic plant, and has been utilized as an alternative adjuvant in the therapy of cancer patients without obvious toxicity. It acts in synergy with antineoplastic drugs and is used clinically to treat various malignancies [389]. It deserves more attention as a potential adjuvant.

Grifola frondosa, commonly known as maitake, is an edible and medicinal mushroom that grows in Asian regions, especially in China, India, Japan, Korea, and some European countries. It has been used for centuries in traditional medicine for different purposes. The anticancer properties of this mushroom are especially attractive.

Several bioactive polysaccharide fractions could be separated from Gf: D-fraction, MD-fraction, X-fraction, Grifolan, MZ-fraction, and MT-α-glucan, which possess different biological activities [409]. For medical usage, in most cases, the so-called "D-Fraction" is prepared via extraction from fruit bodies. In this way, D-fraction is a standardized form of protein-bound β-glucans (proteoglucans) extracted from the fruit bodies of maitake. It predominantly contains β-D-glucans with β-(1→6) main chains and β-(1→4) branches, as well as more common β-(1→3) main chains and β-(1→6) branches [410].

It was shown that in the MDA-MB-231 TNBC cell line, D-fraction favored apoptosis, decreased motility, increased E-cadherin protein levels and β-catenin membrane localization, and reduced activity of MMP-2 and MMP-9 [411,412]. In the corresponding xenograft mouse model, D-fraction also inhibited tumor growth and metastasis.

The inhibitory effect was associated with the cell cycle arrest, diminished motility, and induced apoptosis. D-fraction suppressed hepatoma cells both in vitro and in vivo, which was associated with PI3K/AKT attenuation and an autophagy increase [413]. The Konno group demonstrated the strong synergistic cytotoxicity of D-fraction combined with vitamin C on prostate and renal cancer cells [414,415].

However, numerous studies have shown that the key ability of maitake to affect tumors is hidden in the stimulation of the immune system. Both the innate and acquired immunities are affected by D-fraction. In BALB/C mice, D-fraction blocked more than 60% of breast cancer development and prevented oncogenesis in 26%, with regards to control animals [416]. The other group has shown a long-term immunity activation in MM46-bearing C3H/HeN mice which was associated with an increase in TNF-alpha, IFN-gamma, and macrophage-derived interleukin (IL)-12, as well as the activity of NK cells [417]. Furthermore, D-fraction combined with vitamin C increased the percentage of CD4 + CD8 + T-cells, B-cells, and Treg cells, and also elevated IL-2, IL-12p70, TNF-α, and IFN-γ levels in Heps-bearing mice [418].

In B16 melanoma and colon-26 carcinoma mice, maitake-derived α-glucan (a highly α-1,6-branched α-1,4 glucan, YM-2A) elevated the antitumor immune response through the up-regulation of INF-γ-expressing CD4+ and CD8+ T-cells in the spleen and INF-γ-expressing T-CD8+ cells in tumor-draining lymph nodes. Moreover, orally administered YM-2A increased the expression of the MHC class II and CD86 on dendritic cells and the MHC class II on macrophages in Peyer's patches [419].

The meta-analysis of pre-clinical data revealed that Gf usage upon cancer treatment significantly inhibited tumor growth, and, on the contrary, improved remission rates, and also increased CD4+ and CD8+ T cell percentages, as well as IL-2, IL-12, and TNF-α [420].

Maitake-derived polysaccharide-based drugs were subjected to clinical trials. The Japan group reported cancer regression in about 58.3% of liver cancer patients, 68.8% of breast cancer patients, and 62.5% of lung cancer patients [421]. At the same time, there was only a 10–20% improvement for leukemia, stomach cancer, and brain cancer patients. In another investigation, D-fraction increased NK cell activity, attenuated metastatic progress, and improved the expression of tumor markers in all examined patients [422].

In China, a maitake-derived polysaccharide-based drug was approved by the State Food and Drug Administration (SFDA) in 2010 [423].

Strong antitumor properties and the safety of its use place maitake at the top of biological organisms which should be studied with respect of neoplasia.

***Cordyceps sinensis* (*CS*)** and ***Cordyceps militaris* (*CM*)** are important mushroom species for China and Korea. Both of them are entomopathogenic fungi which parasitize on the larvae of moth caterpillars. However, these mushrooms can be cultivated in a variety of media, including silkworm pupae, rice, and liquid nutrition. They have been used in Chinese medicine because of their anti-inflammatory, anti-microbial, immunostimulant, and antineoplastic properties [424]. The known bioactive compounds of these mushrooms are cordycepin, cordycepic acid, ergothioneine, lovastatin, and polysaccharides [425,426].

In the 4T1 orthotopic xenograft breast mouse model, an extract of Cs inhibited tumor growth and promoted macrophage polarization toward the M1 phenotype [427]. Cm extract was shown to suppress KRAS-driven colorectal cancer by attenuating the RAS/ERK pathway [428]. Another study reported that the Cm extract overcame cisplatin resistance in NSCLC cell lines when proteomic profile analysis revealed H-Ras down-regulation [429]. Other authors have demonstrated that its extract down-regulated hedgehog signaling in NSCLCs via TCTN3 inhibition and GLI1 nuclear translocation suppression [430].

The main pharmacologic activity of CS and CM is attributed to cordycepin. This is 3-deoxyadenosine, which has a similar structure to adenosine but lacks the $3'$-hydroxyl group of the ribose moiety [431]. Adenosine receptors are in the family of G-protein-coupled receptors, which are found in almost all human body tissues and organs. Specific ligands, agonists, or antagonists activate these receptors which modulate tumor growth via a range of signaling pathways [432].

Cordycepin is suggested to act through ADORA2 and ADORA3 receptors. It has been shown that the cordycepin-mediated activation of ADORA3 inhibits growth and induces apoptosis in bladder cancer and murine B16 melanoma, which can be associated with glycogen synthase kinase-3β activation and cyclin D 1 suppression [433–435]. In the HCC model, cordycepin suppressed focal adhesion kinase (FAK) activation which plays an important role in angiogenesis [436,437]. Cordycepin down-regulates PI3/AKT, MAPK/ERK, β-catenin, bcl-2, and cdk2, and also induces JNK, caspase-3 and -9, and PARP cleavage in renal, colon, bladder, lung, breast, prostate, glioblastoma cancer, and leukemia. This compound inhibited cell cycle, motility, invasion, and vascularization, while inducing apoptosis (reviewed in [431,438]). One more mechanism has been proposed for cordycepin neoplastic activity. It activates death receptors (DRs) which induce extrinsic apoptotic pathways [439,440]. With respect to the testicular cancer mouse model, cordycepin suppressed FGFs/FGFRs pathways, ERK1/2, Rb/E2F1, cell cycle, and tumor growth [441].

Cordyceps acid diminished lung cancer development in nude mice which was associated with the inhibition of the Nrf-2/HO-1/NLRP3/NF-κB pathway in tumor tissue [442].

Like other mushrooms discussed, Cordyceps possess immunomodulatory effects. It is assumed that this effect is mainly attributed to polysaccharides. The mushroom is able to increase the production of interleukin (IL)-1β, IL-2, IL-6, IL-8, IL-10, and IL-12, as well as the tumor necrosis factor (TNF)-α, and also induce the phagocytosis of macrophages and mononuclear cells [443–445]. Thus, cordyceps are able to strengthen the immune system, which is an additional bonus for cancer therapy.

A *cordyceps sinensis*-derived polysaccharide provoked apoptosis and autophagy in human colon HCT1166 cells, which were associated with Akt, mTOR inhibition, and AMPK and ULK1 activation [446].

Ergothioneine is a diet-derived amino acid which exhibits antioxidant, cytoprotective, and other activities beneficial to human health [447]. It likely enters the cells by binding the solute carrier family 22, member 4 (SLC22A4), which is an organic cation carrier. Although there is not enough information about the role of ergothioneine in human physiology, there are strong evidences about its protective properties in our organism [447]. Ergothioneine mitigated oxaliplatin-induced peripheral neuropathy in rats (Nishida 2018), provoked necroptosis in colorectal cancer cells [448], and favored adjuvant vaccine cancer immunotherapy by suppressing the function of tumor-associated macrophages [449]. The blood level of ergothioneine was negatively associated with the risk of cardiometabolic disease and mortality [450], as well as chronic peripheral neuropathy upon colorectal cancer chemotherapeutic treatment [451].

Like reishi, shiitake, chaga, and maitake, the natural Cordyceps-derived products are manufactured and commonly sold as healthy food products.

Chaga (*Inonotus obliquus*, the *Hymenochaetaceae* family) is a plant parasitic fungus, predominantly widespread in Russia and in the countries of Northern Europe. Chaga penetrates into the trunks of various tree species through wounds in the bark, but its main host is birch. Chaga has been used in folk medicine, especially in Russia, Baltic countries, Korea, China, and Japan. As a medical plant, it was first mentioned by Hippocrates [359].

Different types of Chaga extracts have demonstrated their antineoplastic properties in both in vitro and in vivo models (reviewed in [452]).

Chaga contains biologically active polysaccharides, hispidin analogues, melanins, ergosterol, sesquiterpenes, triterpenoids, and benzoic acid derivates. Eighty-six of them are listed with the examples of their antineoplastic properties in [452].

In the Lewis lung mice carcinoma model, the extract of chaga decreased the size of tumors by 60%, and, in parallel, reduced the number of metastatic nodules [453].

In the orthotopic 4T1 mouse mammary cancer model, chaga extract induced autophagy, as well as LCIII and AMPK phosphorylation [454]. Authors have also shown that both inotodiol- and trametenolic-acid-enriched fractions displayed cytotoxicity. Tramentolic acid was shown to decrease the expression and activity of P-gp, which reverted multidrug resistance in breast cancer cells [455].

Inonotus obliquus polysaccharides (IOPSs) are considered to be very important biologically active compounds derived from this mushroom. Their hypoglycemic, antioxidant, anti-inflammatory, and neuroprotective properties, among others, have been identified [456].

The intraperitoneal administration of IOPSs at a dose of 30 mg/kg/day led to 4.07-fold increase in the survival rate of B16F10-implanted mice. Moreover, the authors reported that approximately 67% of the initial number of mice survived with no tumor incidence after 60 days of feeding. At the same time, no cytotoxic IOPS activity was observed for both normal and cancer cells in vitro. Thus, the authors suggested that the anti-cancer effects of endopolysaccharides are associated with immunostimulation [457]. However, another study has shown that Inonotus polysaccharides directly activate autophagy through LKB1/AMPK, which provoked MMP loss as well as the down-regulation of glycolysis and respiration, and subsequently elicited the death of lung cancer cells both in vitro and in allograft tumor models [458].

Other bioactive compounds from chaga are hispidin, hispolon, inotodiol, and syringic acid. They were shown to reduce proliferation, invasion, migration, and angiogenesis. On a molecular level, these bioactive compounds attenuated the expression of MMPs and antiapoptotic proteins that, in turn, were mediated by onco-associated signaling pathways: TNF-alpha signaling, Nox/ROS/NF-kB/STAT3, PI3K/AKT, and ERK1/2 [452,459,460].

Inotodiol is lanostane triterpenoid with anticancer properties. It down-regulated β-catenin, c-Myc, and cyclin D1 in breast cancer [461] and suppressed the migration and invasion of ovarian cancer cells through a p53-dependent mechanism [462].

Hispolon is a natural polyphenol compound with antidiabetic and anti-inflammatory activities which may also kill cancer cells through multiple mechanisms (reviewed in [463]). Hispolon attenuated STAT3 signaling, and also induced S-phase arrest and mitochondria-dependent apoptosis in prostate cancer cells [464]. In melanoma cells, it compromised the activities of mitochondrial respiration complexes I and IV, i.e., the level of Bcl-2, and also increased ROS, nitrite, and lipid peroxide levels [465]. Regarding breast cancer, hispolon, on the contrary, attenuated ROS levels, ERK activity, and the expression of Slug, therefore reversing EMT (Zhao 2016). In another study, hispolon degraded cathepsin S in an autophagy-dependent way which suppressed metastasis [466].

Polyketide hispidin exerts a variety of beneficial properties and may help to reduce cancer, metabolic syndrome, cardiovascular, neurodegenerative, and viral diseases (reviewed in [467]). Hispidin induced the microtubule and depolymerization induced lysosomal membrane permeabilization, which resulted in the death of cancer but not normal cell lines [468]. Moreover, it synergized with gemcitabine to inhibit pancreatic cancer stem cells [469].

Thus, like the well-known Asian medical mushrooms, chaga also has strong antineoplastic properties, both in vitro and in vivo.

Despite the fact that chaga is not as well known as reishi, shiitake, or maitake, and thus was not found associated with any clinical trials, the biodiversity of chaga-derived compounds with strong antineoplastic activities makes this mushroom noteworthy. Additionally, it should be kept in mind as a potential anticancer substance, and therefore warrants further studies.

A number of several mushroom-derived compounds are known today with antineoplastic properties and are of primary interest for cancer investigation. These include various mushroom polysaccharides such as lentinan, D-fraction of Grifola frondose, *Trametes versicolor*-derived PSK, gandoderic acid, grifolin, cordycepin, illudin-*S*, antroquinonol, hispidin, hispolon, inotodiol, theanine, phellinulin A, atractylenolide I, phellifuropyranone, meshimakobnol A, and meshimakobnol B (Tables 7 and 8).

Table 7. Others mushrooms and their compounds with strong anti-neoplastic activity.

Mushroom	Active Compounds	Effects	References
Agaricus subrufescens ("mushroom of the sun")	β-glucans (β-(1–3) linked backbone with (1–6) linked side branches); ergosterol	Pre-clinic: various immune stimulatory response. Clinic: increased activity of natural killer (NK) cells, and improved quality of life; increased number of plasmacytoid dendritic cells (DCs), Tregs, IL-5, and IL-7 in the blood.	[470–472]
Phellinus linteus	Polysaccharides, hispolon, phellinulin A, atractylenolide I, phellifuropyranone, meshimakobnol A, and meshimakobnol B	Pre-clinic: down-regulation of PI3K/AKT, ERK1/2, NF-kB Snail and Twist, cyclin D1 and -E, MMP-2 and -9, TGF-α; increased p53, p21, p27, and Bax; suppression of pancreatic CSCs. In clinic: Disease-free and overall survival of pancreatic cancer patients after tumor resection.	[469,473,474]
Hericium erinaceus (Lion's mane)	4-chloro-3,5-dimethoxybenzoic methyl ester, erinacine A, herierin III, herierin IV, and erinacerin G	The epigenetic regulation of FasL and TRAIL; sustained phosphorylation of FAK/AKT/p70S6K and the PAK1 pathways; generation of ROS; apoptosis via activation of JNK, p300, and NFκB p50; increased expression of TNFR, Fas, and FasL.	[475–478]
Trametes versicolor (Turkey tail)	Protein polysaccharide beta-glucan β-1,4 main chain with β-1,3 and β-1,6 side chains (PSKs)	In clinic: PSK, including adjuvant immunochemotherapy, significantly prolonged 5-year survival and disease-free rate for patients with gastric and colorectal cancer; slows progression of advanced non-small cell lung cancer.	[479,480]

Table 8. Selected plants, mushrooms, and their active compounds in the order of their priority to study anticancer capabilities. The priority was suggested based on the available information about the anti-neoplastic efficacy and safety in preclinical and clinical studies.

High Priority		
Plants	**Mushrooms**	**Individual Compounds**
Cephalotaxus harringtonia, Oldenlandia diffusa, Scutellaria barbata, Curcuma longa, Xanthium ssp., *Zingiber officinalis, Hypericum perforatum, Glycyrrhiza glabra, Silybum marianum, Panax americanus and P. ginseng, Aloe vera and A. arborescence, Tabebuia impetiginosa, Viscum album, Allium sativum, Vitis vinifera, Rosmarinus officinalis, Echinacea purpurea, Sanguinaria canadensis*	*Lentinula edodes (Shiitake), Ganoderma lucidum (Reishi), Grifola frondosa (Maitake), Cordyceps sinensis and C. militaris, Agaricus blazei, Trametes versicolor, Phellinus linteus*	Quercetin, kaempferol, ginsenosides (especially Rg3), silibinin, isoliquiritigenin, (−)- epicatechin, oleanolic acid, ursolic acid, hyperforin, hypericin, xanthatin, curcumin, withaferin A, withanone, scutellarein, scutellarin, homoharringtonine and its semi-synthetic derivates, chlorogenic acid, caffeic acid, carnosol, rosmarinic acid, resveratrol, iscodor, helixor A, shogaol, boswellic acids, hispolon, lentinan, cordycepin, echinacoside, and myricetin
Secondary priority		
Betula pubescens, Eremophila galeata, Combretum caffrum, Acacia nilotica, Guera senegalis, Tasmannia lanceolata, Davidsonia pruriens, Elaeocarpus angustifolius, Pittosporum angustifolium, Terminalia ferdinandiana, Aristolochia ringens, Beilschmiedia acuta, Dorstenia psilurus, Aristolochia ringens, Beilschmiedia acuta, Dorstenia psilurus, Echinops giganteus, Imperata cylindrica, Piper capense, Polyscia fulva, Achyrocline satureioides, Aloysia polystachya, Azorella glabra, Ephedra chilensis, Croton lechleri, Laetia corymbulosa, Lepidium meyenii, Leptocarpha rivularis, Passiflora alata, Thevetia peruviana, Menyanthes trifoliata, Ebenus boissieri, Centaurea solstitialis, Arctium lappa, Capraria biflora, Asimina triloba, Aristolochia foetida	*Hericium erinaceus (Lion's mane), Inonotus obliquus (Chaga)*	Gallic acid, combrestastatins, pyrogallol, betulinic acid, guieranone B, harringtonine, isoharringtonine, and doxyharringtonine, aloe-emodin, aloins, leptocarpin, macamide and macaene, corymbulosins, taspine, mulinic acid, achyrobichalcone, 3-O-methylquercetin, arctigenin, lappaol F, solstitialin A, sageone, biflorin, acetogenins, β-sitosterol, stigmasterol, sanguinarine, gandoderic acid, grifolin, illudin-S, lapachol and β-lapachone, carthamidin, carnosic acid, hispidin, inotodiol, syringic acid, p-coumaric acid, caffeoyl quinic acids, viniferin, lectins (ML-I, ML-II, and ML-III) from Viscum album

The antitumor activities of *Grifola frondosa* (Maitake) polysaccharide are reported in a meta-analysis based on preclinical evidence and quality assessment.

5. Why Should Medical Plants and Mushrooms Be Used Today?

At its core, modern western medicine has evolved from the folk medicine of different regions around the world over the past few centuries. As stated earlier, the most frequently used anti-neoplastic therapeutics came from live organisms (Tables S1 and S2, Supplementary Materials). Regarding pharmaceuticals, in the process of its evolution, modern medicine has created a certain set of drugs with a known efficacy, safety, side effects, and known molecular targets. However, it lost a wide profile of pharmacological activity of the plant extracts' initial biological crude material.

Anticancer therapeutics from plants remain extremely important and are still in use to treat various types of neoplasia. They include mitotic poisons from Pacific yew Taxus brevifolia—paclitaxel (Taxol®) and its semi-synthetic dodetaxel (Taxotere®); vinca alkaloids from Madagascar periwinkle (*Catharanthus roseus* L.)—vinblastine (Velban®), vincristine (leurocristin, Oncovin®) and their semi-synthetic derivate vinorelbine (Navelbini®); topoisomerase I inhibitors, i.e., semi-synthetic analogs of camptothecin from Camptotheca acuminata—irinotecan (Camptosar®) and topotecan (Hycamtin®); topoisomerase II inhibitor—etoposide (VP-16, Toposar®), which is a semi-synthetic derivative of 4′-demethylepipodophyllotoxin from Podophyllum peltatum; and omacetaxine (Synribo®)—a semi-synthetic derivate of

homoharringtonine from *Cephalotaxus harringtonia*. These drugs occupy the majority of existing chemotherapeutic schemes.

These examples illustrate the importance of plant-derived chemotherapeutics. However, even today, despite being seemingly irrelevant due to a wide assortment of synthetic anticancer drugs, interest in studies of natural compounds from plants and fungi is constantly increasing according to PubMed statistics (Figure 2). It is interesting to note that, although fungi or their active compounds are not clinically used in the western world today, their known safety and use in clinical practice in China and Japan can lead to an increase in studies on their antineoplastic capabilities. These mushrooms are represented by shiitake, maitake, reishi, and others, and act mainly through the stimulation of the anti-tumor immune system.
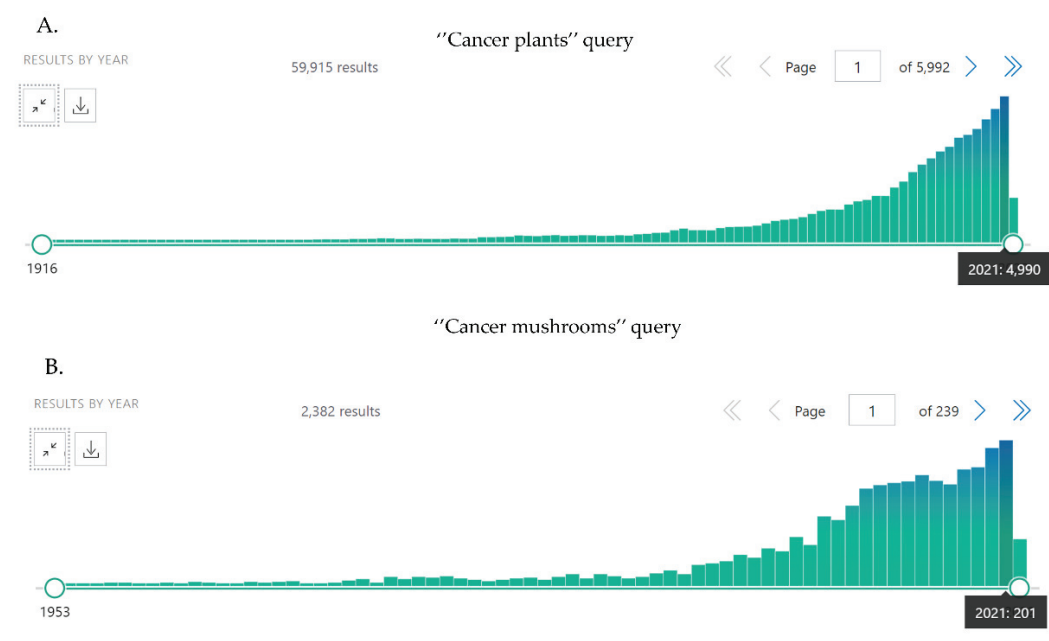
Figure 2. PubMed statistics by years on published articles on plants and fungi with antitumor properties (April 2022). Query on (**A**) "cancer plants" and (**B**) "cancer mushrooms".

One of the actual strategies used to develop anticancer drugs is the search for agents which are capable of simultaneously inhibiting several signaling pathways. A large amount of clinical data highlights that the highly selective inhibition of only one of the signaling pathways in the tumor cell usually leads to a limited response. Another significant problem of targeted therapy is the rapid acquisition of resistance by tumor cells due to the proliferation of cell clones bearing mutations that abolish the effects of the targeted drug. Thus, multitargeted therapy is considered a promising approach.

Based on the examples of plants and mushrooms described above, the anticancer activity of their extracts is attributed to the plethora of biologically active compounds with a number of biological activities. Thus, different compounds may target simultaneously different cellular processes resulting in synergistic effects. In light of this, there may be benefits from sharing them with known strong antineoplastic therapeutics in adjuvant or neoadjuvant therapy. The published data of many in vitro and in vivo experiments described here point to the fact that plant and mushroom substances with anticancer properties often increase susceptibility to genotoxic drugs.

In terms of safety and predictability, the usage of individual compounds for therapy is much better than the plant extract, which is a complex mixture of primary and secondary metabolites. However, the well-known phenomenon states that the pharmacological activities of many bioactive constituents are much weaker than those of the corresponding herbal extracts. Upon separation and purification from herbal extracts, the pharmacological

effects of many bioactive constituents diminish or even disappear [481,482]. In practice, the pharmacokinetics (AUC values) between some herbal extracts and their pure constituents may differ up to 130 times. This phenomenon depends a lot on the pharmacokinetic synergies during intestinal absorption. This means that additional constituents of plant and mushroom extracts increase solubility, reduce first-pass elimination mediated by drug-metabolizing enzymes and drug efflux transporters (ABC transporters), and enhance the membrane permeability of enterocytes (reviewed in [482]).

For instance, in the *Hypericum perforatum* (St. John's) extract, the co-existing constituent hyperoside increased the water solubility of the active compound, hypericin, by 400-fold [483]. The antimalaria agent, artemisinin, which is one of the most important natural drugs, is a substrate of cytochrome P450 enzymes. Artemisia annua extract co-occurs with arteannuin B, which inhibits hepatic cytochromes P450 and doubles the peak serum concentration of artemisinin in vivo [484].

There are evidences that coexisting compounds may change the solubility and bioavailability of their active constituents via the formation of natural nanoparticles, greatly modifying their pharmacological activities [482,485,486].

Another important point is associated with a strong deterioration in the health of patients undergoing chemotherapy. In this case, all of the medical plants and mushrooms described here can significantly improve the physical and mental health of patients due to the anti-inflammatory, hepatoprotective, cardioprotective, immunomodulatory, anxiolytic, and metabolism-normalizing properties. The simultaneous use of plant- and mushroom-derived medical substances along with chemotherapy may ameliorate its toxic impact on normal tissues.

Finally, standardized herbal medicine can be more cost-efficient than most other synthetic compounds.

Based on the information discussed in this review, we divided medical plants, mushrooms, and their active compounds into two priority groups for research and potential of use in antitumor therapy. This priority is suggested based on the available literature on their anti-neoplastic efficacy and safety in preclinical and clinical studies (Table 8). The chemical structures of active compounds with their sources are demonstrated in Figure S1.

6. Limitations of Using Plants and Mushrooms as Medicine

6.1. Bioavailability

Despite the promising antineoplastic activity of several natural herbs and mushrooms, their translation to human studies is limited due to their low bioavailability.

First of all, this is based on poor water solubility. This is a problem limiting the efficiency and application of compounds with significant antineoplastic properties in both animal and human studies. Curcumin, resveratrol, quercetin, hypericin, ursolic acid, silybin, pterostilbene, berberine, betulinic acid, and other valuable compounds are among them [487].

Besides solubility, other reasons affecting bioavailability include an increased intestine metabolism (by both microbiota and enterocytes), absorption and intestinal efflux (the activity of P-gp and other ABC transporters), and the activity of liver drug-metabolizing enzymes. The drug-metabolizing system consists of phase I and phase II drug-metabolizing enzymes which are cytochromes (CYPs), especially CYP3A4, and UDP glucuronosyl-transferases (UGTs), primarily UGT1A1 and 2B1 [482]. These enzymes are active in both hepatocytes and enterocytes.

In preclinical and clinical investigations, curcumin, quercetin, resveratrol, and other promising natural compounds with anticancer properties have displayed problems with the dissolvement into gastrointestinal fluids, permeability across the intestinal epithelium, and "first-pass" metabolism due to the aforementioned molecular limitations which greatly reduce oral bioavailability [488]. To challenge this, chemical modifications of natural molecules can be carried out to improve them. However, after chemical modifications, this

molecule will not be natural anymore, but rather will become a new compound, which will require new exhaustive preclinical studies.

As an alternative, several approaches have been used including nanoparticle formulations, phytosomes, and the use of bioenhancers [488].

To increase bioavailability, self-microemulsifying drug delivery systems (SMEDDSs) are frequently formulated [489]. SMEDDS are isotropic mixtures of oils, surfactants, or (alternatively) co-surfactants and co-solvents [488,490]. To avoid drug precipitation, SMEDDS are supplied with hydrophilic polymers, such as polyvinylpyrrolidone and hydroxypropyl methylcellulose. The use of SMEDDSs significantly improved the stability, effectiveness, and Cmax and AUC values of curcumin, quercetin, and resveratrol [490].

Another way to improve the bioavailability of natural compounds is the application of phosphatidylcholine complexes, called "phytosomes" [487,488,491]. Their effectiveness has been demonstrated regarding silibinin. In prostate cancer patients, phytosomes were able to increase the Cmax of silibinin by up to 100 uM, with an average concentration of 1.2 uM at the end of the trial [492,493].

Phytosomes loaded with quercetin and scorpion venom peptides were able to target breast cancer cells [494]. Thymoquinone-loaded phytosomes exhibited cytotoxic effects in the lung cancer cell line [495].

Taken together, the application of a nanoparticle delivery system is considered as one of the most important ways to improve the bioavailability of herbal therapeutics (reviewed in [487,496,497]).

Piperine is a commonly used "bioenhancer" for many herbal products marketed in the USA [488,498]. This compound inhibits both CYP3A4 and P-glycoprotein. As reported, other inhibitors of CYP and UGT isoforms are α-mangostin, magnobol, peppermint oil, grapefruit juice (naringin), lysergol, chrysin, ginger extract, pterostilbene, silybin, gallic acid ester, genestein, and others (reviewed in [499]).

However, as stated in the previous subsection, one more option to address the challenge with bioavailability is to use herbal and mushroom extracts where a mixture of naturally co-occurring constituents promote the bioavailability and strong pharmacological properties of active compounds.

6.2. Safety

Undoubtedly, two key advantages of modern western medicine are the known profiles of efficacy and safety. International agencies including the Food and Drug Administration (FDA) and the Europe Medicine Agency (EMA) require at least one trail with control phase III significant results to launch a substance into clinics [500]. However, in some cases, drugs which are not approved by the FDA and EMS can be registered in certain countries.

There is a widespread belief that herbal medicine is safe and non-toxic. Despite the fact that herbal medicines are widely considered to be of a lower risk compared to synthetic drugs, they are not completely free from the possibility of toxicity or adverse effects. Thus, herbal and mushroom pharmacological products should be accurately and exhaustively managed.

Several reasons for the unsafety of herbal and mushroom medicine can be recognized: "intrinsic" and "external" toxicities, wrong indication, and herb–drug interactions [501].

"Intrinsic" toxicity is determined by the toxicity of some plants and mushrooms at a normal therapeutic dosage or in overdose. Herbal extracts represent a mixture of dozens of constituents with multiple pharmacological properties. Moreover, active compounds in the form of natural extracts frequently display synergistic effects. As stated by Paracelsus, ''Everything is poison, everything is medicine; either effect is determined by the dose". Even medical plants well-known for being safe for centuries may have serious adverse effects. For instance, it was recently reported that aloe–emodin and aloin—two principle active components of *Aloe vera*—may have hepato- and nephrotoxicity [109] and may even induce the Wnt/β-catenin pathway which may be associated with potential carcinogenesis [121]. Moreover, there are media stories (e.g., https://www.bbc.com/news/stories-45971416;

accessed on 20 February 2022) and scientific reports [502–504] about serious hepatotoxicity in people who consumed excessive amounts of green tea or used its extract as a food supplement. The green-tea-induced hepatotoxicity occurs due to the excessive consumption of (−)-epigallocatechin-3-gallate (EGGG). Its consumption safety level was determined by the European Commission [503,505].

"External toxicity" is associated with the possible environmental pollution of herbal sources with heavy metals, pesticides, and poisons.

As herbal and mushroom extracts are composed of a complex mixture of biologically active constituents, their intake in parallel with the usage of conventional drugs may result in herbal–drug interactions. Herbal–drug interactions display the synergistic or additive actions of herbal products with conventional medications as a result of overlapping affinities for common receptor sites. They may affect different physiological processes (the induction and inhibition of drug-metabolizing enzymes and ABC transporters, the alteration of gastrointestinal functions, and the modulation of the effects of antipsychotic therapeutics) which needs to be taken into account (reviewed in [506]).

All of these issues are addressed by complex investigations and through the procedure of standardization of manufacturing, ranging from pharmacological studies on human physiology to the precise monitoring of the herbal source quality, as well as the quantification of active and marker compounds.

6.3. Standardization

Besides safety, there is another closely related problem. The chemical composition of plants and mushrooms may vary depending on the genetic background and growth conditions. A major source of distrust towards the use of plants in modern medicine is the impossibility of the full standardization of plant material.

Standardization refers to all the information and activities aimed at developing and establishing requirements and control to ensure minimum quantitative and qualitative variations of active biochemicals in a herbal product. This is archived through assurance practices applied to agricultural and manufacturing processes [507]. Thus, standardization guarantees the content of one or more active constituents and marker compounds. This is closely associated with both efficiency and safety. It includes the evaluation of chemical constituents present in a herbal drug. This may involve the quantification of individual compounds of interest or chemical groups (total phenolics, total triterpenic acids, total alkaloids, and tannins). Standardization may use multiple marker-based fingerprint profiles [508]. The step-by-step standardization procedure, from primary culturing to the finished herbal product, is described in another review [509].

Whether the substance is synthetic or natural, the standardized procedure of its preclinical studies should be followed. Recently, the FDA adopted an ICH guideline on the nonclinical evaluation of anticancer drugs, including 41 questions and answers aimed at providing additional clarity about oncology drug development [369].

7. Overcoming Limitations to Integrate Folk and Modern Medicine

To integrate folk and modern medicine, standardization is required to be highly developed. Although this is by far a difficult obstacle, there are well-known examples of successful standardization approaches.

China is an upper–middle-income country with the second largest world economy (https://www.worldbank.org/en/country/china/; accessed on 26 March 2022). However, in China, both western modern medicine and TCM are officially used today, alone or in combination. One of the reasons is that TCM has proven its effectiveness for 2000 years. Now, China's government strongly supports TCM (in the form of CPM), exporting its products to different countries for trials and therapy, and setting up a research partnership with the big international pharmaceutical companies such as Novartis or Astrazeneca, displaying global ambitions [7] (http://www.news.cn/english/2021-10/03/c_13102247 91.htm; accessed on 26 March 2022). The fears of western medicine are related both to

the concern about the safety profile, and a possible reduction in the monopoly currently held by large pharmaceutical corporations. Various aspects such as economic and political components, fears, and real examples of insecurity (both related to efficacy and a lack of evidence in various clinical trials) intertwine and both contribute to and hinder TCM's application in developed countries [8]. Nevertheless, TCM actively continues to develop its niche in the modern world's pharmacology.

In China, the standardization of TCM was set as one priority area to become the standard specification of international traditional medicine, with a lot of TCM standards established [510]. Thus, as demonstrated by China, it is possible to improve traditional medicine like this.

Thus, the standardization of plants and for anticancer clinical trials is also possible. Standardized medical substances derived from herbal sources are applied in different regions of the world. For instance, there are drops, syrups, and tablets used against coughs, which are derived from various companies including Kodelak™ (Moscow, Russia), Herbion™ (Burlington, ON, Canada), Dabur Honitus™ (New Delhi, India), Dr. Müller Syrups™ (Hradec Králové, Czech Rebublic), and Naturactive™ (Boe, France), etc.

Moreover, there are standardized dietary supplements which are manufactured by large world-class companies such as Solgar™ (Leonia, NJ, USA), Himalaya™ (Bangalore, India), NOW™ (Bloomingdale, IL, USA), and others, in accordance with developed standardized protocols. Some of these supplements are consumed worldwide and are derived from plants and mushrooms with strong antineoplastic properties described in this review: *Silybum marianum* (thistle), *Withania somnifera* (Ashwagandha), *Plumbago zeylanica* (Chitrak), *Boswellia serrata* (Boswellia extract), *Curcuma longa* (turmeric-based supplements), *Panax gingseng* (different supplements), *Glyzzhiriza glabra* (licorice), *Hypericum perforatum* (St. John's wort), *Zingiber officinale* (ginger), *Agaricus blazei* (Andosan™, Oslo, Norway), etc. A plausible experimental approach to test the antineoplastic therapeutic properties of these plants and mushrooms can be exerted by using the corresponding supplements in preclinical experiments on animal tumor models. The quality control, standardized constitution, and orally available form can create good opportunities to credibly evaluate their anticancer potential, safety, and other possible beneficial effects on health. It is important to analyze the potential synergy between such supplements and conventional anticancer therapeutics. Taking into account that the bioavailability of active compounds is usually several-fold higher in the form of a herbal or mushroom extract (due to the co-existing constituents), the usage of dietary supplements derived from standardized extracts is very promising.

As was reported earlier, a mixture of naturally co-occurring constituents promotes the bioavailability and strong pharmacological properties of active compounds. Thus, the use of plant and mushroom medical products derived from their standardized extracts may also significantly increase the bioavailability of active compounds without additional manipulations.

One more interesting approach to bring herbs and mushrooms into modern medicine is the concept of "medical food based on certain herbs and mushrooms" [511,512]. In theory, food supplementation with anticancer herbs and mushrooms (e.g., shiitake, reishi, etc.) may help to prevent and reduce tumor growth. Chen and colleagues fed mice with gastric cancer with six medical edible plants used in TCM and observed the suppression of neoplastic growth through several molecular mechanisms [512]. All of the plants used possess well-known anticancer properties.

This new approach seems to be promising but requires more experimental data to confirm its efficiency.

8. Conclusions and Future Perspectives

Summarizing the information discussed above, we would like to highlight several points that should help implement traditional herbal medicine in current medicine:

— To date, a lot of information about a number of plants and mushrooms, and their individual bioactive compounds with well-documented antitumor properties, has been accumulated. Their respective full-scale multi-level studies should be top priorities.

— Despite there being a lot of investigations on the anticancer properties of a certain plant using tumor cell models, only a limited number of studies have been carried out with implication of control non-tumor cell models and subsequent animal studies. As the next step, comprehensive studies on their effectiveness, toxicity to non-cancer cells, and animal tissues in various doses are required to authorize natural-derived extracts and individual compounds into the next pre-clinical or clinical investigation.

— Progress in standardization is highly required to transform anecdotal folk herbal medicine into modern molecular pharmacology with clear mechanisms of action. This process includes investments into big programs regarding investigations, monitoring, and certifications of manufacturing the final product.

— On the examples of etoposide, irino- and topotecan, vinorelbine, docetaxel, and omacetaxine, the development of semi-synthetic derivates of newly identified natural compounds with significant anticancer properties may improve their characteristics and lead to new antineoplastic drugs.

— The study of a synergistic interaction of isolated natural compounds and crude plant- and mushroom-derived extracts with widely used anticancer therapeutics should help define the right dosage and compatibility between the natural and synthetic therapeutics.

— Natural compounds may sensitize tumors for modern therapeutics and be effective in adjuvant and neoadjuvant therapy.

— There is a variety of standardized dietary supplements from plants and mushrooms with presumable antineoplastic properties produced by large world-class companies. The important approach is to test their antitumor potential using animal models, especially in combination with relevant modern therapeutics.

— The pharmacological effects of active compounds are much higher in herbal extracts than in pure compounds due to co-existing constituents which may provide the pharmacokinetic synergy during intestinal absorption and the ''first-path'' metabolism.

— Folk medicine may point to certain plants or mushrooms with highly potent anticancer properties and bioactive compounds. Herewith, the cooperation between cancer researchers and ethnobotanists or ethnomedicine specialists can benefit the development of new therapeutics.

To conclude, a systematic approach in studying the traditional herbal medicine is required to successfully integrate this unique knowledge into modern molecular medicine. This combined knowledge that encompasses both the empirical and theoretical approaches may provide a window of opportunities to facilitate the development of new chemotherapeutic strategies to treat malignancies.

Institutional Review Board Statement: Not applicable.

Informed Consent Statement: Not applicable.

Data Availability Statement: Data sharing not applicable.

Conflicts of Interest: The authors declare no conflict of interest.

References

1. WHO. *CureAll Framework: WHO Global Initiative for Childhood Cancer: Increasing Access, Advancing Quality, Saving Lives*; WHO: Geneva, Switzerland, 2021.
2. Garodia, P.; Ichikawa, H.; Malani, N.; Sethi, G.; Aggarwal, B.B. From ancient medicine to modern medicine: Ayurvedic concepts of health and their role in inflammation and cancer. *J. Soc. Integr. Oncol.* **2007**, *5*, 25–37. [CrossRef] [PubMed]
3. Mann, M.; Pathak, S.R. Ayurveda: A new dimension in the era of modern medicine. In *Synthesis of Medicinal Agents from Plants*; Elsevier: Amsterdam, The Netherlands, 2018; pp. 283–303.
4. Vaghora, B.; Shukla, V. Impact of different phytochemical classes and Ayurvedic plants in battle against cancer. *Skin* **2016**, *13*, 14.
5. Wu, M.; Lu, P.; Shi, L.; Li, S. Traditional Chinese patent medicines for cancer treatment in China: A nationwide medical insurance data analysis. *Oncotarget* **2015**, *6*, 38283. [CrossRef]
6. Zhang, N.; Shi, N.; Li, S.; Liu, G.; Han, Y.; Liu, L.; Zhang, X.; Kong, X.; Zhang, B.; Yuan, W. A Retrospective Study on the Use of Chinese Patent Medicine in 24 Medical Institutions for COVID-19 in China. *Front. Pharmacol.* **2020**, *11*, 574562. [CrossRef] [PubMed]
7. Ovais, M.; Khalil, A.T.; Jan, S.A.; Ayaz, M.; Ullah, I.; Shinwari, W.; Shinwari, Z.K. Traditional Chinese Medicine Going Global: Opportunities for Belt and Road Countries: TCM Importance in the Context of Belt Road Initiative. *Proc. Pak. Acad. Sci. B Life Environ. Sci.* **2019**, *56*, 17–26.
8. Cyranoski, D. Why Chinese medicine is heading for clinics around the world. *Nature* **2018**, *561*, 448. [CrossRef]
9. Katayama, K.; Yoshino, T.; Munakata, K.; Yamaguchi, R.; Imoto, S.; Miyano, S.; Watanabe, K. Prescription of kampo drugs in the Japanese health care insurance program. *Evid. Based Complement. Altern. Med.* **2013**, *2013*, 576973. [CrossRef]
10. Motoo, Y.; Cameron, S. Kampo medicines for supportive care of patients with cancer: A brief review. *Integr. Med. Res.* **2022**, *11*, 100839. [CrossRef]
11. Shimizu, M.; Takayama, S.; Kikuchi, A.; Arita, R.; Ono, R.; Ishizawa, K.; Ishii, T. Kampo medicine treatment for advanced pancreatic cancer: A case series. *Front. Nutr.* **2021**, *8*, 513. [CrossRef]
12. Takayama, S.; Tomita, N.; Arita, R.; Ono, R.; Kikuchi, A.; Ishii, T. Kampo Medicine for various aging-related symptoms: A review of geriatric syndrome. *Front. Nutr.* **2020**, *7*, 86. [CrossRef]
13. Yamakawa, J.-i.; Motoo, Y.; Moriya, J.; Ogawa, M.; Uenishi, H.; Akazawa, S.; Sasagawa, T.; Nishio, M.; Kobayashi, J. Role of Kampo medicine in integrative cancer therapy. *Evid. Based Complement. Altern. Med.* **2013**, *2013*, 139–144. [CrossRef] [PubMed]
14. Watanabe, K.; Matsuura, K.; Gao, P.; Hottenbacher, L.; Tokunaga, H.; Nishimura, K.; Imazu, Y.; Reissenweber, H.; Witt, C.M. Traditional Japanese Kampo medicine: Clinical research between modernity and traditional medicine—The state of research and methodological suggestions for the future. *Evid. Based Complement. Altern. Med.* **2011**, *2011*, 513842. [CrossRef] [PubMed]
15. Ito, A.; Munakata, K.; Imazu, Y.; Watanabe, K. First nationwide attitude survey of Japanese physicians on the use of traditional Japanese medicine (Kampo) in cancer treatment. *Evid. Based Complement. Altern. Med.* **2012**, *2012*, 957082. [CrossRef] [PubMed]
16. Aoyama, T.; Tamagawa, H. The clinical effect of Kampo medicine in multimodal treatment for Gastrointestinal Cancer in Japan. *J. Cancer* **2020**, *11*, 5390. [CrossRef] [PubMed]
17. Rondilla, N.A.; Rocha, I.C.N.; Roque, S.J.; Lu, R.M.; Apolinar, N.L.B.; Solaiman-Balt, A.A.; Abion, T.J.; Banatin, P.B.; Javier, C.V. Folk Medicine in the Philippines: A Phenomenological Study of Health-Seeking Individuals. *Int. J. Med. Stud.* **2021**, *9*, 25–32. [CrossRef]
18. Arnason, J.; Cal, V.; Pesek, T.; Awad, R.; Bourbonnais-Spear, N.; Collins, S.; Otarola-Rojas, M.; Walshe-Roussel, B.; Audet, P.; Ta, C.A. A review of ethnobotany and ethnopharmacology of traditional medicines used by Q'eqchi'Maya Healers of Xna'ajeb'aj Ralch'o'och', Belize. *Botany* **2022**, *100*, 219–230. [CrossRef]
19. Jorim, R.Y.; Korape, S.; Legu, W.; Koch, M.; Barrows, L.R.; Matainaho, T.K.; Rai, P.P. An ethnobotanical survey of medicinal plants used in the eastern highlands of Papua New Guinea. *J. Ethnobiol. Ethnomed.* **2012**, *8*, 47. [CrossRef]
20. Neergheen, V.S.; Kam, A.H.; Pem, Y.; Ramsaha, S.; Bahorun, T. Regulation of cancer cell signaling pathways as key events for therapeutic relevance of edible and medicinal mushrooms. *Proc. Semin. Cancer Biol.* **2020**, *80*, 145–156. [CrossRef]
21. Shoaib, A.; Tabish, M.; Ali, S.; Arafah, A.; Wahab, S.; Almarshad, F.M.; Rashid, S.; Rehman, M.U. Dietary phytochemicals in cancer signalling pathways: Role of miRNA targeting. *Curr. Med. Chem.* **2021**, *28*, 8036–8067. [CrossRef]
22. Oyenihi, O.R.; Oyenihi, A.B.; Erhabor, J.O.; Matsabisa, M.G.; Oguntibeju, O.O. Unravelling the anticancer mechanisms of traditional herbal medicines with metabolomics. *Molecules* **2021**, *26*, 6541. [CrossRef]
23. Hanahan, D.; Weinberg, R.A. Hallmarks of cancer: The next generation. *Cell* **2011**, *144*, 646–674. [CrossRef] [PubMed]
24. Kontomanolis, E.N.; Koutras, A.; Syllaios, A.; Schizas, D.; Mastoraki, A.; Garmpis, N.; Diakosavvas, M.; Angelou, K.; Tsatsaris, G.; Pagkalos, A. Role of oncogenes and tumor-suppressor genes in carcinogenesis: A review. *Anticancer Res.* **2020**, *40*, 6009–6015. [CrossRef] [PubMed]

25. Sanchez-Vega, F.; Mina, M.; Armenia, J.; Chatila, W.K.; Luna, A.; La, K.C.; Dimitriadoy, S.; Liu, D.L.; Kantheti, H.S.; Saghafinia, S. Oncogenic signaling pathways in the cancer genome atlas. *Cell* **2018**, *173*, 321–337.e310. [CrossRef]

26. Witsch, E.; Sela, M.; Yarden, Y. Roles for growth factors in cancer progression. *Physiology* **2010**, *25*, 85–101. [CrossRef] [PubMed]

27. Patranabis, S. Recent Advances in the Therapeutic Development of Receptor Tyrosine Kinases (RTK) against Different Types of Cancer. In *Protein Kinases—Promising Targets for Anticancer Drug Research*; InTechOpen: London, UK, 2021; p. 103.

28. Zou, Z.; Tao, T.; Li, H.; Zhu, X. mTOR signaling pathway and mTOR inhibitors in cancer: Progress and challenges. *Cell Biosci.* **2020**, *10*, 31. [CrossRef] [PubMed]

29. Yun, C.W.; Jeon, J.; Go, G.; Lee, J.H.; Lee, S.H. The dual role of autophagy in cancer development and a therapeutic strategy for cancer by targeting autophagy. *Int. J. Mol. Sci.* **2020**, *22*, 179. [CrossRef]

30. Al-Masri, M.; Paliotti, K.; Tran, R.; Halaoui, R.; Lelarge, V.; Chatterjee, S.; Wang, L.-T.; Moraes, C.; McCaffrey, L. Architectural control of metabolic plasticity in epithelial cancer cells. *Commun. Biol.* **2021**, *4*, 371. [CrossRef]

31. Shuvalov, O.; Petukhov, A.; Daks, A.; Fedorova, O.; Vasileva, E.; Barlev, N.A. One-carbon metabolism and nucleotide biosynthesis as attractive targets for anticancer therapy. *Oncotarget* **2017**, *8*, 23955. [CrossRef]

32. Shuvalov, O.; Daks, A.; Fedorova, O.; Petukhov, A.; Barlev, N. Linking metabolic reprogramming, plasticity and tumor progression. *Cancers* **2021**, *13*, 762. [CrossRef]

33. Daks, A.; Shuvalov, O.; Fedorova, O.; Petukhov, A.; Lezina, L.; Zharova, A.; Baidyuk, E.; Khudiakov, A.; Barlev, N.A. p53-Independent Effects of Set7/9 Lysine Methyltransferase on Metabolism of Non-Small Cell Lung Cancer Cells. *Front. Oncol.* **2021**, *11*, 706668. [CrossRef]

34. Munshi, P.N.; Lubin, M.; Bertino, J.R. 6-thioguanine: A drug with unrealized potential for cancer therapy. *Oncologist* **2014**, *19*, 760–765. [CrossRef] [PubMed]

35. Morgunkova, A.; Barlev, N.A. Lysine methylation goes global. *Cell Cycle* **2006**, *5*, 1308–1312. [CrossRef] [PubMed]

36. Cao, J.; Yan, Q. Cancer epigenetics, tumor immunity, and immunotherapy. *Trends Cancer* **2020**, *6*, 580–592. [CrossRef] [PubMed]

37. Cheng, Y.; He, C.; Wang, M.; Ma, X.; Mo, F.; Yang, S.; Han, J.; Wei, X. Targeting epigenetic regulators for cancer therapy: Mechanisms and advances in clinical trials. *Signal Transduct. Target. Ther.* **2019**, *4*, 62. [CrossRef] [PubMed]

38. Daks, A.; Vasileva, E.; Fedorova, O.; Shuvalov, O.; Barlev, N.A. The Role of Lysine Methyltransferase SET7/9 in Proliferation and Cell Stress Response. *Life* **2022**, *12*, 362. [CrossRef]

39. Vasileva, E.; Shuvalov, O.; Petukhov, A.; Fedorova, O.; Daks, A.; Nader, R.; Barlev, N. KMT Set7/9 is a new regulator of Sam68 STAR-protein. *Biochem. Biophys. Res. Commun.* **2020**, *525*, 1018–1024. [CrossRef]

40. Pottier, C.; Fresnais, M.; Gilon, M.; Jérusalem, G.; Longuespée, R.; Sounni, N.E. Tyrosine kinase inhibitors in cancer: Breakthrough and challenges of targeted therapy. *Cancers* **2020**, *12*, 731. [CrossRef]

41. Zhang, M.; Zhang, L.; Hei, R.; Li, X.; Cai, H.; Wu, X.; Zheng, Q.; Cai, C. CDK inhibitors in cancer therapy, an overview of recent development. *Am. J. Cancer Res.* **2021**, *11*, 1913.

42. Mukherjee, N.; Amato, C.M.; Skees, J.; Todd, K.J.; Lambert, K.A.; Robinson, W.A.; Van Gulick, R.; Weight, R.M.; Dart, C.R.; Tobin, R.P. Simultaneously inhibiting BCL2 and MCL1 is a therapeutic option for patients with advanced melanoma. *Cancers* **2020**, *12*, 2182. [CrossRef]

43. He, P.; Qiu, K.; Jia, Y. Modeling of mesenchymal hybrid epithelial state and phenotypic transitions in EMT and MET processes of cancer cells. *Sci. Rep.* **2018**, *8*, 14323. [CrossRef]

44. Bhatia, S.; Wang, P.; Toh, A.; Thompson, E.W. New insights into the role of phenotypic plasticity and EMT in driving cancer progression. *Front. Mol. Biosci.* **2020**, *7*, 71. [CrossRef] [PubMed]

45. Yu, Z.; Pestell, T.G.; Lisanti, M.P.; Pestell, R.G. Cancer stem cells. *Int. J. Biochem. Cell Biol.* **2012**, *44*, 2144–2151. [CrossRef] [PubMed]

46. Peitzsch, C.; Tyutyunnykova, A.; Pantel, K.; Dubrovska, A. Cancer stem cells: The root of tumor recurrence and metastases. *Proc. Semin. Cancer Biol.* **2017**, *44*, 10–24. [CrossRef]

47. Ermakov, A.; Daks, A.; Fedorova, O.; Shuvalov, O.; Barlev, N.A. Ca2+-depended signaling pathways regulate self-renewal and pluripotency of stem cells. *Cell Biol. Int.* **2018**, *42*, 1086–1096. [CrossRef] [PubMed]

48. Waldman, A.D.; Fritz, J.M.; Lenardo, M.J. A guide to cancer immunotherapy: From T cell basic science to clinical practice. *Nature Rev. Immunol.* **2020**, *20*, 651–668. [CrossRef] [PubMed]

49. Smirnov, S.; Petukhov, A.; Levchuk, K.; Kulemzin, S.; Staliarova, A.; Lepik, K.; Shuvalov, O.; Zaritskey, A.; Daks, A.; Fedorova, O. Strategies to Circumvent the Side-Effects of Immunotherapy Using Allogeneic CAR-T Cells and Boost Its Efficacy: Results of Recent Clinical Trials. *Front. Immunol.* **2021**, *12*, 780145. [CrossRef]

50. Alves-Silva, J.M.; Romane, A.; Efferth, T.; Salgueiro, L. North African medicinal plants traditionally used in cancer therapy. *Front. Pharmacol.* **2017**, *8*, 383. [CrossRef]

51. Mbaveng, A.T.; Kuete, V.; Efferth, T. Potential of Central, Eastern and Western Africa medicinal plants for cancer therapy: Spotlight on resistant cells and molecular targets. *Front. Pharmacol.* **2017**, *8*, 343. [CrossRef]

52. Klopper, R.R.; Gautier, L.; Chatelain, C.; Smith, G.F.; Spichiger, R. Floristics of the angiosperm flora of Sub-Saharan Africa: An analysis of the African Plant Checklist and Database. *Taxon* **2007**, *56*, 201–208.

53. Linder, H.P. The evolution of African plant diversity. *Front. Ecol. Evolut.* **2014**, *2*, 38. [CrossRef]

54. Rather, L.J.; Mohammad, F. *Acacia nilotica* (L.): A review of its traditional uses, phytochemistry, and pharmacology. *Sustain. Chem. Pharm.* **2015**, *2*, 12–30. [CrossRef]

55. Malami, I.; Jagaba, N.M.; Abubakar, I.B.; Muhammad, A.; Alhassan, A.M.; Waziri, P.M.; Yahaya, I.Z.Y.; Mshelia, H.E.; Mathias, S.N. Integration of medicinal plants into the traditional system of medicine for the treatment of cancer in Sokoto State, Nigeria. *Heliyon* **2020**, *6*, e04830. [CrossRef] [PubMed]

56. Barapatre, A.; Meena, A.S.; Mekala, S.; Das, A.; Jha, H. In vitro evaluation of antioxidant and cytotoxic activities of lignin fractions extracted from *Acacia nilotica*. *Int. J. Biol. Macromol.* **2016**, *86*, 443–453. [CrossRef] [PubMed]

57. Zheleva-Dimitrova, D.; Sinan, K.I.; Etienne, O.K.; Ak, G.; Sharmeen, J.B.; Dervisoglu, G.; Ozdemir, F.A.; Mahomoodally, M.F.; Zengin, G. Comprehensive chemical characterization and biological evaluation of two Acacia species: *A. nilotica* and *A. ataxacantha*. *Food Chem. Toxicol.* **2021**, *156*, 112446. [CrossRef]

58. Revathi, S.; Hakkim, F.L.; Kumar, N.R.; Bakshi, H.A.; Rashan, L.; Al-Buloshi, M.; Hasson, S.S.; Krishnan, M.; Javid, F.; Nagarajan, K. Induction of HT-29 colon cancer cells apoptosis by Pyrogallol with growth inhibiting efficacy against drug-resistant *Helicobacter pylori*. *Anticancer Agents Med. Chem.* **2018**, *18*, 1875–1884. [CrossRef]

59. Sakthive, K.; Kannan, N.; Angeline, A.; Guruvayoorappan, C. Anticancer activity of *Acacia nilotica* (L.) Wild. Ex. Delile subsp. indica against Dalton's ascitic lymphoma induced solid and ascitic tumor model. *Asian Pac. J. Cancer Prev.* **2012**, *13*, 3989–3995. [CrossRef]

60. Revathi, S.; Hakkim, F.L.; Kumar, N.R.; Bakshi, H.A.; Sangilimuthu, A.Y.; Tambuwala, M.M.; Changez, M.; Nasef, M.M.; Krishnan, M.; Kayalvizhi, N. In vivo anti cancer potential of pyrogallol in murine model of colon cancer. *Asian Pac. J. Cancer Prev.* **2019**, *20*, 2645. [CrossRef]

61. Al-Nour, M.Y.; Ibrahim, M.M.; Elsaman, T. Ellagic acid, Kaempferol, and Quercetin from *Acacia nilotica*: Promising combined drug with multiple mechanisms of action. *Curr. Pharmacol. Rep.* **2019**, *5*, 255–280. [CrossRef]

62. Thiagarajan, K.; Mohan, S.; Roy, T.K.; Chandrasekaran, R. Antiproliferative effect of *Acacia nilotica* (L.) leaf extract rich in ethyl gallate against human carcinoma cell line KB. *Indian J. Pharmacol.* **2020**, *52*, 488.

63. Dirar, A.I.; Devkota, H.P. Ethnopharmacological uses, phytochemistry and pharmacological activities of *Guiera senegalensis* JF Gmel. (*Combretaceae*). *J. Ethnopharmacol.* **2021**, *267*, 113433. [CrossRef]

64. Adebayo, I.A.; Gagman, H.A.; Balogun, W.G.; Adam, M.A.A.; Abas, R.; Hakeem, K.R.; Nik Him, N.A.I.I.B.; Samian, M.R.B.; Arsad, H. *Detarium microcarpum*, *Guiera senegalensis*, and *Cassia siamea* induce apoptosis and cell cycle arrest and inhibit metastasis on MCF7 breast cancer cells. *Evid. Based Complement. Altern. Med.* **2019**, *2019*, 6104574.

65. Kuete, V.; Eichhorn, T.; Wiench, B.; Krusche, B.; Efferth, T. Cytotoxicity, anti-angiogenic, apoptotic effects and transcript profiling of a naturally occurring naphthyl butenone, guieranone A. *Cell Div.* **2012**, *7*, 16. [CrossRef] [PubMed]

66. Bello, B.A.; Khan, S.A.; Khan, J.A.; Syed, F.Q.; Anwar, Y.; Khan, S.B. Antiproliferation and antibacterial effect of biosynthesized AgNps from leaves extract of *Guiera senegalensis* and its catalytic reduction on some persistent organic pollutants. *J. Photochem. Photobiol. B Biol.* **2017**, *175*, 99–108. [CrossRef]

67. Singh, R.; Kaur, H. Advances in synthetic approaches for the preparation of combretastatin-based anti-cancer agents. *Synthesis* **2009**, *2009*, 2471–2491. [CrossRef]

68. Karatoprak, G.Ş.; Küpeli Akkol, E.; Genç, Y.; Bardakcı, H.; Yücel, Ç.; Sobarzo-Sánchez, E. Combretastatins: An overview of structure, probable mechanisms of action and potential applications. *Molecules* **2020**, *25*, 2560. [CrossRef] [PubMed]

69. Nwankwo, J. Anticancer potentials of phytochemicals from some indigenous food and medicinal plants of West Africa. *Adv. Cancer Prev.* **2017**, *2*, 124–130. [CrossRef]

70. Twilley, D.; Rademan, S.; Lall, N. A review on traditionally used South African medicinal plants, their secondary metabolites and their potential development into anticancer agents. *J. Ethnopharmacol.* **2020**, *261*, 113101. [CrossRef]

71. Sagbo, I.J.; Otang-Mbeng, W. Plants used for the traditional management of cancer in the eastern cape province of south africa: A review of ethnobotanical surveys, ethnopharmacological studies and active phytochemicals. *Molecules* **2021**, *26*, 4639. [CrossRef]

72. Khorombi, T.; Fouché, G.; Kolesnikova, N.; Maharaj, V.; Nthambeleni, R.; Van der Merwe, M.R. Investigation of South African plants for anti cancer properties. *Pharmacology* **2006**, *3*, 494–500.

73. Matowa, P.R.; Gundidza, M.; Gwanzura, L.; Nhachi, C.F. A survey of ethnomedicinal plants used to treat cancer by traditional medicine practitioners in Zimbabwe. *BMC Complement. Med. Ther.* **2020**, *20*, 278. [CrossRef]

74. Akindele, A.J.; Wani, Z.; Mahajan, G.; Sharma, S.; Aigbe, F.R.; Satti, N.; Adeyemi, O.O.; Mondhe, D.M. Anticancer activity of *Aristolochia ringens* Vahl. (Aristolochiaceae). *J. Tradit. Complement. Med.* **2015**, *5*, 35–41. [CrossRef] [PubMed]

75. Ahmad, J.; Ajani, E.; Sabiu, S. Chemical group profiling, in vitro and in silico evaluation of *Aristolochia ringens* on α-amylase and α-glucosidase activity. *Evid. Based Complement. Altern. Med.* **2021**, *2021*, 6679185. [CrossRef] [PubMed]

76. Kuete, V.; Tankeo, S.B.; Saeed, M.E.; Wiench, B.; Tane, P.; Efferth, T. Cytotoxicity and modes of action of five Cameroonian medicinal plants against multi-factorial drug resistance of tumor cells. *J. Ethnopharmacol.* **2014**, *153*, 207–219. [CrossRef] [PubMed]

77. Somaida, A.; Tariq, I.; Ambreen, G.; Abdelsalam, A.M.; Ayoub, A.M.; Wojcik, M.; Dzoyem, J.P.; Bakowsky, U. Potent cytotoxicity of four cameroonian plant extracts on different cancer cell lines. *Pharmaceuticals* **2020**, *13*, 357. [CrossRef]

78. Pieme, C.A.; Guru, S.K.; Ambassa, P.; Kumar, S.; Ngameni, B.; Ngogang, J.Y.; Bhushan, S.; Saxena, A.K. Induction of mitochondrial dependent apoptosis and cell cycle arrest in human promyelocytic leukemia HL-60 cells by an extract from *Dorstenia psilurus*: A spice from Cameroon. *BMC Complement. Altern. Med.* **2013**, *13*, 223. [CrossRef]

79. Kuete, V.; Sandjo, L.P.; Wiench, B.; Efferth, T. Cytotoxicity and modes of action of four Cameroonian dietary spices ethno-medically used to treat cancers: *Echinops giganteus*, *Xylopia aethiopica*, *Imperata cylindrica* and *Piper capense*. *J. EthnoPharmacol.* **2013**, *149*, 245–253. [CrossRef]

80. Sandjo, L.P.; Kuete, V.; Siwe, X.N.; Poumale, H.M.; Efferth, T. Cytotoxicity of an unprecedented brominated oleanolide and a new furoceramide from the *Cameroonian spice*, *Echinops giganteus*. *Nat. Product Res.* **2016**, *30*, 2529–2537. [CrossRef]

81. Jung, Y.-K.; Shin, D. *Imperata cylindrica*: A review of phytochemistry, pharmacology, and industrial applications. *Molecules* **2021**, *26*, 1454. [CrossRef]

82. Wamba, B.E.; Ghosh, P.; Mbaveng, A.T.; Bhattacharya, S.; Debarpan, M.; Depanwita, S.; Saunak, M.M.; Kuete, V.; Murmu, N. Botanical from *Piper capense* Fruit Can Help to Combat the Melanoma as Demonstrated by In Vitro and In Vivo Studies. *Evid. Based Complement. Altern. Med.* **2021**, *2021*, 8810368. [CrossRef]

83. Ulloa Ulloa, C.; Acevedo-Rodríguez, P.; Beck, S.; Belgrano, M.J.; Bernal, R.; Berry, P.E.; Brako, L.; Celis, M.; Davidse, G.; Forzza, R.C. An integrated assessment of the vascular plant species of the Americas. *Science* **2017**, *358*, 1614–1617. [CrossRef]

84. Zhang, J.; Hunto, S.T.; Yang, Y.; Lee, J.; Cho, J.Y. *Tabebuia impetiginosa*: A comprehensive review on Tradit. uses, phytochemistry, and immunopharmacological properties. *Molecules* **2020**, *25*, 4294. [CrossRef] [PubMed]

85. Warashina, T.; Nagatani, Y.; Noro, T. Constituents from the bark of *Tabebuia impetiginosa*. *PhytoChem.* **2004**, *65*, 2003–2011. [CrossRef] [PubMed]

86. Mukherjee, B.; Telang, N.; Wong, G. Growth inhibition of estrogen receptor positive human breast cancer cells by Taheebo from the inner bark of Tabebuia avellandae tree. *Int. J. Mol. Med.* **2009**, *24*, 253–260. [PubMed]

87. Kee, J.-Y.; Han, Y.-H.; Park, J.; Kim, D.-S.; Mun, J.-G.; Ahn, K.S.; Kim, H.-J.; Um, J.-Y.; Hong, S.-H. β-Lapachone inhibits lung metastasis of colorectal cancer by inducing apoptosis of CT26 cells. *Integr. Cancer Ther.* **2017**, *16*, 585–596. [CrossRef]

88. Woo, H.J.; Park, K.-Y.; Rhu, C.-H.; Lee, W.H.; Choi, B.T.; Kim, G.Y.; Park, Y.-M.; Choi, Y.H. β-lapachone, a quinone isolated from Tabebuia avellanedae, induces apoptosis in HepG2 hepatoma cell line through induction of Bax and activation of caspase. *J. Med. Food* **2006**, *9*, 161–168. [CrossRef]

89. Pires, T.C.; Dias, M.I.; Calhelha, R.C.; Carvalho, A.M.; Queiroz, M.-J.R.; Barros, L.; Ferreira, I.C. Bioactive properties of *Tabebuia impetiginosa*-based phytopreparations and phytoformulations: A comparison between extracts and dietary supplements. *Molecules* **2015**, *20*, 22863–22871. [CrossRef]

90. De Melo, J.G.; Santos, A.G.; de Amorim, E.L.C.; de Nascimento, S.C.; de Albuquerque, U.P. Medicinal plants used as antitumor agents in Brazil: An ethnobotanical approach. *Evid. Based Complement. Altern. Med.* **2011**, *2011*, 365359. [CrossRef]

91. Shankar Babu, M.; Mahanta, S.; Lakhter, A.J.; Hato, T.; Paul, S.; Naidu, S.R. Lapachol inhibits glycolysis in cancer cells by targeting pyruvate kinase M2. *PLoS ONE* **2018**, *13*, e0191419. [CrossRef]

92. Zahra, K.; Dey, T.; Mishra, S.P.; Pandey, U. Pyruvate kinase M2 and cancer: The role of PKM2 in promoting tumorigenesis. *Front. Oncol.* **2020**, *10*, 159. [CrossRef]

93. Shuvalov, O.; Kizenko, A.; Petukhov, A.; Fedorova, O.; Daks, A.; Bottrill, A.; Snezhkina, A.V.; Kudryavtseva, A.V.; Barlev, N. SEMG1/2 augment energy metabolism of tumor cells. *Cell Death Dis.* **2020**, *11*, 1047. [CrossRef]

94. Zhao, W.; Jiang, L.; Fang, T.; Fang, F.; Liu, Y.; Zhao, Y.; You, Y.; Zhou, H.; Su, X.; Wang, J. β-Lapachone Selectively Kills Hepatocellular Carcinoma Cells by Targeting NQO1 to Induce Extensive DNA Damage and PARP1 Hyperactivation. *Front. Oncol.* **2021**, *11*, 747282. [CrossRef] [PubMed]

95. Cheng, M.-L.; Lu, Y.-F.; Chen, H.; Shen, Z.-Y.; Liu, J. Liver expression of Nrf2-related genes in different liver diseases. *Hepatobiliary Pancreat. Dis. Int.* **2015**, *14*, 485–491. [CrossRef]

96. Yang, Y.; Zheng, J.; Wang, M.; Zhang, J.; Tian, T.; Wang, Z.; Yuan, S.; Liu, L.; Zhu, P.; Gu, F. NQO1 promotes an aggressive phenotype in hepatocellular carcinoma via amplifying ERK-NRF2 signaling. *Cancer Sci.* **2021**, *112*, 641–654. [CrossRef] [PubMed]

97. Hussain, H.; Green, I.R. Lapachol and lapachone analogs: A journey of two decades of patent research (1997–2016). *Exp. Opin. Ther. Pat.* **2017**, *27*, 1111–1121. [CrossRef]

98. Rone, A.; Oliveira, K.M.; Guedes, A.P.; Dos Santos, P.W.; Aissa, A.F.; Batista, A.A.; Pavan, F.R. A Novel Ruthenium (II) Complex with Lapachol Induces G2/M Phase Arrest through Aurora-B Kinase Down-Regulation and ROS-Mediated Apoptosis in Human Prostate Adenocarcinoma Cells. *Front. Oncol.* **2021**, *11*, 2148.

99. Chen, Q.; Bai, L.; Zhou, X.; Xu, P.; Li, X.; Xu, H.; Zheng, Y.; Zhao, Y.; Lu, S.; Xue, M. Development of long-circulating lapachol nanoparticles: Formation, characterization, pharmacokinetics, distribution and cytotoxicity. *RSC Adv.* **2020**, *10*, 30025–30034. [CrossRef]

100. Beg, M.; Boothman, D.; Khosama, L.; Arriaga, Y.; Verma, U.; Sanjeeviaiah, A.; Kazmi, S.; Fattah, F.; Pilarski, S.; Rodriguez, M. A phase I/Ib, multi-center trial of ARQ-761 (Beta-Lapachone) with gemcitabine/nab-paclitaxel in patients with advanced pancreatic cancer. *Ann. Oncol.* **2019**, *30*, v271. [CrossRef]

101. Tahara, T.; Watanabe, A.; Yutani, M.; Yamano, Y.; Sagara, M.; Nagai, S.; Saito, K.; Yamashita, M.; Ihara, M.; Iida, A. STAT3 inhibitory activity of naphthoquinones isolated from Tabebuia avellanedae. *Bioorg. Med. Chem.* **2020**, *28*, 115347. [CrossRef]

102. Rauwald, H.W.; Maucher, R.; Dannhardt, G.; Kuchta, K. Dihydroisocoumarins, Naphthalenes, and Further Polyketides from *Aloe vera* and *A. plicatilis*: Isolation, Identification and Their 5-LOX/COX-1 Inhibiting Potency. *Molecules* **2021**, *26*, 4223. [CrossRef]

103. Huang, P.-H.; Huang, C.-Y.; Chen, M.-C.; Lee, Y.-T.; Yue, C.-H.; Wang, H.-Y.; Lin, H. Emodin and aloe-emodin suppress breast cancer cell proliferation through ERα inhibition. *Evid. Based Complement. Altern. Med.* **2013**, *2013*, 376123. [CrossRef]

104. Wang, Z.; Tang, T.; Wang, S.; Cai, T.; Tao, H.; Zhang, Q.; Qi, S.; Qi, Z. Aloin inhibits the proliferation and migration of gastric cancer cells by regulating NOX2–ROS-mediated pro-survival signal pathways. *Drug Des. Dev. Ther.* **2020**, *14*, 145. [CrossRef] [PubMed]

105. Sun, R.; Zhai, R.; Ma, C.; Miao, W. Combination of aloin and metformin enhances the antitumor effect by inhibiting the growth and invasion and inducing apoptosis and autophagy in hepatocellular carcinoma through PI3K/AKT/mTOR pathway. *Cancer Med.* **2020**, *9*, 1141–1151. [CrossRef] [PubMed]

106. Pan, Q.; Pan, H.; Lou, H.; Xu, Y.; Tian, L. Inhibition of the angiogenesis and growth of Aloin in human colorectal cancer in vitro and in vivo. *Cancer Cell Int.* **2013**, *13*, 69. [CrossRef] [PubMed]

107. Sanders, B.; Ray, A.M.; Goldberg, S.; Clark, T.; McDaniel, H.R.; Atlas, S.E.; Farooqi, A.; Konefal, J.; Lages, L.C.; Lopez, J. Anti-cancer effects of aloe-emodin: A systematic review. *J. Clin. Transl. Res.* **2018**, *3*, 283. [PubMed]

108. Manirakiza, A.; Irakoze, L.; Manirakiza, S. Aloe and its Effects on Cancer: A Narrative Literature Review. *East Afr. Health Res. J.* **2021**, *5*, 1. [CrossRef]

109. Dong, X.; Zeng, Y.; Liu, Y.; You, L.; Yin, X.; Fu, J.; Ni, J. Aloe-emodin: A review of its pharmacology, toxicity, and pharmacokinetics. *Phytother. Res.* **2020**, *34*, 270–281. [CrossRef]

110. Cheng, C.; Dong, W. Aloe-emodin induces endoplasmic reticulum stress-dependent apoptosis in colorectal cancer cells. *Med. Sci. Monit. Int. Med. J. Exp. Clin. Res.* **2018**, *24*, 6331. [CrossRef]

111. Shen, F.; Ge, C.; Yuan, P. Aloe-emodin induces autophagy and apoptotic cell death in non-small cell lung cancer cells via Akt/mTOR and MAPK signaling. *Eur. J. Pharmacol.* **2020**, *886*, 173550. [CrossRef]

112. Wang, S.; Yan, W.-W.; He, M.; Wei, D.; Long, Z.-J.; Tao, Y.-M. Aloe emodin inhibits telomerase activity in breast cancer cells: Transcriptional and enzymological mechanism. *Pharmacol. Rep.* **2020**, *72*, 1383–1396. [CrossRef]

113. Kosiol, N.; Juranek, S.; Brossart, P.; Heine, A.; Paeschke, K. G-quadruplexes: A promising target for cancer therapy. *Mol. Cancer* **2021**, *20*, 40. [CrossRef]

114. Das, A.; Dutta, S. Binding Studies of Aloe-Active Compounds with G-Quadruplex Sequences. *ACS Omega* **2021**, *6*, 18344–18351. [CrossRef] [PubMed]

115. Li, P.; Ren, K.; Liang, Y.; Liu, J.; Liang, Z.; Zhang, Y. Aloin promotes cell apoptosis by targeting HMGB1-TLR4-ERK axis in human melanoma cells. *EXCLI J.* **2020**, *19*, 641.

116. Tao, H.; Tang, T.; Wang, S.; Wang, Z.; Ma, Y.; Cai, T.; Cheng, X.; Qi, S.; Zhang, Y.; Qi, Z. The molecular mechanisms of Aloin induce gastric cancer cells apoptosis by targeting High Mobility Group Box 1. *Drug Des. Dev. Ther.* **2019**, *13*, 1221. [CrossRef]

117. Birari, L.; Wagh, S.; Patil, K.R.; Mahajan, U.B.; Unger, B.; Belemkar, S.; Goyal, S.N.; Ojha, S.; Patil, C.R. Aloin alleviates doxorubicin-induced cardiotoxicity in rats by abrogating oxidative stress and pro-inflammatory cytokines. *Cancer Chemother. Pharmacol.* **2020**, *86*, 419–426. [CrossRef] [PubMed]

118. Lissoni, P.; Rovelli, F.; Brivio, F.; Zago, R.; Colciago, M.; Messina, G.; Mora, A.; Porro, G. A randomized study of chemotherapy versus biochemotherapy with chemotherapy plus Aloe arborescens in patients with metastatic cancer. *In Vivo* **2009**, *23*, 171–175. [PubMed]

119. Lissoni, P.; Giani, L.; Zerbini, S.; Trabattoni, P.; Rovelli, F. Biotherapy with the pineal immunomodulating hormone melatonin versus melatonin plus *Aloe vera* in untreatable advanced solid neoplasms. *Nat. Immun.* **1998**, *16*, 27–33. [CrossRef]

120. Damani, M.R.; Shah, A.R.; Karp, C.L.; Orlin, S.E. Treatment of ocular surface squamous neoplasia with topical *Aloe vera* drops. *Cornea* **2015**, *34*, 87–89. [CrossRef]

121. Peng, C.; Zhang, W.; Dai, C.; Li, W.; Shen, X.; Yuan, Y.; Yan, L.; Zhang, W.; Yao, M. Study of the aqueous extract of *Aloe vera* and its two active components on the Wnt/β-catenin and Notch signaling pathways in colorectal cancer cells. *J. Ethnopharmacol.* **2019**, *243*, 112092. [CrossRef]

122. Arul, B.; Kothai, R. Anticancer effect of capsaicin and its analogues. In *Capsicum*; IntechOpen: London, UK, 2020.

123. Chapa-Oliver, A.M.; Mejía-Teniente, L. Capsaicin: From plants to a cancer-suppressing agent. *Molecules* **2016**, *21*, 931. [CrossRef]

124. Chakraborty, S.; Adhikary, A.; Mazumdar, M.; Mukherjee, S.; Bhattacharjee, P.; Guha, D.; Choudhuri, T.; Chattopadhyay, S.; Sa, G.; Sen, A. Capsaicin-induced activation of p53-SMAR1 auto-regulatory loop down-regulates VEGF in non-small cell lung cancer to restrain angiogenesis. *PLoS ONE* **2014**, *9*, e99743. [CrossRef]

125. Dai, N.; Ye, R.; He, Q.; Guo, P.; Chen, H.; Zhang, Q. Capsaicin and sorafenib combination treatment exerts synergistic anti-hepatocellular carcinoma activity by suppressing EGFR and PI3K/Akt/mTOR signaling. *Oncol. Rep.* **2018**, *40*, 3235–3248. [PubMed]

126. Lin, Y.-T.; Wang, H.-C.; Hsu, Y.-C.; Cho, C.-L.; Yang, M.-Y.; Chien, C.-Y. Capsaicin induces autophagy and apoptosis in human nasopharyngeal carcinoma cells by downregulating the PI3K/AKT/mTOR pathway. *Int. J. Mol. Sci.* **2017**, *18*, 1343. [CrossRef] [PubMed]

127. Chang, C.-F.; Islam, A.; Liu, P.-F.; Zhan, J.-H.; Chueh, P.J. Capsaicin acts through tNOX (ENOX2) to induce autophagic apoptosis in p53-mutated HSC-3 cells but autophagy in p53-functional SAS oral cancer cells. *Am. J. Cancer Res.* **2020**, *10*, 3230. [PubMed]

128. Friedman, J.R.; Richbart, S.D.; Merritt, J.C.; Brown, K.C.; Denning, K.L.; Tirona, M.T.; Valentovic, M.A.; Miles, S.L.; Dasgupta, P. Capsaicinoids: Multiple effects on angiogenesis, invasion and metastasis in human cancers. *Biomed. Pharmacother.* **2019**, *118*, 109317. [CrossRef] [PubMed]

129. Amantini, C.; Morelli, M.B.; Nabissi, M.; Cardinali, C.; Santoni, M.; Gismondi, A.; Santoni, G. Capsaicin triggers autophagic cell survival which drives epithelial mesenchymal transition and chemoresistance in bladder cancer cells in an Hedgehog-dependent manner. *Oncotarget* **2016**, *7*, 50180. [CrossRef] [PubMed]

130. Fedorova, O.; Daks, A.; Parfenyev, S.; Shuvalov, O.; Netsvetay, S.; Vasileva, J.; Gudovich, A.; Golotin, V.; Semenov, O.; Petukhov, A. Zeb1-mediated autophagy enhances resistance of breast cancer cells to genotoxic drugs. *Biochem. Biophys. Res. Commun.* **2022**, *589*, 29–34. [CrossRef]

131. de Souza, P.O.; Bianchi, S.E.; Figueiró, F.; Heimfarth, L.; Moresco, K.S.; Gonçalves, R.M.; Hoppe, J.B.; Klein, C.P.; Salbego, C.G.; Gelain, D.P. Anticancer activity of flavonoids isolated from *Achyrocline satureioides* in gliomas cell lines. *Toxicol. In Vitro* **2018**, *51*, 23–33. [CrossRef]

132. Soares Machado, M.; Palma, A.; Panelo, L.C.; Paz, L.A.; Rosa, F.; Lira, M.C.; Azurmendi, P.; Rubio, M.F.; Lenz, G.; Urtreger, A.J. Extract from *Aloysia polystachya* induces the cell death of colorectal cancer stem cells. *Nutr. Cancer* **2020**, *72*, 1004–1017. [CrossRef]

133. Lamorte, D.; Faraone, I.; Laurenzana, I.; Trino, S.; Russo, D.; Rai, D.K.; Armentano, M.F.; Musto, P.; Sgambato, A.; De Luca, L. Advances in *Azorella glabra* Wedd. Extract research: In vitro antioxidant activity, antiproliferative effects on acute myeloid leukemia cells and bioactive compound characterization. *Molecules* **2020**, *25*, 4890. [CrossRef]

134. Mellado, M.; Soto, M.; Madrid, A.; Montenegro, I.; Jara-Gutiérrez, C.; Villena, J.; Werner, E.; Godoy, P.; Aguilar, L.F. In vitro antioxidant and antiproliferative effect of the extracts of *Ephedra chilensis* K Presl aerial parts. *BMC Complement. Altern. Med.* **2019**, *19*, 53. [CrossRef]

135. Alonso-Castro, A.J.; Ortiz-Sánchez, E.; Domínguez, F.; López-Toledo, G.; Chávez, M.; de Jesús Ortiz-Tello, A.; García-Carrancá, A. Antitumor effect of *Croton lechleri* mull. arg.(euphorbiaceae). *J. Ethnopharmacol.* **2012**, *140*, 438–442. [CrossRef] [PubMed]

136. Montopoli, M.; Bertin, R.; Chen, Z.; Bolcato, J.; Caparrotta, L.; Froldi, G. *Croton lechleri* sap. and isolated alkaloid taspine exhibit inhibition against human melanoma SK23 and colon cancer HT29 cell lines. *J. Ethnopharmacol.* **2012**, *144*, 747–753. [CrossRef] [PubMed]

137. Suzuki, A.; Saito, Y.; Fukuyoshi, S.; Goto, M.; Miyake, K.; Newman, D.J.; O'Keefe, B.R.; Lee, K.-H.; Nakagawa-Goto, K. Corymbulosins D–H, 2-Hydroxy-and 2-Oxo-clerodane Diterpenes from the Bark of *Laetia corymbulosa*. *J. Nat. Prod.* **2017**, *80*, 1065–1072. [CrossRef] [PubMed]

138. Fu, L.; Wei, J.; Gao, Y.; Chen, R. Antioxidant and antitumoral activities of isolated macamide and macaene fractions from *Lepidium meyenii* (Maca). *Talanta* **2021**, *221*, 121635. [CrossRef] [PubMed]

139. Bosio, C.; Tomasoni, G.; Martínez, R.; Olea, A.F.; Carrasco, H.; Villena, J. Cytotoxic and apoptotic effects of leptocarpin, a plant-derived sesquiterpene lactone, on human cancer cell lines. *Chem. Biol. Interact.* **2015**, *242*, 415–421. [CrossRef]

140. Amaral, R.G.; Gomes, S.V.; Andrade, L.N.; Dos Santos, S.A.; Severino, P.; de Albuquerque Júnior, R.L.; Souto, E.B.; Brandão, G.C.; Santos, S.L.; David, J.M. Cytotoxic, antitumor and toxicological profile of *Passiflora alata* leaf extract. *Molecules* **2020**, *25*, 4814. [CrossRef]

141. Ramos-Silva, A.; Tavares-Carreón, F.; Figueroa, M.; la Torre-Zavala, D.; Gastelum-Arellanez, A.; Rodríguez-García, A.; Galán-Wong, L.J.; Avilés-Arnaut, H. Anticancer potential of *Thevetia peruviana* fruit methanolic extract. *BMC Complement. Altern. Med.* **2017**, *17*, 241. [CrossRef]

142. Kantarjian, H.M.; Talpaz, M.; Santini, V.; Murgo, A.; Cheson, B.; O'Brien, S.M. Homoharringtonine: History, current research, and future directions. *Cancer* **2001**, *92*, 1591–1605. [CrossRef]

143. Kantarjian, H.M.; O'Brien, S.; Cortes, J. Homoharringtonine/omacetaxine mepesuccinate: The long and winding road to food and drug administration approval. *Clin. Lymphoma Myeloma Leuk.* **2013**, *13*, 530–533. [CrossRef]

144. Xie, M.; Jiang, Q.; Li, L.; Zhu, J.; Zhu, L.; Zhou, D.; Zheng, Y.; Yang, X.; Zhu, M.; Sun, J. HAG (homoharringtonine, cytarabine, G-CSF) regimen for the treatment of acute myeloid leukemia and myelodysplastic syndrome: A meta-analysis with 2,314 participants. *PLoS ONE* **2016**, *11*, e0164238. [CrossRef]

145. Gu, L.-F.; Zhang, W.-G.; Wang, F.-X.; Cao, X.-M.; Chen, Y.-X.; He, A.-L.; Liu, J.; Ma, X.-R. Low dose of homoharringtonine and cytarabine combined with granulocyte colony-stimulating factor priming on the outcome of relapsed or refractory acute myeloid leukemia. *J. Cancer Res. Clin. Oncol.* **2011**, *137*, 997–1003. [CrossRef] [PubMed]

146. Winer, E.S.; DeAngelo, D.J. A review of omacetaxine: A chronic myeloid leukemia treatment resurrected. *Oncol. Ther.* **2018**, *6*, 9–20. [CrossRef] [PubMed]

147. Chen, X.-J.; Zhang, W.-N.; Chen, B.; Xi, W.-D.; Lu, Y.; Huang, J.-Y.; Wang, Y.-Y.; Long, J.; Wu, S.-F.; Zhang, Y.-X. Homoharringtonine deregulates MYC transcriptional expression by directly binding NF-κB repressing factor. *Proc. Nat. Acad. Sci. USA* **2019**, *116*, 2220–2225. [CrossRef] [PubMed]

148. Tong, H.; Ren, Y.; Zhang, F.; Jin, J. Homoharringtonine affects the JAK2-STAT5 signal pathway through alteration of protein tyrosine kinase phosphorylation in acute myeloid leukemia cells. *Eur. J. Haematol.* **2008**, *81*, 259–266. [CrossRef]

149. Han, X.; Zhang, X.; Wang, Q.; Wang, L.; Yu, S. Antitumor potential of *Hedyotis diffusa* Willd: A systematic review of bioactive constituents and underlying molecular mechanisms. *Biomed. Pharmacother.* **2020**, *130*, 110735. [CrossRef]

150. Lee, Y.K.; Bae, K.; Yoo, H.-S.; Cho, S.-H. Benefit of adjuvant Tradit. herbal medicine with chemotherapy for resectable gastric cancer. *Integr. Cancer Ther.* **2018**, *17*, 619–627. [CrossRef]

151. Yeh, Y.-C.; Chen, H.-Y.; Yang, S.-H.; Lin, Y.-H.; Chiu, J.-H.; Lin, Y.-H.; Chen, J.-L. *Hedyotis diffusa* combined with *Scutellaria barbata* are the core treatment of Chinese herbal medicine used for breast cancer patients: A population-based study. *Evid. Based Complement. Altern. Med.* **2014**, *2014*, 202378. [CrossRef]

152. Yang, B.; Wang, N.; Wang, S.; Li, X.; Zheng, Y.; Li, M.; Song, J.; Zhang, F.; Mei, W.; Lin, Y. Network-pharmacology-based identification of caveolin-1 as a key target of *Oldenlandia diffusa* to suppress breast cancer metastasis. *Biomed. Pharmacother.* **2019**, *112*, 108607. [CrossRef]

153. Chung, T.-W.; Choi, H.; Lee, J.-M.; Ha, S.-H.; Kwak, C.-H.; Abekura, F.; Park, J.-Y.; Chang, Y.-C.; Ha, K.-T.; Cho, S.-H. *Oldenlandia diffusa* suppresses metastatic potential through inhibiting matrix metalloproteinase-9 and intercellular adhesion molecule-1 expression via p38 and ERK1/2 MAPK pathways and induces apoptosis in human breast cancer MCF-7 cells. *J. Ethnopharmacol.* **2017**, *195*, 309–317. [CrossRef]

154. Lu, P.-H.; Chen, M.-B.; Ji, C.; Li, W.-T.; Wei, M.-X.; Wu, M.-H. Aqueous *Oldenlandia diffusa* extracts inhibits colorectal cancer cells via activating AMP-activated protein kinase signalings. *Oncotarget* **2016**, *7*, 45889. [CrossRef]

155. Chen, Q.; Rahman, K.; Wang, S.-J.; Zhou, S.; Zhang, H. *Scutellaria barbata*: A review on chemical constituents, pharmacological activities and clinical applications. *Curr. Pharm. Des.* **2020**, *26*, 160–175. [CrossRef] [PubMed]

156. Feng, X.M.; Su, X.L. Anticancer effect of ursolic acid via mitochondria-dependent pathways. *Oncol. Lett.* **2019**, *17*, 4761–4767. [CrossRef] [PubMed]

157. Guo, W.; Xu, B.; Wang, X.; Zheng, B.; Du, J.; Liu, S. The analysis of the anti-tumor mechanism of ursolic acid using connectively map approach in breast cancer cells line MCF-7. *Cancer Manag. Res.* **2020**, *12*, 3469. [CrossRef] [PubMed]

158. Liu, T.; Ma, H.; Shi, W.; Duan, J.; Wang, Y.; Zhang, C.; Li, C.; Lin, J.; Li, S.; Lv, J. Inhibition of STAT3 signaling pathway by ursolic acid suppresses growth of hepatocellular carcinoma. *Int. J. Oncol.* **2017**, *51*, 555–562. [CrossRef]

159. Wang, S.; Chang, X.; Zhang, J.; Li, J.; Wang, N.; Yang, B.; Pan, B.; Zheng, Y.; Wang, X.; Ou, H. Ursolic Acid Inhibits Breast Cancer Metastasis by Suppressing Glycolytic Metabolism via Activating SP1/Caveolin-1 Signaling. *Front. Oncol.* **2021**, *11*, 745584. [CrossRef]

160. Lewinska, A.; Adamczyk-Grochala, J.; Kwasniewicz, E.; Deregowska, A.; Wnuk, M. Ursolic acid-mediated changes in glycolytic pathway promote cytotoxic autophagy and apoptosis in phenotypically different breast cancer cells. *Apoptosis* **2017**, *22*, 800–815. [CrossRef]

161. Wang, J.; Jiang, Z.; Xiang, L.; Li, Y.; Ou, M.; Yang, X.; Shao, J.; Lu, Y.; Lin, L.; Chen, J. Synergism of ursolic acid derivative US597 with 2-deoxy-D-glucose to preferentially induce tumor cell death by dual-targeting of apoptosis and glycolysis. *Sci. Rep.* **2014**, *4*, 1–12. [CrossRef]

162. Tang, Z.-Y.; Li, Y.; Tang, Y.-T.; Ma, X.-D.; Tang, Z.-Y. Anticancer activity of oleanolic acid and its derivatives: Recent advances in evidence, target profiling and mechanisms of action. *Biomed. Pharmacother.* **2022**, *145*, 112397. [CrossRef]

163. Li, Y.; Xu, Q.; Yang, W.; Wu, T.; Lu, X. Oleanolic acid reduces aerobic glycolysis-associated proliferation by inhibiting yes-associated protein in gastric cancer cells. *Gene* **2019**, *712*, 143956. [CrossRef]

164. Lee, J.-H.; Yoo, E.-S.; Han, S.-H.; Jung, G.-H.; Han, E.-J.; Jung, S.-H.; Kim, B.S.; Cho, S.-D.; Nam, J.-S.; Choi, C. Oleanolic acid induces apoptosis and autophagy via the PI3K/AKT/mTOR pathway in AGS human gastric cancer cells. *J. Funct. Foods* **2021**, *87*, 104854. [CrossRef]

165. Nie, H.; Wang, Y.; Qin, Y.; Gong, X.G. Oleanolic acid induces autophagic death in human gastric cancer cells in vitro and in vivo. *Cell Biol. Int.* **2016**, *40*, 770–778. [CrossRef] [PubMed]

166. Xiaofei, J.; Mingqing, S.; Miao, S.; Yizhen, Y.; Shuang, Z.; Qinhua, X.; Kai, Z. Oleanolic acid inhibits cervical cancer Hela cell proliferation through modulation of the ACSL4 ferroptosis signaling pathway. *Biochem. Biophys. Res. Commun.* **2021**, *545*, 81–88. [CrossRef] [PubMed]

167. Li, F.; Wang, S.; Niu, M. Scutellarin inhibits the growth and EMT of gastric cancer cells through regulating PTEN/PI3K pathway. *Biol. Pharm. Bull.* **2021**, *44*, 780–788. [CrossRef] [PubMed]

168. Niu, G.; Sun, L.; Pei, Y.; Wang, D. Oleanolic acid inhibits colorectal cancer angiogenesis by blocking the VEGFR2 signaling pathway. *Anti Cancer Agents Med. Chem. Formerly Curr. Med. Chem. Anti-Cancer Agents* **2018**, *18*, 583–590. [CrossRef]

169. Ma, T.-T.; Zhang, G.-L.; Dai, C.-F.; Zhang, B.-R.; Cao, K.-X.; Wang, C.-G.; Yang, G.-W.; Wang, X.-M. *Scutellaria barbata* and *Hedyotis diffusa* herb pair for breast cancer treatment: Potential mechanism based on network pharmacology. *J. Ethnopharmacol.* **2020**, *259*, 112929. [CrossRef]

170. Gao, J.; Yin, W.; Corcoran, O. From *Scutellaria barbata* to BZL101 in cancer patients: Phytochemistry, pharmacology, and clinical evidence. *Nat. Prod. Commun.* **2019**, *14*, 1934578X19880645. [CrossRef]

171. Chen, V.; Staub, R.E.; Fong, S.; Tagliaferri, M.; Cohen, I.; Shtivelman, E. Bezielle selectively targets mitochondria of cancer cells to inhibit glycolysis and OXPHOS. *PLoS ONE* **2012**, *7*, e30300. [CrossRef]

172. Lang, X.; Chen, Z.; Yang, X.; Yan, Q.; Xu, M.; Liu, W.; He, Q.; Zhang, Y.; Cheng, W.; Zhao, W. Scutellarein induces apoptosis and inhibits proliferation, migration, and invasion in ovarian cancer via inhibition of EZH2/FOXO1 signaling. *J. Biochem. Mol. Toxicol.* **2021**, *35*, e22870. [CrossRef]

173. Ha, S.E.; Kim, S.M.; Vetrivel, P.; Kim, H.H.; Bhosale, P.B.; Heo, J.D.; Lee, H.J.; Kim, G.S. Inhibition of cell proliferation and metastasis by scutellarein regulating PI3K/Akt/NF-κB signaling through PTEN activation in hepatocellular carcinoma. *Int. J. Mol. Sci.* **2021**, *22*, 8841. [CrossRef]

174. Zeng, S.; Chen, L.; Sun, Q.; Zhao, H.; Yang, H.; Ren, S.; Liu, M.; Meng, X.; Xu, H. Scutellarin ameliorates colitis-associated colorectal cancer by suppressing Wnt/β-catenin signaling cascade. *Eur. J. Pharmacol.* **2021**, *906*, 174253. [CrossRef]

175. Jiang, Q.; Li, Q.; Chen, H.; Shen, A.; Cai, Q.; Lin, J.; Peng, J. *Scutellaria barbata* D. Don inhibits growth and induces apoptosis by suppressing IL-6-inducible STAT3 pathway activation in human colorectal cancer cells. *Exp. Ther. Med.* **2015**, *10*, 1602–1608. [CrossRef] [PubMed]

176. Wei, L.-H.; Lin, J.-M.; Chu, J.-F.; Chen, H.-W.; Li, Q.-Y.; Peng, J. *Scutellaria barbata* D. Don inhibits colorectal cancer growth via suppression of Wnt/β-catenin signaling pathway. *Chin. J. Integr. Med.* **2017**, *23*, 858–863. [CrossRef] [PubMed]

177. Lin, J.; Feng, J.; Yang, H.; Yan, Z.; Li, Q.; Wei, L.; Lai, Z.; Jin, Y.; Peng, J. *Scutellaria barbata* D. Don inhibits 5-fluorouracil resistance in colorectal cancer by regulating PI3K/AKT pathway. *Oncol. Rep.* **2017**, *38*, 2293–2300. [CrossRef] [PubMed]

178. Chen, F.; Zhong, Z.; Tan, H.Y.; Guo, W.; Zhang, C.; Tan, C.-W.; Li, S.; Wang, N.; Feng, Y. Uncovering the anticancer mechanisms of Chin. herbal medicine formulas: Ther. alternatives for liver cancer. *Front. Pharmacol.* **2020**, *11*, 293. [CrossRef] [PubMed]

179. Fan, Y.; Ma, Z.; Zhao, L.; Wang, W.; Gao, M.; Jia, X.; Ouyang, H.; He, J. Anti-tumor activities and mechanisms of Traditional Chinese medicines formulas: A review. *Biomed. Pharmacother.* **2020**, *132*, 110820. [CrossRef]

180. Wang, K.; Chen, Q.; Shao, Y.; Yin, S.; Liu, C.; Liu, Y.; Wang, R.; Wang, T.; Qiu, Y.; Yu, H. Anticancer activities of TCM and their active components against tumor metastasis. *Biomed. Pharmacother.* **2021**, *133*, 111044. [CrossRef]

181. Liu, S.-H.; Chen, P.-S.; Huang, C.-C.; Hung, Y.-T.; Lee, M.-Y.; Lin, W.-H.; Lin, Y.-C.; Lee, A.Y.-L. Unlocking the Mystery of the Therapeutic Effects of Chinese Medicine on Cancer. *Front. Pharmacol.* **2021**, *2013*, 601785. [CrossRef]

182. Lan, H.-Y.; An, P.; Liu, Q.-P.; Chen, Y.-Y.; Yu, Y.-Y.; Luan, X.; Tang, J.-Y.; Zhang, H. *Aidi injection* induces apoptosis of hepatocellular carcinoma cells through the mitochondrial pathway. *J. Ethnopharmacol.* **2021**, *274*, 114073. [CrossRef]

183. Shi, Q.; Diao, Y.; Jin, F.; Ding, Z. Anti-metastatic effects of Aidi on human esophageal squamous cell carcinoma by inhibiting epithelial-mesenchymal transition and angiogenesis. *Mol. Med. Rep.* **2018**, *18*, 131–138. [CrossRef]

184. Yang, M.; Shen, C.; Zhu, S.-j.; Zhang, Y.; Jiang, H.-l.; Bao, Y.-d.; Yang, G.-y.; Liu, J.-p. Chin. patent medicine *Aidi injection* for cancer care: An overview of systematic reviews and meta-analyses. *J. Ethnopharmacol.* **2022**, *282*, 114656. [CrossRef]

185. Zhao, Z.; Fan, H.; Higgins, T.; Qi, J.; Haines, D.; Trivett, A.; Oppenheim, J.J.; Wei, H.; Li, J.; Lin, H. Fufang *Kushen injection* inhibits sarcoma growth and tumor-induced hyperalgesia via TRPV1 signaling pathways. *Cancer Lett.* **2014**, *355*, 232–241. [CrossRef] [PubMed]

186. Zhu, A.; Wang, F.; Fan, Q.; He, W.; Wang, L.; Zhao, P. Apoptosis and growth arrest of human esophageal squamous cell carcinoma cell EC9706 induced by *Fufangkushen injection*. *Zhonghua Yi Xue Za Zhi* **2011**, *91*, 2797–2800. [PubMed]

187. Lu, Y.; Li, C.-S.; Dong, Q. Chin. herb related molecules of cancer-cell-apoptosis: A minireview of progress between *Kanglaite injection* and related genes. *J. Exp. Clin. Cancer Res.* **2008**, *27*, 31. [CrossRef] [PubMed]

188. Liu, Y.; Zhang, W.; Wang, X.-J.; Liu, S. Antitumor effect of Kanglaite®injection in human pancreatic cancer xenografts. *BMC Complement. Altern. Med.* **2014**, *14*, 228. [CrossRef] [PubMed]

189. Yang, Y.; Sun, M.; Yao, W.; Wang, F.; Li, X.; Wang, W.; Li, J.; Gao, Z.; Qiu, L.; You, R. Compound *Kushen injection* relieves tumor-associated macrophage-mediated immunosuppression through TNFR1 and sensitizes hepatocellular carcinoma to sorafenib. *J. Immunother. Cancer* **2020**, *8*, e000317. [CrossRef] [PubMed]

190. Qi-Yue, Y.; Ting, Z.; Ya-Nan, H.; Sheng-Jie, H.; Xuan, D.; Li, H.; Chun-Guang, X. From natural dye to herbal medicine: A systematic review of chemical constituents, pharmacological effects and clinical applications of indigo naturalis. *Chin. Med.* **2020**, *15*, 127. [CrossRef]

191. Yao, C.-J.; Chow, J.-M.; Yang, C.-M.; Kuo, H.-C.; Chang, C.-L.; Lee, H.-L.; Lai, I.; Chuang, S.-E.; Lai, G.-M. Chinese herbal mixture, Tien-Hsien liquid, induces G2/M cycle arrest and radiosensitivity in MCF-7 human breast cancer cells through mechanisms involving DNMT1 and Rad51 downregulation. *Evid. Based Complement. Altern. Med.* **2016**, *2016*, 3251046. [CrossRef]

192. Yao, C.-J.; Yang, C.-M.; Chuang, S.-E.; Yan, J.-L.; Liu, C.-Y.; Chen, S.-W.; Yan, K.-H.; Lai, T.-Y.; Lai, G.-M. Targeting PML-RARα and oncogenic signaling pathways by Chin. herbal mixture Tien-Hsien liquid in acute promyelocytic leukemia NB4 cells. *Evid. Based Complement. Altern. Med.* **2011**, *2011*, 984154. [CrossRef]

193. Yang, P.-M.; Du, J.-L.; Wang, G.N.-K.; Chia, J.-S.; Hsu, W.-B.; Pu, P.-C.; Sun, A.; Chiang, C.-P.; Wang, W.-B. The Chin. Herbal Mixture Tien-Hsien Liquid Augments the Anticancer Immunity in Tumor Cell–Vaccinated Mice. *Integr. Cancer Ther.* **2017**, *16*, 319–328. [CrossRef]

194. Yin, T.; Yang, G.; Ma, Y.; Xu, B.; Hu, M.; You, M.; Gao, S. Developing an activity and absorption-based quality control platform for Chin. Tradit. medicine: Application to Zeng-Sheng-Ping (Antitumor B). *J. Ethnopharmacol.* **2015**, *172*, 195–201. [CrossRef]

195. Wang, Y.; Yao, R.; Gao, S.; Wen, W.; Du, Y.; Szabo, E.; Hu, M.; Lubet, R.A.; You, M. Chemopreventive effect of a mixture of Chin. Herbs (antitumor B) on chemically induced oral carcinogenesis. *Mol. Carcinogen.* **2013**, *52*, 49–56. [CrossRef] [PubMed]

196. Lim, K.J.; Rajan, K.; Eberhart, C.G. Effects of Zeng Sheng Ping/ACAPHA on malignant brain tumor growth and notch signaling. *Anticancer Res.* **2012**, *32*, 2689–2696. [PubMed]

197. Kuruppu, A.I.; Paranagama, P.; Goonasekara, C.L. Medicinal plants commonly used against cancer in Tradit. *medicine formulae in Sri Lanka. Saudi Pharm. J.* **2019**, *27*, 565–573.

198. Sujatha, V. The Universal and the Global: Contextualising European Ayurvedic Practices. *Soc. Cult. South Asia* **2020**, *6*, 52–73. [CrossRef]

199. Rosenberg, M. The European academy of Ayurveda: 20 years of Ayurvedic education in Germany. *Anc. Sci. Life* **2012**, *32*, 63. [CrossRef] [PubMed]

200. Bhandari, N. Is ayurveda the key to universal healthcare in India? *BMJ* **2015**, *350*, h2879. [CrossRef]

201. Kumar, S.; Jawaid, T.; Dubey, S.D. Ther. plants of Ayurveda; a review on anticancer. *Pharmacogn. J.* **2011**, *3*, 1–11. [CrossRef]

202. Palliyaguru, D.L.; Singh, S.V.; Kensler, T.W. *Withania somnifera*: From Prev. to treatment of cancer. *Mol. Nutr. Food Res.* **2016**, *60*, 1342–1353. [CrossRef]

203. Singh, N.; Bhalla, M.; de Jager, P.; Gilca, M. An overview on ashwagandha: A Rasayana (rejuvenator) of Ayurveda. *Afr. J. Tradit. Complement. Altern. Med.* **2011**, *8*, 208–213. [CrossRef]

204. Widodo, N.; Kaur, K.; Shrestha, B.G.; Takagi, Y.; Ishii, T.; Wadhwa, R.; Kaul, S.C. Selective killing of cancer cells by leaf extract of Ashwagandha: Identification of a tumor-inhibitory factor and the first molecular insights to its effect. *Clin. Cancer Res.* **2007**, *13*, 2298–2306. [CrossRef]

205. Wadhwa, R.; Singh, R.; Gao, R.; Shah, N.; Widodo, N.; Nakamoto, T.; Ishida, Y.; Terao, K.; Kaul, S.C. Water extract of Ashwagandha leaves has anticancer activity: Identification of an active component and its mechanism of action. *PLoS ONE* **2013**, *8*, e77189. [CrossRef]

206. Mehta, V.; Chander, H.; Munshi, A. Mechanisms of anti-tumor activity of *Withania somnifera* (Ashwagandha). *Nutr. Cancer* **2021**, *73*, 914–926. [CrossRef] [PubMed]

207. Kataria, H.; Kumar, S.; Chaudhary, H.; Kaur, G. *Withania somnifera* suppresses tumor growth of intracranial allograft of glioma cells. *Mol. Neurobiol.* **2016**, *53*, 4143–4158. [CrossRef] [PubMed]

208. Moselhy, J.; Suman, S.; Alghamdi, M.; Chandarasekharan, B.; Das, T.P.; Houda, A.; Ankem, M.; Damodaran, C. Withaferin A inhibits prostate carcinogenesis in a PTEN-deficient mouse model of prostate cancer. *Neoplasia* **2017**, *19*, 451–459. [CrossRef] [PubMed]

209. Lee, I.-C.; Choi, B.Y. Withaferin-A—A natural anticancer agent with pleitropic mechanisms of action. *Int. J. Mol. Sci.* **2016**, *17*, 290. [CrossRef] [PubMed]

210. Sultana, T.; Okla, M.K.; Ahmed, M.; Akhtar, N.; Al-Hashimi, A.; Abdelgawad, H.; Haq, I.-U. Withaferin A: From Ancient Remedy to Potential Drug Candidate. *Molecules* **2021**, *26*, 7696. [CrossRef]

211. Kyakulaga, A.H.; Aqil, F.; Munagala, R.; Gupta, R.C. Withaferin a inhibits epithelial to mesenchymal transition in non-small cell lung cancer cells. *Sci. Rep.* **2018**, *8*, 15737. [CrossRef]

212. Hahm, E.-R.; Lee, J.; Kim, S.-H.; Sehrawat, A.; Arlotti, J.A.; Shiva, S.S.; Bhargava, R.; Singh, S.V. Metabolic alterations in mammary cancer Prev. by withaferin A in a clinically relevant mouse model. *J. Nat. Cancer Inst.* **2013**, *105*, 1111–1122. [CrossRef]

213. Kakar, S.S.; Parte, S.; Kelsey Carter, I.G.J.; Worth, C.; Rameshwar, P.; Ratajczak, M.Z. Withaferin A (WFA) inhibits tumor growth and metastasis by targeting ovarian cancer stem cells. *Oncotarget* **2017**, *8*, 74494. [CrossRef]

214. Kim, S.-H.; Singh, S.V. Mammary cancer chemoPrev. by withaferin A is accompanied by in vivo suppression of self-renewal of cancer stem cells. *Cancer Prev. Res.* **2014**, *7*, 738–747. [CrossRef]

215. Nelson, K.M.; Dahlin, J.L.; Bisson, J.; Graham, J.; Pauli, G.F.; Walters, M.A. The essential medicinal chemistry of curcumin: Miniperspective. *J. Med. Chem.* **2017**, *60*, 1620–1637. [CrossRef] [PubMed]

216. Dosoky, N.S.; Setzer, W.N. Chemical composition and biological activities of essential oils of Curcuma species. *Nutrients* **2018**, *10*, 1196. [CrossRef] [PubMed]

217. Sandur, S.K.; Pandey, M.K.; Sung, B.; Ahn, K.S.; Murakami, A.; Sethi, G.; Limtrakul, P.; Badmaev, V.; Aggarwal, B.B. Curcumin, demethoxycurcumin, bisdemethoxycurcumin, tetrahydrocurcumin and turmerones differentially regulate anti-inflammatory and anti-proliferative responses through a ROS-independent mechanism. *Carcinogenesis* **2007**, *28*, 1765–1773. [CrossRef] [PubMed]

218. Giordano, A.; Tommonaro, G. Curcumin and cancer. *Nutrients* **2019**, *11*, 2376. [CrossRef] [PubMed]

219. Sultana, S.; Munir, N.; Mahmood, Z.; Riaz, M.; Akram, M.; Rebezov, M.; Kuderinova, N.; Moldabayeva, Z.; Shariati, M.A.; Rauf, A. Molecular targets for the Manag. of cancer using *Curcuma longa* Linn. phytoconstituents: A Review. *Biomed. Pharmacother.* **2021**, *135*, 111078. [CrossRef]

220. Lev-Ari, S.; Starr, A.; Vexler, A.; Karaush, V.; Loew, V.; Greif, J.; Fenig, E.; Aderka, D.; Ben-Yosef, R. Inhibition of pancreatic and lung adenocarcinoma cell survival by curcumin is associated with increased apoptosis, down-regulation of COX-2 and EGFR and inhibition of Erk1/2 activity. *Anticancer Res.* **2006**, *26*, 4423–4430.

221. Zhao, G.; Han, X.; Zheng, S.; Li, Z.; Sha, Y.; Ni, J.; Sun, Z.; Qiao, S.; Song, Z. Curcumin induces autophagy, inhibits proliferation and invasion by downregulating AKT/mTOR signaling pathway in human melanoma cells. *Oncol. Rep.* **2016**, *35*, 1065–1074. [CrossRef]

222. Li, W.; Zhou, Y.; Yang, J.; Li, H.; Zhang, H.; Zheng, P. Curcumin induces apoptotic cell death and protective autophagy in human gastric cancer cells. *Oncol. Rep.* **2017**, *37*, 3459–3466. [CrossRef]

223. Zhuang, W.; Long, L.; Zheng, B.; Ji, W.; Yang, N.; Zhang, Q.; Liang, Z. Curcumin promotes differentiation of glioma-initiating cells by inducing autophagy. *Cancer Sci.* **2012**, *103*, 684–690. [CrossRef]

224. Almanaa, T.N.; Geusz, M.E.; Jamasbi, R.J. Effects of curcumin on stem-like cells in human esophageal squamous carcinoma cell lines. *BMC Complement. Altern. Med.* **2012**, *12*, 195. [CrossRef]

225. Wang, J.; Wang, C.; Bu, G. Curcumin inhibits the growth of liver cancer stem cells through the phosphatidylinositol 3-kinase/protein kinase B/mammalian target of rapamycin signaling pathway. *Exp. Ther. Med.* **2018**, *15*, 3650–3658. [CrossRef] [PubMed]

226. Yallapu, M.M.; Maher, D.M.; Sundram, V.; Bell, M.C.; Jaggi, M.; Chauhan, S.C. Curcumin induces chemo/radio-sensitization in ovarian cancer cells and curcumin nanoparticles inhibit ovarian cancer cell growth. *J. Ovar. Res.* **2010**, *3*, 11. [CrossRef]

227. Zhang, P.; Lai, Z.-L.; Chen, H.-F.; Zhang, M.; Wang, A.; Jia, T.; Sun, W.-Q.; Zhu, X.-M.; Chen, X.-F.; Zhao, Z. Curcumin synergizes with 5-fluorouracil by impairing AMPK/ULK1-dependent autophagy, AKT activity and enhancing apoptosis in colon cancer cells with tumor growth inhibition in xenograft mice. *J. Exp. Clin. Cancer Res.* **2017**, *36*, 190. [CrossRef] [PubMed]

228. Kong, W.-Y.; Ngai, S.C.; Goh, B.-H.; Lee, L.-H.; Htar, T.-T.; Chuah, L.-H. Is curcumin the answer to future chemotherapy cocktail? *Molecules* **2021**, *26*, 4329. [CrossRef]

229. Farghadani, R.; Naidu, R. Curcumin as an Enhancer of Ther. Efficiency of Chemotherapy Drugs in Breast Cancer. *Int. J. Mol. Sci.* **2022**, *23*, 2144. [CrossRef]

230. Hsu, F.-T.; Liu, Y.-C.; Liu, T.-T.; Hwang, J.-J. Curcumin sensitizes hepatocellular carcinoma cells to radiation via suppression of radiation-induced NF-κB activity. *Biomed Res. Int.* **2015**, *2015*, 363671. [CrossRef]

231. Zoi, V.; Galani, V.; Tsekeris, P.; Kyritsis, A.P.; Alexiou, G.A. Radiosensitization and Radioprotection by Curcumin in Glioblastoma and Other Cancers. *Biomedicines* **2022**, *10*, 312. [CrossRef]

232. Prasad, S.; Tyagi, A.K. Ginger and its constituents: Role in Prev. and treatment of gastrointestinal cancer. *Gastroenterol. Res. Pract.* **2015**. [CrossRef]

233. Mao, Q.-Q.; Xu, X.-Y.; Cao, S.-Y.; Gan, R.-Y.; Corke, H.; Beta, T.; Li, H.-B. Bioactive compounds and bioactivities of ginger (*Zingiber officinale* Roscoe). *Foods* **2019**, *8*, 185. [CrossRef]

234. de Lima, R.M.T.; Dos Reis, A.C.; de Menezes, A.A.P.M.; Santos, J.V.d.O.; Filho, J.W.G.d.O.; Ferreira, J.R.d.O.; de Alencar, M.V.O.B.; da Mata, A.M.O.F.; Khan, I.N.; Islam, A. Protective and therapeutic potential of ginger (*Zingiber officinale*) extract and [6]-gingerol in cancer: A comprehensive review. *Phytother. Res.* **2018**, *32*, 1885–1907. [CrossRef]

235. Habib, S.H.M.; Makpol, S.; Hamid, N.A.A.; Das, S.; Ngah, W.Z.W.; Yusof, Y.A.M. Ginger extract (*Zingiber officinale*) has anti-cancer and anti-inflammatory effects on ethionine-induced hepatoma rats. *Clinics* **2008**, *63*, 807–813. [CrossRef] [PubMed]

236. Kim, S.M.; Kim, C.; Bae, H.; Lee, J.H.; Baek, S.H.; Nam, D.; Chung, W.S.; Shim, B.S.; Lee, S.G.; Kim, S.H. 6-Shogaol exerts anti-proliferative and pro-apoptotic effects through the modulation of STAT3 and MAPKs signaling pathways. *Mol. Carcinog.* **2015**, *54*, 1132–1146. [CrossRef] [PubMed]

237. Saha, A.; Blando, J.; Silver, E.; Beltran, L.; Sessler, J.; DiGiovanni, J. 6-Shogaol from dried ginger inhibits growth of prostate cancer cells both in vitro and in vivo through inhibition of STAT3 and NF-κB signaling. *Cancer Prev. Res.* **2014**, *7*, 627–638. [CrossRef] [PubMed]

238. Kim, Y.-J.; Jeon, Y.; Kim, T.; Lim, W.-C.; Ham, J.; Park, Y.N.; Kim, T.-J.; Ko, H. Combined treatment with zingerone and its novel derivative synergistically inhibits TGF-β1 induced epithelial-mesenchymal transition, migration and invasion of human hepatocellular carcinoma cells. *Bioorg. Med. Chem. Lett.* **2017**, *27*, 1081–1088. [CrossRef]

239. Ray, A.; Vasudevan, S.; Sengupta, S. 6-Shogaol inhibits breast cancer cells and stem cell-like spheroids by modulation of Notch signaling pathway and induction of autophagic cell death. *PLoS ONE* **2015**, *10*, e0137614. [CrossRef]

240. El-Ashmawy, N.E.; Khedr, N.F.; El-Bahrawy, H.A.; Abo Mansour, H.E. Ginger extract adjuvant to doxorubicin in mammary carcinoma: Study of some molecular mechanisms. *Eur. J. Nutr.* **2018**, *57*, 981–989. [CrossRef]

241. Rahimi Babasheikhali, S.; Rahgozar, S.; Mohammadi, M. Ginger extract has anti-leukemia and anti-drug resistant effects on malignant cells. *J. Cancer Res. Clin. Oncol.* **2019**, *145*, 1987–1998. [CrossRef]

242. Liu, C.-M.; Kao, C.-L.; Tseng, Y.-T.; Lo, Y.-C.; Chen, C.-Y. Ginger phytochemicals inhibit cell growth and modulate drug resistance factors in docetaxel resistant prostate cancer cell. *Molecules* **2017**, *22*, 1477. [CrossRef]

243. Almatroudi, A.; Alsahli, M.A.; Alrumaihi, F.; Allemailem, K.S.; Rahmani, A.H. Ginger: A novel strategy to battle cancer through modulating cell signalling pathways: A review. *Curr. Pharm. Biotechnol.* **2019**, *20*, 5–16. [CrossRef]

244. Zadorozhna, M.; Mangieri, D. Mechanisms of chemopreventive and Ther. proprieties of ginger extracts in cancer. *Int. J. Mol. Sci.* **2021**, *22*, 6599. [CrossRef]

245. Iram, F.; Khan, S.A.; Husain, A. Phytochemistry and potential Ther. actions of Boswellic acids: A mini-review. *Asian Pac. J. Trop. Biomed.* **2017**, *7*, 513–523. [CrossRef]

246. Roy, N.K.; Parama, D.; Banik, K.; Bordoloi, D.; Devi, A.K.; Thakur, K.K.; Padmavathi, G.; Shakibaei, M.; Fan, L.; Sethi, G. An update on pharmacological potential of boswellic acids against chronic diseases. *Int. J. Mol. Sci.* **2019**, *20*, 4101. [CrossRef]

247. Gupta, M.; Rout, P.; Misra, L.; Gupta, P.; Singh, N.; Darokar, M.; Saikia, D.; Singh, S.; Bhakuni, R. Chemical composition and bioactivity of *Boswellia serrata* Roxb. essential oil in relation to geographical variation. *Plant Biosyst. Int. J. All Aspects Plant Biol.* **2017**, *151*, 623–629.

248. Ayub, M.A.; Hanif, M.A.; Blanchfield, J.; Zubair, M.; Abid, M.A.; Saleh, M.T. Chemical composition and antimicrobial activity of *Boswellia serrata* oleo-gum-resin essential oil extracted by superheated steam. *Nat. Prod. Res.* **2022**; *in press*.

249. Khajehdehi, M.; Khalaj-Kondori, M.; Baradaran, B. Molecular evidences on anti-inflammatory, anticancer, and memory-boosting effects of frankincense. *Phytother. Res.* **2022**, *36*, 1194–1215. [CrossRef]

250. Ahmed, H.H.; Abd-Rabou, A.A.; Hassan, A.Z.; Kotob, S.E. Phytochemical analysis and anti-cancer investigation of *Boswellia serrata* bioactive constituents in vitro. *Asian Pac. J. Cancer Prev.* **2015**, *16*, 7179–7188. [CrossRef]

251. Hakkim, F.L.; Bakshi, H.A.; Khan, S.; Nasef, M.; Farzand, R.; Sam, S.; Rashan, L.; Al-Baloshi, M.S.; Hasson, S.S.A.A.; Al Jabri, A. Frankincense essential oil suppresses melanoma cancer through down regulation of Bcl-2/Bax cascade signaling and ameliorates heptotoxicity via phase I and II drug metabolizing enzymes. *Oncotarget* **2019**, *10*, 3472. [CrossRef] [PubMed]

252. Takada, Y.; Ichikawa, H.; Badmaev, V.; Aggarwal, B.B. Acetyl-11-keto-β-boswellic acid potentiates apoptosis, inhibits invasion, and abolishes osteoclastogenesis by suppressing NF-κB and NF-κB-regulated gene expression. *J. Immunol.* **2006**, *176*, 3127–3140. [CrossRef]

253. Kunnumakkara, A.B.; Nair, A.S.; Sung, B.; Pandey, M.K.; Aggarwal, B.B. Boswellic acid blocks STAT3 Signaling, proliferation, and survival of multiple myeloma via the protein tyrosine phosphatase SHP-1. *Mol. Cancer Res. MCR* **2009**, *7*, 118. [CrossRef]

254. Shen, Y.; Takahashi, M.; Byun, H.-M.; Link, A.; Sharma, N.; Balaguer, F.; Leung, H.-C.; Boland, C.R.; Goel, A. Boswellic acid induces epigenetic alterations by modulating DNA methylation in colorectal cancer cells. *Cancer Biol. Ther.* **2012**, *13*, 542–552. [CrossRef]

255. Mazzio, E.A.; Lewis, C.A.; Soliman, K.F. Transcriptomic Profiling of MDA-MB-231 cells exposed to *Boswellia Serrata* and 3-O-Acetyl-B-Boswellic Acid; ER/UPR mediated programmed cell death. *Cancer Genom. Proteom.* **2017**, *14*, 409–425.

256. Hussain, H.; Ali, I.; Wang, D.; Hakkim, F.L.; Westermann, B.; Rashan, L.; Ahmed, I.; Green, I.R. Boswellic acids: Privileged structures to develop lead compounds for anticancer drug discovery. *Expert Opin. Drug Discov.* **2021**, *16*, 851–867. [CrossRef] [PubMed]

257. Hussain, H.; Al-Harrasi, A.; Csuk, R.; Shamraiz, U.; Green, I.R.; Ahmed, I.; Khan, I.A.; Ali, Z. Therapeutic potential of boswellic acids: A patent review (1990–2015). *Expert Opin. Ther. Pat.* **2017**, *27*, 81–90. [CrossRef]

258. Takeda, S.; Noguchi, M.; Matsuo, K.; Yamaguchi, Y.; Kudo, T.; Nishimura, H.; Okamoto, Y.; Amamoto, T.; Shindo, M.; Omiecinski, C.J. (−)-Xanthatin up-regulation of the GADD45γ tumor suppressor gene in MDA-MB-231 breast cancer cells: Role of topoisomerase IIα inhibition and reactive oxygen species. *Toxicology* **2013**, *305*, 1–9. [CrossRef] [PubMed]

259. Yu, Y.; Yu, J.; Pei, C.G.; Li, Y.Y.; Tu, P.; Gao, G.P.; Shao, Y. Xanthatin, a novel potent inhibitor of VEGFR2 signaling, inhibits angiogenesis and tumor growth in breast cancer cells. *Int. J. Clin. Exp. Pathol.* **2015**, *8*, 10355. [PubMed]

260. Zhang, L.; Ruan, J.; Yan, L.; Li, W.; Wu, Y.; Tao, L.; Zhang, F.; Zheng, S.; Wang, A.; Lu, Y. Xanthatin induces cell cycle arrest at G2/M checkpoint and apoptosis via disrupting NF-κB pathway in A549 non-small-cell lung cancer cells. *Molecules* **2012**, *17*, 3736–3750. [CrossRef]

261. Tao, L.; Fan, F.; Liu, Y.; Li, W.; Zhang, L.; Ruan, J.; Shen, C.; Sheng, X.; Zhu, Z.; Wang, A. Concerted suppression of STAT3 and GSK3β is involved in growth inhibition of non-small cell lung cancer by xanthatin. *PLoS ONE* **2013**, *8*, e81945. [CrossRef]

262. Tao, L.; Sheng, X.; Zhang, L.; Li, W.; Wei, Z.; Zhu, P.; Zhang, F.; Wang, A.; Woodgett, J.R.; Lu, Y. Xanthatin anti-tumor cytotoxicity is mediated via glycogen synthase kinase-3β and β-catenin. *Biochem. Pharmacol.* **2016**, *115*, 18–27. [CrossRef]

263. Yang, J.; Li, Y.; Zong, C.; Zhang, Q.; Ge, S.; Ma, L.; Fan, J.; Zhang, J.; Jia, R. Xanthatin Selectively Targets Retinoblastoma by Inhibiting the PLK1-Mediated Cell Cycle. *Investig. Ophthalmol. Visual Sci.* **2021**, *62*, 11. [CrossRef]

264. Geng, Y.-d.; Zhang, L.; Wang, G.-Y.; Feng, X.-J.; Chen, Z.-L.; Jiang, L.; Shen, A.-Z. Xanthatin mediates G2/M cell cycle arrest, autophagy and apoptosis via ROS/XIAP signaling in human colon cancer cells. *Nat. Prod. Res.* **2020**, *34*, 2616–2620. [CrossRef]

265. Li, L.; Liu, P.; Xie, Y.; Liu, Y.; Chen, Z.; Geng, Y.; Zhang, L. Xanthatin inhibits human colon cancer cells progression via mTOR signaling mediated energy metabolism alteration. *Drug Dev. Res.* **2022**, *83*, 119–130. [CrossRef]

266. Ma, Y.-Y.; Di, Z.-M.; Cao, Q.; Xu, W.-S.; Bi, S.-X.; Yu, J.-S.; Shen, Y.-J.; Yu, Y.-Q.; Shen, Y.-X.; Feng, L.-J. Xanthatin induces glioma cell apoptosis and inhibits tumor growth via activating endoplasmic reticulum stress-dependent CHOP pathway. *Acta Pharmacol. Sin.* **2020**, *41*, 404–414. [CrossRef]

267. Hashim, Y.; Latimer, C.; Ternan, N.; Abbas, P. Studies of Malaysian plants in prevention and treatment of colorectal cancer. In *Colorectal Cancer*; InTechOpen: London, UK, 2016; Volume 18, pp. 377–394.

268. Mazumder, K.; Biswas, B.; Raja, I.M.; Fukase, K. A review of cytotoxic plants of the Indian subcontinent and a broad-spectrum analysis of their bioactive compounds. *Molecules* **2020**, *25*, 1904. [CrossRef] [PubMed]

269. Meiyanto, E.; Larasati, Y.A. The chemopreventive activity of Indonesia medicinal plants targeting on hallmarks of cancer. *Adv. Pharm. Bull.* **2019**, *9*, 219. [CrossRef] [PubMed]

270. Sithisarn, P.; Rojsanga, P. Anticancer Effects of Some Medicinal Thai Plants. In *Natural Products and Cancer Drug Discovery*; IntechOpen: London, UK, 2017.

271. Nguyen, N.H.; Ta, Q.T.H.; Pham, Q.T.; Luong, T.N.H.; Phung, V.T.; Duong, T.-H.; Vo, V.G. Anticancer activity of novel plant extracts and compounds from Adenosma bracteosum (Bonati) in human lung and liver cancer cells. *Molecules* **2020**, *25*, 2912. [CrossRef] [PubMed]

272. Shuvalov, O.; Fedorova, O.; Tananykina, E.; Gnennaya, Y.; Daks, A.; Petukhov, A.; Barlev, N. An arthropod hormone, ecdysterone, inhibits the growth of breast cancer cells via different mechanisms. *Front. Pharmacol.* **2020**, *11*, 561537. [CrossRef]

273. Zirak, N.; Shafiee, M.; Soltani, G.; Mirzaei, M.; Sahebkar, A. *Hypericum perforatum* in the treatment of psychiatric and neurodegenerative disorders: Current evidence and potential mechanisms of action. *J. Cell. Physiol.* **2019**, *234*, 8496–8508. [CrossRef]

274. Menegazzi, M.; Masiello, P.; Novelli, M. Anti-tumor activity of *Hypericum perforatum* L. and hyperforin through modulation of inflammatory signaling, ROS generation and proton dynamics. *Antioxidants* **2020**, *10*, 18. [CrossRef]

275. Napoli, E.; Siracusa, L.; Ruberto, G.; Carrubba, A.; Lazzara, S.; Speciale, A.; Cimino, F.; Saija, A.; Cristani, M. Phytochemical profiles, phototoxic and antioxidant properties of eleven Hypericum species–A comparative study. *Phytochem.* **2018**, *152*, 162–173. [CrossRef]

276. Alper, M.; Güneş, H. The anticancer and anti-inflammatory effects of *Centaurea solstitialis* extract on human cancer cell lines. *Turk. J. Pharm. Sci.* **2019**, *16*, 273. [CrossRef]

277. Koeberle, A.; Rossi, A.; Bauer, J.; Dehm, F.; Verotta, L.; Northoff, H.; Sautebin, L.; Werz, O. Hyperforin, an anti-inflammatory constituent from St. John's wort, inhibits microsomal prostaglandin E2 synthase-1 and suppresses prostaglandin E2 formation in vivo. *Front. Pharmacol.* **2011**, *2*, 7. [CrossRef]

278. Benedí, J.; Arroyo, R.; Romero, C.; Martín-Aragón, S.; Villar, A.M. Antioxidant properties and protective effects of a standardized extract of *Hypericum perforatum* on hydrogen peroxide-induced oxidative damage in PC12 cells. *Life Sci.* **2004**, *75*, 1263–1276. [CrossRef] [PubMed]

279. Imreova, P.; Feruszova, J.; Kyzek, S.; Bodnarova, K.; Zduriencikova, M.; Kozics, K.; Mucaji, P.; Galova, E.; Sevcovicova, A.; Miadokova, E. Hyperforin exhibits antigenotoxic activity on human and bacterial cells. *Molecules* **2017**, *22*, 167. [CrossRef] [PubMed]

280. Hsu, F.T.; Chen, W.T.; Wu, C.T.; Chung, J.G. Hyperforin induces apoptosis through extrinsic/intrinsic pathways and inhibits EGFR/ERK/NF-κB-mediated anti-apoptotic potential in glioblastoma. *Environ. Toxicol.* **2020**, *35*, 1058–1069. [CrossRef] [PubMed]

281. Merhi, F.; Tang, R.; Piedfer, M.; Mathieu, J.; Bombarda, I.; Zaher, M.; Kolb, J.-P.; Billard, C.; Bauvois, B. Hyperforin inhibits Akt1 kinase activity and promotes caspase-mediated apoptosis involving Bad and Noxa activation in human myeloid tumor cells. *PLoS ONE* **2011**, *6*, e25963. [CrossRef]

282. Quiney, C.; Billard, C.; Faussat, A.; Salanoubat, C.; Ensaf, A.; Nait-Si, Y.; Fourneron, J.; Kolb, J. Pro-apoptotic properties of hyperforin in leukemic cells from patients with B-cell chronic lymphocytic leukemia. *Leukemia* **2006**, *20*, 491–497. [CrossRef]

283. Lorusso, G.; Vannini, N.; Sogno, I.; Generoso, L.; Garbisa, S.; Noonan, D.M.; Albini, A. Mechanisms of Hyperforin as an anti-angiogenic angioPrev. agent. *Eur. J. Cancer* **2009**, *45*, 1474–1484. [CrossRef]

284. Donà, M.; Dell'Aica, I.; Pezzato, E.; Sartor, L.; Calabrese, F.; Della Barbera, M.; Donella-Deana, A.; Appendino, G.; Borsarini, A.; Caniato, R. Hyperforin inhibits cancer invasion and metastasis. *Cancer Res.* **2004**, *64*, 6225–6232. [CrossRef]

285. Sell, T.S.; Belkacemi, T.; Flockerzi, V.; Beck, A. Protonophore properties of hyperforin are essential for its pharmacological activity. *Sci. Rep.* **2014**, *4*, 7500. [CrossRef]

286. Scotti, F.; Löbel, K.; Booker, A.; Heinrich, M. St. John's Wort (*Hypericum perforatum*) products–How variable is the primary material? *Front. Plant Sci.* **2019**, *9*, 1973. [CrossRef]

287. Fulda, S. Betulinic acid for cancer treatment and prevention. *Int. J. Mol. Sci.* **2008**, *9*, 1096–1107. [CrossRef]

288. Zhang, X.; Hu, J.; Chen, Y. Betulinic acid and the pharmacological effects of tumor suppression. *Mol. Med. Rep.* **2016**, *14*, 4489–4495. [CrossRef] [PubMed]

289. Tan, Y.; Yu, R.; Pezzuto, J.M. Betulinic acid-induced programmed cell death in human melanoma cells involves mitogen-activated protein kinase activation. *Clin. Cancer Res.* **2003**, *9*, 2866–2875. [PubMed]

290. Guo, Y.; Zhu, H.; Weng, M.; Wang, C.; Sun, L. Chemopreventive effect of Betulinic acid via mTOR-Caspases/Bcl2/Bax apoptotic signaling in pancreatic cancer. *BMC Complement. Med. Ther.* **2020**, *20*, 178. [CrossRef] [PubMed]

291. Wang, S.; Wang, K.; Zhang, C.; Zhang, W.; Xu, Q.; Wang, Y.; Zhang, Y.; Li, Y.; Zhang, Y.; Zhu, H. Overaccumulation of p53-mediated autophagy protects against betulinic acid-induced apoptotic cell death in colorectal cancer cells. *Cell Death Dis.* **2017**, *8*, e3087. [CrossRef]

292. Potze, L.; Mullauer, F.; Colak, S.; Kessler, J.; Medema, J. Betulinic acid-induced mitochondria-dependent cell death is counterbalanced by an autophagic salvage response. *Cell Death Dis.* **2014**, *5*, e1169. [CrossRef]

293. Zheng, Y.; Liu, P.; Wang, N.; Wang, S.; Yang, B.; Li, M.; Chen, J.; Situ, H.; Xie, M.; Lin, Y. Betulinic acid suppresses breast cancer metastasis by targeting GRP78-mediated glycolysis and ER stress apoptotic pathway. *Oxid. Med. Cell. Longev.* **2019**, *2019*, 8781690. [CrossRef]

294. Saeed, M.E.; Mahmoud, N.; Sugimoto, Y.; Efferth, T.; Abdel-Aziz, H. Betulinic acid exerts cytotoxic activity against multidrug-resistant tumor cells via targeting autocrine motility factor receptor (AMFR). *Front. Pharmacol.* **2018**, *9*, 481. [CrossRef]

295. Nedopekina, D.A.; Gubaidullin, R.R.; Odinokov, V.N.; Maximchik, P.V.; Zhivotovsky, B.; Bel'skii, Y.P.; Khazanov, V.A.; Manuylova, A.V.; Gogvadze, V.; Spivak, A.Y. Mitochondria-targeted betulinic and ursolic acid derivatives: Synthesis and anticancer activity. *MedChemComm* **2017**, *8*, 1934–1945. [CrossRef]

296. Sharma, V.; Katiyar, A.; Agrawal, R. *Glycyrrhiza glabra*: Chemistry and pharmacological activity. *Sweeteners* **2018**, 87–100.

297. Wang, K.-L.; Yu, Y.-C.; Hsia, S.-M. Perspectives on the Role of Isoliquiritigenin in Cancer. *Cancers* **2021**, *13*, 115. [CrossRef]

298. Tian, T.; Sun, J.; Wang, J.; Liu, Y.; Liu, H. Isoliquiritigenin inhibits cell proliferation and migration through the PI3K/AKT signaling pathway in A549 lung cancer cells. *Oncol. Lett.* **2018**, *16*, 6133–6139. [CrossRef] [PubMed]

299. Chen, C.; Shenoy, A.K.; Padia, R.; Fang, D.; Jing, Q.; Yang, P.; Su, S.-B.; Huang, S. Suppression of lung cancer progression by isoliquiritigenin through its metabolite 2, 4, 2', 4'-Tetrahydroxychalcone. *J. Exp. Clin. Cancer Res.* **2018**, *37*, 243. [CrossRef] [PubMed]

300. Bolós, V.; Gasent, J.M.; López-Tarruella, S.; Grande, E. The dual kinase complex FAK-Src as a promising therapeutic target in cancer. *Onco Targets Ther.* **2010**, *3*, 83. [CrossRef] [PubMed]

301. Nag, S.; Qin, J.; Srivenugopal, K.S.; Wang, M.; Zhang, R. The MDM2-p53 pathway revisited. *J. Biomed. Res.* **2013**, *27*, 254.

302. Bohlman, S.; Manfredi, J.J. p53-independent effects of Mdm2. *Mutant p53 and MDM2 in Cancer. Subcell Biochem.* **2014**, *85*, 235–246.

303. Shuvalov, O.; Kizenko, A.; Shakirova, A.; Fedorova, O.; Petukhov, A.; Aksenov, N.; Vasileva, E.; Daks, A.; Barlev, N. Nutlin sensitizes lung carcinoma cells to interferon-alpha treatment in MDM2-dependent but p53-independent manner. *Biochem. Biophys. Res. Commun.* **2018**, *495*, 1233–1239. [CrossRef]

304. Xiang, S.; Chen, H.; Luo, X.; An, B.; Wu, W.; Cao, S.; Ruan, S.; Wang, Z.; Weng, L.; Zhu, H. Isoliquiritigenin suppresses human melanoma growth by targeting miR-301b/LRIG1 signaling. *J. Exp. Clin. Cancer Res.* **2018**, *37*, 184. [CrossRef]

305. Kroll, D.J.; Shaw, H.S.; Oberlies, N.H. Milk thistle nomenclature: Why it matters in cancer research and pharmacokinetic studies. *Integr. Cancer Ther.* **2007**, *6*, 110–119. [CrossRef]

306. Karimi, G.; Vahabzadeh, M.; Lari, P.; Rashedinia, M.; Moshiri, M. "Silymarin", a promising pharmacological agent for treatment of diseases. *Iran. J. Basic Med. Sci.* **2011**, *14*, 308.

307. Won, D.-H.; Kim, L.-H.; Jang, B.; Yang, I.-H.; Kwon, H.-J.; Jin, B.; Oh, S.H.; Kang, J.-H.; Hong, S.-D.; Shin, J.-A. In vitro and in vivo anti-cancer activity of silymarin on oral cancer. *Tumor Biol.* **2018**, *40*, 1010428318776170. [CrossRef]

308. Eo, H.J.; Park, G.H.; Jeong, J.B. Inhibition of Wnt signaling by silymarin in human colorectal cancer cells. *Biomol. Ther.* **2016**, *24*, 380. [CrossRef] [PubMed]

309. Delmas, D.; Xiao, J.; Vejux, A.; Aires, V. Silymarin and Cancer: A Dual Strategy in Both in Chemoprevention and Chemosensitivity. *Molecules* **2020**, *25*, 2009. [CrossRef] [PubMed]

310. Ramasamy, K.; Agarwal, R. Multitargeted therapy of cancer by silymarin. *Cancer Lett.* **2008**, *269*, 352–362. [CrossRef] [PubMed]

311. Kim, S.H.; Choo, G.S.; Yoo, E.S.; Woo, J.S.; Han, S.H.; Lee, J.H.; Jung, J.Y. Silymarin induces inhibition of growth and apoptosis through modulation of the MAPK signaling pathway in AGS human gastric cancer cells. *Oncol. Rep.* **2019**, *42*, 1904–1914. [CrossRef] [PubMed]

312. Mao, J.; Yang, H.; Cui, T.; Pan, P.; Kabir, N.; Chen, D.; Ma, J.; Chen, X.; Chen, Y.; Yang, Y. Combined treatment with sorafenib and silibinin synergistically targets both HCC cells and cancer stem cells by enhanced inhibition of the phosphorylation of STAT3/ERK/AKT. *Eur. J. Pharmacol.* **2018**, *832*, 39–49. [CrossRef]

313. Soleimani, V.; Delghandi, P.S.; Moallem, S.A.; Karimi, G. Safety and toxicity of silymarin, the major constituent of milk thistle extract: An updated review. *Phytother. Res.* **2019**, *33*, 1627–1638. [CrossRef]

314. Shang, A.; Cao, S.-Y.; Xu, X.-Y.; Gan, R.-Y.; Tang, G.-Y.; Corke, H.; Mavumengwana, V.; Li, H.-B. Bioactive compounds and biological functions of garlic (*Allium sativum* L.). *Foods* **2019**, *8*, 246. [CrossRef]

315. Taleb Agha, M.; Baharetha, H.M.; Al-Mansoub, M.A.; Tabana, Y.M.; Kaz Abdul Aziz, N.H.; Yam, M.F.; Abdul Majid, A.M.S. Proapoptotic and antiangiogenic activities of *Arctium lappa* L. on breast cancer cell lines. *Scientifica* **2020**, *2020*. [CrossRef]

316. Li, X.; Lin, Y.-Y.; Tan, J.-Y.; Liu, K.-L.; Shen, X.-L.; Hu, Y.-J.; Yang, R.-Y. Lappaol F, an anticancer agent, inhibits YAP via transcriptional and post-translational regulation. *Pharm. Biol.* **2021**, *59*, 619–628. [CrossRef]

317. He, Y.; Fan, Q.; Cai, T.; Huang, W.; Xie, X.; Wen, Y.; Shi, Z. Molecular mechanisms of the action of Arctigenin in cancer. *Biomed. Pharmacother.* **2018**, *108*, 403–407. [CrossRef]

318. Erenler, R.; Sen, O.; Sahin Yaglioglu, A.; Demirtas, I. Bioactivity-guided isolation of antiproliferative sesquiterpene lactones from *Centaurea solstitialis* L. ssp. solstitialis. *Comb. Chem. High Throughput Screen.* **2016**, *19*, 66–72. [CrossRef] [PubMed]

319. Simsek, E.; Imir, N.; Aydemir, E.A.; Gokturk, R.S.; Yesilada, E.; Fiskin, K. Caspase-mediated apoptotic effects of *Ebenus boissieri* barbey extracts on human cervical cancer cell line hela. *Pharmacogn. Mag.* **2017**, *13*, 254. [CrossRef] [PubMed]

320. Aydemir, E.A.; Simsek, E.; Imir, N.; Göktürk, R.S.; Yesilada, E.; Fiskin, K. Cytotoxic and apoptotic effects of *Ebenus boissieri* Barbey on human lung cancer cell line A549. *Pharmacogn. Mag.* **2015**, *11*, S37. [CrossRef] [PubMed]

321. Imir, N.; Aydemir, E.; Şimşek, E.; Göktürk, R.; Yesilada, E.; Fişkin, K. Cytotoxic and immunomodulatory effects of *Ebenus boissieri* Barbey on breast cancer cells. *Genet. Mol. Res.* **2016**, 15. [CrossRef]

322. Allegra, A.; Tonacci, A.; Pioggia, G.; Musolino, C.; Gangemi, S. Anticancer activity of *Rosmarinus officinalis* L.: Mechanisms of Action and Therapeutic Potentials. *Nutrients* **2020**, *12*, 1739. [CrossRef]

323. Kowalczyk, T.; Sitarek, P.; Skała, E.; Toma, M.; Wielanek, M.; Pytel, D.; Wieczfińska, J.; Szemraj, J.; Śliwiński, T. Induction of apoptosis by in vitro and in vivo plant extracts derived from *Menyanthes trifoliata* L. in human cancer cells. *Cytotechnology* **2019**, *71*, 165–180. [CrossRef]

324. Vervandier-Fasseur, D.; Latruffe, N. The potential use of resveratrol for cancer prevention. *Molecules* **2019**, *24*, 4506. [CrossRef]

325. Aja, I.; Ruiz-Larrea, M.B.; Courtois, A.; Krisa, S.; Richard, T.; Ruiz-Sanz, J.-I. Screening of natural stilbene oligomers from *Vitis vinifera* for anticancer activity on human hepatocellular carcinoma cells. *Antioxidants* **2020**, *9*, 469. [CrossRef]

326. Marvibaigi, M.; Supriyanto, E.; Amini, N.; Abdul Majid, F.A.; Jaganathan, S.K. Preclinical and clinical effects of mistletoe against breast cancer. *Biomed Res. Int.* **2014**, *2014*, 785479. [CrossRef]

327. de Oliveira Melo, M.N.; Oliveira, A.P.; Wiecikowski, A.F.; Carvalho, R.S.; de Lima Castro, J.; de Oliveira, F.A.G.; Pereira, H.M.G.; da Veiga, V.F.; Capella, M.M.A.; Rocha, L. Phenolic compounds from *Viscum album* tinctures enhanced antitumor activity in melanoma murine cancer cells. *Saudi Pharm. J.* **2018**, *26*, 311–322. [CrossRef]

328. Chen, T.; Li, B.; Qiu, Y.; Qiu, Z.; Qu, P. Funct. mechanism of Ginsenosides on tumor growth and metastasis. *Saudi J. Biol. Sci.* **2018**, *25*, 917–922. [CrossRef] [PubMed]

329. Jia, L.; Zhao, Y. Current evaluation of the millennium phytomedicine-ginseng (I): Etymology, pharmacognosy, phytochemistry, market and regulations. *Curr. Med. Chem.* **2009**, *16*, 2475–2484. [CrossRef] [PubMed]

330. Hong, H.; Baatar, D.; Hwang, S.G. Anticancer activities of ginsenosides, the main active components of ginseng. *Evid. Based Complement. Altern. Med.* **2021**, *2021*, 8858006. [CrossRef] [PubMed]

331. Gao, J.-L.; Lv, G.-Y.; He, B.-C.; Zhang, B.-Q.; Zhang, H.; Wang, N.; Wang, C.-Z.; Du, W.; Yuan, C.-S.; He, T.-C. Ginseng saponin metabolite 20 (S)-protopanaxadiol inhibits tumor growth by targeting multiple cancer signaling pathways. *Oncol. Rep.* **2013**, *30*, 292–298. [CrossRef] [PubMed]

332. Zhang, X.; Han, L.; Li, P.; Zhang, S.; Zhang, M.; Li, X.; Chu, J.; Wang, L.; Tu, P.; Zhang, Y. Region-Specific Biomarkers and Their Mechanisms in the Treatment of Lung Adenocarcinoma: A Study of *Panax quinquefolius* from Wendeng, China. *Molecules* **2021**, *26*, 6829. [CrossRef] [PubMed]

333. Ham, S.W.; Kim, J.-K.; Jeon, H.-Y.; Kim, E.-J.; Jin, X.; Eun, K.; Park, C.G.; Lee, S.Y.; Seo, S.; Kim, J.Y. Korean Red ginseng extract inhibits glioblastoma propagation by blocking the Wnt signaling pathway. *J. Ethnopharmacol.* **2019**, *236*, 393–400. [CrossRef]

334. Guo, J.-Q.; Zheng, Q.-H.; Chen, H.; Chen, L.; Xu, J.-B.; Chen, M.-Y.; Lu, D.; Wang, Z.-H.; Tong, H.-F.; Lin, S. Ginsenoside Rg3 inhibition of vasculogenic mimicry in pancreatic cancer through downregulation of VE-cadherin/EphA2/MMP9/MMP2 expression. *Int. J. Oncol.* **2014**, *45*, 1065–1072. [CrossRef]

335. Nag, S.A.; Qin, J.; Wang, W.; Wang, M.-H.; Wang, H.; Zhang, R. Ginsenosides as anticancer agents: In vitro and in vivo activities, structure-activity relationships, and molecular mechanisms of action. *Front. Pharmacol.* **2012**, *3*, 25. [CrossRef]

336. Lerma-Herrera, M.A.; Beiza-Granados, L.; Ochoa-Zarzosa, A.; López-Meza, J.E.; Hernández-Hernández, J.D.; Aviña-Verduzco, J.; García-Gutiérrez, H.A. In vitro cytotoxic potential of extracts from *Aristolochia foetida* Kunth against MCF-7 and bMECs cell lines. *Saudi J. Biol. Sci.* **2021**, *28*, 7082–7089. [CrossRef]

337. Nam, J.-S.; Park, S.-Y.; Lee, S.-O.; Lee, H.-J.; Jang, H.-L.; Rhee, Y.H. The growth-inhibitory effects of pawpaw (*Asimina triloba* [L.] Dunal) roots, twigs, leaves, and fruit against human gastric (AGS) and cervical (HeLa) cancer cells and their anti-inflammatory activities. *Mol. Biology Rep.* **2021**, *48*, 2173–2181. [CrossRef]

338. Wisintainer, G.; Scola, G.; Moura, S.; Lemos, T.; Pessoa, C.; de Moraes, M.; Souza, L.; Roesch-Ely, M.; Henriques, J. O-naphthoquinone isolated from *Capraria biflora* L. induces selective cytotoxicity in tumor cell lines. *Genet. Mol. Res.* **2015**, *14*, 17472–17481. [CrossRef] [PubMed]

339. Barbosa-Jobim, G.S.; Costa-Lira, E.; Ralph, A.C.L.; Gregorio, L.; Lemos, T.L.; Burbano, R.R.; Calcagno, D.Q.; Smith, M.A.; Montenegro, R.C.; Vasconcellos, M.C. Biflorin inhibits the proliferation of gastric cancer cells by decreasing MYC expression. *Toxicol. In Vitro* **2020**, *63*, 104735. [CrossRef] [PubMed]

340. Tang, C.; Gong, L.; Qiu, K.; Zhang, Z.; Wan, L. Echinacoside inhibits breast cancer cells by suppressing the Wnt/β-catenin signaling pathway. *Biochem. Biophys. Res. Commun.* **2020**, *526*, 170–175. [CrossRef] [PubMed]

341. Hosami, F.; Manayi, A.; Salimi, V.; Khodakhah, F.; Nourbakhsh, M.; Nakstad, B.; Tavakoli-Yaraki, M. The pro-apoptosis effects of *Echinacea purpurea* and Cannabis sativa extracts in human lung cancer cells through caspase-dependent pathway. *BMC Complement. Med. Ther.* **2021**, *21*, 37. [CrossRef] [PubMed]

342. Kuttikrishnan, S.; Siveen, K.S.; Prabhu, K.S.; Khan, A.Q.; Akhtar, S.; Mateo, J.M.; Merhi, M.; Taha, R.; Omri, H.E.; Mraiche, F. Sanguinarine suppresses growth and induces apoptosis in childhood acute lymphoblastic leukemia. *Leuk. Lymphoma* **2019**, *60*, 782–794. [CrossRef] [PubMed]

343. Tuzimski, T.; Petruczynik, A.; Plech, T.; Kaproń, B.; Makuch-Kocka, A.; Szultka-Młyńska, M.; Misiurek, J.; Buszewski, B. Determination of Cytotoxic Activity of *Sanguinaria canadensis* Extracts against Human Melanoma Cells and Comparison of Their Cytotoxicity with Cytotoxicity of Some Anticancer Drugs. *Molecules* **2021**, *26*, 1738. [CrossRef]

344. Croaker, A.; King, G.J.; Pyne, J.H.; Anoopkumar-Dukie, S.; Liu, L. *Sanguinaria canadensis*: Traditional medicine, phytochemical composition, biological activities and current uses. *Int. J. Mol. Sci.* **2016**, *17*, 1414. [CrossRef]

345. Singab, A.N.; Youssef, F.S.; Ashour, M.L.; Wink, M. The genus Eremophila (Scrophulariaceae): An ethnobotanical, biological and phytochemical review. *J. Pharm. Pharmacol.* **2013**, *65*, 1239–1279. [CrossRef]

346. Petersen, M.J.; Lund, X.L.; Semple, S.J.; Buirchell, B.; Franzyk, H.; Gajhede, M.; Kongstad, K.T.; Stenvang, J.; Staerk, D. Reversal of ABCG2/BCRP-Mediated Multidrug Resistance by 5, 3′, 5′-Trihydroxy-3, 6, 7, 4′-Tetramethoxyflavone Isolated from the Australian Desert Plant *Eremophila galeata* Chinnock. *Biomolecules* **2021**, *11*, 1534. [CrossRef]

347. An, G.; Morris, M.E. Efflux transporters in cancer resistance: Molecular and Funct. characterization of breast cancer resistance protein. In *Drug Efflux Pumps in Cancer Resistance Pathways: From Molecular Recognition and Characterization to Possible Inhibition Strategies in Chemotherapy*; Elsevier: Amsterdam, The Netherlands, 2020; pp. 67–96.

348. Shalom, J.; Cock, I.E. *Terminalia ferdinandiana* Exell. fruit and leaf extracts inhibit proliferation and induce apoptosis in selected human cancer cell lines. *Nutr. Cancer* **2018**, *70*, 579–593. [CrossRef]

349. Mohanty, S.; Cock, I.E. The chemoTher. potential of *Terminalia ferdinandiana*: Phytochemistry and bioactivity. *Pharmacogn. Rev.* **2012**, *6*, 29. [PubMed]

350. Sakulnarmrat, K.; Fenech, M.; Thomas, P.; Konczak, I. Cytoprotective and pro-apoptotic activities of native Australian herbs polyphenolic-rich extracts. *Food Chem.* **2013**, *136*, 9–17. [CrossRef] [PubMed]

351. Chuen, T.L.; Vuong, Q.V.; Hirun, S.; Bowyer, M.C.; Predebon, M.J.; Goldsmith, C.D.; Sakoff, J.A.; Scarlett, C.J. Antioxidant and anti-proliferative properties of Davidson's plum (*Davidsonia pruriens* F. Muell) phenolic-enriched extracts as affected by different extraction solvents. *J. Herbal Med.* **2016**, *6*, 187–192. [CrossRef]

352. Jamieson, N.; Sirdaarta, J.; Cock, I. The Anti-Proliferative Properties of Australian Plants with High Antioxidant Capacities Against Cancer Cell Lines. *Pharmacogn. Commun.* **2014**, *4*, 71–82.

353. Bäcker, C.; Jenett-Siems, K.; Siems, K.; Wurster, M.; Bodtke, A.; Lindequist, U. Cytotoxic saponins from the seeds of *Pittosporum angustifolium*. *Z. Nat. C* **2014**, *69*, 191–198. [CrossRef]

354. Hawksworth, D.L.; Lücking, R. Fungal diversity revisited: 2.2 to 3.8 million species. *Microbiol. Spectr.* **2017**, *5*, 10. [CrossRef]

355. Nowakowski, P.; Markiewicz-Żukowska, R.; Bielecka, J.; Mielcarek, K.; Grabia, M.; Socha, K. Treasures from the forest: Evaluation of mushroom extracts as anti-cancer agents. *Biomed. Pharmacother.* **2021**, *143*, 112106. [CrossRef] [PubMed]

356. Al-Obaidi, J.R.; Jambari, N.N.; Ahmad-Kamil, E. Mycopharmaceuticals and Nutraceuticals: Promising Agents to Improve Human Well-Being and Life Quality. *J. Fungi* **2021**, *7*, 503. [CrossRef]

357. Keller, N.P. Fungal secondary metabolism: Regulation, function and drug discovery. *Nat. Rev. Microbiol.* **2019**, *17*, 167–180. [CrossRef]

358. Avalos, J.; Limón, M.C. Fungal Secondary Metabolism. *Encyclopedia* **2021**, *2*, 1–13. [CrossRef]

359. Szychowski, K.A.; Skóra, B.; Pomianek, T.; Gmiński, J. *Inonotus obliquus*–from folk medicine to clinical use. *J. Tradit. Complement. Med.* **2021**, *11*, 293–302. [CrossRef] [PubMed]

360. Yukawa, H.; Ishikawa, S.; Kawanishi, T.; Tamesada, M.; Tomi, H. Direct cytotoxicity of *Lentinula edodes* mycelia extract on human hepatocellular carcinoma cell line. *Biol. Pharm. Bull.* **2012**, *35*, 1014–1021. [CrossRef] [PubMed]

361. Israilides, C.; Kletsas, D.; Arapoglou, D.; Philippoussis, A.; Pratsinis, H.; Ebringerová, A.; Hříbalová, V.; Harding, S. In vitro cytostatic and immunomodulatory properties of the medicinal mushroom *Lentinula edodes*. *Phytomedicine* **2008**, *15*, 512–519. [CrossRef] [PubMed]

362. Liu, W.; Gu, J.; Qi, J.; Zeng, X.N.; Ji, J.; Chen, Z.Z.; Sun, X.L. Lentinan exerts synergistic apoptotic effects with paclitaxel in A549 cells via activating ROS-TXNIP-NLRP 3 inflammasome. *J. Cell. Mol. Med.* **2015**, *19*, 1949–1955. [CrossRef] [PubMed]

363. Sun, M.; Zhao, W.; Xie, Q.; Zhan, Y.; Wu, B. Lentinan reduces tumor progression by enhancing gemcitabine chemotherapy in urothelial bladder cancer. *Surg. Oncol.* **2015**, *24*, 28–34. [CrossRef] [PubMed]

364. Zhao, L.; Xiao, Y.; Xiao, N. Effect of lentinan combined with docetaxel and cisplatin on the proliferation and apoptosis of BGC823 cells. *Tumor Biol.* **2013**, *34*, 1531–1536. [CrossRef] [PubMed]

365. Zhang, Y.; Li, Q.; Wang, J.; Cheng, F.; Huang, X.; Cheng, Y.; Wang, K. Polysaccharide from Lentinus edodes combined with oxaliplatin possesses the synergy and attenuation effect in hepatocellular carcinoma. *Cancer Lett.* **2016**, *377*, 117–125. [CrossRef]

366. Wang, Y.; Chen, J.; Han, Q.; Luo, Q.; Zhang, H.; Wang, Y. Construction of doxorubicin-conjugated lentinan nanoparticles for enhancing the cytotoxocity effects against breast cancer cells. *Coll. Surf. A Physicochem. Eng. Asp.* **2019**, *579*, 123657. [CrossRef]

367. Wang, J.; Li, W.; Huang, X.; Liu, Y.; Li, Q.; Zheng, Z.; Wang, K. A polysaccharide from Lentinus edodes inhibits human colon cancer cell proliferation and suppresses tumor growth in athymic nude mice. *Oncotarget* **2017**, *8*, 610. [CrossRef]

368. Ina, K.; Kataoka, T.; Ando, T. The use of lentinan for treating gastric cancer. *Anticancer Agents Med. Chem.* **2013**, *13*, 681–688. [CrossRef]

369. Ina, H.; Yoneda, M.; Kanda, M.; Kodera, Y.; Kabeya, M.; Yuasa, S. Lentinan, a shiitake mushroom beta-glucan, stimulates tumor-specific adaptive immunity through PD-L1 down-regulation in gastric cancer cells. *Med. Chem* **2016**, *6*, 710–714. [CrossRef]

370. Antonelli, M.; Donelli, D.; Firenzuoli, F. Lentinan for Integrative Cancer Treatment: An Umbrella Review. *Multidiscip. Digit. Publ. Inst. Proc.* **2020**, *79*, 1.

371. Zhang, M.; Zhang, Y.; Zhang, L.; Tian, Q. Mushroom polysaccharide lentinan for treating different types of cancers: A review of 12 years clinical studies in China. *Progress Mol. Biol. Translat. Sci.* **2019**, *163*, 297–328.

372. Zhao, H.; Wu, L.; Yan, G.; Chen, Y.; Zhou, M.; Wu, Y.; Li, Y. Inflammation and tumor progression: Signaling pathways and targeted intervention. *Signal Transduct. Target. Ther.* **2021**, *6*, 263. [CrossRef]

373. Basu, A.; Ramamoorthi, G.; Albert, G.; Gallen, C.; Beyer, A.; Snyder, C.; Koski, G.; Disis, M.L.; Czerniecki, B.J.; Kodumudi, K. Differentiation and regulation of TH cells: A balancing act for cancer immunotherapy. *Front. Immunol.* **2021**, *12*, 669474. [CrossRef] [PubMed]

374. Ina, K.; Furuta, R.; Kataoka, T.; Kayukawa, S.; Yoshida, T.; Miwa, T.; Yamamura, Y.; Takeuchi, Y. Lentinan prolonged survival in patients with gastric cancer receiving S-1-based chemotherapy. *World J. Clin. Oncol.* **2011**, *2*, 339. [CrossRef]

375. Howard, R.; Kanetsky, P.A.; Egan, K.M. Exploring the prognostic value of the neutrophil-to-lymphocyte ratio in cancer. *Sci. Rep.* **2019**, *9*, 19673. [CrossRef]

376. Szor, D.J.; Dias, A.R.; Pereira, M.A.; Ramos, M.F.K.P.; Zilberstein, B.; Cecconello, I.; Ribeiro-Júnior, U. Prognostic role of neutrophil/lymphocyte ratio in resected gastric cancer: A systematic review and meta-analysis. *Clinics* **2018**, *73*, e360. [CrossRef]

377. Tavakkoli, M.; Wilkins, C.R.; Mones, J.V.; Mauro, M.J. A novel paradigm between leukocytosis, G-CSF secretion, neutrophil-to-lymphocyte ratio, myeloid-derived suppressor cells, and prognosis in non-small cell lung cancer. *Front. Oncol.* **2019**, *9*, 295. [CrossRef]

378. Matsuoka, H.; Seo, Y.; Wakasugi, H.; Saito, T.; Tomoda, H. Lentinan potentiates immunity and prolongs the survival time of some patients. *Anticancer Res.* **1997**, *17*, 2751–2755.

379. Wang, X.-E.; Wang, Y.-H.; Zhou, Q.; Peng, M.; Zhang, J.; Chen, M.; Ma, L.-J.; Xie, G.-M. Immunomodulatory effect of lentinan on aberrant T subsets and cytokines profile in non-small cell lung cancer patients. *Pathol. Oncol. Res.* **2020**, *26*, 499–505. [CrossRef] [PubMed]

380. Oba, K.; Kobayashi, M.; Matsui, T.; Kodera, Y.; Sakamoto, J. Individual patient based meta-analysis of lentinan for unresectable/recurrent gastric cancer. *Anticancer Res.* **2009**, *29*, 2739–2745. [PubMed]

381. Isoda, N.; Eguchi, Y.; Nukaya, H.; Hosho, K.; Suga, Y.; Suga, T.; Nakazawa, S.; Sugano, K. Clinical efficacy of superfine dispersed lentinan (beta-1, 3-glucan) in patients with hepatocellular carcinoma. *Hepato Gastroenterol.* **2009**, *56*, 437–441.

382. Shimizu, K.; Watanabe, S.; Matsuda, K.; Suga, T.; Nakazawa, S.; Shiratori, K. Efficacy of oral administered superfine dispersed lentinan for advanced pancreatic cancer. *Hepato Gastroenterol.* **2009**, *56*, 240–244.

383. Wang, H.; Cai, Y.; Zheng, Y.; Bai, Q.; Xie, D.; Yu, J. Efficacy of biological response modifier lentinan with chemotherapy for advanced cancer: A meta-analysis. *Cancer Med.* **2017**, *6*, 2222–2233. [CrossRef]

384. Babu, P.D.; Subhasree, R. The sacred mushroom "Reishi"—A review. *Am. Eurasian J. Bot.* **2008**, *1*, 107–110.

385. Suarez-Arroyo, I.J.; Rosario-Acevedo, R.; Aguilar-Perez, A.; Clemente, P.L.; Cubano, L.A.; Serrano, J.; Schneider, R.J.; Martínez-Montemayor, M.M. Anti-tumor effects of *Ganoderma lucidum* (reishi) in inflammatory breast cancer in in vivo and in vitro models. *PLoS ONE* **2013**, *8*, e57431. [CrossRef]

386. Martínez-Montemayor, M.M.; Acevedo, R.R.; Otero-Franqui, E.; Cubano, L.A.; Dharmawardhane, S.F. *Ganoderma lucidum* (Reishi) inhibits cancer cell growth and expression of key molecules in inflammatory breast cancer. *Nutr. Cancer* **2011**, *63*, 1085–1094. [CrossRef]

387. Acevedo-Díaz, A.; Ortiz-Soto, G.; Suárez-Arroyo, I.J.; Zayas-Santiago, A.; Martínez Montemayor, M.M. *Ganoderma lucidum* extract reduces the motility of breast cancer cells mediated by the RAC–lamellipodin Axis. *Nutrients* **2019**, *11*, 1116. [CrossRef]

388. Liang, C.; Tian, D.; Liu, Y.; Li, H.; Zhu, J.; Li, M.; Xin, M.; Xia, J. Review of the molecular mechanisms of *Ganoderma lucidum* triterpenoids: Ganoderic acids A, C2, D, F, DM, X and Y. *Eur. J. Med. Chem.* **2019**, *174*, 130–141. [CrossRef]

389. Sohretoglu, D.; Huang, S. *Ganoderma lucidum* polysaccharides as an anti-cancer agent. *Anti-Cancer Agents Med. Chem.* **2018**, *18*, 667–674. [CrossRef] [PubMed]

390. Radwan, F.F.; Perez, J.M.; Haque, A. Apoptotic and immune restoration effects of ganoderic acids define a new prospective for complementary treatment of cancer. *J. Clin. Cell. Immunol.* **2011**, *11*, 4. [CrossRef] [PubMed]

391. Gill, B.S.; Kumar, S. Ganoderic acid targeting multiple receptors in cancer: In silico and in vitro study. *Tumor Biol.* **2016**, *37*, 14271–14290. [CrossRef] [PubMed]

392. Xia, J.; Dai, L.; Wang, L.; Zhu, J. Ganoderic acid DM induces autophagic apoptosis in non-small cell lung cancer cells by inhibiting the PI3K/Akt/mTOR activity. *Chem. Biol. Interact.* **2020**, *316*, 108932. [CrossRef] [PubMed]

393. Wu, G.-S.; Lu, J.-J.; Guo, J.-J.; Li, Y.-B.; Tan, W.; Dang, Y.-Y.; Zhong, Z.-F.; Xu, Z.-T.; Chen, X.-P.; Wang, Y.-T. Ganoderic acid DM, a natural triterpenoid, induces DNA damage, G1 cell cycle arrest and apoptosis in human breast cancer cells. *Fitoterapia* **2012**, *83*, 408–414. [CrossRef]

394. Chen, N.-H.; Liu, J.-W.; Zhong, J.-J. Ganoderic acid Me inhibits tumor invasion through down-regulating matrix metalloproteinases 2/9 gene expression. *J. Pharmacol. Sci.* **2008**, *108*, 212–216. [CrossRef]

395. Xu, J.; Chen, F.; Wang, G.; Liu, B.; Song, H.; Ma, T. The Versatile Functions of G. Lucidum Polysaccharides and G. Lucidum Triterpenes in Cancer Radiotherapy and Chemotherapy. *Cancer Manag. Res.* **2021**, *13*, 6507. [CrossRef]

396. Pan, H.; Wang, Y.; Wang, Y.; Li, M.; Li, Z.; Xu, J.; Wang, X. *Ganoderma lucidum* polysaccharides induce cytotoxicity in colorectal cancer cells through inducing autophagosome accumulation and inhibiting autophagic flux. *FASEB J.* **2019**, *33*, lb395. [CrossRef]

397. Zhong, J.; Fang, L.; Chen, R.; Xu, J.; Guo, D.; Guo, C.; Guo, C.; Chen, J.; Chen, C.; Wang, X. Polysaccharides from sporoderm-removed spores of *Ganoderma lucidum* induce apoptosis in human gastric cancer cells via disruption of autophagic flux. *Oncol. Lett.* **2021**, *21*, 425. [CrossRef]

398. Su, J.; Li, D.; Chen, Q.; Li, M.; Su, L.; Luo, T.; Liang, D.; Lai, G.; Shuai, O.; Jiao, C. Anti-breast cancer enhancement of a polysaccharide from spore of *Ganoderma lucidum* with paclitaxel: Suppression on tumor metabolism with gut microbiota reshaping. *Front. Microbiol.* **2018**, *9*, 3099. [CrossRef]

399. Jin, H.; Song, C.; Zhao, Z.; Zhou, G. *Ganoderma Lucidum* Polysaccharide, an Extract from *Ganoderma Lucidum*, Exerts Suppressive Effect on Cervical Cancer Cell Malignancy through Mitigating Epithelial-Mesenchymal and JAK/STAT5 Signaling Pathway. *Pharmacology* **2020**, *105*, 461–470. [CrossRef] [PubMed]

400. Hsu, W.-H.; Hua, W.-J.; Qiu, W.-L.; Tseng, A.-J.; Cheng, H.-C.; Lin, T.-Y. WSG, a glucose-enriched polysaccharide from *Ganoderma lucidum*, suppresses tongue cancer cells via inhibition of EGFR-mediated signaling and potentiates cisplatin-induced apoptosis. *Int. J. Biol. Macromol.* **2021**, *193*, 1201–1208. [CrossRef] [PubMed]

401. Cao, Y.; Xu, X.; Liu, S.; Huang, L.; Gu, J. Ganoderma: A cancer immunotherapy review. *Front. Pharmacol.* **2018**, *9*, 1217. [CrossRef]

402. Zhao, R.; Chen, Q.; He, Y.-m. The effect of *Ganoderma lucidum* extract on immunological function and identify its anti-tumor immunostimulatory activity based on the biological network. *Sci. Rep.* **2018**, *8*, 12680. [CrossRef]

403. Chien, C.M.; Cheng, J.-L.; Chang, W.-T.; Tien, M.-H.; Tsao, C.-M.; Chang, Y.-H.; Chang, H.-Y.; Hsieh, J.-F.; Wong, C.-H.; Chen, S.-T. Polysaccharides of *Ganoderma lucidum* alter cell immunophenotypic expression and enhance CD56+ NK-cell cytotoxicity in cord blood. *Bioorg. Med. Chem.* **2004**, *12*, 5603–5609. [CrossRef]

404. Chen, H.-S.; Tsai, Y.-F.; Lin, S.; Lin, C.-C.; Khoo, K.-H.; Lin, C.-H.; Wong, C.-H. Studies on the immuno-modulating and anti-tumor activities of *Ganoderma lucidum* (Reishi) polysaccharides. *Bioorg. Med. Chem.* **2004**, *12*, 5595–5601. [CrossRef]

405. Zhang, S.; Pang, G.; Chen, C.; Qin, J.; Yu, H.; Liu, Y.; Zhang, X.; Song, Z.; Zhao, J.; Wang, F. Effective cancer Immunother. by *Ganoderma lucidum* polysaccharide-gold nanocomposites through dendritic cell activation and memory T cell response. *Carbohydr. Polym.* **2019**, *205*, 192–202. [CrossRef] [PubMed]

406. Guo, C.; Guo, D.; Fang, L.; Sang, T.; Wu, J.; Guo, C.; Wang, Y.; Wang, Y.; Chen, C.; Chen, J. *Ganoderma lucidum* polysaccharide modulates gut microbiota and immune cell function to inhibit inflammation and tumorigenesis in colon. *Carbohydr. Polym.* **2021**, *267*, 118231. [CrossRef]

407. Chiu, H.-F.; Fu, H.-Y.; Lu, Y.-Y.; Han, Y.-C.; Shen, Y.-C.; Venkatakrishnan, K.; Golovinskaia, O.; Wang, C.-K. Triterpenoids and polysaccharide peptides-enriched *Ganoderma lucidum*: A randomized, double-blind placebo-controlled crossover study of its antioxidation and hepatoprotective efficacy in healthy volunteers. *Pharm. Biol.* **2017**, *55*, 1041–1046. [CrossRef]

408. Deng, Y.; Ma, J.; Tang, D.; Zhang, Q. Dynamic biomarkers indicate the immunological benefits provided by Ganoderma spore powder in post-operative breast and lung cancer patients. *Clin. Translat. Oncol.* **2021**, *23*, 1481–1490. [CrossRef]

409. Wu, J.-Y.; Siu, K.-C.; Geng, P. Bioactive ingredients and medicinal values of *Grifola frondosa* (Maitake). *Foods* **2021**, *10*, 95. [CrossRef] [PubMed]

410. De Silva, D.D.; Rapior, S.; Fons, F.; Bahkali, A.H.; Hyde, K.D. Medicinal mushrooms in supportive cancer therapies: An approach to anti-cancer effects and putative mechanisms of action. *Fungal Divers.* **2012**, *55*, 1–35. [CrossRef]

411. Alonso, E.N.; Orozco, M.; Nieto, A.E.; Balogh, G.A. Genes related to suppression of malignant phenotype induced by Maitake D-Fraction in breast cancer cells. *J. Med. Food* **2013**, *16*, 602–617. [CrossRef] [PubMed]

412. Alonso, E.N.; Ferronato, M.J.; Fermento, M.E.; Gandini, N.A.; Romero, A.L.; Guevara, J.A.; Facchinetti, M.M.; Curino, A.C. Antitumoral and antimetastatic activity of Maitake D-Fraction in triple-negative breast cancer cells. *Oncotarget* **2018**, *9*, 23396. [CrossRef] [PubMed]

413. Lin, C.-H.; Chang, C.-Y.; Lee, K.-R.; Lin, H.-J.; Lin, W.-C.; Chen, T.-H.; Wan, L. Cold-water extracts of *Grifola frondosa* and its purified active fraction inhibit hepatocellular carcinoma in vitro and in vivo. *Exp. Biol. Med.* **2016**, *241*, 1374–1385. [CrossRef] [PubMed]

414. Fullerton, S.; Samadi, A.; Tortorelis, D.; Choudhury, M.; Mallouh, C.; Tazaki, H.; Konno, S. Induction of apoptosis in human prostatic cancer cells with beta-glucan (Maitake mushroom polysaccharide). *Mol. Urology* **2000**, *4*, 7–13.

415. Alexander, B.; Fishman, A.I.; Eshghi, M.; Choudhury, M.; Konno, S. Induction of cell death in renal cell carcinoma with combination of D-fraction and vitamin C. *Integr. Cancer Ther.* **2013**, *12*, 442–448. [CrossRef]

416. Roldan-Deamicis, A.; Alonso, E.; Brie, B.; Braico, D.A.; Balogh, G.A. Maitake Pro4X has anti-cancer activity and prevents oncogenesis in BALB c mice. *Cancer Med.* **2016**, *5*, 2427–2441. [CrossRef]

417. Kodama, N.; Komuta, K.; Sakai, N.; Nanba, H. Effects of D-Fraction, a polysaccharide from *Grifola frondosa* on tumor growth involve activation of NK cells. *Biol. Pharm. Bull.* **2002**, *25*, 1647–1650. [CrossRef]

418. Zhao, F.; Guo, Z.; Zhang, Y.; Song, L.; Ma, L.; Zhao, J. Anti-tumor and immunomodulatory effects of *Grifola frondosa* polysaccharide combined with vitamin C on Heps-bearing mice: Based on inducing apoptosis and autophagy. *J. Funct. Foods* **2021**, *87*, 104797. [CrossRef]

419. Masuda, Y.; Nakayama, Y.; Tanaka, A.; Naito, K.; Konishi, M. Antitumor activity of orally administered maitake α-glucan by stimulating antitumor immune response in murine tumor. *PLoS ONE* **2017**, *12*, e0173621. [CrossRef] [PubMed]

420. Zhao, F.; Guo, Z.; Ma, Z.-R.; Ma, L.-L.; Zhao, J. Antitumor activities of *Grifola frondosa* (Maitake) polysaccharide: A meta-analysis based on preclinical evidence and quality assessment. *J. Ethnopharmacol.* **2021**, *280*, 114395. [CrossRef] [PubMed]

421. Kodama, N.; Komuta, K.; Nanba, H. Can maitake MD-fraction aid cancer patients? *Altern. Med. Rev.* **2002**, *7*, 236–239. [PubMed]

422. Kodama, N.; Komuta, K.; Nanba, H. Effect of Maitake (*Grifola frondosa*) D-Fraction on the activation of NK cells in cancer patients. *J. Med. Food* **2003**, *6*, 371–377. [CrossRef] [PubMed]

423. He, Y.; Zhang, L.; Wang, H. The biological activities of the antitumor drug *Grifola frondosa* polysaccharide. *Prog. Mol. Biol. Translat. Sci.* **2019**, *163*, 221–261.

424. Zhou, X.; Gong, Z.; Su, Y.; Lin, J.; Tang, K. Cordyceps fungi: Natural products, pharmacological functions and developmental products. *J. Pharm. Pharmacol.* **2009**, *61*, 279–291. [CrossRef]

425. Yue, K.; Ye, M.; Zhou, Z.; Sun, W.; Lin, X. The genus Cordyceps: A chemical and pharmacological review. *J. Pharm. Pharmacol.* **2013**, *65*, 474–493. [CrossRef]

426. Jędrejko, K.J.; Lazur, J.; Muszyńska, B. *Cordyceps militaris*: An Overview of Its Chemical Constituents in Relation to Biological Activity. *Foods* **2021**, *10*, 2634. [CrossRef]

427. Li, J.; Cai, H.; Sun, H.; Qu, J.; Zhao, B.; Hu, X.; Li, W.; Qian, Z.; Yu, X.; Kang, F. Extracts of *Cordyceps sinensis* inhibit breast cancer growth through promoting M1 macrophage polarization via NF-κB pathway activation. *J. Ethnopharmacol.* **2020**, *260*, 112969. [CrossRef]

428. Seo, H.; Song, J.; Kim, M.; Han, D.-W.; Park, H.-J.; Song, M. *Cordyceps militaris* grown on germinated soybean suppresses KRAS-driven colorectal cancer by inhibiting the RAS/ERK pathway. *Nutrients* **2018**, *11*, 20. [CrossRef]

429. Jeong, M.-K.; Yoo, H.-S.; Kang, I.-C. The extract of *Cordyceps militaris* inhibited the proliferation of cisplatin-resistant a549 lung cancer cells by downregulation of H-Ras. *J. Med. Food* **2019**, *22*, 823–832. [CrossRef] [PubMed]

430. Jo, E.; Jang, H.-J.; Shen, L.; Yang, K.E.; Jang, M.S.; Huh, Y.H.; Yoo, H.-S.; Park, J.; Jang, I.S.; Park, S.J. *Cordyceps militaris* Exerts Anticancer Effect on Non–Small Cell Lung Cancer by Inhibiting Hedgehog Signaling via Suppression of TCTN3. *Integr. Cancer Ther.* **2020**, *19*, 1534735420923756. [CrossRef] [PubMed]

431. Yoon, S.Y.; Park, S.J.; Park, Y.J. The anticancer properties of cordycepin and their underlying mechanisms. *Int. J. Mol. Sci.* **2018**, *19*, 3027. [CrossRef] [PubMed]

432. Fishman, P.; Bar-Yehuda, S.; Synowitz, M.; Powell, J.; Klotz, K.; Gessi, S.; Borea, P. Adenosine receptors and cancer. *Adenosine Recept. Health Dis.* **2009**, *193*, 399–441.

433. Cao, H.-L.; Liu, Z.-J.; Chang, Z. Cordycepin induces apoptosis in human bladder cancer cells via activation of A3 adenosine receptors. *Tumor Biol.* **2017**, *39*, 1010428317706915. [CrossRef]

434. Nakamura, K.; Yoshikawa, N.; Yamaguchi, Y.; Kagota, S.; Shinozuka, K.; Kunitomo, M. Antitumor effect of cordycepin (3′-deoxyadenosine) on mouse melanoma and lung carcinoma cells involves adenosine A3 receptor stimulation. *Anticancer Res.* **2006**, *26*, 43–47.

435. Yoshikawa, N.; Yamada, S.; Takeuchi, C.; Kagota, S.; Shinozuka, K.; Kunitomo, M.; Nakamura, K. Cordycepin (3′-deoxyadenosine) inhibits the growth of B16-BL6 mouse melanoma cells through the stimulation of adenosine A3 receptor followed by glycogen synthase kinase-3β activation and cyclin D1 suppression. *Naunyn Schmiedeberg's Arch. Pharmacol.* **2008**, *377*, 591–595. [CrossRef]

436. Zhao, X.; Guan, J.-L. Focal adhesion kinase and its signaling pathways in cell migration and angiogenesis. *Adv. Drug Deliv. Rev.* **2011**, *63*, 610–615. [CrossRef]

437. Yao, W.-L.; Ko, B.-S.; Liu, T.-A.; Liang, S.-M.; Liu, C.-C.; Lu, Y.-J.; Tzean, S.-S.; Shen, T.-L.; Liou, J.-Y. Cordycepin suppresses integrin/FAK signaling and epithelial-mesenchymal transition in hepatocellular carcinoma. *Anti Cancer Agents Med. Chem.* **2014**, *14*, 29–34. [CrossRef]

438. Jin, Y.; Meng, X.; Qiu, Z.; Su, Y.; Yu, P.; Qu, P. Anti-tumor and anti-metastatic roles of cordycepin, one bioactive compound of *Cordyceps militaris*. *Saudi J. Biol. Sci.* **2018**, *25*, 991–995. [CrossRef]

439. Lee, S.Y.; Debnath, T.; Kim, S.-K.; Lim, B.O. Anti-cancer effect and apoptosis induction of cordycepin through DR3 pathway in the human colonic cancer cell HT-29. *Food Chem. Toxicol.* **2013**, *60*, 439–447. [CrossRef] [PubMed]

440. Lee, H.H.; Kim, S.O.; Kim, G.-Y.; Moon, S.-K.; Kim, W.-J.; Jeong, Y.K.; Yoo, Y.H.; Choi, Y.H. Involvement of autophagy in cordycepin-induced apoptosis in human prostate carcinoma LNCaP cells. *Environ. Toxicol. Pharmacol.* **2014**, *38*, 239–250. [CrossRef] [PubMed]

441. Chang, M.-M.; Hong, S.-Y.; Yang, S.-H.; Wu, C.-C.; Wang, C.-Y.; Huang, B.-M. Anti-cancer effect of cordycepin on FGF9-induced testicular tumorigenesis. *Int. J. Mol. Sci.* **2020**, *21*, 8336. [CrossRef] [PubMed]

442. Wang, J.; Chen, H.; Li, W.; Shan, L. Cordyceps acid alleviates lung cancer in nude mice. *J. Biochem. Mol. Toxicol.* **2021**, *35*, e22670. [CrossRef]

443. Ka Wai Lee, S.; Kwok Wong, C.; Kai Kong, S.; Nam Leung, K.; Wai Kei Lam, C. Immunomodulatory activities of HERBSnSENSES™ Cordyceps—in vitro and in vivo studies. *Immunopharmacol. Immunotoxicol.* **2006**, *28*, 341–360. [CrossRef]

444. Wang, M.; Meng, X.Y.; Le Yang, R.; Qin, T.; Wang, X.Y.; Zhang, K.Y.; Fei, C.Z.; Li, Y.; liang Hu, Y.; Xue, F.Q. *Cordyceps militaris* polysaccharides can enhance the immunity and antioxidation activity in immunosuppressed mice. *Carbohydr. Polym.* **2012**, *89*, 461–466. [CrossRef]

445. Das, G.; Shin, H.-S.; Leyva-Gómez, G.; Prado-Audelo, M.L.D.; Cortes, H.; Singh, Y.D.; Panda, M.K.; Mishra, A.P.; Nigam, M.; Saklani, S. Cordyceps spp.: A review on its immune-stimulatory and other biological potentials. *Front. Pharmacol.* **2021**, *11*, 602364. [CrossRef]

446. Qi, W.; Zhou, X.; Wang, J.; Zhang, K.; Zhou, Y.; Chen, S.; Nie, S.; Xie, M. *Cordyceps sinensis* polysaccharide inhibits colon cancer cells growth by inducing apoptosis and autophagy flux blockage via mTOR signaling. *Carbohydr. Polym.* **2020**, *237*, 116113. [CrossRef]

447. Borodina, I.; Kenny, L.C.; McCarthy, C.M.; Paramasivan, K.; Pretorius, E.; Roberts, T.J.; van der Hoek, S.A.; Kell, D.B. The biology of ergothioneine, an antioxidant nutraceutical. *Nutr. Res. Rev.* **2020**, *33*, 190–217. [CrossRef]

448. D'Onofrio, N.; Martino, E.; Balestrieri, A.; Mele, L.; Cautela, D.; Castaldo, D.; Balestrieri, M.L. Diet-derived ergothioneine induces necroptosis in colorectal cancer cells by activating the SIRT3/MLKL pathway. *FEBS Lett.* **2022**. [CrossRef]

449. Yoshida, S.; Shime, H.; Matsumoto, M.; Kasahara, M.; Seya, T. Anti-oxidative amino acid L-ergothioneine modulates the tumor microenvironment to facilitate adjuvant vaccine immunotherapy. *Front. Immunol.* **2019**, *10*, 671. [CrossRef] [PubMed]

450. Smith, E.; Ottosson, F.; Hellstrand, S.; Ericson, U.; Orho-Melander, M.; Fernandez, C.; Melander, O. Ergothioneine is associated with reduced mortality and decreased risk of cardiovascular disease. *Heart* **2020**, *106*, 691–697. [CrossRef] [PubMed]

451. Winkels, R.M.; Van Brakel, L.; Van Baar, H.; Beelman, R.B.; Van Duijnhoven, F.J.; Geijsen, A.; Van Halteren, H.K.; Hansson, B.M.; Richie, J.P.; Sun, D. Are Ergothioneine Levels in Blood Associated with Chronic Peripheral Neuropathy in Colorectal Cancer Patients Who Underwent Chemotherapy? *Nutr. Cancer* **2020**, *72*, 451–459. [CrossRef] [PubMed]

452. Zhao, Y.; Zheng, W. Deciphering the antitumoral potential of the bioactive metabolites from medicinal mushroom *Inonotus obliquus*. *J. Ethnopharmacol.* **2021**, *265*, 113321. [CrossRef]

453. Arata, S.; Watanabe, J.; Maeda, M.; Yamamoto, M.; Matsuhashi, H.; Mochizuki, M.; Kagami, N.; Honda, K.; Inagaki, M. Continuous intake of the Chaga mushroom (*Inonotus obliquus*) aqueous extract suppresses cancer progression and maintains body temperature in mice. *Heliyon* **2016**, *2*, e00111. [CrossRef]

454. Lee, M.-G.; Kwon, Y.-S.; Nam, K.-S.; Kim, S.Y.; Hwang, I.H.; Kim, S.; Jang, H. Chaga mushroom extract induces autophagy via the AMPK-mTOR signaling pathway in breast cancer cells. *J. Ethnopharmacol.* **2021**, *274*, 114081. [CrossRef]

455. Zhang, Q.; Wang, J.; He, H.; Liu, H.; Yan, X.; Zou, K. Trametenolic Acid B Reverses Multidrug Resistance in Breast Cancer Cells Through Regulating the Expression Level of P-Glycoprotein. *Phytother. Res.* **2014**, *28*, 1037–1044. [CrossRef]

456. Lu, Y.; Jia, Y.; Xue, Z.; Li, N.; Liu, J.; Chen, H. Recent developments in *Inonotus obliquus* (*Chaga mushroom*) polysaccharides: Isolation, structural characteristics, biological activities and application. *Polymers* **2021**, *13*, 1441. [CrossRef]

457. Kim, Y.O.; Park, H.W.; Kim, J.H.; Lee, J.Y.; Moon, S.H.; Shin, C.S. Anti-cancer effect and structural characterization of endo-polysaccharide from cultivated mycelia of *Inonotus obliquus*. *Life Sci.* **2006**, *79*, 72–80. [CrossRef]

458. Jiang, S.; Shi, F.; Lin, H.; Ying, Y.; Luo, L.; Huang, D.; Luo, Z. *Inonotus obliquus* polysaccharides induces apoptosis of lung cancer cells and alters energy metabolism via the LKB1/AMPK axis. *Int. J. Biol. Macromol.* **2020**, *151*, 1277–1286. [CrossRef]

459. Pei, J.; Velu, P.; Zareian, M.; Feng, Z.; Vijayalakshmi, A. Effects of Syringic Acid on Apoptosis, Inflammation, and AKT/mTOR Signaling Pathway in Gastric Cancer Cells. *Front. Nutr.* **2021**, *8*, 788929. [CrossRef] [PubMed]

460. Sung, B.; Pandey, M.K.; Nakajima, Y.; Nishida, H.; Konishi, T.; Chaturvedi, M.M.; Aggarwal, B.B. Identification of a novel blocker of IκBα kinase activation that enhances apoptosis and inhibits proliferation and invasion by suppressing nuclear factor-κB. *Mol. Cancer Ther.* **2008**, *7*, 191–201. [CrossRef] [PubMed]

461. Zhang, X.; Bao, C.; Zhang, J. Inotodiol suppresses proliferation of breast cancer in rat model of type 2 diabetes mellitus via downregulation of β-catenin signaling. *Biomed. Pharmacother.* **2018**, *99*, 142–150. [CrossRef]

462. Zhang, S.-D.; Yu, L.; Wang, P.; Kou, P.; Li, J.; Wang, L.-T.; Wang, W.; Yao, L.-P.; Zhao, X.-H.; Fu, Y.-J. Inotodiol inhibits cells migration and invasion and induces apoptosis via p53-dependent pathway in HeLa cells. *Phytomedicine* **2019**, *60*, 152957. [CrossRef]

463. Sarfraz, A.; Rasul, A.; Sarfraz, I.; Shah, M.A.; Hussain, G.; Shafiq, N.; Masood, M.; Adem, Ş.; Sarker, S.D.; Li, X. Hispolon: A natural polyphenol and emerging cancer killer by multiple cellular signaling pathways. *Environ. Res.* **2020**, *190*, 110017. [CrossRef] [PubMed]

464. Masood, M.; Rasul, A.; Sarfraz, I.; Jabeen, F.; Liu, S.; Liu, X.; Wei, W.; Li, J.; Li, X. Hispolon induces apoptosis against prostate DU145 cancer cells via modulation of mitochondrial and STAT3 pathways. *Pak. J. Pharm. Sci* **2019**, *32*, 2237–2243. [PubMed]

465. Al Saqr, A.; Majrashi, M.; Alrbyawi, H.; Govindarajulu, M.; Fujihashi, A.; Gottumukkala, S.; Poudel, I.; Arnold, R.D.; Babu, R.J.; Dhanasekaran, M. Elucidating the anti-melanoma effect and mechanisms of Hispolon. *Life Sci.* **2020**, *256*, 117702. [CrossRef]

466. Hsin, M.-C.; Hsieh, Y.-H.; Wang, P.-H.; Ko, J.-L.; Hsin, I.-L.; Yang, S.-F. Hispolon suppresses metastasis via autophagic degradation of cathepsin S in cervical cancer cells. *Cell Death Dis.* **2017**, *8*, e3089. [CrossRef]

467. Palkina, K.A.; Ipatova, D.A.; Shakhova, E.S.; Balakireva, A.V.; Markina, N.M. Ther. Potential of Hispidin—Fungal and Plant Polyketide. *J. Fungi* **2021**, *7*, 323. [CrossRef]

468. Lv, L.-X.; Zhou, Z.-X.; Zhou, Z.; Zhang, L.-J.; Yan, R.; Zhao, Z.; Yang, L.-Y.; Bian, X.-Y.; Jiang, H.-Y.; Li, Y.-D. Hispidin induces autophagic and necrotic death in SGC-7901 gastric cancer cells through lysosomal membrane permeabilization by inhibiting tubulin polymerization. *Oncotarget* **2017**, *8*, 26992. [CrossRef]

469. Chandimali, N.; JIN, W.Y.; KWON, T. Combination effects of hispidin and gemcitabine via inhibition of stemness in pancreatic cancer stem cells. *Anticancer Res.* **2018**, *38*, 3967–3975. [CrossRef] [PubMed]

470. Ahn, W.-S.; Kim, D.-J.; Chae, G.-T.; Lee, J.-M.; Bae, S.-M.; Sin, J.-I.; Kim, Y.-W.; Namkoong, S.-E.; Lee, I. Natural killer cell activity and quality of life were improved by consumption of a mushroom extract, *Agaricus blazei* Murill Kyowa, in gynecological cancer patients undergoing chemotherapy. *Int. J. Gynecol. Cancer* **2004**, *14*, 589–594. [CrossRef] [PubMed]

471. Hetland, G.; Tangen, J.-M.; Mahmood, F.; Mirlashari, M.R.; Nissen-Meyer, L.S.H.; Nentwich, I.; Therkelsen, S.P.; Tjønnfjord, G.E.; Johnson, E. Antitumor, anti-inflammatory and antiallergic effects of *Agaricus blazei* mushroom extract and the related medicinal Basidiomycetes mushrooms, *Hericium erinaceus* and *Grifola frondosa*: A review of preclinical and clinical studies. *Nutrients* **2020**, *12*, 1339. [CrossRef] [PubMed]

472. Tangen, J.-M.; Tierens, A.; Caers, J.; Binsfeld, M.; Olstad, O.K.; Trøseid, A.-M.S.; Wang, J.; Tjønnfjord, G.E.; Hetland, G. Immunomodulatory effects of the *Agaricus blazei* Murrill-based mushroom extract AndoSan in patients with multiple myeloma undergoing high dose chemotherapy and autologous stem cell transplantation: A randomized, double blinded clinical study. *Biomed Res. Int.* **2015**, *2015*, 718539. [CrossRef]

473. Lee, S.H.; Hwang, H.K.; Kang, C.M.; Lee, W.J. Potential impact of *Phellinus linteus* on adherence to adjuvant treatment after curative resection of pancreatic ductal adenocarcinoma: Outcomes of a propensity score–matched analysis. *Integr. Cancer Ther.* **2019**, *18*, 1534735418816825. [CrossRef]

474. Chen, W.; Tan, H.; Liu, Q.; Zheng, X.; Zhang, H.; Liu, Y.; Xu, L. A review: The bioactives and pharmacological applications of *Phellinus linteus*. *Molecules* **2019**, *24*, 1888. [CrossRef]

475. Zhang, C.-C.; Cao, C.-Y.; Kubo, M.; Harada, K.; Yan, X.-T.; Fukuyama, Y.; Gao, J.-M. Chemical constituents from *Hericium erinaceus* promote neuronal survival and potentiate neurite outgrowth via the TrkA/Erk1/2 pathway. *Int. J. Mol. Sci.* **2017**, *18*, 1659. [CrossRef]

476. Tung, S.-Y.; Lee, K.-C.; Lee, K.-F.; Yang, Y.-L.; Huang, W.-S.; Lee, L.-Y.; Chen, W.-P.; Chen, C.-C.; Teng, C.-C.; Shen, C.-H. Apoptotic mechanisms of gastric cancer cells induced by isolated erinacine S through epigenetic histone H3 methylation of FasL and TRAIL. *Food Funct.* **2021**, *12*, 3455–3468. [CrossRef]

477. Kuo, H.-C.; Kuo, Y.-R.; Lee, K.-F.; Hsieh, M.-C.; Huang, C.-Y.; Hsieh, Y.-Y.; Lee, K.-C.; Kuo, H.-L.; Lee, L.-Y.; Chen, W.-P. A comparative proteomic analysis of Erinacine A's inhibition of gastric cancer cell viability and invasiveness. *Cell. Physiol. Biochem.* **2017**, *43*, 195–208. [CrossRef]

478. Lee, K.-C.; Lee, K.-F.; Tung, S.-Y.; Huang, W.-S.; Lee, L.-Y.; Chen, W.-P.; Chen, C.-C.; Teng, C.-C.; Shen, C.-H.; Hsieh, M.-C. Induction apoptosis of erinacine a in human colorectal cancer cells involving the expression of TNFR, fas, and fas ligand via the JNK/p300/p50 signaling pathway with histone acetylation. *Front. Pharmacol.* **2019**, *10*, 1174. [CrossRef]

479. TSANG, K.W.; Lam, C.; Yan, C.; Mak, J.; Ooi, G.; Ho, J.; Lam, B.; Man, R.; Sham, J.; Lam, W. Coriolus versicolor polysaccharide peptide slows progression of advanced non-small cell lung cancer. *Resp. Med.* **2003**, *97*, 618–624. [CrossRef] [PubMed]

480. Ohwada, S.; Ikeya, T.; Yokomori, T.; Kusaba, T.; Roppongi, T.; Takahashi, T.; Nakamura, S.; Kakinuma, S.; Iwazaki, S.; Ishikawa, H. Adjuvant immunochemotherapy with oral Tegafur/Uracil plus PSK in patients with stage II or III colorectal cancer: A randomised controlled study. *Br. J. Cancer* **2004**, *90*, 1003–1010. [CrossRef] [PubMed]

481. Li, J.W.-H.; Vederas, J.C. Drug discovery and natural products: End of an era or an endless frontier? *Science* **2009**, *325*, 161–165. [CrossRef] [PubMed]

482. Zhao, Q.; Luan, X.; Zheng, M.; Tian, X.-H.; Zhao, J.; Zhang, W.-D.; Ma, B.-L. Synergistic mechanisms of constituents in herbal extracts during intestinal absorption: Focus on natural occurring nanoparticles. *Pharmaceutics* **2020**, *12*, 128. [CrossRef]

483. Jürgenliemk, G.; Nahrstedt, A. Dissolution, solubility and cooperativity of phenolic compounds from *Hypericum perforatum* L. in aqueous systems. *Int. J. Pharm. Sci.* **2003**, *58*, 200–203.

484. Cai, T.-Y.; Zhang, Y.-R.; Ji, J.-B.; Xing, J. Investigation of the component in Artemisia annua L. leading to enhanced antiplasmodial potency of artemisinin via regulation of its metabolism. *J. Ethnopharmacol.* **2017**, *207*, 86–91. [CrossRef]

485. Gröning, R.; Breitkreutz, J.; Müller, R. Physico-chemical interactions between extracts of *Hypericum perforatum* L. and drugs. *Eur. J. Pharm. Biopharm.* **2003**, *56*, 231–236. [CrossRef]

486. Zhuang, Y.; Yan, J.; Zhu, W.; Chen, L.; Liang, D.; Xu, X. Can the aggregation be a new approach for understanding the mechanism of Tradit. Chin. Medicine? *J. Ethnopharmacol.* **2008**, *117*, 378–384. [CrossRef]

487. Mukherjee, P.K.; Harwansh, R.K.; Bhattacharyya, S. Bioavailability of herbal products: Approach toward improved pharmacokinetics. In *Evidence-Based Validation of Herbal Medicine*; Elsevier: Amsterdam, The Netherlands, 2015; pp. 217–245.

488. Phansalkar, P.S.; Zhang, Z.; Verenich, S.; Gerk, P.M. Pharmacokinetics and bioavailability enhancement of natural products. In *Natural Products for Cancer Chemoprevention*; Springer: Berlin/Heidelberg, Germany, 2020; pp. 109–141.

489. Khedekar, K.; Mittal, S. Self emulsifying drug delivery system: A review. *Int. J. Pharm. Sci. Res.* **2013**, *4*, 4494.

490. Singh, N.; Rai, S.; Bhattacharya, S. A Conceptual Analysis of solid Self-emulsifying drug Delivery System and its Associate Patents for the Treatment of Cancer. *Recent Pat. Nanotechnol* **2021**, *15*, 92–104. [CrossRef]

491. Murugesan, M.P.; Ratnam, M.V.; Mengitsu, Y.; Kandasamy, K. Evaluation of anti-cancer activity of phytosomes formulated from *Aloe vera* extract. *Mat. Today Proc.* **2021**, *42*, 631–636. [CrossRef]

492. Flaig, T.W.; Gustafson, D.L.; Su, L.-J.; Zirrolli, J.A.; Crighton, F.; Harrison, G.S.; Pierson, A.S.; Agarwal, R.; Glodé, L.M. A phase I and pharmacokinetic study of silybin-phytosome in prostate cancer patients. *Investig. New Drugs* **2007**, *25*, 139–146. [CrossRef]

493. Flaig, T.W.; Glodé, M.; Gustafson, D.; van Bokhoven, A.; Tao, Y.; Wilson, S.; Su, L.J.; Li, Y.; Harrison, G.; Agarwal, R. A study of high-dose oral silybin-phytosome followed by prostatectomy in patients with localized prostate cancer. *Prostate* **2010**, *70*, 848–855. [CrossRef] [PubMed]

494. Alhakamy, N.A.; Fahmy, U.A.; Eldin, S.M.B.; Ahmed, O.A.; Aldawsari, H.M.; Okbazghi, S.Z.; Alfaleh, M.A.; Abdulaal, W.H.; Alamoudi, A.J.; Mady, F.M. Scorpion Venom-Functionalized Quercetin Phytosomes for Breast Cancer Management: In Vitro Response Surface Optimization and Anticancer Activity against MCF-7 Cells. *Polymers* **2021**, *14*, 93. [CrossRef] [PubMed]

495. Alhakamy, N.A.; Badr-Eldin, S.M.; Fahmy, U.A.; Alruwaili, N.K.; Awan, Z.A.; Caruso, G.; Alfaleh, M.A.; Alaofi, A.L.; Arif, F.O.; Ahmed, O.A. Thymoquinone-loaded soy-phospholipid-based phytosomes exhibit anticancer potential against human lung cancer cells. *Pharmaceutics* **2020**, *12*, 761. [CrossRef]

496. Muhamad, N.; Plengsuriyakarn, T.; Na-Bangchang, K. Application of active targeting nanoparticle delivery system for chemoTher. drugs and traditional/herbal medicines in cancer therapy: A systematic review. *Int. J. Nanomed.* **2018**, *13*, 3921. [CrossRef]

497. Rehman, M.U.; Khan, A.; Imtiyaz, Z.; Ali, S.; Makeen, H.A.; Rashid, S.; Arafah, A. Current Nano-Therapeutic Approaches Ameliorating Inflammation in Cancer Progression. *Semin. Cancer Biol.* 2022; *Online ahead of print*.

498. Salunkhe, R.; Gadgoli, C.; Naik, A.; Patil, N. Pharmacokinetic Profile and Oral Bioavailability of Diosgenin, Charantin, and Hydroxychalcone from a Polyherbal Formulation. *Front. Pharmacol.* **2021**, *12*, 629272. [CrossRef]

499. Peterson, B.; Weyers, M.; Steenekamp, J.H.; Steyn, J.D.; Gouws, C.; Hamman, J.H. Drug bioavailability enhancing agents of natural origin (bioenhancers) that modulate drug membrane permeation and pre-systemic metabolism. *Pharmaceutics* **2019**, *11*, 33. [CrossRef]

500. Apolone, G.; Joppi, R.; Bertele, V.; Garattini, S. Ten years of marketing approvals of anticancer drugs in Europe: Regulatory policy and guidance documents need to find a balance between different pressures. *Br. J. Cancer* **2005**, *93*, 504–509. [CrossRef]

501. Zhang, J.; Onakpoya, I.J.; Posadzki, P.; Eddouks, M. The safety of herbal medicine: From prejudice to evidence. *Evid. Based Complement. Alternat. Med.* **2015**, *2015*, 316706. [CrossRef]

502. Mazzanti, G.; Menniti-Ippolito, F.; Moro, P.A.; Cassetti, F.; Raschetti, R.; Santuccio, C.; Mastrangelo, S. Hepatotoxicity from green tea: A review of the literature and two unpublished cases. *Eur. J. Clin. Pharmacol.* **2009**, *65*, 331–341. [CrossRef] [PubMed]

503. Hu, J.; Webster, D.; Cao, J.; Shao, A. The safety of green tea and green tea extract consumption in adults–results of a systematic review. *Regul. Toxicol. Pharmacol.* **2018**, *95*, 412–433. [CrossRef] [PubMed]

504. Schmidt, M.; Schmitz, H.-J.; Baumgart, A.; Guedon, D.; Netsch, M.; Kreuter, M.-H.; Schmidlin, C.; Schrenk, D. Toxicity of green tea extracts and their constituents in rat hepatocytes in primary culture. *Food Chem. Toxicol.* **2005**, *43*, 307–314. [CrossRef] [PubMed]

505. Additives, E.P.o.F.; Food, N.S.a.t.; Younes, M.; Aggett, P.; Aguilar, F.; Crebelli, R.; Dusemund, B.; Filipič, M.; Frutos, M.J.; Galtier, P.; et al. Scientific opinion on the safety of green tea catechins. *EFSA J.* **2018**, *16*, e05239.

506. Fasinu, P.S.; Bouic, P.J.; Rosenkranz, B. An overview of the evidence and mechanisms of herb–drug interactions. *Front. Pharmacol.* **2012**, *3*, 69. [CrossRef]

507. Yadav, P.; Mahour, K.; Kumar, A. Standardization and evaluation of herbal drug formulations. *J. Adv. Lab. Res. Biol.* **2011**, *2*, 161–166.

508. Bijauliya, R.K.; Alok, S.; Chanchal, D.K.; Kumar, M. A comprehensive review on standardization of herbal drugs. *Int. J. Pharm. Sci. Res.* **2017**, *8*, 3663–3677.

509. Govindaraghavan, S.; Sucher, N.J. Quality assessment of medicinal herbs and their extracts: Criteria and prerequisites for consistent safety and efficacy of herbal medicines. *Epilepsy Behav.* **2015**, *52*, 363–371. [CrossRef]

510. Wang, J.; Guo, Y.; Li, G.L. Current Status of Standardization of Traditional Chinese Medicine in China. *Evid. Based Complement. Altern. Med.* **2016**, *2016*, 9123103. [CrossRef]

511. Downer, S.; Berkowitz, S.A.; Harlan, T.S.; Olstad, D.L.; Mozaffarian, D. Food is medicine: Actions to integrate food and nutrition into healthcare. *BMJ* **2020**, *369*, m2482. [CrossRef]

512. Chen, X.; Yue, W.; Tian, L.; Li, N.; Chen, Y.; Zhang, L.; Chen, J. A plant-based medicinal food inhibits the growth of human gastric carcinoma by reversing epithelial–mesenchymal transition via the canonical Wnt/β-catenin signaling pathway. *BMC Complement. Med. Ther.* **2021**, *21*, 137. [CrossRef] [PubMed]

MDPI

Article

Design, Synthesis, and Molecular Docking Studies of Curcumin Hybrid Conjugates as Potential Therapeutics for Breast Cancer

Siva S. Panda [1,*]**, Queen L. Tran** [1]**, Pragya Rajpurohit** [2,3]**, Girinath G. Pillai** [4]**, Sean J. Thomas** [1]**, Allison E. Bridges** [2,3]**, Jason E. Capito** [1]**, Muthusamy Thangaraju** [2,3,*] **and Bal L. Lokeshwar** [2,3,5]

[1] Department of Chemistry and Physics, Augusta University, Augusta, GA 30912, USA; queentran29@gmail.com (Q.L.T.); seanjosephthomas@gmail.com (S.J.T.); jcaps79@gmail.com (J.E.C.)
[2] Department of Biochemistry and Molecular Biology, Augusta University, Augusta, GA 30912, USA; pragyaraj2018@gmail.com (P.R.); allison.bridges@ngu.edu (A.E.B.); blokeshwar@augusta.edu (B.L.L.)
[3] Georgia Cancer Center, Augusta University, Augusta, GA 30912, USA
[4] Discovery Chemistry, Nyro Research India, Kochi 682021, India; giribio@gmail.com
[5] Department of Medicine, Medical College of Georgia, Augusta University, Augusta, GA 30912, USA
[*] Correspondence: sipanda@augusta.edu (S.S.P.); mthangaraju@augusta.edu (M.T.)

Abstract: Curcumin (CUR) has received great attention over the past two decades due to its anti-cancer, anti-inflammatory, and antioxidant properties. Similarly, Dichloroacetate (DCA), an pyruvate dehydrogenase kinase 1 (PKD1) inhibitor, has gained huge attention as a potential anticancer drug. However, the clinical utility of these two agents is very limited because of the poor bioavailability and unsolicited side effects, respectively. We have synthesized fusion conjugates of CUR and DCA with an amino acids linker to overcome these limitations by utilizing the molecular hybridization approach. The molecular docking studies showed the potential targets of Curcumin-Modified Conjugates (CMCs) in breast cancer cells. We synthesized six hybrid conjugates named **CMC1-6**. These six CMC conjugates do not show any significant toxicity in a human normal immortalized mammary epithelial cell line (MCF10A) in vitro and C57BL/6 mice in vivo. However, treatment with **CMC1** and **CMC2** significantly reduced the growth and clonogenic survival by colony-formation assays in several human breast cancer cells (BC). Treatment by oral gavage of a transgenic mouse BC and metastatic BC tumor-bearing mice with **CMC2** significantly reduced tumor growth and metastasis. Overall, our study provides strong evidence that CUR and DCA conjugates have a significant anticancer properties at a sub-micromolar concentration and overcome the clinical limitation of using CUR and DCA as potential anticancer drugs.

Keywords: curcumin; DCA; amino acid; molecular hybridization; molecular docking; breast cancer

1. Introduction

Breast cancer (BC) is the second most common cancer in women, with an estimated 290,560 cases in 2022 and 43,780 deaths. BC is a complex biological disease that becomes lethal as it progresses, with limited options for curing it beyond the early stage of localized cancer. Like many other human cancers, BC results from significant alterations in genetic and epigenetic mechanisms and targeting multiple signaling pathways in growth and malignant progression towards incurable lethal disease [1]. Targeting a single-cell signaling pathway is unlikely to prevent or cure BC. Combination therapy (adjuvant therapy) is a current strategy for BC treatment and prevention of its progression [2]. The chemotherapeutic drugs for treating BCs, only target rapidly growing tumor cells but are less lethal to cancer stem cells [3]. However, these anticancer drugs inevitably produce severe, systemic toxicities in patients after chemotherapy. The emergence of resistance to drugs used in chemotherapy and rapid regrowth of tumors is another limitation of chemotherapy. Therefore, the development of novel small molecules that can be used as a

non-toxic adjuvant to chemotherapy is a promising strategy for prolonging the quality and longevity of BC patients.

Curcumin (CUR, **1**) (Figure 1), the spice turmeric's major ingredient, is well-documented for its anti-inflammatory and pro-apoptotic activities against many solid tumors [4,5]. However, CUR is ineffective as an anticancer agent because of its low bioavailability, even at high pharmacological doses [6]. Almost two decades of scientific work on CUR has minimal utility in treating human cancers. Several chemical approaches are utilized, such as optimizing the pharmacological formulations' nano-formulation [7], prodrugs [8], and molecular modifications [9] to increase the bioactivity and potency of CUR. Biological evaluation of the modified form of CUR has mainly been limited to in vitro testing and seldom for their bioavailability by multiple routes, such as oral, intravenous, and intraperitoneal administration [10].
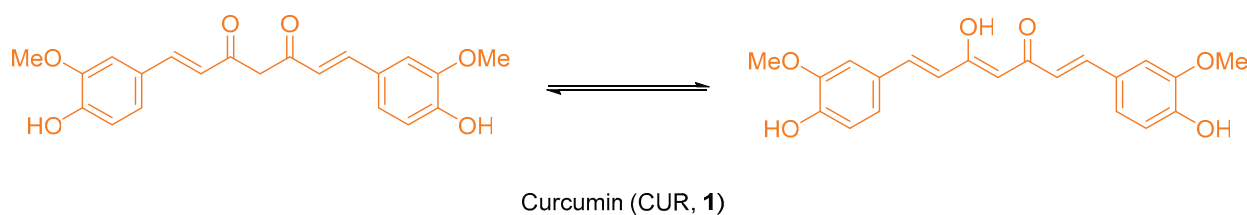
Curcumin (CUR, **1**)

Figure 1. Keto-enol tautomeric forms of curcumin (CUR).

Dichloroacetate (DCA) is another leading natural product against BC since 2007 [11]. DCA targets the pyruvate-led glycolytic pathway in cancer cells because of its structural similarities with pyruvate. DCA could trigger apoptosis of human BC cells, and this is very effective and shows the synergistic effect when used in combination with other drugs [12–15]. A recent report suggests that DCA treatment led to a significant increase in ROS production (up to 15-fold) in hypoxic cancer cells but not in aerobic cells [16]. However, its use in the treatment of BC has been absent as some studies showed unusual adverse toxicity [17].

Several CUR analogs and conjugates have been reported upon in the last decade for their anticancer properties [18,19]. Most of the CUR analogs and conjugates are studied for their anticancer properties against various cell lines [18–20]. However, very few reports on animal studies on synthesized compounds administered orally at a very high dose [21] or other routes [22,23]. We adopted a molecular hybridization approach to synthesize our proposed molecules (Figure 2). Our synthesized compounds overcome the barriers associated with CUR and DCA.
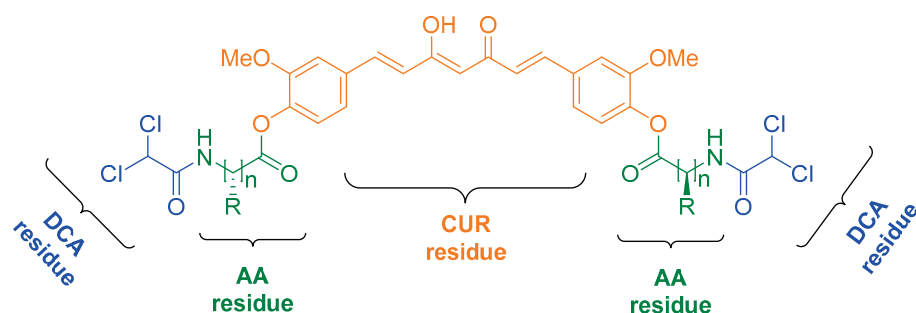
Figure 2. Target hybrid conjugates.

Among various rational drug design strategies, molecular hybridization (conjugation of two or more anticancer molecules via a covalent bond) is an effective and efficient tool for developing new drug candidates for BC. Furthermore, the molecular hybrids could also overcome drug resistance, lower the risk of drug–drug interactions, have cost-effective, synergistic effects, improve interactions with multiple pharmacological sites, and minimize redundant side effects [24–26]. Previously, we reported various conjugates with amino

acids (AAs) of enhanced lipophilic properties, which retain or increase the biological properties with respect to the parent molecule(s) [27]. To aid in the discovery of new drug developments, we have actively explored the molecular hybridization approach to synthesize hybrid conjugates using CUR, DCA, and AAs as building blocks.

In the present study, we have designed and synthesized a set of novel CUR–DCA conjugates with potential anticancer properties against BC using a conjugate chemistry approach employing amino acids as linkers. The well-characterized synthesized hybrid conjugates were screened against a human normal immortalized mammary epithelial cell line (MCF10A), human ER + BC cell line (T47D), and TNBC cell line (MB231) using MTT cell proliferation and colony formation assays. The most potent conjugate was further validated in the spontaneous mouse mammary tumor model (MMTV–PyMT–Tg).

2. Results and Discussion

For our present study, we tried several reaction conditions and coupling reagents to establish an optimized condition to prepare the desired set of CMC conjugates of CUR and DCA with an AA linker in pure form with chiral integrity. We successfully synthesized six CMC conjugates designed using the molecular hybridization approach (**CMC1–6**, Figure 1) and fully characterized by spectral studies.

To better understand the role of the amino acids as a linker, we have also prepared a conjugate of DCA and CUR (**CMC1**) without any linker. For the rest of the conjugates, we used glycine (**CMC2**). *L*-alanine (**CMC3**). β–alanine (**CMC4**). *L*-phenylalanine (**CMC5**) and γ–aminobutyric acid (**CMC6**). All purely synthesized conjugates were screened against BC cell lines, and the most potent ones (**CMC1** and **CMC2**) were further considered for animal studies. The toxicity study was also carried out against a human normal immortalized mammary epithelial cell line (MCF10A) and normal C57BL/6 mice. In addition, the molecular docking studies support the experimental observations.

2.1. Chemistry

The current study is focused on evaluating some CUR–DCA conjugates with and without an amino acid linker to correlate activity, structure, and bioavailability. To synthesize the CUR–DCA conjugates without any linker, DCA was activated by benzotriazole **3** using our previously reported method [28]. The benzotriazole activated DCA **4** treated with CUR in the presence of 4-(dimethylamino)pyridine (DMAP) in tetrahydrofuran (THF) under microwave irradiation. We also synthesized **CMC1** by using an alternative route where DCA was treated with CUR in the presence of *N*-(3-Dimethylaminopropyl)-*N*′-ethyl carbodiimide hydrochloride (EDAC) and DMAP in DCM to obtain the hybrid conjugate of DCA and CUR after recrystallizing with ethanol (Scheme 1). The reaction condition was optimized in our previous report [29]. We found that the alternative route for preparing **CMC1** was more efficient in yield and purity.
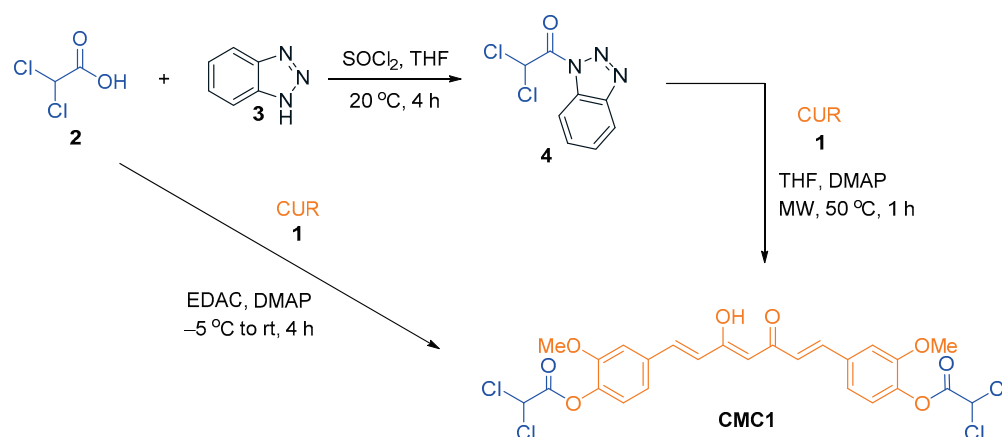
Scheme 1. Synthesis of DCA–curcumin conjugate **CMC1**.

To introduce amino acid as a linker in the conjugate, the benzotriazole activated DCA **4** was treated with amino acids in the presence of triethylamine (TEA) in aqueous acetonitrile at room temperature to form the DCA–amino acid conjugates **5a–e** [30]. Conjugates **5a–e** is further coupled with CUR **1** under optimized reaction conditions to yield the hybrid conjugates **CMC2–6** (Scheme 2).
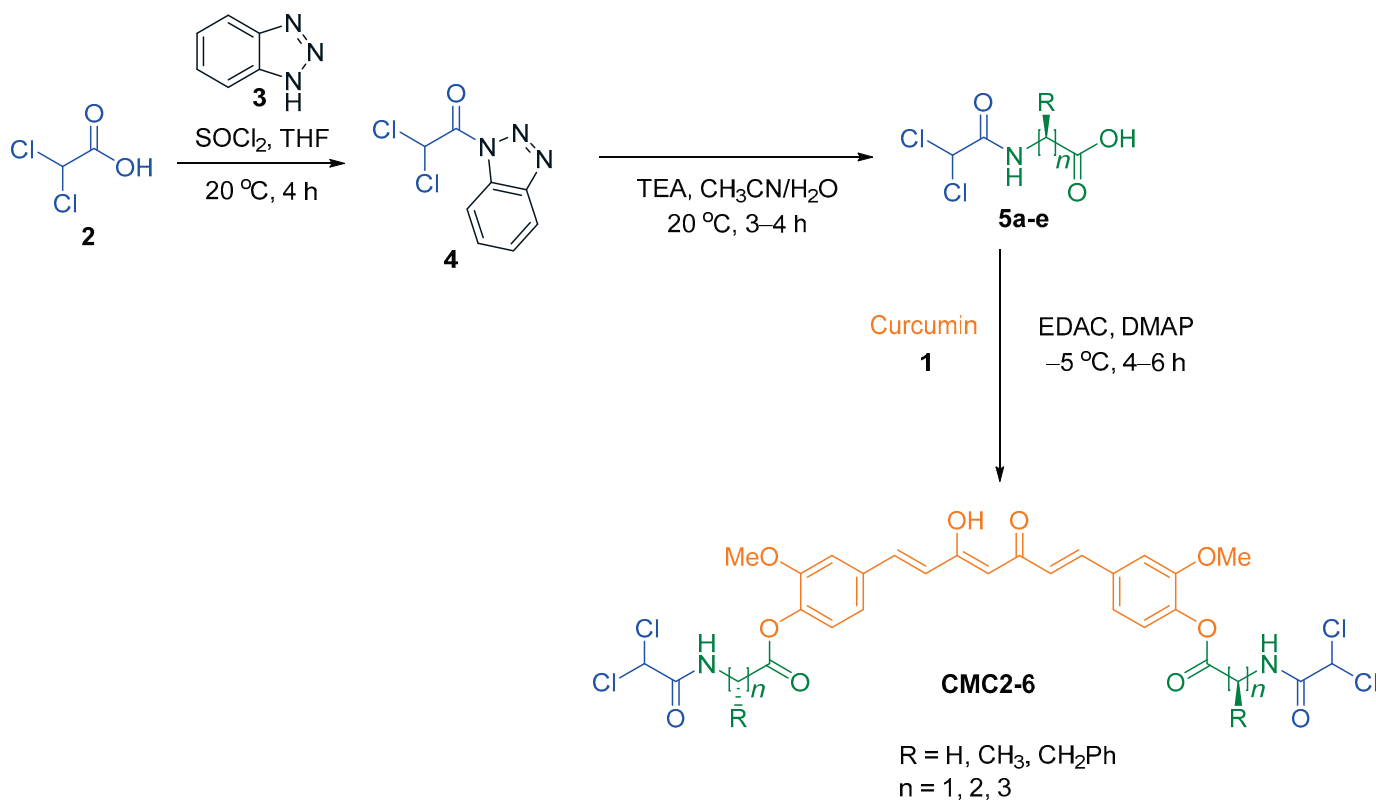
Scheme 2. Synthesis of DCA–curcumin conjugate with amino acid as linker **CMC2–6**.

We successfully synthesized the following six curcumin conjugates (Figure 3) in pure form, which were fully characterized by spectral studies.
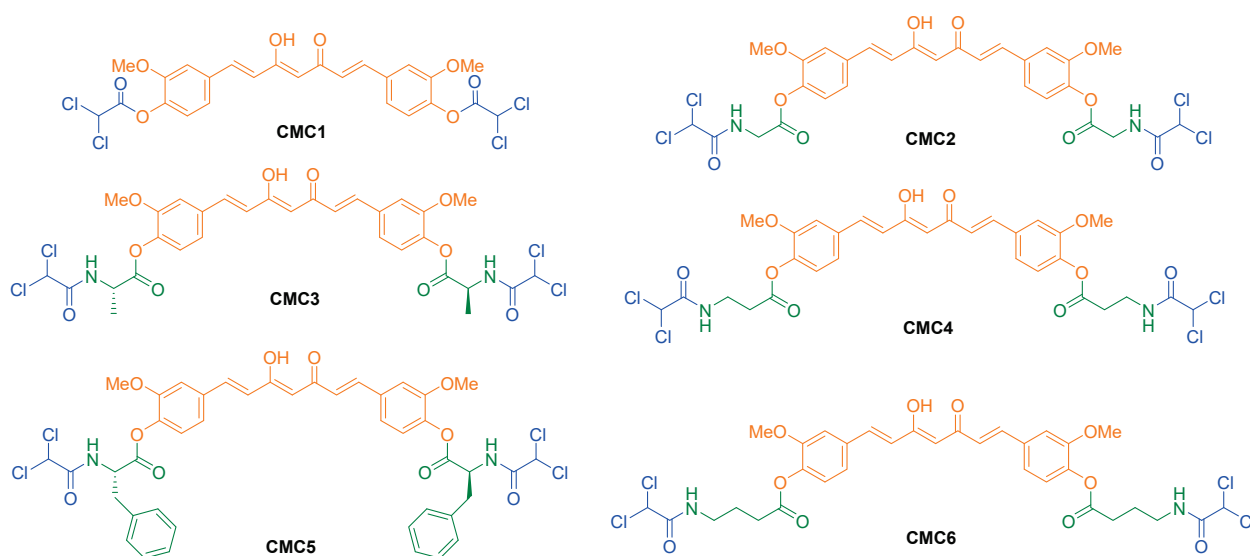
Figure 3. Structures of synthesized CUR and DCA hybrid conjugates **CMC1–6**.

2.2. Biology

We tested the antitumor potential of all six CMC conjugates (**CMC1–6**) in a human normal immortalized mammary epithelial cell line (MCF10A), human ER + BC cell line (T47D), and TNBC cell line (MB231) using MTT (3-(4,5-dimethylthiazol-2yl)-2,5-diphenyltetrazolium bromide) cell proliferation and colony formation assays, as described in our previous manuscripts [30,31]. Our results show that none of these CMC conjugates inhibited cell proliferation in human normal immortalized cell lines, but most of these CMC conjugates are effectively inhibited cell proliferation in both ER + BC and TNBC cell lines at a nanomolar concentration (Figure 4).
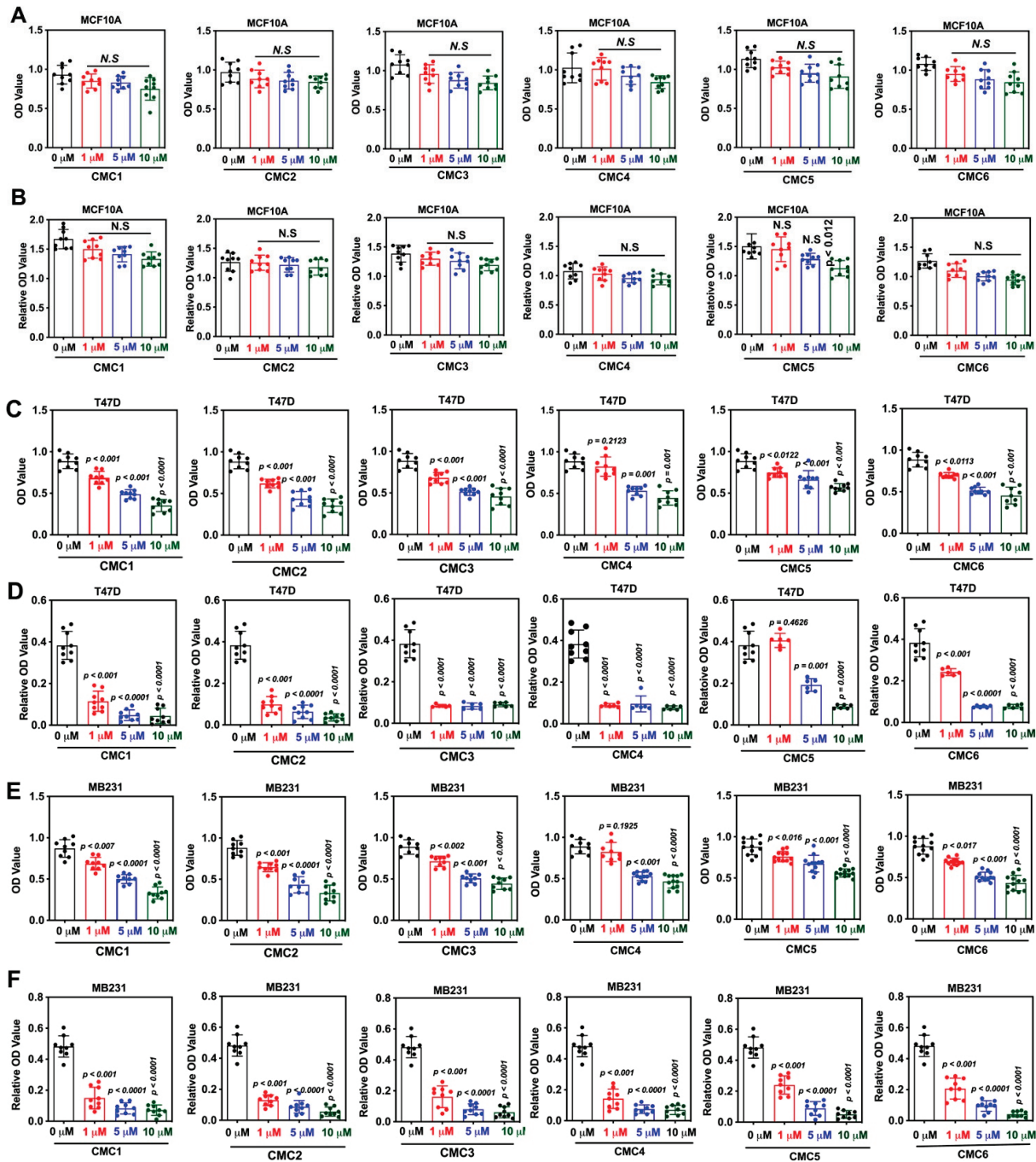
Figure 4. CMC conjugates inhibit human BC cell growth at submicromolar concentration. (**A,C,E**) MTT and (**B,D,F**) colony formation assays were carried out in MCF10A, T47D, and MB231 cells with **CMC1–6** at different concentrations (0, 1, 5, and 10 μM).

We also tested the antitumor potential of the parent CUR and DCA compounds in these cell lines (MCF10A, T47D, and MB231). However, CUR and DCA inhibited cell viability and colony formation in T47D and MB231 cells (Figure 5) but not in MCF10A cells. Based on these results, we calculated EC_{50} values for these conjugates and found that most of these compounds inhibited BC cell growth at submicromolar concentrations (Table 1). These observations provide a strong rationale to test the hypothesis that CMC conjugates would have high antitumor potential and, therefore, it is imperative to establish the antitumor potential of these compounds in BC growth and metastasis. Several curcumin analogs were synthesized and screened against various cancer cell lines according to the literature data. The reported data are all in the range of micromolar to molar concentration [21,23]. However, our synthesized conjugates showed potency at submicromolar concentrations. As shown in Table 1, all CMCs had very low activity against the normal breast epithelial cells, MCF10. The EC_{50} values of CMCs against MCF10A were about 8–16 times that against TNBC cell lines. These results show high tumor specificity.
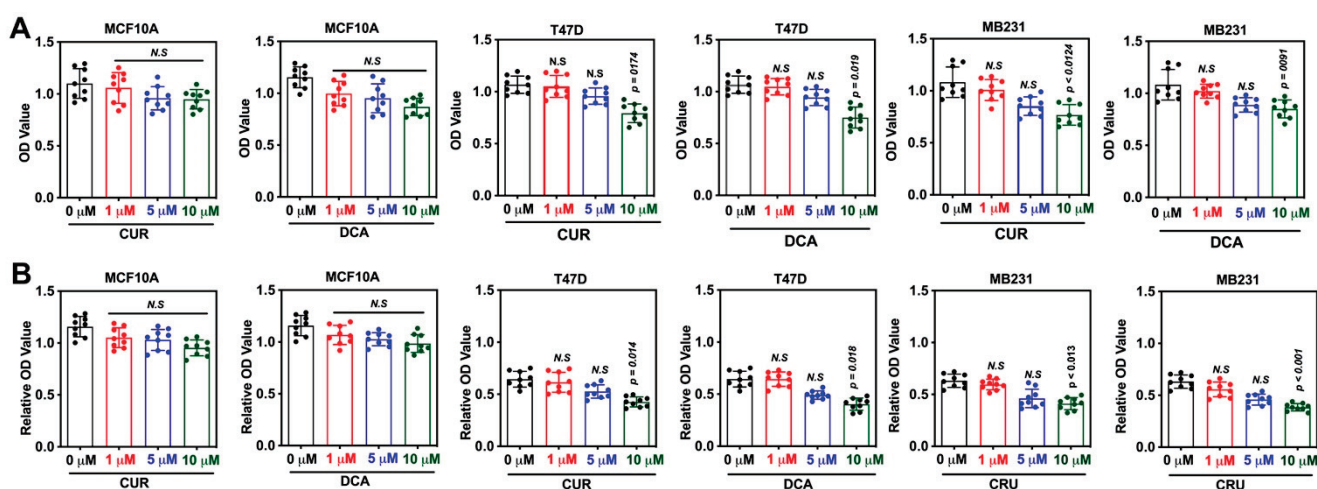
Figure 5. CUR and DCA inhibit cell viability and colony formation, to a lower extent, in human BC cells. (**A**) MTT, and (**B**) colony formation assays were carried out in MCF10A, T47D, and MB231 cells with CUR and DCA at different concentrations (0, 1, 5, and 10 μM).

Table 1. EC_{50} values for CMC compounds were determined by a clonogenic survival assay for two human BC cell lines.

Name of the Compound	EC50 for MCF10A	EC_{50} for T47D Cells	EC_{50} for MB231 Cells
CMC1	8.982 μM	1.648 μM	0.4240 μM
CMC2	9.675 μM	1.421 μM	0.7780 μM
CMC3	9.714 μM	1.595 μM	0.5179 μM
CMC4	8.859 μM	1.255 μM	1.1320 μM
CMC5	9.604 μM	1.245 μM	0.8375 μM
CMC6	9.474 μM	1.372 μM	0.9418 μM

2.3. Toxicity Studies

We tested whether the synthesized conjugates are free of toxicity and safer to use in human normal cells and animal models. We treated human normal immortalized cell line (MCF10A) and normal C57BL/6 mice at different concentrations and time points. We found that none of these conjugates (**CMC1-6**) inhibited cell viability, measured by MTT assay, in human normal immortalized cell lines (Figures 4 and 5). Similarly, treatment of normal C57BL/6 mice with two different concentrations (50 and 100 mg/kg body for 7 days) of

CMC1 and **CMC2** conjugates showed no changes in the body weight, morphology, kidney functions (serum creatinine and blood urea and nitrogen), and liver functions (ALT and AST) (Figure 6A–F). These observations clearly show that CMC conjugates are safer and free of toxicity.
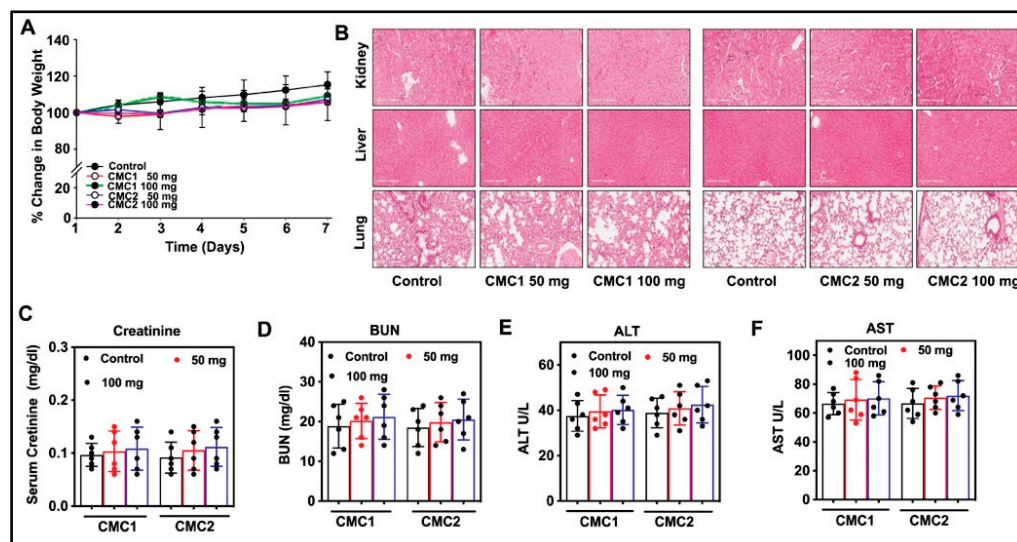
Figure 6. CMC conjugates are safer and do not show any contraindication. Normal C57BL/6 mice (*n* = 6) were treated with **CMC1** and **CMC2** at two different concentrations (50 and 100 mg/kg body) by oral gavage for 7 days. Bodyweight, (**A**) movement, hair loss, food, and water intake were monitored. At the end of the experimental period (7 days after the treatment), mice were euthanized, tissues (kidney, liver, and lung) were collected to monitor morphological changes by H&E staining. Representative images are shown at 20x magnification (**B**). Blood samples were collected to measure Creatinine (**C**), BUN (**D**), ALT (**E**), and AST (**F**) levels. Values are shown as the mean ± SD of 6 animals in each group.

2.4. Animal Studies

We chose and studied the antitumor potential of the most active CMC conjugates, **CMC2**, in a spontaneous mouse mammary tumor model (*MMTV–PyMT–Tg* mice). We chose *MMTV–PyMT–Tg* mouse mainly because the tumor formation and progression in this mouse is characterized by four different stages (hyperplasia, adenoma/mammary intra-epithelial neoplasia, early and late carcinoma) and also mimics human BC; the tumor develops first as ER-positive (ER$^+$) but ultimately becomes ER-negative BC (ER$^-$ BC) [31,32]. We randomly assigned 6-week-old *MMTV–PyMT–Tg* mice into two groups (6 mice in each); one control and one **CMC2** treated (10 mg/kg body, three times a week by oral gavage for 7 weeks). We measured the tumor volume twice a week. Tumor volume was calculated using the formula V = L × W^2/2, where L represents the largest tumor diameter, and W represents the smallest tumor diameter. Mice were euthanized after seven weeks of treatment, and tumor tissues were collected. The total tumor weight was measured. Tumor tissue sections were prepared and stained with Hematoxylin and Eosin (H&E) for morphometric analysis and Ki67 for cell proliferation analysis. As shown in Figure 6, **CMC2** treatment significantly reduced tumor growth without affecting the normal body weight and organ histology (Figure 7A,B) and tumor weight (Figure 7B). **CMC2** treatment significantly reduced tumor growth by inhibiting tumor cell proliferation in the mammary tumor tissue (Figure 7C,D) and lung tumor tissue (Figure 7F,G), reducing lung nodules (Figure 7E) with increased overall survival rate (Figure 7H).
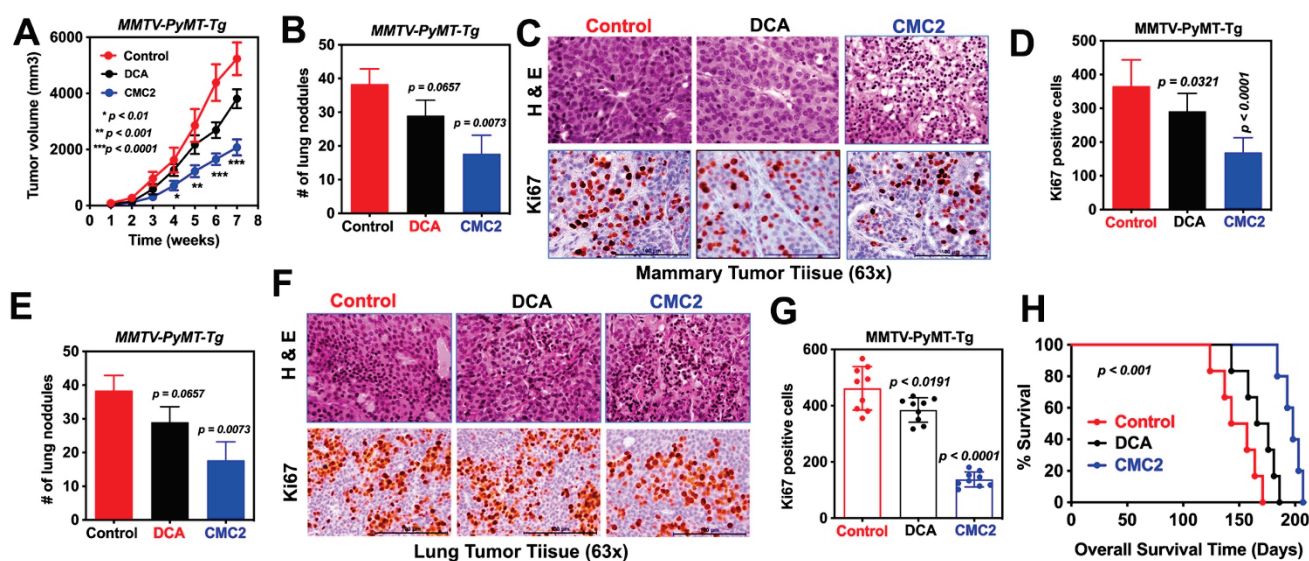
Figure 7. CMC2 treatment inhibits tumor growth in spontaneous mouse mammary tumor models. Six-week-old *MMTV–PyMT–Tg* mice were treated with DCA and **CMC2** (10 mg/kg body for 3× a week for 7 weeks. Control mice received PBS. (**A**) Tumor size was measured twice a week and tumor volume was calculated as described in our previous manuscript [31]. After seven weeks, mice were euthanized, tumor tissue was collected, and measured tumor weight (**B**). Tumor tissue sections were prepared and stained with H&E, and Ki67- and Ki67-positive cells were quantitated manually (**C**,**D**). Lung tissues were collected, visible lung nodules were manually counted (**E**). Lung tissue sections were prepared and stained with H&E and Ki67. The density of Ki67-positive cells per objective field was manually counted (**F**,**G**). Finally, we monitored the overall survival (**H**). Values are shown as mean ± SD of six mice in each group.

Overall, our studies provided evidence for the following three important observations: (**1**) CMC conjugates do not show any adverse side effects like kidney, liver, or lung toxicity. Therefore, these compounds are safe to use for clinical trials; (**2**) CMC conjugates show a potential antitumor activity in both luminal ER-positive (T47D cells) and basal triple-negative breast cancer (TNBC) cells by inhibiting cell growth and colony formation. (**3**) One of the CMC conjugates (**CMC2**) has a strong antitumor potential in vivo by inhibiting tumor growth in the GEM mouse model of BC (*MMTV–PyMT–Tg*), which mimics human BC [33,34].

2.5. Computational Studies

The experimental anticancer data was interesting and promising, which encouraged us to validate the experimental data by docking studies. According to a recent report, CUR inhibits 26S proteasome activity by directly inhibiting dual-specificity tyrosine-regulated kinase 2 (DYRK2) [35,36], and we deployed this target protein for our docking studies. The docking results interpret the most active conjugate of the six synthesized compounds to have a better docking score. Obtaining balanced pharmacokinetic (ADME—Absorption, Distribution, Metabolism, and Excretion) properties of drug-like molecules is one of the most difficult and challenging parts of the drug development process [37].
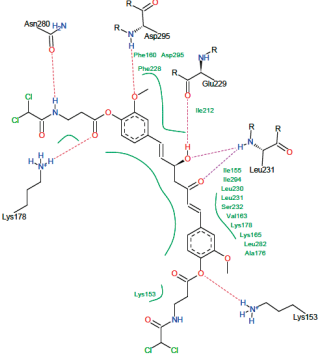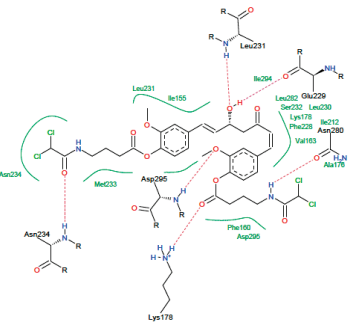
The execution of the molecular docking study is to identify whether CMC compounds modulate T47D and identify potential binding sites for a well-established ER- Breast cancer target (PDB ID:5ZTN). Prediction of binding sites was performed by a combinatorial analysis. Binding site prediction was made by conducting literature reviews on the DYRK2 target. Computational tools such as DoGSiteScorer and ScanProsite were used to predict the binding sites for the same. DoGSiteScorer reported a drug score of 81% having 41% non-polar, 28% polar, 18% of −ve, and 13% of +ve amino acids and including 225 interaction points within the binding pocket. Validation of binding sites was carried out by establishing

a comparative analysis of binding sites obtained from all three sources. Predicted binding sites for DYRK2 include Ile, Ala, Lys, Phe, Leu, and Asp involved in the key binding interactions (Table 2).

Table 2. Molecular docking and predicted ADME properties of CMC compounds.

Name	CMC Docking with DYRK2		dG kJ/mol	Score	L.E
CUR			−24	−29.24	0.22
CMC1			−27	−22.86	0.18
CMC2			−67	−33.02	0.35
CMC3			−21	−16.71	0.11

Table 2. *Cont.*

Name	CMC Docking with DYRK2	dG kJ/mol	Score	L.E
CMC4		−49	−25.09	0.25
CMC6		−58	−21.10	0.28

Molecular docking studies were carried out by FlexX4, which exploits incremental construction algorithms to predict dock scores. The significance of the docking score implies how comfortable the ligand is interacting with the protein. Prediction of binding affinity and ligand efficiency (L.E) were performed by the HYDE algorithm [38]. Chain A of protein was considered for docking study since the amino acid residues present in the binding site were associated with chain A. The top 100 poses of the solutions were generated by considering three different stereo modes of ligands such as E/Z, R/S, and pseudo-R/S. The binding of ligand to protein is driven by the enthalpy-entropy-based hybrid approach.

Even though CUR has a good docking score and comfortably binds to the pocket of the protein target, the compound is not stable while considering desolvation terms and torsional alerts. On the other hand, **CMC2** has acceptable docking scores along with free binding affinity in agreement with desolvation terms and torsional alerts. Docking analysis revealed the selectivity of interactions with key amino acids, surface characteristics, including the regulatory mechanism of the DYRK2. To better characterize and make decisions on drug-like derivatives, we carried out pharmacokinetic studies to predict a few ADME properties to understand the liability. **CMC2** showed optimally balanced properties of aqueous solubility (Sol), HERG liability (HERG II), developmental toxicity (Dev. Tox.), P-glycoprotein substrate/non-substrate (P-gp), and 2D6 isoform of P450 affinity data. The violation of drug-likeness, the Lipinski rule, including oral bioavailability, could be overcome by lead optimization methods to design derivatives within the applicability domain of potency and all pharmacokinetic properties. The predicted ADME data looks promising (Table 3). Even though the orally administered animal studies provided preliminary results, we will investigate the blood serum of the treated animal at different intervals of time to analyze the presence of our conjugate and or the hydrolyzed products and communicate in the future.

Table 3. Predicted ADME properties of CMC compounds.

Name	Log P	Aq. Sol (log mol/L)	HERG II Inhibitor	Dev Tox	CYP2D6 Substrate	P-gp Substrate	HIA %
CUR	3.852	−3.878	+	+	Med	-	84.38
CMC1	5.859	−4.644	-	-	Low	-	81.65
CMC2	4.092	−4.031	-	-	Low	+	66.25
CMC3	4.869	−4.010	-	-	Low	+	68.18
CMC4	4.872	−3.700	-	+	Low	+	61.82
CMC5	7.314	−2.981	+	+	Med	-	81.50
CMC6	5.65	−3.336	-	+	Med	+	67.89

In vitro studies confirmed the significant role of **CMC2** in eliciting anticancer activity. In silico studies conducted on synthesized hybrid conjugates reported the binding affinity, significant interactions as well as bioavailability of these novel compounds concerning curcumin. Out of six hybrid conjugates, **CMC2** exhibited a higher dock score, binding energy as well as ligand efficiency. The binding energy of curcumin was found to be −24 kJ/mol, ligand efficiency 0.22, and dock score of −29.24. However, **CMC2** exhibited a much higher range of these parameters, which indicates the likeliness of this compound to inhibit DYRK2. Even though the docking score of **CMC6** is considerably low, binding energy and ligand efficiency are comparable to **CMC2**. All conjugates showed significant interactions with DYRK2. The comparative analysis of binding interactions revealed the presence of H-bonds with two significant amino-acid residues, Leu231 and Asp295, in all the derivatives. The NH- group of Leu231 made H-bond interactions with the protein, while polar amino acid Asp295 contributes to making stronger interactions with the target protein by donating hydrogen atoms.

Bioavailability studies emphasize the significance of human intestinal absorption, affinity towards P450 isoform CYP2D6, developmental toxicity, hERG inhibition, and lipophilicity. Affinity toward the P450 isoform confirms the metabolic stability of compounds. A low/medium range of affinity is acceptable since higher affinity towards cytochrome P450 results in the decreased therapeutic value of lead-like compounds. This is due to the higher rate of conversion of compounds into metabolic end products before eliciting its therapeutic activity [39]. Developmental toxicity is highly undesirable since this could affect the entire homeostasis process. hERG is a gene encoding the alpha subunit of the potassium ion channel. Drug-induced inhibition of hERG results in the development of cardiac-related disorders [40]. Lipophilicity is an essential parameter depicting the permeability of lead-like molecules into biological membranes.

The curcumin reported for anticancer activity was found to inhibit hERG and possess developmental toxicity, which is not appreciable. However, the hybrid conjugate **CMC2** has the optimal balance for all the above-mentioned parameters. Hence, the potency of **CMC2** in executing anticancer activity is confirmed by in vitro and in silico approaches. **CMC3** got good bioavailability scores which are comparable to **CMC2**. All conjugates exhibited good intestinal absorption profiles, metabolic profiles, and lipophilicity. However, **CMC4**, **CMC5**, and **CMC6** were found to exhibit developmental toxicity, and **CMC5** was reported for hERG inhibition. Hence, future studies focusing on the optimization of these derivatives could bring the most promising lead molecules having anticancer activity.

3. Materials and Methods

Melting points were determined on a capillary tube melting point apparatus equipped with a digital thermometer. NMR spectra were recorded in DMSO-d6 on a Bruker NMR spectrometer operating at 500 MHz for 1H (with TMS as an internal standard) and 125 MHz for 13C. were performed on reverse phase gradient using Agilent (Santa Clara, CA, USA)

1200 series binary pump (G1312B), waters XTerra MS C18 (3.5 mm; 2.1–150 mm) þ Phenomenex C18 security guard column (2–4 mm) using 0.2% acetic acid in H2O/methanol as mobile phases; wavelength $\frac{1}{4}$ 254 nm; and mass spectrometry was done with 6220 Agilent (Santa Clara, CA, USA) TOF in electrospray ionization (ESI) mode with a positive and negative method in both Profile and Centroid mode. HPLC studies were done with 6120 Agilent (quadrupole LC/MS) [29].

3.1. Synthesis of CUR–DCA Hybrid Conjugate (CMC1)

A dried round bottom flask containing a small stir bar was charged with CUR (1.0 equivalent) and DCA (2.0 equivalent) dissolved in DCM (5 mL) along with EDAC (2.5 equivalent) and DMAP (0.5 equivalent). The reaction mixture was cooled down to −5 °C in an ice bath and continued stirring for 4 h. The progress of each mixture was monitored through thin layered chromatography (TLC), and upon completion, the DCM was evaporated under reduced pressure. The residues were treated with 10% saturated sodium carbonate, and the solid obtained was filtered and washed with water (50 mL) followed by 2N HCl (10 mL) and water (50 mL) to give the desired compounds. The products were recrystallized by aqueous ethanol to obtain in pure form.

((1E,3Z,6E)-3-Hydroxy-5-oxohepta-1,3,6-triene-1,7-diyl)bis(2-methoxy-4,1-phenylene) bis(2,2-dichloroacetate) (**CMC1**) (See Supplementary Material).

Light yellow amorphous, yield: 90%, m.p. 145–147 °C; ^{1}H NMR (DMSO-d$_6$) δ: 7.67 (d, *J* = 15.8 Hz, 2H), 7.59 (bs, 2H), 7.39 (d, *J* = 10.2 Hz, 2H), 7.28 (d, *J* = 8.2 Hz, 2H), 7.23 (s, 2H), 7.04 (d, *J* = 15.8 Hz, 2H), 6.21 (s, 1H), 3.87 (s, 6H). ^{13}C NMR (DMSO-d$_6$) δ: 183.1, 165.8, 162.7, 150.8, 139.8, 139.5, 134.8, 125.2, 122.6, 121.5, 112.5, 101.9, 65.8, 64.5, 56.3. HPLC (CHIRIBIOTIC T 15 cm × 4.6 mm in acetonitrile and water): 95.4%. HRMS *m/z* for C$_{25}$H$_{20}$Cl$_4$O$_8$ [M+H]$^+$ Calcd. 588.9945. Found: 588.9984.

3.2. General Method for Preparation of CUR–DCA Hybrid Conjugates with an AA Linker (CMC2–6)

A dried round-bottom flask containing a small stir bar was charged with CUR (1.0 equivalent) and the respective DCA-amino acid conjugates (2.0 equivalent) dissolved in DCM (5 mL) along with EDAC (2.5 equivalent) and DMAP (0.5 equivalent). The reaction mixture was cooled down to −5 °C in an ice bath and stirred for 4–6 h. The DCA-amino acid conjugates were synthesized following our previously reported method (CBDD). The progress of each mixture was monitored through thin layered chromatography (TLC), and upon completion, the DCM was evaporated under reduced pressure. The residues were treated with 10% saturated sodium carbonate, and the solid obtained was filtered and washed with water (50 mL) followed by 2N HCl (10 mL) and water (50 mL) to give the desired compounds. The products were recrystallized by aqueous ethanol to obtain their pure form.

((1E,3Z,6E)-3-Hydroxy-5-oxohepta-1,3,6-triene-1,7-diyl)bis(2-methoxy-4,1-phenylene) bis(2-(2,2-dichloroacetamido)acetate) (**CMC2**) (See Supplementary Material).

Bright yellow amorphous, yield: 92%, m.p. 167–16975 °C; ^{1}H NMR (DMSO-d$_6$) δ: 9.19 (bs, 2H), 7.65 (d, *J* = 15.8 Hz, 2H), 7.54 (bs, 2H), 7.34 (d, *J* = 8.4 Hz, 2H), 7.17 (d, *J* = 8.2 Hz, 2H), 7.00 (d, *J* = 15.8 Hz, 2H), 6.63 (s, 2H), 6.20 (s, 1H), 4.27 (d, *J* = 5.8 Hz, 4H), 3.85 (s, 6H). ^{13}C NMR (DMSO-d$_6$) δ: 183.2, 167.3, 164.3, 151.0, 139.8, 140.4, 139.7, 134.0, 129.7, 124.8, 123.1, 121.4, 112.3, 101.8, 66.3, 56.1, 41.1. HPLC (CHIRIBIOTIC T 15 cm × 4.6 mm in acetonitrile and water): 96.6%. HRMS *m/z* for C$_{29}$H$_{26}$Cl$_4$N$_2$O$_{10}$ [M+Na]$^+$ Calcd. 727.0342. Found: 727.0249.

((1E,3Z,6E)-3-Hydroxy-5-oxohepta-1,3,6-triene-1,7-diyl)bis(2-methoxy-4,1-phenylene) (2S,2′S)-bis(2-(2,2-dichloroacetamido)propanoate) (**CMC3**) (See Supplementary Material).

Yellow amorphous, yield: 89%, m.p. 92–93 °C; ^{1}H NMR (DMSO-d$_6$) δ: 9.24 (d, *J* = 6.6 Hz, 2H), 7.65 (d, *J* = 15.8 Hz, 2H), 7.54 (bs, 2H), 7.35 (d, *J* = 8.2 Hz, 2H), 7.15 (d, *J* = 8.0 Hz, 2H), 7.00 (d, *J* = 15.8 Hz, 2H), 6.52 (s, 2H), 6.21 (s, 1H), 4.63–4.57 (m, 2H), 3.85 (s, 6H), 1.52 (d, *J* = 7.0 Hz, 6H). ^{13}C NMR (DMSO-d$_6$) δ: 183.5, 170.3, 164.0, 151.5, 141.1, 140.2, 134.4, 125.2, 123.5, 121.9, 112.7, 102.2, 66.8, 56.6, 48.9, 17.2. HPLC (CHIRIBIOTIC T 15 cm × 4.6 mm in

acetonitrile and water): 98.6%. HRMS m/z for $C_{31}H_{30}Cl_4N_2O_{10}$ [M+H]$^+$ Calcd. 731.0655. Found: 731.0733.

((1E,3Z,6E)-3-Hydroxy-5-oxohepta-1,3,6-triene-1,7-diyl)bis(2-methoxy-4,1-phenylene) bis(3-(2,2-dichloroacetamido)propanoate) (**CMC4**) (See Supplementary Material).

Light yellow amorphous, yield: 93%, m.p. 140–142 °C; ^{1}H NMR (DMSO-d$_6$) δ: 8.79 (bs, 2H), 7.66 (d, J = 15.8 Hz, 2H), 7.52 (bs, 2H), 7.34 (bs, 2H), 7.18 (d, J = 6.3 Hz, 2H), 7.00 (d, J = 15.8 Hz, 2H), 6.51 (s, 2H), 6.20 (s, 1H), 3.85 (s, 6H), 3.49 (s, 4H), 2.82 (s, 4H). ^{13}C NMR (DMSO-d$_6$) δ: 183.7, 169.6, 164.3, 151.6, 141.2, 140.3, 134.3, 125.1, 123.8, 121.8, 112.5, 102.2, 67.2, 56.5, 36.0, 33.4. HPLC (CHIRIBIOTIC T 15 cm × 4.6 mm in acetonitrile and water): 95.6%. HRMS m/z for $C_{31}H_{30}Cl_4N_2O_{10}$ [M+H]$^+$ Calcd. 731.0655. Found: 731.0545.

((1E,3Z,6E)-3-Hydroxy-5-oxohepta-1,3,6-triene-1,7-diyl)bis(2-methoxy-4,1-phenylene) (2S,2′S)-bis(2-(2,2-dichloroacetamido)-3-phenylpropanoate) (**CMC5**) (See Supplementary Material).

Yellow amorphous, yield: 90%, m.p. 192–194–75 °C; ^{1}H NMR (DMSO-d$_6$) δ: 9.27 (d, J = 7.2 Hz, 2H), 7.66 (d, J = 15.8 Hz, 2H), 7.56 (bs, 2H), 7.35–7.25 (m, 11H), 7.12 (d, J = 7.8 Hz, 2H), 7.02 (d, J = 15.8 Hz, 2H), 6.50 (s, 2H), 6.21 (s, 1H), 4.63–4.57 (m, 2H), 3.85 (s, 6H), 1.52 (d, J = 7.0 Hz, 6H). ^{13}C NMR (DMSO-d$_6$) δ: 183.6, 169.1, 164.1, 151.5, 140.9, 140.2, 136.8, 134.5, 129.8, 128.8, 127.3, 125.3, 123.5, 121.9, 112.8, 102.3, 66.7, 56.6, 54.4, 36.6. HPLC (CHIRIBIOTIC T 15 cm × 4.6 mm in acetonitrile and water): 97.2%. HRMS m/z for $C_{43}H_{38}Cl_4N_2O_{10}$ [M+H]$^+$ Calcd. 883.1281. Found: 883.1318.

((1E,3Z,6E)-3-Hydroxy-5-oxohepta-1,3,6-triene-1,7-diyl)bis(2-methoxy-4,1-phenylene) bis(4-(2,2-dichloroacetamido)butanoate) (**CMC6**) (See Supplementary Material).

Bright yellow amorphous, yield: 96%, m.p. 130–132 °C; ^{1}H NMR (DMSO-d$_6$) δ: 8.68 (bs, 2H), 7.65 (d, J = 15.8 Hz, 2H), 7.52 (bs, 2H), 7.34 (d, J = 8.7 Hz, 2H), 7.17 (d, J = 8.2 Hz, 2H), 6.99 (d, J = 15.8 Hz, 2H), 6.46 (s, 2H), 6.20 (s, 1H), 3.84 (s, 6H), 3.27–3.30 (m, 4H), 2.61 (t, J = 7.5 Hz, 4H), 1.83 (t, J = 7.2 Hz, 4H). ^{13}C NMR (DMSO-d$_6$) δ: 183.2, 170.6, 163.7, 151.1, 140.9, 139.8, 133.7, 124.6, 123.3, 121.4, 112.1, 101.7, 66.9, 56.0, 38.5, 30.5, 24.0. HPLC (CHIRIBIOTIC T 15 cm × 4.6 mm in acetonitrile and water): 98.6%. HRMS m/z for $C_{33}H_{34}Cl_4N_2O_{10}$ [M+Na]$^+$ Calcd. 783.0968. Found: 783.0809.

3.3. MTT Assay

MCF10A, T47D, and MB231 cells (5 × 10^3) were seeded in 96-well plates and incubator at 37 °C with 5% CO$_2$ in MEGM, DMEM, and RPMI medium (100 μL), respectively. After 24 h, the medium was replaced with the CMC conjugates at different concentrations (0, 1, 5, and 10 μM) for 72 h. After 72 h, 10 μL MTT reagent was added to each well and incubated for 2 h for the formation of purple formazan and then added 100 μL detergent to dissociate the formazan precipitate and measured at 570 nm. Values are shown as mean ± SD of three experiments with 3 wells in each, a total of 9 repeats [28].

3.4. Colony Formation Assay

MCF10A, T47D, and MB231 cells (5 × 10^3) were seeded in 24-well plates, and cells were exposed to different CMC conjugates at different concentrations (0, 1, 5, and 10 μM) for 2 weeks, changing the medium for every 3 days with respective CMC conjugates at the indicated concentrations. After 2 weeks, cells were washed with PBS and fixed in 100% methanol for 30 min followed by staining with KaryoMax Giemsa stain for 1 h. The unfound dyes were removed by washing the wells with water and dried overnight at room temperature. Finally, cells were lysed with lysis buffer (1% SDS in 0.2 N NaOH) for 5 min, and the absorbance of the released dye was measured at 630 nm, as described before [28]. Values are shown as mean ± SD of three experiments with 3 wells in each, for a total of 9 repeats.

3.5. Institutional Compliance

The animal experiments reported in this study were approved by the Augusta University IACUC (protocol #2015-0737, approval date 30 July 2021) and Biosafety (protocol #1462, approval date 30 July 2021) Committees.

3.6. Cell Lines

The human non-transformed normal mammary epithelial cell line MCF10A was obtained from the American Type Culture Collection (ATCC). The estrogen receptor-positive breast cancer (ER + BC) cell line MCF7 and triple-negative breast cancer (TNBC) cell line MDA-MB231 (MB231) were obtained from ATCC. Cell lines from ATCC have been thoroughly tested and authenticated, and morphology, karyotyping, and PCR-based approaches were used to confirm the identity of the cell lines. The MCF10A cells were grown in MEGM complete medium; MCF7 cells were grown in DMEM medium with 10% FBS; MDA-MB-231 cells were grown in Leibovitz's L-15 medium with 10% FBS and 1% P/S. All these cell lines have been routinely tested for mycoplasma contamination using the Universal mycoplasma detection kit obtained from ATCC (Manassas, VA, USA), and the last mycoplasma test was performed in July 2021. Mycoplasma-free cell lines were used in all our experiments.

3.7. Animals

C57BL/6 (Stock #000664) and MMTV–PyMT–Tg (Stock #002374) mice were obtained from the Jackson laboratories. All these mice were bred and maintained in Augusta University Animal Facility by the guidelines of the Institutional Animal Care Use Committees. All euthanasia protocols were performed by the regulations and guidelines presented by IACUC and LAS of Augusta University.

Administration of CMC compounds to the mice: For toxicity studies, CMC1 and CMC2 conjugates at two different concentrations (50 and 100 mg/kg body) were given oral gavage daily for 7 days. At the end of the experiment, animals were euthanized, kidneys, liver, and lungs were analyzed for morphological changes. We also collected blood samples to measure Creatinine using a Creatinine assay kit (obtained from Millipore Sigma, Burlington, MA, USA, Catalog # MAK080), Alanine aminotransferase (ALT), using an ALT assay kit (obtained from the Millipore Sigma, Catalog #MAK053), Aspartate aminotransferase (AST), using an AST assay kit obtained from Millipore Sigma, Catalog #MAK055), and blood urea and nitrogen (BUN), using a urea nitrogen assay kit (obtained from ThermoFisher Scientific, Waltham, MA, USA, Catalog #EIABUN) as per the manufacturer's instruction.

Similarly, six-week-old MMTV–PyMT–Tg mice were grouped into two groups—one control and one CMC2 treatment. The control mice received PBS, and the CMC2-treated group received CMC2 conjugate (10 mg/kg body by oral gavage, three times a week) for 7 weeks. We monitored animal weight and measured the tumor volume twice a week. At the end of the experimental period, mice were euthanized, and tumor tissues were harvested and measured for tumor weight. Tumor tissues were processed to extract RNA and protein and fixed in 10% buffered formalin phosphate solution (obtained from Fisher Scientific, Catalog #SF100-4) for morphological analysis.

3.8. Statistical Analysis

Statistical analysis was done using one-way ANOVA followed by the Bonferroni multiple comparison test and also using Student's *t*-test with the two-tail distribution. The software used was Graph Pad Prism, version 8.0, San Diego, CA, USA. A value of $p < 0.05$ was considered statistically significant. GraphPad, Sigma Plot, and Excel programs were used to draw figures.

4. Conclusions

CUR–DCA hybrid conjugates **CMC1-6** were synthesized in good yields by an optimized facile reaction condition. Two of the synthesized conjugates (**CMC1** and **CMC2**)

exhibit enhanced anticancer properties against BC with reduced possible toxicity to human normal immortalized mammary epithelial cell line (MCF10A) and normal C57BL/6 mice. Animal studies suggest **CMC2** is a highly effective and safer therapeutic agent for BC. We believe the hybrid conjugates work as an effective prodrug of curcumin, and DCA provides a synergistic effect. The molecular docking and ADME studies support the drug candidacy of **CMC2** for BC. The potential conjugates need further investigation with different animal models to develop the pharmacokinetic profile to better understand the molecular mechanism and develop safer as well as efficient oral drug candidates for BC.

Supplementary Materials: The following are available online at https://www.mdpi.com/article/10.3390/ph15040451/s1, ^{1}H NMR and ^{13}C NMR of all the synthesized compounds.

Institutional Review Board Statement: The animal study protocol was approved by the Augusta University IACUC (protocol code #2015-0737 and date of approval 30 July 2021) and Biosafety Committees (protocol code #1462 and date of approval 30 July 2021).

Informed Consent Statement: Not applicable.

Data Availability Statement: Data is contained within the article and Supplementary Material.

Conflicts of Interest: The authors declare no conflict of interest.

References

1. Cai, F.-F.; Kohler, C.; Zhang, B.; Wang, M.-H.; Chen, W.-J.; Zhong, X.-Y. Epigenetic therapy for breast cancer. *Int. J. Mol. Sci.* **2011**, *12*, 4465–4476. [CrossRef] [PubMed]
2. Zanardi, E.; Bregni, G.; de Braud, F.; Di Cosimo, S. Better together: Targeted combination therapies in breast cancer. *Semin. Oncol.* **2015**, *42*, 887–895. [CrossRef] [PubMed]
3. Steinbrueck, A.; Sedgwick, A.C.; Brewster, J.T.; Yan, K.C.; Shang, Y.; Knoll, D.M.; Vargas-Zuniga, G.I.; He, X.P.; Tian, H.; Sessler, J.L. Transition metal chelators, pro-chelators, and ionophores as small molecule cancer chemotherapeutic agents. *Chem. Soc. Rev.* **2020**, *49*, 3726–3747. [CrossRef] [PubMed]
4. Liu, D.; Chen, Z. The effect of curcumin on breast cancer cells. *J. Breast Cancer* **2013**, *16*, 133–137. [CrossRef]
5. Banik, U.; Othman, N.H.; Parasuraman, S.; Adhikary, A.K. Curcumin: The spicy modulator of breast carcinogenesis. *J. Exp. Clin. Cancer Res.* **2017**, *36*, 98. [CrossRef]
6. Nelson, K.M.; Walters, M.A.; Dahlin, J.L.; Bisson, J.; Graham, J.; Pauli, G.F. The essential medicinal chemistry of curcumin. *J. Med. Chem.* **2017**, *60*, 1620–1637. [CrossRef]
7. Jamwal, R. Bioavailable curcumin formulations: A review of pharmacokinetic studies in healthy volunteers. *J. Integr. Med.* **2018**, *16*, 367–374. [CrossRef]
8. Bhuket, P.R.N.; El-Magboub, A.; Haworth, I.S.; Rojsitthisak, P. Enhancement of curcumin bioavailability via the prodrug approach: Challenges and prospects. *Eur. J. Drug Metab. Pharmacokinet.* **2017**, *42*, 341–353. [CrossRef]
9. Vyas, A.; Dandawate, P.; Padhye, S.; Ahmad, A.; Sarkar, F. Perspectives on new synthetic curcumin analogs and their potential anticancer properties. *Curr. Pharm. Des.* **2013**, *19*, 2047–2069.

10. Shen, L.; Liu, C.-C.; An, C.-Y.; Ji, H.-F. How does curcumin work with poor bioavailability? Clues from experimental and theoretical studies. *Sci. Rep.* **2016**, *6*, 20872. [CrossRef]

11. Bonnet, S.; Archer, S.L.; Allalunis-Turner, J.; Haromy, A.; Beaulieu, C.; Thompson, R.; Lee, C.T.; Lopaschuk, G.D.; Puttagunta, L. A mitochondria-K$^+$ channel axis is suppressed in cancer and its normalization promotes apoptosis and inhibits cancer growth. *Cancer Cell* **2007**, *11*, 37–51. [CrossRef] [PubMed]

12. Khan, A.; Andrews, D.; Blackburn, A.C. Long-Term stabilization of stage 4 colon cancer using sodium dichloroacetate therapy. *World J. Clin. Cases* **2016**, *4*, 336–343. [CrossRef] [PubMed]

13. Florio, R.; De Lellis, L.; Veschi, S.; Verginelli, F.; di Giacomo, V.; Gallorini, M.; Natale, A.; Amoroso, R.; Cataldi, A.; Cama, A. Effects of dichloroacetate as single agent or in combination with GW6471 and metformin in paraganglioma cells. *Sci. Rep.* **2018**, *8*, 13610. [CrossRef] [PubMed]

14. Parczyk, J.; Ruhnau, J.; Pelz, C.; Schilling, M.; Wu, H.; Piaskowski, N.N.; Eickholt, B.; Kühn, H.; Danker, K.; Klein, A. Dichloroacetate and PX-478 exhibit strong synergistic effects in a various number of cancer cell lines. *BMC Cancer* **2021**, *21*, 481. [CrossRef] [PubMed]

15. Tataranni, T.; Piccoli, C. Dichloroacetate (DCA) and Cancer: An Overview towards Clinical Applications. *Oxid. Med. Cell. Longev.* **2019**, *2019*, 8201079. [CrossRef]

16. Mey, S.D.; Dufait, I.; Jiang, H.; Corbet, C.; Wang, H.; Gucht, M.V.D.; Kerkhove, L.; Law, K.L.; Vandenplas, H.; Gevaert, T.; et al. Dichloroacetate radiosensitizes hypoxic breast cancer cells. *Int. J. Mol. Sci.* **2020**, *21*, 9367. [CrossRef]

17. Stacpoole, P.W.; Martyniuk, C.J.; James, M.O.; Calcutt, N.A. Dichloroacetate-induced peripheral neuropathy. *Int. Rev. Neurobiol.* **2019**, *145*, 211–238.

18. Tomeh, M.A.; Hadianamrei, R.; Zhao, X. A Review of Curcumin and Its Derivatives as Anticancer Agents. *Int. J. Mol. Sci.* **2019**, *20*, 1033. [CrossRef]

19. Agrawal, D.K.; Mishra, P.K. Curcumin and Its Analogues: Potential Anticancer Agents. *Med. Res. Rev.* **2010**, *30*, 818–860. [CrossRef]

20. Lin, L.; Shi, Q.; Nyarko, A.K.; Bastow, K.F.; Wu, C.-C.; Su, C.-Y.; Shih, C.C.-Y.; Lee, K.-H. Antitumor Agents. 250. Design and Synthesis of New Curcumin Analogues as Potential Anti-Prostate Cancer Agents. *J. Med. Chem.* **2006**, *49*, 3963–3972. [CrossRef]

21. Lee, D.-Y.; Hou, Y.-C.; Yang, J.S.; Lin, H.-Y.; Chang, T.-Y.; Lee, K.-H.; Kuo, S.-C.; Hsieh, M.-T. Synthesis, Anticancer Activity, and Preliminary Pharmacokinetic Evaluation of 4,4-Disubstituted Curcuminoid 2,2-bis(Hydroxymethyl)Propionate Derivatives. *Molecules* **2020**, *25*, 479. [CrossRef] [PubMed]

22. Ozawa-Umeta, H.; Kishimoto, A.; Imaizumi, A.; Hashimoto, T.; Asakura, T.; Kakeya, H.; Kanai, M. Curcumin β-D-glucuronide exhibits anti–tumor effects on oxaliplatin-resistant colon cancer with less toxicity in vivo. *Cancer Sci.* **2020**, *111*, 1785–1793. [CrossRef] [PubMed]

23. Hackler, L., Jr.; Ozsvari, B.; Gyuris, M.; Sipos, P.; Fabian, G.; Molnar, E.; Marton, A.; Farago, N.; Mihaly, J.; Nagy, L.I.; et al. The Curcumin Analog C-150, Influencing NF-κB, UPR and Akt/Notch Pathways Has Potent Anticancer Activity In Vitro and In Vivo. *PLoS ONE* **2016**, *11*, e0149832. [CrossRef] [PubMed]

24. Meunier, B. Hybrid molecules with a dual mode of action: Dream or reality? *Acc. Chem. Res.* **2008**, *41*, 69–77. [CrossRef]

25. Tangutur, A.D.; Kumar, D.; Krishna, V.; Kantevari, S. Microtubule targeting agents as cancer chemotherapeutics: An overview of molecular hybrids as stabilizing and destabilizing agents. *Curr. Top. Med. Chem.* **2017**, *17*, 2523–2537. [CrossRef]

26. Gontijo, V.S.; Viegas, F.P.D.; Ortiz, C.J.C.; Silva, M.F.; Damasio, C.M.; Rosa, M.C.; Campos, T.G.; Couto, D.S.; Dias, K.S.T.; Viegas, C. Molecular hybridization as a tool in the design of multi-target directed drug candidates for neurodegenerative diseases. *Curr. Neuropharmacol.* **2020**, *18*, 348–407. [CrossRef]

27. Ibrahim, M.A.; Panda, S.S.; Birs, A.S.; Serrano, J.C.; Gonzalez, C.F.; Alamry, K.A.; Katritzky, A.R. Synthesis and antibacterial evaluation of amino acid-antibiotic conjugates. *Bioorg. Med. Chem. Lett.* **2014**, *24*, 1856–1861. [CrossRef]

28. Panda, S.S.; Hall, C.D.; Scriven, E.; Katritzky, A.R. Aminoacyl Benzotriazolides: Versatile Reagents for the Preparation of Peptides, their Mimetics, and Conjugates. *Aldrichim. Acta* **2013**, *46*, 43–55.

29. Panda, S.S.; Girgis, A.S.; Thomas, S.J.; Capito, J.E.; George, R.F.; Salman, A.; El-Manawaty, M.A.; Samir, A. Synthesis, pharmacological profile, and 2D-QSAR studies of curcumin-amino acid conjugates as potential drug candidates. *Eur. J. Med. Chem.* **2020**, *196*, 112293. [CrossRef]

30. Seliem, I.A.; Panda, S.S.; Girgis, A.S.; Nagy, Y.I.; George, R.F.; Fayad, W.; Fawzy, N.G.; Ibrahim, T.S.; Al-Mahmoudy, A.M.M.; Sakhuja, R.; et al. Design, synthesis, antimicrobial, and DNA gyrase inhibitory properties of fluoroquinolone–dichloroacetic acid hybrids. *Chem. Biol. Drug Des.* **2020**, *95*, 248–259. [CrossRef]

31. Thangaraju, M.; Gopal, E.; Martin, P.M.; Ananth, S.; Smith, S.B.; Prasad, P.D.; Sterneck, E.; Ganapathy, V. SLC5A8 triggers tumor cell apoptosis through pyruvate-dependent inhibition of histone deacetylases. *Cancer Res.* **2006**, *66*, 11560–11564. [CrossRef]

32. Bridges, A.E.; Ramachandran, S.; Pathania, R.; Parwal, U.; Lester, A.; Rajpurohit, P.; Morera, D.S.; Patel, N.; Singh, N.; Korkaya, H.; et al. RAD51AP1 Deficiency reduces tumor growth by targeting stem cell self-renewal. *Cancer Res.* **2020**, *80*, 3855–3866. [CrossRef] [PubMed]

33. Maglione, J.E.; Moghanaki, D.; Young, L.J.; Manner, C.K.; Ellies, L.G.; Joseph, S.O.; Nicholson, B.; Cardiff, R.D.; MacLeod, C.L. Transgenic Polyoma middle-T mice model premalignant mammary disease. *Cancer Res.* **2001**, *61*, 8298–8305. [PubMed]

34. Lin, E.Y.; Jones, J.G.; Li, P.; Zhu, L.; Whitney, K.D.; Muller, W.J.; Pollard, J.W. Progression to malignancy in the polyoma middle T oncoprotein mouse breast cancer model provides a reliable model for human diseases. *Am. J. Pathol.* **2003**, *163*, 2123–2126. [CrossRef]
35. Banerjee, S.; Ji, C.; Mayfield, J.E.; Goel, A.; Xiao, J.; Dixon, J.E.; Guo, X. Ancient drug curcumin impedes 26S proteasome activity by direct inhibition of dual-specificity tyrosine-regulated kinase 2. *Proc. Natl. Acad. Sci. USA* **2018**, *115*, 8155–8160. [CrossRef]
36. Tandon, V.; de la Vega, L.; Banerjee, S. Emerging roles of DYRK2 in cancer. *J. Biol. Chem.* **2021**, *296*, 100233. [CrossRef]
37. Di, L.; Kerns, E.H.; Carter, G.T. Drug-Like property concepts in pharmaceutical design. *Curr. Pharm. Des.* **2009**, *15*, 2184–2194. [CrossRef]
38. Leeson, P.D.; Bento, P.; Gaulton, A.; Hersey, A.; Manners, E.J.; Radoux, C.J.; Leach, A.R. Target-Based evaluation of "Drug-Like" properties and ligand efficiencies. *J. Med. Chem.* **2021**, *64*, 7210–7230. [CrossRef]
39. Zhang, Z.; Tang, W. Drug metabolism in drug discovery and development. *Acta Pharm. Sin. B* **2008**, *8*, 721–732. [CrossRef]
40. Priest, B.; Bell, I.M.; Garcia, M. Channels Role of hERG potassium channel assays in drug development. *Channels* **2008**, *2*, 87–93. [CrossRef]

Article

In Vitro and In Vivo Effects of Ulvan Polysaccharides from *Ulva rigida*

Jorge García-Márquez [1], Bruna Rodrigues Moreira [2], Piedad Valverde-Guillén [3], Sofía Latorre-Redoli [3], Candela T. Caneda-Santiago [3], Gabriel Acién [4], Eduardo Martínez-Manzanares [1,5], Manuel Marí-Beffa [3,6] and Roberto T. Abdala-Díaz [7,*]

[1] Department of Microbiology, Faculty of Science, Andalusian Institute of Blue Biotechnology and Development (IBYDA), Malaga University, Campus Universitario de Teatinos s/n, 29071 Malaga, Spain

[2] Phycology Laboratory, Department of Botany, Biological Sciences Center, Federal University of Santa Catarina, Florianópolis 88040-900, SC, Brazil

[3] Department of Cell Biology, Genetics and Physiology, Faculty of Science, Andalusian Institute of Blue Biotechnology and Development (IBYDA), Malaga University, Campus Universitario de Teatinos s/n, 29071 Malaga, Spain

[4] Department of Chemical Engineering, Almería University, 04120 Almería, Spain; facien@ual.es

[5] Instituto de Investigación Biomédica de Málaga-IBIMA, Hospital Universitario Virgen de la Victoria, Universidad de Málaga, 29071 Málaga, Spain

[6] Networking Biomedical Research Centre in Bioengineering, Biomaterials and Nanomedicine (CIBER-BBN), Málaga Biomedical Research Institute and Nanomedicine Platform (IBIMA BIONAND Platform), 29071 Málaga, Spain

[7] Department of Ecology and Geology, Faculty of Science, Andalusian Institute of Blue Biotechnology and Development (IBYDA), Malaga University, Campus Universitario de Teatinos s/n, 29071 Malaga, Spain

* Correspondence: abdala@uma.es; Tel.: +34-952136652

Abstract: One of the main bioactive compounds of interest from the *Ulva* species is the sulfated polysaccharide ulvan, which has recently attracted attention for its anticancer properties. This study investigated the cytotoxic activity of ulvan polysaccharides obtained from *Ulva rigida* in the following scenarios: (i) in vitro against healthy and carcinogenic cell lines (1064sk (human fibroblasts), HACAT (immortalized human keratinocytes), U-937 (a human leukemia cell line), G-361 (a human malignant melanoma), and HCT-116 (a colon cancer cell line)) and (ii) in vivo against zebrafish embryos. Ulvan exhibited cytotoxic effects on the three human cancer cell lines tested. However, only HCT-116 demonstrated sufficient sensitivity to this ulvan to make it relevant as a potential anticancer treatment, presenting an LC_{50} of 0.1 mg mL^{-1}. The in vivo assay on the zebrafish embryos showed a linear relationship between the polysaccharide concentration and growth retardation at 7.8 hpf mL mg^{-1}, with an LC_{50} of about 5.2 mg mL^{-1} at 48 hpf. At concentrations near the LC_{50}, toxic effects, such as pericardial edema or chorion lysis, could be found in the experimental larvae. Our in vitro study supports the potential use of polysaccharides extracted from *U. rigida* as candidates for treating human colon cancer. However, the in vivo assay on zebrafish indicated that the potential use of ulvan as a promising, safe compound should be limited to specific concentrations below 0.001 mg mL^{-1} since it revealed side effects on the embryonic growth rate and osmolar balance.

Keywords: cytotoxic activity; human cancer cell lines; polysaccharides; *Ulva rigida*; ulvan; zebrafish embryo toxicity test

1. Introduction

According to the World Health Organization, cancer was the second leading cause of death globally in 2020 [1]. Breast cancer is the most prevalent cancer worldwide, whereas colorectal cancer, leukemia, and skin melanoma rank third, thirteenth, and seventeenth amongst the main forms of cancer, according to the Global Cancer Observatory (GCO) of the International Agency for Research on Cancer (IARC) (gco.iarc.fr). The frequency

of this disease is expected to rise to more than 30 million people by 2040, a 56% increase from 2020 (gco.iarc.fr). Effective therapy strategies remain limited even though significant breakthroughs have been made in understanding the different pathways that drive the emergence of cancer. These strategies entail a combination of therapies, such as chemotherapies, which use various chemicals to target malignant and healthy cells [2,3]. Despite promising improvements in targeted therapeutics [4,5], their efficiency is restricted in some situations due to drug resistance [6,7].

Natural product research has emerged as a serious alternative for finding new bioactive compounds, with seaweed being one of the most promising sources of therapeutic candidates due to the vast richness of the marine environment [8]. Seaweeds, which live in harsh environmental and ecological circumstances, have been used for various purposes, including feed, food, and biotechnological applications [9]. This is due to their bioactive and nutritious compounds, which make them a valuable resource [10,11]. Green macroalgae species of *Ulva* are distributed around the world and are capable of occupying diverse habitats because of their tolerance to determinant factors, such as light, temperature, and salinity [12]. They present high growth rates and productivity under very variable conditions, having highly exploitable biochemical profiles [13], including bioactive metabolites that are of interest with regard to many economic applications, such as food, feed, fertilizers, and biomedicine [14].

One of the main bioactive compounds present in *Ulva* species is the sulfated polysaccharide ulvan. The ulvan complex structure varies according to the algae species, the growing location and conditions, and the extraction procedures [15]. Ulvans constitute between 8 and 29 % of the dry weight depending on the *Ulva* species and growing conditions [16]. These complex sulfated polysaccharides are interesting in terms of biomedical applications due to their antioxidant, antitumor, anticoagulant, antiviral, anti-inflammatory, and immune-modulator properties [17–20]. Recent attention has been given to the anticancer properties that ulvans possess because ulvans obtained from different *Ulva* species have demonstrated significant cytotoxic activity against hepatocellular carcinoma (HepG2), human breast cancer (MCF7), human colon carcinoma (HCT-116), and cervical cancer (HeLa) cells [21–24]. Their anticancer activity seems to operate via different pathways, including promoting cancer cell apoptosis, reducing cancer cell proliferation, and stimulating the innate immune response [14]. Furthermore, the pathways affected depend on the source and/or structure of the ulvans [15]. Therefore, specific research should be conducted on each *Ulva* species and cancer cell line.

Polysaccharide extracts have also been tested on living organisms, for example, on zebrafish embryos, in the so-called zebrafish embryo toxicity test (ZFET) [25]. Zebrafish have become an alternative model to rodent toxicity in in vivo assays [26–28]. This model provides important features, namely, rapid external embryonic development, a small size, optical transparency, a large number of offspring, and genetic similarities to humans [29,30]. Furthermore, zebrafish have been reported to have functional homologs for more than 90 of the 450 human genetic dysplasias [31].

Several interesting tests that use these embryos have also been proposed, such as rapid, high-throughput, cost-effective drug and chemical screening tests [29,32–35]. Zebrafish embryos have already been used to test for beneficial fungicidal [36], antioxidant [37–41], anti-inflammatory [40,42–46], immunomodulatory [47–50], genoprotective [51], hepatoprotective [52], disease-resistant [49], and antitumor activities [53]. Conversely, these tests have been employed to show the detrimental toxic effects of drugs and chemicals [25,54–57] leading to limitations in their potential clinical or veterinary use. Among these studies, several works specifically analyzed the effects of algal polysaccharides on zebrafish embryos [39,43,44,58].

In this study, we obtained ulvan polysaccharides from the green macroalga *Ulva rigida*. The in vitro antitumor activity of the ulvans was evaluated with MTT assays using healthy cell lines (1064sk (human fibroblasts) and HACAT (immortalized human keratinocytes)) and carcinogenic cell lines (U-937 (a human leukemia cell line), G-361 (a human malignant

melanoma), and HCT-116 (a colon cancer cell line)). In addition, the cytotoxic activity of the ulvans was evaluated using a zebrafish embryo toxicity test (ZFET) [25].

2. Results

2.1. Ulvan Composition and Structure

2.1.1. Fourier-Transform Infrared Spectroscopy (FTIR)

FTIR spectroscopy of the ulvans from *U. rigida* showed the presence of several functional groups (Figure 1). The strong broad absorption band centered at about 3402 cm^{-1} corresponds to the hydroxyl group (OH) stretching vibration. The weak absorption at 2938 cm^{-1} was due to the stretching vibration of C–H. Two other bands were observed between 1650 and 1430 cm^{-1}, characteristic of the carboxylate groups of uronic acids in the ulvan. The strong absorption at 1640 cm^{-1} was ascribed to the asymmetric stretching mode of the COO– group, and weaker absorption around 1438 cm^{-1} arose from the symmetric COO– stretching mode. The most important absorptions were those revealed at approximately 1260 cm^{-1} and 1056 cm^{-1}, considered the fingerprint region for ulvan [59]. A moderate absorption at the 1200 cm^{-1} wavelength is characteristic of the stretching vibration of the polysaccharide's sulfate ester (S=O), referring to the C–O stretching of the two principal sugars, namely, rhamnose and uronic acid. The absorption peaks at about 850 cm^{-1} correspond to the C–O–S bending vibration of sulfate in the axial position.
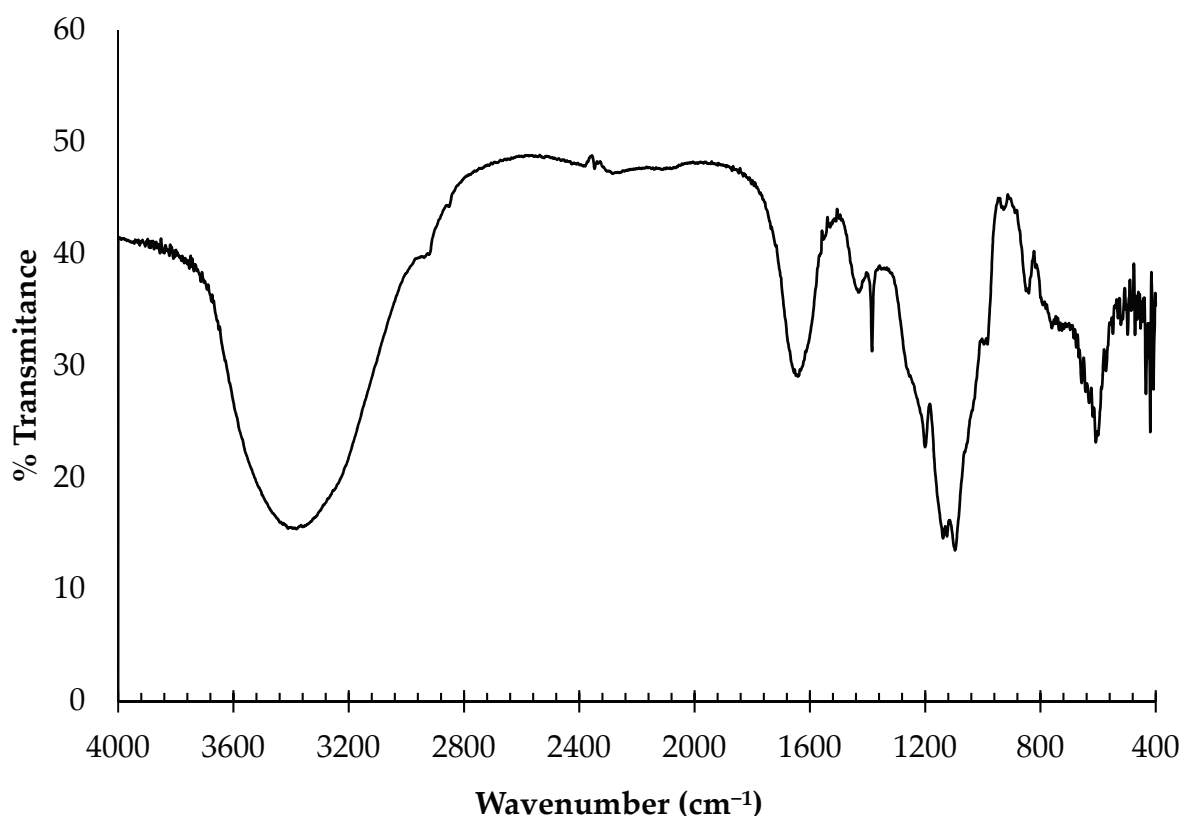
Figure 1. FTIR spectroscopy of ulvans from *U. rigida*.

2.1.2. Gas Chromatography–Mass Spectrometry (GC–MS)

In the GC–MS spectrum of the ulvans from *U. rigida*, the highest peak corresponds to rhamnose, followed by glucuronic acid and xylose (Figure 2). The rhamnose, glucuronic acid, and xylose percentages were 80.60%, 9.14%, and 4.01%, respectively (Table 1). Other monosaccharides, namely, glucose and galactose, were also detected (3.78% and 2.48%, respectively).
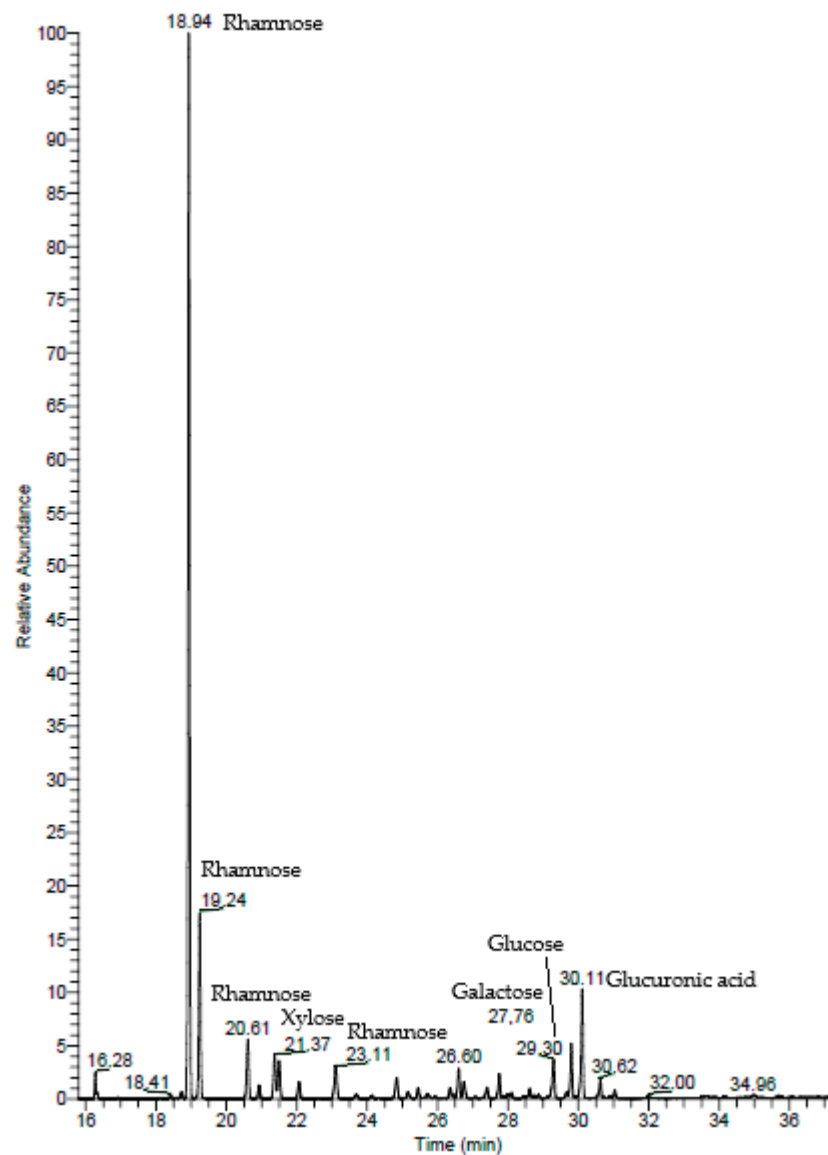
Figure 2. Gas chromatography–mass spectrometry (GC–MS) of ulvans from *U. rigida*.

Table 1. Percentage of monosaccharides for ulvans extracted from *U. rigida*.

Monosaccharide	%
Rhamnose	80.60
Glucuronic acid	9.14
Xylose	4.01
Glucose	3.78
Galactose	2.48

2.2. Cytotoxic Activity of Ulvan Polysaccharides

The cytotoxic activities of the ulvans at different concentrations (ranging from 0.009 to 5 mg mL^{-1}) against the healthy and carcinogenic cell lines are presented in Figure 3. With regard to the cytotoxicity against the healthy cells, a lower cytotoxic effect was observed in the keratinocyte (HACAT) cells, presenting an IC$_{50}$ value of 4.2 $\pm$ 0.5 mg mL^{-1}, than in the fibroblast (1064sK) cells, which exhibited an IC$_{50}$ of 1.2 $\pm$ 0.1 mg mL^{-1} (Figure 3a,b). For the carcinogenic cells, the IC$_{50}$ values were estimated for the colon (HCT-116), leukemia (U-937), and melanoma (G-361) cells as being 0.1 $\pm$ 0.02, 2.4 $\pm$ 0.4, and 4.3 $\pm$ 1.2 mg mL^{-1}, respectively (Figure 3c–e).
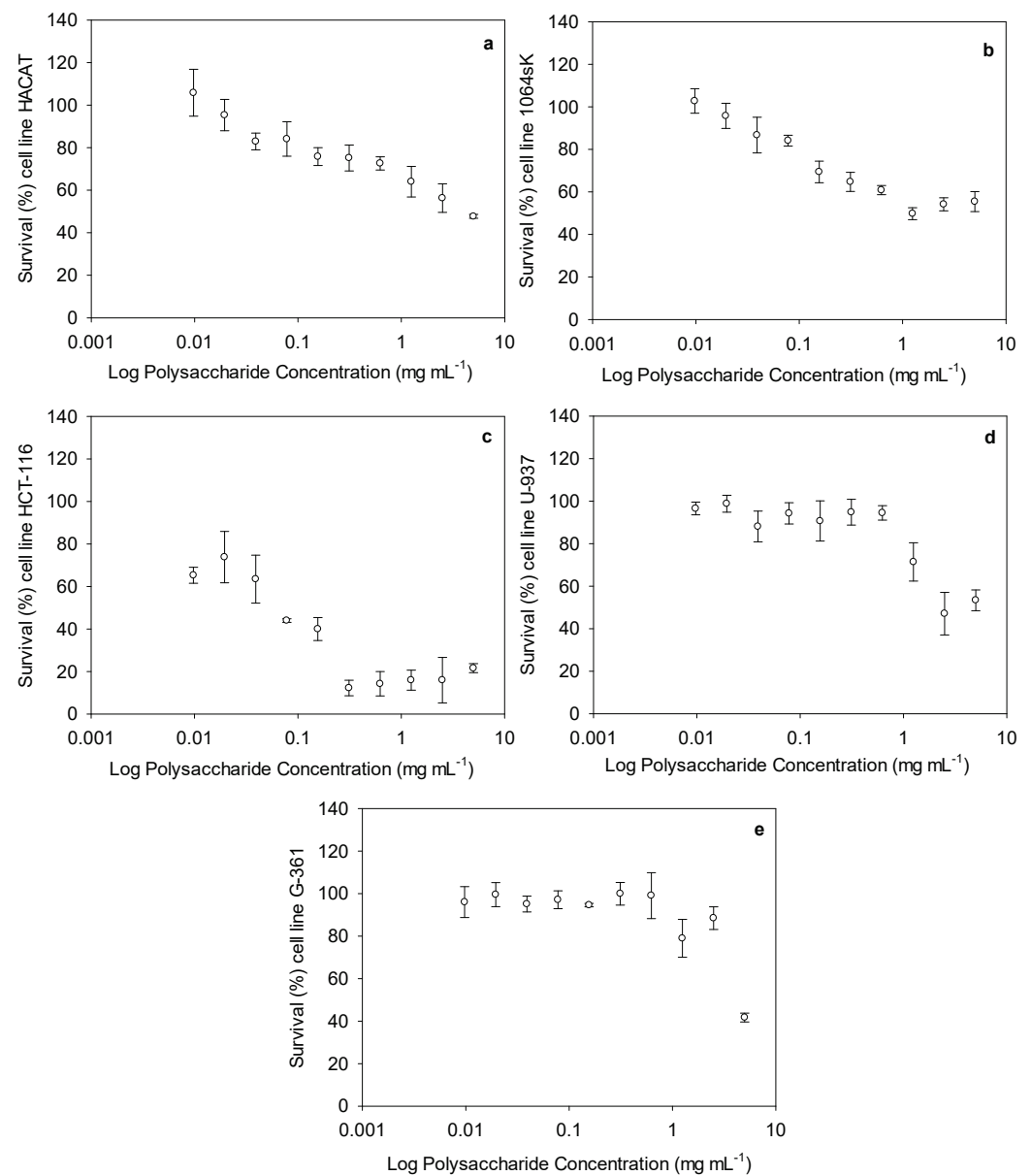
Figure 3. Cytotoxic activity of ulvan polysaccharides, expressed as survival (%) of each cell line depending on the ulvan polysaccharide concentration (mg mL^{-1}). Each figure represents a cell line: (**a**) immortalized human keratinocytes (HACAT), (**b**) human fibroblasts (1064SK), (**c**) human colorectal carcinoma cell line (HCT-116), (**d**) human myeloid leukemia (U-937), and (**e**) human malignant melanoma (G-361).

After obtaining the IC$_{50}$ values, the selectivity index (SI) was also calculated (Table 2). The SI is the ratio obtained by dividing the IC$_{50}$ value of the healthy cells by that of the cancer cells. The higher the SI, the more effective and safer a drug would theoretically be during in vivo treatment. The selectivity between the healthy and cancer cell lines varied for our compound. The highest selectivity indexes were estimated as 40.9 and 11.5, respectively, for the ulvans used against the HCT-116 cells compared to the HACAT and 1064sk cells.

Table 2. Selectivity index (SI) of *U. rigida* polysaccharides.

	Selectivity Index
HACAT/HCT-116	40.9
1064sk/HCT-116	11.5
HACAT/U-937	1.8
1064sk/U-937	0.5
HACAT/G-361	0.9
1064sk/G-361	0.3

2.3. Zebrafish Exposure to Increasing Concentrations of Ulvan Polysaccharides

Several anatomical characteristics were studied to understand how ulvans affect zebrafish embryogenesis. The frequencies of viability, pericardial edema, and hatching were measured daily in zebrafish embryos exposed to increasing ulvan concentrations. As described in the Section 4, other variables, such as the standard length or head–trunk angle (Figure 4), were calculated after digital images were obtained at 72 hpf. Other less frequent anatomical characteristics, such as body abnormalities or short size, body mobility, abnormal head or yolk, curved body or tail, or depigmentation, were eventually annotated when observed.
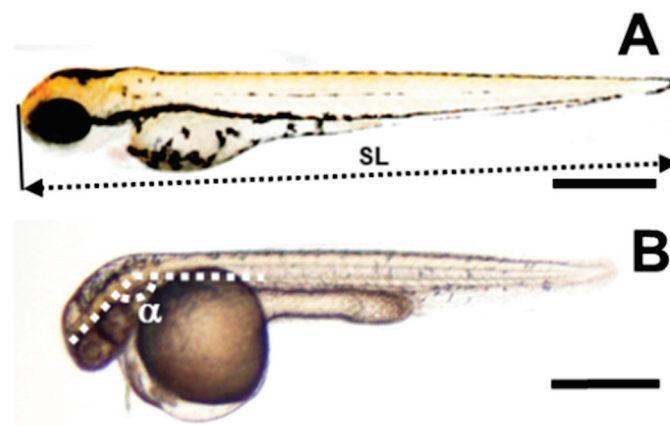
Figure 4. Standard length and head–trunk angle of zebrafish embryos. (**A**) Control untreated zebrafish embryos. The double discontinuous arrow shows the standard length (SL). (**B**) Polysaccharide-treated 72 hpf embryo. α indicates the head–trunk angle as suggested by Kimmel et al. [60]. Bars represent 500 μm.

The increasing ulvan concentrations gradually affected embryo viability. At 48 hpf, the polysaccharides steadily reduced viability (from 100 to 70%) up to about 2.5 mg mL^{-1}, at which point a sharp decline in this index was observed (Figure 5). Following the log-linear regression approach [61], we measured an LC$_{50}$ of 5.127 mg mL^{-1}.

A detailed anatomical description of the 72 hpf embryos exposed to dispersions below the LC$_{50}$ suggests a reduction in the growth rate. To quantify this effect, we measured the standard length and the head–trunk angle, which are two anatomical variables that increase throughout development. The increase in the first variable is gradual over time, whereas the second ranges from 60–70° to 180°. This 180° angle is reached at 72 hpf, and it remains stable through the rest of development [60]. As described in the Section 4, we reproduced data from Kimmel et al. [60] (Figure 6) to obtain four quadratic minimum adjustments that allowed for a linear transformation of these two variables into hours of development (hpf).
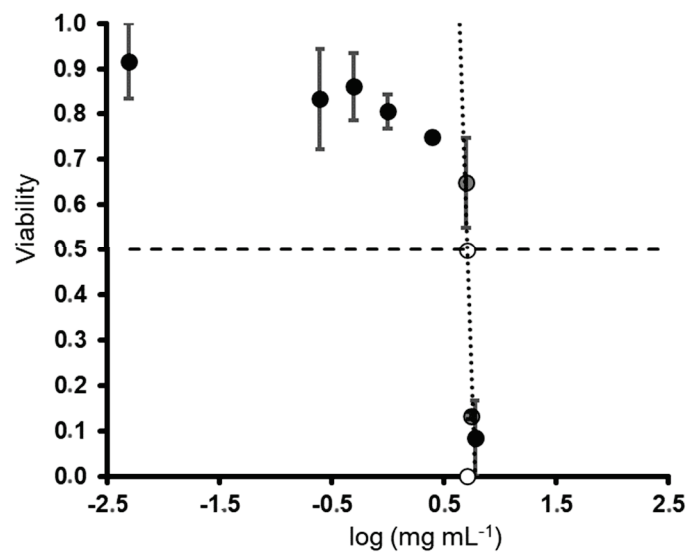
Figure 5. LC_{50} estimation for ulvan polysaccharide treatment of zebrafish 48 hpf embryos. Circles and vertical bars are the means and standard deviations of data from three replicates. Gray, transparent circles are data used to estimate the LC_{50}. The empty circle intersects the regression line and 50 % viability. The white circle is the log (LC_{50}) estimation. Linear adjustment is y = −7.2237x + 5.6279 (R^2 = 0.8357).
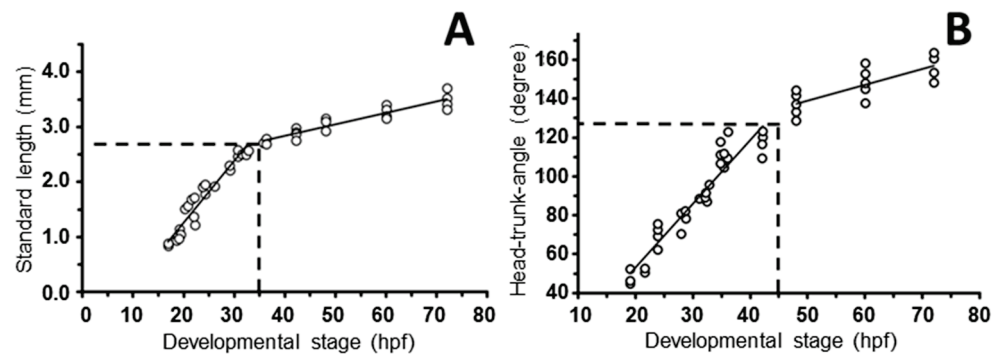

Figure 6. Linear functions used to transform standard lengths and head–trunk angles into hours of post-fertilization development. Graphs show the linear adjustments recovered from approximations to standard length (**A**) and head–trunk angle (**B**) data in Kimmel et al. [60] (Figures 16 and 33, respectively, of Kimmel et al. [60]). Data were obtained using ImageJ 1.50i (nih.gov, accessed on 13 January 2023). The variable transformation functions are (**A**) y = 0.0207x + 2.0153 (R^2 = 0.8716; $p \approx 0.0000$) (greater sizes); y = 0.1124x − 0.9848 (R^2 = 0.931; $p \approx 0.0000$) (lesser sizes); and (**B**) y = 0.8216x + 97.927 (R^2 = 0.6126; $p < 0.00059$) (greater angles); y = 3.2744x − 12.452 (R^2 = 0.9081; $p < 0.000835$) (lesser angles). Discontinuous lines represent the variable transformation limits.

Using this variable transformation method, the stages were estimated from both morphometric variables. The estimated hours post-fertilization showed linear reductions in the concentration of the ulvan polysaccharide dispersions (Figure 7A,B), whereas the embryos exposed to between 0.25 and 1 mg mL^{-1} presented a developmental stage resembling that of the control specimen; the embryos exposed to the highest concentration (5 mg mL^{-1}) showed a significant reduction. The linear reduction slopes obtained for both variables were almost identical (7.3 and 7.4 hpf mL mg^{-1}) (Figures 7A and 7B, respectively), supporting the initial observation of growth delay. Using this method, the dispersion of the data was high (low R^2 values) (Figure 7) when compared with the non-transformed variables (see Figure 6A).
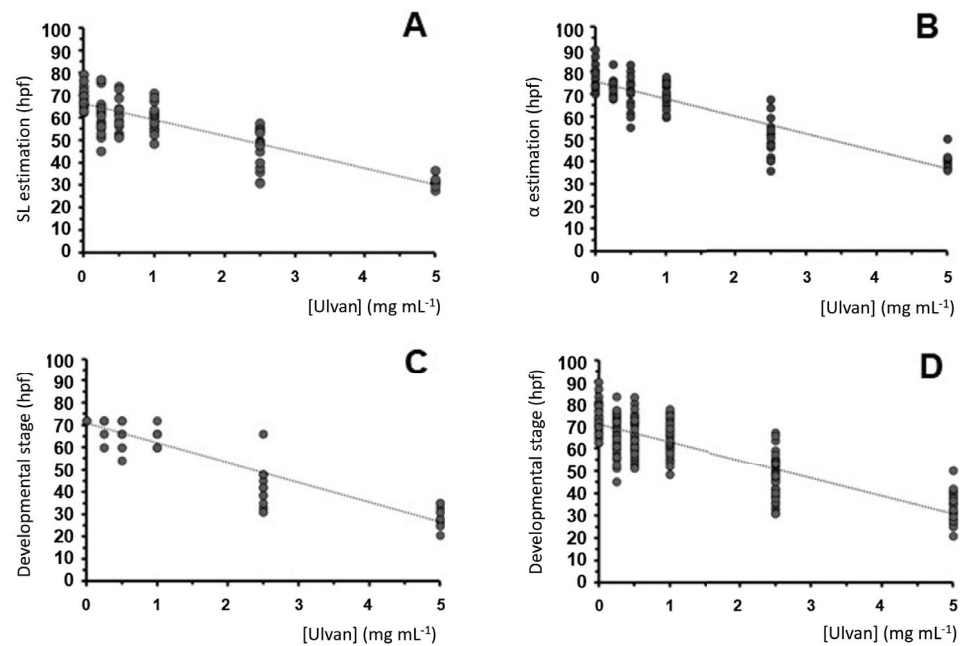
Figure 7. Embryo stage estimation after anatomical variable transformation using data from Kimmel et al. [60] (see Figure 4). (**A–C**) Linear regressions of standard length (**A**), head–trunk α angle (**B**), and anatomical-based estimations (**C**) with respect to the ulvan concentration. (**D**) Linear reduction in the compound stage estimation (**A**+ **B** + **C**) with respect to the ulvan concentration. The linear adjustments are (**A**) y = -7.2x + 66.234 (R^2 = 0.7232; $p \approx 0.0000$), (**B**) y = -7.3294x + 76.026 (R^2 = 0.8003; $p < 0.00015$), (**C**) y = -8.8x + 70.857 (R^2 = 0.8738; $p \approx 0.0000$), and (**D**) y = -7.88x + 71.036 (R^2 = 0.7479; $p < 0.000085$).

Furthermore, a detailed anatomical description of the digital images from each 72 hpf embryo compared to the descriptions provided by Kimmel et al. [60] supported this hypothesis. Several anatomical characteristics (see above) were compared to the data from Kimmel et al. [60] to provide a tentative developmental stage for each embryo. When possible, the vascular pattern was also observed using the *Tg(fli1a:EGFP)y1* transgene to confirm the proposed stage [62]. Almost all the variables supported the occurrence of a growth rate reduction with respect to the ulvan concentration. This anatomy-based estimation also showed a linear decline with regard to the ulvan concentration, having a slightly higher slope of 8.8 hpf mL mg^{-1} (Figure 7C).

To perform a global stage estimation, we calculated the linear variation based on the summary of our three estimations for each embryo (Figure 7D). This global estimation also showed a linear reduction in ulvan concentration with a slope of 7.8 hpf mL mg^{-1} (Figure 7D).

The mean value and standard deviation of each stage estimation are also shown in Table 3. All the experimental conditions differ from those of the control, showing an increasing statistical significance with regard to the ulvan concentration (from $p < 0.05$ * to $p < 0.001$ ***) and proportionally higher standard deviations. All these data support the sub-lethal effects of ulvans at concentrations lower than the LC$_{50}$.

In this study, we further dechorionated the embryos and replicated the experiment at a concentration of 2.5 mg mL^{-1} to rule out the potential involvement of hypoxia caused by chorion pore obliteration resulting from ulvan precipitation. In these replicated experiments, no significant modification was found in the mean delay observed (data not shown).

Table 3. Embryo stage estimation following the anatomical features.

Ulvan (mg mL^{-1})	Head–Trunk Angle (hpf)	Standard Length (hpf)	Developmental Stage (hpf)	Mean Estimation (hpf)
5	40.25 ± 3.55 ***	31.56 ± 2.15 ***	29.90 ± 4.23 ***	33.91 ± 5.56 (13) ***
2.5	49.73 ± 8.94 ***	47.03 ± 8.50 ***	41.64 ± 8.46 ***	46.13 ± 4.12 (16) ***
1	70.10 ± 5.34 ***	59.98 ± 5.56 ***	63.14 ± 3.61 ***	64.41 ± 5.18 (19) ***
0.5	70.62 ± 7.78 **	61.24 ± 6.92 ***	66.80 ± 5.49 **	66.22 ± 4.72 (15) **
0.25	73.06 ± 3.86 **	61.70 ± 8.91 **	69.88 ± 4.21 *	68.21 ± 5.86 (16) **
0	77.61 ± 5.28	69.60 ± 5.02	72.00 ± 0.00	73.07 ± 4.11 (18)

The results are expressed as the mean and standard deviation. $p < 0.05$ (*); $p < 0.01$ (**); $p < 0.001$ (***). Underlined symbols represent non-parametric analysis. N = 97, 99, and 107 for the head–trunk angle, SL, and developmental stage estimations, respectively. The total number of embryos used to calculate the mean estimation are placed in parentheses (total: 97).

Two other toxic effects were frequently observed at sub-lethal concentrations: pericardial edema and chorion lysis (Figure 8). This pericardial edema also augmented in size (Figure 8A,B) along with the increasing ulvan concentration. This effect presented an exponential rather than a linear trend as the ulvan concentration increased (Figure 8C). Larvae with pericardial edemas may also present an apparent increase in yolk sac size. This may be because the yolk is physically displaced by the augmentation of interstitial liquid in the edemas. In our experiments, at concentrations over 2 mg mL^{-1}, a slight amount of precipitate could be found over the plastic well and the yolk sac. At these concentrations, a second effect was also observed. As in cell plasmolysis, extra-chorionic hypertonic ulvan solutions generate chorion shrinkage (Figure 8D). This was not observed at lower concentrations.
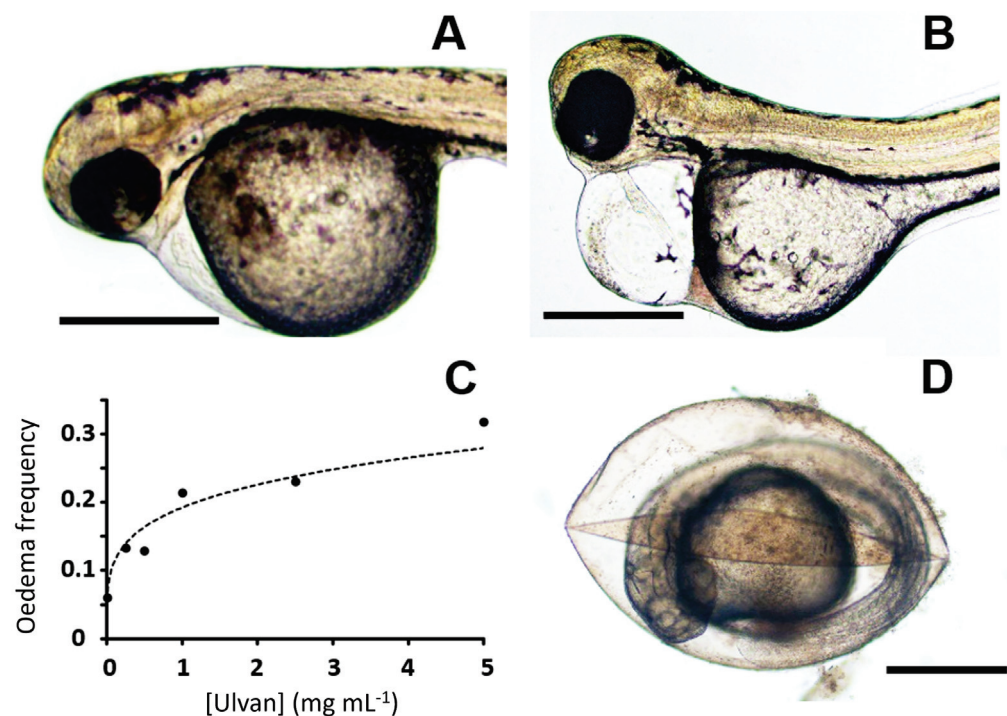
Figure 8. Pericardial edema and chorion lysis increase with the ulvan polysaccharide concentration. Slight (**A**) and significant (**B**) pericardial edemas are seen in zebrafish embryos treated with a 0.25 mg mL^{-1} ulvan concentration. (**C**) Exponential regression of edema frequency versus ulvan polysaccharide concentrations (y = 0.0386x$^{0.2325}$, R^2 = 0.9351). (**D**) Chorion lysis observed at 2.5 mg mL^{-1} ulvan. Bars represent 500 μm.

3. Discussion

Ulvan, the main polysaccharide found on the cell wall of *Ulva* species, is a bioactive compound of great biotechnological interest. Different reviews (see [14,63]) have described the potential of ulvans as an anticancer, immune-modulating, anticoagulant, antiviral,

antihyperlipidemic, and antioxidant molecule. Among the bioactivities mentioned above, the anticancer aspect is always highlighted due to the social impact of the disease and, consequently, the need for therapeutic compounds that act selectively on those cells. In 2018, it was estimated that there were almost 290,000, 1,100,000, and 440,000 new cases of melanoma, colon cancer, and leukemia, respectively, and about 61,000, 555,000, and 310,000 deaths worldwide [64].

Our study provides further evidence of the anticancer effects of ulvan polysaccharides from *U. rigida*. The anticancer activity of ulvan from different sources is highly variable. Ahmed and Ahmed [21] previously showed that the ulvan from *Ulva lactuca* induced antitumor cytotoxic effects against HepG2 (IC$_{50}$ 55.56 µg mL^{-1}) and HCT-116 (IC$_{50}$ 22.65 µg mL^{-1}) human cell lines. Thanh et al. [22] also reported a high cytotoxic effect of ulvan polysaccharides on HepG2, MCF7, and HeLa, obtaining IC$_{50}$ values of 29.67 ± 2.87, 25.09 ± 1.36, and 36.33 ± 3.84 µg mL^{-1}, respectively. In our study, ulvan exhibited cytotoxic effects against the three human cancer cell lines tested. However, only the HCT-116 cells exhibited sufficient sensitivity to this ulvan in terms of its potential as an anticancer treatment, presenting an IC$_{50}$ of 0.1 mg mL^{-1}; however, this was significantly lower than that found by Ahmed and Ahmed [21]. In general, the mechanisms involved in ulvan's anticancer effect are not fully understood. Some preliminary studies indicate that apoptosis may stimulate programmed cell death or reduce DNA replication and cell proliferation [21,22,65,66]. Other scientists have observed that the polysaccharide's structure (the number of monosaccharides, glycosidic linkages, sulfate, carboxyl, and hydroxyl groups) might enhance its contact with tumor cells and boost its anticancer effect [67–69]. This is supported by the FTIR spectra and monosaccharide composition obtained in our results, in which rhamnose, glucuronic acid, and xylose were the most represented (80.60%, 9.14%, and 4.01%, respectively). Furthermore, the tested molecules must present a specific selectivity for cancer cells over healthy cells to be considered a safe cancer treatment compound. This parameter can be stipulated using the selectivity index (SI). According to Weerapreeyakul et al. [70], a promising, safe compound should present an SI > 3. In our study, ulvan exhibited SI values > 3 on the HCT-116 cells compared to the healthy epithelial cells (40.9 for HACAT and 11.5 for 1064sk). Our work supports the polysaccharide's potential as a candidate for use in colon cancer treatment. Unfortunately, this promising effect was not observed in the human myeloid leukemia (U-937) or human malignant melanoma (G-361) cells. It is also worth noting that other authors found only extremely low to moderate cytotoxic activity compared to cancer chemotherapy drugs [71,72]. For example, ulvan from *U. intestinalis* demonstrated no cytotoxic effects on sarcoma 180 tumor cells in vitro at 50–800 µg mL^{-1} but reduced the sarcoma 180 tumor weight by 61–71% in mice dosed with 100–400 mg kg^{-1} [73]. Furthermore, immunological organs (such as the thymus and spleen) were increased in ulvan-treated mice, suggesting that the polysaccharide's anticancer activity stems from its immunomodulatory function. In summary, the anticancer activity of ulvans appears to be mediated through one or more routes, which include enhancing cancer cell apoptosis, decreasing cancer cell growth, and activating the innate immune response. In addition, the affected pathways are altered depending on the ulvan source and/or structure. More research is needed to investigate the structural and chemical components that influence ulvan's ability to reduce the number of cancer cells and to figure out the relationship between them.

To further study the toxicity effects of ulvans in vivo, we conducted a zebrafish embryo toxicity test (ZFET). In general, our data agree with the idea of using zebrafish embryos as an effective system to evaluate the effects of glycans in relatively short procedures. Previous studies [74] suggest a close homology between zebrafish embryogenesis and human carcinogenesis, thus supporting its use as a screening assay to evaluate potential anticancer compounds. In this sense, Rusdi et al. [74] and other studies [25,56] have already evaluated the toxicity of algal and fungal polysaccharides on zebrafish embryos, suggesting either absent [74] or low [25,56,74] toxicity. Nevertheless, the measurement of the LC$_{50}$ of

these polysaccharides has revealed a variable susceptibility of early zebrafish embryos to their presence in the embryo medium.

Although fucoidan from *Fucus vesiculosus* showed no LC_{50}, alginate LC_{50} was measured at 245 µg mL^{-1} after 24 h [74]. A decline in zebrafish embryo survival (from about 75% at 48 hpf to 23% at 72 hpf) was also reported when using 5 mg mL^{-1} of exopolysaccharides from a fungus species, *Ganoderma applanatum*. In contrast, its endopolysaccharides showed a viability decline from about 75% at 72 hpf to 32% at 96 hpf [56]. These results suggest an LC_{50} higher than that found for *F. vesiculosus* alginate at 24 h or ulvans in our study at 48 hpf (5.2 mg mL^{-1}). Moreover, 5 mg mL^{-1} of natural mycelial biomass from *Lignosus rhinoceros* showed a survival rate decline between 72 hpf (65%) and 96 hpf (5%), while 5 mg mL^{-1} of exopolysaccharides showed a 50 % zebrafish mortality rate at 72 hpf [25]. In these cases, fungal exopolysaccharides presented slightly higher LC_{50} values than those found for ulvans, whereas those of endopolysaccharides and mycelial extracts were even higher. These effects mimic the anticancer activity discussed above and further support the case for ulvans as a candidate cancer treatment compound. From this comparison, the ulvans tested in our study seem to be a better option for a potential anticancer product than others from brown algae [74] or fungi [25,56] species, although they are less effective than *Fucus* alginate [74].

A teratogenic effect on zebrafish pigmentation has also been described at lower polysaccharide concentrations, molecularly related to the interference of several tyrosine kinase downstream effectors in carcinogenesis [74,75]. In our study, ulvans between 0.1 and 5 mg mL^{-1} linearly delayed pigmentation and embryonic development at a rate of 7.6 hpf per mg mL^{-1}. Partial hypoxia generated by the obliteration of chorionic pores [76] from ulvan precipitates was initially considered the potential cause of this delay. Our results ruled out this hypothesis because of the delay observed in our experiment on dechorionated embryos.

Recent studies have proposed alternative assays to the ZFET test, such as the zebrafish embryo acute toxicity test (ZET) or the General and Behavioral Embryo Toxicity Assay [28]. In both tests, several phenotypes have been proposed to describe toxicity. The most critical phenotypes in these tests are developmental abnormalities; a short body size; body mobility and position; a slow heartbeat; pericardial, yolk or head edemas; an abnormally sized or darkened head, yolk or liver; a curved body or tail; or pigment abnormalities [28]. Our study associated a short body size, an abnormal head size, and pigment abnormalities with signs of developmental delay, all of which are phenotypes included in the scoring panel of the ZET [28] and ZFET [25] tests. Three different estimations of this effect were evaluated to support our hypothesis: anatomical descriptions, the standard length, and the head–trunk angle. This association is not explicitly included in the ZET and ZFET assays. Parallel to our study, we conducted experiments with five other polysaccharides from algal and fungal species in search of an appropriate positive control [77]. In certain instances, this developmental delay effect has also been observed, suggesting a new toxic phenotype produced by increasing algal and fungal polysaccharide concentrations (Abdala-Díaz and Marí-Beffa, in preparation). Furthermore, the variables used to support the occurrence of this phenomenon always show high dispersion estimates. This suggests a potential variable susceptibility of zebrafish embryos to this type of substance in the culture medium. This new growth delay effect of algal polysaccharides may also be tested over cancer and zebrafish development in xenograft experiments [78]. These experiments are currently underway and will be published elsewhere. In our results, no other teratogenic defects were consistently associated with the ulvan concentration.

Finally, new osmolar and toxicity effects were observed at the highest viable concentrations, such as chorion lysis and pericardial edema. In principle, chorion lysis may be caused by osmolar imbalance and increased water loss. Moreover, in various substances, pericardial edema is a well-established toxicity symptom seen in zebrafish embryos [79]. In our study, we did not test whether zebrafish toxicity is associated with inflammation or any other cell stress process. In principle, the food, feed, fertilizing, and biomedical modulatory effects of ulvan [12,14] could be accompanied by relevant metabolic perturba-

tions that might induce toxicity and affect osmolar imbalance and embryonic growth as the concentration increases from 0.25–1 mg mL^{-1}.

The lowest ulvan concentration in our study, 0.25 mg mL^{-1}, is higher than the 0.05 mg mL^{-1} of *Spirulina maxima* pectins, a concentration within the range of the above-mentioned cytotoxic IC$_{50}$ indexes [21,22], which stimulates larval fin regeneration [58]. Studies on the immunomodulatory effects of *U. rigida* ulvans in model organisms are also in progress to support the beneficial effects of these compounds at concentrations within the colon cancer cytotoxic LC$_{50}$ range (data not shown).

4. Materials and Methods

4.1. Ulvan Preparation

Ulva rigida was cultivated in 500 L aerated semi-circular fiberglass tanks under natural outdoor conditions at the facilities of the Andalusian Institute of Blue Biotechnology and Development (IBYDA) at Malaga University (Málaga, Spain). The algal biomass was harvested weekly, washed gently with abundant natural seawater, and dried at 60 °C for 24 h. Afterwards, the biomass was milled to obtain a fine powder (50 μm) and stored at −20 °C. Ulvan was then extracted from the powdered sample using the ethanol precipitation method according to Béress et al. [80]. The *U. rigida* powder was submerged in 95% ethanol (a biomass-to-ethanol ratio of 1:10) until de-pigmentation was apparent. Subsequently, the de-pigmented biomass was suspended in distilled water and heated at 90 °C for 2 h. The solution was then centrifuged for 15 min at 6000 rpm at room temperature. The supernatant was concentrated to 1/5th of the original volume. Following this, five times the volume of 95% ice-cold ethanol was added to the concentrated solution and stored at 4 °C. The precipitate that formed was collected via centrifugation at 12,000 rpm for 10 min at 4 °C, washed twice with absolute ethanol, and freeze-dried.

4.2. Chemical Composition and Structure of Ulvans

4.2.1. Fourier-Transform Infrared Spectroscopy (FTIR)

The FTIR spectra of the *U. rigida* ulvans were obtained by pressing 13 mm diameter self-supporting pressed discs comprising a mixture of ulvans and KBr (1% *w/w*) with a hydraulic press at a force of 15.0 tcm^{-2} for 2 min. The FTIR spectra were obtained in the 400–4000 cm^{-1} region using a Thermo Nicolet Avatar 360 IR spectrophotometer (Thermo Electron Inc., Franklin, MA, USA), having a resolution of 4 cm^{-1}, with a deuterated triglycine sulfate (DTGS) detector and OmnicTM 7.2 software (bandwidth of 50 cm^{-1} and an enhancement factor of 2.6). Thermo Nicolet OMNIC software was used for baseline correction to smooth the baseline of each spectrum. To compare the sample spectra to those in the spectral collection, the OMNIC correlation algorithm was used.

4.2.2. Gas Chromatography–Mass Spectrometry (GC–MS)

The GC–MS of the ulvans was determined following the methodology described in detail by Parra-Riofrío et al. [81,82]. In brief, GC–MS analyses were carried out using a Trace GC gas chromatograph (Thermo Fisher Scientific, Franklin, MA, USA), a Triplus RSH autosampler (Thermo Fisher Scientific, Franklin, MA, USA), and a DSQ quadrupole mass spectrometer (Thermo Fisher Scientific, Franklin, MA, USA). The identification of monosaccharides in the polysaccharide samples was carried out by comparing the retention time and mass spectra of monosaccharide standards, previously analyzed under identical conditions (glucose, galactose, mannose, arabinose, xylose, rhamnose, ribose, fucose, galacturonic acid, and glucuronic acid). The compounds were identified by comparing the mass spectra with those in the National Institute of Standards and Technology (NIST 2014) library.

4.3. Cytotoxic Effect Assay

Five human cell lines, 1064sk (human fibroblasts; CIC cell bank of CIC of the Universidad de Granada, Spain), HACAT (immortalized human keratinocytes; ATCC, Manassas, VA, USA), U-937 (human leukemia cell line; ATCC, Manassas, VA, USA), G-361 (human

malignant melanoma; ATCC, Manassas, VA, USA), and HCT-116 (colon cancer cell line; ATCC, Manassas, VA, USA), were used for the assays. The cells were cultured in either Dulbecco's Modified Eagle's Medium (DMEM) (Capricorn Scientific, Ebsdorfergrund, Germany, ref. DMEM-HPSTA), for the 1064sk, U-937, and HCT-116 cells, or in RPMI-1640 medium (BioWhittaker, ref. BE12-167F), for the HACAT and G-361 cells, both containing 10% Fetal Bovine Serum (FBS, Biowest, ref. S1810-500), 1% penicillin–streptomycin solution $100\times$ (Capricorn Scientific, ref. PS-B), and 0.5% amphotericin B (Biowest ref. L0009-100). The cells were maintained sub-confluent at 37 °C in humidified air containing 5% CO_2.

The cytotoxic effect on the cell lines mentioned above was measured using an MTT assay. The cells were incubated independently in 96-well plates, containing 1×10^4 cell/well for 1064sk and 6×10^3 cell/well for the other cell lines, with different ulvan concentrations (ranging from 0.009 to 5 mg mL^{-1}) at 37 °C in a humid atmosphere with 5% CO_2 for 72 h. As a control, the same cell lines were used without treatment. The trial was carried out following the method proposed by Abdala-Díaz et al. [83]. The cytotoxicity was calculated, and it is expressed as the inhibition concentration at 50% (IC$_{50}$ values). The analyses were carried out in three independent experiments. In addition, the selectivity index (SI) was calculated as the ratio of dividing the IC$_{50}$ value of the healthy cell lines by that of the cancer cell lines.

4.4. Zebrafish Husbandry and Embryo Collection

The zebrafish (*Danio rerio*) embryos were the offspring of mating AB wild-type and/or *Tg(fli-1: EGFP) y1* adults. The adults were obtained from the breeding stock at the fish facilities belonging to the Centre of Experimentation and Animal Behavior at the University of Málaga, where they were cultured in a 12:12 h light:dark photoperiod following standard procedures [61,62]. The adults were the offspring of fish obtained from the Zebrafish International Resource Centre (ZIRC, Eugene, OR). The eggs were collected after fertilization and then bleached, washed, and incubated at 28 ± 0.1 °C in a Petri dish with an embryo medium. The fish were handled in accordance with notification A/ES/12/I-22 (activity A/ES/12/24) of the National Laws. The Universidad de Málaga Bioethics Commission approved the experiments as part of the grants BIO2014-56092-R and UMA18-FEDERJA-274.

4.5. Zebrafish Embryo Toxicity Assay

The AB wild-type or *Tg(fli-1:EGFP)y1* embryos were placed in 96-well plates (1 fish per well using 300 μL embryo medium) at 4 h post-fertilization (4 hpf) [84]. Each replicate comprised 8 embryos immersed in the embryo medium with a specific polysaccharide concentration (from 0.25 to 6.5 mg mL^{-1}), comprising 56 embryos per experiment and including both negative and positive controls. The embryos were immersed for three days following the ZFET procedure [25] without further modifications. The concentrations were obtained by diluting 5 or 10 mg mL^{-1} stock solutions. The stock solutions were prepared from polysaccharide lyophilized powder and stored at 4 °C after preparation. The embryo medium served as the negative control [84]. Polysaccharides from the macroalga *Sarcopeltis skottsbergii* and the fungus *Calvatia* (in preparation) were used as positive controls in parallel experiments. Both polysaccharides presented a relevant LC$_{50}$ and a significant induction of growth delay at lower concentrations. LPS was discarded as a positive control due to its well-known inflammatory effects [77]. Each experiment was run at least three times with a minimum of 24 embryos for each experimental condition. Basic statistics were obtained from the data described below. After the experiments, the live embryos were euthanized using MS-222 (0.2 mg mL^{-1}) over-anesthetization and stored as organic waste following the University of Málaga procedures.

4.6. Phenotypic Analysis

In the ZFET, several phenotypes were annotated to support the toxic effects of the reagents tested. The following were used in this test: embryo viability, hatching, and heart rate [25]; tail malformations; or the absence of fins, the gut, or melanophores [56].

Other phenotypes, such as the standard length, head–trunk angle [60], or pericardial edema, were estimated for each living specimen at the end of the experiment. Additional characteristics were used for an anatomical comparison with a standard embryological atlas [60]; these were the shape of the eyes, cochlea, and pec and tail fins; the form and size of the yolk sac, the notochord, and the craniofacial skeleton; and the pigment distribution (see Table 3 for the number of measured embryos). The analysis was performed under a magnifying microscope (Nikon SMZ-445 model) or using digital images obtained with a Nikon Microphot-FX Fluorescence Research Microscope with a Nikon DS-L1 digital camera. The lethal concentration that kills 50% of the sample (LC_{50}) was estimated from mortality/viability data following a linear regression test [61]. To estimate the growth delay, the actual age of the embryos was compared to three different stage estimations made from embryo anatomy, the standard length, and the head–trunk angle. The last two variables were transformed into a potential developmental stage using data from Kimmel et al. [60] (see the Results Section 2.2). The quantitative variables were measured from digital images using the ImageJ 1.50i settings (National Institutes of Health, Bethesda, MD, USA) and verified in a single-blind evaluation.

4.7. Statistical Analysis

Statistical differences between the means were calculated using the Student *t*-test. Linear regressions were calculated using a least squares analysis. The statistical analyses were performed using the Statistical Package for the Social Sciences software (IBM, SPSS-version 25), Statgraphics software (Statgraphics Technologies, Inc., The Plains, VA, USA), or the Excel program (Microsoft Office, Windows 11, Redmond, WA, USA). Significant differences were noted when $p < 0.05$ (*), $p < 0.01$ (**), and $p < 0.001$ (***).

5. Conclusions

Our in vitro study supports the potential use of polysaccharides extracted from *U. rigida* as candidates for treating human colon cancer. This is further supported by our zebrafish toxicity and phenotypic assay. These in vivo tests revealed the side effects of these molecules on zebrafish development, such as developmental abnormalities and delay. Perturbations of cancer or development-associated signaling pathways may be underlying these phenocopies as previously suggested by other authors. Ulvans may be a promising, safe compound at concentrations below 0.1–0.2 mg mL^{-1}.

References

1. Siegel, R.L.; Miller, K.D.; Fuchs, H.E.; Jemal, A. Cancer Statistics. *CA Cancer J. Clin.* **2021**, *71*, 7–33. [CrossRef] [PubMed]
2. Abotaleb, M.; Kubatka, P.; Caprnda, M.; Varghese, E.; Zolakova, B.; Zubor, P.; Opatrilova, R.; Kruzliak, P.; Stefanicka, P.; Büsselberg, D. Chemotherapeutic agents for the treatment of metastatic breast cancer: An update. *Biomed. Pharmacother.* **2018**, *101*, 458–477. [CrossRef] [PubMed]
3. Schirrmacher, V. From chemotherapy to biological therapy: A review of novel concepts to reduce the side effects of systemic cancer treatment (Review). *Int. J. Oncol.* **2019**, *54*, 407–419. [CrossRef] [PubMed]
4. Zeng, X.; Liu, C.; Yao, J.; Wan, H.; Wan, G.; Li, Y.; Chen, N. Breast cancer stem cells, heterogeneity, targeting therapies and therapeutic implications. *Pharmacol. Res.* **2021**, *163*, 105320. [CrossRef]
5. Zhong, L.; Li, Y.; Xiong, L.; Wang, W.; Wu, M.; Yuan, T.; Yang, W.; Tian, C.; Miao, Z.; Wang, T.; et al. Small molecules in targeted cancer therapy: Advances, challenges, and future perspectives. *Signal Transduct. Target. Ther.* **2021**, *6*, 201. [CrossRef]
6. Si, W.; Shen, J.; Zheng, H.; Fan, W. The role and mechanisms of action of microRNAs in cancer drug resistance. *Clin. Epigenet.* **2019**, *11*, 25. [CrossRef]
7. Craig, M.; Jenner, A.L.; Namgung, B.; Lee, L.P.; Goldman, A. Engineering in Medicine to Address the Challenge of Cancer Drug Resistance: From Micro-and Nanotechnologies to Computational and Mathematical Modeling. *Chem. Rev.* **2021**, *121*, 3352–3389. [CrossRef]
8. Gutiérrez-Rodríguez, A.G.; Juárez-Portilla, C.; Olivares-Bañuelos, T.; Zepeda, R.C. Anticancer activity of seaweeds. *Drug Discov. Today* **2018**, *23*, 434–447. [CrossRef]
9. Costa, M.; Cardoso, C.; Afonso, C.; Bandarra, N.M.; Prates, J.A.M. Current knowledge and future perspectives of the use of seaweeds for livestock production and meat quality: A systematic review. *J. Anim. Physiol. Anim. Nutr.* **2021**, *105*, 1075–1102. [CrossRef]
10. Makkar, H.P.S.; Tran, G.; Heuzé, V.; Giger-Reverdin, S.; Lessire, M.; Lebas, F.; Ankers, P. Seaweeds for livestock diets: A review. *Anim. Feed Sci. Technol.* **2016**, *212*, 1–17. [CrossRef]
11. Alves, C.; Silva, J.; Pinteus, S.; Gaspar, H.; Alpoim, M.C.; Botana, L.M.; Pedrosa, R. From Marine Origin to Therapeutics: The Antitumor Potential of Marine Algae-Derived Compounds. *Front. Pharmacol.* **2018**, *9*, 777. [CrossRef]
12. Mantri, V.A.; Kazi, M.A.; Balar, N.B.; Gupta, V.; Gajaria, T. Concise review of green algal genus *Ulva* Linnaeus. *J. Appl. Phycol.* **2020**, *32*, 2725–2741. [CrossRef]
13. Mata, L.; Magnusson, M.; Paul, N.A.; de Nys, R. The intensive land-based production of the green seaweeds *Derbesia tenuissima* and *Ulva ohnoi*: Biomass and bioproducts. *J. Appl. Phycol.* **2016**, *28*, 365–375. [CrossRef]
14. Kidgell, J.T.; Magnusson, M.; de Nys, R.; Glasson, C.R.K. Ulvan: A systematic review of extraction, composition and function. *Algal Res.* **2019**, *39*, 101422. [CrossRef]
15. Tran, T.T.V.; Huy, B.T.; Truong, H.B.; Bui, M.L.; Thanh, T.T.T.; Dao, D.Q. Structure analysis of Sulphated polysaccharides extracted from green seaweed *Ulva lactuca*: Experimental and density functional theory studies. *Mon. Chem.* **2018**, *149*, 197–205. [CrossRef]
16. Robic, A.; Sassi, J.F.; Dion, P.; Lerat, Y.; Lahaye, M. Seasonal variability of physicochemical and rheological properties of ulvan in two *Ulva* species (Chlorophyta) from the Brittany coast. *J. Phycol.* **2009**, *45*, 962–973. [CrossRef] [PubMed]
17. Venkatesan, J.; Lowe, B.; Anil, S.; Manivasagan, P.; Kheraif, A.A.A.; Kang, K.H.; Kim, S.K. Seaweed polysaccharides and their potential biomedical applications. *Starch—Stärke* **2015**, *67*, 381–390. [CrossRef]
18. Cunha, L.; Grenha, A. Sulfated Seaweed Polysaccharides as Multifunctional Materials in Drug Delivery Applications. *Mar. Drug.* **2016**, *14*, 42. [CrossRef]
19. Tanna, B.; Mishra, A. Nutraceutical Potential of Seaweed Polysaccharides: Structure, Bioactivity, Safety, and Toxicity. *Compr. Rev. Food Sci. Food Saf.* **2019**, *18*, 817–831. [CrossRef]
20. Tziveleka, L.A.; Ioannou, E.; Roussis, V. Ulvan, a bioactive marine sulphated polysaccharide as a key constituent of hybrid biomaterials: A review. *Carbohydr. Polym.* **2019**, *218*, 355–370. [CrossRef]
21. Ahmed, O.M.; Ahmed, R.R. Anti-Proliferative and Apoptotic Efficacies of Ulvan Polysaccharides against Different Types of Carcinoma Cells *In Vitro* and *In Vivo*. J. Cancer Sci. Ther. **2014**, *6*, 202–208. [CrossRef]

22. Thanh, T.T.; Quach, T.M.; Nguyen, T.N.; Vu Luong, D.; Bui, M.L.; Tran, T.T. Structure and cytotoxic activity of ulvan extracted from green seaweed *Ulva lactuca*. *Int. J. Biol. Macromol.* **2016**, *93 Pt A*, 695–702. [CrossRef]

23. Xie, C.; Lu, X.; Han, L.; Xu, J.; Wang, Z.; Jiang, L.; Wang, K.; Zhang, H.; Ren, F.; Tang, Y. Biomimetic Mineralized Hierarchical Graphene Oxide/Chitosan Scaffolds with Adsorbability for Immobilization of Nanoparticles for Biomedical Applications. *ACS Appl. Mater. Interfaces* **2016**, *8*, 1707–1717. [CrossRef] [PubMed]

24. Hu, Z.; Hong, P.; Cheng, Y.; Liao, M.; Li, S. Polysaccharides from *Enteromorpha tubulosa*: Optimization of extraction and cytotoxicity. *J. Food Process. Preserv.* **2018**, *42*, e13373. [CrossRef]

25. Usuldin, S.R.A.; Wan-Mohtar, W.A.A.Q.I.; Ilham, Z.; Jamaludin, A.A.; Abdullah, N.R.; Rowan, N. *In vivo* toxicity of bioreactor-grown biomass and exopolysaccharides from Malaysian tiger milk mushroom mycelium for potential future health applications. *Sci. Rep.* **2021**, *11*, 23079. [CrossRef] [PubMed]

26. Bai, H.; Kong, W.W.; Shao, C.L.; Li, Y.; Liu, Y.Z.; Liu, M.; Guan, F.F.; Wang, C.Y. Zebrafish Embryo Toxicity Microscale Model for Ichthyotoxicity Evaluation of Marine Natural Products. *Mar. Biotechnol.* **2016**, *18*, 264–270. [CrossRef] [PubMed]

27. Cassar, S.; Adatto, I.; Freeman, J.L.; Gamse, J.T.; Iturria, I.; Lawrence, C.; Muriana, A.; Peterson, R.T.; Van Cruchten, S.; Zon, L.I. Use of Zebrafish in Drug Discovery Toxicology. *Chem. Res. Toxicol.* **2020**, *33*, 95–118. [CrossRef]

28. Achenbach, J.C.; Leggiadro, C.; Sperker, S.A.; Woodland, C.; Ellis, L.D. Comparison of the Zebrafish Embryo Toxicity Assay and the General and Behavioral Embryo Toxicity Assay as New Approach Methods for Chemical Screening. *Toxics* **2020**, *8*, 126. [CrossRef]

29. Dooley, K.; Zon, L.I. Zebrafish: A model system for the study of human disease. *Curr. Opin. Genet. Dev.* **2000**, *10*, 252–256. [CrossRef]

30. Kari, G.; Rodeck, U.; Dicker, A.P. Zebrafish: An emerging model system for human disease and drug discovery. *Clin. Pharmacol. Ther.* **2007**, *82*, 70–80. [CrossRef]

31. Marí-Beffa, M.; Mesa-Román, A.B.; Duran, I. Zebrafish Models for Human Skeletal Disorders. *Front. Genet.* **2021**, *12*, 675331. [CrossRef] [PubMed]

32. Tran, T.C.; Sneed, B.; Haider, J.; Blavo, D.; White, A.; Aiyejorun, T.; Baranowski, T.C.; Rubinstein, A.L.; Doan, T.N.; Dingledine, R.; et al. Automated, quantitative screening assay for antiangiogenic compounds using transgenic zebrafish. *Cancer Res.* **2007**, *67*, 11386–11392. [CrossRef] [PubMed]

33. Tobia, C.; De Sena, G.; Presta, M. Zebrafish embryo, a tool to study tumor angiogenesis. *Int. J. Dev. Biol.* **2011**, *55*, 505–509. [CrossRef]

34. Wilkinson, R.N.; van Eeden, F.J. The zebrafish as a model of vascular development and disease. *Prog. Mol. Biol. Transl. Sci.* **2014**, *124*, 93–122. [CrossRef]

35. García-Caballero, M.; Quesada, A.R.; Medina, M.A.; Marí-Beffa, M. Fishing anti(lymph)angiogenic drugs with zebrafish. *Drug Discov. Today* **2018**, *23*, 366–374. [CrossRef] [PubMed]

36. Wang, S.H.; Chen, C.C.; Lee, C.H.; Chen, X.A.; Chang, T.Y.; Cheng, Y.C.; Young, J.J.; Lu, J.J. Fungicidal and anti-biofilm activities of trimethylchitosan-stabilized silver nanoparticles against *Candida* species in zebrafish embryos. *Int. J. Biol. Macromol.* **2020**, *143*, 724–731. [CrossRef]

37. Kang, M.C.; Kim, S.Y.; Kim, Y.T.; Kim, E.A.; Lee, S.H.; Ko, S.C.; Wijesinghe, W.A.; Samarakoon, K.W.; Kim, Y.S.; Cho, J.H.; et al. *In vitro* and *in vivo* antioxidant activities of polysaccharide purified from aloe vera (*Aloe barbadensis*) gel. *Carbohydr. Polym.* **2014**, *99*, 365–371. [CrossRef] [PubMed]

38. Cai, Z.N.; Li, W.; Mehmood, S.; Pan, W.J.; Wang, Y.; Meng, F.J.; Wang, X.F.; Lu, Y.M.; Chen, Y. Structural characterization, in vitro and in vivo antioxidant activities of a heteropolysaccharide from the fruiting bodies of *Morchella esculenta*. *Carbohydr. Polym.* **2018**, *195*, 29–38. [CrossRef]

39. Raguraman, V.; Abraham, L., S.; Jyotsna, J.; Palaniappan, S.; Gopal, S.; Thirugnanasambandam, R.; Kirubagaran, R. Sulfated polysaccharide from *Sargassum tenerrimum* attenuates oxidative stress induced reactive oxygen species production in *in vitro* and in zebrafish model. *Carbohydr. Polym.* **2019**, *203*, 441–449. [CrossRef]

40. Wang, W.; Liu, J. Efficient extraction, antioxidant activities and anti-inflammation of polysaccharides from *Notopterygium franchetii* Boiss. *Carbohydr. Polym.* **2020**, *248*, 116783. [CrossRef] [PubMed]

41. Yang, Y.; Qiu, Z.; Li, L.; Vidyarthi, S.K.; Zheng, Z.; Zhang, R. Structural characterization and antioxidant activities of one neutral polysaccharide and three acid polysaccharides from *Ziziphus jujuba* cv. Hamidazao: A comparison. *Carbohydr. Polym.* **2021**, *261*, 117879. [CrossRef]

42. Iman, V.; Mohan, S.; Abdelwahab, S.I.; Karimian, H.; Nordin, N.; Fadaeinasab, M.; Noordin, M.I.; Noor, S.M. Anticancer and anti-inflammatory activities of girinimbine isolated from *Murraya koenigii*. *Drug Des. Dev. Ther.* **2016**, *11*, 103–121. [CrossRef] [PubMed]

43. Fernando, I.P.S.; Sanjeewa, K.K.A.; Samarakoon, K.W.; Lee, W.W.; Kim, H.S.; Kang, N.; Ranasinghe, P.; Lee, H.S.; Jeon, Y.J. A fucoidan fraction purified from *Chnoospora minima*; a potential inhibitor of LPS-induced inflammatory responses. *Int. J. Biol. Macromol.* **2017**, *104 Pt A*, 1185–1193. [CrossRef]

44. Jayawardena, T.U.; Fernando, I.P.S.; Lee, W.W.; Sanjeewa, K.K.A.; Kim, H.S.; Lee, D.S.; Jeon, Y.J. Isolation and purification of fucoidan fraction in *Turbinaria ornata* from the Maldives; Inflammation inhibitory potential under LPS stimulated conditions in in-vitro and in-vivo models. *Int. J. Biol. Macromol.* **2019**, *131*, 614–623. [CrossRef] [PubMed]

45. Wang, S.; Ni, L.; Fu, X.; Duan, D.; Xu, J.; Gao, X. A Sulfated Polysaccharide from Saccharina japonica Suppresses LPS-Induced Inflammation Both in a Macrophage Cell Model via Blocking MAPK/NF-κB Signal Pathways *In Vitro* and a Zebrafish Model of Embryos and Larvae *In Vivo*. *Mar. Drugs* **2020**, *18*, 593. [CrossRef] [PubMed]

46. Siddhu, N.S.S.; Guru, A.; Satish Kumar, R.C.; Almutairi, B.O.; Almutairi, M.H.; Juliet, A.; Vijayakumar, T.M.; Arockiaraj, J. Pro-inflammatory cytokine molecules from *Boswellia serrate* suppresses lipopolysaccharides induced inflammation demonstrated in an *in-vivo* zebrafish larval model. *Mol. Biol. Rep.* **2022**, *49*, 7425–7435. [CrossRef]

47. Watzke, J.; Schirmer, K.; Scholz, S. Bacterial lipopolysaccharides induce genes involved in the innate immune response in embryos of the zebrafish (*Danio rerio*). *Fish Shellfish Immunol.* **2007**, *23*, 901–905. [CrossRef]

48. Shi, Z.; An, L.; Zhang, S.; Li, Z.; Li, Y.; Cui, J.; Zhang, J.; Jin, D.Q.; Tuerhong, M.; Abudukeremu, M.; et al. A heteropolysaccharide purified from leaves of *Ilex latifolia* displaying immunomodulatory activity *in vitro* and *in vivo*. *Carbohydr. Polym.* **2020**, *245*, 116469. [CrossRef]

49. Rajapaksha, D.C.; Edirisinghe, S.L.; Nikapitiya, C.; Dananjaya, S.; Kwun, H.J.; Kim, C.H.; Oh, C.; Kang, D.H.; De Zoysa, M. *Spirulina maxima* Derived Pectin Nanoparticles Enhance the Immunomodulation, Stress Tolerance, and Wound Healing in Zebrafish. *Mar. Drugs* **2020**, *18*, 556. [CrossRef]

50. Zhang, S.; An, L.; Li, Z.; Wang, H.; Shi, L.; Zhang, J.; Li, Y.; Jin, D.Q.; Tuerhong, M.; Ohizumi, Y.; et al. An active heteropolysaccharide from the rinds of *Garcinia mangostana* Linn.: Structural characterization and immunomodulation activity evaluation. *Carbohydr. Polym.* **2020**, *235*, 115929. [CrossRef]

51. Eid, J.I.; Al-Tuwaijri, M.M.; Mohanty, S.; Das, B. Chaga mushroom (*Inonotus obliquus*) polysaccharides exhibit genoprotective effects in UVB-exposed embryonic zebrafish (*Danio rerio*) through coordinated expression of DNA repair genes. *Heliyon* **2021**, *7*, e06003. [CrossRef] [PubMed]

52. Xiong, G.; Deng, Y.; Cao, Z.; Liao, X.; Zhang, J.; Lu, H. The hepatoprotective effects of *Salvia plebeia* R. Br. extract in zebrafish (*Danio rerio*). *Fish Shellfish Immunol.* **2019**, *95*, 399–410. [CrossRef]

53. Zhang, S.; Song, Z.; Shi, L.; Zhou, L.; Zhang, J.; Cui, J.; Li, Y.; Jin, D.Q.; Ohizumi, Y.; Xu, J.; et al. A dandelion polysaccharide and its selenium nanoparticles: Structure features and evaluation of antitumor activity in zebrafish models. *Carbohydr. Polym.* **2021**, *270*, 118365. [CrossRef] [PubMed]

54. Hu, Y.L.; Qi, W.; Han, F.; Shao, J.Z.; Gao, J.Q. Toxicity evaluation of biodegradable chitosan nanoparticles using a zebrafish embryo model. *Int. J. Nanomed.* **2011**, *6*, 3351–3359. [CrossRef]

55. Sanjeewa, K.K.A.; Fernando, I.P.S.; Kim, S.Y.; Kim, H.S.; Ahn, G.; Jee, Y.; Jeon, Y.J. In vitro and in vivo anti-inflammatory activities of high molecular weight sulfated polysaccharide; containing fucose separated from Sargassum horneri: Short communication. *Int. J. Biol. Macromol.* **2018**, *107 Pt A*, 803–807. [CrossRef]

56. Wan-Mohtar, W.A.A.Q.I.; Ilham, Z.; Jamaludin, A.A.; Rowan, N. Use of Zebrafish Embryo Assay to Evaluate Toxicity and Safety of Bioreactor-Grown Exopolysaccharides and Endopolysaccharides from European *Ganoderma applanatum* Mycelium for Future Aquaculture Applications. *Int. J. Mol. Sci.* **2021**, *22*, 1675. [CrossRef]

57. Vijayakumar, S.; Chen, J.; Kalaiselvi, V.; Tungare, K.; Bhori, M.; González-Sánchez, Z.I.; Durán-Lara, E.F. Marine polysaccharide laminarin embedded ZnO nanoparticles and their based chitosan capped ZnO nanocomposites: Synthesis, characterization and *in vitro* and *in vivo* toxicity assessment. *Environ. Res.* **2022**, *213*, 113655. [CrossRef]

58. Edirisinghe, S.L.; Rajapaksha, D.C.; Nikapitiya, C.; Oh, C.; Lee, K.A.; Kang, D.H.; De Zoysa, M. *Spirulina maxima* derived marine pectin promotes the *in vitro* and *in vivo* regeneration and wound healing in zebrafish. *Fish Shellfish Immunol.* **2020**, *107 Pt A*, 414–425. [CrossRef]

59. Yaich, H.; Amira, A.B.; Abbes, F.; Bouaziz, M.; Besbes, S.; Richel, A.; Blecker, C.; Attia, H.; Garna, H. Effect of extraction procedures on structural, thermal and antioxidant properties of ulvan from *Ulva lactuca* collected in Monastir coast. *Int. J. Biol. Macromol.* **2017**, *105*, 1430–1439. [CrossRef]

60. Kimmel, C.B.; Ballard, W.W.; Kimmel, S.R.; Ullmann, B.; Schilling, T.F. Stages of embryonic development of the zebrafish. *Dev. Dyn.* **1995**, *203*, 253–310. [CrossRef]

61. Ocaña, M.C.; Martínez-Poveda, B.; Marí-Beffa, M.; Quesada, A.R.; Medina, M.A. Fasentin diminishes endothelial cell proliferation, differentiation and invasion in a glucose metabolism-independent manner. *Sci. Rep.* **2020**, *10*, 6132. [CrossRef] [PubMed]

62. Isogai, S.; Horiguchi, M.; Weinstein, B.M. The vascular anatomy of the developing zebrafish: An atlas of embryonic and early larval development. *Dev. Biol.* **2001**, *230*, 278–301. [CrossRef] [PubMed]

63. Priyanka, K.R.; Rajaram, R.; Sivakumar, S.R. A critical review on pharmacological properties of marine macroalgae. *Biomass Convers. Biorefinery* **2022**, *1*, 1–25. [CrossRef]

64. Bray, F.; Ferlay, J.; Soerjomataram, I.; Siegel, R.L.; Torre, L.A.; Jemal, A. Global cancer statistics 2018: GLOBOCAN estimates of incidence and mortality worldwide for 36 cancers in 185 countries. *CA Cancer J. Clin.* **2018**, *68*, 394–424. [CrossRef] [PubMed]

65. Abd-Ellatef, G.F.; Ahmed, O.M.; Abdel-Reheim, E.S.; Abdel-Hamid, A.Z. *Ulva lactuca* polysaccharides prevent Wistar rat breast carcinogenesis through the augmentation of apoptosis, enhancement of antioxidant defense system, and suppression of inflammation. *Breast Cancer (Dove Med. Press)* **2017**, *9*, 67–83. [CrossRef] [PubMed]

66. Hussein, U.K.; Mahmoud, H.M.; Farrag, A.G.; Bishayee, A. Chemoprevention of Diethylnitrosamine-Initiated and Phenobarbital-Promoted Hepatocarcinogenesis in Rats by Sulfated Polysaccharides and Aqueous Extract of *Ulva lactuca*. *Integr. Cancer Ther.* **2015**, *14*, 525–545. [CrossRef] [PubMed]

67. Majee, S.B.; Avlani, D.; Biswas, G.R. Pharmacological, pharmaceutical, cosmetic and diagnostic applications of sulphated polysaccharides from marine algae and bacteria. *Afr. J. Pharm. Pharmacol.* **2017**, *11*, 68–77. [CrossRef]

68. Liao, D.-w.; Cheng, C.; Liu, J.-p.; Zhao, L.-y.; Huang, D.-c.; Chen, G.-t. Characterization and antitumor activities of polysaccharides obtained from ginger (*Zingiber officinale*) by different extraction methods. *Int. J. Biol. Macromol.* **2020**, *152*, 894–903. [CrossRef]

69. Miao, J.; Regenstein, J.M.; Qiu, J.; Zhang, J.; Zhang, X.; Li, H.; Zhang, H.; Wang, Z. Isolation, structural characterization and bioactivities of polysaccharides and its derivatives from Auricularia-A review. *Int. J. Biol. Macromol.* **2020**, *150*, 102–113. [CrossRef]

70. Weerapreeyakul, N.; Nonpunya, A.; Barusrux, S.; Thitimetharoch, T.; Sripanidkulchai, B. Evaluation of the anticancer potential of six herbs against a hepatoma cell line. *Chin. Med.* **2012**, *7*, 15. [CrossRef]

71. Shao, P.; Chen, X.; Sun, P. In vitro antioxidant and antitumor activities of different sulfated polysaccharides isolated from three algae. *Int. J. Biol. Macromol.* **2013**, *62*, 155–161. [CrossRef] [PubMed]

72. Matloub, A.A.; Aglan, H.A.; Mohamed El Souda, S.S.; Aboutabl, M.E.; Maghraby, A.S.; Ahmed, H.H. Influence of bioactive sulfated polysaccharide-protein complexes on hepatocarcinogenesis, angiogenesis and immunomodulatory activities. *Asian Pac. J. Trop. Med.* **2016**, *9*, 1200–1211. [CrossRef] [PubMed]

73. Jiao, L.; Li, X.; Li, T.; Jiang, P.; Zhang, L.; Wu, M.; Zhang, L. Characterization and antitumor activity of alkali-extracted polysaccharide from *Enteromorpha intestinalis*. *Int. Immunopharmacol.* **2009**, *9*, 324–329. [CrossRef] [PubMed]

74. Rusdi, N.A.; Ku, C.S.; Yu, K.-X.; Lau, B.F.; Chung, L.Y.; Kiew, L.V. Assessment of Potential Anticancer Activity of Brown Seaweed Compounds Using Zebrafish Phenotypic Assay. *Nat. Prod. Commun.* **2019**, *14*, 1–5. [CrossRef]

75. Colanesi, S.; Taylor, K.L.; Temperley, N.D.; Lundegaard, P.R.; Liu, D.; North, T.E.; Ishizaki, H.; Kelsh, R.N.; Patton, E.E. Small molecule screening identifies targetable zebrafish pigmentation pathways. *Pigment Cell Melanoma Res.* **2012**, *25*, 131–143. [CrossRef]

76. Duan, Z.; Duan, X.; Zhao, S.; Wang, X.; Wang, J.; Liu, Y.; Peng, Y.; Gong, Z.; Wang, L. Barrier function of zebrafish embryonic chorions against microplastics and nanoplastics and its impact on embryo development. *J. Hazard. Mater.* **2020**, *395*, 122621. [CrossRef]

77. Ko, E.Y.; Heo, S.J.; Cho, S.H.; Lee, W.; Kim, S.Y.; Yang, H.W.; Ahn, G.; Cha, S.H.; Kwon, S.H.; Jeong, M.S.; et al. 3 Bromo 5 (ethoxymethyl) 1,2 benzenediol inhibits LPS-induced pro-inflammatory responses by preventing ROS production and downregulating NF-κB in vitro and in a zebrafish model. *Int. Immunopharmacol.* **2019**, *67*, 98–105. [CrossRef]

78. Brown, H.K.; Schiavone, K.; Tazzyman, S.; Heymann, D.; Chico, T.J.A. Zebrafish xenograft models of cancer and metastasis for drug discovery. *Expert Opin Drug Discov.* **2017**, *12*, 379–389. [CrossRef]

79. Truong, L.; Tanguay, R.L. Evaluation of Embryotoxicity Using the Zebrafish Model. *Methods Mol. Biol.* **2017**, *1641*, 325–333. [CrossRef]

80. Béress, A.; Wassermann, O.; Tahhan, S.; Bruhn, T.; Béress, L.; Kraiselburd, E.N.; Gonzalez, L.V.; de Motta, G.E.; Chavez, P.I. A new procedure for the isolation of anti-HIV compounds (polysaccharides and polyphenols) from the marine alga *Fucus vesiculosus*. *J. Nat. Prod.* **1993**, *56*, 478–488. [CrossRef]

81. Parra-Riofrío, G.; García-Márquez, J.; Casas-Arrojo, V.; Uribe-Tapia, E.; Abdala-Díaz, R.T. Antioxidant and Cytotoxic Effects on Tumor Cells of Exopolysaccharides from *Tetraselmis suecica* (Kylin) Butcher Grown Under Autotrophic and Heterotrophic Conditions. *Mar. Drugs* **2020**, *18*, 534. [CrossRef] [PubMed]

82. Parra-Riofrío, G.; Casas-Arrojo, V.; Pino-Selles, R.; García-Márquez, J.; Abdala-Díaz, R.T.; Uribe-Tapia, E. Adaptation of autotrophic to heterotrophic culture of *Porphyridium purpureum* (Bory) K.M. Drew & R.Ross: Characterization of biomass and production of exopolysaccharides. *J. Appl. Phycol.* **2021**, *33*, 3603–3615. [CrossRef]

83. Abdala Díaz, R.T.; Casas Arrojo, V.; Arrojo Agudo, M.A.; Cárdenas, C.; Dobretsov, S.; Figueroa, F.L. Immunomodulatory and Antioxidant Activities of Sulfated Polysaccharides from *Laminaria ochroleuca*, *Porphyra umbilicalis*, and *Gelidium corneum*. *Mar. Biotechnol.* **2019**, *21*, 577–587. [CrossRef] [PubMed]

84. Jin, J.; Nguyen, T.T.H.; Kim, C.; Kim, D. Antimelanogenesis Effects of Fungal Exopolysaccharides Prepared from Submerged Culture of *Fomitopsis castanea* Mycelia. *J. Microbiol. Biotechnol.* **2019**, *29*, 1204–1211. [CrossRef] [PubMed]

MDPI